CODEN: JASMAN 4966

THE JOURNAL of the Acoustical Society of America

Vol. 104, No. 2, Pt. 1 August 1998

MEETING PROGRAM SUMMARY **NORFOLK MEETING** **12–16 OCTOBER 1998**
Norfolk, Virginia
(see pp. 649–650)

(Continued)

CONTENTS—*Continued from preceding page*

(Continued)

CONTENTS—*Continued from preceding page*

STRUCTURAL ACOUSTICS AND VIBRATION [40]

ACOUSTIC SIGNAL PROCESSING [60]

PHYSIOLOGICAL ACOUSTICS [64]

PSYCHOLOGICAL ACOUSTICS [66]

SPEECH PRODUCTION [70]

MUSIC AND MUSICAL INSTRUMENTS [75]

(Continued)

CONTENTS—*Continued from preceding page*

BIOACOUSTICS [80]

LETTERS TO THE EDITOR

ERRATA

CUMULATIVE AUTHOR INDEX

NOTES CONCERNING ARTICLE ABSTRACTS

1. The number following the abstract copyright notice is a Publisher Item Identifier (PII) code that provides a unique and concise identification of each individual published document. This PII number should be included in all document delivery requests for copies of the article.
2. PACS numbers are for subject classification and indexing. See June and December issues for detailed listing of acoustical classes and subclasses.
3. The initials in brackets following the PACS numbers are the initials of the JASA Associate Editor who accepted the paper for publication.

Document Delivery: Copies of journal articles can be ordered from the new Articles in Physics online document delivery service (URL: http://www.aip.org/articles.html).

SOUNDINGS

This front section of the *Journal* includes acoustical news, views, reviews, and general tutorial or selected research articles chosen for wide acoustical interest and written for broad acoustical readership.

ACOUSTICAL NEWS—USA

Elaine Moran
Acoustical Society of America, 500 Sunnyside Boulevard, Woodbury, New York 11797

Editor's Note: *In order to provide broad coverage of members' activities, readers of this Journal are asked to submit items on awards, appointments, and other activities about themselves or their colleagues. Deadline dates for news items and notices are 2 months prior to publication.*

Joshua E. Greenspon edits for 25 years

Joshua E. Greenspon

Dr. Joshua E. Greenspon retired recently as an Associate Editor for General Linear Acoustics after 25 years of editorial service to the *Journal*. Throughout this time this department of the *Journal* has been one of the most active. During the past decade Dr. Greenspon has handled an average of 103 submissions per year, which is believed to be a record for a single associate editor. In addition to diligence, faithfulness, and competence, he has shown great diplomatic skill when needed, and has helped many authors to improve their articles and letters before publication.

The Society has honored Dr. Greenspon with the Silver Medal in Engineering Acoustics in 1989 ''for his leadership in and contributions to the solution of underwater radiation and scattering problems.'' He received his Dr. Eng. in Applied Mechanics from The Johns Hopkins University in 1956, while doing research at the David Taylor Model Basin on ship vibration and shock. After working for the Martin Company on theory and tests for wing panel flutter, in 1958 he formed his own engineering company, JG Engineering Research Associates, working under contract to the U.S. Navy on problems in underwater acoustics and structural acoustics, and also for the Army and NASA on structural vibration and vulnerability. His outstanding and sustained *Journal* editorial work has been performed at his JG Engineering Research office to which the *Journal* and Society express gratitude for support services. Congratulations and thanks to Dr. Greenspon!

DANIEL W. MARTIN
Editor-in-Chief

Dale E. Chimenti becomes new Associate Editor of the *Journal*

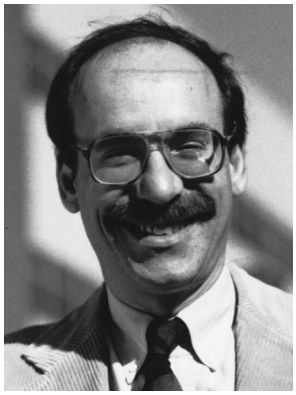

Dale E. Chimenti

In May 1998 Professor Dale E. Chimenti of the Aerospace Engineering and Engineering Mechanics Department at the Iowa State University, Ames, Iowa, became a new Associate Editor of the *Journal* for papers in Linear Acoustics (PACS 43.20). He succeeded Dr. Joshua E. Greenspon who completed 25 years of faithful and effective service for which the Editor-in-Chief expresses his deep appreciation (see news item above).

Dale Chimenti received a B.A. in physics from Cornell College in Iowa in 1968. He received the M.S. in 1972 and Ph.D. in 1974, also in physics, from Cornell University. His thesis research dealt with electronic transport properties in metals and electromagnetic generation of acoustic waves. From 1974 to 1976 Dr. Chimenti pursued postdoctoral research in superconductivity at Argonne National Laboratory. He continued this work from 1976 to 1978 under DFG sponsorship as a von Humboldt Fellow at the University of Tuebingen. In 1978 he joined the Nondestructive Evaluation Branch at the Air Force Materials Laboratory in Dayton, OH, where he performed research on ultrasonics with applications to NDE. There he also managed the Air Force's Advanced NMDE Technology Program, and chaired TTCP PTP-5, an international defense panel on NDE. In 1989 Dr. Chimenti accepted a research professorship in the Department of Materials Science and Engineering at The Johns Hopkins University, also serving as Associate Director of the Center for NDE. In 1993 he moved to Iowa State University, where he is currently a professor in Aerospace Engineering and Engineering Mechanics and a senior scientist in the Center for NDER. Dale's research interests lie in elastic wave propagation in anisotropic layered or inhomogeneous media, composite materials, leaky guided waves, and ultrasonics for materials characterization. He has published widely, including 17 articles in our *Journal*, and is co-editor of the series ''Review of Progress in Quantitative Nondestructive Evaluation.'' He also serves as Editor-in-Chief of NDT&E International.

The Editor-in-Chief and his colleagues welcome Professor Chimenti to membership on the Editorial Board.

DANIEL W. MARTIN
Editor-in-Chief

James M. Hillenbrand becomes new Associate Editor of the *Journal*

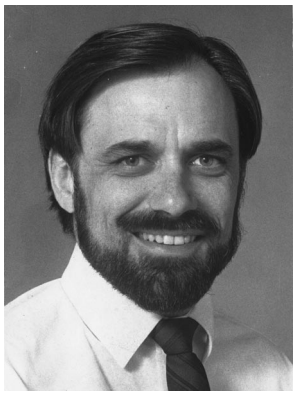

James M. Hillenbrand

Winifred Strange

In July 1998 Professor James M. Hillenbrand of the Department of Speech Pathology and Audiology at the Western Michigan University, Kalamazoo, Michigan, became a new Associate Editor of the *Journal* for papers in Speech Perception (PACS 43.71). He succeeded Professor Winifred Strange of the University of South Florida, who served a three-year term of faithful and effective service. The Editor-in-Chief is happy to express his deep appreciation to Professor Strange and to her institution for support services.

James M. Hillenbrand received a B.S. in 1974, and an M.S. in 1975 in Speech and Hearing Science from Indiana University. He received a Ph.D. in Speech and Hearing Science in 1980 from the University of Washington.

From 1980 to 1985 he was on the faculty of the Department of Com-

munication Science and Disorders at Northwestern University. From 1985 to 1988 he was Director of Research for the Intelligent Systems Division of RIT Research Corporation in Rochester, New York. Since 1988 Professor Hillenbrand has been on the faculty of Western Michigan University.

Hillenbrand's principal research interests have been in speech perception, synthesis, and voice. He has authored or co-authored over 25 research publications, many of them in our *Journal*, and served as an associate editor of the *Journal of Speech and Hearing Research* from 1991 to 1994. He is a member of the Technical Committee on Speech Communication.

The Editor-in-Chief and his colleagues welcome Professor Hillenbrand to membership on the Editorial Board.

DANIEL W. MARTIN
Editor-in-Chief

Virginia Richards receives award from National Academy of Sciences

ASA member Virginia Richards, of the Department of Psychology at the University of Pennsylvania, was awarded the prestigious Troland Research Award from the National Academy of Sciences (NAS) on 27 April at the NAS annual meeting in Washington, DC. This award of $35,000 is given annually to each of two recipients to support their research in experimental psychology. Dr. Richards was chosen ''for her contributions to auditory perception, especially to the understanding of the envelope and energy cues that contribute to detecting signals in noise.''

Regional Chapter News

Cincinnati: The January 1997 lecturer was Dr. Robert Dooling (Univ. of Maryland) whose topic was ''Hearing and Vocal Learning in Birds: A Model for Human Language.''

The February meeting speaker was Dr. Christy Holland who discussed and demonstrated the noise generated during magnetic resonance imaging (MRI).

In April, Dr. Daniel Martin lectured on ''The Singing Voice.'' Following the lecture, the group attended a concert by the Knox Presbyterian Church Choir.

The May meeting featured a case study on highway noise barriers presented by Dr. Ernest Weiler and a discussion and demonstration of a unique amplification device by Dr. Roger Adelman.

At the September meeting Christa Themann discussed the early data from the NIOSH survey of noise exposure and hearing status in farm families. Sharon Hepfner presented recent developments in and new applications for hearing protection devices.

A joint meeting with the Columbus, OH chapter was attended in October for the guest lecture on the development of an intraoral hearing aid.

In December, we honored Dr. Daniel W. Martin for his outstanding contributions and service to the ASA and our chapter with a luncheon. The large gathering heard several speakers, including Dr. Martin's longtime friend Dr. Mead Killion.

SHARON T. HEPFNER
President, Cincinnati Chapter ASA

Report to the Auditor

Published herewith is a condensed version of our auditor's report for calendar year ended 31 December 1997.

Independent Auditors' Report

To the Executive Council
Acoustical Society of America

We have audited the accompanying statements of financial position of the Acoustical Society of America as of December 31, 1997 and the related statements of activity and cash flows for the year then ended. These financial statements are the responsibility of the Society's management. Our responsibility is to express an opinion on the financial statements based on our audit.

We conducted our audit in accordance with generally accepted auditing standards. Those standards require that we plan and perform the audit to obtain reasonable assurance about whether the financial statements are free of material misstatement. An audit includes examining, on a test basis, evidence supporting the amounts and disclosures in the financial statements. An audit also includes assessing the accounting principles used and significant estimates made by management, as well as evaluating the overall financial statement presentation. We believe that our audit provides a reasonable basis for our opinion.

In our opinion, the financial statements referred to above present fairly, in all material respects, the financial position of the Acoustical Society of America as of December 31, 1997 and the changes in its net assets and its cash flows for the year then ended in conformity with generally accepted accounting principles.

CONROY, SMITH & CO.
5 May 1998
New York, NY

ACOUSTICAL SOCIETY OF AMERICA
STATEMENTS OF FINANCIAL POSITION
AS OF 31 DECEMBER 1997
(With Comparative Totals For 1996)

	1997	1996
Assets:		
Cash and cash equivalents	$ 291,383	$ 681,225
Accounts receivable	227,177	285,485
Marketable securities	5,134,080	3,978,955
Furniture, fixtures and equipment — net	101,165	112,526
Other assets	270,367	309,756
Total assets	$6,024,172	$5,367,947
Liabilities:		
Accounts payable and accrued expenses	$ 234,484	$ 129,029
Deferred revenue	836,905	1,048,038
Deferred rent liability	46,228	41,326
Total liabilities	$1,117,617	$1,218,393
Net assets:		
Unrestricted	$3,882,375	$3,272,177
Temporarily restricted	472,038	391,476
Permanently restricted	552,142	485,901
Total net assets	$4,906,555	$4,149,554
Total liabilities and net assets	$6,024,172	$5,367,947

ACOUSTICAL SOCIETY OF AMERICA
STATEMENTS OF ACTIVITY
FOR THE YEAR ENDED 31 DECEMBER 1997
(With Comparative Totals For 1996)

	1997	1996
Unrestricted net assets:		
Revenue		
Dues	$ 522,273	$ 508,513
Publishing	2,204,176	2,217,577
Standards	270,506	313,893
Meetings	295,101	305,231
Interest and dividends	168,799	133,759
Unrealized gain (loss)	161,509	252,935
Other	90,786	99,870
Realized gain (loss)	340,162	34,089
Total unrestricted revenue	$4,053,312	$3,865,867
Expenses:		
Publishing	$1,820,558	$1,823,241
Standards	428,281	411,513
Administrative and general	485,402	510,838
Meetings	452,926	313,000
Other expenses	263,711	177,563
Total expenses	$3,450,878	$3,236,155
Increase in net assets	$ 602,434	$ 629,712
Net assets released from restrictions:		
Satisfaction of program restrictions	7,764	4,041
Increase in unrestricted net assets and reclassifications	$ 610,198	$ 633,753
Temporarily restricted net assets:		
Contributions	$ 2,861	$20,301
Investment income	65,004	21,213
Unrealized gain (loss)	20,461	31,949
Release of restrictions	(7,764)	(4,041)
Increase (decrease) in temporarily restricted net assets	$ 80,562	$ 69,422
Permanently restricted net assets:		
Investment income	$ 80,680	$ 27,616
Unrealized gain (loss)	25,377	41,597
Expenses	(39,816)	(15,583)
Increase (decrease) in permanently restricted net assets	$ 66,241	$ 53,630
Increase in net assets	$ 757,001	$ 756,805
Net assets, beginning of year	4,149,554	3,392,749
Net assets, end of year	$4,906,555	$4,149,554

ACOUSTICAL SOCIETY OF AMERICA
STATEMENTS OF CASH FLOWS
FOR THE YEAR ENDED 31 DECEMBER 1997
(With Comparative Totals For 1996)

	Total All Funds	
	1997	**1996**
Operating Activities		
Increase in net assets	$ 757,001	$ 756,805
Adjustments to reconcile net income to net cash provided by operating activities:		
Depreciation and amortization	26,919	23,973
Unrealized (gain) loss on marketable securities	(207,347)	(326,481)
Changes in operating assets and liabilities:		
(Increase) decrease in accounts receivable	58,308	6,989
Decrease (increase) in other assets	39,389	(86,703)
Increase (decrease) in accounts payable and accrued expenses	105,455	(120,073)
Increase in deferred rent liability	4,902	4,903
Increase (decrease) in deferred revenue	(211,133)	160,381
Net cash flows provided by operating activities	$ 573,494	$ 419,794
Investing Activities		
Purchase of furniture, fixtures, equipment and leasehold improvements	($ 15,557)	($ 31,014)
Proceeds from sale of securities	4,564,188	2,097,286
Purchase of securities	(5,511,967)	(5,714,531)
Net cash (used in) provided by investing activities	($ 963,336)	($3,648,259)
Increase (decrease) in cash and cash equivalents	($ 389,842)	($3,228,465)
Cash and cash equivalents, beginning of year	681,225	3,909,690
Cash and cash equivalents, end of year	$ 291,383	$ 681,225

Revisions to Membership List

New Associates

Artinano, Pedro, P&A Consultores de Acustica, c./Saturnino Calleja 7, Madrid 28002 Spain
Bajdek, Christopher J., Harris Miller Miller & Hanson, Inc., 15 New England Executive Park, Burlington, MA 01803
Bajic, Branko, I Ferensica 33, Zagreb 10000, Croatia
Balabaev, Sergey M., Utkinskaya 13, ap. 10, Vladivostak 690091, Russia
Balachandran, Balakumar, Mechanical Engineering, Univ. of Maryland, College Park, MD 20742-3035
Bielecki, Robert J., 523 Beaverkill Road, Olivebridge, NY 12461
Bird, Michael T., AETC, Inc., 8910 University Center Lane, Suite 900, San Diego, CA 92122-1012
Bogdanowicz, Kenneth J., Wave Mechanics, Inc., 118 South Fullerton Avenue, Montclair, NJ 07042
Bollard, Paul A., Bollard Acoustical Consulting, 7909 Walerga Road, Suite 112-143, Antelope, CA 95843
Burrows, John M., Sonar Systems Dept., DERA Winfrith, Winfrith Technology Centre, Dorchester, Dorset DT2 8XJ, U.K.
Campbell, Murray D., Physics and Astronomy, Univ. of Edinburgh, Mayfield Road, Edinburgh EH9 3JZ, U.K.
Cerami, Victoria J., Cerami & Associates, Inc., 518 Fifth Avenue, New York, NY 10036
Chang, Pi Sheng, 1529 Ambergrove Drive, San Jose, CA 95131
Chen, Kejian, Medical College of Ohio, Otolaryngology Dept., 3000 Arlington Avenue, Toledo, OH 43614
Chung, Jae Soo, 2025 Jolley Drive, Burbank, CA 91504
Ciao, Quinsan, Virginia Technical Univ., 201 Cowgull, Blacksburg, VA 24060
Clifton, Mark A., Acoustics & Structural Vibrations, Engineering Technology Center, 240 Oral School Road, Suite 105, Mystic, CT 06355
Cote, Marc G., Cavanaugh Tocci Associates, Inc., 327F Boston Post Road, Sudbury, MA 01776
Crayme, Kirk N., 15456 Forest Park Drive, Grand Haven, MI 49417
De Vries, Martin P., BMT Biomechanics, Univ. of Groningen, Bloemsingel 10, Groningen 9712KZ, The Netherlands
Djordjevic, B. Boro, Johns Hopkins University, CNDE/102 Maryland Hall, 3400 North Charles Street, Baltimore, MD 21218
Donlagic, Denis, Sernceva Ulica 5, Maribor 2000, Slovenia
Dosso, Stan E., School of Earth and Ocean Sci., Univ. of Victoria, Victoria, BC V8W 3P6, Canada
Durabb, Jr., Richard K., 3601 Karen Drive, Chalmette, LA 70043,
Ead, Richard M., 825 Middlebridge Road, Wakefield, RI 02879
Eggenschwiler, Kurt, Acoustics, EMPA, Ueberlandstr. 123, Duebendorf CH-8600, Switzerland
Eilar, Douglas K., 321 North Willowspring Drive, Encinitas, CA 92024
Fang, Wen-Tsun, F6, 113, Chien-Kuo North Rd., Sec. 2, Taipei 104, Taiwan
Fire, Kevin M., Communication Sciences & Disorders, Univ. of North Dakota, P.O. Box 8040, Grand Forks, ND 58202-8040
Fujioka, Taira, Ridge Corporation, 7808 Bryn Mawr Drive, Dallas, TX 75225
Galvin, John J. III, Auditory Perception Lab., House Ear Inst., 2100 West 3rd Street, 5th Floor, Los Angeles, CA 90057-1922
Gates, Edward M., Mechanical Engineering, CSU Pomona, 3801 West Temple, Pomona, CA 91768
Goyal, K. C., 121 Mohalla Chaudharian, Hisar 125001, India
Green, Grant D., 1626 Parkhills Avenue, Los Altos, CA 94024
Hamel, Tim A., 48941 Denton Road, #309, Belleville, MI 48111
Hertlein, Bernard H., 3478 Glen Flora Avenue, Gurnee, IL 60031
Hewlett, Dean A. K., Audio Tag, Nokia R+D Ltd., Ashwood House, Pembroke Broadway, Camberley, Surrey GU15 3XD, England
Higgins, Owen S., Electronic Specialty Company, P.O. Box 400, 1325 Dunbar Avenue, Dunbar, WV 25064
Honeycutt, Richard A., 404 Olivia Drive, Lexington, NC 27295
Huffman, Thomas B., Stanley Associates, 2231 Crystal Drive, Suite 1101, Arlington, VA 22202
Il'nskii, Yurii, MacroSonic Corp., 1570 East Parham Road, Richmond, VA 23228
Jamali, Naseem Z., Books and Research, Inc., 32 Main Street, Hastings, NY 10706
Joitke, Paul L., 9380 Hartland Road, Fenton, MO 48430
Juve, Daniel, Acoustique, Ecole Centrale de Lyon, 36 Avenue Guy de Collongue, BP 163, Ecully 69131 Cedex, France
Karlson, Karl D., NVH, MIRA North America, 47523 Clipper Street, Plymouth, MI 48170
Kimble, Bart W., 404 Green Court, Johnstown, OH 43031
Klesenski, Kevin, 522 Paco Drive, Los Altos, CA 94024
Londo, Shawn P., Strategic Systems Dept., Johns Hopkins Univ., Applied Physics Lab., 11100 Johns Hopkins Road, Laurel, MD 20723-6099
Maev, Roman G., Dept. of Physics, Univ. of Windsor, 401 Sunset Avenue, Windsor, ON N9B 3P4, Canada
Martin, Martha A., Beyond the Classroom, 909 Marina Village Parkway, #238, Alameda, CA 94501
McGuigan, Kevin G., Physics Dept., Royal College of Surgeons in Ireland, 123 St. Stephen's Green, Dublin 2, Ireland
Men, Theresa, ATL Ultrasound, Inc., 22100 Bothell Everett Highway, Bothell, WA 98021
Mourad, Pierre D., 109 NW 49th Street, Seattle, WA 98107
Nakayama, Kazuo, Dept. of English Teaching, Faculty of Education, Yamagata University, Kyoyuokyoiku Building #1, 1-4-12 Kojirakawa, Yamagata 990-8560, Japan
Nguyen, Phat, Produits Acoustiques PN Inc., 10858 St. Vital, Montreal-Norb QC H1H 4T4, Canada
Nutting, Michael J., 74 Theodore Drive, Leominster, MA 01453
Park, Patrick E., 121 Olive Street, #12, Glendale, CA 91206
Parzynski, Paul, 55300 Parkview Drive, Shelby Township, MI 48316-1069
Patro, Tangi N., 14427 Wellesley, Dearborn, MI 48126
Peterson, D. Kent, 1325 Holly Avenue, Los Altos, CA 94024
Phillips, James N. III, Hobart Ground Power, 1177 Trade Road, East, Troy, OH 45373,
Pollack, Martin L., Lockeed Martin, Knolls Atomic Power Lab., P.O. Box 1072, Schenectady, NY 12301
Prager, Bradley T., 668 Falkland Road, Victoria, BC V8S 4L5, Canada
Pulchner, Martin W., Pilchner Schoustal, Inc., 376 Queen Street East, Toronto, ON M5A 1T1, Canada
Richardson, James R., 20 St. Benedicts Close, Aldershot, Hampshire GU11 3NL, U.K.
Richardson, Suzanne D., 3220 Duval Road, #3303, Austin, TX 78759
Rossi, Pietro, c/o Cuncnav Op-Via Della Storta 701, Roma 00123, Italy
Russell, Ian J., School of Biological Sciences, University of Sussex, Falmer, Brighton BN1 9QG, U.K.
Ryaboy, Vyacheslav M., 3701 Parkview Lane, #23B, Irvine, CA 92612
Schneider, Albrecht, Inst. of Musicology, Univ. of Hamburg, Neue Rabenstr. 13, Hamburg D-20354, Germany
Schulz, Mark J., 2903 Latta Drive, Summerfield, NC 27358
Schutte, Harm K., Biomedical Technology, Groningen Voice Research Lab., Bloemsingel 10, Groningen 9712KZ, The Netherlands
Segev-Gilad, Sima, Voice Identification Lab., National Police Headquarters, DIFS, Sheik Jarakh, Jerusalem 91906, Israel
Shaughnessy, Thom, P.O. Box 607, New Britain, CT 06050
Smith, Malcolm J., 2065 Brunswick Street, Apt. 403, Halifax NS B3K 5T8, Canada
Steinschneider, Mitchell, Department of Neurology, Albert Einstein College of Medicine, Kennedy Center, Room 322, 1300 Morris Park Avenue, Bronx, NY 10461
Sundkvist, Karl E., Goodyear Tire and Rubber Company, D460G, Technical Center, P.O. Box 3531, Akron, OH 44309-3531
Svinth, Fred M., Jack Evans & Assoc., Inc., 5806 Mesa Drive, Suite 380, Austin, TX 78731-3742
Thorpe, Cornelius W., National Voice Center, Univ. of Sydney, East Street, Lidcombe, NSW 2141, Australia
Tressler, James F., Naval Research Lab., Code 7130, Physical Acoustic, 4555 Overlook Avenue, SW, Washington, DC 20375-5350
Truckenbrodt, Hubert, Dept. of Linguistics, Rutgers University, 18 Seminary Place, New Brunswick, NJ 08901-1184
Tschiegg, Richard D., 7407 Brandenburg Court, Sykesville, MD 21784
Uscinski, Barry J., Applied Mathematics & Theoretical Physics, University of Cambridge, Silver Street, Cambridge CB3 9EW, U.K.
Valerio, Rubens A., Engineering, Periodical Consulting, Rue Peixoto Gomide, 996 Conjunto 501, Sao Paulo, SP 01409-900, Brazil
Vigness, Kathleen J., P.O. Box 425, Saunderstown, RI 02874
Vincent, Harold T., 161 Woodmist Way, North Kingstown, RI 02852
Vlaming, Marcel S., P.O. Box 80002, 5600 JB Eindhoven, The Netherlands
Wang, Rongqing, Sound Scattering of Underwater Target, Measure and Control Technique Inst., 14 Binhaijie, P.O. Box 67, Dalian, Liaoning 116013, P. R. China
White, James D., Dept. of Physics, SUNY Potsdam, Potsdam, NY 13676

Wieland, David L., Wieland Associates, 23276 South Pointe Drive, #114, Laguna Hills, CA 92653
Wilson, M. Lee, Shimoda Services, Inc., 7602 Stoneywood Drive, Austin, TX 78731
Wyatt, James H., 12648 Crescent Drive, Carmel, IN 46032
Zhou, Xiaoru, Pilchner Schoustal Inc., 376 Queen Street, East, Toronto, ON M5A 1T1, Canada

New Students

Berger, Thomas K., 3819 Miramar Street, Apt. B, La Jolla, CA 92037
Birdsong, Charles B., Mechanical Engineering, Michigan State Univ., 2553 Engineering Building, East Lansing, MI 48824-1226
Buehler, Matthew R., Audiology and Speech Pathology, Univ. of Tennessee Knoxville, 457 South Stadium Hall, Knoxville, TN 37996-0740
Bukhala, Zeeky A., Electric Power Engineering, Rensselaer Polytechnic Inst., 110 8th Street, Troy, NY 12180
Busenitz, John A., 1201 Lindberg Road, West Lafayette, IN 47906
Cherepennikov, Valery V., Radiophysical, Univ. of Nizhny Novgorod, Gagarin Avenue 23, Nizhny Novgorod 603600, Russia
Constan, Zachary A., 4464 Janice Lee Drive, B-211, Okemos, MI 48864
Curra, Francesco P., Applied Physics Lab., Univ. of Washington, 1013 NE 40th Street, Seattle, WA 98105
Dallal, Michael, 75 Dickenson Place, Great Neck, NY 11023
Davenny, Ben C., 14 Woodvale Street, Portland, ME 04102
DeLong, Caroline M., Marine Mammal Research Program, Hawaii Inst. of Marine Biology, P.O. Box 1106, Kailua, HI 96734
D'Hooge, Jan R., K. E. Leuven, Univ. Hospital Gasthuisberg, Cardiology, Herestraat 49, Leuven 3000, Belgium
Dorado, David, Cava Alta 25, 2th, Madrid 28005, Spain
Duncan, Scott D., Apt. 507, 770 Wonderland Road, South, London, ON N6K 1M3, Canada
Elliott, Christopher M., 4512-308 Baymar Drive, Raleigh, NC 27612
Fitzgerald, Matthew B., 835 Ridge, #508, Evanston, IL 60202
Gage, Nicole M., 2535 Juanita Way, Laguna Beach, CA 92651
Gallun, Frederick J., 1555 Oxford Street, #201, Berkeley, CA 94709
Granat, Cristel, 52 Allee de la Blancharde, Gif Sur Yvette 91190, France
Habibzadeh-Vaneghi, Houshang, Graduate School of Engineering, Shizouka Univ., 3-5-1 Johoku, Hamamatsu, Shizuoka-Ken 432, Japan
Hahn, Thomas R., Physics, UCSD, 9500 Gilman Drive, La Jolla, CA 92093-0238
Hardiman, James E., Electrical and Computer Eng., Univ. of Massachusetts, Dartmouth, 285 Old Westport Road, North Dartmouth, MA 02747-2300
Harne, Catherine M., 114 Meadow View Lane, Kennett Square, PA 19348
Haviland, Genevieve M., 1016 3rd Street, North, St. Petersburg, FL 33701
Hock, Davis A., 2414 Cedarwood Avenue, Lawrence, KS 66046
Hornsby, Benjamin W. Y., Hearing and Speech Science, Vanderbilt University, 1114 19th Avenue, South, Nashville, TN 37212
Houix, Olivier, IRCAM, 1 place Igor-Stravinsky, Paris F-75004, France
Hynes, Shelly F., 138 Fern Street, Natchitoches, LA 71457
Jaeseung, Choi, Electrical Engineering, Information Processing Lab., Osaka City Univ., 3-3-138 Sugimoto, Sumiyoshi-ku, Osaka 558-0022, Japan
Kalantar-Zadeh, Kourosh, No. 24, Shahid Akbari St., Kargar Shomali Ave., Tehran 14146, Iran
Kilfoyle, Daniel B., 406 Suppewissett Road, Falmouth, MA 02540
Kim, Seongil, Marine Physical Lab., Scripps Inst. of Oceanography, Mail Code 0238, Univ. of California, San Diego, La Jolla, CA 92093-0238
Kite, Thomas D., 5200 North Lamar, #D301, Austin, TX 78751
Ledevedec, Pierre Ph., Allee du Chateau, Menthon St., Bernard 74290, France
Lewis, Julie A., 1823B Blake Street, Berkeley, CA 94703
Lin, Chris C., 680 Leff Street, San Luis Obispo, CA 93401
Magill, Brian F., 247 East Irvin Avenue, Apt. B, State College, PA 16801
Michel, Nathalie C., GAUS, Univ. de Sherbroke, 2000 Bd. de L'Universite, Sherbrooke, QC J1K 9R1, Canada
Mitchell, Elle, P.O. Box 231032, Old State House Station, Hartford, CT 06123-1032
Muller, Barbara S., Psychology, Univ. of Geneva, Rte. de Drize 9, Geneva GE 1227, Switzerland
Oelze, Michael L., National Center for Physical Acoustics, Univ. of Mississippi, Coliseum Drive, University, MS 38677
Pasicznyk, Paula P., Hearing and Speech Sciences, Vanderbilt University, 1114 19th Avenue, South, Nashville, TN 37212
Petculescu, Andi G., Physics and Astronomy, Ohio University, Clippinger Labs., Room 251, Athens, OH 45701
Petculescu, Gabriela, Physics, Ohio University, Clippinger Labs., Room 251, Athens, OH 45701
Pinus, Alexander B., 1124 Green Street, Philadelphia, PA 19123
Plyler, Patrick N., Audiology & Speech Pathology, Univ. of Tennessee, 457 South Stadium Hall, Knoxville, TN 37996-0740
Potty, Gopu R., 2900 Kingstown Road, #112, Kingston, RI 02881
Pyper, Edward A., 580 North 100 East, #2, Provo, UT 84606
Ressler, Patrick H., Dept. of Oceanography, Texas A&M Univ, MS 3146, College Station, TX 77843-3146
Richards, Christopher M., 614 Anna Rose Run, Westerville, OH 43081
Romano, Lisa J., 291 Avenue ''W,'' Brooklyn, NY 11223
Rout, Ayasakanta, Audiology and Speech Sciences, Purdue Univ., 1353 Heavillon Hall, West Lafayette, IN 47907
Sampedro Noya, Francesc, Joseph, c/o Santa Eugenia, 48 3 2a, Girona, Catalunya 17005, Spain
Schutz, Elijah A., 265 SW 11th, Corvallis, OR 97331
Sheppard, Erin M., 314 Murphy Street, Murphysboro, IL 62966
Slaton, William V., Thermoacoustics, National Center for Physical Acoustics, Coliseum Drive, University, MS 38677
Smart, Ronald D., Dept. of Food Science, Pennsylvania State Univ., 125 Borland Lab., University Park, PA 16802
Vassilakis, Pantelis N., 1517 Armacost, #201, West Los Angeles, CA 90025
Wadsworth, Glenn J., National Center for Physical Acoustics, Coliseum Drive, University, MS 38677
Wakabayashi, Midori, 4817 Sheboygan Avenue, #402, Madison, WI 53705
Weatherly, Kirk A., 5200 Coe Avenue, #1186, Seaside, CA 93955
Wilson, Weston, 20 South Bryant Avenue, #209, Edmond, OK 73034
Xie, Qiang, Dept. of Welding Engineering, Ohio State Univ., 1248 Arthur E. Adams Drive, Columbus, OH 43221
Zheng, Hua, 407 1/2 East Stoughton Street, Apt. 7, Champaign, IL 61820-4341
Zimmerman, Eric J., 5980 Chesbro Avenue, San Jose, CA 95123

Associates Elected Members

R. Akahane-Yamada, C. W. Allen, B. A. J. Angelsen, Y. Chevalier, G. D. Dorrance, E. J. Feleppa, G. Furnell, J. D. Geiler, J. B. Gubelmann, R. Hill, Y. Irie, K. H. Kaliski, M. P. Kerr, C. A. Krajewski, S. Kuwahara, P. J. Loughlin, G. M. Martin, K. I. Maslov, S. M. Mayevskyyi, V. B. Mit'ko, H. Miura, V. I. Passechnik, A. Protopapas, J. M. Pyne, D. C. Ricks, P. M. J. Sas, J. Sun, J. D. Szymanski, J. Tabrikian, H. Takata, S. K. Tomar, R. Varela, A. C. Zander

Students to Associates

J. S. Allen, R. R. Andre, R. K. Andrew, S. N. Backhaus, B. A. Bard, J. R. Benki, M. H. W. Budhiantho, T. M. Chan, P. P. Chang, B. V. Chapnik, Y.-C. Chiang, C.-H. Choi, D. Colton, F. Cummins, N. Currey, X. Dong, Y. Dorfman, A. Economou, J. D. Estep, J. J. Finneran, M. S. Fozo, Q.-J. Fu, W. G. Gardner, M. J. Gregan, E. Healy, M. Hicks, J. H. Irwin, Jr., E. R. Maniet, Jr., D. Kapolka, M. Kato, B. F. Katz, D. M. Kenney, L. L. Koenig, H. Kosaki, R. S. Kulkarni, B. J. Landsberger, B.-G. Lee, Y.-H. Lin, D. Lin, J. P. Maillard, P. Masson, P. G. May, J. A. Nelson, J. G. Neuhoff, R. S. Newman, A. E. Ozelame, J. S. O'Neill, M. Pedersen, M. Pell, A. R. Pilon, G. J. T. Ramsay, J. M. Riley, R. A. Roberts, E. J. Rosenberg, L. S. Rossi, A. M. Sampath, G. P. Scavone, J. R. Schoepflin, S. A. K. Seddoh, V. V. Shah, S. A. Shaw, W. S. Shepard, S. A. Singh, A. R. Smith, J.-H. So, E. Soltano, C. Stamoulis, G. R. Stanley, G. Starr, P. A. Stucky, A. Tsuchida, J. S. Vipperman, M. S. Vitevitch, Y. Wang, R. Wayland, K. R. Weninger, N. A. Whitmal, C. R. Winkel, B. D. Womack, R. A. Wright

Associates to Students

J. R. Bishop, P. S. Wilson

Resigned

E. Gross—*Fellow*

H. R. Bauer, P. J. Benson, D. Butler, R. D. Doolittle, F. E. Geib, Jr., J. V. Long, A. G. McKay, T. D. McNeal, R. F. Naunton, H. Otsubo, H. A. Schenck, A. Sfaoui, R. H. Stokes, D. C. Tate, E. P. Vehslage, L. E. Volaitis—*Members*

J. D. Alexander, W. H. Bailey, J. W. Boughman, M. C. Brown, D. Chan, C. Fassbender, Q. Hu, J. H. Rose, Jr., H. J. Kim, L. Kondic, J. C. Makous, G.

C. Marean, E. Mayfield, J. L. van Niekerk, R. A. Rodgers, Y. Sakurai, G. Thielemann, S. A. Thorpe, C. A. Zala—*Associates*

S. K. Boegli, I. B. Clark, R. R. Patka, R. D. Susanto—*Students*

Deceased

E. L. Hamilton, R. E. Williams—*Fellows*

M. W. Keyes, J. C. Myers, C. W. Oliphant—*Members*

J. Lacagnino—*Associate*

Fellows	810
Members	2784
Associates	2887
Students	882
	7363

USA Meetings Calendar

Listed below is a summary of meetings related to acoustics to be held in the U.S. in the near future. The month/year notation refers to the issue in which a complete meeting announcement appeared.

1998

9–14 Aug. International Acoustic Emission Conference, Hawaii, HI [Karyn S. Downs, Lockheed Martin Astronautics, P.O. Box 179, M.S. DC3005, Denver, CO 80201; Tel.: 303-977-1769; Fax: 303-971-7698; E-mail: karyn.s.downs@lmco.com].

13–17 Sept. American Academy of Otolaryngology—Head and Neck Surgery, San Francisco, CA [American Academy of Otolaryngology—Head and Neck Surgery, One Prince St., Alexandria, VA 22314 Tel.: 703-836-4444; Fax: 703-683-5100].

18–19 Sept. 6th Annual Conference on Management of the Tinnitus Patient, Iowa City, IA [Richard Tyler, Univ. of Iowa, Dept. of Otolaryngology—Head & Neck Surgery, 200 Hawkins Dr., C21GH, Iowa City, IA 52242; Tel: 319-356-2471; Fax: 319-353-6739; E-mail: rich-tyler@uiowa.edu].

12–16 Oct. 136th meeting of the Acoustical Society of America, Norfolk, VA [ASA, 500 Sunnyside Blvd., Woodbury, NY 11797, Tel.: 516-576-2360; Fax: 516-576-2377; E-mail: asa@aip.org, WWW: http://asa.aip.org].

1999

15–19 March Joint meeting: 137th meeting of the Acoustical Society of America/Forum Acusticum [Acoustical Society of America, 500 Sunnyside Blvd., Woodbury, NY 11797, Tel.: 516-576-2360; Fax: 516-576-2377; E-mail: asa@aip.org; WWW: asa.aip.org].

27–30 June ASME Mechanics and Materials Conference, Blacksburg, VA [Mrs. Norma Guynn, Dept. of Engineering Science and Mechanics, Virginia Tech, Blacksburg, VA 24061-0219; Fax: 540-231-4574; E-mail: nguynn@vt.edu; WWW: http://www.esm.vt.edu/mmconf/]. Deadline for receipt of abstracts: 15 January 1999.

ACOUSTICAL NEWS—INTERNATIONAL

Walter G. Mayer
Physics Department, Georgetown University, Washington, DC 20057

A new Society: Indonesia

According to a report in *Acoustics Australia* [Vol. 26, No. 1, p. 27 (1998)] the Indonesian Acoustics and Vibration Society (IAVS) was recently founded with the cooperation of universities, civilian government agencies, the Indonesian Navy, aircraft industry, and other industrial companies. The structure of the new society is similar to that of the Australian Acoustical Society, some of whose members were involved in the founding of the new society. The society aims to conduct short courses and distribute information in the areas of acoustics and vibrations since this field is relatively new among industry practitioners.

The society hopes to attract scientists, engineers, and others from all parts of Indonesia who are concerned with acoustics and vibrations in their daily work. The main program of IAVS clearly is to introduce the society within Indonesia as well as internationally, and to have its first meeting this year. The office of the society is based in Jakarta; the address is Indonesian Acoustics and Vibration Society, Jl. Cemara 13, Blok-S, Kebayoran Baru, Jakarta 12110, Indonesia. The Fax number is +62 21 573 7753.

Société Française d'Acoustique—Cinquantenaire!

The French Acoustical Society (S.F.A.), which, many years ago, was known as G.A.L.F. (Group of French-Language Acousticians), celebrates its 50th birthday this year. The various interest groups of the society will hold meetings to celebrate this event, some of which will hold more than one meeting, like the Physical Acoustics/Underwater Sound/Ultrasonics group which has scheduled four meetings from March through the Fall, in Lyon, Le Havre, Brest, and Bordeaux, respectively. Regional Chapters also have scheduled meetings to commemorate the occasion, all of which will come to a grand finale the week before Christmas with four meetings in Paris in various locations like the Palais de la Découverte, the Musée de la Musique, and the Conservatoire.

Papers published in JASJ(E)

A listing of Invited Papers and Regular Papers appearing in the latest issue of the English language version of the *Journal of the Acoustical Society of Japan*, JASJ(E), was published for the first time in the January 1995 issue of the Journal. This listing is continued below.

The May issue of JASJ(E), Vol. 19, No. 3 (1998) contains the following papers:

K. Soetanto, S. Takeuchi, and M. Okujima ''Numerical investigation on nonlinear response of free microbubble illuminated with ultrasonic pulse''
R. Makarewicz and K. Masuda ''Highway noise under favorable conditions of generation and propagation''
T. Okubo and K. Fujiwara ''Efficiency of a noise barrier with an acoustically soft cylindrical edge''
H. Zheng, H. Yamaoka, N. Gohda, H. Noguchi, and A. Kaneko ''Design of the acoustic tomography system for velocity measurement with an application to the coastal sea''
A. Omoto, T. Matsui, and K. Fujiwara ''The behavior of an adaptive algorithm with a moving primary source''

International Meetings Calendar

Below are announcements of meetings to be held abroad. Entries preceded by an * are new or updated listings with contact addresses given in parentheses. Month/year listings following other entries refer to issues of the *Journal* which contain full calendar listings or meeting announcements.

September 1998

7–8	*__British Society of Audiology Annual Conference__, University of Hull, UK. (BSA, 80 Brighton Road, Reading RG6 1PS, UK; Fax: +44 0118 935 1915; e-mail: bsa@b-s-a.demon.co.uk; www.b-s-a.demon.co.uk)
7–9	**Nordic Acoustical Meeting 98**, Stockholm. *10/97*
14–15	*__Annual Meeting of the Austrian Acoustical Society,__ Graz, Austria. (E. Benes, IAP, Vienna University of Technology, Wiedner Hauptstrasse 8–10/134, 1040 Wien, Austria; Fax: +43 1 586 42 03; www.kfs.oeaw.ac.at/aaa/home.html)
14–16	**Biot Conference on Poromechanics**, Louvain-la-Neuve. *10/97*
14–16	**ACUSTICA 98**, Lisbon. *10/97*
14–18	**35th International Conference on Ultrasonics and Acoustic Emission**, Chateau of Třešt'. *10/97*
16–18	**International Conference on Noise & Vibration Engineering**, Leuven. *6/98*
17–18	**Annual Meeting of INCE/Japan**, Tokyo. *6/98*
17–18	**5th Mexican Congress on Acoustics**, Querétaro, Qro. *6/98*
21–25	**4th European Conference on Underwater Acoustics**, Rome. *4/98*
24–26	**Autumn Meeting of the Acoustical Society of Japan**, Yamagata. *6/98*

October 1998

4–7	**euro-noise 98**, Munich. *4/98*
12–16	**International Conference on Signal Processing (ICSP'98)**, Beijing. *6/98*
14–16	**16th Yugoslav Conference on Noise and Vibration**, Niš. *6/98*
15–16	*__Autumn Meeting Swiss Acoustical Society__, Dübendorf, Switzerland. (SGA, Postfach, 8600 Dübendorf, Switzerland)
28–30	*__Acoustics Week in Canada__, London, ON, Canada. (Margaret Cheesman, Hearing HealthCare Research Unit, University of Western Ontario, Elborn College, London, ON N6G 1H1, Canada; Fax: +1 519 661 3805; e-mail: cheesman@audio.hhcru.uwo.ca)
31–2	**AES International Conference ''Audio, Acoustics, and Small Spaces,''** Copenhagen. *6/98*

November 1998

11–13	**1st Asia Pacific Conference on Acoustics and Vibration** (APAV 98), Singapore. *6/98*
12–15	**Institute of Acoustics (UK) Autumn Conference: Speech and Hearing**, Windermere. *4/98*
16–18	**Inter-Noise 98**, Christchurch. *4/96*
20	**Recreational Noise**, Queenstown. *10/97*
23–27	**ICBEN 98: Biological Effects of Noise**, Sydney. *6/98*
30–4	**5th International Conference on Spoken Language Processing**, Sydney. *6/97*

December 1998

15–16	**Sonar Signal Processing**, Loughborough. *4/98*

March 1999

15–19	**Joint Meeting of EAA Forum Acusticum, and 137th Meeting of the Acoustical Society of America**, Berlin. *6/97*

April 1999

27–29	*__International Conference on Vibration, Noise, and Structural Dynamics__, Venice, Italy. (D. Hill, Stafford-

shire University, P.O. Box 333, Beaconside, Stafford ST18 0DF, UK; Fax: +44 1785 353552)

May 1999

10–14 **4th International Conference on Theoretical and Computational Acoustics**, Trieste. *6/98*

24–26 *__2nd International Conference on Emerging Technologies in NDT__, Athens, Greece. (A. Anastassopoulos, Envirocoustics S.A., Eleftheriou Venizelou 7 & Delfon, 14452 Athens, Greece; Fax: +30 1 28 46 805; e-mail: envac@acci.gr)

June 1999

28–30 **1st International Congress of the East European Acoustical Association**, St. Petersburg. *10/97*

28–1 **Joint Conference of Ultrasonics International '99 and World Congress on Acoustics '99 (UI99/WCU99)**, Lyngby. *6/98*

July 1999

4–9 **10th British Academic Conference in Otolaryngology**, London. *10/97*

5–8 **6th International Congress on Sound and Vibrations**, Copenhagen. *2/98*

September 1999

1–4 **15th International Symposium on Nonlinear Acoustics (ISNA-15)**, Göttingen. *10/97*

15–17 *__British Society of Audiology Annual Conference__, Buxton, UK. (BSA, 80 Brighton Road, Reading RG6 1PS, UK; Fax: +44 0118 935 1915; e-mail: bsa@b-s-a.demon.co.uk; www.b-s-a.demon.co.uk)

October 2000

3–5 **WESTPRAC VII**, Kumamoto. *6/98*

BOOK REVIEWS

James F. Bartram
94 Kane Avenue, Middletown, Rhode Island 02842

These reviews of books and other forms of information express the opinions of the individual reviewers and are not necessarily endorsed by the Editorial Board of this Journal.

Editorial Policy: *If there is a negative review, the author of the book will be given a chance to respond to the review in this section of the Journal and the reviewer will be allowed to respond to the author's comments. [See ''Book Reviews Editor's Note,'' J. Acoust. Soc. Am.* ***81****, 1651 (May 1987).]*

Deaf Architects & Blind Acousticians?—A Guide to the Principles of Sound Design

Robert E. Apfel

Apple Enterprise Press, 25 Science Park, Box 4, New Haven, CT 06511.
xii+105 pp. Price: $24.95 + @2.00 S&H in USA, foreign delivery available.

Perhaps the most difficult task that an accomplished acoustician can meet is one of explaining the fundamentals of acoustics to a lay audience. This was what Robert E. Apfel, a former president of ASA, set out to do and he did it admirably in this new paperback, *Deaf Architects & Blind Acousticians?—A Guide to the Principles of Sound Design.* The book is intended to acquaint the architecture student, the architect, and the civic planner, all of whom are likely to be mathematically challenged, with the importance of including the acoustical environment in the overall design plan. Because of Apfel's fame as an effective teacher, this reviewer took a gamble on adopting the text sight unseen for a course he is teaching in the School of Architecture at the City College of New York. Judging from the enthusiastic response on the part of the students, the gamble paid off. Apfel effectively met the challenge of describing acoustical principles without resorting to post-high school mathematics. As can be inferred from the title of the book, Apfel is a very witty man, and he maintains that wit throughout the text.

The introduction begins with a discussion of the nature of light and sound and then launches into a description of high and low pitched sounds. The essentialness of sound to bats and cetaceans, as well as to humans, are outlined, and then the relationship $\lambda = c/f$ is discussed.

The mechanism of human hearing is described simply without ''talking down'' to the reader. Major aspects of psychoacoustics are touched upon: sensitivity of human hearing according to frequency and sound level intensity, the cocktail party effect, sensitivity to the change in decibels, A-weighting of decibels, etc.

In the discussion of acoustic spaces, five general criteria are listed: (a) sufficient loudness, (b) good distribution of sound everywhere, (c) adequate clarity, (d) absence of echoes, and (e) absence of extraneous sounds. A simple but illuminating discussion of direct and indirect sound paths follows, with explanations of reverberation time and the effect of varying absorption coefficients of surrounding surfaces. Apfel describes the room as a musical instrument complete with resonance modes, discusses the effect of curved surfaces, and he includes several case studies (e.g., the Kresge Auditorium at MIT, Teatro y Centro de Arte in Guyaquil, Ecuador, Jones Hall in Houston, Texas). The problem of designing a multi-purpose hall which can function as an opera house and theater and concert hall is treated with a description of how the interior architecture can be varied to meet the function. Apfel also stresses the importance of quiet HVAC operation and installation of a proper sound amplification system. He also enumerates the reasons for quiet spaces; namely, protection against hearing loss, speech interference, and annoyance. Construction techniques promoting acoustical and vibrational isolation are described, complete with tables on transmission loss (TL) and sound transmission class (STC) for common building elements, and noise criteria (NC) ratings for acceptable background levels in a room according to its usage. It would be useful to include a plot of NC curves versus octave-band center frequency in this text. There is also a discussion of classroom acoustics (after all, the modern science of architectural acoustics began over a century ago with W. C. Sabine's dealing with an outrageously echoic Harvard lecture hall!). Outdoor acoustic effects are not forgotten—building layout can generate echoes between adjacent structures, foliage constitute ineffective noise barriers but berms can be effective, and window placement should be configured away from noise sources and positioned to avoid cross talk transmission from other windows. Four appendices follow the main text. Appendix A contains the sound absorption data for common building materials and furnishings (including members of an audience), and Appendix B lists TL loss data for common building elements, Appendix C is one that should be reviewed almost at the onset of an acoustics course for architectural students, for it constitutes a very brief survey of simple mathematical techniques for dealing with logarithms and decibels. Appendix D should not be skipped, for it deals with transmission through simple and composite walls or floor–ceiling construction, complete with examples (one example shows how a relatively small hole can greatly deteriorate the effectiveness of an entire wall in insulating sound). The only glaring error in the entire book (aside from a couple of obvious typos) appears on the sixth line of page 99, where an equation should read:

$$\mathrm{TL} = 20 = 10 \log 1/\tau_1$$

instead of

$$\mathrm{TL} = 20 = 1/\tau_1 .$$

It should be noted that for each book purchased directly from Apple Enterprise Press, $5.00 will be donated to the Acoustical Society Foundation. For sales via other parties (e.g., bookstores and eventually www.amazon.com), there will be a proportionally smaller amount, depending on the net return to the publisher.

In summation, this is a great text for use in courses for non-acousticians. And in an era of $80-and-up textbooks, this paperback is a downright steal.

N.B.: We have just learned that the error on page 99 will be found only in those copies from the first printing, as it has been corrected in subsequent printings.

DANIEL R. RAICHEL
CUNY Graduate School
Mechanical Engineering Department
City College of New York
New York, New York 10031

REVIEWS OF ACOUSTICAL PATENTS

Daniel W. Martin
7349 Clough Pike, Cincinnati, Ohio 45244

The purpose of these acoustical patent reviews is to provide enough information for a Journal reader to decide whether to seek more information from the patent itself. Any opinions expressed here are those of reviewers as individuals and are not legal opinions. Printed copies of United States Patents may be ordered at $3.00 each from the Commissioner of Patents and Trademarks, Washington, DC 20231.

Reviewers for this issue:

GEORGE L. AUGSPURGER, *Perception Incorporated, Box 39536, Los Angeles, California 90039*
HARVEY H. HUBBARD, *325 Charleston Way, Newport News, Virginia 23606*
SAMUEL F. LYBARGER, *101 Oakwood Road, McMurray, Pennsylvania 15317*
D. LLOYD RICE, *11222 Flatiron Drive, Lafayette, Colorado 80026*
ERIC E. UNGAR, *Acentech Incorporated, 33 Moulton Street, Cambridge, Massachusetts 02138*

5,708,191

43.35.Zc ULTRASONIC FLUID DENSITOMETRY AND DENSITOMETER

Margaret S. Greenwood and Jason C. Lail, assignors to Battelle Memorial Institute
13 January 1998 (Class 73/32 A); filed 5 April 1996

An ultrasonic fluid densitometer has a wedge partially immersed in fluid. The material of the wedge is selected to have an acoustic impedance near that of the fluid. Ultrasonic transducers transmit and receive ultrasonic

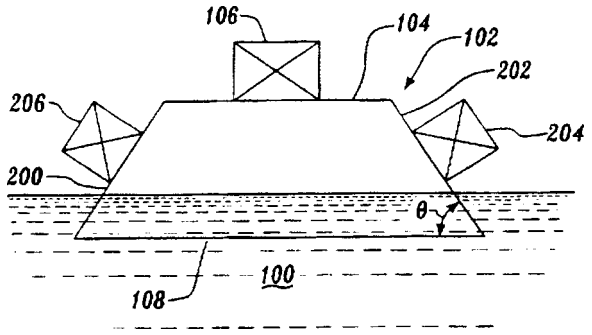

signals internally reflected within the wedge. The density of the fluid is determined from the measured reflection of ultrasound at the wedge-fluid interface.—DWM

5,682,434

43.38.Ja WEARABLE AUDIO SYSTEM WITH ENHANCED PERFORMANCE

James H. Boyden, assignor to Interval Research Corporation
28 October 1997 (Class 381/187); filed 7 June 1995

You can enjoy your very own personal stereo system without wearing earphones. Sound pressure produced by transducers in cavity **50** is conducted through tubes **56** and **58** to suitable locations near the wearer's ears. Additional tweeters **60** and **62** reproduce left and right high-frequency information. The chamber and tubes form a Helmholtz resonator which,

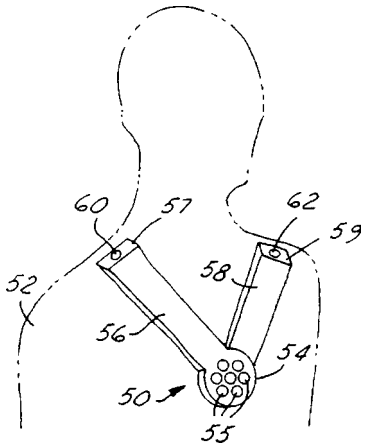

through suitable geometry, can have a resonance frequency of around 150 Hz, and presumably produce constant amplitude at the user's ears below this frequency, ''...consistent with using a transducer or array with sufficient displacement to yield desired output acoustic pressures.''—GLA

5,684,884

43.38.Fx PIEZOELECTRIC LOUDSPEAKER AND A METHOD FOR MANUFACTURING THE SAME

Chitose Nakaya *et al.*, assignors to Hitachi Metals, Ltd.
4 November 1997 (Class 381/190); filed in Japan 31 May 1994

An improved piezoelectric loudspeaker is made up of a sheet in which multiple piezoelectric devices are arranged in an organic material, an impedance matching support layer that maintains desired curvature, and a support frame. The patent includes numerous illustrations and response graphs—GLA

5,710,395

43.38.Ja HELMHOLTZ RESONATOR LOUDSPEAKER

Paul Wilke, Vienna, Austria
20 January 1998 (Class 181/153); filed 28 March 1995

If you had hoped to make your fortune by converting unsold barbecue kettles into loudspeaker enclosures, the idea is probably covered in this patent. Among other goals, the novel shape provides ''...a speaker enclosure

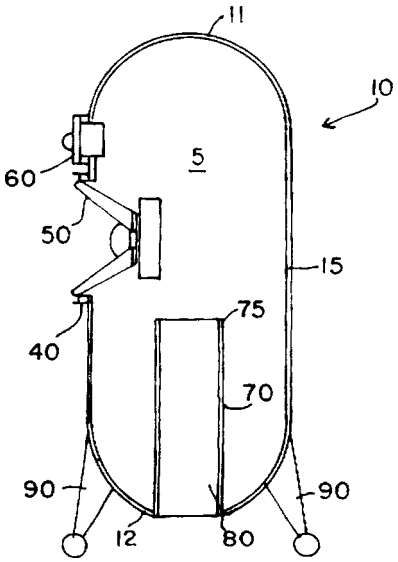

fabricated from a thin material without requiring the use of additional sound absorbing material.''—GLA

5,715,322

43.38.Ja THROAT DEVICE INTERCONNECTING A PLURALITY OF DRIVE UNITS AND A HORN

Tsutomu Yoshioka *et al.*, assignors to TOA Corporation
3 February 1998 (Class 381/182); filed in Japan 25 August 1992

In high-power public address systems it is sometimes desirable to couple two or more high-frequency drivers to a single horn. Conventional ''Y'' or ''T'' couplers may introduce unwanted high-frequency rolloff because of unequal path lengths and resulting phase interference. Most such

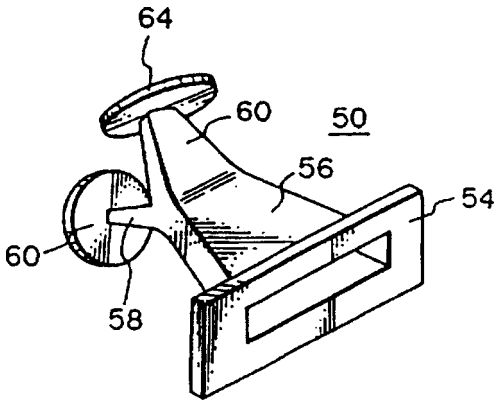

devices couple circular driver apertures to a circular horn throat. However, the throat of a constant-directivity horn might just as well be a narrow rectangle, which can be split into two even narrower slits, allowing phase-coherent summation through the full bandwidth of the drivers.—GLA

5,710,752

43.38.Ne APPARATUS USING ONE OPTICAL SENSOR TO RECOVER AUDIO INFORMATION FROM ANALOG AND DIGITAL SOUNDTRACK CARRIED ON MOTION PICTURE FILM

Charles Gordon Seagrave *et al.*, assignors to Dolby Laboratories Licensing Corporation
20 January 1998 (Class 369/97); filed 7 June 1995

This is the latest continuation-in-part of four earlier filings dating back to February 1991. The patent document is clearly written and describes Dolby's analog/digital film recording system in detail.—GLA

5,692,042

43.38.Si SPEAKERPHONE CONTROLLED BY A COMPARATOR WITH HYSTERESIS

Frank Sacca, assignor to Casio PhoneMate, Incorporated
25 November 1997 (Class 379/387); filed 31 May 1995

Speakerphones try to maintain the illusion of full duplex communication while controlling send and receive gains in a manner that prevents acoustic feedback. The speakerphone utilizes inexpensive analog circuitry and a standard telephone line interface. The patent document includes a good comparison of other schemes and clearly explains the operation of the design.—GLA

5,706,344

43.38.Si ACOUSTIC ECHO CANCELLATION IN AN INTEGRATED AUDIO AND TELECOMMUNICATION SYSTEM

Brian M. Finn, assignor to Digisonix, Incorporated
6 January 1998 (Class 379/410); filed 29 March 1996

Consider the problems inherent in a dual-location conference. At each location there is a speaker's podium with a microphone connected to the local speech amplification system. But each amplification system must also reproduce speech from the other location. The two systems are typically connected via a dial-up telephone link. The patent describes a ''robust'' echo cancellation scheme employing a modified FIR LMS filter.—GLA

5,680,464

43.38.Vk SOUND FIELD CONTROLLING DEVICE

Masayuki Iwamatsu, assignor to Yamaha Corporation
21 October 1997 (Class 381/18); filed in Japan 30 March 1995

The device is intended for use in home theaters. Sound tracks encoded in various Dolby formats are processed to provide the kind of spacious, enveloping surround sound that would be heard in an exhibition theater. Four surround loudspeakers are required for playback and each is driven from its own synthesized surround channel.—GLA

5,692,050

43.38.Vk METHOD AND APPARATUS FOR SPATIALLY ENHANCING STEREO AND MONOPHONIC SIGNALS

Timothy J. Hawks, assignor to Binaura Corporation
25 November 1997 (Class 381/1); filed 15 June 1995

The system encompasses a broad range of features intended to enhance stereophonic signals, to transform mono into enhanced pseudo-stereo, and various combinations thereof. In all cases, monophonic compatibility is maintained. The patent document includes considerable mathematics and 20 circuit diagrams. More than 60 previous patents are referenced.—GLA

5,703,955

43.38.Vk METHOD AND APPARATUS FOR MULTICHANNEL SOUND REPRODUCTION

Peter Fels *et al.*, assignors to Deutsche Telekom AG
30 December 1997 (Class 381/18); filed in Germany 9 November 1994

Even with five discrete channels available for stereophonic recording and reproduction, seating locations for good listening may be limited to a relatively small area, depending upon one's definition of good listening. To what extent can everyone in the audience be presented with the same overall stereo sound stage while maintaining accurate localization of individual

sound sources? This is a method of processing and combining signals to achieve ''... a higher proportion in the overall room size for acoustic/visual use.'' The patent document is short and interesting.—GLA

5,710,818

43.38.Vk APPARATUS FOR EXPANDING AND CONTROLLING SOUND FIELDS

Toshitaka Yamato *et al.*, assignors to Fujitsu Ten Limited
20 January 1998 (Class 381/1); filed in Japan 1 November 1990

This is yet another method for correcting the asymmetric geometry of listener and loudspeakers in an automobile. Numerous charts and illustrations help to explain how the goal is accomplished and why the apparatus is an improvement.—GLA

5,687,948

43.40.Tm VIBRATION ISOLATION SYSTEM INCLUDING A PASSIVE TUNED VIBRATION ABSORBER

Gerald P. Whiteford and Paul T. Herbst, assignors to Lord Corporation
18 November 1997 (Class 248/635); filed 26 September 1995

This patent describes several arrangements in which an elastomeric mount is combined with one or more tuned vibration absorbers, with each absorber consisting of a mass and an elastomeric resilient element. The absorbers are to be tuned so that their natural frequencies are between about 0.90 and 0.99 times the machinery's dominant operating frequency, and are intended at this operating frequency to increase the impedance against which the isolator acts, thus increasing its isolation effectiveness.—EEU

5,684,249

43.40.Yq GROUND VIBRATION PROPERTIES DETECTION METHOD AND EQUIPMENT THEREOF

Yorimasa Abe *et al.*, assignors to Fe Lime Industry Corporation and Western Japan Geography Survey Company
4 November 1997 (Class 73/146); filed in Japan 15 November 1995

This patent relates to the measurement of the vibrations induced in road surfaces by loads that simulate those associated with vehicle passages. A device is described for dropping selected heavy weights from various heights onto the road surface, either one time or repetitively at selected repetition rates. A cushioning arrangement between the impacting weight and the road is used to reduce the noise, to protect the road surface, and to ensure that the weight impacts on a flat surface rather than on a potentially irregular road surface. The resulting road surface vibrations are sensed conventionally by accelerometers placed at various distances from the impact point and are evaluated by means of Japanese standard vibration level recorders.—EEU

5,619,179

43.50.Fe METHOD AND APPARATUS FOR ENHANCING ELECTRONICALLY GENERATED SOUND

Blaine Smith, assignor to Sharper Image Corporation
8 April 1997 (Class 340/384.72); filed 31 October 1994

A personal sound masking device includes independent noise generators for right and left channels. A variety of effects can then be produced by controlling clock rates and processing the two signals.—GLA

5,676,300

43.50.Gf SOUND REDUCTION APPARATUS FOR PNEUMATIC NAILING MACHINE

Takashi Nakazato and Masaru Sekita, assignors to Max Co.
14 October 1997 (Class 227/130); filed in Japan 7 November 1994

This patent relates to the control of noise from the exhaust air of nailing machines. The exhaust air is ducted into an expansion chamber from which it flows to the atmosphere through a number of slits. The detailed geometry of the slits and their enlarged area results in a lower velocity and less turbulent exhaust flow which in turn generates lower exhaust flow noise levels.—HHH

5,680,889

43.50.Gf LOW NOISE BALL VALVE ASSEMBLY

Henry W. Boger, assignor to Dresser Industries, Incorporated
28 October 1997 (Class 137/625.32); filed 23 September 1996

This patent relates to the control of noise in ball valves used for the throttling of compressible fluids. The rotable ball portion of the valve is configured in such a manner that the fluid flows through a large number of smaller passages, thus producing aerodynamic noise having relatively high frequencies. Since these high frequencies are not effective in exciting structural vibrations in the downstream piping system, less associated noise is radiated to the surrounding areas.—HHH

5,696,360

43.50.Gf SOUND ABSORBING MOTOR MOUNT FOR ELECTRICAL ACTUATING DRIVES IN MOTOR VEHICLES

Peter Tiemeyer, assignor to Siemens Aktiengesellschaft
9 December 1997 (Class 181/205); filed in European Patent Office 8 August 1994

This patent applies to the sound-absorbing mounting of electrical actuating devices in motor vehicles. Elastic sound-absorbing intermediate layers, which are subjected substantially to tensile stresses, are coupled be-

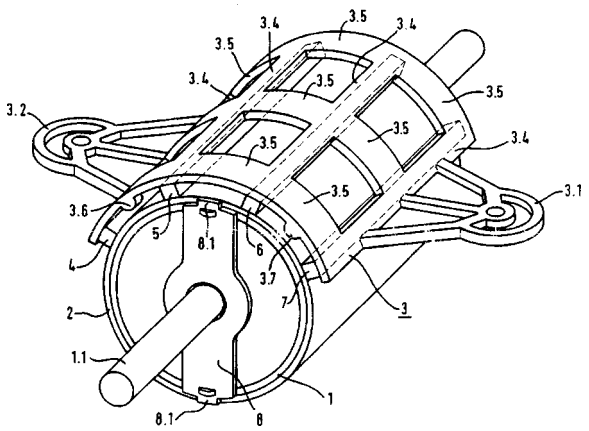

tween the mounting part and the carrier part. These axial direction members, which run essentially like webs, are manufactured as injection molded plastic parts attached to either the mounting or carrier parts.—HHH

5,702,231

43.50.Gf APPARATUS AND METHOD FOR REDUCING NOISE EMISSIONS FROM A GAS TURBINE ENGINE INLET

Robert P. Dougherty, assignor to The Boeing Company
30 December 1997 (Class 415/119); filed 9 August 1996

This patent relates to the control of fan noise emissions in the forward direction during takeoff and landing of turbofan engine powered airplanes. Beneficial changes in the noise radiation patterns are said to occur by means of selective and asymmetric application of passive acoustical linings (honeycomb with perforated surface sheets) in the region of the forward extremities of the nacelle.—HHH

5,709,440

43.50.Gf TRACK NOISE SUPPRESSION

Gaetan Lecours, assignor to Bombardier, Inc., Montreal, Canada
20 January 1998 (Class 305/178); filed 1 February 1995

This patent relates to the control of noise from tracked vehicles such as snowmobiles. It is said that unpleasant pure tone noise can be greatly reduced by ensuring that the driving lugs of the endless belt track of reinforced rubber are offset transversely, and that the ground engaging lugs have a variable longitudinal spacing.—HHH

5,713,161

43.50.Gf NOISE PROTECTION SCREEN

Arend Johan Veldhoen, assignor to Durisol Materials Limited
3 February 1998 (Class 52/144); filed in The Netherlands 4 February 1994

This patent relates to the use of free-standing walls for noise shielding, as, for instance, along roadways. Absorbent materials and tuned resonators are included to give noise reduction over a range of frequencies. A unique

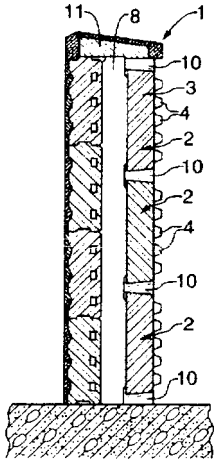

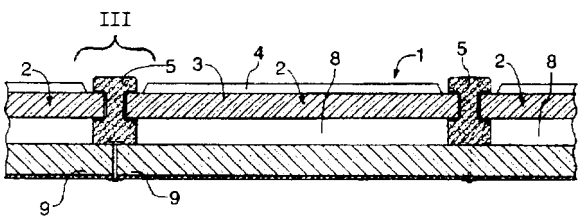

feature of construction is the use of wood fiber concrete elements for absorption.—HHH

5,707,338

43.64.Ha STAPES VIBRATOR

Theodore P. Adams *et al.*, assignors to St. Croix Medical, Incorporated
13 January 1998 (Class 600/25); filed 2 August 1996

The patent shows a piezoelectric transducer mounted between the neck and the footplate of the stapes to vibrate the oval window or perilymph of the cochlea. An electronic unit supplies the electrical input signal. The arrangement is said to be advantageous for middle-ear implantable systems.—SFL

5,729,612

43.66.Qp METHOD AND APPARATUS FOR MEASURING HEAD-RELATED TRANSFER FUNCTIONS

Jonathan Stuart Abel and Scott Haines Foster, assignors to Aureal Semiconductor, Incorporated
17 March 1998 (Class 381/56); filed 5 August 1994

This method and apparatus is intended to derive head-related transfer functions specific to the particular listener involved (depending upon individual anatomical properties). Transducer **210** generates a sound field in response to a test signal from control **100**. Transducers **309** in the left ear and **310** in the right ear respond to the sound field by sending signals to control **100**. Position sensors **220** at or near transducer **210**, and **320** mounted on the test subject's head, provide signals to control **100** to estab-

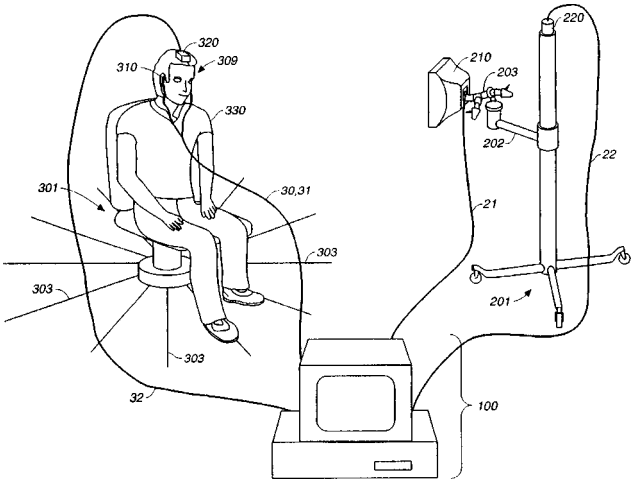

lish the relative positions. The patent shows a flow diagram of a process for deriving head-related transfer functions that are said to eliminate the need for anechoic surroundings, to reduce effects of test subject movements during measurements, to eliminate inaccuracies caused by acoustic effects in the ear canal, and to eliminate inaccuracies introduced by transducer acoustical properties. Six of the referenced publications are from this *Journal* over the time period from 1977–1992.—DWM

5,717,770

43.66.Ts PROGRAMMABLE HEARING AID WITH FUZZY LOGIC CONTROL OF TRANSMISSION CHARACTERISTICS

Oliver Weinfurtner, assignor to Siemens Audiologische Technik GmbH
10 February 1998 (Class 381/68.2); filed in European Patent Office 23 March 1994

The use of a fuzzy logic controller in modern, programmable hearing aids is said to improve the signal processing functions, particularly for adapting the dynamic range of the input signal to the generally restricted

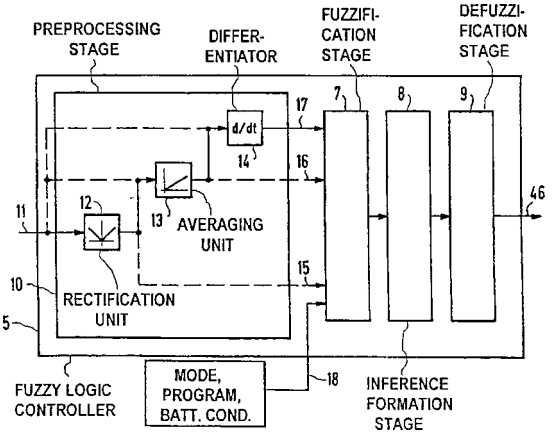

dynamic range of the hearing impaired person. Circuits for producing the desired processing are shown.—SFL

5,717,771

43.66.Ts PROGRAMMABLE HEARING AID MEANS WORN IN THE AUDITORY CANAL

Joseph Sauer *et al.*, assignors to Siemens Audiologische Technik GmbH
10 February 1998 (Class 381/68.6); filed in Germany 1 March 1995

The patent shows an electrical line connected to a programmable hearing aid worn in the auditory canal. At the ear canal entrance the outer end of

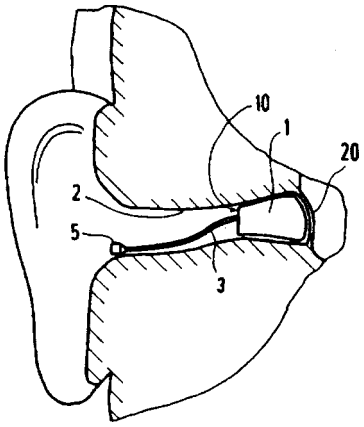

the line is provided with a connector **5** to which signals from programming equipment can be transmitted with the hearing aid in place.—SFL

5,718,001

43.66.Vt PROTECTIVE EAR COVERING DEVICE

Jacquelin E. Wright, Alexandria, VA
17 February 1998 (Class 2/209); filed 24 May 1996

The patent shows a pair of ear coverings joined by a hollow strap under the chin. A drawstring with its ends under the chin permits tightening the fit of the coverings as desired.—SFL

5,718,002

43.66.Vt HEARING PROTECTIVE EYEWEAR

Ronald M. Pavlac, Eagan, MN
17 February 1998 (Class 2/423); filed 7 January 1997

The patent shows a pair of protective safety glasses with extensions added to cover the ears partially.—SFL

5,704,000

43.72.Ar ROBUST PITCH ESTIMATION METHOD AND DEVICE FOR TELEPHONE SPEECH

Kumar Swaminathan and Murthy Vemuganti, assignors to Hughes Electronics
30 December 1997 (Class 395/2.16); filed 10 November 1994

This LP residual autocorrelation pitch tracker computes the autocorrelation of the LP residual for speech segments of 7.5-ms duration. The pitch candidates from each segment are then combined using a smoothing process based on a distortion minimization technique.—DLR

5,710,865

43.72.Ar METHOD OF BOUNDARY ESTIMATION FOR VOICE RECOGNITION AND VOICE RECOGNITION DEVICE

Yoshiharu Abe, assignor to Mitsubishi Denki Kabushiki Kaisha
20 January 1998 (Class 395/2.57); filed in Japan 22 March 1994

This voice endpoint detection system uses hidden Markov model (HMM) techniques to evaluate the probability that a beginning or ending voice endpoint has occurred during an analysis interval. Specific state sequences in the HMM are trained to match the speech endpoints for specific utterance initial and final phonemes.—DLR

5,706,394

43.72.Dv TELECOMMUNICATIONS SPEECH SIGNAL IMPROVEMENT BY REDUCTION OF RESIDUAL NOISE

Woodson Dale Wynn, assignor to AT&T
6 January 1998 (Class 395/2.28); filed 30 November 1993

This noise reducer operates on line spectral pair (LSP) speech data to reduce the effect of background noise on the transmitted speech signal. A noise spectrum is accumulated by averaging nonspeech frames identified by

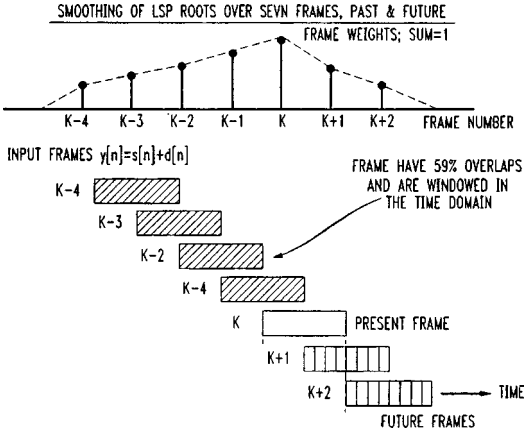

voice detection. The LSP coefficients are then time smoothed and the resulting spectra are further refined based on knowledge of the background spectrum.—DLR

5,710,862

43.72.Dv METHOD AND APPARATUS FOR REDUCING AN UNDESIRABLE CHARACTERISTIC OF A SPECTRAL ESTIMATE OF A NOISE SIGNAL BETWEEN OCCURRENCES OF VOICE SIGNALS

Steven Adam Urbanski, assignor to Motorola, Incorporated
20 January 1998 (Class 395/2.35); filed 30 June 1993

This speech noise reduction system includes a speech activity detector and averages the signal spectrum during nonspeech periods. Spectral subtraction is performed using the average spectrum to modify the transmitted signal during nonspeech periods.—DLR

5,699,480

43.72.Ew APPARATUS FOR IMPROVING DISTURBED SPEECH SIGNALS

Rainer Martin, assignor to Siemens Aktiengesellschaft
16 December 1997 (Class 395/2.14); filed in Germany 7 July 1995

When a patient is placed into the magnetic field of a tomography machine, a microphone allowing patient-to-doctor communication is said to pick up large amounts of disturbing noise, presumably mostly low-frequency noise. In this apparatus, two independent microphone channels

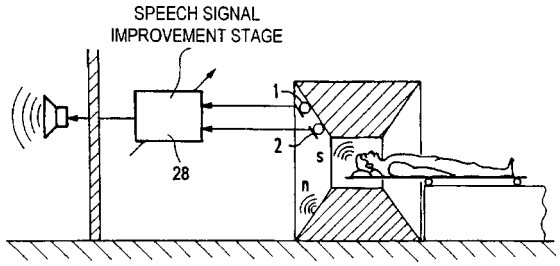

are divided into three bands, with each band being separately processed. A low band is high-pass filtered. A mid-band is weighted so as to be particularly sensitive to speech pauses. A high band is damped during pauses. The signals are recombined to produce clean output speech.—DLR

5,692,098

43.72.Gy REAL-TIME MOZER PHASE RECODING USING A NEURAL-NETWORK FOR SPEECH COMPRESSION

Michael Thomas Kurdziel, assignor to Harris
25 November 1997 (Class 395/2.11); filed 30 March 1995

This patent uses a neural network to implement the Mozer phase adjustment method of speech compression as patented in the early 1980s. The input speech signal is whitened to remove spectral tilt, and spectral magnitudes are determined by Fourier transform. A neural net performs a Mozer phase encoding on the magnitude spectrum. After an inverse transform, half of the signal has values near zero and need not be transmitted.—DLR

5,699,479

43.72.Gy TONALITY FOR PERCEPTUAL AUDIO COMPRESSION BASED ON LOUDNESS UNCERTAINTY

Jonathan Brandon Allen *et al.*, assignors to Lucent Technologies, Incorporated
16 December 1997 (Class 395/2.14); filed 6 February 1995

This speech compression system makes use of some new findings in the psychoacoustics of hearing to compute a better masking function for the perceptual weighting used to reduce the impact of quantization noise. New

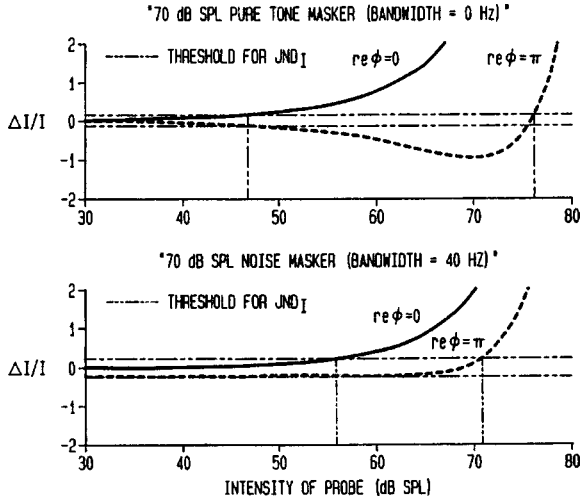

studies have shown that masking levels are a function of the loudness uncertainty. This system uses an amplitude variation measure to approximate the desired masking levels.—DLR

5,701,390

43.72.Gy SYNTHESIS OF MBE-BASED CODED SPEECH USING REGENERATED PHASE INFORMATION

Daniel W. Griffin and John C. Hardwick, assignors to Digital Voice Systems, Incorporated
23 December 1997 (Class 395/2.15); filed 22 February 1995

In a multiband excitation (MBE) vocoder, the speech signal is filtered into bands and voiced/unvoiced decisions are made independently for each band. This patent presents a MBE vocoder in which special attention is given to maintaining the correct phase of harmonic components within those bands selected as voiced.—DLR

5,704,001

43.72.Gy SENSITIVITY WEIGHTED VECTOR QUANTIZATION OF LINE SPECTRAL PAIR FREQUENCIES

William R. Gardner, assignor to QUALCOMM, Incorporated
30 December 1997 (Class 395/2.28); filed 4 August 1994

In this line spectral pair (LSP) vocoder, linear prediction vectors are first computed for each speech frame. The LP coefficients are converted to LSPs in a way that provides a sensitivity measure for each pair. The LSPs are then quantized using the sensitivity measures to minimize the overall spectral distortion.—DLR

5,704,002

43.72.Gy PROCESS AND DEVICE FOR MINIMIZING AN ERROR IN A SPEECH SIGNAL USING A RESIDUE SIGNAL AND A SYNTHESIZED EXCITATION SIGNAL

Dominique Massaloux, assignor to France Telecom Etablissement
30 December 1997 (Class 395/2.29); filed in France 12 March 1993

A large class of speech vocoders uses a long-term predictor (LTP) typically consisting of from one to three predictor coefficients applied at time indices offset by a long-term delay coefficient. This device speeds up the process of finding optimal LTP coefficients through the use of a predefined LTP dictionary having a roughly logarithmic rate of change of delay values.—DLR

5,706,392

43.72.Gy PERCEPTUAL SPEECH CODER AND METHOD

Randy G. Goldberg and James L. Flanagan, assignors to Rutgers, The State University of New Jersey
6 January 1998 (Class 395/2.19); filed 1 June 1995

This multiband excitation (MBE) speech vocoder uses the masking characteristics of human auditory perception to limit the bandwidth required for high-quality reproduction. Following MBE analysis, coded frames are

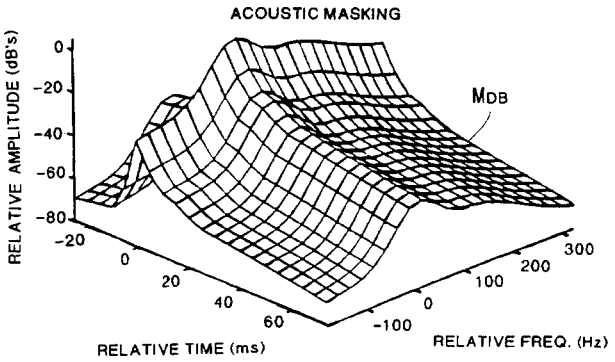

passed to a masker module to determine whether any or all parts of the frame are inaudible due to masking. If so, the bits which would be transmitted for those portions are discarded.—DLR

5,704,006

43.72.Ja METHOD FOR PROCESSING SPEECH SIGNAL USING SUB-CONVERTING FUNCTIONS AND A WEIGHTING FUNCTION TO PRODUCE SYNTHESIZED SPEECH

Naoto Iwahashi, assignor to Sony Corporation
30 December 1997 (Class 395/2.68); filed in Japan 13 September 1994

This speech synthesis system is based on the analysis of human speech such that the output quality is improved and a particular voice pattern can be produced. The analysis consists of the determination of a set of weightings in the form of radial basis functions which may be used to map the linear

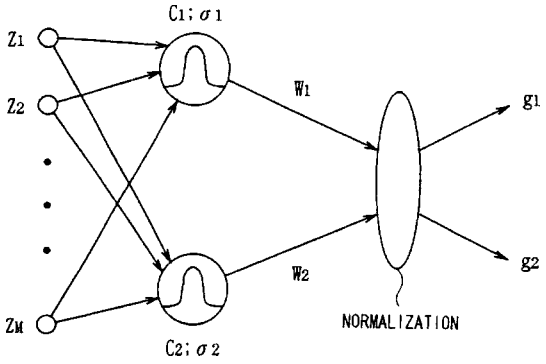

prediction spectral vectors from one speaker's configuration to that of another. Mapping functions may be obtained with a small amount of training speech, but improve when more training is available.—DLR

5,689,618

43.72.Kb ADVANCED TOOLS FOR SPEECH SYNCHRONIZED ANIMATION

Elon Gasper and Richard Wesley, assignors to Bright Star Technology, Incorporated
18 November 1997 (Class 395/2.85); filed 19 February 1991

This tool for generating lip-synchronized video displays uses a simple table-lookup approach to associate lip shapes with speech sounds. The system can create animated figures which can be used as is or as a guide in

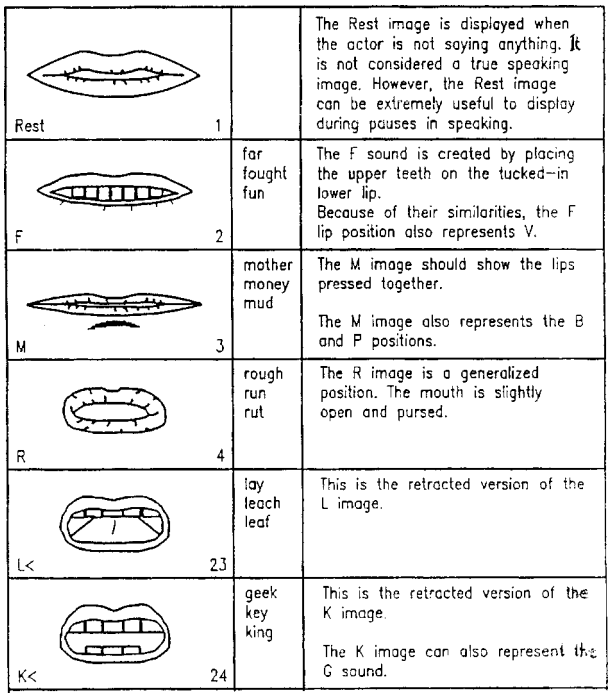

overlaying other footage of real actors, etc. A control language gives the sequence designer considerable flexibility in constructing images lip synced to a given script. The figure shows a few examples.—DLR

5,696,819

43.72.Kb SPEECH COMMUNICATION APPARATUS

Shinichi Suizu and Yuji Umemoto, assignors to Kabushiki Kaisha Toshiba
9 December 1997 (Class 379/390); filed in Japan 29 January 1993

This telephone speech enhancer includes both a typical echo canceller circuit and a center clipping stage to remove any remaining low-level echo signal. The center clipping circuit is disabled under certain conditions depending on the setting of a receiver volume control and the received and transmitted channel gain settings.—DLR

5,704,004

43.72.Ne APPARATUS AND METHOD FOR NORMALIZING AND CATEGORIZING LINEAR PREDICTION CODE VECTORS USING BAYESIAN CATEGORIZATION TECHNIQUE

Tze Fen Li *et al.*, assignors to Industrial Technology Research Institute, Taiwan
30 December 1997 (Class 395/2.52); filed 1 December 1993

This patent discloses the comparator portion of a speech recognition system based on syllable pattern matching. The LP cepstral coefficients for a number of frames covering a syllable are reduced by time normalization to a set of standard syllable features. A probability-based comparison between

standard and test features yields the syllable classification for the speech segment.—DLR

5,704,005

43.72.Ne SPEECH RECOGNITION APPARATUS AND WORD DICTIONARY THEREFOR

Hitoshi Iwamida, assignor to Fujitsu Limited
30 December 1997 (Class 395/2.63); filed in Japan 28 January 1994

The patent describes more or less typical phonetic speech recognition systems except that the basic recognition unit is not phoneme sized but a phoneme sequence called a ''subword.'' The word dictionary gives the ''spelling'' of each word in subwords and includes a weighting value for the importance of each subword match to the overall word matching score.—DLR

5,710,864

43.72.Ne SYSTEMS, METHODS AND ARTICLES OF MANUFACTURE FOR IMPROVING RECOGNITION CONFIDENCE IN HYPOTHESIZED KEYWORDS

Biing-Hwang Juang *et al.*, assignors to Lucent Technologies, Incorporated
20 January 1998 (Class 395/2.47); filed 29 December 1994

In this keyword spotter system, the test input utterance is matched against a variety of word models, including the target words and a number of closely competing nontarget words. Relative scores between target words and competing false targets indicate when a keyword has been spoken.—DLR

5,723,804

43.75.Gh ELECTRIC MONOPHONIC/ STEREOPHONIC STRINGED RESONATOR INSTRUMENT

D. Michael Replogle, assignor to Gibson Guitar Corporation
3 March 1998 (Class 84/726); filed 10 July 1996

Some acoustic guitars (DOBRO® and NATIONAL) have resonator assemblies mounted in the body which mechanically amplify the sound produced when the strings are played, and which add distinctive timbral characteristics to the tone. In this patent, in addition to a string vibration pickup, there is a vibration transducer mounted on the resonator. The pickup and resonator outputs are separately amplified and either mixed for a monophonic output channel or supplied separately to stereophonic output channels.—DWM

5,723,805

43.75.Gh VIBRATION TRANSDUCER DEVICE FOR STRINGED MUSICAL INSTRUMENTS

Robert J. Lacombe, Ville Ste-Catherine, PQ, Canada
3 March 1998 (Class 84/727); filed 12 July 1996

Under and separate from metallic strings **30** of this guitar are three magnetic field generating bars **32**, **34**, and **36**. Each bar contains cylindrical magnets alternately polarized to create for each string a separate magnetic

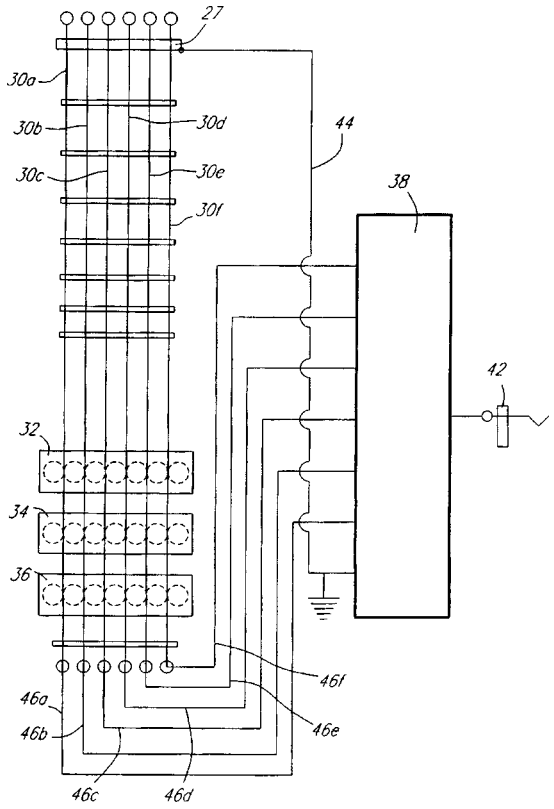

field within which to vibrate, generating electric potentials in each string for separate amplification or other electronic processing in mixer **38**.—DWM

5,717,155

43.75.Tv SYNTHESIZER DETECTING PITCH AND PLUCKING POINT OF STRINGED INSTRUMENT TO GENERATE TONES

Andreas Szalay, assignor to Yamaha Corporation
10 February 1998 (Class 84/723); filed in Japan 16 June 1995

Electronic synthesizers are often connected to electric guitar outputs for generating accompanying synthesized tones under the control of the output from the guitar pickups. The pickup output signal is typically detected by the synthesizer for frequency coordination of the guitar tone with the synthesizer tone. In this patent the plucking point is also detected ''in

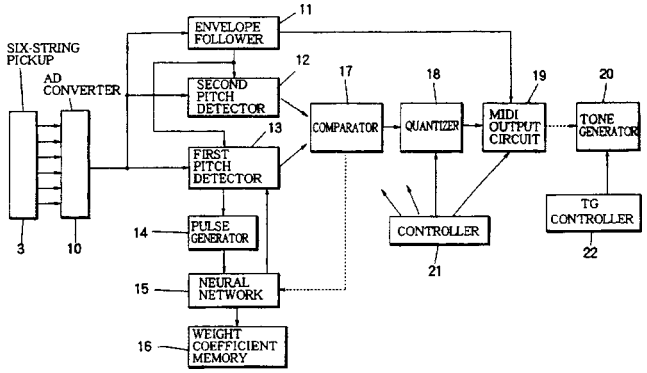

order to control a timbre in response to the plucking point.'' The plucking point is detected by having two frequency detectors operating at different speed with an additional detector processing the waveform signal ''to measure a time interval between a pair of the peaks so as to detect a plucking point.''—DWM

5,726,374

43.75.Tv KEYBOARD ELECTRONIC MUSICAL INSTRUMENT WITH GUITAR EMULATION FUNCTION

Paul B. Vandervoort, Reno, NV
10 March 1998 (Class 84/638); filed 21 November 1995

This polyphonic electronic keyboard musical instrument triggers arpeggio chords to simulate a strumming guitar sound. Signals resulting from chord or key selection are triggered sequentially or alternately at a selectable rate. Two arpeggiated chords of alternating direction may be produced ''as a result of one triggering device cycle [cycling] from one state to the other and back again.''—DWM

5,717,769

43.80.Qf ADAPTER FOR REVERSIBLE CONVERSION OF STANDARD STETHOSCOPES TO MULTIMEDIA AND TELEMEDICINE READY STETHOSCOPES

Christopher A. Williams, Wallingford, PA
10 February 1998 (Class 381/67); filed 10 February 1995

The patent shows a T-shaped adapter that is placed in the tube from the chest piece to the binaurals of a stethoscope to allow it to function in the usual manner. A microphone is placed in the bottom leg of the T to provide an electrical signal for electronic storage, etc.—SFL

Measurements of macrosonic standing waves in oscillating closed cavities[a)]

Christopher C. Lawrenson, Bart Lipkens, Timothy S. Lucas, David K. Perkins, and Thomas W. Van Doren
MacroSonix Corporation, 1570 East Parham Road, Richmond, Virginia 23228

(Received 6 November 1997; revised 30 April 1998; accepted 4 May 1998)

Measurements of macrosonic standing waves in gases in oscillating closed cavities are shown. The strong dependence of the pressure waveform upon cavity shape is demonstrated. This dependence is exploited to provide control of harmonic phase and amplitude, thus avoiding shocks and enabling resonant waveforms to reach macrosonic pressures. The exploitation of this dependence is referred to as resonant macrosonic synthesis (RMS). Power is delivered to the cavity by oscillating it with a linear actuator (entire resonator drive). Standing wave overpressures in excess of 340% of ambient pressure are demonstrated in RMS cavities, compared to maximum overpressures of 17% observed in cylindrical resonators. Ratios of maximum to minimum pressures of 27 were observed in RMS cavities compared to 1.3 for cylinders. Measurements are shown for four axisymmetric cavity shapes: cylinder, cone, horn-cone hybrid, and bulb. Cavities were filled with nitrogen, propane, or refrigerant R-134a (1,1,1,2-tetrafluoroethane). Physical effects which can be observed at macrosonic pressures are demonstrated. These effects include nonlinearly generated dc pressures of 40% of ambient pressure as well as hardening and softening resonance behavior for the same gas but different cavity shape. RMS, together with the entire resonator drive, provides high-power transduction of energy through resonant sound waves and opens a wide range of new commercial applications for macrosonic waves.
[S0001-4966(98)04508-1]

PACS numbers: 43.10.Ln, 43.25.Gf [MAB]

INTRODUCTION

Nonlinear effects in high-amplitude standing waves are strongly dependent on the interior shape of the resonant cavity (resonator). Precise exploitation of this dependency comprises the subject of this paper, and constitutes a new technology referred to as resonant macrosonic synthesis (RMS).

In this paper experimental results for mechanically driven standing waves in gases show peak acoustic overpressures exceeding 340% of ambient pressure, with corresponding peak-to-peak pressures of over 1.37 MPa. At this pressure, calculations using the model developed by Il'inskii *et al.*[1] show Mach numbers exceeding 0.50. By comparison, the literature reports overpressures up to 10% of ambient for mechanically driven standing waves,[2–5] 50% of ambient for thermoacoustically driven standing waves,[6] and approximately 50% of ambient for combustion-driven Helmholtz resonators.[7]

High-amplitude waveform distortion caused by the nonlinear properties of a fluid can lead to the formation of shock waves. Shocks are particularly relevant to the topic of high-amplitude waves since they can impose overpressure limits. (Overpressure is defined as the difference between the wave's peak pressure and the medium's ambient pressure). For finite-amplitude plane traveling waves, the pressure limit imposed by shock formation is known as *acoustic saturation*.[8] Acoustic saturation can occur for waves propagating in a free-field and in waveguides.

Significant experimental and theoretical work has been conducted in the field of finite-amplitude standing acoustic waves in gases. Yet, little experimental attention seems to have been directed towards the question of how large an overpressure can be achieved. A particularly relevant question is whether acoustic saturation will invariably lead to overpressure limits for standing waves in gases, as is the case for plane traveling waves.

Researchers have asserted that overpressure limits do exist. Keller[9] derived the piston displacement amplitude for which shocks will occur in both progressive waves and for standing waves in a tube. Keller states that this limiting amplitude is the same for both progressing and standing sound waves, without distinguishing as to what effect a particular resonator geometry may have on this limiting amplitude. Temkin[10] began a paper on standing shock waves in tubes by stating, ''the amplitudes of propagating and standing acoustic waves of finite strength in fluids have limiting values that are of practical interest.'' Swift[11] stated that standing wave amplitudes in gases are likely to be limited to Mach numbers of less than 0.10 by nonlinear effects. The questions regarding standing wave overpressure limits appear to have remained open.

In this paper we show overpressure amplitudes which far exceed previously predicted and demonstrated values. Consequently, an important relative comparison can be made. In gases, mechanically driven standing waves can now

[a)]''Selected research articles'' are ones chosen occasionally by the Editor-in-Chief that are judged (a) to have a subject of wide acoustical interest, and (b) to be written for understanding by broad acoustical readership.

provide pressures across a domain once offered only by positive displacement and kinetic machines.

A. Resonant macrosonic synthesis

Resonant macrosonic synthesis is defined as the synthesis, or deliberate shaping, of a resonant acoustic waveform by designing the shape of the resonator to give the desired result.[12] In other words, RMS exploits the influence of the shape of the cavity upon the phases and amplitudes of harmonic components of the wave in order to synthesize a desired waveform.

The following terms are used throughout this paper. *Harmonic amplitude* refers to the amplitude of a particular harmonic component of a pressure waveform. *Harmonic phase* refers to the phase of a particular harmonic component of a pressure waveform with respect to the fundamental frequency component of the waveform. The fundamental component of the pressure waveform is referenced as the first harmonic.

A specific resonator shape exhibits a unique modal spectrum. It has been known for some time that the amplitude and phase of harmonics of a standing wave are influenced by the modal spectrum of the cavity in which the standing wave is excited.[13] If each harmonic m of a family of harmonics is frequency coincident with a mode n of a family of modes of the resonator for $m=1$ to ∞, then the resonator is referred to as *consonant*.[14] Conversely, if the harmonics are not frequency coincident with modes, then we refer to the resonator as *dissonant*. Real resonators always have some degree of dissonance due to the dispersive effects of energy dissipation as well as geometric imperfections. Dissonance plays an important role in determining the nonlinear characteristics of a resonator.

High-amplitude sine waves have been desirable for many applications of finite-amplitude standing waves. For example, in the field of thermoacoustics, the additional energy dissipation associated with harmonics reduces system efficiency.[4,15] A further example is the calibration of high-intensity microphones where high-amplitude sine waves with low harmonic generation are sometimes required.[3] Thus, it seems the typical use of dissonance for finite-amplitude standing waves was to eliminate, or at least to minimize, unwanted harmonics. When primary importance is given to reducing harmonic amplitude, then little attention need be given to harmonic phase.

In contrast, harmonics provide the raw materials, or synthesis building blocks, of RMS. By controlling both harmonic phase and amplitude it is possible to synthesize a continuum of extremely high overpressure unshocked waveforms, including sine waves. The factors which make this possible, and which we will demonstrate in this paper, are: (i) shocks occur only when harmonics possess a particular phase and amplitude *relative to the fundamental*, (ii) the relative phase and amplitude of harmonics can be controlled with resonator shape, and (iii) the overpressure at which shock waves and saturation occur is strongly dependent on resonator shape. When combined, these principles lead to the simple concept of RMS. Out of the infinite family of possible synthesized macrosonic waveforms, shocks are merely a special case. Thus, unshocked waveforms can be synthesized at extremely high overpressures.

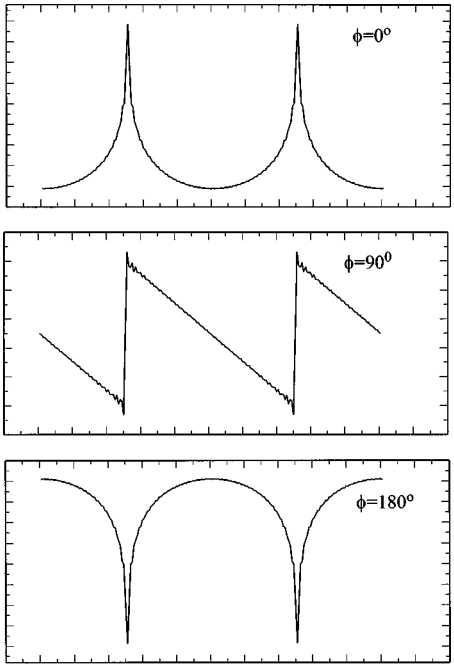

FIG. 1. Waveforms constructed with identical harmonic amplitudes but different phases.

Pressure waves of several different shapes are demonstrated in this paper. As alluded to above, the shape of the wave depends on both the amplitudes and the phases of the harmonics relative to the fundamental. An example of how phase affects the waveform is given by using this equation:

$$p(t)=\sum_{n=0}^{\infty}\frac{1}{n}\cos\left(n\omega_1 t+\frac{\pi\phi_n}{180}\right), \tag{1}$$

where ω_1 is the fundamental frequency (in rad/s) and ϕ_n is the phase angle in degrees of the harmonic n relative to the fundamental. Note that ϕ_1, the phase angle of the fundamental with respect to itself, is always 0 degrees.

Figure 1 shows three waveforms generated by Eq. (1) for the first 40 harmonics. For all three waveforms the harmonic amplitudes $1/n$ are identical and only the phases ϕ_n are changed. For all n such that $\phi_n=\phi$, as ϕ is varied from 0 to 180 degrees an exact sawtooth waveform appears when $\phi=90$ degrees. We refer the $\phi=0$ degrees waveform as a u wave, and the $\phi=180°$ waveform as an m wave. Examples of all of these waveforms, as well as variations of them, are given in the results section.

B. Resonators

With proper design, simple resonator geometries can provide quite dramatic results. In this paper measurements of macrosonic standing waves in rigid closed axisymmetric cavities are shown. Data is presented for a cylinder, a cone, a composite shape with an exponential horn section and a conical section, and a bulb-type shape.

Noncylindrical resonators are, in general, dissonant; modal frequencies are not integer multiples of the fundamen-

tal mode frequency. This is not the case for purely axial modes in a rigid-walled cylindrical cavity with rigid end caps.

Analytical methods for accurately predicting the waveform within an arbitrarily shaped resonator are beyond the scope of this paper. A companion paper provides details regarding a specific analytical approach.[1]

As mentioned previously, when harmonic wavelengths become small with respect to the dimensions of the resonator, it becomes more difficult to provide a desired harmonic phase. This difficulty is compounded by the fact that the modal spectral density increases substantially with frequency. The inability to control harmonic phases at higher frequencies can lead to the formation of what we refer to as *micro-shocks*. The shock front of a micro-shock does not span the entire peak-to-peak pressure of the waveform, as is the case for a sawtooth-type shock wave. Micro-shocks can appear as high-frequency spikes on the pressure waveform. The family of harmonics comprising a micro-shock is a subset of the total number of harmonics present in the resonator. Many micro-shocks can exist simultaneously.

Micro-shock formation may lead to acoustic saturation. Depending on resonator design, micro-shocks can occur at overpressures of a few percent of ambient, or not until overpressures of more than 100%. The specific overpressure at which micro-shocks appear is determined by the geometry of the resonator.

Changing the shape of the resonator also changes the power consumption of the resonator for a given pressure amplitude and working gas, due to changes in thermoviscous boundary layer losses, turbulence, and micro-shocks. Resonator shape changes will also affect the impedance match between the resonator and the motor by which power is delivered.

C. Power delivery system

Hundreds of watts of acoustic power can be put to practical use in RMS resonators. However, high-power mechanical-to-acoustic transduction is not a trivial task.

Consider, for example, the case of a moving piston being coupled to an open end of a cylindrical resonator which is otherwise closed. If the resonator is driven at the lowest axial mode, the dynamic pressure at each end is 180 degrees out of phase. Unless the resonator is rigidly restrained, it will oscillate along its cylindrical axis in response to the dynamic pressure of the standing wave, in which case the standing wave performs work on the resonator. This will reduce the pressure in the cavity. To remedy this the resonator would have to be either rigidly restrained or extremely massive. Since the acoustic pressures can generate hundreds of pounds of dynamic force on the resonator, rigid restraint would be difficult.

These problems are overcome by a drive system referred to as entire resonator drive; the entire closed resonator is oscillated, rather than just having a moving piston or diaphragm at one end.[12,16,17] This approach assumes that the walls of the resonator are rigid and do not flex, so that the entire resonator moves as a rigid body. Unlike the piston case, the motion of the entire resonator makes potentially all of its inner surface area available for transferring power to the gas. This drive technology has been used to deliver more than 700 W to a gas-filled cavity of about 1 l volume. A closed cavity prevents problems associated with sliding or flexing seals and also allows fluids at pressures significantly higher or lower than atmospheric to be used and studied.

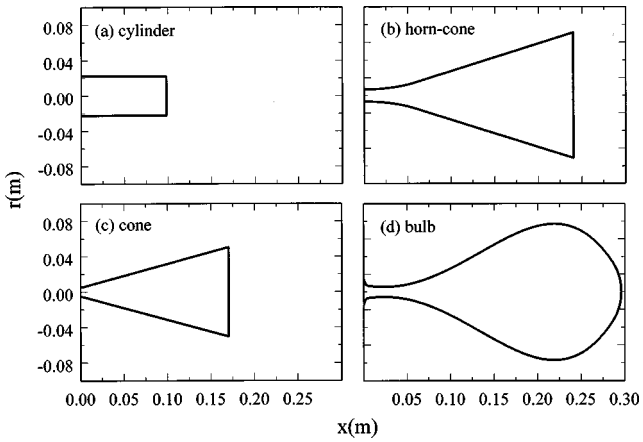

FIG. 2. Interior geometry of resonators: (a) cylinder, (b) horn-cone, (c) cone, and (d) bulb.

D. Commercial motivation

Gas pressures large enough to serve commercial needs have typically been provided by positive-displacement and kinetic machines, such as reciprocating, rotary, screw, and centrifugal pumps and compressors.

The elevated pressure amplitudes enabled by RMS and entire resonator driving can be used to provide practical high-power commercial devices. Currently, working acoustic gas compressors and acoustic liquid pumps have been successfully built and tested. These devices use both the oscillating pressure (with valves) and nonlinearly generated dc pressure gradients (without valves) inside the resonator as pumping mechanisms.

When evaluating commercial applications for resonators it is helpful to calculate a pressure ratio based on the peak-to-peak pressure of the waveform. Pressure ratio is defined by

$$\text{pressure ratio} = \frac{p_{\max}}{p_{\min}},$$

where $p_{\max}$ is the highest absolute pressure and $p_{\min}$ is the lowest absolute pressure measured on the pressure signal at any given point in the resonator. Pressure ratios in excess of 27 have been measured in RMS-designed resonators. This compares to maximum usable pressure ratios we have measured in cylinders, which are on the order of 1.3.

For commercial compressors, pressure ratios from discharge to suction are on the order of 2 to 20. Refrigerator compressors need to achieve pressure ratios of about 10. Commercial air compressors need to achieve pressure ratios of between 3 and 13. Thus, the pressures created using RMS-designed resonators can cover the range of many commercial applications when combined with high-speed valves.

For use in practical devices, not only the peak-to peak pressure amplitude and pressure ratio are important. The shape of the pressure waveform is important for compressor applications because it determines the duration and magnitude of the force for driving flow through the valves. Examples are shown in the following sections of waveform variations that can be created with different resonator geometries.

Pumping efficiency is an important requirement for practical machines. The power consumption mechanisms in acoustic pumps and compressors lead to potentially greater pumping efficiencies when compared to conventional machines because the mechanisms for energy dissipation are quite different and are potentially smaller for acoustic compressors.

I. EXPERIMENTAL APPARATUS AND METHOD

In this section descriptions of resonator geometry, instrumentation, and experimental procedure are given. All experiments were performed for closed resonators filled with a gas of constant quiet-condition density.

A. Resonator geometry

Results are reported for the following resonators: cylinder, cone, horn-cone, and bulb. The interior geometry of each resonator is shown in Fig. 2. All of these resonators were axisymmetric, and their geometries are described by the following equations, where all dimensions are in meters. For the cylinder the radius is

$$r(x)=0.0222 \quad \text{for} \quad 0\leqslant x\leqslant 0.10. \tag{2}$$

For the cone, the radius is

$$r(x)=0.0056+0.2680\cdot x \quad \text{for} \quad 0\leqslant x\leqslant 0.17. \tag{3}$$

The geometry of the horn-cone is

$$\begin{aligned} &r(x)=r_{th}\cosh(mx) \quad \text{for} \quad 0\leqslant x\leqslant 0.06,\\ &r(x)=r_c+\alpha\cdot x \quad \text{for} \quad 0.06\leqslant x\leqslant 0.24, \end{aligned} \tag{4}$$

where

$$r_c=r_{th}\cosh(mx)\big|_{0.06}, \quad \alpha=r_{th}m\sinh(mx)\big|_{0.06},$$

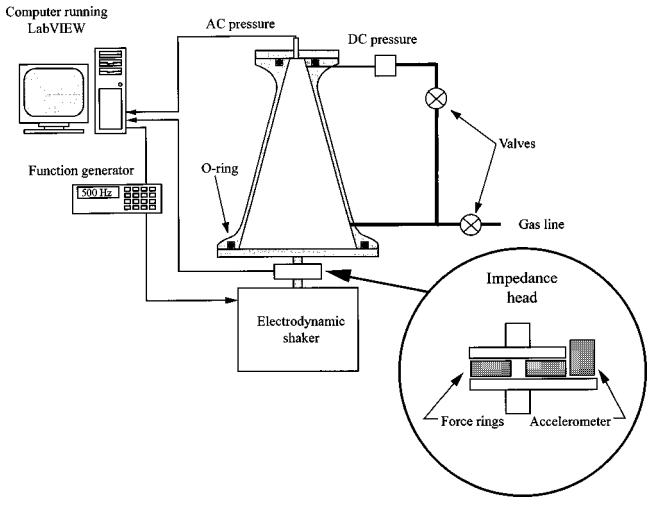

FIG. 3. Experimental apparatus.

where $r_{th}=0.0068$ m and m is 23.86 m^{-1}. For the bulb resonator the radius is given by

$$r(x)=\begin{cases} 0.007-0.15x+4.1x^2-9.9\times10^4x^3-9\times10^6x^4 \\ \quad \text{for} \quad -0.00508\leqslant x\leqslant 0, \\ l\left[a_0+a_1\left(\dfrac{x}{l}\right)+a_2\left(\dfrac{x}{l}\right)^2+a_3\left(\dfrac{x}{l}\right)^3+a_4\left(\dfrac{x}{l}\right)^4\right] \\ \quad \text{for} \quad 0<x\leqslant 0.28, \\ \sqrt{0.00380-(x-0.229)^2} \quad \text{for} \quad 0.28<x\leqslant 0.291, \end{cases} \tag{5}$$

where $a_0=0.025$, $a_1=-0.15$, $a_2=1.15$, $a_3=0.0$, $a_4=-0.9$, and $l=0.28$ m.

With the exception of the cylinder, all of the resonators were machined from billet aluminum. The resonator end caps were bolted on with O-ring seals (see Fig. 3) providing a pressure-tight joint. The cylinder was formed from a brass tube with brass plates soldered onto each end.

Typically, researchers have gone to great lengths to eliminate gross resonator motion and flexing of the resonator walls. For example, Cruikshank[2] used approximately 352 kg of hardware, and Coppens and Sanders[5] used a steel tube with a wall thickness of 28.6 mm. A typical RMS resonator, which depends on motion of the entire resonator for power transfer, has aluminum walls approximately 3.56 mm thick. Finite-element analyses of RMS resonators show negligible wall stresses and flexing at the elevated pressure amplitudes and accelerations reported in this paper. The RMS resonators are lightweight (less than 2 kg for the resonators described above) and portable.

B. Instrumentation

Figure 3 shows a typical experimental configuration, including the resonator, motor, and electronics. The resonators were rigid closed cavities bolted to the motor through an impedance head used to measure power transferred to the resonator. The motor was a LabWorks model ET-127 voice coil shaker capable of generating about 2200 N at the frequencies of interest.

Since significant power was dissipated in the resonators, the gas contained in the cavity tended to heat during experiments. Because of this heating (and the associated resonance frequency shift) it was necessary to use a resonance locking scheme in order to keep the drive frequency locked to the acoustic resonance. A computer program implemented in LabVIEW® by National Instruments was used to sample the dynamic pressure in the resonator and the acceleration of the resonator. The LabVIEW® control program program then adjusted the drive frequency so that the phase between pressure and acceleration matched a target value. Note that this target phase was not in general 90 degrees. Because the entire resonator moves in response to both the drive force and to the acoustic reaction forces, the drive phase for maximum pressure amplitude depends on the mass of the cavity.

Precise drive frequency control was required, due to the high resonance quality factor (Q) of each resonator. (Q factors were typically on the order of 500.) A Stanford Research

model DS345 function generator was used and provided 0.01 Hz or better resolution over a range of frequencies of 450–1050 Hz for the experiments reported below.

PCB® Piezotronics Inc. piezoelectric ballistic-type pressure transducers (such as model 113A26) were used to measure dynamic pressures inside the resonators. The pressure transducers were mounted in the resonator wall so that their faces were flush with the interior resonator surface.

Static pressure changes due to nonlinear effects and heating of the gas were measured. For this measurement a fitting was constructed which had a 0.1-mm through-hole of 2.54 cm length. The small tube acted as a low-pass acoustic filter and greatly reduced dynamic pressure variations. One end of this fitting was mounted in the resonator wall with the end flush with the inside resonator surface. The other end was attached via a short flexible hose to a strain-gauge-type static pressure transducer (Omega model PX-811).

Power transfer to the resonator was measured with an impedance head mounted between the resonator and the motor (see Fig. 3). The impedance head used three PCB® force rings (model 201A05) mounted equidistant from the axis of a rigid stainless steel fixture to which was also mounted a PCB® accelerometer (model 353B02). The force transducer arrangement was designed to reduce the possibility of cross-axis errors from side-to-side oscillations of the resonator. Force measurements (which included both the input force from the motor and acoustic reaction forces) ranged up to about 4500 N. Accelerations of up to about 100 g were measured in the experiments, so the rigid-body displacements of the resonators were very small. For example, 100 g at 500 Hz would give a peak displacement of only 0.1 mm.

A LabVIEW® program was used to measure the phase between force and acceleration for the power measurement. Phase measurement errors were about ± 0.5 degrees. We estimate the experimental error for our power measurements to be $\pm 3\%$.

Essentially all of the power delivered to the resonators was at the drive frequency. We measured no significant power flow either into or out of the resonator at the higher harmonic frequencies. This lack of power flow is not surprising since, with the exception of the cylindrical resonator, the harmonic frequencies do not coincide with the modal frequencies. Thus, the distortion components in the drive signal cannot generate significant pressure amplitudes and no appreciable power flow is created.

However, this does not imply that energy dissipation is not present at harmonic frequencies in the resonator. The power flows from the motor, through the impedance head, and into the resonator at the drive frequency. Inside the resonator some of the energy is pumped by nonlinear processes to distortion components of the standing waves at harmonic frequencies, where the energy is then dissipated.

C. Experimental procedure

Two basic types of experiments were conducted. In the first type, the drive amplitude was increased in steps while the drive frequency was locked to the fundamental resonance. At each drive amplitude the acquired data included pressure waveform and static pressure (at either or both ends of the resonator), resonator acceleration, force, power delivered to the resonator, and resonator temperature.

In the second type of experiment, the drive frequency was swept through the fundamental resonance of the cavity while holding drive amplitude constant. Sweeps were run both for increasing and decreasing frequencies, and were performed at several different drive amplitudes. The same data were acquired as for the first experiment type.

For the pressure waveforms shown in the next section we report harmonic amplitudes p_n and phases ϕ_n. Waveforms can be reconstructed from these values by using the relation

$$p(t)=\sum_{n=0}^{N} p_n \cos\left(2\pi n f_1 t+\frac{\pi\phi_n}{180}\right), \tag{6}$$

where f_1 is the fundamental resonance frequency (in Hz) of the resonator and N is the number of harmonics to be used in the reconstruction. Note that $\phi_0=\phi_1=0$ degrees.

II. RESULTS

Several different phenomena are discussed here. First, high-pressure amplitude waveforms are presented. These waveforms are demonstrations of the effect of resonator geometry on pressure amplitude and waveform. Next, the evolution of the pressure waveforms and harmonic distortion at increasing amplitudes is presented. Then, effects such as hardening and softening behavior in frequency response curves are shown. Finally, measurements for several different types of gas are contrasted. For the experiments described below, all of the resonators were driven at their lowest resonance frequency, and the pressure waveforms were measured at the ends (antinodes) of each resonator.

A. High-pressure amplitude waveforms

This section provides a comparison of pressure waveforms for three different resonator geometries: horn-cone, cylinder, and cone (see geometries in Fig. 2). The results in this section were obtained with resonators charged at room temperature, 22 °C, with $p_0=301$ kPa of refrigerant 134a (R-134a). Note that, while the ambient density inside the resonators remained constant during the experiments, the pressure rose due to heating. For the data presented here p_0 is reported for the condition at which waveforms were collected.

Figure 4 shows a pressure waveform measured at the small end of the horn-cone resonator. The waveform is of quite high amplitude, and has multiple micro-shocks on the higher pressure regions. The peak pressure $p_{\max}$ is 1446 kPa and the minimum pressure $p_{\min}$ is 53.1 kPa, so that the peak-to-peak amplitude of the waveform is 1390 kPa. Thus, not only does the wave reach very high peak and peak-to-peak pressures, the waveform also reaches down to low pressures. Another way of expressing the amplitude of the wave is with the pressure ratio: $p_{\max}/p_{\min}=27$.

To obtain the waveform shown in Fig. 4, the power delivered to (and dissipated by) the resonator was 144 W.

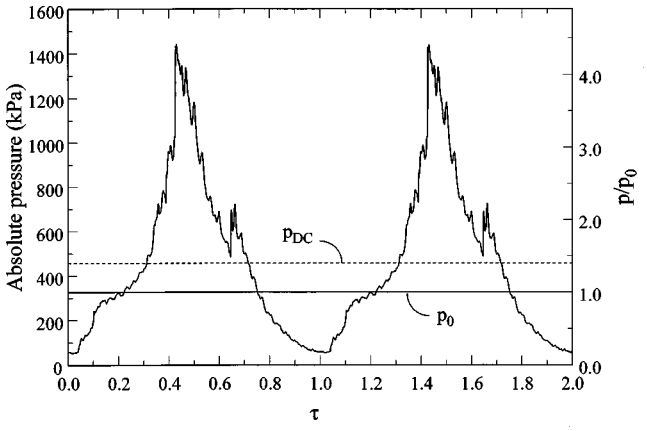

FIG. 4. Waveform at small end of horn-cone resonator charged with R-134a ($p_0 = 327$ kPa).

The quiet-condition static pressure, measured immediately after the waveform was taken and represented by the solid horizontal line in the figure, was $p_0 = 327$ kPa, and the resonance frequency was 481.8 Hz. Using the value of p_0 measured with heating, the relative maximum pressure amplitude p_{max}/p_0 is 4.42 and the minimum p_{min}/p_0 is 0.163.

Table I provides the amplitudes of the fundamental frequency, second through tenth harmonic, and dc components of the waveform in Fig. 4. The table also shows the phases of the harmonics relative to the fundamental frequency component. During the test, the static pressure at the small end resonator (represented by the dashed line) rose to 458 kPa. Thus, the nonlinear processes inside the resonator generated a static pressure increase (from the quiet-condition) of 131 kPa, or 40% of the quiet condition pressure, at the throat-end pressure antinode.

In Fig. 5(a), a waveform measured at the small end of the horn-cone resonator is compared to a waveform measured at one end of the cylindrical resonator. Harmonic amplitudes and phases for the two waveforms are shown in Table II. The waveforms were measured for a power input of 41.7 W, and the final p_0 was 311 kPa for the cylinder and 306 kPa for the horn-cone. A comparison of the total pressure amplitudes for each resonator is shown in Table III. The resonance frequencies were 808.3 Hz for the cylinder and

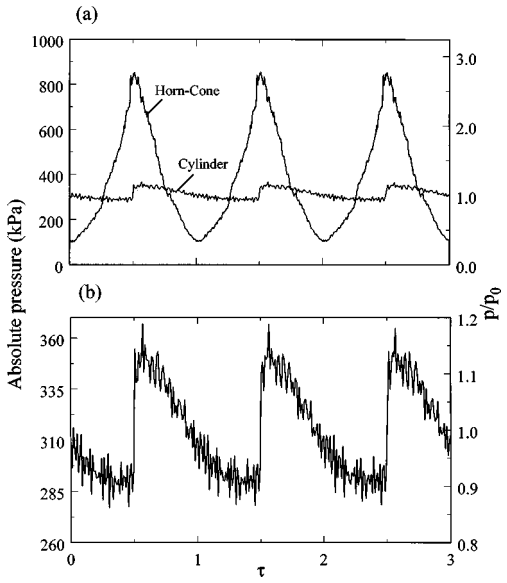

FIG. 5. Waveforms at one end of cylinder and small end of horn-cone for 41.7 W of power input. Resonators were filled with R-134a ($p_0 = 311$ kPa for cylinder and 306 kPa for horn-cone).

463.6 Hz for the horn-cone. The comparison of the waveforms for the cylinder and the horn-cone gives a good demonstration of the changes that can be made in the standing wave pressure field by changing resonator geometry. For the same ''cost'' measured in watts, the horn-cone gives much higher ''return'' in pressure amplitude.

The peak-to-peak pressure amplitude is 95.2 kPa for the cylinder's waveform shown in Fig. 5(b), and the pressure ratio is 1.36. This pressure ratio was achieved with about 1600 N from the shaker. While slight increases in the pressure ratio might be gained with higher forces, for practical purposes the cylinder reached acoustic saturation. The saturation is demonstrated by the fact that for a pressure amplitude of 17.3 kPa peak-to-peak, the cylinder only dissipated 0.06 W. Increasing the pressure amplitude by a factor of 5.8 (17.3 to 95.2 kPa) required 700 times more power (0.06 to 41.7 W). Since the pressure ratio that is achievable in a cylinder is limited and since it takes a considerable amount of power to generate the small pressure ratios, the cylinder

TABLE I. Harmonic amplitudes and phases at small end of horn-cone resonator filled with R-134a ($p_0 = 327$ kPa).

	Small end of horn-cone resonator	
Harmonic	Pressure (kPa)	Phase (degrees)
dc	131	⋯
1	449	0
2	118	−1
3	112	28
4	84	51
5	45	24
6	23	33
7	11	113
8	15	97
9	19	94
10	12	102

TABLE II. Harmonic amplitudes and phases for 41.7 W of power delivery to cylinder and horn-cone resonators filled with R-134a ($p_0 = 311$ kPa for cylinder and 306 kPa for horn-cone).

	Cylinder		Horn-cone	
Harmonic	Pressure (kPa)	Phase (degrees)	Pressure (kPa)	Phase (degrees)
dc	3.5	⋯	69.0	⋯
1	26.9	0	310.5	0
2	10.4	58	69.0	0
3	6.9	140	35.2	2
4	4.8	−150	13.1	−14
5	3.5	−71	15.9	49
6	3.5	0	13.8	66
7	2.8	72	6.2	52
8	2.1	157	2.1	34
9	2.1	−131	4.1	66
10	1.4	−74	4.1	112

TABLE III. Comparison of performance for cylinder and horn-cone with 41.7 W power delivery. Resonators were filled with R-134a.

Resonator	Power (W)	p_{max} (kPa)	p_{min} (kPa)	pk–pk pressure (kPa)	$\frac{p_{max}}{p_{min}}$	p_0 (kPa)
Cylinder	41.7	360	264	95.2	1.36	311
Horn-cone	41.7	833	104	729	8.03	306

would impose practical limits for pumping or compressor applications.

For the same power input as for the cylinder (41.7 W), the horn-cone resonator achieved a peak-to-peak pressure amplitude of 729 kPa, and the resulting pressure ratio was 8.03. For the same factor of 5.8 pressure increase as described for the cylinder, the horn-cone only required an increase of a factor of 50 in the delivered power (peak-to-peak pressure increased from 126 to 729 kPa). Unlike the cylinder, the horn-cone resonator is well suited for use in compressor and pumping applications, because usefully high pressures can be obtained for a reasonable amount of input power.

The waveform shown in Fig. 5 for the cylinder is not a perfect sawtooth. Rather, it is composed of large shocks connected by half sine waves overlaid with high-frequency spikes (micro-shocks). There is good agreement between this measured waveform and previously reported measurements and predictions of waveforms in cylindrical resonators.[1,2,18,19]

While there appear to be some small shocks at the peak of the horn-cone resonator waveform, the basic shape is nothing like the sawtooth observed in the cylinder. This can be attributed to the RMS design (of which the carefully designed dissonance is a part) of the horn-cone which gives the desired high-amplitude unshocked waveform. In contrast, the cylindrical resonator is consonant (or nearly so), and thus has longitudinal resonance frequencies that are nearly integer multiples of the lowest resonance frequency. In Fig. 6 measurements of the first eight longitudinal resonance frequencies of the horn-cone resonator filled with R-134a are shown. The vertical dashed lines mark the harmonics of the 472-Hz fundamental (drive) frequency and the triangles mark longitudinal mode frequencies. This particular dissonance pattern shows a symmetry between modal spectra and harmonic spectra. Odd–even adjacent harmonics (e.g., harmonics 1 and 2) bracket a single mode and even–odd adjacent harmonics bracket two modes.

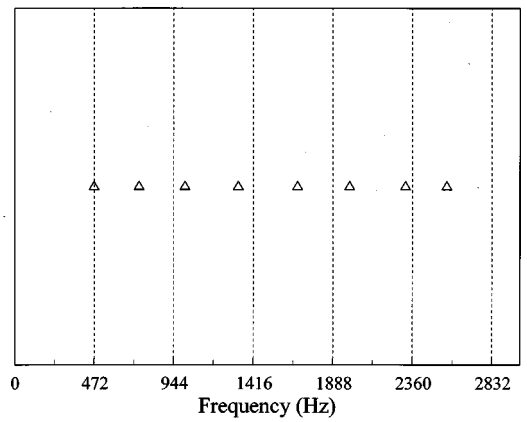

FIG. 6. Frequencies of longitudinal resonances (×'s) and harmonic frequencies (vertical dashed lines) for excitation of fundamental resonance of horn-cone resonator filled with R-134a.

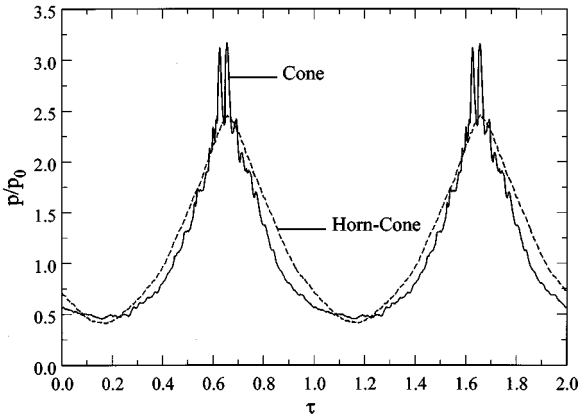

FIG. 7. Comparisons of waveforms at small ends of cone and horn-cone resonators for $p_1/p_0=0.9$. Resonators were filled with R-134a ($p_0=325$ kPa for cone and 306 kPa for horn-cone).

The response of both a dissonant (horn-cone) and consonant (cylinder) resonator is markedly different, as discussed above. The dissonant resonator is able to achieve much higher pressure amplitudes than the consonant resonator. Two of the goals of RMS resonator designs are to (1) create high-amplitude unshocked waves, and (2) create waves of a specific shape. To use RMS to create a high-amplitude unshocked wave it is not sufficient simply to construct a dissonant resonator, as is shown in Fig. 7 where a waveform at the small end of the (dissonant) cone resonator (resonance frequency of 604.0 Hz, $p_0=325$ kPa with heating) is compared to a waveform at the small end of the horn-cone resonator. The relative amplitude p_1/p_0 is 0.9 for both waveforms. For the same fundamental amplitude, the cone has shocks and the horn-cone does not. Thus, the change in geometry between the two dissonant resonators leads to shock formation at different amplitudes. Also, even though both resonators are dissonant, the shape of the wave for each is also different. The differences in the waveform can also be seen in Table IV, which shows relative harmonic amplitudes and phases for the waveforms in Fig. 7. Harmonic amplitudes are larger for the cone, with the exception of the dc component.

From the examples shown above we may draw several conclusions. First, to achieve unshocked pressure waves in gases with amplitudes much higher than about $p_1/p_0=0.1$ the resonator must be dissonant. Second, the amplitude at which a dissonant resonator will shock depends on the specific geometry of the resonator. Last, the shape of the wave obtained in a dissonant resonator depends on the resonator geometry.

Now we will discuss further some of the physical mechanisms related to the behavior of consonant and dissonant resonators. When a dissonant resonator such as the horn-cone is driven at a resonance frequency, nonlinear processes pump energy into higher harmonics, but the energy at

TABLE IV. Relative harmonic amplitudes and phases for cone and horn-cone for $p_1/p_0=0.9$ for resonators filled with R-134a ($p_0=325$ kPa for cone and 306 kPa for horn-cone).

	Cone		Horn-cone	
Harmonic	Pressure (p_n/p_1)	Phase (degrees)	Pressure (p_n/p_1)	Phase (degrees)
dc	0.111	⋯	0.205	⋯
1	1.000	0	1.000	0
2	0.394	1	0.204	0
3	0.170	−2	0.089	1
4	0.089	8	0.027	0
5	0.064	19	0.032	8
6	0.065	29	0.021	12
7	0.055	32	0.007	8
8	0.035	27	0.003	10
9	0.037	32	0.004	13
10	0.026	42	0.005	32

the higher harmonics is not strongly resonance amplified. The dissonance prevents efficient transfer of energy from the fundamental to higher harmonics. In the cylinder resonator nonlinear processes pump energy to harmonic frequencies that coincide with resonances of the cavity, so this pumping process is relatively more efficient than in the horn-cone. Thus, in the cylinder significant harmonic amplitudes occur at much smaller fundamental amplitudes than for the horn-cone.

The proximity of harmonic frequencies to modal frequencies (such as that shown in Fig. 6) cannot in general be used to predict the shape of the wave or exact amplitudes and phases of harmonics. It is not sufficient that a harmonic frequency coincide with a mode frequency in order to have a large amplitude for that harmonic; the spatial and temporal distribution of the nonlinear sources inside the cavity must be such that the mode can be excited. The actual amplitude and phase of harmonics in standing waves at the elevated pressures p_1/p_0 reported here also depend on a range of contributions including boundary layer effects, turbulence, and hardening or softening behavior of the resonance at which the cavity is excited. These contributions can be accounted for in RMS designs with tools such as those described by Il'inski *et al.*[1]

Other researchers have discussed some of the same issues as we have here. Coppens and Sanders[14] measured finite-amplitude distortion in standing waves in rectangular cavities, where certain families of modes had frequencies that were not integer multiples, but their cases were limited to low pressure amplitudes. Gaitan and Atchley[4] and Oberst[3] also built dissonant resonators, but neither reported pressure amplitudes p_1/p_0 greater than about 0.1. The RMS technology together with entire resonator drive enable amplitudes p_1/p_0 greater than 1.3, or more than an order of magnitude larger.

To summarize, the maximum practical pressure amplitude of a standing wave depends very strongly on the shape of the cavity in which the wave is generated. Acoustic saturation in standing waves is very significant for the cylinder, but less so for the resonators examined here. Also, the cavity shape affects not only the amplitude of the wave and its harmonic components, but also the phase of the harmonics and therefore the shape of the wave.

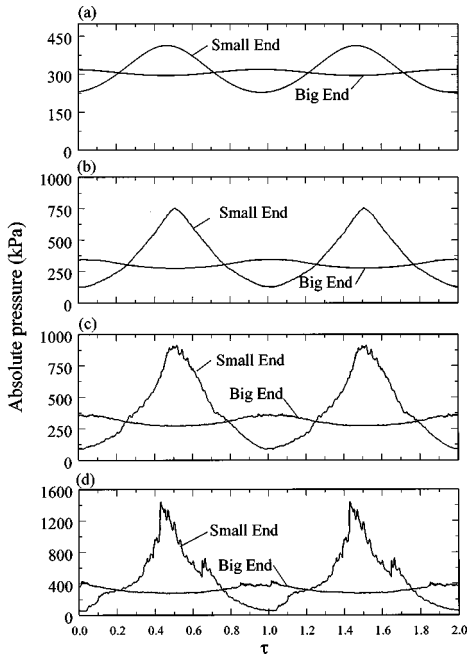

FIG. 8. Evolution of pressure waveforms at big and small ends of the horn-cone resonator being excited at its fundamental mode. Resonator was filled with R-134a.

B. Pressure distribution and evolution

In the previous section waveforms for different resonators were compared. In this section, details of the evolution and distribution of the pressure field inside the resonators are discussed. As in the previous section, the experiments described here were performed with resonators filled with R-134a at an initial pressure of 301 kPa.

Figure 8(a)–(d) shows the evolution of the pressure waveform at the small and big ends of the horn-cone resonator [filled with R-134a, (a): $p_0=306$ kPa, (b): $p_0=307$ kPa, (c): $p_0=309$ kPa, (d): $p_0=327$ kPa] for increasing drive amplitude. Figure 9(a) shows the waveforms at the small end for the four drive amplitudes and Fig. 9(b) shows the waveforms at the big end. Since the resonator is driven at its fundamental mode, there is a 180-degree phase shift between the waveforms measured at the big and small ends. In Fig. 8(a) the waveform at both ends of the resonator is nearly sinusoidal.

It is interesting to note that for Fig. 8(b), the peak overpressure ($p_{\max}/p_0$) amplitude is 2.32, more than twice the ambient pressure, yet the waveform is very smooth (with a ''*u*-wave'' shape), and no shocks are present. This is in contrast to the waveform in the cylinder (see Fig. 4), which shows strong shocks for an overpressure of only 1.1.

In Fig. 8(c) small ripples appear in the waveform at the small end. At a relative maximum pressure amplitude of 4.42 [Fig. 8(d)], the waveform for the horn-cone contains several distinct shocks. Table V shows the pressure amplitudes p_n of the first ten harmonics and the dc component of the waveform of Fig. 8(d) for the small and big ends. The table also

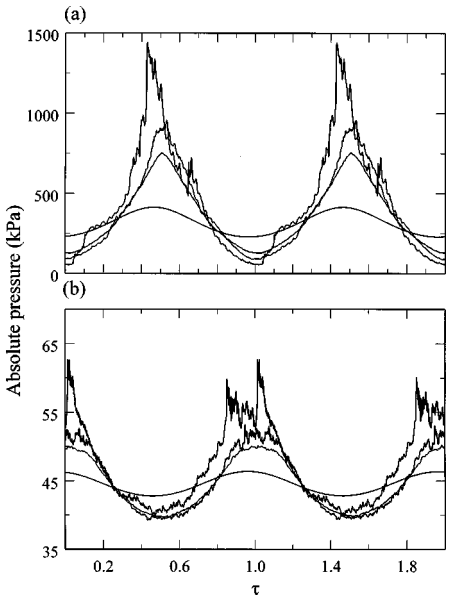

FIG. 9. Evolution of pressure waveforms at big and small ends of the horn-cone resonator being excited at its fundamental mode. Graph (a) shows waveforms for small end and graph (b) shows waveforms for the big end. Resonator was filled with R-134a.

shows the relative phase of each harmonic ϕ_n with respect to the fundamental.

The difference in amplitude of the nonlinearly generated dc pressure between the ends of the horn-cone is 131 kPa for the highest drive amplitude (see Table V). This difference in dc pressure can be used as a pumping mechanism to create low compression ratio pumps without valves. Although the amplitude of the waveform at the mouth end is smaller, nonlinear effects still exist, as evidenced by the shocks shown in Fig. 8(d).

The previous discussion has been directed at the shape and amplitude of the waveforms obtained in various resonator shapes. Another way to study differences between resonators is to compare the amount of nonlinear distortion present for a range of fundamental component pressure amplitudes.

Qualitative measurements of the effect of cavity geometry on nonlinear distortion of waveforms are shown in Fig.

TABLE V. Harmonic amplitudes and phases at big and small ends of horn-cone resonator filled with R-134a ($p_0 = 327$ kPa).

	Small end		Big end	
Harmonic	Pressure (kPa)	Phase (degrees)	Pressure (kPa)	Phase (degrees)
dc	131	⋯	0.0	⋯
1	449	0	55.2	0
2	118	−1	11.0	6
3	112	28	2.1	−104
4	84	51	4.1	−162
5	45	24	4.1	−149
6	23	33	6.2	−140
7	11	113	3.5	−125
8	15	97	1.4	−125
9	19	94	0.7	−158
10	12	102	1.4	98

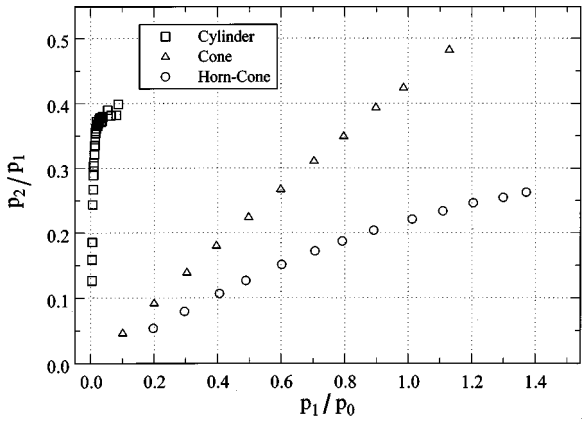

FIG. 10. Relative second harmonic amplitude p_2/p_1 for a range of fundamental frequency amplitudes (p_1/p_0) for three different resonator geometries. Resonators were filled with R-134a.

10, where the relative amplitudes of the second harmonic (p_2/p_1) are plotted for increasing fundamental amplitude p_1/p_0. The ambient pressure p_0 includes pressure changes due to heating, but not from nonlinearly generated dc pressure. All of the resonators had the same initial pressure charge of R-134a. For the cylindrical resonator, very high levels of second harmonic (about 40%) are obtained for very low levels of the fundamental (p_1/p_0 less than 0.1). The cone and horn-cone exhibit much less harmonic generation; the ratio of second harmonic to fundamental is much lower for a given p_1/p_0. This is again an illustration of the fact that both the horn-cone and cone are dissonant resonators. For the cone the second harmonic increases almost linearly with fundamental amplitude, while for the horn-cone the second harmonic increases linearly at first, but the rate of increase drops for higher fundamental amplitudes. The horn-cone has a lower second harmonic amplitude than the cone. Comparisons of amplitudes of higher harmonics between resonators show similar behavior as in Fig. 10; harmonic amplitude shows a strong dependence on resonator geometry.

Now we will examine the evolution of the harmonic amplitudes and phases in more detail. For the cone resonator, Fig. 11 shows the dc pressure and the relative amplitudes and phases of the second through fifth harmonics for a range of fundamental amplitudes. Note that it is not, in general, possible to tell when a waveform develops shocks simply by examining the amplitudes in the frequency spectrum; harmonic phases must also be considered. Also note that the phases of the harmonic components relative to the fundamental can vary substantially with fundamental amplitude. This phase amplitude dependence is not surprising in light of the nonlinear hardening behavior (described in detail in the next section) observed for the lowest mode of the cone resonator. When the amplitude at the fundamental mode (frequency f) is increased, the frequency of this resonance increases by an amount Δf, which causes a corresponding increase in the nth harmonic frequency of $n\Delta f$. Consequently, the higher harmonic frequencies can be swept near and/or through higher modes of the cavity, causing substantial changes in harmonic phase. Also, the large overpressures

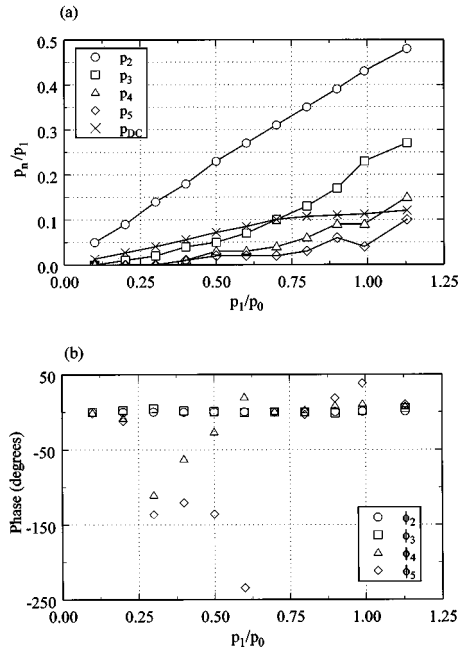

FIG. 11. Relative harmonic amplitudes p_n/p_1 and phases ϕ_n for a range of fundamental frequency amplitudes (p_1/p_0) for cone resonator. Resonator was filled with R-134a.

of the fundamental mode can significantly alter the local ambient conditions of the gas. These changes in local conditions can result from the large temperature changes that occur over an acoustic cycle and also from nonlinear effects such as the large dc pressure and density gradients from end to end in the resonator. This effect can alter the modal frequencies, causing further amplitude-sensitive phase changes. All of these effects can be modeled and do not prohibit good resonator design.

As mentioned in the Introduction, a measure of the suitability of a particular resonator design for use in a compressor application is the the power input necessary to generate a certain pressure ratio $p_{\max}/p_{\min}$. A comparison of the cylinder, cone, and horn-cone resonators is shown in Fig. 12. The pressure ratio in the cylinder is very limited, yet the power dissipated is significant. For the cone, a pressure ratio of about 12 is obtained for a power input of 100 W, while for

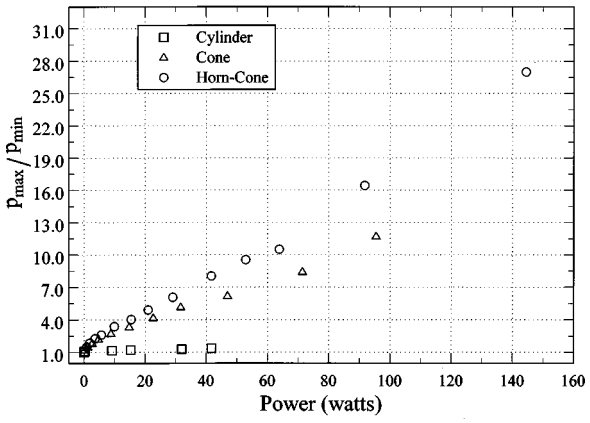

FIG. 12. Pressure ratios $p_{\max}/p_{\min}$ for cone, horn-cone, and cylinder. Resonators were filled with R-134a.

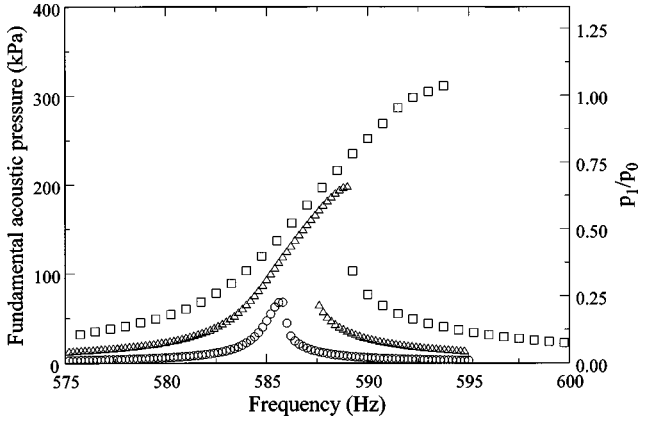

FIG. 13. Frequency response curves measured at the small end of the cone resonator. Resonator was filled with R-134a.

the same dissipation a pressure ratio of 17 is achieved in the horn-cone.

C. Frequency effects

All of the data presented in the previous sections of this paper were measured for resonators being excited ''on-resonance,'' where resonance in this case is defined as the maximum pressure amplitude achievable for a given drive force amplitude. In this section, effects in resonators being driven near-, as well as on-resonance are examined. As in the previous sections, the experiments described here were performed with resonators filled with R-134a at an initial pressure of 301 kPa.

Figure 13 shows frequency response curves for the cone resonator at three drive amplitudes. Pressure was monitored at the small end of the resonator during the frequency sweeps. The pressure shown in the plot is only for the fundamental frequency component. However, the basic shapes and behaviors of the resonance curves are the same when peak-to-peak pressures are used.

At the lowest drive amplitude a single-valued response curve was obtained, and the curve could be reproduced with upwards or downwards frequency sweeps. However, even at this lowest drive level a nonlinear hardening behavior is observed; the resonance curve ''leans'' towards high frequency. This low amplitude sweep had a resonance quality factor (Q) of about 500.

As shown in Fig. 13, the two higher drive amplitude response curves are multi-valued and strong hysteresis is present. For these two curves the low-frequency segment was taken from an upward sweep, and the high-frequency segment was taken from a downward sweep that immediately followed the upward sweep. Care was taken to sweep quickly enough so that heating or cooling of the gas in the resonator would not change the sound speed and thus shift the resonance frequencies, yet slowly enough that transients did not affect the measurements. The resonator temperature was monitored during the sweeps to confirm that heating and the resultant sound speed changes did not affect the resonance curves. The maximum resonance frequency change during the test due to heating is estimated at less than 0.1% (0.6 Hz).

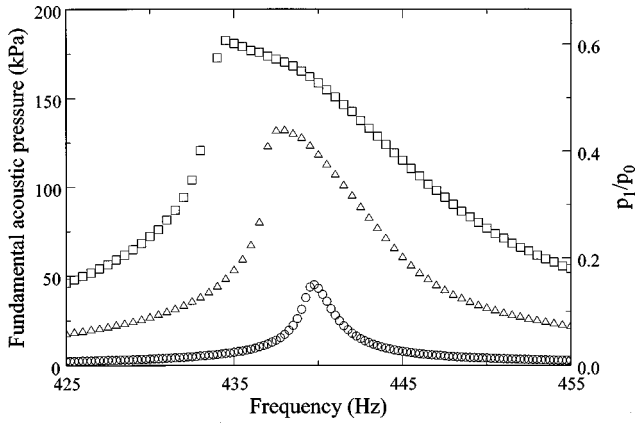

FIG. 14. Frequency response curves measured at the small end of the bulb resonator. Resonator was filled with R-134a.

As stated in the previous sections, the nonlinear characteristics of a gas-filled resonant cavity are mostly influenced by the cavity geometry. In Fig. 14, the frequency response curves for a bulb resonator are presented. Unlike the cone resonator, the bulb resonator exhibits a softening behavior. However, measurements for the bulb do not exhibit the strong hysteresis shown for the cone. Thus, for frequency sweep experiments performed with the same gas conditions, and similar pressure amplitudes, the bulb and cone exhibit *much* different behavior. If the properties of the gas in the cavities were the primary factor influencing nonlinear behavior, we would expect to see similar frequency response curves.

In Fig. 15 the results of three frequency sweeps for the cylindrical resonator are shown. While the resonance curves show the asymmetry associated with a hardening behavior (similar to the curves in Fig. 13), there is no hysteresis and no measurable shift in resonance frequency. The lack of frequency shift is in agreement with the results presented by Il'inskii *et al.*[1] However, the results are in disagreement with the results presented by Cruikshank[2] and Coppens and Sanders.[5] Both Cruikshank and Coppens and Sanders reported increases in resonance frequency on the order of 0.5 Hz for a fundamental frequency of about 100 Hz. This 0.5% resonance frequency increase would equate to about 4 Hz for

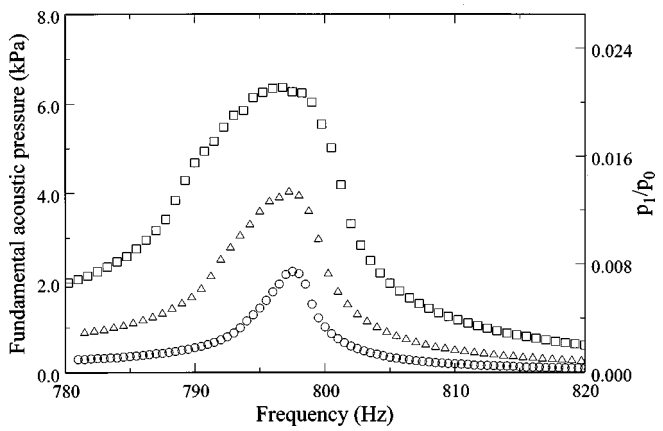

FIG. 15. Frequency response curves measured at one end of the cylinder resonator. Resonator was filled with R-134a.

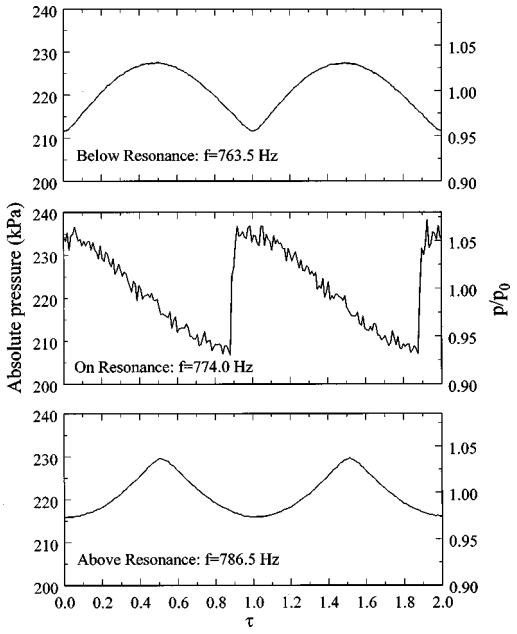

FIG. 16. Waveforms in cylinder (filled with R-134a) just before resonance (graph a), on resonance (graph b), and just after resonance (graph c).

our experiment. One possible source of the discrepancy is the difference in the driving mechanisms. While both Cruikshank and Coppens and Sanders employed a piston drive at one end and a rigid cap at the other end, the results presented here are obtained with the entire resonator drive system described previously. A second possible explanation for the discrepancy is the heating of the resonator during a sweep test. The dissipation in the resonator will cause the resonator and gas to heat, and results in an increase in the sound speed and therefore the resonance frequency of the cylinder. The increase in gas temperature raises the speed of sound at the rate of 0.17% per °C increase in gas temperature for a 20 °C initial temperature. The frequency changes observed by Cruikshank and by Coppens and Sanders could be attributed to an increase in ambient temperature in the tube of 3 °C. From measurements on the resonator body, we estimate that the total temperature change during our frequency sweep experiments was less than 0.5 °C. Therefore, the shape of the resonance curves in our experiments should not be affected by temperature changes.

The graphs in Fig. 16 show waveforms measured in the cylinder just before resonance (763.5 Hz), on resonance (774.0 Hz), and just after resonance (786.5 Hz). The shape of the waveforms is very similar to that predicted by Chester[18] and measured by Cruikshank.[2] The waveform in Fig. 16(a) is an ''*m* wave.'' For the ''*m* wave,'' the second and higher harmonics are all out of phase with the fundamental frequency component. On resonance [Fig. 16(b)] the waveform is shocked. The waveform in Fig. 16(c) is an inverted version (''*u* wave'') of that shown in Fig. 16(a). The shape results from the second and higher harmonics being (in general) in phase with the fundamental frequency component.

The change in waveform for the cylindrical resonator as it is swept through resonance is different than the behavior with the cone, horn-cone, and bulb resonators. For the cylinder resonator, all of the harmonics of the fundamental fre-

TABLE VI. Gas properties for experiments with nitrogen, propane, and R-134a. All properties are for approximately 20 °C.

	Nitrogen	Propane	R-134a
Pressure p_0 (kPa)	110	319	306
Density (kg/m^3)	1.26	6.11	13.8
Sound speed (m/s)	341	239	154
Coefficient of nonlinearity (β)	1.20	1.08	1.08

quency sweep through higher modes as the fundamental sweeps. Thus, both harmonic amplitudes and phases relative to the fundamental change substantially. For the noncylindrical resonators, harmonic frequencies, in general, do not correspond to modal frequencies. Harmonic frequency components grow as the fundamental is resonance amplified, but (unlike in the cylinder) the basic character of the waveform (i.e., ''*u* wave'' or ''*m* wave'') does not change as it does in the cylinder.

D. Effect of fluid properties

While the general characteristics of the waveform are determined by the resonator shape, changes in fluid properties will also make predictable changes in the waveform. All of the data previously presented in this paper were collected using R-134a, which is a relatively dense, low-sound-speed gas used for vapor-compression cooling systems in refrigerators and automotive air-conditioners.

In this section performance is described for the horn-cone resonator filled with three different gases: nitrogen, propane, and R-134a. Properties for these gases are shown in Table VI. The gases were chosen to give a range of densities and sound speeds, and also as examples of gases used for applications such as compressors. To give a relative comparison of the nonlinearity for each gas, the table includes the coefficient of nonlinearity, which for an ideal gas is defined by

$$\beta = 1 + \frac{\gamma - 1}{2}, \tag{7}$$

where γ is the ratio of specific heats.

In Fig. 17 comparisons of waveforms are shown for nitrogen ($p_0 = 110$ kPa), propane ($p_0 = 319$ kPa), and R-134a ($p_0 = 306$ kPa). Waveforms were measured at the throat of the horn-cone resonator for $p_1/p_0 = 1.0$. The resonance frequencies when the waveforms were captured were: $f_{\text{nitrogen}} = 1039.6$ Hz, $f_{\text{propane}} = 753.6$ Hz, and $f_{\text{R-134a}} = 463.6$ Hz. The waveforms are very similar for each gas, except that the nitrogen waveform is shifted up in pressure compared to the other two. Table VII shows relative amplitudes and phases for the first ten harmonic and dc components of the waveforms shown in Fig. 17. The amplitudes of the dc component and the second through fourth harmonics are somewhat higher for the nitrogen. This is consistent with the higher β, which will tend to give higher energy transfer to distortion components of the wave. The higher dc pressure gives the upward shift in the waveform seen in Fig. 17. The phases of the harmonics through the fourth are nearly the same, but

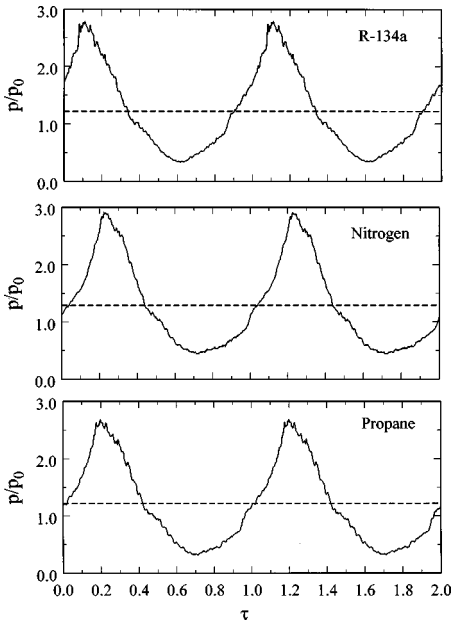

FIG. 17. Comparison of waveforms at small end of horn-cone resonator for $p_1/p_0 = 1.0$ in R-134a, nitrogen, and propane.

above the fourth harmonic, the phases vary somewhat from waveform to waveform. This may be due to differences in damping and frequency-related dispersive effects unique to each gas. While there were measurable differences in waveform for each gas, the basic shape of the wave which results for the RMS design remained constant.

Figure 18 shows p_2/p_1 for a range of fundamental amplitudes as a measurement of nonlinearity for nitrogen, propane, and R-134a. Again, the results are basically consistent with the calculated coefficients of nonlinearity above. It does appear that the effective nonlinearity for the propane experiments was higher than that for R-134a, which is contrary to the calculated values, although the measured differences are not large.

E. Applications

By enabling very-high-amplitude standing wave pressures with RMS and enabling delivery of large power with

TABLE VII. Relative harmonic amplitudes and phases for horn-cone resonator filled with nitrogen, propane, and R-134a. Relative pressure amplitude is $p_1/p_0 = 1.0$.

	Nitrogen		Propane		R-134a	
Harmonic	Pressure (p_n/p_1)	Phase (degrees)	Pressure (p_n/p_1)	Phase (degrees)	Pressure (p_n/p_1)	Phase (degrees)
dc	0.299	⋯	0.219	⋯	0.222	⋯
1	1.000	0	1.000	0	1.000	0
2	0.287	1	0.228	0	0.222	0
3	0.128	−2	0.116	1	0.114	2
4	0.075	8	0.054	0	0.043	−14
5	0.028	19	0.039	8	0.051	49
6	0.041	29	0.042	12	0.045	66
7	0.028	32	0.019	8	0.021	52
8	0.002	27	0.005	10	0.007	34
9	0.014	32	0.023	13	0.014	66
10	0.019	42	0.018	32	0.013	112

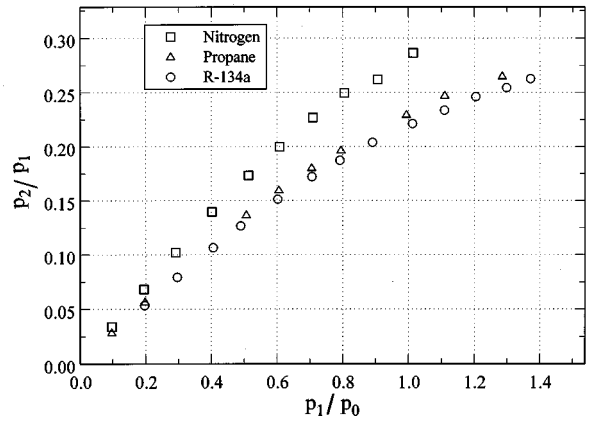

FIG. 18. Relative harmonic amplitude p_2/p_1 at small end of horn-cone resonator as a measure of relative nonlinearity in R-134a, nitrogen, and propane.

entire resonator drive, a number of practical applications can be addressed. These applications include process control; process reactors for the chemical and pharmaceutical industries; chambers for separation, agglomeration, levitation, mixing, and pulverization; oil-less compressors for air compression, refrigeration, comfort air-conditioning, and natural gas; noncontaminating compressors and pumps for commercial gases, ultra-pure, and hazardous fluids; and the conversion of combustible fuels into electric power with RMS pulse combustion. Figure 19 shows ranges of pressure ratios that might be needed for several different compressor applications. With single or multiple stages, RMS devices are capable of delivering the needed pressures.

In order to create the high pressures needed for practical applications, power consumption of the resonator is important. The comparison of the waveforms between consonant and dissonant resonators demonstrates the large changes that can be made in the standing wave pressure field by changing resonator geometry. For the same ''cost'' measured in watts, dissonant resonators (designed with RMS) give a much higher ''return'' in pressure amplitude. Even comparing different dissonant resonator designs, power can be changed. For example, in the cone a pressure ratio of about 12 is obtained for a power input of 100 W, while for the same dissipation a pressure ratio of 17 is achieved in the horn-cone. For applications that require a high efficiency, the horn-cone is better than the cone, since it generates a higher pressure ratio for a given power input.

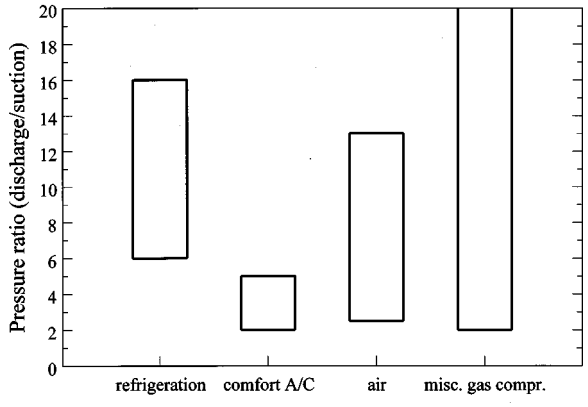

FIG. 19. Pressure ratios (discharge/suction) for several compressor applications.

As demonstrated by the differences in the waveforms for the cone and horn-cone resonators, using RMS resonator geometry can be changed to give different waveforms. This is important in applications such as compressors where flow through valves depends on not only the pressure amplitude, but also the shape of the pressure wave.

One effect that can be exploited to give valveless compressors is the change in dc pressure between ends of RMS resonators. This pressure delta can be large enough (40% of ambient for the horn-cone) to create significant flows with no mechanical components moving relative to each other in the flow stream.

If resonators designed with RMS are to be used for applications where the working gas changes, the results obtained for the different gases are very important. The data show that a resonator designed to give an unshocked waveform with a certain shape and relative amplitude should work fairly consistently with different gases, and therefore several applications can be addressed with a single resonator design. Of course, this ignores performance of components such as valves and motors, but that discussion is beyond the scope of this paper.

III. SUMMARY AND CONCLUSIONS

The capability to synthesize unshocked waveforms of very large amplitude by careful design of the shape of a resonator has been demonstrated. Pressure amplitudes more than an order of magnitude larger than those obtained in an acoustically saturated cylindrical resonator have been measured. Within the range of pressure amplitudes studied for the other resonators described acoustic saturation did not appear to be present.

A key technological component in the generation of these macrosonic standing waves is the entire resonator drive system, which provides a practical method of transferring hundreds of watts of power into the standing wave.

Interesting physical effects of macrosonic standing waves were apparent. Strong hardening and softening resonance behavior in resonators of different geometry filled with the same gas were observed. For a given gas and a fixed power delivery, the dominant factor affecting the peak pressure amplitude is the geometry of the resonator, with different resonator shapes providing tremendous differences in pressure amplitudes. The particular properties of the gas, such as sound speed, density, or compressibility, do not appear to present absolute physical limitations on pressure amplitudes.

In conclusion, the pressure amplitudes produced were limited only by available drive force, which can be increased. The issue of what standing wave overpressures can ultimately be generated remains an open question. However, a significant benchmark is that acoustics can now span the pressure ranges necessary for many important commercial applications.

ACKNOWLEDGMENTS

The authors would like to express their gratitude to the following MacroSonix employees who made vital contributions to this work: Mark Skapin and Kevin Cosgrove (prototype machinists) for their patience in fabricating our often challenging hardware, and Chris Meade (design/drafter) for clearly conveying our ideas to the machine shop. The authors are also grateful to Dr. Joe Keith, Dr. Yurii Il'inskii, and Dr. Evgenia Zabolotskaya for their comments and corrections to earlier drafts of this paper.

[1] Y. Il'inskii, B. Lipkens, T. Lucas, T. W. Van Doren, and E. Zabolotskaya, ''Non-linear standing waves in an acoustical resonator,'' J. Acoust. Soc. Am. (to be published).

[2] D. B. Cruikshank, Jr., ''Experimental investigation of finite-amplitude acoustic oscillations in a closed tube,'' J. Acoust. Soc. Am. **52**, 1024–1036 (1972).

[3] H. Oberst, ''A method for the production of extremely powerful standing waves in air,'' Akust. Zh. **5**, 27–38 (1940). The article was translated by R. T. Beyer.

[4] D. F. Gaitan and A. A. Atchley, ''Finite amplitude standing waves in harmonic and anharmonic tubes,'' J. Acoust. Soc. Am. **93**, 2489–2495 (1993).

[5] A. B. Coppens and J. V. Sanders, ''Finite-amplitude standing waves in rigid-walled tubes,'' J. Acoust. Soc. Am. **43**, 516–529 (1968).

[6] U. A. Muller and N. Rott, ''Thermally Driven Acoustic Oscillations, Part VI: Excitation and Power,'' J. Appl. Math. Phys. **34**, 609–626 (1983).

[7] A. A. Puttnam, F. E. Belles, and J. A. C. Kentfield, ''Pulse Combustion,'' Prog. Energy Combust. Sci. **12**, 43–79 (1986).

[8] D. A. Webster and D. T. Blackstock, ''Finite-amplitude saturation of plane sound waves in air,'' J. Acoust. Soc. Am. **62**, 518–523 (1977).

[9] J. B. Keller, ''Finite-amplitude sound waves,'' J. Acoust. Soc. Am. **25**, 212–216 (1953).

[10] S. Temkin, ''Propagating and standing sawtooth waves,'' J. Acoust. Soc. Am. **45**, 224–227 (1969).

[11] G. W. Swift, ''Thermoacoustic engines,'' J. Acoust. Soc. Am. **84**, 1145–1180 (1988).

[12] T. S. Lucas and T. W. Van Doren, ''Resonant Macrosonic Synthesis,'' U.S. Patent 5,515,684 (1996).

[13] A. B. Coppens and J. V. Sanders, ''Finite-amplitude standing waves within real cavities,'' J. Acoust. Soc. Am. **58**, 1133–1140 (1975).

[14] A. B. Coppens and A. A. Atchley, ''Nonlinear standing waves in cavities,'' in *Encyclopedia of Acoustics* (Wiley, New York, 1997), pp. 237–246

[15] G. W. Swift, ''Analysis and performance of a large thermoacoustic engine,'' J. Acoust. Soc. Am. **92**, 1551–1563 (1992).

[16] T. S. Lucas, ''Acoustic resonator having mode-alignment-canceled harmonics,'' U.S. Patent 5,579,399 (1996).

[17] D. T. Blackstock, ''Finite-amplitude motion of a piston in a shallow, fluid-filled cavity,'' J. Acoust. Soc. Am. **34**, 796–802 (1962). The entire resonator drive shares one characteristic with a proposal by Blackstock, who presented theory for a device to be used for measuring fluid properties. Blackstock also proposed oscillating a cavity, but his resonator contained a moving diaphragm or piston that separated the cavity into two fluid-filled spaces. To the best of the authors' knowledge, no versions of Blackstock's chamber have been built.

[18] W. Chester, ''Resonant oscillations in closed tubes,'' J. Fluid Mech. **18**, 44–64 (1964).

[19] R. Betchov, Phys. Fluids **1**, 205–212 (1958).

Perceptual evaluations of spectral and temporal modifications of deaf speech[a)]

Grace H. Yeni-Komshian
University of Maryland, College Park, Maryland 20742

H. Timothy Bunnell
The duPont Hospital for Children, Wilmington, Delaware 19899

(Received 14 February 1997; revised manuscript received 6 February 1998; accepted 10 March 1998)

The perceptual effect of modifying speech produced by deaf talkers was investigated to discover the changes necessary for disordered speech to be judged normal. Recordings of passages read by three deaf talkers were used as material. For the first two experiments, a three-syllable word was extracted from the deaf talkers' passages and from a similar passage recorded by a hearing talker. Each of the deaf speech samples was paired with the normal speech sample to generate various continua that differed in the spectral and temporal modifications applied to them. Within each continuum, the individual stimuli varied in the shape of the spectrum envelope and were produced by linear interpolation of LPC analysis parameters between the deaf and normal speech end points. Results suggest that correcting the temporal component of deaf speech alone is not enough to make it sound normal. Spectral corrections that approximate about 70% of normal appear to be necessary for the deaf speech samples to be judged normal. A third experiment made use of a 10-syllable segment of speech in which the relative contributions of spectral and temporal adjustments were investigated. The general conclusion of these three experiments is that spectral adjustments are more important to perceptual judgments of normality than temporal adjustments. © *1998 Acoustical Society of America.* [S0001-4966(98)05506-4]

PACS numbers: 43.10.Ln, 43.71.−k, 43.70.Dn, 43.72.Ew [WS]

INTRODUCTION

A major concern in speech therapy is to determine how habilitation efforts should be emphasized or sequenced to achieve intelligible and normal sounding speech. For example, should therapy focus on correcting mispronunciation of segmental phonemes or should the focus be on correcting timing and intonation? One way of answering this question is to apply corrections to disordered speech and evaluate the perceptual outcome of the corrections. Although the effects of this type of correction can be studied in any kind of disordered speech, most of the relevant research is based on modifications applied to speech produced by deaf children.

An early study along these lines was reported by Levitt (1973); he synthesized various versions of the word *better* using parameters modeled after recordings from deaf children. Some of the synthetic versions included adjustments to timing and formant trajectories so that the deaf children's speech more nearly resembled normal speech. Ten versions of the word were used in a paired comparison task in which listeners were instructed to indicate the member of the pair which sounded most like natural speech. The ten versions included natural productions as well as synthetic versions. Rankings based on paired comparisons between synthetic and natural speech tokens suggested that duration adjustments had the strongest effects on naturalness ratings. However, the unaltered versions were ranked as being more natural sounding than even the duration-adjusted synthetic versions except in the case of one child who had very poor articulation.

Subsequently, Osberger and Levitt (1979) worked with recordings of sentences produced by 13- to 15-year-old children with congenital severe to profound hearing loss. The recorded sentences were digitized and the waveforms were modified to correct six types of timing errors. All other aspects of the speech samples were left unchanged. Judges were asked to write what they heard and an intelligibility measure was calculated. The only timing adjustment that produced an improvement in intelligibility was correction of relative timing errors. This correction involved matching the ratio of the stressed-to-unstressed vowels in each syllable produced by the children to the median value of the normal speaker.

A series of studies by Maasen and Povel (1984a, b, 1985) examined the effects of various computer based corrections on the intelligibility of sentences produced by deaf children. The speech of 12- to 14-year-old Dutch children, who had congenital sensorineural hearing loss of 90 dB or more, was used in the experiments. The deaf children were asked to produce sentences that were only recently introduced into their class reading material. Normal hearing children of the same age were also asked to produce the same set of sentences. Digital signal processing techniques, including LPC analysis and resynthesis were used to modify speech samples produced by the deaf children along the dimensions of timing, fundamental frequency, and the spectral compo-

[a)]''Selected research articles'' are ones chosen occasionally by the Editor-in-Chief that are judged (a) to have a subject of wide acoustical interest, and (b) to be written for understanding by broad acoustical readership.

nents of vowels and consonants. When appropriate, the characteristics of the speech produced by the normal hearing children were used for the corrections. Small but significant improvements in intelligibility were noted for correction of suprasegmental aspects of speech such as timing and fundamental frequency (intonation); however, when the corrections were applied to segmental aspects of speech (vowels and consonants), a major improvement in intelligibility was noted. The authors offer the general recommendation that, to improve intelligibility, it is more important to work on correcting problems in articulation than in timing and intonation. The authors also stress that this conclusion applies to the speech of deaf children who have acquired a steady voice and thus do not have problems with maintaining phonation. It could be that in instances where maintaining phonation is a problem, the relative contribution of suprasegmental corrections would be enhanced.

In the present set of experiments, the focus is on delineating the spectral and temporal characteristics of speech that are associated with a perceptual shift from disordered to normal speech. The aim is to discover the range and extent of spectral and temporal modifications that need to be applied to samples of deaf speech to be perceptually judged normal. The perceptual question, thus, is aimed at acceptability of speech as normal and not whether it is intelligible. Although work described above has generally pointed to the importance of segmental over suprasegmental factors in determining the intelligibility of deaf speech, the role of these factors in determining normal speech quality beyond intelligibility has not been examined and is addressed in the present experiments.

We report on three perceptual studies which made use of synthesized speech stimuli that differed along a deaf to normal continuum. The general approach was to analyze the speech samples produced by deaf and normal hearing speakers and synthesize a series of intermediate stimuli that together with the endpoint stimuli formed a continuum spanning the distance between the deaf and the normal speech samples.

I. EXPERIMENT 1

A. Introduction

The specific questions asked in this experiment were: (a) given normal timing and intonation, to what extent must the spectral properties of deaf speech approximate normal speech before it is reliably perceived as ''normal,'' and (b) what is the extent of perceived improvement in deaf speech if only the spectral envelope is changed without altering deaf timing and prosody?

The questions asked in experiment 1 were examined by the use of two sets of continua. One set examined whether the imposition of normal speech timing on the deaf talker's speech in and of itself made the speech sample sound normal; and if not, how close should the spectrum of the deaf speech sample be to the normal sample before it is judged to be normal. Using another set of continua, we inquired whether spectral modifications alone would make the deaf speech samples be perceived as normal.

B. Method

1. Subjects

Six female graduate students in Speech and Hearing from the University of Maryland participated as listeners in the study. They were all native speakers of English.

2. Stimuli

Recordings of the rainbow passage read by about 50 deaf students, enrolled at Gallaudet University, were reviewed. The recordings of three male talkers (identified as #35, #37, and #40) were selected because they were marginally intelligible and because each talker consistently attempted to pronounce all the segmental components of the passage they were asked to read. A normal hearing adult male talker (HTB) recorded the same passage; his speech samples were paired with similar tokens produced by the deaf talkers.

The word *beautiful* was extracted from the rainbow passage recorded by the four talkers and was used to generate stimuli for the six continua used in experiment 1. The three deaf talkers' productions of the word *beautiful* were identifiable as three-syllable words. Talkers #35 and #40 produced words which contained the expected consonant and vowel segments, and although they sounded disordered, the words were identifiable as *beautiful*. Talker #37 produced the word with a neutralized, flaplike /t/, and generally had the most disordered speech. The duration of this word for speaker #35 was 589 ms, for #37 was 464 ms, for #40 was 374 ms, and for the normal hearing speaker it was 684 ms. The deaf speakers, therefore, had faster speaking rates than the normal hearing speaker for this word.

Each token produced by a deaf talker was paired with the normal hearing talker's production of the same word to generate three continua, one for each deaf talker. The stimuli in these continua had normal timing and intonation and spanned the deaf to normal distance in ten spectral steps. Another set of three continua differed from the first set in that all stimuli retained the deaf talker's timing and intonation. Each of these three continua had different timing and intonation per the original deaf talker's productions.

There were several steps in the construction of the test stimuli. First, LPC analyses of the three deaf and one normal speech samples were carried out. Source (residual) and spectral (inverse filter) estimates were derived in successive 5-ms analysis frames. Inverse filtering was used to remove the spectral information specified by the LPC parameters, and whatever else was left (i.e., the residual signal) was considered to be source information. Next, an asymmetrical Dynamic Time Warping (DTW) algorithm was used to match frames of spectral information between deaf and normal pairs of words.

To temporally adjust the speech samples produced by the deaf talkers with the timing of the normal talker, LPC parameter files were edited by removing extraneous frames and inserting interpolated frames, where necessary, to optimally align the frames of the deaf and normal talkers per the DTW results. The temporally aligned deaf talkers' parameters were then used for residual excited LPC synthesis (ex-

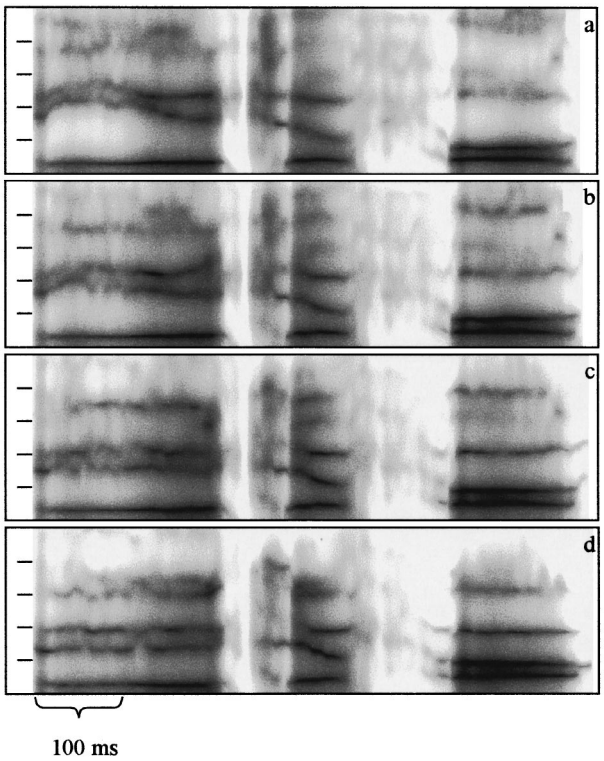

FIG. 1. LPC smoothed narrow-band spectrograms for the 90% normal endpoint (a), 60% normal token (b), 30% normal token (c), and deaf talker endpoint (d) in the continuum for deaf talker #35 from experiment 1. Frequency in 1-kHz increments is shown in the left border of each spectrogram, and a 100-ms time interval is illustrated along the bottom of panel (d). All panels share a common time base.

citing the LPC filters with the normal talker's residual signal). The same procedure was used to temporally align the token produced by the normal hearing talker to each of the tokens produced by the three deaf talkers. Thus the time alignment procedures meant that each of the three deaf speech samples was altered to be matched and paired with the normal speech for one set of continua; and the normal speech sample was modified three times to be paired with each of the three deaf speech samples for the second set of continua. In all cases, the residual excitation signal used for synthesis was derived from the utterance for which timing and intonation were being modeled. That is, normal timing continua were synthesized with the residual from normal speech; and the deaf timing continua were synthesized with the residuals from the associated deaf speaker's speech.

Finally, a ten-step spectral continuum was created for each of the six deaf-normal pairings of the word *beautiful* by linearly interpolating the LPC synthesis parameters (reflection coefficients) of every time frame. In each continuum, stimulus 1 was synthesized using the LPC parameters of the deaf talkers, stimulus 2 was synthesized using LPC parameters linearly interpolated to 10%, of the distance (in the LPC parameter space) between the deaf and normal hearing talkers, stimulus 3 approximated the normal LPC parameters by 20%, and so on up to stimulus 10 which approximated the normal LPC parameters by 90%.

Figure 1 illustrates the acoustic consequences of this interpolation procedure for stimuli in one of the continua (for deaf talker #35 aligned to normal speech timing). In this figure, LPC smoothed spectrograms are shown for the two endpoint stimuli [Fig. 1(a) and (d)] and for two intermediate stimuli (the 30% and 60% cases).[1] As this figure shows, the consequences of the interpolation procedure for formant frequencies are generally well-behaved and result in a graded progression from formant patterns associated with one talker to those of another. This is generally true in the case (as here) where the steps are relatively small with respect to the range of differences in the parameter space.

To summarize, there were six continua, three were formed by matching each of the disordered samples to the timing and intonation of the normal speech sample; and the residual used for synthesis was derived from normal speech. The other three continua were formed by matching the normal sample to the timing and intonation of each of the three disordered samples; and the residual used for synthesis was derived from each of the three deaf speakers.

3. Procedure

The listeners were tested individually. A computer system was used to present the stimuli to the listeners and to record their responses. The listeners were informed that the stimuli consisted of synthesized speech tokens based on the productions of deaf talkers saying the word *beautiful* which were altered in various ways. They were instructed to make their judgments, as to whether each token sounded normal or disordered to them.

The ten stimuli within each continuum were presented in ten randomizations, and the order in which each continuum was presented within a set was also randomized. The order in which the normal timing and the deaf timing continua were presented was counterbalanced. The subjects responded to the stimuli in each continuum twice. Trials were presented as a two-alternative forced choice task in which subjects were instructed to label the stimulus as either ''normal'' or ''disordered.''

C. Results

The results based on the continua in which the deaf talkers' speech was initially modified to match the normal talker's timing are illustrated in Fig. 2. This figure displays percent ''normal'' responses as a function of change in the spectrum of the stimulus for talkers #35, #37, and #40. On the *x*-axis, stimulus 1 represents the deaf speech end of the continuum and stimulus 10 the normal speech end of the continuum.

It can be seen that all the responses to the stimuli that were not modified spectrally (stimulus step 1) were rated as disordered (not normal) demonstrating that simply correcting the timing of the deaf speech samples to normal, without making any changes in the spectrum, does not make the stimuli sound normal. As the stimuli in a continuum approach the spectrum of the normal talker, however, there is an ordered increase in the proportion of ''normal'' responses corresponding to spectral modification in the stimuli.

The average number of times each stimulus was judged to be normal by the subjects was entered in a two-way

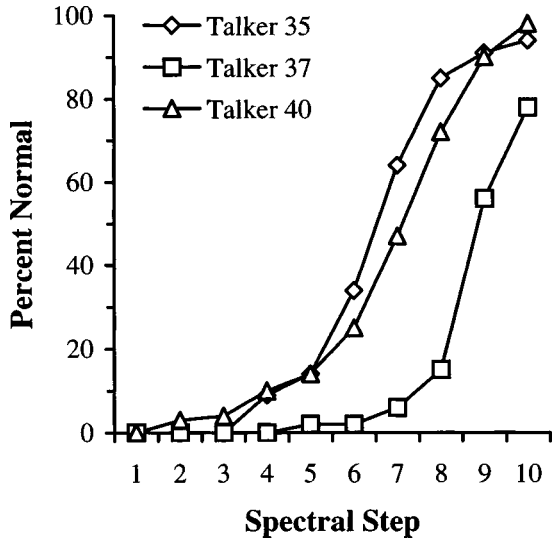

FIG. 2. Percent normal ratings given to the stimuli in three spectral continua based on the speech of deaf talkers #35, #37, and #40. All stimuli were synthesized and modeled on the timing and residual of the normal hearing talker. Continuum step 1 is the deaf end of the continuum.

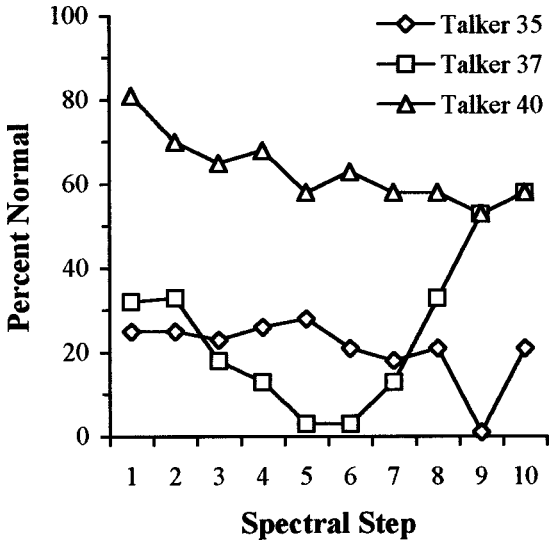

FIG. 3. Percent normal ratings given to the stimuli in three spectral continua based on the speech of deaf talkers #35, #37, and #40. All stimuli were synthesized and modeled on the speech timing and residual of the three deaf talkers. Continuum step 1 is the deaf end of the continuum.

ANOVA with talkers (three levels) and spectral steps (ten levels) as within subjects variables. Multiple group comparisons and simple main effects were calculated when appropriate. The results of the analysis revealed a significant main effect for talkers [$F(2,10)=15.43$, $p<0.0009$], spectral steps [$F(9,45)=50.93$, $p<0.0001$], and a significant interaction between talkers and spectral steps [$F(18,90)=4.39$, $p<0.0001$]. Talker #37 received significantly fewer normal ratings than talkers #35 and #40 who did not differ from each other. The interaction revealed that the difference among the talkers was significant only for stimuli that approached normal spectral patterns (spectral steps 6–10). The spectral steps effect, as seen in Fig. 2, showed that the speech of all talkers was consistently rated disordered at the deaf end of the continuum and was more likely to be rated normal at the other end of the continuum. Further analysis of the spectral steps factor showed three groupings of the stimuli: spectral steps 1–6 received very low normal ratings (0%–20%) and did not differ among themselves, spectral steps 7–8 received significantly higher normal ratings (40%–57%) and did not differ from each other, and spectral steps 9–10 received the highest ratings (79%–85%).

In contrast, the listeners' responses regarding the stimuli that were based on the deaf talker's timing was varied and somewhat unstable. The listeners frequently commented that they found the stimuli in these three continua difficult to judge. Some indicated that they did not hear clear differences among the stimuli within a continuum to enable them to respond reliably. The results are shown in Fig. 3.

Similar statistical analyses were carried out on the ratings of these stimuli, namely a two-way ANOVA was done with talkers (three levels) and spectral steps (ten levels) as within subjects variables. There was a significant main effect for talkers [$F(2,10)=7.84$, $p<0.009$], and group comparisons indicated that speaker #40 received significantly more normal speech ratings than speakers #35 and #37. The main effect of spectral steps was not significant, and as can be seen in Fig. 3 there was no correspondence between spectral changes in the stimuli and the ratings of the listeners. A significant interaction between talkers and spectral steps [$F(18,90)=2.03$, $p<0.02$] was due to a dip in ''normal'' speech ratings for talker #37 at the center of the continuum.

D. Discussion

A 70% ''normal'' rating was used as a cut off score indicative of normal speech. This criterion was used to examine the group means listed in Figs. 2 and 3. The criterion of normal speech was reached for some of the stimuli in the continua based on normal timing (Fig. 2) however, almost all the means of the continua based on deaf timing (Fig. 3) were below this cut off point. Looking at the group means in Fig. 2, normal speech ratings was reached at stimulus 8 (70% normal spectrum) for deaf speakers #35 and #40, and stimulus 10 (90% normal spectrum) for deaf speaker #37. It can be concluded that in these temporally adjusted stimuli, and for two out of the three deaf talkers, only the stimuli that approximated the normal spectrum by about 70% or better were judged to be normal. Deaf speaker #37 was less intelligible than the other two speakers. Although his token of the word *beautiful* did not contain any missing segments and listeners could identify the word easily, his pronunciation of individual segments deviated more from normal than for the other two deaf speakers. Consequently, the spectral difference between his productions and the normal talker was more than for the other deaf talkers.

One interpretation of the results for the set of continua based on deaf timing and intonation (Fig. 3) is that the presence of normal timing and intonation is a precondition for speech to be judged normal. That is, with disordered timing and intonation, spectral modifications do not play a consistent role in contributing to what is perceived as normal speech. Instead, the results suggest that listener judgments

were not affected by the spectral adjustments in these continua.

In general, the results of experiment 1 suggest that spectral changes in the context of normal timing bring about a perceptual shift in judgment toward normal speech; however, the same spectral changes in the context of deaf speech timing do not produce a reliable perceptual shift to normal. However, there are several confounding factors to be considered as well. First, by design, timing and intonation were confounded in this experiment. Although intonation did not seem particularly disruptive for any of the talkers, it is unclear if effects are due specifically to timing, or to intonation, or to both combined. Second, because residual excitation was used, it is possible that spectral information retained in the residual signal tended to bias or confound the results. If the all-pole LPC model was a poorer fit to the deaf speech (e.g., because of greater nasality) than to the normal speech, we would expect the residual signals from the deaf speech to retain more of the deaf speech spectral features. Consequently, in resynthesis, more of the deaf spectral features would be preserved, even at the normal speech end of the spectral continua. Experiment 2 was designed to address these issues and examine the timing (independent of intonation) in greater detail.

II. EXPERIMENT 2

A. Introduction

In experiment 2 an attempt was made to separate the effects of timing from the effects of possible artifacts (due to the residual of deaf speech) by using a neutral signal to excite the LPC vocoder for synthesis. The question asked in this experiment was: how would partial timing adjustments of deaf speech influence judgments of normality? In other words, is there a trade-off between temporal and spectral adjustments of deaf speech?

B. Method

1. Subjects

Another group of seven female graduate students in Speech and Hearing from the University of Maryland participated as listeners in the study. They were all native speakers of English.

2. Stimuli

The same original tokens of the word *beautiful* produced by deaf talkers #35 and #40 and the normal talker were used to generate the stimuli in this experiment. To test the effect of timing and spectral adjustments factorially, spectral change continua were created for five levels of timing adjustment relative to the difference between deaf and normal timing: (1) no temporal change; (2) a 25% change toward normal; (3) a 50% change toward normal; (4) a 75% change toward normal; and (5) a complete (100%) match with normal timing.

The timing adjustments to create end point stimuli for each of the five continua were based on linear temporal expansion or compression of syllables within the deaf and normal speech. Consequently, a syllable originally produced by a deaf talker with the same duration as the normal talker's corresponding syllable would not vary in duration over the five steps of the temporal continuum. A speech waveform time compression and expansion program developed by the second author was used to produce time-altered waveforms from the original speech tokens. The program achieved the desired syllable durations by repeating or deleting brief signal epochs which corresponded to pitch periods in voiced regions and to similar sized chunks of waveform in unvoiced regions of the stimuli (a more detailed description of the algorithm is given in the Appendix). A study by Pitt and Samuel (1995) showed that even substantial time compression produced by using this algorithm results in an acceptably small loss of intelligibility for normal speech.

Following the time alignment procedure, the same general procedures for synthesis used in experiment 1 were followed. For these stimuli, however, the LPC vocoder excitation signal was generated by matching a synthetic glottal pulse and noise model to the residual of the (in some cases time-altered) normal speech. This synthetic source function made use of the Rosenberg (1971) glottal waveform approximation, adjusted for use with the LPC vocoder, during voiced regions of speech and used Gaussian noise for voiceless excitation. The synthetic source could also contain mixed (glottal pulses+noise) excitation signals.

As in experiment 1, each of the continua consisted of spectral steps that were created by linearly interpolating LPC reflection coefficients between the tokens of the deaf and normal hearing talkers. However, in experiment 2, seven rather than ten spectral steps were used. In addition, at each of the spectral steps, the $F0$ did not change, i.e., there were no pitch variations associated with spectral steps; the $F0$ contour was that of the normal talker for all stimuli. In all, the stimuli for the ten continua created for this experiment made use of speech samples from two deaf talkers at five timing levels and seven spectral steps.

The no temporal change condition (Time 1: deaf timing) is in essence a replication of the second part of experiment 1. For this set of stimuli, however, a synthesized neutral source which modeled normal intonation was used to drive the vocoder. Thus temporal and spectral factors were varied orthogonally over the various experimental continua, but intonation and other source features were held constant.[2]

3. Procedure

The test setting, instructions to the listeners, computer system for stimulus delivery and response recording were similar to the ones used in experiment 1.

The seven stimuli within each continuum were presented in ten randomizations, and the order in which each continuum was presented was also randomized. The order in which the continua based on the tokens of speaker #35 and speaker #40 were presented was counterbalanced.

C. Results

The results of this experiment are shown in Fig. 4. The figure shows averaged group judgments for the two talkers.

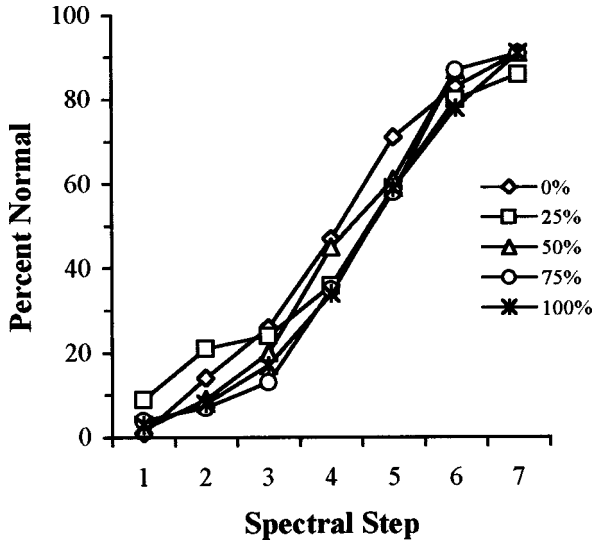

FIG. 4. Percent normal ratings given to stimuli in five spectral continua, each representing a different level of timing adjustment (from 0% normal time to 100% normal time). All stimuli were synthesized by using a synthetic source (glottal pulse and noise) matched to the residual of normal speech. The responses are averaged over stimuli based on the speech of talkers #35 and #40.

Each of the five lines in the figure represents a different timing level. The subjects' responses were entered into a three-way ANOVA with talkers (two levels), temporal adjustment (five levels) and spectral steps (seven levels) as within subjects variables. The main effects for talkers and for temporal adjustment were not significant; however, the main effect for spectral steps was highly significant [$F(2,24) = 126.45$, $p < 0.0001$]. There was, in addition, a significant interaction between talkers and temporal adjustment [$F(4,24) = 6.78$, $p < 0.0008$]; no other interaction was significant.

The significant spectral steps factor revealed that there was an orderly increase in the number of normal speech ratings as the spectral steps were modified in the direction of normal. Further analysis of this factor indicated that stimuli in spectral steps 6 and 7 received significantly more ratings of normal than all other stimuli. At the other end of the continuum, spectral step stimulus 1 received significantly fewer ratings of normal than all other stimuli. The intermediate stimuli were either significantly different from their adjacent steps (spectral steps 4 and 5) or only overlapping with their adjacent steps (spectral steps 2 and 3).

The temporal adjustment factor was not significant, revealing that the stimuli with and without temporal adjustment were rated at the same level of normality. This finding suggests that using a neutral source but keeping the deaf speech timing intact can produce perceptual ratings of normal speech. That is, spectral modifications applied to speech tokens with deaf timing, but using a neutral sound source, produced perceptual ratings that were reliably judged to be normal. The criterion of 70% normal was reached for stimuli in spectral steps 6 and 7.

The interpretation of the significant interaction between talkers and temporal adjustment is not interesting; it indicates that deaf speaker #40 had slightly higher average normal ratings than speaker #35 at temporal adjustment levels 1 and 2 and the difference between the 2 speakers was reversed at temporal adjustment levels 4 and 5.

D. Discussion

The findings of this experiment support those of experiment 1 by demonstrating the perceptual importance of spectral modifications applied to deaf speech. That is, as the spectrum of the stimuli approached that of the normal speech, there was a concomitant perceptual shift in the direction of normal. Furthermore, and in contrast to the results of experiment 1, the results of this experiment indicate that spectral modifications of the stimuli had the same perceptual impact, independent of adjustments in syllable timing. That is, normal timing does not appear to be a precondition to speech being judged normal, and there does not seem to be a trade-off between spectral and temporal modifications. The only variable that affected perceptual judgments was the change in the spectrum of the stimuli.

It could be concluded, at this point, that the problems with evaluating the stimuli synthesized with the deaf residuals to create deaf timing in experiment 1, had to do with the effects of using the deaf residual and were not related to deaf timing per se. However, with a stimulus item of only three syllables, it is possible that timing effects were just too small to be observed. Consequently, experiment 3 was designed to extend these results to stimuli of more complex rhythmical structure.

III. EXPERIMENT 3

A. Introduction

The aim of this experiment was to extend the results of the previous experiments to phrase-length speech tokens since it is possible that timing effects are better assessed in such materials. Additionally, rather than fixing the intonation pattern to model the properties of normal intonation in all stimuli, we allowed the intonation pattern to vary from disordered to normal in a manner that was redundant with spectral changes while still orthogonally varying the timing dimension alone. It was thought that this might increase the perceptual differences between the normal and non-normal ends of the continua and hence provide more opportunity to observe effects of timing, especially at the non-normal end of the continua.

B. Method

1. Subjects

A third group of eight female graduate students in Speech and Hearing from the University of Maryland participated as listeners in the study. They were all native speakers of English.

2. Stimuli

The speech sample used in this experiment was a ten-syllable phrase from the rainbow passage: *When the sunlight strikes raindrops in the air*. The speech of deaf speaker #37 was used because it was reasoned that the least intelligible

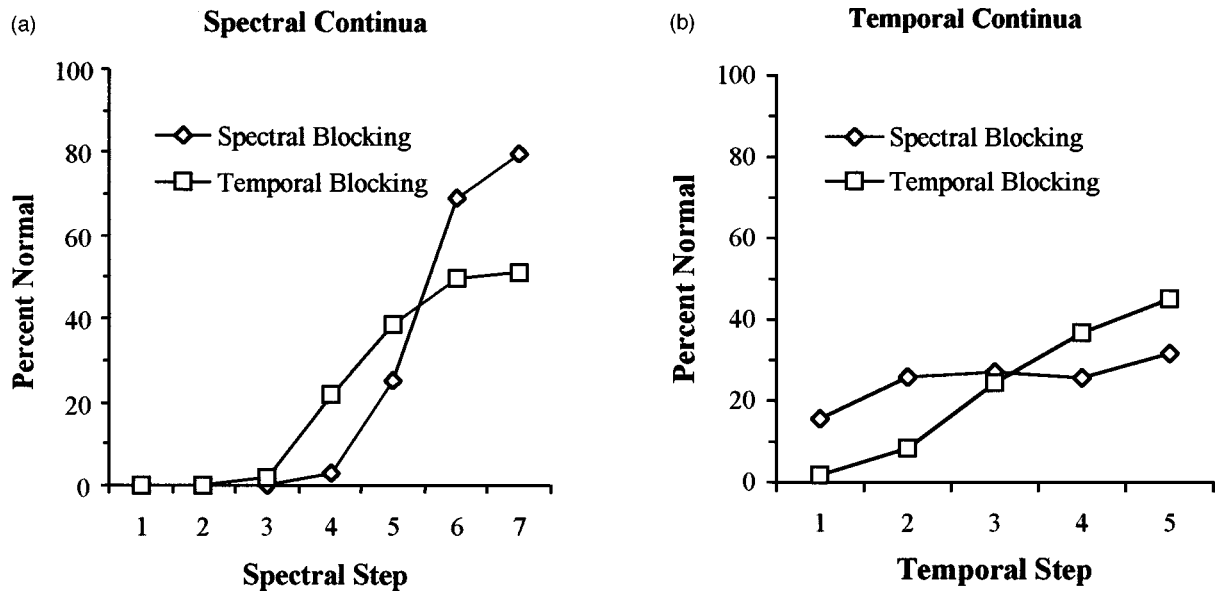

FIG. 5. Percent normal ratings given to the stimuli in experiment 3. (a) Listeners' ratings demonstrating the perceptual effect of spectral adjustments in spectral block trials and temporal block trials, and (b) ratings demonstrating the perceptual effect of temporal adjustments in spectral block trials and temporal block trials.

speaker might show the greatest timing adjustment effect. Speaker #37's pronunciation of this phrase contained all of the consonantal and vowel segments, although segments tended to be nasalized, and friction energy was very weak for all fricative segments. The duration of this phrase as produced by speaker #37 was 3517 ms. A normal-hearing male speaker's recording of this phrase was selected from previously digitized materials for use as the normal template. This was a different speaker than the normal-hearing male speaker in the previous experiments. The duration of the normal phrase was 2464 ms.

The procedure for creating five different temporal adjustments was the same as in experiment 2, that is, phrases for both talkers were first aligned by linear expansion or compression of syllable durations to target patterns representing each of the five temporal steps. These time aligned endpoint stimuli were then analyzed to obtain LPC parameters for synthesis.

The synthesis excitation signal in this experiment was a simple pulse train for voiced segments and Gaussian noise for voiceless segments. In these series, the timing of the stimuli was separated from intonation which varied from deaf to normal redundantly with spectral changes.

The stimuli consisted of five continua, one for each timing adjustment, each of which had seven spectral steps ranging from deaf to normal spectral characteristics; thus there were 35 different stimuli in all. With these stimuli, however, the usual linear interpolations for the spectral steps from deaf to normal were also accompanied with linear interpolations of $F0$ and amplitude. That is, the intonation contour also changed linearly from deaf to normal within each continuum.

3. Procedure

The test setting, instructions to the listeners and computer system for stimulus delivery and response recording were similar to the ones used in experiment 2.

The stimuli within each continuum were presented in ten randomizations, and the order in which each continuum was presented was also randomized. Subjects in this experiment were presented the 35 stimuli blocked in two counterbalanced orders: (a) trials that were blocked for spectral steps (within each continuum, the temporal adjustment of the stimuli was constant and the spectral steps varied), and (b) trials that were blocked for temporal adjustment (within each continuum, the spectral modification of the stimuli was constant and the temporal adjustments varied). The format of the trials blocked for spectral steps was the same as that used in experiments 1 and 2. It was assumed that the spectral blocking would enhance the spectral effect and temporal blocking would enhance the temporal effect.

C. Results

The results based on the spectral block and temporal block trials are presented in Fig. 5(a) for the seven spectral steps and in Fig. 5(b) for the five temporal steps. A comparison between the values shown for experiment 3 and those shown for experiments 1 and 2 reveals an overall drop in the incidence of normal speech ratings, presumably reflecting the use of only the least intelligible talker (#37). To assess the relative contributions of spectral and temporal modifications, and whether these factors contribute independently to perception of normality, a log-linear analysis was used. This analysis models data in hierarchically structured frequency tables by determining the minimum number of factors (main effects) and interactions needed to account for the data.

For the present analysis, two seven by five tables of frequencies were constructed. Each table represented a different blocking factor (either spectral or temporal blocking) and the rows and columns of each table were the seven spectral and five temporal steps. Thus the complete dataset formed a three-dimensional ($7\times5\times2$) table for analysis. The results of this analysis showed a significant spectral ef-

fect (χ^2df=6, 1741.7, $p<0.0001$) and significant temporal effect (χ^2df=4, 266.41, $p<0.0001$). The main effect of block was not significant. It also revealed significant interactions for spectral by block (χ^2df=6, 108.53, $p<0.0001$) and temporal by block (χ^2df=4, 132.12, $p<0.0001$) effects; however, the interaction between spectral and temporal factors was not significant. Finally, the three-way interaction was not significant.

Figure 5(a) plots the means involved in the significant spectral by block interaction, and in Fig. 5(b) the means for the significant temporal by block interaction are shown. The parameter in each panel is the blocking factor. In Fig. 5(a), it can be seen that the effects of spectral changes are enhanced when stimuli are blocked spectrally, and similarly it can be seen in Fig. 5(b) that temporal changes are enhanced when stimuli are blocked temporally. However, the magnitude of spectral effects, Fig. 5(a), is substantially greater than the magnitude of the temporal effects, Fig. 5(b).

IV. GENERAL DISCUSSION

Experiment 3 extended the results of the previous experiments to speech stimuli of longer duration, allowed intonation to vary independently of timing (although redundantly with spectral factors), and further used presentation blocking to enhance possible temporal and spectral effects. Despite these differences, the results of all experiments suggest that spectral features contribute more to the perception of normality than temporal features. It was never possible to produce a criterion level of 70% normal judgments by altering the temporal structure of deaf speech without spectral modification as well. In experiment 2, with short three-syllable stimuli and normal intonation, spectral changes in the absence of temporal changes were sufficient to produce at least 70% judgments of normal. In experiment 3, a combination of temporal and spectral changes were needed to produce 70% or higher normal ratings, but spectral effects were both stronger than, and independent of, the temporal effects. Only in experiment 1 did it appear that normal timing and intonation were prerequisite to judgments of normal, and in that experiment, the conclusion is suspect because of the possible confounding of spectral and temporal information within the deaf speech residual signals used for synthesis.

The temporal disruption associated with speech disorders is often large (Darley *et al.*, 1975) and appears to be correlated with both intelligibility and naturalness (Linebaugh and Wolf, 1984). Nonetheless, studies evaluating the relative contributions of temporal and spectral factors to speech intelligibility generally support the view that spectral factors are more important (Maasen and Povel, 1984a, b, 1985). One reason for undertaking the present study was the possibility that the subjective impression of the importance of timing in speech disorders would be reflected more in judgments of normality than in measures of intelligibility. However, the findings of the present experiments tend to parallel those of experiments in which the intelligibility measure is used and show the predominance of spectral factors in normality judgments as well.

It is necessary to qualify this conclusion by noting that the distinction between spectral and temporal features in speech is somewhat arbitrary. In preparing the stimuli for experiments 2 and 3, the syllable level was chosen as the level at which timing was manipulated. That is, syllable durations were linearly expanded or compressed to align deaf and normal utterances. Thus temporal features were associated with rhythmic structure and with segmental durations in constant proportion to the durations of their parent syllables; while spectral features were associated with the redistribution of segmental durations within a syllable and more fine-grained variations in articulatory patterns, even thought such variations implicitly involve timing as well. For instance, subtle features such as the way vowel offglides are patterned, and the pattern of vocalic transitions associated with CV and VC gestures, as well as less subtle features such as the relative durations of vowels and surrounding consonants within the same syllable fell into the category of spectral effects. For experiment 2, which involved only the word *beautiful*, it does not appear that a finer-grained definition of timing would have made any difference. However, it is possible that effects of timing could have been more pronounced in experiment 3 if timing had been adjusted at the segmental or sub-segmental level (as in experiment 1).

To explore this further, three spectrograms from stimuli in experiment 3 are shown in Fig. 6. The top panel [Fig. 6(a)] shows the LPC spectrogram of the synthetic version of the deaf talker's production of the ten-syllable test phrase. The central panel [Fig. 6(b)] shows the spectrogram of the same phrase after timing adjustment to align syllable onsets with those in the normal talker's phrase. The bottom panel [Fig. 6(c)] is the spectrogram of the synthetic version of the normal talker's production. Vertical lines running through all three panels indicate the approximate temporal alignment points used in the signal processing. Perceptual differences between the stimuli associated with panels (a) and (b) would be attributed to temporal modification while differences in perception between stimuli associated with panels (b) and (c) would be attributed to spectral modification.

Several features are worth noting in this figure. First, the normal talker neutralizes the /ð/ of *when the*, replacing the /nð/ with a dentalized nasal which is released into schwa [see the leftmost two regions of Fig. 6(c)]. This is a pattern which is typical of connected speech (Manuel *et al.*, 1992). The deaf talker produces these two words with a very brief nasal stop in the coda of *when*, virtually no nasal murmur, a period of silence, between *when* and *the*, and replaces /ð/ with what is perceptually a weak unaspirated /d/ [see the leftmost two regions of Fig. 6(b) and (a)]. These articulatory differences between the talkers certainly have both temporal and spectral components. It is possible that temporal factors would have appeared to be more important had a very fine-grained temporal restructuring of the spectral features in the deaf talker's utterance been used. For instance, by lengthening the end of *when* while shortening the silent interval following *when*, something similar to the normal talker's nasal murmur might have resulted. However, given that the spectrum at the end of the deaf talker's *when* is different than the normal talker's nasal murmur, such fine-grained temporal restructuring might only have resulted in a different but equally unnatural-

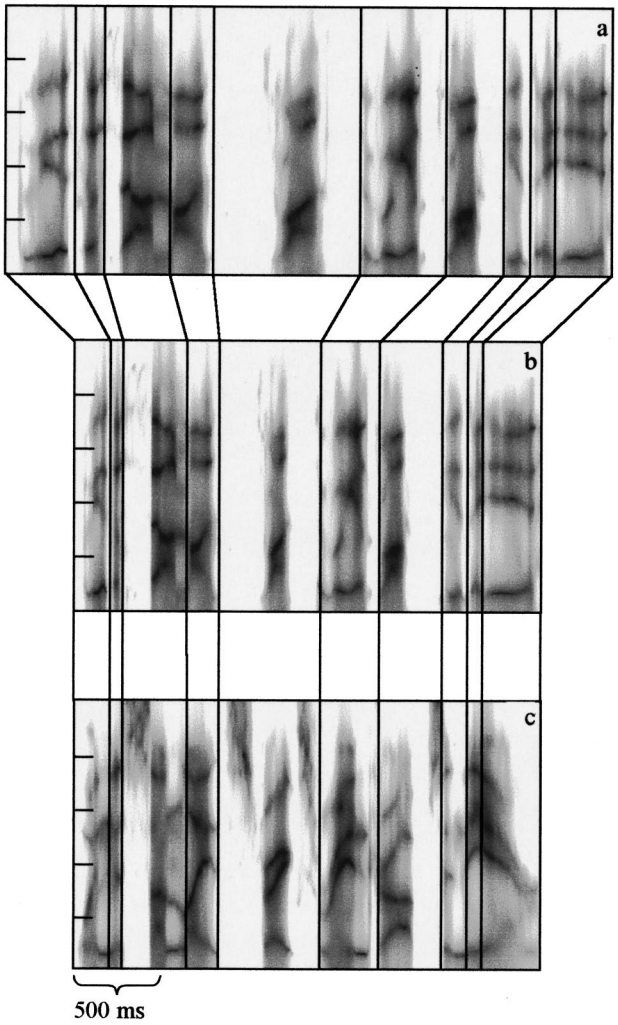

FIG. 6. LPC smoothed narrow band spectrograms for three stimuli in experiment 3. (a) Original deaf talker's phrase, (b) deaf talker's phrase temporally aligned to the normal talker's phrase, and (c) normal talker's phrase. All spectrograms are derived from the synthetic versions of the stimuli used in the experiment. Vertical lines are drawn through each panel to illustrate alignment points for the temporal adjustments. Frequency in kHz is indicated within each panel. The common timescale is indicated in ms below panel (c). The phrase is: when the sunlight strikes raindrops in the air.

sounding utterance. Moreover, practical limitations in the signal processing typically result in distortions when a segment of speech is extended in duration by more than a factor of 2 or 3, thus reducing perceived normality.

The differences between the talkers for *when the* are the most extreme of the examples that can be seen in Fig. 6. In other cases, there may be smaller segmental or subsegmental temporal differences which, in the present analysis, will be attributed to spectral changes. However, inspection of the overall differences between the spectrograms in Fig. 6 suggests that spectral, not temporal differences dominate the differences between these tokens. In addition to the absence of virtually any friction energy visible in the deaf talker's phrase, every voiced region shows marked differences in formant frequencies and formant trajectories which for the most part could not be resolved by temporal restructuring, nor accounted for by simple differences in, for example, vocal tract length. Given these considerations, the conclusion that spectral rather than temporal factors are most crucial in determining perceived normality is warranted.

Applying these results to clinical practice suggests that it is more important to achieve improvements at the segmental level rather than in speech timing as the outcome of clinical treatment. This was also the conclusion drawn by Maasen and Povel (1984a, b, 1985) who worked with speech samples from deaf children in the Netherlands. However, it is worth bearing in mind that these results speak to the desired outcome of treatment and do not necessarily imply that the course of effective treatment must focus on segmental articulation to the exclusion of prosodic, and particularly timing factors. Indeed, it is possible that the best training to achieve improvements at the segmental level builds on establishing a well-grounded timing strategy. Our experiments cannot address this issue, but our findings in conjunction with results of previous studies clearly show the importance of improved segmental articulation as an outcome of speech therapy.

The findings of this set of experiments are also in accord with results of studies on computer enhancement of disordered speech (e.g., Bunnell *et al.*, 1992; Bunnell, and Polikoff, in preparation). These investigators adjusted the timing of short sentences produced by dysarthric talkers to achieve temporal alignment at the segmental level with normal speech exemplars of the same sentences. A total of 740 sentences (74 sentences and 10 talkers) were presented to listeners in both original and time-aligned form. Segmental intelligibility was measured using a closed response set identification task for three keywords in each sentence. Overall, and in nearly all specific contrasts, segmental intelligibility was either unchanged or slightly lowered as a result of temporal alignment with normal speech. These authors conclude that, while adjusting the temporal structure of dysarthric speech may produce objectively more natural timing, significant improvements in segmental intelligibility are unlikely to be observed without adjustments to the spectral structure as well. That is, it is more important to directly work on improving the spectral properties of the signal than on adjusting its temporal features.

In summary, in experiment 1, the timing of disordered speech samples was modified to fit the temporal structure and prosody of normal speech and then spectral adjustments were applied to the speech samples. Another set of stimuli was used to investigate whether spectral modifications alone would make deaf speech samples be perceived as normal. In experiment 2, we evaluated the contribution of temporal modifications in more detail. In experiment 3, we used a longer sample of speech and again examined the relative contribution of spectral and temporal modifications to the perception of normal speech. In all experiments our general conclusion is that the contributions of spectral adjustments to normality judgments are more effective than temporal adjustments.

ACKNOWLEDGMENTS

The authors thank James J. Mahshie for providing them with the deaf speech samples. They also thank Peggy M. Schmid for her help in collecting the data and all the listeners for their cooperation.

APPENDIX: METHOD USED FOR TIME COMPRESSION AND EXPANSION

The algorithm for time compression and expansion was developed for use in altering the temporal structure of dysarthric speech (Bunnell *et al.*, 1992). However, it has been used by a number of investigators for temporal modification of normal speech as well (e.g., Gordon-Salant and Fitzgibbons, 1993; Pitt and Samuel, 1995). The procedure works by copying an input waveform file to an output waveform file occasionally duplicating or skipping short sections of the input waveform to achieve a required timescale modification. For voiced regions of the input file, the segments copied are (with high probability) individual pitch periods, thus maintaining the fundamental frequency of the speech being compressed or expanded in time. For unvoiced regions of the input, the same segment selection criteria leads to choosing portions of the waveform which are of approximately pitch period length.

The general design of a program implementing this algorithm is illustrated in the flowchart shown in Fig. A1. After initializing various data registers, the program chooses a waveform epoch (pitch period or unvoiced region of short duration), appends the epoch to the output, computes the new duration of the output file, and then computes a location within the input file from which to select the next epoch based on the timescaled duration of the output waveform.

The most difficult part of this process is selecting epochs to copy. A variety of methods for pitch period location have been tried for use in this algorithm, including inverse filtering techniques (e.g., Markel, 1972) and wavelet analysis (e.g., Kadambe and Boudreaux-Bartels, 1992). However, for most laboratory speech (i.e., good signal to noise ratio and stable recording channel characteristics), a simple approach based on detecting features within a low-pass filtered copy of the input waveform often performs nearly as well as more elaborate techniques, at relatively low computational cost. For this approach, the input waveform is low-pass filtered at 850 Hz so that it will be likely to include oscillations due to $F1$, but not $F2$. The filtered waveform is then searched in the region from which a segment is to be copied to locate the largest excursion between a waveform minimum and adjacent (preceding or following) maximum. From the location of the maximum, the preceding positive-going waveform zero crossing is then taken as the start of a pitch period. Using similar logic, the start of the immediately following pitch period is also located (subject to parameters which constrain the likely $F0$ and jitter for the speech), and from that the duration of the pitch period to be copied is determined. To avoid compounding errors, this process is restarted as an independent search each time a pitch period is to be located.

When the input speech signal is not voiced, the same logic is used to locate some waveform feature within the input which can serve as the start of a waveform epoch to be copied. On occasions where there is too little energy below 850 Hz to leave useful minima and maxima in the filtered waveform, the search returns to the center of the input sequence as the next location of a pitch period and 10 ms as the period duration.

Finally, each epoch is isolated with a small amount (generally 1.5 ms) of prior waveform context which is used for overlap blending of the epoch with the tail of the output waveform. The blending process is a weighted averaging of the samples in the overlap region with corresponding samples in the tail of the output waveform. A weighting factor is linearly incremented from zero to 1.0 over the duration of the overlap region to increase the contribution of the new data to the average while a complementary weight is applied to samples from the tail of the output waveform. This eliminates small waveform discontinuities which might arise when epochs are either duplicated or skipped due to differences in the timescales of the input and output waveforms.

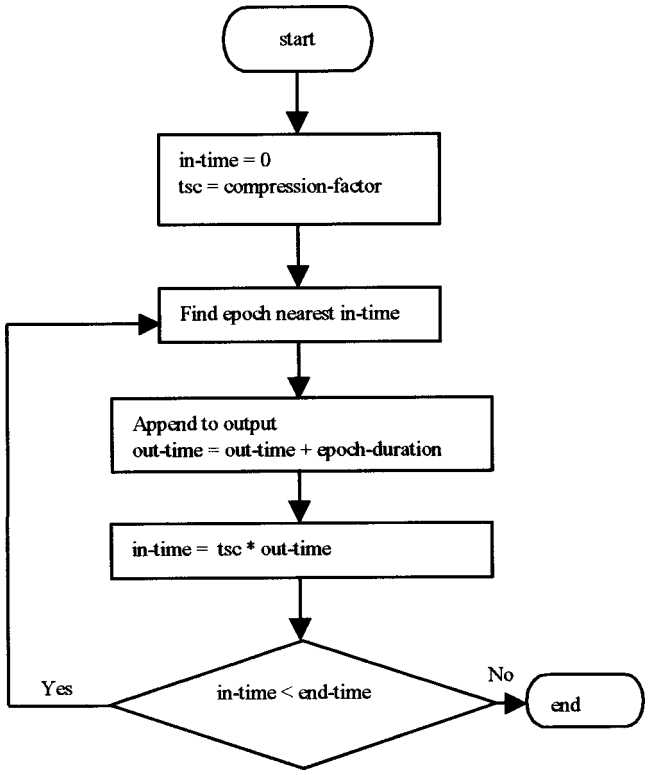

FIG. A1. Flowchart illustrating method used for time scale modification of speech in experiments 2 and 3.

[1]The LPC smoothing was computed with a 25-ms Hanning window and 12 inverse filter coefficients using the preemphasized (6 dB/oct) speech waveform. This display format provides roughly the frequency resolution of a narrowband spectrogram without imaging the voice harmonics, thus giving a clear view of the consequences of the interpolation vis-a-vis formant frequencies.

[2]It is, of course, impossible to completely separate intonation pattern from timing since intonation is a pattern defined over time. However, in so far as intonation could be describe in ordinal terms, the pattern was fixed for all stimuli.

Bunnell, H. T., and Polikoff, J. B. (**in preparation**). ''Toward enhancement of dysarthric speech: Perceptual effects of temporal modifications.''

Bunnell, H. T., Polikoff, J. B., Peters, S. M., Kadambe, S., and Mineo, B. (**1992**). ''Progress in computer enhancement of dysarthric speech,'' Presentation to the fourth meeting of the International Society of Augmentative and Alternative Communication, Philadelphia, USA, August, 1992.

Darley, F. L., Aronson, A. E., and Brown, J. R. (**1975**). *Motor Speech Disorders* (Saunders, Philadelphia, PA).

Gordon-Salant, S., and Fitzgibbons, P. (**1993**). ''Temporal factors and speech recognition performance in young and elderly listeners,'' J. Speech Hear. Res. **36**, 1276–1285.

Kadambe, S., and Boudreaux-Bartels, G. F. (**1990**). ''A pitch detector based on even detection using the dyadic wavelet transform,'' Proceedings of the

International Conference on Spoken Language Processing, Kobe, Japan, Vol. 1, pp. 469–472.
Levitt, H. (**1973**). ''Speech processing aids for the deaf: An overview,'' IEEE Trans. Audio Electroacoust. **AU-21**, 269–273.
Linebaugh, C. W., and Wolf, V. E. (**1984**). ''Relationship between articulation rate, intelligibility, and naturalness in spastic and ataxic speakers,'' in *The Dysarthrias: Physiology-Acoustics-Perception-Management*, edited by M. R. McNeil, J. C. Rosenbek, and A. E. Aronson (College Hill, San Diego).
Maasen, B., and Povel, D. J. (**1984a**). ''The effect of correcting temporal structure on the intelligibility of deaf speech,'' Speech Commun. **3**, 123–135.
Maasen, B., and Povel, D. J. (**1984b**). ''The effect of correcting fundamental frequency on the intelligibility of deaf speech and its interaction with temporal aspects,'' J. Acoust. Soc. Am. **76**, 1673–1681.
Maasen, B., and Povel, D. J. (**1985**). ''The effect of segmental and suprasegmental corrections on the intelligibility of deaf speech,'' J. Acoust. Soc. Am. **78**, 877–886.
Manuel, S. Y., Shattuck-Hufnagel, S., Huffman, M., Stevens, K. N., Carlson, R., and Hunnicutt, S. (**1992**). ''Studies of vowel and consonant reduction,'' Proceedings of the International Conference on Spoken Language Processing, Banff, Canada, Vol. 1, pp. 943–946.
Markel, J. D. (**1972**). ''The SIFT algorithm for fundamental frequency estimation,'' IEEE Trans. Audio Electroacoust. **AU-20**, 367–377.
Osberger, M. J., and Levitt, H. (**1979**). ''The effect of timing errors on the intelligibility of deaf children's speech,'' J. Acoust. Soc. Am. **66**, 1316–1324.
Pitt, M. A., and Samuel, A. G. (**1995**). ''Lexical and sublexical feedback in auditory word recognition,'' Cogn. Psychol. **29**, 149–188.
Rosenberg, A. (**1971**). ''Effect of glottal pulse shape on the quality of natural vowels,'' J. Acoust. Soc. Am. **49**, 583–590.

An approximation to the planar harmonic Green's function at branch points in wave-number domain

Eugene J. Danicki
Polish Academy of Sciences, IPPT, 00-049 Warsaw, Poland

(Received 15 April 1997; revised 1 October 1997; accepted 7 April 1998)

An arbitrary anisotropic piezoelectric half-space is considered, and harmonic wave field in both time and space on its surface. A planar harmonic Green's function, dependent on the wave number, is involved in the matrix relation between complex amplitudes of the applied traction and the resulting particle displacement on the surface of the half-space. An approximation to this function is derived, being valid in the vicinity of the cutoff slownesses of bulk waves, for certain cases of the shape of the slowness curves at the cutoffs. The Stroh formalism is adopted and a new theorem is proved for this purpose. This approximation is useful in any analysis of the wave field carried out by means of the methods of complex variable, for example in finding the singular points or determining the type of branch points (at the cutoff wave numbers of bulk waves) on the complex plane of a wave number. The branch points of square and cubic root type are discussed. The approximation parameters are derived from the matrix dependences at a given branch point. The computed examples are presented for effective surface dielectric permittivity of quartz substrate. © *1998 Acoustical Society of America.* [S0001-4966(98)02008-6]

PACS numbers: 43.20.Bi, 43.20.Gp, 43.20.Jr, 43.35.Pt [JEG]

INTRODUCTION

In this paper, we consider a planar harmonic Green's function **G** for piezoelectric half-space, which is involved in the equation

$$[U_i \;\; -E_1]^T = \mathbf{G}(r)[T_{3i} \;\; D_3]^T, \tag{1}$$

where $U_i = \partial u_i / \partial x_1$, u_i is the particle displacement ($\mathbf{U} = \mathbf{u}_{,1}$), $E_1 = -\varphi_{,1}$ is the tangential electric field, φ is the electric potential, T_{3i} is the stress component (a traction on the surface of the body, **T**), and D_3 is the electric flux density (normal component), all on the surface of the considered arbitrarily anisotropic piezoelectric half-space $x_3 \leqslant 0$, where they are assumed to be harmonic functions of x_1 and time t in the form ($j = \sqrt{-1}$)

$$\exp(j\omega t - jrx_1), \tag{2}$$

with angular frequency ω and wave number r (a real spectral variable).

Equation (1) is the Fourier transform of the relation

$$[\mathbf{U} \;\; -E_1{}^T](x_1,t) = \int\int \mathbf{G}(x_1 - x_1'; t - t') \times [\mathbf{T} \;\; D_3]^T(x_1', t')\, dx_1'\, dt' \quad \text{at } x_3 = 0.$$

The above notations for the wave-field components are extended to their complex amplitudes dependent on r, for example, $\mathbf{U} = -jr\mathbf{u}$. It will be later assumed that the wave field in the body (for $x_3 < 0$) depends on x_3 according to $\exp(j\omega t - jrx_1 - jsx_3)$, with s being generally a complex number.

At given frequency ω, the matrix **G** is a function of r. It results directly from the energy conservation law that **G** is an anti-Hermitian matrix for r above the cutoff wave number of bulk waves k_s. In this case, there are no propagating modes in the body that can carry energy from the surface sources (e.g., an applied traction) to infinity. **G** has a pole at $r = k_R$, where k_R is the wave number of the surface acoustic wave (SAW). In piezoelectrics, there are two characteristic wave numbers of SAWs, for metallized surface ($\varphi = 0$), and for isolated surface ($D_3 = 0$), k_0 and k_x, respectively, $k_{0,x} > k_s$.

In the theory of SAW devices, of particular interest is the so-called effective surface permittivity $D_3/E_1 = -G_{44}^{-1}(r)$. Its useful approximation,[1] valid for $|r| > k_s$ ($\sqrt{r^2} = |r|$ for real r), is

$$\frac{D_3}{E_1} = j\epsilon_e \frac{r^2 - k_x^2}{r^2 - k_0^2} \frac{\sqrt{r^2}}{r}. \tag{3}$$

This approximation neglects the bulk waves entirely. A more general approximation has been introduced for certain cases of piezoelectric crystals[2] that accounts for the slowest bulk wave. It has the form

$$\frac{D_3}{E_1} = j\epsilon_e \frac{\sqrt{r^2 - k_s^2} - \beta\sqrt{r^2}}{\sqrt{r^2 - k_s^2} - \alpha\sqrt{r^2}} \frac{\sqrt{r^2}}{r}, \tag{4}$$

that is valid in the vicinity of the cutoff wave number of bulk waves k_s. In fact, it is quite accurate for $r > k_s$, including $k_{0,x}$; α and β are the approximation coefficients. This equation accounts for the most important bulk wave for SAW devices. This is the wave propagating with velocity close to the SAW velocity, carrying energy almost parallel to the surface of the substrate. This is because, at the cutoff wave number, the direction of the Poynting vector, being normal to the slowness curve $(r,s)/\omega$, is parallel to x_1. Such waves decay slowly (due to diffraction) along x_1. This property is exploited in certain SAW devices for signal transmission along the substrate surface.[3]

In Eq. (4), there is a branch point of the square-root type on the complex plane of wave number r. It will be shown below, that this type of branch point is connected with slow-

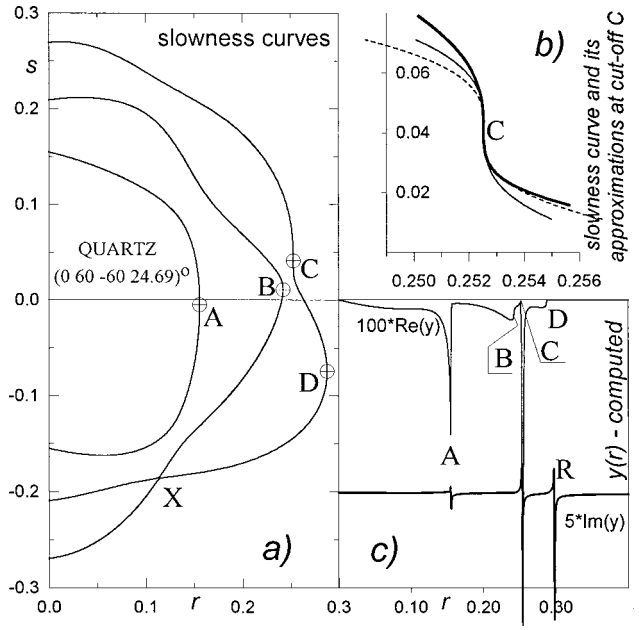

FIG. 1. (a) Slowness curves of quartz in the sagital plane described by Euler angles (0°, 60°, −60°) and with subsequent rotation in the sagital plane by 24.6904°. Cutoff wave numbers are marked by letters A–D. X marks the point where slowness curves do not cross each other (this is due to piezoelectric coupling of these two shear waves); the curves approach each other and then diverge what makes the approximation of such slowness curves extremely difficult. Somewhat similar is the case of two slowness curves near points C and B. (b) The approximation to the slowness curve (thick line) at cutoff C, thin solid line: approximated with parameter a evaluated from Eq. (27) (this approximation is of equal quality on both sides of the cutoff), and thin dashed line: slowness curve approximated with $1.75a$. This produces better approximation at the right-hand side of the cutoff, whose domain of y is more important in Fig. 2. (c) The computed $y(r)=G_{44}^{-1}(r)$ in a broad domain. Points A–D correspond to the cutoff slownesses in the subplot at the left-hand side. R marks a pair of a zero and a pole of y corresponding to the Rayleigh waves.

ness curves that can be approximated, at the cutoff, by a parabola. In this paper, we further generalize the approximation to the planar harmonic Green's function by:

(1) Considering arbitrary cutoff wave numbers of bulk modes (there can be many cutoffs; Fig. 1 presents four cutoff wave numbers, A, B, C, and D), that propagate in arbitrary anisotropic piezoelectric half-space.

(2) And considering more complicated cases of slowness shape at the cutoff (in Fig. 1, A, B, and D are cutoffs where the slowness curves have parabolic approximations that result in the above-mentioned branch points of the square-root type, and C is the cutoff where the slowness curve has a point of inflection, this will result in a branch point of Airy, cubic root type).

In Eq. (4), the slowness curve is assumed to be a parabola such that the wave vector of bulk wave (r,s) has its x_3 component dependent on r like $s\sim\sqrt{k_s^2-r^2}$. Generally, the slowness can exhibit higher-order curvatures $s\sim(k_s-r)^{1/n}$, with $n\leqslant 6$. In this paper, we discuss cases of $n=2$ and 3. These are the most fundamental cases; there are only isolated points with higher n on the entire slowness surfaces (for all sagital planes). For nonpiezoelectric bodies, similar cases were considered in Ref. 4. For completeness of the presentation we will necessarily repeat certain results of that paper with new derivation.

As discussed elsewhere in the literature,[5] evaluating **G** is quite a difficult task. As mentioned above, the proposed approximation at the cutoff wave numbers of bulk modes allows us to account for the most important waves carrying energy along the surface of the body. The remaining waves, and **G** in the remaining domain of r, can thus be treated with a reduced accuracy, or even neglected in some applications.

I. BOUNDARY VALUE PROBLEM

For our purposes, the best suited is the Stroh formalism generalized to piezoelectric body in Ref. 6. With details presented in this paper[6] and also in Appendix A, the constitutive equations and equations of motion of arbitrary anisotropic body can be transformed into the following eigenvalue problem for real and nonsymmetric matrix **H**, dependent on spectral variable r (and ω, which is assumed to be constant in our considerations)

$$\mathbf{HF}=q\mathbf{F}, \tag{5}$$

where $q=s/r$, s is the z component of the wave vector of the harmonic wave field assumed in the body $\exp(j\omega t-jrx-jsz)$ ($x=x_1$, $z=x_3<0$, and there is no dependence on $y=x_2$). The vector

$$\mathbf{F}=[U_1\ \ U_2\ \ U_3\ \ -E_1\ \ T_{31}\ \ T_{32}\ \ T_{33}\ \ D_3]^T \tag{6}$$

comprises all the wave-field components that will be later involved in boundary conditions at $z=0$, on the surface of piezoelectric half-space.

There are eight eigenvalue–eigenvector pairs $\{q_i,\mathbf{F}^{(i)}\}$ satisfying Eq. (5) and the normalization condition

$$\mathbf{F}^{(i)*}\cdot\mathbf{F}^{(i)}=1, \tag{7}$$

but only half of them satisfy the radiation condition at $z\to-\infty$, which is ($s_i=rq_i$)

$$\text{Im } s_i>0, \quad \text{or} \quad \Pi_3^{(i)}<0 \quad \text{if Im } s_i=0, \tag{8}$$

where Π_3 is the z component of the Poynting vector of the ith bulk propagating mode, the slowness and polarization vectors of which are described by $(r,rq_i)/\omega$ and $\mathbf{F}^{(i)}$, respectively (if Im $q_i\neq 0$ then it is an evanescent bulk mode, vanishing deep in the body). It is shown in Appendix A that

$$\Pi_3=\frac{1}{2}\frac{\omega}{r}\,\text{Re}\,\overline{\mathbf{T}}\cdot\overline{\mathbf{U}}^*, \tag{9}$$

where the asterisk means complex conjugation and $\overline{\mathbf{T}}$ and $\overline{\mathbf{U}}$ are parts of **F**

$$\overline{\mathbf{U}}=\begin{bmatrix}\mathbf{U}\\ -E_1\end{bmatrix},\quad \overline{\mathbf{T}}=\begin{bmatrix}\mathbf{T}\\ D_3\end{bmatrix}. \tag{10}$$

Only the $(q_i,\mathbf{F}^{(i)})$ satisfying radiation condition (8) are included in the solution for the wave field from the $z<0$ domain. They are numbered by $i=1-4$ in the representation of the wave field inside the body

$$\mathbf{F}(x,z)=\sum_{i=1}^{4} C_i\mathbf{F}^{(i)} \exp(j\omega t-jrx-js_iz),$$

$$s_i=rq_i, \quad z<0, \tag{11}$$

where C_i are unknown constants to be evaluated from the boundary conditions at $z=0$. These conditions are usually stated for T_{3i}, $i=1,2,3$ and D_3, that is for $\mathbf{T}$.

Once $\mathbf{C}=[C_i]$ is evaluated, we obtain the solution for $\partial u_i/\partial x$ and $E_1=-\partial\varphi/\partial x$ at $z=0$, that is for $\mathbf{U}$

$$\mathbf{C}=[\check{\mathbf{F}}^{(1)}\ \check{\mathbf{F}}^{(2)}\ \check{\mathbf{F}}^{(3)}\ \check{\mathbf{F}}^{(4)}]^{-1}\ \overline{\mathbf{T}},$$

$$\overline{\mathbf{U}}=[\hat{\mathbf{F}}^{(1)}\ \hat{\mathbf{F}}^{(2)}\ \hat{\mathbf{F}}^{(3)}\ \hat{\mathbf{F}}^{(4)}]\mathbf{C}. \tag{12}$$

In the above equation, $\overline{\mathbf{T}}$ is assumed to be given at $z=0$, and the inverted caret denotes the column vector of the last four components of $\mathbf{F}^{(i)}$, while the caret denotes the column vector of its first four components [neglecting indices, $\hat{\mathbf{F}}$ is $\mathbf{U}$, and $\check{\mathbf{F}}$ is $\mathbf{T}$ in Eq. (10)].

From the above equation, we obtain immediately Eq. (1), where

$$\mathbf{G}=[\hat{\mathbf{F}}^{(i)}][\check{\mathbf{F}}^{(k)}]^{-1}, \quad i,k=1,2,3,4 \tag{13}$$

with evident notations for the two 4×4 matrices involved.

The purpose of this paper is to analyze some special cases of the above equation, namely the cases where $[\check{\mathbf{F}}^{(i)}]^{-1}$ is close to the singular matrix. This can happen at $r\approx k_x$ (a SAW wave number), where the determinant of $[\check{\mathbf{F}}^{(i)}]$ is zero. Indeed, the Rayleigh wave has $\mathbf{U}$ different from zero, thus $\mathbf{C}$ is different from zero, but $\overline{\mathbf{T}}=0$ as stated for Rayleigh waves, hence $[\check{\mathbf{F}}^{(i)}]\mathbf{C}$ must be zero.

There is yet another cause of singularity of the matrix $[\check{\mathbf{F}}^{(i)}]^{-1}$ which is thoroughly discussed in the section below. The matrix $\mathbf{H}$ can be defective. This happens at the cutoff k_s of any bulk wave mode. At such a point, two eigenvalues become one, and two corresponding eigenvectors of the matrix become one as well. This is easily seen in Fig. 1 at cutoff A. For smaller r, we easily get two solutions for s on the inner slowness curve (and two corresponding eigenvalues defined by s/r), at points where the vertical line starting from r crosses this slowness curve. The corresponding two bulk modes propagate in slightly different directions and surely their polarizations are described by two different eigenvectors $\mathbf{F}$. But at cutoff, $r=k_s$, there is only one solution for s, and only one corresponding bulk wave, thus only one eigenvector $\mathbf{F}$ exists instead of two existing for $r\neq k_s$. In other words, two eigenvectors melt into one at $r=k_s$. Hence two columns of the matrix $[\check{\mathbf{F}}^{(i)}]^{-1}$ are the same at $r=k_s$. This makes the matrix singular.

II. DEFECTIVE MATRIX H AND ITS EIGENVECTORS

The slowness curves are usually evaluated from the Christoffel equation. It is evident that the Stroh formalism must yield the solution for $s_i=rq_i$ that falls on the slowness curves, for real s_i, and eigenvectors of $\mathbf{H}$ describe the corresponding bulk wave polarization. r and $s_i=rq_i$ are x and z projections of the wave vector of bulk wave $\mathbf{k}_i$ ($\mathbf{k}_i/\omega$ is the slowness vector). If r is small, there can be up to six such vectors, for different s_i. For larger r, some s_i become complex because $\mathbf{k}_i$ is not large enough to make the x projection equal r. Such s_i correspond to evanescent modes which are not usually inferred from the Christoffel equations. For $r>k_s$, all s_i concern evanescent modes, k_s is the cutoff wave number of all bulk waves. Similarly, we can define a cutoff wave number of a given bulk mode r_0, at which the number of real solutions to s_i drops, or rises by 2, as shown in Fig. 1.

Two eigenvalues of $\mathbf{H}$ are always complex (for real r). They can be called ''electrostatic solutions'' because by neglecting piezoelectric coupling, they describe electric field in the body governed by $D_{i,i}=0$. These two solutions to q are usually close to $\pm j$.

Investigating the eigenvalues for r close to r_0, we notice that two (or more) $s_i=rq_i$ converge to the same s_0. The same concerns $\mathbf{F}^{(i)}$ describing polarization of the corresponding bulk waves, which converge to one $\mathbf{F}^0$. It means that two eigenvectors of $\mathbf{H}$ become one, and thus the system of eigenvectors cannot span the whole eight-dimensional space of solutions. The matrix $\mathbf{H}$ is defective[7] at r_0.

Usually, the slowness curve of the given bulk propagating mode can be approximated by a parabola, $r-r_0=a(s-s_0)^2$, and the corresponding eigenvalues are $q_i=(s_0\pm\sqrt{(r-r_0)/a})/r_0$ (for $r\approx r_0$). There are cases, however (see Refs. 4 and 8), where the approximation is $r-r_0\sim(s-s_0)^n$, $n>2$, and at such a point, more than two eigenvectors melt into one; the matrix $\mathbf{H}$ can be multiple defective.

In this paper we do not consider r exactly at the cutoff. That is, with $r\neq r_0$ assumed, the matrix $\mathbf{H}$ has all its eigenvectors independent and spanning the space of the solution sought for in the form of expansion (11). However, for $r\approx r_0$, we can take advantage of the above discussion and find the eigenvalues from approximation to the slowness curve rather than from Eq. (5), as well as to find approximate eigenvectors. For this purpose, we must consider each case of the type of the slowness curves at the cutoff separately.

A. Case of parabolic approximation

Let us first consider a parabolic approximation to the slowness curve at cutoff r_0. We propose the following approximations to q and $\mathbf{F}$ for $r\approx r_0$:

$$q=q_0+\delta, \quad \mathbf{F}=\mathbf{F}^0+\delta\mathbf{F}'+\cdots, \quad \delta=\pm\sqrt{\epsilon/a},$$
$$\epsilon=r-r_0. \tag{14}$$

The matrix $\mathbf{H}$ depends on r smoothly, and for r close to $r_0\neq0$, Eq. (5) can be rewritten in the form

$$(\mathbf{H}_0+\epsilon\dot{\mathbf{H}})(\mathbf{F}^0+\delta\mathbf{F}'+\delta^2\ddot{\mathbf{F}})=(q_0+\delta)(\mathbf{F}^0+\delta\mathbf{F}'+\delta^2\ddot{\mathbf{F}}), \tag{15}$$

where $\mathbf{H}_0=\mathbf{H}(r_0)$ and $\dot{\mathbf{H}}=\partial\mathbf{H}/\partial r$ at r_0. Note that $\epsilon\sim\delta^2$, and that all higher-order components are dropped in the above equation.

Expanding Eq. (15) in powers of δ we obtain

$$\mathbf{H}_0\mathbf{F}^0=q_0\mathbf{F}^0 \tag{16}$$

that defines the ordinary existing eigenvalue-eigenvector pair at $r=r_0$, and

$$(\mathbf{H}_0-q_0\mathbf{I})\mathbf{F}'=\mathbf{F}^0 \tag{17}$$

($\mathbf{I}$ is the identity matrix) that defines the generalized eigenvector $\mathbf{F}'$ of the defective matrix $\mathbf{H}_0$. It is made unique by applying the normalization condition (7) to $\mathbf{F}$ expanded in Eq. (14). This results in (both $\mathbf{F}^0$ and $\mathbf{F}'$ are real vectors)

$$\mathbf{F}^0 \cdot \mathbf{F}' = 0. \tag{18}$$

To solve the set of equations (17), the determinant of which equals zero, we replace one of the equations by Eq. (18) (a similar technique can be applied for other generalized eigenvectors considered below).

The last equation that results from (15)

$$(\mathbf{H}_0 - q_0\mathbf{I})\ddot{\mathbf{F}} + a\dot{\mathbf{H}}\mathbf{F}^0 = \mathbf{F}' \tag{19}$$

allows us to evaluate a, the parameter describing the curvature of the slowness curve at the cutoff $(r_0, s_0)/\omega$. First, we define the left eigenvector $\mathbf{E}^0$

$$\mathbf{E}^0(\mathbf{H}_0 - q_0\mathbf{I}) = 0 \tag{20}$$

satisfying the well-known equation for the defective matrices

$$\mathbf{E}^0\mathbf{F}^0 = 0. \tag{21}$$

It is shown in Appendix A that

$$\mathbf{E}^0 = [\check{\mathbf{F}}^{0T}\hat{\mathbf{F}}^{0T}]. \tag{22}$$

Hence multiplying Eq. (19) on the left by $\mathbf{E}^0$ and using (20) we get

$$a = \frac{\mathbf{E}^0\mathbf{F}'}{\mathbf{E}^0\dot{\mathbf{H}}\mathbf{F}^0}. \tag{23}$$

Note that a has a different sign depending on whether the slowness is a convex or concave curve, and whether r_0 is positive or negative.

Summarizing, if we know that r_0 is the cutoff wave number, and that the slowness curve can be approximated by a parabola, the above reasoning allows us to obtain approximations for eigenvalues and eigenvectors as functions of r in the vicinity of r_0, with accuracy up to $\delta \sim (r - r_0)^{1/2}$, which is of an order greater than $r_0 - r$. There are two solutions for $\{q_i, \mathbf{F}^{(i)}\}$, for different signs of δ, and they can be extended for imaginary values of δ, that is for r on both sides of r_0.

Only one of these solutions satisfies the radiation condition and will be included in the expansion (11) to the field inside the body. If δ is imaginary, the choice is simply based on the rule (8) for complex q_i. Thus we discuss only the case of real δ and q_i. As it is known, the direction of the Poynting vector of the propagating bulk mode is perpendicular to its slowness curve.[9,10] For example with $a < 0$, $r_0 > 0$, at cutoff (r_0, s_0), the normal to the slowness curve is parallel to the x axis, and any move down along the slowness curve results in the normal directed down into the bulk of the body, producing $\Pi_3 < 0$ as required by Eq. (8). This means that for $q = q_0 + \delta$, with $\delta = -\sqrt{(r - r_0)/a}$ real and negative, the corresponding eigenvector $\mathbf{F}^0 + \delta\mathbf{F}'$ satisfies the radiation condition. It thus results from Eq. (9) that

$$\Pi_3 = \frac{\omega}{2r}(\check{\mathbf{F}}^0 + \delta\check{\mathbf{F}}') \cdot (\hat{\mathbf{F}}^0 + \delta\hat{\mathbf{F}}')^* < 0.$$

Noticing that for real q both $\mathbf{F}^0$ and $\mathbf{F}'$ are real and satisfying Eq. (18), we conclude that, for the considered case of $\epsilon \sim \delta^2$,

$$a\,\frac{\omega}{r}\,\mathbf{E}^0\mathbf{F}' < 0, \tag{24}$$

where $\mathbf{E}^0$ is given by Eq. (22). Exactly at the cutoff ($\delta = 0$), the mode $\mathbf{F}^0$ produces $\Pi_3 = 0$ (its Poynting vector is parallel to the x axis), thus

$$\check{\mathbf{F}}^0 \cdot \check{\mathbf{F}}^0 = 0, \tag{25}$$

which confirms Eq. (21).

B. Higher-order approximations

A similar discussion can be carried out for multiple defective matrix $\mathbf{H}$ at cutoff r_0, where

$$\begin{aligned} &q = q_0 + \delta, \quad \mathbf{F} = \mathbf{F}^0 + \delta\mathbf{F}' + \delta^2\mathbf{F}'' + \cdots, \\ &\epsilon = r - r_0 = a\,\delta^3. \end{aligned} \tag{26}$$

Accounting for the normalization conditions for $\mathbf{F}$, Eq. (5) results in

$$\begin{aligned} &(\mathbf{H}_0 - q_0\mathbf{I})\mathbf{F}^0 = 0, \quad (\mathbf{H}_0 - q_0\mathbf{I})\mathbf{F}' = \mathbf{F}^0, \\ &(\mathbf{H}_0 - q_0\mathbf{I})\mathbf{F}'' = \mathbf{F}', \quad \mathbf{F}^0 \cdot \mathbf{F}' = 0, \quad \mathbf{F}^0 \cdot \mathbf{F}'' = -\tfrac{1}{2}\,\mathbf{F}' \cdot \mathbf{F}', \\ &a = \frac{\mathbf{E}^0\mathbf{F}''}{\mathbf{E}^0\dot{\mathbf{H}}\mathbf{F}^0}, \end{aligned} \tag{27}$$

where $\mathbf{F}'$ and $\mathbf{F}''$ are generalized eigenvectors of the second and third ranks, respectively, $(\mathbf{H}_0 - q_0\mathbf{I})^3\mathbf{F}'' = 0$. There are three different values of $\delta = (\epsilon/a)^{1/3}$, and three different pairs $\{q_i, \mathbf{F}^{(i)}\}$ resulting from Eqs. (27).

The last case considered in this section is

$$\begin{aligned} &q = q_0 + \delta, \quad \mathbf{F} = \mathbf{F}^0 + \delta\mathbf{F}' + \delta^2\mathbf{F}'' + \delta^3\mathbf{F}''' + \cdots, \\ &\epsilon = r - r_0 = a\,\delta^4, \\ &(\mathbf{H}_0 - q_0\mathbf{I})\mathbf{F}^0 = 0, \quad (\mathbf{H}_0 - q_0\mathbf{I})\mathbf{F}' = \mathbf{F}^0, \\ &(\mathbf{H}_0 - q_0\mathbf{I})\mathbf{F}'' = \mathbf{F}', \quad (\mathbf{H}_0 - q_0\mathbf{I})\mathbf{F}''' = \mathbf{F}'', \\ &\mathbf{F}^0 \cdot \mathbf{F}' = 0, \quad \mathbf{F}^0 \cdot \mathbf{F}'' = -\tfrac{1}{2}\,\mathbf{F}' \cdot \mathbf{F}', \\ &\mathbf{F}^0 \cdot \mathbf{F}''' = -\mathbf{F}' \cdot \mathbf{F}'', \quad a = \frac{\mathbf{E}^0\mathbf{F}'''}{\mathbf{E}^0\dot{\mathbf{H}}\mathbf{F}^0}. \end{aligned} \tag{28}$$

Note the difference between this case and that considered in Ref. 4 of two simultaneous cutoffs at the same r_0 but at two different s_0's, with parabolic approximations to the slowness curves at both of them. In such a case $\delta \sim \epsilon^{1/2}$, while in the above case we have $\delta \sim \epsilon^{1/4}$. The analysis that is presented in the next section, however, will be similar for all the cases.

It is worth noting that applying improper approximation to $\epsilon = a\,\delta^n$, by assuming $n = 2$ instead of the proper value 3, for instance, Eqs. (23) will produce $a = 0$ due to $\mathbf{E}^0\mathbf{F}' = 0$ in the case of $n = 3$. This means that, knowing that r_0/ω is the cutoff slowness, we can try an approximation with $n = 2$; then, if $a = 0$, with $n = 3$, and if still $a = 0$ results from Eqs. (27), try $n = 4$ and Eq. (28), etc.

Interesting equations result from the consideration concerning the Π_1 component of the Poynting vector of the $\mathbf{F}^0$ mode. The normal to the slowness is inclined to x_1 by $3a\delta^2/r_0$ for the case $n=3$, and $4a\delta^3/r_0$ for $n=4$, thus $\Pi_3 \sim \delta^2\Pi_1$ or $\sim\delta^3\Pi_1$, respectively. By evaluating Π_3 from expansion (14) we notice that terms proportional to δ in the $n=3$ case, and to both δ and δ^2 for $n=4$, must vanish. This results in

$$\begin{aligned} &\mathbf{E}^0\mathbf{F}'=0, \quad \mathbf{E}^0\mathbf{F}''=\mathbf{E}'\mathbf{F}', \quad n=3, \\ &\mathbf{E}^0\mathbf{F}'=0, \quad \mathbf{E}^0\mathbf{F}''=0, \quad \mathbf{E}'\mathbf{F}'''=\mathbf{E}''\mathbf{F}''=0, \quad n=4, \end{aligned} \tag{29}$$

i.e., relations which are also known from the matrix analysis. Indeed, multiplying on the left $(\mathbf{H}_0-q_0\mathbf{I})\mathbf{F}''=\mathbf{F}'$ by $\mathbf{E}'$, then noticing that $\mathbf{E}'(\mathbf{H}_0-q_0\mathbf{I})=\mathbf{E}^0$, analogously to Eq. (27), we get the second of Eqs. (29). In the same way we obtain the remaining identities in Eqs. (29) that do not directly result from the energy conservation law.

III. GREEN'S FUNCTION NEAR THE CUTOFFS

The remaining eigenvalue–eigenvector pairs $\{q_i,\mathbf{F}^{(i)}\}$ depend on r regularly, and because $r=r_0+a\delta^n$, they can be considered to be *constants* for small δ, with accuracy better than $|\delta|^{n-1}$. There are six such pairs for the case $n=2$, and five for $n=3$. Only some of them satisfy the radiation conditions at $z\to-\infty$ and are included in Eq. (13). There must be four pairs altogether satisfying Eqs. (8), including all pairs $\{q_0+\delta,\mathbf{F}^0+\delta\mathbf{F}'+\delta^2\mathbf{F}''+\cdots\}$ satisfying the radiation condition at $-\infty$. From the latter set, there is one such pair for the case $n=2$, and one or two pairs for the case $n=3$, depending on the shape of the slowness curve at the cutoff slowness $(r_0,s_0)/\omega$. In the example of Fig. 1, at the point C, the real solution to δ does not satisfy Eqs. (8) and is not included in Eqs. (12). For convenience, we choose this simplest case for detailed discussion. Then the well-known relation[10]

$$G_{ij}(-r)=-G^*_{ji}(r) \tag{30}$$

gives the required result for the other case, where the propagating mode at cutoff satisfies the radiation conditions (for the sake of completeness, we remark here that $-\mathbf{G}^T$ is the planar harmonic Green's function for the upper half-space, $z>0$).

The analysis presented in previous sections has been carried out with accuracy to $|\delta|^{n-1}$: $\mathbf{F}^0+\delta\mathbf{F}'+\cdots$ does not include the term $\delta^n\sim\epsilon$ (*infinitesimal* ϵ) and higher. Thus we cannot expect better accuracy of the approximated $\mathbf{G}$. It can be improved, however, by making it to hold its physical correctness for *finite* δ, and this requires certain higher-order terms to be included in this improved approximation to $\mathbf{G}$. The physical correctness means particularly, that the energy conservation law is satisfied by the solution evaluated by means of the approximate $\mathbf{G}$ for all possible surface forces $\mathbf{T}$ applied. This is discussed below in details.

A. Case $\epsilon=a\delta^2$

We rewrite Eqs. (12) in a somewhat symbolic form

$$\begin{aligned} &\overline{\mathbf{T}}=[\check{\mathbf{F}}^0+\delta\check{\mathbf{F}}' \quad \check{\mathbf{F}}^{(e)} \quad \cdots \quad \check{\mathbf{F}}^{(p)}]\mathbf{C}=\check{\mathbf{F}}\mathbf{C}, \\ &\overline{\mathbf{U}}=[\hat{\mathbf{F}}^0+\delta\hat{\mathbf{F}}' \quad \hat{\mathbf{F}}^{(e)} \quad \cdots \quad \hat{\mathbf{F}}^{(p)}]\mathbf{C}=\hat{\mathbf{F}}\mathbf{C}, \end{aligned} \tag{31}$$

where index e marks evanescent modes (there is at least one evanescent mode involved), and p-propagation modes (at most two). Note the order of eigenvectors in 4×4 matrices in the above equation (the ellipsis stands for either evanescent or propagating modes). C_n are the amplitudes of the corresponding modes excited in the body by the applied force $\mathbf{T}$.

The solution to $\overline{\mathbf{T}}=\check{\mathbf{F}}\mathbf{C}$, with accuracy to δ, is[11]

$$\begin{aligned} &C_1=\frac{1}{1+\delta p}\,d_{1j}\overline{T}_j, \quad \mathbf{d}=[\hat{\mathbf{F}}^0 \quad \hat{\mathbf{F}}^{(e)} \quad \cdots \quad \hat{\mathbf{F}}^{(p)}]^{-1}=[d_{kj}], \\ &C_k=d_{kj}\overline{T}_j-\check{F}'_k\,\frac{\delta}{1+\delta p}\,d_{1j}\overline{T}_j, \quad k=2,3,4, \\ &p=\sum_l d_{1l}\check{F}'_l, \quad \check{F}'_l=F'_{4+l}, \quad l=1,2,3,4 \end{aligned} \tag{32}$$

(summation convention applied), which substituted to Eqs. (31) yields

$$\begin{aligned} \overline{U}_i=G_{ij}\overline{T}_j&=\frac{\hat{F}^0_i+\delta\hat{F}'_i}{1+\delta p}\,d_{1j}\overline{T}_j \\ &\quad+\hat{F}^{(k)}_i\left(d_{kj}-\frac{\delta\hat{F}'_k}{1+\delta p}\,d_{1j}\right)\overline{T}_j, \quad k=e,p. \end{aligned} \tag{33}$$

Note that C_k, $k=e,p$ is the δ-dependent amplitude of the evanescent or the propagating mode the polarization of which, described by $\mathbf{F}^{(k)}$, is considered to be constant (being dependent on r, the polarization depends on δ^2 that is negligible). The vector $\mathbf{F}^{(1)}=\mathbf{F}^0+\delta\mathbf{F}'$, however, properly describes the varying polarization of this perturbed mode at the cutoff, for δ small.

In the rigorous analysis, for δ infinitesimally small, there is not much sense in keeping δ in the denominator in Eq. (32), since $(1+\delta p)^{-1}=1-\delta p$. However, we will later attempt to use the expression for $\mathbf{G}(\delta)$ for larger (finite) δ, and in spite of that

$$\mathbf{F}^0+\delta\mathbf{F}'=\mathbf{F}^0+\frac{\delta}{1+\delta\tau}\,\mathbf{F}'$$

to within the accuracy of δ, the latter behaves quite differently when δ is *finite*, particularly if τ is large. We will exploit this in construction of such expression for $\mathbf{G}(\delta)$ which, remaining rigorous for infinitesimal δ, does not lead to violation of the energy conservation law for finite δ. The accuracy of such an approximation to $\mathbf{G}$ is subjected to numerical verification.

To discuss the energy conservation law, we first evaluate the power delivered to the body by the applied surface force $\mathbf{T}$ at $z=0$

$$P=\Pi_3(z=0)=\frac{\omega}{2r}\,\mathrm{Re}\{\overline{\mathbf{T}}^T\mathbf{G}^*\overline{\mathbf{T}}^*\}=\frac{\omega}{2r}\,\mathrm{Re}\{\overline{\mathbf{T}}^{T*}\mathbf{G}\overline{\mathbf{T}}\}. \tag{34}$$

For convenience of the subsequent discussion, we apply the modal amplitudes t_n to express $\overline{\mathbf{T}}^T=\mathbf{t}^T\check{\mathbf{F}}^T$ and $\overline{\mathbf{T}}=\check{\mathbf{F}}\mathbf{t}$, which substituted into the above equation yield

$$P=\frac{\omega}{2r}\,\mathrm{Re}\{\mathbf{t}^{T*}\tilde{\mathbf{G}}\mathbf{t}\},\quad \tilde{\mathbf{G}}=\check{\mathbf{F}}^{T*}\mathbf{G}\check{\mathbf{F}}=\check{\mathbf{F}}^{T*}\hat{\mathbf{F}} \tag{35}$$

(note that the indices n, m of the matrix $[\tilde{G}_{nm}]$ are the mode indices).

Let us apply imaginary δ, thus the mode $\mathbf{F}^0+\delta\mathbf{F}'$ becomes the evanescent one. Applying $t_p=0$ for all propagating modes involved in (35), the power P must be zero because there are no propagating modes in the body to carry the energy to $-\infty$.

$$\mathrm{Re}\{\mathbf{t}^{T*}\bar{\mathbf{G}}\mathbf{t}\}=0,$$

$$\bar{\mathbf{G}}=\left[\check{\mathbf{F}}^0+\frac{\delta}{1+\delta\tau}\,\check{\mathbf{F}}'\ \cdots\ \check{\mathbf{F}}^{(e)}\right]^{T*}\left[\hat{\mathbf{F}}^0+\frac{\delta}{1+\delta\tau}\,\hat{\mathbf{F}}'\ \cdots\ \hat{\mathbf{F}}^{(e)}\right], \tag{36}$$

$$\delta=j|\delta|,$$

where the ellipsis stands for another evanescent mode. Thus the corresponding part of the matrix $\bar{\mathbf{G}}$ must be anti-Hermitian ($n,m=1,2,...$, except p)

$$\bar{G}_{nm}=-\bar{G}^*_{mn}, \tag{37}$$

and we will require this not only for infinitesimal δ, but for its finite values as well. Moreover, we will require that both the numerator and denominator in the expression for $\mathbf{G}(\delta)$ should not include higher powers of δ. This is reasonable: the solution to the eigenvalue problem is only this accurate for infinitesimal δ.

Still using symbolic notation where e stays for any index of evanescent modes (there can be more column vectors $\mathbf{F}^{(e)}$ in the discussed matrices), we obtain for $\mathbf{G}$

$$\begin{bmatrix} \left(\check{\mathbf{F}}^0+\frac{\delta^*}{1+\delta^*\tau^*}\,\check{\mathbf{F}}'\right)\cdot\left(\hat{\mathbf{F}}^0+\frac{\delta}{1+\delta\tau}\,\hat{\mathbf{F}}'\right) & \left(\check{\mathbf{F}}^0+\frac{\delta^*}{1+\delta^*\tau^*}\,\check{\mathbf{F}}'\right)\cdot\hat{\mathbf{F}}^{(e)} \\ \check{\mathbf{F}}^{(e)}\cdot\left(\hat{\mathbf{F}}^0+\frac{\delta}{1+\delta\tau}\,\hat{\mathbf{F}}'\right) & \check{\mathbf{F}}^{(e)*}\cdot\hat{\mathbf{F}}^{(e)} \end{bmatrix}. \tag{38}$$

Noticing that

$$\check{\mathbf{F}}^{(e)*}\cdot\left(\hat{\mathbf{F}}^0+\frac{\delta}{1+\delta\tau}\,\hat{\mathbf{F}}'\right)=-\hat{\mathbf{F}}^{(e)*}\cdot\left(\check{\mathbf{F}}^0+\frac{\delta}{1+\delta\tau}\,\check{\mathbf{F}}'\right) \tag{39}$$

on the basis of the orthogonality properties discussed in Appendix A, we easily conclude that $G_{21}=-G^*_{12}$. It results from (A15) that G_{22} is purely imaginary, thus $G_{22}=-G^*_{22}$, and we need only to analyze G_{11}, which should also be purely imaginary for $\mathbf{G}$ to be an anti-Hermitian matrix

$$\mathrm{Re}\{G_{11}\}=\frac{1}{|1+\delta\tau|^2}\,\mathrm{Re}\{\delta(1+\delta^*\tau^*)(\check{\mathbf{F}}^0\cdot\hat{\mathbf{F}}'+\hat{\mathbf{F}}^0\cdot\check{\mathbf{F}}') +|\delta|^2\check{\mathbf{F}}'\cdot\hat{\mathbf{F}}'\}=0 \tag{40}$$

($\delta=j|\delta|$ is purely imaginary); this requires that

$$\mathrm{Re}\{\tau\}=-\frac{1}{2}\,\frac{\mathbf{E}'\mathbf{F}'}{\mathbf{E}^0\mathbf{F}'}, \tag{41}$$

while $\mathrm{Im}\{\tau\}$ is arbitrary. This is a free parameter which can be used to improve the approximation to $\mathbf{G}$.

Applying $\delta\mathbf{F}'/(1+\delta\tau)$ instead of $\delta\mathbf{F}'$ in Eqs. (33), we finally get

$$G_{ij}=\hat{F}^{(m)}_i d_{mj}+\frac{\delta}{1+\delta(p+\tau)}\,(\hat{F}'_i-\hat{F}^{(m)}_i d_{ml}\check{F}'_l)d_{1j}, \tag{42}$$

where we have introduced the notation $F^{(1)}_i=F^0_i$ for convenience; $F^{(m)}_i$, $m=2,3,4$ are the remaining eigenvectors satisfying the radiation condition. Note that $\delta=(s-s_0)/r_0=\sqrt{(r-r_0)/a}$ is also subjected to conditions (8).

This formula satisfies the requirements stated earlier: part of $\mathbf{G}$ that does not depend on the propagating modes is an anti-Hermitian matrix for any finite $\delta=\sqrt{\epsilon/a}$, $\epsilon=r-r_0$, and $\mathbf{G}$ includes terms up to δ in both the numerator and denominator of Eq. (42), similarly to Eq. (4). In the most interesting case, where $r_0=k_s$, the matrix $\mathbf{G}$ is anti-Hermitian for any $|r|>k_s$, where δ is purely imaginary. Its asymptotic value for $r\to\infty$ can be used to set the free parameter $\mathrm{Im}\{\tau\}$. The Rayleigh wave number evaluated from the approximate $\mathbf{G}$ and compared to its correct value can be also applied as another criterion for this same purpose.[12]

Note that $\delta=(s-s_0)/r_0=\sqrt{(r-r_0)/a}$ has incorrect asymptotics for $r\to\infty$, where $|s|\sim|r|$. This is why we applied in Ref. 3 the improved formula: $\delta=[0.5k_s(r^2-k_s^2)/(ar^2)]^{1/2}$ that resulted in Eq. (4).

B. Case $\epsilon=a\delta^3$, $ar_0<0$

We consider the case of $a<0$, $r_0>0$, where the real solution to δ does not satisfy the radiation condition at $z\to-\infty$. The eigenvalue satisfying it is

$$\delta=|\epsilon/a|^{1/3}\begin{cases} e^{j2\pi/3}=-1/2+j\sqrt{3}/2, & \epsilon<0,\\ e^{j\pi/3}=1/2+j\sqrt{3}/2, & \epsilon>0. \end{cases} \tag{43}$$

The approximation for the other case, $a>0$, can be obtained by using Eq. (30).

With accuracy to δ^3, we apply

$$\mathbf{F}^0+\delta\mathbf{F}'+\delta^2\mathbf{F}''=\mathbf{F}^0+\frac{\delta}{1+\delta^2\eta}\,\mathbf{F}'+\frac{\delta^2}{1+\delta\tau}\,\mathbf{F}'', \tag{44}$$

where η and τ are parameters which will be evaluated in the analysis that follows. Equation (12) becomes

$$\overline{\mathbf{T}}=\left[\check{\mathbf{F}}^0+\frac{\delta}{1+\delta^2\eta}\,\check{\mathbf{F}}'+\frac{\delta^2}{1+\delta\tau}\,\check{\mathbf{F}}''\ \cdots\ \check{\mathbf{F}}^{(n)}\right]\mathbf{C},$$
$$\overline{\mathbf{U}}=\left[\hat{\mathbf{F}}^0+\frac{\delta}{1+\delta^2\eta}\,\hat{\mathbf{F}}'+\frac{\delta^2}{1+\delta\tau}\,\hat{\mathbf{F}}''\ \cdots\ \hat{\mathbf{F}}^{(n)}\right]\mathbf{C},\quad n=2,3,4. \tag{45}$$

The solution to $\mathbf{C}$ is

$$C_1=\frac{d_{1j}}{1+d_{1l}[\,\delta\check{F}_l'/(1+\delta^2\eta)+\delta^2\check{F}_l''/(1+\delta\tau)]}\,\overline{T_j},$$
$$C_n=d_{nj}\overline{T_j}-\frac{d_{nl}[\,\delta\check{F}_l'/(1+\delta^2\eta)+\delta^2\check{F}_l''/(1+\delta\tau)]}{1+d_{1l}[\,\delta\check{F}_l'/(1+\delta^2\eta)+\delta^2\check{F}_l''/(1+\delta\tau)]}\,d_{1j}\overline{T_j}. \tag{46}$$

It is evident that the parameter η brings terms $\sim\delta^4$ that are beyond the accuracy of our analysis. This is the reason why we have put $\eta=0$.

To obtain the constraints for τ, we consider the matrix $\overline{\mathbf{G}}$ which is

$$\overline{\mathbf{G}}=\left[\check{\mathbf{F}}^0+\delta\check{\mathbf{F}}'+\frac{\delta^2}{1+\delta\tau}\,\check{\mathbf{F}}''\ \cdots\ \check{\mathbf{F}}^{(e)}\right]^{T*}\times\left[\hat{\mathbf{F}}^0+\delta\hat{\mathbf{F}}'+\frac{\delta^2}{1+\delta\tau}\,\hat{\mathbf{F}}''\ \cdots\ \hat{\mathbf{F}}^{(e)}\right]. \tag{47}$$

Note that δ has the complex value given by Eq. (43).

We easily notice that $G_{21}=-G_{12}^*$ on the strength of the orthogonality properties of the eigenvectors, and that G_{22} is purely imaginary. We thus need to make $\mathrm{Re}\{\overline{G_{11}}\}=0$. Evaluating the above term by term, we get for terms with δ

$$\frac{1}{|1+\delta\tau|^2}\,\mathrm{Re}\{\delta\check{\mathbf{F}}^0\cdot\hat{\mathbf{F}}'+\delta^*\check{\mathbf{F}}'\cdot\hat{\mathbf{F}}^0\}=0, \tag{48}$$

which is satisfied due to $\mathbf{E}^0\mathbf{F}'=0$, for terms δ^2 we get

$$\begin{aligned}&\mathrm{Re}\{(\delta\tau+\delta^*\tau^*)(\delta\check{\mathbf{F}}^0\cdot\hat{\mathbf{F}}'+\delta^*\check{\mathbf{F}}'\cdot\hat{\mathbf{F}}^0)+\delta\delta^*\check{\mathbf{F}}'\cdot\hat{\mathbf{F}}'\\&\quad+\delta^2\check{\mathbf{F}}^0\cdot\hat{\mathbf{F}}''+\delta^{*2}\check{\mathbf{F}}''\cdot\hat{\mathbf{F}}^0\}\\&\quad=\tfrac{1}{2}\,|\epsilon/a|^{2/3}\,\mathrm{Re}\{\mathbf{E}'\mathbf{F}'-\mathbf{E}^0\mathbf{F}''+j(\cdots)\}\\&\quad=0\end{aligned} \tag{49}$$

because $\mathbf{E}'\mathbf{F}'=\mathbf{E}^0\mathbf{F}''$, terms with δ^3 yield the following condition:

$$\mathrm{Re}\{\tau\}=-\frac{1}{2}\,\frac{\mathbf{E}'\mathbf{F}''}{\mathbf{E}^0\mathbf{F}''} \tag{50}$$

in order to make the corresponding part of $\overline{G}_{11}$ purely imaginary, and the last term $\sim\delta^4$ produces another constraint

$$(\mathrm{Im}\{\tau\})^2=3(\mathrm{Re}\{\tau\})^2-\frac{\mathbf{E}''\mathbf{F}''}{\mathbf{E}'\mathbf{F}'}. \tag{51}$$

The ambiguity of $\pm\mathrm{Im}\{\tau\}$ must be resolved by comparison of the computed and approximated values of $\mathbf{G}$.

The above constraints determine both the real and imaginary parts of τ; there is no free parameter for adjusting the approximation of $\mathbf{G}(\delta)$.

Substituting the above into Eqs. (45) and (44), we finally obtain

$$G_{ij}=\hat{F}^{(m)}d_{mj}+\frac{(1+\delta\tau)\,\delta\hat{F}_i'+\delta^2\hat{F}_i''-\hat{F}^{(m)}d_{ml}[(1+\delta\tau)\,\delta\hat{F}_l'+\delta^2\hat{F}_l'']}{1+\delta\tau+d_{1l}[(1+\delta\tau)\,\delta\hat{F}_l'+\delta^2\hat{F}_l'']}\,d_{1j}, \tag{52}$$

where δ depends on $\epsilon=r-r_0$ as given in Eq. (43).

C. Case $\epsilon=a\delta^4$ and concluding remarks

The approximation to the slowness curve of both forms, $\epsilon\sim\delta^3$, and $\epsilon\sim\delta^4$, are limited to a small domain of δ. Indeed, it is known that $|s|\sim|r|$ for large $|r|$, and thus $s\sim(q_0+\delta)r$ is not a proper asymptotics for s (for large $|\delta|$). This shows that the validity domain of approximation to $\mathbf{G}$ in the considered case can be rather narrow. Moreover, it is shown below that there is a serious difficulty in obtaining the physically correct $\mathbf{G}(\delta)$ for finite δ: there are too many constraints on the parameter τ.

The case $\epsilon\sim\delta^4$ is much more difficult because the radiation conditions admit two perturbed eigenvectors in Eqs. (12) and (13). To simplify the discussion, we consider only the case of $r_0=k_s>0$, $a<0$. There are only evanescent modes for $r>k_s$, and only one propagating mode, the perturbed one, if r is just below k_s:

$$\begin{aligned}&\delta_1=\delta,\ \ \mathbf{F}^0+\delta_1\mathbf{F}'+\delta_1^2\mathbf{F}''+\frac{\delta_1}{1+\tau\delta_1}\,\mathbf{F}''',\\&\delta_2=j\,\delta,\ \ \mathbf{F}^0+\delta_2\mathbf{F}''+\delta_2^2\mathbf{F}''+\frac{\delta_2}{1+\tau\delta_2}\,\mathbf{F}''',\\&\delta=\begin{cases}j\,|\epsilon/a|^{1/4}, & \epsilon<0,\\ |\epsilon/a|^{1/4}e^{j\pi/4}, & \epsilon>0\end{cases}\end{aligned} \tag{53}$$

(note that the same formula, taken for two different δ, expresses both the perturbed values of $\mathbf{F}$). Above, we have introduced the parameter τ in advance, like in the cases discussed previously.

For $\epsilon<0$, the matrix $\overline{\mathbf{G}}$ is (the propagating mode is not included)

$$\overline{\mathbf{G}}=[\check{\mathbf{F}}^0+\delta\check{\mathbf{F}}'+\ \cdots\ \check{\mathbf{F}}^{(e)}][\hat{\mathbf{F}}^0+\delta\hat{\mathbf{F}}'+\ \cdots\ \hat{\mathbf{F}}^{(e)}]. \tag{54}$$

The discussion similar to that carried out previously produces the following conditions for τ

$$\mathrm{Re}\{\tau\}=-\frac{1}{2}\frac{\mathbf{E}'\mathbf{F}'''}{\mathbf{E}^0\mathbf{F}'''},\quad |\tau|^2=\frac{\mathbf{E}''\mathbf{F}'''}{\mathbf{E}^0\mathbf{F}'''}-\frac{\mathbf{E}'''\mathbf{F}'''}{\mathbf{E}'\mathbf{F}'''} \tag{55}$$

resulting from terms δ^4 and δ^6 of $\underline{\overline{G}}_{11}$, correspondingly.

For $\epsilon>0$ ($r>k_s$), the matrix $\mathbf{G}$ includes both the perturbed evanescent modes, corresponding to eigenvalues δ_1 and δ_2. We need to check only whether G_{11} is purely imaginary. Again, the terms δ^4 and δ^6 produce the same conditions as previously for $\epsilon<0$, and the term δ^5 requires additionally that

$$(\mathrm{Im}\{\tau\})^2=3(\mathrm{Re}\{\tau\})^2-\frac{\mathbf{E}''\mathbf{F}'''}{\mathbf{E}^0\mathbf{F}'''}. \tag{56}$$

This means that τ can be evaluated only if

$$\left(\frac{\mathbf{E}'\mathbf{F}'''}{\mathbf{E}^0\mathbf{F}'''}\right)^2-2\frac{\mathbf{E}''\mathbf{F}'''}{\mathbf{E}^0\mathbf{F}'''}+\frac{\mathbf{E}'''\mathbf{F}'''}{\mathbf{E}'\mathbf{F}'''}=0. \tag{57}$$

If this is the case, $\mathbf{G}(\delta)$ depends on one variable δ because δ_2 depends on δ_1 similarly in both cases $\epsilon>0$ and $\epsilon<0$. We do not discuss this case further.

IV. NUMERICAL EXAMPLES

It has been found convenient to apply the following units in numerical analysis: $t[10^6$ s], ω[MHz], $x[10^{-3}$ m], $r[1/\mathrm{mm}]$, $u[10^{-9}$ m], ϕ[V], $T[10^3$ N/m$^2]$, $D[10^{-6}$ C/m$^2]$, and $g[10^3$ kg/m$^3]$, $c[10^9$ N/m$^2]$, $e[$C/m$^2]$, the value of dielectric constant of vacuum $\epsilon_0[10^9$ F/m$]=0.008\,854\,2$.

In applications, we frequently need only one diagonal element of $\mathbf{G}$, namely G_{44}, that plays an important role in the theory of SAW devices.[3,13] It can be more easily evaluated from the above analysis than from the standard computation based on Eq. (13) (evaluated for subsequent values of r). This is because $\mathbf{G}(r)$ varies very rapidly in some tiny domains of r (at cutoffs). This is shown in the example presented below for quartz.

We applied quartz because its bulk waves are known to be strongly dependent on the propagation direction. This allowed us to choose such orientation of the substrate surface, that both cutoff types are simultaneously present (at different r_0's) on the same sagital plane: $\epsilon\sim\delta^2$ at points A, B, and D in Fig. 1, and $\epsilon\sim\delta^3$ at point C in this figure.

To make the reference easy, in the neighboring figure (bottom right drawing in Fig. 1) the computed function of $y=G_{44}^{-1}=-D_3/E_1$ is shown. We easily notice that the most interesting domains of y fall in the vicinity of the cutoff slownesses, A–D. The letter R marks the domain of $y(r)$ describing the Rayleigh wave; y has a zero and a pole there, and their relative distance describes the piezoelectric coupling coefficient of this wave. Note that both the zero and the pole of y reside above the cutoff wave number of the bulk waves, point D, where $\mathrm{Re}\{y\}=0$. This is typical of Rayleigh waves.

We also easily notice similar sharp variation of $\mathrm{Im}\{y\}$ at other cutoffs, A and B, but $y(r)$ has no pole there because $\mathrm{Re}\{y\}$ is different from zero, for real values of r. There can be a pole, however, for complex r. Such a pole is very difficult[6] to find by direct computations based on Eq. (13), and very easy to find from Eq. (C5), for instance, resulting from the approximation introduced in this paper. This is one of the possible applications of the presented theory. Another application concerns evaluation of the generated wave field at the substrate surface by integration of a certain expression[5] on the complex plane of r. This requires evaluation of the residuum at the pole of $y(r)$. This is again easy by using Eq. (C5), for instance.

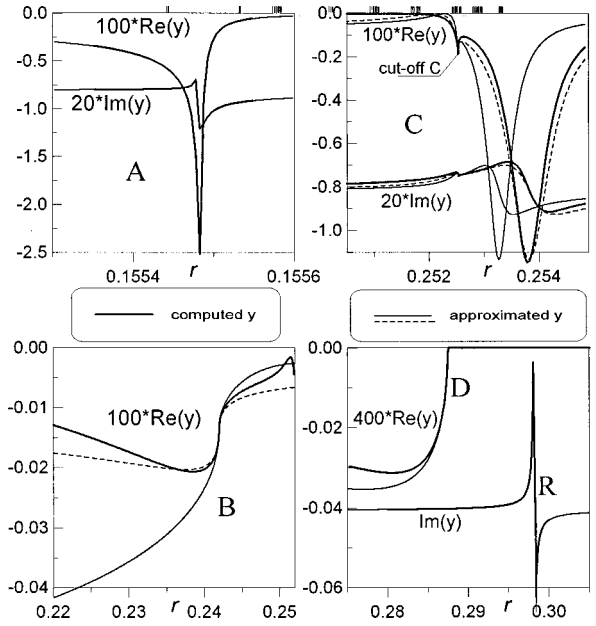

FIG. 2. Detailed plots of computed y around cutoff wave numbers (thick lines), for comparison with the approximate y (thin solid and dashed lines). Subplots A–D correspond to cutoffs A–D in Fig. 1. Solid lines concern approximations as directly evaluated from the equations presented in the paper, and dashed lines present approximations somehow improved in broader domain of r. In case C, the improvement of the approximation to the slowness curve in the domain at the right-hand side of the cutoff produces the improved approximation to y in the same domain. In case B, the chosen free approximation parameter ($\mathrm{Im}\{\tau\}=-j10$) results in a somewhat better fit to the computed y in broader domain around the cutoff.

The approximate (thin lines) and computed values of y (thick lines) are shown in the above-mentioned important domains of r, A, B, C, and D in four subsequent figures marked correspondingly in Fig. 2. Case A does not require explanation. The agreement between the computed and approximate values is excellent. This is because the cutoff A is well separated from the next cutoff, B, and thus the assumption of independence of the other eigenvalues on δ, Eqs. (31), is satisfied sufficiently well in this narrow domain of r that is presented in this figure.

This does not always happen, however. In such cases the approximation can be valid in a narrower domain of r (case D), can be somewhat improved (case B and C), or can require another theory (for example, if two cutoffs are extremely close to each other, the case that is not discussed in this paper). In any case, the validity of a particular approximation is subjected to numerical verification by computed values.

Two approximations are drawn in case C ($\epsilon\sim\delta^3$): for computed parameter a from Eqs. (27) (thin solid line), and for parameter a greater by 75% (dashed line). The parameter a is responsible for approximation of the slowness curve at

cutoff. Because of the complicated shape of this curve, it cannot be well approximated by the curve like $r \sim s^3$ in the broader domain, and Eqs. (27) produce an approximation which is equally good on both sides of the cutoff (see the upper right subplots in Fig. 1 presenting the slowness curves: the thick line is the computed slowness, the solid line is the approximate one with parameter a, and the dashed line is that for the parameter $1.75a$ instead of a).

Better approximation to the slowness curve on the right-hand side of the cutoff results in a better approximation to y in the same domain of r, to the right of r_0. The corrected a has improved the approximation to y in a quite wide domain of r and for quite large values of δ. This example clearly shows that better approximation to $s(r)$, obtained by changing only one parameter, a, can produce better approximation to $\mathbf{G}(\delta)$, without changing many other parameters resulting from $\mathbf{F}'$, $\mathbf{F}''$, etc. We should stress, however, that for original a, the approximation in the tiny domain around the cutoff C is excellent. Changing the value of a, we can better match the computed and approximate curves for *larger* ϵ.

The other cutoff slownesses are of the type $r \sim s^2$, where we have one approximation parameter free, $\mathrm{Im}\{\tau\}$. This can be used for certain improvement of the approximation to $\mathbf{G}$, if necessary. We applied $\mathrm{Im}\{\tau\}=0$ in cases A and D, and obtained good approximations to y (in Fig. 2 the computed y in certain narrower domains is shown, because otherwise some of the thin lines of approximate y would be invisible under the thick lines representing the computed y). It is worth noting that in case D, for r much larger than $r_0 = k_s$, the positions of both the zero and pole of $\mathrm{Im}\{y\}$ are very well approximated in the domain marked by R. This is important because these points are the wave numbers of Rayleigh waves propagating at the free and metallized substrate surface. Hence the evaluated approximation to y at k_s determines the Rayleigh wave velocity and its piezoelectric coupling coefficient relatively well. This is an interesting result because it can be exploited in the numerical investigation of surface waves in piezoelectric crystals.

In case B, however, $\mathrm{Im}\{\tau\}=0$ produces approximate y (thin solid line) that diverges fast from the computed y (thick line), if $r < r_0$. The approximation can be somewhat improved in this area of *large* ϵ by applying $\mathrm{Im}\{\tau\}=-j10$ (dashed line). This poorer fit can be attributed to the proximity of the cutoff slowness C. This makes invalid the assumption that only one, the perturbed eigenvector, depends strongly on δ and the other eigenvectors are *constant*. Moreover, the value of y is rather small in the case B, thus prone to perturbation by small inaccuracies in eigenvectors. Let us stress again that in the tiny domain at the cutoff B, the approximation is excellent.

V. CONCLUSIONS

The proposed approximation to the Green's function $\mathbf{G}$ is shown to be excellent at cutoff slownesses well separated from the neighboring cutoffs, particularly when y is large due to its almost vanishing denominator, the case represented by Eq. (C5), for instance. The denominator can have zero for complex r and one of the applications of the presented analysis is the search for such zeros. This is usually necessary in searching for new waves and modes.[3,13–15]

The impulse response of the body to the applied surface traction that is the time and spatial Fourier transformation of $\mathbf{G}$,[8,16] has distinctive features corresponding to the bulk waves propagating parallely to the surface of the body. They are the waves at cutoffs in spectral domain. Having correct approximation to $\mathbf{G}(r)$, we can evaluate these important features analytically, by applying inverse Fourier transforms of relatively simple functions. Indeed, it is a common method of evaluating far wave field excited by the pointlike source by closing the integration path on the complex plane of spectral variable r in infinity. The most important contribution to the wave field results from the residuum at the pole of the harmonic Green's function,[3,17] that is at zero of the above discussed denominator. This clearly shows the possible area of applications of the presented analysis and the approximation to the planar harmonic Green's function in the spectral domain of the wave number.

ACKNOWLEDGMENTS

This paper is dedicated to His Holiness Pope John Paul II. Financial support was provided by the State Committee for Scientific Research under Grant No. 7 T07A 049 13.

APPENDIX A: DERIVATION AND PROPERTIES OF THE MATRIX *H* AND ITS EIGENVECTORS

The constitutive equations for a piezoelectric body[10]

$$T_{ij} = c_{ijkl} u_{k,l} + e_{kij} \varphi_{,k}, \qquad D_j = e_{jkl} u_{k,l} - \epsilon_{jk} \varphi_{,k}, \tag{A1}$$

can be rewritten in a somewhat symbolic form

$$\begin{bmatrix} T_{i3} \\ D_3 \end{bmatrix} = \begin{bmatrix} c_{i3j1} & e_{1i3} \\ e_{31j} & -\epsilon_{31} \end{bmatrix} \begin{bmatrix} u_j \\ \varphi \end{bmatrix}_{,1} + \begin{bmatrix} c_{i3j3} & e_{3i3} \\ e_{33j} & -\epsilon_{33} \end{bmatrix} \begin{bmatrix} u_j \\ \varphi \end{bmatrix}_{,3}, \tag{A2}$$

and similarly for $[T_{i1} D_1]^T$. The equations of motion

$$T_{i3,3} + T_{31,1} + g\omega^2 u_i = 0, \qquad D_{3,3} + D_{1,1} = 0, \tag{A3}$$

after substitution of $[T_{i1}\ D_1]^T_{,1}$ evaluated from the constitutive equations, yield

$$\begin{bmatrix} T_{i3} \\ D_3 \end{bmatrix}_{,3} + g\omega^2 \begin{bmatrix} u_i \\ 0 \end{bmatrix} + \begin{bmatrix} c_{i11j} & e_{1i1} \\ e_{11j} & -\epsilon_{11} \end{bmatrix} \begin{bmatrix} u_j \\ \varphi \end{bmatrix}_{,11} + \begin{bmatrix} c_{i13j} & e_{3i1} \\ e_{13j} & -\epsilon_{13} \end{bmatrix} \begin{bmatrix} u_j \\ \varphi \end{bmatrix}_{,31} = 0. \tag{A4}$$

Now, we can combine (A2) and (A4) to form one system of equations

$$\begin{bmatrix} c_{i33j} & e_{3i3} & \mathbf{0} & 0 \\ e_{33j} & -\epsilon_{33} & 0 & 0 \\ c_{i13j} & e_{3i1} & \mathbf{I} & 0 \\ e_{13j} & -\epsilon_{13} & 0 & 1 \end{bmatrix} \begin{bmatrix} u_{j,13} \\ \varphi_{,13} \\ T_{j3,3}+g\omega^2 u_i \\ D_{3,3} \end{bmatrix}$$

$$+ \begin{bmatrix} c_{i31j} & e_{1i3} & -\mathbf{I} & 0 \\ e_{31j} & -\epsilon_{31} & 0 & -1 \\ c_{i11j} & e_{1i1} & \mathbf{0} & 0 \\ e_{11j} & -\epsilon_{11} & 0 & 0 \end{bmatrix} \begin{bmatrix} u_{j,1} \\ \varphi_{,1} \\ T_{j3} \\ D_3 \end{bmatrix}_{,1} = 0, \tag{A5}$$

which, solved with respect to the first vector, yields

$$[\mathbf{u}_{,1} \quad -E_1 \quad \mathbf{T} \quad D_3]_{,3}^T = \mathbf{h}[\mathbf{u}_{,1} \quad -E_1 \quad \mathbf{T} \quad D_3]_{,1}^T - g\omega^2[\mathbf{0} \quad \mathbf{u} \quad 0]^T, \quad \mathbf{h} = -\mathbf{z}^{-1}\mathbf{x}, \tag{A6}$$

where $\mathbf{z}$ and $\mathbf{x}$ are 8×8 matrices in (A5), $\mathbf{0}=[0000]$. These matrices and the matrix $\mathbf{h}$ do not depend on r.

Replacing the x_1 and x_3 derivatives by $-jr$ and $-js$, respectively, we easily get Eq. (5). The dependence of $\mathbf{H}$ on r results only from the term $g\omega^2/r^2$ in its 5th to 7th rows: the matrix $\mathbf{H}$ is $\mathbf{h}$, except that $H_{4+i,i}=h_{4+i,i}+g\omega^2/r^2$, $i=1,2,3$.

The above derivation gives us the MATLAB-style[18] code for evaluation of $\mathbf{h}$ for given material constants in abbreviated notations c_{IJ}, e_{iJ}, and ϵ_{ij} contained in the 9×9 table[9] **mat**. It is presented in Appendix B.

Substitution of (A2) into (A4), and the application of $r=k\cos\vartheta$, $s=k\sin\vartheta$ results in the pseudo-Christoffel equation

$$\overline{\Gamma}[\mathbf{U} \quad -E_1]^T = gv^2[\mathbf{U} \quad 0]^T, \quad v=\omega/k. \tag{A7}$$

Eliminating E_1 from the above, we obtain an eigenvalue problem for the Christoffel matrix $\mathbf{\Gamma}$, that is $\mathbf{\Gamma U}=\lambda\mathbf{U}$, $\lambda=gv^2$. We introduce the additional rotation of the coordinate system in the sagital plane (the fourth component of **eu** in Appendix B), which makes the given point $k(\vartheta)$ become a point of cutoff slowness (r_0,s_0) in the rotated system.[3] To find the angle of this rotation, we can exploit the relation for $d\lambda/d\vartheta=\mathbf{U}^T(d\mathbf{\Gamma}/d\vartheta)\mathbf{U}$, where λ is the eigenvalue and $\mathbf{U}$ is the normalized eigenvector of $\mathbf{\Gamma}$. We obtain $s_0/r_0=-0.5\lambda_{,\vartheta}/\lambda$.

Below we investigate useful properties of eigenvectors of the matrix $\mathbf{H}$ that result from the energy conservation law which is known[20] to be satisfied by any solution to Eqs. (A2) and (A4). Consider a slab of certain thickness in the x direction, and extend from the body surface to $z\to-\infty$. There is a wave field expressed by Eq. (11). We will consider several cases of wave fields composed of two modes $\mathbf{F}^{(i)}$, but we should notice first that, due to x-translational invariance, equal power enters the slab from its left side and leaves it at its right-hand side. Thus we can neglect the consideration of the x component of the Poynting vector, focusing only on its z component.

The power delivered to the slab through its upper surface S is[10]

$$P=S\Pi_3, \quad \Pi_3=\tfrac{1}{2}\,\mathrm{Re}\{-T_{3i}(j\omega u_i)^*+\varphi(j\omega D_3)^*\} \tag{A8}$$

and because the area of the bottom surface of the slab is the same S, we can neglect S. The above formula can be easily transformed into Eq. (9), and substituting expansion (11), we get

$$\Pi_3(z=0)=\tfrac{1}{2}\,\mathrm{Re}\{(C_1\check{\mathbf{F}}^{(1)}+C_2\check{\mathbf{F}}^{(2)})\cdot(C_1\hat{\mathbf{F}}^{(1)}+C_2\hat{\mathbf{F}}^{(2)})^*\}. \tag{A9}$$

For the sake of the energy conservation law, the same value must appear at the bottom side of the slab, that is at $z<0$

$$\Pi_3(z\to-\infty)=\frac{1}{2}\mathrm{Re}\left\{\left(\sum_i C_i\check{\mathbf{F}}^{(i)}e^{-js_iz}\right)\times\left(\sum_k C_k\hat{\mathbf{F}}^{(k)}e^{-js_kz}\right)^*\right\}. \tag{A10}$$

Consider two propagating modes in the wave field, $\mathbf{F}^{(p)}$ and $\mathbf{F}^{(q)}$, both of them real.

$$\Pi_3=\frac{\omega}{2r}\,\check{\mathbf{F}}\cdot\hat{\mathbf{F}} \tag{A11}$$

is the z component of the Poyting vector of such modes. The difference between $\Pi_3(z=0)$ and $\Pi_3(z\to-\infty)$ is

$$\Delta\Pi_3=\frac{\omega}{2r}\,\mathrm{Re}\{C_pC_q^*\check{\mathbf{F}}^{(p)}\cdot\hat{\mathbf{F}}^{(q)}e^{j(s_q-s_p)z} + C_p^*C_q\check{\mathbf{F}}^{(q)}\cdot\hat{\mathbf{F}}^{(p)}e^{j(s_p-s_q)z}\}, \tag{A12}$$

must be zero for any C_i, $i=p,q$, $p\neq q$. We conclude that

$$\check{\mathbf{F}}^{(p)}\cdot\hat{\mathbf{F}}^{(q)}+\check{\mathbf{F}}^{(q)}\cdot\hat{\mathbf{F}}^{(p)}=0, \quad p\neq q. \tag{A13}$$

Note that the above equation is true for any propagating modes (real eigenvectors), independently of their propagation direction.

Similar considerations can be carried out for the set of one propagating (p), and the other evanescent (e) modes, vanishing at $z\to-\infty$ (thus only p-mode carries power at the bottom side of the considered slab). We easily obtain (with details presented in the next case below) that the necessary condition for $\Delta\Pi_3$ to vanish for arbitrary real C_p (this does not constrain the reasoning) and complex C_e is

$$\check{\mathbf{F}}^{(p)}\cdot\hat{\mathbf{F}}^{(e)}+\check{\mathbf{F}}^{(e)}\cdot\hat{\mathbf{F}}^{(p)}=0. \tag{A14}$$

Note that similar reasoning is true for the slab extending from $z=0$ to $z\to\infty$, thus the above result holds for any modes, satisfying the radiation conditions (8) or not.

In the last case we have the set of two evanescent modes, e and c, both satisfying (8) and having arbitrary complex amplitudes. But first, we consider only one evanescent mode. Because there is not any power carried at large $|z|$ (no wave field there) Π_3 evaluated at $z=0$ must vanish (we cannot deliver any power to an evanescent mode). This yields

$$\mathrm{Re}\{\check{\mathbf{F}}^{(e)}\cdot\hat{\mathbf{F}}^{(e)*}\}=0. \tag{A15}$$

For two modes, the necessary condition for vanishing Π_3 at $z=0$ is

$$\mathrm{Re}\{C_e C_c^* \check{\mathbf{F}}^{(e)} \cdot \hat{\mathbf{F}}^{(c)*} + C_e^* C_c \check{\mathbf{F}}^{(c)} \cdot \hat{\mathbf{F}}^{(e)*}\} = 0 \tag{A16}$$

for any C_e, C_c. This equation is similar to $\mathrm{Re}\{(a+jb)(c+jd)+(a-jb)(e+jf)\}=0$ for any a, b, requiring that $c=-e$ and $d=f$, that is $c+jd=-(e+jf)^*$. Finally we obtain

$$\check{\mathbf{F}}^{(e)} \cdot \hat{\mathbf{F}}^{(c)*} + \check{\mathbf{F}}^{(e)} \cdot \hat{\mathbf{F}}^{(c)*} = 0, \quad e \neq c \tag{A17}$$

and similarly for the case of both modes vanishing at $z \to \infty$. Note that if $\mathbf{F}^{(e)}$ is an eigenvector, then $\mathbf{F}^{(e)*}$ is another one, however, at q_e^* instead of q_e, and vanishing at $z \to \infty$ instead of $-\infty$. Thus the above equation can be interpreted as the orthogonality relation for two modes from two different families, satisfying radiation conditions at different $z \to \pm\infty$.

Now we can repeat the above reasoning for a finite slab, extending from $z=0$ to a certain finite z, and for a wave field composed of two evanescent modes: e, vanishing at $z \to -\infty$, and c, vanishing at ∞. Using Eq. (A15), we easily arrive at the conclusion

$$\mathrm{Re}\{(1 - C_e C_c^* e^{j(s_c^* - s_e)z}) \check{\mathbf{F}}^{(e)} \cdot \hat{\mathbf{F}}^{(c)*} + (1 - C_e^* C_c e^{j(s_e^* - s_c)z}) \check{\mathbf{F}}^{(c)} \cdot \hat{\mathbf{F}}^{e*}\} = 0, \tag{A18}$$

and finally to Eq. (A16), but now for modes from two different families. Note, however, that if $\mathbf{F}^{(c)}$ is the mode vanishing at ∞, then $\mathbf{F}^{(c)*}$ is the mode vanishing at $-\infty$, that is the mode from the same family as $\mathbf{F}^{(e)}$. The above equation expresses the orthogonality relation of two modes satisfying the same radiation condition.

All the above equations, when compared with the known orthogonality relations of the left and right eigenvectors

$$\mathbf{E}^{(i)} \mathbf{F}^{(j)} = 0, \quad i \neq j, \tag{A19}$$

prove the following

Theorem: The left and the right eigenvectors of the matrix $\mathbf{H}$ are

$$\mathbf{E}^{(i)} = [\check{\mathbf{F}}^{(i)T} \quad \hat{\mathbf{F}}^{(i)T}], \quad \mathbf{F}^{(i)} = \begin{bmatrix} \hat{\mathbf{F}}^{(i)} \\ \check{\mathbf{F}}^{(i)} \end{bmatrix}, \quad \mathbf{E}^{(i)} \mathbf{F}^{(j)} = 0, \quad i \neq j, \tag{A20}$$

which gives us the left eigenvectors without solving the corresponding left eigenvalue problem for nonsymmetric $\mathbf{H}$: if $\mathbf{F} = [U_1 \ U_2 \ U_3 \ -E_1 \ T_{31} \ T_{32} \ T_{33} \ D_3]^T$ is the right eigenvector, then the corresponding left eigenvector is $\mathbf{E} = [T_{31} \ T_{32} \ T_{33} \ D_3 \ U_1 \ U_2 \ U_3 \ -E_1]$. This theorem, when applied to expansion (14) and similar expansion for $\mathbf{E}$, results in

Corollary:

$$\mathbf{E}^0 = [\check{\mathbf{F}}^{0T} \ \ \hat{\mathbf{F}}^{0T}], \quad \mathbf{E}' = [\check{\mathbf{F}}'^T \ \ \hat{\mathbf{F}}'^T], \tag{A21}$$

and similarly for $\mathbf{E}''$, $\mathbf{E}'''$. It also allows us to rewrite (A8) in the form

$$\Pi_3^{(n)} = \frac{\omega}{4r} \mathrm{Re}\{\mathbf{E}^{(n)} \mathbf{F}^{(n)*}\}. \tag{A22}$$

(Numerical hint: Typical numerical programs[21] give us the eigenvalue–eigenvector pairs in arbitrary order. We can use the above theorem to order them when they are evaluated for subsequent points of r. To do this we evaluate the product of $\mathbf{E}^{(i)}$ from the previous r with $\mathbf{F}^{(j)}$ from the current r, and accordingly reorder the latter to get almost a diagonal matrix $[\mathbf{E}^{(i)}][\mathbf{F}^{(j)}]$. This is useful for making figures, for instance.)

It is instructive to evaluate the Poynting vector of the mode $\mathbf{F}^0$. Below we show an example of evaluation for the case of $r \sim a s^4$ $(n=4)$. First, we evaluate

$$\Pi_3 = \frac{\omega}{2r} \mathrm{Re}\{(\check{\mathbf{F}}^0 + \delta \check{\mathbf{F}}' + \delta^2 \check{\mathbf{F}}'' + \delta^3 \check{\mathbf{F}}'') \times (\hat{\mathbf{F}}^0 + \delta \hat{\mathbf{F}}' + \delta^2 \hat{\mathbf{F}}'' + \delta^3 \hat{\mathbf{F}}''')^*\}. \tag{A23}$$

Neglecting all terms of higher-order than δ^3, taking into account Eqs. (29), and $\mathbf{E}^0 \mathbf{F}''' = \mathbf{E}' \mathbf{F}''$, that results from $(\mathbf{H}^0 - q_0 \mathbf{I}) \mathbf{F}''' = \mathbf{F}''$ multiplied on the left by $\mathbf{E}'$, we easily get

$$\Pi_3 = \frac{\omega}{r_0} \mathrm{Re}\{\delta\} \mathrm{Re}\{\delta^2\} \mathbf{E}^0 \mathbf{F}'''. \tag{A24}$$

For real δ, the considered mode is the propagating one, the Poynting vector of which is perpendicular to the slowness curve. For small δ, the absolute value of the full Poynting vector of the mode is described by $\mathbf{F}^0$, and its dependence on δ is negligible. Thus $\Pi_3 = \alpha \Pi_1$, where α is the angle between the x axis and the normal to the slowness curve: $\alpha \approx dr/ds = 4(a/r_0)\delta^3$. Hence

$$\frac{\omega}{r_0} \delta^3 \mathbf{E}^0 \mathbf{F}''' = 4 \frac{a}{r_0} \delta^3 \Pi_1, \tag{A25}$$

where a is given by Eq. (28). This yields

$$\Pi_1 = \frac{\omega}{4} \mathbf{E}^0 \dot{\mathbf{H}} \mathbf{F}''', \quad \dot{\mathbf{H}} = -2g \frac{\omega^2}{r_0^3} \begin{bmatrix} \mathbf{0} & \mathbf{0} \\ \mathbf{I}' & \mathbf{0} \end{bmatrix}, \quad \mathbf{I}' = \mathrm{diag}(1110), \tag{A26}$$

where we have assumed that $\mathbf{E}^0$ and $\mathbf{F}'''$ are real. Noticing the component order in both these vectors, given explicitly below Eq. (A20), and remembering that $(-\omega^2/r_o^2) U_i^2 = |\partial u_i / \partial t|^2$, we get

$$\Pi_1 = v_0 \mathscr{E}, \quad \mathscr{E} = \frac{1}{2} g \sum_i |u_{i,t}|^2, \quad v_0 = \frac{\omega}{r_0}, \tag{A27}$$

what is the already well-known relation.[9]

APPENDIX B: MATLAB-STYLE CODE FOR THE MATRIX H

In the SAW literature,[19] three Euler angles are used to describe the orientation of the coordinate system x_i with respect to the crystallographic axes. Here we will use additional rotation of the coordinate system in the sagital plane $x_2 = 0$; thus the vector **eu** contains three Euler angles and this angle of additional rotation. In the code, **a** is the cosine matrix of tensor transformation, and **b** is its Cartesian product. The transformed tensors are stored in the matrix **td** that represents the dependence of $[T_{ij} \ D_j]$ on $[u_{k,l} \ \varphi_{,l}]$. This helps us to evaluate matrices **z** and **x** which appear in Eq. (A6), and finally to obtain the matrix **h**. The matrix **mat** is the table of material constants[9,10] (with relative dielectric constants) in units described in Sec. IV above.

```
a=[1 0 0; 0 -1 0; 0 0 -1]*...
[cos(eu(3)) sin(eu(3)) 0; -sin(eu(3)) cos(eu(3)) 0; 0 0 1]*...
 [1 0 0; 0 cos(eu(2)) sin(eu(2)); 0 -sin(eu(2)) cos(eu(2))]*...
 [cos(eu(1)) sin(eu(1)) 0; -sin(eu(1)) cos(eu(1)) 0; 0 0 1];
a=[cos(eu(4)) 0 -sin(eu(4)); 0 1 0; sin(eu(4)) 0 cos(eu(4))]*a;
mat=zeros(9); load mat; mat(7:9,7:9)=-.0088542*mat(7:9,7:9);
b=zeros(9); b=[a(1,1)*a a(1,2)*a a(1,3)*a; a(2,1)*a ...
            a(2,2)*a a(2,3)*a; a(3,1)*a a(3,2)*a a(3,3)*a];
td([1 5 9 6 3 2 10 11 12],[1 5 9 6 3 2 10 11 12])=mat;
td([4 7 8],:)=td([2 3 6],:);td(:,[4 7 8])=td(:,[2 3 6]);
             td(1:9,:)=b*td(1:9,:); td(10:12,:)=a*td(10:12,:);
             td(:,1:9)=td(:,1:9)*b';td(:,10:12)=td(:,10:12)*a';
z=zeros(8);z(1:4,1:4)=td([7 8 9 12],3:3:12); z(5:8,5:8)=eye(4);
x=zeros(8);x(1:4,1:4)=td([7 8 9 12],1:3:10);x(1:4,5:8)=-eye(4);
     z(5:8,1:4)=td(1:3:10,3:3:12);x(5:8,1:4)=td(1:3:10,1:3:10);
h=-z\x
```

APPENDIX C: THE IDENTITY FOR PERTURBED MATRIX G'

Below, an identity is presented without proof, for the matrix components of the matrix $\mathbf{G}'$. The proposition results from transformation[2] of Eq. (33) involving $\bar{U}_i$, $\bar{T}_j$ [defined in Eqs. (10)], and G_{ij}, rewritten below in the form

$$[U_i \quad -E_1]^T = G_{ij}[T_j \quad D_3]^T, \qquad G_{ij} = G^0_{ij} + \frac{\delta}{1+\delta\eta}\, G'_{ij}, \tag{C1}$$

to another matrix equation, having replaced electric amplitudes

$$[U_i \quad D_3]^T = \underline{G}_{ij}[T_j \quad -E_1]^T \tag{C2}$$

in its left- and right-hand sides.

From the original equation we obtain

$$D_3 = \frac{1+\delta\eta}{G^0_{44}(1+\delta\eta)+\delta G'_{44}}\,(-E_1) - \frac{G^0_{4j}(1+\delta\eta)+\delta G'_{4j}}{G^0_{44}(1+\delta\eta)+\delta G'_{44}}\, T_j, \tag{C3}$$

which, substituted into the remaining equations (C1) yields, among others, the expression involved in the relation between U_i and T_j

$$U_i = \frac{[\delta^2/(1+\delta\eta)]G'_{ij}G'_{44} - [\delta^2/(1+\delta\eta)]G'_{i4}G'_{4j} + \cdots}{G^0_{44}(1+\delta\eta)+\delta G'_{44}}\, T_j + \cdots .$$

This term exhibits singularity at $1+\delta\eta=0$, the same as in the original equation (C1), and another singularity, at $G^0_{44}(1+\delta\eta)+\delta G'_{44}=0$. If the ''old'' singularity really exists, then there would be two surface modes (two Rayleigh waves, for instance, when $T_j=0$) for metallized surfaces of piezoelectrics. This does not happen, hence the first singularity must vanish on the strength of

Conjecture

$$G'_{44}G'_{ij} = G'_{i4}G'_{4j}, \tag{C4}$$

which is perfectly satisfied in numerical examples.

Accounting for this, we finally obtain that $\underline{G}$ involved in (C2) is

$$\begin{bmatrix} G^0_{ij}-\dfrac{G^0_{i4}G^0_{4j}}{G^0_{44}}+\delta\,\dfrac{G'_{ij}G^0_{44}+G^0_{i4}G^0_{4j}(G'_{44}/G^0_{44})-G^0_{i4}G'_{4j}-G'_{i4}G^0_{4j}}{G^0_{44}+\delta(G'_{44}+\eta G^0_{44})} & \dfrac{G^0_{i4}+\delta(G'_{i4}+\eta G^0_{i4}}{G^0_{44}+\delta(G'_{44}+\eta G^0_{44})} \\ \dfrac{G^0_{44}+\delta(G'_{4j}+\eta G^0_{4j})}{G^0_{44}+\delta(G'_{44}+\eta G^0_{44})} & \dfrac{1+\delta\eta}{G^0_{44}+\delta(G'_{44}+\eta G^0_{44})} \end{bmatrix}. \tag{C5}$$

The dispersive equation for surface waves, for example, immediately results from the above. Indeed, for the free metallized surface, $T_j=0$ and $E_1=0$, thus for nontrivial solution for U_j, D_3, the denominator that appears in all the above matrix components must vanish. This gives the dispersive equation $1+\delta(\eta+G'_{44}/G^0_{44})=0$, $\delta=\sqrt{(r-r_0)/a}$, determining the SAW wave number $r=k_0$ for metallized substrate surface (the cutoff $r_0=k_s$ is assumed for the considered case). Similarly, for any other cutoff r_0, there can be zero of the above denominator, at r taking complex values due to complex values of η and G'_{44}.

[1] K. A. Ingebrigtsen, ''Surface waves in piezoelectrics,'' J. Appl. Phys. **40**, 2960–2963 (1969).
[2] E. Danicki, ''Propagation of transverse surface acoustic waves in rotated Y-cut quartz substrates under heavy periodic metal electrodes,'' IEEE Trans. Sonics Ultrason. **SU-30**, 304–312 (1983).
[3] E. Danicki, ''New theory of SSBW devices,'' IEEE Ultrason. Symp. Proc., 235–239 (1980).
[4] D. M. Barnett, J. Lothe, and S. A. Gundersen, ''Zero curvature transonic states and free surface waves in anisotropic elastic media,'' Wave Motion **12**, 341–360 (1990).
[5] V. K. Tewary, M. Mahapatra, and C. M. Fortunko, ''Green's function for anisotropic half-space solids in frequency space and calculation of mechanical admittance,'' J. Acoust. Soc. Am. **100**, 2960–2963 (1996).
[6] E. L. Adler, ''SAW and pseudo-SAW properties using matrix methods,'' IEEE Trans. Ultrason. Ferroelectr. Freq. Control **41**, 699–705 (1994).
[7] J. H. Wilkinson, *The Algebraic Eigenvalue Problem* (Clarendon, Oxford, 1965), Chap. 1.
[8] C.-Y. Wang and J. D. Achenbach, ''Lamb's problem for solids of general anisotropy,'' Wave Motion **24**, 227–244 (1996).
[9] E. Dieulesaint and D. Royer, *Ondes Élastiques Dans Les Solides* (Masson, Paris, 1974), Chap. 5.
[10] B. A. Auld, *Elastic Fields and Waves in Solids* (Wiley, New York, 1973), Vol. 1, Chaps. 7 and 8, and Vol. 2, Chap. 10.
[11] E. Danicki, ''Interfacial waves in an elastic body fractured by periodic cracks,'' J. Acoust. Soc. Am. **100**, 2942–2948 (1996).
[12] E. Danicki and W. Laprus, ''Singularities of the planar Green function in the spectral domain,'' IEEE Ultrason. Symp. Proc. Vol. 1, 225–228 (1996).
[13] W. Laprus and E. Danicki, ''Piezoelectric interfacial waves in lithium niobate and other crystals,'' J. Appl. Phys. **81**, 855–861 (1997).
[14] E. Danicki, ''An approximation to surface admittance of Y-rotated langasite,'' Arch. Acoust. **20**, 91–94 (1995).
[15] E. Danicki and W. D. Hunt, ''On spurious bulk wave excitation in SAW grating reflectors on GaAs (001)(110),'' Arch. Acoust. **20**, 171–175 (1995).
[16] V. K. Tewary and C. M. Fortunko, ''A computationally efficient representation for propagation of elastic waves in anisotropic media,'' J. Acoust. Soc. Am. **91**, 1888–1896 (1992).
[17] A. Mourad, C. Desmet, W. Lauriks, H. Coufal, and J. Thoen, ''The Green's function for surface acoustic waves: Comparison between theory and experiment,'' J. Acoust. Soc. Am. **100**, 1538–1541 (1996).
[18] *MATLAB, User's Guide* (The Math Works, Inc., 1993).
[19] E. A. Oliner, *Acoustic Surface Waves* (Springer-Verlag, Berlin, 1978), Chap. 6.
[20] W. Nowacki, *Efekty Elektromagnetyczne w Cialach Stalych Odksztalcalnych* (in Polish) (PWN, Warszawa, 1983).
[21] B. T. Smith, J. M. Boyle, G. S. Garbow, Y. Ikebe, V. C. Klema, and C. B. Moler, *Lecture Notes in Computer Sciences, Matrix Eigensystem Routines—EISPACK Guide* (Springer-Verlag, Heidelberg, 1970).

Sound attenuation in a cylindrical tube due to evaporation–condensation

Yi Mao[a)]
National Center for Physical Acoustics, University of Mississippi, University, Mississippi 38677

(Received 10 April 1996; revised 28 August 1997; accepted 2 September 1997)

The influence of evaporation–condensation processes on sound propagation in a cylindrical tube was studied in an attempt to understand sound attenuation in porous materials. In this theoretical model, the tube wall is assumed to be rigid and kept at constant temperature. Water in a very thin layer on the wall is allowed to evaporate into or condense from the gas/vapor mixture due to the sound field propagating in the tube. In addition to the acoustical, thermal, and vorticity modes in Kirchhoff's theory, there exists a mass-diffusion mode. Sound attenuation was obtained after applying the boundary conditions at the tube wall for these four modes. Analytical expressions for the asymptotic behavior in both high- and low-frequency limits were derived. While the sound attenuation due to viscosity could be identified, those due to thermal conduction and evaporation–condensation were coupled. The sound attenuation due to the evaporation–condensation process was significant when the concentration of vapor in the tube was high, but it still underestimated the experimental results in porous materials. [S0001-4966(97)04912-6]

PACS numbers: 43.20.Bi, 43.20.Hq, 43.20.Mv [JEG]

INTRODUCTION

The equations describing sound propagation in a gas-filled cylindrical tube were formally solved more than a century ago. Kirchhoff[1] gave the solution in the form of a complicated, complex transcendental equation. The approximate analytic solutions in the limits of high and low frequencies were first obtained by Kirchhoff[1] and Rayleigh.[2] Higher-order approximations were given later by Weston.[3] Numerical solutions of Kirchhoff's transcendental equation by Shields *et al.*[4] and the ''low reduced frequency solution'' by Tijdeman[5] provide a complete view of sound propagation in cylindrical tubes. There is a long list of authors who derived analytic solutions directly from fundamental equations or performed numerical calculations by introducing some simplifying assumptions. Interested readers may refer to the literature by Helmholtz,[6] Crandall,[7] Kerris,[8] Zwikker and Kosten,[9] Iberall,[10] Rohmann and Grogan,[11] Garlach and Parker,[12] Tsao,[13] Karam and Franke,[14] and Scarton and Rouleau.[15]

Several experimental studies of sound propagation in sandstone have demonstrated that a small amount of absorbed moisture has a large effect on velocities and attenuation. Pandit and King[16] measured elastic velocities and the quality factor, Q, on specimens of Berea sandstone as water vapor content was increased by exposure to an environment of increasing relative humidity. The velocity showed a 20%–30% decrease when relative humidity increased to 0.98%. The quality factor, Q, fell sharply from ~ 200 to ~ 50 during the initial increase (about 0.01% by weight) in the moisture content but changed very little upon further addition of water vapor. Spencer[17] also observed a significant reduction of stiffness and quality factor Q due to a small amount (1.1 g H_2O, corresponding 7% of pore volume) of water in a sample of Navajo sandstone. O'Hara[18] observed a logarithmic decrement (directly related to attenuation) three times greater for ''air dry'' than for ''vacuum dry'' in an experiment on Berea sandstone. In these measurements, the higher logarithmic decrement resulted from the existence of a small amount of water in ''air dry'' Berea sandstone.

When small amounts of water are present in the pore spaces, the air/vapor mixture undergoes a condensation–evaporation process near the pore wall during an acoustic cycle. Mehl *et al.*[19] have measured the condensation–evaporation effect on sound speed in an acoustic resonator. In the latter, the acoustic wave in the mixture drives the condensation–evaporation process, while in the sandstone experiments, the Biot-type one wave does. To model the condensation–evaporation effect, we allowed the frame to be rigid. The matrix elasticity can be added to the mass-transfer model in the manner that Biot incorporated rigid frame pore-wall effects in a poro-elastic model.[20] It is important to point out that the essence of the effects of condensation–evaporation can be captured in a rigid-wall tube model.

For theoretical simplicity, we also consider sound propagation in a cylindrical tube rather than real pores in a sandstone. The theory presented here modifies Kirchhoff's theory[1,2] by including condensation–evaporation in the model. The method is straightforward. First, we obtained a general solution to the wave equation for a gas/vapor mixture confined in the tube. The general solution is a superposition of the four possible modes in the mixture. Application of the boundary conditions resulted in an equation for the wave number for sound propagating along the axis of the tube. The wave number is complex; its real and imaginary parts are related to the phase velocity and the attenuation in the tube. Because of the mutual mass diffusion between the vapor and air molecules involved in our model, the analysis is complicated. In the high- and low-frequency limits, however, analytical solutions have been derived.

[a)]Present address: Tuboscope Vetco Pipeline Services, 2835 Holmes Rd., Houston, TX 77001, 713-766-5410.

I. THEORETICAL MODEL

Consider a wave propagating in a gas/vapor mixture confined in a tube of an infinite length. The wall of the tube is always covered with a thin layer of water. The gas in the tube is able to exchange water molecules with this layer through evaporation–condensation. The goal is to obtain attenuation of the sound traveling down the tube.

The same assumptions used in Kirchhoff's theory apply. The tube has a rigid wall and its heat capacity (or heat conductivity) is large so temperature fluctuations are negligible. The gas/vapor mixture in the tube is assumed to be an ideal gas. Only plane waves are considered; all higher modes are ignored.

Because of the evaporation–condensation process at the surface, the density of vapor molecules near the interface is different from that in the bulk of the gas. This creates a gradient in the density of water vapor. As a result, mutual diffusion between the gas and vapor has to be considered. Another complication here is the water layer between the tube wall and the gas/vapor mixture. For a complete solution, one has to solve the wave equations in the three regions, respectively, and make them meet the boundary conditions at these two interfaces. However, if the thickness of the water layer is thin enough, all physical quantities will be uniform in the layer. In this way, the layer is just an extension of the wall and only one interface is taken under consideration. In other words, the problem can be treated as if the gas/vapor mixture had an immediate interface with the solid wall which could exchange water molecule just as if it were water. Under this thin layer assumption, the analysis will be greatly simplified.

II. FUNDAMENTAL EQUATIONS AND FOUR MODES IN A GAS/VAPOR MIXTURE

For a gas/vapor mixture, there are the following fundamental equations:[21] the mass conservation law for the gas, the mass conservation law for the vapor, the Navier–Stokes equation, the Kirchhoff–Fourier equation, the diffusion equation for the mixture, the equation of state for an ideal gas, and the thermodynamic relation for energy:

$$\frac{\partial \rho_1}{\partial t}+\nabla\cdot(\rho_1\boldsymbol{\nu}_1)=0, \tag{1}$$

$$\frac{\partial \rho_2}{\partial t}+\nabla\cdot(\rho_2\boldsymbol{\nu}_2)=0, \tag{2}$$

$$\rho\frac{D\boldsymbol{\nu}}{Dt}=-\nabla p+\mu\nabla^2\boldsymbol{\nu}+\left(\frac{\mu}{3}+\beta\right)\nabla(\nabla\cdot\boldsymbol{\nu}), \tag{3}$$

$$\rho\frac{Du}{Dt}-\frac{p}{\rho}\frac{D\rho}{Dt}=\frac{\mu}{2}\sum_{ij}\left(\frac{\partial \nu_i}{\partial x_j}+\frac{\partial \nu_j}{\partial x_i}-\nabla\cdot\boldsymbol{\nu}\delta_{ij}\right)^2+\lambda\nabla^2T-kT\left[\frac{n_1}{\gamma_1-1}\nabla\cdot(\boldsymbol{\nu}_1-\boldsymbol{\nu})+\frac{n_2}{\gamma_2-1}\nabla\cdot(\boldsymbol{\nu}_2-\boldsymbol{\nu})\right], \tag{4}$$

$$\boldsymbol{\nu}_1-\boldsymbol{\nu}_2=-\frac{n^2}{n_1n_2}D_{12}\left(\nabla\frac{n_1}{n}+\frac{n_1n_2(m_2-m_1)}{n\rho p}\nabla p\right), \tag{5}$$

$$p=\left(\frac{\rho_1}{m_1}+\frac{\rho_2}{m_2}\right)kT, \tag{6}$$

and

$$\rho u=\left(\frac{\rho_1}{m_1(\gamma_1-1)}+\frac{\rho_2}{m_2(\gamma_2-1)}\right)kT. \tag{7}$$

The subscripts 1 and 2 are for gas and vapor, respectively, and a quantity without a subscript is for the mixture. The terms ρ, m, n, $\boldsymbol{\nu}$, and T are, respectively, the density, the molecular mass, the molecular number density, the velocity, and the temperature. The quantities μ, β, λ, and D_{12} are the coefficients of shear viscosity, bulk viscosity, thermal conductivity, and mutual diffusion. In addition, k is Boltzmann's constant, γ is the specific-heat ratio, u is the internal energy per unit mass, and $D/Dt=d/dt+\boldsymbol{\nu}\cdot\nabla$.

The above set of equations has been solved for a small disturbance from equilibrium.[21] There are four modes of wave motion. In the linear region, each mode can exist independently in the gas/vapor mixture and their interaction occurs only at a boundary. In a tube, these boundary interactions transfer energy from the acoustical mode into the other three highly attenuated modes so that the acoustical mode in the tube is more rapidly attenuated than in open space. At a given (circular) frequency, ω, these four modes satisfy four different Helmholtz equations $\nabla^2F+xF=0$, with $x(=\hat{\mathbf{k}}^2c^2/\omega^2)$ being one of four characteristic values x_A, x_T, x_M, and x_V listed below; F is the variation of a physical quantity and c is the sound speed in the mixture. Three of the allowed modes are irrotational which satisfy $\nabla\times\mathbf{v}=0$:[21]

acoustic mode:

$$x_A=1+(\gamma g_1-g_2)\varepsilon_k-(\gamma-1)\varepsilon_\lambda-\varepsilon_\mu, \tag{8}$$

thermal mode (entropy mode):

$$x_T=\frac{1}{\varepsilon_\lambda}+\frac{(\gamma-1)(\varepsilon_\lambda-g_2\varepsilon_\kappa)(\varepsilon_\lambda-\varepsilon_\mu)}{\varepsilon_\lambda(\varepsilon_\lambda-\gamma g_1\varepsilon_\kappa)}, \tag{9}$$

mass diffusion mode:

$$x_M=\frac{1}{\gamma g_1\varepsilon_\kappa}-\frac{(\gamma g_1-g_2)(\varepsilon_\lambda-g_1\varepsilon_\kappa)(\gamma g_1\varepsilon_\kappa-\varepsilon_\mu)}{\gamma g_1^2\varepsilon_\kappa(\varepsilon_\lambda-\gamma g_1\varepsilon_\kappa)}. \tag{10}$$

The last one is a rotational, vorticity mode, which satisfies $\nabla\times v=0$. Because the vorticity mode is decoupled from the mutual diffusion, Pierce's[22] solution applies to this case:

$$\text{Vorticity mode:}\quad x_V=(4/3\mu+\beta)/(\mu\varepsilon_\mu). \tag{11}$$

Those quantities which appear in Eqs. (8)–(11) are defined as

$$\varepsilon_\mu=\frac{i\omega(\frac{4}{3}\mu+\beta)}{\overline{\rho}\overline{c}^2},$$

$$\varepsilon_\lambda=\frac{i\omega\lambda}{\overline{\rho}\overline{c}_p\overline{c}^2},\quad \epsilon_\kappa=\frac{i\omega D_{12}(m_1+m_2)n}{\overline{\rho}\overline{c}^2},$$

$$g_1=\overline{p}_1^*m_1^*+\overline{p}_2^*m_2^*,\quad g_2=\overline{\rho}_1^*m_1^*+\overline{\rho}_2^*m_2^*, \tag{12}$$

$$m_1^*=\frac{m_1}{m_1+m_2},\quad m_2^*=\frac{m_2}{m_1+m_2},$$

$$\overline{p}_1^*=\frac{\overline{n}_1k\overline{T}}{\overline{\rho}\overline{c}^2},\quad \overline{p}_2^*=\frac{\overline{n}_2k\overline{T}}{\overline{\rho}\overline{c}^2},\quad \overline{\rho}_1^*=\frac{\overline{\rho}_1}{\overline{\rho}},\quad \overline{\rho}_2^*=\frac{\overline{\rho}_2}{\overline{\rho}}.$$

Each mode leads to different relations between physical quantities such as pressure, particle velocities of vapor, gas and their mixture, temperature, densities, etc. Because the medium is a dynamic system, a temperature gradient will no longer result in only a temperature field. For example, a thermal mode has not only a temperature field but also an accompanying nonzero particle velocity field and an accompanying nonzero density field.

III. FOUR MODES IN CYLINDRICAL COORDINATES (R,Θ,Z)

The four modes are building blocks for a description of wave propagation in a gas/vapor mixture. A general solution is just a linear superposition of these four modes. In a tube, solutions of the four modes should be expressed in terms of cylindrical coordinates.

In addition to those quantities defined by Eq. (12) it is useful to introduce additional quantities:[21]

$$\nabla^*=\frac{c\nabla}{\omega},\quad r^*=\frac{\omega r}{c},\quad z^*=\frac{\omega z}{c},$$

$$\tilde{\rho}_1^*=\frac{\tilde{\rho}_1}{\overline{\rho}},\quad \tilde{\rho}_2^*=\frac{\tilde{\rho}_2}{\overline{\rho}}, \tag{13}$$

and

$$\tilde{p}^*=\frac{\tilde{p}}{\overline{\rho}\overline{c}^2},\quad \tilde{T}^*=\frac{\tilde{T}}{\overline{T}},\quad \boldsymbol{\nu}^*=i\frac{\boldsymbol{\nu}}{c}.$$

A superscript * stands for a dimensionless quantity, a bar ''-'' for the equilibrium value and ''$\sim$'' for the variation about equilibrium. In the new symbol system, the Helmholtz equation $\nabla^2F+xF=0$ becomes $\nabla^{*2}F^*+\mathbf{x}F^*=0$.

Solutions are understood to have an extra factor $e^{i\omega t}$. All four modes have a common factor $\exp(-ik_z^*z^*)$ since the wave travels in z direction. The goal is to find k_z^*. The real and imaginary parts of k_z^* are related to the phase velocity and the attenuation of wave in the tube. Due to the assumption introduced earlier, the solutions are θ independent. The solutions for the three irrotational modes are the same except for different characteristic values of x. Solutions for two types of waves, rotational and irrotational, are required:

(1) Vorticity mode $x_V=(4/3\mu+\beta)/(\mu\varepsilon_\mu)$. Only the vorticity mode is rotational. The r component ν_r^* and z component ν_z^* satisfy the following equations with $x=x_V$:

$$\nabla^{*2}\nu_r^*-\frac{\nu_r^*}{r^{*2}}+\mathbf{x}\nu_r^*=0,$$

$$\nabla^{*2}\nu_z^*+\mathbf{x}\nu_z^*=0, \tag{14}$$

$$\nabla^*\cdot\boldsymbol{\nu}=0.$$

The solution is found to be

$$\nu_r^*=Aik_z^*J_1(k_r^*r^*)\exp(-ik_z^*z^*),$$

$$\nu_z^*=Ak_r^*J_0(k_r^*r^*)\exp(-ik_z^*z^*), \tag{15}$$

where $k_r^*=\sqrt{(x-k_z^{*2})}$ and A is an undetermined constant.

For the vorticity mode, the particle velocities for gas and vapor are the same, i.e., $\boldsymbol{\nu}^*=\boldsymbol{\nu}_1^*=\boldsymbol{\nu}_2^*$ and $\tilde{T}^*=\tilde{p}^*=\tilde{\rho}^*=0$.

(2) Acoustical mode ($x=x_A$), thermal mode ($x=x_T$), and mass diffusion mode ($x=x_M$): Three modes are irrotational. The r and z components of $\boldsymbol{\nu}^*$, $\boldsymbol{\nu}_1^*$, and $\boldsymbol{\nu}_2^*$ satisfy the following equations with x equal to x_A, x_T, x_M:

$$\nabla^{*2}\nu_r^*-\frac{\nu_r^*}{r^{*2}}+\mathbf{x}\nu_r^*=0,$$

$$\nabla^{*2}\nu_z^*+\mathbf{x}\nu_z^*=0, \tag{16}$$

$$\boldsymbol{\nabla}^*\times\boldsymbol{\nu}=0.$$

Any two of the velocities $\boldsymbol{\nu}^*$, $\boldsymbol{\nu}_1^*$, and $\boldsymbol{\nu}_2^*$, can be expressed in terms of the other.[21] The solution of Eq. (16) for $\boldsymbol{\nu}_2^*$ is expressed as

$$\nu_{2r}^*=Ak_z^*J_1(k_r^*r^*)\exp(-ik_z^*z^*),$$

$$\nu_{2z}^*=Aik_r^*J_0(k_r^*r^*)\exp(-ik_z^*z^*), \tag{17}$$

where $k_r^*=\sqrt{(x-k_z^{*2})}$ and A is an undetermined constant. The velocities $\boldsymbol{\nu}^*$ and $\boldsymbol{\nu}_1^*$ in terms of $\boldsymbol{\nu}_2^*$ are as follows:

$$\nu_r^*=(1-\rho_1^*G)\nu_{2r}^*,\quad \nu_z^*=(1-\rho_1^*G)\nu_{2z}^*, \tag{18}$$

$$\nu_{1r}^*=(1-G)\nu_{2r}^*,\quad \nu_{1z}^*=(1-G)\nu_{2z}^*, \tag{19}$$

where G is a mode-dependent parameter and it has to have the same subscript as x,

$$G=\frac{1-(\gamma\varepsilon_\lambda+\varepsilon_\mu+1)x+\varepsilon_\lambda(1+\gamma\varepsilon_\mu)x^2}{\overline{\rho}_1^*-[(\gamma\varepsilon_\lambda+\varepsilon_\mu+1-1/\gamma)\overline{\rho}_1^*+\overline{p}_1^*]x+\varepsilon_\lambda\gamma(\overline{p}_1^*+\overline{\rho}_1^*\varepsilon_\mu)x^2}. \tag{20}$$

For later usage, other relations are derived[21] and listed below:

$$\nabla^*\cdot\boldsymbol{\nu}^*=\frac{(1-\rho_1^*G)x\nu_{2r}^*}{ik_z^*}, \tag{21}$$

$$\tilde{\rho}_2^*=\nabla^*\cdot\boldsymbol{\nu}_2^*=\frac{x\nu_{2r}^*}{ik_z^*}, \tag{22}$$

$$\tilde{T}^*=\frac{(\gamma-1)(1-\rho_1^*G)x\nu_{2r}^*}{ik_z^*(1-x\gamma\varepsilon_\lambda)}. \tag{23}$$

IV. GENERAL SOLUTION IN TERMS OF THE FOUR MODES IN CYLINDRICAL COORDINATES (R,Θ,Z)

Any solution in the tube can now be written as a superposition of four modes. For example, the temperature variation in the mixture is a summation of $\tilde{T}_A^*$, $\tilde{T}_T^*$, $\tilde{T}_M^*$, and $\tilde{T}_V^*$, where the subscripts ''A,'' ''T,'' ''M,'' and ''V'' are attached to indicate a quantity in the acoustical, thermal, mass-diffusion, and vorticity modes, respectively. These subscripts will be added when needed. Since each mode has an undetermined constant, a general solution contains four corresponding undetermined constants, A_A, A_T, A_M, and A_V.

For the temperature variation,

$$\tilde{T}^*=\left[A_V\frac{x_V}{i(1-x_V\gamma\varepsilon_\lambda)}J_0(k_{rV}^*r^*)+\sum_{i=A,T,M}A_i\frac{(1-\rho_1^*G_i)x_i}{i(1-x_i\gamma\varepsilon_\lambda)}J_0(k_{ri}^*r^*)\right]\times(\gamma-1)\exp(-ik_z^*z^*). \tag{24}$$

For the gradient of the temperature variation in the radial direction,

$$\frac{\partial\tilde{T}^*}{\partial r^*}=-\left[A_V\frac{x_Vk_{rV}^*}{i(1-x_V\gamma\varepsilon_\lambda)}J_1(k_{rV}^*r^*)+\sum_{i=A,T,M}A_i\frac{(1-\rho_1^*G_i)x_ik_{ri}^*}{i(1-x_i\gamma\varepsilon_\lambda)}J_1(k_{ri}^*r^*)\right]\times(\gamma-1)\exp(-ik_z^*z^*). \tag{25}$$

For the velocity of gas,

$$\begin{aligned}\nu_{1r}^*&=\left[A_Vik_z^*J_1(k_{rV}^*r^*)+\sum_{i=A,T,M}A_i(1-G_i)\times k_{ri}^*J_1(k_{ri}^*r^*)\right]\exp(-ik_z^*z^*),\\ \nu_{1z}^*&=\left[A_Vk_{rV}^*J_0(k_{rV}^*r^*)+\sum_{i=A,T,M}A_i(1-G_i)\times ik_z^*J_0(k_{ri}^*r^*)\right]\exp(-ik_z^*z^*).\end{aligned} \tag{26}$$

For the velocity of vapor,

$$\begin{aligned}\nu_{2r}^*&=\left[A_Vik_z^*J_1(k_{rV}^*r^*)+\sum_{i=A,T,M}A_ik_{ri}^*J_1(k_{ri}^*r^*)\right]\times\exp(-ik_z^*z^*),\\ \nu_{2z}^*&=\left[A_Vk_{rV}^*J_0(k_{rV}^*r^*)+\sum_{i=A,T,M}A_ik_z^*J_0(k_{ri}^*r^*)\right]\times\exp(-ik_z^*z^*).\end{aligned} \tag{27}$$

For velocity of mixture,

$$\begin{aligned}\nu_r^*&=\left[A_Vik_z^*J_1(k_{rV}^*r^*)+\sum_{i=A,T,M}A_i(1-\rho_1^*G_i)\times k_{ri}^*J_1(k_{ri}^*r^*)\right]\exp(-ik_z^*z^*),\\ \nu_z^*&=\left[A_Vk_{rV}^*J_0(k_{rV}^*r^*)+\sum_{i=A,T,M}A_i(1-\rho_1^*G_i)\times ik_z^*J_0(k_{ri}^*r^*)\right]\exp(-ik_z^*z^*).\end{aligned} \tag{28}$$

For vapor density variations,

$$\tilde{\rho}_2^*=\boldsymbol{\nabla}^*\cdot\boldsymbol{\nu}_2^*=\left[A_Vix_Vk_z^*J_1(k_{rV}^*r^*)+\sum_{i=A,T,M}A_ix_ik_{ri}^*J_1(k_{ri}^*r^*)\right]\frac{\exp(-ik_z^*z^*)}{ik_z^*}. \tag{29}$$

In writing out the above, Eqs. (15) and (17)–(23) were used. We could list the general solution for other quantities, but they are not needed below.

V. BOUNDARY CONDITIONS

The general solution obtained above is, in fact, a family of solutions because A_A, A_T, A_M, and A_V can take on any value. However, sound traveling in the tube is well defined when physical properties and the geometrical configuration are given. To find this specific solution, boundary conditions are needed to restrict the choice of A_A, A_T, A_M, and A_V. Actually, boundary conditions impose three relations among these four undetermined constants.

For our model, there are four boundary conditions:

(1) the gas cannot penetrate the boundary:

$$\nu_{1r}^*|_{r^*=R^*}=0; \tag{30}$$

(2) the gas/vapor mixture can not slip against the boundary:

$$\nu_z^*|_{r^*=R^*}=0; \tag{31}$$

(3) the temperature on the wall remains constant:

$$\tilde{T}^*|_{r^*=R^*}=0; \tag{32}$$

(4) the vapor pressure at the boundary depends only on the temperature there:

$$\left[\overline{p_2^*}\tilde{\rho}_2^*+\left(\overline{p_2}-\frac{\partial\overline{p_2^*}}{\partial\tilde{T}^*}\right)\tilde{T}^*\right]\Bigg|_{r^*=R^*}=0. \tag{33}$$

Because of the third boundary condition above, the last condition can be reduced to

$$\tilde{\rho}_2^*|_{r^*=R^*}=0. \tag{34}$$

VI. SOUND ATTENUATION

Inserting the general solution equations (24)–(29) into these boundary conditions (30)–(32) and (34), we obtain a set of four homogeneous linear equations for A_A, A_T, A_M, and A_V. The condition for this set of equations to have a nonzero

solution is that the determinant of the matrix constructed from the coefficients of A_A, A_T, A_M, and A_V must be zero, i.e.,

$$\mathrm{Det}[M]=0, \tag{35}$$

where

$$M=\begin{pmatrix} \frac{k_z^{*2}}{k_{rV}^{*2}}F(k_{rV}^*) & F(k_{rA}^*)(1-G_A)\left(\frac{1}{x_A}-\gamma\varepsilon_\lambda\right) & F(k_{rT}^*)(1-G_T)\left(\frac{1}{x_T}-\gamma\varepsilon_\lambda\right) & F(k_{rM}^*)(1-G_M)\left(\frac{1}{x_M}-\gamma\varepsilon_\lambda\right) \\ 1 & (1-\overline{\rho_1^*}G_A)\left(\frac{1}{x_A}-\gamma\varepsilon_\lambda\right) & (1-\overline{\rho_1^*}G_T)\left(\frac{1}{x_T}-\gamma\varepsilon_\lambda\right) & (1-\overline{\rho_1^*}G_M)\left(\frac{1}{x_M}-\gamma\varepsilon_\lambda\right) \\ 0 & (1-\overline{\rho_1^*}G_A) & (1-\overline{\rho_1^*}G_T) & (1-\overline{\rho_1^*}G_M) \\ 0 & (1-x_A\gamma\varepsilon_\lambda) & (1-x_T\gamma\varepsilon_\lambda) & (1-x_M\gamma\varepsilon_\lambda) \end{pmatrix} \tag{36}$$

and $F(k_{ri}^*)$ is defined as

$$F(k_{ri}^*)=k_{ri}^*\frac{J_1(k_{ri}^*R^*)}{J_0(k_{ri}^*R^*)}, \quad i=A,T,M,V. \tag{37}$$

Some algebraic manipulations have been employed to write down the above simplified matrix.

A value of k_z^* satisfying Eq. (35) reflects the existence of a wave traveling down the tube with a phase velocity $c/\mathrm{Re}(k_z^*)$ and an attenuation $\mathrm{Im}(k_z^*)$ per $c/\omega=\lambda/2\pi$, where $\mathrm{Re}(k_z^*)$ and $\mathrm{Im}(k_z^*)$ are the real and imaginary parts of k_z^*, and λ is the wavelength in an infinite medium. The solution of the problem has been reduced to mathematically solving Eq. (35), which is in the form of a complex transcendental equation. Because the left-hand side of Eq. (35) is a complicated function of k_z^*, it usually has to be solved numerically.

We could derive Kirchhoff's equation from the matrix M. The last column of the matrix M is due to the mass diffusion mode and the last row is due to the boundary condition regarding the vapor. Neither exist in Kirchhoff's model. If we had taken the upper-left 3×3 submatrix (formed from the matrix M by deleting the last column and the last row), and kept only the lowest order for x_A and x_T and set both G_A and G_T to be zero in this 3×3 submatrix, Eq. (35) would be Kirchhoff's result.

VII. HIGH- AND LOW-FREQUENCY LIMITS

Although Eq. (35) is complicated, an analytical solution can be derived in either the high- or low-frequency limit. Before deriving these analytic solutions, the orders of magnitude of some physical parameters need to be considered. The three parameters, ε_μ, ε_λ, and ε_κ, are all much less than one, and can be treated as small quantities. Consequently, x_A is on the order of one, while x_V, x_T, and x_M are much larger than one. Also, G_A and G_T are found to be small quantities and G_M is of order one. The radius of the tube is small compared to the acoustical wavelength. For small values of the argument of the Bessel functions,

$$\frac{J_1(k_{rA}^*R^*)}{J_0(k_{rA}^*R^*)}=-\frac{k_{rA}^*R^*}{2}\left(1+\frac{(k_{rA}^*R^*)^2}{8}+\frac{(k_{rA}^*R^*)^4}{48}+\cdots\right). \tag{38}$$

In the high-frequency limit, the frequency is high or the radius of the cylindrical tube is large compared to the boundary-layer thicknesses for the vorticity, thermal, and mass-diffusion modes. In other words, $|k_{ri}^*R^*|\gg1$ for $i=V,T,M$, so that the Bessel functions for large arguments can be employed:

$$\frac{J_1(k_{ri}^*R^*)}{J_0(k_{ri}^*R^*)}\approx i. \tag{39}$$

Using the stated approximations above and keeping only the largest two terms, an analytical solution for the high-frequency limit is given by

$$k_z^{*2}=x_A\left(1-\frac{2i}{R^*\sqrt{x_V}}-\frac{2(\gamma-1)i}{R^*\sqrt{x_T}}R_h\right), \tag{40}$$

where

$$R_h=\frac{\gamma(1-G_M)\sqrt{x_T}(x_M\gamma-x_T)+(\gamma-1)(G_M\overline{\rho_1^*}x_T-x_M\gamma)\sqrt{x_M}}{(\gamma-1)[\gamma(x_T-x_M)-(\gamma-1)G_M\overline{\rho_1^*}x_T]\sqrt{x_M}}. \tag{41}$$

Equation (40) reduces to Rayleigh's high-frequency solution when R_h is set equal to 1 and only the largest term of the x's are kept.

The last two terms in the parentheses of Eq. (40) account for attenuation in the tube. The first term is due to viscosity. The second term, which was purely due to the thermal conduction in Kirchhoff's model, is coupled with the mass-diffusion loss. The attenuation due to thermal conduction and mass diffusion cannot be easily separated. In fact, substituting R_h into Eq. (40), the solution has some symmetry between x_T and x_M. This result is not surprising because the mass diffusion is thermal in nature.

Because the last two terms in the parentheses of Eq. (40) are small, the analytical solution can be approximated by

$$k_z^*=\sqrt{x_A}\left(1-\frac{i}{R^*\sqrt{x_V}}-\frac{(\gamma-1)i}{R^*\sqrt{x_T}}R_h\right). \tag{42}$$

It is clear now that the real part of R_h is the ratio of the attenuation coefficients due to thermal effect in the wet and dry tubes.

Figure 1 displays the ratio of the attenuation in saturated air to the attenuation in dry air as a function of

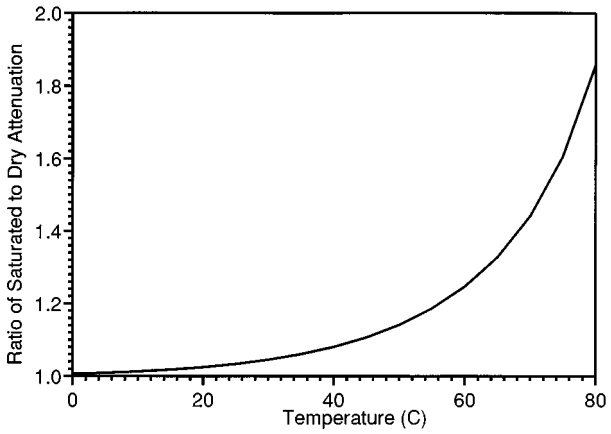

FIG. 1. The temperature dependence of the ratio of the attenuation in a wet tube to that in a dry tube in the high-frequency limit.

temperature.[23–25] Note that this ratio is independent of frequency as long as the conditions for the high-frequency limit are met.

For the low-frequency limit, assume that the frequency is low or the radius of the cylindrical tube is small compared to the boundary-layer thicknesses for the vorticity, thermal, and mass-diffusion modes; that is, $|k_{ri}^* R^*| \ll 1$ for $i = V,T,M$. The Bessel functions with arguments associated with each of the four modes will be approximated by

$$\frac{J_1(k_{ri}^* R^*)}{J_0(k_{ri}^* R^*)} = -\frac{k_{ri}^* R^*}{2}\left(1+\frac{(k_{ri}^* R^*)^2}{8}+\frac{(k_{ri}^* R^*)^4}{48}+\cdots\right). \tag{43}$$

The solution in low-frequency limits can be written as

$$k_z^{*2} = \frac{8x_A\gamma}{x_V R^{*2}}\frac{G_M(x_M\gamma - x_T)}{[\gamma(x_M - x_T)+(\gamma-1)G_M\overline{\rho_1^*}x_T]} + O((k_{ri}^* R^*)^2). \tag{44}$$

Kirchhoff's solution results in the expression

$$k_z^{*2} = \frac{8x_A\gamma}{x_V R^{*2}}\left(1+\frac{x_V R^{*2}}{6}-\frac{(\gamma-1)x_T R^{*2}}{8}\right). \tag{45}$$

Figure 2 displays the ratio of the attenuation in saturated air in a tube to the attenuation in dry air in a tube in the low-frequency limit calculated using Eqs. (44) and (45).[23–25] Note that this ratio is frequency independent in the range of validity of the low-frequency approximation.

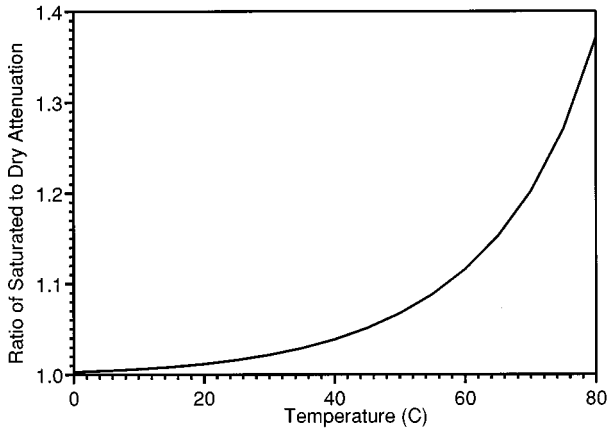

FIG. 2. The temperature dependence of the ratio of the attenuation in a wet tube to that in a dry tube in the low-frequency limit.

VIII. DISCUSSION AND CONCLUSIONS

In the high-frequency limit, the ratio of wet to dry attenuation is small at temperature less than 40 °C. At extreme temperatures the ratio approaches 1.9. In the low-frequency limit, corresponding to narrow tubes and low frequency, the ratio of wet to dry attenuation is even smaller, only approaching 1.4 at high temperatures. The relative effect is larger in the high frequency case since the thermal effects are proportionately larger in the wide tube limit. For narrow tubes, the propagation is approximately isothermal.

In summary we have demonstrated that moisture generally influences the attenuation of sound propagating in a tube and causes a significant increase in attenuation at high temperatures. This result only qualitatively agrees with experimental results in sandstone. At low temperatures where the gas/vapor mixture has a small fraction of vapor, this theory predicts a moderate increase in attenuation; experiments in sandstone yield at least three times higher attenuation.

The discrepancy may be due to the difference in geometry between the connected pore spaces in sandstone or may be due to the assumed boundary conditions in the present calculation. In particular, the assumption of constant temperature wall and water layer temperature may lead to an underestimation of attenuation.

ACKNOWLEDGMENTS

I would like to acknowledge the contributions of Dr. James Sabatier and Dr. Richard Raspet in editing and revising the article to its final form. I also would like to thank Dr. Henry E. Bass for his helpful suggestions and wish to acknowledge gratefully the financial support of the Office of Naval Research.

[1] G. Kirchhoff, ''Ueber den einfluss der wärmeleitung in einem gase auf die schallbewegung,'' Poggendorfer Annalen **134**, 177–193 (1868).
[2] Lord Rayleigh, *Theory of Sound* (Macmillan, London, 1896), 2nd ed., Vol. II.
[3] D. E. Weston, ''The theory of the propagation of plane sound waves in tubes,'' Proc. Phys. Soc. London, Sec. B **66**, 695–709 (1953).
[4] F. D. Shields, K. P. Lee, and W. J. Wiley, ''Numerical solution for sound velocity and absorption in cylindrical tubes,'' J. Acoust. Soc. Am. **37**, 724–729 (1965).
[5] H. Tijdeman, ''On the propagation of sound waves in cylindrical tubes,'' J. Sound Vib. **39**, 1–33 (1975).
[6] H. V. Helmholtz, ''Verhandlungen der Naturhistorisch-Medizinischen Vereins zu Heidelberg,'' **III**, 16 (1863).
[7] I. B. Crandall, *Theory of Vibrating Systems and Sound* (von Nostrand, New York, 1927).
[8] W. Kerris, ''Einfluss der rohrleitung bei der messung periodisch schwankender drücke,'' Zentralblatt für wissenschaftliches berichtwesen (Adlerhof F. B., Berlin, 1939), p. 1140.
[9] C. Zwikker and C. W. Kosten, *Sound Absorbing Materials* (Elsevier, New York, 1949).
[10] A. S. Iberall, ''Attenuation of oscillatory pressures in instrument lines,'' J. Res. Natl. Bur. Stand. **45**, 85–108 (1950).
[11] C. P. Rohmann and E. C. Grogan, ''On the dynamics of pneumatic transmission lines,'' Trans. Am. Soc. Mech. Eng. **79**, 853–874 (1957).

[12] C. R. Garlach and J. D. Parker, ''Wave propagation in viscous fluid lines including higher mode effects,'' J. Basic Eng. Am. **89**, 782–788 (1967).
[13] S. Tsao, ''Numerical solutions of transients in pneumatic networks-transmission line calculations,'' J. Appl. Mech. Am. **35**, 588–595 (1968).
[14] J. T. Karam and M. E. Franke, ''The frequency response of pneumatic lines,'' J. Basic Eng. Am. **90**, 853–874 (1969).
[15] H. A. Scarton and W. T. Rouleau, ''Axisymmetric waves in compressible Newtonian liquids contained in rigid tubes: Steady periodic mode shapes and dispersion by the method of eigenvalues,'' J. Fluid Mech. **58**, 595–621 (1973).
[16] B. I. Pandit and M. S. King, ''The variation of elastic wave velocities and quality factor Q of a sandstone with moisture content,'' Can. J. Earth Sci. **16**, 2177–2195 (1979).
[17] J. W. Spencer, ''Stress relaxations at low frequencies in fluid-saturated rocks: Attenuation and modulus dispersion,'' J. Geophys. Res. **86**, 1803–1812 (1981).
[18] S. G. O'Hara, ''Influence of pressure, temperature, and pore fluid on the frequency-dependent attenuation of elastic waves in Berea sandstone,'' Phys. Rev. A **32**, 472–488 (1985).
[19] J. B. Mehl and M. R. Moldover, ''Precondensation phenomena in acoustic measurements,'' J. Chem. Phys. **77**, 455–465 (1982).
[20] M. A. Biot, ''Theory of propagation of elastic waves in a fluid-saturated porous solid. II. Higher frequency range,'' J. Acoust. Soc. Am. **28**, 179–191 (1956).
[21] Y. Mao, ''The dynamics of freely oscillating gas-vapor bubble,'' Doctoral dissertation, University of Mississippi (1993).
[22] A. D. Pierce, *Acoustics: An Introduction to its Physical Principles and Applications* (Acoustical Society of America, New York, 1989), pp. 519–523.
[23] The values and temperature dependence of μ, β, and λ are calculated from the formulas on p. 513 of Ref. 22. The values and temperature dependence of γ and c_p are calculated using formulas on p. 28 and 29 of Ref. 22.
[24] The value and temperature dependence of D_{12} is developed from p. 600 of J. V. Hirschfelder, C. F. Curtiss, and R. B. Byrd, *Molecular Theory of Gases and Liquids* (Wiley, New York, 1954).
[25] The vapor pressure as a function of temperature is calculated from the formula on p. 169 of *Physical Acoustics XVII*, edited by W. P. Mason and R. N. Thurston (Academic, New York, 1984).

A novel boundary integral formulation for three-dimensional analysis of thin acoustic barriers over an impedance plane

L. A. de Lacerda
Brunel University, Department of Mechanical Engineering, Uxbridge, Middlesex UB8 3PH, United Kingdom and COPPE/UFRJ, Programa de Engenharia Civil, Cx.P. 68506, 21945 Rio de Janeiro, Brazil

L. C. Wrobel
Brunel University, Department of Mechanical Engineering, Uxbridge, Middlesex UB8 3PH, United Kingdom

H. Power
Wessex Institute of Technology, Ashurst Lodge, Ashurst, Southampton SO40 7AA, United Kingdom

W. J. Mansur
COPPE/UFRJ, Programa de Engenharia Civil, Cx.P. 68506, 21945 Rio de Janeiro, Brazil

(Received 20 March 1997; revised 21 April 1998; accepted 4 May 1998)

This article presents a three-dimensional formulation for the analysis of acoustic barriers over an impedance plane as infinitely thin structures. The barriers are therefore modeled as simple surfaces rather than volumetric structures. Using this approach, the problems caused by near-singular integrations and near-degenerate systems of equations are averted, and mesh generation is made easier. A dual-boundary-element method is used in the analysis, involving the simultaneous solution of standard and hypersingular boundary integral equations. An optimization procedure is used to speed up the assembling of the system of equations, increasing the applicability of the method to a wider range of frequencies. © *1998 Acoustical Society of America.* [S0001-4966(98)04808-5]

PACS numbers: 43.20.Fn, 43.20.Rz, 43.50.Gf, 43.28.Fp [JEG]

INTRODUCTION

Acoustic barriers have been widely used as a means of noise abatement from road traffic. Several empirical and numerical methods have been developed, based on different approaches, to predict the insertion loss in the field behind the barrier. Among them, the boundary integral equation method permits the analysis of barriers of complex shapes and complicated boundary conditions. In this formulation, the problem is recast in terms of boundary integral representations using a Green's function which directly satisfies the Sommerfeld radiation condition. Therefore, only interior boundaries need to be discretized. Accurate results can be obtained using a sufficient number of elements per wavelength. The drawback of the method is that it requires large amounts of CPU time and memory, especially for three-dimensional problems at high frequencies. The standard boundary integral formulation also presents some difficulties for the analysis of very thin bodies, in the form of near-singularities and near-degeneracy of the final system of equations.

Filippi and Dumery[1] and Terai[2] developed efficient boundary integral techniques to analyze the scattering of sound waves by thin rigid screens in unbounded regions using a slender body theory. This technique makes use of a hypersingular boundary integral equation and only requires discretization of the screen axis. The formulation was later extended by Kawai and Terai[3] to analyze outdoor sound propagation and its attenuation by thin rigid barriers over a rigid ground. The formulation also used a hypersingular integral equation over the barrier axis and avoided discretization of the infinite plane ground by modifying the free-space Green's function through the method of images.

Numerical solutions for two-dimensional problems in which both the barrier and the ground are treated as absorptive have been presented by Hothersall *et al.*[4] and de Lacerda *et al.*[5] However, no such numerical formulations have been derived for three-dimensional problems.

The present paper extends Kawai and Terai's work by considering the infinite ground as homogeneously absorptive. In this case the method of images is no longer sufficient to derive a Green's function which takes into account the properties of the ground. Nevertheless, a Green's function for this problem has been found and represented in closed integral form by many authors.[6–10] Different asymptotic representations were also suggested for these integrals, depending on the frequency, ground absorption, and relative position between source and receiver. The general approach adopted in this work for evaluating the Green's function basically uses numerical quadrature in the ''near'' field and an asymptotic expansion presented by Kawai *et al.*[10] for the ''far'' field, derived from the modified steepest descent method. The ''near'' and ''far'' field positions will be defined later in this paper.

Because the thin barriers themselves will also be considered as absorptive, contrary to previous works where they were always treated as rigid, we formulate a dual-boundary-element method which simultaneously applies a standard and a hypersingular integral equation at each side of the barrier.[5] Evaluation of the Green's function is very expensive and has to be performed at every integration point, together with its first and second derivatives. It will be shown that the second derivatives of the Green's function, required in the hypersingular boundary integral equation, do not demand extra com-

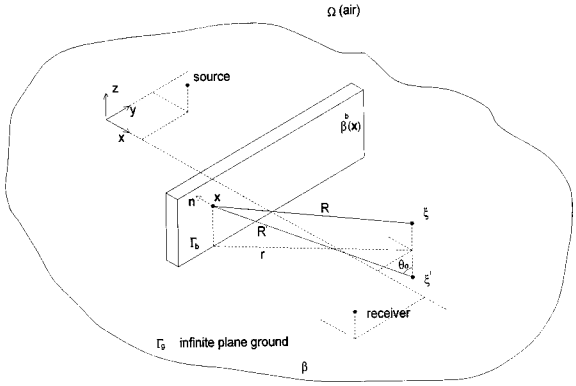

FIG. 1. Three-dimensional model for outdoor sound propagation.

putational effort since their terms can be represented as functions of the Green's function and its first derivatives, already used in the standard boundary integral equation. Another advantage of modeling the barrier (or its attachments) as a surface rather than a volumetric structure is the reduction in the CPU time for the system assembly. Numerical aspects concerning the accurate evaluation of the Green's function and its derivatives are also discussed.

Computer speed and memory define a threshold of applicability in every large numerical analysis. In the present problem, computational efforts increase with increasing barrier sizes or frequencies of excitation. An optimization procedure is proposed for the analysis of simple shaped barriers in order to reduce the CPU time required for assembling the system of equations. This very simple and effective approach, which basically avoids repetitive integrations over homogeneous patches of the mesh, is explained in Sec. IV. Finally, some examples are presented and results compared to standard boundary element analyses.

I. MATHEMATICAL FORMULATION AND GREEN'S FUNCTION

Consider the problem of outdoor sound propagation and its attenuation using thin acoustic barriers sketched in Fig. 1.

The domain Ω is assumed free from any pressure or temperature variations and wind effect. All boundaries are locally reacting and the barrier, represented by Γ_b, may have different surface treatments on each side and within any side. The plane ground (Γ_g) is homogeneous and has a normalized surface admittance β. If the ground is rigid, then $\beta=0$; but if absorbing, β is a complex number with $\mathrm{Re}(\beta)>0$. Different models[11,12] were suggested for the computation of the admittance depending on certain properties of the surface. The model used in this work depends only on the frequency, flow resistivity, and thickness of the absorptive layer.[11]

Linear sound propagation for this exterior problem is governed by the Helmholtz equation (e^{-iwt} time dependence)

$$\nabla^2\phi(\mathbf{x})+k^2\phi(\mathbf{x})=h(\mathbf{x}), \tag{1}$$

mixed boundary conditions

$$q(\mathbf{x})=\frac{\partial\phi(\mathbf{x})}{\partial\mathbf{n}(\mathbf{x})}=ik\beta\phi(\mathbf{x}), \quad \mathbf{x}\in\Gamma_g, \tag{2}$$

$$q(\mathbf{x})=\frac{\partial\phi(\mathbf{x})}{\partial\mathbf{n}(\mathbf{x})}=ik\beta^b(\mathbf{x})\phi(\mathbf{x}), \quad \mathbf{x}\in\Gamma_b, \tag{3}$$

and the Sommerfeld radiation condition at infinity, where ϕ is the velocity potential, k is the wave number, $h(\mathbf{x})$ is a known source in the domain, ∇^2 is the Laplacian operator, $\mathbf{n}(\mathbf{x})$ is the unit outward normal vector at $\mathbf{x}$, and $\beta^b(\mathbf{x})$ is the admittance of the barrier surface.

Substituting $h(\mathbf{x})$ by the Dirac delta function and solving Eqs. (1) and (2) with $\beta=0$, the following Green's function is obtained:

$$G_0(\boldsymbol{\xi},\mathbf{x})=\frac{1}{4\pi R}e^{ikR}+\frac{1}{4\pi R'}e^{ikR'}, \tag{4}$$

where R is the distance from the source to the field point and R' is the distance from the image of the source (with respect to the plane ground) to the field point. The first and second terms in Eq. (4) correspond to the direct and reflected waves, respectively.

If the plane ground is absorptive, the sound field due to a spherical wave cannot be described by Eq. (4) alone and a correction term corresponding to the radiated wave is added to the Green's function,

$$G(\boldsymbol{\xi},\mathbf{x})=G_0(\boldsymbol{\xi},\mathbf{x})+G_\beta(\boldsymbol{\xi},\mathbf{x}) \tag{5}$$

This special Green's function must satisfy Eqs. (1) and (2) as well as the Sommerfeld radiation condition. A proper integral representation and efficient evaluation of the correction term has been the subject of study of many authors.[6–10] Kawai *et al.*[10] give the following representation:

$$G_\beta(\boldsymbol{\xi},\mathbf{x})=-\frac{ik\beta}{4\pi}\times\int_L\frac{e^{ik(\cos\theta(z(\mathbf{x})+z(\boldsymbol{\xi})))}H_0^{(1)}(kr\sin\theta)\sin\theta}{\beta+\cos\theta}\,d\theta, \tag{6}$$

where θ is a complex variable, L is a path in the θ plane defined by $(-\pi/2+i\infty\rightarrow-\pi/2\rightarrow\pi/2\rightarrow\pi/2-i\infty)$, and r is the horizontal distance between source and field points, as indicated in Fig. 1. By using a modified steepest descent method, Kawai *et al.*[10] efficiently evaluated this integral for large values of kR'; their asymptotic results are used in this work. A numerical Gaussian quadrature suggested in Ref. 13 is used for smaller values of kR', but with a cubic coordinate transformation to enhance its accuracy.

For application of the dual-boundary-element method, normal derivatives of the Green's function of first and second order are required as follows:

$$\frac{\partial G(\boldsymbol{\xi},\mathbf{x})}{\partial\mathbf{n}(\mathbf{x})}=\frac{\partial G_0(\boldsymbol{\xi},\mathbf{x})}{\partial\mathbf{n}(\mathbf{x})}+\frac{\partial G_\beta(\boldsymbol{\xi},\mathbf{x})}{\partial\mathbf{n}(\mathbf{x})}, \tag{7}$$

$$\frac{\partial G(\boldsymbol{\xi},\mathbf{x})}{\partial\mathbf{n}(\boldsymbol{\xi})}=\frac{\partial G_0(\boldsymbol{\xi},\mathbf{x})}{\partial\mathbf{n}(\boldsymbol{\xi})}+\frac{\partial G_\beta(\boldsymbol{\xi},\mathbf{x})}{\partial\mathbf{n}(\boldsymbol{\xi})}, \tag{8}$$

$$\frac{\partial^2 G(\boldsymbol{\xi},\mathbf{x})}{\partial \mathbf{n}(\mathbf{x})\partial \mathbf{n}(\boldsymbol{\xi})}=\frac{\partial^2 G_0(\boldsymbol{\xi},\mathbf{x})}{\partial \mathbf{n}(\mathbf{x})\partial \mathbf{n}(\boldsymbol{\xi})}+\frac{\partial^2 G_\beta(\boldsymbol{\xi},\mathbf{x})}{\partial \mathbf{n}(\mathbf{x})\partial \mathbf{n}(\boldsymbol{\xi})}, \tag{9}$$

where $\mathbf{n}(\boldsymbol{\xi})$ is the unit outward normal vector at $\boldsymbol{\xi}$ ($\boldsymbol{\xi}$ at the boundary). Derivatives of $G_0(\boldsymbol{\xi},\mathbf{x})$ can easily be found[3] and computed while derivatives of $G_\beta(\boldsymbol{\xi},\mathbf{x})$ can be decomposed in the form

$$\frac{\partial G_\beta(\boldsymbol{\xi},\mathbf{x})}{\partial \mathbf{n}(\mathbf{x})}=\frac{\partial G_\beta(\boldsymbol{\xi},\mathbf{x})}{\partial z(\mathbf{x})}\frac{\partial z(\mathbf{x})}{\partial \mathbf{n}(\mathbf{x})}+\frac{\partial G_\beta(\boldsymbol{\xi},\mathbf{x})}{\partial r(\boldsymbol{\xi},\mathbf{x})}\frac{\partial r(\boldsymbol{\xi},\mathbf{x})}{\partial \mathbf{n}(\mathbf{x})}, \tag{10}$$

$$\frac{\partial G_\beta(\boldsymbol{\xi},\mathbf{x})}{\partial \mathbf{n}(\boldsymbol{\xi})}=\frac{\partial G_\beta(\boldsymbol{\xi},\mathbf{x})}{\partial z(\boldsymbol{\xi})}\frac{\partial z(\boldsymbol{\xi})}{\partial \mathbf{n}(\boldsymbol{\xi})}+\frac{\partial G_\beta(\boldsymbol{\xi},\mathbf{x})}{\partial r(\boldsymbol{\xi},\mathbf{x})}\frac{\partial r(\boldsymbol{\xi},\mathbf{x})}{\partial \mathbf{n}(\boldsymbol{\xi})}, \tag{11}$$

$$\begin{aligned}\frac{\partial^2 G_\beta(\boldsymbol{\xi},\mathbf{x})}{\partial \mathbf{n}(\mathbf{x})\partial \mathbf{n}(\boldsymbol{\xi})}=&\left(\frac{\partial^2 G_\beta(\boldsymbol{\xi},\mathbf{x})}{\partial r(\boldsymbol{\xi},\mathbf{x})^2}-\frac{1}{r(\boldsymbol{\xi},\mathbf{x})}\frac{\partial G_\beta(\boldsymbol{\xi},\mathbf{x})}{\partial r(\boldsymbol{\xi},\mathbf{x})}\right)\frac{\partial r(\boldsymbol{\xi},\mathbf{x})}{\partial \mathbf{n}(\mathbf{x})}\\&\times\frac{\partial r(\boldsymbol{\xi},\mathbf{x})}{\partial \mathbf{n}(\boldsymbol{\xi})}+\frac{\partial^2 G_\beta(\boldsymbol{\xi},\mathbf{x})}{\partial r(\boldsymbol{\xi},\mathbf{x})\partial z(\mathbf{x})}\frac{\partial r(\boldsymbol{\xi},\mathbf{x})}{\partial \mathbf{n}(\boldsymbol{\xi})}n_3\\&+\frac{\partial^2 G_\beta(\boldsymbol{\xi},\mathbf{x})}{\partial r(\boldsymbol{\xi},\mathbf{x})\partial z(\boldsymbol{\xi})}\frac{\partial r(\boldsymbol{\xi},\mathbf{x})}{\partial \mathbf{n}(\mathbf{x})}m_3\\&+\frac{\partial^2 G_\beta(\boldsymbol{\xi},\mathbf{x})}{\partial z(\mathbf{x})\partial z(\boldsymbol{\xi})}n_3 m_3,\end{aligned} \tag{12}$$

where n_3 and m_3 are the vertical components of the unit normal vectors $\mathbf{n}(\mathbf{x})$ and $\mathbf{n}(\boldsymbol{\xi})$, respectively, and $r(\boldsymbol{\xi},\mathbf{x})=r$. The term $\partial G_\beta(\boldsymbol{\xi},\mathbf{x})/\partial r(\boldsymbol{\xi},\mathbf{x})$, directly differentiated from Eq. (6), is represented by

$$\begin{aligned}\frac{\partial G_\beta(\boldsymbol{\xi},\mathbf{x})}{\partial r(\boldsymbol{\xi},\mathbf{x})}=&-\frac{ik^2\beta}{4\pi}\\&\times\int_L\frac{e^{ik(\cos\theta(z(\mathbf{x})+z(\boldsymbol{\xi})))}H_1^{(1)}(kr\ \sin\theta)\sin^2\theta}{\beta+\cos\theta}\,d\theta.\end{aligned} \tag{13}$$

The procedure to evaluate this integral, the same applied to the integral in Eq. (6), is briefly explained in Sec. III. All other derivatives of $G_\beta(\boldsymbol{\xi},\mathbf{x})$ in Eqs. (10)–(12) can be expressed as functions of $G_\beta(\boldsymbol{\xi},\mathbf{x})$, $\partial G_\beta(\boldsymbol{\xi},\mathbf{x})/\partial r(\boldsymbol{\xi},\mathbf{x})$ and exponential terms. Their expressions are

$$\frac{\partial G_\beta(\boldsymbol{\xi},\mathbf{x})}{\partial z(\mathbf{x})}=\frac{\partial G_\beta(\boldsymbol{\xi},\mathbf{x})}{\partial z(\boldsymbol{\xi})}=-ik\beta\left(G_\beta(\boldsymbol{\xi},\mathbf{x})+\frac{e^{ikR'}}{2\pi R'}\right), \tag{14}$$

$$\begin{aligned}\frac{\partial^2 G_\beta(\boldsymbol{\xi},\mathbf{x})}{\partial z(\mathbf{x})\partial z(\boldsymbol{\xi})}=&-ik\beta\left(\frac{\partial G_\beta(\boldsymbol{\xi},\mathbf{x})}{\partial z(\mathbf{x})}+\left(ik-\frac{1}{R'}\right)\right.\\&\left.\times(z(\mathbf{x})+z(\boldsymbol{\xi}))\frac{e^{ikR'}}{2\pi R'^2}\right),\end{aligned} \tag{15}$$

$$\begin{aligned}\frac{\partial^2 G_\beta(\boldsymbol{\xi},\mathbf{x})}{\partial r(\boldsymbol{\xi},\mathbf{x})\partial z(\mathbf{x})}=&\frac{\partial^2 G_\beta(\boldsymbol{\xi},\mathbf{x})}{\partial r(\boldsymbol{\xi},\mathbf{x})\partial z(\boldsymbol{\xi})}\\=&-ik\beta\left(\frac{\partial G_\beta(\boldsymbol{\xi},\mathbf{x})}{\partial r(\boldsymbol{\xi},\mathbf{x})}+\left(ik-\frac{1}{R'}\right)r\,\frac{e^{ikR'}}{2\pi R'^2}\right),\end{aligned} \tag{16}$$

$$\begin{aligned}\frac{\partial^2 G_\beta(\boldsymbol{\xi},\mathbf{x})}{\partial r(\boldsymbol{\xi},\mathbf{x})^2}=&-k^2 G_\beta(\boldsymbol{\xi},\mathbf{x})-\frac{1}{r(\boldsymbol{\xi},\mathbf{x})}\frac{\partial G_\beta(\boldsymbol{\xi},\mathbf{x})}{\partial r(\boldsymbol{\xi},\mathbf{x})}\\&-\frac{\partial^2 G_\beta(\boldsymbol{\xi},\mathbf{x})}{\partial z(\mathbf{x})\partial z(\boldsymbol{\xi})}.\end{aligned} \tag{17}$$

Once all the above derivatives are properly evaluated, the Green's function and its normal derivatives are established and the boundary element method can be efficiently used.

II. DUAL-BOUNDARY-ELEMENT METHOD

The standard integral representation formula for the boundary-value problem stated in the previous section, with a Green's function G which implicitly satisfies the boundary condition (2), is given by

$$\begin{aligned}\alpha(\boldsymbol{\xi})\phi(\boldsymbol{\xi})=&\int_{\Gamma_b}G(\boldsymbol{\xi},\mathbf{x})q(\mathbf{x})d\Gamma-\int_{\Gamma_b}\frac{\partial G(\boldsymbol{\xi},\mathbf{x})}{\partial \mathbf{n}(\mathbf{x})}\phi(\mathbf{x})d\Gamma\\&+\phi_I(\boldsymbol{\xi}),\end{aligned} \tag{18}$$

where $\phi_I(\boldsymbol{\xi})$ is the known contribution coming from monofrequency concentrated sources and $\alpha(\boldsymbol{\xi})$ is 1 or $\frac{1}{2}$ depending on whether $\boldsymbol{\xi}$ is inside the domain Ω or at a smooth part of the boundary, respectively. Discretizing the boundary Γ_b into $(2N_b+N_e)$ elements and applying the discretized form of Eq. (18) at each nodal point, a system of $(2N_b+N_e)$ equations and $(2N_b+N_e)$ unknowns is obtained (assuming that simple constant elements are used; N_b is the number of elements at each side of the barrier and N_e the number of elements at the edges). In order to obtain a satisfactory accuracy, a minimum number of elements per wavelength is necessary. In low-frequency analysis larger elements could be used, but since acoustic barriers are usually thin and may be composed of thin attachments, near singular integrations appear when integrating over elements on the other side of the structure. Therefore, the thickness of the barrier, in the low-frequency range, defines how refined the mesh should be. Also, if the structure is very thin, a near degenerate system of equations could arise.[14]

In order to avoid these difficulties, the thin barrier is modeled as a surface ($\overline{\Gamma}_b$) which is the limit when the thickness of the structure tends to zero. Assuming the normal direction $\overline{\mathbf{n}}$ to $\overline{\Gamma}_b$ is coincident with the normal to the shadowed side, the integral equation for a point in the domain is written as

$$\begin{aligned}\phi(\boldsymbol{\xi})=&\int_{\overline{\Gamma}_b}\frac{\partial G(\boldsymbol{\xi},\mathbf{x})}{\partial \overline{\mathbf{n}}(\mathbf{x})}\Delta\phi(\mathbf{x})d\Gamma+\int_{\overline{\Gamma}_b}G(\boldsymbol{\xi},\mathbf{x})\Sigma q(\mathbf{x})d\Gamma\\&+\phi_I(\boldsymbol{\xi}),\end{aligned} \tag{19}$$

where $\Delta\phi(\mathbf{x})=\phi^+(\mathbf{x})-\phi^-(\mathbf{x})$, $\Sigma q(\mathbf{x})=q^+(\mathbf{x})+q^-(\mathbf{x})$, and the superscripts $+$ and $-$ indicate the illuminated and shadowed sides of the barrier, respectively. Taking $\boldsymbol{\xi}$ to the boundary one finds

$$\frac{1}{2}\Sigma\phi(\boldsymbol{\xi})-\int_{\overline{\Gamma}_b} G(\boldsymbol{\xi},\mathbf{x})\Sigma q(\mathbf{x})d\Gamma = \int_{\overline{\Gamma}_b} \frac{\partial G(\boldsymbol{\xi},\mathbf{x})}{\partial \overline{\mathbf{n}}(\mathbf{x})}\Delta\phi(\mathbf{x})d\Gamma+\phi_I(\boldsymbol{\xi}), \tag{20}$$

where $\Sigma\phi(\boldsymbol{\xi})=\phi^+(\boldsymbol{\xi})+\phi^-(\boldsymbol{\xi})$. The boundary conditions at each side are represented by

$$q^+(\mathbf{x})=ik\beta^+(\mathbf{x})\phi^+(\mathbf{x}), \tag{21}$$

$$q^-(\mathbf{x})=ik\beta^-(\mathbf{x})\phi^-(\mathbf{x}), \tag{22}$$

but for Eq. (20) the quantity $\Sigma q(\mathbf{x})$ can also be expressed as a linear combination of $\Sigma\phi(\mathbf{x})$ and $\Delta\phi(\mathbf{x})$:

$$\Sigma q(\mathbf{x})=\frac{ik}{2}(\beta^+(\mathbf{x})+\beta^-(\mathbf{x}))\Sigma\phi(\mathbf{x})+\frac{ik}{2}(\beta^+(\mathbf{x})-\beta^-(\mathbf{x}))\Delta\phi(\mathbf{x}). \tag{23}$$

Applying Eq. (20) over N_b elements of the contour $\overline{\Gamma}_b$ produces twice as many unknowns as equations. Another N_b equations can be obtained by differentiating the boundary integral equation (19) with respect to the direction $\overline{\mathbf{n}}(\boldsymbol{\xi})$. After taking the limit when $\boldsymbol{\xi}$ tends to the boundary, assuming $\overline{\mathbf{n}}(\boldsymbol{\xi})$ as the normal direction at $\boldsymbol{\xi}$, one finds

$$\frac{1}{2}\Delta q(\boldsymbol{\xi})+\int_{\overline{\Gamma}_b}\frac{\partial G(\boldsymbol{\xi},\mathbf{x})}{\partial\overline{\mathbf{n}}(\boldsymbol{\xi})}\Sigma q(\mathbf{x})\,d\Gamma = -\oint\!\!\!\!\!\!=_{\overline{\Gamma}_b}\frac{\partial^2 G(\boldsymbol{\xi},\mathbf{x})}{\partial\overline{\mathbf{n}}(\boldsymbol{\xi})\partial\overline{\mathbf{n}}(\mathbf{x})}\Delta\phi(\mathbf{x})\,d\Gamma-\frac{\partial\phi_I(\boldsymbol{\xi})}{\partial\overline{\mathbf{n}}(\boldsymbol{\xi})}, \tag{24}$$

where $\Delta q(\boldsymbol{\xi})=q^+(\boldsymbol{\xi})-q^-(\boldsymbol{\xi})$ can also be represented, like $\Sigma q(\mathbf{x})$, as a combination of $\Sigma\phi(\boldsymbol{\xi})$ and $\Delta\phi(\boldsymbol{\xi})$, namely

$$\Delta q(\boldsymbol{\xi})=\frac{ik}{2}(\beta^+(\boldsymbol{\xi})-\beta^-(\boldsymbol{\xi}))\Sigma\phi(\boldsymbol{\xi})+\frac{ik}{2}(\beta^+(\boldsymbol{\xi})+\beta^-(\boldsymbol{\xi}))\Delta\phi(\boldsymbol{\xi}). \tag{25}$$

The sign in the second integral indicates its interpretation as a Hadamard finite part integral.[15] Equation (24) is a hypersingular integral equation which, when applied over N_b elements together with Eq. (20), produces a well-conditioned system of $2N_b$ equations.[14] After applying the boundary conditions (23) and (25) and solving the system for $\Sigma\phi(\mathbf{x})$ and $\Delta\phi(\mathbf{x})$, values of velocity potential at field points are obtained from Eq. (19). Note that, in this case, the computation at field points is carried out with integrations over N_b elements rather than $(2N_b+N_e)$ as in the standard equation (18).

The dual formulation applied to this problem has an extra advantage over the standard formulation which is a faster assembling of the system of equations. This happens not only due to the smaller number of equations (absence of edge elements), but also because the computation of the correction term and its r derivative are performed a reduced number of times. The computation of $G_\beta(\boldsymbol{\xi},\mathbf{x})$ and $\partial G_\beta(\boldsymbol{\xi},\mathbf{x})/\partial r(\boldsymbol{\xi},\mathbf{x})$ are extremely expensive compared to $G_0(\boldsymbol{\xi},\mathbf{x})$, and must be performed at every integration point. Since in the nonthickness barriers every integration point geometrically belongs to ''two'' elements (same position on different sides of the barrier), computation of these terms is performed simultaneously for both standard and hypersingular equations reducing the associated computer time for this task in approximately 50%. Also, these equations are applied over N_b rather than $(2N_b+N_e)$ elements, which reduces the computing time by another 50%. In total, it is expected that the matrix assembly will be at least four times faster than in the standard boundary element method.

For particular cases where the barrier is rigid at both sides, only one-half of the total number of equations is necessary. Equation (24) is applied alone over N_b elements and solved to obtain $\Delta\phi(\mathbf{x})$. Afterwards, potential values at field points can be computed from Eq. (19).

III. EVALUATION OF $G_\beta(\boldsymbol{\xi},\mathbf{x})$ AND $\partial G_\beta(\boldsymbol{\xi},\mathbf{x})/\partial r(\boldsymbol{\xi},\mathbf{x})$

During the assembling process, the Green's function and its derivatives are integrated over the elements. Gaussian quadrature is used with a certain number of integration points. This number is not fixed and should always be kept to a minimum necessary due to the expensive computation of the correction term and its derivatives. It basically depends on the distance from the source point to the element under integration, the size of the element, and, of course, the required accuracy. A range from 1–36 integration points is used in this work.

If the admittance of the plane ground is $\beta\neq 0$, then $G_\beta(\boldsymbol{\xi},\mathbf{x})$ and $\partial G_\beta(\boldsymbol{\xi},\mathbf{x})/\partial r(\boldsymbol{\xi},\mathbf{x})$ must be calculated at each integration point and for this an efficient and sufficiently accurate evaluation of integrals in Eqs. (6) and (13) is required. Using a modified steepest descent method both integrals can be expressed in the form

$$\int_0^\infty F(\mu)e^{-kR'\mu^2}\,d\mu+\text{eventual pole contribution}, \tag{26}$$

where $F(\mu)$ is a function which has poles at positions defined by β and θ_0.[10] A nondimensional limit of 23 was chosen for kR', such that for values of kR' above this limit asymptotic expressions are used, otherwise numerical quadrature is employed. This choice guarantees absolute errors from the asymptotic expressions of less than 10^{-5}. Kawai *et al.*[10] give asymptotic expressions for $G_\beta(\boldsymbol{\xi},\mathbf{x})$ and similar expressions for the r-derivative are found to be:

for $\theta_0=0$ ($\gamma=\cos\theta_0=1$):

$$\frac{\partial G_\beta(\boldsymbol{\xi},\mathbf{x})}{\partial r(\boldsymbol{\xi},\mathbf{x})}=0, \tag{27}$$

for θ_0 close to 0 ($\gamma\geqslant 0.9$):

$$\frac{\partial G_\beta(\boldsymbol{\xi},\mathbf{x})}{\partial r(\boldsymbol{\xi},\mathbf{x})}=\frac{ik\beta}{2\pi R'}e^{i(kR'-\pi)}\frac{\sqrt{1-\gamma^2}}{\gamma+\beta}\times(1-ab_1(1-F^*(kR'a))), \tag{28}$$

for θ_0 not close to 0 ($\gamma<0.9$):

$$\frac{\partial G_\beta(\boldsymbol{\xi},\mathbf{x})}{\partial r(\boldsymbol{\xi},\mathbf{x})} = \frac{ik^2\beta}{4}\sqrt{\frac{2}{\pi kR'}}\, e^{i(kR'-\pi/4-kr\sqrt{1-\gamma^2})} \times \frac{(1-\gamma^2)}{\gamma+\beta} H_1^{(1)}(kr\sqrt{1-\gamma^2}) \times (1-ab_2(1-F^*(kR'a))), \tag{29}$$

where

$$a = 1+\beta\gamma-\sqrt{1-\beta^2}\sqrt{1-\gamma^2}, \tag{30}$$

$$b_1 = \frac{8+3\gamma^2+6\gamma\beta-5\beta^2}{4(\gamma+\beta)^2}, \tag{31}$$

$$b_2 = b_1+\frac{3\gamma^2}{4(1-\gamma^2)}, \tag{32}$$

$$F^*(z) = \sqrt{\pi z}e^{-i(z+\pi/4)}\ \mathrm{erfc}(\sqrt{-iz}). \tag{33}$$

These asymptotic expressions already take into account the eventual presence of pole contributions.

For the numerical evaluation ($kR'<23$) of the integral in expression (26), due to the fast decay of the exponential function, it is sufficient to truncate the upper limit of integration at $\mu=5$ or less depending on the value kR'. Over this range, a variable number of integration points is placed depending on the angle θ_0. If an existing pole is close to the path of integration ($|\beta|$ and γ very small), a larger number of points is used as well as a third-degree coordinate transformation[16] in order to concentrate the Gauss points in a position of the path which is closer to the pole.

Contributions from poles must be added according to the values of β and a. If $\mathrm{Im}\{\beta\}<0$ and $\mathrm{Re}\{a\}<0$, the following value is added:

$$\frac{k^2\beta}{2} H_1^{(1)}(kr\sqrt{1-\beta^2})\sqrt{1-\beta^2}e^{-ik(z(\mathbf{x})+z(\boldsymbol{\xi}))\beta}. \tag{34}$$

Only one-half of this value is added if the pole is over the path;[17] in this case, the integration in expression (26) is performed in the Cauchy principal value sense.

IV. MATRIX ASSEMBLY OPTIMIZATION

An optimization technique was developed to speed up the system assembly. It takes into account the homogeneity of patches in the global mesh and avoids repeating integrations over similar elements within the patch. The technique is limited to simple geometries, though very efficient if all the mesh can be represented by just one patch which is the case of standard barrier shapes.

Consider a rectangular patch of N by M elements. Usually, $(NM)^2$ element integrations are required, where each element integration (I) can be decomposed into a sum of direct (D) and image (R) integrations,

$$I_{ij} = D_{ij}+R_{ij}, \tag{35}$$

where i is the element which contains the collocation point ξ, j is the element being integrated, D corresponds to the direct wave, R corresponds to the reflected/radiated waves, and I can be any element integral in both standard and hypersingular equations.

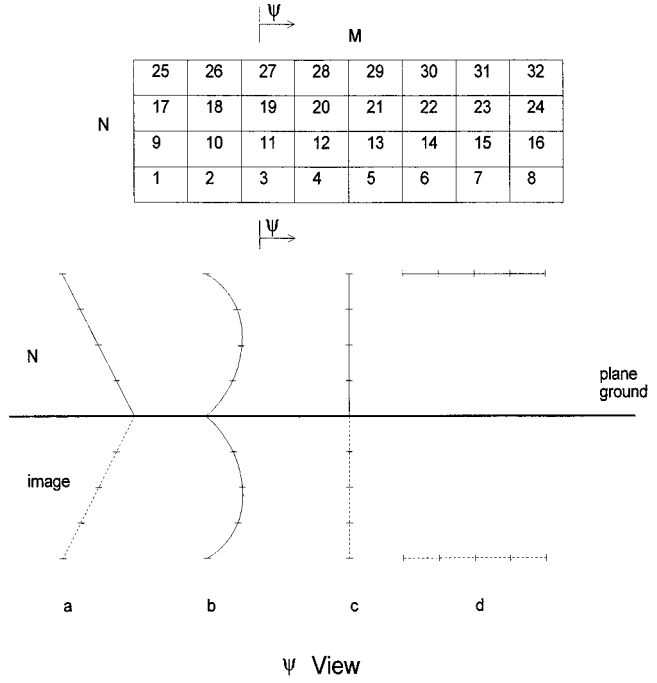

FIG. 2. Homogeneous patch of N by M elements and some possible positions above the plane ground.

Figure 2 shows a homogeneous patch and an appropriate element numbering sequence. In the proposed approach, the following cases are considered for the direct and image integrations.

A. Direct integration

1. Planar patch [Fig. 2(a)]

Once all D_{i1} integrations are carried out, it is possible to associate any other D_{ij} integration within this patch to one similar from D_{i1}, for example, $D_{8\ 9}=D_{16\ 1}$, $D_{25\ 10}=D_{18\ 1}$, etc. Therefore, the number of D integrations is reduced from $(NM)^2$ to NM.

2. Nonplanar patch [Fig. 2(b)]

Once all D_{i1} integrations are carried out, it is possible to associate any integration over the elements on the same line of 1 (2 to 8) to one similar from D_{i1}, for example, $D_{9\ 2}=D_{10\ 1}$, $D_{16\ 6}=D_{11\ 1}$, etc. The other elements in the same column of 1 are integrated like element 1 (D_{i9}, D_{i17}, and D_{i25}) and the same procedure is applied to the elements on the respective lines. The reduction in this case is from $(NM)^2$ to N^2M. Usually, N is much smaller than M since in an acoustic barrier N is associated with the height while M is associated with the length.

B. Image integration

1. Planar patch parallel to the ground [Fig. 2(d)]

In this case, R integrations are performed exactly like in case A 1. The image of element 1 is integrated with the collocation point in all the other elements (R_{i1}) and other R_{ij} integrations within this patch can be associated to one from R_{i1}. The reduction is from $(NM)^2$ to NM integrations.

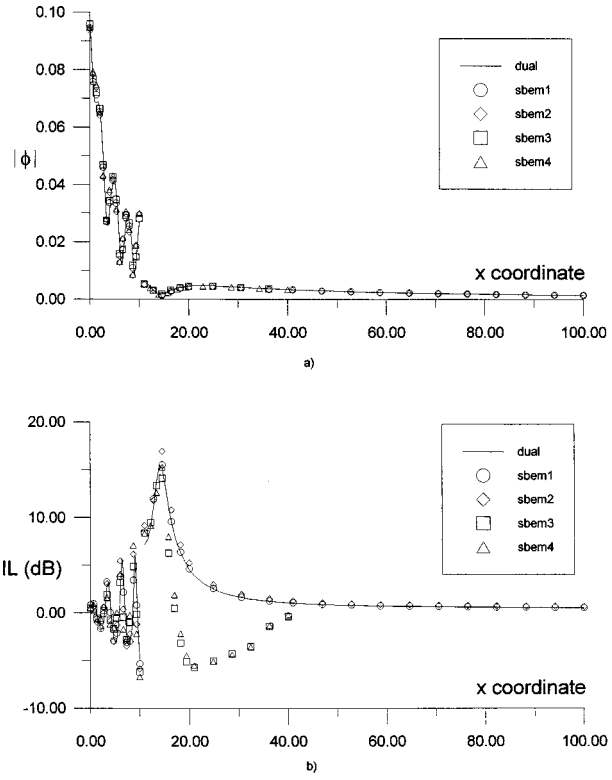

FIG. 3. Velocity potential and insertion loss at field points (0.0 to 100.0, 0.0, 1.5) for a frequency of 63 Hz and an all rigid barrier (3×10).

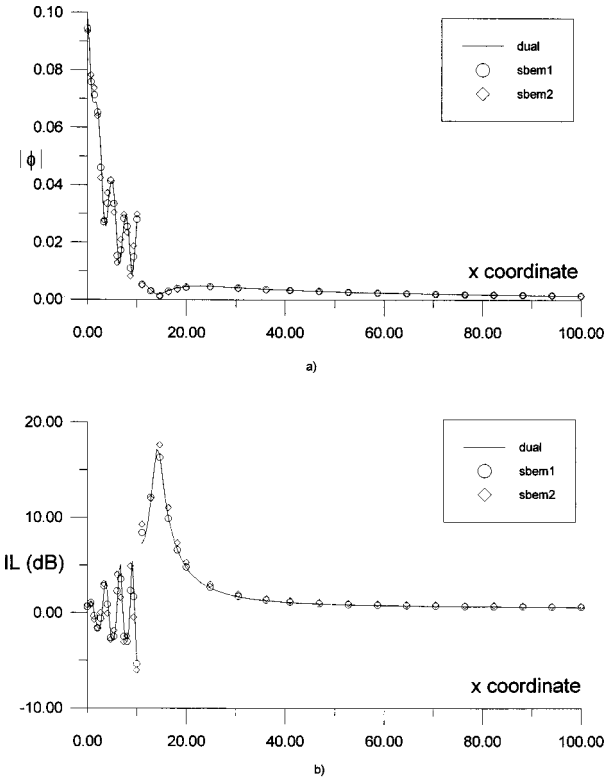

FIG. 4. Velocity potential and insertion loss at field points (0.0 to 100.0, 0.0, 1.5) for a frequency of 63 Hz and an absorptive/rigid barrier (3×10).

2. Inclinated or curved patch with one side parallel to the ground [Fig. 2(a) and (b)]

The procedure in this case is exactly like in case A 2. The only particularity is that the elements on the same line of 1 have to be on the side of the patch which is parallel to the ground. The reduction is from $(NM)^2$ to N^2M integrations.

3. Vertical patch with one side parallel to the ground [Fig. 2(c)]

In this last case, the line of element 1 is the closest and also parallel to the ground. Initially, the image of the element 1 is integrated (R_{i1}). The integration over the image of elements in the same line of 1 are associated like in case B 2. Element 9, which is just above element 1, can also be associated to previous integrations R_{i1} except when the collocation point is at the highest line of the patch. Therefore, an extra M integrations of the image of element 9 are necessary; after that, the other elements on the line of 9 are associated like in case B 2. The same procedure is carried out for the element just above 9. It can be associated to R_{i9} but also needs an extra M element integrations when the collocation point is at the highest line. In total, the reduction is from $(NM)^2$ to $(2N-1)M$ integrations in this case.

V. NUMERICAL TESTS

Numerical results obtained from the analysis of a vertical barrier with different boundary element approaches are compared. The following symbols are used:

dual—proposed dual formulation [Eqs. (20) and (24)].

dual opt—*dual* with the optimization procedures of Sec. IV.

*sbem*1—standard boundary element formulation [Eq. (18)] with barrier thickness of 0.30 m.

*sbem*2—like *sbem*1 but barrier thickness of 0.60 m.

sbem2 opt—*sbem*2 with the optimization procedures of Sec. IV.

*sbem*3—standard boundary element formulation with ground discretization and barrier thickness of 0.30 m.

*sbem*4—like *sbem*3 but barrier thickness of 0.60 m.

Consider a plane vertical barrier with height $h=3.0$ m and length $l=10.0$ m located over a plane ground ($z=0$) which has a normalized admittance characterized by a flow resistivity $\sigma=300\,000$ Ns m^{-4} (grassland) and the frequency of the sound source. The barrier is parallel to the plane yz and its geometrical center is at the coordinate $x=10.5$ m. A unit monofrequency point source is located at the position (0.0 m, 0.0 m, 0.75 m). In the first set of results, values of the velocity potential modulus and insertion loss (IL) at field points located at (0.0→100.0 m, 0.0 m, 1.5 m) are plotted. Results for source frequencies of 63 and 100 Hz are shown in Figs. 3–6. Two types of barrier surface conditions are considered: (1) both sides are rigid; (2) absorptive illuminated side and rigid shadowed side. In case 2 the surface treatment is characterized by a material of $\sigma=20000$ Ns m^{-4} with a depth of 0.1 m. The larger side of any element in the discretization was never greater than one-sixth of the wavelength in all analyses.

The limitation of using *sbem*3 and *sbem*4 is evident in Fig. 3 where more than 1000 elements were necessary to model a restricted range of the ground. Despite the good

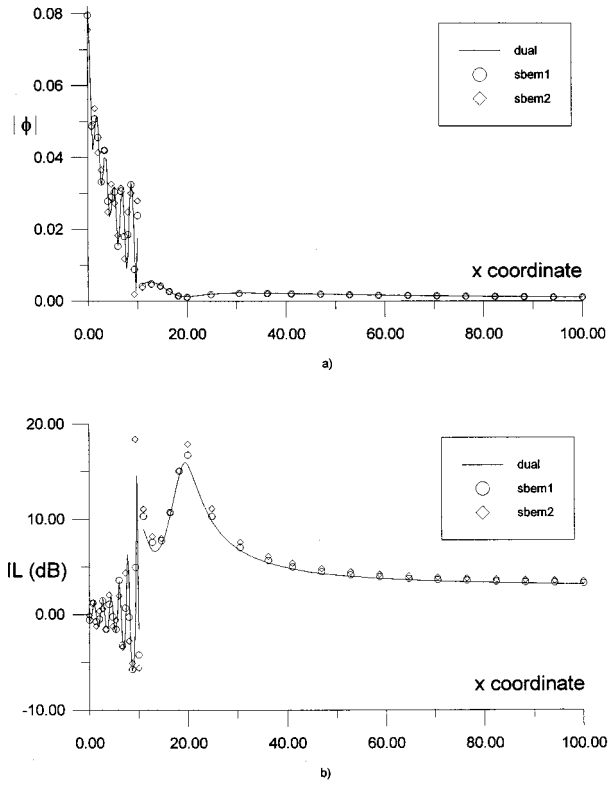

FIG. 5. Velocity potential and insertion loss at field points (0.0 to 100.0, 0.0, 1.5) for a frequency of 100 Hz and an all rigid barrier (3×10).

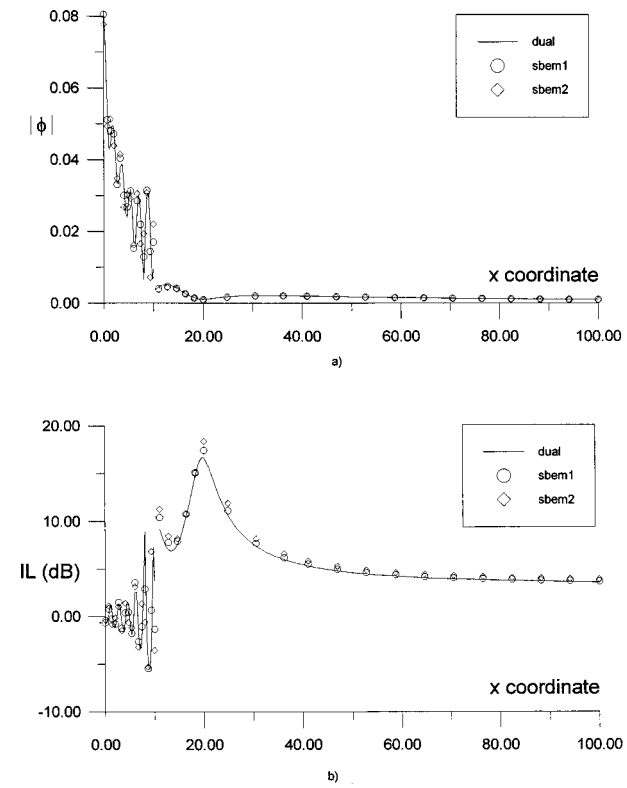

FIG. 6. Velocity potential and insertion loss at field points (0.0 to 100.0, 0.0, 1.5) for a frequency of 100 Hz and an absorptive/rigid barrier (3×10).

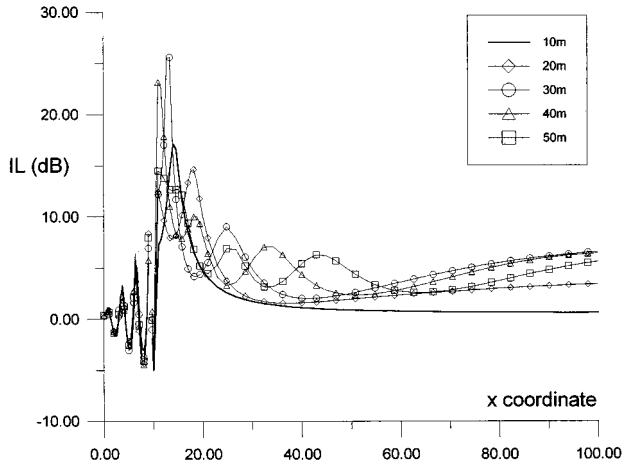

FIG. 7. Insertion loss at field points (0.0 to 100.0, 0.0, 1.5) for a frequency of 63 Hz and an absorptive/rigid barrier, for barriers of different lengths.

velocity potential results in this range [Fig. 3(a)], insertion loss values are very much influenced by the truncation of the mesh [Fig. 3(b)].

The agreement between the *dual*, *sbem*1, and *sbem*2 formulations was very good throughout. The cut in the solid curves (dual BEM results) at $x=10.5$ m (the barrier axis) accounts for the fact that the velocity potential is different at each side of the barrier; this can also be observed for the standard BEM results. Similar meshes were used in all the tests apart from the presence of edge elements, but a more refined mesh would be necessary in the *sbem* approach if a more realistic thickness ($\approx$0.10 m) was to be modelled.

Figure 7 shows the influence of the barrier length on the IL results for a source of frequency of 63 Hz and the same surface treatment mentioned before in the illuminated side. The gain of a few decibels in the overall range, by increasing the length of the barrier, is evident in the figure.

A comparison between the time necessary for assembling the system, for the dual and standard formulations, in the case of a 10.0-m-long vertical barrier of the previous example, is shown in Fig. 8. A SUN station 2 was used with

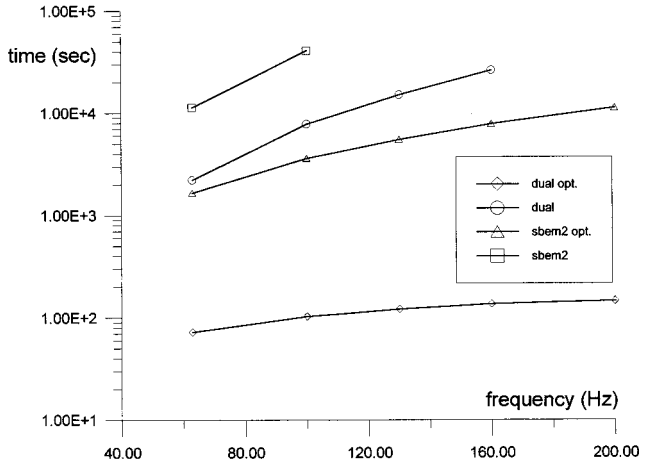

FIG. 8. Time comparisons for dual and standard boundary element formulations.

similar meshes for each frequency. The results from *dual* and *sbem*2 confirm the expectations of Sec. II, i.e., the former is approximately four times faster than the latter. Large time reductions were obtained by using the optimization procedures of Sec. IV, especially for the *dual opt* case where less than 3 min were necessary compared to nearly 3 h for *sbem*2 *opt* for a frequency of 200 Hz. Despite the speed-up of the assembly with *dual opt*, when higher frequencies are to be analyzed, memory and system solution time still offer problems to be tackled in the near future.

VI. CONCLUSIONS

This paper has presented a three-dimensional dual boundary element formulation for studying sound propagation around thin acoustic barriers over a homogeneous impedance ground. The formulation applies two integral equations, the standard Helmholtz integral representation and its hypersingular counterpart, over the barrier axis. Because the Green's function adopted directly incorporates the boundary condition at the absorbing ground, only the barrier axis needs to be discretized, leading to substantial savings in computer time and memory.

Several tests were performed to assess the theoretical and numerical developments. Comparison of results with those for barriers of decreasing thickness, obtained using the standard formulation, displayed convergence to the nonthickness cases.

For the same frequency and discretization, it was shown that the time required to assemble the system of equations with the dual formulation is four times faster than the standard one. An optimization algorithm was also developed which avoids repetitive integrations over similar patches in the global mesh, i.e., situations where the relative position of the source point with respect to the element to be integrated have already been calculated. A speed-up of two orders of magnitude was achieved for higher frequencies, making it feasible to proceed the analysis to reasonably high frequencies using a simple workstation.

ACKNOWLEDGMENT

The first author would like to acknowledge the financial support provided by CAPES, Ministry of Education, Brazil.

[1] P. Filippi and G. Dumery, ''Etude théorique et numérique de la diffraction par un écran mince,'' Acustica **21**, 343–359 (1969).
[2] T. Terai, ''On calculation of sound fields around three dimensional objects by integral equation methods,'' J. Sound Vib. **69**, 71–100 (1980).
[3] Y. Kawai and T. Terai, ''The application of integral equation methods to the calculation of sound attenuation by barriers,'' Appl. Acoust. **31**, 101–117 (1990).
[4] D. C. Hothersall, S. N. Chandler-Wilde, and N. M. Hajmirzae, ''The efficiency of single noise barriers,'' J. Sound Vib. **146**, 303–322 (1991).
[5] L. A. de Lacerda, L. C. Wrobel, and W. J. Mansur, ''A dual boundary element formulation for sound propagation around barriers over an infinite plane,'' J. Sound Vib. **202**, 235–247 (1997).
[6] U. Ingard, ''On the reflection of a spherical sound wave from an infinite plane,'' J. Acoust. Soc. Am. **23**, 329–335 (1951).
[7] A. R. Wenzel, ''Propagation of waves along an impedance boundary,'' J. Acoust. Soc. Am. **55**, 956–963 (1974).
[8] C. F. Chien and W. W. Soroka, ''Sound propagation along an impedance plane,'' J. Sound Vib. **43**, 9–20 (1975).
[9] S. I. Thomasson, ''Reflection of waves from a point source by an impedance boundary,'' J. Acoust. Soc. Am. **59**, 780–785 (1976).
[10] T. Kawai, T. Hidaka, and T. Nakajima, ''Sound propagation above an impedance boundary,'' J. Sound Vib. **83**, 125–138 (1982).
[11] M. E. Delany and E. N. Bazley, ''Acoustical properties of fibrous absorbent materials,'' Appl. Acoust. **3**, 105–116 (1970).
[12] K. Attenborough, ''Acoustical impedance models for outdoor ground surfaces,'' J. Sound Vib. **99**, 521–544 (1985).
[13] S. N. Chandler-Wilde and D. C. Hothersall, ''Sound propagation above an inhomogeneous impedance plane,'' J. Sound Vib. **98**, 475–491 (1985).
[14] G. Krishnasamy, F. J. Rizzo, and Y. Liu, ''Boundary integral equations for thin bodies,'' Int. J. Numer. Methods Eng. **37**, 107–121 (1994).
[15] J. Hadamard, *Lectures in Cauchy's Problem in Linear Partial Differential Equations* (Yale U.P., New Haven, 1923).
[16] J. C. F. Telles, ''A self-adaptive co-ordinate transformation for efficient numerical evaluation of general boundary element integrals,'' Int. J. Numer. Methods Eng. **24**, 959–973 (1987).
[17] S. N. Chandler-Wilde and D. C. Hothersall, ''Efficient calculation of the Green function for acoustic propagation above a homogeneous impedance plane,'' J. Sound Vib. **180**, 705–724 (1995).

Sound propagation from a point source over extended-reaction ground

Kai Ming Li, Tim Waters-Fuller, and Keith Attenborough
Engineering Mechanics Discipline, Faculty of Technology, The Open University, Milton Keynes MK7 6AA, United Kingdom

(Received 17 December 1997; accepted for publication 17 April 1998)

Through comparisons with numerical predictions, with data from laboratory experiments and with outdoor data obtained over snow, heuristic modifications of the classical analytical approximation for the field due to a point source above an impedance plane are shown to be adequate for predicting sound propagation from a point source close to layered porous media with extended reaction. The main deficiencies are for extremely low flow resistivities and at close ranges. It is shown that multiple layering offers a possible explanation for previously reported difficulties in obtaining theoretical fits to propagation data over snow [J. Acoust. Soc. Am. **77**, 67–73 (1985)]. © *1998 Acoustical Society of America.* [S0001-4966(98)00808-X]

PACS numbers: 43.20.Fn, 43.20.Fp [ANN]

INTRODUCTION

Materials used as sound absorbents often have lower flow resistivities than would permit the assumption of local reaction when predicting sound fields close to their surfaces. This is important, for example, when characterizing the acoustical properties of a material by free-field measurements. The prediction of sound propagation above relatively low-flow resistivity outdoor ground surfaces such as snow, forest floors, some cultivated soils, and porous asphalt is of interest also. It is well known that snow, forest floors, and porous asphalt may offer flow resistivities of the order of 10 kPa s m^{-2} or less.[1]

Prediction of sound propagation over such surfaces involves calculation of sound fields above surfaces of extended reaction and often above multiple layering. There are established numerical methods for such calculations involving the fast field program (FFP)[2] or transfer matrices.[3] To predict propagation from a point source over semi-infinite or hard-backed layers with extended reaction an approximation has been employed that represents a heuristic extension of the classical Weyl–van der Pol theory for electromagnetic waves.[4,5] In this paper we examine the accuracy of this potentially useful approximation and consider its extension to multiple layers with extended reaction. In Sec. II we outline the relevant theoretical developments including asymptotic approximations. In Sec. III we compare resulting theoretical predictions with experimental data obtained in laboratory experiments over artificial materials and over snow outdoors. Finally, in Sec. IV we offer some concluding remarks.

I. THEORY

A. Formulation of the problem

The problem considered is that of the propagation of sound from a point source over a plane ground of extended reaction beneath a homogeneous atmosphere (see Fig. 1). Time dependence $\exp(-i\omega t)$ is understood. The ground may be modeled as either a layered or a semi-infinite rigid porous medium. The sound field, $p(r,z)$ can be represented by a Bessel integral[6] as

$$p(r,z)=\int_0^\infty \kappa P(\kappa,z)J_0(\kappa r)\ d\kappa, \tag{1}$$

where

$$P(\kappa,z)=\frac{1}{2iK_0}\{\exp\,[iK_0|z-z_s|] + V_0\,\exp\,[iK_0(z+z_s)]\}, \tag{2}$$

$$K_0=+\sqrt{k_0^2-\kappa^2}, \tag{3}$$

z and z_s are, respectively, the receiver and source heights, r is the horizontal range, $k_0(\equiv\omega/c_0)$ is the wave number, ω is the angular frequency of the source, and c_0 and ρ_0 are the sound speed and density of air, respectively. We are interested primarily in the problem where both the source and receiver are above the ground, i.e., $z,\ z_s>0$. In Eq. (2), V_0 is the plane wave reflection coefficient of the sound wave interacting with the ground surface of extended reaction. It can be determined by

$$V_0=\frac{(K_0/\rho_0)(V_1e^{iK_1d_1}+e^{-iK_1d_1})+(K_1/\rho_1)(V_1e^{iK_1d_1}-e^{-iK_1d_1})}{(K_0/\rho_0)(V_1e^{iK_1d_1}+e^{-iK_1d_1})-(K_1/\rho_1)(V_1e^{iK_1d_1}-e^{-iK_1d_1})}, \tag{4}$$

where

$$K_1=+\sqrt{k_1^2-\kappa^2}, \tag{5}$$

and d_1, $k_1(\equiv\omega/c_1)$, ρ_1, and c_1 are the thickness, complex wave number, density, and speed of sound of the first layer if the ground is layered. The plane wave reflection coefficient

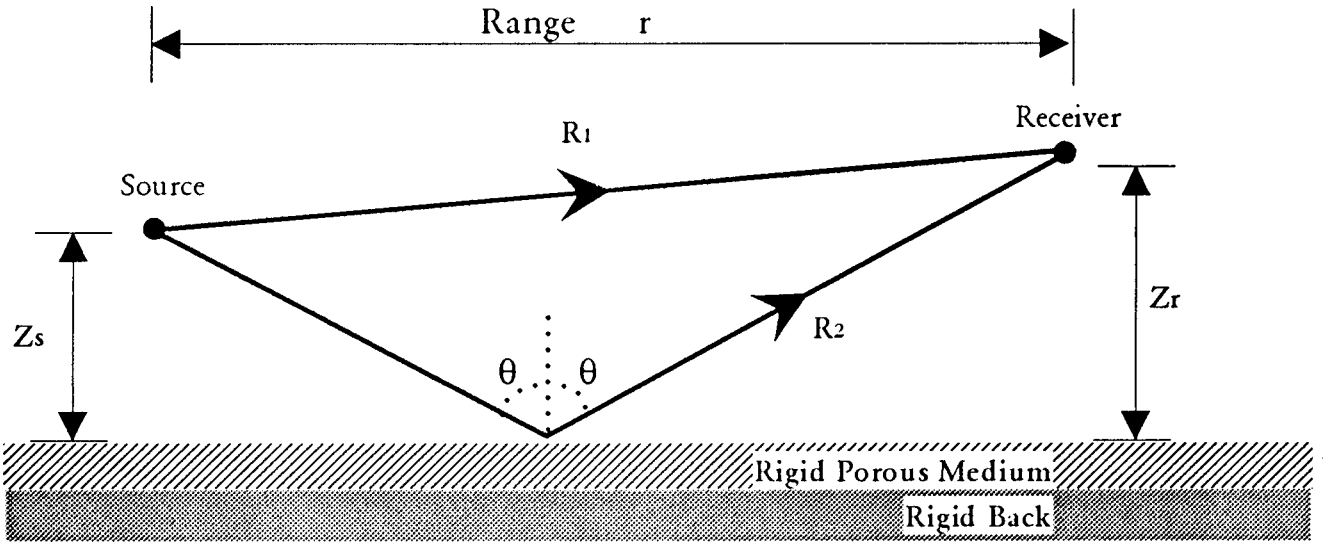

FIG. 1. The source/receiver geometry: a hard-backed layered ground is shown.

V_1 depends on the properties of subsequent layers. The reflection coefficient V_1 is 1 for a hard backing and -1 for a ''pressure-release'' backing. The layer thickness d_1 tends to infinity if the ground is semi-infinite. The factor $\exp(iK_1d_1)$ tends to zero as d_1 takes a large value, since the imaginary part of K_1 is nonzero and positive. In this case, V_0 becomes

$$V_0=\frac{(K_0/\rho_0)-(K_1/\rho_1)}{(K_0/\rho_0)+(K_1/\rho_1)}, \tag{6}$$

which is the well-known form[6] for a semi-infinite externally reacting ground. It is interesting that V_0 is ''relatively'' independent of V_1 beyond a certain depth. We can determine the minimum depth for which the ground can be treated as semi-infinite by noting that

$$\cosh(x)\approx\sinh(x) \tag{7}$$

for $x>6$ (accurate to five significant figures and 1.2×10^{-3}% of difference). Hence the condition for a semi-infinite externally reacting ground may be stated simply as

$$\mathrm{Im}\,(\sqrt{k_1^2-\kappa^2}\,d_1)>6. \tag{8}$$

By writing $k_1=k_R+i\,k_X$, it is then straightforward to show that the minimum depth d_m can be written as

$$d_m>6/k_X \tag{9}$$

for normal incidence (where $\kappa=0$), and

$$d_m>6\left[\sqrt{\frac{(k_R^2-k_X^2-1)^2}{4}+(k_Rk_X)^2}-\frac{k_R^2-k_X^2-1}{2}\right]^{-1/2} \tag{10}$$

for grazing incidence (where $\kappa=1$).

B. Reflection coefficient in a layered ground above a hard-backed layer

In a layered ground, the reflection coefficient can be derived in an analogous manner. The plane wave reflection coefficient of the jth layer is

$$V_j=\frac{(K_j/\rho_j)(V_{j+1}e^{iK_{j+1}d_{j+1}}+e^{-iK_{j+1}d_{j+1}})+(K_{j+1}/\rho_{j+1})(V_{j+1}e^{iK_{jn+1}d_{j+1}}-e^{-iK_{j+1}d_{j+1}})}{(K_j/\rho_j)(V_{j+1}e^{iK_{j+1}d_{j+1}}+e^{-iK_{j+1}d_{j+1}})-(K_{j+1}/\rho_{j+1})(V_{j+1}e^{iK_{jn+1}d_{j+1}}-e^{-iK_{j+1}d_{j+1}})}, \tag{11}$$

where the subscript j denotes the corresponding parameters at the jth layer. Suppose that the ground can be modeled by L layers with the $(L+1)$th layer as the hard backing. We then have $V_{L+1}=1$ and

$$V_L=\frac{(iK_L/\rho_L)-(K_{L+1}/\rho_{L+1})\tan(K_{L+1}d_{L+1})}{(iK_L/\rho_L)+(K_{L+1}/\rho_{L+1})\tan(K_{L+1}d_{L+1})}. \tag{12}$$

Substituting Eq. (11) into Eq. (4) with $j=1,2,\ldots,L-1$ in turn and using Eq. (12), we can determine the plane wave reflection coefficient V_0 at the surface of the layered ground. It is fairly straightforward to determine the reflection coefficient when L is small.

For a single layer, we have

$$V_0=\frac{(iK_0/\rho_0)-(K_1/\rho_1)\tan(K_1d_1)}{(iK_0/\rho_0)+(K_1/\rho_1)\tan(K_1d_1)}. \tag{13}$$

For a double layer, the plane wave reflection coefficient is

$$V_0=\frac{(iK_0/\rho_0)[1-g_1\tan(K_1d_1)\tan(K_2d_2)]-(K_1/\rho_1)[\tan(K_1d_1)+g_1\tan(K_2d_2)]}{(iK_0/\rho_0)[1-g_1\tan(K_1d_1)\tan(K_2d_2)]+(K_1/\rho_1)[\tan(K_1d_1)+g_1\tan(K_2d_2)]}. \tag{14}$$

The dimensionless parameter, g_1, in Eq. (14) is given by

$$g_1=\frac{\rho_1}{\rho_2}\frac{K_2}{K_1}. \tag{15}$$

In the limiting case where d_2 is vanishingly small (i.e., a hard-backed layer), it is obvious that Eq. (14) reduces to Eq. (13), as it should. Moreover, for large values of d_1 (i.e., a semi-infinite ground), Eq. (14) can be simplified to give Eq. (6). It is enlightening to start with a more general expression [Eq. (14)] that can be reduced to previous expressions [Eqs. (6) and (13)] in special cases.

For $L>2$ there is increasing complexity in the expression for the plane wave reflection coefficient, V_0. The number of terms in the denominator and numerator of Eq. (4) increases as 2^L. So, for example, the presence of four layers in the ground means that there are 16 terms in both numerator and denominator of the reflection coefficient. Nevertheless, numerical implementation on a digital computer for an arbitrary number of layers is straightforward.

II. ASYMPTOTIC SOLUTION AND ITS VALIDATION

Asymptotic theories are available to compute the sound field above a semi-infinite porous ground[7] or a finite hard-backed layer of porous ground.[8–11] The approximation for semi-infinite media with extended reaction is fairly convenient for computation;[9] however, analytical approximations for layered media are not as simple or straightforward. Moreover, a study by Nicolas *et al.*[5] suggests that these more elaborate theories are not satisfactory for smaller values of k_0r. Our preliminary numerical calculations support their views. Also, we find that the more elaborate theory is not satisfactory for small flow resistivities. In the light of these preliminary analyses, we choose a simpler approximation that is, in essence, a heuristic extension of the classical Weyl–Van der Pol formula.[12] Introducing an effective admittance β_e, the sound field can be approximated by

$$p(r,z)=\frac{e^{ik_0R_1}}{4\pi R_1}+\{R_p+(1-R_p)F(w)\}\frac{e^{ik_0R_2}}{4\pi R_2}, \tag{16}$$

where

$$F(w)=1+i\sqrt{\pi}w\,\exp(-w^2)\,\mathrm{erfc}(-iw), \tag{17}$$

$$w=(\tfrac{1}{2}ik_1R_2)^{1/2}(\cos\theta+\beta_e), \tag{18}$$

$$R_p=\frac{\cos\theta-\beta_e}{\cos\theta+\beta_e}. \tag{19}$$

For a semi-infinite ground, the effective admittance is

$$\beta_e=m_1\sqrt{n_1^2-\sin^2\theta}, \tag{20}$$

for a hard-backed layer, the effective admittance is

$$\beta_e=-im_1\sqrt{n_1^2-\sin^2\theta}\,\tan(k_0d_1\sqrt{n_1^2-\sin^2\theta}), \tag{21}$$

and, finally, for a double layer with a hard backing, the effective admittance can be determined according to

$$\beta_e=-im_1\sqrt{n_1^2-\sin^2\theta}\left\{\frac{\tan(k_0d_1\sqrt{n_1^2-\sin^2\theta})+\bar{g}_1\tan(k_0d_2\sqrt{n_2^2-\sin^2\theta})}{1+\bar{g}_1\tan(k_0d_1\sqrt{n_1^2-\sin^2\theta})\tan(k_0d_2\sqrt{n_2^2-\sin^2\theta})}\right\}, \tag{22}$$

where

$$\bar{g}_1=\frac{m_2\sqrt{n_2^2-\sin^2\theta}}{m_1\sqrt{n_1^2-\sin^2\theta}}, \tag{23}$$

$$n_j=k_j/k_0\quad\text{and}\quad m_j=\rho_0/\rho_j\quad\text{with}\quad j=1,2. \tag{24}$$

Here, θ is the angle of incidence and $\bar{g}_1$ is a dimensionless ratio characterizing the change of media properties from the first layer to the second, cf. Eq. (15). It is straightforward to generalize β_e for an arbitrary number of layers, but the details will not be given here.

To validate the asymptotic expressions, a numerical method based on the fast field formulation (FFP)[13] has been developed. For numerical convenience, and for comparison with predictions reported previously,[5] we employ a one-parameter model[14] to determine the complex propagation constant, k_j, although it is known that this model overpredicts the attenuation constant [Ref. 5, p. 104]. The real and imaginary parts of k_j are given by

$$\begin{aligned}k_R/k_0&=1+10.8(\sigma/\sigma f)^{0.70},\\ k_X/k_0&=10.3(\sigma/f)^{0.59},\end{aligned} \tag{25}$$

where σ is the effective flow resistivity of the porous ground in cgs units (1 cgs unit=1 kPa s m^{-2}), and f is the frequency. In addition, the normalized impedance of the porous ground is determined by

$$\begin{aligned}Z_R&=1+9.08(\sigma/f)^{0.75},\\ Z_X&=11.9(\sigma/f)^{0.73},\end{aligned} \tag{26}$$

where Z_R and Z_X are the corresponding real and imaginary parts and $1/Z_j=m_jn_j$.

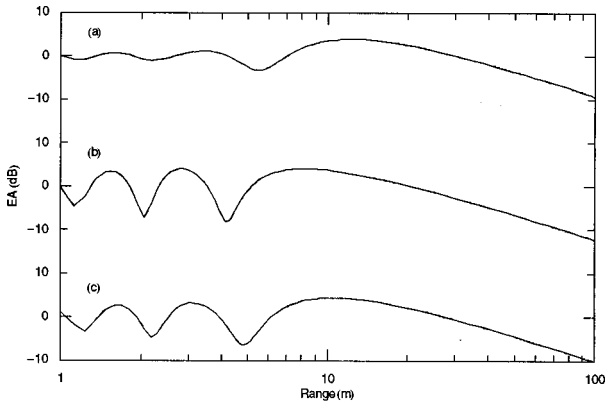

FIG. 2. The prediction of excess attenuation (EA) versus distance with source and receiver heights of 1.0 m and frequency of 1 kHz. Asymptotic and FFP predictions coincide. (a) Semi-infinite medium with $\sigma=12$ kPa m s^{-2}. (b) A hard-backed layer with $d=0.015$ m and $\sigma=12$ kPa m s^{-2}. (c) Two layers with $\sigma_1=12$ kPa m s^{-2} and $\sigma_2=20$ kPa m s^{-2} and both layers have a thickness of 0.015 m.

Figure 2 shows a comparison of the predictions according to the fast field program with those due to the heuristic approximation. The excess attenuation (EA) is calculated by comparing the total sound fields with their corresponding free-field predictions. The source and receiver are 1.0 m above the porous ground and the effective flow resistivities are, respectively, 12.0 and 20.0 kPa m s^{-2}, and layer thickness is 0.015 m where appropriate. It is useful that predictions of the heuristic approximation agree remarkably well (to within 0.5 dB) with those of the fast field program even for multiple layers. We have found that the agreement is less satisfactory when both the source and receiver are close to ground, for small values of flow resistivity and at shorter ranges. This is illustrated in Fig. 3 by the relatively poor agreement between predictions when the source and receiver heights are 0.01 m, the corresponding effective flow resistivities are 1.0 and 10.0 kPa m s^{-2}, and the layer thickness is the same as in the previous case.

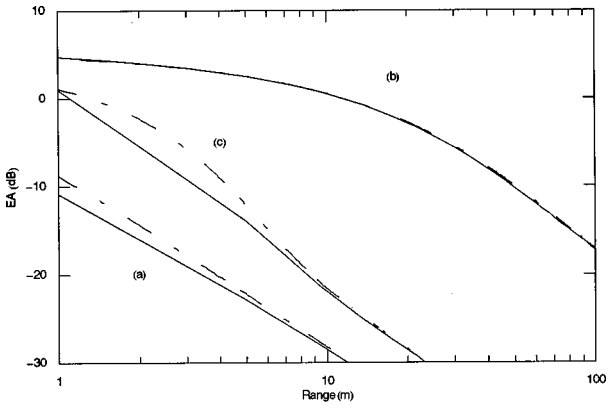

FIG. 3. Same as Fig. 2 except that the source and receiver are situated at 0.01 m above ground. Asymptotic and FFP predictions are represented by solid and broken lines respectively. (a) Semi-infinite medium with $\sigma=1$ kPa m s^{-2}. (b) A hard-backed layer with $d=0.015$ m and $\sigma=1$ kPa m s^{-2}. (c) Two layers with σ_1 and σ_2 of 1 and 10 kPa m s^{-2}, respectively. Both layers have a thickness of 0.015 m.

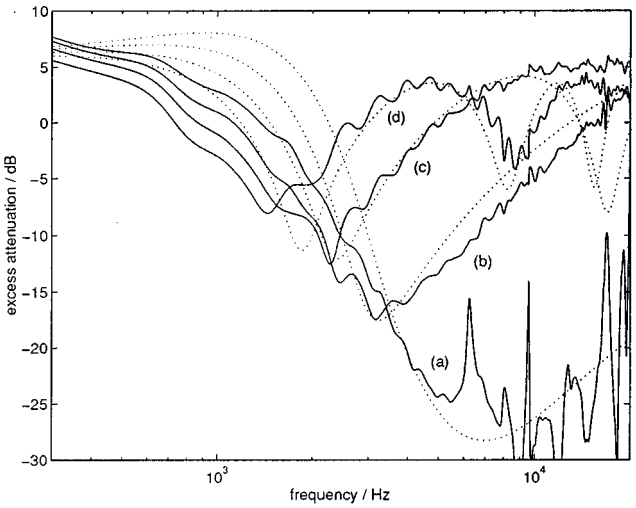

FIG. 4. Measurements of excess attenuation spectra (solid lines) at a horizontal range of 1 m obtained over a single 0.8-cm-thick layer of fiberglass on an acoustically hard backing with source and receiver heights at (a) grazing incidence, (b) 5 cm, (c) 10 cm, and (d) 15 cm. Also shown are predictions (dotted lines) obtained with Eqs. (16)–(19), (21), (25), and (26), using $\sigma=23$ kPa s m^{-2}.

III. COMPARISONS WITH EXPERIMENTAL DATA

A. Laboratory data

A Tannoy driver fitted with a tube 15 cm long and 3 cm internal diameter has been used as a point source and suspended in a fixed position in an anechoic chamber of wedge-tip to wedge-tip internal dimensions $3\times3\times3$ m^3. A Bruel & Kjaer type 4311 1.3-cm diam ($\frac{1}{2}$ in.) condenser microphone fitted with a preamplifier and suspended 1 m away, at the same height (0.145 m) as the center of the speaker tube, was used as the receiver for all of the experiments. A PC-based maximum length sequence system analyzer (MLSSA)[15] was used both as the signal generator for the Tannoy and as the analyzer for subsequent signal processing. The MLSSA system controls the source output to be in the form of a pseudo-random sequence of pulses. The microphone signal is analyzed with respect to the known output sequence, thus eliminating background noise effects.

Both source and receiver were suspended by light flexible strings. A reference measurement, carried out with the floor removed, was used as the direct field in subsequent processing. A varnished hardwood board measuring $1.2\times1.2\times0.02$ m^3 (thick) was used as an acoustically hard boundary to support various porous layers. Surfaces of extended reaction were formed from 0.8 and 1.4-cm-thick layers of fiberglass. A nonhard substrate was provided by a layer of felt which was 1.2 cm thick. The spectrum level at the microphone was measured with and without the porous surfaces and without altering the source–receiver geometry. After processing and FFT (fast Fourier transformation), each spectrum level was divided by the direct field measured earlier. All the steps were carried out with the MLSSA software, the final output being the desired excess attenuation spectrum.

Figures 4–6 show data for the sound pressure level relative to free field (henceforth called either relative SPL or excess attenuation) obtained with single layers of the porous

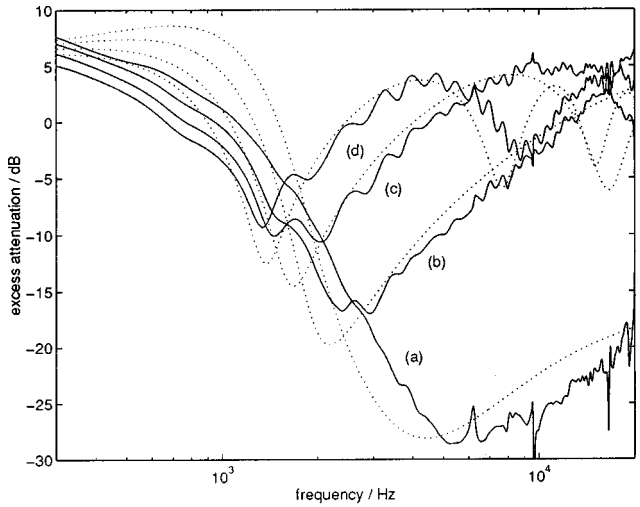

FIG. 5. Same as Fig. 4 except that the thickness of fiberglass is 1.4 cm.

materials placed on the varnished wooden board. The data are plotted above 300 Hz only since the radiated sound power from the point source used is too small for accurate measurement at lower frequencies. Also shown are predictions obtained with Eqs. (16)–(19), (21), (25), and (26) and fixed values of the single parameter (σ): 23 kPa s m^{-2} for the fiberglass and 160 kPa s m^{-2} for the felt. Figures 4 and 5 show the measured and predicted relative SPL spectra above a single layer of fiberglass of thicknesses 0.8 and 1.4 cm, respectively. Figure 6 shows the measured and predicted relative SPL spectra above a single layer of felt. Predictions at lower frequencies above the fiberglass layers are poor, although it is clear that somewhat better agreement is obtained over the felt than over the fiberglass. Nevertheless the agreement was considered adequate to use these effective flow resistivity values for predicting relative SPL spectra over composite layers. It should be noted that the effective flow resistivity of the felt layer is sufficiently high for it to be regarded as locally reacting.

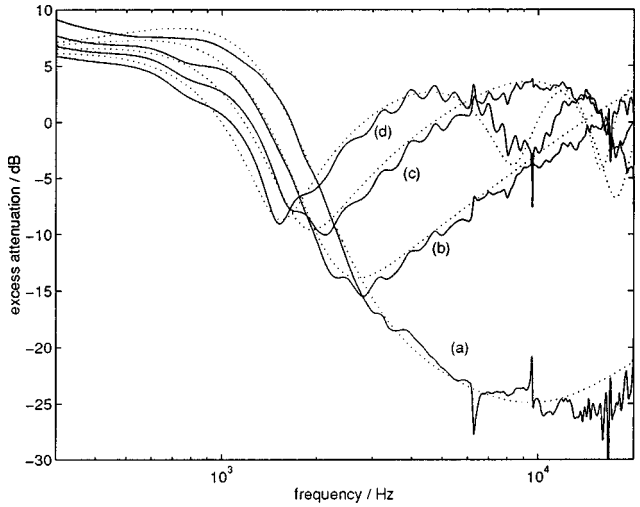

FIG. 6. Measurements of excess attenuation spectra (solid lines) at a horizontal range of 1 m obtained over a single 1.2-cm-thick layer of felt on an acoustically hard backing with source and receiver heights at (a) grazing incidence, (b) 5 cm, (c) 10 cm, and (d) 15 cm. Also shown are predictions obtained with Eqs. (16)–(19), (21), (25), and (26), using $\sigma=160$ kPa s m^{-2}.

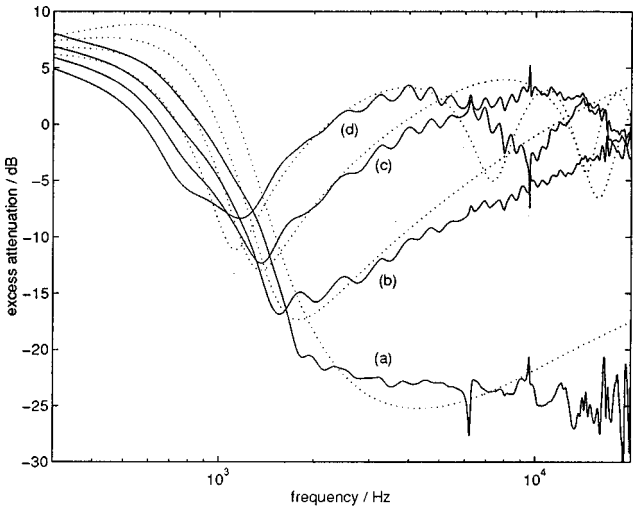

FIG. 7. Measurements of excess attenuation spectra (solid lines) at a horizontal range of 1 m obtained over a double-layer structure of 0.8-cm-thick fiberglass and 1.2-cm-thick felt on an acoustically hard backing with source and receiver heights at (a) grazing incidence, (b) 5 cm, (c) 10 cm, and (d) 15 cm. Also shown are predictions obtained with Eqs. (16)–(19) and (22)–(26), using $\sigma_1=23$ kPa s m^{-2} and $\sigma_2=160$ kPa s m^{-2}.

Next, we consider measurements of the sound field above composite layers of porous materials formed by placing a layer of fiberglass on top of the felt which, in turn, is secured on the varnished wooden board with double-sided tape. Figures 7 and 8 show, respectively, the measured relative SPL spectra above composite layers with 0.8- and 1.4-cm-thick layers of fiberglass on top of 1.2-cm-thick layer of felt. Theoretical predictions are shown also with the effective admittance determined according to Eq. (22). Again, the same flow resistivities are used (23 kPa s m^{-2} for the fiberglass and 160 kPa s m^{-2} for the felt) in the theoretical predictions.

It should be noted that fiberglass is anisotropic and anisotropy is not included in the modeling reported here. The discrepancies between predictions and data may be attributed to the simplistic single-parameter characterization of the fi-

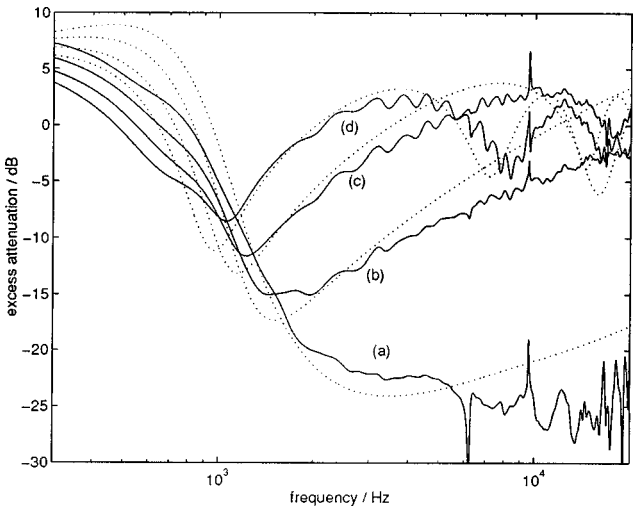

FIG. 8. Same as Fig. 7 except that the thickness of fiberglass layer is 1.4 cm.

berglass layers (Figs. 4 and 5). Nevertheless, the measured and predicted influence of reducing the impedance of the substrate on the primary interference dip is clear.

B. Outdoor data over snow

Nicolas *et al.*[5] have reported an extensive series of measurements over layers of snow from 5 to 50 cm thick and at propagation distances up to 15 m and compared their data to theoretical predictions based on the heuristic extended-reaction layer formula discussed earlier. Discrepancies were found between these predictions and the data above snow layers less than 20 cm thick and below 200 Hz even after allowing (heuristically) for extended reaction [Eqs. (16)–(19) and (21)]. In particular it was observed that the data obtained above 6-, 8-, and 10-cm layers of snow, while conforming to predictions of relative SPL over finite layers with extended reaction above acoustically hard backing at higher frequencies, behaved more like predictions of the relative SPL spectra above semi-infinite media with extended reaction at frequencies below 200 Hz [see Fig. 4(a)–(c) in Ref. 5]. Nicolas *et al.* were able to improve the qualitative agreement by means of a model[16] for the acoustical properties of a medium with an exponentially varying porosity profile. Another reason for the discrepancies between predictions and data above snow layers that has been suggested is finer layering within the snow.[1] Figure 9 shows that the measured behavior over snow layers, nominally 6, 8, and 10 cm thick, may be attributed to multiple layering. In Fig. 7, the predicted flow resistivity of the surface layer is higher than that of the second layer, which is expected in most practical situations. It should be noted that the values for the flow resistivities and layer thicknesses are intended to be indicative only and these parameters are listed in Table I for reference. No systematic attempts to obtain best fit have been employed. We also remark that the predicted thickness for the first layer is somewhat thinner than those measured thicknesses reported in Ref. 5. The fundamental limitations of the impedance model (Delaney and Bazley) used in the present analysis mean that we should treat all predicted flow resistivities and layer thicknesses as effective parameters.

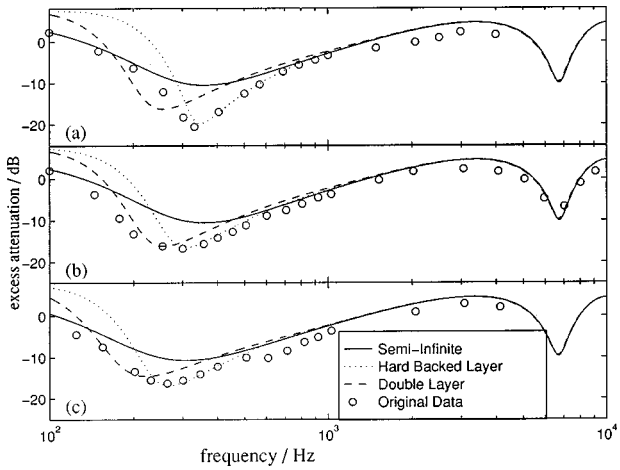

FIG. 9. Excess attenuation data (circles) obtained with source height 0.6 m, receiver height 0.3 m, and horizontal range 7.5 m and reported by Nicolas *et al.* [Ref. 5, Fig. 4(a)–(c)] over (a) 6-cm-thick layer of ''snow over ice,'' (b) 8-cm-layer of ''new snow over asphalt,'' and (c) 10-cm-thick layer of ''freshly-fallen snow above 50 cm of old hardened snow covered previously with a crust of ice.'' Also shown are predictions assuming semi-infinite (continuous lines), hard-backed single layer (dotted lines), and hard-backed double layer (broken lines), respectively, using the parameter values shown in Table I.

IV. CONCLUSION

This paper has contributed theoretical and experimental investigations into the sound field due to a point source above a ground with extended reaction. It has been demonstrated that the heuristic formula is satisfactory in most practical situations above a layered porous ground. Clearly the heuristic formula offers computational advantages over numerical methods such as the FFP for predicting sound fields above multiply layered extended reaction materials. A formula for finding the minimum depth of an externally reacting porous material that can be treated as a semi-infinite ground has been derived. This could be used to provide guidance for the thickness of the porous materials over a hard or nonhard backing required to simulate semi-infinite media with extended reaction in laboratory measurements. Finally, multiple layering has been demonstrated as a possible explanation of previous difficulties in obtaining theoretical predictions that match data obtained outdoors over snow.[5]

TABLE I. The layer thicknesses and flow resistivities used in Fig. 9.

	(a)	(b)	(c)
Hard backed layer (dotted line)	$\sigma=15$ kPa m s^{-2} $d=6$ cm	$\sigma=15$ kPa m s^{-2} $d=8$ cm	$\sigma=10$ kPa m s^{-2} $d=10$ cm
Semi-infinite ground (solid line)	$\sigma=15$ kPa m s^{-2}	$\sigma=15$ kPa m s^{-2}	$\sigma=10$ kPa m s^{-2}
Double layer (broken line)	$\sigma_1=10$ kPa m s^{-2} $d_1=8$ cm $\sigma_2=15$ kPa m s^{-2} $d_2=3$ cm	$\sigma_1=10$ kPa m s^{-2} $d_1=10$ cm $\sigma_2=55$ kPa m s^{-2} $d_2=1$ cm	$\sigma_1=8$ kPa m s^{-2} $d_1=12$ cm $\sigma_2=15$ kPa m s^{-2} $d_2=3$ cm

ACKNOWLEDGMENTS

The study was supported by the BBSRC (UK) through Grant Ref. No. CTE 02649, and by the EPSRC (UK) through Grant Ref. No. GR/L15326.

[1] K. Attenborough, ''Ground parameter information for propagation modeling,'' J. Acoust. Soc. Am. **92**, 418–427 (1992).
[2] Z. Hu and J. S. Bolton, ''Sound propagation from an arbitrarily oriented multi-pole placed near a plane, infinite impedance surface,'' J. Sound Vib. **170**, 637–669 (1994).
[3] J. F. Allard, *Sound Propagation in Porous Media: Modelling Sound Absorption Materials* (Chapman and Hall, London, 1993).
[4] C. Howorth, ''Sound propagation over rigid porous layers,'' Ph.D. thesis, The Open University, 1991.
[5] J. Nicolas, J. L. Berry, and G. A. Diagle, ''Propagation of sound above a finite layer of snow,'' J. Acoust. Soc. Am. **77**, 67–73 (1985).
[6] L. M. Brekhovskikh, *Waves in Layered Media* (Academic, New York, 1980), 2nd ed.
[7] K. Attenborough, S. I. Hayek, and J. M. Lawther, ''Propagation of sound above a porous half-space,'' J. Acoust. Soc. Am. **68**, 1493–1501 (1980).
[8] D. Habault and P. J. T. Filippi, ''Ground effect analysis: Surface wave and layer potential representation,'' J. Sound Vib. **79**, 529–550 (1981).
[9] P. J. T. Filippi, ''Extended sources radiation and Laplace type integral representation: application to wave propagation above and within layered media,'' J. Sound Vib. **91**, 64–85 (1983).
[10] T. L. Richards, K. Attenborough, N. W. Heap, and A. P. Watson, ''Penetration of sound from a point source into a rigid porous medium,'' J. Acoust. Soc. Am. **78**, 956–963 (1985).
[11] S. I. Thomasson, ''Sound propagation above a layer with a large refractive index,'' J. Acoust. Soc. Am. **61**, 659–674 (1977).
[12] C. F. Chien and W. W. Soroka, ''Sound propagation along an impedance plane,'' J. Sound Vib. **43**, 9–20 (1975).
[13] T. L. Richards and K. Attenborough, ''Accurate FFT-based Hankel transforms for prediction of outdoor sound propagation,'' J. Sound Vib. **109**, 157–167 (1986).
[14] M. E. Delany and E. N. Bazley, ''Acoustical properties of fibrous absorbent materials,'' Appl. Acoust. **3**, 105–116 (1970).
[15] D. D. Rife and J. Van der Kooy, ''Transfer-function measurements with Maximum-Length Sequences,'' J. Audio Eng. Soc. **37**(6), 419–443 (1989).
[16] R. J. Donato, ''Impedance models for grass-covered ground,'' J. Acoust. Soc. Am. **61**, 1449–1452 (1977).

The complementary operators method applied to acoustic finite-difference time-domain simulations

John B. Schneider[a)]
School of Electrical Engineering and Computer Science, Washington State University, Pullman, Washington 99164-2752

Omar M. Ramahi[b)]
Digital Equipment Corporation PKO3-1/R11, 129 Parker Street, Maynard, Massachusetts 01754

(Received 17 April 1997; revised 2 April 1998; accepted 7 April 1998)

The complementary operators method (COM) has recently been introduced as a mesh-truncation technique for open-domain radiation problems in electromagnetics. The COM entails the construction of two solutions that employ absorbing boundary conditions (ABCs) with complementary behavior, i.e., the reflection coefficients associated with the two ABCs are exactly opposite each other. The average of these solutions then yields a new solution in which the errors caused by artificial reflections from the termination of grid are nearly eliminated. In this work, COM is introduced for the finite-difference time-domain (FDTD) solution of acoustics problems. The development of COM is presented in terms of Higdon's absorbing boundary operators, but generalization to non-Higdon operators is straightforward. The effectiveness of COM in comparison to other absorbing boundary conditions is demonstrated with numerical experiments in two and three dimensions. © *1998 Acoustical Society of America.* [S0001-4966(98)01808-6]

PACS numbers: 43.20.Fn, 43.20.Gp, 43.20.Px [JEG]

INTRODUCTION

The finite-difference time-domain (FDTD) method was first introduced by Yee in 1966[1] for the study of electromagnetic scattering problems. A similar method has been developed for simulation of acoustic and elastic wave propagation (e.g., Refs. 2 and 3). The method is simple, both conceptually and in terms of implementation. It is robust and can be used to study accurately a wide range of complex phenomena. Since the FDTD method can be computationally expensive, a great deal of research has been, and continues to be, concerned with finding ways to decrease computational cost, both in memory and run time, while preserving or increasing accuracy. Arguably the most active area of this research is concerned with grid termination techniques for open-domain problem. The way in which the grid is terminated, i.e., the absorbing boundary condition (ABC), often dictates the size of the grid needed to obtain an accurate solution and hence is intimately tied to computational cost. This a consequence of the fact that a simulation employing an ABC of lower accuracy generally requires a larger grid than one employing an ABC of higher accuracy to obtain results of comparable quality.

Most open-domain problems require that the FDTD grid be terminated with an ABC. Open-domain problems need not be terminated with an ABC if a grid can be constructed that is so large that the boundaries of the computational domain are causally isolated from all regions of interest. Unfortunately, this approach is infeasible for nearly all realistic simulations. Global ABCs do exist which are nominally exact (e.g., Ref. 4). However, these ABCs require, for each terminal point of the grid, an integration over a surface which bounds the interior of the computational domain. Therefore, global ABCs are exceeding costly for time-domain simulations and have not proven to be useful in practical applications. Alternatively, local ABCs merely depend upon the field in the immediate vicinity of each terminal node and are far less costly than global ABCs. However, local ABCs are inherently imperfect and always reflect some spurious energy back into the computational domain. Typically the closer a local ABC is brought to the source of outgoing fields, whether an active element or a scatterer, the greater is the reflected energy (moving the ABC closer to the source of fields implies decreasing the size of the grid). This a consequence of the inability of traditional local ABCs to absorb evanescent energy and the fact that local ABCs typically perform poorly at grazing incidence. Nevertheless, the computational savings afforded by local ABCs outweigh their disadvantages and thus local ABCs are the ones most commonly used today. (In the remainder of the paper only local ABCs are discussed so that the ''local'' adjective will be dropped.)

There is another distinct approach to the termination of the FDTD grid that relies upon the use of an absorbing material. In such an approach, the absorbing material is placed adjacent to the terminal boundaries. The material is designed to absorb the energy from outgoing waves so that the amount of energy that reenters the interior of the grid via reflection from the grid termination is small. Straightforward material-based termination techniques have been available for several years (see, for example, Refs. 5, 6). An improved technique, employing a nonphysical split-field formulation, was recently presented by Bérenger.[7] This technique, known as the perfectly matched layer (PML) method, was presented in the context of electromagnetic problems, but it has been adapted

[a)]Electronic mail: schneidj@eecs.wsu.edu
[b)]Electronic mail: Omar.Ramahi@digital.com

for acoustic and elastic modeling.[8–12] The performance of the PML method is such that it has attracted the attention of several researchers. Unfortunately, the quest to improve the PML method has led many researchers to put aside the search for further improvements in differential equation-based ABCs. Nevertheless, as shown here, there are still tremendous improvements that can be made in the application of such ABCs. Thus it is nearly certain that the full potential of both differential equation-based and material-based grid truncation schemes has not yet been realized.

In this paper we provide the theoretical foundation for a new grid truncation technique known as the complementary operators method (COM) and show its application to problems in acoustics. The superiority of the technique over other differential equation-based ABCs is demonstrated via two- and three-dimensional examples. The COM requires that two simulations be performed. In one simulation an ABC is used that reflects energy in a known manner. In the other simulation, the complement of the ABC is used so that the energy reflected by the ABC has the same magnitude but opposite phase. Then, the results of the two simulations are averaged to obtain a solution that is free of most of the energy introduced by ABC reflections. The COM was first presented in the electromagnetics literature where it was shown to yield excellent results even when using a much smaller grid than required by other traditional ABCs.[13–15] Because of the ease with which the COM can be implemented and the significant impact it can have on accuracy and computational cost, this method has the potential to increase greatly the class of acoustics problems to which FDTD can successfully be applied.

The complementary ABCs (or boundary operators) required by the COM can be formulated from a general class of boundary operators;[15] however, in this paper we present the method specifically in terms of the Higdon ABC.[16,17] Section I provides a review of Higdon's boundary operators in their differential form and demonstrates the construction of complementary operators of arbitrary order. Section II details the implementation of the COM in the FDTD scheme. Section III provides results from two- and three-dimensional simulations that demonstrate the efficacy of the COM.

Our primary goals here are to present the theory behind the COM and to show the significant advantages it has over other differential equation-based grid truncation methods. Comparison of the COM with other grid termination techniques, such as the PML method, has been investigated elsewhere. The results presented in Refs. 18 and 19 show that the COM can yield results that are superior to the PML method while at the same time being less computationally costly. It should be noted that there is no ''best'' test with which to compare material-based and differential equation-based grid termination techniques. Instead, many different tests are required to isolate specific aspects of the techniques (e.g., performance at grazing angles, absorption of evanescent energy, and broadband behavior).

Finally, we note that there is an alternative implementation of the COM method to the one presented here.[20] The scheme presented in Ref. 20, named the concurrent complementary operators method or C-COM, does not require two separate simulations, i.e., the complementary boundary operators are realized using a single simulation. The cost associated with this implementation is an increase in memory usage (but that cost ''buys'' a decrease in total run time). The implementation of a C-COM solution is a straightforward extension to a COM solution and thus this paper concentrates on the basic formulation of COM for acoustic simulations. The reader interested in a concurrent formulation is referred to Ref. 20. We further note that programs that currently employ a Higdon (or Higdon-like) ABC can be modified to use the COM by making changes that are trivial (a simple change of coefficients is all that is required of the existing code and then results must be averaged). To realize a C-COM solution, additional changes must be made to the existing code.

I. DIFFERENTIAL FORM OF BOUNDARY OPERATOR

The first-order, coupled, differential equations governing linear acoustics are

$$\frac{\partial \mathbf{v}}{\partial t} = -\frac{1}{\rho}\,\nabla p, \tag{1}$$

$$\frac{\partial p}{\partial t} = -c^2 \rho \nabla \cdot \mathbf{v}, \tag{2}$$

where $\mathbf{v}$ is velocity, p is pressure, ρ is density, and c is the speed of sound. The standard FDTD algorithm is obtained by approximating the derivatives in Eqs. (1) and (2) by second-order accurate central differences. The evaluation points for pressure and velocity are spatially and temporally offset from each other so that leapfrog scheme can be constructed to express future fields in terms of past fields (see, for example, Ref. 2 or 8 for details). The usual leapfrog update equations cannot be applied to pressure nodes on the terminal boundary of the computational domain since not all of the needed adjacent fields are available there (i.e., a velocity node is needed that is outside of the grid). Instead, to update these pressure nodes, an auxiliary equation must be used that expresses the boundary value in terms of current or past values of the field in the interior of the grid and past values of the field on the boundary itself. Perhaps the most popular such auxiliary equation is provided by the Higdon boundary operator. The remainder of this section provides the theory behind the differential form of this operator and shows how it can be implemented in a manner suitable for use in the COM. The next section details the discrete form of this operator which, although similar to the continuous operator in many respects, is fundamentally different.

The general Mth-order Higdon boundary operator B^M operates on the pressure p at the termination of a computation domain as follows:

$$B^M p = \prod_{m=1}^{M} B_m p = 0, \tag{3}$$

where

$$B_m = \frac{\partial}{\partial x} + \frac{\xi_m}{c}\frac{\partial}{\partial t} + \alpha_m \tag{4}$$

and ξ_m and α_m are parameters. For arbitrary boundaries, the first partial derivative in Eq. (4) should be taken with respect to the outward normal to the boundary, but the x direction is used here to be consistent with subsequent analysis. Superscripts will be used for the overall order of a boundary operator while a subscript will be used to indicate the constituent components. Thus an individual term B_m is a first-order operator whereas the operator B^M is the Mth-order operator obtained from the product $B_1 B_2 \cdots B_M$. When α_m is zero, B_m will yield perfect absorption of plane waves incident at an angle θ_m such that $\xi_m = \cos(\theta_m)$. The parameter α_m was proposed by Higdon as a means of controlling stability of the operator.[17] Additionally, as discussed in Ref. 21, the α_m parameters can be used to absorb evanescent energy (which would otherwise experience unimodular reflection).

Assume that a plane is incident, perhaps obliquely, on a boundary corresponding to a constant x plane. Further assume, without loss of generality, that this boundary corresponds to $x=0$ and over this boundary the Higdon ABC operates on the pressure as given in Eq. (3). The plane wave has unit magnitude and its x component of propagation is in the positive direction. The total pressure in the computational domain will be the superposition of the incident wave and the wave reflected from the boundary

$$p(x,y,z,t) = e^{(j\omega t - jk_x x - jk_y y - jk_z z)} + R^M e^{(j\omega t + jk_x x - jk_y y - jk_z z)}, \tag{5}$$

where k_x, k_y, and k_z (which may be complex) are the x, y, and z components of the wave vector, respectively, ω is frequency, and R^M is the reflection coefficient of the Mth-order boundary operator.

The reflection coefficient is obtained by applying Eqs. (3)–(5) and solving for R^M. The result is

$$R^M = (-1)^{M-1} \prod_{m=1}^{M} R_m(\xi_m, \alpha_m), \tag{6}$$

where

$$R_m(\xi_m, \alpha_m) = -\frac{-jk_x + j\xi_m k + \alpha_m}{jk_x + j\xi_m k + \alpha_m}. \tag{7}$$

As before, the superscript indicates the overall order of the ABC and the subscript indicates constituent components. If the first-order operator B_m were to operate by itself, R_m would be the resulting reflection coefficient. The total reflection coefficient R^M can be obtained from the product of the individual R_m's [with a sign correction as shown in Eq. (6)].

Consider the reflection coefficient R_M associated with the first-order operator B_M when α_M is zero and when ξ_M either is zero or approaching infinity:

$$R_M(\xi_M = 0, \alpha_M = 0) = 1, \tag{8}$$

$$\lim_{\xi_M \to \infty} R_M(\xi_M, \alpha_M = 0) = -1. \tag{9}$$

The operator B_M corresponding to Eq. (8) is functionally equivalent to differentiation with respect to x as is evident from inspection of Eq. (4) with ξ and α set to zero. Similarly, the operator corresponding to Eq. (9) is equivalent to differentiation with respect to t. This is clearly seen in the context of Eq. (3) if both sides are divided by ξ_M prior to taking the limit.

We define Mth-order complementary boundary operators as operators whose corresponding reflection coefficients are given by

$$R_0^M = R_M(\xi_M = 0, \alpha_M = 0) R^{M-1} = -R^{M-1}, \tag{10}$$

$$R_\infty^M = \lim_{\xi_M \to \infty} R_M(\xi_M, \alpha_M = 0) R^{M-1} = R^{M-1}. \tag{11}$$

These operators are labeled B_0^M and B_∞^M, and corresponds to the operators that have $\alpha_M = 0$ and ξ_M equal to zero or approaching infinity, respectively. The reflection coefficients of these two Mth-order operators are the same in magnitude as the reflection coefficient of an operator of order $M-1$, but, significantly, these reflection coefficients have opposite signs. By performing two simulations, one using B_0^M and once using B_∞^M, and averaging the results, the spurious reflections associated with one ABC will be canceled by the reflections associated with the other ABC. However, as will be discussed below, not all ABC-related errors are eliminated by averaging the two solutions.

One must consider the operators in their finite-difference form, as is done in the next section, rather than their continuous form to understand fully their behavior. For example, since R_∞^M is equal to R^{M-1}, it appears that one of the complementary solutions can be obtained using the reduced-order boundary operator B^{M-1} (i.e., since the reflection coefficients associate with B^{M-1} is R^{M-1}, there is no need to use the higher-order operator B_∞^M). However, when implemented in discrete form, the phase shift associated with $R_M(\xi_M = 0, \alpha_M = 0)$ is not exactly 180 degrees. The actual phase shift is a function of the coarseness of the grid, the incident angle, and the frequency. The amount that this phase shift differs from the desired value must be accounted for to obtain the most accurate solution possible. As will be shown in the next section, a similar phase shift is produced by the finite-difference equivalent of $\lim_{\xi_M \to \infty} R_M(\xi_M, \alpha_M = 0)$ and this additional term in the operator ensures complete complementarity of the discrete forms of R_0^M and R_∞^M.[13,15]

Although operators can be used that are exactly complementary in both their continuous and discrete forms, the solution obtained by averaging the two complementary solutions is not completely free of ABC errors. To illustrate this fact, imagine a plane wave obliquely incident on a boundary that is near the corner of the computational domain (it suffices to think of a corner in a two-dimensional problem). In the simulation employing B_0^M the field reflected from the boundary will be scaled by $-R^{M-1}$. If this energy subsequently strikes the other boundary associated with the corner (i.e., the one orthogonal to the first boundary), it will be scaled by $(R^{M-1})^2$. For the simulation employing the B_∞^M boundary operator, the field reflected from the first boundary will be scaled by R^{M-1}. After striking the other boundary, it also will be scaled by $(R^{M-1})^2$. Therefore, when the results are averaged, all the errors associated with a single reflections from the ABCs will cancel while the errors associated with double reflections will add. More generally, errors associated with an odd number of reflections will cancel while

those associated with an even number of reflections will add. This also holds for reflections between the ABC and any scatterer within the computational domain. It should be emphasized that R^{M-1} is typically small so that reducing the error by the square of this amount is substantial.

II. FINITE-DIFFERENCE IMPLEMENTATION

Here we consider the discrete form of the boundary operators described in the previous section. The pressure is assumed to be available at discrete points in space–time and we adopt the standard FDTD notation for those points:

$$p^n_{i,j,k}=p(i\Delta x,j\Delta y,k\Delta z,n\Delta t), \tag{12}$$

where Δx, Δy, and Δz, are the spatial step sizes and Δt is the temporal step size. The operators **I**, **S**, and **T** are defined to be the identity, spatial shift, and temporal shift operators, respectively. Functionally, they perform as follows:

$$\mathbf{I}p^n_{i,j,k}=p^n_{i,j,k}, \tag{13}$$

$$\mathbf{S}p^n_{i,j,k}=p^n_{i+1,j,k}, \tag{14}$$

$$\mathbf{T}p^n_{i,j,k}=p^{n+1}_{i,j,k}. \tag{15}$$

Assuming the last grid point in the x direction is $i_{\max}$, the discrete form of Eq. (3) that would be applied to the boundary node is

$$\prod_{m=1}^{M}\left[\frac{\mathbf{I}-\mathbf{S}^{-1}}{\Delta x}\,\frac{\mathbf{I}+\mathbf{T}^{-1}}{2}+\frac{\xi_m}{c}\,\frac{\mathbf{I}+\mathbf{S}^{-1}}{2}\,\frac{\mathbf{I}-\mathbf{T}^{-1}}{\Delta t}+\alpha_m\,\frac{\mathbf{I}+\mathbf{S}^{-1}}{2}\,\frac{\mathbf{I}+\mathbf{T}^{-1}}{2}\right]p^{n+1}_{i_{\max},j,k}=0. \tag{16}$$

This equation is used to obtain $p^{n+1}_{i_{\max},j,k}$ in terms of pressures interior to the grid and previous values of the pressure on the boundary. In order to employ central differences, the discrete form of the boundary operator incorporates spatial and temporal averaging. The reader is referred to Refs. 16 and 17 for further details concerning the implementation of the discrete form of the boundary operator. Carrying out the multiplications and regrouping in terms of the **I**, **S**, and **T** operators, Eq. (16) can be written

$$\prod_{m=1}^{M}\left[\mathbf{I}+a_m\mathbf{S}^{-1}+b_m\mathbf{T}^{-1}+c_m\mathbf{S}^{-1}\mathbf{T}^{-1}\right]p^{n+1}_{i_{\max},j,k}=0, \tag{17}$$

where

$$a_m=\frac{-1+\xi_m\Delta x/c\Delta t+\alpha_m\Delta x/2}{1+\xi_m\Delta x/c\Delta t+\alpha_m\Delta x/2}, \tag{18}$$

$$b_m=\frac{1-\xi_m\Delta x/c\Delta t+\alpha_m\Delta x/2}{1+\xi_m\Delta x/c\Delta t+\alpha_m\Delta x/2}, \tag{19}$$

$$c_m=\frac{-1-\xi_m\Delta x/c\Delta t+\alpha_m\Delta x/2}{1+\xi_m\Delta x/c\Delta t+\alpha_m\Delta x/2}. \tag{20}$$

The finite-difference equivalent of Eqs. (3) and (4) are thus

$$\tilde{B}^M p^{n+1}_{i_{\max},j,k}=\prod_{m=1}^{M}\tilde{B}_m p^{n+1}_{i_{\max},j,k}=0, \tag{21}$$

where

$$\tilde{B}_m=\mathbf{I}+a_m\mathbf{S}^{-1}+b_m\mathbf{T}^{-1}+c_m\mathbf{S}^{-1}\mathbf{T}^{-1}. \tag{22}$$

The tildes distinguish the discrete operators from the continuous ones. Now consider the discrete from of Eq. (5)

$$p^n_{i,j',k}=e^{(j\omega n\Delta t-j\tilde{k}_x i\Delta x-j\tilde{k}_y j'\Delta y-j\tilde{k}_z k\Delta z)}+\tilde{R}^M e^{(j\omega n\Delta t+j\tilde{k}_x i\Delta x-j\tilde{k}_y j'\Delta y-j\tilde{k}_z k\Delta z)}. \tag{23}$$

A prime has been added to the spatial index in the y direction to distinguish it from the symbol j used to represent $\sqrt{-1}$. The tilde on wave vector components emphasizes that the numeric wave vector differs from the continuous one since the dispersion relation in an FDTD grid differs slightly from the true one.

Using Eq. (23) in (21) and, without loss of generality, letting $i_{\max}$ equal zero, one can solve for the numeric reflection coefficient $\tilde{R}^M$

$$\tilde{R}^M=(-1)^{M-1}\prod_{m=0}^{M}\tilde{R}_m(\xi_m,\alpha_m), \tag{24}$$

where

$$\tilde{R}_m(\xi_m,\alpha_m)=-\frac{1+a_m e^{j\tilde{k}_x\Delta x}+b_m e^{-j\omega\Delta t}+c_m e^{j\tilde{k}_x\Delta x-j\omega\Delta t}}{1+a_m e^{-j\tilde{k}_x\Delta x}+b_m e^{-j\omega\Delta t}+c_m e^{-j\tilde{k}_x\Delta x-j\omega\Delta t}}. \tag{25}$$

As with the continuous operators, $\tilde{R}_m$ is the reflection coefficient obtained when using the first-order operator $\tilde{B}_m$ by itself and $\tilde{R}^M$ is the product of the $\tilde{R}_m$'s with a correction made for the sign.

Motivated by the analysis of the previous section, we consider $\tilde{R}_M$ when α_M is zero and ξ_M is either zero or approaching infinity. However, since Eq. (25) gives $\tilde{R}_M$ in terms of a_M, b_M, and c_M, it is helpful first to obtain these coefficients directly from Eqs. (18) to (20). For the two cases of interest here, the sets of coefficients are

$$\tilde{R}_M(\xi_M=0,\alpha_M=0)\Rightarrow a_M=-1;\quad b_M=1;\quad c_M=-1, \tag{26}$$

$$\lim_{\xi_M\to\infty}\tilde{R}_M(\xi_M,\alpha_M=0)\Rightarrow a_M=1;\quad b_M=-1;\quad c_M=-1. \tag{27}$$

Using these in Eq. (25) yields

$$\tilde{R}_M(\xi_M=0,\alpha_M=0)=\exp(j\tilde{k}_x\Delta x), \tag{28}$$

$$\lim_{\xi_M\to\infty}\tilde{R}_M(\xi_M,\alpha_M=0)=-\exp(j\tilde{k}_x\Delta x). \tag{29}$$

As was the case for the continuous operators (Refs. 8 and 9), these two reflection coefficients are exactly complementary. The discrete form of Eqs. (10) and (11) is thus

$$\tilde{R}^M_0=\tilde{R}_M(\xi_M=0,\alpha_M=0)\tilde{R}^{M-1}=-\exp(j\tilde{k}_x\Delta x)\tilde{R}^{M-1}, \tag{30}$$

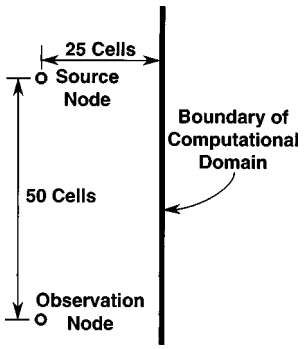

FIG. 1. Sketch of geometry used to test numerical complementarity. The boundary is terminated using either $\tilde{B}_0^2$ or $\tilde{B}_\infty^2$. Boundaries other than the one shown are sufficiently far away so that no energy is reflected by them over the duration of the simulation. The reference solution is obtained with the same spacing between the source and observation point, but all boundaries are causally isolated from the observation point.

$$\tilde{R}_\infty^M = \lim_{\xi_M \to \infty} \tilde{R}_M(\xi_M, \alpha_M = 0)\tilde{R}^{M-1} = \exp(j\tilde{k}_x \Delta x)\tilde{R}^{M-1}, \tag{31}$$

which have the corresponding boundary operators $\tilde{B}_0^M$ and $\tilde{B}_\infty^M$ given by

$$\tilde{B}_0^M = [\mathbf{I} - \mathbf{S}^{-1} + \mathbf{T}^{-1} - \mathbf{S}^{-1}\mathbf{T}^{-1}] \prod_{m=1}^{M-1} [\mathbf{I} + a_m \mathbf{S}^{-1} + b_m \mathbf{T}^{-1} + c_m \mathbf{S}^{-1}\mathbf{T}^{-1}], \tag{32}$$

$$\tilde{B}_\infty^M = [\mathbf{I} + \mathbf{S}^{-1} - \mathbf{T}^{-1} - \mathbf{S}^{-1}\mathbf{T}^{-1}] \prod_{m=1}^{M-1} [\mathbf{I} + a_m \mathbf{S}^{-1} + b_m \mathbf{T}^{-1} + c_m \mathbf{S}^{-1}\mathbf{T}^{-1}]. \tag{33}$$

It is important to note, as is clear from Eqs. (30) and (31), that these two discrete boundary operators are, as were the continuous operators, exactly complementary. The fact that complementarity is also preserved numerically (i.e., when implemented using finite-precision arithmetic) will be shown in the next section.

III. NUMERICAL RESULTS

In this section two problems are considered to study the behavior of the ABCs. The first is simply propagation in a homogeneous region while the second is propagation about a pressure-release (Dirichlet boundary condition) sphere. Although analytic solutions are available for both these problems, comparisons are made to reference solutions also obtained from FDTD simulations. If results were compared to analytic solutions, numerical artifacts inherent in the FDTD technique other than those caused by the grid termination (e.g., grid dispersion) could make meaningful interpretation difficult. Hence, the FDTD reference solutions, which use large grids to eliminate boundary errors over the duration of the simulations, permit the ABC errors to be separated from any other numeric artifacts.

First we demonstrate that the numerical implementation of $\tilde{B}_0^M$ and $\tilde{B}_\infty^M$ yields complementary results even when the error associated with the individual operators is large. Consider the two-dimensional problem depicted in Fig. 1 which

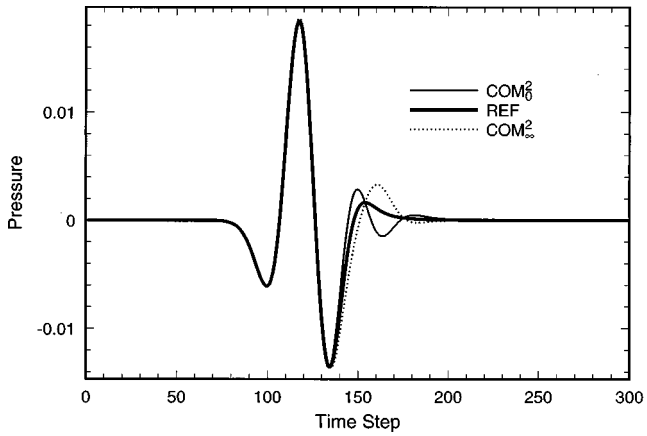

FIG. 2. Pressure at the observation point. The units of pressure here, as in all other plots, can be chosen arbitrarily.

is, ideally, the equivalent of a point source (three-dimensional line source) radiating in a homogeneous medium. The source is realized by adding a Ricker wavelet to the update equations for the source node. (This yields a transparent source that introduces fields into the computational domain without scattering them. See Ref. 22 for further discussion of the implementation of transparent sources.) The maximum value of the source function is unity (arbitrary units). The discretization is such that the peak frequency of the wavelet is sampled at 32 points per wavelength. The Courant number ($c\Delta t/\Delta x$) is 0.95 times the two-dimensional limit of $1/\sqrt{2}$ and the spatial step size is the same throughout the grid. Three simulations were performed. In the first, the boundary operator was $\tilde{B}_0^2$ with $\xi_1 = 1$ and $\alpha_1 = 0$ (these parameters will provide perfect absorption for a plane wave normally incident on the boundary); in the second, the boundary operator was $\tilde{B}_\infty^2$ with, again, $\xi_1 = 1$ and $\alpha_1 = 0$; the third simulation was a reference solution in which all the boundaries of the computational domain were causally isolated from the observation point over the duration of the simulation. We label the results from these three simulations COM_0^2, COM_∞^2, and REF.

Figure 2 shows the results of the three simulations recorded over 300 time steps. Note that the solutions obtained using $\tilde{B}_0^2$ and $\tilde{B}_\infty^2$ differ substantially from the reference solution. The errors are comparable to that of a first-order Higdon ABC by itself (the errors differ only in phase). To show that the error in the two ABC-terminated solutions are complementary, Fig. 3 shows plots of the difference between the reference solution and the complementary solutions, i.e., plots of the error in the two solutions. Note that these error plots appear to be exactly opposite each other. The ultimate COM solution for this problem, which we label COM^2, is the average of the two complementary run; thus at each time step $\mathrm{COM}^2 = (\mathrm{COM}_0^2 + \mathrm{COM}_\infty^2)/2$. A plot of COM^2 is indistinguishable from the reference solution and does not warrant a separate figure. Instead, it is instructive to plot the error in COM^2. Figure 4 shows the logarithm (base 10) of the absolute value of the difference between REF and COM^2 as a function of time. The significance of this plot is that the difference between the two solutions hovers around the numeric noise floor for double precision numbers. (Double pre-

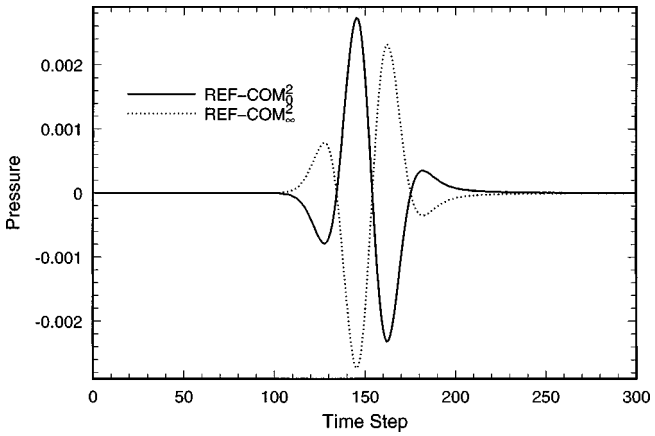

FIG. 3. Difference between the reference solution and the two solutions that used complementary boundary operators.

cision arithmetic yields between 14 and 15 digits of precision. Given that the peak value of the observed pressure has a magnitude of approximately 10^{-2}, the numeric noise floor should be in the range of 10^{-16} to 10^{-17}. This is precisely the range of errors seen in Fig. 4.) We must add, however, that this problem was constructed so that there are no multiple reflections. As was mentioned at the end of Sec. I, the ABC-induced errors associated with an even numbers of multiple reflections add rather then cancel.

To demonstrate the performance of the COM in three dimensions, we consider the pressure about a pressure-release sphere (i.e., the Dirichlet boundary condition is enforced over the surface of the sphere) that is insonified by an isotropic point source. This problem is designed to provide a stringent environment for testing the performance of ABCs and is not, per se, designed to provide a realistic model of any particular physical system. Thus this study was performed all in terms of nondimensional units, e.g., the number of points per wavelength and the Courant number.

The computational domain is 39 cells$\times$39 cells $\times$39 cells; the sphere has a radius of ten cells and is centered in the computation space. The spatial step sizes are the same in all directions, i.e., $\Delta x=\Delta y=\Delta z=\delta$. The Courant number, $c\Delta t/\delta$ is $1/\sqrt{3.1}$ which is approximately 98% of the three-dimensional limit. Figure 5 shows a slice through the middle of the computational domain. (Although drawn as a

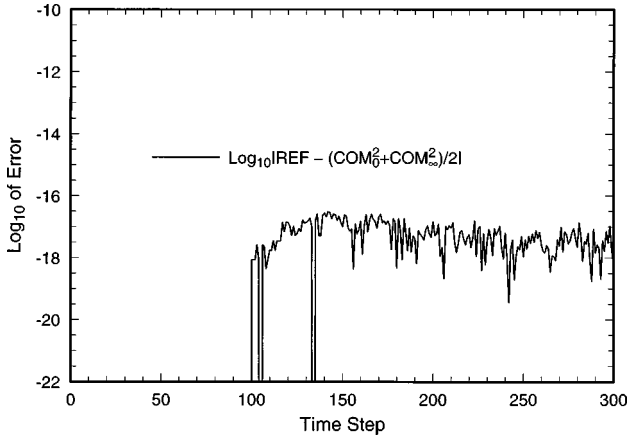

FIG. 4. Log base 10 of the error in the COM solution.

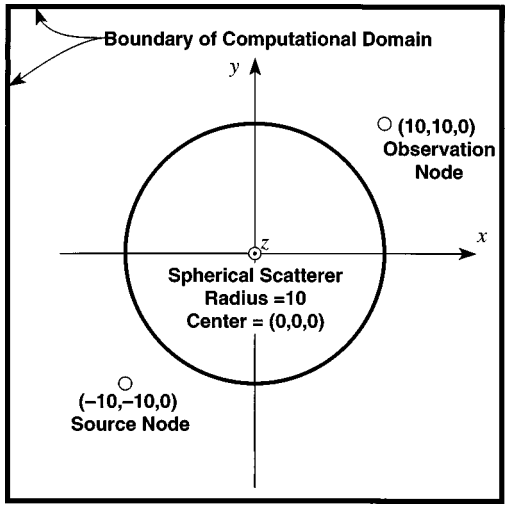

FIG. 5. Cross section of three-dimensional problem showing the source and observation points. Coordinates are relative to the center of the sphere. The boundary is terminated using either $\tilde{B}_0^4$ or $\tilde{B}_\infty^4$. The reference solution is obtained using a large grid that causally isolated the boundaries from the observation point over the duration of the simulation.

continuous circle, the actual boundary of the spherical scatterer follows the staircased boundary inherent in Cartesian-cell FDTD simulations.) The source node is a pressure node where the pressure is given by a Ricker wavelet. However, unlike before, the usual update equation does not apply at this one node. In that sense the source node itself is ''hard,'' i.e., it will scatter any field incident upon it. The discretization is such that there are 20 points per wavelength at the peak spectral content of the wavelet. Hence, the diameter of the sphere corresponds to one wavelength of the most energetic portion of the insonification. The locations of the source and observation points are as shown in Fig. 5. Since the observation point is on the opposite side of the sphere from the source and the boundary of the computational domain is, at its closest point, only nine cells away from the sphere, the quality of the ABC significantly influences the observed field. Since the fields at the observation point are small relative to the peak amplitude of the source pulse, the source function was scaled by a factor of 5000. This was done solely to facility plotting and, since the units of pressure can be chosen arbitrarily, has no effect on the interpretation of the results.

The boundary is terminated either using $\tilde{B}_0^4$, $\tilde{B}_\infty^4$, or $\tilde{B}^4$. We label the associated solutions COM_0^4, COM_∞^4, and HIG^4, respectively. (HIG^4 solution is that which is obtained using the standard fourth-order Higdon ABC.) The solution obtained by the average of COM_0^4 and COM_∞^4 is labeled COM^4. The parameter α_m was zero for all the first-order constituent components of these boundary operators, while ξ_m was unity (except, of course, where ξ was used to establish complementary behavior in $\tilde{B}_0^4$ and $\tilde{B}_\infty^4$). Thus no attempt was made to ''tune'' the ABC parameters to the particular problem at hand or optimize the coefficient for a general problem. However, it should be noted that if a set of parameters can be found that improves the performance of the Higdon ABC, the benefit realized by using the same set of parameters in a COM formulation should be even greater (i.e.,

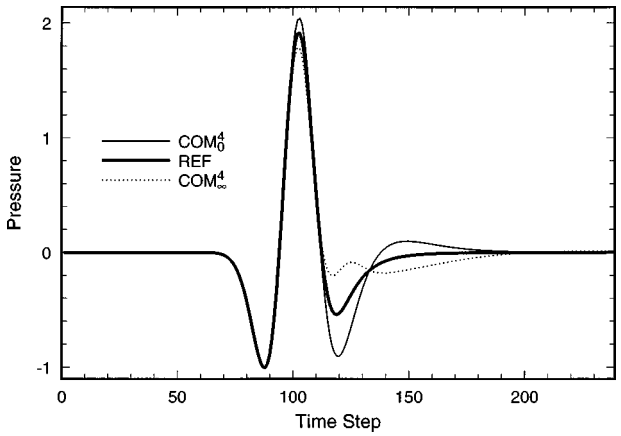

FIG. 6. Pressure at observation point obtained using either the boundary operator $\tilde{B}_0^4$ (COM$_0^4$) or $\tilde{B}_\infty^4$ (COM$_\infty^4$). The reference solution is free of all ABC errors.

the square of that realized using an uncomplemented formulation).

Note that the reflection coefficients, and hence the ABC-induced errors, for the COM$_0^4$ and COM$_\infty^4$ solutions are comparable to that of a third-order Higdon ABC. The reflection coefficient for the HIG^4 solution, on the other hand, is the smaller reflection coefficient of the fourth-order Higdon ABC. But, all these solutions require the same computational resources in terms of backstorage of fields and number of operations—they only differ in the coefficients used in the boundary-node update equations. Given the size of the reflection coefficient in each simulation, the HIG^4 should give better results than either COM$_0^4$ or COM$_\infty^4$ individually. However, the import question is: How does HIG^4 compare to COM^4?

Figure 6 shows the reference solution (obtained using a large grid which is free of all ABC errors) together with COM$_\infty^4$ and COM$_0^4$. There are obvious and significant errors, but, given the design of this ''test bed,'' the errors are not surprising. Figure 7 shows the reference solution together with HIG^4 and COM^4. As anticipated, HIG^4 is more accurate than either COM$_0^4$ or COM$_\infty^4$. However, COM^4 is obviously more accurate than HIG^4. Since it is difficult to tell the difference between the reference solution and COM^4 when plotting the entire pulse, an inset shows a plot of the trailing portion of the pulse with the vertical scale magnified by approximately ten. On this scale the slight errors in COM^4 can be seen.

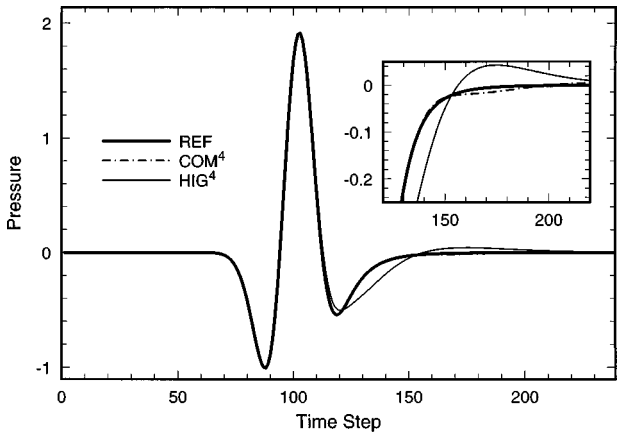

FIG. 7. Pressure at observation point obtained using the average of the two complementary results (COM^4) and obtained using a Higdon fourth-order operator (HIG^4). The inset box shows the pressure from time step 120 to 220 with the vertical scale magnified by a factor of 10.

IV. CONCLUSIONS

By averaging the results obtained from two simulations in which complementary boundary operators are used, ABC-related errors can be significantly reduced. The final result is superior to that which can be obtained using a higher-order ABC by itself. The construction of complementary operators is relatively simple. In fact, any acoustic code which currently employs a Higdon ABC can be modified with little effort to use complementary operators. One merely has to employ different sets of coefficients for the boundary update equations (i.e., other than a change of constants, no other modifications are needed). The cost of using the COM is that two simulations must be performed. However, given the quality of the results obtained, this cost can be more than offset by the use of a smaller computational domain (see Ref. 15 for a discussion of this point). Additionally, in situations where one is willing to trade an increase in memory for a reduction in total computation time, a concurrent-COM scheme has been presented elsewhere.[20]

As demonstrated here, the COM applies equally well to two- and three-dimensional acoustics problems. It is further anticipated that the complementary operators method can be applied to problems in elastic propagation and this will be the subject of future investigations.

ACKNOWLEDGMENT

This work was supported by Digital Equipment Corporation and the Office of Naval Research, Code 321OA.

[1] K. S. Yee, ''Numerical solution of initial boundary value problems involving Maxwell's equations in isotropic media,'' IEEE Trans. Antennas Propag. **14**, 302–307 (1966).
[2] D. Botteldooren, ''Acoustical finite-difference time-domain simulation in a quasi-Cartesian grid,'' J. Acoust. Soc. Am. **95**, 2313–2319 (1994).
[3] J. Virieux, ''*P-SV* wave propagation in heterogeneous media: Velocity-stress finite difference method,'' Geophysics **51**, 889–901 (1986).
[4] J. De Moerloose and D. De Zutter, ''Surface integral representation radiation boundary condition for the FDTD method,'' IEEE Trans. Antennas Propag. **41**, 890–896 (1993).
[5] R. Holland and J. W. Williams, ''Total-field versus scattered-field finite-difference codes: A comparative assessment,'' IEEE Trans. Nucl. Sci. **NS-30**, 4583–4588 (1983).
[6] C. Cerjan, D. Kosloff, R. Kosloff, and M. Reshef, ''A nonreflecting boundary condition for discrete acoustic and elastic wave equations,'' Geophysics **50**, 705–708 (1985).
[7] J.-P. Berenger, ''A perfectly matched layer for the absorption of electromagnetic waves,'' J. Comput. Phys. **114**, 185–200 (1994).
[8] J. G. Maloney and K. E. Cummings, ''Adaptation of FDTD techniques to acoustic modeling,'' in *11th Annual Review of Progress in Applied Computational Electromagnetics*, Vol. 2 (Monterey, CA), pp. 724–731, Mar. 1995.
[9] F. D. Hastings, J. B. Schneider, and S. L. Broschat, ''Application of the perfectly matched layer (PML) absorbing boundary condition to elastic wave propagation,'' J. Acoust. Soc. Am. **100**, 3061–3069 (1996).
[10] W. C. Chew and Q. H. Liu, ''Perfectly matched layers for elastodynamics:

A new absorbing boundary condition,'' J. Comput. Acoust. **4**, 341–359 (1996).
[11] X. Yuan, D. Borup, J. W. Wiskin, M. Berggren, R. Eidens, and S. A. Johnson, ''Formulation and validation of Berenger's PML absorbing boundary for the FDTD simulation of acoustic scattering,'' IEEE Trans. Ultrason. Ferroelectr. Freq. Control **44**, 816–822 (1997).
[12] Q. H. Liu and J. Tao, ''The perfectly matched layer for acoustic waves in absorptive media,'' J. Acoust. Soc. Am. **102**, 2072–2082 (1997).
[13] O. Ramahi, ''Application of the complementary operator method to the finite-difference–time domain solution of the three-dimensional radiation problem,'' Microwave Opt. Technol. Lett. **9**, 147–149 (1995).
[14] O. M. Ramahi, ''Complementary operators: A method to annihilate artificial reflections arising from the truncation of the computational domain in the solution of partial differential equations,'' IEEE Trans. Antennas Propag. **43**, 697–704 (1995).
[15] O. M. Ramahi, ''Complementary boundary operators for wave propagation problems,'' J. Comput. Phys. **133**, 113–128 (1997).
[16] R. L. Higdon, ''Absorbing boundary conditions for difference approximations to the multi-dimensional wave equation,'' Math. Comput. **47**, 437–459 (1986).
[17] R. L. Higdon, ''Numerical absorbing boundary conditions for the wave equation,'' Math. Comput. **49**, 65–90 (1987).
[18] J. Schneider and O. M. Ramahi, ''A comparison and evaluation of the PML and COM mesh truncation techniques for FDTD simulation,'' in *IEEE Antennas and Propagat. Soc. Int. Symp.* (Montréal, Canada), Vol. 3, pp. 1904–1907, July 1997.
[19] O. M. Ramahi and J. B. Schneider, ''Comparative study of the PML and C-COM mesh-truncation techniques,'' IEEE Microwave Guid. Wave Lett. **8**, 55–57 (1998).
[20] O. M. Ramahi, ''Concurrent implementation of the complementary operators method in 2-D space,'' IEEE Microwave Guid. Wave Lett. **7**, 165–167 (1997).
[21] J. Fang, ''Absorbing boundary conditions applied to model wave propagation in microwave integrated-circuits,'' IEEE Trans. Microwave Theory Tech. **42**, 1506–1513 (1994).
[22] J. B. Schneider, C. L. Wagner, and S. L. Broschat, ''Implementation of transparent sources embedded in acoustic finite-difference time-domain grids,'' J. Acoust. Soc. Am. **103**, 136–142 (1998).

Measurement of acoustic stop bands in two-dimensional periodic scattering arrays

W. M. Robertson and J. F. Rudy III
Department of Physics and Astronomy, Middle Tennessee State University, Murfreesboro, Tennessee 37132

(Received 24 August 1997; revised 30 March 1998; accepted 7 April 1998)

The experimental observation of acoustic stop bands in two-dimensional periodic arrays using an impulse response technique is reported. The frequencies of the stop-band centers are consistent with simple theoretical considerations based on the spacing between layers along the high symmetry directions of the regular arrays. The phase information extracted from the Fourier analysis is used to construct the acoustic dispersion relation for frequencies above and below the stop band. Measurements are reported for both square and triangular scattering arrays. © *1998 Acoustical Society of America.* [S0001-4966(98)01908-0]

PACS numbers: 43.20.Gp, 43.20.Ye, 43.20.Fn [JEG]

The nature of wave propagation in two- and three-dimensional periodic structures has received considerable attention, in particular for electromagnetic radiation. The motivation for this interest is that in periodic dielectric structures the process of coherent scattering and interference offers the potential to engineer the properties of the radiation field, including the creation of photonic band gaps–frequency intervals over which propagation is forbidden. The ability to manipulate the propagation properties of electromagnetic radiation has a number of fundamental consequences for processes such as the Anderson localization of light[1] and photon-dressed atoms.[2,3] In addition, a number of practical applications have been proposed including narrow bandpass filters,[4] enhanced surface mounted microwave antennas,[5] sharp bend radius waveguides,[6] and the zero threshold laser.[7]

Recently, several authors have investigated theoretically the comparable process of acoustic wave propagation in periodic scattering arrays.[8–13] The motivation is the possibility of creating materials that tailor the propagation properties of acoustic waves for applications such as filters, noise and vibration isolation, and acoustic wave guiding. The theoretical consideration of this problem has been addressed by solving the elastic wave equation for a number of acoustic scattering array configurations. The inherent symmetry of the periodic array permits the acoustic wave dispersion to be solved, for a periodic sample of infinite extent, using plane wave expansion techniques similar to those used to find the electronic band structure in solid state physics. Because the theoretical techniques have been adapted from solid state band structure calculations, much of the terminology has also carried over, including the concept of a band gap, the Brillouin zone, and the representation of acoustic wave dispersion in the reduced zone scheme. The differences between the nature of electron wave functions, and electromagnetic and acoustic waves are accounted for in adapting these techniques from one regime to another.

For the electromagnetic case there is now a rich body of theoretical calculations that has proven to match well with experiment.[14] In contrast, the experimental work on acoustic wave band structure is just beginning. One of the first experiments[15] made elegant use of a sculpture that consisted of an array of regularly spaced metal rods to measure the acoustic wave transmission along various high symmetry directions of the lattice of rods. Using a broadband sound source and a spectrum analyzer, the authors observed a reduction of the acoustic transmission at specific frequencies consistent with the array spacing. Because the filling factor of the sculpture was too small, the measurements did not exhibit complete acoustic band gaps[16] but rather a suppression of the density of acoustic states.

In the experiments described here we made measurements on two-dimensional arrays of metal cylinders in air designed, using the criteria cited in Ref. 16, to have complete band gaps. The measurements were made using an impulse response technique to determine the transmission function over a broad frequency bandwidth. A key advantage of the impulse response technique is that it is possible to extract not only the frequency intervals that define the band gaps but also to determine the dispersion relation for acoustic waves in the array at frequencies above and below the band gap.

A schematic representation of the experimental configuration is shown in Fig. 1. The basic experiment consisted of playing an impulse signal through the speaker and recording the acoustic signal arriving at the microphone. Experiments were performed with and without the sample—a two-dimensional array of cylindrical rods—in place. The modification of the transmission due to the sample was determined by comparing the Fourier transforms of the recorded time-domain data. The impulse signal was a computer sound file created numerically. Various impulse signals were explored, the most successful in giving broad spectral content being signals that were generated by taking the second derivative of a Gaussian. The width in time of the Gaussian could be varied to adjust the range of frequency components.

The impulse was fed to the stereo output of the computer's sound card. One channel of the impulse was fed to the speaker; the second output was directed to the trigger input of the data acquisition card. A number of successive impulse signals (typically between 200 and 500) were recorded and averaged to eliminate background noise. A pretrigger mode of the data acquisition card (National Instruments Lab-PC$^+$)

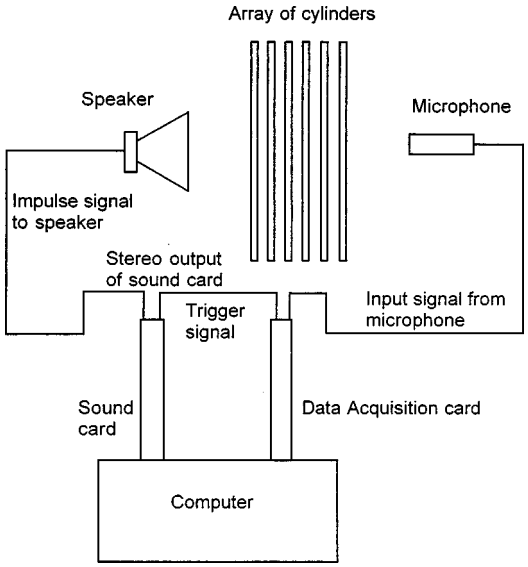

FIG. 1. Schematic diagram of the experimental configuration.

was used to measure information before the trigger pulse. Because the trigger pulse was derived directly from the electrical signal sent to the speaker, the relative timing of the signals justified the add and average method and allowed a comparison of timing between experiments with different samples. Typical time-domain data are shown in Fig. 2 both for the impulse alone, and for the impulse after passing through a square array of rods five layers thick. The initial flat response indicates that the averaging successfully extinguishes the random background noises. The oscillations after the pulse are signals that add coherently in the averaging process and are due to ringing of the speaker and to the reverberations in the room. As described in the results section below, time windowing was used to reduce the effect of the reverberant field.

The samples used for the experiments consisted of two-dimensional arrays of 2.34-cm-diam electrical conduit arranged in either a square or triangular pattern. A wooden base was drilled with the appropriate pattern to hold the cylindrical conduit in place. The cylinders were approximately 1 m in length and could be reconfigured in the holder to make arrays of different dimensions.

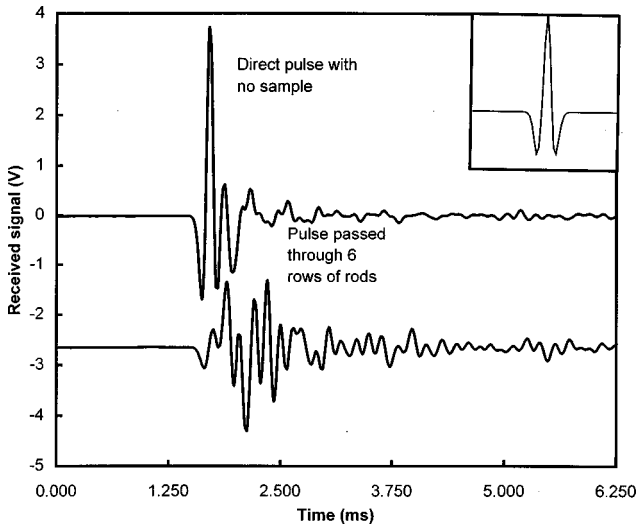

FIG. 2. Time domain wave forms recorded with no sample [upper trace] and a sample of rods 6 rows deep×10 rows wide [lower trace] between the speaker and microphone. The inset at the upper right shows the form of the electrical pulse fed to the speaker.

Theoretical considerations indicate that the filling factor—the fraction of the sample occupied by the scattering rods—determines whether an array will exhibit a complete band gap. For the square sample, the filling factor, F, is given by the relation

$$F=\frac{\pi d^2}{4a^2}, \tag{1}$$

where d is the diameter of the cylinders and a the spacing between nearest neighbors. The square array was built with $a=3.7$ cm and $d=2.34$ cm leading to a filling factor of $F=0.31$. The results of Ref. 16 suggested that for the square array a minimum filling factor of 0.3 was required for the appearance of complete acoustic stop bands. In the absence of theoretical guidelines for the triangular lattice we chose a filling factor of $F=0.366$. Experiments in electromagnetics suggest that the triangular lattice typically exhibits a larger stop band than the square lattice.[17–19] Simple geometry gives the filling factor for the triangular lattice as

$$F=\frac{2\pi d^2}{a^2\sqrt{3}}. \tag{2}$$

Using the same set of conduit rods as for the square lattice with diameter, $d=2.34$ cm, led us to adopt a spacing $a=3.7$ cm.

Fourier transforms of the time-domain data were performed in order to analyze the impulse response results acquired in the experiments. The time-domain wave form in Fig. 2, with no sample in the path between the speaker and the microphone, shows that the reverberant field contributes significantly for long times after the initial pulse. To minimize the effect of this reverberation, windowing of the time signal was used before the Fourier analysis. This procedure reduces the frequency resolution but achieves a better measure of the effect of the sample under test. Total time windows of 6 ms were typically chosen resulting in a frequency step of 166 Hz. Figure 2 also shows that the initial pulse is not exactly the same as the electrical wave form fed to the speaker by the sound card. There is a distinct after pulse due to the limitations of the speaker. These features lead to corresponding features in the Fourier transformed data.

The Fourier analysis of the time domain data from Fig. 2 is shown in Fig. 3(a) which plots the magnitude of the Fourier components for the two time wave forms. The filled circular data points correspond to the case with no sample and the open squares represent the data for transmission through six rows of the square lattice along the ΓX direction. The no-sample Fourier transform shows a dip at about 3500 Hz which is due to the response of the speaker. For transmission through the array of cylinders, there is a clear attenuation from about 3000 Hz to 5500 Hz. This region of reduced transmission is the acoustic stop band. A simple calculation can be used to confirm that the gap is centered at

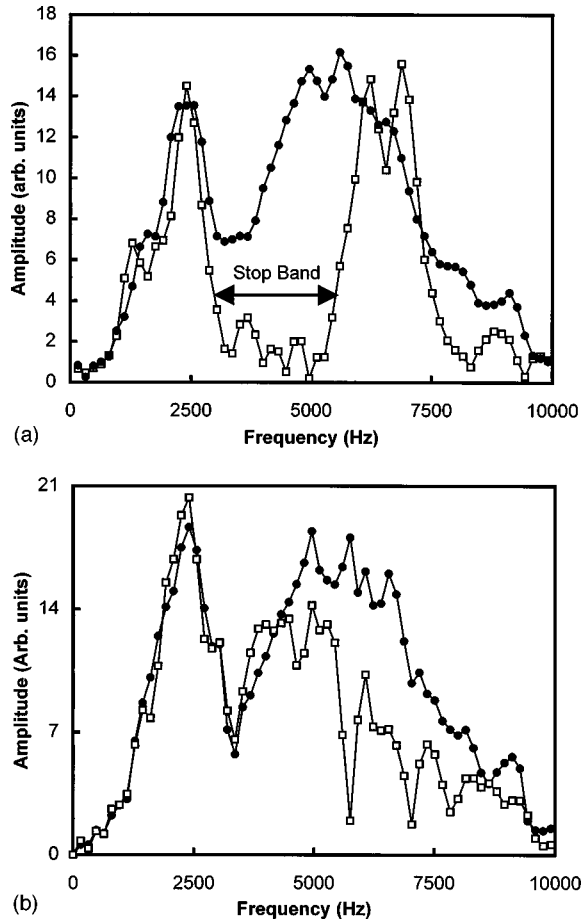

FIG. 3. (a) Fourier amplitude transmitted through 6 rows of rods along the ΓX direction of the square lattice (curve with open squares). The Fourier components in the direct pulse with no sample is represented by the curve with filled circles. (b) Fourier amplitude transmitted through 6 rows of rods along the ΓM direction of the square lattice (curve with open squares). The Fourier components in the direct pulse with no sample is represented by the curve with filled circles.

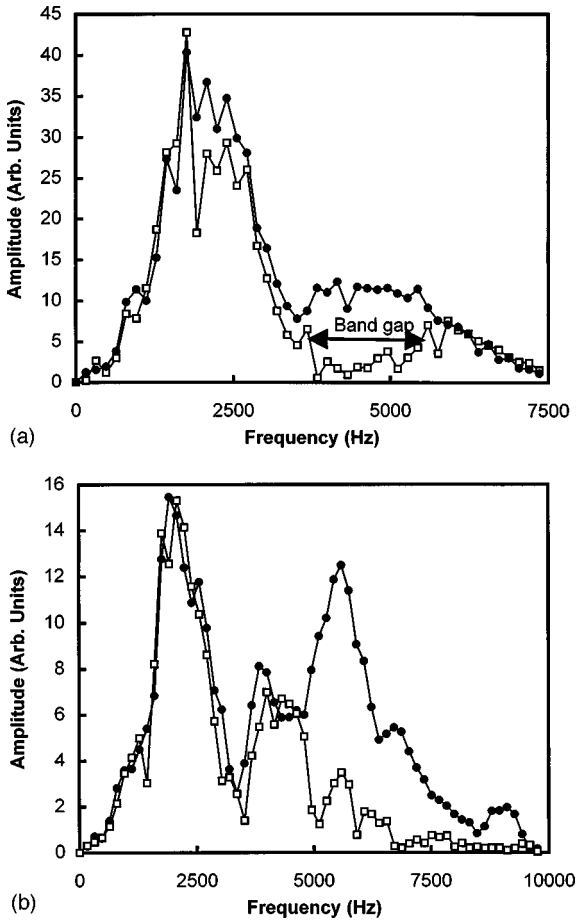

FIG. 4. (a) Fourier amplitude transmitted through 4 rows of rods along the ΓX direction of the triangular lattice (curve with open squares). The Fourier components in the direct pulse with no sample is represented by the curve with filled circles. (b) Fourier amplitude transmitted through 6 rows of rods along the ΓJ direction of the triangular lattice (curve with open squares). The Fourier components in the direct pulse with no sample is represented by the curve with filled circles.

the correct frequency. The periodicity along the ΓX direction is 3.7 cm, the spacing between adjacent layers. The coherent scattering from these equally spaced layers opens up a band gap at the Brillouin zone edge $k_{\mathrm{BZ}}=\pi/a$. The dispersion in the vicinity of the band gap will be modified, but the center frequency of the band gap is approximately given by assuming linear dispersion and using k_{BZ}. Thus

$$\omega = v k_{\mathrm{BZ}} = v \frac{\pi}{a}, \tag{3}$$

which can be rearranged to give

$$f_c = \frac{v}{2a}. \tag{4}$$

Using $a=3.7$ cm and $v=340$ m/s gives a center frequency of 4595 Hz in good agreement with the experimental observation.

Figure 3(b) shows the Fourier components for propagation along the ΓM direction of the square lattice. In this case the spacing between layers is given by $a/\sqrt{2}$; thus the simple formula predicts a center frequency for the stop band of 6498 Hz. The amplitude data in this case are less compelling. There is a clear suppression in the transmission beginning at about 5000 Hz and continuing out through the highest frequency of 10 000 Hz; however, it is difficult to identify a clear band gap from this data alone. In the case of small band gaps, the phase information extracted from the Fourier transformed data proved to be a more powerful tool to elucidate the characteristics of the band gap. A description of the analysis of the phase data, including its use to determine the acoustic dispersion relation, is given below.

Results for transmission experiments on the triangular lattice are shown in Fig. 4(a) and (b). In each case a reference spectrum is shown in addition to the spectrum for transmission through a sample. Figure 4(a) shows transmission amplitudes for propagation along the ΓX direction of the triangular lattice. A well-defined gap is observed between 3800 and 5800 Hz. Again a simple calculation of the frequency of the gap center is given by arguments similar to those presented for the square lattice resulting in

$$f_c = \frac{v}{a\sqrt{3}}, \tag{5}$$

which predicts a center gap frequency for $a = 3.7$ cm of 5305 Hz.

Figure 4(b) shows the transmitted amplitudes for propagation along the ΓJ direction of the triangular lattice. There is no clearly defined band gap, only a suppression of the transmitted amplitude that begins at 5000 Hz and continues through the highest frequencies measured. As for the ΓM direction of the square lattice, the phase data are more indicative of the exact location of the band gap.

To obtain valid data with the impulse response technique requires the use of time windowing of the raw data to exclude spurious reflections from objects other than the sample under test. The first unwanted reflections in the experiment described here came from the holder used to affix the cylindrical rods in position. In an experimental series exploring the propagation along a given direction, the holder was always left in position, even in the case of no rods, so that differences in the Fourier spectra would be solely due to the addition of the scattering cylindrical rods. Series of experiments typically consisted of measuring a reference wave form with no sample followed by a wave form for transmission through 1 row of rods, then 2 rows, etc. The earliest unwanted reflections from the holder can arrive as early as 2 ms after the arrival of the direct pulse. The effect of these reflections can be eliminated by choosing a very short time window with the consequential reduction in frequency resolution. In analyzing the data the time window was chosen as a compromise between desired frequency resolution and acceptable noise due to spurious reflections.

The results presented thus far exploit the amplitude data obtained by Fourier analysis of the impulse data. Because the signal recorded by the microphone is directly proportional to the pressure amplitude of the acoustic wave, the corresponding phase data can be used to derive the phase velocity of the acoustic wave at each frequency and hence to determine the acoustic dispersion relation. The phase data can also be used as a more sensitive marker of the presence of a band gap than the amplitude data, particularly when the band gap is small. This determination is accomplished by locating the frequency intervals over which the phase data indicate anomalous dispersion.

The use of phase data to determine the gap positions is illustrated by the results plotted in Fig. 5. Figure 5(a) shows the amplitude data extracted from the two time-domain wave forms of Fig. 2 after truncation with a short time window of 2.5 ms. Figure 5(b) plots the corresponding relative phase delay at each frequency. The relative phase data are found from the transmission function obtained by dividing the complex Fourier transform of the sample time-domain wave form by that of the reference. The phase of the complex transmission function is the relative phase delay of the wave traveling through the scattering array compared to transmission through air. The phase delay for normal dispersion has a negative slope as expected, whereas for frequencies in the band gap, where transmission is forbidden, the phase exhibits anomalous dispersion with positive slope. The anomalous dispersion serves as a clearer indicator of the presence of the band gap than the suppression of the amplitude alone. For large band gaps the extent of the gap is clear in both amplitude and phase as shown by Fig. 5(a) and (b), respectively. However, in cases in which there is no clear gap in the amplitude data, such as that shown in Fig. 4(b) for propagation along the ΓJ direction of the triangular lattice, the phase data

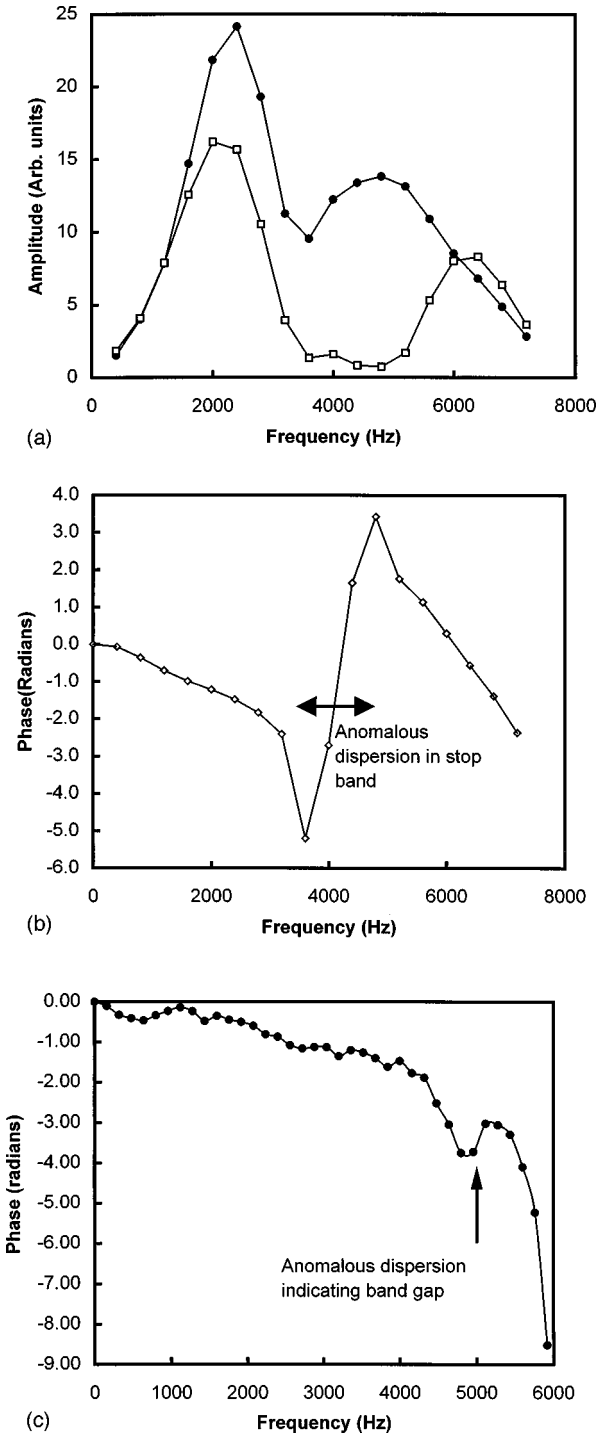

FIG. 5. (a) Fourier amplitude transmitted through 6 rows of rods along the ΓX direction of the square lattice (curve with open squares). The Fourier components in the direct pulse with no sample is represented by the curve with filled circles. The data are the same as for Fig. 3(a) only with a shorter time window of 2.5 ms to reduce the effect of reflections. (b) The phase delay data for propagation along the ΓX direction showing the anomalous dispersion of the phase within the band gap. (c) The phase delay for propagation along the ΓJ direction of the triangular lattice in which the band gap, although small, is again clearly indicated by the same anomalous dispersion characteristic.

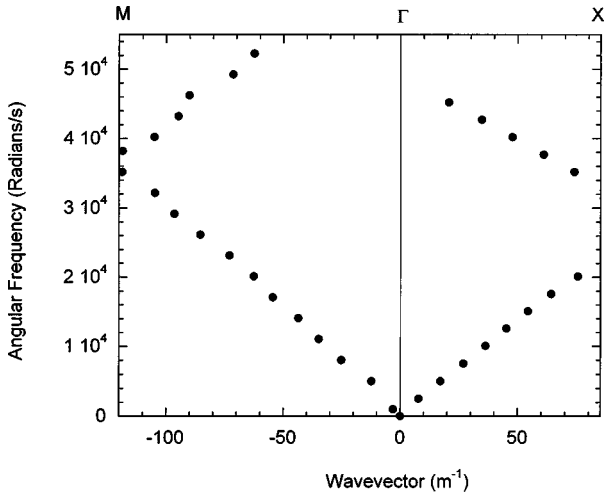

FIG. 6. The acoustic dispersion relation for propagation along the ΓX and ΓM directions in the square lattice. The data are represented in the reduced zone scheme in which the bands are folded back to lie within the first Brillouin zone.

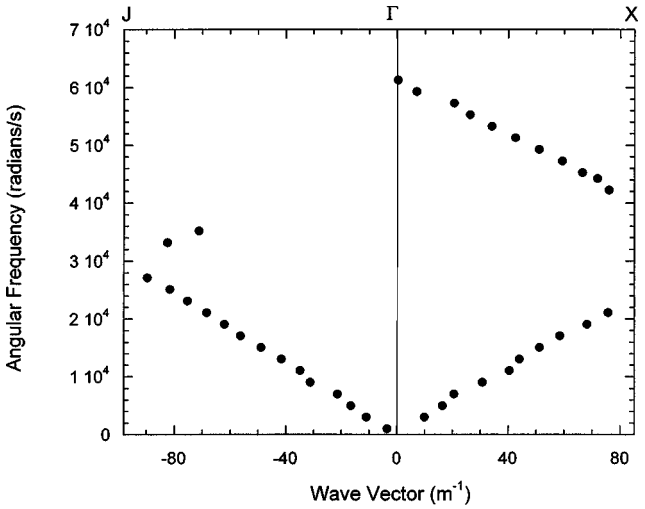

FIG. 7. The acoustic dispersion relation for propagation along the ΓX and ΓJ directions in the triangular lattice. The data are represented in the reduced zone scheme in which the bands are folded back to lie within the first Brillouin zone.

can prove more insightful. Figure 5(c) shows the phase data corresponding to the amplitude data of Fig. 4(b). As shown in the figure, there is a clear anomalous dispersion signature indicative of the presence of a gap. Note that to successfully resolve the small band gap in this case required higher frequency resolution which was achieved by the use of a larger time window and concomitantly noisier data.

More importantly the phase data can be used to determine the dispersion relation for acoustic waves propagating in the array. The phase velocity of acoustic waves, $v(f)$, at each frequency, f, can be recovered from the experimental phase data using the relation

$$v(f)=\frac{v_0}{v_0\phi/2\pi fL+1}, \tag{6}$$

where v_0 is the speed of sound in air, ϕ is the phase delay, and L is the thickness of the sample. Because the phase velocity is related to the angular frequency, ω, and wave vector, k, by

$$v(f)=\frac{\omega}{k}, \tag{7}$$

it is possible to determine the dispersion relation, ω vs k, for the acoustic waves. The experimentally determined dispersion relation for propagation along the high symmetry directions of the square lattice is shown in Fig. 6. The right hand side of the figure shows dispersion along the ΓX direction and the left hand sections shows dispersion along ΓM. The plot makes use of the reduced zone scheme in which the data for wave vectors beyond the zone edge, $k_{\mathrm{BZ}}=\pi/a$, are folded back to lie within the first Brillouin zone. A comparable plot for propagation along the high symmetry directions of the triangular lattice is shown in Fig. 7. In both cases the dispersion results are in close agreement with theoretical calculations for the band structures of these samples.[20]

In conclusion, the experiments on two-dimensional periodic samples show that it is possible both to determine the frequencies of the acoustic stop bands and to measure the acoustic dispersion relation for propagation in a two-dimensional scattering array. The continuation of this experimental technique to three-dimensional samples that exhibit a stop band in all propagation directions is of particular interest. From the point of view of finding applications of acoustic band gap systems it is important to realize that for two-dimensional arrays the predicted stop band exists only for propagation in a plane perpendicular to the rods and containing the speaker and the microphone. At sufficiently steep angles above and below this plane the periodicity of the array is not correct to maintain the stop band. The absence of a stop band for out-of-plane propagation means that for most practical applications a simple two-dimensional array will be of limited value. For strong acoustic suppression either three-dimensional periodic arrays with stop bands in all propagation directions are necessary, or the judicious use of a combination of two-dimensional arrays and guided waves will be required such as that described recently for electromagnetic waves.[21] This work demonstrates that the impulse response technique can serve as an important characterization tool for such samples.

ACKNOWLEDGMENT

This work was supported by a Cottrel College grant from the Research Corporation.

[1] S. John, Phys. Rev. Lett. **58**, 2486 (1987).
[2] S. John and J. Wang, Phys. Rev. Lett. **64**, 2418 (1990).
[3] S. John and J. Wang, Phys. Rev. B **43**, 12772 (1991).
[4] M. M. Sigalas, J. S. McCalmont, K.-M. Ho, and G. Tuttle, Appl. Phys. Lett. **68**, 3525 (1996).
[5] E. R. Brown, C. D. Parker, and E. Yablonovitch, J. Opt. Soc. Am. B **10**, 404 (1993).
[6] R. D. Meade, A. Devenyi, J. D. Joannopoulos, O. L. Alerhand, D. A. Smith, and K. Kash, J. Appl. Phys. **75**, 4753 (1994).
[7] E. Yablonovitch, Phys. Rev. Lett. **58**, 2059 (1987).
[8] M. S. Kushwaha, P. Halevi, L. Dobrzynski, and B. Djafari-Rouhani, Phys. Rev. Lett. **71**, 2002 (1993).

[9] M. Sigalas and E. N. Economou, Solid State Commun. **86**, 141 (1993).
[10] M. S. Kushwaha, P. Halevi, G. Martinez, L. Dobrzynski, and B. Djafari Rouhani, Phys. Rev. B **49**, 2313 (1994).
[11] M. M. Sigalas, J. Acoust. Soc. Am. **101**, 1256 (1997).
[12] M. S. Kushwaha and P. Halevi, J. Acoust. Soc. Am. **101**, 619 (1997).
[13] M. M. Sigalas and E. N. Economou, Europhys. Lett. **36**, 241 (1996).
[14] W. Robertson, G. Arjavalingam, R. D. Meade, K. D. Brommer, A. M. Rappe, and J. D. Joannopoulos, Phys. Rev. Lett. **68**, 2023 (1992).
[15] R. Martinez-Sala, J. Sancho, J. V. Sanchez, V. Gomez, J. Llinares, and F. Meseguer, Nature (London) **378**, 241 (1995).
[16] M. S. Kushwaha, Appl. Phys. Lett. **70**, 3218 (1997).
[17] P. R. Villeneuve and M. Piche, Phys. Rev. B **46**, 4969 (1992).
[18] M. Plihal and A. A. Maradudin, Phys. Rev. B **44**, 8565 (1991).
[19] R. D. Meade, K. D. Brommer, A. M. Rappe, and J. D. Joannapoulos, Appl. Phys. Lett. **61**, 495 (1992).
[20] M. S. Kushwaha, private communication.
[21] J. S. Foresi *et al.*, Nature (London) **390**, 143 (1997).

Potential for the presence of additional stop bands in the modal response of regularly ribbed cylinders

G. Maidanik and K. J. Becker
David Taylor Model Basin (NSWC/CD), 9500 MacArthur Boulevard, West Bethesda, Maryland 20817-5700

(Received 30 December 1997; accepted for publication 14 May 1998)

When, in a given frequency band, the magnitude of the line impedance of the ribs approaches and exceeds the line impedance of a moderately damped shell, to which the ribs are attached, a stop band emerges. This stop band need not coincide with any of the usual series of stop bands that are associated with the spacing regularity of the ribs. In this sense, this stop band is dubbed ''additional.'' The enhancement in the magnitude of the line impedance of the ribs may be caused by a resonance; e.g., if the line impedance of the ribs is commensurate with that of a sprung mass and the loss factor of this dynamic system is low, at resonance, the magnitude of the line impedance of the ribs is relatively high. This resonance enhancement in the line impedance of the ribs may contribute an additional stop band centered about the resonance frequency of the resonant ribs. Examples of additional stop bands in the response of regularly ribbed cylinders are cited and displayed in this paper. [S0001-4966(98)06208-0]

PACS numbers: 43.20.Tb, 43.20.Ks, 43.20.Bi [DEC]

INTRODUCTION

In a recent paper, computations were displayed of the modal response of regularly ribbed cylinders.[1] In this reference the many phenomena in the response of panels, hybrid cylinders and natural cylinders were investigated; e.g.,

(1) The surface admittances of uniform shells were formulated and numerically investigated.

(2) The role of fluid loading on these admittances were also formulated and numerically investigated.

(3) The relationship between the three forms of a shell were discussed and commonalities and differences were emphasized. (A hybrid cylinder is defined in Ref. 1 to designate a cylindrical shell from which curvature effects are artificially removed. This removal renders the surface impedance of the hybrid cylinder commensurate with that of a panel. A natural cylinder is one for which this removal is not rendered: the surface impedance of a natural cylinder accounts for curvature effects.[2])

(4) The dispersive loci were exhibited and investigated. The membrane free waves in the natural cylinders were defined and their characteristics were contrasted with those of the flexural free waves which exist in all the three forms of the shell considered.

(5) The influence of damping, the mechanical damping and, indirectly, the radiative damping, was investigated.

(6) The ribs were defined in simple terms. However, in this definition only line impedances of ribs that were either mass or stiffness controlled were available. The differences between these controlled forms were also considered.

(7) The phenomena of aliasing and pass and stop bands were formulated, discussed, and displayed. It was argued that these phenomena are manifest in the drive in lieu of the ribs. The first phenomenon, that of aliasing, resides completely in the modal drive in lieu of the ribs. This phenomenon is directly related to the equi-separations between adjacent ribs and is not predicted on the interactions among the ribs via the shell. On the other hand, the second phenomenon, that of pass and stop bands, arises in direct consequence of the interactions among the ribs via the shell; in the absence of these interactions this phenomenon is absent. When the aliasing phenomenon resides in the modal drive in lieu of the ribs and the interactions among the ribs via the shell are accounted for, the phenomenon of pass and stop bands is present in this drive[3] (cf. Appendix).

(8) The computations were performed in two Fourier conjugate axial domains; these conjugate axial domains comprise the k domain and the x domain. The computations in the first domain were displayed on the $\{(ak),(\omega/\omega_c)\}$ plane and in the second on the $\{(x/a),(\omega/\omega_c)\}$ plane, where (x/a) and (ak) are a Fourier conjugate pair. In this format, a pair of corresponding displays are complementary. It was noted that situations exist in which the interpretation of data was more readily conducted in one domain than in another, even though the two domains are Fourier conjugate domains. This proved particularly relevant to the interpretation of pass and stop bands. In the x domain a pass band is merely a frequency band in which the transmission of vibration from a localized external drive position to a localized observation position that is removed a few bays away, hardly encounters more attenuation than is indicated by the distributed damping on an unribbed shell. On the other hand, a stop band in a similar geometrical situation, will indicate a more severe attenuation. A Fourier transformation of the (n)th modal drive in lieu of the ribs in the k domain $P_{sn}(k,\omega)$ into its counterpart $p_{sn}(x,\omega)$ in the x domain may thus be efficacious. In Ref. 1 the transformation was carried out by means of a double-sum technique.[4] This technique is particularly, but not exclusively, useful with respect to the phenomenon of pass and stop bands of regularly ribbed panels and/or cylinders. The exclusivity is with respect to the regularity of the spacings between adjacent ribs.

It is to be assumed that the reader is familiar with the material presented in Ref. 1. This familiarity is assumed not only with respect to the items just stated, but, in particular,

with respect to the format in which the displays are presented and interpreted. The story told in this paper is an extension to the story presented in Ref. 1. This extension, however, relates merely to the description of the ribs. Whereas in Ref. 1 the modal line impedance $Z_{sn}(\omega)$ of the ribs was either mass controlled or stiffness controlled, in the present paper the modal line impedance $Z_{sn}(\omega)$ of the ribs is allowed to transit, as a function of frequency, from mass controlled to stiffness controlled. The region of transition occupies a narrow frequency band that is centered at a modal resonance frequency $(\omega=\omega_n)$. Through that transition the magnitude of the modal line impedance of the ribs is significant compared with the ''modal line impedance'' of the shell to which the ribs are attached. It is convenient to express the modal line impedance $Z_{sn}(\omega)$ of the ribs in the dual and simplified forms

$$Z_{sn}(\omega)\simeq Z_s(\omega)=(i\omega M)\begin{cases}A(\omega/\omega_0) & (1a)\\ A'(\omega/\omega_0), & (1b)\end{cases}$$

where M is a line mass, the factor $A(\omega/\omega_0)$ is a resonance bearing factor, the factor $A'(\omega/\omega_0)$ is a ''false'' resonance bearing factor and, finally, it is noted that the modal line impedance is assumed, for simplicity sake, to be independent of the mode index (n). Specifically

$$A(\omega/\omega_0)=[e_0(\omega/\omega_0)+\alpha(\omega/\omega_0)^2(1-i\eta_0)]\times[e_0(\omega/\omega_0)-(\omega/\omega_0)^2(1-i\eta_0)]^{-1}, \quad (2a)$$

$$A'(\omega/\omega_0)=\mathrm{Re}\{A(\omega/\omega_0)+(2)^{-1/2}\ \mathrm{Im}\ A(\omega/\omega_0)\}\times\{U[(\omega_0/\omega_c)-(\omega/\omega_c)]-U[(\omega/\omega_c)-(\omega_0/\omega_c)]\}, \quad (2b)$$

where

$$e_0(\omega/\omega_0)=\exp[1-(\omega/\omega_0)^{\gamma}],\qquad \alpha=[1+(\beta\omega/\omega_c)^2]^{-1},\quad \omega_0^2=(K_0/M), \quad (3)$$

and (ω_0) is the resonance frequency, (η_0) is a loss factor, (K_0) is a line stiffness parameter and (γ) and (β) are chosen constants.[3] A standard rib is to be defined

$$(M/mb)=0.2,\quad (\omega_0/\omega_c)=2.5\times10^{-1},\qquad \eta_0=3\times10^{-1},\quad \gamma=8,\quad \beta=5, \quad (4)$$

where (b) is the separation distance between adjacent ribs, (ω_c) is the critical frequency of the flexural waves with respect to the fluid speed of sound (c), and (m) is the surface mass of the plating of the shell.[1,3] The computations to be carried out in this paper are based on the standard rib stated in Eq. (4). The factor $A(\omega/\omega_0)$ is commensurate with a point reacting rib the line impedance of which approximately characterizes a ''sprung mass.'' [5,6] With $A(\omega/\omega_0)$, however, the transition, with increasing frequency, from mass controlled to stiffness controlled is sharper and the magnitude of the line impedance in the stiffness controlled region is sustained as compared with a conventional sprung mass.[3] In the transition region, the line impedance assumes, under this factor, a resistance controlled form that substantially duplicates that of a conventional sprung mass; in this transition region the line impedance is resistance controlled (real) and of a magnitude that is inversely proportional to the loss factor.[3,5,6] The resistance controlled region spans a narrow frequency band centered about the resonance frequency (ω_0). The factor $A'(\omega/\omega_0)$ duplicates the factor $A(\omega/\omega_0)$ in the mass and stiffness controlled regions; it differs in the transition region just discussed. Whereas $A(\omega/\omega_0)$ in Eq. (1a) renders the line impedance $Z_s(\omega)$ real (resistance controlled) at and in the vicinity of the resonance frequency (ω_0), $A'(\omega/\omega_0)$ in Eq. (1b) renders the line impedance $Z_s(\omega)$ imaginary (reactive) at and in the vicinity of the resonance frequency (ω_0). The transition in the line impedance in Eq. (1b), from moderate mass controlled to moderate stiffness controlled is abrupt.[3] Nonetheless, the magnitude of the line impedance, as stated in Eqs. (1), is significant, at and in the vicinity of the resonance frequency, compared with the magnitude of the line impedance of the shell to which the rib is attached. The duality stated in Eqs. (1) is merely a device to facilitate an examination of the decisive role that a resistance controlled line impedance for the ribs may play in the control of the modal response of the shell when the ribs resonate. A resonating rib, in this case, may provide at resonance a damping mechanism for the shell. In Eq. (1b) this damping mechanism is made artificially absent without changing appreciably the magnitude of the line impedance at the resonance frequency (ω_0). The examination is, thereby, facilitated by contrasting data obtained inserting Eq. (1a) with data obtained inserting Eq. (1b).[3]

Reiterating, the present paper extends the data presented in Ref. 1 to situations in which the ribs are resonating in a frequency region defined by the resonance frequency (ω_0). The line impedance of these ribs is mass controlled below and is stiffness controlled above the resonance (ω_0). At and in the vicinity of this resonance frequency, the line impedance of these ribs possesses a magnitude that is significant compared with that of the line impedance of the shell to which the ribs are attached. Moreover, provision is made to investigate whether the resistance controlled line impedance of the ribs at resonance influences the modal response data. The provision is rendered by artificially assigning a corresponding line impedance to the ribs that lacks the resistance controlled character.[3]

I. MODAL RESPONSE OF A REGULARLY RIBBED CYLINDER IN WHICH RIBS RESONATE

As Eqs. (1) and (2) attest, at resonance ribs present a line impedance of significant magnitude to the shell at each location of a rib. As was previously shown, when the magnitude of the line impedance of a rib, at a given frequency, approaches and exceeds the magnitude of the line impedance of a moderately damped shell to which the ribs are attached, the vibrational propagation away from the position of a line drive is substantially attenuated, whether the frequency matches a pass or an amber band.[7] It is this increase in attenuation that is here identified with an additional stop band; it is an increase in attenuation of propagation that substantially exceeds that which exists on a moderately damped ribless shell that is dubbed a stop band (cf. Appendix). The additional stop band so defined occurs at a frequency and possesses a bandwidth that is commensurate with the reso-

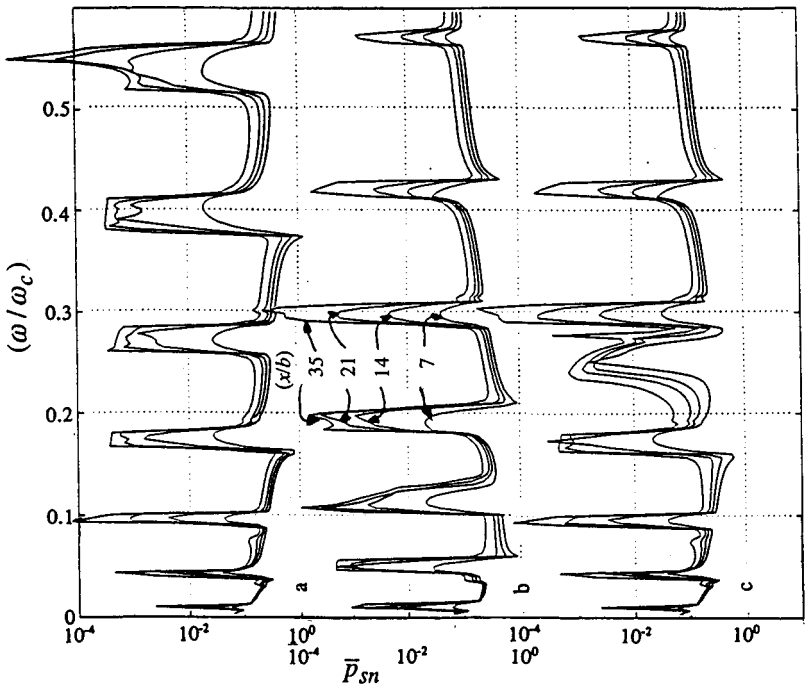

FIG. 1. Normalized modal drive $\overline{p}_{sn}(x,\omega)$ in lieu of ribs on a **hybrid** cylinder as a function of the normalized frequency (ω/ω_c) at the positions $(x/b)=7$, 14, 21, and 35. (a) Mass controlled ribs $[(\omega_0/\omega_c)=10]$; (b) stiffness controlled ribs $[(\omega_0/\omega_c)=10^{-2}]$; (c) $(\omega_0/\omega_c)=2.5\times10^{-1}$.

nance frequency and the bandwidth in which the line impedance of the ribs reigns supreme. Chandiramani recently reported a similar finding, except that the high magnitude in the line impedance of the ribs results from the introduction of a rotational inertia into the motion of the ribs.[8] This rotational inertia significantly enhanced the magnitude of the line impedance of the ribs in a regularly ribbed shell. This enhancement occurs at a specific resonance frequency (ω^0). The result of this enhancement is to introduce an additional stop band at (ω^0), especially if this resonance frequency is not coincident with a stop band due to the regularity of the ribs on the shell.[8] With this very definition, were the resonance of the ribs such as to bring a substantial diminution in the line impedance of the ribs at resonance so that this line impedance becomes insignificant compared to the line impedance of the shell, an additional pass band may occur at and in the vicinity of that resonance frequency. This phenomenon will be especially noticeable if this resonance frequency falls within an otherwise stop or amber band (cf. Appendix). An additional pass band of this kind is not discussed herein. Here the resonance of the ribs, as already stated, brings about a substantial increase in the line impedance of the ribs resulting in an additional stop band. This additional stop band is particularly conspicuous if the resonance frequency of the ribs falls within an otherwise pass or amber band. In the present paper, an emergence of such an additional pass band is investigated à la Ref. 1. In this vein the phenomenon is investigated computationally and is exhibited in the drive in lieu of the ribs. Indeed, the additional pass band is highlighted by comparing with results obtained in Ref. 1, which are computed in the absence of resonating ribs, to those computed herein, which are computed for resonating ribs, as defined in Eqs. (1)–(4). In this paper, the results displayed in Ref. 1 that pertain to ribs that are moderately mass controlled are obtained by changing the standard normalized resonance frequency (ω_0/ω_c) from 2.5×10^{-1} to 10. Similarly, the results displayed in Ref. 1 that pertain to ribs that are moderately stiffness controlled are obtained by changing the standard normalized resonance frequency (ω_0/ω_c) from 2.5×10^{-1} to 10^{-2}. The normalized modal drives $\overline{p}_{sn}(x,\omega)$ in lieu of the ribs on a hybrid and a natural cylinder as a function of the normalized frequency (ω/ω_c) for the normalized axial distances $(x/b)=7$, 14, 21, and 35 are presented in Figs. 1 and 2, respectively. To accentuate the stop bands, the stop bands in these and in subsequent figures are featured as prominences. This is accomplished by a reversal to a common practice: The low values in $\overline{p}_{sn}(x,\omega)$ are set atop the high values in this quantity. In Figs. 1 and 2 the mode index (n) is set to the standard value of zero and the fluid loading parameter ϵ_c is set to the standard value of 10^{-2}, where

$$\epsilon_c=[(\rho c)/(\omega_c m)], \tag{5}$$

and (ρ) is the fluid density. It is noted that changes in the fluid loading parameter are instituted here, as in Ref. 1, through changes in the density (ρ) only. The emergence of an additional stop band when the standard ribs, as defined in Eq. (4), are employed is clearly discernible in Figs. 1(c) and 2(c); the additional stop band is appropriately located at and in the vicinity of the resonance frequency (ω_0) of the ribs. It is noted that below that resonance frequency, the displays are governed by a moderate line impedance that is mass controlled and above that resonance by a moderate line impedance that is stiffness controlled. This observation is confirmed in Fig. 1 by Fig. 1(a) and (b), and in Fig. 2 by Fig. 2(a) and (b). Figure 2 is repeated in Fig. 3 except that the standard mode index (n) of zero is changed to unity. Except for the very low frequency range, only minor differences are noted between Figs. 2 and 3. In particular, the additional stop band at $(\omega/\omega_0)\simeq1$, remains loud and clear. The influence of

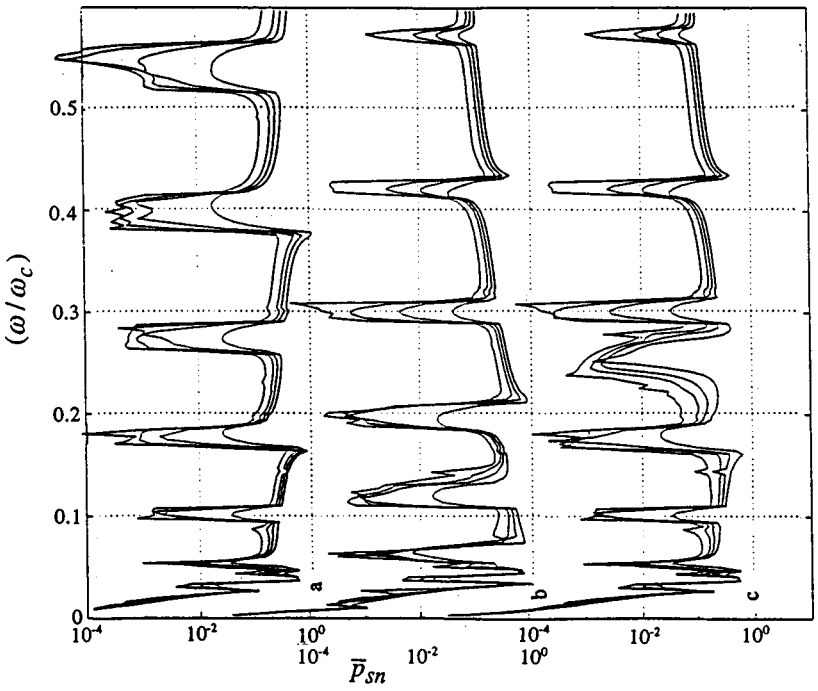

FIG. 2. As in Fig. 1 except for the change to a **natural** cylinder. (a) Mass controlled ribs $[(\omega_0/\omega_c)=10]$; (b) stiffness controlled ribs $[(\omega_0/\omega_c)=10^{-2}]$; (c) $(\omega_0/\omega_c)=2.5\times10^{-1}$.

fluid loading on the additional stop band at $(\omega/\omega_0)\simeq 1$ is depicted in Fig. 4. Figure 4(b) is identical to Fig. 2(c), both with the standard fluid loading parameter $\epsilon_c=10^{-2}$. In Fig. 4(a) the fluid loading parameter ϵ_c is changed from the standard value of 10^{-2} to 10^{-4} and in Fig. 4(c) to 10^{-1}. The mollifying influence that an increase in fluid loading has on any response phenomenon is recalled and is clearly discernible in Fig. 4; the influence on the additional stop band is of particular interest in this paper.

Figure 5 repeats Fig. 2 except that the standard factor $A(\omega/\omega_0)$ in Eqs. (1a) and (2a) is replaced by the factor $A'(\omega/\omega_0)$ in Eqs. (1b) and (2b). The additional stop band at $(\omega/\omega_0)\simeq 1$ is substantially duplicated; the additional stop band in Fig. 5(c) is sharper and more pronounced than the corresponding one in Fig. 2(c). One may argue that the mollifying influence of the damping, that is associated with the resistance controlled line impedance of the ribs, is responsible for that difference. Indeed, Fig. 6, which repeats Fig. 4 except for the change from $A(\omega/\omega_0)$ to $A'(\omega/\omega_0)$, shows that the mollifying influence of the fluid loading on the additional stop band renders Fig. 6(c), in this respect, more commensurate with Fig. 4(c), whereas Fig. 6(a) is, in this

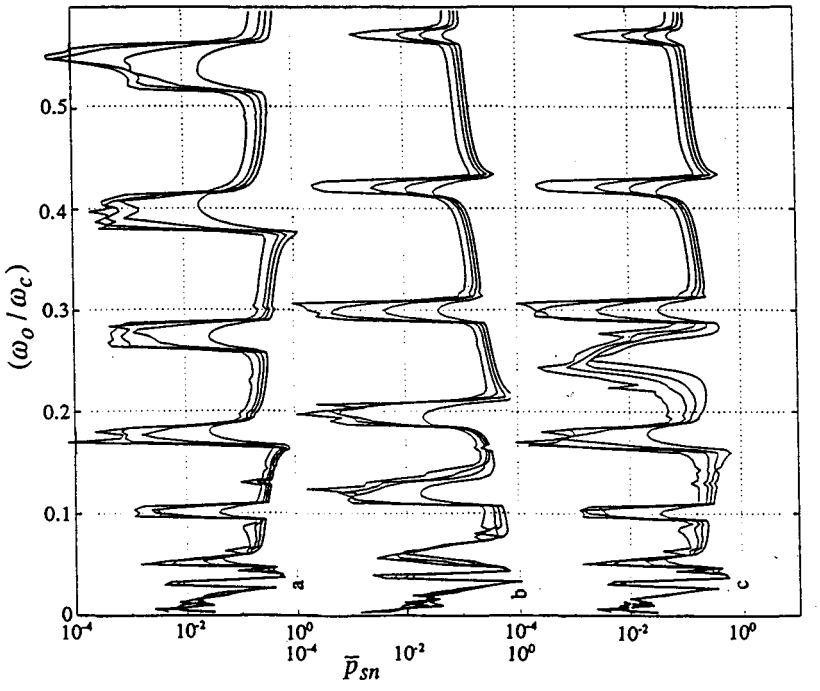

FIG. 3. As in Fig. 2 except for the change from the standard mode index (n) of zero to unity. (a) Mass controlled ribs $[(\omega_0/\omega_c)=10]$; (b) stiffness controlled ribs $[(\omega_0/\omega_c)=10^{-2}]$; (c) $(\omega_0/\omega_c)=2.5\times10^{-1}$.

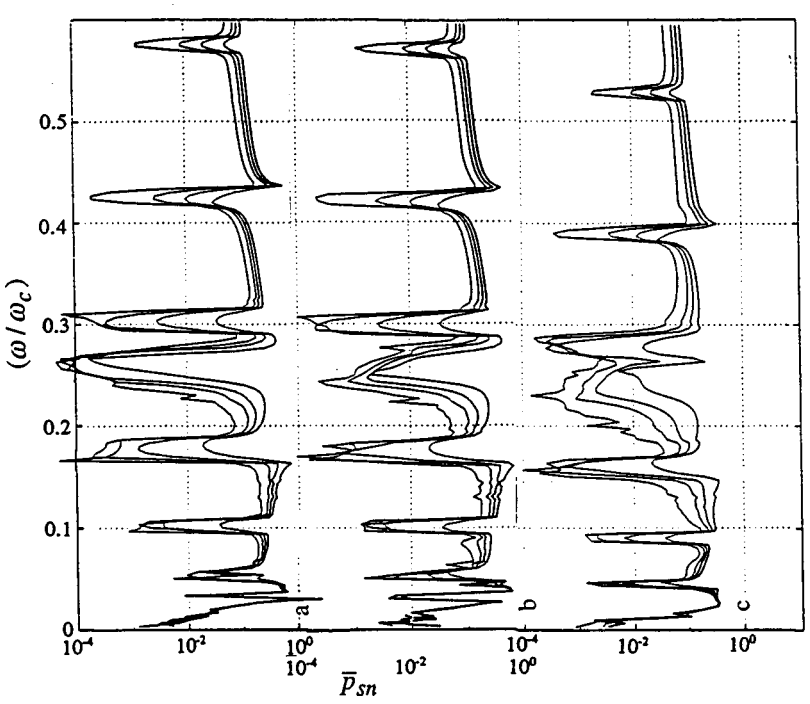

FIG. 4. As in Fig. 3(c) except for a change in the fluid loading parameter (ϵ_c). (a) (ϵ_c) is decreased from 10^{-2} to 10^{-4}; (b) unchanged [$\epsilon_c = 10^{-2}$]; (c) (ϵ_c) is increased from 10^{-2} to 10^{-1}.

respect, even less commensurate with Fig. 4(a) than is Fig. 6(b) with Fig. 4(b). It is noted that the mollifying effects of the fluid loading are related not merely to the reactive portion, but also to the dissipation provided by radiation. In this manner, the resemblance of the additional pass band in Figs. 6(c) and 4(c) may be explained. Nonetheless, it is suggested that the emergence of the additional stop band, as such, is related more to the high magnitude that the line impedance of the ribs presents to the shell than to the detailed characteristic of this line impedance; e.g., whether it is resistance controlled or reactive.[3,7,8]

II. COMPLEMENTARITY IN THE MODAL RESPONSE OF A REGULARLY RIBBED CYLINDER IN WHICH RIBS RESONATE

It was argued in Refs. 1 and 3 that there is advantage in complementing displays in two Fourier conjugate domains; the (axial) x-domain and the (axial) k domain.[1,3] Figures 1–6 depict the drive $\bar{p}_{sn}(x,\omega)$ in lieu of the ribs on the $\{(x/a),(\omega/\omega_c)\}$ plane, with four values of (x/a) chosen discretely [cf. Fig. 1(b)]. Can displays pertaining to the normalized drive $\bar{P}_{sn}(k,\omega)$ in lieu of the ribs be plotted on the

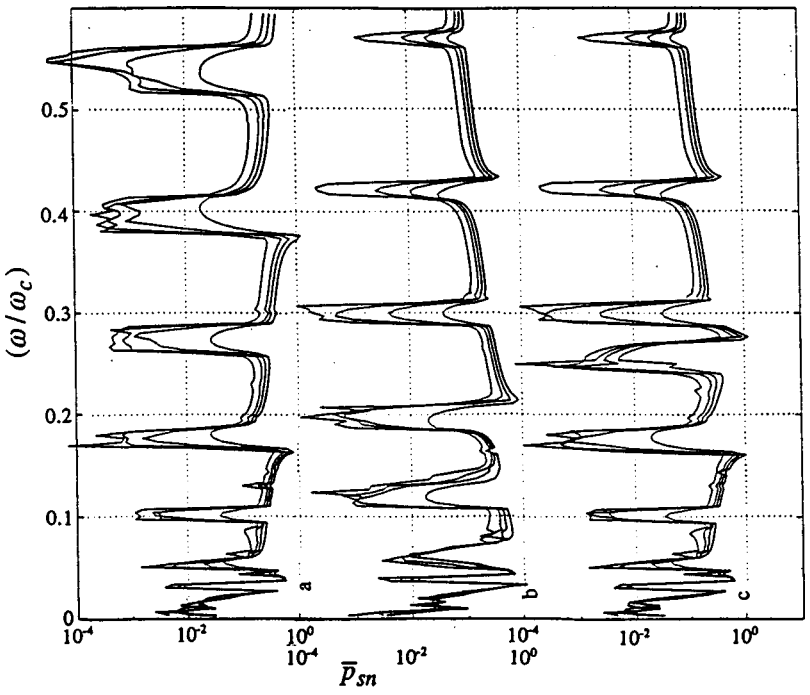

FIG. 5. As in Fig. 2 except that $A(\omega/\omega_0)$ [Eq. (2a)] is replaced by $A'(\omega/\omega_0)$ [Eq. (2b)]. (a) Mass controlled ribs [$(\omega_0/\omega_c)=10$]; (b) stiffness controlled ribs [$(\omega_0/\omega_c)=10^{-2}$]; (c) $(\omega_0/\omega_c)=2.5\times10^{-1}$.

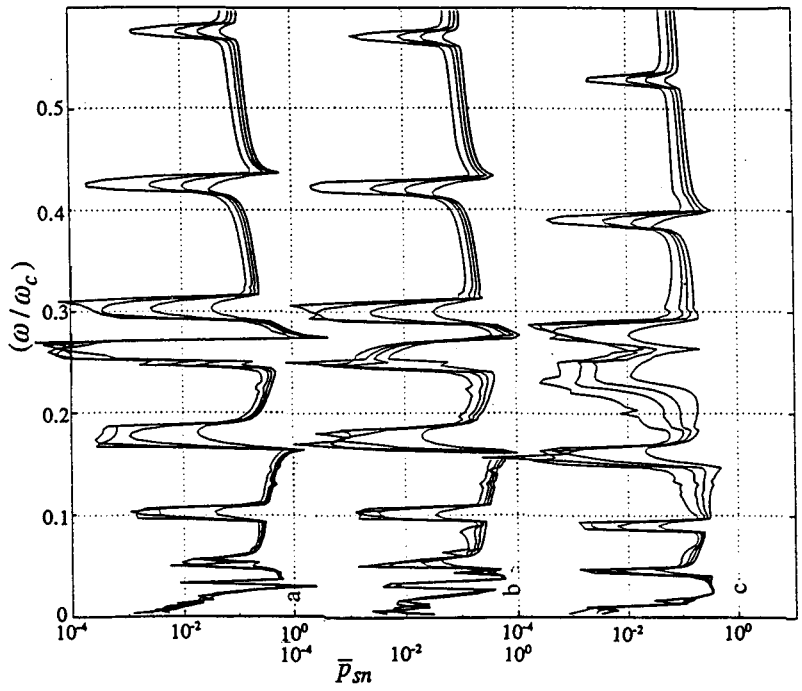

FIG. 6. As in Fig. 5(c) except that $A(\omega/\omega_0)$ [Eq. (2a)] is replaced by $A'(\omega/\omega_0)$ [Eq. (2b)] and a change in the fluid loading parameter (ϵ_c). (a) (ϵ_c) is decreased from 10^{-2} to 10^{-4}; (b) unchanged [$\epsilon_c = 10^{-2}$]; (c) (ϵ_c) is increased from 10^{-2} to 10^{-1}.

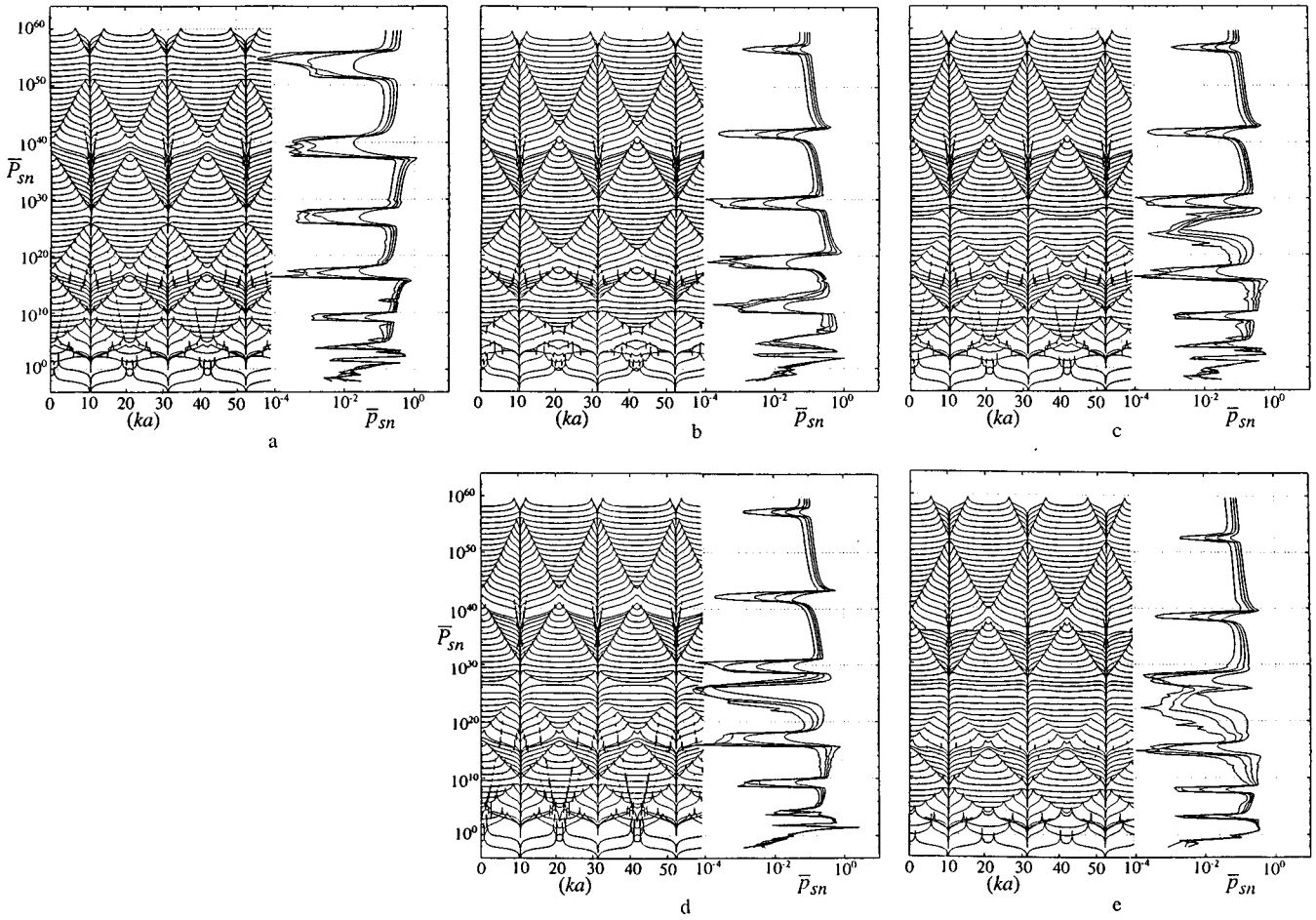

FIG. 7. Complementarity pertaining, respectively, to Fig. 2(a), (b), and (c) and Fig. 4(a) and (c). (a) Mass controlled ribs [$(\omega_0/\omega_c) = 10$]; (b) stiffness controlled ribs [$(\omega_0/\omega_c) = 10^{-2}$]; (c) $(\omega_0/\omega_c) = 2.5 \times 10^{-1}$; (d) as in (c) except that (ϵ_c) is decreased from 10^{-2} to 10^{-4}; (e) as in (c) except that (ϵ_c) is increased from 10^{-2} to 10^{-1}.

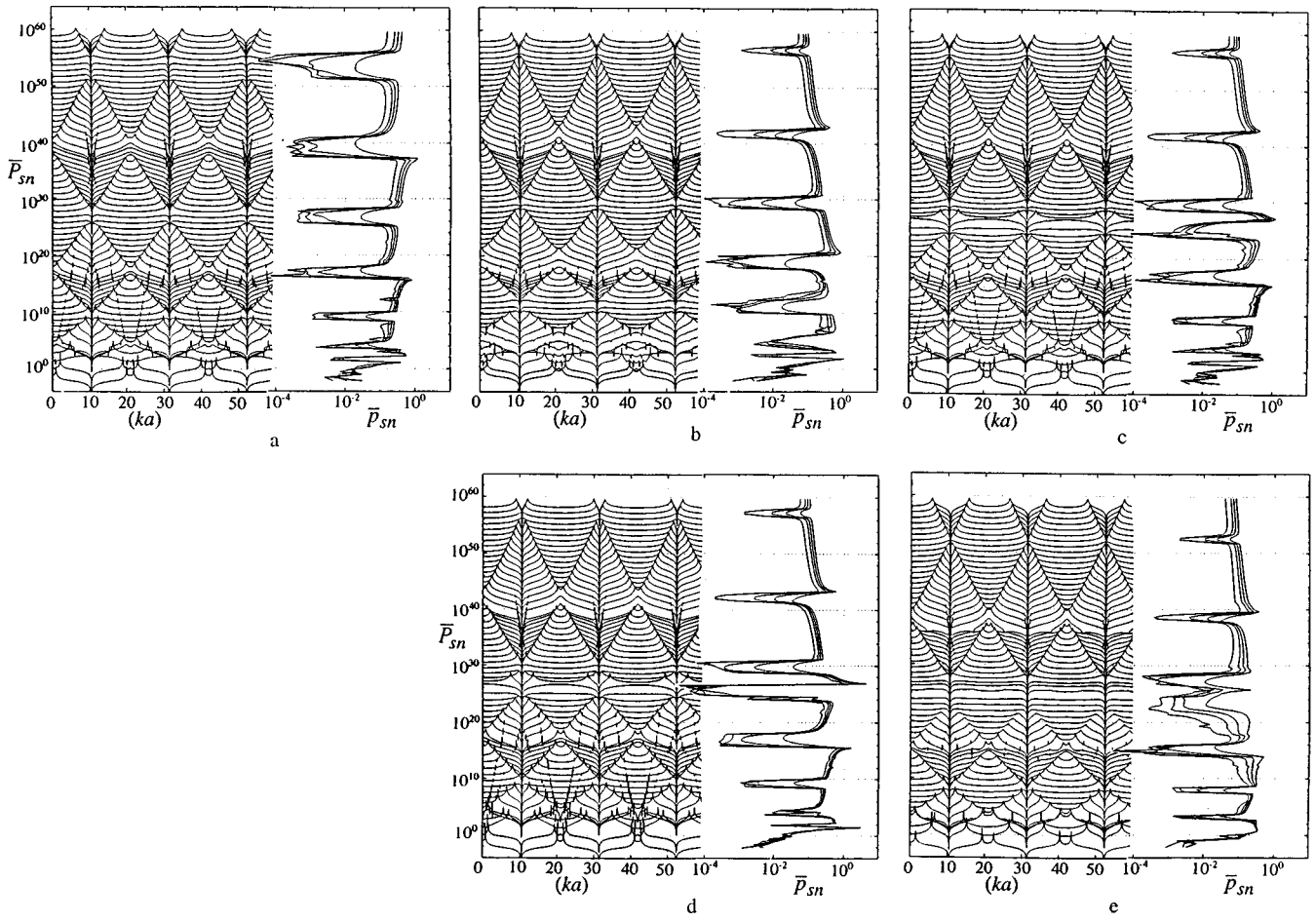

FIG. 8. Complementarity pertaining, respectively, to Fig. 5(a), (b), and (c) and Fig. 6(a) and (c). (a) Mass controlled ribs $[(\omega_0/\omega_c)=10]$; (b) stiffness controlled ribs $[(\omega_0/\omega_c)=10^{-2}]$; (c) $(\omega_0/\omega_c)=2.5\times10^{-1}$; (d) as in (c) except that (ϵ_c) is decreased from 10^{-2} to 10^{-4}; (e) as in (c) except that (ϵ_c) is increased from 10^{-2} to 10^{-1}.

$\{(ak),(\omega/\omega_c)\}$ plane and be complemented with those presented in the format of Figs. 1–6? In particular, can these complemented pairs of figures include the emergence of the additional stop band? The answer is, of course, in the affirmative.[1,3] Displays on the $\{(ak),(\omega/\omega_c)\}$ plane are usually presented in a waterfall format; this format is amply explained in Refs. 1 and 3. The frequency waterfall format displays the quantity $\bar{P}_{sn}(k,\omega)$ as a function of (ka) on a stepwise frequency axis, where (a) is the radius of the cylinder. The stepwise frequency axis is to be interpreted in the form: $\bar{P}_{sn}\equiv\log[|P_{sn}\{k,(q+1)\Delta\omega\}|10^q]$. In Figs. 7 and 8 the normalized frequency range spans $(2\omega_r/\omega_c)\leqslant(\omega/\omega_c)\leqslant0.6$ and is, thus, governed by $\Delta(\omega/\omega_c)=0.01$ and $0\leqslant q\leqslant59$, where ω_r is the ring frequency and ω_c is the critical flexural frequency. In these figures, the normalized frequency, on the stepwise frequency axis, is identified by the frequency pseudonym 10^q; e.g., in Fig. 7(a) the position marked 10^{30} locates the origin for the curve of $\bar{P}_{sn}(k,\omega)$ pertaining to the normalized frequency $(\omega/\omega_c)=31\Delta(\omega/\omega_c)=0.31$. In Figs. 7 and 8 the stepwise frequency axis is adapted for the depiction of $\bar{p}_{sn}(x,\omega)$ so that the two superposed displays are rendered compatible; notwithstanding that $\bar{p}_{sn}(x,\omega)$ is more finely distributed in the frequency domain than is the frequency waterfall depicting $\bar{P}_{sn}(k,\omega)$. In this manner the complementarity, between the corresponding pairs of displays, in this side by side format, is achieved. The complemented pairs are depicted in Figs. 7 and 8. In Fig. 7 and the standard factor $A(\omega/\omega_0)$ of Eq. (2a) is employed; in Fig. 8 the factor is changed to $A'(\omega/\omega_0)$ of Eq. (2b). Also Fig. 7(a)–(e) depict computations displayed in Figs. 2(a)–(c) and 4(a) and (c), respectively, and Fig. 8(a)–(e) depict computations displayed in Figs. 5(a)–(c) and 6(a) and (c), respectively. The additional stop band is just as clearly deciphered in $\bar{P}_{sn}(k,\omega)$ as it is in $\bar{p}_{sn}(x,\omega)$. Which one of the complemented pair is the more interpretable is ''in the eyes of the beholder,'' notwithstanding that the availability of both is of interpretive advantage.[1,3]

APPENDIX

The pass bands and stop bands exhibit a decreased and an increased attenuation caused by a constructive and a destructive coherence in the phases of the interactions among the regularly spaced ribs, respectively.[9] Any device that will weaken the interactions and/or the phase coherence will weaken the distinction between the pass and stop bands; adjacent pass and stop bands will then tend to merge into an amber band.[7,9] The attenuation that is associated with amber bands is commensurate with that determined for a model of a ribbed shell from which phase information is removed; e.g.,

as determined in a bay-by-bay energy analysis (EA) or even by statistical energy analysis (SEA).[7] When the damping of the shell and the line impedance of the ribs are moderate, the displays of the characteristics of the pass and stop bands are moderately exhibited; e.g., the attenuation in a pass band is nearly that on a ribless shell and the attenuation in a stop band is substantially higher than in an adjacent amber band. Of course, if the damping in the shell and/or the line impedance of the ribs are light or heavy in the extreme, the displays may not be moderately exhibited.[7] In particular, if the line impedance of the ribs approaches and exceeds the line impedance of the shell, the attenuation in a pass or an amber band may surpass the attenuation in the corresponding moderate amber band and thus become an apparent stop band. When this band is compared to the moderate stop bands on either side, it qualifies as an additional stop band. Similarly, if the line impedance of the ribs becomes negligible compared with the line impedance of the shell, the attenuation in a stop or an amber band may nearly match that of a pass band in a moderate situation. It is within this context that the additional stop and/or additional pass bands are classified. However, in this paper, only situations that pertain to additional stop bands are considered; additional pass bands are not considered herein.

[1] G. Maidanik and K. J. Becker, ''Computation of the modal response of regularly ribbed cylinders,'' J. Acoust. Soc. Am. **101**, 2452–2472 (1997).

[2] G. Maidanik and K. J. Becker, ''Phenomenon of leaky free waves in the modal response of a uniform cylinder,'' J. Acoust. Soc. Am. **102**, 1372–1382 (1997).

[3] G. Maidanik and K. J. Becker, ''Phenomena of aliasing and pass and stop bands in the drive in lieu of ribs on cylinder shells,'' NSWCCD-SIG-96/072-7030 (July 1996).

[4] G. Maidanik and K. J. Becker, ''A double-sum technique for performing a Fourier transformation,'' J. Acoust. Soc. Am. **101**, 2448–2451 (1997).

[5] M. Strasberg and D. Feit, ''Vibration damping of large structures induced by attached small resonance substructures,'' J. Acoust. Soc. Am. **94**, 1814–1815 (1993).

[6] G. Maidanik, ''Power dissipation in a sprung mass attached to a master structure,'' J. Acoust. Soc. Am. **98**, 3527–3533 (1995).

[7] G. Maidanik and J. Dickey, ''Quadratic and energy estimates of the partial response of ribbed panels,'' J. Acoust. Soc. Am. **94**, 1435–1444 (1993); ''Influence of variations in the loss factor of a panel and line impedance of attached ribs,'' J. Acoust. Soc. Am. **94**, 1445–1452 (1993).

[8] K. L. Chandiramani, ''Effects of rib bending on Bloch wave structure of a rib-stiffened plate,'' J. Acoust. Soc. Am. **102**, 3130A (1997).

[9] G. Maidanik and J. Dickey, ''Localization and delocalization in periodic one-dimensional dynamic systems,'' Acustica **73**, 119–128 (1991).

Numerical and experimental study of finite-amplitude standing waves in a tube at high sonic frequencies

L. Elvira-Segura and E. Riera-Franco de Sarabia
Instituto de Acústica, C.S.I.C. Serrano 144, 28006 Madrid, Spain

(Received 28 April 1997; revised 26 March 1998; accepted 20 April 1998)

Finite-amplitude standing waves in an air-filled tube are studied numerically and experimentally. The standing wave is excited at one end of the rigid-walled tube and a rigid cap is assumed at the other end. The one-dimensional nonlinear second order wave equation is solved numerically using a finite element algorithm based on the Bubnov–Galerkin method. Viscous and thermal losses at the walls of the tube are taken into account. An experimental setup is developed for the study of standing waves at high sonic frequencies. The acoustic field is measured along the tube axis with a fine calibrated probe. Experimental data of pressure distributions for the fundamental frequency (9.5 kHz) and the second harmonic (19 kHz) are compared with the numerical results, as a function of the tube length. © *1998 Acoustical Society of America.* [S0001-4966(98)06207-9]

PACS numbers: 43.25.Gf [MAB]

INTRODUCTION

In this paper, an experimental and numerical study of high-frequency sonic standing waves in a rigid-walled tube is presented. Nonlinear effects up to second order are taken into account. Viscous and thermal attenuation at the walls of the tube are also considered.

The experimental study of finite-amplitude effects in rigid-walled, gas-filled closed cavities has generally been restricted to the frequencies in the range of 10 Hz–500 Hz.[1–7] Gaete[8,9] investigated the saturation effect on nonlinear standing waves at 20 kHz; nevertheless, no theoretical validation of these results was presented in his work. Pressure detection at one end of the tube is the typical method used to characterize the acoustic field inside a cavity. However, for high sonic frequencies, the wavelength becomes comparable to the size of commercially available microphones and the acoustic field is therefore affected by this invasive measurement method. In this work, an experimental device for measuring nonlinear standing waves in gases at high frequencies is presented.

The measurement of nonlinear standing waves provides an interesting method for the characterization of gases.[10] High-frequency sound waves would permit the construction of small devices for such characterization. Similarly, the use of high frequencies could be interesting if material and gas properties are being studied for practical applications in macrosonic processes (acoustic agglomeration, defoaming, ultrasonic cleaning,...). These processes often work with frequencies in the range of tenths of kHz.[11]

A second order wave equation is numerically solved to obtain a theoretical description of the acoustic field inside a tube. To solve this equation an original finite element algorithm was developed.[12] This method has proved to give accurate results when it is compared with analytical solutions. In this work, numerical results are compared with experimental data in order to validate the empirical method for measuring nonlinear standing waves in a gas. Reciprocally, the absorption coefficient and the nonlinear parameter can be determined from the measurements when they are compared with the results predicted by the numerical algorithm. These tools (numerical algorithm and experimental setup) therefore provide a suitable method for characterizing gases.

I. THEORY

This study considers a one-dimensional nonlinear standing wave inside a tube with rigid walls. Second-order terms are retained to obtain the wave equation. Viscous and thermal losses at the walls of the tube are also considered, it being assumed that bulk absorption in the gas is negligible compared with the absorption effects at the walls. No exact solution of this nonlinear equation has been reported until now. However, a perturbation approach has been used to obtain an analytical solution in the neighborhood of resonance.[1] In this paper, a finite element algorithm is used to solve the wave equation. This method is not restricted to resonance conditions.

A. Second order wave equation

The wave equation is derived from the continuity equation, the equation of state for a perfect gas, the force equation, and the thermal and viscous absorption at the walls of the tube. Lagrangian coordinates are used as they are preferred for applying the boundary conditions at the ends of the tube. In terms of the displacement ξ, the second order wave equation has the form:[1]

$$(1-\sigma)\xi''-\frac{1}{c_0^2}\ddot{\xi}+\frac{\sigma}{\omega}\dot{\xi}''-2\beta\xi'\xi''=0, \tag{1}$$

where the quotes denote derivation with respect to the Lagrangian spatial coordinate and the dots stand for derivation with respect to time. β is the nonlinearity parameter. For a gas it can be expressed as

$$\beta=\frac{\gamma+1}{2}, \tag{2}$$

where γ is the ratio of specific heats. Absorption effects are taken into account through the parameter σ which can be expressed as[13]

$$\sigma(\omega)=\frac{P_t}{S_t}\left(\sqrt{\frac{\eta}{2\omega\rho_0}}+(\gamma-1)\sqrt{\frac{\kappa}{2\omega\rho_0 c_P}}\right), \tag{3}$$

where P_t and S_t are the perimeter and the cross section of the tube, respectively, η is the dynamic viscosity parameter, κ is the thermal conductivity, and c_P is the specific heat coefficient at constant pressure.

From the displacement obtained by solving Eq. (1), other acoustic parameters can be calculated. Pressure and velocity are usually chosen to characterize the acoustic field. To compare theory with experiments, pressure expressed in Eulerian coordinates has to be derived, as it is in fact the magnitude that is measured. In a second order approach, it has the form

$$\begin{aligned} p^E &\approx p^L-\xi\left[\frac{\partial p^L}{\partial a}\right]_{x=a} \\ &\approx -c_0^2\rho_0\xi'+c_0^2\rho_0\,\frac{\gamma+1}{2}\,\xi'^2-\frac{P_t}{S_t}\sqrt{\frac{\kappa}{2\omega\rho_0 c_p}} \\ &\quad\times(\gamma-1)\left(\frac{1}{\omega}\,\dot{\xi}'-\xi'\right)+c_0^2\rho_0\xi\xi''. \end{aligned} \tag{4}$$

The superscript ''L'' denotes Lagrangian coordinates and ''E'' denotes Eulerian coordinates. Equation (4) is the same as the expression obtained by Wang and Lee[14] if the third term, relating to thermal absorption, is omitted as it was in their approach.

B. Finite element algorithm

A finite element algorithm was proposed to solve the nonlinear Eq. (1). This method is not restricted to resonance conditions. Another advantage of the method is that different boundary conditions can be applied with no additional complication of the algorithm.

If periodic excitation is assumed, the displacement can be expressed in terms of a Fourier discrete expansion:

$$\begin{aligned} \xi(a,t) &= g_0(a)+\sum_{i=1}^{\infty} g_i(a)\cos(i\omega t)+h_i(a)\sin(i\omega t) \\ &= \sum_{i=0}^{\infty} g_i(a)\cos(i\omega t)+h_i(a)\sin(i\omega t). \end{aligned} \tag{5}$$

When this expansion is substituted into Eq. (1), an infinite set of equations is obtained:

$$(1-\sigma_i)g_i''+\frac{\omega_i^2}{c_0^2}\,g_i+\sigma_i h_i''=fc_i, \tag{6a}$$

$$i=0,1,2,\ldots,$$

$$(1-\sigma_i)h_i''+\frac{\omega_i^2}{c_0^2}\,h_i-\sigma_i g_i''=fs_i, \tag{6b}$$

where $\omega_i=i\omega$, and the terms on the right are infinite series of nonlinear terms:

$$fc_0=\beta\left(2g_0'g_0''+\sum_{j=1}^{\infty} g_j'g_j''+h_j'h_j''\right), \tag{7a}$$

$$fc_i=\beta\left(\frac{1}{2}\sum_{j=0}^{i}(g_j'g_{i-j}''+g_j''g_{i-j}'-h_j'h_{i-j}''-h_j''h_{i-j}')+\sum_{j=i}^{\infty}(g_j'g_{j-i}''+g_j''g_{j-i}'+h_j'h_{j-i}''+h_j''h_{j-i}')\right), \tag{7b}$$

$$fs_i=\beta\left(\frac{1}{2}\sum_{j=0}^{i}(h_j'g_{i-j}''+h_j''g_{i-j}'+g_j'h_{i-j}''+g_j''h_{i-j}')+\sum_{j=i}^{\infty}(h_j'g_{j-i}''+h_j''g_{j-i}'-g_j'h_{j-i}''-g_j''h_{j-i}')\right),$$

$$i=1,2,\ldots. \tag{7c}$$

If the excitation is sinusoidal, nonlinear terms of high order tend to vanish. In a second order approach, only $i=0,1,2$ must be retained, and the infinite set of Eqs. (6) become a set of five equations:

$$g_0''=\beta(g_1'g_1''+h_1'h_1''), \tag{8a}$$

$$(1-\sigma_1)g_1''+\frac{\omega^2}{c_0^2}\,g_1+\sigma_1 h_1''=0, \tag{8b}$$

$$(1-\sigma_1)h_1''+\frac{\omega^2}{c_0^2}\,h_1-\sigma_1 g_1''=0, \tag{8c}$$

$$(1-\sigma_2)g_2''+\frac{(2\omega)^2}{c_0^2}\,g_2+\sigma_2 h_2''=\beta(g_1'g_1''-h_1'h_1''), \tag{8d}$$

$$(1-\sigma_2)h_2''+\frac{(2\omega)^2}{c_0^2}\,h_2-\sigma_2 g_2''=\beta(h_1'g_1''+g_1'h_1''). \tag{8e}$$

To solve this differential system numerically, the region where the standing wave is excited is divided into a discrete set of elements, connected by points called nodes. The Bubnov–Galerkin[15] method (one of the most important finite element methods) is applied to this problem and five matrix equations are obtained:

$$(\mathbf{M_i}+\mathbf{K_i})\mathbf{dg_i}+\mathbf{C_i}\mathbf{dh_i}=\mathbf{FCc_i}+\mathbf{FNc_i},\quad \mathbf{i}=0,1,2, \tag{9a}$$

$$(\mathbf{M_i}+\mathbf{K_i})\mathbf{dh_i}-\mathbf{C_i}\mathbf{dg_i}=\mathbf{FCs_i}+\mathbf{FNs_i},\quad \mathbf{i}=1,2, \tag{9b}$$

where $\mathbf{dg_i}$ and $\mathbf{dh_i}$ are the unknowns and relate to the Fourier components of the displacements at the nodes. $\mathbf{M_i}$, $\mathbf{K_i}$, and $\mathbf{C_i}$ are the mass matrix, the stiffness matrix, and the absorbing matrix, respectively. $\mathbf{FCc_i}$ and $\mathbf{FCs_i}$ take into account the boundary conditions of the specific problem, and $\mathbf{FNc_i}$ and $\mathbf{FNs_i}$ are the nonlinear terms. These matrices can be written in their integral form as

$$\mathbf{K_k}=(1-\sigma_k)\int[\varphi'^i][\varphi'^j]da, \tag{10a}$$

$$\mathbf{M_k}=-\frac{\omega^2}{c_0^2}\,k^2\int[\varphi^i][\varphi^j]da, \tag{10b}$$

$$\mathbf{C_k}=\sigma_k\int[\varphi'^i][\varphi'^j]da, \tag{10c}$$

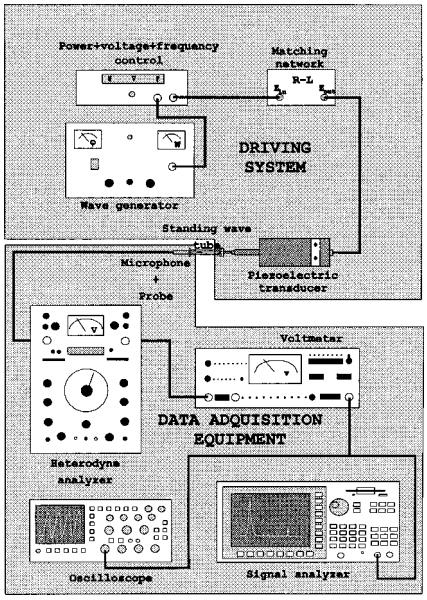

FIG. 1. Experimental setup.

$$\mathbf{FCc_k} = (1-\sigma_k)[dg_{ki}\ \varphi'^i\varphi^j|_{a_{\text{ini}}}^{a_{\text{fin}}}] + \sigma_k[dh_{ki}\ \varphi'^i\varphi^j|_{a_{\text{ini}}}^{a_{\text{fin}}}], \tag{10d}$$

$$\mathbf{FCs_k} = (1-\sigma_k)[dh_{ki}\ \varphi'^i\varphi^j|_{a_{\text{ini}}}^{a_{\text{fin}}}] - \sigma_k[dg_{ki}\ \varphi'^i\varphi^j|_{a_{\text{ini}}}^{a_{\text{fin}}}], \tag{10e}$$

$$\mathbf{FNc_k} = -\int [fc_k][\varphi^j]da, \tag{10f}$$

$$\mathbf{FNs_k} = -\int [fs_k][\varphi^j]da. \tag{10g}$$

In these equations, functions φ are the set of interpolating polynomials used to approach displacements.

II. EXPERIMENTS

The experimental setup for measuring the sound pressure inside a tube is shown in Fig. 1. It consists of a driving system to excite the standing wave, a rigid-walled tube of variable length, and data acquisition equipment.

A. Driving system

The acoustic standing wave inside the tube is excited by a narrow-band and high power piezoelectric transducer.[16] Its natural frequency of resonance is 9500 Hz. The transducer is constructed from an assembly of two paired disks of simple piezoelectric PZT ceramics sandwiched between two metallic cylindrical rods (one of them made of stainless steel and the other one made of a titanium alloy, Ti6Al4V), to increase the vibration amplitude on the radiating face and to improve matching to the load. The sandwich transducer is a half-wave resonant length-expander structure. Coupling between the piezoelectric elements and the metal end sections and increase of a tensile strength are achieved by mechanically prestressing the assembly in the axial direction by means of a bolt.

In this experimental study, the sandwich transducer is followed by a half-wave length resonant element made of titanium alloy with a change in cross-sectional area, which

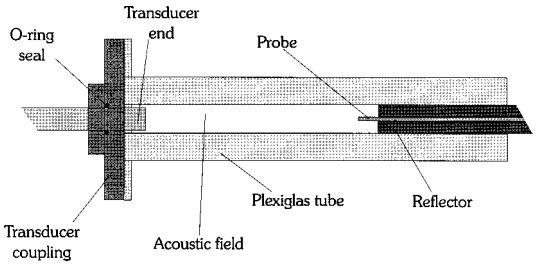

FIG. 2. Schematic diagram of the standing wave tube.

produces displacement amplification at the working end. The amplification factor depends on the ratio of the areas of the larger and smaller cross sections.

The coupling element, made of the same titanium alloy, is one of the most critical parts of the experimental setup. It has a 4-mm-diam cylindrical ending, coupling the transducer to the internal diameter of the tube. This matching has to be as hermetic as possible to avoid pressure leakage. Mechanical friction between the transducer oscillating at 9500 Hz and the static clamp joint to the tube is reduced by a neoprene oil-lubricated O-ring seal. Such undesirable friction may cause energy losses and uncontrolled impedance changes, thereby making the transducer unstable.

The electronic system used to drive the transducer consists of a high power wave generator, which implements a feedback stage to automatically adjust the excitation frequency to the resonant frequency of the transducer. A matching network is inserted at the generator output to achieve a good energy transfer to the load. This network has a resistive element to increase the stability of the system by widening the electric bandwidth.[17]

B. Acoustic chamber

The acoustic chamber is a cylindrical tube made of plexiglas. It is divided into three modules (a 25-mm module and two 50-mm modules) to work with different tube lengths. It has a 4-mm inner diameter. For these dimensions, the cutoff frequency is 50 kHz, and no transverse modes can propagate for the frequency components of the excitation signal under study.

The walls of the tube are 4 mm thick, and the energy transmission from air to plexiglas is negligible, with the result that the assumption of rigid walls holds for the tube under study.

A cylindrical piece made of brass closes the tube at the opposite side of the transducer. It is flat ended to work as a plane reflector. A hole is bored at its axis to allow the acoustic probe to move through it, so that the pressure can be measured at different points along the tube. The reflector can also move through the tube, changing the effective chamber length (Fig. 2).

C. Measuring system

Data acquisition is one of the most important experimental aspects of the present work. There are no commercially available acoustic sensors suited to the measuring conditions required. Piezoelectric and membrane microphones

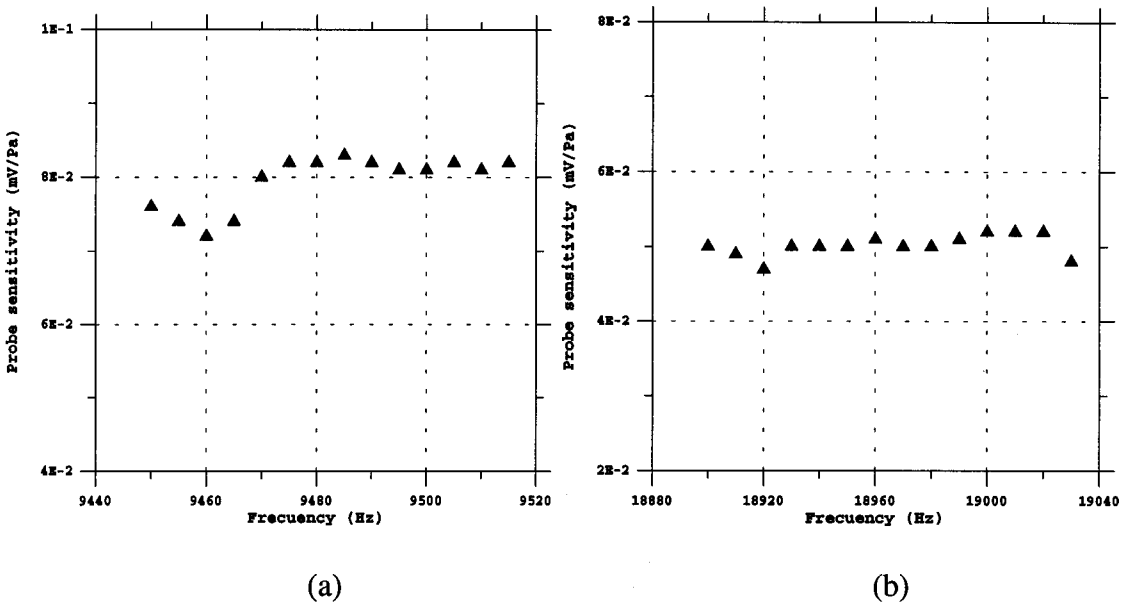

FIG. 3. Sensor sensitivity (microphone+probe) for the fundamental (a) and the second harmonic (b).

need a relatively high cross section with respect to the diameter of the tubes involved, in order to have good sensitivity. It must be noted that the measuring technique is invasive, and that the acoustic field must be perturbed as little as possible.

The solution adopted is similar to that used by Gaete:[8,9] A fine probe with a diameter of 0.8 mm is coupled to a commercial condenser Brüel & Kjær, 1/8-in. microphone. The frequency response of this microphone is flat within ± 0.5 dB from 20 Hz to 60 kHz. The measurements with this technique have two significant disadvantages. First of all, the acoustic signal is strongly attenuated, making high harmonics hardly detectable. On the other hand, the frequency response of the probe is not flat and a careful calibration is needed at the working frequencies (in this case, the resonant frequency of the transducer and its second harmonic).

The spectrum of the electrical signal received from the microphone is visualized in real time on a HP 35670A signal dynamic analyzer. The electric values obtained for the fundamental frequency and the second harmonic must be corrected by means of the calibrated sensitivity (Fig. 3) of the sensor (microphone plus probe).

III. RESULTS

Different measurements were made to explore the acoustic field inside the tube. In this section, experimental data are compared with the numerical predictions obtained using the finite element algorithm presented previously.

A. Pressure distribution inside the tube

The pressure distribution is explored along the axis of the chamber for different tube lengths. The second harmonic is clearly detected only when the length of the tube corresponds to a resonance of this frequency (19 kHz). This situation is achieved near the resonance and antiresonance tube length of the fundamental frequency. For different sizes of tube, only the fundamental frequency could be distinguished from the noise. Figures 4 and 5 plot these results, showing a good agreement between numerical and experimental data.

B. Experimental determination of the absorption coefficient

Discrepancies of about 10%–20% are often reported in the literature between the Kirchhoff–Rayleigh absorption coefficient (due to viscous and thermal effects) and experiments.[1,18] Therefore, an empirical determination of this coefficient is needed to characterize the acoustic chamber and to compare the experimental data with the numerical results. It is important to notice that the theoretical value of this coefficient was based on the assumption that absorption takes place only along the lateral walls. Nevertheless, this hypothesis would fail if the area corresponding to the ends of the tube is not negligible compared with the area of these lateral walls.

From linear theory, if a tube is driven at its resonant frequency, the pressure can be found from the equation:

$$pr_{\mathrm{rms}}=\frac{1}{\sqrt{2}}\,\rho_0 c_0^2 k_0\,\frac{\xi_0}{\alpha L_{\mathrm{res}}}. \tag{11}$$

On the other hand, if the length of the tube is adjusted to fit antiresonance conditions, the pressure is obtained by

$$pa_{\mathrm{rms}}=\frac{1}{\sqrt{2}}\,\rho_0 c_0^2 k_0 \xi_0. \tag{12}$$

From Eqs. (11) and (12), the absorption coefficient can be derived:

$$\alpha=\frac{1}{L_{\mathrm{res}}}\,\frac{pa_{\mathrm{rms}}}{pr_{\mathrm{rms}}}. \tag{13}$$

Using this equation an absorption coefficient of 1.81 m^{-1} is obtained. The theoretical value calculated using Eq. (3) was 1.48 m^{-1}. This value is 18% below the measured

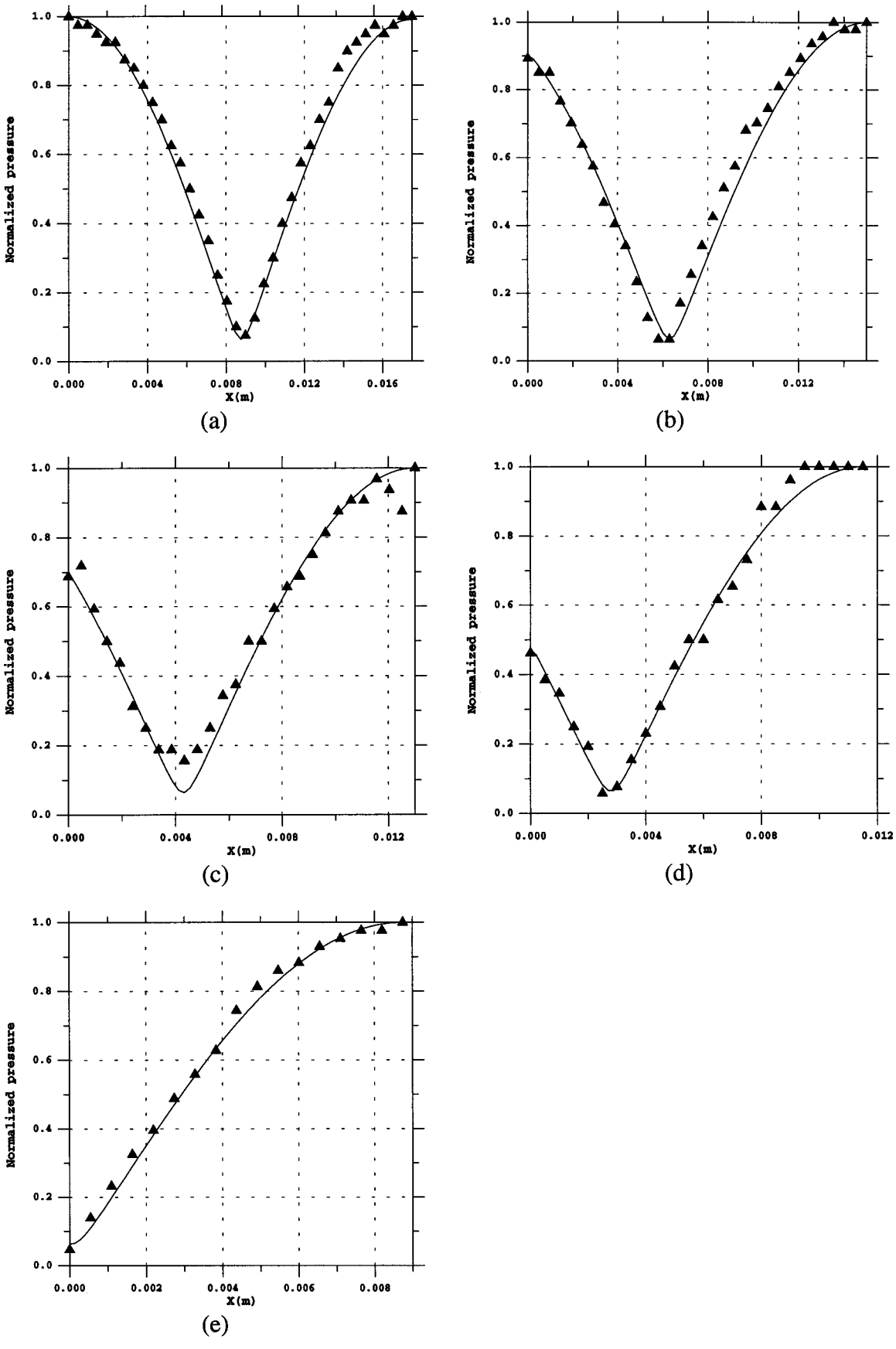

FIG. 4. Pressure distribution inside the tube for the fundamental component of the frequency. Tube lengths are 18 mm (a), 15 mm (b), 13 mm (c), 11 mm (d), and 9 mm (e). Numerical (———) and experimental (▲) results.

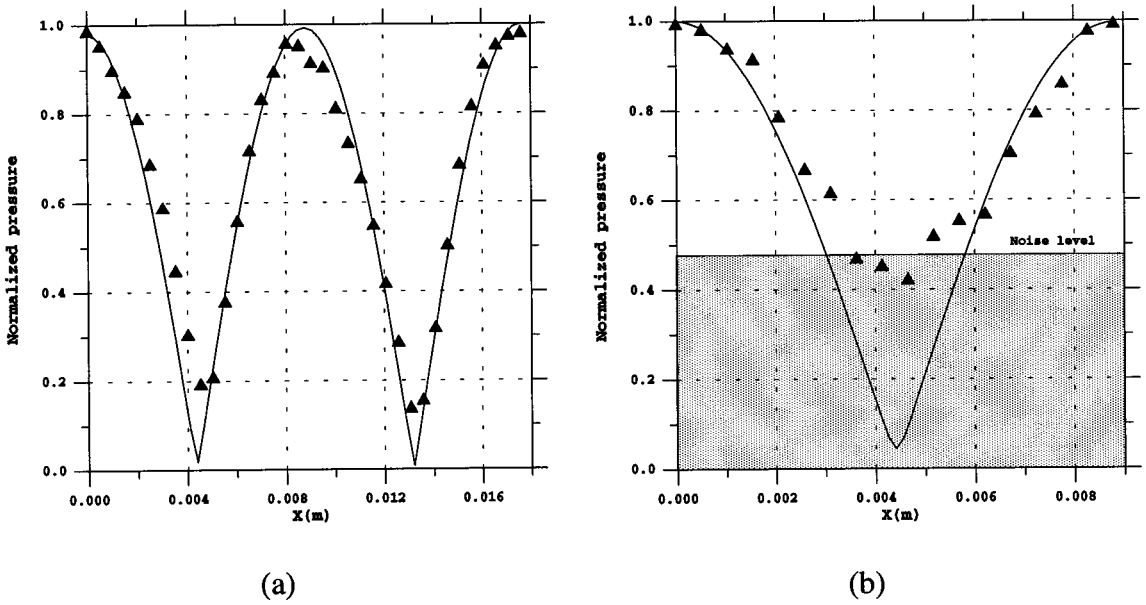

FIG. 5. Pressure distribution inside the tube for the second harmonic frequency component. Tube lengths are 18 mm (a) and 9 mm (b). Numerical (———) and experimental (▲) results.

result, and it is therefore consistent with other authors' findings.

C. Absolute pressure results

Measurements of the pressure at the reflector were made for different tube lengths. Figure 6 shows some of these results. A good agreement is found between experimental data and numerical predictions. A more careful study near resonance is interesting from the point of view of practical applications. Figure 7 plots the experimental pressure of the second harmonic versus the fundamental. A parabolic regression curve, in keeping with theoretical predictions, is plotted with a continuous line. As a result of this quadratic relationship, if the second harmonic pressure divided by the square of the fundamental pressure is plotted versus the tube length, the results will be unaffected by the vibration amplitude of the transducer. Figure 8 shows a comparison between numerical and experimental results. The vertical line marks the fundamental frequency resonance. It can be seen that the peak of the figure does not match with this frequency. As it has been pointed out,[1] this is due to the difference between the absorption coefficient of the two frequency components.

IV. CONCLUSIONS

Finite-amplitude standing waves in one-dimensional tubes were studied numerically and experimentally. The numerical approach was based on a finite element algorithm applied to the second order nonlinear wave equation, with viscous and thermal absorption taken into account.

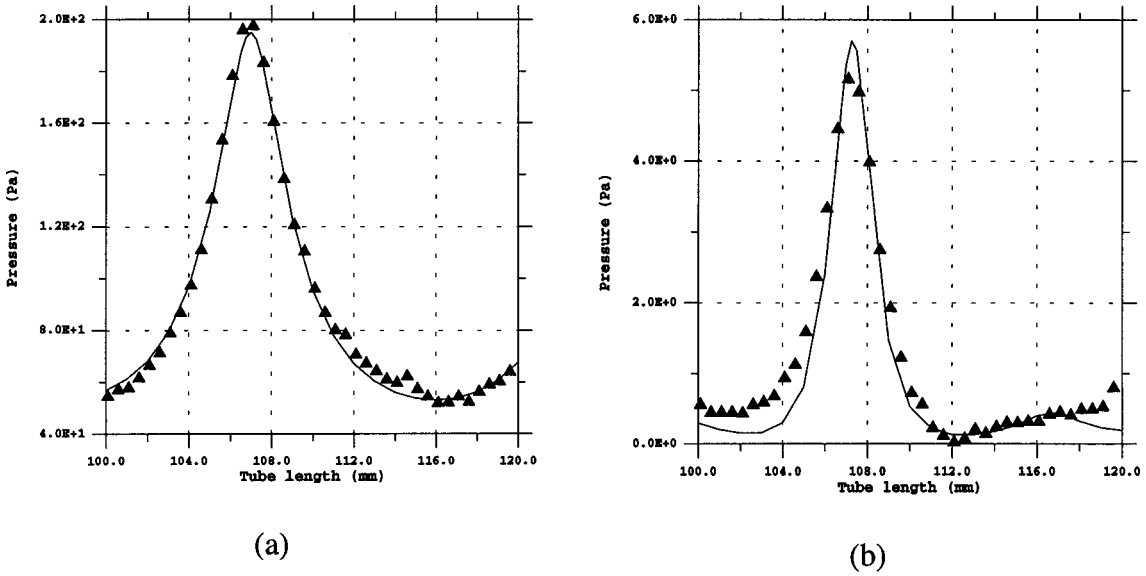

FIG. 6. Fundamental (a) and second harmonic (b) rms pressure at the reflector as a function of the tube length. Numerical (———) and experimental (▲) results.

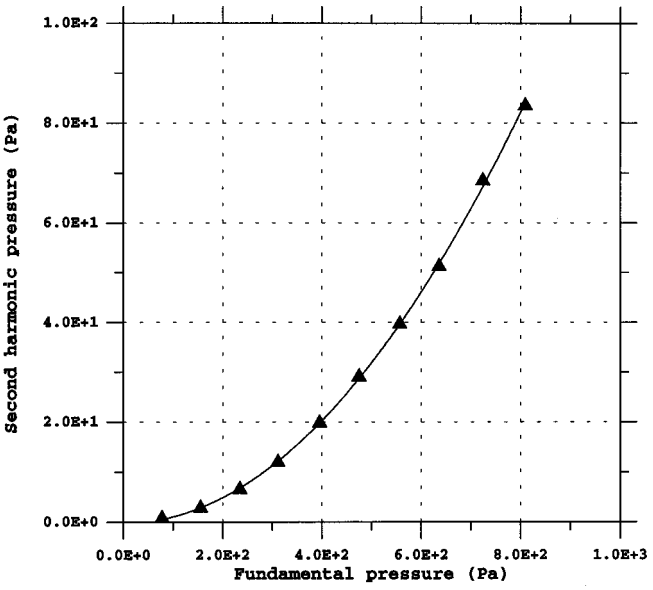

FIG. 7. Second harmonic as a function of the fundamental component. Parabolic regression (———) and experimental (▲) results.

The experimental work carried out was consistent with numerical results. This procedure can lead to an interesting method for characterizing gases. The absorption coefficient can be determined from pressure measurements at the reflector for both resonance and antiresonance conditions. On the other hand, the nonlinearity parameter β, can be determined from the curve fitting of fundamental and second harmonic values near resonance.

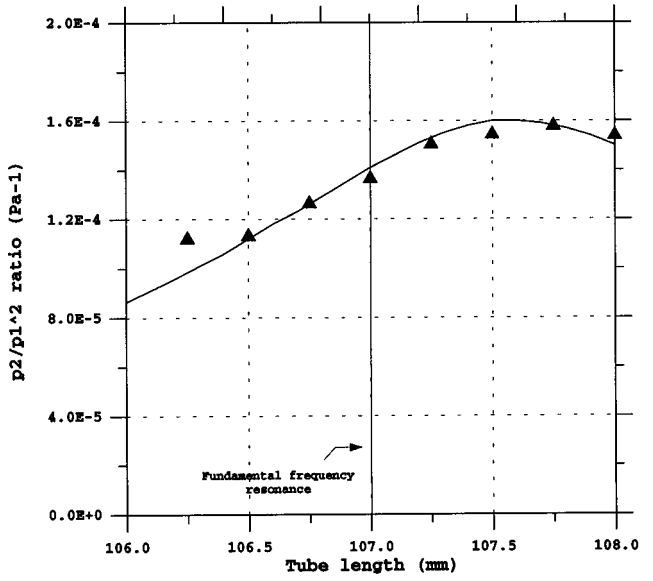

FIG. 8. Plot of the $p_2/(p_1)^2$ ratio as a function of the tube length, near resonance. Numerical (———) and experimental (▲) results. Vertical line indicates the resonance of the fundamental frequency component.

The use of a fine probe has shown to be an adequate method for measuring pressure in small tubes at high frequencies. This will permit small devices to be made for the characterization of gases although there are no commercially available sensors suitable for measuring pressure in these conditions.

ACKNOWLEDGMENTS

The work presented in this paper was supported by the research Grant No. PN91-02621490 from the Spanish Ministry of Education and Science; by two research projects: CICYT-AMB96-1211-C02-01 and CICYT-TAP93-0230, from the Spanish Ministry of Education and Culture.

[1] A. B. Coppens and J. V. Sanders, ''Finite-amplitude standing waves in rigid-walled tubes,'' J. Acoust. Soc. Am. **43**, 516–529 (1968).
[2] D. B. Cruikshank, Jr., ''Experimental investigation of finite-amplitude acoustic oscillations in a closed tube,'' J. Acoust. Soc. Am. **52**, 1024–1036 (1972).
[3] W. Chester, ''Resonant oscillations in closed tubes,'' J. Fluid Mech. **18**, 44–64 (1964).
[4] D. F. Gaitan and A. A. Atchley, ''Finite amplitude standing waves in harmonic and anharmonic tubes,'' J. Acoust. Soc. Am. **93**, 2489–2495 (1993).
[5] R. A. Saenger and G. E. Hudson, ''Periodic shock waves in resonating gas columns,'' J. Acoust. Soc. Am. **32**, 961–970 (1960).
[6] R. G. Zaripov and M. A. Ilhamov, ''Non-linear gas oscillations in a pipe,'' J. Sound Vib. **42**, 245–257 (1976).
[7] D.-Y. Maa and K. Liu, ''Nonlinear standing waves: Theory and experiments,'' J. Acoust. Soc. Am. **98**, 2753–2763 (1995).
[8] L. F. Gaete-Garretón, ''Fenómenos no-lineales en ondas ultrasónicas de alta intensidad. Saturación acústica,'' Ph. D. Dissertation, Universidad Complutense de Madrid, 1981.
[9] L. Gaete-Garretón and J. A. Gallego-Juárez, ''Propagation of finite-amplitude ultrasonic waves in air. II. Plane waves in a tube,'' J. Acoust. Soc. Am. **73**, 768–773 (1983).
[10] L. L. Beranek, *Acoustic Measurements* (Wiley, New York, and Chapman & Hall, London, 1959), Chap. 7, pp. 321–336.
[11] J. A. Gallego-Juárez, ''Nonlinear effects in ultrasonic processing applications,'' in the Proceedings of the 15th International Congress on Acoustics, Trondheim (Norway), June 1995, Vol. I, pp. 41–45.
[12] L. Elvira, ''Desarrollo y validación de un método de elementos finitos para el estudio de ondas acústicas estacionarias no lineales,'' Ph.D. dissertation, Universidad Complutense de Madrid, 1996.
[13] D. E. Weston, ''The theory of the propagation of plane sound waves in tubes,'' Proc. Phys. Soc. London, Sec. B **66**, 695–709 (1953).
[14] C. P. Lee and T. G. Wang, ''Acoustic radiation pressure,'' J. Acoust. Soc. Am. **94**, 1099–1109 (1993).
[15] O. C. Zienkiewicz, *The Finite Element Method* (McGraw-Hill, UK, 1977), 3rd ed., Chap. 3, pp. 42–65.
[16] J. A. Gallego-Juŕez, G. Rodríguez-Corral, J. L. San Emeterio, and F. Montoya-Vitini, European Patent N° E P 450 030, 1991.
[17] C. Campos-Pozuelo and J. A. Gallego-Juárez, ''Finite amplitude standing waves in metallic rods,'' J. Acoust. Soc. Am. **97**, 875–881 (1995).
[18] P. Mariens, ''Kirchoff-Helmholtz absorption in wide and in capillary tubes at audible frequencies,'' J. Acoust. Soc. Am. **29**, 442–445 (1957).

Boundary effect on a parametrically excited soliton

Xinlong Wang[a)]
Institute of Acoustics and State Key Laboratory of Modern Acoustics, Nanjing University, Nanjing 210093, People's Republic of China

(Received 15 July 1997; revised 10 April 1998; accepted 20 April 1998)

It has been proved experimentally that a boundary has the ''mirror effect'' on a parametrically excited soliton. The numerical simulation with the parametrically driven and damped nonlinear Schrödinger equation reproduces the observed interesting phenomena, in particular, the periodical collisions and reflections of the boundary soliton. The dynamical behaviors of the soliton are further concluded as a stability diagram in the space of control parameters. In addition, the internal dynamics including the collision-reflection mechanism of the boundary soliton is also explored tentatively. © *1998 Acoustical Society of America.* [S0001-4966(98)06407-8]

PACS numbers: 43.25.Rq [MAB]

INTRODUCTION

Solitons and their dynamics in integrable systems, such as in KdV, Sine-Gordon, and nonlinear Schrödinger (NLS) ones, have been well studied. However, the situations become much more complicated and yet more attractive for some real physical systems. An example is the *nonpropagating surface-wave soliton* observed by Wu *et al.*[1] in Faraday's vibrating water channel. This type of soliton is usually characterized with the adjective *parametrically excited*, with reference to the variations of the vertical driving parameters. They appear as some highly localized wave envelopes ψ that modulate the transverse surface-wave mode (0,1) along the channel. Hence, they are virtually a one-dimensional localized object, although the wave motion in the water trough is typically a three-dimensional problem. So far several special, even unique, dynamical aspects of the solitons have been revealed in experiments,[2,3] in particular, the basic dynamical modes of soliton–soliton interactions,[4–6] the synchronous spatiotemporal oscillations of multiple solitons, and the oscillatory one-dimensional surface-wave patterns of multisolitons.[7]

There have been two theoretical models for describing the solitonic phenomena. One was proposed by Larraza and Putterman.[8] By using the multiple-scales method, they derived an NLS equation that controls the time evolution of the complex solitary-wave envelope ψ. A time-independent solution to the equation confirms the existence of the so-called *nonpropagating* or *standing* soliton. The other model was set up by Miles.[9] In his theory, Miles took account of the external vertical drive, as well as the damping and water surface-tension effects, so the resulting equation for ψ is a parametrically driven and damped nonlinear Schrödinger (PDNLS) equation. As a result, the time-independent localized solution to the equation not only agrees with the existence of the nonpropagating soliton, but also explains how the soliton depends on the drive and the other physical effects. With Miles' equation, several other authors[10–13] have explored the nonlinear dynamics of the standing soliton. Their results show that the soliton can even exhibit some complex bifurcation and chaotic behaviors under different driving conditions. On the other hand, our recent computer simulations have confirmed that the PDNLS equation also can describe the rich multisoliton phenomena satisfactorily.[5,7]

In most cases, for simplicity, one usually treats the solitary-wave problem as if the soliton existed in an unbounded channel. The present work, however, emphasizes the boundary effect on the solitary-wave system. In Sec. I, we describe the experimental observations[4] of the behavior of a soliton created near one end wall, and demonstrate the existence of the ''*mirror effect*'' on the boundary soliton. These interesting observations are then numerically simulated with the PDNLS equation in Sec. II. The numerical results show that Miles's model can well describe the physics of the observed phenomena. Next, in Sec. III, we analyze the stability of the boundary soliton and inspect the parameter region for the stable existence of the soliton, while in Sec. IV, we attempt to study the internal dynamics of the soliton–boundary interaction. The results reveal the mechanism of the constant collisions and reflections of the boundary solitons. Our conclusions and remarks are given in the final section.

I. DESCRIPTIONS OF EXPERIMENTAL PHENOMENA

The main experimental aspects of the boundary effect can be found in our previous report.[4] Here we describe the observed phenomena in more detail. The experimental setup is quite simple, and is essentially the same as that of Wu *et al.*[1] We use a Plexiglas trough of length L and width W, filled with water to a (static) depth h. The trough then is fixed on a horizontal table that vibrates vertically almost in the sinusoidal form $z_0 = A\cos 2\omega t$, where A and $2f$ $(=\omega/\pi)$ are the driving amplitude and frequency, respectively (the higher harmonics of the vertical vibration are measured to be at least 50 dB lower than the fundamental component). By adding a small amount of saponin, we minimize the water surface tension coefficient T_1 down to about 37.6 dyn·cm^{-2}, to make the soliton formation easier. In what follows, we always assume the fluid to be confined to the rectangular region $0<x<L$, $0<y<W$, and $-h<z<0$ in the static state. With this setup, Wu's nonpropagating

a)Electronic mail: xlwang@nju.edu.cn

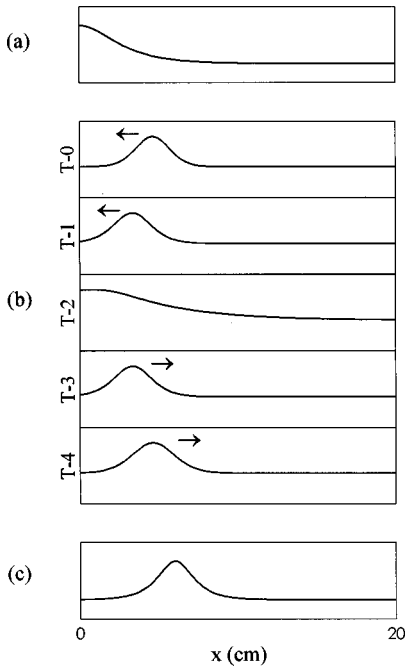

FIG. 1. Interactions of a boundary soliton with a boundary. (a) Attached ($A<A_1$); (b) oscillating ($A_1<A<A_2$) in a period: $T-0\rightarrow T-1\rightarrow T-2\rightarrow T-3\rightarrow T-4$; (c) standing ($A>A_2$).

soliton[1] can be repeated easily if we select a very long trough (i.e., $L \gg W,h$) and form the soliton in the middle of the trough ($X \sim L/2$).

A. Periodic reflections and collisions

To observe the boundary effect on a soliton, we select a water trough of dimension $L\times W\times h=20\times 3\times 2$ cm^3. In this trough, we can generate a soliton near the left end wall ($x=0$) by manually applying a finite disturbance on the water surface near the boundary, if the driving parameters (A,f) are properly adjusted. To depress the possible excitation of the longitudinal surface-wave modes which usually originate from the other end wall, we put some absorbent material such as cotton on the remote end ($x=L$). As a result, the formed soliton can be stabilized in a larger parameter range.

Now let us fix $f=4.8$ Hz and change A to see how the boundary soliton behaves. We observe that, when A is smaller than a critical threshold A_1 (~ 0.7 mm), the soliton first moves toward, and then, collides with the boundary. The collision appears to be ''inelastic;'' after the collision, the soliton is attached to the boundary, keeping itself standing and displaying only half its symmetric wave envelope, as shown in Fig. 1(a). However, when $A>A_1$, e.g., $A=0.71$ mm, we find that the collision is ''elastic,'' that is, after the collision, the soliton no longer is attached to the boundary, but suddenly ''bounces back'' to a definite distance about 5 cm from the boundary, at which it begins to approach the boundary again. The collision-reflection process is shown in Fig. 1(b). Consequently, the soliton oscillates slowly in the vicinity of the left boundary. The repetition frequency of the collisions varies slightly with (A,f), but is typically 0.1 Hz, much smaller than Faraday's resonant frequency $f=4.8$ Hz. If we further increase A, we find that the slow oscillation diminishes; when A is larger than another critical threshold A_2 (~ 1 mm), no matter how close to the wall, the soliton is rejected by the boundary and eventually stands apart from the boundary about 7 cm, greater than the width of the wave envelope, as shown in Fig. 1(c). At a very large A, the soliton appears to be quite unstable and the excitations of other wave modes become unavoidable.

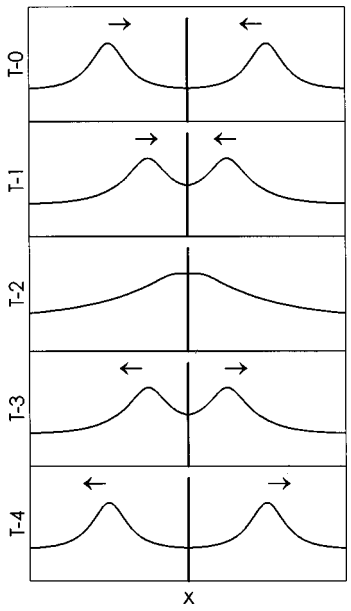

FIG. 2. Oscillations of the two solitons in the bound-state after inserting a partition board at its symmetric center.

B. ''Mirror effect''

The behavior of the boundary soliton remind us of the oscillating bound state.[1,5] By a *bound state* we mean a pair of strongly interacting solitons of like polarity. A direct comparison shows that the boundary soliton behaves essentially the same as any individual in the bound state.[5] To reveal their relationship, we further have carried out the second experiment as follows. In the same water trough as used above (Sec. I A), we form an oscillating bound state at a proper driving parameter, say, $A=0.71$ mm and $f=4.8$ Hz. After the formation, we vertically dip a smooth, rigid, and thin hydrophilic board (such as a Plexiglas one) exactly at the symmetric center of the soliton pair, so that the fluid on both sides is completely partitioned off. Surprisingly, we find that the operation does not change the behavior of solitons, and each soliton oscillates as before, as if there were no partition board. The interesting phenomenon is illustrated in Fig. 2.

From the two experiments, it can be seen clearly that the soliton–soliton interaction in the bound state is completely equivalent to the soliton–boundary interaction. Therefore, we conclude that a boundary (i.e., an end wall) has a ''*mirror effect*'' on a soliton, and the soliton–boundary interaction can be regarded as the interaction between the soliton and its virtual image.

II. NUMERICAL SIMULATIONS

A. Theoretical background

As mentioned in the Introduction, the theoretical model proposed by Miles[9] incorporates both the driving and damping effects, so it might better reflect the experimental situation. In fact, with the PDNLS equation, we have successfully reproduced various multisoliton interaction phenomena.[5–7] We attempt to use the model again to interpret the observed phenomena for the boundary soliton. By rescaling the variables, we can rewrite the one-dimensional model equation in the form

$$i\left(\frac{\partial\psi}{\partial\tau}+\alpha\psi\right)+\frac{\partial^2\psi}{\partial X^2}+2|\psi|^2\psi+\beta\psi+\gamma\psi^*=0, \tag{1}$$

where the asterisk denotes complex conjugate, and α is the linear damping coefficient of the dominant mode (0,1). In the equation, the dimensionless driving parameters, (β,γ), are related to the experimental ones, (ω,A), by

$$\beta=\frac{\omega^2-\omega_{01}^2}{2\omega_{01}^2},\quad \gamma=\frac{\omega^2 A}{g}, \tag{2}$$

where g is the acceleration of gravity, ω_{01} is the linear angular eigenfrequency of the first transverse surface-wave mode (0,1), and

$$\omega_{01}^2=gkT,\quad (k=\pi/W,\ T\equiv\tanh kh).$$

The dimensionless spatial and temporal variables, (X,τ), are mapped to the physical ones, (x,t), through

$$X=\nu kx,\quad \tau=\omega t, \tag{3}$$

where the pure number ν is defined by

$$\nu\equiv 2\sqrt{\frac{T}{T+kh(1-T^2)}}. \tag{4}$$

Note that the optional small parameter $\epsilon(0<\epsilon\ll 1)$, introduced by Miles[9] is implicit in ψ, α, β, and γ in the present formulation; hence $\psi=O(\epsilon)$, $\alpha=O(\epsilon)$, $\beta=O(\epsilon)$, and $\gamma=O(\epsilon)$. For the details, as well as the incorporation of water surface tension, one may refer to Miles' contribution.[9] If the water surface tension is neglected, then in our experiment, the pure number $\nu\approx 1.884$, and the linear eigenfrequency $f_{01}(=\omega_{01}/2\pi)\approx 5.022$ Hz; so $f<f_{01}$ and $\beta\approx -0.0432<0$.

In an unbounded channel, Eq. (1) admits a stationary one-soliton solution $\psi=\psi_s(X)$

$$\psi_s(X)=\pm a_0 ie^{-i\vartheta_0}\ \mathrm{sech}\left(\frac{X-X_0}{\lambda}\right)\quad (-\infty<X<\infty), \tag{5}$$

where X_0 is the ''mass center'' of the soliton, $\lambda=a_0^{-1}$, and

$$a_0=\sqrt{-\beta+\gamma\cos 2\vartheta_0}$$
$$\vartheta_0=\frac{1}{2}\arcsin\left(\frac{\alpha}{\gamma}\right).$$

This solution can describe a soliton standing far from both end walls $(0\ll X_0\ll L)$. In the present situation, however, the soliton dynamics is significantly affected by the left end wall, and the boundary condition at the wall must be taken into account.

B. Boundary conditions

Now we examine the boundary conditions that the solitary-wave function $\psi(X,\tau)$ must satisfy. Let $\xi(x,y,t)$ and $\Phi(x,y,z,t)$ denote the surface displacement and the velocity potential of the fluid, respectively. In terms of the envelope function $\psi(x,t)$, the dominant terms of ξ and Φ can be expressed, respectively, as

$$k\xi=\frac{T}{\sqrt{\delta}}[\psi e^{-i\omega t}+\text{c.c.}]\cos ky+O(\epsilon^2),$$
$$\Phi=\frac{1}{\sqrt{\delta}}\left(\frac{-i\omega}{k^2}\right)[\psi e^{-i\omega t}-\text{c.c.}]\cos ky\ \frac{\cosh k(z+h)}{\cosh kh}+O(\epsilon^2), \tag{6}$$

where c.c. denotes complex conjugate, and

$$\delta=\tfrac{1}{8}(6T^4-5T^2+16-9T^{-2})$$

[note that $\psi=O(\epsilon)$ in our formulation]. Obviously, at the remote end wall $(x=L)$, $\xi\approx 0$, and thus, both ψ and ψ_X can be reasonably assumed to be zeros.

As we know, $\xi_x=0$ at the symmetrical center of the bound state, while the experiment described in Sec. I B clearly tells us that $\xi_x=0$ still holds true at the boundary $x=0$. It immediately follows from the first formula of Eq. (6) that

$$\frac{\partial}{\partial x}(\psi e^{-i\omega t}+\text{c.c.})=0\quad (x=0). \tag{7}$$

In general, $\xi_x\neq 0$ for nonlinear surface waves incident on the wall. However, in the present case, the solitary-wave envelope varies at a much larger scale than the transverse wave profile, i.e., the (0,1) mode. Hence, despite of the nonlinearity and the existence of the damping and surface-tension effects, it is reasonable to assume $\xi_x\approx 0$ at $x=0$, although $\xi_x\neq 0$ at the lateral walls $y=0,W$. One the other hand, the rigid boundary condition $\Phi_x=0$ at $x=0$ requires, from the second formula of Eq. (6), that

$$\frac{\partial}{\partial x}(\psi e^{-i\omega t}-\text{c.c.})=0,\ (x=0). \tag{8}$$

Combining both conditions, (7) and (8), and noting the linear mapping Eq. (3), we finally obtain the boundary condition for the solitary-wave envelope $\psi(X,\tau)$

$$\frac{\partial\psi}{\partial X}=0\quad (X=0). \tag{9}$$

C. Simulation results

To the author's knowledge, there is no way to get an analytical soliton solution to the boundary-value problem at present. We integrate Eq. (1), together with boundary condition (9), by using the same numerical algorithm as before.[5] The computation error is controlled within 10^{-6}. The effectiveness of the algorithm has been verified with a single soli-

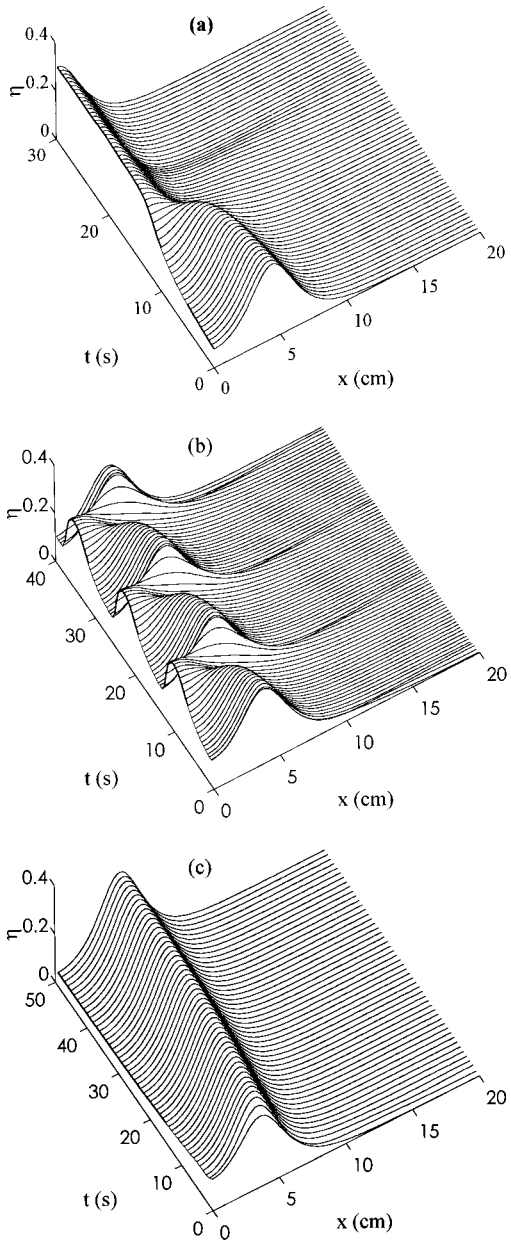

FIG. 3. Numerical simulations of the time evolution of a boundary soliton [$\eta = \mathrm{Im}(\psi)$]. (a) The boundary soliton becomes an attached one as γ is decreased from 0.065 53 to 0.065 51 (or A:0.0706→0.070 58 mm); (b) when $\gamma = 0.0659$, the soliton oscillates near the boundary; (c) when γ is increased from 0.066 83 to 0.078 89 (or A:0.072→0.085 mm), the soliton is rejected from the boundary. In all cases, $\alpha = 0.045\,48$ and $\beta = -0.064\,23$ (or $f = 4.8$ Hz).

ton located at the trough center $x = L/2$ ($L = 20$ cm). For the parameters at which a single soliton is stable, the numerical solution converges soon to the analytical one (5), even if the given initial wave envelope deviates from the solution very much. The stability and the rapid convergence of the algorithm are partially due to the existence of the physical damping effect (in some conservative systems, as a computational trick, one often introduces pseudo-damping to achieve the same purpose).[14]

Applying the algorithm to Eqs. (1) and (9), we find that the experimental phenomena described in Sec. I all can be simulated numerically. Figure 3 shows the numerical results

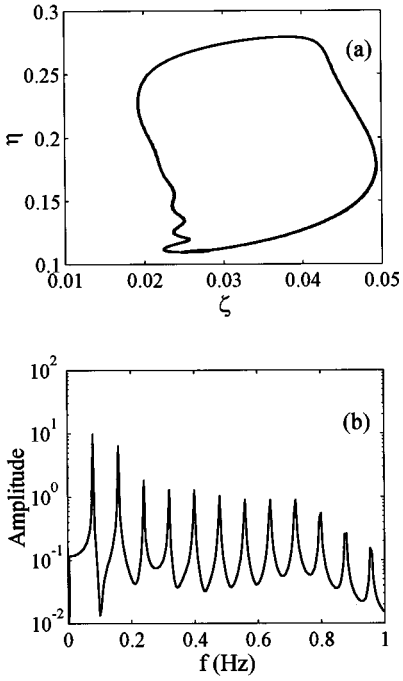

FIG. 4. (a) Phase trajectory of (ξ, η). (b) Frequency spectrum of η at $x = 0$, where $\zeta = \mathrm{Re}(\psi)$ and $\eta = \mathrm{Im}(\psi)$. (Control parameters: $\alpha = 0.045\,48$, $\beta = -0.064\,23$, and $\gamma = 0.0659$).

corresponding to the three cases, (a), (b), and (c), in Fig. 1. In the computation, we take $\alpha = 0.045\,48$. Using the computer-generated data, we have constructed the phase trajectory of the solitary-wave motion. Figure 4(a) gives an example at $x = 0$. The limit cycle in the figure indicates the periodicity of the constant collision-reflection process. The corresponding FFT spectrum is plotted in Fig. 4(b). As can be directly read from the spectrum, the period of the oscillation is about 10 s, consistent with the experimentally measured value.

III. THE STABILITY DIAGRAM

Now we survey the parameter region for the stable existence of the boundary soliton. For a given trough, Eq. (1) contains three adjustable parameters, α, β, and γ. In fact, there are only two independent ones among the three. This can be made clear through applying the simple variable transformation,

$$X' = \sqrt{-\beta}X, \quad \tau' = -\beta\tau, \qquad (10)$$

$$\phi(X', \tau') = \frac{\psi(X, \tau)}{\sqrt{-\beta}},$$

to Eq. (1), which immediately produces

$$i(\phi_{\tau'} + \alpha'\phi) + \phi_{X'X'} + (-1 + 2|\phi|^2)\phi + \gamma'\phi^* = 0. \qquad (11)$$

In the rescaled equation (11), the new control parameters (α', γ') are given by

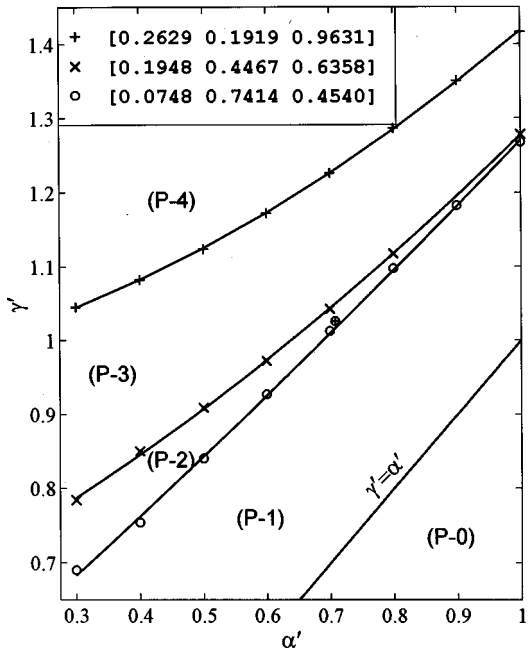

FIG. 5. Stability diagram. (P-0) ($\gamma' < \alpha'$) no soliton; (P-1) attached boundary soliton; (P-2) oscillating boundary soliton; (P-3), standing boundary soliton; (P-4) unstable boundary soliton. The three symbols, ''○,'' ''×,'' and ''+,'' label the computed data points of the three border lines that separate the different subregions. These data are best fitted, respectively, in the form $\gamma' = a\alpha'^2 + b\alpha' + c$, and the coefficient [$a$ b c] are given in the up left corner. The point labeled by ''⊕'' in (P-2) corresponds to the parameters used in the experiment for the oscillating boundary soliton.

$$\alpha' \equiv -\frac{\alpha}{\beta}, \quad \gamma' \equiv -\frac{\gamma}{\beta}. \tag{12}$$

We thus need to survey the parameter region only in the (α', γ') plane (note that $\beta < 0$).

As we can see from Fig. 3(b), the right boundary ($x = L$) still has a little influence on the soliton near the left boundary when $L = 20$ cm. To further exclude the unwanted influence, we take a longer trough $L \times W \times h = 34 \times 3 \times 2$ cm^3 in locating the parameter region. Plotted in Fig. 5 is the stability diagram in the (α', γ') plane for this case. We have further investigated the diagrams for several longer troughs ($L > 34$ cm), and the results are almost the same as the one in the figure. Therefore, the given diagram is valid even for the semi-infinitesimal case, $x \in (0, \infty)$. In the diagram, the whole parameter plane is divided into five domains. Among them, (P-1), (P-2), and (P-3) are the stability regions for the boundary soliton, which correspond to the three different experimental cases, (a), (b), and (c), in Fig. 1, respectively. Below the straight line $\gamma' = \alpha'$, i.e., in the subregion (P-0), no soliton can be supported, because of the insufficient energy fed to the system. The periodical collision-reflection phenomenon occurs only if (α', γ') falls into the narrow parameter band (P-2).

We find that all the three stability subregions can extend to much large value of α', but, except for (P-1), they cannot be extrapolated to $\alpha' = 0$ [$\alpha \to 0$, or $\beta \to -\infty$, see Eq. (12)]; when $\alpha' < 0.3$, the boundary soliton becomes unstable, due to the strong radiation of continuous waves from it. Even in the range of $0.3 < \alpha' < 0.45$, the collision behavior appears to be somewhat irregular. This explains two experimental facts: (1) the soliton is more stable and its shape looks smoother in dirty water than in clean water; (2) at a very low frequency f, which corresponds to very low damping as can be seen from definitions (2) and (12), the soliton is easily destroyed by a small disturbance, and instead, the longitudinal modes soon prevail. We will elaborate the chaotic problem elsewhere in more detail.

IV. THE DYNAMICS OF A BOUNDARY SOLITON

Phenomenologically, the oscillating boundary soliton bears a close analogy with an elastic ball freely falling on a rigid horizontal plane in classical mechanics. At first sight, one might expect that something familiar with a falling ball would also be found in the soliton–boundary interaction, for instance, the momentum of the soliton would reverse its direction at each collision. Now let us examine whether such a statement holds true for the boundary soliton.

We attempt to explore the internal dynamics of the boundary soliton through investigating two dynamical quantities: the ''particle number'' N and the ''momentum'' M. They are defined, respectively, as[5]

$$N \equiv \frac{1}{2a_0} \int_0^\infty |\psi(X,\tau)|^2 \, dX, \tag{13}$$

$$M \equiv \frac{1}{2} i \int_0^\infty (\psi\psi_X^* - \psi^*\psi_X) dX. \tag{14}$$

We have assumed that the upper limits L of both integrations approach infinity, for in the considered case the right boundary is far from the boundary soliton. In definition (13), we divide the integration by a normalization factor ($2a_0$), so that $N = 1$ for a single soliton in an unbounded channel, as is easily verified by substituting formula (5) into (13). In fact, N characterizes the strength of the soliton, while M is proportional to the average momentum of fluid, as is proved in the Appendix [see formula (A2)]. In the exactly integrable NLS system, both N and M are conserved in the time evolution of solitons, but we see that, in the damped and parametrically driven system, they are no longer conserved in general.

By invoking Eq. (1) and taking account of the boundary condition (9), we can derive from (13) and (14) that

$$\begin{aligned} &\frac{dN}{d\tau} + 2\alpha N = \frac{\gamma}{a_0} r, \\ &\frac{dM}{d\tau} + 2\alpha M = -s, \end{aligned} \tag{15}$$

where

$$\begin{aligned} &r \equiv \int_0^\infty \mathrm{Im}(\psi^2) dX, \\ &s \equiv [|\psi|^4 + \tfrac{1}{2}(|\psi|^2)_{XX}]_{X=0}. \end{aligned} \tag{16}$$

In the derivations, we have used the boundary conditions, $\psi(\infty, \tau) \to 0$ and $\psi_X(\infty, \tau) \to 0$. When the solitary-wave envelope remains standing, i.e., $(\alpha', \gamma') \in$ (P-1) or (P-3) in Fig.

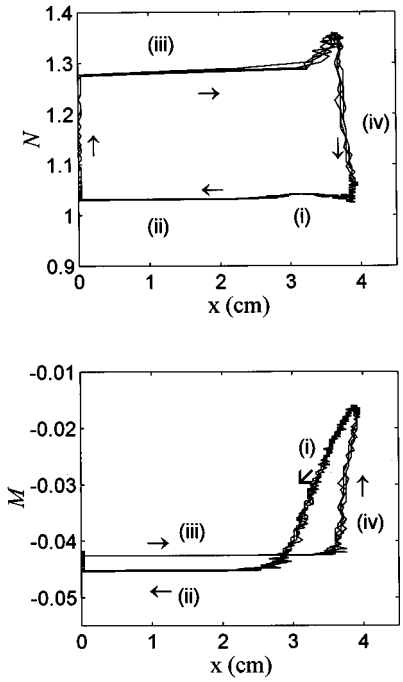

FIG. 6. Variations of N and M versus soliton ''position'' X_0 (the control parameters $\alpha'=0.708$ and $\gamma'=1.0259$). The arrows indicate the directions of motion. The process is divided into four stages as described below. (i) The soliton starts moving toward the boundary very slowly; (ii) when it moves to $x\approx 3$ cm, it is attracted to the boundary rapidly; (iii) next, it is reflected to $x\approx 3.8$ cm all at once; and then, (iv) it recedes to the original position slowly.

5, both r and s are time independent. Thus we have the following explicit steady solutions to (15):

$$N_\infty \equiv \lim_{\tau\to\infty} N = \frac{\gamma}{2\alpha a_0}\, r,$$
$$M_\infty \equiv \lim_{\tau\to\infty} M = -\frac{s}{2\alpha}. \tag{17}$$

For $(\alpha',\gamma')\in$(P-1), the boundary soliton displays only half its symmetrical envelope in the steady state. Thus the analytical solution (5) is still valid if we set $X_0=0$ and assume $X>0$. Substituting the solution into Eq. (16) produces $r=a_0\sin 2\vartheta_0$ and $s=0$. Hence, $N_\infty=\frac{1}{2}$ (half soliton), and $M_\infty=0$. For $(\alpha',\gamma')\in$(P-3), the soliton is standing apart from the boundary, i.e., $X_0>0$, after a transient process. In this case, N_∞ is calculated to be a little greater than 1. Since $X=0$ is the minimum of $|\psi|$, $(|\psi|^2)_{XX}>0$, and thus, s is a positive constant. It follows from Eq. (17) that $M_\infty<0$. With the increase of γ' (or A), the soliton moves away from the boundary more and more, and its wave envelope approaches the one-soliton solution (5). Therefore, $N\downarrow 1$ and $M\uparrow 0$. The situation is somewhat complicated for $(\alpha',\gamma')\in$(P-2). Within the domain (P-2), the boundary soliton oscillates as shown in Fig. 3(b). In this case, we are incapable of obtaining an explicit asymptotic solution to Eq. (15), so we have to resort to numerical ones again. Using the same computed data as used in Fig. 3(b), we can define the soliton ''position'' $X_0(\tau)$ as the one at which the solitary-wave amplitude $|\psi|$ reaches its maximum. Figure 6 illustrates how N and M vary with the ''position'' X_0, respectively. The labels (i), (ii), (iii), and (iv), in the figures identify four consecutive stages in one collision period: *slowly attracting→rapidly attracting→rapidly reflecting→slowly receding.*

To conclude, we have seen that the momentum M of a boundary soliton vanishes for the control parameters $(\alpha',\gamma')\in$(P-1), while in the other two cases, i.e., $(\alpha',\gamma')\in$(P-2) and (P-3), $M<0$, even if the soliton is standing. In the oscillation case, i.e., $(\alpha',\gamma')\in$(P-2), the momentum fluctuates periodically, but never change its direction, although the soliton seems to ''bounce back'' immediately after each collision at $X_0=0$. Moreover, the collision-reflection process is irreversible, as is indicated by the hysteresis phenomenon in Fig. 6. The internal process might be explained as follows. The damping effect would dissipate the energy of the boundary soliton, and thus, the soliton tends to be absorbed by the boundary (i.e., $N:1\to\frac{1}{2}$), but the strong parametric excitation in the case of $(\alpha',\gamma')\in$(P-2) could recreate the soliton at a large distance from the boundary, resulting in a net momentum always flowing to the boundary. In the standing case of $(\alpha',\gamma')\in$(P-3), the annihilation-recreation process becomes stationary as being due to the stronger excitation of the system.

V. CONCLUSIONS AND REMARKS

The following aspects can be obtained from our experimental and theoretical work.

(1) A boundary has ''mirror effect'' on a soliton. As a result, the soliton behaves as the same as one of the identical solitons in the bound state.

(2) The behavior of the boundary soliton can be described by the PDNLS equation.

(3) Although the collision behavior of the boundary soliton seems similar to that of a freely falling ball, *namely*, a ping-pong ball, the internal dynamics is quite different, and the periodical collision-reflection process is attributed to the dynamical balance between energy dissipation and parametric excitation.

At the moment, we point out that, although Miles' equation models the experimental phenomena quite well, the cubic order approximation still has some limitation in fully explaining the complex nonlinear phenomena. For instance, our experiment shows that the range of the driving amplitude A for the stable existence of a boundary soliton is quite large. For instance, $\Delta A=A_2-A_1\sim 0.3$ mm at $f=4.8$ Hz, which corresponds to $\Delta\gamma'\sim 0.43$ at $\alpha'=0.708$. However, we can read from Fig. 5 that the computed range is about 0.2, nearly half the experimental value. Actually, we have observed that the peak value of the solitary-wave envelope can even reach up to 2 cm under a strong excitation of the system (remember that the static water depth $h=2$ cm). In such a situation, higher order nonlinear terms might play a significant role in the soliton dynamics. In spite of the limitation, we can see that Miles' model is quite successful in interpreting the observed phenomena, and so far it might be the best choice in theoretically dealing with surface-wave solitons.

Finally, we mention that there exist a number of nonlinear resonant phenomena in other physical media that can also be modeled by the PDNLS equation.[12,13,15–17] We expect that

the same or similar solitary-wave phenomena as observed in the oscillating water trough could be found in these physical systems.

ACKNOWLEDGMENT

The work is supported by the National Natural Science Foundation of China under Grant No. 19774029.

APPENDIX: MOMENTUM OF FLUID

The momentum of the 3-D fluid motion is formulated as

$$\mathbf{I}=\rho\int_0^{\infty}dx\int_0^{W}dy\int_{-h}^{\xi}dz\ \boldsymbol{\nabla}\Phi(x,y,z,t), \tag{A1}$$

where

$$\boldsymbol{\nabla}=\left(\frac{\partial}{\partial x},\frac{\partial}{\partial y},\frac{\partial}{\partial z}\right),$$

ρ is the density of water, and $\Phi(x,y,z,t)$ is the velocity potential of fluid (note that the upper limit for x: $L\rightarrow\infty$ in our experiment). By invoking expressions (6), neglecting the terms of higher order than $O(\epsilon^2)$, and averaging $\mathbf{I}$ over the fast oscillation ($f=\omega/2\pi$) of mode (0,1), we finally obtain

$$\langle\mathbf{I}\rangle\equiv\frac{\omega}{2\pi}\int_0^{2\pi/\omega}\mathbf{I}\ dt=\rho W\cdot\left(\frac{\nu T}{\delta}\cdot\frac{\omega}{k^2}\right)\cdot M\cdot\mathbf{e}_{\mathbf{x}}+o(\epsilon^2), \tag{A2}$$

where $\mathbf{e}_{\mathbf{x}}$ denotes the unit vector in the x direction, ν is defined in formula (4), and M is the soliton ''momentum'' defined in formula (14).

[1] J. Wu, R. Keolian, and I. Rudnick, Phys. Rev. Lett. **52**, 1421 (1984).
[2] R. J. Wei, B. R. Wang, Y. Mao, X. Zheng, and G. Miao, J. Acoust. Soc. Am. **88**, 469 (1990).
[3] X. N. Chen and R. J. Wei, J. Fluid Mech. **259**, 291 (1994).
[4] X. L. Wang and R. J. Wei, Phys. Lett. A **192**, 1 (1994).
[5] X. L. Wang and R. J. Wei, Phys. Rev. Lett. **78**, 2744 (1997).
[6] X. L. Wang and R. J. Wei, Phys. Lett. A **227**, 55 (1997).
[7] X. L. Wang and R. J. Wei, Phys. Rev. E **57**, 2405 (1998); Chin. Phys. Lett. **15**, 275 (1998).
[8] A. Larraza and S. Putterman, J. Fluid Mech. **148**, 443 (1984).
[9] J. W. Miles, J. Fluid Mech. **148**, 451 (1984).
[10] E. W. Laedke and K. H. Spatchek, J. Fluid Mech. **223**, 589 (1991).
[11] H. Friedel, E. W. Laedke, and K. H. Spatschek, J. Fluid Mech. **284**, 341 (1995).
[12] I. V. Barashenkov, M. M. Bogdan, and V. I. Korobov, Europhys. Lett. **15**, 113 (1991).
[13] M. Bondila, I. V. Barashenkov, and M. M. Bogdan, Physica D **87**, 314 (1995).
[14] William H. Press *et al.*, *Numerical Recipes: The Art of Scientific Computing* (Cambridge U.P., New York, 1985).
[15] B. Denardo *et al.*, Phys. Rev. Lett. **68**, 1730 (1992).
[16] V. E. Zakharov, V. S. L'vov, and S. S. Staroninets, Sov. Phys. Usp. **17**, 896 (1975).
[17] H. Yamazaki and M. Mino, Prog. Theor. Phys. Suppl. **98**, 400 (1989).

Nonlinear, low-frequency sound generation in a bubble layer: Theory and laboratory experiment

Lev A. Ostrovsky
University of Colorado, CIRES/NOAA Environmental Technology Laboratory, 325 Broadway, R/E/ET1, Boulder, Colorado 80303 and Institute of Applied Physics, Nizhmy, Novgorod, Russia

Alexander M. Sutin, Irina A. Soustova, Alexander I. Matveyev, and Andrey I. Potapov
Institute of Applied Physics, Russian Academy of Sciences, 46 Uljanova St., 46, Nizhny Novgorod 603600, Russia

(Received 15 July 1997; revised 1 April 1998; accepted 4 May 1998)

The difference-frequency sound generation as a result of interaction of two high-frequency harmonic waves in a bubble layer in water is investigated both theoretically and experimentally. Because the sound speed in the layer is less than that outside, the layer has resonance properties. As was shown before, this can considerably increase the efficiency of the nonlinear frequency transformation. However, unlike the cases considered before, the layer resonance is practically achievable only at the low (difference) frequency, whereas the high-frequency signal (pump) resonates at individual bubbles and then it strongly dissipates. Here the results of an experiment with a bubble layer with a thickness of about 10 cm in an anechoic tank are presented. One of the incident (primary) wave frequencies was 60 kHz, whereas the other could be varied, thus providing the low-frequency signal in the range of 0.8–14.8 kHz. Due to the first-mode layer resonance, this secondary signal had a pronounced maximum at a frequency of 2.4 kHz. The high attenuation of pump waves was due to resonant bubbles. A theory which agrees with the experimental results reasonably well, is developed for this type of interaction. [S0001-4966(98)04608-6]

PACS numbers: 43.25.Yw, 43.30.Hw, 43.30.Qd [MAB]

INTRODUCTION

It is common knowledge that the presence of gas bubbles in water causes strong nonlinearity for acoustic waves. One of the most known nonlinear effects is the difference-frequency signal generation by two primary pump waves of close frequencies. Since the 1960s, this effect has been used in parametric acoustic arrays, which can provide high-radiation directivity for a rather small size of pump radiator.[1,2] The main disadvantage of parametric arrays is their low efficiency. In the early 1980s, it was suggested to enhance parametric radiation by using the high nonlinearity of bubbles.[3] This idea was verified experimentally,[4] and later several cases of parametric radiation from a bubble layer were investigated theoretically and experimentally.[5–7] Due to the wide bubble-radii distribution in real conditions, the resonance bubbles played a definitive role in these experiments. However, along with strong nonlinearity, high resonance losses were involved (in fact, these two factors are proportional to each other for resonant bubbles), which kept the efficiency of the system still far from being optimal. Recently[8] it was suggested that resonance oscillations of the entire bubble layer be used instead of individual bubble resonances. In this situation the bubbles are small enough to behave quasistatically. The main effect of small, nonresonant bubbles is to decrease the sound speed so that the jumps of acoustic impedance occur at the layer boundaries. The boundary then becomes a planar resonator. It was shown that the use of resonance modes of the layer at both high (primary) and low (secondary) frequencies increases the efficiency of the frequency conversion up to a few percent in energy, which is a rather high value for such systems.[8] However, in real experiments it is practically impossible to create bubbles so small that all of them are out of resonance for all working frequencies. This is realistic for the difference-frequency signal, but hardly achievable for the high-frequency pump waves. Hence the use of layer resonance should be restricted to the low-frequency signal and combined with the highly damped pump still in resonance with a group of individual bubbles from the entire bubble population widely distributed in radii.

This paper presents theoretical and experimental investigations of low-frequency generation under exactly these conditions, when the difference frequency is below resonance for the bulk of bubbles whereas there are bubbles resonant at the frequencies of primary waves. The nonlinearity in such a system is due to these pump-resonance bubbles; they also provide high attenuation of primary waves. At the same time, for the difference frequency, the sound velocity is significantly less than that in ''pure'' water, so that the bubble layer works as a resonator.

I. THEORY

We consider a planar bubble layer of thickness l (Fig. 1). Two high-frequency acoustic waves with close frequencies, ω_1 and ω_2, are incident from the left on the boundary of the layer. We are interested in the nonlinear effect of frequency down conversion. The efficiency of this process depends on the bubble size distribution function and on the frequencies

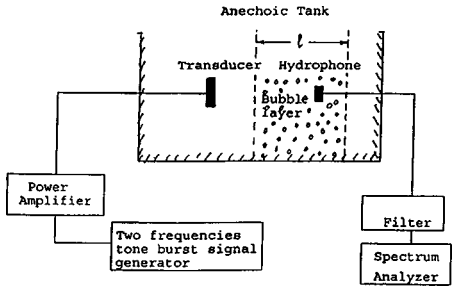

FIG. 1. Experimental setup.

of the interacting waves. In experiments, we used electrolysis to produce bubbles with a radii of the order of 300 μm or smaller. The corresponding single-bubble resonance frequencies were from several kilohertz upward. As already mentioned, it is difficult to generate acoustical waves with frequencies out of resonance for all bubbles (in our case much less than 10 kHz) with high enough amplitude to provide nonlinearity. We used the pump frequencies of about 60 kHz generated by a resonance transducer. The bubbles resonant at about that frequency provided the maximum nonlinearity but also the maximum pump attenuation, so that the source of the difference-frequency wave was in fact concentrated near the left boundary of the layer, where the pump wave attenuates.

In general, theoretical description of this problem should be based on the wave equation for acoustic pressure, p_a,

$$c_0^{-2}\frac{\partial^2 p_a}{\partial t^2}-\frac{\partial^2 p_a}{\partial x^2}=\rho_0\frac{\partial^2 \beta}{\partial t^2}, \tag{1}$$

where c_0 and ρ_0 are the unperturbed sound speed and density of water, respectively, and $\beta(x,t)$ is the bubble volume fraction, together with the equation for a single bubble oscillation (see, e.g., Ref. 9)

$$\frac{\partial^2 v}{\partial t^2}+\omega_R^2 v+\hat{f}v-\frac{1}{8\pi R^3}\left[3(1+\gamma)\omega_R^2 v^2+2v\frac{\partial v}{\partial t}+\left(\frac{\partial v}{\partial t}\right)^2\right]$$

$$=-\frac{4\pi R}{\rho_0}p_a. \tag{2}$$

Here, v is the bubble volume perturbation, $\omega_R=R^{-1}(3\gamma p_0/\rho_0)^{1/2}$ is the resonance frequency of the bubble of radius R (surface tension is not important in the range considered), γ is the polytropic index for the gas, and p_0 is the static pressure in water. The operator $\hat{f}$ characterizes frequency-dependent losses for a linear harmonic wave of frequency ω, and it defines the single-bubble damping rate δ. This system of equations should be supplemented by the bubble radii distribution function $n(R,\mathbf{r})$ so that the bubble volume fraction is

$$\beta=\int_{R_{\min}}^{R_{\max}} v(R)n(R)dR. \tag{3}$$

We shall solve the problem of difference-frequency wave generation with the commonly used perturbation method. For each of the high-frequency waves, we neglect the nonlinearity and represent the pump in the form of a traveling and attenuating biharmonic wave

$$p_h=P_0[\cos(\omega_1 t-k_1 x)+\cos(\omega_2 t-k_2 x)]e^{-\alpha x}, \tag{4}$$

where P_0 is the wave amplitude at the left boundary of the layer, $\omega_{1,2}$ and $k_{1,2}$ are the frequencies and wave numbers of the pump waves, respectively, and $\alpha(\omega)$ is the wave spatial damping rate, which is supposed to be the same for both pump waves due to the closeness of their frequencies. As mentioned above, in our case $\alpha l\gg 1$, so that the effect of the right boundary for these waves can be neglected. If the damping is associated mainly with resonance bubbles, the known formula[10] can be used

$$\alpha(\omega)=725R_\omega^3 n(R_\omega), \tag{5}$$

where R_ω is the radius of bubbles resonant at frequency ω.

Now, the problem of resonance excitation of the standing wave at the difference frequency $\Omega=\omega_1-\omega_2$ in the layer can be solved in a way similar to that used in Ref. 8, but with a different spatial distribution of the pump. If this frequency lies far below the resonance frequencies of the bubbles, and total gas void fraction β is small, the relative wave impedance n and the sound speed c are defined by (Ref. 10)

$$n=\frac{\rho_0 c_0}{\rho c}=\frac{1}{1+1.6\times 10^4\beta}. \tag{6}$$

Such a nonresonant wave propagates without a strong damping in the medium, so the Q factor of the layer is mainly determined by the energy leakage at boundary impedance jumps. This is the case for the difference-frequency wave. The nonresonant bubbles mainly change the sound velocity for this wave, which is determined by the total gas void fraction in the layer.

Substituting (4) into (1), (2), and (3), in the framework of the standard perturbation procedure, we obtain a linear equation for the pump waves [for them the nonlinear terms in square parentheses of (2) are omitted], and a linear equation with a forcing for the small difference-frequency signal p_Ω (cf. Refs. 4 and 8):

$$\frac{\partial^2 p_\Omega}{\partial t^2}-c_0^2\frac{\partial^2 p_\Omega}{\partial x^2}=\frac{\epsilon}{\rho_0 c_0^2}\frac{\partial^2 (p_h^2)_\Omega}{\partial t^2}. \tag{7}$$

Here $\epsilon\simeq 0.039\delta^{-1}n(R_\omega)\lambda^4$ ($\lambda=2\pi/k$ is the pump wavelength) is the nonlinearity parameter that is due to the bubbles resonant at pump frequencies[4] (we suppose that the difference frequency Ω is smaller than the width of the resonance curve at frequencies $\omega_{1,2}$). The right-hand part of Eq. (7) gives the component of the nonlinear forcing at the frequency Ω.

At the end of the layer, the following boundary conditions must be met:

$$\left(\frac{\partial}{\partial t}\mp c_0\frac{\partial}{\partial x}\right)p_\Omega=0, \tag{8}$$

which means the absence of a low-frequency wave incident onto the layer.[8] It is seen from Eqs. (4) and (5) that

$$(p_h^2)_\Omega=P_0^2 e^{-2\alpha x}\cos(\Omega t-Kx), \tag{9}$$

where $K=k_2-k_1=\Omega/c$.

Representing $p_\Omega = \frac{1}{2}P(x)[\exp(-i\Omega t) + \text{c.c.}]$, we have

$$\frac{d^2P}{dx^2} + K^2P = \frac{\epsilon\Omega^2}{\rho_0 c_0^4} P_0^2 e^{-2\alpha x} = Se^{-2\alpha x} \tag{10}$$

[we omitted Kx in the argument of cos in Eq. (9) because of $K\alpha \ll 1$]. The solution of Eq. (10) reads

$$P = \frac{1}{2} A \exp(iKx) + \frac{1}{2} B \exp(-iKx) - \frac{S}{4\alpha^2} e^{-2\alpha x}, \tag{11}$$

where A and B are constants (and we again omitted K^2 in $K^2 + \alpha^2$).

The condition at the right boundary, $x = L$, readily gives $B = rAe^{2iKL}$, where $r = (1-n)/(1+n)$ is the reflection coefficient. Substituting all this into Eq. (8) for the left boundary ($x = 0$), we find

$$A = \frac{2i(2\alpha c_0 - i\Omega)S/4\alpha^2}{c_0 K(1 - re^{2iKL}) + \Omega(1 + re^{2iKL})}. \tag{12}$$

The linear resonance frequencies of the layer are

$$\Omega_l = \frac{l\pi c}{L}, \tag{13}$$

where $l = 1,2,\ldots$. We then simplify the expression in Eq. (12) by considering small vicinities of the resonances, when $KL = l\pi + s$ and $s \ll \pi$. We also use the inequalities $\Omega/c_0 \ll \alpha$ and $n \ll 1$. As a result we have

$$A = \frac{ic_0 S}{\alpha\Omega(2 - is/n)}, \tag{14}$$

which, in particular, gives the resonance function for the amplitude of the difference-frequency signal:

$$|A| = \frac{c_0 S}{\alpha\Omega\sqrt{4 + (L\Delta\omega/cn)^2}}, \tag{15}$$

where $\Delta\omega = cs/L$ is the frequency deviation from resonance. In exact resonance we have

$$|A| = \frac{c_0 S}{2\alpha\Omega} = \frac{\epsilon\Omega P_0^2}{2\alpha\rho_0 c_0^3}. \tag{16}$$

This value is the same for all modes, and it does not depend on the layer length. Moreover, as shown in Ref. 11, the level of the difference-frequency wave for the case of high pump wave attenuation does not depend on the bubble concentration $n(R_\omega)$: the nonlinear parameter ϵ_- and the pump attenuation coefficient α are both proportional to bubble density so that the ratio ϵ/α is conserved. For the near-surface region when the pressure is close to atmospheric pressure, this ratio reads[11,12]

$$\epsilon/\alpha = 5.3 \times 10^4 \lambda/\delta. \tag{17}$$

Note that in resonance, the pressure amplitude of the low-frequency wave radiated from the layer is practically the same as that inside the layer, but this ratio is less for particle velocity by a factor n.

II. EXPERIMENT

The experimental setup is shown in Fig. 1. Experimental studies were carried out in a laboratory tank of dimensions $4 \times 5 \times 3$ m. Although the tank walls were covered by absorbing rubber, the experiments were performed in a pulsed regime, which enabled us to better discriminate the direct signal in the layer from the waves reflected from the walls. Hydrogen bubbles were generated electrolytically, with wires placed over a 70×10-cm foil-covered plate 1.5 m below the water surface, thus forming a bubble layer of thickness l of about 10 cm. The measurements were started 30–40 min after switching the system on, to ensure that a stationary bubble distribution has been established. The pump source was a circular transducer of 10-cm diameter, placed 30 cm before the bubble layer. The generator produced the tone burst signal 2.78 ms in duration, at two carrier frequencies. One of them, $f_1 = 60$ kHz, was kept constant, and the other, f_2, could be varied between 45.2 and 59.2 kHz with steps of 0.4 kHz, so that the difference-frequency waves lay in the frequency band of 0.8–14.8 kHz.

The signal received by the hydrophone (Brüel&Kjaer 8101) was amplified and went through a low-pass filter to ensure that no nonlinear cross modulation occurred in the subsequent electronics. The leading part of the resultant signal was then processed by a spectrum analyzer. The signal was analyzed in a 2.5-ms temporal window so as to pass the signal in the bubble layer only and to avoid receiving a signal reflected from the tank walls. In the limits of this window, the fast Fourier transform with Hanning's window was used, which enabled us to measure the spectrum of the low-frequency component.

The experiments were started with the pump-wave pressure measurements. The pump amplitudes were kept constant at the level of about 2 kPa each. The receiving hydrophone was placed about 20 cm behind the layer. Due to bubbles, the pump waves had a very high attenuation. The level of the pump signal received after passing through the bubble layer for the electrolysis plate voltage of 40 V was 25 dB below the level measured without bubbles, so that the damping rate was about 0.28 cm^{-1} (for these measurements, averaging over 32 pulses was used). Using Eq. (5) and the known damping rate, resonance bubble concentration, $n(\omega_{1,2})$, has been estimated as approximately 2500 cm^{-4}, the corresponding resonance bubble radius is about 50 μm. For higher electrolysis voltages the attenuation decreased to 9–12 dB at 75 V, and larger fluctuations were observed in the attenuation level. The error of attenuation measurements did not exceed 1 dB.

Then the low-frequency signals were studied. First, the sound speed in the bubble layer was measured by using a tone burst signal with the same duration of 2.78 ms and carrier frequency of about 6.4 kHz, the limited size of the tank did not allow us to use much lower frequencies in the pulsed regime. The sound speed was calculated from the time delay between transmitted and received signals in the presence of bubbles and with the bubble generator turned off, respectively. This direct measurement at 6.4 kHz gives $c = 1100$–1300 m/s, depending on the plate voltage (Table I), with a preciseness of about 30 m/s.

TABLE I. Experimental results for two values of voltage.

Electrolysis voltage, V	40	75
Pump wave attenuation, dB	25	9–12
First resonance frequency, kHz	2.4	2.4
Sound speed, m/s (1st resonance)	480	480
Second resonance frequency, kHz	6	5.6
Sound speed, m/s (2nd resonance)	1200	1120
Sound speed at 6.4 kHz (by time of flight)	1300	1100
Difference-frequency signal, Pa (1st resonance, exper.)	2	1.8
Difference-frequency signal, Pa (1st resonance, theory)	3.3	3.3

At measurements or resonance curves of the layer (the dependence of the difference-frequency signal amplitude on its frequency) the receiving hydrophone was placed inside the bubble layer, at about 2.5 cm from its rear side. An averaging over eight pulses was used in this case. The result is shown in Fig. 2. One can see a pronounced resonance at about 2.4 kHz. Considering the layer thickness, this means that the sound speed at this frequency is about 480 m/s. According to the formula (6), this corresponds to the total void fraction of $\beta \simeq 7 \times 10^{-4}$ (for all bubbles smaller than 1.3 mm in radius).

A second (albeit smoother) resonance peak is seen at the frequency of 5.6–6 kHz, depending on the plate voltage. This corresponds to $c = 1120-1200$ m/s for the first mode, which is close to the value obtained from the time-of-flight measurement at 6.4 kHz. This means that we again deal with the first mode of the layer, but the sound speed is higher than that at 2.4 kHz. Such a frequency dispersion indicates that the bubble size distribution function effectively drops in a size range corresponding to resonant frequencies in the interval between 6 and 2.4 kHz. Indeed, it is a well-known effect that sound speed for low-frequency waves in the bubble layer can be much less than in pure water, but it becomes higher with increasing frequency. This is caused by the contribution of resonant bubbles that provide mainly the wave damping rather than the phase shift (note that a similar effect was observed for subsurface bubble layer in sea[10]).

The experimental results are summarized in Table I for two values of voltage. The error of all measurements does not exceed 1 to 2 dB.

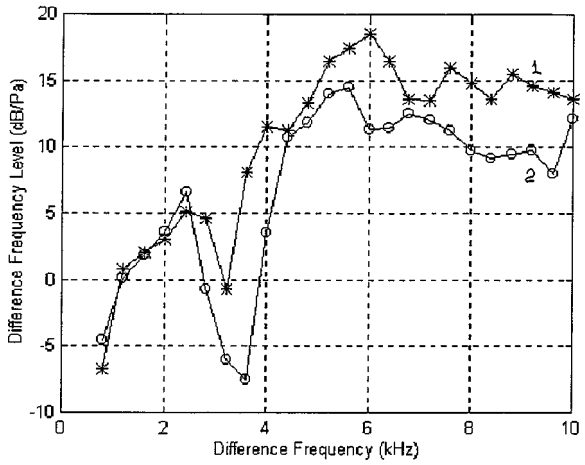

FIG. 2. The dependence of the difference-frequency signal amplitude in the bubble layer on its frequency. Curve 1 was obtained at 40 V on the plate; curve 2 is for 75 V.

Theoretical estimates obtained from Eq. (16) give the value of about 3 Pa for the maximum level of the difference-frequency field in the layer. The value of a single bubble decrement $\delta = 0.1$ was used (see Ref. 12). The observed acoustical pressure in the first resonance was about 2 Pa. Taking into account the aforementioned problems, one may call this reasonably good agreement between theory and experiment.

III. CONCLUSIONS

In this paper, the theory describing the downward frequency transformation in a resonance bubble layer was developed for a realistic case when the pump is resonant with individual bubbles and hence is damped quickly near the input side of the layer whereas the low-frequency signal is resonant with a layer mode. The results of probably the first experiment where the difference-frequency signal was generated in a resonance bubble layer were also demonstrated. These results enabled us to measure the total gas void fraction and to obtain some data regarding the bubble distribution with radii. It is worth noting that the common methods of evaluating the void fraction are inapplicable here: the direct measurement of a traveling wave attenuation [see Eq. (6)] is good for the pump frequencies but not for the difference frequencies due to the limits of propagation path, whereas the bubbles are still too small to use microscopic observations. Therefore the resonance method could be a unique tool for measuring bubbles in the corresponding size range. Most of the data are in satisfactory agreement with the developed theory. Further, we suggest that measurements be performed in better controlled conditions with a larger bubble concentration in order to enhance the quality factor of the layer resonator and to decrease the low-frequency dispersion due to lowering the layer resonance frequency. Thus the efficiency of nonlinear signal transformation can be increased.

The effects considered here can be applied to measurements of subsurface bubble layers in the sea. In principle, such a method enables one simultaneously to measure the bubble void fraction and the thickness of the bubble layer. In addition, the parametric mechanism of low-frequency generation in a bubble layer can affect the ambient noise spectrum in the ocean.

ACKNOWLEDGMENTS

This work was supported by Office of Naval Research (Science Opportunity Program) and Russian Foundation of Basic Research, Grant No. 97-05-64711.

[1] R. J. Urick, *Principles of Underwater Sound* (McGraw-Hill, New York, 1983), 3rd ed.
[2] T. G. Muir, L. A. Thompson, L. R. Cox, and H. G. Frey, ''A low-frequency parametric research tool for ocean acoustics,'' in *Bottom-Interacting Ocean Acoustics*, edited by W. A. Kuperman and F. B. Jensen (Plenum, New York, 1980), pp. 467–483.
[3] H. C. Woodsum, ''Enhancement of parametric efficiency by saturation suppression,'' J. Sound Vib. **69**, 27–33 (1980).
[4] L. Kustov, V. Nazarov, L. Ostrovsky, A. Sutin, and S. Zamolin, ''Para-

metric acoustic radiator with a bubble layer,'' Acoust. Lett. **6**, 15–17 (1982).
[5] V. E. Nazarov and A. M. Sutin, ''Far-field characteristics of a parametric sound radiator with a bubble layer,'' Sov. Phys. Acoust. **30**, 477–479 (1984).
[6] L. M. Kustov, V. E. Nazarov, and A. M. Sutin, ''Nonlinear sound scattering by a bubble layer,'' Sov. Phys. Acoust. **32**, 500–503 (1986).
[7] T. Asada and Y. Watanabe, ''Experiments of parametric amplification using nonlinear vibration of bubbles under water,'' in *Frontiers of Nonlinear Acoustics: Proceedings of 12th ISNA*, edited by M. F. Hamilton and D. T. Blackstock (Elsevier, London, 1990), pp. 485–490.
[8] O. A. Druzhinin, L. A. Ostrovsky, and A. Prosperetti, ''Low-frequency acoustic wave generation in a resonant bubble-layer,'' J. Acoust. Soc. Am. **100**, 3570–3580 (1996).
[9] O. V. Rudenko and S. I. Soluyan, *Theoretical Foundations of Nonlinear Acoustics* (Plenum, New York, 1977).
[10] C. S. Clay and H. Medwin, *Acoustical Oceanography: Principles and Applications* (Wiley, New York, 1977).
[11] Yu. A. Kobelev and A. M. Sutin, ''Difference-frequency sound generation in a liquid containing bubbles of different sizes,'' Sov. Phys. Acoust. **26**, 485–487 (1980).
[12] K. A. Naugolnykh and L. A. Ostrovsky, *Nonlinear Wave Processes in Acoustics* (Cambridge U.P., New York, 1998).

Coherence functions of plane and spherical waves in a turbulent medium with the von Karman spectrum of medium inhomogeneities

V. E. Ostashev
Department of Physics, New Mexico State University, Las Cruces, New Mexico 88003-8001

B. Brähler and V. Mellert
Arbeitsgruppe Akustik, Fachbereich Physik, Universität Oldenburg, Oldenburg D-26111, Germany

G. H. Goedecke
Department of Physics, New Mexico State University, Las Cruces, New Mexico 88003-8001

(Received 14 May 1997; revised 8 April 1998; accepted 13 April 1998)

This paper deals with line-of-sight sound propagation in a medium with the von Karman spectra of temperature and medium velocity fluctuations. The mean sound field, the coherence functions of plane and spherical waves and their coherence radii in such a medium are calculated analytically and numerically. It is found that the temperature and medium velocity contributions to these statistical moments of a sound field may differ significantly. The coherence functions of plane and spherical waves for the von Karman spectrum of medium inhomogeneities have been compared with those for the Kolmogorov and Gaussian spectra. The latter two spectra have been used widely in theories of sound propagation in random media. It is shown that, in limiting cases, the coherence functions calculated for the von Karman spectrum coincide with those calculated for the Kolmogorov and Gaussian spectra. This result supports the use of the Gaussian spectrum in theories of sound propagation in random media. © *1998 Acoustical Society of America.* [S0001-4966(98)00308-7]

PACS numbers: 43.28.Fp, 43.20.Bi, 43.20.Fn [LCS]

INTRODUCTION

The theory of sound propagation in random media is important for many concerns of atmospheric and oceanic acoustics, aeroacoustics and for considering sound propagation through turbulent flows of gases and fluids.[1–3] Random inhomogeneities in a medium can be caused by temperature fluctuations $\tilde{T}$ and medium velocity fluctuations $\mathbf{v}$. The theory of sound propagation in a medium with temperature fluctuations is similar to that of electromagnetic wave propagation in media with light velocity fluctuations. The latter theory has been developed extensively during the last 30–40 years.[3–5] On the other hand, not so many results have been obtained in the theory of sound propagation in moving random media, i.e., in media with temperature and medium velocity fluctuations. The classical and latest results of this theory have been summarized in Refs. 6 and 7.

In theories of waves in random media, the coherence function Γ of an electromagnetic or sound field and its coherence radius are two of the most important statistical characteristics of the field. For example, they are of primary importance for source detection and ranging; an optimal length of an array of microphones, which is used in source detection and ranging, is of the order of a coherence radius. In electrodynamics, Γ has been calculated for the case of plane wave propagation in a medium with the von Karman spectrum of light velocity fluctuations.[8] The von Karman spectrum has been used widely in the theory of turbulence.[3,9] The main goal of the present paper is to calculate the coherence functions Γ of plane and spherical sound waves and their coherence radii in a medium with the von Karman spectra of temperature and medium velocity fluctuations. In a limiting case, the coherence function can be expressed as a product of the mean sound fields. The mean sound field in a medium with the von Karman spectra of temperature and medium velocity fluctuations is calculated in the paper also.

Another goal of the paper is to show that, in limiting cases, the coherence functions of plane and spherical waves calculated for the von Karman spectrum of medium inhomogeneities coincide with those calculated for the Kolmogorov and Gaussian spectra. The Kolmogorov and Gaussian spectra of medium inhomogeneities have been used widely in the literature for calculating the statistical moments of a sound field.[1,3,10–13]

We shall also compare the temperature and medium velocity contributions to the statistical moments of plane and spherical waves in a medium with the von Karman spectrum of medium inhomogeneities. In the recent references,[6,7,14,15] these contributions have been shown to be different for the case of sound propagation in media with the Kolmogorov and Gaussian spectra of medium inhomogeneities. Also it has been shown in these references that the temperature and medium velocity contributions to the statistical moments of a sound field were assumed incorrectly to be the same in previous theories of sound propagation in random media.

The paper is organized as follows. The starting equations for the coherence function and the mean sound field in a medium with arbitrary spectra of temperature and medium velocity fluctuations are presented in Sec. I. The von Karman, Kolmogorov, and Gaussian spectra of temperature and medium velocity fluctuations are considered in Sec. II A. Section II B deals with the calculation of the mean sound

field in a medium with the von Karman spectrum of medium inhomogeneities. The coherence functions of plane and spherical waves and their coherence radii are calculated analytically and numerically in Secs. II C and II D for the case of the von Karman spectrum of temperature and medium velocity fluctuations. Conclusions are summarized in Sec. III.

I. STARTING EQUATIONS

A. Parabolic equation and Markov approximation

The coherence function and the mean sound field will be calculated by using the parabolic equation method and Markov approximation. In the parabolic equation method, the sound field $p(\mathbf{R})$ satisfies the equation[6,7]

$$2ik\frac{\partial p}{\partial x}+\nabla_{\perp}^2 p+2k^2\left(1+\frac{\varepsilon_{\mathrm{mov}}}{2}\right)p=0. \tag{1}$$

Here $\mathbf{R}=(x,\mathbf{r})$ are the Cartesian coordinates with the x-axis in the direction of sound propagation (i.e., from source to receiver), $\mathbf{r}=(y,z)$, $k=2\pi/\lambda$ is the wave number of a sound wave, λ is the wavelength, and $\nabla_{\perp}=(\partial/\partial y,\partial/\partial z)$. Furthermore, in Eq. (1) $\varepsilon_{\mathrm{mov}}=\varepsilon-2v_x/c_0$ are fluctuations in the square of the acoustic refractive index in a moving random medium, $\varepsilon=c_0^2/(c_0+\tilde{c})^2-1$ are those in a motionless random medium, c_0 and $\tilde{c}$ are the mean and fluctuating values of the adiabatic sound speed $c=c_0+\tilde{c}$, and v_x is the x component of the medium velocity vector $\mathbf{v}$. We shall assume that fluctuations ε are caused by fluctuations in the temperature:[6] $\varepsilon=-2\tilde{c}/c_0+O(\tilde{c}^{\,2}/c_0^2)=\beta_c\tilde{T}/T_0+O(\tilde{T}^2/T_0^2)$. Here T_0 is the mean value of the temperature $T=T_0+\tilde{T}$, and $\beta_c=2(T_0/c_0)\,(\partial c_0/\partial T_0)$. Since ε is proportional to $\tilde{T}$ and for the sake of brevity, ε will be referred to hereinafter as temperature fluctuations.

Also we shall assume that temperature and medium velocity fluctuations are statistically homogeneous and isotropic, do not correlate, and that $\nabla\cdot\mathbf{v}=0$ and $\langle\mathbf{v}\rangle=0$, where $\langle\rangle$ means ensemble average. In this case, the correlation function of the random field $\varepsilon_{\mathrm{mov}}$ is given by[6]

$$B_{\mathrm{eff}}(\mathbf{R})=\langle\varepsilon_{\mathrm{mov}}(\mathbf{R_1}+\mathbf{R})\varepsilon_{\mathrm{mov}}(\mathbf{R_1})\rangle$$
$$=B_{\varepsilon}(R)+\frac{4}{c_0^2}\left[B_{RR}(R)+\frac{r^2}{2R}\frac{d}{dR}B_{RR}(R)\right]. \tag{2}$$

Here $B_{\varepsilon}(R)=\langle\varepsilon(\mathbf{R_1}+\mathbf{R})\varepsilon(\mathbf{R_1})\rangle$ is the correlation function of temperature fluctuations, and $B_{RR}(R)=\langle v_R(\mathbf{R_1}+\mathbf{R})v_R(\mathbf{R_1})\rangle$ is the longitudinal correlation function of medium velocity fluctuations, where $v_R(\mathbf{R})$ is a component of the vector $\mathbf{v}$ in the direction of the vector $\mathbf{R}$.

In the Markov approximation, $B_{\mathrm{eff}}(\mathbf{R})$ is proportional to the delta function $\delta(x)$[5,6]

$$B_{\mathrm{eff}}(x,r)=\delta(x)2\pi\int_{-\infty}^{\infty}\int_{-\infty}^{\infty}d^2\kappa\,\exp(i\boldsymbol{\kappa}\cdot\mathbf{r})\Phi_{\mathrm{eff}}(0,\kappa), \tag{3}$$

where $\boldsymbol{\kappa}=(\kappa_y,\kappa_z)$ is a vector whose components are the wave numbers of turbulence in y and z directions, Φ_{eff} is the effective three-dimensional spectral density, and κ and r are the moduli of $\boldsymbol{\kappa}$ and $\mathbf{r}$. In the considered case of statistically homogeneous and isotropic turbulence, Φ_{eff} and B_{eff} depend only on the moduli of $\boldsymbol{\kappa}$ and $\mathbf{r}$, respectively, and $\Phi_{\mathrm{eff}}(0,\kappa)$ is given by[6]

$$\Phi_{\mathrm{eff}}(0,\kappa)=\Phi_{\varepsilon}(\kappa)+4F(\kappa)/c_0^2. \tag{4}$$

Here $\Phi_{\varepsilon}(\kappa)$ and $F(\kappa)$ are the three-dimensional spectral densities of temperature and medium velocity fluctuations, which are related to B_{ε} and B_{RR} by[3,9]

$$B_{\varepsilon}(R)=\frac{4\pi}{R}\int_0^{\infty}d\kappa\,\kappa\sin(\kappa R)\Phi_{\varepsilon}(\kappa), \tag{5}$$

$$B_{RR}(R)=4\pi\int_0^{\infty}d\kappa_1\cos(\kappa_1 R)\int_{\kappa_1}^{\infty}d\kappa\,\frac{\kappa^2-\kappa_1^2}{\kappa}F(\kappa), \tag{6}$$

where κ_1 is an integration variable.

B. Coherence function and mean sound field

The coherence function of a sound field is determined by $\Gamma(x,\mathbf{r_1},\mathbf{r_2})=\langle p(x,\mathbf{r_1})p^*(x,\mathbf{r_2})\rangle$. It is worthwhile introducing new transverse coordinates $\mathbf{r}=\mathbf{r_1}-\mathbf{r_2}$ and $\mathbf{r_+}=(\mathbf{r_1}+\mathbf{r_2})/2$, and denoting the coherence function by $\Gamma(x,\mathbf{r},\mathbf{r_+})$. The mean sound field will be denoted by $\langle p(x,\mathbf{r})\rangle$. Using the parabolic equation method, Markov approximation and results known for electromagnetic wave propagation in a turbulent medium,[3–5] the equations for Γ and $\langle p(x,\mathbf{r})\rangle$ have been derived for plane and spherical waves in a medium with arbitrary spectra of temperature and medium velocity fluctuations.[14,15] The coherence function of a plane wave in a statistically isotropic medium depends only on the modulus of the vector $\mathbf{r}$ and is given by

$$\Gamma_p(x,r)$$
$$=I_p\exp\left\{-\pi^2k^2x\int_0^{\infty}d\kappa\,\kappa[1-J_0(\kappa r)]\Phi_{\mathrm{eff}}(0,\kappa)\right\}. \tag{7}$$

Hereinafter, the subscript p will refer to a plane wave. Furthermore, in Eq. (7) x is a distance of wave propagation in a random medium, J_0 is the Bessel function, and I_p is proportional to the intensity of a plane wave in a medium without random inhomogeneities. The coherence function of a spherical wave is given by

$$\Gamma_s(x,\mathbf{r},\mathbf{r_+})=\frac{I_s}{(4\pi x)^2}\exp\left\{\frac{ik\mathbf{r}\cdot\mathbf{r_+}}{x}-\pi^2k^2x\right.$$
$$\left.\times\int_0^1 dt\int_0^{\infty}d\kappa\,\kappa[1-J_0(\kappa rt)]\Phi_{\mathrm{eff}}(0,\kappa)\right\}, \tag{8}$$

where the subscript s refers to a spherical wave, I_s is proportional to the intensity of a spherical wave in a medium without random inhomogeneities, and t is an integration variable.

The mean sound field $\langle p(x,\mathbf{r})\rangle$ of a plane or spherical wave, calculated by using the parabolic equation method and Markov approximation, exponentially decreases with the distance x

$$\langle p(x,\mathbf{r})\rangle = p_0(x,\mathbf{r})e^{-\gamma x}. \tag{9}$$

Here $p_0(x,\mathbf{r})$ is a sound field in a medium without random inhomogeneities, so that $p_0 = I_p^{1/2}\exp(ikx)$ and $p_0 = I_s^{1/2}\exp(ikR)/4\pi R$ for plane and spherical waves, respectively, and γ is the attenuation coefficient of the mean field due to sound scattering by temperature and medium velocity fluctuations

$$\gamma = \frac{\pi^2 k^2}{2}\int_0^\infty d\kappa\,\kappa\,\Phi_{\text{eff}}(0,\kappa). \tag{10}$$

In the limiting case $\Phi_{\text{eff}}(0,\kappa) = \Phi_\varepsilon(\kappa)$, i.e., when there are no medium velocity fluctuations, Eqs. (7)–(10) coincide with those known for electromagnetic wave propagation.[3–5]

II. THEORY AND NUMERICAL RESULTS

A. Spectra of turbulence

For the von Karman spectrum, the three-dimensional spectral densities of temperature and medium velocity fluctuations are given by (e.g., Ref. 7)

$$\begin{aligned}\Phi_\varepsilon^{\text{vK}}(\kappa) &= AC_\varepsilon^2(\kappa^2+\kappa_0^2)^{-11/6},\\ F^{\text{vK}}(\kappa) &= (11/6)AC_v^2\kappa^2(\kappa^2+\kappa_0^2)^{-17/6}.\end{aligned} \tag{11}$$

Hereinafter, the superscript vK will refer to the von Karman spectrum. Also in Eq. (11) $A = 5/(18\pi\Gamma(1/3)) = 0.033$, $\Gamma(1/3)$ is the Gamma-function, κ_0 is a characteristic wave number of the turbulence, and C_ε^2 and C_v^2 are the structure parameters of the random fields ε and $\mathbf{v}$, characterizing the intensity of turbulence. Strictly speaking, $\Phi_\varepsilon^{\text{vK}}(\kappa)$ and $F^{\text{vK}}(\kappa)$ in Eq. (11) should also contain a sharp cutoff factor like $\exp(-\kappa^2/\kappa_m^2)$, where $\kappa_m = 5.92/\eta_0$, and η_0 is the Kolmogorov microscale of turbulence. But this factor can be omitted since for most cases of sound propagation in random media $\lambda \gg \eta_0$.[6,7] Note that $F^{\text{vK}}(\kappa)$ contains a factor κ^2. This factor is a consequence of the assumption that $\nabla\cdot\mathbf{v} = 0$.[9] On the other hand, $\Phi_\varepsilon^{\text{vK}}(\kappa)$ is the three-dimensional spectral density of temperature fluctuations which is not required to have a factor κ^2. Following classical theories of waves in random media,[3–5] we assume that $\Phi_\varepsilon^{\text{vK}}$ does not have this factor and is given by Eq. (11). Modeling homogeneous and isotropic turbulence by an ensemble of turbules[16] also shows that $\Phi_\varepsilon^{\text{vK}}(\kappa)$ does not contain the factor κ^2 analogous to that in equation for $F^{\text{vK}}(\kappa)$.

It follows from Eqs. (4) and (11) that, for the von Karman spectrum, the effective three-dimensional spectral density Φ_{eff} is given by

$$\Phi_{\text{eff}}^{\text{vK}}(0,\kappa) = A\left(C_\varepsilon^2 + \frac{22}{3}\frac{C_v^2}{c_0^2}\frac{\kappa^2}{\kappa^2+\kappa_0^2}\right)(\kappa^2+\kappa_0^2)^{-11/6}. \tag{12}$$

Substituting the functions $\Phi_\varepsilon^{\text{vK}}$ and F^{vK} from Eq. (11) into Eqs. (5) and (6) and calculating the integrals over κ yields the correlation functions $B_\varepsilon(R)$ and $B_{RR}(R)$ for the von Karman spectrum

$$B_\varepsilon^{\text{vK}}(R) = \frac{\Gamma(1/3)}{\pi 2^{2/3}\sqrt{3}}C_\varepsilon^2\kappa_0^{-2/3}(\kappa_0 R)^{1/3}K_{1/3}(\kappa_0 R), \tag{13}$$

$$B_{RR}^{\text{vK}}(R) = \frac{\Gamma(1/3)}{\pi 2^{2/3}\sqrt{3}}C_v^2\kappa_0^{-2/3}(\kappa_0 R)^{1/3}K_{1/3}(\kappa_0 R). \tag{14}$$

Here $K_{1/3}$ is the modified Bessel function of the order 1/3. Substituting Eqs. (13) and (14) into Eq. (2) one obtains the correlation function $B_{\text{eff}}(\mathbf{R})$ for the von Karman spectrum

$$B_{\text{eff}}^{\text{vK}}(\mathbf{R}) = \frac{\Gamma(1/3)\kappa_0^{-2/3}(\kappa_0 R)^{1/3}}{\pi 2^{2/3}\sqrt{3}}\left\{C_\varepsilon^2 K_{1/3}(\kappa_0 R) + \frac{4C_v^2}{c_0^2}\left[K_{1/3}(\kappa_0 R) - \frac{\kappa_0 r^2}{2R}K_{2/3}(\kappa_0 R)\right]\right\}. \tag{15}$$

For this spectrum, the variance σ_{mov}^2 of the random field ε_{mov} can be obtained from Eq. (15)

$$\sigma_{\text{mov},vK}^2 = B_{\text{eff}}^{\text{vK}}(0) = \frac{\Gamma^2(1/3)\kappa_0^{-2/3}}{\pi 2^{4/3}\sqrt{3}}\left\{C_\varepsilon^2 + \frac{4C_v^2}{c_0^2}\right\}. \tag{16}$$

The Kolmogorov and Gaussian spectra have most widely been used previously for calculating the statistical moments of a sound field propagating in a random medium.[1,3,4,7] For the Kolmogorov spectrum, the three-dimensional spectral densities of temperature and medium velocity fluctuations, Φ_ε and F, and the structure functions of temperature and medium velocity fluctuations, D_ε and D_{RR}, are given by[3,9]

$$\Phi_\varepsilon^{\text{K}}(\kappa) = AC_\varepsilon^2\kappa^{-11/3},\quad F^{\text{K}}(\kappa) = (11/6)AC_v^2\kappa^{-11/3}, \tag{17}$$

$$D_\varepsilon^{\text{K}}(R) = C_\varepsilon^2 R^{2/3},\quad D_{RR}^{\text{K}}(R) = C_v^2 R^{2/3}. \tag{18}$$

Here the superscript K refers to the Kolmogorov spectrum. A comparison between Eqs. (11) and (17) reveals that $\Phi_\varepsilon^{\text{vK}}(\kappa) \approx \Phi_\varepsilon^{\text{K}}(\kappa)$ and $F^{\text{vK}}(\kappa) \approx F^{\text{K}}(\kappa)$ if $\kappa \gg \kappa_0$. For the Kolmogorov spectrum, the correlation functions B_ε^{K} and B_{RR}^{K} do not exist. Note that, if the correlation function $B(R)$ of a random field does exist, it is related to the structure function $D(R)$ of this field by[3,5]

$$D(R) = 2[B(0) - B(R)]. \tag{19}$$

For the Gaussian spectrum, the three-dimensional spectral densities of temperature and medium velocity fluctuations and the corresponding correlation functions are given by[1,6]

$$\Phi_\varepsilon^{\text{G}}(\kappa) = \frac{\sigma_\varepsilon^2 l^3}{8\pi^{3/2}}e^{-\kappa^2 l^2/4},\quad F^{\text{G}}(\kappa) = \frac{\sigma_v^2\kappa^2 l^5}{32\pi^{3/2}}e^{-\kappa^2 l^2/4}, \tag{20}$$

$$B_\varepsilon^{\text{G}}(R) = \sigma_\varepsilon^2 e^{-R^2/l^2},\quad B_{RR}^{\text{G}}(R) = \sigma_v^2 e^{-R^2/l^2}. \tag{21}$$

Hereinafter, the superscript G will refer to the Gaussian spectrum. In Eqs. (20) and (21), l is the correlation length of medium inhomogeneities, and σ_ε^2 and σ_v^2 are the variances of ε and v_R. The functions $\Phi_\varepsilon^{\text{vK}}(\kappa)$ and $\Phi_\varepsilon^{\text{G}}(\kappa)$, and the functions $F^{\text{vK}}(\kappa)$ and $F^{\text{G}}(\kappa)$ have similar dependences on κ if $\kappa \ll \kappa_0$ and $\kappa \ll 1/l$.

The relationship between C_ε^2, C_v^2, κ_0 in Eq. (11) and σ_ε^2, σ_v^2, l in Eq. (20) can be obtained by comparing the correlation functions $B_\varepsilon^{\text{vK}}(R)$ and $B_\varepsilon^{\text{G}}(R)$, and by comparing

the correlation functions $B_{RR}^{\mathrm{vK}}(R)$ and $B_{RR}^{\mathrm{G}}(R)$. We shall assume that the variance of ε is the same for both the von Karman and Gaussian spectra: $B_{\varepsilon}^{\mathrm{vK}}(0)=B_{\varepsilon}^{\mathrm{G}}(0)$; and similarly for the variance of v_R: $B_{RR}^{\mathrm{vK}}(0)=B_{RR}^{\mathrm{G}}(0)$. Substitution of Eqs. (13), (14), and (21) into these equalities allows one to express σ_{ε}^2 in terms of κ_0 and C_{ε}^2, and σ_v^2 in terms of κ_0 and C_v^2:

$$\sigma_{\varepsilon}^2=\frac{\Gamma^2(1/3)}{\pi 2^{4/3}\sqrt{3}}C_{\varepsilon}^2\kappa_0^{-2/3}\cong 0.523C_{\varepsilon}^2\kappa_0^{-2/3},$$
$$\sigma_v^2=\frac{\Gamma^2(1/3)}{\pi 2^{4/3}\sqrt{3}}C_v^2\kappa_0^{-2/3}\cong 0.523C_v^2\kappa_0^{-2/3}. \tag{22}$$

To obtain the relationship between l and κ_0, we shall assume that the correlation functions $B_{\varepsilon}^{\mathrm{vK}}(R)$ and $B_{\varepsilon}^{\mathrm{G}}(R)$ have the same integral length, and that the integral length of $B_{RR}^{\mathrm{vK}}(R)$ and $B_{RR}^{\mathrm{G}}(R)$ is also the same:

$$\int_0^{\infty}dRB_{\varepsilon}^{\mathrm{vK}}(R)=\int_0^{\infty}dRB_{\varepsilon}^{\mathrm{G}}(R),$$
$$\int_0^{\infty}dRB_{RR}^{\mathrm{vK}}(R)=\int_0^{\infty}dRB_{RR}^{\mathrm{G}}(R). \tag{23}$$

Substituting $B_{\varepsilon}^{\mathrm{vK}}(R)$ and $B_{\varepsilon}^{\mathrm{G}}(R)$ from Eqs. (13) and (21) into Eq. (23) and calculating the integrals over R yields the relationship between l and κ_0:

$$l=\frac{2\Gamma(5/6)}{\Gamma(1/3)}\kappa_0^{-1}\cong 0.843\kappa_0^{-1}. \tag{24}$$

The same relationship is obtained when substituting $B_{RR}^{\mathrm{vK}}(R)$ and $B_{RR}^{\mathrm{G}}(R)$ from Eqs. (14) and (21) into Eq. (23) and calculating the integrals over R.

Equations (22) and (24) are important relationships obtained in the paper. They allow one to express σ_{ε}^2, σ_v^2, and l appearing in the Gaussian spectra in terms of C_{ε}^2, C_v^2, and κ_0 appearing in the von Karman spectra. Also these relationships allow us to compare the von Karman, Kolmogorov and Gaussian spectra. It is worthwhile to do such a comparison in the space domain, i.e., to compare the structure functions of temperature and medium velocity fluctuations for the spectra involved.

The structure functions of temperature and medium velocity fluctuations for the von Karman spectrum, $D_{\varepsilon}^{\mathrm{vK}}(R)$ and $D_{RR}^{\mathrm{vK}}(R)$, can be obtained by substitution of Eqs. (13) and (14) into Eq. (19). These structure functions, normalized by σ_{ε}^2 and σ_v^2, are given by

$$D_{RR}^{\mathrm{vK}}(R)/\sigma_v^2=D_{\varepsilon}^{\mathrm{vK}}(R)/\sigma_{\varepsilon}^2$$
$$=2[1-(2^{2/3}/\Gamma(1/3))(\kappa_0R)^{1/3}K_{1/3}(\kappa_0R)]. \tag{25}$$

For the Kolmogorov spectrum, the normalized structure functions of temperature and medium velocity fluctuations can be obtained from Eqs. (18) and (22)

$$D_{RR}^{\mathrm{K}}(R)/\sigma_v^2=D_{\varepsilon}^{\mathrm{K}}(R)/\sigma_{\varepsilon}^2=(\pi 2^{4/3}\sqrt{3}/\Gamma^2(1/3))(\kappa_0R)^{2/3}. \tag{26}$$

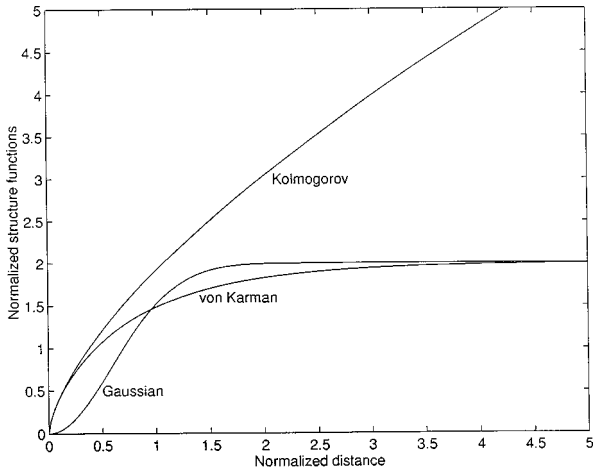

FIG. 1. The normalized structure functions for temperature (medium velocity) fluctuations for the von Karman, Kolmogorov and Gaussian spectra versus the normalized distance κ_0R.

For the Gaussian spectrum, the structure functions of temperature and medium velocity fluctuations, $D_{\varepsilon}^{\mathrm{G}}(R)$ and $D_{RR}^{\mathrm{G}}(R)$, can be obtained by the substitution of Eq. (21) into Eq. (19). The structure functions, normalized by σ_{ε}^2 and σ_v^2, are given by

$$D_{RR}^{\mathrm{G}}(R)/\sigma_v^2=D_{\varepsilon}^{\mathrm{G}}(R)/\sigma_{\varepsilon}^2=2[1-\exp(-R^2/l^2)]. \tag{27}$$

It follows from Eqs. (25)–(27) that the normalized structure functions of temperature fluctuations coincide with those of medium velocity fluctuations. The normalized structure functions of temperature and medium velocity fluctuations for the von Karman, Kolmogorov and Gaussian spectra versus κ_0R are plotted in Fig. 1. It is seen from the figure that, as one would expect for $\kappa_0R\ll 1$ (this corresponds to $\kappa\gg\kappa_0$), the normalized structure function for the von Karman spectrum coincides with that for the Kolmogorov spectrum. In the opposite limiting case $\kappa_0R\gg 1$ (this corresponds to $\kappa\ll\kappa_0$), the normalized structure function for the von Karman spectrum coincides with that for the Gaussian spectrum. This is a consequence of the relationships $B_{\varepsilon}^{\mathrm{vK}}(0)=B_{\varepsilon}^{\mathrm{G}}(0)$, $B_{RR}^{\mathrm{vK}}(0)=B_{RR}^{\mathrm{G}}(0)$ and those in Eq. (23), assumed above. Because of these equalities one would expect that the mean sound field and the coherence function calculated for the von Karman spectrum must coincide with those calculated for the Kolmogorov and Gaussian spectra in limiting cases. However, only rigorous analysis, which is presented below in Secs. II B–II D, can prove such equivalences and give their ranges of applicability.

B. Mean sound field

Substituting Eq. (12) into Eq. (10) and calculating the integral over κ yields the equation for the attenuation coefficient γ of the mean sound field for the von Karman spectrum of medium inhomogeneities

$$\gamma^{\mathrm{vK}}=\gamma_{\varepsilon}^{\mathrm{vK}}+\gamma_v^{\mathrm{vK}}=\frac{3}{10}\pi^2Ak^2\kappa_0^{-5/3}\left(C_{\varepsilon}^2+\frac{4C_v^2}{c_0^2}\right). \tag{28}$$

Here $\gamma_{\varepsilon}^{\mathrm{vK}}$ and γ_v^{vK} are the temperature and medium velocity contributions to γ^{vK}. Equation (28) is a new result in theories

of waves in random media. This equation is valid both for plane and spherical waves. For convenience in comparing the temperature and medium velocity contributions to γ and, below, to Γ, we shall assume that

$$C_\varepsilon^2 = 4C_v^2/c_0^2. \tag{29}$$

If this equality were valid, the temperature and medium velocity fluctuations would make the same contributions to the variance $\sigma^2_{\mathrm{mov},vK}$ of the random field $\varepsilon_{\mathrm{mov}}$, calculated for the von Karman spectrum and given by Eq. (16). Since the von Karman spectrum becomes the Kolmogorov one for $\kappa_0 \to \infty$, Eq. (29) is also used for comparing the temperature and medium velocity contributions to the statistical moments of a sound field for the Kolmogorov spectrum of medium inhomogeneities. For the Gaussian spectrum, it can be shown from Eqs. (2) and (21) that the variance of the random field $\varepsilon_{\mathrm{mov}}$ is given by $B^{\mathrm{G}}_{\mathrm{eff}}(0) = \sigma_\varepsilon^2 + 4\sigma_v^2/c_0^2$. The temperature and medium velocity contributions to the variance are the same if $\sigma_\varepsilon^2 = 4\sigma_v^2/c_0^2$. This relationship can also be obtained from Eq. (29) by replacing C_ε^2 and C_v^2 by their values from Eq. (22).

If Eq. (29) is valid, $\gamma_\varepsilon^{\mathrm{vK}} = \gamma_v^{\mathrm{vK}}$, i.e., the temperature and medium velocity contributions to γ^{vK} are the same.

For $\kappa_0 \to 0$ in Eq. (28), one finds that the attenuation coefficient γ^{K} for the Kolmogorov spectrum tends to infinity. Hence the mean sound field $\langle p \rangle = 0$ for this case.

For the Gaussian spectrum, the attenuation coefficient γ^{G} has been calculated in Ref. 14

$$\gamma^{\mathrm{G}} = \gamma_\varepsilon^{\mathrm{G}} + \gamma_v^{\mathrm{G}} = \frac{\sqrt{\pi} k^2 l}{8}\left(\sigma_\varepsilon^2 + \frac{4\sigma_v^2}{c_0^2}\right). \tag{30}$$

Here $\gamma_\varepsilon^{\mathrm{G}}$ and γ_v^{G} are the temperature and medium velocity contributions to γ^{G}. Substituting Eqs. (22) and (24) into Eq. (30) and comparing the resulting equation with Eq. (28), it can be shown that $\gamma_\varepsilon^{\mathrm{vK}} = \gamma_\varepsilon^{\mathrm{G}}$, $\gamma_v^{\mathrm{vK}} = \gamma_v^{\mathrm{G}}$ and, hence, $\gamma^{\mathrm{vK}} = \gamma^{\mathrm{G}}$. These equalities actually are a consequence of the assumed integral relationships between $B_\varepsilon^{\mathrm{vK}}$ and $B_\varepsilon^{\mathrm{G}}$, and between B_{RR}^{vK} and B_{RR}^{G}, given by Eq. (23). Indeed, taking into account that Φ_{eff} is the Fourier transform of B_{eff}, Eq. (10) can be written as $\gamma = (k^2/4)\int_0^\infty dx B_{\mathrm{eff}}(x,0)$. Substitution of Eq. (2) into the integrand of this equation yields

$$\gamma = \gamma_\varepsilon + \gamma_v = \frac{k^2}{4}\int_0^\infty dx\left[B_\varepsilon(x) + \frac{4}{c_0^2}B_{RR}(x)\right]. \tag{31}$$

It can be shown easily from this equation and Eq. (23) that $\gamma_\varepsilon^{\mathrm{vK}} = \gamma_\varepsilon^{\mathrm{G}}$, $\gamma_v^{\mathrm{vK}} = \gamma_v^{\mathrm{G}}$, and $\gamma^{\mathrm{vK}} = \gamma^{\mathrm{G}}$.

C. Coherence function of a plane wave

To calculate the coherence function Γ_p^{vK} of a plane wave in a medium with the von Karman spectra of temperature and medium velocity fluctuations, we substitute $\Phi_{\mathrm{eff}}^{\mathrm{vK}}$ from Eq. (12) into Eq. (7). Calculations of the integral over κ in the resulting equation are presented in the Appendix. As a result, one obtains

$$\Gamma_p^{\mathrm{vK}}(x,r) = I_p \Gamma_{p,\varepsilon}^{\mathrm{vK}}(x,r)\Gamma_{p,v}^{\mathrm{vK}}(x,r). \tag{32}$$

Here $\Gamma_{p,\varepsilon}^{\mathrm{vK}}$ and $\Gamma_{p,v}^{\mathrm{vK}}$ are the factors of Γ_p^{vK} due to sound scattering by temperature and medium velocity fluctuations with the von Karman spectrum, given by

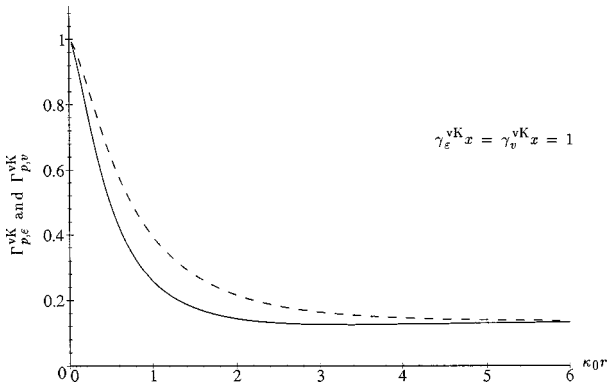

FIG. 2. The temperature ($\Gamma_{p,\varepsilon}^{\mathrm{vK}}$, dashed line) and medium velocity ($\Gamma_{p,v}^{\mathrm{vK}}$, solid line) contributions to the coherence function of a plane wave for the von Karman spectrum.

$$\Gamma_{p,\varepsilon}^{\mathrm{vK}}(x,r) = \exp\left\{-\frac{3}{5}\pi^2 A C_\varepsilon^2 k^2 \kappa_0^{-5/3} x\left[1 - \frac{\Gamma(1/6)}{\pi}\left(\frac{\kappa_0 r}{2}\right)^{5/6} \times K_{5/6}(\kappa_0 r)\right]\right\}, \tag{33}$$

$$\Gamma_{p,v}^{\mathrm{vK}}(x,r) = \exp\left\{-\frac{12}{5}\pi^2 A \frac{C_v^2}{c_0^2} k^2 \kappa_0^{-5/3} x\left[1 - \frac{\Gamma(1/6)}{\pi}\left(\frac{\kappa_0 r}{2}\right)^{5/6} \times \left(K_{5/6}(\kappa_0 r) - \frac{\kappa_0 r}{2}K_{1/6}(\kappa_0 r)\right)\right]\right\}, \tag{34}$$

where $K_{5/6}$ and $K_{1/6}$ are the modified Bessel functions of the order 5/6 and 1/6, respectively. Using Eq. (28) for $\gamma_\varepsilon^{\mathrm{vK}}$ and γ_v^{vK}, $\Gamma_{p,\varepsilon}^{\mathrm{vK}}$ and $\Gamma_{p,v}^{\mathrm{vK}}$ can be rewritten as:

$$\Gamma_{p,\varepsilon}^{\mathrm{vK}}(x,r) = \exp\left\{-2\gamma_\varepsilon^{\mathrm{vK}} x\left[1 - \frac{\Gamma(1/6)}{\pi}\left(\frac{\kappa_0 r}{2}\right)^{5/6} K_{5/6}(\kappa_0 r)\right]\right\}, \tag{35}$$

$$\Gamma_{p,v}^{\mathrm{vK}}(x,r) = \exp\left\{-2\gamma_v^{\mathrm{vK}} x\left[1 - \frac{\Gamma(1/6)}{\pi}\left(\frac{\kappa_0 r}{2}\right)^{5/6} \times \left(K_{5/6}(\kappa_0 r) - \frac{\kappa_0 r}{2}K_{1/6}(\kappa_0 r)\right)\right]\right\}. \tag{36}$$

Equation (35) has been obtained in Ref. 8, while Eq. (36) is a new result. It follows from these equations that the temperature and medium velocity contributions to the coherence function, $\Gamma_{p,\varepsilon}^{\mathrm{vK}}$ and $\Gamma_{p,v}^{\mathrm{vK}}$, are different even if Eq. (29) is valid. Moreover, $\Gamma_{p,\varepsilon}^{\mathrm{vK}}(x,r) > \Gamma_{p,v}^{\mathrm{vK}}(x,r)$ for all values of r and $\gamma_\varepsilon^{\mathrm{vK}} x = \gamma_v^{\mathrm{vK}} x$ since $K_{1/6}(\kappa_0 r) > 0$ for $\kappa_0 r > 0$. The functions $\Gamma_{p,\varepsilon}^{\mathrm{vK}}(x,r)$ and $\Gamma_{p,v}^{\mathrm{vK}}(x,r)$ are plotted in Fig. 2 for $\gamma_\varepsilon^{\mathrm{vK}} x = \gamma_v^{\mathrm{vK}} x = 1$.

Another way to compare the coherence functions $\Gamma_{p,\varepsilon}^{\mathrm{vK}}(x,r)$ and $\Gamma_{p,v}^{\mathrm{vK}}(x,r)$ is to compare their coherence radii

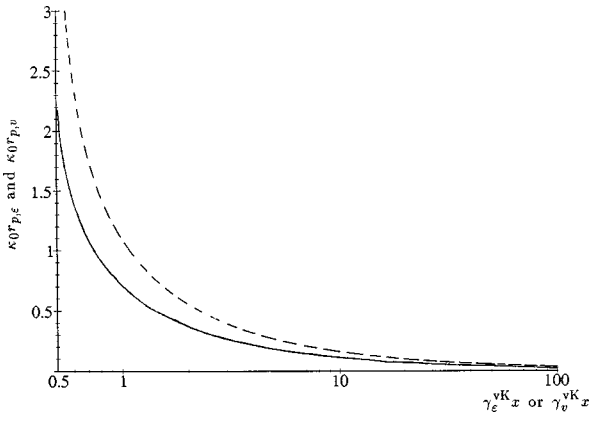

FIG. 3. The normalized coherence radii $\kappa_0 r_{p,\varepsilon}$ (dashed line) and $\kappa_0 r_{p,v}$ (solid line) for a plane wave and the von Karman spectrum.

$r_{p,\varepsilon}$ and $r_{p,v}$, which are the most important characteristics of the coherence functions. The coherence radii $r_{p,\varepsilon}$ and $r_{p,v}$ are determined by the following equations:

$$\Gamma_{p,\varepsilon}^{\mathrm{vK}}(x, r_{p,\varepsilon}) = \Gamma_{p,\varepsilon}^{\mathrm{vK}}(x,0)/e,$$
$$\Gamma_{p,v}^{\mathrm{vK}}(x, r_{p,v}) = \Gamma_{p,v}^{\mathrm{vK}}(x,0)/e. \tag{37}$$

According to Eqs. (37), the coherence radii determine a separation between two points on a wavefront, at which the coherence functions are decreased by a factor of e. It follows from Eqs. (35)–(37) that the coherence radii $r_{p,\varepsilon}$ and $r_{p,v}$ satisfy the following equations:

$$2\gamma_\varepsilon^{\mathrm{vK}} x\left[1 - \frac{\Gamma(1/6)}{\pi}\left(\frac{\kappa_0 r_{p,\varepsilon}}{2}\right)^{5/6} K_{5/6}(\kappa_0 r_{p,\varepsilon})\right] = 1, \tag{38}$$

$$2\gamma_v^{\mathrm{vK}} x\left[1 - \frac{\Gamma(1/6)}{\pi}\left(\frac{\kappa_0 r_{p,v}}{2}\right)^{5/6}\left(K_{5/6}(\kappa_0 r_{p,v}) - \frac{\kappa_0 r_{p,v}}{2} K_{1/6}(\kappa_0 r_{p,v})\right)\right] = 1. \tag{39}$$

It is seen from Eqs. (38) and (39) that the normalized coherence radii $\kappa_0 r_{p,\varepsilon}$ and $\kappa_0 r_{p,v}$ depend only on $\gamma_\varepsilon^{\mathrm{vK}} x$ and $\gamma_v^{\mathrm{vK}} x$, respectively. The normalized coherence radii are obtained by numerical solution of these equations and are plotted in Fig. 3 as functions of $\gamma_\varepsilon^{\mathrm{vK}} x = \gamma_v^{\mathrm{vK}} x$. In the figure, $\gamma_\varepsilon^{\mathrm{vK}} x = \gamma_v^{\mathrm{vK}} x \geqslant 1/2$. Note that Eq. (38) has no solution for $\kappa_0 r_{p,\varepsilon}$ if $\gamma_\varepsilon^{\mathrm{vK}} x < 1/2$ since the expression in the square brackets in Eq. (38) is always less than 1. Equation (39) has either two or no solutions for $\kappa_0 r_{p,v}$ if $\gamma_v^{\mathrm{vK}} x < 1/2$, which are not discussed here for brevity. Figure 3 shows that $r_{p,\varepsilon} > r_{p,v}$ for all values of $\gamma_\varepsilon^{\mathrm{vK}} x = \gamma_v^{\mathrm{vK}} x$. Also it is seen from the figure that $\kappa_0 r_{p,\varepsilon} \to \infty$ if $\gamma_\varepsilon^{\mathrm{vK}} x \to 1/2 + 0$. On the other hand, $\kappa_0 r_{p,v}$ reaches the finite value 2.26 for $\gamma_v^{\mathrm{vK}} x = 1/2$. It also follows from Fig. 3 that $\kappa_0 r_{p,\varepsilon} \to 0$ and $\kappa_0 r_{p,v} \to 0$ if $\gamma_\varepsilon^{\mathrm{vK}} x = \gamma_v^{\mathrm{vK}} x \to \infty$. The ratio $r_{p,\varepsilon}/r_{p,v}$ of the coherence radii tends to infinity for $\gamma_\varepsilon^{\mathrm{vK}} x = \gamma_v^{\mathrm{vK}} x \to 1/2 + 0$, rapidly drops to a value of about 1.5 for $\gamma_\varepsilon^{\mathrm{vK}} x = \gamma_v^{\mathrm{vK}} x \sim 1$, and reaches the minimal value $(11/6)^{3/5} = 1.44$ if $\gamma_\varepsilon^{\mathrm{vK}} x = \gamma_v^{\mathrm{vK}} x \to \infty$.

Let us compare the coherence function Γ_p^{vK} calculated for the von Karman spectrum with those calculated for the Kolmogorov and Gaussian spectra. To do this, we shall consider two limiting cases of Eqs. (35) and (36). The first limiting case is $\kappa_0 r \ll 1$ or $r \ll \lambda$. Expanding the functions $K_{5/6}(\kappa_0 r)$ and $K_{1/6}(\kappa_0 r)$ into series in terms of $\kappa_0 r$, one obtains

$$\Gamma_{p,\varepsilon}^{\mathrm{vK}}(x,r) = \exp\left\{-2\gamma_\varepsilon^{\mathrm{vK}} x\left[\frac{3\pi 2^{1/3}}{5\Gamma^2(5/6)}(\kappa_0 r)^{5/3} - \frac{3}{2}(\kappa_0 r)^2 + O(\kappa_0 r)^{11/3}\right]\right\} \quad \text{if} \quad \kappa_0 r \ll 1, \tag{40}$$

$$\Gamma_{p,v}^{\mathrm{vK}}(x,r) = \exp\left\{-2\gamma_v^{\mathrm{vK}} x\left[\frac{11\pi 2^{1/3}}{10\Gamma^2(5/6)}(\kappa_0 r)^{5/3} - 3(\kappa_0 r)^2 + O(\kappa_0 r)^{11/3}\right]\right\} \quad \text{if} \quad \kappa_0 r \ll 1. \tag{41}$$

Now we compare Eqs. (40) and (41) with the temperature and medium velocity contributions to the coherence function of a plane wave for the Kolmogorov spectrum, given by

$$\Gamma_{p,\varepsilon}^{\mathrm{K}}(x,r) = \exp(-BC_\varepsilon^2 k^2 r^{5/3} x),$$
$$\Gamma_{p,v}^{\mathrm{K}}(x,r) = \exp\left(-B\frac{22}{3}\frac{C_v^2}{c_0^2} k^2 r^{5/3} x\right), \tag{42}$$

where $B = [\sqrt{3}\Gamma^2(1/3)]/[2^{7/3} 5\Gamma(2/3)] = 0.364$. The equation for $\Gamma_{p,\varepsilon}^{\mathrm{K}}$ is presented in Ref. 4. According to the theory developed in Ref. 6, the equation for $\Gamma_{p,v}^{\mathrm{K}}$ is obtained from the equation for $\Gamma_{p,\varepsilon}^{\mathrm{K}}$ by replacing C_ε^2 by $(22/3)C_v^2/c_0^2$. Substituting the values of $\gamma_\varepsilon^{\mathrm{vK}}$ and γ_v^{vK}, given by Eq. (28), into Eqs. (40) and (41) and omitting terms proportional to $(\kappa_0 r)^2$ and $(\kappa_0 r)^{11/3}$, one obtains that $\Gamma_{p,\varepsilon}^{\mathrm{vK}}(x,r) = \Gamma_{p,\varepsilon}^{\mathrm{K}}(x,r)$ and $\Gamma_{p,v}^{\mathrm{vK}}(x,r) = \Gamma_{p,v}^{\mathrm{K}}(x,r)$. Thus in the limiting case $\kappa_0 r \ll 1$, the temperature contributions to the coherence functions for the von Karman and Kolmogorov spectrum are the same, and so are the medium velocity contributions to Γ for these spectra. This result is due to the fact that the structure functions of temperature fluctuations for the von Karman and Kolmogorov spectra coincide for $\kappa_0 R \ll 1$ (see Fig. 1), and hence so do the structure functions of medium velocity fluctuations.

The second limiting case is $\kappa_0 r \gg 1$. Replacing $K_{5/6}(\kappa_0 r)$ and $K_{1/6}(\kappa_0 r)$ in Eqs. (35) and (36) by their asymptotes for large values of arguments yields

$$\Gamma_{p,\varepsilon}^{\mathrm{vK}}(x,r) = \exp\left\{-2\gamma_\varepsilon^{\mathrm{vK}} x \times\left[1 - \frac{\Gamma(1/6)(\kappa_0 r)^{1/3}}{\sqrt{\pi} 2^{4/3}} e^{-\kappa_0 r}\right]\right\} \quad \text{if} \quad \kappa_0 r \gg 1, \tag{43}$$

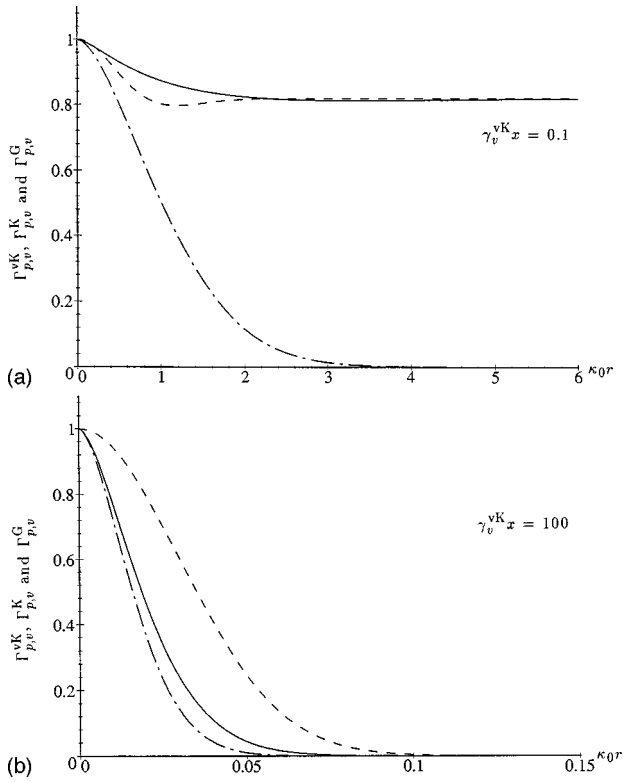

FIG. 4. The medium velocity contributions to the coherence function of a plane wave for the von Karman ($\Gamma_{p,v}^{vK}$, solid line), Kolmogorov ($\Gamma_{p,v}^{K}$, dash-dotted line) and Gaussian ($\Gamma_{p,v}^{G}$, dashed line) spectra. (a) $\gamma_v^{vK}x=0.1$ and (b) $\gamma_v^{vK}x=100$.

$$\Gamma_{p,v}^{vK}(x,r)=\exp\left\{-2\gamma_v^{vK}x\left[1-\frac{\Gamma(1/6)(\kappa_0 r)^{1/3}}{\sqrt{\pi}2^{7/3}}\times\left(\frac{19}{9}-\kappa_0 r\right)e^{-\kappa_0 r}\right]\right\} \quad \text{if} \quad \kappa_0 r\gg 1. \tag{44}$$

Let us compare these equations with the temperature and medium velocity contributions to the coherence function of a plane wave for the Gaussian spectrum, given by Ref. 14

$$\Gamma_{p,\varepsilon}^{G}(x,r)=\exp\{-2\gamma_\varepsilon^{G}x[1-e^{-r^2/l^2}]\},$$
$$\Gamma_{p,v}^{G}(x,r)=\exp\left\{-2\gamma_v^{G}x\left[1-\left(1-\frac{r^2}{l^2}\right)e^{-r^2/l^2}\right]\right\}. \tag{45}$$

For $\kappa_0 r\gg 1$, second terms in the square brackets in Eqs. (43)–(45) can be neglected. Taking into account that $\gamma_\varepsilon^{vK}=\gamma_\varepsilon^{G}$ and $\gamma_v^{vK}=\gamma_v^{G}$, one obtains $\Gamma_{p,\varepsilon}^{vK}=\Gamma_{p,\varepsilon}^{G}=\exp(-2\gamma_\varepsilon^{vK}x)$ and $\Gamma_{p,v}^{vK}=\Gamma_{p,v}^{G}=\exp(-2\gamma_v^{vK}x)$. Thus if $\kappa_0 r\gg 1$, the temperature contributions to the coherence functions for the von Karman and Gaussian spectra are the same, so are the medium velocity contributions to Γ for these spectra. This is due to the fact that the structure functions for temperature and medium velocity fluctuations for the von Karman spectrum coincide with those for the Gaussian spectrum for $\kappa_0 R\gg 1$, see Fig. 1.

The medium velocity contributions to the coherence functions for the von Karman, Kolmogorov and Gaussian spectra versus $\kappa_0 r$ are plotted in Fig. 4(a) and (b) for $\gamma_v^{vK}x=0.1$ and $\gamma_v^{vK}x=100$, respectively. It is seen from the figures that $\Gamma_{p,v}^{vK}(x,r)\approx\Gamma_{p,v}^{K}(x,r)$ for $\kappa_0 r\ll 1$, and that $\Gamma_{p,v}^{vK}(x,r)\approx\Gamma_{p,v}^{G}(x,r)$ for $\kappa_0 r\gg 1$. The same result has been obtained above analytically. It follows from Fig. 4(a) that $\Gamma_{p,v}^{vK}(x,r)\approx\Gamma_{p,v}^{K}(x,r)$ for rather small values of $\kappa_0 r$, which are less than 0.1. This is due to the fact that the ratio of the second and first terms in the square brackets in Eq. (41) is of the order of $(\kappa_0 r)^{1/3}$. This ratio tends to zero rather slowly when $\kappa_0 r\to 0$.

Figure 4(a) and (b) for the coherence functions for $\gamma_v^{vK}x=0.1$ and 100, and similar figures for the coherence functions for other values of $\gamma_v^{vK}x$, which have been obtained but not presented in the paper, allow us to make the following conclusion. For $\gamma_v^{vK}x<0.5$, the coherence function $\Gamma_{p,v}^{G}(x,r)$ approximates the coherence function $\Gamma_{p,v}^{vK}(x,r)$ practically for all values of r, while $\Gamma_{p,v}^{K}(x,r)$ and $\Gamma_{p,v}^{vK}(x,r)$ are different for most values of r [e.g., see Fig. 4(a)]. If $\gamma_v^{vK}x$ is greater than 1 and less than 30 or so, $\Gamma_{p,v}^{vK}(x,r)$ is somewhere between $\Gamma_{p,v}^{K}(x,r)$ and $\Gamma_{p,v}^{G}(x,r)$. Finally, for large values of $\gamma_v^{vK}x\geqslant 100$, the coherence function $\Gamma_{p,v}^{K}(x,r)$ approximates the coherence function $\Gamma_{p,v}^{vK}(x,r)$ rather well, while $\Gamma_{p,v}^{G}(x,r)$ and $\Gamma_{p,v}^{vK}(x,r)$ differ significantly [see Fig. 4(b)]. Note that the same conclusion is valid for the temperature contributions to the coherence functions, $\Gamma_{p,\varepsilon}^{vK}(x,r)$, $\Gamma_{p,\varepsilon}^{K}(x,r)$, and $\Gamma_{p,\varepsilon}^{G}(x,r)$, if they are compared for small, moderate and large values of $\gamma_\varepsilon^{vK}x$.

D. Coherence function of a spherical wave

Using Eqs. (7) and (8), the coherence function Γ_s of a spherical wave can be expressed in terms of the coherence function Γ_p of a plane wave (e.g., see Ref. 7)

$$\Gamma_s(x,\mathbf{r},\mathbf{r}_+)=\frac{I_s}{(4\pi x)^2}\exp\left\{\frac{ik\mathbf{r}\cdot\mathbf{r}_+}{x}+\int_0^1 dt\,\ln\frac{\Gamma_p(x,rt)}{I_p}\right\}. \tag{46}$$

Substituting $\Gamma_p^{vK}(x,r)$ from Eqs. (32), (35), and (36) into Eq. (46), one obtains the following equation for the coherence function of a spherical wave in a medium with the von Karman spectra of temperature and medium velocity fluctuations

$$\Gamma_s^{vK}(x,\mathbf{r},\mathbf{r}_+)=\frac{I_s\exp\{ik\mathbf{r}\cdot\mathbf{r}_+/x\}}{(4\pi x)^2}\Gamma_{s,\varepsilon}^{vK}(x,r)\Gamma_{s,v}^{vK}(x,r). \tag{47}$$

Here $\Gamma_{s,\varepsilon}^{vK}(x,r)$ and $\Gamma_{s,v}^{vK}(x,r)$ are the factors of Γ_s^{vK} due to sound scattering by temperature and medium velocity fluctuations, given by

$$\Gamma_{s,\varepsilon}^{vK}(x,r)=\exp\left\{-\frac{2\gamma_\varepsilon^{vK}x}{\kappa_0 r}\times\int_0^{\kappa_0 r}dt\left[1-\frac{2^{1/6}t^{5/6}}{\Gamma(5/6)}K_{5/6}(t)\right]\right\}, \tag{48}$$

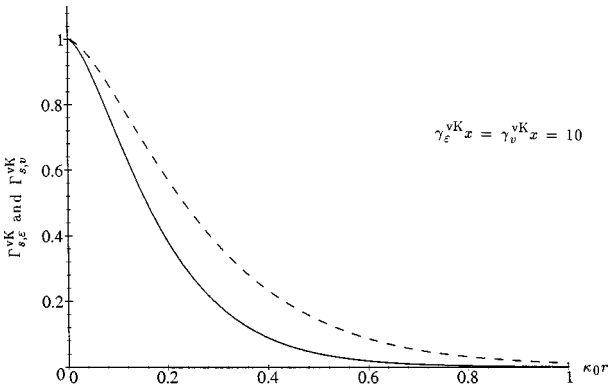

FIG. 5. The temperature ($\Gamma_{s,\varepsilon}^{\rm vK}$, dashed line) and medium velocity ($\Gamma_{s,v}^{\rm vK}$, solid line) contributions to the coherence function of a spherical wave for the von Karman spectrum.

$$\Gamma_{s,v}^{\rm vK}(x,r)=\exp\left\{-\frac{2\gamma_v^{\rm vK}x}{\kappa_0 r}\int_0^{\kappa_0 r}dt\left[1-\frac{2^{1/6}t^{5/6}}{\Gamma(5/6)}\times\left(K_{5/6}(t)-\frac{t}{2}K_{1/6}(t)\right)\right]\right\}. \tag{49}$$

Equations (48) and (49) are new results obtained in this paper. It follows from Eqs. (48) and (49) and the inequality $K_{1/6}(t)>0$ that $\Gamma_{s,\varepsilon}^{\rm vK}(x,r)>\Gamma_{s,v}^{\rm vK}(x,r)$. $\Gamma_{s,\varepsilon}^{\rm vK}(x,r)$ and $\Gamma_{s,v}^{\rm vK}(x,r)$ are plotted in Fig. 5 for $\gamma_\varepsilon^{\rm vK}x=\gamma_v^{\rm vK}x=10$, respectively.

The equations for the coherence radii $r_{s,\varepsilon}$ and $r_{s,v}$ of the coherence functions $\Gamma_{s,\varepsilon}^{\rm vK}(x,r)$ and $\Gamma_{s,v}^{\rm vK}(x,r)$ can be obtained from Eqs. (48) and (49):

$$2\gamma_\varepsilon^{\rm vK}x\int_0^{\kappa_0 r_{s,\varepsilon}}dt\left[1-\frac{2^{1/6}t^{5/6}}{\Gamma(5/6)}K_{5/6}(t)\right]=\kappa_0 r_{s,\varepsilon}, \tag{50}$$

$$2\gamma_v^{\rm vK}x\int_0^{\kappa_0 r_{s,v}}dt\left[1-\frac{2^{1/6}t^{5/6}}{\Gamma(5/6)}\left(K_{5/6}(t)-\frac{t}{2}K_{1/6}(t)\right)\right]=\kappa_0 r_{s,v}. \tag{51}$$

The normalized coherence radii $\kappa_0 r_{s,\varepsilon}$ and $\kappa_0 r_{s,v}$ are obtained by numerical solution of Eqs. (50) and (51). They are plotted in Fig. 6 as functions of $\gamma_\varepsilon^{\rm vK}x=\gamma_v^{\rm vK}x$. It follows from the figure that $r_{s,\varepsilon}>r_{s,v}$ for all values of $\gamma_\varepsilon^{\rm vK}x=\gamma_v^{\rm vK}x$. Also it is seen from the figure that $r_{s,\varepsilon}\to 0$ and $r_{s,v}\to 0$ if $\gamma_\varepsilon^{\rm vK}x=\gamma_v^{\rm vK}x\to\infty$, and that $r_{s,\varepsilon}\to\infty$ and $r_{s,v}\to\infty$ if $\gamma_\varepsilon^{\rm vK}x=\gamma_v^{\rm vK}x\to 1/2+0$. The ratio $r_{s,\varepsilon}/r_{s,v}$ of the coherence radii is 2 for $\gamma_\varepsilon^{\rm vK}x=\gamma_v^{\rm vK}x=1/2$ and tends to the minimal value $(11/6)^{3/5}=1.44$ for $\gamma_\varepsilon^{\rm vK}x=\gamma_v^{\rm vK}x\to\infty$.

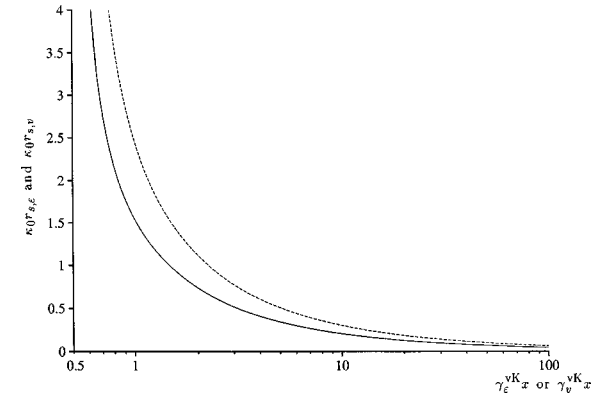

FIG. 6. The normalized coherence radii $\kappa_0 r_{s,\varepsilon}$ (dashed line) and $\kappa_0 r_{s,v}$ (solid line) for a spherical wave and the von Karman spectrum.

Now we compare the coherence function of a spherical wave for the von Karman spectrum with those for the Kolmogorov and Gaussian spectra. First consider the limiting case $\kappa_0 r\ll 1$. Expanding the functions $K_{5/6}(t)$ and $K_{1/6}(t)$ in Eqs. (48) and (49) into series in terms of t and calculating the integrals over t, one obtains

$$\Gamma_{s,\varepsilon}^{\rm vK}(x,r)=\exp\left\{-2\gamma_\varepsilon^{\rm vK}x\left[\frac{9\pi(\kappa_0 r)^{5/3}}{2^{8/3}5\Gamma^2(5/6)}-\frac{(\kappa_0 r)^2}{2}+O(\kappa_0 r)^{11/3}\right]\right\}\quad\text{if}\quad\kappa_0 r\ll 1, \tag{52}$$

$$\Gamma_{s,v}^{\rm vK}(x,r)=\exp\left\{-2\gamma_v^{\rm vK}x\left[\frac{33\pi(\kappa_0 r)^{5/3}}{2^{11/3}5\Gamma^2(5/6)}-(\kappa_0 r)^2+O(\kappa_0 r)^{11/3}\right]\right\}\quad\text{if}\quad\kappa_0 r\ll 1. \tag{53}$$

The temperature and medium velocity contributions to the coherence function of a spherical wave for the Kolmogorov spectrum are given by

$$\Gamma_{s,\varepsilon}^{\rm K}(x,r)=\exp\{-\tfrac{3}{8}BC_\varepsilon^2k^2r^{5/3}x\},\qquad \Gamma_{s,v}^{\rm K}(x,r)=\exp\left\{-\frac{11}{4}B\frac{C_v^2}{c_0^2}k^2r^{5/3}x\right\}. \tag{54}$$

The equation for $\Gamma_{s,\varepsilon}^{\rm K}$ is presented in Ref. 4. The equation for $\Gamma_{s,v}^{\rm K}$ is obtained from the equation for $\Gamma_{s,\varepsilon}^{\rm K}$ by replacing C_ε^2 by $(22/3)C_v^2/c_0^{2\,6}$. In Eqs. (52) and (53), the terms proportional to $(\kappa_0 r)^2$ and $(\kappa_0 r)^{11/3}$ can be omitted for the considered case $\kappa_0 r\ll 1$. Then, replacing $\gamma_\varepsilon^{\rm vK}$ and $\gamma_v^{\rm vK}$ by their values given by Eq. (28), it can be shown from Eqs. (52)–(54) that $\Gamma_{s,\varepsilon}^{\rm vK}(x,r)=\Gamma_{s,\varepsilon}^{\rm K}(x,r)$ and $\Gamma_{s,v}^{\rm vK}(r)=\Gamma_{s,v}^{\rm K}(r)$. In other words, if $\kappa_0 r\ll 1$, the temperature contributions to the coherence function for the von Karman and Kolmogorov spectra are equal and so are the medium velocity contributions to the coherence functions for these spectra.

Let us consider the opposite limiting case $\kappa_0 r\gg 1$. Replacing $\Gamma_p(r)$ in Eq. (46) by its asymptotic for large t, given by Eqs. (32), (43), and (44), and then calculating the integrals over t yields

$$\Gamma_{s,\varepsilon}^{\rm vK}(x,r)=\exp\left\{-2\gamma_\varepsilon^{\rm vK}x\left[1-\frac{\sqrt{\pi}\gamma(4/3,\kappa_0 r)}{\Gamma(5/6)2^{1/3}\kappa_0 r}\right]\right\}\quad\text{if}\quad\kappa_0 r\gg 1, \tag{55}$$

$$\Gamma_{s,v}^{\rm vK}(x,r)=\exp\left\{-2\gamma_v^{\rm vK}x\left[1-\frac{7\sqrt{\pi}\gamma(4/3,\kappa_0 r)}{9\Gamma(5/6)2^{4/3}\kappa_0 r}\right]\right\}\quad\text{if}\quad\kappa_0 r\gg 1. \tag{56}$$

Here $\gamma(4/3,\kappa_0 r)$ is the incomplete gamma-function.

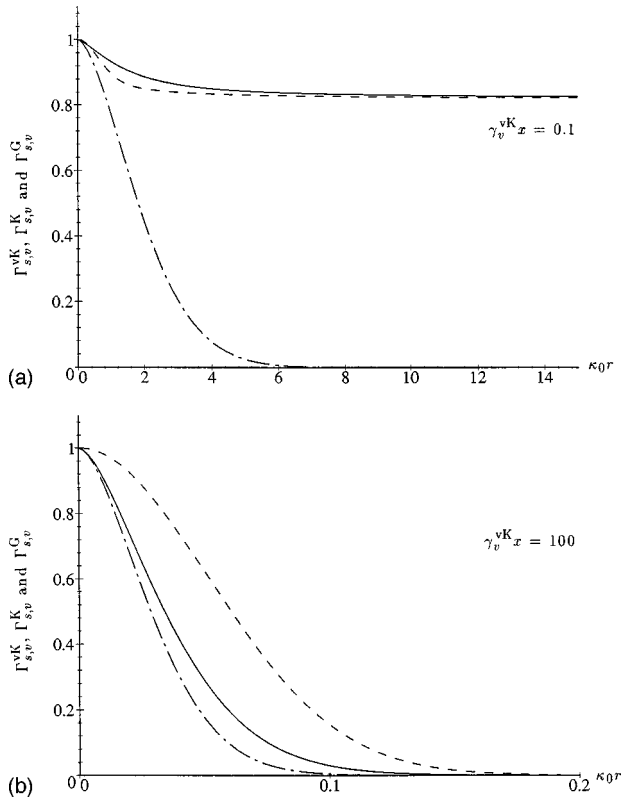

FIG. 7. The medium velocity contributions to the coherence function of a spherical wave for the von Karman ($\Gamma_{s,v}^{vK}$, solid line), Kolmogorov ($\Gamma_{s,v}^{K}$, dash-dotted line) and Gaussian ($\Gamma_{s,v}^{G}$, dashed line) spectra. (a) $\gamma_v^{vK}x=0.1$ and (b) $\gamma_v^{vK}x=100$.

The temperature and medium velocity contributions to Γ for the Gaussian spectrum are given by[15]

$$\Gamma_{s,\varepsilon}^{G}(x,r)=\exp\left\{-2\gamma_\varepsilon^{G}x\left[1-\frac{\sqrt{\pi}l}{2r}\mathrm{erf}\left(\frac{r}{l}\right)\right]\right\}, \tag{57}$$

$$\Gamma_{s,v}^{G}(x,r)=\exp\left\{-2\gamma_v^{G}x\left[1-\frac{\sqrt{\pi}l}{4r}\mathrm{erf}\left(\frac{r}{l}\right)-\frac{1}{2}e^{-r^2/l^2}\right]\right\}, \tag{58}$$

where $\mathrm{erf}(r/l)$ is the error-function. For the considered case $\kappa_0 r\gg 1$, only the first terms in the square brackets in Eqs. (55)–(58) need be retained. Taking also into account that $\gamma_\varepsilon^{vK}=\gamma_\varepsilon^{G}$ and $\gamma_v^{vK}=\gamma_v^{G}$ yields $\Gamma_{s,\varepsilon}^{vK}=\Gamma_{s,\varepsilon}^{G}=\exp(-2\gamma_\varepsilon^{vK}x)$ and $\Gamma_{s,v}^{vK}=\Gamma_{s,v}^{G}=\exp(-2\gamma_v^{vK}x)$. These relationships coincide with those obtained for the case of plane wave propagation.

The functions $\Gamma_{s,v}^{vK}(x,r)$, $\Gamma_{s,v}^{K}(x,r)$, and $\Gamma_{s,v}^{G}(x,r)$ are plotted in Fig. 7(a) and (b) for $\gamma_v^{vK}x=0.1$ and $\gamma_v^{vK}x=100$, respectively. It follows from the figures that $\Gamma_{s,v}^{vK}(x,r)\approx\Gamma_{s,v}^{K}(x,r)$ for small values of $\kappa_0 r$, and that $\Gamma_{s,v}^{vK}(x,r)\approx\Gamma_{s,v}^{G}(x,r)$ for large values of $\kappa_0 r$. Also it can be shown from Fig. 7(a) and (b) and similar figures for other values of $\gamma_v^{vK}x$, which have been obtained but not presented in the paper, that, for small values of $\gamma_v^{vK}x<0.5$, $\Gamma_{s,v}^{G}(x,r)$ approximates $\Gamma_{s,v}^{vK}(x,r)$ practically for all values of r, while $\Gamma_{s,v}^{K}(x,r)$ differs from $\Gamma_{s,v}^{vK}(x,r)$ significantly [e.g., Fig. 7(a)]. If $\gamma_v^{vK}x$ is greater than 1 and less than 30 or so, $\Gamma_{s,v}^{vK}(x,r)$ is somewhere between $\Gamma_{s,v}^{K}(x,r)$ and $\Gamma_{s,v}^{G}(x,r)$. Finally, for large values of $\gamma_v^{vK}x\geqslant 100$, $\Gamma_{s,v}^{K}(x,r)$ approximates $\Gamma_{s,v}^{vK}(x,r)$ rather well, while $\Gamma_{s,v}^{G}(x,r)$ and $\Gamma_{s,v}^{vK}(x,r)$ are significantly different [Fig. 7(b)]. The same result is valid for the temperature contributions to the coherence functions, $\Gamma_{s,\varepsilon}^{vK}(x,r)$, $\Gamma_{s,\varepsilon}^{K}(x,r)$, and $\Gamma_{s,\varepsilon}^{G}(x,r)$, when comparing them for different values of $\gamma_\varepsilon^{vK}x$.

III. CONCLUSIONS

Line-of-sight sound propagation of plane and spherical waves in a medium with the von Karman spectra of temperature and medium velocity fluctuations has been considered. The mean sound field, the coherence functions of plane and spherical waves and their coherence radii have been calculated analytically and numerically. The temperature and medium velocity contributions to the attenuation coefficient of the mean sound field are shown to be the same provided that $C_\varepsilon^2=4C_v^2/c_0^2$, see Eq. (29). On the other hand, the temperature and medium velocity contributions to the coherence functions of plane and spherical waves and their coherence radii are different. Note that in previous theories of sound propagation in random media, the temperature and medium velocity contributions to the statistical moments of a sound field were assumed incorrectly to be the same.

It has been shown that, in the limiting cases $\kappa_0 r\ll 1$ and $\kappa_0 r\gg 1$, the coherence functions of plane and spherical waves for the von Karman spectrum of medium inhomogeneities coincide with those calculated for the Kolmogorov and Gaussian spectra. The coherence functions of plane and spherical waves for the spectra involved have also been compared for different values of $\gamma_\varepsilon^{vK}x=\gamma_v^{vK}x$. It is shown that, for small values of $\gamma_\varepsilon^{vK}x=\gamma_v^{vK}x<0.5$, the coherence function for the von Karman spectrum can be approximated by that for the Gaussian spectrum practically for all values of $\kappa_0 r$ and differs significantly from that for the Kolmogorov spectrum. For moderate values of $\gamma_\varepsilon^{vK}x=\gamma_v^{vK}x$ from 1 to 30 or so, the coherence function for the von Karman spectrum is somewhere between those for the Kolmogorov and Gaussian spectra. Finally, for large values of $\gamma_\varepsilon^{vK}x=\gamma_v^{vK}x\geqslant 100$, the coherence function for the von Karman spectrum can be approximated by that for the Kolmogorov spectrum and differs markedly from that for the Gaussian spectrum.

Note that the von Karman spectrum is a more ''realistic'' spectrum of medium inhomogeneities than the Gaussian one. There has always been a concern whether one can use the Gaussian spectrum in theories of waves in random media. The approximate coincidence between the coherence functions of plane and spherical waves for the von Karman and Gaussian spectra, shown above for $\kappa_0 r\gg 1$ or for small values of $\gamma_\varepsilon^{vK}x=\gamma_v^{vK}x$, supports the use of the Gaussian spectrum in theories of waves in random media. Note that such a coincidence will probably occur if other ''reasonable,'' finite spectra with relationships similar to those in (22) and (23) are used instead of the Gaussian spectrum. However, the Gaussian spectrum has been almost exclusively chosen from such spectra in the literature. Therefore it is worthwhile to compare the coherence function Γ and other statistical moments of a sound field for the von Karman and Gaussian spectra.

In the atmosphere, inhomogeneities of the order of or greater than the outer scale of turbulence $1/\kappa_0$ are anisotropic

(e.g., Ref. 12). Therefore some precautions must be taken when using the results obtained in the present paper for studies of sound propagation through a turbulent atmosphere. However, these results can be directly applied to the study of sound propagation through a turbulent jet where the medium velocity fluctuations are isotropic and their spectrum can be approximated fairly well by the von Karman spectrum. The coherence function of a spherical wave after passing through a turbulent jet has been measured.[17] A comparison between these measurements and theoretical predictions of the coherence function has been reported.[18] The geometry of the experiment involved was a bit different from that considered in the present paper because the source was located at a certain distance from the turbulent jet so there was no interaction of sound with turbulence on the path leg from source to the jet. However, the coherence function is calculated in Ref. 18 by the same approach as that used in the present paper and is similar to $\Gamma_{s,v}^{\mathrm{vK}}$ given by Eq. (49). Reference 18 has clearly shown that the theoretical predictions of the coherence function based on the approach of the present paper are in good agreement with experimental data from Ref. 17 while those based on the previous theories do not agree with experimental data.

ACKNOWLEDGMENTS

This material is partly based upon work done by V. E. Ostashev and G. Goedecke that was supported by the U.S. Army Research Office under Contract No. DAAH04-95-1-0593. We would like to thank the Associate Editor Louis Sutherland and the reviewers for many useful comments to the paper.

APPENDIX: CALCULATIONS OF THE COHERENCE FUNCTION FOR A PLANE WAVE

In this Appendix, the coherence function $\Gamma_p^{\mathrm{vK}}(x,r)$ of a plane wave in a medium with the von Karman spectra of temperature and medium velocity fluctuations is calculated. Substitution of $\Phi_{\mathrm{eff}}^{\mathrm{vK}}$ from Eq. (12) into Eq. (7) yields the equation for Γ_p^{vK}:

$$\Gamma_p^{\mathrm{vK}}(x,r)=I_p\exp\left\{-\pi^2Ak^2x\int_0^\infty d\kappa\,\frac{\kappa[1-J_0(\kappa r)]}{(\kappa^2+\kappa_0^2)^{11/6}}\times\left(C_\varepsilon^2+\frac{22}{3}\,\frac{C_v^2}{c_0^2}\,\frac{\kappa^2}{\kappa^2+\kappa_0^2}\right)\right\}. \tag{A1}$$

Let $\Gamma_p^{\mathrm{vK}}(x,r)=I_p\Gamma_{p,\varepsilon}^{\mathrm{vK}}(x,r)\Gamma_{p,v}^{\mathrm{vK}}(x,r)$, where $\Gamma_{p,\varepsilon}^{\mathrm{vK}}$ and $\Gamma_{p,v}^{\mathrm{vK}}$ are the temperature and medium velocity factors of Γ_p^{vK}. Then,

$$\Gamma_{p,\varepsilon}^{\mathrm{vK}}(x,r)=\exp\{-\pi^2AC_\varepsilon^2k^2x(I_1-I_2)\}, \tag{A2}$$

$$\Gamma_{p,v}^{\mathrm{vK}}(x,r)=\exp\left\{-\frac{22}{3}\,\pi^2A\frac{C_v^2}{c_0^2}k^2x(I_3-I_4)\right\}, \tag{A3}$$

where the integrals I_1, I_2, I_3, and I_4 are given by

$$I_1=\int_0^\infty d\kappa\,\frac{\kappa}{(\kappa^2+\kappa_0^2)^{11/6}},\quad I_2=\int_0^\infty d\kappa\,\frac{\kappa J_0(\kappa r)}{(\kappa^2+\kappa_0^2)^{11/6}},$$
$$I_3=\int_0^\infty d\kappa\,\frac{\kappa^3}{(\kappa^2+\kappa_0^2)^{17/6}},\quad I_4=\int_0^\infty d\kappa\,\frac{\kappa^3J_0(\kappa r)}{(\kappa^2+\kappa_0^2)^{17/6}}. \tag{A4}$$

The integral I_1 is straightforward: $I_1=(3/5)\kappa_0^{-5/3}$. The integral I_2 can be calculated by using a reference integral from Ref. 19:

$$I_2=\frac{2^{1/6}3}{5\Gamma(5/6)}\left(\frac{r}{\kappa_0}\right)^{5/6}K_{5/6}(\kappa_0 r). \tag{A5}$$

Substituting I_1 and I_2 into Eq. (A2), one obtains the desired formula for $\Gamma_{p,\varepsilon}^{\mathrm{vK}}$:

$$\Gamma_{p,\varepsilon}^{\mathrm{vK}}(x,r)=\exp\left\{-\frac{3}{5}\,\pi^2AC_\varepsilon^2k^2\kappa_0^{-5/3}x\times\left[1-\frac{\Gamma(1/6)}{\pi}\left(\frac{\kappa_0 r}{2}\right)^{5/6}K_{5/6}(\kappa_0 r)\right]\right\}. \tag{A6}$$

Calculation of the integral I_3 is straightforward: $I_3=(18/55)\kappa_0^{-5/3}$. Calculation of the integral I_4 is more involved. Using Ref. 19, one obtains

$$I_4=\frac{18}{55}\kappa_0^{-5/3}{}_1F_2\left(2;\frac{1}{6},1;\frac{\kappa_0^2r^2}{4}\right)+\frac{\Gamma(-5/6)r^{5/3}}{2^{8/3}\Gamma(11/6)}{}_1F_2\left(\frac{17}{6};\frac{11}{6},\frac{11}{6};\frac{\kappa_0^2r^2}{4}\right). \tag{A7}$$

Here ${}_1F_2$ is the generalized hypergeometric function. The generalized hypergeometric function ${}_1F_2(2;\frac{1}{6},1;\kappa_0^2r^2/4)$ on the right hand side in Eq. (A7) can be written in the following equivalent form:

$$\begin{aligned}{}_1F_2\left(2;\frac{1}{6},1;\frac{\kappa_0^2r^2}{4}\right)&=\Gamma\left(\frac{1}{6}\right)\sum_{n=0}^\infty[1+n]\frac{(\kappa_0^2r^2/4)^n}{\Gamma(n+1/6)n!}\\&=\Gamma\left(\frac{1}{6}\right)\left\{\sum_{n=0}^\infty\frac{(\kappa_0^2r^2/4)^n}{\Gamma(n+1-5/6)n!}+\frac{\kappa_0^2r^2}{4}\sum_{n=0}^\infty\frac{(\kappa_0^2r^2/4)^n}{\Gamma(n+1+1/6)n!}\right\}\\&=\Gamma\left(\frac{1}{6}\right)\{(\kappa_0r/2)^{5/6}I_{-5/6}(\kappa_0r)+(\kappa_0r/2)^{11/6}I_{1/6}(\kappa_0r)\}.\end{aligned} \tag{A8}$$

The first line in this equation is obtained from a definition of ${}_1F_2$. Removing the square brackets in this line yields the second line. When writing the third line, we have taken into account that the first series in the second line is equal to $(\kappa_0 r/2)^{5/6} I_{-5/6}(\kappa_0 r)$, where $I_{-5/6}$ is the modified Bessel function, while the second series is equal to $(\kappa_0 r/2)^{11/6} I_{1/6}(\kappa_0 r)$.

The generalized hypergeometric function ${}_1F_2(\frac{17}{6};\frac{11}{6},\frac{11}{6};\kappa_0^2 r^2/4)$ can be manipulated similarly:

$$
\begin{aligned}
{}_1F_2\left(\frac{17}{6};\frac{11}{6},\frac{11}{6};\frac{\kappa_0^2 r^2}{4}\right) &= \Gamma\left(\frac{11}{6}\right)\sum_{n=0}^{\infty}\left[1+\frac{6n}{11}\right]\frac{(\kappa_0^2 r^2/4)^n}{\Gamma(n+11/6)n!} \\
&= \Gamma\left(\frac{11}{6}\right)\left\{\sum_{n=0}^{\infty}\frac{(\kappa_0^2 r^2/4)^n}{\Gamma(n+1+5/6)n!}+\frac{6}{11}\,\frac{\kappa_0^2 r^2}{4}\sum_{n=0}^{\infty}\frac{(\kappa_0^2 r^2/4)^n}{\Gamma(n+1+11/6)n!}\right\} \\
&= \Gamma(\tfrac{11}{6})\{(\kappa_0 r/2)^{-5/6} I_{5/6}(\kappa_0 r)+\tfrac{6}{11}(\kappa_0 r/2)^{1/6} I_{11/6}(\kappa_0 r)\}. \qquad \text{(A9)}
\end{aligned}
$$

Substituting ${}_1F_2(2;\frac{1}{6},1;\kappa_0^2 r^2/4)$ and ${}_1F_2(\frac{17}{6};\frac{11}{6},\frac{11}{6};\kappa_0^2 r^2/4)$ from Eqs. (A8) and (A9) into Eq. (A7), using the equality $I_{11/6}(\kappa_0 r)=I_{-1/6}(\kappa_0 r)-(5/3\kappa_0 r)I_{5/6}(\kappa_0 r)$, and taking into account that $K_{-\nu}(z)=K_\nu(z)=(\pi/2)[I_{-\nu}(z)-I_\nu(z)/\sin(\pi\nu)]$, one obtains the formula for I_4:

$$
I_4=\frac{2^{1/6}9\Gamma(1/6)}{55\pi}\left(\frac{r}{\kappa_0}\right)^{5/6}\left[K_{5/6}(\kappa_0 r)-\frac{\kappa_0 r}{2}K_{1/6}(\kappa_0 r)\right]. \qquad \text{(A10)}
$$

Substitution of I_3 and I_4 into Eq. (A3) results in the desired formula for $\Gamma^{\mathrm{vK}}_{p,v}$

$$
\begin{aligned}
\Gamma^{\mathrm{vK}}_{p,v}(r)=\exp\Bigg\{&-\frac{12}{5}\pi^2 A\frac{C_v^2}{c_0^2}k^2\kappa_0^{-5/3}x\Bigg[1-\frac{\Gamma(1/6)}{\pi}\left(\frac{\kappa_0 r}{2}\right)^{5/6} \\
&\times\left(K_{5/6}(\kappa_0 r)-\frac{\kappa_0 r}{2}K_{1/6}(\kappa_0 r)\right)\Bigg]\Bigg\}. \qquad \text{(A11)}
\end{aligned}
$$

Note that the integral I_4 has been calculated independently in Ref. 20 by making the substitution $J_0(x)=(2/x)J_1(x)-J_2(x)$ in Eq. (A4) and then using reference integrals. Both approaches give the same result, Eq. (A10), that confirms its validity.

[1] L. A. Chernov, *Wave Propagation in a Random Medium* (Dover, New York, 1960).
[2] S. M. Flatte, R. Dashen, W. H. Munk, K. M. Watson, and F. Zachariasen, *Sound Transmission Through a Fluctuating Ocean* (Cambridge U. P., New York, 1979).
[3] V. I. Tatarskii, *The Effects of the Turbulent Atmosphere on Wave Propagation* (Israel Program for Scientific Translation, Jerusalem, 1971).
[4] A. Ishimaru, *Wave Propagation and Scattering in Random Media* (Academic, New York, 1978).
[5] S. M. Rytov, Yu. A. Kravtzov, and V. I. Tatarskii, *Principles of Statistical Radio Physics. Part 4. Wave Propagation Through Random Media* (Springer-Verlag, Berlin, 1989).
[6] V. E. Ostashev, ''Sound propagation and scattering in media with random inhomogeneities of sound speed, density, and medium velocity (Review Article),'' Waves Random Media **4**, 403–428 (1994).
[7] V. E. Ostashev, *Acoustics in Moving Inhomogeneous Media* (E & FN SPON, An Imprint of Thompson Professional, London, 1997).
[8] R. F. Fante, ''Mutual coherence function and frequency spectrum of a laser beam propagating through atmospheric turbulence,'' J. Opt. Soc. Am. **64**, 592–598 (1974).
[9] J. O. Hinze, *Turbulence* (McGraw-Hill, New York, 1975).
[10] G. A. Daigle, J. E. Piercy, and T. F. W. Embleton, ''Line-of-sight propagation through atmospheric turbulence near the ground,'' J. Acoust. Soc. Am. **74**, 1505–1513 (1983).
[11] W. E. McBride, H. E. Bass, R. Raspet, and K. E. Gilbert, ''Scattering of sound by atmospheric turbulence: A numerical simulation above a complex impedance boundary,'' J. Acoust. Soc. Am. **90**, 3314–3325 (1991).
[12] D. K. Wilson and D. W. Thomson, ''Acoustic propagation through anisotropic, surface-layer turbulence,'' J. Acoust. Soc. Am. **96**, 1080–1095 (1994).
[13] D. Di Iorio and D. M. Farmer, ''Separation of current and sound speed in the effective refractive index for a turbulent environment using reciprocal acoustic transmission,'' J. Acoust. Soc. Am. **103**, 321–329 (1998).
[14] V. E. Ostashev, V. Mellert, R. Wandelt, and F. Gerdes, ''Propagation of sound in a turbulent medium I. Plane waves,'' J. Acoust. Soc. Am. **102**, 2561–2570 (1997).
[15] V. E. Ostashev, F. Gerdes, V. Mellert, and R. Wandelt, ''Propagation of sound in a turbulent medium II. Spherical waves,'' J. Acoust. Soc. Am. **102**, 2571–2578 (1997).
[16] G. H. Goedecke and H. J. Auvermann, ''Acoustic scattering by atmospheric turbules,'' J. Acoust. Soc. Am. **102**, 759–771 (1997).
[17] Ph. Blanc-Benon, ''Moment d'ordre deux en deux points d'une onde acoustique sphérique après traversée d'une turbulence cinématique,'' Rev. Cethedec **79**(2), 21–29 (1984).
[18] V. E. Ostashev, Ph. Blanc-Benon, and D. Juvé, ''Coherence function of a spherical acoustic wave after passing through a turbulent jet,'' C. R. Acad. Sci., Ser. II: Mec. Phys., Chim., Sci. Terre Univers **326**, 39–45 (1998).
[19] A. P. Prudnikov, Y. A. Brychkov, and O. A. Marichev, *Integrals and Series* (Gordon and Breach, New York, 1986).
[20] D. K. Wilson, ''Performance bounds for acoustic angle-of-arrival arrays operating in atmospheric turbulence,'' J. Acoust. Soc. Am. **103**, 1306–1319 (1998).

Numerical simulation of remote acoustic sensing of ocean temperature in the Fram Strait environment

Konstantin A. Naugolnykh
Environmental Technology Laboratory, Boulder, Colorado 80303

Ola M. Johannessen
Nansen Environmental and Remote Sensing Center/Geophysical Institute, University of Bergen, Bergen, Norway

Igor B. Esipov, Oleg B. Ovchinnikov, Yury I. Tuzhilkin, and Viktor V. Zosimov
N. Andreyev Acoustics Institute, Moscow, Russia 117036

(Received 20 February 1997; accepted for publication 8 May 1998)

An important part of the general problem of the Arctic climate change is the monitoring of the Fram Strait, which lies between Greenland and Spitsbergen. For this reason it is reasonable to apply acoustic methods which are proven to be effective in acoustic ocean thermometry, acoustic tomography, etc. Knowledge of the main peculiarities of sound signal propagation in this region is needed to estimate the feasibility of applying remote acoustic methods. To this end computer simulation of sound signal propagation in the Fram Strait environment was performed, based on oceanographic data obtained by the R/V POLARSTERN expedition. The presence of stable eigenrays in Fram Strait environmental conditions is demonstrated, typical values of acoustic signal travel time fluctuations due to environmental variations are determined, and the temperature effect on the signal travel time variation is considered. Sensitivity estimates for measurement of the average ocean temperature across Fram Strait is considered in two approaches: by calculating travel time changes along selected stable eigenrays, and by determining the cumulative sum of the whole envelope of the signals passed along water-borne paths. © *1998 Acoustical Society of America.* [S0001-4966(98)05808-1]

PACS numbers: 43.30.Pc, 43.30.Qd [DLB]

INTRODUCTION

General circulation models (GCMs) predict global warming, which is most visible in the Arctic region.[1–5] A potentially effective way to measure ocean and region scale average ocean temperature over time is to use the Acoustic Thermometry method. This method's effectiveness has been demonstrated by several experimental projects. The Heard Island Feasibility Test (HIFT)[6] demonstrated that even at global ranges, acoustic signals permit phase-coherent processing and thus yield favorable signal-to-noise levels. The Trans-Arctic Acoustic Propagation Experiment (TAP)[7–9] showed that the modal dependence of signal travel times is apparently consistent with a warming of the Atlantic Intermediate Water in the Arctic Ocean. The Greenland Sea Tomography Experiment, at path lengths of $l \simeq 200$ km, was successfully performed to study deep-water formation,[10,11] gyre circulation dynamics and acoustic noise,[11,12] and sound propagation and scattering.[13,14]

To use the Acoustic Thermometry method for global climate change monitoring, it is necessary to separate ambient variability from global warming. This cannot be done without determining the boundary conditions, particularly in such a crucial area as the Fram Strait between Greenland and Spitsbergen, where the warm Atlantic water flows into the Arctic basin. A promising method of permanently monitoring temperature and current velocity of the Atlantic water penetrating into the Arctic Ocean through the Fram Strait is acoustic signal travel time measurement in the cross section of the strait, which has a typical width of 300 km and depth of 2700 m. The method is based on the fact that the propagation time of acoustic pulses along the rays connecting a source and a receiver (eigenrays) is determined primarily by the distributions of temperature and longitudinal stream velocity components. This allows the acquisition of appropriate data from acoustic measurements in an acoustic tomography framework.[15] Knowledge of the main peculiarities of sound signal propagation in the Fram Strait environment is needed to estimate the feasibility of applying remote acoustic methods. It is necessary to consider several questions: Are there any stable eigenrays in the Fram Strait environment; what is the typical value of acoustic signal travel time fluctuation due to environmental variations in comparison to the effects of ice scattering and rough surface; and what is the temperature effect on the signal travel time variation? First approach is to estimate the sensitivity of acoustic measurements to the average temperature in the Fram Strait cross section. These are the main issues to which this paper is addressed.

Sound wave propagation in the Fram Strait is strongly dependent on the variable environmental conditions. Oceanic mesoscale eddies have diameters of 20–50 km, lifetimes of at least 20 days, vertical structures penetrating to depths of 500–1000 m with the most significant variations over the first 100 m, and advection rates of 5–15 km per day.[16,17] These inhomogeneities influence the sound signal propagation, giving rise to fluctuations in the signal's travel time. The fluctuations act as ''background noise'' in measure-

ments of the average time of signal propagation, which in turn depends on the average ocean temperature along the propagation path.

It should be noted that eddies and vortex pairs in the Fram Strait have relatively short lifetimes, length scales, and timescales compared to mid-ocean eddies.[18–20] This fact allows us to reduce the random influences of the environmental variation on the signal travel time measurement by averaging with respect to the pathway and the time of measurement. Corresponding estimates is given in Sec. II. Strong temperature changes associated with ocean fronts often occur in the region of a mid-ocean eddy, causing strong sound-speed gradients and consequently anomalous acoustic propagation.[21,22]

Normal modes and rays are commonly employed representations of the acoustic field generated by a point source in water. Since the signal frequency range in most underwater acoustic applications is from several hundred to a thousand Hz (which is optimal for acoustical probing at distances of several hundred kilometers), the variation of the refractive properties of the medium is small over the acoustic wavelength, and one can use a geometric acoustical ray representation.[23] The basic parameter for the ray calculation is the sound-speed value, or refractive index distribution over the ocean in the area of interest. This is a function of all three spatial coordinates plus time.

We limit our study to a Fram Strait winter environment disturbed by the presence of ocean eddies measured in March, considering the environmental perturbations as due to the processes that occur next to an ice edge[24] and therefore the most emphasized amplitude. That is why we hope to obtain an upper estimate of the feasibility of acoustic methods to detect the temperature trend when upper ocean layer heating occurs.

The oceanographic model used in our approach is described in the first section. We develop numerical models for acoustic signal propagation in the region under consideration, with different subsurface layer temperatures. Two approaches are used. The first or ''deterministic'' approach is based on selecting the most stable rays and determining the time variation of the signal propagating along them due to environmental variations. The second or ''statistical'' approach consists of defining trends in the signal arrival spectrum caused by the temperature changes, and computing average parameters of the arriving signal ensemble. In a complex environment such as the Fram Strait, many closely spaced multipaths exist which are difficult to resolve. Therefore it is more effective to use broad characteristics of the entire arrivals in a lower resolution inversion. The signal arrival time fluctuations caused by ocean inhomogeneity are obtained both from computational experiments and from analytical estimates. By comparing the magnitude of the fluctuations induced by temperature changes with the regular variations in arrival time, it is possible to estimate the sensitivity of the acoustic method.

I. OCEANOGRAPHIC MODEL

To model the sound propagation in the Fram Strait, a region along 79 °N latitude was chosen where an oceanographic cross section was performed by the R/V POLARSTERN expedition in March 1993. A map of the region with the main currents scheme,[25] as well as the positions of the acoustic transmitter (T) and receiver (R), is shown in Fig. 1. Figure 2 shows the isolines of sound speed in the vertical cross section of the strait along the sound pathway, as received by parabolic interpolation of the experimental data obtained by R/V POLARSTERN, and reflects the acoustic features of this region.

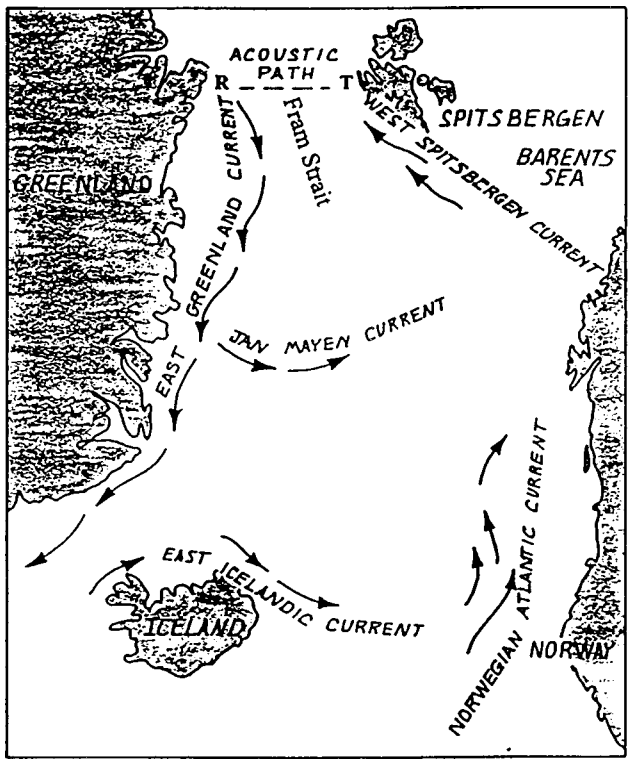

FIG. 1. Ocean currents structure (B. G. Hurdle, 1986, Ref. 13) and the Fram Strait acoustical pathway. T and R indicate transmitter and receiver positions.

As is seen in Fig. 2, the larger spatial variations in sound speed on this pathway were observed in the upper layers of the ocean. The ocean inhomogeneities that lead to changes in

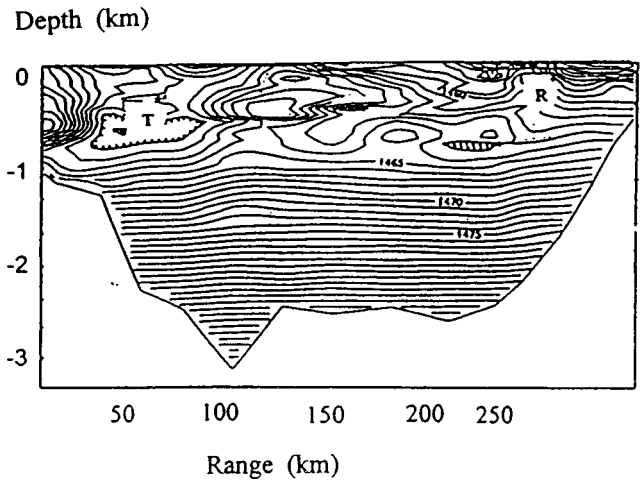

FIG. 2. Isolines of the sound velocity in the Fram Strait cross section. Depth in m, distance in km, T and R indicate transmitter and receiver positions.

sound speed can be assumed to vary randomly in time and space. The horizontal spatial scale of the sound-speed inhomogeneity has been shown to be about of 30 km, and the sound speed can vary by 10 m/s at such a spatial scale. The position of the sound source was chosen carefully; it had to allow us to select certain eigen rays emitted at angles of moderate slope.

Rays from a shallow source will be propagated mostly in the subsurface waveguide through a number of oceanographic inhomogeneities. These inhomogeneities can strongly affect the rays so they change their structure (through a number of reflections from the sea surface). This makes the signal propagation process more complicated for the problem under consideration. For a deeper source the length of the ray cycle increases and the number of ray interceptions with the perturbed subsurface layer decreases at the strait width. In addition, the deeper rays can touch the bottom and scatter there.

The rays chosen for modeling should enter the region of temperature variation, stay there sufficiently long with respect to propagation time, and be stable as well. These demands are conflicting, but a compromise can be reached by properly positioning the sound source and receiver. In accordance with Snell's Law, a ray will cross a surface if its sound speed at the lowest depth of its turn exceeds its speed next to the surface. Taking into account that in a subsurface layer the sound speed is about 1460 m/s (see Fig. 2), for such a critical speed the value 1475 m/s was taken, which was observed at a depth of 1800 m. With this consideration in mind, we consider the pathway in the eastern part of the Fram Strait. The sound source is placed in our model at a depth of 500 m, 160 km distant from Prince Karl Land coast in a region of the ocean of more than 1800 m in depth, and the receiver is placed 200 km to the west of the source at depths of 100, 200, and 300 m. Only water-borne rays are taken into account. The main bottom ray train is separated from the water-borne rays for different environmental realizations at time interval 30–70 ms. Only one or pair of them (depending on environmental realization) is mixed with the water-borne ray train (with those ones which exit at the angle more than 0.09 rad). For example, for omnidirectional source only two rays exist which once touch bottom in time interval of 136.95 s. These rays could be separated by the angle resolution array application. The vertical array of 10–30 m long can separate the water-borne rays which exit angle does not exceed the range of -0.08 to $+0.08$ rad. Bottom rays exist only for more steeper exit angles—more than 0.09 rad. Among water-borne rays, stable rays are present in this source–receiver configuration. These rays have a maximum of five sea surface interceptions. Such rays are stable in the sense that variations of the ocean environment will not change the number of reflections from the sea surface. They reflect from the surface, crossing the subsurface layer where the most water temperature variation takes place, but not touching the bottom.

Vertical profiles of sound speed, calculated at different points based on the measurements made by Polarstern in March 1993, are presented in Fig. 3. The environment under consideration is characterized by a minimum value of $c(z)$ at

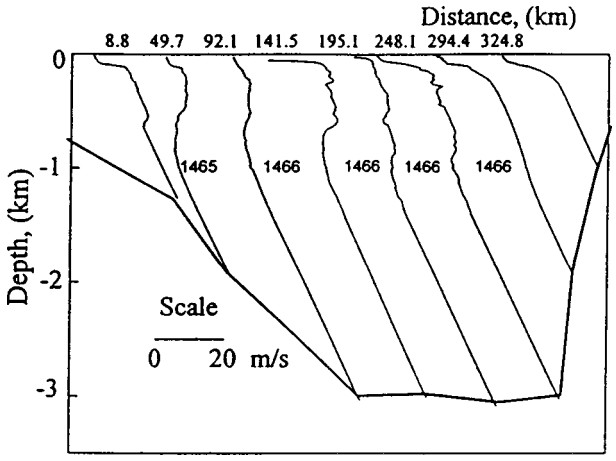

FIG. 3. Sound velocity profiles at different distances along the trace. Labels indicate the sound speed (in m/s) at the 1-km depth.

the sea surface (subsurface sound waveguide), which is typical for winter. In the east part of the path (left side of Fig. 3) one more $c(z)$ minimum is at the depth of 600 m. It corresponds to the warm water inlet from the Atlantic at the horizon of 100–400 m depth. In the western part of the strait the cold and less saline Arctic water does not penetrate to large depths and flows in a subsurface layer. The second minimum of $c(z)$ vanishes there. These profiles were considered as initial steps to further calculations of the sound propagation in a variable environment. Then, two ensembles of sound speed distributions were constructed. One was obtained by shifting the sound speed field horizontally to simulate oceanographic variability and numerically estimate the signal arrival time fluctuations. Another set of profiles was generated to model the ocean surface layer heating.

We consider isotropic ocean turbulence in each horizontal plane of our model. This means that the spatial scale of correlation of random oceanographic inhomogeneities is the same in any direction in a horizontal plane. Therefore, when we are shifting oceanographic data in any direction by more than the scale of spatial correlation we obtain an oceanographic realization for which the statistical properties will be uncorrelated with the initial realization. This provides the possibility of calculating typical values of the signal travel time variation in a changing environment. We choose a path far from the area where warm currents occur in our simulation because one cannot regard this oceanographic inhomogeneity as a random one. Further, it was assumed that the temperature changes take place in the upper 200-m layer, which is the most perturbed layer of the ocean.[16,17] The corresponding sound speed variations were approximated as follows:[15]

$$\frac{\Delta c}{c} \simeq \alpha \Delta T, \quad \alpha = 3.09 \times 10^{-3}/^{\circ}\mathrm{C}. \tag{1}$$

ΔT is an ocean water temperature variation in °C. The variations in sound speed were added to the initial sound-speed profiles in the upper 200-m subsurface layer. The modified sound-speed profiles were obtained by exponential matching of the profiles used initially in the deeper layer of the ocean.

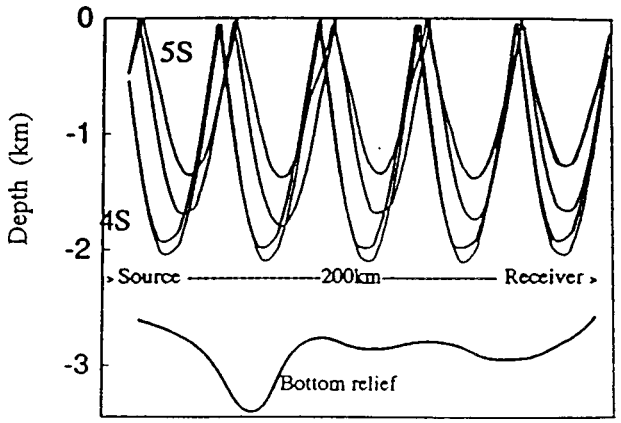

FIG. 4. Paths of the 4s and 5s rays along the trace. Rays 4s and 5s contacted the sea surface four and five times, respectively.

II. VARIATION IN TRAVEL TIME OF SIGNALS DUE TO WARMING OF THE UPPER OCEAN LAYER

Statistical ensembles of the sound-speed fields were constructed from specific parts of the general hydrographic data distribution presented in Fig. 2. The space between source and receiver forms a stationary path of 200 km length. Figure 4 shows an example of paths for which the acoustic signal is touching the sea surface four or five times. Inhomogeneity variation on the acoustical pathway was modeled following Ref. 26 by shifting of the measured environment pattern (plotted in Fig. 2) with respect to both source–receiver and bottom configuration with a 10-km step of each. In the process of computer modeling 11 pattern of environmental conditions on the path of 200 km between source and receiver were considered. The total environmental shift was 100 km, which corresponds roughly to the three spatial intervals of the arrival time correlation function so the main features of the travel time variation has been taken into account. As a result this model gives the possibility of calculating a typical value of the signal travel time variation due to changing ocean inhomogeneities.

The warming of the upper layer of the sea also affects acoustic signal travel time. For good travel time resolution, it is necessary to use broadband high-frequency signals that have periods smaller than the time delay of interest. To avoid excessive wave damping the frequency should not be too high. In experiments using long paths in the ocean (more than 1000 km), signals of several tens of Hz are used. The sound signal path in the Fram Strait is a few hundred kilometers long; therefore, signals with frequencies of several hundred Hz should be used. The sound field in this frequency range normally can be analyzed by ray representation. One can consider the signal travel time as the propagation time along one of the rays between the transmitter and the receiver. If the depths of the transmitter and the receiver are appropriately chosen, the signal travel time along one of several rays can differ significantly from the travel time along other rays. Thus if the signal frequency band is relatively broad, it is possible to separate the signals passing along the different rays.

A numerical code was used to calculate the ray structure of the sound field. This provides the sound field level through both coherent and noncoherent summations of the sound signals propagating along different rays in the inhomogeneous ocean. The code takes into account the sound wave attenuation in a homogeneous ocean, anomalies of sound signal propagation due to inhomogeneities of the medium and sound signal damping due to the sound signal reflection at the sea surface and sea bottom. At program input, the sound-speed distribution in the ocean is given, and the positions of the sound source and receiver are specified. Propagation times for the sound signal along the pathway were calculated for different surface layer temperatures. The amplitudes and arrival times of acoustic signals, propagating along different rays, vary as the environment changes. Stable rays sensitive to surface temperature variation were chosen for the simulations. Three receiver positions were considered at depths of 100 m (R_1), 200 m (R_2), and 300 m (R_3), respectively. The ray pattern is presented in Fig. 4. The rays are presented for signal reception at levels of 100 m and 300 m. One of them (Ray 4s) propagates initially downward and experiences four reflections; the other (Ray 5s) propagates initially upward and has five contacts with the sea surface.

TABLE I. Arrival times of signals.

Receiver depth (m)	Mean value Ray 5s time (s)	rms arrival time fluctuations (ms)
100	137.027 41	32.0
200	137.014 50	29.0
300	137.003 14	27.1

The variation of the hydrographic environment changes the ray paths and can lead to the disappearance of some of the rays. Ray 4s at receiver R_1 is absent for the initial environmental condition; it appears after the first shift and disappears again on the fourth shift. For receiver R_3, Ray 4s disappears at the final shift. At all receivers, Ray 4s disappears at the four-step shift to the right, while at the three-step shift this ray disappears only at receivers R_1 and R_2. In all the other cases, this ray is stable.

Table I shows the arrival times of signals propagated along Ray 5s for receivers placed at depths of 100 m, 200 m, and 300 m, along with root-mean-square (rms) values of arrival time fluctuations averaged over 11 realizations.

Ray 5s is emitted upward from the source, therefore it propagates in the upper inhomogeneous layer for a longer time than Ray 4s, which makes it more sensitive to the environmental variations along this route. Table I demonstrates that arrival time fluctuations along the moderately steep ray due to mesoscale inhomogeneities are on the order of 30 ms.

Travel times for sound signals propagating along Rays 4s and 5s were calculated for different temperatures of the upper 200-m subsurface layer. Typical results are given in Fig. 5, where the amplitudes and arrival times of the signal propagating along the different rays are presented. In Fig. 6, the propagation times for Rays 4s and 5s, received at different levels (R_1—100 m, R_2—200 m, R_3—300 m), are presented as a function of change in ocean temperature. Figure 6 shows that the 5s ray remains as a stable one in a rather restricted interval of temperature variation (about 0.5 °C),

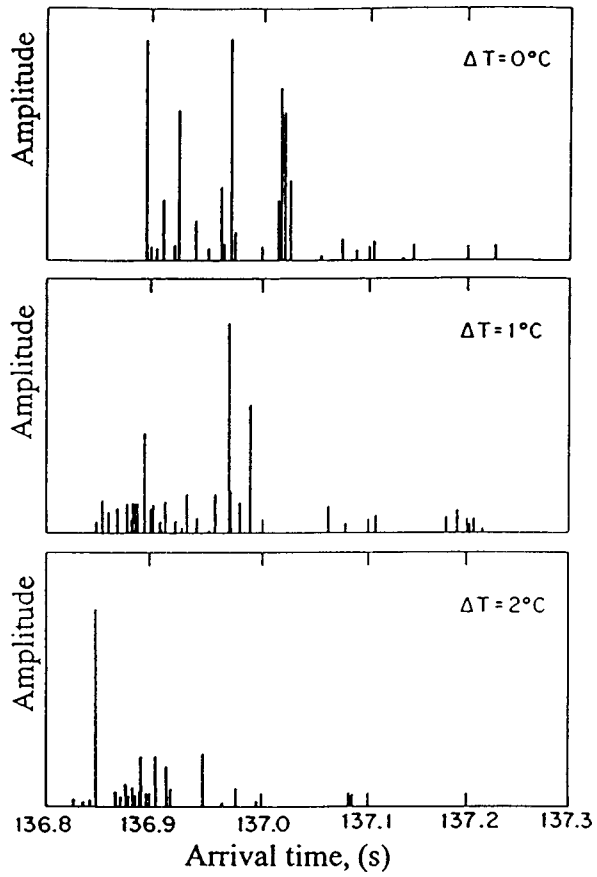

FIG. 5. Arrival patterns for different subsurface layer temperature. Distance between transmitter and receiver is 200 km, source depth 500 m, receiver depth 300 m. ΔT represents temperature change from the initial state.

while the 4s ray is proved to be stable in a more vast area of temperature change. The slopes of the curves correspond to gradients of 29 ms/°C for Ray 4s and 37 ms/°C for Ray 5s.

Increasing the average temperature leads to subsurface sound refraction. Calculation shows that Ray 5s is stable up to a temperature increment of about 0.5 °C. Ray 4s, having a steeper slope at the source, continues to exist for temperature increases up to 2 °C. A smaller degree of heating in upper ocean layers can be measured using the rays with gentle

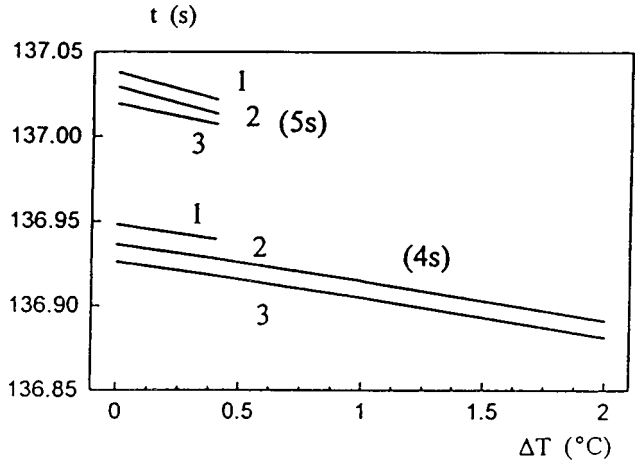

FIG. 6. Propagation time t variation as a function of the temperature change for 4s and 5s rays. Curves 1, 2, and 3 correspond to receiver depth 100 m, 200 m, and 300 m.

slopes, as long as they are stable enough with respect to the effects of mesoscale inhomogeneities. However, in such a case the exit angles should be sufficiently large to prevent the ray's changing type due to mesoscale inhomogeneity.

Numerical evaluation of the signal propagation time and its variation shows that warming of the ocean's upper layer can be measured and averaged by using acoustic travel time techniques. The sensitivity of temperature evaluation depends on the signal processing procedure. For one travel time measurement, the error will be on the order of the of the signal fluctuation, or 30 ms (Table I), corresponding to a temperature measurement error of about 1 °C.

The warming of the ocean's upper layer is on a larger timescale, however, compared to that of mesoscale variability. This means that it is possible to apply well-known signal processing methods to suppress undesirable signal fluctuations.[27] In this case, the fluctuation of the signal arrival time will decrease as the inverse of the square root of the number of statistically independent measurements. The evaluation of sensitivity can be performed on the timescales of ocean warming and mesoscale inhomogeneities. For the typical mesoscale eddies, having diameters of 20–50 km and drift rates of 5–15 km per day, one can estimate the time correlation interval for the environmental variation in any cross section as about 3 days. In the case of a homogeneous random process, the signal storage procedure can suppress the travel time fluctuations up to $\sqrt{365/3}\approx 10$ times per year observations. Appropriate acoustic feasibility to measure mean subsurface layer temperature can reach $\sim$0.1 °C over a year-long monitoring period. For a more precise evaluation, it is necessary to use data on seasonal variation of the environment.

Standard sound sources at frequencies of several hundred Hz usually have a signal frequency band of about 100 Hz; this leads to time resolution of signal arrivals of 10 ms. The closely arriving rays produce an interference pattern, the structure of which varies with environmental change. To some degree this can be considered as noise and be suppressed by averaging procedures.

In addition to mesoscale inhomogeneities, acoustic signal fluctuations can be produced by other types of environmental perturbations, for example, by the effects of surface or internal waves. Waves can affect the arrival time of a signal propagating along the rays and mask the effects of ocean temperature change. The motion of surface waves affects the rays reflecting at the sea surface,[28,29] and causes the arrival times of the signals to fluctuate. The rms of the signal phase fluctuations is determined mainly by the Rayleigh parameter $\Delta\theta = 2q\xi \sin\chi$, where q is the signal wave number, ξ is the rms surface displacement, and χ is the grazing angle measured from the smoothed surface. The propagation time fluctuations are determined by the equation $\Delta\tau \simeq \sqrt{n}\Delta\theta/\omega$, where ω is signal frequency and n is the number of ray surface contacts. For the grazing angle $\chi \sim 0.1$ rad, $n=4$, and for $q \simeq 4m^{-1}$ (for signal frequency 1 kHz), one can obtain an estimation $\Delta\tau \sim 1$ ms for the surface root-mean-square roughness value $\xi \simeq 1$ m. Somewhat more complicated is the problem of estimating the influence of ice on the travel time fluctuations. Theoretical research conducted with respect to

the Greenland Sea tomography experiment[14] shows that the acoustic signal can be influenced by the ice covered sea surface in the rms travel time fluctuation of $\Delta\tau \sim 1-10$ ms for a path 121 km long when the acoustic ray comes to the water–ice interface four times in a variety of ice cover conditions. The travel time change due to ice interface is approximately proportional to the propagating range (number of reflections). Therefore we can conclude that the $c(z)$ variation leads to stronger travel time fluctuations than the ice cover in the environmental conditions under consideration. This result is closely related with the remark of Jin *et al.*[14] that the ice travel time signals can be negligible at Greenland Sea for paths of hundred km long; and only for newly formed keels, which have very low shear sound speed, the ice induced errors are appreciable.

As to the effects of internal waves, one can refer to the results of a field experiment done in the Barents Sea polar front region.[30] For shallow water sound transmission, $\Delta\tau \simeq 10$ ms was registered there for high-frequency internal waves (more then 10 cycles per day). It is possible that in deeper water, such as that in Fram Strait where perturbations are concentrated in a subsurface layer, the travel time fluctuations for steep rays will not exceed 10 ms, which fluctuations can be suppressed by storage signal processing.

III. CUMULATIVE SIGNAL STORAGE

Another method of signal processing is to deal with signals as a whole, without considering that separate parts propagate along different rays. Increasing ocean temperature generally leads to decreasing propagation times. To detect this trend against the random travel time fluctuations, it is natural to use a statistical approach. One procedure is to use an algorithm based on cumulative sum considerations. The cumulative summation procedure is widely used in seismology for investigating the statistical spreading of earthquake shocks in time.[31] In our case we consider the cumulative sum with respect to the total train of arrival times t_i, corresponding to the signal propagation along the different rays. When one arranges the signal arrival times in order of increasing value $t_1 < t_2 < t_3 \ldots < t_N$, the cumulative sum can be written as

$$S(t) = \frac{1}{N} \begin{cases} 0 & t < t_1 \\ i & t_i \leqslant t < t_{i+1}. \\ N & t > t_N \end{cases} \tag{2}$$

The normalization factor $1/N$ is used to compare the results of the calculation for signal realizations with different numbers of rays. The cumulative sum computation procedure is as follows:

- the signal threshold is defined;
- the appropriate amplitude of the signal propagating along the chosen rays is normalized to 1 if its value is higher than the threshold; otherwise it is set to 0;
- the normalized amplitude of each successive signal is added to the sum of normalized amplitudes of the preceding signals in order of signal arrival time;

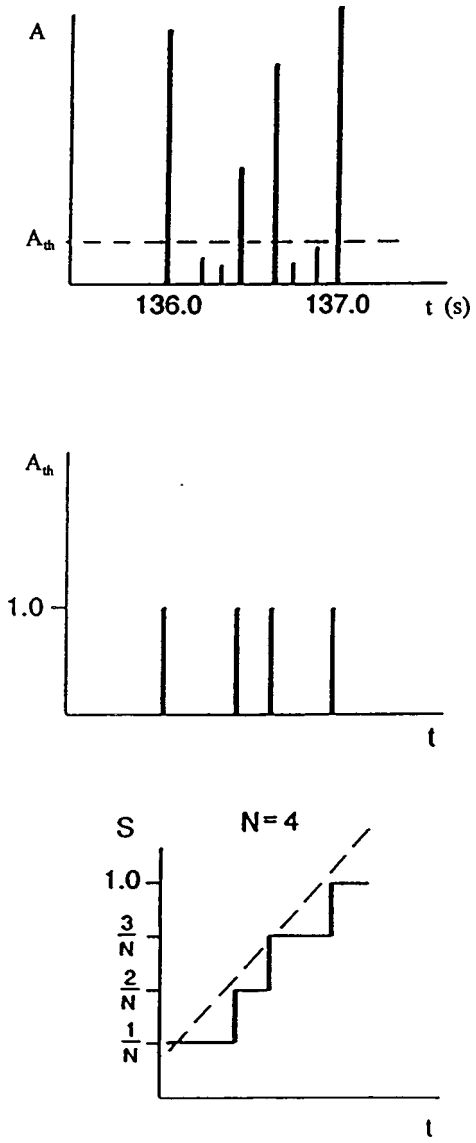

FIG. 7. Schematic outline of the cumulative sum derivation. Arrival pattern (a); exceeding the threshold amplified and limited signals (b); cumulative sum (solid line) and the regression line (dotted line) as a function of the arrival time (c).

- the total sum is normalized with respect to the number of terms in the series.

Thus the cumulative sum corresponds to a transfer function for the medium in which the sound signal propagates. The following analysis of the cumulative sum is based on the computation of the linear regression coefficients of $S(t)$ with respect to the time t_i of signal arrival. In other words, the coefficients a and b are defined for the expression $at_i + b$ in accord with the least-squares method of minimizing

$$\sum_{i=1}^{N} (S(t_i) - at_i - b)^2. \tag{3}$$

This procedure is outlined in Fig. 7, which shows the arrival signal pattern [Fig. 7(a)], the threshold signal [Fig. 7(b)], and the cumulative sum (solid line) and regression line (dotted line) [Fig. 7(c)] as a function of time. Regression lines corresponding to different temperatures of the layer are

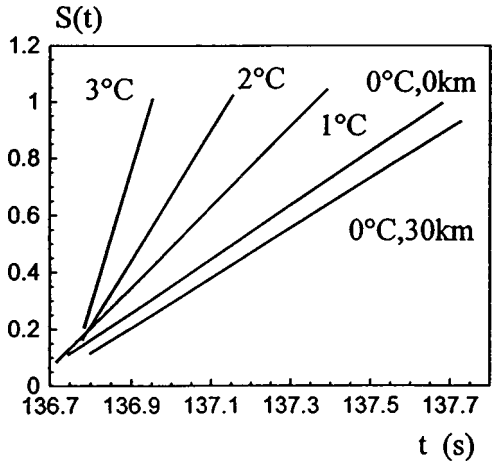

FIG. 8. Cumulative sum S regression lines versus signal arrival times for different subsurface layer temperatures. Labels indicate the subsurface layer temperature increase ΔT and the hydrographic pattern shift. Label (0 °C, 0 km) corresponds to initial environment realization, (0 °C, 30 km) to that shifted at 30 km and (ΔT °C) to the realization with increased subsurface layer temperature.

presented in Fig. 8 as a function of signal arrival times. In Fig. 8, labels indicate the subsurface layer temperature increase ΔT ($\Delta T=0$ corresponds to the initial state of the environment) and the hydrographic pattern shift. So (0 °C, 0 km) corresponds to the initial environment realization (0 °C, 30 km) to that shifted at 30 km, and (ΔT °C, 0) to the realization with increased subsurface layer temperature. The difference in slope of these two lines indicates the influence of ''background noise'' produced by mesoscale inhomogeneities. The other lines correspond to different degrees of warming of the upper surface layer. It can be seen from the plot that the slope of the lines increases as the temperature of the ocean's subsurface layers increases. The regression line slope a as a function of water temperature is presented in Fig. 9. The following illustrates the temperature dependence of the regression line slope. The cumulative sum magnitude is normalized; therefore the slope of the regression line depends only upon the duration of the travel time difference

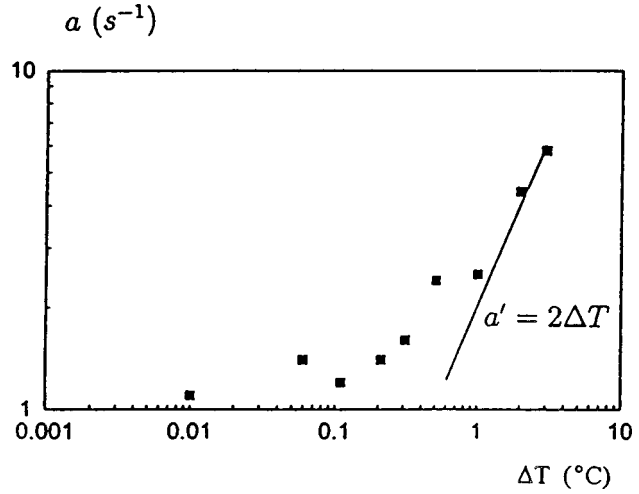

FIG. 9. The dependance of the regression line slope a upon the temperature of the subsurface layer; circles present the result of numerical calculation; solid line corresponds to Eq. (11).

$\tau=t_N-t_1$, where t_N, t_1 are the Nth and the 1st signal arrival times, respectively. The steep rays are first to arrive and the axial rays are last. For a winter-type hydrographic environment the waveguide axis is located near the sea surface, so heating of the subsurface layer hastens the axial signal propagation and decreases the arrival-signal pattern duration. This effect can be approximated as follows.

Introducing a linear approximation for the cumulative sum

$$S(\Delta t_i)=a'\Delta t_i+b', \tag{4}$$

where a', b' are constants, and bearing in mind that $S(0)=1/N$ and $S(\tau)=1$, one gets $b'=1/N\ll 1$ and

$$a'\tau+b'\simeq a'\tau=1. \tag{5}$$

The signal train duration τ is related to the hydrographic data as follows:

$$\tau(\Delta T)\simeq\frac{1}{c_0^2}\,\Delta c(\Delta T). \tag{6}$$

We point out here that $\Delta c(\Delta T)$ depends on the subsurface layer depth h, where temperature increases can be presented as a first approximation as $\Delta c(\Delta T)=\Delta c_0-(h/H)\alpha'\Delta T$, Δc_0 being the sound-speed dispersion essential for waveguide sound propagation at the initial temperature, H is the depth of the transmitter, $\alpha'\Delta T$ corresponds to the sound-speed variation with the change in the mean temperature of the ocean's upper layer, and $\alpha'=\alpha c_0$, where α is defined by Eq. (1). Really, the faster ones are the deeper water rays which come to the subsurface area only a few times and therefore are only slightly influenced by the temperature variation. The most dependent on temperature are the shallow water rays. They propagate mainly in a layer with thickness of the order H, where H is the transmitter depth. Thus the temperature effect on the most influenced shallow water rays would be weighted by the factor h/H. Then:

$$a'\simeq\frac{1}{\tau(\Delta T)}\simeq\frac{c_0^2}{l\Delta c(\Delta T)}=\frac{c_0^2}{l(\Delta c_0-\alpha c\Delta T h/H)}, \tag{7}$$

or for $\alpha'\Delta T\ll\Delta c_0$:

$$a'\simeq\frac{c_0^2}{l\Delta c_0}\left(1+\frac{h\alpha'\Delta T}{H\Delta c_0}\right). \tag{8}$$

The temperature increment of the slope $a'_T=da'/dT$ is therefore equal:

$$a'_T=\frac{h\alpha' c_0^2}{Hl\Delta c_0^2}.$$

The value Δc_0 can be estimated from the signal train duration τ_0 at the initial mean temperature as

$$\Delta c_0\simeq\frac{\tau_0 c_0^2}{l}; \tag{9}$$

therefore,

$$a'_T\simeq\frac{h\alpha' l}{H\tau_0^2 c_0^2}. \tag{10}$$

As one can see in Fig. 5, the signal train duration τ_0 is about 0.3 s. Thus for the path length $l=200$ km, subsurface layer thickness $h=200$ m, transmitter depth $H=500$ m, temperature factor $\alpha c_0 \simeq 4.5$ m/s/°C, and $c_0^2 \simeq 2\times 10^6$ m^2/s^2, one gets estimates of the slope temperature increment a_T':

$$a_T' = 2 \ \ \mathrm{s}^{-1}(^\circ\mathrm{C})^{-1}, \tag{11}$$

which corresponds in order of magnitude to the results of the computer calculations presented in Fig. 9.

It is worthwhile to note that the cumulative sum with temperature dependence is quite independent of the detailed features of the environmental conditions. Computations show a similar dependence of the cumulative sum on the ocean surface layer temperature when the environmental features are shifted by 30 km, i.e., more than the typical mesoscale distance for the conditions considered here.

IV. CONCLUSION

Numerical simulation of acoustic sensing of ocean temperature shows the main peculiarity of the acoustics method application in such a crucial Arctic zone as Fram Strait, which lies between Greenland and Spitsbergen. Signal travel time variations caused by temperature changes in the upper 200-m surface layer were calculated using ray theory for sound propagation on a path 200 km long. The modeling demonstrated the presence of stable acoustic rays, which do not change their type under ocean temperature variation. For the source–receiver configuration considered here (source at the depth of 500 m and the set of receivers at depths of 100, 200, and 300 m), calculations reveal water-borne rays which exit from the source at the angles of -0.08 to $+0.08$ rad, and intersect the surface from 2 to 8 times. Among these are stable rays in this source–receiver configuration. These rays intersect the sea surface a maximum of five times, but they remain stable only in a restricted range of temperature change (about 0.5 °C). Rays with the smaller number of surface intersections prove to be more stable but less sensitive to the temperature variations.

Two approaches are considered in the modeling. One of them is based on selecting the stable rays and determining the travel time variation. The second one consists of defining the trend in the signal-arrival spectrum caused by the temperature changes, and computing average parameters of the arriving signal ensemble.

The arrival time fluctuations were investigated for changing oceanographic data. Environmental data variation was provided by shifting the entire sound-speed pattern horizontally with respect to the transmitter-bottom-receiver configuration for a distance essentially more than the scale of ocean turbulence spatial correlation. For isotropic ocean turbulence in each horizontal plane, when the spatial scale of correlation of random oceanographic inhomogeneities is the same in any direction in the horizontal plane, we obtain the rms travel time fluctuations, for a signal propagated along the 5s ray, close to 30 ms. This value is noticeably larger than signal fluctuations due to surface scattering and ice cover influences.

The temperature influence on the stable rays was evaluated as a gradient of 29 ms/°C for Ray 4s and 37 ms/°C for Ray 5s.

In the course of implementing the second approach there were obtained the broad characteristics of wave arrival groups to calculate the cumulative sum of signal amplitudes. The temperature dependence of the arrival-pattern duration leads to variation in the slope of the cumulative sum regression line. The analytical evaluation of the derivative of this regression line slope with respect to temperature is in agreement with the numerical results. The advantage of this method is that it is based only on relative measurements of arrivals duration. Measurement of the regression line slope does not require as sophisticated an apparatus to match the receiver and the source clock as is required for travel time measurements. The cumulative sum procedure suggested for signal processing presents the possibility of determining the average temperature along an acoustic pathway in the ocean without considering detailed arrival features.

To estimate the heat inflow from the Atlantic Ocean to the Arctic basin, which is important for monitoring global climate changes, it is also necessary to determine the stream velocity distribution in the Fram Strait cross section. The problems related to current velocity acoustic monitoring under Fram Strait's environmental conditions will be considered later.

ACKNOWLEDGMENTS

The work was performed with the help of several people; in particular, the contributions of Dr. K. D. Sabinin, H. Sagen, Dr. J. Shaw, and Dr. V. V. Tatarskii are gratefully acknowledged. We are grateful to Dr. J. F. Lynch for a very stimulating review and interesting suggestions. The project was partially supported by NATO Linkage Grant (E.NVIR.L G 960352)528 (96) LVdC).

[1] U. Cubasch, G. Hegerl, A. Hellbach, H. Hock, U. Mikolajewicz, B. Santer, and R. Voss, ''A climate change simulation starting at an early time of industrialization,'' Climate Dynamics **11**, 71–84 (1995).

[2] J. Mitchell, T. Johnes, J. Gregory, and S. Tett, ''Climate response to increasing level of greenhouse gases and sulphate aerosols,'' Nature (London) **376**, 224–226 (1990).

[3] K. Hasselmann, L. Bengtasson, U. Cubash, G. Hegerl, H. Rodhe, E. Roeckner, H. von Storch, R. Voss, and J. Wasckewitz, ''Detection of anthropogenic climate change using a fingerprint method,'' Technical Report 168, Max-Planck-Institute fur Meteorology (1995).

[4] O. M. Johannessen, M. W. Miles, and E. Bjorgo, ''The Arctic's shrinking sea ice,'' Nature (London) **376**, 126–127 (1995).

[5] O. M. Johannessen, E. Bjargo, and M. W. Milas, ''Global warming and the Arctic,'' Science **271**, 129 (1996).

[6] W. H. Munk, R. C. Spindel, A. Baggeroer, and T. G. Birdsail, ''The Heard Island Feasibility Test,'' J. Acoust. Soc. Am. **96**, 2330–2342 (1994).

[7] P. N. Mikhalevsky, A. B. Baggeroer, A. N. Gavrilov, and M. Slavinsky, ''Continuous wave and *M*-sequence transmission across the Arctic,'' J. Acoust. Soc. Am. A **96**, 3235 (1994).

[8] P. N. Mikhalevsky, A. N. Gavrilov, and A. B. Baggeroer, ''Are faster than predicted arrival times seeing Arctic ocean warming?'' J. Acoust. Soc. Am. A **97**, 3234 (1995).

[9] P. N. Mikhalevsky, A. Gavrilov, A. B. Baggeroer, and M. Slavinsky, ''Experiment Tests Use of Acoustics to monitor temperature and ice in the Arctic Ocean,'' EOS Trans. Am. Geophys. Union **76**, 265–272 (1995).

[10] P. E. Worcester, J. F. Lynch, W. M. L. Morawitz, R. Pawlowicz, P. J. Sutton, B. D. Cornuelle, O. M. Johannessen, W. H. Munk, W. B. Owens, R. Shuchman, and R. C. Spindel, ''Evolution of the large-scale tempera-

ture field in the Greenland Sea during 1988-89 from tomographic measurements,'' Geophys. Res. Lett. **20**, 2211–2214 (1993).
[11] R. Pawlowicz, J. F. Lynch, W. B. Owens, P. F. Worcester, W. M. L. Morawitz, and P. J. Sutton, ''Thermal evolution of the Greenland Sea Gyre in 1988–89,'' J. Geophys. Res. **100**, 4727–4750 (1995).
[12] J. F. Lynch, H. X. Wu, R. Pawlowicz, P. Worcester, R. E. Keenan, H. C. Graber, O. M. Johannessen, P. Wadhams, and R. A. Shuchman, ''Ambient noise measurements in the 200–300 Hz band from the Greenland Sea tomography experiment,'' J. Acoust. Soc. Am. **94**, 1015 (1993).
[13] G. Jin, J. F. Lynch, R. Pawlowicz, and P. Worcester, ''Acoustic scattering losses in the Greenland Sea marginal ice zone during the 1988–89 tomography experiment,'' J. Acoust. Soc. Am. **96**, 3045–3053 (1994).
[14] G. Jin, J. F. Lynch, R. Pawlowicz, and P. Wadhams, ''Effects of sea ice cover on acoustic ray travel times, with applications to the Greenland Sea tomography experiment,'' J. Acoust. Soc. Am. **94**, 1044–1057 (1993).
[15] W. Munk, P. Worcester, and C. Wunch, *Ocean Acoustic Tomography* (Cambridge U. P., Cambridge, 1995).
[16] O. M. Johannessen, J. A. Johannessen, E. Svendsen, R. A. Schuchman, W. J. Campbell, and E. Josberger, ''Ice-edge eddies in the Fram Strait marginal ice zone,'' Science **236**, 427–429 (1987).
[17] C.-S. Chiu, J. F. Lynch, and O. M. Johannessen, ''Tomographic resolution of mesoscale eddies in the marginal ice zone: A preliminary study,'' J. Geophys. Res. **92**, 6886–6902 (1987).
[18] A. R. Robenson (Ed.), *Eddies in Marine Science* (Springer-Verlag, New York, 1983).
[19] J. A. Johannessen, O. M. Johannessen, E. Svendsen, R. Shuchman, T. Manley, W. Campbell, E. Josberger, S. Sandven, J. C. Gascard, T. Olaussen, K. Davidson, and J. VanLeer, ''Mesoscale eddies in the Fram Strait Marginal Ice Zone during the 1983 and 1984 experiments,'' J. Geophys. Res. **92**, 6754–6772 (1987).
[20] O. M. Johannessen, S. Sandven, W. P. Budgell Johnny, A. Johannessen, and R. A. Shuchman, ''Observation and simulation of ice tongues and vortex pairs in the marginal ice zone,'' The Polar Oceans and Their Role in Shaping the Global Environment, Geophysical Monograph, **85**.
[21] L. E. Mellberg, O. M. Johannessen, D. N. Connors, G. Botseas, and D. Browning, ''Model acoustic propagation through an ice edge eddy in the East Greenland Sea marginal ice zone,'' J. Geophys. Res. **92**, 6857–6868 (1987).
[22] L. E. Melberg, O. M. Johannessen, D. N. Connors, G. Botseas, and D. G. Browning, ''Acoustic propagation in the western Greenland Sea frontal zone,'' J. Acoust. Soc. Am. **89**, 2144–2156 (1991).
[23] L. M. Brekhovskikh, *Waves in Layered Media* (Academic, Orlando, FL, 1980), 2nd ed.
[24] O. M. Johannessen, J. A. Johannessen, S. Sandven, and K. L. Davidson, ''Preliminary results of the Marginal Ice Zone Experiment (MIZEX) summer operations,'' *Environment of the Nordic Seas*, edited by B. Hurdle (Springer-Verlag, New York, 1985), pp. 665–679.
[25] B. G. Hurdle, *The Nordic Seas* (Springer-Verlag, New York, 1986).
[26] W. J. Emery, T. J. Reich, J. A. DeSanto, R. N. Baer, and J. P. Dugan, ''Mesoscale variations in the deep sound channel and effects on low frequency propagation,'' J. Acoust. Soc. Am. **66**, 831–841 (1979).
[27] H. L. Van Trees, *Detection, Estimation and Modulation Theory*, Part 1 (Wiley, New York, 1968).
[28] I. B. Burlakova, Y. A. Dubovskoy, A. L. Zeigman, A. G. Nechaev, M. M. Slavinskiy, and N. M. Smirnof, ''On the possibility of acoustic tomography of the waved surface of the ocean,'' Acust. Zh. **34**, 423–430 (1988) (in Russian) [Sov. Phys. Acoust. **34**, 246 (1988)].
[29] D. Rubenstein and M. H. Brill, ''Acoustic variability due to internal waves and surface waves in shallow water,'' in *Ocean Variability and Acoustic Propagation*, edited by J. Potter and Warn-Varnas (Kluwer Academic, The Netherlands, 1991), pp. 225–228.
[30] J. F. Lynch, G. Jin, R. Pawlowicz, D. Ray, and A. J. Plueddemann, ''Acoustic travel-time perturbations due to shallow-water internal waves and internal tides in the Barents Sea Polar Front: theory and experiment,'' J. Acoust. Soc. Am. **99**, 803–821 (1996).
[31] J. J. Kagan and L. Knopoff, ''Stochastic synthesis of earthquake catalog,'' J. Geophys. Res. **86**, 2853–2862 (1981).

Effects of elastic heterogeneities and anisotropy on mode coupling and signals in shallow water

Minkyu Park
Geophysics Program, Box 351650, University of Washington, Seattle, Washington 98195

Robert I. Odom
Applied Physics Laboratory, University of Washington, 1013 NE 40th Street, Seattle, Washington 98105

(Received 8 April 1997; revised 6 May 1998; accepted 12 May 1998)

Coupled mode theory is applied to acoustic/elastic wave propagation in shallow water to examine the effects of lateral heterogeneities and transverse isotropy on mode coupling and signals. A numerical code is developed by applying the invariant imbedding technique to the coupled mode theory. From the code, the reflection and transmission matrices and the forward/backward-propagating wave fields in the frequency domain are generated for a range-dependent medium. The effect of transverse isotropy of bottom sediment layers is also considered. Time domain signals are synthesized with a 2-Hz bandwidth between 10 Hz and 12 Hz for the excitation by a unit line force and for an incident fundamental mode. The generation of higher overtones and the decay of the fundamental mode propagating in a range-dependent medium are clearly shown. [S0001-4966(98)06508-4]

PACS numbers: 43.30.Bp, 43.30.Ft, 43.30.Gv, 43.30.Hw [SAC-B]

INTRODUCTION

This paper treats computational aspects of modeling seismo-acoustic propagation in shallow water at low frequencies. The model is one in which the frequency and bottom geoacoustic properties are such that the bottom cannot be treated as either a perfectly rigid reflector or as a simple bulk absorber.

The shallow water/bottom/subbottom system form a waveguide which, in the most general case, may contain range-dependent geometry and material properties. The bottom may also be anisotropic, but we are limited here to the relatively simple case of transverse isotropy (TI). The bottom may also be poroelastic. However, we do not include that in this work.

For our treatment of the range-dependent shallow water signal propagation problem, we use Maupin's (1988) formulation in terms of local coupled modes. Maupin's theory is quite general, and treats models containing both fluid and elastic layers. The elastic layers may be anisotropic, and both range-dependent geometry and range-dependent material properties are included. Nonplanar boundaries are handled in an exact manner by transforming inhomogeneous boundary conditions to homogeneous boundary conditions and adding a source term to the equation of motion.

Odom *et al.* (1996) studied the effect of transversely isotropic sediments on normal modes and their coupling in shallow water. We have developed code which includes the effects of bottom shear, transverse isotropy, and quite general range dependence.

A brief outline of Maupin's coupled mode theory, and its transformation to a numerically stable form by the invariant imbedding technique are introduced in the first section.

In the second section, the reflection and transmission matrices, the forward-propagating and backward-propagating wave in the frequency domain, and signals in the time domain are numerically generated for a realistic range-dependent shallow water model.

I. THEORY

In this section, we present the method based on Maupin's (1988) coupled mode theory. First, we briefly summarized the coupled mode theory for layered fluid-elastic media (Maupin, 1988). Next, we introduce the invariant imbedding technique (IIT) as applied to coupled mode theory by Kennett (1984). The evolution equation is converted to coupled differential Riccati equations for the transmission matrix and the reflection matrix. The transmission matrix accounts for the interaction between the modes of the incident wave and those of the transmitted (or forward-propagating) wave, and the reflection matrix describes the coupling to the reflected (or backward-propagating) wave. In the Appendix, we also represent the source as a decomposition of local modes.

A. Mode coupling in range-dependent media

Because our shallow water model consists of a fluid layer over an elastic bottom, we employ the coupled mode theory based on the local mode representation, as formulated by Maupin (1988) for fluid–elastic media. Only a brief outline of the theory, required for the development in the following subsections, is therefore given in this paper. Details are given in Maupin (1988) and summarized in Odom *et al.* (1996). For the numerical implementation in the following section, the range dependence is assumed to be confined in the interval $[x_L, x_R]$ as illustrated in Fig. 1, and the boundary conditions for the equation of motion are set according to that interval.

The particle displacement vector $\mathbf{w}=(w_x, w_y, w_z)$ is Fourier transformed with respect to y and t:

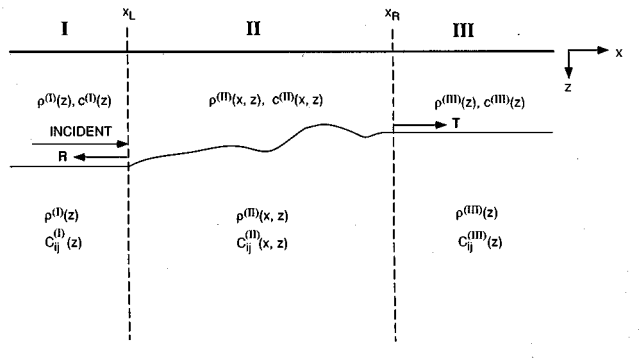

FIG. 1. The figure illustrates the geometry of the range-dependent medium modeled by the coupled Riccati equations, Eq. (31) and Eq. (32). The range-dependent region (II) is sandwiched between two plane layered (range-independent) regions (I) and (III) that need not be the same. The integration of Eq. (31) and Eq. (32) proceeds backward from the point x_R to the point x_L.

$$\mathbf{w}(x,z,k_y,\omega)=\int_{-\infty}^{+\infty}\int_{-\infty}^{+\infty}\mathbf{w}(x,y,z,t)\times\exp(ik_y y-i\omega t)dy\ dt. \tag{1}$$

The stress is

$$\tau=(\mathbf{T}(\hat{\mathbf{x}}_1)\ \ \mathbf{T}(\hat{\mathbf{x}}_2)\ \ \mathbf{T}(\hat{\mathbf{x}}_3))=(\mathbf{t}\ \ \mathbf{t}_2\ \ \mathbf{t}_3), \tag{2}$$

where the unit vectors of coordinates are $(\hat{\mathbf{x}}_1,\hat{\mathbf{x}}_2,\hat{\mathbf{x}}_3)=(\hat{\mathbf{x}},\hat{\mathbf{y}},\hat{\mathbf{z}})$ and the traction vector is $\mathbf{t}_i=(\tau_{ix},\tau_{iy},\tau_{iz})^T$ for $i=1,2,3$. By introducing the six-component displacement-stress vector $\mathbf{u}=(\mathbf{w},\mathbf{t})^{\mathbf{T}}$, the equation of motion and the constitutive law for elasticity can be written as the first-order system:

$$\frac{\partial\mathbf{u}}{\partial x}=A\mathbf{u}-\mathbf{F}^S+\mathbf{F}^0 \tag{3}$$

with the boundary conditions

$$[\mathbf{t}_3]_m=[\mathbf{w}]_m=0, \tag{4}$$

where the traction vector on the vertical plane whose surface normal is $\hat{\mathbf{x}},\mathbf{t}=\mathbf{t}_1=(\tau_{xx},\tau_{xy},\tau_{xz})^T$, and the external source $\mathbf{F}^S$ and the effective source $\mathbf{F}^0$ resulting from nonplanar boundaries are

$$\mathbf{F}^S=\begin{Bmatrix}\mathbf{0}\\ \mathbf{f}^S\end{Bmatrix}, \tag{5}$$

$$\mathbf{F}^0=\begin{Bmatrix}\mathbf{0}\\ [\mathbf{t}]_m\delta(z-h_m(x))\end{Bmatrix}. \tag{6}$$

The source $\mathbf{F}^S$ is the external source for the problem, i.e., the source such as an explosion that provides the initial excitation. The source $\mathbf{F}^0$ is a localized volume force located along the interface which is converted from a traction discontinuity at the interface by the representation theorem (Burridge and Knopoff, 1964). This source $\mathbf{F}^0$ depends linearly on the solution of the local plane layered problem. We refer the reader to Maupin's (1988) original work or to the summary given in Odom *et al.* (1996) for details. The square brackets $[\cdot]_m$ in Eq. (4) indicate the jump of the enclosed quantity across the mth interface, taken from bottom to top. The range coordinate, x in Eq. (3), represents the propagation direction and the differential operator A on the r.h.s. of Eq. (3) contains only the derivatives with respect to the depth coordinate, z. For horizontal transmission in transversely isotropic elastic media, the displacement-stress vector can be written as

$$\mathbf{u}=(w_x\quad 0\quad w_z\quad \tau_{xx}\quad 0\quad \tau_{xz})^T \quad \text{for Rayleigh } (P\text{-}SV) \text{ waves,} \tag{7}$$

$$\mathbf{u}=(0\quad w_y\quad 0\quad 0\quad \tau_{xy}\quad 0)^T \quad \text{for Love } (SH) \text{ waves,} \tag{8}$$

and in a fluid layer

$$\mathbf{u}=\left(\frac{1}{i\omega}V_x\ \ 0\ \ 0\ \ p\ \ 0\ \ 0\right)^T \quad \text{for acoustic waves,} \tag{9}$$

where the symbol P represents the compressional waves, SV the vertically polarized shear waves, and SH the horizontally polarized shear waves. In Eq. (9), p is the pressure, V_x is the x component of the velocity. The matrix differential operator A is

$$A=\begin{pmatrix}A^{11} & A^{12}\\ A^{21} & A^{22}\end{pmatrix}. \tag{10}$$

For a TI elastic medium, the submatrices of the differential operator A are

$$A^{11}=\begin{pmatrix}0 & ik_y\dfrac{A-2N}{A} & \dfrac{F}{A}\dfrac{\partial}{\partial z}\\ ik_y & 0 & 0\\ \dfrac{\partial}{\partial z} & 0 & 0\end{pmatrix}, \tag{11}$$

$$A^{12}=\begin{pmatrix}\dfrac{1}{A} & 0 & 0\\ 0 & \dfrac{1}{N} & 0\\ 0 & 0 & \dfrac{1}{L}\end{pmatrix}, \tag{12}$$

$$A^{21}=\begin{pmatrix} -\rho\omega^2 & 0 & 0 \\ 0 & -\rho\omega^2-\dfrac{\partial}{\partial z}\left(L\dfrac{\partial}{\partial z}\right) & ik_y\dfrac{2NF}{A}\dfrac{\partial}{\partial z}+\dfrac{\partial}{\partial z}(ik_yL) \\ 0 & ik_yL\dfrac{\partial}{\partial z}+\dfrac{\partial}{\partial z}\left(ik_y\dfrac{2NF}{A}\right) & -\rho\omega^2-\dfrac{\partial}{\partial z}\left(\dfrac{AC-F^2}{A}\dfrac{\partial}{\partial z}\right)+k_y^2L \end{pmatrix}, \tag{13}$$

$$A^{22}=\begin{pmatrix} 0 & ik_y & -\dfrac{\partial}{\partial z} \\ ik_y\dfrac{A-2N}{A} & 0 & 0 \\ -\dfrac{\partial}{\partial z}\dfrac{F}{A} & 0 & 0 \end{pmatrix}, \tag{14}$$

where the elastic parameters in a TI medium are defined for horizontal transmission as (Takeuchi and Saito, 1972)

$$\sqrt{\frac{A}{\rho}}\equiv\alpha_H \quad \text{for } P \text{ waves}, \tag{15}$$

$$\sqrt{\frac{L}{\rho}}\equiv\beta_V \quad \text{for } SV \text{ waves}, \tag{16}$$

$$\sqrt{\frac{N}{\rho}}\equiv\beta_H \quad \text{for } SH \text{ waves}, \tag{17}$$

and for vertical transmission, they are given by

$$\sqrt{\frac{C}{\rho}}\equiv\alpha_V \quad \text{for compressional waves}, \tag{18}$$

$$\sqrt{\frac{L}{\rho}}\equiv\beta_V \quad \text{for shear waves}. \tag{19}$$

α and β represent the compressional and shear velocities, respectively, and subscripts H and V denote the horizontal and vertical propagation directions. For a fluid layer, the differential operator A is

$$A^{12}=\begin{pmatrix} \dfrac{1}{\omega^2}\dfrac{\partial}{\partial z}\left(\dfrac{1}{\rho}\dfrac{\partial}{\partial z}\right)+\eta & 0 & 0 \\ 0 & 0 & 0 \\ 0 & 0 & 0 \end{pmatrix}, \tag{20}$$

$$A^{21}=\begin{pmatrix} -\omega^2\rho & 0 & 0 \\ 0 & 0 & 0 \\ 0 & 0 & 0 \end{pmatrix}, \tag{21}$$

$$A^{11}=A^{22}=\mathbf{0}, \tag{22}$$

where ρ is the density and η is the compressibility such that the sound speed $c=(1/\eta\rho)^{1/2}$. In 1-D range-independent and 2-D range-dependent media, the matrix differential operator A can be written in block diagonal form indicating the separation of the *P-SV* terms from the *SH*. This block diagonal form is also possible for TI media.

We represent the solution of the equation-of-motion (3) as the superposition of forward (+) and backward (−) propagating local modes $\mathbf{u}^r(z;x,\pm k^r)$ multiplied by the range-dependent mode amplitude $c_r(x)$, where a set of local modes at $x=x'$ are computed from the locally equivalent depth-dependent but range-*independent* structure:

$$\mathbf{u}=\begin{Bmatrix}\mathbf{w}\\ \mathbf{t}\end{Bmatrix}=\sum_r c_r^{\pm}(x)\exp\left(\mp i\int_{x_s}^{x}k^r(\xi)d\xi\right)\begin{Bmatrix}\mathbf{w}^r(z;x)\\ \mathbf{t}^r(z;x)\end{Bmatrix}, \tag{23}$$

where $k(\zeta)$ is the local horizontal wave number, and x_s denotes the source point.

The decomposition into forward- and backward-propagating waves in a continuously varying inhomogeneous medium is not unique. Continuously varying in this case means that all derivatives with respect to x are continuous, i.e., the medium properties w.r.t. range are represented by so-called C^∞ functions. Derivatives are considered continuous if they vary slowly on the order of the wavelength. A derivative for a given order may be considered discontinuous if the change in the medium property derivative occurs on an interval small with respect to the wavelength. If the *n*th range derivative of the medium property is discontinuous, the reflection coefficient at the location of the discontinuity will be $\mathcal{O}(\epsilon^n)$ where $\epsilon=\lambda/L$. The length of the inhomogeneous region is L and the wavelength is λ. Schelkunoff (1951) gives a particularly clear discussion of the details of reflection from an inhomogeneous medium. The nonuniqueness of the decomposition into forward- and backward-propagating waves is not a problem as long as it is consistently applied. A discussion of the nonuniqueness with an example is given by Sluijter (1970).

By substituting Eq. (23) into the equation of motion (3), the evolution equation for the range-dependent mode amplitudes is expressed in terms of both forward (+) and backward (−) propagating modes (Marquering and Snieder, 1995):

$$\frac{\partial}{\partial x}\begin{pmatrix}\mathbf{c}^+(x)\\ \mathbf{c}^-(x)\end{pmatrix}=\begin{pmatrix}\mathbf{B}^{++}(x) & \mathbf{B}^{+-}(x)\\ \mathbf{B}^{-+}(x) & \mathbf{B}^{--}(x)\end{pmatrix}\begin{pmatrix}\mathbf{c}^+(x)\\ \mathbf{c}^-(x)\end{pmatrix}, \tag{24}$$

with the boundary conditions

$$\mathbf{c}^+=\mathbf{c}^0 \quad \text{at } x=x_L, \tag{25}$$

$$\mathbf{c}^-=0 \quad \text{at } x=x_R. \tag{26}$$

The left boundary condition is the excitation at the beginning of the inhomogeneous section at $(x=x_L)$, and is in fact, the response at $(x=x_L)$ due to the source $\mathbf{f}^S$. This is discussed further in the Appendix. Matrices $\mathbf{B}^{++}$, $\mathbf{B}^{+-}$, $\mathbf{B}^{-+}$, and $\mathbf{B}^{--}$ are the $n\times n$ matrices of complex values and describe forward-to-forward, forward-to-backward, backward-to-forward, and backward-to-backward coupling, respectively.

Vectors $\mathbf{c}^+$ and $\mathbf{c}^-$ are $n\times 1$ column vectors, where n is the appropriate number of modes required to accurately model the signal. The elements of matrices $\mathbf{B}^{++}$, $\mathbf{B}^{+-}$, $\mathbf{B}^{-+}$, and $\mathbf{B}^{--}$ depend linearly on the range gradients of the material properties and quadratically on the local medium eigenfunctions. The derivation of $\mathbf{B}$ matrices follows from the effective source term $\mathbf{F}^0$ in Eq. (6) and the orthogonality of the local modes. A complete discussion is given by Maupin (1988), and a summary is in Odom *et al.* (1996).

B. Invariant imbedding

If we specify a geometry defined by a heterogeneous region sandwiched between two homogeneous (plane layered) regions, and assume a signal incident from the left onto the heterogeneous region, Eq. (24) defines a $2n\times 2n$ boundary value problem (BVP) for the amplitudes of the forward- and backward-propagating modes. A schematic of a range-dependent medium is shown in Fig. 1. The boundary values are $\mathbf{c}^+(x_L)$, known at $x=x_L$ on the left side of the heterogeneous region, and $\mathbf{c}^-(x_R)=0$ on the right side of the heterogeneous region at $x=x_R$. Stable numerical solution of the two point boundary value problem defined by Eq. (24) and the two boundary values is problematic due to the presence of both growing and decaying mode amplitudes within the heterogeneous region. This situation is exacerbated if the heterogeneous region is extended in range. Kennett (1984) and Marquering and Snieder (1995) applied the invariant imbedding technique (IIT) to the evolution equation (24) and its boundary conditions (25) and (26). The main strategy of IIT is to reformulate the original BVP in terms of the associated initial value problems (IVP's) via the Riccati transformation (e.g., Dieci, 1992).

The procedure (Marquering and Snieder, 1995) is to define a transmission matrix $\mathbf{T}(x_R,x_L)$ that connects the $\mathbf{c}^+(x_L)$ on the left side of the heterogeneous region with the $\mathbf{c}^+(x_R)$ on the right side of the heterogeneous region

$$\mathbf{c}^+(x_R)=\mathbf{T}(x_R,x_L)\mathbf{c}^+(x_L). \tag{27}$$

In addition a reflection matrix $\mathbf{R}(x_R,x_L)$ is defined that relates the backscattered component $\mathbf{c}^-(x_L)$ from the heterogeneous region to the forward-propagating component $\mathbf{c}^+(x_L)$ at the left side of the heterogeneous region

$$\mathbf{c}^-(x_L)=\mathbf{R}(x_R,x_L)\mathbf{c}^+(x_L). \tag{28}$$

We differentiate Eqs. (27) and (28) with respect to x_L

$$\frac{\partial}{\partial x_L}\mathbf{c}^+(x_L)=\frac{\partial}{\partial x_L}\mathbf{T}\mathbf{c}^+(x_L)+\mathbf{T}\frac{\partial}{\partial x_L}\mathbf{c}^+(x_L)=0, \tag{29}$$

$$\frac{\partial}{\partial x_L}\mathbf{c}^-(x_L)=\frac{\partial}{\partial x_L}\mathbf{R}\mathbf{c}^+(x_L)+\mathbf{R}\frac{\partial}{\partial x_L}\mathbf{c}^+(x_L). \tag{30}$$

The derivatives of the amplitude vectors are replaced with their expressions from Eq. (24), and $\mathbf{c}^-(x_L)$ can be removed from the equation using Eq. (28). After removing a common factor of $\mathbf{c}^+(x_R)$, we arrive at coupled matrix differential Riccati equations (DRE) for the reflection and transmission matrices for the heterogeneous region:

$$\frac{\partial}{\partial x_L}\mathbf{R}=\mathbf{B}^{-+}+\mathbf{B}^{--}\mathbf{R}-\mathbf{R}\mathbf{B}^{++}-\mathbf{R}\mathbf{B}^{+-}\mathbf{R} \tag{31}$$

and

$$\frac{\partial}{\partial x_L}\mathbf{T}=-\mathbf{T}\mathbf{B}^{++}-\mathbf{T}\mathbf{B}^{+-}\mathbf{R}, \tag{32}$$

with the initial conditions

$$\mathbf{T}(x_R,x_R)=\mathbf{I}\quad\text{and}\quad\mathbf{R}(x_R,x_R)=\mathbf{0}. \tag{33}$$

$\mathbf{I}$ is the $n\times n$ identity matrix.

Now we investigate the existence and the stability of the solutions of coupled matrix DRE's (31) and (32) from the properties of the coupling matrix $\mathbf{B}$. We can decompose the coupling matrix into the amplitude and the phase:

$$B_{qr}^{++}=\frac{1}{k^q-k^r}\hat{B}_{qr}^{++}\exp\left\{i\int_{x_s}^{x}(k^q(\xi)-k^r(\xi))d\xi\right\}, \tag{34}$$

$$B_{qr}^{+-}=\frac{1}{k^q+k^r}\hat{B}_{qr}^{+-}\exp\left\{i\int_{x_s}^{x}(k^q(\xi)+k^r(\xi))d\xi\right\}, \tag{35}$$

$$B_{qr}^{-+}=\frac{1}{-k^q-k^r}\hat{B}_{qr}^{-+}\exp\left\{i\int_{x_s}^{x}(-k^q(\xi)-k^r(\xi))d\xi\right\}, \tag{36}$$

$$B_{qr}^{--}=\frac{1}{-k^q+k^r}\hat{B}_{qr}^{--}\exp\left\{i\int_{x_s}^{x}(-k^q(\xi)+k^r(\xi))d\xi\right\}. \tag{37}$$

The amplitude $\hat{B}_{qr}$ is a function of material properties and the eigenfunctions of qth and rth modes. Since the eigenfunctions of qth backward-propagating mode equals that of the forward-propagating mode, and the eigen wave number k_q is merely replaced with $-k_q$ for the backward-propagating mode, the amplitude $\hat{\mathbf{B}}$ becomes

$$\hat{B}_{qr}^{++}=\hat{B}_{qr}^{+-}=\hat{B}_{qr}^{-+}=\hat{B}_{qr}^{--}\equiv\hat{B}_{qr}. \tag{38}$$

From the anti-Hermicity of the coupling matrix $\hat{\mathbf{B}}$ (Maupin, 1988),

$$\{\mathbf{B}^{++}\}^\dagger=-\mathbf{B}^{++}, \tag{39}$$

$$\{\mathbf{B}^{+-}\}^\dagger=\mathbf{B}^{-+}, \tag{40}$$

$$\{\mathbf{B}^{--}\}^\dagger=-\mathbf{B}^{--}, \tag{41}$$

it can be proved that the amplitude $\hat{\mathbf{B}}$ is also anti-Hermitian, e.g.,

$$\{B_{qr}^{++}\}^\dagger=-\frac{1}{k^q-k^r}\hat{B}_{qr}^\dagger\exp\left(i\int_{x_s}^{x}(k^q(\xi)-k^r(\xi))d\xi\right), \tag{42}$$

$$-B_{qr}^{++}=\frac{1}{k^q-k^r}\hat{B}_{qr}\exp\left(i\int_{x_s}^{x}(k^q(\xi)-k^r(\xi))d\xi\right), \tag{43}$$

where $\dagger$ represents the adjoint. Therefore, by equating Eq. (42) and Eq. (43),

$$\hat{\mathbf{B}}^\dagger=-\hat{\mathbf{B}}. \tag{44}$$

If we assume that there is no wave propagation in the y-direction, i.e., the wave number $k_y=0$, and there is no mode

coupling between Rayleigh waves (*P-SV*) and Love waves (*SH*), then the elements of $\hat{\mathbf{B}}$ become pure real [see Eq. (25) of Maupin, 1988] and the amplitude matrix $\hat{\mathbf{B}}$ becomes antisymmetric:

$$\hat{\mathbf{B}}^T = -\hat{\mathbf{B}}, \tag{45}$$

where T is the transpose. From the antisymmetry of $\mathbf{B}$, the following properties can be derived:

$$\{\mathbf{B}^{--}\}^T = -\mathbf{B}^{++}, \tag{46}$$

$$\{\mathbf{B}^{+-}\}^T = \mathbf{B}^{+-}, \tag{47}$$

$$\{\mathbf{B}^{-+}\}^T = \mathbf{B}^{-+}, \tag{48}$$

i.e., the coupling matrix $\mathbf{B}(x)$ is the particular (pointwise) Hamiltonian (Dieci, 1992):

$$\hat{\mathbf{B}}(x) = \begin{pmatrix} \mathbf{B}^{++} & \mathbf{B}^{+-} \\ \mathbf{B}^{-+} & -\mathbf{B}^{++T} \end{pmatrix}, \tag{49}$$

and $\mathbf{B}^{+-T} = \mathbf{B}^{+-}$, $\mathbf{B}^{-+T} = \mathbf{B}^{-+}$. When the coupling matrix $\mathbf{B}(x)$ is the particular Hamiltonian, the DRE for the reflection matrix (31) becomes the *symmetric* DRE. Under condition (49), all solutions of Eq. (31) are symmetric (Dieci, 1992):

$$\mathbf{R}^T(x_R, x_L) = \mathbf{R}(x_R, x_L), \tag{50}$$

and existence and monotonicity properties are guaranteed, which do not generally hold for other DRE's. The symmetry of the reflection matrix reduces the number of matrix elements to be numerically solved from N^2 to $N(N+1)/2$. It also provides a useful check on the accuracy of computation for the test.

For numerical computation of the transmission and the reflection matrices, the DRE for the transmission matrix equation (32) must be solved after the DRE for the reflection matrix equation (31) is numerically integrated backward from the point X_R.

One advantage of the invariant imbedding approach is that there are built in checks on the accuracy. The reflection matrix $\mathbf{R}$ can be checked for symmetry. In addition, energy conservation demands that

$$|\mathbf{R}|^2 + |\mathbf{T}|^2 = \mathbf{I}. \tag{51}$$

Other numerically stable techniques for solving the coupled mode evolution equation (24) are Mattheij's (1985) continuous decoupling transform, employed by Evans (1986a,b) for a range-dependent fluid medium, and the very powerful Lanczos method used by Knobles (1994).

Mattheij's continuous decoupling transformation was used by Evans (1986a) to stabilize the Thomson (1950)–Haskell (1953) propagator matrix technique. The dependent variables in the Thomson–Haskell method are usually the stress and displacement, whereas the IIT takes $\mathbf{R}$ and $\mathbf{T}$ as the dependent variables. Because the two methods are solving the same boundary value problem, it is of course possible to transform one method to the other (Buchen and Ben-Hador, 1996). There are, however, significant algorithmic differences between Mattheij's stabilized Thomson–Haskell method and the IIT (Evans, 1986b). Knobles (1994) found Lanczos' method to converge rapidly, and it appear to have numerical advantages for very large problems. Although we have found the computation of the local mode bases to be the most time consuming aspect of the problem.

We have adopted the IIT because of the built in numerical checks stated above, and easily accessible intermediate products of the computation.

II. NUMERICAL RESULTS

In this section we study the effect of the transverse isotropy, and the range dependence on the coupling matrix, the transmission matrix, the reflection matrix, the forward-propagating and the backward-propagating wave fields in the frequency domain, and the synthetic signals for a range-dependent shallow model. The code DISPER80 (Saito, 1988) is used to generate the eigenfunctions of the local modes, from which the coupling matrix B_{qr} is computed. By numerically integrating the coupled DRE Eqs. (31) and (32), the transmission matrix $\mathbf{T}$ and the reflection matrix $\mathbf{R}$ are computed for a given frequency. The forward-propagating and the backward-propagating wave fields in the frequency domain are generated from the the matrices $\mathbf{T}$ and $\mathbf{R}$. Signals in the time domain are synthesized from the inverse Fourier transformation of the spectral wave field.

The computations were carried out on a Sun SPARCstation LX. The numerical process consists of four steps. The first step is calculating the eigenfunctions of the local modes for each point in range at one fixed frequency. The eigenfunctions for a set of local modes for our test problem require 2.6-Mbyte disk storage when only the first four modes are computed. A disk space problem may be encountered when generating multiple modes at multiple frequencies. This problem can be overcome because the eigenfunctions are no longer necessary after computing the transmission/reflection matrices at a particular frequency. That is, all local normal modes, except at the receiver point and the source point, can be deleted at the end of the first step. For our computational model (Fig. 2), it takes 20 s of CPU time to compute a set of four eigenfunctions at a single range point for one frequency using double precision. We found that at higher frequencies (20 Hz) for our low shear speed model, quadruple precision was necessary to generate accurate eigenfunctions. This significantly increased the computation time. At the second step, the coupling matrix $\mathbf{B}$ is computed from the eigenfunctions. The reflection/transmission matrices $\mathbf{R}$ and $\mathbf{T}$ are computed by numerical integration of the coupled DRE, which takes 143-s CPU time for one frequency for our test model. Next, the wave fields in the frequency domain are generated from matrices $\mathbf{R}$ and $\mathbf{T}$. As the last step, the signals in the time domain are synthesized by inverse Fourier transforming the wave fields generated for multiple frequency points. The third and the fourth steps take relatively less CPU time than the first and the second steps.

A. Computational model

Our computational model consists of a heterogeneous region ($0\ \text{m} \leqslant x \leqslant 76\ \text{m}$) and two homogeneous (plane layered) regions ($x < 0\ \text{m}$) and ($x > 76\ \text{m}$). The slope of the interfaces in the heterogeneous region varies up to 45°, and the

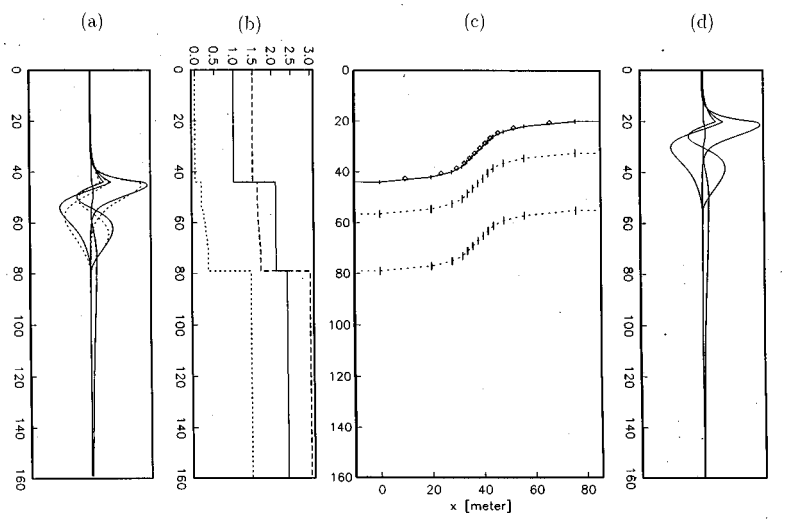

FIG. 2. The range-dependent shallow water model with transversely isotropic sediments [based on the data of Berge *et al.* (1991) Table I]. (a) Normal modes of an isotropic medium (solid lines) and a transversely isotropic (TI) medium (dotted lines) at $x=0$ m. (b) Density (solid line), compressional wave velocity (broken line), and shear wave velocity (dotted line) at $x=0$ m. (c) Two-dimensional shallow water structure. ◇ indicates the point where local normal modes are computed. (d) Normal modes of an isotropic medium at $x=76$ m.

material properties in each layer are assumed constant. The material properties of the homogeneous region ($x>76$ m) are the same as the model of Odom *et al.* (1996), which was taken from Berge *et al.* (1991). The model structure, the velocity, and the density profiles are illustrated in Fig. 2. The model consists of an isovelocity water layer over sediment layers followed by the hard bottom. The thickness of a water layer varies from 44 m to 20 m as x increases from 0 m to 76 m. The sediment layers are made of 12.5-m-thick TI upper layers, followed by 12.5-m-thick isotropic lower layers. There is a large contrast in the velocities and the density between the sediments and a hard bottom. The TI layer is characterized by $\eta'=0.012$ and $\phi'=0$, where the dimensionless parameters (Takeuchi and Saito, 1972) are:

$$\eta'=1-\eta=1-\frac{F}{A-2L}, \tag{52}$$

and

$$\phi'=1-\phi=1-\frac{C}{A}. \tag{53}$$

Values of

$$\eta'=0 \quad \text{and} \quad \phi'=0 \tag{54}$$

indicate isotropy. The departure from isotropy increases as η' and/or ϕ' change from 0. In Fig. 2, the vertical displacement eigenfunction of the first four local modes are plotted against depth at 10 Hz. The first mode, whose phase velocity is 145.6 m/s, propagates along the water/sediment interface, i.e., a Stoneley wave (Scholte wave). The energy of the second and the third modes are mainly confined within the sediment layers, while the fourth mode radiates into the hard bottom.

The coupling matrix **B** is computed from the eigen wave numbers and eigenfunctions of the local modes. These coupling matrices become the coefficient matrices of the coupled matrix DRE which will be solved in the following subsection. The plots of **B** are presented in Odom *et al.* (1996).

B. Reflection and transmission matrices and forward- and backward-propagating wave fields

In this subsection, we describe the numerical solution of the matrix DRE's Eqs. (31) and (32). We solved for the reflection and transmission matrices with FORTRAN code written for the direct numerical integration of complex matrix DRE's. The code is built around a module CDRIV2 from the SLATEC library, which solves the initial value problem for systems of first-order ordinary differential equations (Gear, 1971).

First, the matrix DRE (31) for the reflection matrix **R** is numerically integrated backward from $x_R=76$ m to $x_L=0$ m with the initial value (33) at x_R. From the computed coupling matrices and reflection matrix, the matrix DRE (32) is similarly solved for the transmission matrix **T**.

From the transmission and the reflection matrices, the range-dependent mode amplitudes $c_q^+(x_r)$ and $c_q^-(x_r)$ at the receiver point ($\mathbf{r}=\mathbf{r}_r$) are computed by relations (27) and (28) and the initial values c_q^0 of Eq. (A7):

$$c_q^+(x_r)=\sum_r T_{qr}(x_R,x_L)c_r^0$$

$$=\sum_r T_{qr}(x_R,x_L)\{i\mathbf{w}^{r*}(z_s;x_s)\cdot\mathbf{f}^s\}, \tag{55}$$

$$c_q^-(x_r)=\sum_r R_{qr}(x_R,x_L)c_r^0$$

$$=\sum_r R_{qr}(x_R,x_L)\{i\mathbf{w}^{r*}(z_s;x_s)\cdot\mathbf{f}^s\}, \tag{56}$$

where the source $\mathbf{f}^s$ is assumed to be located at the point $\mathbf{r}=\mathbf{r}_s=(x_s,0,z_s)$ and the receiver point and the source point are assumed to be placed outside the heteregeneous region, i.e., $x_s\leqslant x_R<x_L\leqslant x_r$. Then the spectral wave fields at the receiver point are generated as a function of depth with a given frequency:

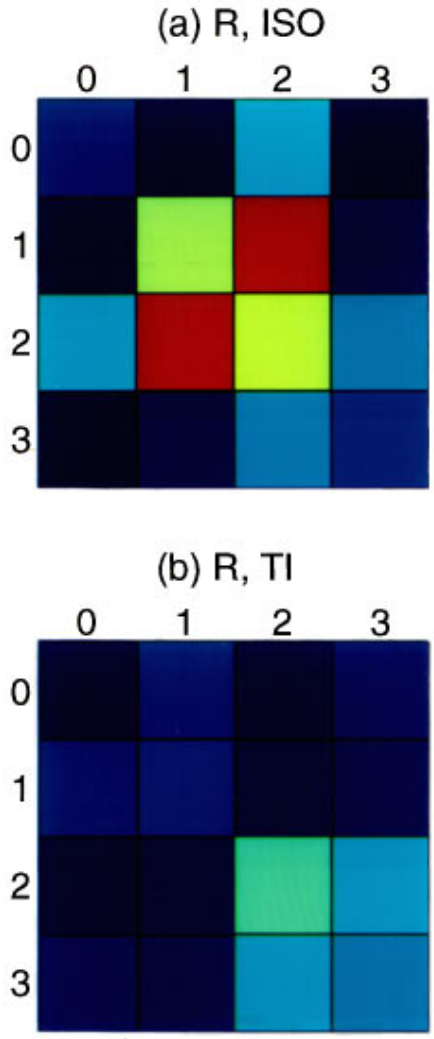

FIG. 3. The reflection matrices computed at 10 Hz for (a) an isotropic model and (b) a TI model. The real parts are plotted. Columns and rows represent incident modes and outgoing modes, respectively.

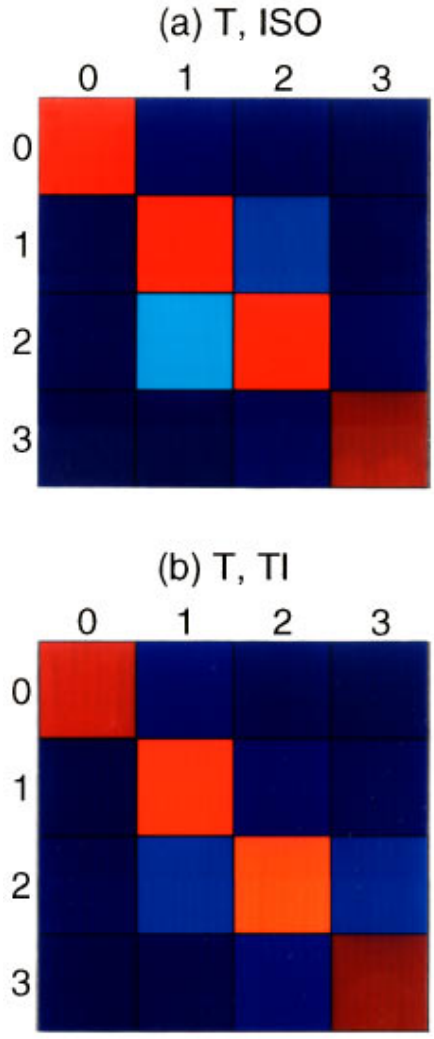

FIG. 4. The transmission matrices computed at 10 Hz for (a) an isotropic model and (b) a TI model. The real parts are plotted. Columns and rows represent incident modes and outgoing modes, respectively.

$$\mathbf{u}^{+}(z;x_r,\omega)=\sum_q g(k_qR)c_q^{+}(x_r)\mathbf{u}^q(z)\exp\left(-i\int_{x_s}^{x_r}k^q(\xi)d\xi\right)$$

$$=\sum_{q,r} g(k_qR)T_{qr}(x_R,x_L)\{i\mathbf{w}^{r*}(z_s;x_s)\cdot\mathbf{f}^{s}\}\mathbf{u}^q(z)$$

$$\times\exp\left(-i\int_{x_s}^{x_r}k^q(\xi)d\xi\right), \tag{57}$$

$$\mathbf{u}^{-}(z;x_r,\omega)=\sum_q g(k_qR)c_q^{-}(x_r)\mathbf{u}^q(z)\exp\left(i\int_{x_s}^{x_r}k^q(\xi)d\xi\right)$$

$$=\sum_{q,r} g(k_qR)R_{qr}(x_R,x_L)\{i\mathbf{w}^{r*}(z_s;x_s)\cdot\mathbf{f}^{s}\}$$

$$\times\mathbf{u}^q(z)\exp\left(i\int_{x_s}^{x_r}k^q(\xi)d\xi\right), \tag{58}$$

where $g(k_qR)$ represents geometric spreading function (Aki and Richards, 1980):

$$g(k_qR)=\sqrt{\frac{2}{\pi k_qR}}=\sqrt{\frac{2}{\pi k_q(x_r-x_s)}}. \tag{59}$$

The computed reflection matrices are shown in Fig. 3 for both an isotropic model and a TI model. In the case of an isotropic model, the most prominent elements are R_{23} or R_{32}, which describe mode coupling from c_2^{+} to c_3^{-} or from c_3^{+} to c_2^{-}. Those two modes, the second and the third modes, propagate just above the sediment-basement boundary, which has a large impedance contrast. The large impedance contrast, and relatively high amplitude of the second and third modes at the sediment-basement interface result in the strong coupling produced by the rising basement.

Addition of transverse isotropy to sediments suppresses the reflected energy of all the elements R_{qr} for q and $r=1,2,3,4$. The greater material stiffness for horizontally propagating waves in the TI medium generally reduces the amplitude of the low-order TI modes, $\{c_1^{+},c_2^{+},c_3^{+},c_4^{+}\}$, whose energy mostly propagates in the sediments, more than the higher modes (Odom *et al.*, 1996). The element R_{44} therefore becomes relatively stronger. As the fractional

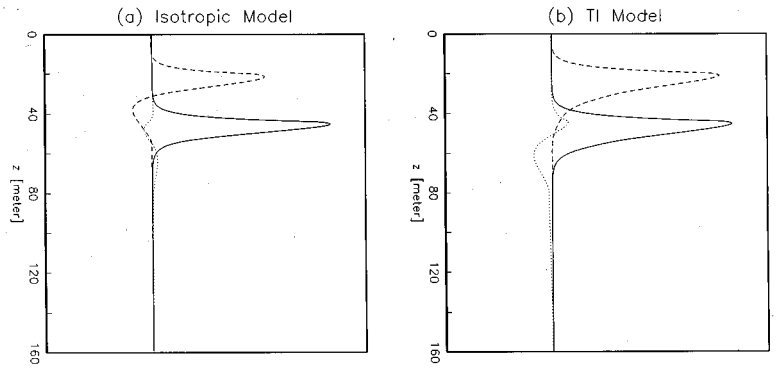

FIG. 5. The vertical components of the displacement wave field are generated for an isotropic model and for a TI model when incident wave is a fundamental mode. The solid line is used for the incident wave $w_z^+(z;x=x_L,\ f=10\ \text{Hz})$, the broken line for the forward-propagating wave $w_z^+(z;x=x_R,\ f=10\ \text{Hz})$, and the dotted line the backward-propagating wave $w_z^-(z;x=x_L,\ f=10\ \text{Hz})$. The backward-propagating waves are ten times magnified for comparison.

amount of modal energy in sediments decreases, the reflection from the range dependence in sediment layers also decreases.

Figure 4 shows the transmission matrices for both an isotropic and a TI model. The diagonal terms of the transmission matrices, which describe the self-coupling of modes, are much stronger than the off-diagonal terms. Especially T_{44} (coupling from c_4^+ to c_4^+) is stronger, which means that the fourth mode is transmitted through the heterogeneous region almost without disturbance. That is because the fourth mode mostly propagates in the homogeneous hard bottom, which is placed below the heterogeneous sediments. The T_{23} and T_{32} elements indicate coupling between c_2^+ and c_3^+ for the same reason that R_{23} or R_{32} are strong.

The computed reflection matrix $\mathbf{R}$ is symmetric to machine precision as demanded by Eq. (51). In addition, the off-diagonal terms of $|\mathbf{R}|^2+|\mathbf{T}|^2$ are on the order of 10^{-5} as required by energy conservation.

The generated wave fields at 10 Hz are presented for the two cases when the incident wave is a fundamental mode (Fig. 5) and when the excitation is a unit line force (Fig. 6) for both an isotropic model and a TI model. In Fig. 5, the shape of the wave field in an isotropic model is changed from the fundamental mode form to the oscillating form indicative of mixed modes after the transmission. This indicates that some amount of the fundamental mode energy is converted to the higher modes after transmission. The energy is spread over a greater depth range. The incident Stoneley wave along the water sediment interface is partly converted to higher-order modes propagating in the sediment. For a TI model the effect of the lateral heterogeneity on the transmitted wave field is less than for the equivalent isotropic model. For both cases the conversion to backward-propagating waves is quite small. [Note that the backward propagating wave fields in Fig. 5(a) and (b) have been multiplied by a factor of 10.]

The spectral wave fields are also generated for the excitation by a unit line force, which shows more complicated coupling among all four modes (Fig. 6).

C. Synthetic signals

Signals in the time domain are synthesized by inverse Fourier transforming the spectral wave fields

$$\mathbf{u}^+(t;x_r,z_r)=\int_{-\infty}^{\infty}\mathbf{u}^+(z;x_r,\omega)\,\delta(z-z_r)\exp(i\omega t)\,d\omega. \tag{60}$$

For that purpose, the spectral wave fields are generated from 10 Hz to 12 Hz with 0.2-Hz increments. The time domain signals are 5 s long with a 2-Hz bandwidth between 10 Hz and 12 Hz.

Spectra with such a narrow bandwidth exhibit significant sidelobes in the time domain. To suppress the sidelobes and to generate realistic signals, a Hanning window is applied to the spectra before the transformation.

In Fig. 7, the arrival preceding the fundamental mode appears after transmission through the range-dependent region, which clearly indicates the mode coupling from the fundamental mode to higher modes with higher group velocities. Synthetic signals for the excitation by a unit line force show both mode coupling and dispersion of modes (Fig. 8). Due to mode coupling among the multiple local modes, the shape of the signals becomes very complicated

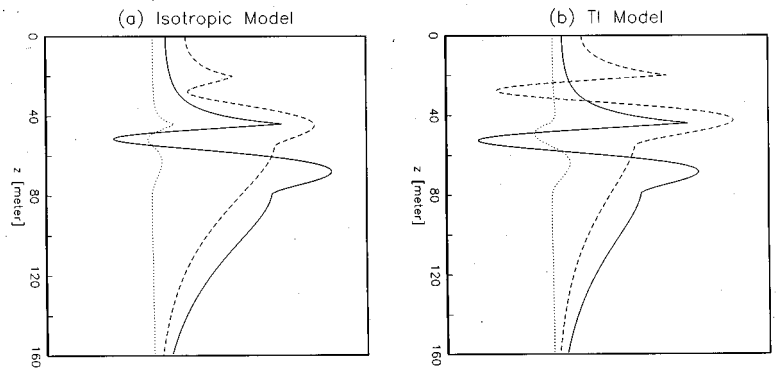

FIG. 6. Same as Fig. 6 except that excitation is a unit line force.

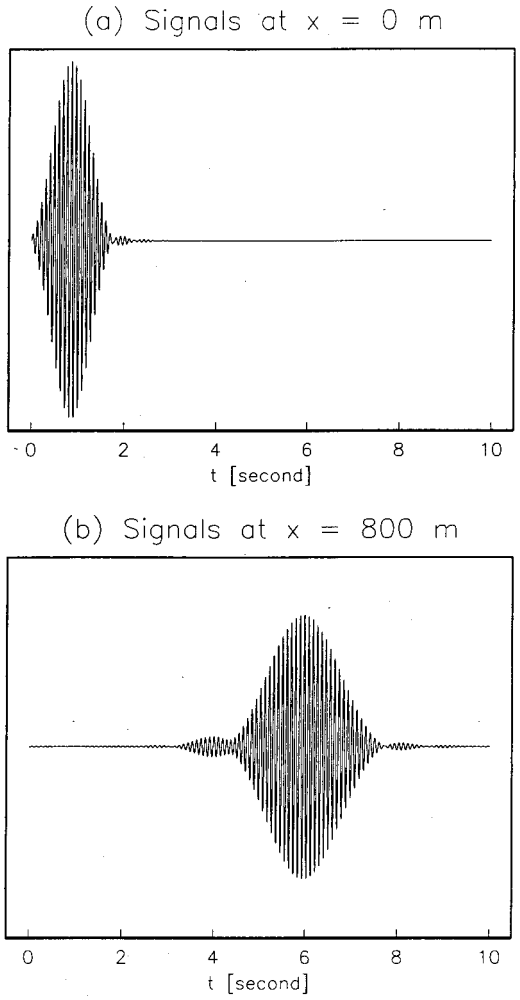

FIG. 7. Synthetic signals (a) at $(x,z)=(0\text{ m},40\text{ m})$ and (b) at $(x,z)=(800\text{ m},20\text{ m})$ with a 2-Hz bandwidth between 10 Hz and 12 Hz when incident wave is fundamental mode.

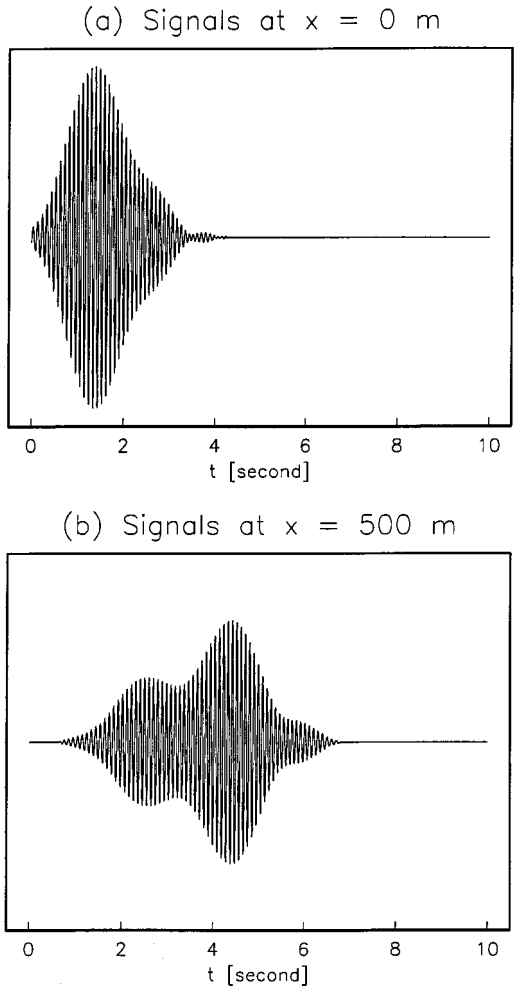

FIG. 8. Synthetic signals (a) at $(x,z)=(0\text{ m},40\text{ m})$ and (b) at $(x,z)=(500\text{ m},20\text{ m})$ with a 2-Hz bandwidth between 10 Hz and 12 Hz when a unit line force is excited at $(x,z)=(0\text{ m},20\text{ m})$ in water.

after transmission through the range-dependent zone and the presence of propagation induced dispersion, and it is much more difficult to interpret those signals.

III. SUMMARY AND CONCLUSIONS

We have developed a numerical code for simulation in range-dependent media from the coupled mode theory for fluid-elastic media. A realistic range-dependent shallow water model, which may also include transversely isotropic sediment layers, is introduced. We have computed the transmission and the reflection matrices, the forward/backward-propagating wave fields, and the time domain signals for a realistic range-dependent model. The numerical results reveal the various and complicated effects of the range dependence and transverse isotropy on the shape of the wave field in the frequency domain and the signals in the time domain. The effects are caused by the energy conversion to different modes due to coupling, broadening of the energy propagation channel (waveguide) and the change in geometry of the propagation channel.

Probably the greatest advantage to employing coupled modes for investigating range-dependent wave propagation is the physical insight provided. There are five different computational products that can be examined: (1) The coupling matrix **B** describe how much of mode r is mixed into mode q; (2) The reflection and transmission matrices **R** and **T** give information on which modes have been transmitted or reflected by the structure essentially defining the spatial pass bands and the stop bands of the structure; (3) Single mode results in transform (mode) space; (4) Multi-mode results in transform space; (5) Time domain signals.

The coupled mode solution we have presented contains only the discrete modes. The completeness of the modal description of the seismo-acoustic field requires the inclusion of the branch line integral, which we have omitted. This is an omission that must be dealt with in the future. If we assume our model is terminated at some depth with a rigid boundary, the discrete modes provide an adequate representation for times up to the point at which reflection from the assumed deep rigid boundary begin to arrive at the receiver.

Coupled mode computations are quite different from finite difference (FD) and finite element (FE) solutions for range-dependent media. Coupled mode solutions provide a number of intermediate computational products not available from FD and FE computations. FD computations suffer from grid dispersion and are difficult to apply on an irregular free surface. Coupled modes do not suffer from grid disper-

sion and can be applied to irregular free surfaces with no difficulty.

One of the main disadvantages of coupled modes is that computation of the local mode sets can be very time consuming for very irregular models, and/or high frequencies. However, because the local modes do not interact until the Ricatti equation must be solved, their computation can be handled very efficiently by a parallel computer with one mode set assigned to each node.

ACKNOWLEDGMENTS

This research was supported by the Office of Naval Research, Grant No. N00014-95-1-0470 and Grant No. N00014-96-10233. We thank an anonymous reviewer for his careful review of an earlier version of the manuscript.

APPENDIX: MODE AMPLITUDE INITIAL VALUES AND SOURCE REPRESENTATION

For our 2-D range-dependent model, a unit line source is used to represent the wave excitation. The normal mode decomposition of the source is derived from the product of the Green's function and the sources in this Appendix. The purpose of this section is to derive the value of the vector $\mathbf{c}^0$ for the left boundary condition of Eq. (24). The general solution for a range-dependent medium is represented as an integral of a product of the Green's function for a local depth-dependent structure and the external source and the effective source excited by range dependence. The dyadic form of the Green's function for a six-dimensional displacement-stress vector is (Park, 1997)

$$G_{ij}(\mathbf{r},\mathbf{r}')=\sum_r u_i^r(z;x,\omega)u_j^{r*}(z';x',\omega)e^{i(\phi_r(x)+\pi/2)}, \tag{A1}$$

where

$$\phi_r(x)=\int_{x_s}^{x} k^r(\xi)d\xi. \tag{A2}$$

Following Park (1997), the integral of the product of the Green's function (A1) and the sources $\mathbf{F}^S$ of Eq. (5) and $\mathbf{F}^0$ of Eq. (6) yields the total solution for a range-dependent medium:

$$\mathbf{u}(x,z;\omega)=\int \sum_j G_{ij}(\mathbf{r},\mathbf{r}')(F_j^S+F_j^0)dV',$$

$$=\sum_r c_r(x)\mathbf{u}^r(z;x,\omega)e^{i\phi_r(x)}, \tag{A3}$$

where the range-dependent modal coefficient c_r is

$$c_r(x)=\int_{x_s}^{x}\langle \mathbf{u}^r(z';x'),\mathbf{F}^s\rangle dx'+\int_{x_L}^{x}\langle \mathbf{u}^r(z';x'),\mathbf{F}^0\rangle dx', \tag{A4}$$

the Hermitian inner product is defined as (Maupin, 1988)

$$\langle \mathbf{u},\mathbf{v}\rangle\equiv\int_0^\infty \mathbf{u}^\dagger\mathbf{X}\mathbf{v}\,dz, \tag{A5}$$

and the matrix $\mathbf{X}$ is

$$\mathbf{X}=\begin{pmatrix}0 & -i\\ i & 0\end{pmatrix}\otimes\begin{pmatrix}1 & 0 & 0\\ 0 & 1 & 0\\ 0 & 0 & 1\end{pmatrix}=\begin{pmatrix}\mathbf{0} & -i\mathbf{I}\\ i\mathbf{I} & \mathbf{0}\end{pmatrix}. \tag{A6}$$

The range-dependent modal coefficient $c_r(x)$, Eq. (A4), can be represented as the sum of two separate integrals. The first integral on the right is the contribution from the line source located to the left of the range-dependent section at $(x,z=x_s,z_s)$. The second integral contains all the contributions from the effective sources in the range dependent section of the wave guide. It is just the first integral that provides us with the excitation at the left boundary of the range-dependent section. The initial condition on c_r is

$$\begin{aligned}c_r^0&\equiv c_r(x=x_L)\\ &=\int_{x_s}^{x_L}\langle \mathbf{u}^r(z';x'),\mathbf{F}^s\rangle dx'\\ &=\int_{x_s}^{x_L}\left\{\int_0^\infty \mathbf{u}^r(z';x')\mathbf{X}\mathbf{F}^s dz\right\}dx'\\ &=\int_{x_s}^{x_L}\left\{\int_0^\infty \mathbf{w}^{r*}(z';x')\cdot\mathbf{f}^s e^{i\pi/2}dz\right\}dx'.\end{aligned} \tag{A7}$$

The initial condition on c_r, Eq. (A7), is a representation of the source in terms of the modal decomposition. For a unit line source in the spectral domain,

$$\mathbf{f}^s(x,z,\omega)\equiv\begin{Bmatrix}\mathbf{f}_x\\ \mathbf{f}_y\\ \mathbf{f}_z\end{Bmatrix}\tilde{g}(\omega)\,\delta(x-x_s)\,\delta(z-z_s), \tag{A8}$$

where the source time function is Fourier transformed:

$$\hat{g}(\omega)=\int_{-\infty}^{\infty} g(t)\exp(-i\omega t)dt. \tag{A9}$$

The representation of the source becomes

$$\begin{aligned}c_r^0=i\{&w_x^r(z_s;x_s,\omega)f_x\\ &+w_z^r(z_s;x_s,\omega)f_z\}\tilde{g}(\omega)\quad\text{for Rayleigh waves,}\end{aligned} \tag{A10}$$

$$c_r^0=iw_y^r(z_s;x_s,\omega)f_y\tilde{g}(\omega)\quad\text{for Love waves,} \tag{A11}$$

$$c_r^0=\frac{1}{\omega}V_x^r(z_s;x_s,\omega)f_x\tilde{g}(\omega)\quad\text{for acoustic waves.} \tag{A12}$$

Aki, K., and Richards, P. G. (**1980**). *Quantitative Seismology, Vol. I* (W. H. Freeman, New York).

Berge, P. A., Mallick, S., Fryer, G. J., Barstow, N., Carter, J. A., Sutton, G. H., and Ewing, J. I. (**1991**). ''*In situ* measurement of transverse isotropy in shallow-water marine sediments,'' Geophys. J. Int. **104**, 241–254.

Buchen, P. W., and Ben-Hador, R. (**1996**). ''Free mode surface-wave computations,'' Geophys. J. Int. **124**, 869–887.

Burridge, R., and Knopoff, L. (**1964**). ''Body-force equivalents for seismic dislocations,'' Bull. Seismol. Soc. Am. **54**, 1875–1888.

Dieci, L. (**1992**). ''Numerical integration of the differential Riccati equation and some related issues,'' SIAM (Soc. Ind. Appl. Math.) J. Numer. Anal. **29**, 781–815.

Evans, R. (**1986a**). ''The decoupling of stepwise coupled modes,'' J. Acoust. Soc. Am. **80**, 1414–1418.

Evans, R. (**1986b**). ''The decoupling of seismic waves,'' Wave Motion **8**, 321–328.
Gear, C. W. (**1971**). *Numerical Initial Value Problems in Ordinary Differential Equations* (Prentice-Hall, Englewood Cliffs, NJ).
Haskell, N. A. (**1953**). ''The dispersion of surface waves on multilayered media,'' Bull. Seismol. Soc. Am. **43**, 17–34.
Kennett, B. L. N. (**1984**). ''Guided-wave propagation in laterally varying media—I. Theoretical development,'' Geophys. J. R. Astron. Soc. **79**, 235–255.
Knobles, D. P. (**1994**). ''Solutions of coupled-mode equations with a large dimension in underwater acoustics,'' J. Acoust. Soc. Am. **96**, 1741–1747.
Marquering, H., and Snieder, R. (**1995**). ''Surface-wave mode coupling for efficient forward modelling and inversion of body-wave phases,'' Geophys. J. Int. **120**, 186–208.
Mattheij, R. M. M. (**1985**). ''Decoupling and stability of algorithms for boundary value problems,'' SIAM (Soc. Ind. Appl. Math.) Rev. **27**, 1–44.
Maupin, V. (**1988**). ''Surface waves across 2-D structures: a method based on coupled local modes,'' Geophys. J. **93**, 173–185.
Odom, R. I., Park, M., Mercer, J. A., Crosson, R. S., and Paik, P. (**1996**). ''Effects of transverse isotropy on modes and mode coupling in shallow water,'' J. Acoust. Soc. Am. **100**, 2079–2092.
Park, M. (**1997**). ''Effects of anisotropy and lateral heterogeneities on elastic waves and mode coupling in shallow water,'' Ph.D. dissertation, University of Washington.
Saito, M. (**1988**). ''DISPER80: A Subroutine Package for the Calculation of Seismic Normal-Mode Solutions,'' in *SEISMOLOGICAL ALGORITHMS: Computational Methods and Computer Programs*, edited by D. Doornbos (Academic, San Diego, CA), pp. 293–319.
Schelkunoff, S. A. (**1951**). ''Remarks concerning wave propagation in stratified media,'' Commun. Pure Appl. Math. **4**, 117–128.
Sluijter, F. W. (**1970**). ''Arbitrariness of dividing the total field in an optically inhomogeneous medium into direct and reversed waves,'' J. Opt. Soc. Am. **60**, 8–10.
Takeuchi, H., and Saito, M. (**1972**). ''Seismic surface waves,'' in *Seismology: Surface Waves and Earthguake Oscillations* (Methods in Computational Physics, Vol. 11), edited by B. A. Bolt (Academic, New York), pp. 217–295.
Thomson, W. T. (**1950**). ''Transmission of elastic waves through a stratified solid medium,'' J. Appl. Phys. **21**, 89–93.

Extracting in-plane bistatic scattering information from a monostatic experiment

Paul C. Hines, D. Vance Crowe, and Dale D. Ellis
Defence Research Establishment Atlantic, P.O. Box 1012, Dartmouth, Nova Scotia B2Y 3Z7, Canada

(Received 22 September 1997; accepted for publication 24 April 1998)

Acoustic backscatter data were collected from the ocean bottom at four sites on the Sohm Abyssal Plain. The bottom sediment at the four sites varied from mud/clay to silt/gravel. Using a simple array consisting of a free-flooding-ring projector which was omnidirectional in azimuth, and an omnidirectional hydrophone, data were collected over the frequency range of 800–2400 Hz [Hines and Barry, J. Acoust. Soc. Am. **92**, 315–323 (1992)]. To obtain sufficient signal-to-noise ratio without impairing spatial resolution, 200-Hz-wide linear FM pulses were employed. By deploying the array at a height of 500 m above the seabed, bottom backscatter data were obtained at grazing angles down to 4 degrees before the onset of the first surface return. For data arriving after the first-bottom–first-surface interaction, the geometry approximates an in-plane bistatic experiment. Estimates of the in-plane bistatic scattering strength were obtained for pairs of incident and scattered grazing angles $(\phi_i, \phi_s) < (50 \text{ degrees}, 88 \text{ degrees})$, at frequencies of 900, 1200, and 1600 Hz. At one site the grazing angle dependence matched Lambert's rule; at all other sites the data exhibited a steeper slope than that of Lambert's rule. There was insufficient data to extract the frequency dependence. The fathometer returns were used to estimate the normal-incidence bottom loss at the four sites. The measured bottom loss ranged from a low of 2 dB to a high of 16 dB. The in-plane bistatic data and the monostatic data were compared to examine the validity of the separable and half-angle approximations [Ellis and Crowe, J. Acoust. Soc. Am. **89**, 2207–2214 (1991)]. The separable approximation provided a reasonable fit to the data at three of the four sites; the half-angle approximation did not match the data well at any of the sites. [S0001-4966(98)01208-9]

PACS numbers: 43.30.Gv, 43.30.Hw, 43.30.Ft [DLB]

INTRODUCTION

In recent years, interest in bistatic scattering from the seabed has increased dramatically. This poses a challenge for the experimentalist since bistatic experiments are more difficult to perform than are monostatic experiments. Perhaps more importantly, the former are significantly more costly since separating the receiver and the transmitter requires, at the very least, separate kits for transmit and receive, and in some cases a second research vessel. For these reasons, it is germane to examine what information about bistatic scattering strength one can obtain using a simple monostatic geometry. In fact, for data arriving at the receiver after the first-surface–first-bottom interaction (S1B1), it will be demonstrated that the geometry approximates that of an in-plane bistatic experiment.

Previously, Hines and Barry[1] reported on a monostatic backscatter experiment in which data were collected at four sites on the Sohm Abyssal Plain. Using a simple array consisting of a free-flooding-ring projector which was omnidirectional in azimuth, and an omnidirectional hydrophone, data were collected over the frequency range of 800–2400 Hz using linear FM pulses 200 Hz in bandwidth. The array was deployed to a nominal depth of 5000 m and bottom backscatter data were obtained at grazing angles down to 4 degrees before the onset of the first surface return. As noted earlier, for data arriving after the first-surface–first-bottom interaction (S1B1), the geometry approximates an in-plane bistatic experiment. Therefore, the in-plane bistatic data and the monostatic data can be compared to examine the validity of the separable and half-angle approximations used in some bistatic scattering models.[2] In this paper the experimental geometry and the bottom topography of the four sites are described. Next, the bistatic geometry is explained and the data are interpreted in light of the bistatic arrivals. Then, we present an algorithm for extracting the in-plane bistatic scattering strength from the data. Finally, the in-plane bistatic and monostatic data are compared using the separable and half-angle approximations.

I. THE EXPERIMENT

The acoustic array, depicted schematically in Fig. 1, consisted of an omnidirectional hydrophone receiver and a free-flooding-ring projector suspended 1.6 m below the hydrophone. The projector was omnidirectional in azimuth with a source level in the horizontal plane that varied from 197 to 203 dB *re*: 1 μPa at 1 m, depending on the frequency band of the transmitted pulse. The two-sided vertical beamwidth, measured to the -3 dB down points, varied from 64 to 74 degrees over the frequency range of interest. The hydrophone was mounted in a shrouded cage to minimize flow-induced noise. A 350-kg weight was suspended from the array in order to keep the array vertical. The array was deployed from the quarterdeck of the research vessel CFAV QUEST via a 5000-m electromechanical cable. In a typical experiment, the array was deployed to a position 450–500 m

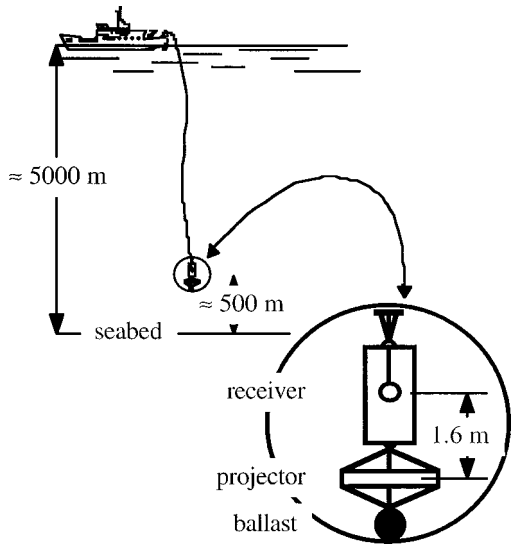

FIG. 1. Schematic diagram of experimental array configuration.

from the bottom depending on the water depth at the site. All backscatter measurements were taken with QUEST drifting.

To obtain sufficient signal-to-noise ratio without impairing spatial resolution, a linear FM (LFM) pulse was employed for the incident signal. The bandwidth of the pulse was 200 Hz and the sampling rate was 7222 Hz. Although the experiment was performed at center frequencies of 900, 1200, 1600, 2000, and 2300 Hz, examination of the bistatic returns was limited to 900, 1200, and 1600 Hz. This was done because the projector had a null at steep grazing angles at the two highest frequencies which severely reduced the bistatic returns. A sequence of 16 pulses, 4 s in duration, was transmitted for each frequency band, with a dwell time of 45 s allocated between pulses; the dwell ensured that returns from consecutive pulses would not interfere with one another. During analysis the recorded data were heterodyned down in frequency to base band, low-pass filtered, and subsampled by a factor of 25 to reduce data processing and storage requirements. The time series recorded for each pulse was matched filtered using fast convolution. Matched filtering the data obtained a spatial resolution (to the -3-dB points) of approximately ± 2 m.

II. ENVIRONMENTAL DESCRIPTION

A. Benthic topography

Bottom backscatter measurements were taken at four sites on the Sohm Abyssal Plain. The bottom topography at Sites A, B, and C was essentially flat. Site D exhibited gently undulating sediment waves, the crests of which ran east–west. The peak-to-peak amplitude of the sediment waves was approximately 5 m and the mean wavelength was 300 m. Qualitative descriptions of the four sites are contained in Refs. 3 and 4 and are as follows: Site A contains graded sediments[5] composed primarily of small-grained silt and clay. Sites B and C are on the distal edge of a turbidity current that resulted from an underwater earthquake. Although the turbidity current has since subsided, its action resulted in more large-grained sand being deposited in the area than is typical of the silt/clay bottom associated with the Sohm Abyssal Plain. The sediment at Sites B and C is graded. Site D lies on the main stream of the turbidity current flow. The turbidity current has deposited a thick layer of ungraded gravel/sand in the area. Table I of Ref. 1 gives a description of the bottom sediments obtained from core samples in the vicinity of the four sites.

TABLE I. Average sea conditions observed at the four sites during the experiment.

Site	Wind speed ($\mathrm{m\cdot s^{-1}}$)	Wind direction (degrees)	Sea state	Significant wave height[a] $H_{1/3}$ (m)
A	5 ± 1	305 ± 5[b]	2–4	$\approx$1.0–1.5
B	1 ± 1	N/A	0–1	<0.5
C	8 ± 1	255 ± 5	4–5	$\approx$2.5
D	5 ± 1	270 ± 5	2–4	$\approx$1.5

[a]Significant wave height is defined as the average peak-to-trough height of the $\frac{1}{3}$ largest waves.

[b]For several hours prior to the start of the experiment, the wind direction at Site A had been 280 degrees. This resulted in slightly calmer seas at Site A relative to Site D, even though the wind speed was the same at both sites.

B. The water column

Table I contains qualitative information on the wind velocity and sea state observed at the four sites during the experiment. The conditions ranged from almost calm to a 2.5-m significant wave height with small amounts of spray. As will be shown in Sec. V, sea conditions have a direct bearing on the range of grazing angles over which estimates of bottom-bistatic scatter were obtained.

Sound-speed profiles were calculated for each site by merging historical data with expendable bathythermograph (XBT) measurements taken at each of the four sites. The resulting profiles are shown in Fig. 2(a) and (b). These were used in conjunction with the arrival time of surface and bottom reflections to compute the water depth and the height of the source above the bottom. The profiles were also used to convert arrival time to path length and grazing angle for the measured reverberation.

III. THE IN-PLANE BISTATIC GEOMETRY

Figure 3 shows a schematic of the two bottom-bistatic scattered paths, BB1 and BB2, for the experiment.[6] Along each path there is a specular reflection from the surface. In addition, path BB2 has a specular reflection from the seabed. In the limit of a perfectly flat sea, the surface reflection will not introduce any loss along the path. However, the loss associated with the bottom reflection must be accounted for when computing the bistatic scattering strength. Note that each of the two bottom-bistatic scattered paths are themselves composed of two scattered returns. This results from the vertical symmetry of the transmitter and receiver beam patterns, which generates an up-going and a down-going wave. Because the source and receiver are colocated, these contributions arrive at the receiver at the same time. Further-

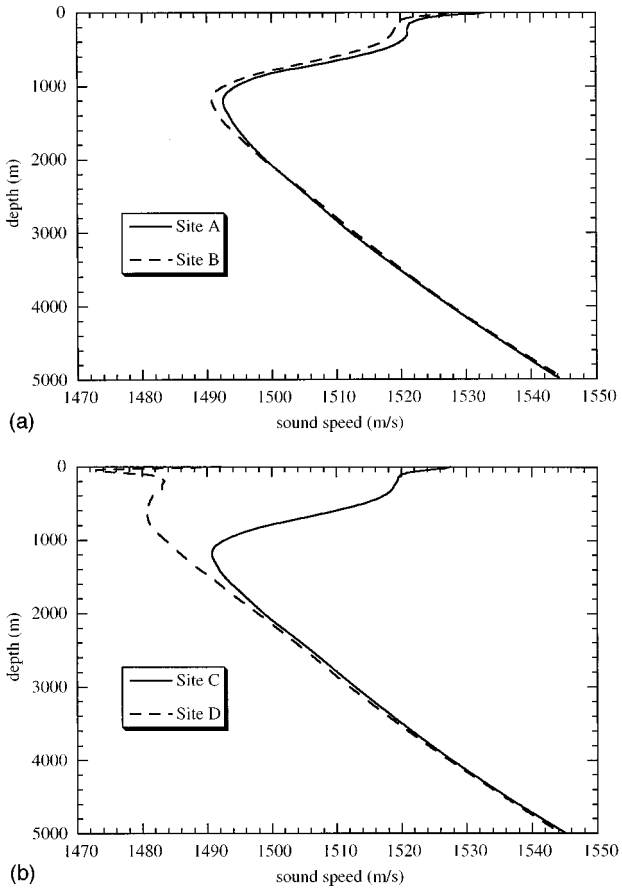

FIG. 2. Sound-speed profiles for Sites A and B (a), and Sites C and D (b).

more, since the receive and transmit beam patterns are not identical, the up-going and down-going paths are not equal in amplitude, except at normal incidence.

Associated with each of the bottom-bistatic paths is a surface-bistatic path which arrives cotemporally with the bottom-bistatic path. The surface-bistatic paths are shown in Fig. 4 along with the bottom-bistatic paths. Typically, scattering from the surface-bistatic path dominates the reverberation at steep grazing angles, and scatter from the bottom-bistatic path dominates the reverberation at intermediate and shallow grazing angles. The transition angle from surface-dominated scatter to bottom-dominated scatter is a function of sea state, seabed roughness, and seabed inhomogeneities.

For completeness one should note that there is a surface-scatter–bottom-scatter path associated with each of the bottom-bistatic paths. However, contributions arriving along this twice-scattered path will be substantially smaller than those of the single-scatter paths and have been neglected in this study.

IV. ESTIMATING THE BOTTOM LOSS

Figure 5 shows the average intensity of the reverberation time series at all four sites for a frequency of 900 Hz. Each curve was obtained by averaging 16 pings. The peak at time $t=0$ in all four curves results from electronic cross talk between the transmitter and the receiver during transmission. The data enclosed by the dashed box are expanded in Fig. 6 for clarity. During pulse transmission, the receive circuitry is

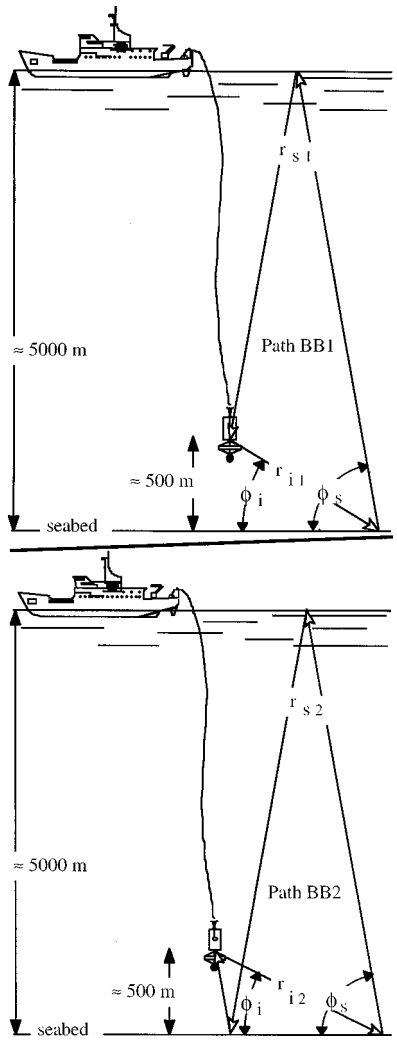

FIG. 3. The two bottom-bistatic scatter paths labeled BB1 and BB2.

shut down to prevent overload. This means that reverberation during the first 4 s will have a reduced source level and reduced range resolution since the full pulse is not available for FM processing. For example, 1 s after completion of the transmit pulse, only the energy scattered from the final 1 s of the transmit pulse is available to the receiver. Thus the received level is reduced by 75% from what one would obtain with the full 4-s pulse. Furthermore, since the bandwidth of the linear FM pulse is reduced by 75%, then so too is the range resolution. These factors account for the artificially low received level for the first bottom return which occurs at approximately $t=0.6$ s.

Figure 6 shows an expanded view of the first-surface return (S1), the first-surface–first-bottom return (S1B1), and the first-surface–second-bottom return (S1B2) for Sites A and B. The difference in levels of the S1 and S1B1 returns at each site gives a qualitative measure of the bottom loss at normal incidence. Of the 900-Hz data, Sites A and B had the maximum and minimum bottom losses, respectively. It might appear that Site B exhibits a negative bottom loss since the magnitude of the S1B1 return is slightly greater than that of the S1 return. This is because the S1B1 return consists of equal contributions from the up-going and down-going waves which, as noted earlier, results from the vertical

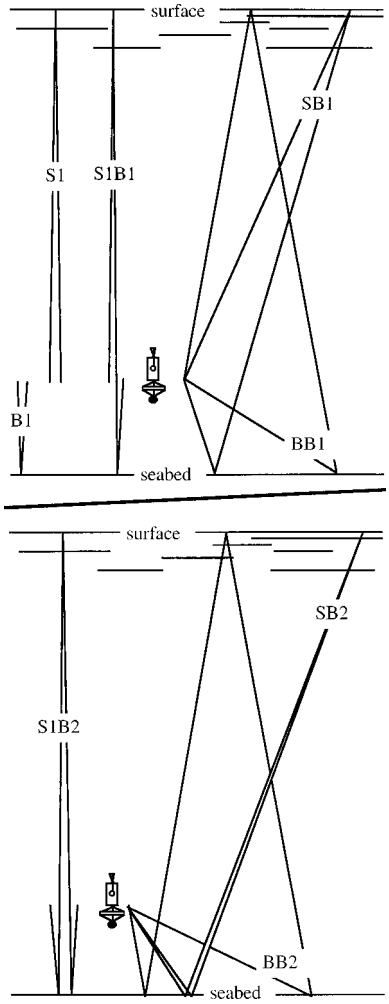

FIG. 4. The surface-bistatic scatter paths, SB1 and SB2, coincident in time with the bottom-bistatic scatter paths. The bottom-bistatic scatter paths are reprinted from Fig. 3 for comparison. Also shown in the figure are the first bottom return (B1), the first surface return (S1), the first-surface–first-bottom return (S1B1), and the first-surface–second-bottom return (S1B2).

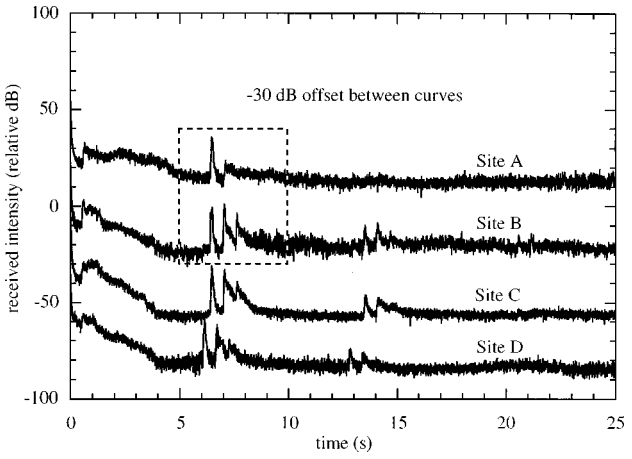

FIG. 5. Time series of the average intensity of the reverberation collected at all four sites at a frequency of 900 Hz. The portion of the figure enclosed by the dashed box is expanded in Fig. 6.

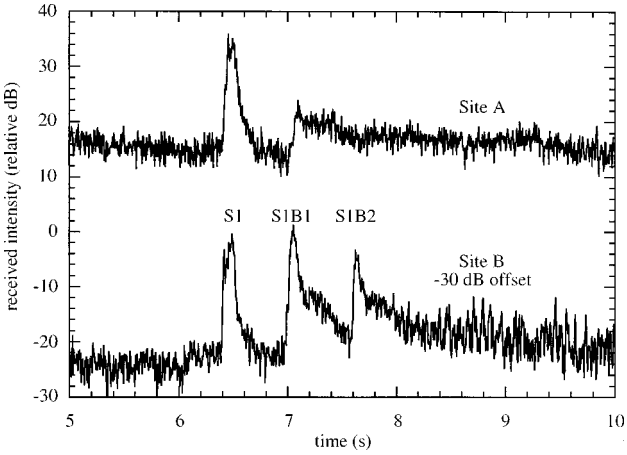

FIG. 6. Expanded view of that portion of the reverberation time series enclosed by the dashed box in Fig. 5.

symmetry of the transmitter and receiver beam patterns.

The normal incidence bottom loss in decibels, BL, was estimated for each site at each frequency using the following equation:

$$\mathrm{BL}=|\mathrm{S1}|-|\mathrm{S1B1}|-\Delta\mathrm{PL}+3\ \mathrm{dB}, \tag{1}$$

where $|\mathrm{S1}|$ and $|\mathrm{S1B1}|$ represent the *magnitude* of the S1 and S1B1 returns, ΔPL accounts for the difference in propagation loss along the S1 and S1B1 paths ($\mathrm{BL}>0$, $\Delta\mathrm{PL}>0$), and the 3 dB accounts for the up- and down-going contributions to S1B1. For the present experiment, the S1B1 path is approximately 10% longer than the S1 path; this increased the propagation loss along S1B1 by about 0.8 dB. Table II contains the normal incidence bottom loss estimates for the four sites at all three frequencies.

V. EXTRACTING THE BOTTOM-BISTATIC SCATTERING STRENGTH FROM THE MEASURED INTENSITY

The method for obtaining the bottom-bistatic scattering strength is more complicated if there is a significant contribution from surface scattering. First, the procedure will be outlined assuming there is no surface-scattered contribution to the received intensity. Following that, a correction will be introduced to remove the surface scattered component of the intensity. Prior to converting the measured intensity to bistatic scattering strength, the data were corrected for ambient noise contamination.

TABLE II. Normal incidence bottom loss in decibels, BL, estimated at the four sites at the three frequencies.

	BL (dB)		
Site	900 Hz	1200 Hz	1600 Hz
A	11.8	16.1	9.9
B	1.5	3.8	3.7
C	2.0	3.2	3.0
D	3.5	4.4	6.7

A. Reducing the measured intensity to a single, bottom-bistatic component in the *absence* of surface scatter

The procedure to reduce the measured intensity to a single, bottom-bistatic component in the *absence* of surface scatter is as follows:

(i) *Calculate the source/receiver depth and the water depth.* These depths are computed using the sound-speed profile and the travel times for the normal incidence specular returns S1 and S1B1.

(ii) *Calculate the two bottom-bistatic scattered paths and the associated scattered angles for the experiment.* The two paths, labeled BB1 and BB2, are shown schematically in Fig. 3. For a given incident path length from the source to the bottom, denoted r_{i1} and r_{i2}, there is only one specularly reflected path back to the receiver, denoted r_{s1} and r_{s2}. Clearly, there is associated with each path a unique incident and scattered grazing angle. Note that although the effect of ray curvature is not depicted in the figure, it was accounted for in the path-length calculations.

(iii) *Convert arrival times for the bistatic paths to range and grazing angle.* With the bistatic path lengths and angles defined, the sound-speed data can be used to convert arrival time of the measured intensity to grazing angle and path length to and from the scattering patch.

(iv) *Subtract out the path BB2 contribution to the scattered intensity.* In order to compute the in-plane bistatic scattering strength, we must relate the measured intensity to a single pair of incident and scattered grazing angles. This requires that we reduce the problem to a single path. The procedure for subtracting out contributions from path BB2 is somewhat involved and the details are left to Appendix A.

(v) *Separate the up-going and down-going contributions of path BB1.* Recall from Sec. III that each of the paths is composed of an up-going and down-going component that are not of equal intensity. Because the down-going component dominates over most grazing angles, we opt to subtract out the up-going component. The procedure for removing the up-going contribution is contained in Appendix A.

At this point one has reduced the measured intensity I_d to contributions from a single bottom-bistatic path, in the absence of any surface roughness. Using this data one can compute the in-plane bottom-bistatic scattering strength (BISS). Prior to examining the in-plane BISS, however, we shall note the corrections to the algorithm if the water surface is not flat.

B. Reducing the measured intensity to a single, bottom-bistatic component in the *presence* of surface scatter

As noted previously, there is a surface-bistatic path whose time of flight is exactly equal to that of the bottom-bistatic path. If, as is usually the case, the ocean surface is not perfectly flat, then energy arriving via the surface-bistatic path will corrupt measurements of the bottom-bistatic scattered intensity. The two surface-bistatic paths,[7] labeled SB1 and SB2, are shown schematically in Fig. 4. These paths correspond to bottom-bistatic paths BB1 and BB2 from Fig. 3. The modifications to the algorithm, necessary to reduce the measured intensity to a single, bottom-bistatic component in the *presence* of surface scatter, follow. To simplify the discussion, comments are restricted to removing the contributions from surface-bistatic path SB1. The procedure to remove path SB2 contributions is a straightforward extension of this.

(i) *Calculate the surface backscattered intensity as a function of grazing angle using the data arriving after S1 until S1B1.* Using the source depth and the sound-speed profile, arrival times can be converted to range and grazing angle. Note that for the geometry of this experiment, all ray paths associated with surface scatter are steep. This makes corrections for ray curvature unnecessary.

(ii) *Calculate the surface-bistatic scattered paths that arrive cotemporally with the two bottom-bistatic paths shown in Fig. 3.* The two surface paths, labeled SB1 and SB2, are shown schematically in Fig. 4.

(iii) *Use the measured surface backscattered intensity to estimate the surface-bistatic scattered intensity.* If the source-receiver is close to the seabed (close in this case is relative to the total water depth), then the incident and scattered angles will be approximately equal[8] for the surface-bistatic paths. In this case the surface-bistatic angles can be approximated by their average—denoted ϕ_{avg}—(also referred to as the half-angle) and the up-going and down-going surface-bistatic contributions are approximately equal. Therefore, the surface-bistatic scattered intensity in dB, denoted BI_{sur}, can be approximated by

$$\text{BI}_{\text{sur}} \approx I_{\text{sur}} - \text{BL} - \Delta\text{PL}_{\text{sur}} + \Delta A_{\text{sur}} + 3 \text{ dB}, \tag{2}$$

where I_{sur} is the surface backscattered intensity, BL is the normal incidence bottom loss from Eq. (1), $\Delta\text{PL}_{\text{sur}}$ and ΔA_{sur} account for the difference in propagation loss and insonified area between the surface backscatter path and the surface-bistatic path, respectively ($\Delta\text{PL}_{\text{sur}}$, $\Delta A_{\text{sur}} > 0$), and the 3-dB correction accounts for the up-going and down-going contributions to the bistatic path, which are approximately equal. Implicit in Eq. (2) is the assumption that the BL is approximately constant for steep grazing angles.

Once the surface-bistatic scatter contribution has been estimated, it is simply subtracted from the total intensity and the bottom-bistatic scattered intensity is reduced to a single component as before.

Figure 7 shows a plot of the total intensity measured at Site C at 1600 Hz, alongside the component of bistatic surface scatter computed using Eq. (2). The intensity is plotted as a function of the surface-bistatic half-angle ϕ_{avg}. Also labeled on the horizontal axis is the bottom-bistatic incident

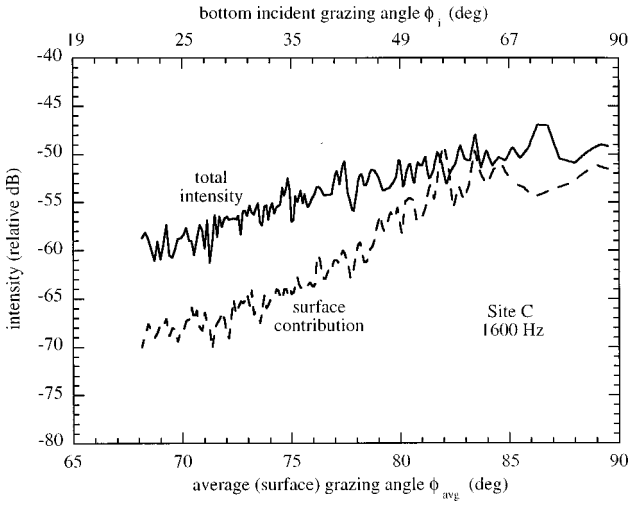

FIG. 7. Comparison of the total intensity to that contributed by surface-bistatic scatter.

grazing angle ϕ_i associated with these arrivals. Choosing the highest frequency at the site with the highest winds approximates[9] a worst case scenario in terms of the surface-scatter contributions. In the figure surface-bistatic scatter dominates the data down to about $(\phi_i, \phi_s) = (55 \text{ degrees}, 88 \text{ degrees})$. This corresponds to a surface half-angle of $\phi_{\text{avg}} \approx 82$ degrees. The transition angle at which surface-bistatic scatter (rather than bottom-bistatic scatter) dominates the intensity occurred in the region of $50 \text{ degrees} < \phi_i < 60$ degrees for all sites and frequencies.

Figure 8 plots the surface-bistatic intensity at 1600 Hz at all four sites as a function of the averaged grazing angle ϕ_{avg}. Also labeled on the horizontal axis is the bottom-bistatic incident grazing angle ϕ_i associated with these arrivals. The surface scattered intensity correlates well with the measured wind speed below about 80 degrees grazing. However, as the data approach normal incidence, the intensity at Site B rises more rapidly than at the other sites. This is possibly because the data are transitioning from (incoherent) scatter to (coherent) reflection, and one would expect the highest coherent reflection at the calmest site.

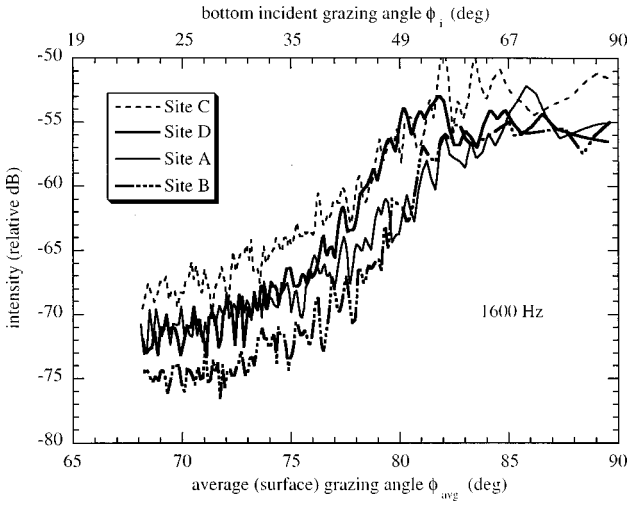

FIG. 8. Estimate of the surface-bistatic intensity at 1600 Hz at all four sites, as a function of the averaged surface-bistatic grazing angle ϕ_{avg}.

Before proceeding, there are two issues related to surface roughness that require some comment. The first is that as ocean roughness increases, bubbles at the air/sea interface can cause a significant loss of intensity of the surface reflection for paths BS1 and BS2. However, for the wind speeds, frequencies, and near-vertical grazing angles encountered in this experiment, the losses expected[10] are less than 1 dB. The second issue is that some time spreading of the surface-reflected signal will result from motion of the sea surface and the source/receiver.[11] Note, however, that (a) the time spreading will be symmetrical about the coherent peak (because the motion is approximately sinusoidal) and (b) for steep angles the surface reflection coefficient will remain approximately constant. This means that spreading of the coherent reflection will have little impact on the averaged scattered intensity since losses at one grazing angle will be compensated for by gains from another.

C. Computing the bottom-bistatic scattering strength (BISS)

In the previous segment, we outlined the algorithm to extract the bottom-bistatic contributions of the down-going portion of path BB1 from the total measured intensity. With the data thus reduced, the bottom-bistatic scattered intensity contributions from path BB1, I_d, were converted to bistatic scattering strength BISS employing the definition

$$\text{BISS} = 10 \log_{10}\left(\frac{I_d r_{i1}^2 r_{s1}^2}{I_0 A}\right), \tag{3}$$

where I_d is the intensity of the scattered wave measured at the receiver, I_0 is the intensity of the incident wave measured at the transmitter, r_{i1} is the path length from transmitter to the scattering patch of area A, and r_{s1} is the return path length from the scattering patch to the receiver. Due to the geometry of the problem, computing the insonified area is somewhat complicated. The details of this procedure are presented in Appendix B.

As noted earlier, when the rays approach normal incidence, surface scatter began to dominate the total intensity. In this situation, estimating the bottom-scattered component of the total intensity becomes error prone. For this reason, estimates of the bottom BISS from the present data set are limited to grazing angles of $(\phi_i, \phi_s) < (50 \text{ degrees}, 88 \text{ degrees})$ for all sites and frequencies. In the following section, the bottom-bistatic scattering strength data are presented as a function of frequency and location.

VI. THE BOTTOM-BISTATIC SCATTERING STRENGTH DATA

Figures 9–12 show the measured grazing angle dependence of the bistatic scattering strength at frequencies of 900, 1200, and 1600 Hz for each of the four sites. Prior to drawing any general inferences from the data, the reader should note that at Site B (Fig. 10), high levels of ambient and system noise combined with low bottom-bistatic scattering strengths to reduce the amount of valid data collected at shallow grazing angles. This accounts for the absence of data in that figure for angles of $\phi_i < 20$ degrees at 900 Hz and ϕ_i

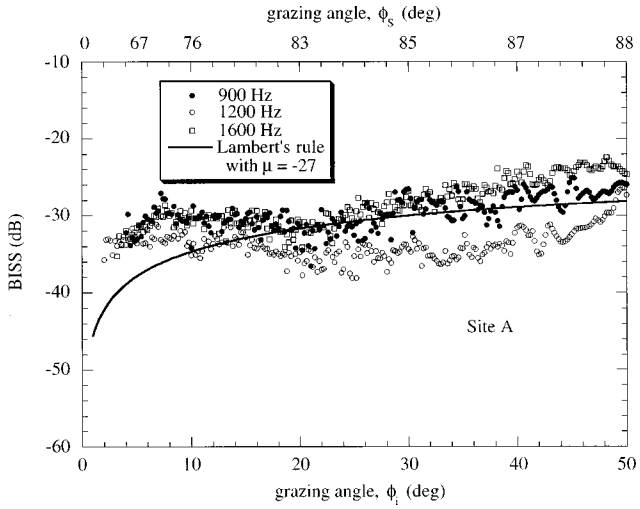

FIG. 9. The measured grazing angle dependence of the bottom-bistatic scattering strength at frequencies of 900, 1200, and 1600 Hz at Site A.

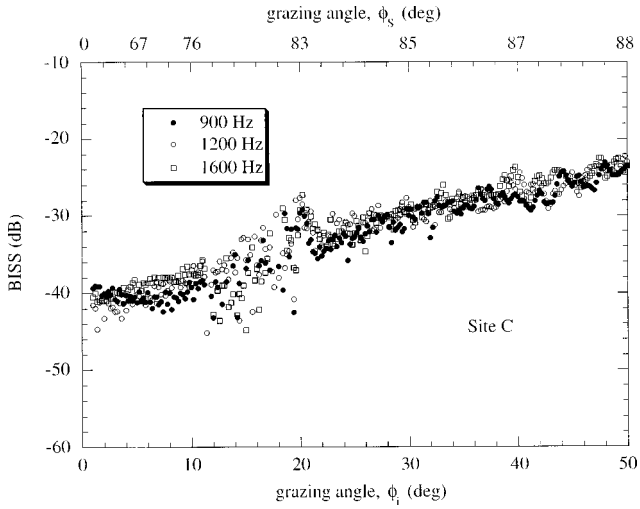

FIG. 11. The measured grazing angle dependence of the bottom-bistatic scattering strength at frequencies of 900, 1200, and 1600 Hz at Site C.

<10 degrees for the higher frequencies. The high noise level also accounts for the large spread in the data for $\phi_i < 20$ degrees. This is because small fluctuations in the total intensity lead to large fluctuations in the estimate of the bottom-scattered signal when the data are corrected for the ambient noise contribution. The data at $\phi_i < 20$ degrees were plotted in spite of the uncertainties brought about by the noise contributions because the general trend of the data is still evident.

With measurements at only three frequencies, it is rather difficult to extract the frequency dependence from the data. It is clear, nonetheless, that only Site A shows any significant spread with frequency; this is especially noticeable at $\phi_i > 30$ degrees and is consistent with the backscatter data collected at the site. (See Fig. 8 of Ref. 1.)

At Sites B, C, and D, the data show a peak at approximately $\phi_i = 20$ degrees. This peak results from the arrival of S1B2 (recall Fig. 6) as well as the steep angle arrivals of the surface scatter from path SB2 (recall Fig. 4). The BISS calculation corrects for both of these contributions. However, as discussed previously, the accuracy of the result diminishes substantially if the contribution from bottom-bistatic scatter does not dominate the total intensity. This leads to the increased spread of the data points in the region 15 degrees $< \phi_i < 20$ degrees. There is no evidence of the peak at Site A because of the high bottom loss.

The grazing angle dependence of the BISS at Sites B, C, and D is approximately the same. Site A, however, exhibits a gentler slope. In fact, at Site A, Lambert's rule provides a reasonable match down to approximately $\phi_i = 15$.

Clearly, the data contained in Figs. 9–12 cover only a small percentage of the total set of in-plane bistatic angles. However, they effectively double the information provided by backscatter data alone. This can be seen in Fig. 13 which represents a grid of all possible pairs of in-plane incident and scattered grazing angles, (ϕ_i, ϕ_s). The diagonal line represents $\phi_i = \phi_s$, that is, backscatter data. The thick dashed line represents the data set shown in Figs. 9–12. The thin dashed line represents the additional data available from the present

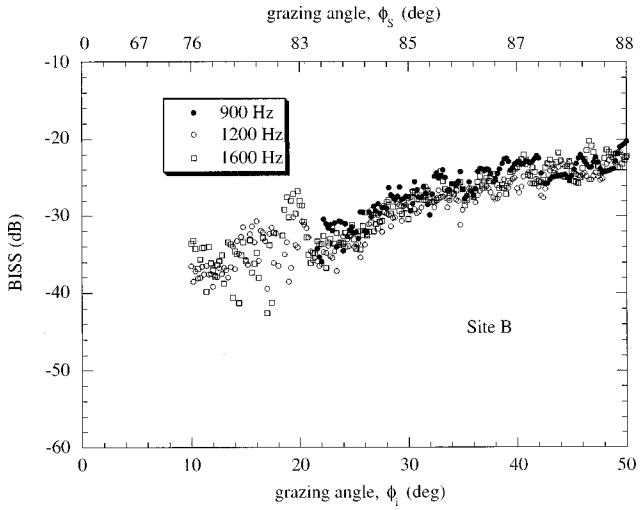

FIG. 10. The measured grazing angle dependence of the bottom-bistatic scattering strength at frequencies of 900, 1200, and 1600 Hz at Site B.

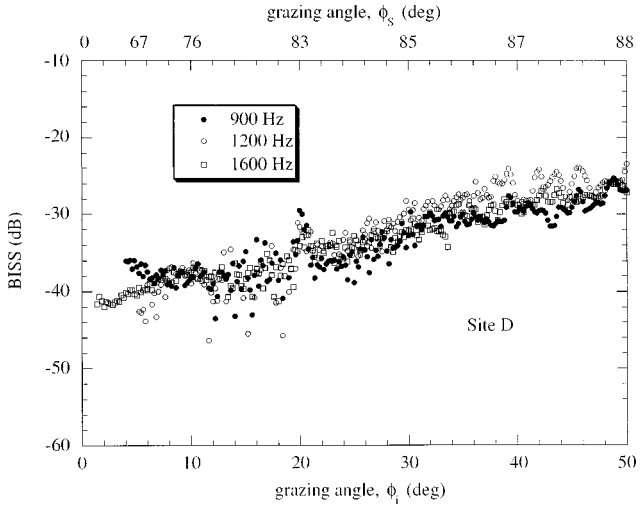

FIG. 12. The measured grazing angle dependence of the bottom-bistatic scattering strength at frequencies of 900, 1200, and 1600 Hz at Site D.

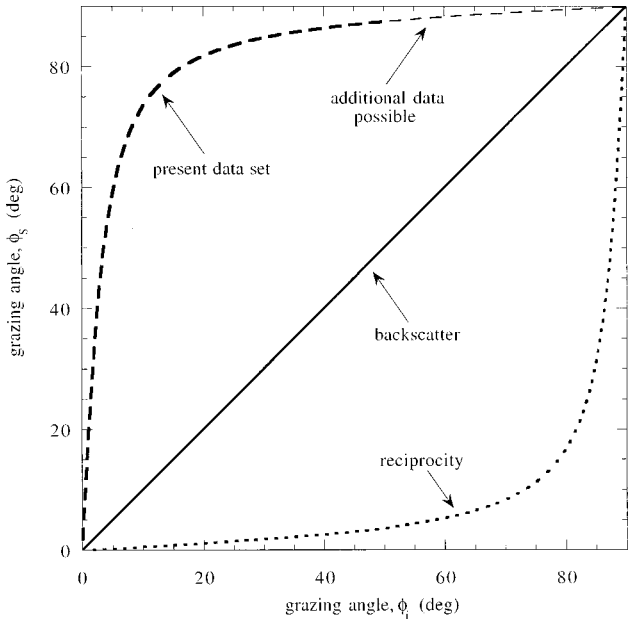

FIG. 13. Grid of all possible pairs of in-plane incident and scattered grazing angles, (ϕ_i, ϕ_s). The diagonal line represents backscatter data. The thick dashed line represents the data set shown in Figs. 9–12. The thin dashed line represents additional data available in the absence of surface scatter. Dots represent the reciprocal of the dashed curves.

experiment in the absence of surface scatter. Furthermore, if there is reciprocity in the scattered field, then $\mathrm{BISS}(\phi_i, \phi_s) = \mathrm{BISS}(\phi_s, \phi_i)$ and one obtains the corresponding curve given by the dots. Finally, by performing the same experiment at several depths, a significant portion of the grid can be filled since the pairing of (ϕ_i, ϕ_s) for the experiment depends on the ratio of the sonar depth to water column depth. Specifically, the relationship of ϕ_i to ϕ_s in the absence of ray curvature is given by

$$\frac{\sin(\phi_i)}{\sin(\phi_s)} = \frac{1-d/w}{1+d/w}\,\frac{(R/w)^2+4d/w}{(R/w)^2-4d/w}, \tag{4}$$

where d is the sonar depth, w is the water depth, and R is the total length of path BB1 as sketched in Fig. 3. Thus, for a fixed water depth, varying the parameter d generates a family of ϕ_i vs. ϕ_s curves.

The grazing angle dependence at the four sites is in qualitative agreement with the backscattering strength (BSS) data of Ref. 1, Figs. 4–7. Furthermore, the geometry of the experiment provides a rare opportunity to compare the BSS of the bottom with the BISS for almost the exact same patch of bottom at almost the exact same time. We shall make such a comparison in the following section.

VII. COMPARING THE BISTATIC AND MONOSTATIC SCATTERING STRENGTH USING THE SEPARABLE AND HALF-ANGLE APPROXIMATIONS

In Ref. 2, the authors propose two expressions to relate backscatter to bistatic scatter functions. These are referred to as the separable approximation BISS_s given by

$$\mathrm{BISS}_s(\phi_i, \phi_s, \theta) \approx \frac{\mathrm{BSS}(\phi_i) + \mathrm{BSS}(\phi_s)}{2} \tag{5}$$

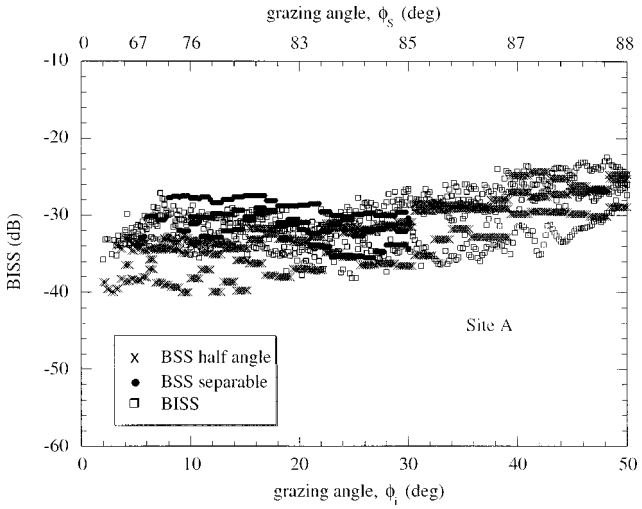

FIG. 14. Comparison of the grazing angle dependence at Site A of the bistatic-scattering strength to the backscattering strength using the separable and half-angle approximations.

and the half-angle approximation BISS_h given by

$$\mathrm{BISS}_h(\phi_i, \phi_s, \theta) \approx \mathrm{BSS}[(\phi_i + \phi_s)/2], \tag{6}$$

where θ is the azimuthal scattered angle, and ϕ_i and ϕ_s are the (in-plane) incident and scattered grazing angles. For in-plane bistatic data $\theta = 0$.[12]

Figures 14–17 compare the grazing angle dependence of the BISS at each of the four sites to the BSS at those sites using the separable and half-angle approximations. The 900-, 1200-, and 1600-Hz data are all plotted using a single variable since the data are approximately independent of frequency. Most of the BSS data used in the figures are published in Figs. 4–7 of Ref. 1. However, the steep angle BSS data used to obtain the separable approximation are previously unpublished data from the same experiment. Note that the separable approximation is limited to $(\phi_i, \phi_s) \leqslant (30\ \text{degrees}, 85\ \text{degrees})$ because of the lack of BSS data

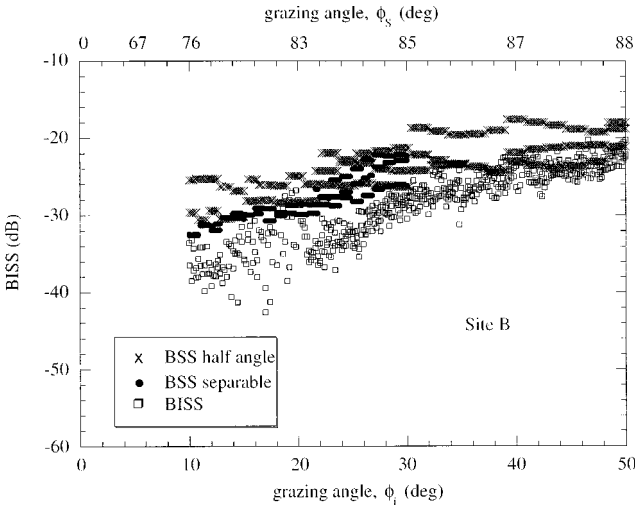

FIG. 15. Comparison of the grazing angle dependence at Site B of the bistatic-scattering strength to the backscattering strength using the separable and half-angle approximations.

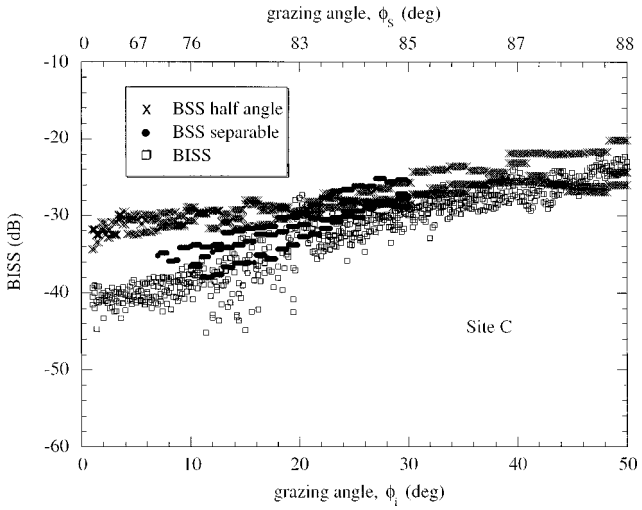

FIG. 16. Comparison of the grazing angle dependence at Site C of the bistatic-scattering strength to the backscattering strength using the separable and half-angle approximations.

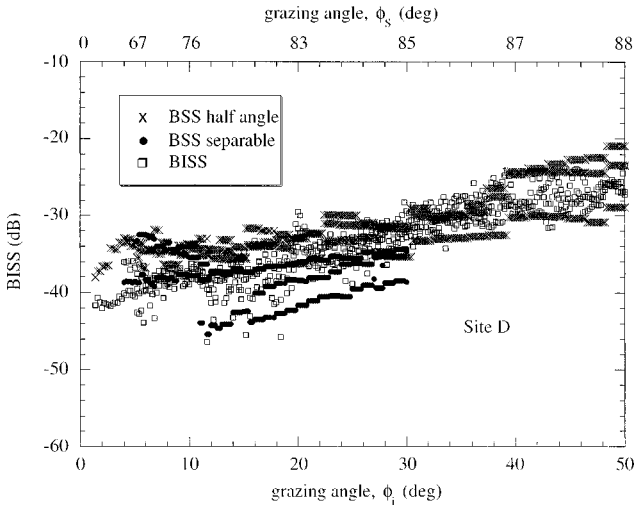

FIG. 17. Comparison of the grazing angle dependence at Site D of the bistatic-scattering strength to the backscattering strength using the separable and half-angle approximations.

for $\phi \geqslant 85$ degrees. The half-angle approximation does not suffer this limitation since it only requires the BSS at the *average* of the two angles.

Clearly, there is only a limited amount of data with which to compare the two approximations. Nonetheless, for the data set examined, the separable approximation provides the better fit—particularly at Sites A, C, and D—where agreement between the BSS and BISS data obtained using Eq. (5) is reasonable. Even at Site B, the separable approximation is better than the half-angle approximation, although neither fit could be considered acceptable. It is interesting to note that although Sites B and C are similar in bottom type, grain size, and bottom loss, the sites differ in the quality of fit to the approximations. This suggests that sediment properties in addition to roughness and grain size play an important role in scattering phenomena.

VIII. SUMMARY AND CONCLUSIONS

In summary, acoustic backscatter data were collected at four sites on the Sohm Abyssal Plain. The four sites are referred to as A, B, C, and D. At all four sites the bottom was reasonably smooth, the predominant difference from site to site being the mean grain sizes comprising the bottom sediment. For data arriving after the first-surface–first-bottom interaction, the geometry approximates an in-plane bistatic experiment. A detailed procedure for extracting the in-plane bottom-bistatic scattering strength (BISS) from a monostatic geometry was presented. The fathometer returns were used to estimate the normal-incidence bottom loss at the four sites. The measured bottom loss ranged from a low of 2 dB to a high of 16 dB. Furthermore, since the bistatic angles are a function of the ratio of sonar depth to water column depth, the experiment can be performed for several sonar depths. This will increase the density of points in the grid of in-plane bistatic scattering angles. The geometry of the experiment also provided an opportunity to compare the backscattering strength (BSS) of the bottom with the BISS to examine the validity of the separable and half-angle approximations.

Estimates of the BISS were obtained for pairs of incident and scattered grazing angles $(\phi_i, \phi_s) < (50$ degrees, 88 degrees). In the present data set, surface scatter contaminated estimates of the bottom-bistatic scattering strength at steeper angles. However, in the absence of both surface roughness and platform motion, estimates at steeper angles are possible.

At Site A, the grazing angle dependence matched Lambert's rule with a scattering coefficient of $\mu = -27$ dB for $(\phi_i, \phi_s) > (15$ degrees,80 degrees); at all other sites the data exhibited a steeper slope than that of Lambert's rule.

Only Site A showed any significant spread with frequency and the spread occurred primarily for $(\phi_i, \phi_s) > (30$ degrees,85 degrees); however, noting that measurements were taken at only three frequencies, it is speculative to extract the frequency dependence (or independence) of the data.

Comparison of the bistatic data to the monostatic arrivals indicated that the separable approximation provided a reasonable fit to the data at Sites A, C, and D; at Site B, however, the separable approximation over estimated the bistatic data by some 6 dB. The half-angle approximation did not match the data well at any of the sites.

ACKNOWLEDGMENTS

The authors wish to acknowledge the scientific and technical contributions of Patrick Barry, Philip Southern, and Mark O'Connor of the Defence Research Establishment Atlantic, Dartmouth, Canada.

APPENDIX A: ADDITIONAL DETAILS ON REDUCING MEASURED INTENSITY TO SINGLE-PATH BISTATIC INTENSITY

1. Separating the contributions from paths BB1 and BB2

In order to compute the in-plane bistatic scattering strength, we must relate the measured intensity to a single pair of incident and scattered grazing angles. This requires

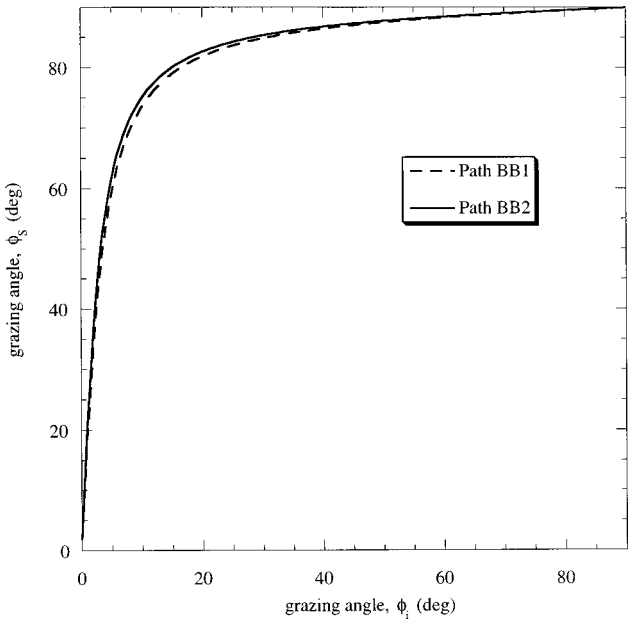

FIG. A1. Comparison of the relationship of ϕ_i to ϕ_s for paths BB1 and BB2. The dashed curve is ϕ_i vs ϕ_s for path BB1, replotted from Fig. 13 and the solid curve is ϕ_i vs ϕ_s for path BB2.

that we reduce the problem to a single path. We begin by noting that although the first arrivals on path BB2 lag those of path BB1 by approximately 0.6 s (recall Fig. 6), the relationship of (ϕ_i, ϕ_s) for both paths is almost identical for the experiment. This is shown in Fig. A1; the dashed curve is ϕ_i vs ϕ_s for path BB1, replotted from Fig. 13, and the solid curve is ϕ_i vs ϕ_s for path BB2. This means that we can use the intensity of arrivals on path BB1 to estimate the intensity of path BB2 arrivals at some later time. This procedure is similar to using the surface backscatter to predict the surface-bistatic scatter as discussed in Sec. V. We write

$$\begin{aligned} \mathrm{BI}_{\mathrm{BB2}}(t+\delta t, \phi_i, \phi_s) \approx & \mathrm{BI}_{\mathrm{BB1}}(t, \phi_i, \phi_s) \\ & - \mathrm{BL} - \Delta \mathrm{PL}_{\mathrm{BB}}(\phi_i, \phi_s) \\ & + \Delta A_{\mathrm{BB}}(\phi_i, \phi_s), \end{aligned} \tag{A1}$$

where $\mathrm{BI}_{\mathrm{BB2}}$ and $\mathrm{BI}_{\mathrm{BB1}}$ are the bottom-bistatic intensities from paths BB1 and BB2, respectively, BL is the normal incidence bottom loss from Eq. (1), and $\Delta \mathrm{PL}_{\mathrm{BB}}$ and ΔA_{BB} account for the difference in propagation loss and insonified area between paths BB1 and BB2 ($\Delta \mathrm{PL}_{\mathrm{BB}}$, $\Delta A_{\mathrm{BB}} > 0$). The arguments t and $t+\delta t$ in the bistatic intensity terms serve to highlight the fact that, although the angle pairs are the same for both paths, the arrival times corresponding to those angles are different. Implicit in Eq. (A1) is the assumption that the BL is approximately constant for steep grazing angles.

2. Separating path BB1 intensity into contributions from the up-going and down-going components

As noted earlier, the vertical symmetry of the transmitter and receiver beam patterns generates an up-going and a down-going wave; and because the source and receiver are colocated, these contributions arrive at the receiver at the same time. Writing the total intensity from path BB1 as a sum of these two components yields

$$I_{\mathrm{BB1}} = I_u + I_d, \tag{A2}$$

where I_{BB1} is the total intensity from path BB1, and I_u and I_d are, respectively, the up-going and down-going components and the two components are assumed to be uncorrelated. The two components are related to each other by

$$I_u = I_d G, \tag{A3}$$

where G is the ratio of the transducer beam pattern gain (in linear units) between the incident and scattered angles. Combining Eqs. (A2) and (A3) and solving for I_d yields

$$I_d = \frac{I_{\mathrm{BB1}}}{G+1} \tag{A4}$$

for the down-going component of the bottom-bistatic scattered intensity.

APPENDIX B: CALCULATION OF THE INSONIFIED AREA

In this Appendix we calculate the area insonified by the bottom-bistatic returns. To simplify the discussion, comments are restricted to the area insonified for path BB1. The procedure to calculate the insonified area for path BB2 is a straightforward extension of this. Figure B1 shows a schematic of the geometry for the problem. A pulse of length τ propagates[13] from the sonar and insonifies a patch of length $\Delta x = x_o - x_i$. The area A insonified is given by

$$A = \pi(x_0^2 - x_1^2). \tag{B1}$$

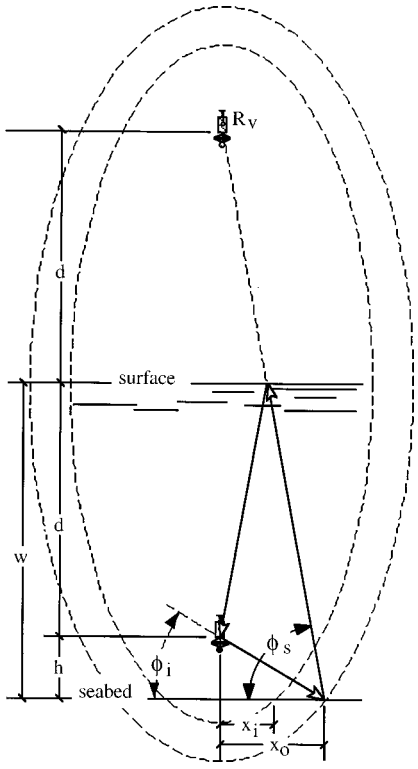

FIG. B1. Schematic showing a cross section of the insonified area A used in the calculation of the bottom-bistatic scattering strength.

The length Δx is a function, not only of pulse length, but also the path from source-to-patch-to-receiver. To solve for the length we recall that the intersection of the bistatic path with the bottom, as shown in Fig. B1, represents a single point on an ellipse of constant travel time. The foci of this ellipse are at the source and at the *virtual* receiver location, denoted R_v in the figure. The virtual receiver is directly above the source at a height d above the water–air interface. Thus, $x_o - x_i$ is simply the intersection of the bottom with the two ellipses that correspond to the leading and trailing edges of the pulse.

Returning to Fig. B1, the major axis of the ellipse is parallel to the y axis for the present geometry. The problem is further simplified by defining $y=0$ to correspond to the seabed and defining $x=0$ such that the y axis intercepts the foci. This obtains for the equation of the ellipse:

$$\frac{x^2}{\beta^2}+\frac{(y-w)^2}{\alpha^2}=1, \tag{B2}$$

where α is half the total path length, $\beta=\sqrt{\alpha^2-d^2}$, w is the distance from the seabed to the water–air interface, and d is the distance from the sonar to the water–air interface. Solving Eq. (B2) for x and recalling that the seabed corresponds to $y=0$ yields

$$x=\sqrt{\beta^2[1-w^2/\alpha^2]}. \tag{B3}$$

For any pair of (ϕ_i,ϕ_s) we calculate the corresponding path length and obtain α and β. These values are inserted into Eq. (B3) to obtain x_i. Then x_o is computed by increasing the total path length by an amount corresponding to $c_{\text{avg}}\tau$, where c_{avg} is the average sound speed in the water column. The insonified area is obtained by inserting the values for x_o and x_i into Eq. (B1). It should be noted that if $\Delta x \ll x_i$, then Eq. (B1) can be approximated with

$$A=2\pi x_{\text{avg}}\Delta x, \tag{B4}$$

where $x_{\text{avg}}=(x_o+x_i)/2$ and[14] $\Delta x=c_{\text{avg}}\tau/(\cos\phi_i+\cos\phi_s)$. Finally, for the simple backscatter case, the foci collapse to a single point, the ellipse reduces to a circle, and we obtain the familiar form $\Delta x=c_{\text{avg}}\tau/(2\cos\phi)$.

[1] P. C. Hines and P. J. Barry, ''Measurements of acoustic backscatter from the Sohm Abyssal Plain,'' J. Acoust. Soc. Am. **92**, 315–323 (1992).

[2] D. D. Ellis and D. V. Crowe, ''Bistatic reverberation calculations using a three-dimensional scattering function,'' J. Acoust. Soc. Am. **89**, 2207–2214 (1991).

[3] D. R. Horn, M. Ewing, B. M. Horn, and M. N. Delach, ''Turbidites of the Hatteras and Sohm Abyssal Plains, Western North Atlantic,'' Mar. Geol. **11**, 287–323 (1971).

[4] J. E. Hughes-Clarke, ''The Geological Record of the 1929 'Grand Banks' Earthquake and its Relevance to Deep-Sea Clastic Sedimentation,'' Ph.D. thesis, Dalhousie University, Halifax, Canada, 1988.

[5] J. Gilluly, A. C. Waters, and A. O. Woodford, *Principles of Geology* (Freeman, San Francisco, 1959), 2nd ed., p. 332.

[6] Although not indicated in the figure, ray curvature resulting from the nonconstant sound-speed profile was accounted for when computing path lengths and grazing angles.

[7] Note that surface bistatic path SB2 is in fact monostatic, but this does not change the procedure.

[8] For our geometry, the incident and scattered angles for surface bistatic path SB1 were within 3 degrees of one another.

[9] We use the word ''approximates'' here because one must remember that the bottom scattering strength varied from site to site independent of the surface scattering strength. Therefore, to come up with a true ''worst case,'' one must consider the relative contributions of the surface and bottom scattering strengths.

[10] J. C. Novarini and D. R. Bruno, ''Effects of the sub-surface bubble layer on sound propagation,'' J. Acoust. Soc. Am. **72**, 510–514 (1982) (see Fig. 6).

[11] Due to the relatively wide bandwidth of the pulses, any frequency spread will be inconsequential.

[12] Note that in Ref. 2 the authors use θ to represent the in-plane angles and ϕ to represent the azimuthal angle.

[13] For the linear FM pulses used in this experiment, $\tau \equiv 1/\text{bandwidth}$.

[14] D. D. Ellis, ''A shallow-water normal-mode reverberation model,'' J. Acoust. Soc. Am. **97**, 2804–2814 (1995) [see Eq. (22)].

Acoustic scattering by a partially buried three-dimensional elastic obstacle

Raymond Lim
Coastal Systems Station/Dahlgren Division, Naval Surface Warfare Center, Code R22, 6703 West Highway 98, Panama City, Florida 32407-7001

(Received 7 October 1997; accepted for publication 25 March 1998)

A transition-matrix solution for the spectral scattering response of an elastic obstacle that penetrates a plane-stratified fluid host is formulated. The field scattered from the segment in each layer is expanded in a global outgoing basis centered on that segment and these segment fields are superposed at the field point. A manageable structure for the transition matrix is maintained by using the boundary conditions to couple these segment fields to the interior field of the obstacle via exterior surface field expansions centered on the primary origin of the obstacle. Two formulations are presented and compared in which the surface fields are expanded in either the standard set of regular spherical eigenfunctions of the Helmholtz equation or the spherical harmonics. Numerical tests for an axisymmetric spheroid indicate both formulations are viable but exhibit different convergence and stability characteristics. However, in both cases, convergence is better for flattened shapes (oblate) than elongated shapes (prolate). Examples are presented to illustrate environmental effects on the backscatter by a bubble and elastic spheres and spheroids that penetrate a water/sediment interface. [S0001-4966(98)02207-3]

PACS numbers: 43.30.Gv, 43.20.Fn [DLB]

INTRODUCTION

While relevant to many disciplines, the acoustic scattering response of a bounded elastic body embedded in a generally inhomogeneous environment is difficult to predict deterministically. Nevertheless, techniques have been developed to model this response, though with limitations that depend on the technique chosen. Finite-difference time-domain solutions[1–3] appear to have the widest applicability, allowing one to treat almost arbitrary environment and scatterer configurations. However, the computational intensity of the solution increases rapidly with frequency and configuration dimensionality, attenuation and dispersion effects are not easy to incorporate, and approximations made to the wave equation and boundary conditions yield a solution whose fidelity is not easy to assess without established benchmarks.

Benchmark quality solutions are more often pursued with analytic and semianalytic frequency domain techniques based on the Helmholtz integral equation. Here, geometric and/or symmetry constraints may be applied to formulate scattering solutions that are faster to implement and converge to an exact solution of the Helmholtz equation with all the proper boundary conditions obeyed. For example, when the environment is assumed to consist of homogeneous plane-stratified layers, numerically viable solutions exist for two- and three-dimensional bounded elastic obstacles embedded in fluid,[4–9] elastic,[10–13] and even poroelastic[14,15] layers. These form the basis for fundamental analysis and provide explicit checks for the more numerical approaches.

Nevertheless, a drawback exists in many of these benchmark solutions; few allow the obstacle to penetrate the layers of the environment due to constraints imposed to ensure convergence. While the hybrid method formulated by Gerstoft and Schmidt[13] and the recent boundary integral equation method of Fawcett[8,9] may be used to consider penetration, these approaches have yet to be extended to model the scattering by three-dimensional obstacles. Aside from some formal results by Bahar[16] in electromagnetic scattering, there seem to be very few analytical treatments of wave scattering by three-dimensional bounded obstacles that penetrate the layers of an inhomogeneous environment. This paper will attempt to remove this deficiency by formulating a transition (T) matrix for calculating the acoustic field scattered by a bounded elastic body that penetrates an arbitrary number of layers of a plane-stratified fluid. The viability of the solution is checked numerically for the case of a homogeneous elastic spheroid at the interface of two fluid half-spaces.

The organization of the paper is as follows. In Section I, some background material and hypotheses needed to develop the required T matrix are first presented. In particular, the basis functions and Green's dyadics needed to expand the fields in a plane-layered fluid medium are given and the range of convergence of the required expansions are discussed. A scattering solution is then obtained by decomposing the scattered field into contributions from segments defined by the host layering and deriving a T matrix for the scattering by each segment. The segment T matrices are formulated in two ways that differ by how the surface fields are expanded. In Sec. II, some of the assumptions made to obtain the resulting solutions are checked. Some implications on scattering calculations with simpler obstacle arrangements (e.g., scattering in an unbounded homogeneous host and next to a boundary) are discussed. The results are then tested on a penetrating spheroid. Difficulties in the numerical implementation are discussed. The final section summarizes the results of the paper and discusses future directions to pursue.

I. THEORY

A. Background

In the subsequent development, frequency-domain field solutions to integral representations of the Helmholtz equation are sought. These solutions will be formulated as vector displacement fields expanded in a basis of eigenfunction solutions to the Helmholtz equation. The $e^{-i\omega t}$ time factor inherent in steady-state solutions will be suppressed. To account for scattering by a three-dimensional bounded obstacle in the fluid host, required regular and outgoing vector basis sets will be adapted from the scalar bases found appropriate in past applications[6] for expanding potential fields in plane-stratified fluids. Thus for fields that are regular in a homogeneous region containing the origin, the regular basis functions are given by the standard set of spherical partial waves used in free-field applications. Expressed in spherical field coordinates, $\mathbf{r}=(r,\theta,\phi)$, these are

$$\hat{\Psi}_{pml}(\mathbf{r})=\frac{1}{k_0}\,\nabla \mathrm{j}_l(k_0 r)Y_{pml}(\theta,\phi), \tag{1}$$

where k_0 is the wave number of the layer containing the coordinate origin of the basis, j_l is an lth order spherical Bessel function, and $Y_{pml}(\theta,\varphi)$ is a normalized spherical harmonic defined by

$$Y_{pml}(\theta,\phi)\equiv\left(\epsilon_m\,\frac{2l+1}{4\pi}\,\frac{(l-m)!}{(l+m)!}\right)^{1/2}\times P_l^m(\cos\theta)\begin{pmatrix}\cos m\phi, & p=e\\ \sin m\phi, & p=o\end{pmatrix}. \tag{2}$$

Here $P_l^m(\cos\theta)$ is an associated Legendre function, $\epsilon_m=2$ for $m>0$, and $\epsilon_0=1$. Completeness of the regular basis is assured by specifying the indices shown so that the parity index p is either even (e) or odd (o), the order index takes the values $l=0,1,...,\infty$, and the rank index $m=0,1,...,l$.

In outgoing propagation of the displacement field, it will be convenient to use eigenfunctions that account for the stratifications of the host. This is accomplished by choosing an outgoing basis that satisfies the proper boundary conditions imposed at all the interfaces of the host. The scalar partial-wave basis $\psi_{pml}(\mathbf{r})$ derived in Ref. 6 may be adapted to obtain a suitable basis of vector partial waves in the cylindrical field coordinates $\mathbf{r}=(\zeta,z,\phi)$ as

$$\Psi_{pml}(\mathbf{r})=\frac{\nabla}{k_0}\,\psi_{pml}(\mathbf{r})$$

$$=\left(\frac{\epsilon_m}{2\pi}\right)^{1/2}\frac{\nabla}{k_0}\begin{pmatrix}\cos m\phi, & p=e\\ \sin m\phi, & p=o\end{pmatrix}\int_0^\infty\frac{q\,dq}{k_0 h_0}\,J_m(q\zeta)e^{ih_0 a_0}\,\frac{(B_{ml}(h_0/k_0)^{-1}+V_0 e^{-2ih_0 b_0}B_{ml}(-h_0/k_0)^{-1})}{1-u_0V_0e^{2ih_0(a_0-b_0)}}$$

$$\times W_{0\to f}e^{-ih_f b_f}\,\frac{(e^{ih_f z}+U_f e^{ih_f(2a_f-z)})}{1-U_fV_fe^{2ih_f(a_f-b_f)}},\quad z>0 \tag{3a}$$

$$=\left(\frac{\epsilon_m}{2\pi}\right)^{1/2}\frac{\nabla}{k_0}\begin{pmatrix}\cos m\phi, & p=e\\ \sin m\phi, & p=o\end{pmatrix}\int_0^\infty\frac{q\,dq}{k_0 h_0}\,J_m(q\zeta)e^{-ih_0 b_0}\,\frac{(B_{ml}(-h_0/k_0)^{-1}+U_0 e^{2ih_0 a_0}B_{ml}(h_0/k_0)^{-1})}{1-U_0\nu_0e^{2ih_0(a_0-b_0)}}$$

$$\times W_{0\to f}e^{ih_f a_f}\,\frac{(e^{-ih_f z}+V_f e^{-ih_f(2b_f-z)})}{1-U_fV_fe^{2ih_f(a_f-b_f)}},\quad z<0. \tag{3b}$$

Here the indices span the same ranges as those of the regular functions, $h_{(0,f)}=\sqrt{k_{(0,f)}^2-q^2}$ with $\mathrm{Im}(h_{(0,f)})\geqslant 0$ to ensure convergence of the integral, k_f is the wave number in the layer at the field point $\mathbf{r}$, $a_{(0,f)}$ and $b_{(0,f)}$ are the vertical (z) coordinates of the upper and lower boundaries of the layer containing either the origin or the field point, respectively, J_m is a cylindrical Bessel function, and

$$B_{ml}\left(\frac{h_0}{k_0}\right)=i^{l-m}\left(\frac{2l+1}{2}\,\frac{(l-m)!}{(l+m)!}\right)^{1/2}P_l^m\left(\frac{h_0}{k_0}\right)$$

$$\equiv B_{ml}\left(-\frac{h_0}{k_0}\right)^{-1}. \tag{4}$$

The remaining coefficients are standard potential field reflection and transmission coefficients.[17] $W_{0\to f}$ is the total transmission coefficient for propagating the plane-wave components of the out-going multipole field through the layers between the origin and field point. U_0 and V_0 are the total plane-wave reflection coefficients at the upper and lower boundaries, respectively, of the layer containing the origin. Similarly, U_f and V_f are total plane-wave reflection coefficients at upper and lower boundaries of the layer containing the field point. Finally, a lower-case u or v is used to denote a partial plane-wave reflection coefficient. When the layer with the field point is above the origin, u_0 is the reflection coefficient at the upper boundary of the origin layer that would result by ignoring the layers above the field point. When the layer with the field point is below the origin, v_0 is the reflection coefficient at the lower boundary of the origin layer that would result by ignoring the layers below the field point.

An expansion for the Green's dyadic $\mathbf{G}(\mathbf{r}_s,\mathbf{r})$ in a plane-

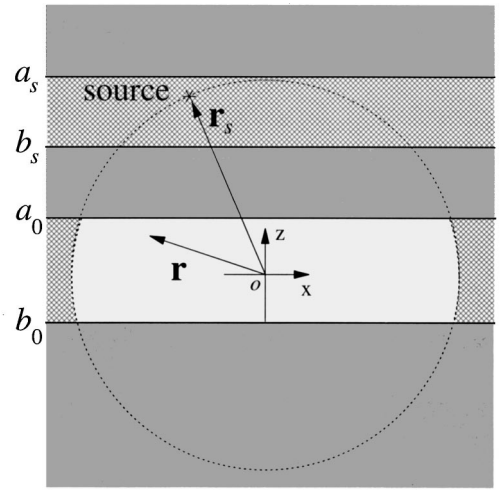

FIG. 1. The convergence region of the expansion of the Green's dyadic for $|\mathbf{r}_s|>|\mathbf{r}|$ is depicted. The expansion is expected to converge to physically valid results for $\mathbf{r}$ within the unshaded spherical segment bounded by the interfaces at $z=a_0$ and $z=b_0$.

stratified fluid can now be formulated with the basis sets specified, provided one of either the source position $\mathbf{r}_s$ or the field point $\mathbf{r}$ are contained within a homogeneous region around the origin. This follows from an expansion of the exact integral form of the potential field Green's function $G(\mathbf{r}_s,\mathbf{r})$ as derived in Ref. 6 (see comments under Ref. 12 of that article). Scaled to suppress units, the dyadic is given by

$$\mathbf{G}(\mathbf{r}_s,\mathbf{r})=\boldsymbol{\nabla}\boldsymbol{\nabla}_s G(\mathbf{r}_s,\mathbf{r})/k_s^3$$

$$=i\left(\frac{k_0}{k_s}\right)^3\frac{\rho_s}{\rho_0}\sum_{pml}\Psi_{pml}(\mathbf{r}_s)\hat{\Psi}_{pml}(\mathbf{r}),\quad |\mathbf{r}_s|>|\mathbf{r}| \tag{5a}$$

$$=i\sum_{pml}\Psi_{pml}(\mathbf{r})\hat{\Psi}_{pml}(\mathbf{r}_s),\quad |\mathbf{r}|>|\mathbf{r}_s|, \tag{5b}$$

where ρ_0 and ρ_s are the densities of the layers containing the origin and source, respectively, and the gradient operators $\boldsymbol{\nabla}$ and $\boldsymbol{\nabla}_s$ operate with respect to $\mathbf{r}$ and $\mathbf{r}_s$, respectively.

A remark on the conditions imposed in Eq. (5) are in order. These are the same as the conditions imposed to ensure convergence of the Green's dyadic in an unbounded homogeneous medium, but their validity here has not been proven. In past applications of Eq. (5), weaker convergence assumptions were stipulated. For example, to formulate the multiple-scattering T matrix in Ref. 6, it was sufficient to assume that Eq. (5a) converges for $\mathbf{r}$ at least within the largest origin-centered sphere that excludes the source and all layer boundaries. In the development to follow, stronger statements are needed and, although given without proof, the conditions imposed above are consistent with intuitive notions of convergence radii as determined by where the singularities of $\mathbf{G}(\mathbf{r}_s,\mathbf{r})$ lie.[18] In this paper, these conditions will be assumed sufficient for convergence of the expansions given. However, using the basis sets specified above, it should be understood that Eq. (5) is not valid everywhere convergence is implied. Since the radius of convergence can now cross over other layers, the values that these expansions converge to will not be valid when the argument of the regular functions are outside the origin layer. This is illustrated in Fig. 1.

To expand the displacements in the interior of the scatterer, additional basis functions will be needed. Since the obstacle will be assumed elastic, homogeneous, reasonably smooth, and not too aspherical the standard spherical elastic partial-wave functions[19] can be used. Adopting the same normalization as Boström,[20] the outgoing set is given by

$$\Phi_{1pml}(\mathbf{r})\equiv\left(\frac{\overline{k}}{\overline{\kappa}}\right)^{3/2}\left\{\frac{d\mathrm{h}_l^{(1)}(\overline{kr})}{d(\overline{kr})}\mathscr{A}_{1pml}(\theta,\phi)+\frac{[l(l+1)]^{1/2}\mathrm{h}_l^{(1)}(\overline{kr})}{\overline{kr}}\mathscr{A}_{3pml}(\theta,\phi)\right\}, \tag{6a}$$

$$\Phi_{2pml}(\mathbf{r})\equiv\mathrm{h}_l^{(1)}(\overline{\kappa r})\mathscr{A}_{2pml}(\theta,\phi), \tag{6b}$$

$$\Phi_{3pml}(\mathbf{r})\equiv l(l+1)^{1/2}\left[\frac{\mathrm{h}_l^{(1)}(\overline{\kappa r})}{\overline{\kappa r}}\right]\mathscr{A}_{1pml}(\theta,\phi)+\left[\frac{d\mathrm{h}_l^{(1)}(\overline{\kappa r})}{d(\overline{\kappa r})}+\frac{\mathrm{h}_l^{(1)}(\overline{\kappa r})}{\overline{\kappa r}}\right]\mathscr{A}_{3pml}(\theta,\phi), \tag{6c}$$

where $\overline{k}$ and $\overline{\kappa}$ are the compressional and shear wave numbers, respectively, of the medium inside the obstacle, $\mathrm{h}_l^{(1)}$ is an lth-order spherical Hankel function of the first kind and the $\mathscr{A}_{\tau pml}(\theta,\phi)$, $\tau=1,2,3$ are vector spherical harmonics defined by

$$\mathscr{A}_{1pml}(\theta,\phi)\equiv\hat{\mathbf{r}}Y_{pml}(\theta,\phi),$$

$$\mathscr{A}_{2pml}(\theta,\phi)\equiv[l(l+1)]^{-1/2}\boldsymbol{\nabla}\times[\mathbf{r}Y_{pml}(\theta,\phi)], \tag{7}$$

$$\mathscr{A}_{3pml}(\theta,\phi)\equiv[l(l+1)]^{-1/2}r\boldsymbol{\nabla}Y_{pml}(\theta,\phi).$$

Here the l, m, and p indices span the same ranges as for the exterior functions above and τ labels the three possible elastic modes: $\tau=1$ for the compressional mode, $\tau=2$ for the spherical T shear mode, and $\tau=3$ for the spherical S shear mode. In addition to the outgoing functions, a regular basis $\hat{\Phi}_{\tau pml}(\mathbf{r})$ is defined in the same way except $\mathrm{h}_l^{(1)}$ is replaced by j_l.

Wave propagation in the interior of the elastic scatterer will be represented by the free-field Green's dyadic $\overline{\mathbf{G}}(\mathbf{r}_s,\mathbf{r})$. This can be expanded in terms of the interior basis functions in the well-known unitless form,[19]

$$\overline{\mathbf{G}}(\mathbf{r}_s,\mathbf{r})=i\sum_{\tau pml}\Phi_{\tau pml}(\mathbf{r}_s)\hat{\Phi}_{\tau pml}(\mathbf{r}),\quad |\mathbf{r}_s|>|\mathbf{r}|, \tag{8a}$$

$$=i\sum_{\tau pml}\Phi_{\tau pml}(\mathbf{r})\hat{\Phi}_{\tau pml}(\mathbf{r}_s),\quad |\mathbf{r}|>|\mathbf{r}_s|. \tag{8b}$$

The final ingredients needed to formulate a T matrix are surface integral representations of the Helmholtz equation for the interior and exterior fields of the scatterer. Appropri-

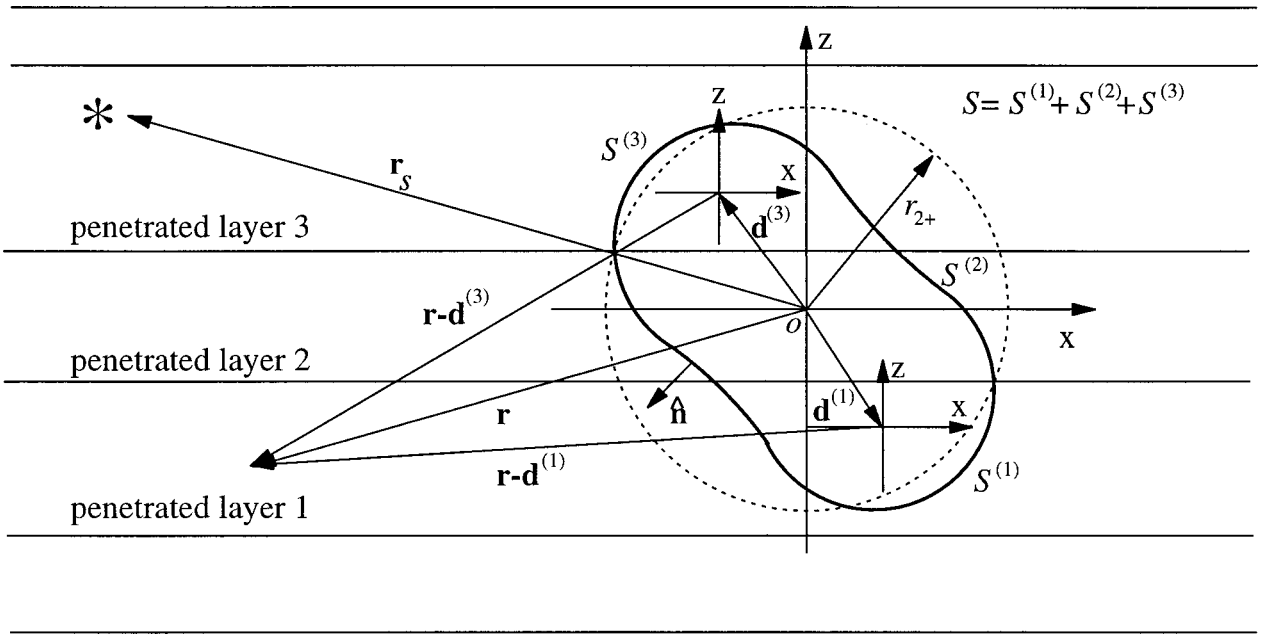

FIG. 2. An approach to determine the field scattered by an obstacle that penetrates three layers of a plane-stratified host is depicted. The field scattered by the segment in each layer is superposed to form the total scattered field at **r**. The dotted circle of radius r_{2+} depicts the spherical surface outside of which the field scattered by the middle segment, expanded around the primary origin at o, is proposed to converge.

ate representations for displacement fields have been derived by Pao and Varatharajulu[21] for an obstacle in an infinite homogeneous host. These expressions remain applicable even when the host is layered but the Green's dyadics used in them for the exterior propagation must be chosen to satisfy all the boundary conditions of the layered host in order to avoid extending the surface integrals over the host's interfaces. Given an elastic obstacle bounded by a surface S and the exterior and interior Green's dyadics expanded in Eqs. (5) and (8), the surface integrals proposed by Pao and Varatharajulu may be adapted in the form,

$$\mathbf{u}^{\mathrm{inc}}(\mathbf{r}) + \frac{1}{\omega^2}\int_S \left(\frac{k'^3}{\rho'}\right)[\mathbf{u}_+(\mathbf{r}')\cdot(\hat{\mathbf{n}}\cdot\Xi(\mathbf{r}',\mathbf{r})) - \mathbf{t}_+(\mathbf{r}')\cdot\mathbf{G}(\mathbf{r}',\mathbf{r})]dA' = \begin{cases}\mathbf{u}(\mathbf{r}), & \mathbf{r}\ \text{outside}\ S,\\ 0, & \mathbf{r}\ \text{inside}\ S,\end{cases} \tag{9}$$

$$-\frac{\overline{\kappa}^3}{\overline{\rho}\omega^2}\int_S [\mathbf{u}_-(\mathbf{r}')\cdot(\hat{\mathbf{n}}\cdot\overline{\Xi}(\mathbf{r}',\mathbf{r})) - \mathbf{t}_-(\mathbf{r}')\cdot\overline{\mathbf{G}}(\mathbf{r}',\mathbf{r})]dA' = \begin{cases}\mathbf{u}(\mathbf{r}), & \mathbf{r}\ \text{inside}\ S,\\ 0, & \mathbf{r}\ \text{outside}\ S.\end{cases} \tag{10}$$

The primed wave number and density correspond to values in the exterior at the area element dA' on S. These parameters are placed inside the integral in case $\mathbf{r}'$ crosses a layer boundary as it is integrated over S. On the left side of Eq. (9), the first term is the part of the total displacement field **u** that would exist without the elastic obstacle; i.e., the incident source field. Within brackets, $\mathbf{u}_\pm$ and $\mathbf{t}_\pm$ are the total displacement and surface traction fields, respectively, evaluated on S as it is approached from the outside $(+)$ or the inside $(-)$. The quantities Ξ and $\overline{\Xi}$ are exterior and interior Green's stress triadics, respectively, and $\hat{\mathbf{n}}$ is the outward unit vector normal to S at dA'.

Both the tractions and the surface normal components of the stress triadic share the same form as functionals of other field components. In the host, they are given by

$$\begin{Bmatrix}\mathbf{t}_+(\mathbf{r}')\\ \hat{\mathbf{n}}\cdot\Xi(\mathbf{r}',\mathbf{r})\end{Bmatrix} = \lambda'\hat{\mathbf{n}}\nabla'\cdot\begin{Bmatrix}\mathbf{u}_+(\mathbf{r}')\\ \mathbf{G}(\mathbf{r}',\mathbf{r})\end{Bmatrix}, \tag{11}$$

where λ' is the Lamé parameter of the fluid at $\mathbf{r}'$ and ∇' operates with respect to $\mathbf{r}'$. For the elastic medium inside S, these tractions and triadic components are

$$\begin{Bmatrix}\mathbf{t}_-(\mathbf{r}')\\ \overline{\Xi}(\mathbf{r}',\mathbf{r})\end{Bmatrix} = \overline{\lambda}\hat{\mathbf{n}}\nabla'\cdot\begin{Bmatrix}\mathbf{u}_-(\mathbf{r}')\\ \overline{\mathbf{G}}(\mathbf{r}',\mathbf{r})\end{Bmatrix} + 2\overline{\mu}\hat{\mathbf{n}}\cdot\nabla'\begin{Bmatrix}\mathbf{u}_-(\mathbf{r}')\\ \overline{\mathbf{G}}(\mathbf{r}',\mathbf{r})\end{Bmatrix} + \overline{\mu}\hat{\mathbf{n}}\times\left(\nabla'\times\begin{Bmatrix}\mathbf{u}_-(\mathbf{r}')\\ \overline{\mathbf{G}}(\mathbf{r}',\mathbf{r})\end{Bmatrix}\right), \tag{12}$$

where $\overline{\lambda}$ and $\overline{\mu}$ are elastic Lamé parameters.

B. General formulation

The total acoustic field due to a point source in a plane-stratified fluid containing a bounded elastic obstacle can be formulated as the superposition of a part represented by the Green's dyadic outlined above [Eq. (5)] and a part scattered by the obstacle. Since the Green's dyadic is easily computed via well-documented techniques (e.g., fast-field algorithms[22,23]), the focus of this section is the part of the field due to the presence of the obstacle. Henceforth, the incident source field will be assumed to be formed from a superposition of known point sources. Figure 2 illustrates the problem for a single point source at $\mathbf{r}_s$ and an obstacle that penetrates three layers of its host. To proceed, expansions for an incident point source field in a multilayered fluid host, the interior field of an obstacle that penetrates N layers of the host, and the resulting scattered field are proposed in the form

$$\mathbf{u}^{\mathrm{inc}}(\mathbf{r})=\sum_{pml}\alpha_{pml}(\mathbf{r}_s)\hat{\Psi}_{pml}(\mathbf{r}), \tag{13}$$

$$\mathbf{u}^{\mathrm{int}}(\mathbf{r})=\sum_{\tau pml}\beta_{\tau pml}\hat{\Phi}_{\tau pml}(\mathbf{r}), \tag{14}$$

$$\mathbf{u}^{\mathrm{sca}}(\mathbf{r})=\sum_{j=1}^{N}\sum_{pml}\gamma_{pml}^{(j)}\Psi_{pml}(\mathbf{r}-\mathbf{d}^{(j)}) \equiv\sum_{j=1}^{N}[\mathbf{u}^{\mathrm{sca}}(\mathbf{r}-\mathbf{d}^{(j)})]^{(j)}, \tag{15}$$

where the $\alpha_{pml}(\mathbf{r}_s)$ coefficients are specified by comparison with Eq. (5a); i.e.,

$$\alpha_{pml}(\mathbf{r}_s)=Fi\left(\frac{k_0}{k_s}\right)^3\frac{\rho_s}{\rho_0}\Psi_{pml}(\mathbf{r}_s). \tag{16}$$

Here the scale factor F is included to account for the field units. Note that the scattered field is composed of expansions around origins that may be different from the primary obstacle origin that the other fields are referenced to. This is motivated by the convergence limitations discussed earlier on the expansion of the layered host's Green's dyadic when layers must be crossed. By expressing the scattering in this way, as a superposition of contributions scattered from each segment j bounded by $S^{(j)}$ in the corresponding penetrated layer, the limitations of the Green's dyadic expansions will not be a problem in the following development. As illustrated for the middle segment in Fig. 2, it will be assumed that the expansion of the field scattered by segment j will converge for $\mathbf{r}$ outside the sphere centered on $\mathbf{d}^{(j)}$ and circumscribing this segment. The primary goal will be to determine the coefficients $\gamma_{pml}^{(j)}$ in terms of the given $\alpha_{pml}(\mathbf{r}_s)$. This will be done using techniques parallel to those formulated by Boström[20,24] for treating scattering in a homogeneous fluid host.

First, since Eq. (15) is not generally expected to converge on the surface S of the obstacle, a mathematical representation of Huygens' principle is needed to allow the boundary conditions at the surface of the obstacle to be satisfied. This is obtained by using the expansions of $\mathbf{G}(\mathbf{r}_s,\mathbf{r})$ in Eq. (5) to expand the stress triadic components in Eq. (11) in terms of the exterior bases and then putting this and the expansions for $\mathbf{u}^{\mathrm{inc}}(\mathbf{r})$, $\mathbf{u}^{\mathrm{sca}}(\mathbf{r})$, and $\mathbf{G}(\mathbf{r}_s,\mathbf{r})$ into Eq. (9). Note that the integration in Eq. (9) is understood to represent a superposition of fields propagated from sources residing on S. Therefore when the field point is specified inside S, Eq. (5a) is the appropriate expansion of the Green's dyadic to use. Since the regular partial waves are complete and linearly independent, the following relation results for the incident source field coefficients by collecting factors of like regular functions:

$$\alpha_{pml}(\mathbf{r}_s)=-i\frac{k_{(0)}^3}{\rho_{(0)}\omega^2}\sum_{j=1}^{N}\int_{S^{(j)}}[\hat{\mathbf{n}}\cdot\mathbf{u}_+(\mathbf{r})\lambda_j\boldsymbol{\nabla}\cdot\Psi_{pml}(\mathbf{r}) -\hat{\mathbf{n}}\cdot\mathbf{t}_+(\mathbf{r})\hat{\mathbf{n}}\cdot\Psi_{pml}(\mathbf{r})]dA. \tag{17}$$

A subscript j is used here to label material parameters associated with the layer of the host containing the jth segment of the obstacle. However, the subscript (0) labels material parameters of the layer that contains the primary origin; e.g., if the origin is in segment j', $k_{(0)}=k_{j'}$.

When the field point is specified outside S in Eq. (9), $\mathbf{u}^{\mathrm{sca}}(\mathbf{r})=\mathbf{u}(\mathbf{r})-\mathbf{u}^{\mathrm{inc}}(\mathbf{r})$ is replaced with a sum of expansions centered on several displaced origins at $\mathbf{d}^{(j)}$, $1\leqslant j\leqslant N$. To obtain an expression for the coefficients, the integral over the surface segment $S^{(j)}$ is performed with the Green's dyadic and the stress triadic components also expanded around $\mathbf{d}^{(j)}$. These are obtained from Eq. (5b) by replacing $\mathbf{r}$ and $\mathbf{r}_s$ with $\mathbf{r}-\mathbf{d}^{(j)}$ and $\mathbf{r}_s-\mathbf{d}^{(j)}$. With these expansions inserted into Eq. (9), the following relation is found for the scattered field coefficients by collecting factors of like outgoing partial waves at each of the auxiliary origins:

$$\gamma_{pml}^{(j)}=i\frac{k_j^3}{\rho_j\omega^2}\int_{S^{(j)}}[\hat{\mathbf{n}}\cdot\mathbf{u}_+(\mathbf{r})\lambda_j\boldsymbol{\nabla}\cdot\hat{\Psi}_{pml}(\mathbf{r}-\mathbf{d}^{(j)}) -\hat{\mathbf{n}}\cdot\mathbf{t}_+(\mathbf{r})\hat{\mathbf{n}}\cdot\hat{\Psi}_{pml}(\mathbf{r}-\mathbf{d}^{(j)})]dA\,. \tag{18}$$

The regular external partial waves in the integrand are evaluated with the material parameters of the layer containing segment j, where they are centered. Note that, while Eq. (18) leads to a unique solution for the scattered field satisfying Eq. (9), the $\gamma_{pml}^{(j)}$ coefficients are not specified uniquely because the outgoing functions centered on different origins are not independent of each other. These coefficients may be specified in other ways but the choice made above is consistent with associating the field scattered by segment j with the part of the scattered field expanded around $\mathbf{d}^{(j)}$. Since it is the uniqueness of the total scattered field solution rather than that of the individual expansions around $\mathbf{d}^{(j)}$ that is needed, Eq. (18) will suffice for the subsequent development.

Equations (17) and (18) embody Huygens' principle by allowing field quantities defined off S [such as $\mathbf{u}^{\mathrm{sca}}(\mathbf{r})$] to be related to field quantities on S. Therefore boundary conditions can now be applied. For a fluid–elastic interface these are

$$\hat{\mathbf{n}}\cdot\mathbf{u}_+(\mathbf{r})=\hat{\mathbf{n}}\cdot\mathbf{u}_-(\mathbf{r}),\quad \text{on } S, \tag{19}$$

$$\hat{\mathbf{n}}\cdot\mathbf{t}_+(\mathbf{r})=\hat{\mathbf{n}}\cdot\mathbf{t}_-(\mathbf{r}),\quad \text{on } S, \tag{20}$$

$$\hat{\mathbf{n}}\times\mathbf{t}_-(\mathbf{r})=0,\quad \text{on } S. \tag{21}$$

For scattering in a homogeneous fluid host, Boström has demonstrated two viable methods of applying these boundary conditions to obtain scattering solutions. These differ in how the surface fields are expanded and, consequently, how quickly the solutions converge for different obstacle shapes. In the following, it will be demonstrated how both of these methods may be extended to treat scattering in a plane-stratified host.

In the first method, the first two conditions are put into Eqs. (17) and (18) directly. Since Eq. (14) is expected to be convergent and differentiable out to the interior surface of the scatterer;[25] this can then be used to expand $\mathbf{u}_-(\mathbf{r})$ and $\mathbf{t}_-(\mathbf{r})$. The result is

$$\alpha_{pml}(\mathbf{r}_s)=-i\sum_{\tau p'm'l'}Q_{pml;\tau p'm'l'}\beta_{\tau p'm'l'}, \tag{22}$$

$$\gamma_{pml}^{(j)} = i \sum_{\tau p' m' l'} \hat{Q}_{pml;\tau p' m' l'}^{(j)} \beta_{\tau p' m' l'}, \tag{23}$$

where

$$Q_{pml;\tau p' m' l'} = \frac{k_{(0)}^3}{\rho_{(0)}\omega^2} \sum_{j=1}^{N} \int_{S^{(j)}} [\hat{\mathbf{n}} \cdot \hat{\Phi}_{\tau p' m' l'}(\mathbf{r}) \lambda_j \boldsymbol{\nabla} \cdot \Psi_{pml}(\mathbf{r}) - \hat{\mathbf{n}} \cdot \mathbf{t}_-(\hat{\Phi}_{\tau p' m' l'}(\mathbf{r})) \hat{\mathbf{n}} \cdot \Psi_{pml}(\mathbf{r})] dA, \tag{24}$$

$$\hat{Q}_{pml;\tau p' m' l'}^{(j)} = \frac{k_j^3}{\rho_j \omega^2} \int_{S^{(j)}} [\hat{\mathbf{n}} \cdot \hat{\Phi}_{\tau p' m' l'}(\mathbf{r}) \lambda_j \boldsymbol{\nabla} \cdot \hat{\Psi}_{pml}(\mathbf{r} - \mathbf{d}^{(j)}) - \hat{\mathbf{n}} \cdot \mathbf{t}_-(\hat{\Phi}_{\tau p' m' l'}(\mathbf{r})) \hat{\mathbf{n}} \cdot \hat{\Psi}_{pml}(\mathbf{r} - \mathbf{d}^{(j)})] dA. \tag{25}$$

The functional dependence of $\mathbf{t}_-$ is explicitly displayed here to indicate it is no longer an unknown quantity.

There are not yet enough relations in Eqs. (22) and (23) to solve for all the unknowns present. To complete the solution, the last of the interior integral equations in Eq. (10) is used. Expansions for $\overline{\mathbf{G}}$ and $\overline{\Xi}$ obtained from Eqs. (8b) and (12) are inserted and the boundary conditions in Eqs. (19) and (21) are applied with the result

$$\frac{\overline{\kappa}^3}{\overline{\rho}\omega^2} \int_S [(\hat{\mathbf{n}} \times \mathbf{u}_-(\mathbf{r})) \cdot \mathbf{t}_-(\hat{\Phi}_{\tau pml}(\mathbf{r})) + \hat{\mathbf{n}} \cdot \mathbf{u}_+(\mathbf{r}) \hat{\mathbf{n}} \cdot \mathbf{t}_-(\hat{\Phi}_{\tau pml}(\mathbf{r})) - \hat{\mathbf{n}} \cdot \mathbf{t}_-(\mathbf{r}) \hat{\mathbf{n}} \cdot \hat{\Phi}_{\tau pml}(\mathbf{r})] dA = 0. \tag{26}$$

Equation (14) may be used to expand the unknown interior surface displacement and traction here but another expression is needed for the normal component of the exterior surface displacement present in the second term. The external displacement is not generally continuous upon crossing an interface of the host. However, the boundary condition in Eq. (19) ensures that the surface normal component of this field will be continuous on S if the interior field is continuous on S. Since the obstacle is elastic and smooth, its shear rigidity is expected to help smooth variations in the normal surface displacements along S. Therefore it will be assumed feasible to expand this field component in a convenient and complete basis set such as spherical harmonics or regular spherical partial waves. The present formulation will make use of the regular functions for this expansion; i.e.,

$$\hat{\mathbf{n}} \cdot \mathbf{u}_+(\mathbf{r}) = \sum_{pml} \xi_{pml} \hat{\mathbf{n}} \cdot \hat{\Psi}_{pml}(\mathbf{r}; k_+). \tag{27}$$

The wave-number dependence of the regular functions in this expansion need not be set equal to that of the layer containing the origin to ensure a complete basis. Therefore this dependence is displayed parametrically as k_+ because it will be convenient to adjust k_+ to optimize convergence later.

Upon inserting Eqs. (14) and (27) into Eq. (26), the following relation between the interior and exterior surface field expansion coefficients is found:

$$\sum_{p' m' l'} P_{\tau pml;p' m' l'}(k_+) \gamma_{p' m' l'} + \sum_{\tau' p' m' l'} R_{\tau pml;\tau' p' m' l'} \beta_{\tau' p' m' l'} = 0, \tag{28}$$

where

$$P_{\tau pml;p' m' l'}(k_+) = \frac{\overline{\kappa}^3}{\overline{\rho}\omega^2} \int_S \hat{\mathbf{n}} \cdot \hat{\Psi}_{p' m' l'}(\mathbf{r}; k_+) \times \hat{\mathbf{n}} \cdot \mathbf{t}_-(\hat{\Phi}_{\tau pml}(\mathbf{r})) dA, \tag{29}$$

$$R_{\tau pml;\tau' p' m' l'} = \frac{\overline{\kappa}^3}{\overline{\rho}\omega^2} \int_S [(\hat{\mathbf{n}} \times \hat{\Phi}_{\tau' p' m' l'}(\mathbf{r})) \cdot \mathbf{t}_-(\hat{\Phi}_{\tau pml}(\mathbf{r})) - \hat{\mathbf{n}} \cdot \mathbf{t}_-(\hat{\Phi}_{\tau' p' m' l'}(\mathbf{r})) \hat{\mathbf{n}} \cdot \hat{\Phi}_{\tau pml}(\mathbf{r})] dA. \tag{30}$$

Except for displaying the parametric dependence on k_+, Eq. (28) is the same relation used in Ref. 20 to complete the T matrix for scattering in a homogeneous fluid. By combining Eq. (28) with Eqs. (22) and (23), an analogous T matrix results for scattering in a stratified fluid, but now from each segment of the obstacle. Using a matrix notation, this is given by

$$\boldsymbol{\gamma}^{(j)} = \mathbf{T}^{(j)} \alpha(\mathbf{r}_s), \tag{31}$$

where

$$\mathbf{T}^{(j)} = -\hat{\mathbf{Q}}^{(j)} \mathbf{R}^{-1} \mathbf{P}(k_+) (\mathbf{Q} \mathbf{R}^{-1} \mathbf{P}(k_+))^{-1}. \tag{32}$$

In these equations, it is understood that $\mathbf{Q}$, $\hat{\mathbf{Q}}^{(j)}$, $\mathbf{P}(k_+)$, and $\mathbf{R}$ are matrices containing elements given by Eqs. (24), (25), (29), and (30), respectively, and $\alpha(\mathbf{r}_s)$ and $\boldsymbol{\gamma}^{(j)}$ are vectors with elements specified by Eqs. (16) and (31), respectively. Of course, each multiplication implies a vector contraction over the full range of spherical indices between the factors. It is useful to note that the square matrix $\mathbf{R}$ is symmetric[20] although the symmetry usually associated with the T matrix is lost in each of the $\mathbf{T}^{(j)}$ matrices.

The second method to derive T matrices for the obstacle segments involves applying the boundary conditions in a different way so that all the surface fields may be expanded in spherical harmonics. This cannot be done with the above approach because, unlike Eq. (14), field expansions in the spherical harmonics are not differentiable on S in the normal direction. To proceed, only the first boundary condition [Eq. (19)] is used in Eqs. (17) and (18) and the surface fields remaining to be specified are expanded as

$$\mathbf{u}_-(\mathbf{r}) = \sum_{\tau pml} \beta_{\tau pml} \mathscr{A}_{\tau pml}(\theta, \phi), \tag{33}$$

$$\hat{\mathbf{n}} \cdot \mathbf{t}_+(\mathbf{r}) = k_+ \lambda_+ \sum_{pml} \xi_{pml} Y_{pml}(\theta, \phi). \tag{34}$$

In Eq. (34), the wave number k_+ and Lamé parameter λ_+ are dummy variables retained for dimensional convenience. They may be set to unity later for numerical implementations without affecting the final results. Also, in regard to the viability of this expansion, note that the surface normal component of the external traction is assumed to be reasonably

smooth even when crossing host interfaces. This is based on the assumption of smoothly varying tractions along the interior surface of the elastic obstacle and the boundary condition in Eq. (20). The manipulations prescribed now lead to the relations

$$\alpha_{pml}(\mathbf{r}_s) = -i \sum_{\tau p' m' l'} L_{pml;\tau p' m' l'} \beta_{\tau p' m' l'} + i \sum_{p' m' l'} M_{pml;p' m' l'} \xi_{p' m' l'}, \tag{35}$$

$$\gamma_{pml}^{(j)} = i \sum_{\tau p' m' l'} \hat{L}_{pml;\tau p' m' l'}^{(j)} \beta_{\tau p' m' l'} - i \sum_{p' m' l'} \hat{M}_{pml;p' m' l'}^{(j)} \xi_{p' m' l'}, \tag{36}$$

where

$$L_{pml;\tau p' m' l'} = \frac{k_{(0)}^3}{\rho_{(0)} \omega^2} \sum_{j=1}^{N} \int_{S^{(j)}} \hat{\mathbf{n}} \cdot \mathscr{A}_{\tau p' m' l'}(\theta, \phi) \times \lambda_j \nabla \cdot \Psi_{pml}(\mathbf{r}) dA, \tag{37}$$

$$M_{pml;p' m' l'} = \frac{k_{(0)}^3 k_+ \lambda_+}{\rho_{(0)} \omega^2} \sum_{j=1}^{N} \int_{S^{(j)}} Y_{p' m' l'}(\theta, \phi) \times \hat{\mathbf{n}} \cdot \Psi_{pml}(\mathbf{r}) dA, \tag{38}$$

$$\hat{L}_{pml;\tau p' m' l'}^{(j)} = \frac{k_j^3}{\rho_j \omega^2} \int_{S^{(j)}} \hat{\mathbf{n}} \cdot \mathscr{A}_{\tau p' m' l'}(\theta, \phi) \lambda_j \times \nabla \cdot \hat{\Psi}_{pml}(\mathbf{r} - \mathbf{d}^{(j)}) dA, \tag{39}$$

$$\hat{M}_{pml;p' m' l'}^{(j)} = \frac{k_j^3 k_+ \lambda_+}{\rho_j \omega^2} \int_{S^{(j)}} Y_{p' m' l'}(\theta, \phi) \times \hat{\mathbf{n}} \cdot \hat{\Psi}_{pml}(\mathbf{r} - \mathbf{d}^{(j)}) dA. \tag{40}$$

To completely resolve all unknowns, the last of the interior integral equations in Eq. (10) is employed once again by inserting expansions for $\mathbf{G}$ and $\overline{\overline{\Xi}}$ and applying the remaining two boundary conditions [Eqs. (20) and (21)]. This yields

$$\frac{\overline{\kappa}^3}{\overline{\rho} \omega^2} \int_S [\mathbf{u}_-(\mathbf{r}) \cdot \mathbf{t}_-(\hat{\Phi}_{\tau pml}(\mathbf{r})) - \hat{\mathbf{n}} \cdot \mathbf{t}_+(\mathbf{r}) \hat{\mathbf{n}} \cdot \hat{\Phi}_{\tau pml}(\mathbf{r})] dA = 0. \tag{41}$$

When Eqs. (33) and (34) are used here, the relations needed to complete the scattering solution are obtained; i.e.,

$$\sum_{\tau' p' m' l'} \hat{D}_{\tau pml;\tau' p' m' l'} \beta_{\tau' p' m' l'} - \sum_{p' m' l'} \hat{E}_{\tau pml;p' m' l'} \xi_{p' m' l'} = 0, \tag{42}$$

where

$$\hat{D}_{\tau pml;\tau' p' m' l'} = \frac{\overline{\kappa}^3}{\overline{\rho} \omega^2} \int_S \mathscr{A}_{\tau' p' m' l'}(\theta, \phi) \cdot \mathbf{t}_-(\hat{\Phi}_{\tau pml}(\mathbf{r})) dA, \tag{43}$$

$$\hat{E}_{\tau pml;p' m' l'} = \frac{\overline{\kappa}^3 k_+ \lambda_+}{\overline{\rho} \omega^2} \int_S Y_{p' m' l'}(\theta, \phi) \hat{\mathbf{n}} \cdot \hat{\Phi}_{\tau pml}(\mathbf{r}) dA. \tag{44}$$

Except for leaving k_+ and λ_+ unspecified in $\hat{E}$, Eq. (42) is the same relation used in Ref. 24 to complete the T matrix for scattering in a homogeneous fluid. By solving Eqs. (35), (36), and (42) via matrix algebra, an analogous T matrix results for scattering from each segment of the obstacle in a stratified fluid. In matrix notation, this is

$$\mathbf{T}^{(j)} = -(\hat{\mathbf{L}}^{(j)} \hat{\mathbf{D}}^{-1} \hat{\mathbf{E}} - \hat{\mathbf{M}}^{(j)})(\mathbf{L} \hat{\mathbf{D}}^{-1} \hat{\mathbf{E}} - \mathbf{M})^{-1}. \tag{45}$$

Both Eqs. (32) and (45) represent formally exact solutions to the scattered field provided the assumptions regarding convergence of the various expansions used are valid. However, their convergence properties and numerical stability differ for obstacles of different shape and could therefore compliment each other in applications. This will be investigated for partially buried spheroids in the next section.

II. NUMERICAL APPLICATIONS

At this point, it is worthwhile to test the basic formulations on a few simple examples. Rather than attempting to optimize these formulations for computational speed or making a detailed analysis of scattering by partially buried obstacles, the emphasis is on demonstrating the viability of some of the basic assumptions made and uncovering the limitations in implementing these formulations numerically. Since spheroids are a convenient canonical shape for this kind of testing, this section will deal exclusively with such obstacles. More optimal formulations, experimental verifications, and investigations of the dynamics observed will be relegated to later efforts.

A. Acoustic scattering in a homogeneous host

First, the viability of decomposing the scattering solution as a superposition of fields scattered from segments of the obstacle is demonstrated. For this, a 3:1 aluminum prolate spheroid suspended in water is used. The density, compressional sound speed, and shear sound speed, respectively, used for the spheroid are 2.7 g/cm^3, 6.35×10^5 cm/s, and 3.05×10^5 cm/s. For water, the density and sound speed used are 1.0 g/cm^3 and 1.50×10^5 cm/s. A unit-amplitude plane wave is incident on the spheroid centered on the origin and the scattered amplitude is calculated $100a$ (a is the radius of the sphere circumscribing the spheroid) from the origin in the backscatter direction. In Fig. 3, the end-on and broadside backscatter responses of the spheroid are plotted as a function of the scaled wave number of water, ka. A resolution of 200 line-connected points is maintained in both curves.

Calculations based on the method described by Boström in Ref. 20 are used for the benchmark. These are given by the solid lines in Fig. 3. Circles superposed over the solid lines correspond to a calculation of the same responses but with the scattered field formed as a sum of contributions from three segments of the spheroid. The spheroid is segmented by dividing it into three equal length parts and auxiliary origins for the scattered field calculations are placed along the axis of the spheroid at midlength in each segment.

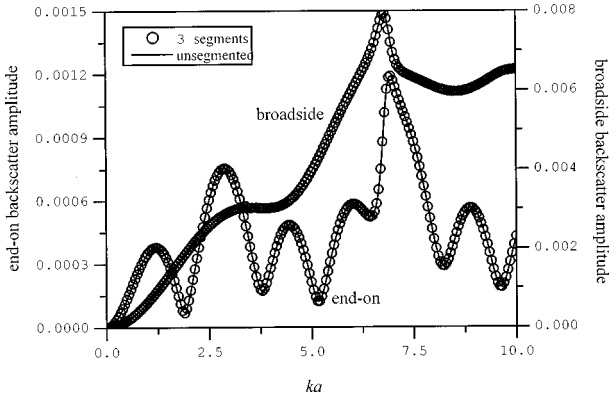

FIG. 3. Comparison of segmented T-matrix calculations with standard approach for a 3:1 aluminum prolate spheroid in water. The incident field is a unit-amplitude plane wave and the backscatter is determined $100a$ away.

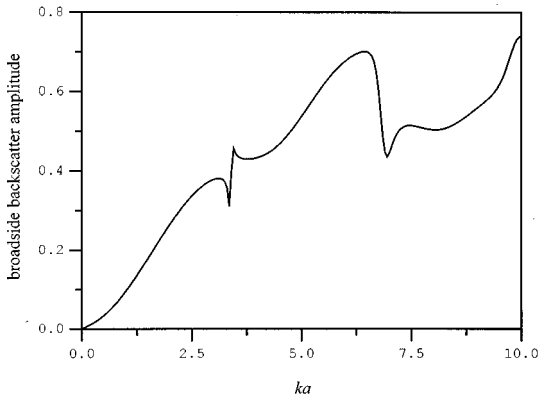

FIG. 4. Segmented T-matrix calculation for the same spheroid in Fig. 3 except 2 segments are used and the field is determined at $0.65a$ from the center of the obstacle for a broadside-oriented plane wave.

The segment T matrices are determined from the method embodied in Eq. (32) where the material parameters of the host layers (including k_+) have all been set to those of water. This simplifies the formulation considerably since the outgoing basis functions reduce to those of an unbounded homogeneous medium. Aside from these simplifications and those that could be incorporated due to the symmetry of the obstacle as described in Ref. 20, no special matrix techniques were used in the calculations. Surface integrals were simplified by performing the ϕ integration analytically and then using Gaussian quadrature for integration along the remaining surface coordinate. Matrix products involving an inversion such as $\mathbf{R}^{-1}\mathbf{P}(k_+)$ were performed with Gaussian elimination. The numerical precision of all calculations was about 15 significant figures. The maximum matrix truncations used in these calculations were 22 l and m values for the broadside calculations and 28 l values (with $m=0$ only) for the end-on calculations.

The plotted results clearly demonstrate the viability of scattering calculations with segmented T matrices. Calculations involving more segments have also been tried and all reproduce the benchmark. However, in maintaining the same precision in the final answer, the convergence of the individual segment fields is generally not observed to be any faster than for the entire obstacle using the standard formulation of Boström. Therefore aside from checking that the segmented approach works, there seems little reason to use it for scattering in a unbounded homogeneous host unless there is a need for the scattered field to converge closer to the obstacle than outside the circumscribing sphere. For example, consider the field backscattered to the Cartesian point $(-0.65a,\ 0,\ 0)$ when a unit-amplitude plane wave traveling in the positive x direction is incident broadside on the 3:1 spheroid above. Boström's method does not converge for points so close to the surface. However, per the assumptions made concerning the convergence of Eq. (15), it is expected that convergence should be possible with the spheroid segmented into two halves with the auxiliary origins for the scattered field at midlength in each segment. The corresponding calculation confirms this and Fig. 4 demonstrates this aspect of the segmented approach.

B. Acoustic scattering next to an interface

One of the problems with existing T-matrix formulations[4–6,10,11] for acoustic scattering by obstacles near an interface is that they are not expected to be applicable if the obstacle comes too close to the interface, even if it does not penetrate. The reason is that interactions between the obstacle and the interface in these formulations are taken into account by superposing effects translated from image positions. These translations are not expected to converge if the translation distance is shorter than the radius of the sphere that circumscribes the obstacle; hence, it cannot be too close to the host interfaces. The approach presented in the present paper eliminates the need to restrict the obstacle distance from host interfaces by formulating the T matrix without isolating the interactions in a matrix of translations. Instead, the interactions are directly accounted for in the mathematical representation of Huygens's principle embodied in Eqs. (17) and (18). This approach is also expected to be applicable when there is no interface penetration, by specifying the obstacle as a single segment in Eq. (32) or (45). The trade-off compared with the previous formulations is that, even for axisymmetric obstacles, the outgoing expansion basis, Eq. (3), leads to two-dimensional numerical integrations in evaluating the elements of $\mathbf{Q}$ in Eq. (32) or $\mathbf{L}$ and $\mathbf{M}$ in Eq. (45); i.e., the surface integral and the integral over horizontal wave number are not separated. Nevertheless, efficient means of evaluating these integrals are available and a test of the stability of the present approach with nearby interfaces will be presented.

The case to be considered involves scattering by an obstacle in the ocean bottom. The field scattered into the water half-space by a 1:3 oblate aluminum spheroid just under a water/sediment interface is determined. Material parameters for the spheroid and water are taken to be the same as in the previous example. The sediment is modeled as an attenuating fluid with density and (complex) sound speed given by 2.0 g/cm^3 and $(1.7\times10^5, -2.4\times10^3)$cm/s. Since the host is formed from two homogeneous half-spaces, the outgoing basis functions needed in the scattered field expansion and the T matrix may be simplified to

$$\Psi_{pml}(\mathbf{r})$$

$$= \left(\frac{\epsilon_m}{2\pi}\right)^{1/2} \frac{\nabla}{k_0} \begin{pmatrix} \cos m\phi, & p=e \\ \sin m\phi, & p=o \end{pmatrix} \int_0^\infty \frac{q\ dq}{k_0 h_0} B_{ml}\left(\frac{h_0}{k_0}\right)^{-1}$$

$$\times J_m(q\zeta) e^{ih_0 a_0} W_{0\to f} e^{ih_f(z-a_0)}, \quad z > a_0, \tag{46a}$$

$$= \left(\frac{\epsilon_m}{2\pi}\right)^{1/2} \frac{\nabla}{k_0} \begin{pmatrix} \cos m\phi, & p=e \\ \sin m\phi, & p=o \end{pmatrix} \int_0^\infty \frac{q\ dq}{k_0 h_0} B_{ml}\left(\frac{h_0}{k_0}\right)^{-1}$$

$$\times J_m(q\zeta) e^{ih_0 a_0} U_0 e^{-ih_0(z-a_0)}$$

$$+ \frac{1}{k_0} \nabla[\mathrm{h}_l^{(1)}(k_0 r) Y_{pml}(\theta,\phi)], \quad z < a_0. \tag{46b}$$

Here the reflection and transmission coefficients take the well-known form:[26]

$$W_{0\to f} = (1+U_0)\rho_0/\rho_f, \tag{47}$$

$$U_0 = \frac{\rho_f h_0 - \rho_0 h_f}{\rho_f h_0 + \rho_0 h_f}. \tag{48}$$

In all the results presented henceforth, the integrals in Eq. (46) as well as the surface integrals in the T matrix were done numerically by applying 32 point Gauss quadrature to enough segments of the specified integration contours to attain a stable, converged result. Generally, a criterion of error less than 1 part in 10^{10} was used to automatically terminate integrals over infinite ranges. However, the q integrations as specified in Eqs. (3) and (46) can be unstable due to singularities of the integrand on or near the real q axis. These were avoided by analytically deforming the integration contour in two ways. If the cylindrical coordinate ζ was not too large, standard arguments[27] were used to deform the contour into the fourth quadrant of the complex q plane on the physical sheet of the root functions, h_0 and h_f. This integration contour is depicted in Fig. 5(a). When ζ became large enough to slow the integration down (due to rapid oscillation of the integrand), the contour was rotated as follows:

$$\int_0^\infty q\ dq\ J_m(q\zeta) f(h_j) = \frac{1}{2} \int_C q\ dq\ H_m^{(1)}(q\zeta) f(h_j). \tag{49}$$

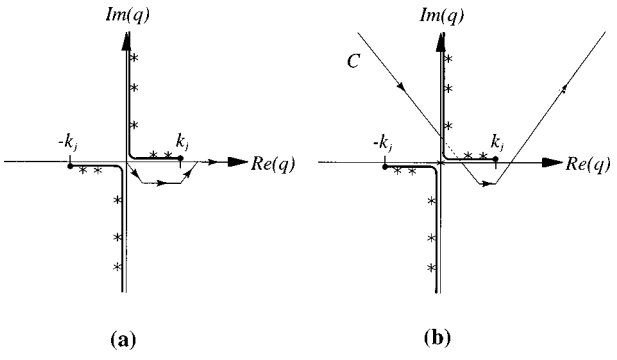

FIG. 5. Integration contours used to evaluate outgoing basis functions. Heavy lines and asterisks represent branch cuts and poles, respectively. Note that the contour in (b) passes under the physical sheet to avoid the pole at the origin.

Here $H_m^{(1)}$ is a cylindrical Hankel function and the contour C encloses the singularities that displace into the top half of the physical complex q plane when the host layers are made attenuating. The singularity of $H_m^{(1)}$ at the origin is avoided by taking the integration contour under the physical sheet when branch cuts are crossed on going around the origin. This integration contour is depicted in Fig. 5(b).

With these considerations input both into Eqs. (32) (setting k_+ equal to the wave number of the sediment containing the spheroid) and (45), the backscatter response of the oblate spheroid can be calculated and compared to previous formulations. A case study is presented in Table I. The axis of the spheroid is oriented normal to the planar interface and its center is considered at the three depths (d): $0.34a, a$, and $2a$. The incident field originates from an on-axis harmonic point source in the water $100a$ above the spheroid's center. The displacement amplitude backscattered to the source position is calculated and this is scaled by the displacement amplitude due to a free-field source in water $100a$ away by setting the scale factor F in Eq. (16) to

$$F = \left| \frac{4\pi}{k_s} \left(\frac{d\mathrm{h}_0^{(1)}(k_s r)}{d(k_s r)} \right)^{-1} \right|_{r=100a}. \tag{50}$$

A frequency corresponding to $k_f a = 5$ is used and results for five different truncations of the l index of the T matrix are shown. (Here and in all subsequent calculations, k_f and k_s are both equal to the wave number of water.) In Table I, the present T-matrix formulations are tested and compared both with each other and with a reference formulation described in Ref. 5 which superposes effects translated from image positions.

Table I demonstrates good agreement between the reference approach and those developed in the present work when the obstacle is centered at least as far away from the interface as the radius of its circumscribing sphere. Note that both the reference approach and that based on Eq. (32) also display ill-conditioning problems when the truncation is overspecified. This has been observed before in free-field scattering calculations with a T matrix using regular spherical partial waves to expand the obstacle surface fields.[24,28] Since the surface fields in both the reference solution and Eq. (32) were treated this way, it is understandable that they would have similar convergence characteristics. On the other hand, when spherical harmonics are used to expand the surface fields, calculations remain stable with higher truncations but convergence is slower. This aspect of using spherical harmonic surface field expansions was observed before with spheroids by Boström;[24] although it was also found that these expansions yielded stable T matrices for more diverse obstacle shapes.

The performance exhibited by the various methods grows more interesting when the spheroid is brought very close to the interface ($d = 0.34a$). Although the reference formulation appears to converge, the values produced at each truncation became sensitive to the number of Gauss quadrature points in the integrations. The source of the sensitivity seemed to be in the part of the T matrix that accounts for interactions with the interface. This sensitivity (about 2% to

TABLE I. The displacement amplitude backscattered by a 1:3 oblate Al spheroid at $k_f a = 5$ and for three burial depths below a water/sediment interface. Five truncations of the l index are shown and numerical performance of the matrix formulations in Eqs. (32), (45), and a standard reference formulation are compared.

		l truncation				
d	Method	20	23	25	28	40
	Ref.	0.009 81	0.009 84	0.009 91	0.009 92	0.009 91
$0.34a$	Eq. (32)	0.010 26	0.010 26	0.010 26	0.010 26	0.161 94
	Eq. (45)	0.010 20	0.010 23	0.010 24	0.010 25	0.010 26
	Ref.	0.011 38	0.011 38	0.011 38	0.011 38	0.021 18
a	Eq. (32)	0.011 38	0.011 38	0.011 38	0.011 38	0.027 32
	Eq. (45)	0.011 34	0.011 36	0.011 37	0.011 37	0.011 38
	Ref.	0.010 55	0.010 55	0.010 55	0.010 55	0.024 33
$2a$	Eq. (32)	0.010 55	0.010 55	0.010 55	0.010 55	0.068 40
	Eq. (45)	0.010 49	0.010 52	0.010 53	0.010 54	0.010 55

3%) could not be reduced with increasing the number of quadrature points; thus, the answer obtained from the reference method might be questionable. However, the other two methods retain the same level of stability seen at the other depths. Here the rate of convergence is little affected by proximity to the interface and the fact that both of these methods converge to the same answer lends strength to it being the true answer.

While it was expected that the reference formulation would break down, it is noteworthy that its predictions remained within a few percent of the true answer for each of the truncations. Since the reference formulation is also fastest to implement (as much as four times faster in obtaining the results above), it is tempting to use it beyond its usual range of validity. Nonetheless, its apparent stability should be accepted with caution given the inability to finally converge to the correct answer.

C. Acoustic scattering by an obstacle penetrating an interface

The final tests of the scattering solutions in Eqs. (32) and (45) will involve an obstacle allowed to penetrate through an interface of the host. The same water/sediment environment and aluminum obstacle parameters examined above will be used. As before, a backscattered field will be calculated in the water half-space. The outgoing basis functions required to evaluate the T-matrix segment in the sediment and expand the field scattered from this segment remain the same as in Eq. (46) except for redefining coordinate origins when needed. However, for the segment in the water half-space, outgoing functions centered in this half-space are also needed. From Eq. (3), these may be expressed in the simplified form

$$\Psi_{pml}(\mathbf{r}) = \left(\frac{\epsilon_m}{2\pi}\right)^{1/2} \frac{\nabla}{k_0} \begin{pmatrix} \cos m\phi, & p=e \\ \sin m\phi, & p=o \end{pmatrix} \times \int_0^\infty \frac{q\,dq}{k_0 h_0} B_{ml}\left(\frac{h_0}{k_0}\right) J_m(q\zeta) e^{-ih_0 b_0} V_0 e^{ih_0(z-b_0)} + \frac{1}{k_0} \nabla[\mathrm{h}_l^{(1)}(k_0 r) Y_{pml}(\theta,\phi)], \quad z > b_0, \tag{51}$$

with V_0 given by the same expression used for U_0 in Eq. (48) except with the understanding that the interpretation of the subscripts is now reversed; i.e., the origin layer for these basis functions is water rather than sediment. Of course b_0, the vertical coordinate of the interface below, is also measured relative to the segment origin set in the water.

In the calculations to follow, the auxiliary origin for each of the axisymmetric segments is placed along the axis of the segment at the midpoint of its vertical dimension. The primary origin, for the incident and surface field expansions, is always placed at the midpoint of the obstacle. If the midpoint is on the water/sediment interface, the outgoing basis functions needed in Eqs. (24), (37), or (38) are evaluated assuming the primary origin is on the sediment side of the interface. The unspecified external surface wave number k_+ in Eq. (32) is chosen by setting it to the value appropriate for aluminum. This choice follows from numerical trials that indicate greater stability in the resulting T matrix when smaller values for this parameter are used. (Of course, there is no reason other than convenience for choosing a value for k_+ that corresponds to one of the materials used; an arbitrary value would work also.) With these details accounted for, some examples are considered.

First, the stability of the formulations embodied in Eqs. (32) and (45) for half-buried spheroids are considered as a function of aspect ratio (axial length/width). As in previous calculations, no special matrix techniques were used to enhance stability and 15 figure precision was used. An on-axis point source is used to illuminate a spheroid from $20a$ above its center and the backscatter is calculated at the source location. In Table II, backscattered displacement amplitudes are presented for seven aspect ratios from 1:3 oblate to 3:1 prolate and 5 truncations of the l index. For convenience, the backscatter is scaled by the source strength in free-field $20a$ away; i.e., Eq. (50) is used with $r = 20a$. For this exercise, a frequency corresponding to $k_f a = 5$ is chosen.

Table II demonstrates that a segmented T matrix can be used to calculate with high accuracy the scattering by three-dimensional obstacles that penetrate a host layer. However, convergence is at least as sensitive to obstacle shape and how the surface fields are treated as it is in free-field scattering. For aspect ratios less than 1, faster convergence is still the

TABLE II. Displacement amplitudes backscattered by an Al spheroid half-buried at a water/sediment interface for $k_f a = 5$. Seven aspect ratios for the spheroid are considered. Numerical performance of the matrix formulations in Eqs. (32) and (45) are assessed by comparing results at five truncations of the l index.

Aspect ratio	Method	l truncation				
		20	23	25	28	40
0.333 33	Eq. (32)	0.123 83	0.123 80	0.123 79	0.123 78	0.243 86
	Eq. (45)	0.123 15	0.123 73	0.123 87	0.123 93	0.123 96
0.5	Eq. (32)	0.013 59	0.103 60	0.103 60	0.103 60	0.103 60
	Eq. (45)	0.103 50	0.103 58	0.103 58	0.103 59	0.103 60
0.666 67	Eq. (32)	0.065 55	0.065 56	0.065 56	0.065 56	0.065 56
	Eq. (45)	0.065 54	0.065 55	0.065 55	0.065 56	0.065 56
1	Eq. (32)	0.066 09	0.066 10	0.066 10	0.066 10	0.066 10
	Eq. (45)	0.066 09	0.066 10	0.066 10	0.066 10	0.066 10
1.5	Eq. (32)	0.021 56	0.021 62	0.021 81	0.021 39	0.020 99
	Eq. (45)	0.021 69	0.021 70	0.021 70	0.021 70	0.021 70
2	Eq. (32)	0.053 98	0.056 97	0.055 45	0.058 32	0.089 40
	Eq. (45)	0.010 35	0.010 80	0.007 88	0.009 53	0.009 58
3	Eq. (32)	0.050 85	0.086 33	0.347 84	0.206 87	0.134 93
	Eq. (45)	0.003 52	0.003 88	0.002 82	0.004 42	0.002 92

norm for spheroids with surface fields expanded in regular partial waves rather than spherical harmonics. Here the only caveat to be noted in the use of regular partial waves is possible ill-conditioning when the truncation is overspecified. As the obstacle grows more spherical the difference in performance disappears and both methods seem to become more stable. But, the situation seems to reverse for prolate objects. Here the method based on spherical harmonics appears to perform better. At an aspect ratio of 1.5, the method based on regular partial waves is clearly starting to have problems while the other method remains stable.

Nevertheless, both methods appear to lose effectiveness for higher aspect ratios. When the ratio reaches 2, the approach using Eq. (32) is clearly producing incorrect results and that using Eq. (45) exhibits much slower convergence. The poor stability of Eq. (32) tends to coincide with poor condition numbers when manipulating matrices with Gaussian elimination; thus, ill-conditioned inverses may be to blame. Notably, the stability (and the matrix condition numbers) sometimes improved by going to higher frequency. This is consistent with ill-conditioning problems in T-matrix solutions, which tend to occur with higher truncations as the frequency is raised. Therefore if convergence improves fast enough to overtake ill-conditioning problems, better results are obtained.

The difficulties exhibited above are expected to be typical and not limited to the present set of system parameters. However, that does not preclude their resolution. The sensitivity of these problems to how the surface fields are expanded suggests that the answer lies in identifying a more appropriate choice of basis for representing these fields. For example, to model elongated obstacles that penetrate layers of the host, a more useful basis for the surface fields might be spheroidal harmonics. While this choice will not be implemented here, the generality of the formulation leading to Eq. (45) makes this choice straightforward to incorporate.

To conclude this section, a few sample calculations of backscatter spectra will be presented to further illustrate the formulations. Figures 6 and 7 demonstrate how the spectral response of an aluminum sphere is modified by three states of burial at the planar water/sediment interface previously specified. In Fig. 6, a point source in the water half-space $20a$ directly above the sphere is used. In Fig. 7, the source is still in the water, $20a$ from the sphere, but now lies on a line that slants 45° from horizontal and passes through the sphere center. For both cases, the amplitude of the displacement field backscattered to the source is plotted over the range $0 \leqslant k_f a \leqslant 10$ for the center of the sphere $1.1a$ above, centered on, and $1.1a$ below the interface. (Note that centering the sphere on the interface leads to no computational advantages; it is merely a convenient choice for the purpose of

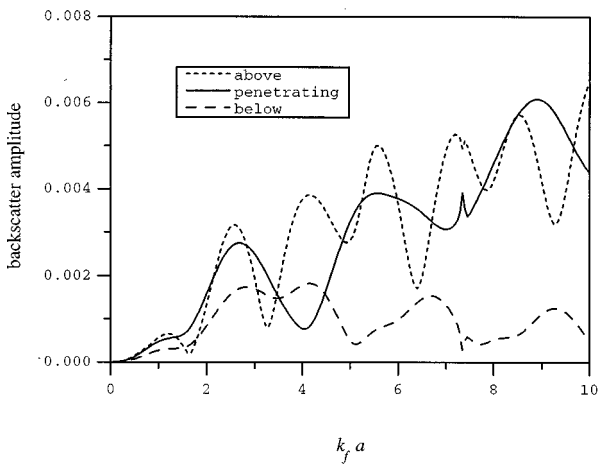

FIG. 6. Backscatter amplitudes for an aluminum sphere of radius a above, below, and centered on a water/sediment interface. The spheres above and below are centered $1.1a$ from the interface. A point source is in the water half-space, $20a$ above the sphere. Amplitudes are scaled by the source strength at one radius from the source.

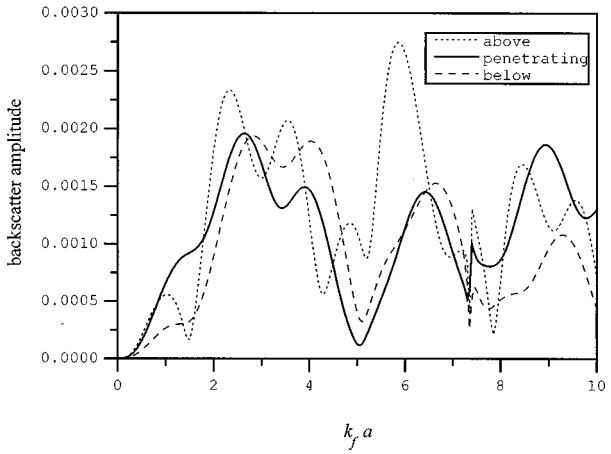

FIG. 7. The spheres above and below are centered $1.1a$ from the interface. A point source is $20a$ from the sphere in the water half-space on a line slanted 45° from the horizontal and passing through the center of the sphere. Amplitudes are scaled by the source strength at one radius from the source.

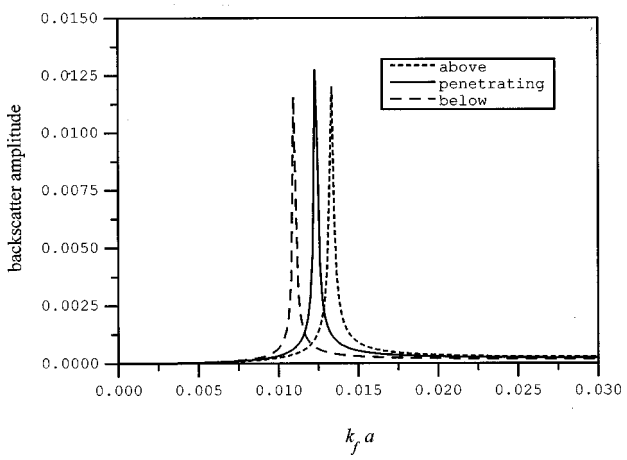

FIG. 8. Backscatter amplitudes for an air bubble of radius a above, below, and centered on a water/sediment interface. The bubbles above and below are $1.1a$ from the interface. A point source in the water half-space, $20a$ above the bubble, is used.

illustration.) The maximum l and m truncations used in the calculations were 23 (although only $m=0$ was required for Fig. 6) and 200-point resolution is maintained in each curve. All amplitudes are scaled by the free-field source strength at one radius from the source.

In these examples, oscillations associated with interference of specularly scattered sound from the sphere with radiation of circumnavigating Franz waves are seen to be strongly modified by the local environment. It is notable that, when the source is directly overhead, the lower backscatter predicted for the completely buried sphere is not due to attenuation of the diffracted field by the sediment. Removing attenuation from the calculations produces a minor enhancement of the buried spectrum compared to the relative difference between the buried and partly buried or unburied spectra. In fact, the amplitude of the buried spectrum here is closer to that of a free-field sphere in water (not shown) than the other two cases. This suggests that a more likely explanation for the general disparity in amplitude is that the partly buried and unburied spectra are enhanced by the waves that are normally diffracted or scattered forward by the sphere but are now reflected up by the interface. This seems to be consistent with the spectra obtained when the source is moved to the side; since much of the energy diffracted or scattered in the forward direction could now reflect off the water/sediment interface at a different specular angle, any enhancement due to the surface is less pronounced. Of course, this disparity is expected to become pronounced again if the source is moved closer to the water/sediment interface, especially as the frequency increases. Due to high reflection near and beyond the incident angle that would be ''critical'' for the equivalent nonattenuating bottom, the illumination of the buried sphere would decrease while that of the unburied sphere would increase.

While the inhomogeneous host produces strong changes in the backscatter spectra, positions of the sphere's normal-mode resonances are not altered much. The sharp feature at about $k_f a=7.35$ in both Figs. 6 and 7 is a resonance of the sphere in the $l=1$ partial wave that is normally associated with a whispering gallery wave. It is manifested as a peak or dip depending on how it interferes with the background field, but it appears at the same frequency irrespective of burial state or source location. Broader features associated with resonances of the Rayleigh wave are also present but less conspicuous; e.g., see the dip in the unburied sphere spectrum of Fig. 7 just below $k_f a=8$. These features are less helpful in locating the corresponding resonances but they also occur about where they normally do in the free-field spectrum.

As a final example, Fig. 8 demonstrates how the spectral scattering response around the monopole resonance of a spherical air bubble is modified by the same burial states used with the aluminum sphere. A point source in the water half-space $20a$ above the bubble is used and the amplitude of the displacement field backscattered to the source is plotted out to $k_f a=0.03$. The sound speed and density used for air are 344 m/s and 0.001 29 g/cm^3. An acceptably low shear speed was used in the T matrix to approach a fluid limit for the elastic obstacle without introducing numerical problems. [In this regard, it is remarkable that stability of the scattering solution did not appear to be compromised by the obstacle's low shear strength even though this might cause exterior field expansions such as Eqs. (27) or (34) to converge poorly at the intersection of the bubble surface with the host interface.] The maximum T-matrix truncation used here was $8l$ values. As before, Fig. 8 is plotted with 200 point resolution and the displacement amplitude is scaled by the free-field source strength at one radius from the source. Note that the effect of the local environment on the dynamics of the bubble is primarily inertial; the monopole shifts in frequency in accord with the local mass loading.

III. SUMMARY AND CONCLUSIONS

A viable way to calculate the field scattered by a three-dimensional, bounded, elastic obstacle that penetrates layers of a plane-stratified fluid host is to formulate a T matrix for the scattering by each segment of the obstacle in a given

layer. This can be done without introducing the convergence problems encountered in past T-matrix formulations for obstacles brought near interfaces by accounting for obstacle–host interactions directly in the representation of Huygens' principle that is derived from the Helmholtz integral equations. To accomplish this, the outgoing fields of all segments and the Green's dyadic for the layered host are expanded in outgoing bases that obey the boundary conditions of the host. A suitable set of functions for this purpose has been specified in previous work and a slightly modified version is used here. By using the representation of Huygens' principle, boundary conditions on the obstacle surface are used to couple the scattered segment field expanded around each segment origin to the interior surface field of the obstacle. By using surface field expansions that remain centered on the primary origin of the obstacle, a T matrix is obtained for each segment in a familiar form. The final result is a solution to the Helmholtz equation that is formally exact provided assumptions regarding the convergence of the Green's dyadics and field expansions are valid. Also, in common with scattering solutions based on the T-matrix approach, the present solution remains insensitive to the nonuniqueness problems associated with other approaches such as the boundary element method.[29–31]

However, the segmented T-matrix formulations come with a few practical caveats. Since the outgoing basis functions used require an integration over horizontal wave number, they cannot be computed as quickly as basis sets normally used in an unbounded medium. Fast techniques for accurately evaluating these functions need to be found to allow the present formulations to be used over higher frequency ranges or to model nonaxisymmetric obstacle–host arrangements. Possible solutions include the use of asymptotic approximations for these integrals, evaluation with fast-field methods such as those used to compute the Green's dyadic,[22,23] or applying adaptive integration techniques.[32] Another problem lies in the range of obstacle shapes that can be treated with the present approach without numerical instability. This range is sensitive to how the surface fields are treated. Two standard methods of expanding these fields were tried in this work but numerical tests of both formulations suggest that the range of applicable shapes will be more limited than in free-field scattering problems. Nevertheless, this problem can perhaps be ameliorated by replacing the spherical harmonic basis used in Eq. (45) with one better suited to the geometry of the obstacle. For example, the spheroidal harmonics may be the ideal choice for elongated obstacles even though they are not popular as a basis set because they are not as easy to compute as the spherical functions. The success of spheroidal functions in T-matrix formulations for elongated obstacles has been discussed elsewhere.[33,34]

The utility of the present work is in making possible benchmark quality predictions for more realistic scattering problems. The examples given in the previous section reflect an interest in ocean acoustics although extensions to other areas are possible. In principle, the present methods can be extended to allow scattering in elastic or poroelastic layered hosts since suitable basis sets and expansions of the layered medium Green's dyadics in these basis sets are available.[14] Such extensions would be of interest in nondestructive evaluation and geophysical exploration as well as ocean acoustics. Another, more straightforward extension would be to make the obstacle inhomogeneous within the present framework. Since the segmented T matrix treats the interior field of the obstacle in the same manner as in standard formulations, it should be possible to incorporate interior layering in analogy to an existing approach.[24] These extensions will be investigated in later work.

ACKNOWLEDGMENTS

This work was supported by the Office of Naval Research's Ocean Acoustics Program (Program Manager: Jeff Simmen) and the Coastal Systems Station's Independent Research Program.

[1] K. S. Yee, ''Numerical solution of initial boundary value problems involving Maxwell's equations in isotropic media,'' IEEE Trans. Antennas Propag. **AP-14**, 302–307 (1966).
[2] R. A. Stephen, ''A review of finite difference methods for seismoacoustics: Problems at the seafloor,'' Rev. Geophys. **26**, 445–458 (1988).
[3] R. A. Stephen and S. A. Swift, ''Modeling seafloor geoacoustic interaction with a numerical scattering chamber,'' J. Acoust. Soc. Am. **96**, 973–990 (1994).
[4] A. Karlsson, ''Scattering from inhomogeneities in layered structures,'' J. Acoust. Soc. Am. **71**, 1083–1092 (1982).
[5] R. H. Hackman and G. S. Sammelmann, ''Multiple scattering analysis for a target in an oceanic waveguide,'' J. Acoust. Soc. Am. **84**, 1813–1825 (1988).
[6] R. Lim, ''Multiple scattering by many bounded obstacles in a multilayered acoustic medium,'' J. Acoust. Soc. Am. **92**, 1593–1612 (1992).
[7] M. G. Imhof, ''Multiple multipole expansions for acoustic scattering,'' J. Acoust. Soc. Am. **97**, 754–763 (1995).
[8] J. A. Fawcett, ''The computation of the scattered pressure field from a cylinder embedded between two half-spaces with different densities,'' J. Acoust. Soc. Am. **99**, 2435–2438 (1996).
[9] J. A. Fawcett, ''Acoustic scattering from cylindrical objects embedded between two half-spaces,'' J. Acoust. Soc. Am. **100**, 3053–3060 (1996).
[10] A. Boström and G. Kristensson, ''Elastic wave scattering by a three-dimensional inhomogeneity in a half-space,'' Wave Motion **2**, 335–353 (1980).
[11] A. Boström and A. Karlsson, ''Broad-band synthetic seismograms for a spherical inhomogeneity in a many-layered elastic half-space,'' Geophys. J. R. Astron. Soc. **89**, 527–547 (1987).
[12] A. Lakhtakia, V. V. Varadan, and V. K. Varadan, ''Reflection characteristics of an elastic slab containing a periodic array of circular elastic cylinders: P and SV wave analysis,'' J. Acoust. Soc. Am. **83**, 1267–1275 (1988).
[13] P. Gerstoft and H. Schmidt, ''A boundary element approach to ocean seismoacoustic facet reverberation,'' J. Acoust. Soc. Am. **89**, 1629–1642 (1991).
[14] R. Lim, ''Scattering by an obstacle in a plane-stratified poroelastic medium: Application to an obstacle in ocean sediments,'' J. Acoust. Soc. Am. **95**, 1223–1244 (1994).
[15] R. Lim, ''Acoustics of layered poroelastic obstacles in poroelastic hosts,'' in *Proceedings Design Technical Conference: Acoustics Vibrations and Rotating Machines* (ASME, New York, 1995), Vol. 2, Pt. 3B.
[16] E. Bahar, ''Depolarization of electromagnetic waves excited by distributions of electric and magnetic sources in inhomogeneous multilayered structures of arbitrarily varying thickness. Generalized field transforms,'' J. Math. Phys. **14**, 1502–1515 (1973).
[17] See, for example, L. M. Brekhovskikh and O. A. Godin, *Acoustics of Layered Media I: Plane and Quasi-Plane Waves* (Springer-Verlag, Berlin, 1990), Sec. 2.5. However, remember that pressure field and potential field transmission coefficients are scaled differently.
[18] A heuristic justification of the convergence assumption can be argued by looking for the singularities of the exact integral representation of the Green's dyadic. The integral representation is given by applying gradients,

as prescribed above Eq. (5a), to Eq. (9) or (10) from Ref. 6. To find where the closest singularity of the Green's dyadic lies, one inspects the leading asymptotic large q behavior of the integrand since this behavior determines whether the integral will diverge or not. By doing so, one can demonstrate that its large q behavior approaches that of the integrand in the free-field Green's dyadic with source at the physical source location. [To see this, one can either use reflection and transmission coefficients for specific cases or make the physically motivated assumptions that the reflection coefficients remain finite as a function of q and the transmission coefficients behave, for large q, like a constant multiplied by a propagation factor appropriate for the thickness transmitted through.] This suggests that the physical source location is the closest singularity and the same convergence radius appropriate for the free-field expansions will apply. Note that if one expands the denominators of the integrands in geometric series and looks at the terms with more propagation and reflection-coefficient factors, one can demonstrate that their large q behavior approaches that of free-field Green's dyadic integrands with ''image'' source locations, which are farther away.

[19] P. M. Morse and H. F. Feshbach, *Methods of Theoretical Physics* (McGraw-Hill, New York, 1953), Chap. 13.

[20] A. Boström, ''Scattering of stationary acoustic waves by an elastic obstacle immersed in a fluid,'' J. Acoust. Soc. Am. **67**, 390–398 (1980).

[21] Y.-H. Pao and V. Varatharajulu, ''Huygens' principle, radiation conditions, and integral formulas for the scattering of elastic waves,'' J. Acoust. Soc. Am. **59**, 1361–1371 (1976).

[22] F. R. DiNapoli and R. L. Deavenport, ''Theoretical and numerical Green's function field solution in a plane multilayered medium,'' J. Acoust. Soc. Am. **67**, 92–105 (1980).

[23] H. Schmidt and F. B. Jensen, ''A full wave solution for propagation in multilayered viscoelastic media with application to Gaussian beam reflection at fluid–solid interfaces,'' J. Acoust. Soc. Am. **77**, 813–825 (1985).

[24] A. Boström, ''Scattering of acoustic waves by a layered elastic obstacle in a fluid—An improved null field approach,'' J. Acoust. Soc. Am. **76**, 588–593 (1984).

[25] P. C. Waterman, ''Matrix theory of elastic wave scattering,'' J. Acoust. Soc. Am. **60**, 567–580 (1976).

[26] See, for example, L. M. Brekhovskikh, *Waves in Layered Media* (Academic, New York, 1980), 2nd ed., Sec. 3.

[27] See, for example, L. B. Felsen and N. Marcuvitz, *Radiation and Scattering of Waves* (Prentice-Hall, Englewood Cliffs, NJ, 1973), Sec. 5.3.

[28] W. Tobocman, ''Comparison of the T-matrix and Helmholtz integral equation methods for wave scattering calculations,'' J. Acoust. Soc. Am. **77**, 369–374 (1984).

[29] H. A. Schenck, ''Improved integral formulation for acoustic radiation problems,'' J. Acoust. Soc. Am. **44**, 41–58 (1968).

[30] A. J. Burton and G. F. Miller, ''The application of integral equation methods to the numerical solution of some exterior boundary value problems,'' Proc. R. Soc. London, Ser. A **323**, 201–210 (1971).

[31] R. P. Shaw and S. C. Huang, ''The fictitious eigenvalue difficulty in the T-matrix and the BEM methods for exterior wave scattering,'' J. Acoust. Soc. Am. **86**, 839–842 (1989).

[32] S. Ivansson and I. Karasalo, ''A higher-order adaptive integration method for wave propagation in range-independent fluid–solid media,'' J. Acoust. Soc. Am. **92**, 1569–1577 (1992).

[33] R. H. Hackman, ''Acoustic scattering from elastic solids,'' in *Underwater Scattering and Radiation, Phys. Acoust., vol. 22*, edited by A. D. Pierce and R. N. Thurston (Academic, San Diego, 1994), pp. 1–194.

[34] R. H. Hackman and R. Lim, ''Development and application of the spheroidal coordinate based T matrix solution to elastic wave scattering,'' Radio Sci. **29**, 1035–1049 (1994).

Wave propagation in range-dependent poro-acoustic waveguides

Joseph F. Lingevitch and Michael D. Collins
Naval Research Laboratory, Washington, DC 20375

(Received 4 April 1997; revised 9 January 1998; accepted 16 April 1998)

The parabolic equation method is extended to handle range-dependent poro-acoustic waveguides. A poro-acoustic medium is the limiting case of a poro-elastic medium in which the shear wave speed vanishes. Recent experiments indicate that this is a relevant limit [Chotiros, ''Biot model of sound propagation in water-saturated sand,'' J. Acoust. Soc. Am. **97**, 199–214 (1995)]. Energy-conserving and single-scattering techniques are developed for handling vertical interfaces. The single-scattering solution is extended to problems involving fluid layers above poro-acoustic sediments. Improved rational function approximations are developed by rotating the branch cut [Milinazzo *et al.*, ''Rational square-root approximations for parabolic equation algorithms,'' J. Acoust. Soc. Am. **101**, 760–766 (1997)]. [S0001-4966(98)05507-6]

PACS numbers: 43.30.Gv, 43.30.Ky, 43.30.Ma, 43.20.Mv [SAC-B]

INTRODUCTION

The theory of poro-elasticity has been proposed as a model for sediments to account for acoustic properties not explained by the fluid and elastic theories.[1–6] For example, recent experiments have shown bottom penetration below the critical grazing angle.[7] Since a poro-elastic sediment supports slow and fast compressional waves, the slow wave may be the mechanism for bottom penetration. The same experiments also suggest that the shear wave speed can be an order of magnitude smaller than the compressional wave speeds. This would imply that the limiting case of vanishing shear wave speed, a poro-acoustic sediment, is physically relevant.[8] The poro-acoustic formulation has the advantage that the small length scale associated with the shear wave need not be resolved. For lossless media, the vector wave equation of poro-acoustics is a self-adjoint generalization of the scalar wave equation of acoustics.

In this paper, we implement a parabolic equation (PE) formulation of the poro-acoustic equations and compare methods for treating vertical interfaces in range-dependent media. The PE method can be used to solve wave equations when the field is dominated by outgoing energy.[9] For range-independent propagation, the PE is an exact factorization of the wave equation into its incoming and outgoing components; range dependence couples the incoming and outgoing waves. Accurate PE modeling of the outgoing wave in range-dependent environments has been carefully studied for acoustic propagation.[10–13] The energy conserving PE conserves the outgoing energy flux across vertical interfaces in range-dependent environments and is motivated by the WKB solution for a slowly varying medium. The single-scattering method imposes exact interface conditions at a vertical interface but neglects multiple-scattering events. Both methods yield accurate results for acoustic propagation when the backscattered energy is negligible. In contrast, pressure conserving solutions in the same environments lead to amplitude errors in the transmitted field. We extend the energy-conserving and single-scattering interface conditions to poro-acoustic media and compare them with the pressure conserving solution.

Rotated Padé approximations of the square root of an operator provide improved stability.[14] We extend this approach to more general operators. This approach is based on matching derivatives with a function whose branch cut has been rotated off the negative real line into the lower half of the complex plane. Rotated Padé approximations are useful for accurately treating the evanescent as well as propagating modes in a waveguide. They are of interest in this paper because they provide improved convergence of the iteration formula in the single-scattering method.

In Sec. I, the poro-acoustic sediment parameters and equations of motion are defined. The rotated Padé approximation for the PE operators is formulated in Sec. II. In Sec. III, the vertical interface conditions for a poro-acoustic waveguide and fluid/poro-acoustic waveguide are examined. In Sec. IV, several examples illustrate propagation in range-dependent poro-acoustic waveguides.

I. PORO-ACOUSTIC EQUATIONS OF MOTION

In this section, the poro-acoustic PE is derived for a range-independent region. Range-dependent environments are approximated as a series of range-independent regions separated by vertical interfaces. The field is propagated through each range-independent region with the PE method. Approximate interface conditions are enforced at the vertical interfaces to estimate the transmitted field. The vertical interface conditions are discussed in Sec. III.

We consider a stratified medium in the vertical direction parametrized by Cartesian coordinates, where x is the range from the source and z is the depth below a free surface. The poro-acoustic equations of motion are a vector generalization of the scalar Helmholtz equation for pressure.[8] In terms of the pore fluid stress σ and the total stress σ_{zz}, they are

$$\frac{\partial^2 \mathbf{p}}{\partial x^2} + R\,\frac{\partial}{\partial z}\left(R^{-1}\,\frac{\partial \mathbf{p}}{\partial z}\right) + K^2 \mathbf{p} = \mathbf{0}, \tag{1}$$

$$\mathbf{p} = \begin{pmatrix} \sigma_{zz} \\ \sigma \end{pmatrix}, \tag{2}$$

$$R=\begin{pmatrix}\rho & \rho_f\\ \rho_f & \rho_c\end{pmatrix}, \tag{3}$$

$$L=\begin{pmatrix}\lambda & C\\ C & M\end{pmatrix}, \tag{4}$$

$$K^2=\omega^2 RL^{-1}, \tag{5}$$

where ω is the circular frequency of the time-harmonic source.

A poro-acoustic medium is defined by ten material parameters: porosity α, pore fluid density ρ_f, fluid bulk modulus K_f, solid density ρ_b, added mass coefficient τ, fluid viscosity η, permeability κ, frame bulk modulus K_b, and the bulk modulus of the sediment grains K_r. In general, K_b is complex to allow for attenuation by the frame; the other material parameters are real quantities. The densities ρ and ρ_c in Eq. (3) are related to the material parameters by

$$\rho=(1-\alpha)\rho_b+\alpha\rho_f, \quad \rho_c=\frac{\rho_f(1+\tau)}{\alpha}+i\frac{\eta}{\kappa\omega}. \tag{6}$$

The moduli C, M, and λ in Eq. (4) are related to K_b, K_f, K_r, α by the relations in Refs. 7 and 15. A poro-acoustic medium supports slow and fast compressional waves with complex wave speeds $\overline{c_j}$ $(j=1,2)$ given in terms of the material parameters by,[15]

$$\overline{c_j}=\left(\frac{F\pm\sqrt{F^2-4EG}}{2E}\right)^{1/2}, \tag{7}$$

$$E=\rho\rho_c-\rho_f^2, \quad F=\lambda\rho_c+\rho M-2\rho_f C, \quad G=\lambda M-C^2. \tag{8}$$

An alternative parametrization of the problem is to specify six of the ten material parameters along with the complex wave speeds, $\overline{c_j}=c_j(1+i\epsilon\beta_j)^{-1}$, where $\epsilon=(40\pi\log_{10}e)^{-1}$ and c_j, β_j are the wave speeds and attenuations (dB/λ) of the slow and fast compressional waves. For the examples, we take $\rho_f=1$ g/cm^3, $K_f=2.25\times10^9$ Pa, $\eta=10^{-3}$ kg m^{-1} s^{-1} and $\tau=0.8$, which are the values determined by Chotiros for water-saturated sand.[7] In addition, we specify the porosity and solid density in each example. The remaining material parameters κ, K_b (complex), and K_r are determined by numerically inverting Eq. (7) using the Newton–Raphson method. This parametrization is more natural in the context of studies in wave propagation since it specifies the wave speeds and attenuations but is complicated by the fact that the inverse mapping may fail to yield physically reasonable values for κ, K_b, and K_r. For the parameter inversions we require κ, Re(K_b), and K_r to be positive and $|K_b|/K_r<1$. The positivity conditions follow from the physical interpretation of the permeability[16] and the bulk moduli.[17] The inequality in the bulk moduli ratio is a statement that poro-acoustic frame is more compressible than the sediment grains.

For a homogeneous poro-acoustic medium, we may define slow and fast wave potentials. Substituting a plane-wave solution,

$$\mathbf{p}=\mathbf{t}\exp(i\mathbf{k}\cdot\mathbf{x}), \tag{9}$$

into Eq. (1), we obtain the eigenvalue problem,

$$K^2\mathbf{t}_j=k_j^2\mathbf{t}_j, \tag{10}$$

where $k_j^2=\omega^2 c_j^{-2}$ are the eigenvalues corresponding to the slow and fast compressional waves. The slow and fast potentials ϕ_1 and ϕ_2 are defined by the relation,

$$\mathbf{p}=T\begin{pmatrix}\phi_1\\ \phi_2\end{pmatrix}, \tag{11}$$

where the columns of T are the eigenvectors $\mathbf{t}_1$ and $\mathbf{t}_2$. The potentials are utilized in the examples of Sec. IV to illustrate the propagation of the slow and fast waves in poro-acoustic media.

The boundary condition for Eq. (1) at a free surface is vanishing $\mathbf{p}$. At a horizontal interface between two poro-acoustic media, the interface conditions are continuity of fluid stress, total stress, solid displacement, and balance of fluid flow:

$$[\mathbf{p}]=\left[R^{-1}\frac{\partial\mathbf{p}}{\partial z}\right]=\mathbf{0}, \tag{12}$$

where $[\cdot]$ denotes the jump across the interface.[8] These conditions are analogous to the scalar interface conditions for fluid media. At a horizontal fluid/poro-acoustic interface, there is continuity of normal stresses and balance of fluid flow:

$$p\mathbf{e}=\mathbf{p}, \quad \rho_f^{-1}\frac{\partial p}{\partial z}=\mathbf{e}^T R^{-1}\frac{\partial\mathbf{p}}{\partial z}, \quad \mathbf{e}=\begin{pmatrix}-1\\ -1\end{pmatrix}, \tag{13}$$

where p is the acoustic pressure in the fluid. The minus sign in the definition of $\mathbf{e}$ accounts for the fact that the normal stress in a fluid is the negative of the pressure.[18]

The poro-acoustic PE is based on the factorization of Eq. (1) into incoming and outgoing components. In a range-independent environment, this factorization is exact because the two components are decoupled. The outgoing component satisfies

$$\frac{\partial\mathbf{p}}{\partial x}=ik_0(I+X)^{1/2}\mathbf{p}, \tag{14}$$

$$X=k_0^{-2}\left(R\frac{\partial}{\partial z}R^{-1}\frac{\partial}{\partial z}+K^2-k_0^2 I\right), \tag{15}$$

where k_0 is a characteristic wave number and I is the identity operator. The split-step Padé solution of Eq. (14),

$$\mathbf{p}(x+\Delta x,z)=\exp(ik_0\Delta x(I+X)^{1/2})\mathbf{p}(x,z), \tag{16}$$

provides higher-order accuracy in $k_0\Delta x$ than the finite-difference solution and permits larger range steps for increased computational efficiency.[19]

An initial condition for the PE can be generated using the self-starter.[8] Placing a line source on the right-hand side of Eq. (1), we obtain

$$\frac{\partial^2\mathbf{p}}{\partial x^2}+R\frac{\partial}{\partial z}\left(R^{-1}\frac{\partial\mathbf{p}}{\partial z}\right)+K^2\mathbf{p}=2i\mathbf{s}\delta(x)\delta(z-z_0), \tag{17}$$

$$\mathbf{s}=\begin{pmatrix}s_1\\ s_2\end{pmatrix}, \tag{18}$$

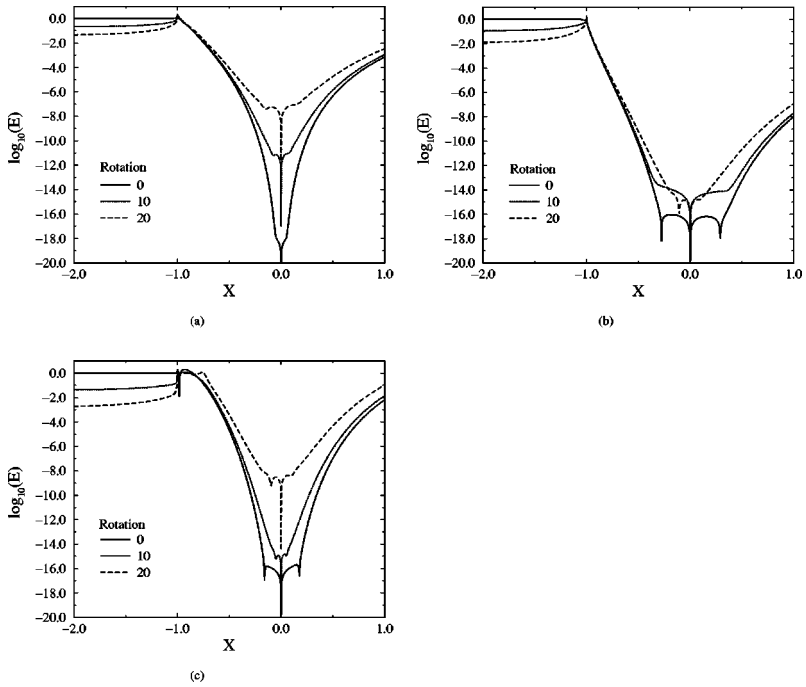

FIG. 1. The error in the rotated Padé approximation as a function of X, Δx, and the branch cut rotation angle for the case $\gamma=0$. The rotation angles in degrees are relative to the negative real axis. For no rotation, the Padé approximations are very accurate for the propagating portion of the spectrum ($X>1$) but inaccurate for the evanescent modes ($X<1$). Rotating the branch cut into the lower half-plane significantly increases the accuracy of the approximation for the evanescent modes. The number of Padé terms n and range step sizes Δx are (a) $n=6$, $\Delta x=2\lambda$ (b) $n=10$, $\Delta x=2\lambda$, (c) $n=10$, $\Delta x=5\lambda$.

where s_1 and s_2 can be chosen to excite an arbitrary combination of fast and slow waves. Integrating Eq. (17) over a small interval centered on $x=0$ and using the continuity of $\mathbf{p}$, we obtain the condition,

$$\lim_{x\to 0^+} \frac{\partial \mathbf{p}}{\partial x} = i\mathbf{s}\delta(z-z_0). \tag{19}$$

Replacing the x derivative by the square root of the depth operator using Eq. (14), we obtain

$$\lim_{x\to 0^+} k_0(I+X)^{1/2}\mathbf{p}=\mathbf{s}\delta(z-z_0). \tag{20}$$

The solution of Eq. (20) is singular at $z=z_0$. A numerically useful initial condition is obtained by introducing a smooth intermediate solution $\mathbf{q}$ satisfying

$$k_0(I+X)^2\mathbf{q}=\mathbf{s}\delta(z-z_0). \tag{21}$$

The singularity at the source is avoided by propagating the intermediate solution out in range to $x=x_0$. The pressure is then given by

$$\mathbf{p}(x_0,z)=(I+X)^{3/2}\exp(ik_0x_0(1+X)^{1/2})\mathbf{q}. \tag{22}$$

In the next section, we derive rotated Padé approximations of the operator in Eq. (22).

II. ROTATED PADÉ APPROXIMATIONS

PE techniques such as the self-starter and split-step Padé solution discussed in Sec. I and the energy-conserving and single-scattering solutions discussed in Sec. III require rational approximations to functions of the form,

$$h(X)=\exp(\gamma\log(1+X)+ik_0\Delta x(-1+(1+X)^{1/2})), \tag{23}$$

where γ is a constant. This function has a branch point at $X=-1$. The physically meaningful branch cut corresponds to $\mathrm{Im}(X)=0$ and $\mathrm{Re}(X)<-1$. The second term in the exponent of Eq. (23) is the split-step Padé operator of Eq. (16) with an additional factor of $\exp(-ik_0\Delta x)$.

A rational approximation $g(X)$ of the function $h(X)$ is of the form,

$$g(X)=\prod_{j=1}^{n}\frac{1+a_{j,n}X}{1+b_{j,n}X}. \tag{24}$$

One method for determining the coefficients $a_{j,n}$ and $b_{j,n}$ is to match $2n-m$ derivatives at $X=0$ and impose m stability constraints.[20] Matching derivatives enforces accuracy of the approximation over the propagating spectrum ($X>-1$). The stability constraints require that the evanescent spectrum ($X<-1$) decays as the solution is advanced in range. Another method for stabilizing the evanescent modes is to match $2n$ derivatives (a Padé approximation) with a function whose branch cut is rotated relative to the negative real line. This method has been applied to the square-root operator and has the advantage that some of the evanescent modes may be accurately approximated for sufficient rotation angles.[14] We extend this method to more general functions of $(1+X)$. Although the branch cut rotation interpretation only applies when $\Delta x=0$, the approach is also effective when $\Delta x\neq 0$.

Let $h_\theta(X)$ denote the function whose branch cut is rotated through the angle θ with respect to the negative real axis. Then h_θ is related to h by a coordinate rotation,

$$h_\theta(X)=h(e^{i\theta}(1+\chi)-1), \tag{25}$$

where the rotated coordinate χ is defined by the transformation

$$\chi = e^{-i\theta}(1+X) - 1. \tag{26}$$

The rotated Padé coefficients are determined numerically by matching $2n$ derivatives at $\chi = 0$,

$$h(e^{i\theta}(1+\chi)-1) \cong h(e^{i\theta}-1)\prod_{j=1}^{n} \frac{1+A_{j,n}\chi}{1+B_{j,n}\chi}. \tag{27}$$

The coefficients are independent of θ for the case $\Delta x = 0$. Substituting for χ in terms of X in Eq. (27), we obtain the rotated Padé approximation for h_θ,

$$h_\theta(X) \cong g_\theta(X) = \left(h(e^{i\theta}-1)\prod_{j=1}^{n} \frac{1+A_{j,n}(e^{-i\theta}-1)}{1+B_{j,n}(e^{-i\theta}-1)} \right) \times \prod_{j=1}^{n} \frac{1+\overline{a}_{j,n}X}{1+\overline{b}_{j,n}X}, \tag{28}$$

$$\overline{a}_{j,n} = \frac{e^{-i\theta}A_{j,n}}{1+A_{j,n}(e^{-i\theta}-1)}, \quad \overline{b}_{j,n} = \frac{e^{-i\theta}B_{j,n}}{1+B_{j,n}(e^{-i\theta}-1)}. \tag{29}$$

The approximation error $E = |g_\theta(X) - h_\theta(X)|$ for the case $\gamma = 0$ as a function of X, Δx, and the branch cut rotation angle is shown in Fig. 1. The Padé approximation is very accurate for the propagating portion of the spectrum ($X > -1$) when the branch cut is along the negative real axis ($\theta = 0$) but inaccurate for the evanescent modes ($X < -1$). Positive rotation angles reduce the error in the evanescent modes by orders of magnitude while simultaneously decreasing the accuracy over the propagating portion of the spectrum. The error plots were generated with quadruple precision numerics to avoid artifacts due to roundoff error. For the examples in Sec. IV, the rotation angle is 45°.

III. INTERFACE CONDITIONS FOR RANGE-DEPENDENT PROBLEMS

In many cases of interest, the environment is range-dependent. The PE factorization, however, is based on the assumption that the incoming and outgoing waves are decoupled. Several methods have been implemented to correct the PE for range dependence. The energy conserving PE is motivated by the WKB solution in gradually range-dependent environments and conserves the forward propagating energy. This method provides accurate solutions for the acoustic case[10,11] and is therefore of interest for poro-acoustic waveguides. The single-scattering method imposes exact vertical interface conditions but neglects multiple-scattering events. Single scattering and energy-conserving solutions agree for problems involving gradual range dependence.[10,11] The single-scattering method provides the reflected field and is applicable to studying backscatter.[12,21]

In this section, the details of the energy-conserving PE and single-scattering method are developed for a poro-acoustic waveguide. We extend the single-scattering method to problems involving coupling to fluid layers. In this case, slow and fast compressional waves of the poro-acoustic medium couple with the fluid compressional wave. The rotated Padé approximation provides improved convergence of the single-scattering iteration formula, extending its applicability to interfaces with large contrast in material properties.

To implement the energy-conserving and single-scattering interface conditions, a range-dependent environment is approximated as a series of range-independent regions separated by vertical interfaces. The field is propagated through each range-independent region with the PE method. Energy conservation or single scattering is then applied at the vertical interfaces between the range-independent regions.

A. Energy conservation

The WKB solution suggests that energy is the appropriate quantity to conserve across vertical interfaces in a gradually range-dependent medium.[10] Although energy flux is nonlinearly related to pressure, an equivalent linear condition for conserving energy is derived by expanding the pressure in normal modes and using the orthogonality property. This method has been applied to fluid and elastic media.[11,22] The energy flux condition for a poro-acoustic medium,

$$R_A^{-1/2}(I+X_A)^{1/4}\mathbf{p}_A = R_B^{-1/2}(I+X_B)^{1/4}\mathbf{p}_B \tag{30}$$

is derived similarly.[8] The subscripts A and B refer to incident and transmitted quantities. The fourth root operator is approximated by a rotated Padé approximation. The square root of the density matrix is well defined in the lossless case. For a medium in which loss is a perturbation, we take the real part of the density matrix to estimate the transmitted energy flux.

B. Single scattering

The single-scattering method solves for the transmitted and reflected fields utilizing the exact interface conditions but ignoring multiple-scattering events. In this section we derive the single-scattering formula for fluid and poro-acoustic media. We generalize the scattering formula to problems involving fluid layers. An iteration procedure for solving the scattering formula is developed and is implemented with rotated Padé approximations.

The vertical interface conditions in a fluid medium are continuity of pressure and normal displacement,

$$[p] = \left[\frac{1}{\rho_f}\frac{\partial p}{\partial x} \right] = 0, \tag{31}$$

where the brackets denote the jump across the interface and p is the pressure in the fluid. The vertical interface conditions in a poro-acoustic medium are continuity of fluid stress, total stress, solid displacement, and balance of fluid flow,

$$[\mathbf{p}] = \left[R^{-1}\frac{\partial \mathbf{p}}{\partial x} \right] = \mathbf{0}. \tag{32}$$

At a fluid/poro-acoustic interface, the conditions are continuity of total stress, fluid stress, and balance of fluid flow,

$$p\mathbf{e} = \mathbf{p}, \quad \frac{1}{\rho_f}\frac{\partial p}{\partial x} = \mathbf{e}^T R^{-1}\frac{\partial \mathbf{p}}{\partial x}, \tag{33}$$

where **e** is defined in Eq. (13). These conditions are analogous to the horizontal interface conditions discussed in Sec. I.

A general interface condition incorporating all of the preceding cases may be written as

$$[\mathbf{p}]=\mathbf{0}, \tag{34}$$

$$\left[MR^{-1}\frac{\partial \mathbf{p}}{\partial x}\right]=\mathbf{0}, \tag{35}$$

where the vector pressure in the fluid is $\mathbf{p}=p\mathbf{e}$, the density matrix in the fluid is

$$R=\begin{pmatrix}\rho_f & 0\\ 0 & \rho_f\end{pmatrix}, \tag{36}$$

and M is one of the following:

$$\begin{pmatrix}1 & 0\\ 0 & 1\end{pmatrix},\quad \begin{pmatrix}1 & 0\\ -1 & 1\end{pmatrix},\quad \begin{pmatrix}1 & 1\\ 0 & 0\end{pmatrix}. \tag{37}$$

At a fluid/fluid or poro-acoustic/poro-acoustic interface, M is the identity. For the fluid/fluid case, this amounts to applying Eq. (31) twice. At a fluid/poro-acoustic interface, M on the fluid side is the second matrix of Eq. (37) and M in the poro-acoustic medium is the last matrix of Eq. (37). The first row of Eq. (35) corresponds to the stress balance in Eq. (33); the second row equates the components of **p** in the fluid. One advantage to this matrix formulation is that it allows the straightforward implementation of the single-scattering method to fluid/fluid, poro-acoustic/poro-acoustic, and fluid/poro-acoustic waveguides. In fluid/poro-acoustic waveguides, M depends on depth.

Applying the single-scattering approximation, we decompose the pressure at the interface into incident $\mathbf{p}_i$, reflected $\mathbf{p}_r$, and transmitted $\mathbf{p}_t$ components. Substituting into Eqs. (34) and (35), we obtain

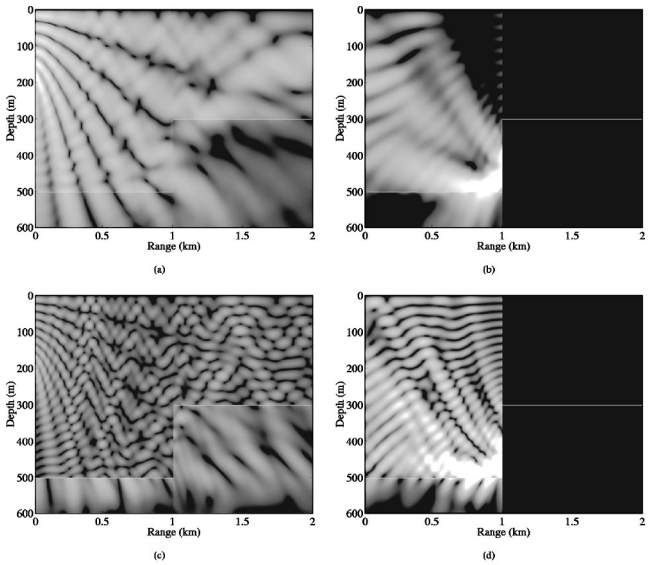

FIG. 2. Transmission loss for scattering from a step in example A, which involves two poro-acoustic layers. The thickness of the top layer is 500 m before the step and 300 m beyond the step, which is located 1 km from the source. The bottom layer approximates a half-space. The top row is the transmission loss of the fast wave and the bottom row is the slow wave. The left column is the outgoing waves and the right column is the reflected waves. The scale of the TL for the outgoing wave is 15–45 dB; for the reflected signal, the scale is 40–60 dB.

$$\mathbf{p}_i+\mathbf{p}_r=\mathbf{p}_t, \tag{38}$$

$$M_A R_A^{-1}\frac{\partial}{\partial x}(\mathbf{p}_i+\mathbf{p}_r)=M_B R_B^{-1}\frac{\partial}{\partial x}\mathbf{p}_t. \tag{39}$$

The range derivatives are replaced with depth operators from the PE factorization,

$$M_A L_A(\mathbf{p}_i-\mathbf{p}_r)=M_B L_B \mathbf{p}_t, \tag{40}$$

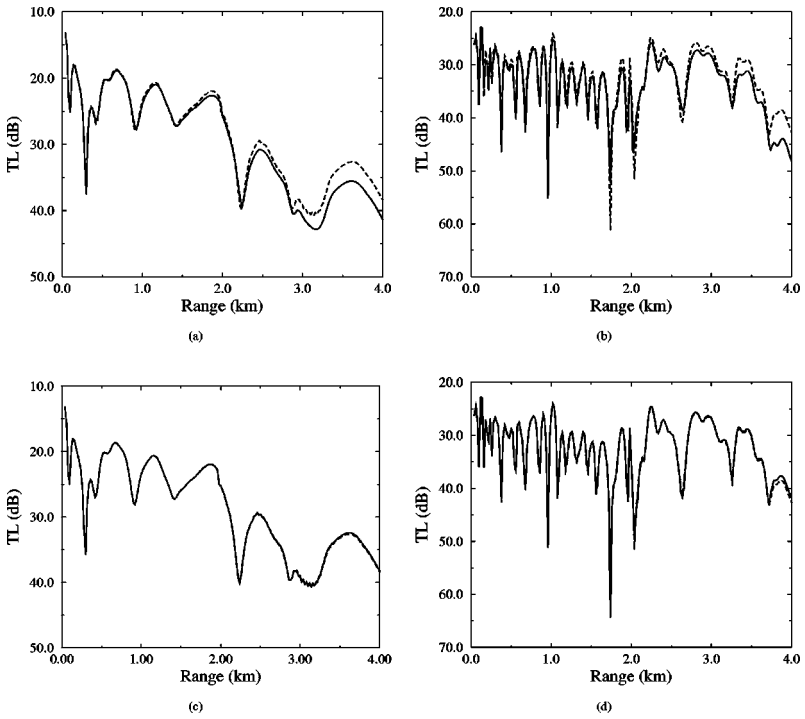

FIG. 3. Comparison of pressure-conserving, energy-conserving, and single-scattering solutions for the poro-acoustic wedge in example B. The fast-wave TL (a) and slow-wave TL (b) for the pressure-conserving (solid) and energy-conserving (dashed) solutions. The fast-wave TL (c) and slow-wave TL (d) for the energy-conserving (solid) and single-scattering (dashed) solutions. The energy conservation and the single-scattering method are in agreement. The pressure-conserving solution exhibits an amplitude error relative to the other methods.

where $L=R^{-1}(I+X)^{1/2}$. Note that the reflected field has a negative factor since it is incoming. The PE operator in the fluid is defined by,

$$X=k_0^{-2}\left(\rho_f\frac{\partial}{\partial z}\frac{1}{\rho_f}\frac{\partial}{\partial z}+k^2-k_0^2\right)\begin{pmatrix}1&0\\0&1\end{pmatrix}, \tag{41}$$

where $k=\omega c_f^{-1}$ is the acoustic wave number for the fluid and c_f is the sound speed in the fluid. Eliminating $\mathbf{p}_t$ in Eq. (40) with Eq. (38), we obtain an operator equation for the reflected field,

$$M_A L_A(\mathbf{p}_i-\mathbf{p}_r)=M_B L_B(\mathbf{p}_i+\mathbf{p}_r). \tag{42}$$

Iterative solutions of the single-scattering equations for fluid and elastic media are derived in Refs. 12 and 21. The solution of Eq. (42) is derived similarly. At a fluid/poro-acoustic interface, only one of the matrices M_A and M_B is invertible depending on whether the interface is a fluid/poro-acoustic or a poro-acoustic/fluid transition. To account for both cases, two iteration formulas are derived, each based on inverting a different combination of operators,

$$\mathbf{p}_r=\frac{\tau-2}{\tau}\mathbf{p}_r+\frac{1}{\tau}(I-L_A^{-1}M_A^{-1}M_B L_B)(\mathbf{p}_i+\mathbf{p}_r), \tag{43}$$

$$\mathbf{p}_r=\frac{\tau-2}{\tau}\mathbf{p}_r+\frac{1}{\tau}(I-L_B^{-1}M_B^{-1}M_A L_A)(\mathbf{p}_r-\mathbf{p}_i), \tag{44}$$

where $\tau\geqslant 2$ is a convergence parameter. With the rotated Padé approximation, the iteration formula converges for relatively large material parameter contrasts. The transmitted field is computed from the continuity of stress condition at the interface. For some problems involving multiple fluid and poro-acoustic layers, neither M_A nor M_B is invertible. This would be the case if a vertical interface consisted of both fluid/poro-acoustic and poro-acoustic/fluid transitions. In this event, the single scattering can be approximated with a two-step implementation: a single scattering of the fluid/poro-acoustic interfaces followed by a scattering from the poro-acoustic/fluid interfaces.

IV. EXAMPLES

To illustrate the implementation of the poro-acoustic PE we consider several examples. The material parameters chosen for examples A and B are not intended to be realistic; they serve to illustrate the implementation of the PE and the vertical interface conditions. Examples C and D are based on material parameters measured by Chotiros for water-saturated sand.[7]

For example A, the single-scattering method is applied to a poro-acoustic stair-step interface located 1 km from a line source. The top layer is 500-m thick before the step and 300-m thick beyond the step. The source depth is 200 m and the frequency is 25 Hz. In the upper layer, the fast/slow attenuations are 0, 0.1 dB/λ with porosity, density, and fast/slow wave speeds: 0.4, 1.5 g/cm^3, 1600 m/s, 1100 m/s. In the lower layer, the fast/slow wave attenuations are 0, 0.1 dB/λ above 500 m and linearly increase to 0.1, 1.0 dB/λ at 600 m. The porosity, density, and fast/slow wave speeds are 0.3, 2 g/cm^3, 1800 m/s, 1300 m/s. For this example, the number of Padé terms is 10, the range step is 20 m, and the depth grid step is 2 m. The top row in Fig. 2 is the fast wave potential and the bottom row is the slow wave potential; the left column corresponds to the outgoing field and the right column is the reflected field. The reflected signal is about 25 dB below the transmitted signal. This example illustrates the robustness of the iteration formula for a relatively large contrast in poro-acoustic parameters across a stair-step discontinuity. It also shows that the backscattered energy is small relative to the transmitted energy.

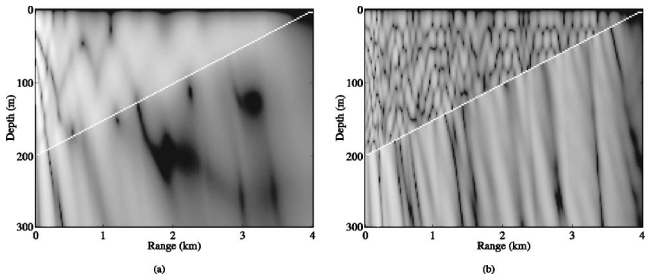

FIG. 4. Transmission loss for the poro-acoustic wedge in example B. The fast wave interacts with the sloping bottom where some of the energy is transmitted as a slow wave into the lower half-space. The scale of transmission loss is 15 dB (white) to 50 dB (black). Fast-wave TL (a), slow-wave TL (b).

Example B is a comparison of the fast and slow wave transmission loss for an upsloping sediment computed by using three different methods at the vertical interface: pressure continuity, single scattering, and energy conservation. The bottom slopes linearly from 200-m depth at the source to zero at 4 km in range. A 25-Hz line source is placed at a depth of 100 m. The poro-acoustic parameters in this example are identical to those in example A except for the

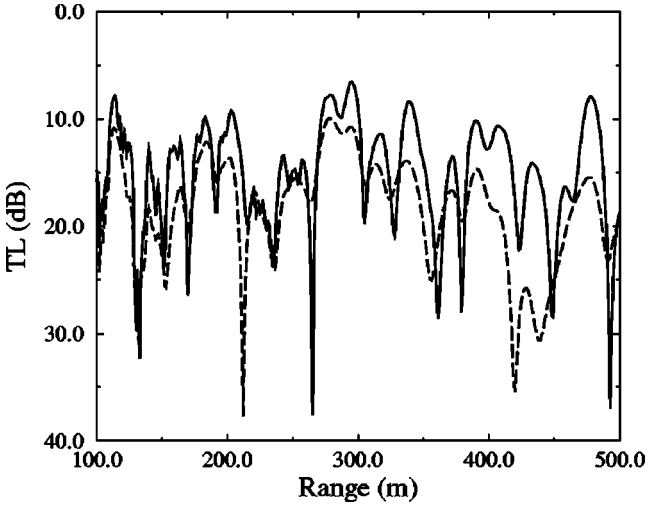

FIG. 5. Transmission loss in a range-independent fluid/poro-acoustic waveguide in example C. The sound speed in the water column is 1500 m/s. Two models for the lower layer are considered: (1) a fluid (1650 m/s sound speed) and (2) a poro-acoustic sediment (1650 m/s fast wave, 1000 m/s slow wave). The source and receiver depths are 10 m, the frequency is 1000 Hz, and the water depth is 20 m. The TL curves are for: fluid bottom (solid) and poro-acoustic bottom layer (dashed). The poro-acoustic parameters have been chosen to approximate the experimentally measured values of Chotiros for water-saturated sand. The slow poro-acoustic wave modifies the TL relative to the fluid sediment case by permitting energy to escape into the lower layer.

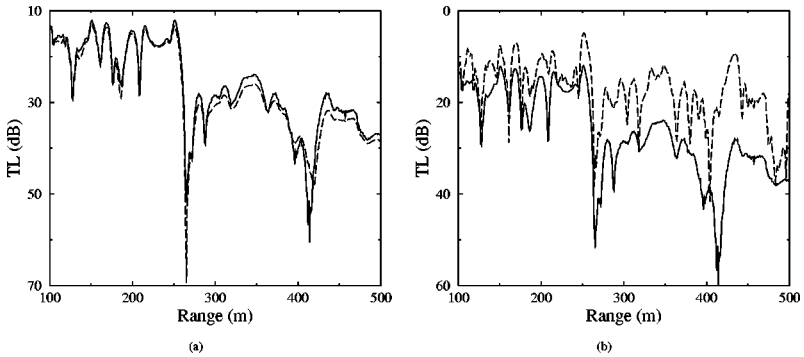

FIG. 6. Transmission loss in the range-dependent fluid/poro-acoustic waveguide of example D. The bottom slopes linearly from 20 m at the source to 0 m at 500 m from the source. All other parameter values are identical to those in example C. The figures compare the single-scattering solution (solid) to the pressure-conserving solution (dashed) for the fluid/poro-acoustic waveguide (a). The single-scattering TL for the fluid/poro-acoustic waveguide (solid) is also compared to the TL for a fluid/fluid waveguide (dashed) (b). The fluid sediment sound speed is identical to the fast wave speed of the poro-acoustic medium.

porosity in the lower layer, which is 0.2 in this case. The computational parameters for this example are: 6 Padé terms, 20-m range step, and 2-m depth grid spacing. Figure 3 shows the transmission loss for the fast- and slow-wave potentials at the receiver depth of 100 m. The single-scattering and energy-conserving solutions are in agreement. The pressure conserving solution exhibits an amplitude error relative to the energy-conserving and single-scattering results that is similar to the error observed in the acoustic case.[10] Figure 4 illustrates the transmission loss in the fast and slow waves for example B.

Example C compares propagation in fluid/fluid and fluid/poro-acoustic waveguides for a range-independent case. The upper layer is 20 m of water with a constant sound speed of 1500 m/s. A 1000-Hz line source is 10 m below the free surface. The bottom layer is modeled as a fluid or a poro-acoustic medium. For the fluid/fluid case, the wave speed, attenuation, and density of the bottom are 1650 m/s, 0 dB/λ, and 2.65 g/cm^3. For the fluid/poro-acoustic case, the fast wave speed, attenuation, and density are identical to the parameters in the bottom layer of the fluid waveguide, and the porosity, slow wave speed, and slow wave attenuation are 0.39, 1000 m/s and 0.1 dB/λ. The transmission loss (TL) curves for both waveguides are shown in Fig. 5. The poro-acoustic sound speeds and densities were chosen to match the values measured by Chotiros for a sandy sediment.[7] The poro-acoustic waveguide allows energy to escape into the lower half-space through coupling between the fluid and the poro-acoustic slow wave. For this example, the number of Padé terms is 8, the range step is 1 m, and the depth grid spacing is 0.025 m.

Example D is a range-dependent case with the same material and computational parameters as the previous example. The bottom slopes linearly from 20-m depth at the source to 0 m at a range of 500 m. The TL curves in Fig. 6(a) compare the pressure-conserving and single-scattering solutions for the fluid/poro-acoustic waveguide. The pressure-conserving solution exhibits an amplitude error relative to the single-scattering solution. In Fig. 6(b) the single-scattering solution for the fluid/poro-acoustic waveguide is compared to the energy-conserving solution for a fluid/fluid waveguide. A significant amount of energy couples into the slow wave and escapes into the bottom.

V. CONCLUSION

The PE method has been implemented to study propagation in poro-acoustic and fluid/poro-acoustic waveguides. Rotated Padé approximations have been used to accurately approximate the evanescent modes for the PE operators. In the single-scattering solution, the rotated Padé approximations yield improved convergence of the iterative solution for greater material parameter contrasts than was previously possible.

In range-dependent poro-acoustic waveguides, energy conservation and the single-scattering solutions yield consistent results while the pressure-conserving solution exhibits an amplitude error. This is consistent with observations in acoustic propagation. Range dependence in fluid/poro-acoustic waveguides is approximated by the single-scattering method. For sediment parameters based on the values measured by Chotiros, the slow poro-acoustic wave can be a significant mechanism for energy loss into the bottom.

ACKNOWLEDGMENTS

This work was supported by the Office of Naval Research and a National Research Council-NRL Research Associateship.

[1] M. A. Biot, ''Theory of propagation of elastic waves in a fluid-saturated porous solid,'' J. Acoust. Soc. Am. **28**, 168–191 (1956).
[2] M. A. Biot, ''Mechanics of deformation and acoustic propagation in porous media,'' J. Appl. Phys. **33**, 1482–1498 (1962).
[3] M. A. Biot, ''Generalized theory of acoustic propagation in porous dissipative media,'' J. Acoust. Soc. Am. **34**, 1254–1264 (1962).
[4] M. Stern, A. Bedford, and H. R. Millwater, ''Wave reflection from a sediment layer with depth-dependent properties,'' J. Acoust. Soc. Am. **77**, 1781–1788 (1985).
[5] R. D. Stoll and T. K. Kan, ''Reflection of acoustic waves at a water-sediment interface,'' J. Acoust. Soc. Am. **70**, 149–156 (1981).
[6] T. Yamamoto, ''Acoustic propagation in the ocean with a poro-elastic bottom,'' J. Acoust. Soc. Am. **73**, 1587–1596 (1983).
[7] N. P. Chotiros, ''Biot model of sound propagation in water-saturated sand,'' J. Acoust. Soc. Am. **97**, 199–214 (1995).
[8] M. D. Collins, J. F. Lingevitch, and W. L. Siegmann, ''Wave propagation in poro-acoustic media,'' Wave Motion **25**, 265–272 (1997).
[9] F. B. Jensen, W. A. Kuperman, M. B. Porter, and H. Schmidt, *Computational Ocean Acoustics* (AIP, New York, 1994), pp. 343–412.
[10] M. B. Porter, F. B. Jensen, and C. M. Ferla, ''The problem of energy conservation in one-way models,'' J. Acoust. Soc. Am. **89**, 1058–1067 (1991).
[11] M. D. Collins and E. K. Westwood, ''A higher-order energy-conserving parabolic equation for range-dependent ocean depth, sound speed and density,'' J. Acoust. Soc. Am. **89**, 1068–1075 (1991).
[12] M. D. Collins and R. B. Evans, ''A two-way parabolic equation for acoustic backscattering in the ocean,'' J. Acoust. Soc. Am. **91**, 1357–1368 (1992).
[13] M. D. Collins, ''The rotated parabolic equation and sloping ocean bottoms,'' J. Acoust. Soc. Am. **87**, 1035–1037 (1990).
[14] F. A. Milinazzo, C. A. Zala, and G. H. Brooke, ''Rational square-root

approximations for parabolic equation algorithms,'' J. Acoust. Soc. Am. **101**, 760–766 (1997).
[15] M. D. Collins, W. A. Kuperman, and W. L. Siegmann, ''A parabolic equation for poro-elastic media,'' J. Acoust. Soc. Am. **98**, 1645–1656 (1995).
[16] C. S. Yih, *Dynamics of Nonhomogeneous Fluids* (Macmillian, New York, 1965).
[17] H. Kolsky, *Stress Waves in Solids* (Dover, New York, 1963).
[18] G. K. Batchelor, *An Introduction to Fluid Dynamics* (Cambridge U.P., New York, 1967).
[19] M. D. Collins, ''A split-step Padé solution for the parabolic equation method,'' J. Acoust. Soc. Am. **93**, 1736–1742 (1993).
[20] M. D. Collins, ''Higher-order Padé approximations for accurate and stable elastic parabolic equations with application to interface wave propagation,'' J. Acoust. Soc. Am. **89**, 1050–1057 (1991).
[21] M. D. Collins, ''A two-way parabolic equation for elastic media,'' J. Acoust. Soc. Am. **93**, 1815–1825 (1993).
[22] M. D. Collins, ''An energy-conserving parabolic equation for elastic media,'' J. Acoust. Soc. Am. **94**, 975–982 (1993).

Some physical models for estimating scattering of underwater sound by algae

Evgeni L. Shenderov
Research and Development Institute ''Morfizpribor,'' 46 Chkalovski pr., St. Petersburg, 197376, Russia

(Received 1 December 1995; accepted for publication 15 April 1998)

A theoretical study of scattering of underwater sound waves by algae has been performed. The dependenies of sound level in reflected waves on parameters of algae (sizes, biomass) are determined. To this purpose, the physical models corresponding to typical algae species are developed. Scattering of sound by algae is treated as diffraction of a sound wave on a random system of three-dimensional bent elastic bodies. Sound pressure in the waves scattered by acoustically semitransparent bent plates and rods corresponding to alga leaves and stems is computed. The statistical properties of algae (roughness, inclination) are taken into account. The theoretical estimations are compared with experimental values. The obtained results can be used for the development of the methods of exploration of the continental shelf and also for the assessment algae resources. © *1998 Acoustical Society of America.* [S0001-4966(98)05207-2]

PACS numbers: 43.30.Gv, 43.30.Sf, 43.20.Fn [JHM–DLB]

INTRODUCTION

The products of processing of seaweeds (algae) are used in industry very extensively. Several million tons of seaweeds per year are necessary for the chemical and food industry. But there exist the problems of search for algae and assessment of their resources. The means of underwater visual observations using diver equipment allow exploration of a small bottom area. Aerial photography gives the possibility of surveying bigger areas, however, it has its own severe limitations. The search is possible only in transparent water in calm weather and with low position of the sun. But even under these conditions it is limited to shallow water (down to 10 m). Using the underwater television helps determine the seaweeds type but only in transparent water and on small bottom area. Of great potential is the hydroacoustical method of search. There is some information on the successful application of the method for the assessment of the algae resources.[1–7] The use of echosounders to measure the height of water plants is reported in Refs. 1 and 2. The estimation of the biomass is carried through by determining the relationship between the height and the biomass. The estimation of biomass by direct measurements of the amplitude of reflected acoustic signal was described in Refs. 4, 6 and 7. We know of just one short paper[5] where authors report on measurements of sound reflection properties of some algae. The knowledge of these properties is necessary to work out the methods of establishing a relationship between the scattered sound wave amplitude and the algae biomass. Besides, the dependencies give grounds for choosing optimal operation modes of the sounders. The best way of doing this is extensive studies of sound scattering by different algae in the sea. But measurements of this kind are very difficult and expensive. Therefore it is expedient to develop a theory describing the basic dependencies of the amplitude of sound signals scattered by the algae on some of their parameters. The main difficulty in the development of such a theory is that the elastic constants of algae have never been measured and may be specified only hypothetically. Nonetheless, as shown below, satisfactory results can be obtained even under considerably great uncertainty of boundary conditions. The attempts to derive some physical models to describe scattering of sound from algae are presented below.

This paper is organized as follows. In Sec. I we describe the shape of the algae which are the most important commercially. Section II deals with some scattering properties of algae that can be represented as wide bent plates with sparse disposition of plants. The properties for dense disposition are considered in Sec. III. In Sec. IV we deal with seaweeds shaped like intertwined wires. Comparison of the theoretical and experimental results is carried out in Sec. V.

I. TYPICAL SHAPES OF SOME IMPORTANT ALGAE

Let us consider the typical shapes of algae[8] from the point of view of their sound reflection properties. The most important commercially are the brown algae-*Laminariaceae*. They have prolate leaves with rows of the pits and bulges. *L. saccharina* may be as big as 7 m. *L. japonica* has a length of 2–6 m, sometimes up to 12 m. The width of the plates is 0.1–1 m. Stems are of cylindrical shape. The biomass of some algae thickets may amount to 140 kg/m^2. *L. angustata* has long narrow plates with a groove along the middle of a plate. The length may be as big as 22 m. *L. digitata* has a wide oval or wedge-shaped cleft plates which may be hemispherical. The width is up to 1 m. *Alaria fistulosa*, besides bent plates has a hollow rib containing gas. The length of some plants may reach 41 m. Another commercially important species is the red algae. *Ulva* has wide, great bent plates. *Gelidiales* and *Anfeltia plicata* resemble much bent, intertwined wires with diameters of several millimeters.

Thus the most typical shapes of algae are bent plates and cylinders. Note that the gas-filled bubbles may exist on the surface of some algae species. These bubbles can drastically enhance the sound reflection properties of algae and the sound absorption in algae thickets but we did not take the bubbles into account in our calculations. There may be two cases: the sparsely located plants and dense layers of plants.

In the first case one can consider the individual plants and neglect multiple scattering. In the second case it is necessary to consider the interaction between the plants. Below we consider both cases.

II. SPARSE DISPOSITIONS OF PLANTS

A. Scattering of sound by a leaf

If individual plants do not overlap, one can neglect the interaction of reflected sound waves and consider each plant on its own. Note that they cannot be modeled with plane plates and straight cylinders. It will be shown below that the optimal frequency range lies higher than 100 kHz. Hence the order of the sound wavelength magnitude is several millimeters. The roughness of the leaves and stems exceed this value many times. Plane plates and straight cylinders reflect the waves only in a very narrow solid angle in the space and the reflected waves are unlikely to arrive at the receiver. Meanwhile bent bodies reflect waves in wide solid angles and the probability of returning sound waves to reach the receiver is very high. A leaf may be considered as a three-dimensional (3-D) rough surface with a given reflection coefficient A. All sizes of the roughness greatly exceed the wavelength. We shall assume the surface to be described by the random function $z=f(x,y)$ with Gaussian correlation function

$$\langle z(x_1+x,y_1+y)z(x_1,y_1)\rangle=\overline{h^2}\,\exp[-(x^2+y^2)/(2l^2)], \tag{1}$$

where $\overline{h^2}$ is the height variance, l is the interval of correlation, and $\langle\ \rangle$ denote the ensemble averaging. We shall consider that the local radii of curvature exceed the wavelength, hence the wave is reflected at every point as if from the respective infinite tangential plane. Further, we shall assume the surface to be gently sloping, so that reflections between different parts of the leaf and shadowing of one projection by another can be neglected. As long as this holds, the region of very small grazing angles is excluded, i.e., we suppose that $\cos\theta \geqslant (kR)^{-1/3}$, where R is the local radius of curvature,[9] $k=\omega/c$, c is the velocity of sound in water and θ is the angle of incidence of a sound wave on a leaf.

One can represent the scattered sound field as a sum of two parts: a coherent component and an incoherent one,[9] i.e., $I_{\text{scat}}=I_{\text{coh}}+I_{\text{incoh}}$. The intensity of the coherent component is defined[10–12] as $I_{\text{coh}}=I_i A^2 A_{\text{eff}}^2(\theta)D_{\text{refl}}^2(\theta)$, where I_i is the incident wave intensity, A is the reflection coefficient for the plane plate, $A_{\text{eff}}(\theta)=\exp(-2k^2\overline{h^2}\cos^2\theta)$ is the effective reflection coefficient for a rough hard plate, $D_{\text{refl}}^2(\theta)$ is the angular dependence of intensity of sound reflected from the plane plate in the back direction. For a plate of sizes more than wavelength this dependence is sharp and the probability of the receiver to fall within a narrow solid angle is low. Besides the strong exponential dependence of the quantity $A_{\text{eff}}(\theta)$ on the wave height of the roughness results in that the coherent component can be neglected.

Let a spherical wave be incident on a plate. The sound pressure in this wave is

$$p_i=-\frac{ik\rho cQ}{4\pi r}\exp(ikr), \tag{2}$$

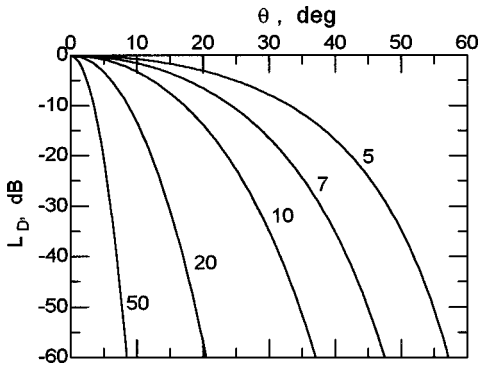

FIG. 1. Directivity patterns of sound wave backscattering by a random rough surface. The numbers near the curves are the ratio $l/2\overline{h}$, $L_D=20\log_{10}D(\theta)$.

where ρ is the water density, Q is the strength of the radiator, and r is the distance between the running point on the scattering surface and the radiator. The wave intensity at the plate is described as

$$I_i=\frac{k^2\rho cQ^2}{2(4\pi)^2 r_0^2}. \tag{3}$$

We shall suppose that the sizes of the plate are significantly less than the distance r_0 between the plate center and the radiator–receiver. The intensity of the incoherent part of the backscattered field is described as[10]

$$I_{\text{incoh}}=\frac{k^2\rho cQ^2}{2(4\pi)^2}\frac{S_0A^2}{4\pi r_0^4}\left(\frac{l}{2h}\right)^2\frac{1}{\cos^2\theta}\times\exp\left(-\frac{l^2}{4h^2}\tan^2\theta\right), \tag{4}$$

where S_0 is the plate area. The factor 2 in the term $(l/(2\overline{h}))^2$ is absent in Ref. 10. This is a repetition of a typographic error in Ref. 11 where the expression was obtained for the first time. To show the necessity of this factor, one can check the law of conservation of energy using the equation describing bistatic scattering by a 3-D rough surface in Refs. 10 and 11:

Define the backscattering cross section as

$$\sigma_{\text{scat}}=r_0^2 I_{\text{scat}}/I_i. \tag{5}$$

Taking I_{incoh} as I_{scat}, one obtains from Eqs. (3) and (4)

$$\sigma_{\text{scat}}=A^2S_0\left(\frac{l}{2h}\right)^2D^2(\theta), \tag{6a}$$

$$D(\theta)=\frac{1}{\cos\theta}\exp\left(-\frac{l^2}{8h^2}\tan^2\theta\right) \tag{6b}$$

is the directivity pattern of the scattered field (Fig. 1).

Despite the simplicity of these expressions, it is very difficult to use them for calculations since the statistical parameters of leaves l and $\overline{h}$ are unknown. To obtain such quantities it is necessary to perform complicated measurements of the leaf shape *in situ*. It is much simpler to estimate the specific length of undulations and the maximum height of the roughness. For this reason we consider below the scat-

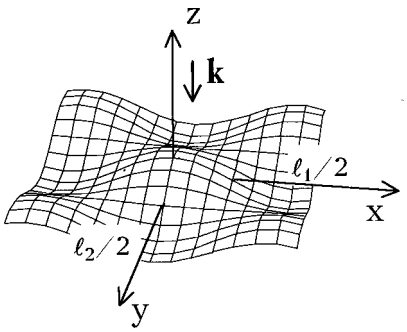

FIG. 2. The bent part of a leaf.

tering of sound on a 3-D periodic surface, then compare the results with Eq. (6a) and find the conversion factor relating the values obtained from two different models. Let the shape of the leaf surface be described by the product

$$f(x,y)=h\ \cos(2\pi x/l_1)\cos(2\pi y/l_2), \tag{7}$$

where $l_1=L_1/n_1$ and $l_2=L_2/n_2$ are the periods of undulations, L_1 and L_2 are the principal sizes of the leaf, and n_1 and n_2 are the numbers of undulations in two directions. Assuming that all sizes are large as compared to the wavelength, one can use the Kirchhoff approximation[13]

$$p_{\text{scat}}=-\frac{k^2\rho cQ}{8\pi^2}A\int\int_{S'}\frac{\exp(i2kr)}{r^2}\cos\ \alpha\ dS. \tag{8}$$

Here S' is the part of the surface which is seen from the point observation (Fig. 2). Applying the stationary phase method to Eq. (8), we obtain [13] the radius of the equivalent sphere for one point of stationary phase (i.e., for one point of specular reflection)

$$a_{\text{sph}}=A\sqrt{|R_1R_2|}, \tag{9}$$

where R_1 and R_2 are the principal radii of curvature at the points of specular reflection. The last formula differs from the known value of the equivalent radius[13–15] of a curved surface only by the factor A. The value $(R_1R_2)^{-1}$ is the Gaussian curvature of the surface at the point of stationary phase. The backscattering cross section is defined as $\sigma_0=a_{\text{sph}}^2/4$. Then for one point of stationary phase

$$\sigma_0=A^2|R_1R_2|/4, \tag{10}$$

where $R_1=1/f''_{xx}$, $R_2=l/f''_{yy}$, primes denote the second derivatives to corresponding coordinates. Therefore the cross section is described as

$$\sigma_0=\frac{A^2l_1^2l_2^2}{64\pi^4h^2}. \tag{11}$$

Note that if the radiator–receiver is located in the far field, the integral in Eq. (8) may be evaluated explicitly. The result in the case $kh\gg1$ coincides with Eq. (11). The value (11) has been obtained for one point of stationary phase. In total there are $2n_1\times2n_2$ such points, for there are two points of stationary phase on each period of undulations. Since we consider all sizes to be substantially larger than the wavelength, the waves reflected from these points are superimposed with random phases. The resultant envelope is described[16] by the Rayleigh probability density function. The contribution of all points in the total intensity exceeds the contribution of one point by $2n_1\times2n_2$ times. Hence the backscattering cross section for the whole leaf σ_{leaf} should exceed the value determined by Eq. (11) by $4n_1n_2$ times. The result is

$$\sigma_{\text{leaf}}=\frac{A^2S_0}{16\pi^4}\frac{l_1l_2}{h^2}, \tag{12}$$

where $S_0\approx L_1L_2$ is the leaf area. Compare the values for a random surface and a periodic one and equate Eq. (6a) under normal incidence and Eq. (12). We will consider that $l_1=l_2$. Having taken into account that for 3-D cosine surface $\underline{h}=h/2$, we obtain the relationship

$$l=l_1/(2\pi^{3/2}). \tag{13}$$

As an example, consider a leaf with $L_1=L_2=0.5$ m, $l_1=l_2=0.2$ m, $h=0.025$ m. Then $n_1=n_2=2.5$ and we obtain using Eq. (12) that $a_{\text{leaf}}=2\sqrt{\sigma_{\text{leaf}}}=0.2A$, m.

B. Estimation of the reflection coefficient

We assume the radii of curvature to be sufficiently greater than the wavelength. Therefore the effect of curvature on sound reflection properties may be neglected, and one can suppose that the leaf reflects the sound wave at every point as a plane plate located tangentially at this point. It follows from the results obtained in Sec. II A that at high frequencies only the points of stationary phase are to be taken into account. At these points the wave is incident on the leaf normally. The reflection and transmission coefficients are defined as

$$A=\frac{i(w^{-1}-w)\sin\ k_1h_1}{2\cos\ k_1h_1-i(w+w^{-1})\sin\ k_1h_1}, \tag{14}$$

$$B=\frac{2\exp(-ikh_1)}{2\cos\ k_1h_1-i(w+w^{-1})\sin\ k_1h_1}, \tag{15}$$

where $w=\rho_1c_1/\rho c$; ρ_1, ρ, c_1, and c are the densities and the wave velocities in the leaf and water, respectively; $k_1=\omega/c_1$; h_1 is the leaf thickness. We suppose that the thickness is in the range 0.002–0.02 m. The values of density and velocity in the seaweeds are unlikely to have ever been measured, so they may be prescribed only presumably. The majority of algae does not lay on the bottom and stays suspended in water. Hence the density must be on order of 0.9 to 1.0. In materials like wood, the velocity of the longitudinal wave in the transversal directions is typically 1500–2000 m/s. The seaweeds consist basically of water and the velocity should be a little less than that in wood. During the estimation we considered the velocity to be in the range 1200–1800 m/s.

The results of calculations are presented in Fig. 3. at low frequencies (or at low values of frequency thickness products), i.e., at $k_1h_1\ll1$, one can write down Eq. (14) as $|A|\sim|1-w^{-1}|\pi fh_1/c_1$. it is seen from Fig. 3 that the reflection coefficient increases up to $fh_1=300$–500 kHz mm. to increase the reflected signal in this frequency range it is necessary to increase the operating frequency.

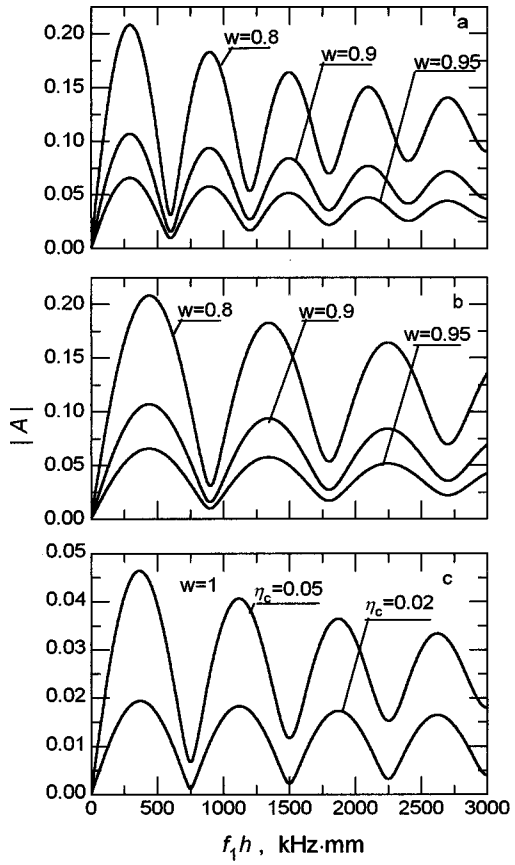

FIG. 3. The reflection coefficient. (a) $c_1=1200$ m/s, $\eta_c=0.05$; (b) $c_1=1800$ m/s, $\eta_c=0.05$; (c) the reflection coefficient for layers with a very low acoustical contrast, $\rho_1=\rho=1000$ kg/m^3, $c_1=c=1500$ m/s. Note the scale change in (c).

The resonant structure of the curves is typical only of an ideal plate of constant thickness without energy absorption. In actual fact the leaf is a more intricate object with the inhomogeneity of structure and variations of thickness. Therefore the periodic pattern of the curves will be essentially smoothed and we obtain a constant value. Consequently, the increasing of the operating frequency up to some limiting frequency increases the reflection coefficient, however, the further increasing of frequency does not practically affect it. As an example, it can be pointed out that for the plate thickness of 2 mm this limiting frequency is about 250 kHz.

To estimate the minimal value of the reflection coefficient, it is useful to note that, even if the densities and the velocities of sound in the material of the leaf and in water are the same but there exist loss of energy in the leaf, the reflection coefficient is not equal to zero. Let us change c_1 for complex value $\hat{c}_1=c(1-i\eta_c)$. From Eq. (14) we obtain approximately at $\eta_c \ll 1$, $|A| \approx \eta_c |1-\text{oscil.term}|$. The typical values of η_c for wood and some plastics are 0.02–0.05. Then one can suppose that this coefficient for algae is about the same. Therefore the reflection coefficient of layers with a very low acoustical contrast is not zero [see Fig. 3(c)].

Returning to the example in the previous section and taking an average value of the reflection coefficient on order of 0.1, we obtain that the equivalent radius of the leaf at high frequencies is $\sim$0.02 m. The backscattering cross section is

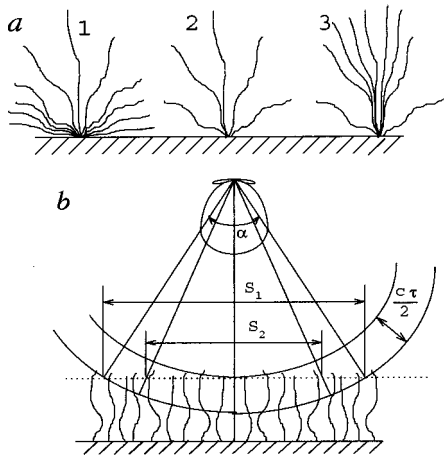

FIG. 4. The seeweeds on the bottom. (a) The typical kinds of leaf inclinations. 1-predominantly horizontal inclination, 2-uniform distribution, 3-predominantly vertical inclination; (b) the insonified bottom area. The effective thickness of the layer with scatterers contributing to the scattered wave is $c\tau/2$.

$\sigma_{\text{leaf}} \approx 10^{-4}$ m^2. We point out for a comparison that the equivalent radius of a fish of length 0.2 m is approximately the same. Such fishes are detected by echosounders at distances of some dozen meters. Hydroacoustical methods allow even weaker targets to be registered. It was reported in Ref. 17 that the sound signals reflected from objects very transparent acoustically, such as jellyfish, have been recorded at frequencies of 120 and 200 kHz. The equivalent radius was about 0.15–0.4 cm.

C. The statistical summation of scattered signals

In summation of the scattered signals from all leaves, one has to take into account that the signals add with random phases, i.e., it is necessary to sum the sound intensities and not the pressures. The different leaves are inclined relative to the direction of the incident wave and the angle of inclination is random. We shall consider three typical cases [Fig. 4(a)]: predominantly horizontal disposition, uniform distribution, and predominantly vertical disposition. The densities of probabilities of the inclination angles for these cases can be described by the following functions

$$P_1(\theta)=\frac{1}{\pi}\cos\theta, \quad P_2(\theta)=\frac{1}{2\pi}, \quad P_3(\theta)=\frac{2}{\pi^2}\sin\theta. \tag{16}$$

The indexes refer to the cases in Fig. 4(a), θ is the angle between the normal to the median plane of the leaves and the direction of the wave vector. These functions satisfy the normalization condition

$$\int_0^{\pi/2}\int_0^{2\pi} P_j(\theta)\sin\theta\, d\theta\, d\varphi=1, \quad j=1,2,3,$$

where we suppose the distributions to be nondependent on azimuthal angle φ. Note that the azimuthal dependence may appear if there are underwater currents and leaves are inclined to one side. Let us introduce a factor to specify the mean value of the angle dependence of the scattered wave

with regard to the above-mentioned densities of probabilities of inclination

$$K_j = \int_0^{\pi/2} \int_0^{2\pi} P_j(\theta) D^2(\theta) \sin\,\theta\, d\theta\, d\varphi, \quad j = 1,2,3.$$

Note that it is impossible to use a ray-optical approach to describe the angular dependence of the scattered wave, since at oblique incidence there will be points on the surface, where the radii of curvature turn into infinity (the points of inflection) and the angular dependence will have the singularity. Therefore we shall use the function Eq. (6b) as a more appropriate one for a random rough surface. So we have

$$K_j = 2\pi \int_0^{\pi/2} P_j(\theta)\, \frac{\sin\,\theta}{\cos^2\,\theta} \exp\left(-\frac{l^2}{4h^2} \tan^2\,\theta \right) d\theta. \tag{17a}$$

The coefficients K_j decrease as the surface becomes more gently sloped, because the pattern of the scattering becomes sharper and only a small part of sound energy propagates in the backward direction. For the large values of the ratio l/h the integral Eq. (17a) is evaluated approximately. The results are

$$K_1 \approx 4(\overline{h}/l)^2, \quad K_2 \approx 2(\overline{h}/l)^2, \quad K_3 \approx (\overline{h}/l)^3 8/\sqrt{\pi}. \tag{17b}$$

The total backscattering cross section can be written down as

$$\sigma = \sigma_{\text{leaf}} \frac{S K_{\text{proj}} K_j K_\tau}{S_0 \langle \cos\,\theta \rangle_j}. \tag{18a}$$

Note that the cross section is actually not dependent on leaf area S_0 since σ_{leaf} in Eq. (12) is proportional to S_0. To calculate the insonified area S on the bottom, it is necessary to take into account that the area (S_1) within the main lobe of the directivity pattern of the transducer may differ from the area (S_2) of the bottom limited by the spot related to the finite thickness of the insonified layer $c\tau/2$ [see Fig. 4(b)]. Therefore $S = \min(S_1, S_2)$, where $S_1 = \pi r_0^2 \alpha_1 \alpha_2/4$ and α_1, α_2 are the widths of the main lobe of the directivity pattern of the transducer in two planes (at the level -3 dB), $S_2 \approx \pi r_0 c\tau$. We suppose, to simplify, that this pattern is constant within the main lobe and zero elsewhere.

The coefficient K_{proj} is determined by the relative projection of the leaves on the bottom, i.e., by the ratio of total area of the projections of all leaves (if observed from the surface) to the area of the bottom in the given location. If the leaves do not overlap, $K_{\text{proj}} \leqslant 1$. The coefficient K_τ is determined by the sound pulse duration. It is known from the theory of volume reverberation that the thickness of the layer which contributes to the scattered field is $c\tau/2$, where τ is the pulse duration. The factor 1/2 appears for the reason that only the scatterers, located in the half of the layer of thickness $c\tau$, contribute to the reflected field, while the waves scattered by other scatterers have no time to catch up with the reflected pulse. We define this coefficient as $K_\tau = c\tau/(2H)$, where H is the average height of the plants. Since the pulses, reflected from the plants and from the bottom, should be separated, $K_\tau \leqslant 1$. The value $\langle \cos\,\theta \rangle_j$ is the cosine of the angle of inclination averaged over the solid angle,

$$\langle \cos\,\theta \rangle_j = \int_0^{\pi/2} \int_0^{2\pi} P_j(\theta) \cos\,\theta\, \sin\,\theta\, d\theta\, d\varphi.$$

For the densities of probabilities given by Eq. (16) we obtain

$$\langle \cos\,\theta \rangle_1 = 2/3, \quad \langle \cos\,\theta \rangle_2 = 0.5,$$

$$\langle \cos\,\theta \rangle_3 = 4/(\pi 3) = 0.42.$$

The frequency dependence of the backscattering cross section is determined only by that of the reflection coefficient in Eq. (12) since other factors in Eq. (18a) are not dependent on frequency. Hence the cross section increases as f^2 for thin leaves or at low frequencies (approximately up to $fh = 300-500$ kHz mm) and remains constant for thick leaves and high frequencies.

Let us return to the example considered in the previous section and suppose that the distribution of inclination of the leaves over all vertical angles is uniform, $r_0 = 30$ m, $\alpha_1 = \alpha_2 = 0.2$ rad, $S_0 = 0.25$ m^2, $l_1 = 0.2$ m, $\overline{h} = h/2 = 0.0125$ m, $K_{\text{proj}} = K_\tau = 1$, $\tau = 5 \times 10^{-4}$ s. Then $\langle \cos\,\theta \rangle_2 = 0.5$, $l = l_1/(2\pi^{3/2}) = 0.02$ m and $K_2 \approx 1$. The area $S_1 = 30$ m^2, $S_2 = 75$ m^2. Hence $S = 30$ m^2. Using Eq. (18a) we obtain $\sigma = 0.02$ m^2. The radius of the equivalent sphere is ~ 0.3 m. It is a comparatively big value.

It is very important to note that the final expression Eq. (18a) depends in a very weak way on the parameter (l_1/h) which specifies the roughness. Let us assume that $l_1 = l_2$. Then it is clear from Eqs. (12) and (18a) that σ_{leaf} is proportional to $(l_1/h)^2$, but the coefficients K_1 and K_2 in Eq. (17b) are approximately in inverse proportion to this ratio since h and l are proportional to h and l_1, respectively. From Eqs. (12), (17b), and (18a) one obtains the estimation

$$\sigma \approx \beta A^2 S K_{\text{proj}} K_\tau, \tag{18b}$$

where $\beta = 0.15$ for predominantly horizontal distribution and $\beta = 0.1$ for random distribution. This expression is not dependent on the parameters of roughness. It can be explained the following way. When the ratio (l_1/h) increases (i.e., the leaf becomes flatter) the signal reflected from a leaf at normal incidence of the wave also increases, however, the directivity pattern of scattering becomes sharper and, with random summation of the scattered waves, the energy arriving at the receiver decreases. These two effects compensate each other and the total reflected signal remains approximately constant, in any case, for predominantly horizontal and random distributions. For predominantly vertical distribution, as seen from Eqs. (17b), K_3 is proportional to $(h/l)^3$. Hence there is no full compensation, and some dependence of the result on the roughness parameters is retained in some degree, but it is weaker than the one in Eq. (12). Therefore it is possible to get a stable estimate even if the statistical parameters of the leave roughness are unknown.

III. DENSE DISPOSITION OF PLANTS ON THE BOTTOM. REFLECTION OF SOUND FROM THE SYSTEM OF LAYERS WITH RANDOM DISTANCES BETWEEN THEM

We shall consider now a dense disposition of seeweeds, when the plants overlap repeatedly and form a multilayer continuous coverage. In this case it is necessary to regard this coverage as a rough surface with some average reflection coefficient. For a thick multilayer system, this coverage can be represented as a half-infinite stack of layers. We shall use the approximate approach and consider that the problem can be simplified by breaking it down into two problems: the calculation of the reflection coefficient for a plane half-infinite system of layers with random distances between them and the calculation of sound scattering from a rough surface with a known reflection coefficient. The reflection coefficient for half-infinite systems of layers separated by layers of media with the same properties as the outer medium is described as follows[18]

$$A_L=\{1-(B_1^2-A^2)u-\sqrt{[1-(B_1^2-A^2)u]^2-4A^2u}\}/(2Au), \tag{19}$$

where A is the reflection coefficient for one plate expressed by Eq. (14), B_1 is the transmission coefficient without the phase factor in the numerator in Eq. (15), i.e., $B_1=B\exp(ikh_1)$, $u=\exp(i2kh_2)$, where h_2 is the distance between the plates.

We shall consider the distance h_2 to be a random quantity with the Gaussian density of probability

$$P(h_2)=\frac{1}{\sqrt{2\pi}h_\sigma}\exp[-(h_2-\overline{h_2})^2/2h_\sigma^2], \quad h_2\geqslant 0, \tag{20}$$

and $P(h_2)=0$ at $h_2<0$. Here h_σ^2 is the variance of h_2 and $\overline{h_2}$ is the mean value. We suppose the distance h_2 to vary slow by along the layers. Then the slopes of rough surfaces relative to their median planes are small and we can apply Eq. (19) with averaging over h_2. The averaged value of the reflection coefficient is

$$\langle A_L\rangle=\left(\int_0^\infty P(h_2)|A_L(h_2)|^2dh_2\Big/\int_0^\infty P(h_2)dh_2\right)^{1/2}. \tag{21}$$

If the standard deviation h_σ exceeds the wavelength, then the average value of the reflection coefficient should not really depend on $\overline{h_2}$ and h_σ. The resonance maxima of the curves in Ref. 18 disappear after averaging. Therefore the distances between the layers need not to be known. The reflection coefficient for a stack of layers is greater than the one for a single layer (compare Figs. 3 and 5). Even for plates with a very low acoustical contrast [Fig. 5(c)] the reflection coefficient retains the values of about 0.02–0.1.

From Eq. (18b) we can obtain the backscattering cross section for very dense coverage and predominantly horizontal disposition in the case $l/h\gg 1$. It is necessary to let $K_{\text{proj}}=1$ and to substitute $\langle A_L\rangle$ for A. So

$$\sigma=0.12\langle A_L\rangle^2 SK_\tau.$$

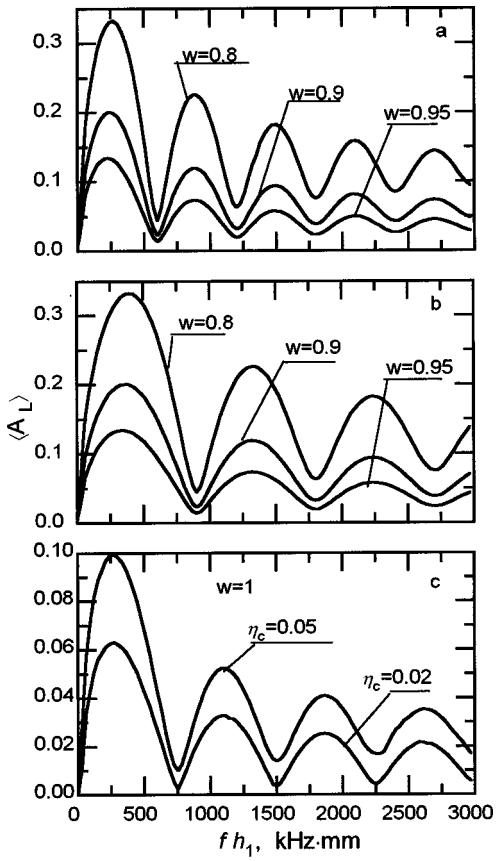

FIG. 5. The mean value of the reflection coefficient averaging over distances between the layers. $h_\sigma=\overline{h_2}$, (a) $c_1=1200$ m/s, $\eta_c=0.05$; (b) $c_1=1800$ m/s, $\eta_c=0.05$; (c) the mean value of the reflection coefficient averaged over distances between the layers with a very low acoustical contrast, $\rho_1=\rho=1000$ kg/m^3, $c_1=c=1500$ m/s. Note the scale change in (c).

For example, if $\langle A_L\rangle=0.1$, $S=30$ m^2, $K_\tau=1$, then $\sigma=0.036$ m^2, i.e., the radius of the equivalent sphere is $\sim$0.35 m. For leaves with a very low acoustical contrast ($c_1=1500$ m/s, $\rho_1=1000$ kg/m^3) and small but finite loss coefficient $\eta_c=0.02$, we obtain $\langle A_L\rangle\approx\eta_c=0.02$, $\sigma=0.0016$ m^2 and the radius is 0.08 m. Thus the cross section for the objects with a very low acoustical contrast is comparatively large.

IV. SCATTERING OF SOUND BY A SYSTEM OF CURVED INTERTWINED STEMS

Consider another kind of algae (for example, *Anfeltia*) which constitutes an intricate system of intertwined bent rods of cylindrical cross section, similar to rope or wire knots. These stems are located comparably sparsely and there is good reason to believe that the distances between them far exceed their diameter. Therefore the sound wave travels through the system without noticeable attenuation. In this case we can consider the total scattered field to be determined by the sum of contributions of fields scattered by all stems in the insonified volume (i.e., in the layer of thickness $c\tau/2$) without interaction between them. As earlier we take into account that the stems are flexible. Then one can neglect shear stresses and describe the acoustical properties of the stems by the density ρ_1 and the velocity of longitudinal wave c_1.

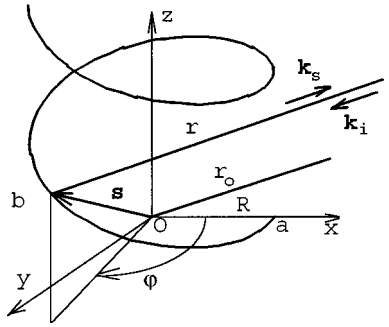

FIG. 6. Reflection of sound from a cylinder bent to a screw line.

Estimation of the target strength of some biological objects based on conception of the objects as bent cylinders was performed in Refs. 19 and 20 (see also the comments of Stanton and Foote[21] to Ref. 19). It was supposed that the axis of the cylinder is bent in one plane. In our case, when the lengths of the rods are large, it is impossible to describe the acoustical properties of such a system adequately with the help of a physical model such as a rod bent in one plane, since this model should be an in-phase summation of scattered waves in the direction normal to this plane. This phenomenon will significantly increase the backscattered field. However, it is impossible to believe that in a real situation the stems could lie in one plane to the accuracy of a small fraction of the wavelength. Practically, they are bent in space and the focusing of sound is unlikely. Hence it is necessary to consider the axes of stems to be 3-D curved lines which have the nonzero values not only of the curvature but of the twist. The simplest model of such a curve is a screw line (Fig. 6). The radius R of the screw line is much greater than the wavelength and the radius of the cylinder a. The pitch d of the screw is much greater than a, but the wave radius of the cylinder is arbitrary. In this case we can consider the sound to be scattered by every element of the curve as it would be scattered by a long cylinder located tangentially to the curve on this element. This assumption corresponds to the Kirchhgoff approximation in respect to the coordinate along the curve, however, the scattering of sound by the cylinder is calculated exactly. We shall derive the backscattering cross section in the same way as in Refs. 14 and 22. The solution of a problem related with scattering of a spherical sound wave described by Eq. (2) from an the infinite cylinder under the condition $kr_0 \gg 1$ can be written down as[14]

$$p_{\text{inf}} = -ik\rho cQ \frac{\exp(ikr)}{4\pi r} \frac{\exp(ikr - i\pi/4)}{\sqrt{\pi kr}} \Phi_s(\pi), \quad (22)$$

where $\Phi_s(\pi)$ is the function describing the scattering of sound in the backward direction (form function). The tables of this function for acoustically hard and soft cylinders are presented in Ref. 13. For the elastic cylinder this function is given by[13,14]

$$\Phi_s(\pi) = \sum_{n=0}^{\infty} \epsilon_n (-1)^n d_n, \quad (23a)$$

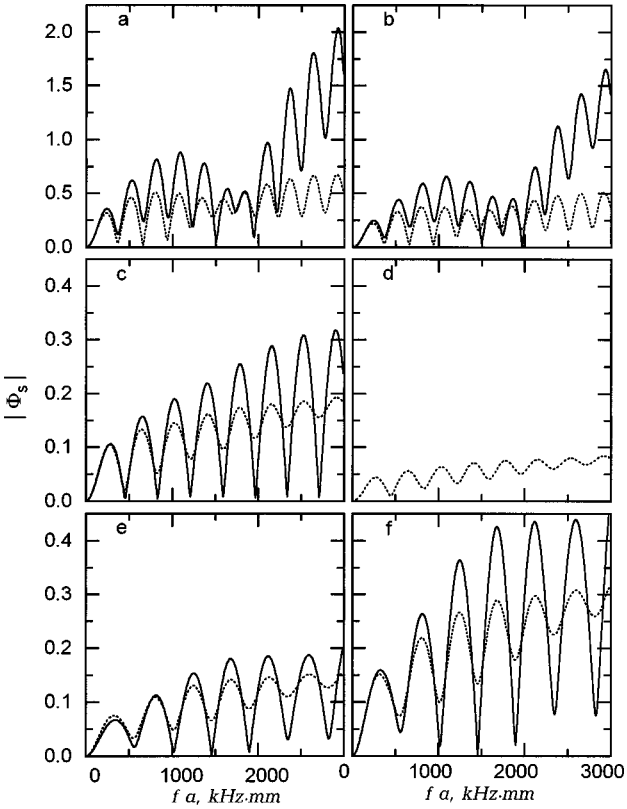

FIG. 7. Form function of the cylinders with different velocities of longitudinal waves. (a) $w=0.9$, $c_1=1200$ m/s, (b) $w=1.0$, $c_1=1200$ m/s, (c) $w=0.9$, $c_1=1500$ m/s, (d) $w=1.0$, $c_1=1500$ m/s, (e) $w=0.9$, $c_1=1800$ m/s, (f) $w=1.0$, $c_1=1800$ m/s, solid lines: $\eta_c=0$, dotted lines: $\eta_c=0.05$. Note the scale change in (a) and (b).

$$d_n = -\frac{J_n(ka) + J_n'(ka) Z_n/(i\rho c)}{H_n^{(1)}(ka) + H_n^{(1)'}(ka) Z_n/(i\rho c)}, \quad (23b)$$

where $\epsilon_n = 1$ if $n=0$ and 2 otherwise, J_n and $H_n^{(1)}$ are Bessel and Hankel functions, and Z_n are the input impedances of the elastic cylinder. For a cylinder with shear stresses neglected (''acoustically liquid cylinder'') impedances are written down as $Z_n = -i\rho_1 c_1 J_n(k_1 a)/J_n'(k_1 a)$, $k_1 = \omega/c_1$ is the wave number of a longitudinal wave in the cylinder. Frequency dependence of the form function is of an oscillating nature (Fig. 7). The oscillations are explainable by the cylinder resonances and by the peripherical waves traveling around the cylinder. The comprehensive discussion of such phenomena is presented in Ref. 23.

To take into account the loss of energy in the stems, we supposed the velocity c_1 to be complex as was done in Sec. II B, and computed the values of Bessel functions $J_n(k_1 a)$ of complex argument. These results are presented in Fig. 7 by the dotted lines. Note that, even if $c_1 = c$ and $\rho_1 = \rho$ [see Fig. 7(d)] the scattered field does not vanish.

Let us derive on this basis the sound pressure scattered by a cylinder with an axis curved in space. The expression (22) is the product of a spherical wave radiated by a spherical source and a cylindrical wave radiated by some sources situated on the axis of the bent cylinder (''virtual sources''). We will find the strength q of these sources on a unit length and next integrate the sound pressure radiated by them along

the screw line. The sound pressure radiated by sources situated on an infinite straight line is written as[14]

$$p=\frac{k\rho cq}{4}\sqrt{\frac{2}{\pi kr}}\exp(ikr-i\pi/4).$$

By equating this value to the scattered sound pressure Eq. (22), we obtain the strength of the virtual sources

$$q=-\frac{4iQ}{\sqrt{2}}\frac{\exp(ikr)}{4\pi r}\Phi_s(\pi). \tag{24}$$

The sound pressure radiated by such sources is determined as the line integral

$$p_{\text{scat}}=-\frac{ik\rho c}{4\pi}\int_l \frac{q\ \exp(ikr)}{r}\,dl. \tag{25}$$

For a point of observation located in far field one can consider the rays r and r_0 to be parallel. Then $r\approx r_0-\mathbf{k}_s\mathbf{s}$. The coordinates of a running point on the curve and the components of the wave-number vector are

$$x=R\ \cos\ \varphi,\quad y=R\ \sin\ \varphi,\quad z=\varphi d/(2\pi),$$

$$k_x=k\ \cos\ \theta,\quad k_y=0,\quad k_z=k\ \sin\ \theta.$$

We shall integrate over one period of the curve. The distance along the curve between the points a and b is described as $l=\varphi[R^2+(d/2\pi)^2]^{1/2}$. Then from Eq. (25) we obtain

$$p_{\text{scat}}=-k\rho cQ\ \frac{\exp(2ikr_0)}{4\pi r_0}\ \frac{\Phi_s(\pi)}{\pi r_0\sqrt{2}}\ F_l, \tag{26}$$

$$\begin{aligned}F_l&=\int_l \exp(-i2\mathbf{ks})\,dl\\&=R[1+g^2]^{1/2}\int_0^{2\pi}\exp[-i2kR(\cos\ \theta\ \cos\ \varphi\\&\quad+\varphi g\ \sin\ \theta)]\,d\varphi,\end{aligned} \tag{27}$$

where $g=d/(2\pi R)$. Note that if $kd\ \sin\ \theta/\pi$ is an integer the integral can be expressed via the Bessel functions. We shall use the stationary phase method. There are two stationary points $\varphi_0^{(1)}=\sin^{-1}(g\ \tan\ \theta)$, $\varphi_0^{(2)}=\pi-\varphi_0^{(1)}$ on a period of the screw line. These stationary points may exist only if $\theta\leqslant\theta_{\max}$, where $\theta_{\max}=\tan^{-1}(1/g)$. If the angle of incidence exceeds $\theta_{\max}$, there are no reflected sound rays arriving at the receiver. In this case in ray-optical approximation the reflected waves are absent. Having evaluated the integral, we obtain for the stationary point of number $j(j=1,2)$

$$F_l=\sqrt{1+g^2}\sqrt{\frac{\pi R}{k}}\ \frac{\exp[-i2kR(u(\theta)+\varphi_0^{(j)}g\ \sin\ \theta)-i\ \text{sign}(\cos\ \varphi_0^{(j)})\pi/4]}{\sqrt{u(\theta)}}, \tag{28}$$

where $u(\theta)=\sqrt{\cos^2\theta-g^2\sin^2\theta}$. At $\theta=\theta_{\max}$ this expression has a weak singularity. At this angle the phase function has an inflection point and two stationary points merge together. However, further on we shall average the intensity of the scattered wave over all angles of incidence and this singularity will not prevent the integration.

Since the real curve has a nonregular shape the contributions of all stationary points add with random phases. Hence we should sum up the wave intensities. Using Eqs. (26) and (28), we write down the intensity of the wave due to one stationary point

$$I_{\text{scat}}^{(0)}(\theta)=I_i\ \frac{l_1}{4\pi^2r_0^2}\ \frac{|\Phi_s(\pi)|^2}{k\ \sin\ \theta_{\max}}\ \frac{1}{u(\theta)}\quad(|\theta|\leqslant\theta_{\max}), \tag{29}$$

where I_i is the intensity of the incident wave described by Eq. (3), $l_1=2\pi R\sqrt{1+g^2}$. Note that the limiting case $k\to 0$ is inadmissible, since the method of stationary phase is valid only if $kR\gg 1$, the same holds for the limiting case $d\to 0$. In the last case, the elements of the curve are nearly planar rings and there arises the focusing in the direction of the axis. In reality it is impossible because we consider the curve to have a nonregular shape.

The curve may be oriented at arbitrary angles relative to the direction of the incident wave. For a random system of intertwined stems we can regard the density of probability of the angles θ to be constant and write it down as $1/4\pi$. Then the value of $I_{\text{scat}}^{(0)}(\theta)$ averaged over solid angle 4π is determined by

$$\begin{aligned}\langle I_{\text{scat}}^{(0)}\rangle&=\frac{1}{4\pi}\int_\Omega I_{\text{scat}}^{(0)}(\theta)\,d\Omega\\&=I_i\ \frac{l_1|\Phi_s(\pi)|^2}{4\pi^2r_0^2k\ \sin\ \theta_{\max}}\\&\quad\times\frac{1}{4\pi}\int_0^{2\pi}\int_{\pi/2-\theta_{\max}}^{\pi/2+\theta_{\max}}\frac{\sin\ \alpha\ d\alpha\ d\varphi}{u(\pi/2-\alpha)}.\end{aligned}$$

Using the definition, Eq. (5), we obtain after the integration the backscattering cross section for one stationary point averaged over the solid angle

$$\langle\sigma_0\rangle=l_1|\Phi_s(\pi)|^2/(8\pi k). \tag{30}$$

The number of stationary points can be calculated from the biomass of algae. The total length of the stems is $l=M/(\pi a^2\rho_1)$. This length accommodates $l/l_1=M/(\pi a^2\rho_1 l_1)$ periods of the curve. Two stationary points are located on each period. Hence the number of stationary points is obtained as $n=2M/(\pi a^2\rho_1 l_1)$. The total backscattering cross section is defined as $\sigma=n\langle\sigma_0\rangle$. From Eqs. (30) and (31) we get

TABLE I. The masses and the sizes of the specimens used in Ref. 5.

			L. saccarina		
Specimen	1	2	3	4	5
M, kg	0.50	0.33	0.80	0.80	0.58
Size, m	0.85×0.57	0.70×0.45	2.0×0.53	1.05×0.88	0.97×0.80
			L. digitata		
Specimen	6		7	8	
M, kg	0.56		0.40	0.70	
Size, m	0.80×0.90		0.90×0.39	1.7×0.45	

$$\sigma = \frac{M|\Phi_s(\pi)|^2}{4\pi^2 a^2 k \rho_1}. \tag{31}$$

This quantity is not dependent on the curve parameters R and d (of course, in the high-frequency approximation used here). It may be explained in the following way. If the curve becomes more winding, then the radii of curvature decrease and the scattered sound pressure falls down. But in this case the number of stationary points increases and compensates the above-mentioned reductions. Therefore one does not have to know the specific geometric parameters of the curve.

Let us consider an example: $a = 2\times10^{-3}$ m, $f = 250$ kHz, $\rho_1 = 1000$ kg/m^3. From Fig. 7 we take an average value $|\Phi_s(\pi)| = 0.05$. If $M = 1$ kg, we obtain $\sigma \approx 0.2\times10^{-4}$ m^2/kg. Returning to the example at the end of Sec. II C, we take the insonified bottom area $S = 30$ m^2 and $\tau = 0.5\times10^{-4}$ s. The effective insonified volume is $V = Sc\tau/2 = 11$ m^3. If one assumes that there are 5 kg of algae in 1 m^3 of water, the total insonified biomass is 55 kg. Hence the total backscattering cross section is $\sim10^{-3}$ m^2. The radius of the equivalent sphere is ~6 cm.

Frequency dependence of σ is described by the function Φ_s and by the quantity k in the denominator. At low values of the wave radius of the cylinder, there exists a Rayleigh scattering and $|\Phi_s|$ increases as f^2. Therefore σ is proportional to f^3. At high values of the wave radius $|\Phi_s| \sim f^{1/2}$ (see Ref. 14) and σ oscillates with increasing frequency but does not grow. The boundary between these frequency ranges is about $fa \sim 300-500$ kHz mm (Fig. 7).

V. COMPARISON OF THE ESTIMATION WITH EXPERIMENT

The results of measurements of backscattering cross section of some kinds of algae are presented in Ref. 5. The authors measured the sound pressure reflected from leaves of *Laminariae: L. saccarina* and *L. digitata*. The measurements were fulfilled at the frequencies 50, 70, and 200 kHz under normal incidence of wave on the leaf. The sizes and masses of the specimens are given in the Table I. The thicknesses of the leaves were 1–5 mm. The leaves were fixed below an acoustical transducer at the depth of 9 m. Magnitudes of reflected sound pulses were compared with the ones for a reference sphere. For calculation of the backscattering cross section the authors of Ref. 5 used the definition $\sigma_{bs} = 4\pi r_0^2 I_{\text{scat}}/I_0$, which differs from the definition Eq. (5) by the factor 4π. Therefore for comparison of the theoretical and the experimental results we have recalculated the values presented in Ref. 5. Using the physical model presented in Sec. II. we have calculated the backscattering cross section per 1 kg of mass. For the estimation we used the values of the roughness adopted in the above-mentioned examples. As the maximal and the minimal values of the reflection coefficient we took 0.2 and 0.05, respectively. The upper and lower bound of estimates and the results of experiments are given in Fig. 8. The cross section increases with increasing frequency. Behavior of this increasing is in agreement with the discussion in Sec. II. The wave thickness of the plates, i.e., kh_1, was 0.15–1.5 and the values fh_1 were 35–400 kHz mm. It is seen from Fig. 3 that such values correspond, in the main, to the frequency range where the reflection coefficient increases, but the maximum values of this product (about 400 kHz mm) correspond to the thickness about a quarter of the wavelength and the increasing of the reflection coefficient slows down. Despite a dispersion of the experimental results and the hypothetical nature of the values of parameters adopted in calculations, one can consider the behavior of the experimental results to be in agreement with the physical model.

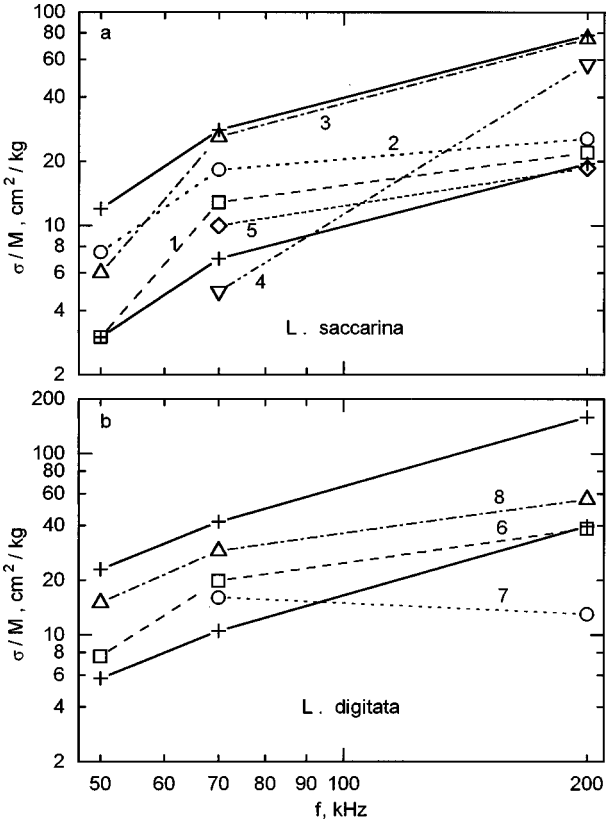

FIG. 8. Comparison of the estimates with the results of experiment, presented in Ref. 6. Upper and lower solid lines are the envelops of the maximal and the minimal calculated values. Numbers on the graph correspond to the specimens in Table I.

VI. CONCLUSIONS

Some physical models for describing the sound reflection properties of algae are suggested. These models are rough, acoustically half-transparent layers, stacks of layers, and cylinders with curved axes. The random disposition of

such elements in the space is taken into account. Despite a great uncertainty of values of the algae elastic parameters, it has turned out to be possible to calculate the sound-scattering cross section of some algae species, the estimated values being in agreement with the experimental results.

The magnitude of the reflected signal increases with increasing frequency up to the values of the products fh_1 or fa on order of 300–500 kHz mm. Further increasing of these parameters does not significantly affect the reflected wave intensity. When dealing with sparse disposition of the plants, the reflected signal intensity is dependent on biomass, and the measurements of this intensity under a condition of appropriate calibration can give the estimates of biomass on the large bottom area. For a very dense distribution of the plants the reflected signal depends only slightly on the biomass.

The important result is that the backscattering cross section after averaging over the angles of inclination is not dependent on the geometrical parameters of the leaves and the stems bending. This result is in agreement with the statement in Ref. 20, where the model of bend cylinder with averaging over angles of orientation was used for estimation of target strength of zooplankton. It was pointed out there that the backscattering cross section of a single scatterer is dramatically dependent upon the curvature, but the curvature becomes a much lesser factor once averaged over an aggregation of animals. Independence or weak dependence of backscattering cross section upon the shape make it possible to obtain stable estimates even if the parameters of the shape are unknown. Of course, the most reliable data on the strongly stochastic objects such as algae can be obtained only during the *in situ* measurements. But the results of an approximate estimation will be useful for choosing operation modes of echosounders and analysis of results.

ACKNOWLEDGMENTS

The author would like to thank Dr. G. C. Gaunaurd for his approval to begin this work, and Professor V.S. Levin (biological sciences), who has attracted my attention to this subject. The research described in this publication was made possible in part by Grant No. NVB 000 from the International Science Foundation and Grant No. NVB 300 from the Russian Government.

[1] C. J. Stant and S. Hanley, ''A recording echosounder for the assessing submerged aquatic plant populations in shallow lakes,'' Aquat. Botany **21**, 327–394 (1985).

[2] C. M. Duarte, ''Use of echosounder tracing to estimate the aboveground biomass of submerged plants in lakes,'' Can. J. Fish. Aquat. Sci. **44**, 732–735 (1987).

[3] Y. Maniwa, ''Investigation of the form of ultrasonic wave reflected from sea bottom, fish shoal and sea plants,'' Techn. Rept. Fish Boat **11**, 157–175 (1958) (in Japanese).

[4] E. N. Gavrilov and V. V. Pestricov, ''Optimal operation modes of compact echosounders in scouting for laminaria,'' in *Modern Methods of Research on Sea Macrophytes* (preprint, PINRO, Murmansk, 1992), pp. 28–32.

[5] E. N. Gavrilov and V. V. Pestricov, ''Experimental studies to determine the reflective capacity of marine macrophytes,'' in *Modern Methods of Research on Sea Macrophytes* (Ref. 4), pp. 33–39.

[6] V. V. Pestricov, ''Investigation of laminaria stocks in the Barents Sea with echosounder Shkipper-607'' in *Modern Methods of Research on Sea Macrophytes* (Ref. 4), pp. 40–47.

[7] A. L. Sorokin and V. V. Pestricov, ''Using of the fish searching echosounders in artography of the sea macrophytes,'' Rybnoye khozyaystvo (Fish industry in Russian) **11**, 58 and 59 (1986).

[8] *Life of Plants*, in 6 volumes, edited by A. A. Fedorov (Prosveshcheniye, Moskva, 1977, in Russian), Vol. 3, Algae, Lichens.

[9] J. A. Ogilvy, ''Wave scattering from rough surfaces,'' Rep. Prog. Phys. **50**, 1553–1608 (1987).

[10] F. G. Bass and I. M. Fuks, *Wave Scattering from Statistically Rough Surfaces* (Pergamon, Oxford, 1979).

[11] M. A. Isakovich, ''Scattering of waves from statistically rough surface,'' Trudy Akusticheskogo Instituta AN SSSR (in Russian) **5**, 152–251 (1969).

[12] E. L. Thorsos, ''The validity of Kirchhoff approximation for rough surface scattering using a Gaussian roughness spectrum,'' J. Acoust. Soc. Am. **83**, 78–92 (1988).

[13] E. L. Shenderov, *Wave Problems in Hydroacoustics* (Sudostroyeniye, Leningrad, 1972). English translation: Joint Publications Research Service, Report JPRS-58146 (National Technical Information Service, Springfield, VA, 1973).

[14] E. L. Shenderov, *Radiation and Scattering of Sound* (Sudostroyeniye, Leningrad, 1989, in Russian).

[15] T. K. Stanton, ''Simple approximate formulas for backscattering of sound by spherical and elongated objects,'' J. Acoust. Soc. Am. **86**, 1499–1510 (1989).

[16] T. K. Stanton, ''Volume scattering: Echo peak PDF,'' J. Acoust. Soc. Am. **77**, 1358–1366 (1985).

[17] I. B. Andreyeva and V. G. Samovolkin, *Scattering of Sound by Sea Animals* (Agropromizdat, Moskva, 1986, in Russian).

[18] E. L. Shenderov, ''Reflection of plane sound wave from half-infinite periodic transversely isotropic set of layers,'' J. Acoust. Soc. Am. **101**, 1239–1249 (1997).

[19] M. C. Macaulay, ''A generalized target strength model for euphausiids with applications to other zooplankton,'' J. Acoust. Soc. Am. **95**, 2452–2466 (1994).

[20] T. K. Stanton, D. Chu, P. H. Wiebe, and C. S. Clay, ''Average echoes from randomly oriented random-length finite cylinders: Zooplankton models,'' J. Acoust. Soc. Am. **94**, 3463–3472 (1993).

[21] T. K. Stanton and K. G. Foote, ''Comment on Average echoes from randomly oriented random-length finite cylinders: Zooplankton models,'' J. Acoust. Soc. Am. **98**, 1807–1809 (1995).

[22] T. K. Stanton, ''Sound scattering by the cylinders of finite length. III. Deformed cylinders,'' J. Acoust. Soc. Am. **86**, 691–705 (1989).

[23] G. C. Gaunaurd, ''Elastic and acoustic resonance wave scattering,'' Appl. Mech. Rev. **42**, 143–191 (1989).

Separation of interfering acoustic scattered signals using the invariants of the time-reversal operator. Application to Lamb waves characterization

Claire Prada and Mathias Fink
Laboratoire Ondes et Acoustique, Université Paris 7, C.N.R.S. UMR 7587, E.S.P.C.I., 10 rue Vauquelin, 75352, Paris Cedex 05, France

(Received 18 August 1997; accepted for publication 23 April 1998)

The D.O.R.T. method (in French, Décomposition de l'Opérateur de Retournement Temporel) is a scattering analysis technique using arrays of transducers. The method was shown to be effective in detecting and focusing on pointlike scatterers in Prada *et al.* [J. Acoust Soc. Am. **99**, 2067–2076 (1996)]. Here the D.O.R.T. method is extended to other geometries, applying it to an air-filled cylindrical shell embedded in water. It is shown that the diagonalization of the time-reversal operator permits the various elastic components of the scattered field to be extracted. For the considered cylinder, these components are mainly three circumferential waves ($A0$, $A1$, and $S0$ Lamb modes). Each Lamb mode is shown to correspond to an invariant of the time-reversal operator. The dispersion curves of these waves are calculated from the invariants. In particular, the cutoff frequency of the $A1$ mode is found and provides the thickness of the shell. Finally, resonance frequencies of the shell are deduced from the frequency dependence of the eigenvalues of the time-reversal operator. [S0001-4966(98)03408-0]

PACS numbers: 43.30.Jx, 43.40.Rj, 43.60.Pt [DLB]

INTRODUCTION

Detection and identification of a scattering object by remote sensing techniques is an important problem in a variety of applications. Among them, the reconstruction of internal flaws in ultrasonic nondestructive testing and target classification in underwater acoustics have been widely studied. The scattering of acoustic waves by an elastic body that has dimensions greater than a wavelength is a complex phenomenon. The incident wave is converted into several modes that propagate in and around the object. These waves radiate into the surrounding medium and contribute to the scattered field. In order to understand the scattering process and relate it to the characteristics of the scatterer, it is necessary to identify and separate the various contributions to the signal. In some cases, the modes propagate at different velocities so that their contribution to the signals occur at different times, and they can then be distinguished with time-domain techniques using highly resolved broadband pulses. However, signals from various modes may overlap in time, rendering their identification difficult. This is the case for the problem that we examine in this paper, the scattering of ultrasound from an air-filled cylindrical shell immersed in water. The goal of this paper is to show how the construction of the invariants of the time-reversal process permits the separation and identification of the modes which contribute to the scattered field. The construction of these invariants is an essential part of the D.O.R.T. method (in French, Décomposition de l'Opérateur de Retournement Temporel).

Methods for identifying and separating the various modes that contribute to the signal backscattered from a cylindrical shell have been the subject of many theoretical works.[1,2] Experimental methods such as ''The Method of Isolation and Identification of Resonance''[3] and the short pulse methods[4,5] have proven to be useful. In these methods, the phase velocity of the wave is deduced from the vibrational modes of the shell at its resonance frequencies. Optical remote sensing techniques have also been used to generate and detect circumferential waves. These techniques have the great advantage of providing a local measurement of the field.[6] More recently, this problem was studied with time-reversal mirrors.[7,8]

Acoustic time-reversal mirrors have been widely used since they were first described in 1989.[9–15] A time-reversal mirror consists of an array of transmit/receive transducers. Each element of the array is connected to its own electronic circuitry: a receiving amplifier, an A/D converter, storage memory, and a programmable transmitter. All the channels are processed in parallel for the transmission and reception of the ultrasonic waves. Such a system is able to transmit an ultrasonic wave, to detect the backscattered wave, and then to synthesize a time-reversed version of this wave. This process is performed in less than 1 ms, which can be considered as real time for most scattering media. The time-reversal mirror converts a divergent wave into a convergent one. One consequence is that it can be used to focus on a reflective target through an inhomogeneous medium. If the medium contains several scatterers, the process can be iterated in order to focus on the most reflective one.[9,16]

As shown by Thomas,[7] this system can also be used to study scattering by an elastic shell. He has investigated the two-dimensional (2-D) problem of a thin, air-filled cylindrical shell with dimensions $a=10\,\text{mm}$, $b/a=0.95$, and $ka\approx 125$ under normal incidence (a is the outer radii, b the inner radii, and k the wave number in the loading medium). Two waves propagating around the shell were detected: the first can be considered as a S_0 Lamb wave and the second as an A_0 Lamb wave. As the contributions of these circumfer-

ential waves occur at different times, they could be selected temporally with a proper time window and then time reversed. This process allowed each wave to be generated separately. The points at which the incident wave converts into circumferential waves were determined and the phase velocity of each wave was deduced from the distance between these points. This method is limited to the case in which circumferential waves do not interfere and thus can be time resolved. In the case considered by Thomas, the frequency range included the cutoff frequency of the second antisymmetrical Lamb wave A_1. This highly dispersive wave interfers with A_0 and S_0 and could not easily be distinguished in the scattered signals. As we shall see now, the D.O.R.T. method solves this problem and allows one to treat all three modes simultaneously.

The D.O.R.T. method was derived from the theoretical study of iterative time-reversal mirrors,[16] and applies to detection and focusing with large arrays of transducers. This method shares some of the principles used in eigenvector decomposition techniques for passive source detection.[17,18] However, these last techniques assume statistically uncorrelated sources and requires averaging of the measured data, while the D.O.R.T. is active and deterministic.

The D.O.R.T. method consists of determining the invariants of the time reversal process. The calculation is performed offline after the measurement of the response functions of the array in the presence of the scattering medium. It is not a real-time procedure; however, it can still be applied in many experimental situations. Its practical advantage is that it does not require the complex programmable emitters of the time-reversal mirrors. As already mentioned, the main interest is that it allows one to separate scattered waves that overlap in time and cannot be separated by time windowing. This method was applied to selective focusing in media containing several targets.[19,20] It was shown that for N pointlike and well-resolved targets of different reflectivities, the number of independent invariants is equal to N. Furthermore, each invariant provides a phase and amplitude law to be applied to the transducer array in order to focus selectively on one of the targets.

In the first part, we review the principles of the D.O.R.T. method. In the second part, the D.O.R.T. method is applied to the detection of Lamb waves on a thin cylindrical shell. It is shown that although the signals due to the various Lamb waves overlap in time, they can nonetheless be separated into the contribution from individual modes. The dispersion curves and the resonance spectrum of the various modes are determined experimentally.

I. PRINCIPLE OF THE D.O.R.T. METHOD

The D.O.R.T. method relies on a matrix formalism describing the scattering experiment. For a given transducer array and a given scattering medium, the time-reversal process is characterized in the frequency domain by a complex matrix. This matrix is obtained from the interelement impulse response functions which can be measured straightforwardly. As shown further, this matrix is Hermitian and its eigenvectors are independent invariants of the time-reversal process. These invariants are related to the structure of the scattering medium and they carry valuable information about this medium. The D.O.R.T. method consists of the determination and analysis of these eigenvectors.

A. The transfer matrix and the time-reversal operator

An array of N transducers placed in front of a time invariant scattering medium is considered as a linear and invariant system of N inputs and N outputs. The N received signals $r_l(t)$, $1 \leqslant l \leqslant N$ depend on the N transmitted signals $e_m(t)$, $1 \leqslant m \leqslant N$ through the linear relation

$$r_l(t) = \sum_{m=1}^{N} k_{lm}(t) \underset{t}{\otimes} e_m(t), \quad 1 \leqslant l \leqslant N. \tag{1}$$

Here, $k_{lm}(t)$ is the impulse response function from the element m to the element l. These interelement response functions take into account all the propagative effects through the medium under investigation as well as the acousto-electric responses of the two elements. In the Fourier domain, Eq. (1) simplifies using a matrix formula:

$$R(\omega) = \mathbf{K}(\omega) E(\omega), \tag{2}$$

where $E(\omega)$ and $R(\omega)$ are the vectors of the Fourier transforms of the transmitted and received signals. $\mathbf{K}(\omega)$ is the $N \times N$ transfer matrix of the system.

The matrix relation between transmitted and received signals leads to an expression for the transmitted signal after two successive time-reversal operations. Let E^0 be the initial input vector signal. The output signal is then $R^0 = \mathbf{K} E^0$.

The time-reversal operation is equivalent to phase conjugation in the frequency domain, so that the new transmitted signal E^1 is the phase conjugate of the previous received signal R^0

$$E^1 = \mathbf{K}^* E^{0*}.$$

The new received signal is then

$$R^1 = \mathbf{K} E^1 = (\mathbf{K}^* \mathbf{K} E^0)^*.$$

$\mathbf{K}^*\mathbf{K}$ is called the time-reversal operator.

As a consequence of the well-known reciprocity theorem the response from element number m to element number l is equal to the response from element number l to element number m, so that the matrix $\mathbf{K}$ is symmetrical. The symmetry of $\mathbf{K}$ implies that $\mathbf{K}^*\mathbf{K}$ is Hermitian positive. In consequence, it can be diagonalized in an orthogonal basis and has real positive eigenvalues. An eigenvector corresponds to an invariant of the time-reversal operation. Two invariants correspond to contributions to the scattered field that are independent solutions of the wave equation. Each of these waves can exist alone even though they are usually superimposed in the experiments.

B. The D.O.R.T. method

The first step of the D.O.R.T. procedure is the measurement of the interelement impulse responses of the system. This measurement can be done with any multiplexed system by $N \times N$ transmit–receive operations. The components of the transfer matrix $\mathbf{K}$ are obtained by a Fourier transform of each signal. The second step is the diagonalization of the

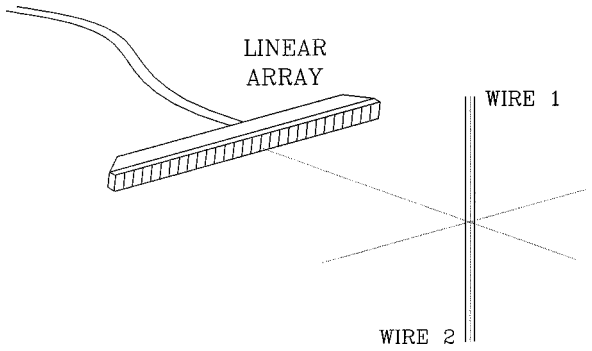

FIG. 1. Experimental setup for two symmetrical wires.

time-reversal operator $\mathbf{K}^*\mathbf{K}$ at a chosen frequency. The eigenvalues distribution contains interesting information on the scattering medium. In the case of pointlike scatterers, the number of significant eigenvalues is exactly the number of scatterers provided they are resolved by the system. More generally, this number corresponds to the number of independent secondary sources in the medium.[16,19,20] The third step is to backpropagate each eigenvector. This can be done either numerically or experimentally. In our case, the propagating medium is homogeneous and the numerical backpropagation can be computed.

C. Experiment with two scatterers in a symmetrical geometry

The results presented in Sec. II can be illuminated by the results obtained in the simple case of two identical pointlike scatterers in a symmetrical geometry. The calculation of the eigenvectors for two pointlike scatterers was presented in a recent paper.[9] In the case of two identical scatterers placed symmetrically with respect to the array of transducers, the expression of the eigenvectors simplifies. Let $H_{il}(\omega)$ be the response of scatterer number i ($i=1,2$) to transducer number l ($1 \leqslant l \leqslant N$). We have shown that the two eigenvectors are

$$V_+ = (H_{11}^* + H_{21}^*, \ldots, H_{1N}^* + H_{2N}^*)$$

and

$$V_- = (H_{11}^* - H_{21}^*, \ldots, H_{1N}^* - H_{2N}^*).$$

They correspond to the phase conjugate of the sum and difference of the responses of each scatterer to the array.

In the experiment, a linear array of 128 transducers spaced 0.417 mm and of central frequency 3 MHz was used. The target was made of two wires placed perpendicular to the array in a symmetrical geometry at the depth of 92 mm and separated by 2 mm (Fig. 1). The time-reversal operator is measured for this configuration and its diagonalization at 3 MHz reveals two main eigenvectors V_+ and V_-. The modulus of the components of those two vectors (Fig. 2) correspond to the interference pattern of two sources oscillating in phase (V_+) and opposite phase (V_-). The numerical backpropagation of V_+ and V_- at the depth of the wires confirms this interpretation [Fig. 3(a) and (b)]: the field is focused at the position of the wires, where the phase of the field is equal for V_+ and opposite V_-.

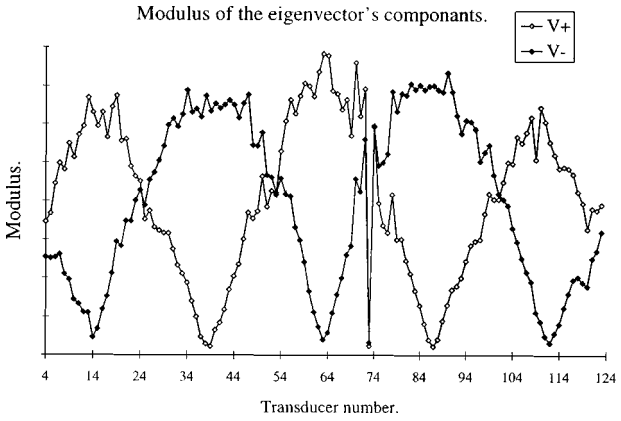

FIG. 2. Modulus of the components of the two eigenvectors versus array element (transducer 73 failed).

II. APPLICATION TO LAMB WAVES

A. Circumferential waves and time reversal

A circumferential wave propagating in a thin hollow cylinder ($b/a=0.95$) can be considered a Lamb wave. It is generated at a given angle of incidence θ with respect to the normal to the surface. According to Snell's law, this angle satisfies the relation

$$\sin(\theta) = \frac{c_0}{c_\phi},$$

where c_0 is the sound velocity in water and c_ϕ is the phase velocity of the Lamb wave. While propagating around the cylinder, it radiates into the fluid at the opposite angle with

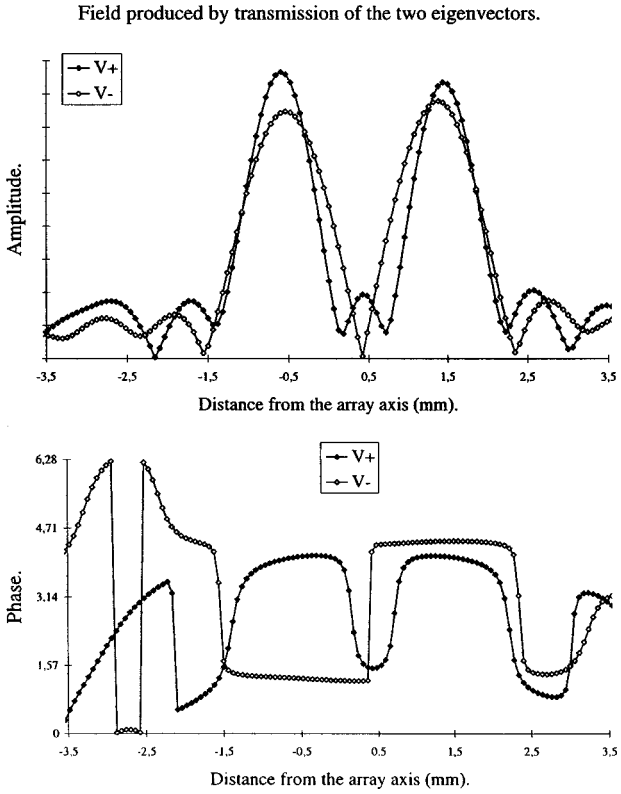

FIG. 3. Amplitude and phase of the field produced by transmission of the two eigenvectors.

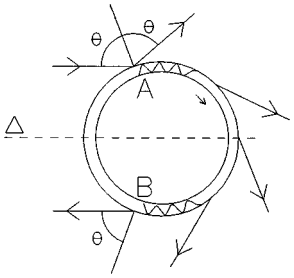

FIG. 4. Generation and radiation of a Lamb wave on a thin hollow cylinder.

respect to the normal to the surface. For a plane wave of incident direction Δ, two Lamb waves are generated at points A and B symmetrical with respect to Δ (Fig. 4). These waves radiate from B and A back to the source. From the direction of observation Δ, the radiated wave appears to be emitted from a pair of secondary sources in A and B. The distance d_{AB} between generation and radiation points A and B is given by the simple relation

$$d_{AB}=D\,\frac{c_0}{c_\phi},$$

where D is the diameter of the cylinder.

Using an array of transducers, a wave can be focused at the surface of the cylinder (Fig. 5). As the wave is locally plane within the focal zone the same approach as before can be used: A Lamb wave is generated at point A if the Snell's law is satisfied. Turning around the shell, the Lamb wave radiates from the opposite point B toward the array. After one time reversal, this wave radiates towards the array from point A. Thus it appears that this wave is invariant under two successive time-reversal processes. Consequently, it should be associated to an eigenvector of the time-reversal operator **K*K**. In fact, due to the symmetry of the system, the focusing in A and B are both associated to the two same eigenvectors just like in the case of two symmetrical pointlike scatterers (Sec. I D).

B. Experiment

The array is linear and made of 96 rectangular transducers. The array pitch is 0.417 mm and the central frequency is

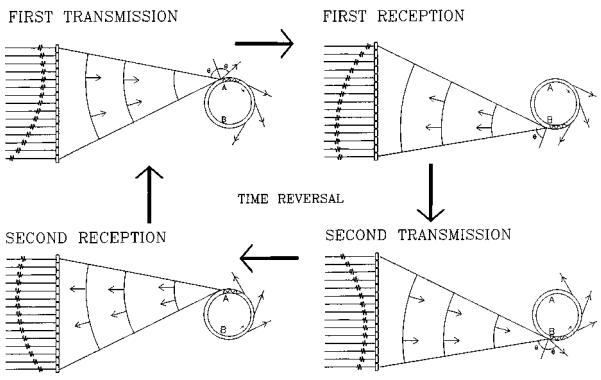

FIG. 5. Lamb waves are invariants of the time-reversal process: A wave focused on point A generates a Lamb wave which radiates towards the array from point B. After two successive time-reversal processes of this Lamb wave, the transmitted wave is similar to the first one, consequently this wave is associated to an invariant of the time-reversal process.

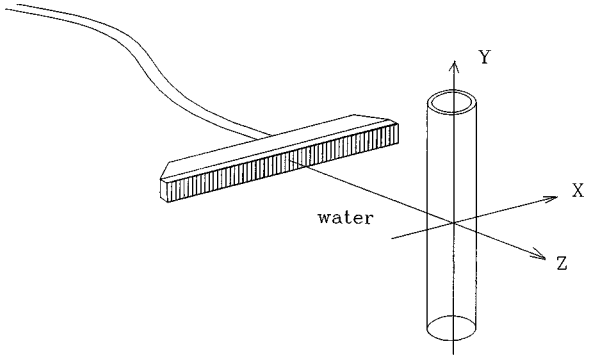

FIG. 6. Experimental setup.

3 MHz with 60% bandwidth. The sampling frequency of received signals is 20 MHz. The steel cylinder of diameter 20 mm and thickness approximately 0.6 mm is placed perpendicular to the array of transducer at a depth of 80 mm symmetrically with respect to the array axis (Fig. 6). For such cylinder and frequency range, the radiation of three Lamb waves should be observed: A_0, S_0, and A_1 as shown on the dispersion curves (Fig. 7).

1. Analysis of the echo

A short pulse is launched by the center element of the array. The echo of the cylinder is recorded on the 96 elements (Fig. 8). The first wavefront corresponds to the strong specular echo. The signal observed later is the elastic part of the echo. Between 15 and 25 μs, two pairs of wavefronts with interference fringes can be distinguished. Those wavefronts correspond to the radiation of two circumferential waves that have turned once around the shell. The one coming first is identified as the S_0 Lamb mode and the second as the A_0 Lamb mode. Interfering with those well-defined wavefronts is the contribution of the highly dispersive A_1 wave.

2. Separation of the modes

To separate these contributions we now apply the D.O.R.T. method. After the measurement of the 96×96 in-

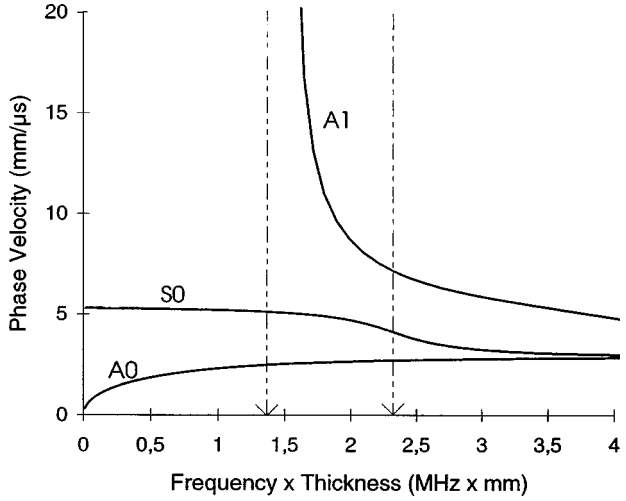

FIG. 7. Dispersion curves of Lamb waves for a steel plate.

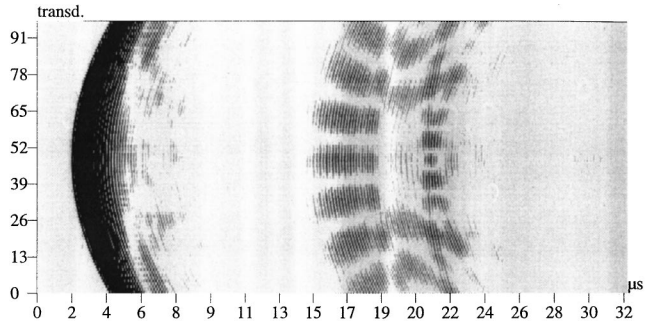

FIG. 8. Echo of the shell received by all the elements of the array after transmission by the central element.

terelement impulse responses, the whole process remains numerical. Only the elastic part of the signal is used to calculate the time-reversal operator (between 15 and 25 μs). At 3.05 MHz, the diagonalization of the time-reversal operator has six main eigenvalues. The modulus of the components of each eigenvector (1–6) is represented versus the array element (Fig. 9). The interference fringes are easily observed. They are equivalent at one frequency of the interference pattern observed on the echoes. As in the experiment on two wires (1.4), it means that an eigenvector corresponds to the interference of two coherent point sources.

The numerical backpropagation of each eigenvector allows us to determine the distance between the sources (Fig. 10). Each pair of sources corresponds to one particular Lamb wave. At this frequency, the first and second eigenvectors are associated to the wave S_0, the third and fourth to the wave A_1, and the fifth and sixth to the wave A_0.

The same calculation is done at several frequencies from 2.2 to 4 MHz so that the dispersion curves for the three

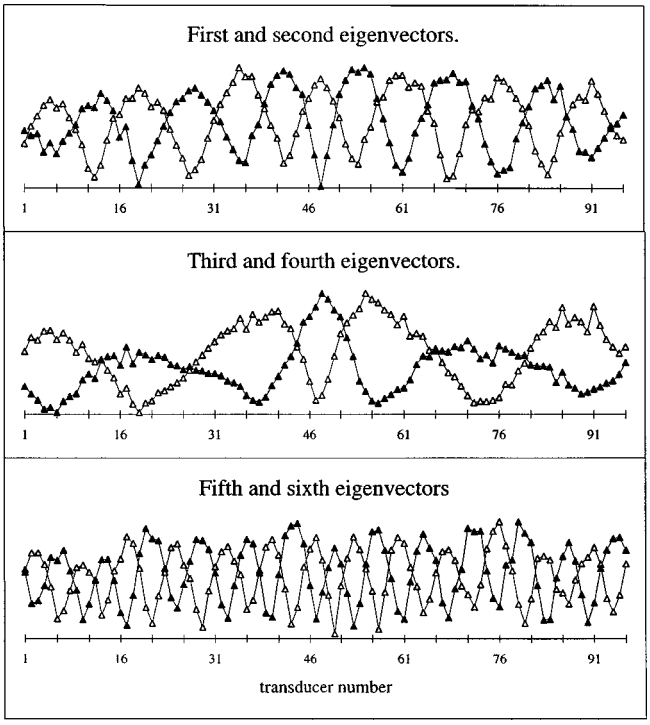

FIG. 9. Modulus of the components of the first six eigenvectors (from top to bottom 1-2, 3-4, 5-6).

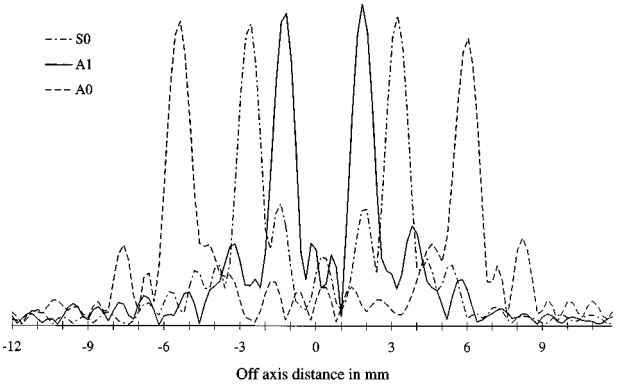

FIG. 10. Pressure patterns obtained by backpropagation of eigenvectors 1, 3, and 5.

waves can be plotted (Fig. 11). These curves are very close to the theoretical curves obtained for a steel plate of thickness 0.6 mm. In particular, the determination of the cutoff frequency of the wave A_1 allows us to tell the thickness of the shell.

3. Resonance frequencies of the shell

The eigenvalue associated to one particular wave depends on the frequency, it is proportional to the level of the contribution of the wave to the scattered field. The generation and reradiation coefficients of the wave are responsible for these fluctuations. Moreover, if the dynamic and duration of the recorded signals allow us to detect several turns of the wave around the shell, a fast modulation of the corresponding eigenvalue is induced, the maxima corresponding to the resonance frequencies of the shell. In the experiment, the wave A_0 is attenuated so fast that only one turn can be observed. But several turns of A_1 and S_0 waves contribute to the scattered field. To take into account these multiple turns the time-reversal operator was calculated using 40 μs of the signal. Then the eigenvalues were calculated from 2.2 to 3.8 MHz. The first six eigenvalues of the time-reversal operator are represented versus frequency (Fig. 12). The two curves

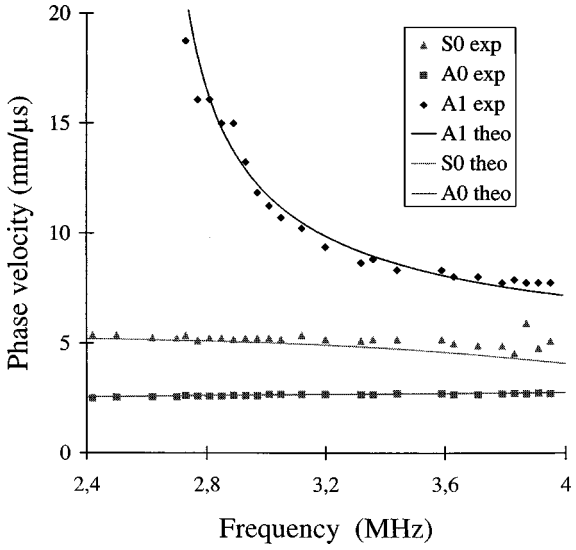

FIG. 11. Dispersion curves: $V_\phi(\omega)$ theory and D.O.R.T. method.

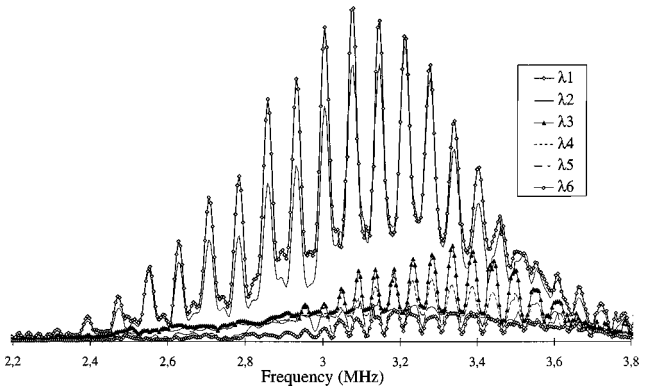

FIG. 12. Eigenvalues of the time-reversal operator obtained from the elastic echo of the shell.

$\lambda_1(\omega)$ and $\lambda_2(\omega)$ correspond to the wave S_0. Their maxima occur at the resonance frequencies of the shell corresponding to this wave. The width of the peaks is mainly due to the length of the recorded signals which allow us to see only three turns of the S_0 wave around the shell. Similar observations can be done for the wave A_1. This wave is associated to the eigenvalues λ_3 and λ_4 around its resonance frequencies and to λ_5 and λ_6 near its antiresonance frequencies. The resonnance peaks are well defined although the contribution of the wave A_1 is weaker than the one of S_0.

To confirm this interpretation, the first eigenvalue $\lambda_1(\omega)$ is compared to the spectrum of the S_0 wave. This last spectrum was obtained by a time-reversal operation as described in Ref. 7. A signal of 40 μs was used to perform the FFT so that only three turns around the shell could be seen. The agreement between the two curves is good (Fig. 13).

4. Limits

One limitation of the D.O.R.T. method is that the generation points of the circumferential waves need to be resolved in space. In the case of two waves of close phase velocities, the separation may not be possible. This explains partly the reason why the velocity of the A_1 wave could not be measured closer to the cutoff frequency. As the phase velocity increases, the two generation points get closer and are no more resolved by the system.

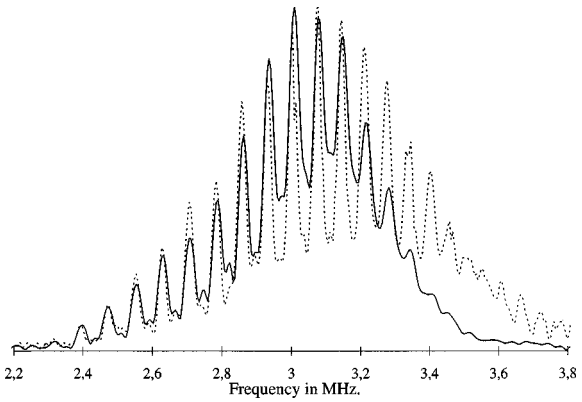

FIG. 13. First eigenvalues of the time-reversal operator (dot line) and experimental spectrum of the $S0$ wave (solid line).

Another limit that we encountered was due to the electronics of the system. The programmable generators we used were built for the time-reversal mirror and could only deliver 20 V peak to peak on each channel. To measure the interelement responses, a more classical generator should be used to get up to 100 V on one channel. This would provide a much better signal-to-noise ratio. Together with the measurement of longer signals, it should allow a more precise determination of the resonance frequencies of the shell.

III. CONCLUSION

The D.O.R.T. method is a new approach to inverse scattering. It allows one to sort various waves contributing to the scattered field and provides information that was previously unavailable. The method was applied to an air-filled stainless-steel cylindrical shell. The circumferential pseudo-Lamb waves A_0, S_0, and A_1 were separated. The dispersion curves of these waves were obtained allowing determination of the thickness of the shell. The eigenvalues of the time-reversal operator provided the resonance frequencies associated with S_0 and A_1 waves and close resonance frequencies of the two different modes were distinguished. Better results should be obtained in the future using electronic devices that provide a higher signal-to-noise ratio for the interelement response signals. Furthermore, the generalization of the method to separate transmit and receive arrays of transducers will widen the domain of the application of this method which should now be applied to other types of scattering problems.

ACKNOWLEDGMENT

The authors wish to express their gratitude to Professor Daniel Royer for many helpful discussions.

[1] N. Gespa, ''La diffusion acoustique par des cibles elastiques de forme géometrique simple,'' Théories et Expérience, CEDOCAR, 1986.
[2] H. Uberall, *Acoustic Resonance Scattering* (Gordon and Breach, New York, 1992).
[3] J. L. Izbicki, G. Maze, and J. Ripoche, ''Influence of the free modes of vibration on the acoustic scattering of a circular cylindrical shell,'' J. Acoust. Soc. Am. **80**, 1215–1219 (1986).
[4] M. Talmant and G. Quentin, ''Backscattering of a short ultrasonic pulse from thin cylindrical shells,'' J. Appl. Phys. **63**, 1857–1863 (1988).
[5] P. Rembert, A. Cand, P. Pareige, M. Talmant, G. Quentin, and J. Ripoche, ''The short pulse method of isolation and identification of resonances: Comparison with a quasiharmonic method and application to axisymmetrical scatterers,'' J. Acoust. Soc. Am. **92**, 3271–3277 (1992).
[6] D. Royer, E. Dieulesaint, and Ph. Leclaire, ''Remote sensing of the thickness of hollow cylinder from optical excitation and detection of Lamb waves,'' in Proceedings of the 1989 Ultrasonic Symposium pp. 1163–1166, IEEE Cat. 89CH2791-2.
[7] J. L. Thomas, P. Roux, and M. Fink, ''Inverse scattering analysis with an acoustic time-reversal mirror,'' Phys. Rev. Lett. **72**, 637–640 (1994).
[8] C. Prada, J. L. Thomas, P. Roux, and M. Fink, ''Acoustic time-reversal and inverse scattering,'' in *Proccedings of the Second International Symposium on Inverse Problems*, edited by H. D. Bui, M. Tanaka, *et al.* (A. A. Balkema, Rotterdam, 1994), pp. 309–316.
[9] C. Prada, F. Wu, and M. Fink, ''The iterative time-reversal mirror: A solution to self-focusing in the pulse echo mode,'' J. Acoust. Soc. Am. **90**, 1119–1129 (1991).
[10] C. Prada, ''Retournement temporel des ondes ultrasonores: Application à la focalisation,'' Thèse de doctorat de l'Université Paris VII, 1991.
[11] M. Fink, ''Time reversal of ultrasonic fields-Part I: Basic principles,'' IEEE Trans. Ultrason. Ferroelectr. Freq. Control **39**, 555–566 (1992).

[12] F. Wu, J. L. Thomas, and M. Fink, ''Time reversal of ultrasonic fields-Part II: Experimental results,'' IEEE Trans. Ultrason. Ferroelectr. Freq. Control **39**, 567–578 (1992).
[13] D. Cassereau and M. Fink, ''Time-reversal of ultrasonic fields-Part III: Theory of the closed time-reversal cavity,'' IEEE Trans. Ultrason. Ferroelectr. Freq. Control **39**, 579–592 (1992).
[14] M. Fink, ''Time-reversal mirrors,'' J. Phys. D **26**, 1333–1350 (1993).
[15] M. Fink, ''Time-reversed acoustics,'' Phys. Today **50**(3), 34–40 (March 1997).
[16] C. Prada, J. L. Thomas, and M. Fink, ''The iterative time-reversal process: analysis of the convergence,'' J. Acoust. Soc. Am. **97**, 62–71 (1995).
[17] G. Bienvenu and L. Kopp, ''Optimality of high resolution array processing using the eigensystem approach,'' IEEE Trans. Acoust., Speech, and Signal Process. **31**, 1235–1247 (1983).
[18] R. O. Schmidt, ''Multiple emitter location and signal parameter estimation,'' IEEE Trans. Antennas Propag. **AP-34**, 276–281 (1986).
[19] C. Prada and M. Fink, ''Eigenmode of the time-reversal operator: a solution to selective focusing in multiple-target media,'' Wave Motion **20**, 151–163 (1994).
[20] C. Prada, S. Manneville, D. Spoliansky, and M. Fink, ''Decomposition of the time reversal operator: Application to detection and selective focusing on two scatterers,'' J. Acoust. Soc. Am. **99**, 2067–2076 (1996).

Ocean acoustic inversion with estimation of *a posteriori* probability distributions

Peter Gerstoft[a)]
SACLANT Undersea Research Centre, I-19138 La Spezia, Italy

Christoph F. Mecklenbräuker[b)]
Ruhr-University Bochum, D-44780 Bochum, Germany

(Received 2 June 1997; accepted for publication 16 April 1998)

Inversion methods are applied in ocean acoustics to infer parameters which characterize the environment. The objective of this paper is to provide such estimates, and means of evaluating the inherent uncertainty of the parameter estimates. In a Bayesian approach, the result of inversion is the *a posteriori* probability density for the estimated parameters, from which all information such as mean, higher moments, and marginal distributions can be extracted. These are multidimensional integrals of the *a posteriori* probability density, which are complicated to evaluate for many parameters. Various sampling options are examined and it is suggested that ''importance sampling'' based on a directed Monte Carlo method, such as genetic algorithms, is the preferred method. The formulation of likelihood functions and maximum-likelihood objective functions for multifrequency data on a vertical array is discussed. *A priori* information about the parameters may be used in the formulation. Shallow-water acoustic data obtained at several frequencies using a vertical array is used to illustrate the applicability of the technique. [S0001-4966(98)05307-7]

PACS numbers: 43.30.Pc, 43.60.Pt [DLB]

INTRODUCTION

From a Bayesian point of view, the solution to an inverse problem is fully characterized by *a posteriori* probability distributions of the unknown parameters. Information about these parameters is assessed by moments of the *a posteriori* distributions, such as the mean, covariance, and marginal distributions. This improves on the usual practice of calculating only a single point-estimate of the parameters: Accuracy of the inversion can be estimated in this way.

In a real problem, the numerical evaluation of *a posteriori* distributions is limited by computational resources. Importance sampling, as performed by simulated annealing (SA) and genetic algorithms (GA), can considerably reduce the number of operations required. The main advantage of the above concept is that it not only provides the best possible parameter estimates, but also calculates moments of the *a posteriori* distributions associated with these parameters. The Monte Carlo method[1] and the simulated annealing method[2] were developed as methods to evaluate multidimensional integrals.

Part of the inverse problem is to find an environment in which a forward model can produce a replica with a good match to the observed data. A representative environment is chosen empirically and a set of parameters $\mathbf{m}$ is selected as unknown. It is assumed that the true model vector is contained in the parameter set $\mathcal{M}$. An objective function $\phi(\mathbf{m})$ that compares the data and the replica is selected. Then, optimization is carried out to find the optimum model parameter vector $\hat{\mathbf{m}}=(\hat{m}^1,\ldots,\hat{m}^M)$ that minimizes the selected objective function.

To understand the inverse problem and its solution, it is important to study uncertainties, ambiguities, and resolution aspects of the unknown parameters. For deterministic local methods, these are limited to a neighborhood surrounding the local estimate, e.g., Refs. 3 and 4. A good discussion of these aspects for underwater acoustics is found in Ref. 5. Estimation of uncertainties from global methods have been discussed in Refs. 6–11 for the related geophysical problem, and in Refs. 12 and 13 for ocean acoustic problems. Retrieving parameters using global optimization methods has frequently been discussed in ocean acoustics.[12,14–16]

The superiority of stochastic global methods for uncertainty estimation stems from their ability to sparsely sample the parameter space $\mathcal{M}$.[17] For present applications, fast estimation of the moments of the *a posteriori* distributions is more important than precision.

The motivation for the present study is that *a posteriori* distributions as described in Ref. 12 have been used with success in a series of previous papers. It has worked well for making comparisons between retrieved parameters and giving an indication of the convergence of the optimization method. However, it is based on an empirical weighting and fails to give a performance indication for *different* inversion approaches. Only a likelihood based *a posteriori* distribution can show the improvement in performance when using more frequencies, or the differing performance using a near or far array.

Before measurement, the information about the models is reflected in the *a priori* distribution $\rho(\mathbf{m})$ and after the experiment, the information about the models is reflected in

[a)]Now at Marine Physical Laboratory, Scripps Institution of Oceanography, University of California, San Diego, La Jolla, CA 92093-0704; Electronic mail: gerstoft@mpl.ucsd.edu
[b)]Now at Siemens A.G., A-1100 Vienna, Austria; Electronic mail: christoph.mecklenbraeuker@siemens.at

the *a posteriori* distribution $\sigma(\mathbf{m})$. These distributions are related through the likelihood function $\mathscr{L}(\mathbf{m})$, which is a measure for the goodness of fit between the observed data and the data generated using a computational acoustic model and the environment $\mathbf{m}$ (Bayes Theorem)

$$\sigma(\mathbf{m}) = \mathscr{L}(\mathbf{m})\rho(\mathbf{m}). \tag{1}$$

When maximizing $\sigma(\mathbf{m})$ the maximum *a posteriori* (MAP) estimate of the parameters is obtained and when maximizing $\mathscr{L}(\mathbf{m})$ the maximum likelihood (ML) parameter estimate is obtained.

To find the best solution, global optimization is carried out by minimizing an objective function $\phi(\mathbf{m})$. In this paper, the objective function is chosen proportional to the log-likelihood function, but often it is selected on a more empirical basis. The likelihood function depends on the stochastic model for the data: differing probabilistic models for signal and noise result in different likelihood and objective functions.

I. EVALUATION OF *A POSTERIORI* DISTRIBUTIONS

Due to multidimensionality, often $M > 10$, the *a posteriori* distribution is not susceptible to graphic display, and mainly integral properties of the distribution are of interest. From the *a posteriori* probability distribution, information will be extracted to describe the solution. The following quantities are of interest: the MAP solution $\hat{\mathbf{m}}^{\mathrm{MAP}}$ where

$$\hat{\mathbf{m}}^{\mathrm{MAP}} \equiv \arg \max_{\mathbf{m} \in \mathscr{M}} \sigma(\mathbf{m}), \tag{2}$$

the expectation $\mathsf{E}_\sigma[\mathbf{m}]$ where

$$\mathsf{E}_\sigma[\mathbf{m}] \equiv \int_{\mathscr{M}} \mathbf{m}\sigma(\mathbf{m})d\mathbf{m}, \tag{3}$$

where $d\mathbf{m} = dm^1 \cdots dm^M$, the covariance matrix $\mathsf{Cov}_\sigma[\mathbf{m}]$ where

$$\mathsf{Cov}_\sigma[\mathbf{m}] \equiv \mathsf{E}_\sigma\{[\mathbf{m} - \mathsf{E}_\sigma(\mathbf{m})][\mathbf{m} - \mathsf{E}_\sigma(\mathbf{m})]^T\}, \tag{4}$$

the one-dimensional (1D) marginal *a posteriori* probability densities $\sigma^i(m^i)$ for parameter m^i

$$\sigma^i(m^i) \equiv \int \sigma(\mathbf{m})dm^1 \cdots dm^{i-1}dm^{i+1} \cdots dm^M, \tag{5}$$

and higher dimensional marginals are defined similarly to Eq. (5). The marginal distributions are the most important in interpreting the inverse result.

A. Integration of *a posteriori* distributions

For solving the inverse problem, Eq. (2), global optimization methods such as simulated annealing and genetic algorithms have been used. However, in order to characterize the solution by Eqs. (3)–(5) the multidimensional integration must be carried out. The evaluation of these integrals has been addressed in Refs. 10 and 11 for the similar geophysical inversion problem. They suggested and evaluated the following three methods for estimation of the integral.

1. Numerical integration (grid search)

Although the most precise and direct method, numerical integration is extremely computationally intensive for M parameters each discretized to k values. It requires k^M forward model evaluations. For $k = 100$ and $M = 10$, this is a prohibitively large number 10^{20}, as for each of these points, a forward model that takes about one CPU-second must be evaluated. This approach is practical only for a very small number of parameters, e.g., $M \leqslant 4$.

2. Monte Carlo integration

In Monte Carlo integration the integration points are selected at random from a uniform distribution. It is not necessary to evaluate the integral at all points as in a grid search. In contrast to classical computing methods, the efficiency of Monte Carlo integration depends only weakly on the dimension and geometric details of the problem. Thus even for high dimensions, M, and complicated boundaries of the parameter set $\mathscr{M}$, the numerical effort remains moderate. The integral is evaluated at randomly selected points from a uniform distribution. The disadvantage is that many of these points will be located in areas contributing little to the integral.

3. Importance sampling

In importance sampling, some knowledge about the integrand is exploited such that a nonuniform distribution is used for generating the integration points. Most of the function evaluations are concentrated in areas which contribute significantly to the integral instead of distributing the points evenly. The integrals can be evaluated using fewer forward models at a reduced variance of the estimated integral. The model space $\mathscr{M}$ is sampled nonuniformly according to a generating distribution g. The integrand is evaluated only at these sample points. Both GA and SA use a generating distribution to select the next point in the model space.

Consider the evaluation of the multidimensional integral,[18]

$$\theta = \int_{\mathscr{M}} f(\mathbf{m})\sigma(\mathbf{m})d\mathbf{m} \equiv \mathsf{E}_\sigma[f(\mathbf{m})], \tag{6}$$

where $f\sigma$ represents any of the integrands given in Eqs. (3)–(5). The integral is estimated by the weighted arithmetic mean using N_{obs} independent identical distributed (i.i.d.) samples $\mathbf{m}_1, \mathbf{m}_2, \ldots, \mathbf{m}_{N_{\mathrm{obs}}}$ from the distribution $g(\mathbf{m})$,

$$\hat{\theta} = \frac{1}{N_{\mathrm{obs}}} \sum_{i=1}^{N_{\mathrm{obs}}} \frac{f(\mathbf{m}_i)\sigma(\mathbf{m}_i)}{g(\mathbf{m}_i)}. \tag{7}$$

It can be shown, Appendix A and Ref. 18, that the variance of $\hat{\theta}$ is minimized if the generating distribution is selected

$$g^{\mathrm{MV}}(\mathbf{m}) = \frac{|f(\mathbf{m})|\sigma(\mathbf{m})}{\int_{\mathscr{M}} |f(\mathbf{m})|\sigma(\mathbf{m})d\mathbf{m}}. \tag{8}$$

Thus in order to reduce the variance, the generating distribution should be selected proportional to $|f|\sigma$. In practical cases, this optimal solution cannot be select due to complicated behavior of $|f|\sigma$. Further, if the integrand is known *a*

priori then there is no reason for estimating it. However, it is expected that selections of g which are ''close'' to g^{MV} will give satisfactory performance.

If the integral is evaluated using a generating distribution $g(\mathbf{m})$ without correcting for $g(\mathbf{m})$ in the denominator, it is seen from Eq. (A1) that the estimate will be biased. Since global estimation methods concentrate most of their numerical effort around the optimal values, they will tend to overestimate parts of the integral for these regions unless special bias corrections are introduced. This will result in an unknown error in the estimates.

Global optimization methods use a generating distribution for selecting the next model vector. This distribution will in general change as the optimization evolves. Thus they are carrying out importance sampling, but with an unknown generating distribution. For SA at a constant temperature T it can be shown that after a large number of iterations the sampling distribution is proportional to $\exp(-\phi(\mathbf{m})/T)$. For more details see Ref. 10 and Sec. I B.

When the MAP solution Eq. (2) is found using SA or GA, a large number N_{obs} of candidate solutions $\mathbf{m}_i$ ($i=1,...,N_{\mathrm{obs}}$) are drawn at random from the model set $\mathscr{M}$. By using the values of the objective function at these sample points $\mathbf{m}_i$, importance sampling can be used in evaluating the integrals Eqs. (3)–(5). When using GA or SA with fast cooling (as usual), the precise distribution of the samples is not known. It should also be made clear that the generating distribution is related in a nonlinear fashion (through GA or SA) to the objective function and not to the preferred distribution $|f|\sigma = |f|\mathscr{L}\rho$. This is not considered a problem as both $|f|$ and ρ are much smoother than $\mathscr{L}$ and the objective function is related to $\mathscr{L}$.

For the N_{obs} observations, the *a posteriori* probability for the kth model vector is estimated by

$$\hat{\sigma}(\mathbf{m}_k) = \frac{\mathscr{L}(\mathbf{m}_k)\rho(\mathbf{m}_k)}{\sum_{j=1}^{N_{\mathrm{obs}}} \mathscr{L}(\mathbf{m}_j)\rho(\mathbf{m}_j)}. \tag{9}$$

For the ith parameter m^i in the model vector the marginal probability distribution for obtaining the particular value κ can be found by summing Eq. (9):

$$\hat{\sigma}^i(\kappa) = \sum_{k=1}^{N_{\mathrm{obs}}} \hat{\sigma}(\mathbf{m}_k)\,\delta(m_k^i - \kappa), \tag{10}$$

where δ is the delta function. In the particular implementation, several independent GA searches are carried out in parallel. It is found for several parallel runs that saving the last obtained model vectors in a population suffices in each of the parallel runs.[12]

When displaying the marginal probability distributions, Eq. (5), they are all scaled so that the areas under each curve are one when the search interval is scaled from 0 to 1. This dictates the y axis and all plots from the same inversion have the same y axis, there is no scale on the y axis as it is mostly used for comparisons. With this choice of scaling the distributions depend on the search interval for each parameter.

B. Comparison to previous probability estimates

Previously,[12] the *a posteriori* distributions were estimated based on a semiempirical approach. Knowing that the likelihood function is usually related to the objective function $\phi(\mathbf{m})$ through an exponential $\mathscr{L} = \exp(-\phi(\mathbf{m})/\hat{\nu})$ (Ref. 6, cf. Appendix B), where $\hat{\nu}$ is the estimated noise power, the following scaling was used:

$$\mathscr{L}_{\mathrm{emp}}(\mathbf{m}) = \exp(-[\phi(\mathbf{m}) - \phi(\mathbf{m}_0)]/T), \tag{11}$$

where ϕ is any objective function and $\mathbf{m}_0$ is the estimated parameter vector, corresponding to the optimal value of the objective function. T is the ''temperature.'' Experimentally, it was found that a good value for T was the average of the 50 best objective functions obtained during the optimization, minus the best value of the objective function. It should be noted that this value of T is not intended to estimate the noise, but to produce a reasonable value with which to estimate the uncertainties of the parameters. The advantage of this scheme is that it works irrespective of the stochastic model for the data or likelihood function used. But for multifrequency inversions it is not suitable as different distributions cannot be directly compared. In this case, a likelihood-based *a posteriori* density, Eqs. (1) and (3)–(5) give better results.

C. Computational procedure

Depending on the model used for the error or noise distribution of the data, a specific likelihood function results. Prior knowledge about the error distribution is required. Usually this is not completely available and some simple and reasonable approximations must be used. Two special cases are considered for multifrequency vertical array data. The noise distribution on each hydrophone is assumed complex Gaussian and zero mean. First, in Sec. I C 1 it is assumed that the noise is independent on each *hydrophone* and second, in Sec. 1 C 2 it is assumed independent for each *significant mode*.

Often, a distinction is made between errors due to noise in the data and errors due to an incomplete forward model, because neither the theory nor the environmental model is adequate. If both error types belong to the same distribution, there is no reason to consider them separately.[19] Here only one error term is considered.

Recently, there has been progress in describing both errors using Kriging.[20] Both noise and modeling errors are assumed zero-mean Gaussian and are independent. The modeling errors are assumed to possess a given correlation structure depending on the ''distance'' between two environmental models. This correlation structure is chosen empirically. Clearly, the same values of the model parameters correspond to the same values of the model errors.

1. Multifrequency matched field processing

The relation between the observed complex-valued data vector $\mathbf{q}(\omega_l)$ on an N-element hydrophone antenna array and the predicted data $\mathbf{p}(\mathbf{m},\omega_l)$ at an angular frequency ω_l is described by the model

$$\mathbf{q}(\omega_l) = \mathbf{p}(\mathbf{m},\omega_l) + \mathbf{e}(\omega_l), \tag{12}$$

where $\mathbf{e}(\omega_l)$ is the error term. The predicted data is given by $\mathbf{p}(\mathbf{m},\omega_l)=\mathbf{w}(\mathbf{m},\omega_l)S(\omega_l)$, where the complex deterministic source term $S(\omega_l)$ is unknown. The transfer function $\mathbf{w}(\mathbf{m},\omega_l)$ is obtained using an acoustic propagation model and an environmental model $\mathbf{m}$.[21]

The errors are assumed to be additive, they stem from many sources: errors in describing the environment, errors in the forward model, instrument and measurements errors, and noise in the data. For the predicted acoustic field ''reasonably close'' to the true field, this error term is assumed complex Gaussian distributed, stationary with zero mean and diagonal covariance matrix $\nu(\omega_l)\mathbf{I}$, where the error power spectrum ν is unknown. Thus the data $\mathbf{q}(\omega_l)$ on the receiving array are also complex Gaussian distributed with mean $\mathbf{p}(\omega_l,\mathbf{m})$ and the covariance matrix $\nu(\omega_l)\mathbf{I}$. For the derivation of a maximum-likelihood estimate, it is further assumed that the data are uncorrelated across frequency and time. The source term $S(\omega_l)$ varies across time snapshots whereas the error power spectral density $\nu(\omega_l)$ is constant. In the following, $\mathbf{q}_l=\mathbf{q}(\omega_l)$, etc., is abbreviated, where $\{\omega_l|l=1,...,L\}$ is the processed frequencies. Under the above assumptions the covariance matrix $\mathbf{R}_l=\mathsf{E}[\mathbf{q}_l\mathbf{q}_l^\dagger]=\mathbf{p}_l(\mathbf{m})\mathbf{p}_l^\dagger(\mathbf{m})+\nu_l\mathbf{I}$. The likelihood function[22] becomes

$$\mathscr{L}(\mathbf{m})\propto\prod_{l=1}^{L}\ \frac{1}{\nu_l^N}\exp\left(-\frac{\phi_l(\mathbf{m})}{\nu_l}\right), \tag{13}$$

where (the dagger refers to the Hermitian transpose and ''tr'' is the trace operation)

$$\phi_l(\mathbf{m})=\mathrm{tr}\ \hat{\mathbf{R}}_l-\frac{\mathbf{w}_l^\dagger(\mathbf{m})\hat{\mathbf{R}}_l\mathbf{w}_l(\mathbf{m})}{\mathbf{w}_l^\dagger(\mathbf{m})\mathbf{w}_l(\mathbf{m})}. \tag{14}$$

Optimization for ν_l yields the closed form ML solution

$$\hat{\nu}_l=\frac{1}{N}\ \phi_l(\mathbf{m}). \tag{15}$$

The $N\times N$ Hermitian matrix $\hat{\mathbf{R}}_l$ denotes the estimated cross-spectral density matrix of the observed data in ''phone-space,'' see Sec. 1 C 3. With these definitions the log-likelihood function is

$$\log|\mathscr{L}(\mathbf{m})|\propto\log\left[\prod_{l=1}^{L}\ \phi_l^{-N}(\mathbf{m})N^N\exp(-N)\right]\propto-\log[\phi(\mathbf{m})], \tag{16}$$

where the ML-objective function $\phi(\mathbf{m})$ to be minimized is

$$\phi(\mathbf{m})=\prod_{l=1}^{L}\ \phi_l(\mathbf{m})=\prod_{l=1}^{L}\left(\mathrm{tr}\ \hat{\mathbf{R}}_l-\frac{\mathbf{w}_l^\dagger(\mathbf{m})\hat{\mathbf{R}}_l\mathbf{w}_l(\mathbf{m})}{\mathbf{w}_l^\dagger(\mathbf{m})\mathbf{w}_l(\mathbf{m})}\right). \tag{17}$$

For details, see Appendix B. Using a global optimization procedure, the minimum $\hat{\phi}^{\mathrm{ML}}$ for the ML solution $\hat{\mathbf{m}}^{\mathrm{ML}}$ is estimated. The estimate, Eq. (15), is biased. The bias stems from the degrees of freedom in the estimated parameters: source signal S and nonlinear parameters $\mathbf{m}$.[23] For simplicity this bias is neglected here. The noise power spectral density is estimated, Eq. (15), $\hat{\nu}_l^{\mathrm{ML}}=1/N\,\phi_l(\hat{\mathbf{m}}^{\mathrm{ML}})$, and the likelihood function is given by

$$\mathscr{L}(\mathbf{m})=p(\mathbf{m}|\mathbf{q})\propto\prod_{l=1}^{L}\ (\hat{\nu}_l^{\mathrm{ML}})^{-N}\exp\left(-\frac{\phi_l(\mathbf{m})}{\hat{\nu}_l^{\mathrm{ML}}}\right)$$
$$\propto\prod_{l=1}^{L}\ \exp\left(-N\,\frac{\phi_l(\mathbf{m})-\hat{\phi}_l^{\mathrm{ML}}}{\hat{\phi}_l^{\mathrm{ML}}}\right). \tag{18}$$

The problem, as addressed above, is then to integrate this multidimensional probability distribution. Often this integral can be evaluated with sufficient accuracy using the information from the global search. In some cases it might be necessary to increase the sampling of the model space in order to obtain convergence.

The likelihood function, Eq. (18), has a stronger maximum when more hydrophones are used. When inverting observed data, there is a limit to how much useful information can be obtained by adding additional hydrophones, as they then become strongly correlated. At high signal-to-noise ratio (SNR) it is expected that the main error contribution is due to inadequate forward modeling. Further, the number of uncorrelated hydrophones is approximately the same as the number of propagating modes, because this limits the degrees of freedom in the random part of the acoustic wave field. The number of uncorrelated hydrophones is estimated as the rank of the covariance matrix.

2. Multifrequency matched mode processing

Normal modes provide a complete description of the field at long ranges, and thus one can equivalently process the data in the phone-space or in the modal-space. The matched mode approach is described by Tolstoy,[24] Hinich,[25] and Shang.[26] Modal processing is discussed here as an alternative noise estimate when there are more hydrophones than propagating modes.

The observed field of N sensors is assumed approximately expressed via a set of J *significant* normal modes, expressed in a $N\times J$ matrix $\mathbf{V}(\omega_l,\mathbf{m})=[\mathbf{v}_1(\omega_l,\mathbf{m}),\ldots,\mathbf{v}_J(\omega_l,\mathbf{m})]$. The typical vector $\mathbf{v}_j(\mathbf{m})$ contains spatial samples of the jth normal mode at the receiver array locations. The set of normal modes will be determined based on the environment. The corresponding complex valued modal amplitudes (the breve refers to the mode-space) $\breve{\mathbf{q}}(\omega)=(\breve{q}_1,\ldots,\breve{q}_J)'$.

$$\mathbf{q}(\omega_l)\approx\sum_{j=1}^{J}\ \mathbf{v}_j(\omega_l,\mathbf{m})\breve{q}_j=\mathbf{V}(\omega_l,\mathbf{m})\breve{\mathbf{q}}(\omega). \tag{19}$$

There should be more hydrophones than modes, $N>K$. This relationship can be inverted in a least-squares sense and estimates the vector of modal amplitudes $\breve{\mathbf{q}}_l=\breve{\mathbf{q}}(\omega_l)$ in the mode-space from the observation $\mathbf{q}_l=\mathbf{q}(\omega_l)$ in phone-space.

$$\breve{\mathbf{q}}_l=[\mathbf{V}_l^\dagger(\mathbf{m})\mathbf{V}_l(\mathbf{m})]^{-1}\mathbf{V}_l^\dagger(\mathbf{m})\mathbf{q}_l. \tag{20}$$

Note that the modes $\mathbf{V}_l(\mathbf{m})$ and thus modal amplitudes depend on the environment. When optimizing the environment $\mathbf{m}$ the modal amplitudes will change with the environment.

A simple relationship between the observed modal amplitudes $\breve{\mathbf{q}}_l$ and synthetic generated modal amplitudes is assumed

$$\check{\mathbf{q}}_l = \check{\mathbf{p}}_l(\mathbf{m}) + \check{\mathbf{e}}_l(\mathbf{m}), \tag{21}$$

where $\check{\mathbf{p}}_l(\mathbf{m}) = S_l \check{\mathbf{w}}_l(\mathbf{m})$ is the complex-valued modal amplitudes of the synthetic data and $\check{\mathbf{e}}_l$ represents the error term for each mode. It is assumed that the noise covariance matrix is diagonal for the J significant modes and the noise power $\check{\nu}$ is identical for all J modes. Using a similar approach to that in Sec. 1 C 1, the objective function is

$$\check{\phi}_l(\mathbf{m}) = \mathrm{tr}\,\hat{\hat{\mathbf{R}}}_l - \frac{\check{\mathbf{w}}_l^\dagger(\mathbf{m})\hat{\hat{\mathbf{R}}}_l\check{\mathbf{w}}_l(\mathbf{m})}{\check{\mathbf{w}}_l^\dagger(\mathbf{m})\check{\mathbf{w}}_l(\mathbf{m})}, \tag{22}$$

where $\hat{\hat{\mathbf{R}}}_l$ is the estimated covariance matrix of the modes. But using the expression for the modes, Eq. (19), the objective function in mode-space, Eq. (22), is seen to be equivalent to the objective function in phone-space, i.e., Eq. (14) expressed in the phone-space

$$\check{\phi}_l(\mathbf{m}) \approx \phi_l(\mathbf{m}). \tag{23}$$

The noise estimate is obtained using the approximation in Eq. (19),

$$\hat{\check{\nu}}_l = \frac{1}{J}\,\hat{\check{\phi}}_l^{\mathrm{ML}} \approx \frac{1}{J}\,\hat{\phi}_l^{\mathrm{ML}}. \tag{24}$$

The likelihood function becomes

$$\mathscr{L}(\mathbf{m}) = p(\mathbf{m}|\mathbf{q}) \propto \prod_{l=1}^{L} (\hat{\check{\nu}}_l^{\mathrm{ML}})^{-J} \exp\left(-\frac{\check{\phi}_l(\mathbf{m})}{\hat{\check{\nu}}_l^{\mathrm{MD}}} \right)$$
$$\propto \prod_{l=1}^{L} \exp\left(-J\,\frac{\phi_l(\mathbf{m}) - \hat{\phi}_l^{\mathrm{ML}}}{\hat{\phi}_l^{\mathrm{ML}}} \right). \tag{25}$$

The advantage of this formulation is that it does not depend directly on the number of hydrophones, but only on the number of propagating modes. For many hydrophones ($N \gg J$) this likelihood function seems more realistic. A formal definition for J is not yet clear. In either case, J is less or equal to the number of propagating modes. For simplicity, J is assumed to be independent of frequency. Only the objective function is affected by the choice of J. All the propagating modes are incorporated in the forward model.

3. Estimation of the covariance matrix

In order to estimate the covariance matrix $\mathbf{R}_l$, the received time signal is divided into K time frames. Each frame was short-time Fourier transformed using the multiple-windows technique described in Refs. 27 and 28,

$$\mathbf{q}_{k,p}(\omega) = \sum_{t=0}^{T-1} \nu_t^p \mathbf{q}(t+kT) e^{-j\omega t}, \quad \text{for } \begin{cases} k = 0,\ldots,K-1 \\ p = 0,\ldots,P-1 \end{cases}, \tag{26}$$

where ν^p is a special set of P orthonormal data tapers.[27,28] The correlation matrix $\mathbf{R}$ was estimated at each selected frequency ω_l as the ensemble average

$$\hat{\mathbf{R}}(\omega_l) = \frac{1}{KP} \sum_{k=0}^{K-1} \sum_{p=0}^{P-1} \mathbf{q}_{k,p}(\omega_l)\mathbf{q}_{k,p}^\dagger(\omega_l). \tag{27}$$

In order to obtain a good estimation of the noise, it is required that $KP \gg N$, where N is the number of hydrophones. In order to ''just'' estimate the signal and the unknown parameters $\mathbf{m}$, the number of averages KP can be much smaller for a received signal with sufficient SNR. In this paper, the evaluation of the inversion accuracy is addressed. Therefore modeling errors in $\mathbf{p}(\mathbf{m},\omega)$ and additive noise must be distinguished. This implies the necessity of a stable noise estimate (27), and thus a larger number of averages than if only parameter estimates $\hat{\mathbf{m}}$ are needed.

D. Including the *a priori* probability distribution

Usually, when solving inverse problems, the question is, ''What is the environmental model for this given data set?'' This is normally an ill-posed question. A better question is, ''What can be inferred from the data about the environmental model given some environmental information?'' Thus some *a priori* information should be included in the inverse problem. *A priori* information is always used in global inversion schemes. The model structure is selected based on *a priori* knowledge and uniform *a priori* distributions are used between the minimum and maximum bounds for the parameters.

One possibility is to include the *a priori* model in the objective function, e.g., Refs. 6 and 29. This has the disadvantage that the distribution must be known explicitly. For Gaussian *a priori* distribution the objective function consists of two terms, one measuring the match between observed and synthetic data and the second penalizing the deviation from the *a priori* model. This approach is used in linearized inversions in order to regularize the solution.

Here a simple approach is used: the obtained likelihood function is multiplied with the *a priori* distribution, according to Eq. (1). This distribution can be arbitrary, for example, a smoothed distribution obtained from inversion of other data. For illustration in Sec. II A 3 a simple triangular distribution is used:

$$\rho(m^i) \propto \begin{cases} (m^i - m_u^i)/(m_m^i - m_u^i), & \text{for } m_m^i < m^i < m_u^i \\ (m^i - m_l^i)/(m_m^i - m_l^i), & \text{for } m_l^i < m^i < m_m^i \\ 0, \quad \text{otherwise}, \end{cases} \tag{28}$$

where $m_l^i < m_m^i < m_u^i$ are the abscissa of lower bound, maximum, and upper bound of the *a priori* distribution, respectively.

A priori information is also used in the parametrization of the forward model. The choices made when doing this have a significant influence on the inverse solution, probably more than including *a priori* information for each parameter. In discretizing the environment, the physics should be carefully considered and described efficiently. Shape functions[30] are a useful method to obtain an efficient description which provides a mapping between the environmental model and the numerical forward model. This could, for example, be used to limit the search to only positive gradients in the sediment, or to obtain a more efficient description of the environment (see the example in Sec. II A 3).

It is assumed for simplicity that there is a vanishing correlation between the *a priori* distributions of the indi-

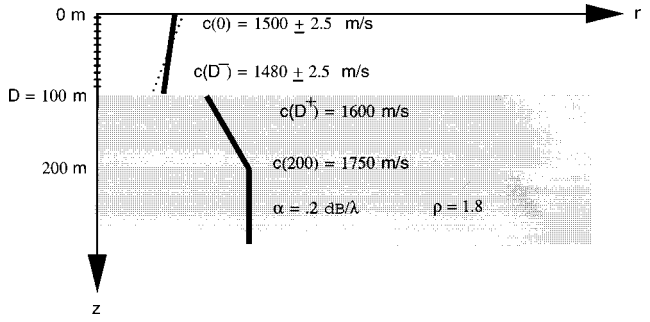

FIG. 1. The environment for the sspmis case. The source coordinates are (9.3 km, 78 m) for SNR=40 dB and (9.6 km, 82 m) for SNR=10 dB.

vidual parameters. Thus $\rho(\mathbf{m})=\rho^1(m^1)\rho^2(m^2)\cdots$. Although for correlated parameters, the model search can be limited using a correlated *a priori* distribution, this approach appears unpractical and, instead, shape functions are used for mapping correlated model vectors to a new representation with lower correlation.

II. EXAMPLES

The examples illustrate the integration of the *a posteriori* distributions and how phone-space and mode-space based likelihood functions affect the estimates. Only in Sec. II A 3, a nonuniform *a priori* distribution is used.

The objective function Eq. (17) was optimized and the SNAP normal mode code[21] was used as a forward model. For likelihood functions, either the empirical, the multifrequency matched field, or the multifrequency matched mode models are used. The GA parameters were as in Refs. 12 and 31: the reproduction rate was 0.5, the permutation probability was 0.05, and the crossover rate was 0.8.

A. SSP-mismatch case

This case corresponds to the sound-speed mismatch from the 1993 Matched field workshop,[32] Fig. 1. It is based on a synthetic data set from a normal-mode code using a 250-Hz source in shallow water. The data are received on the 20 hydrophones spanning the entire water column. White Gaussian noise was added to the data vectors to obtain a SNR of either 40 or 10 dB.[32] This corresponds precisely to the likelihood function developed in Sec. I C 1.

Only four parameters are unknown in this case; the source range and depth and the ocean sound speed at the top and the bottom. Each of the parameters can assume 51 discrete values. For an exhaustive search this requires evaluation of $51^4=7\times10^6$ forward models. It took 5 days of CPU time on a DEC-Alpha 500/266 to evaluate all models. For the genetic algorithm 4×10^4 forward models were evaluated in half an hour of CPU time.

1. Without a priori information

A uniform *a priori* distribution is assumed. To display the marginal distribution, the integral, Eq. (5), is evaluated. When using an exhaustive search, i.e., evaluating each point in the integration corresponding to Sec. I A 1, the result

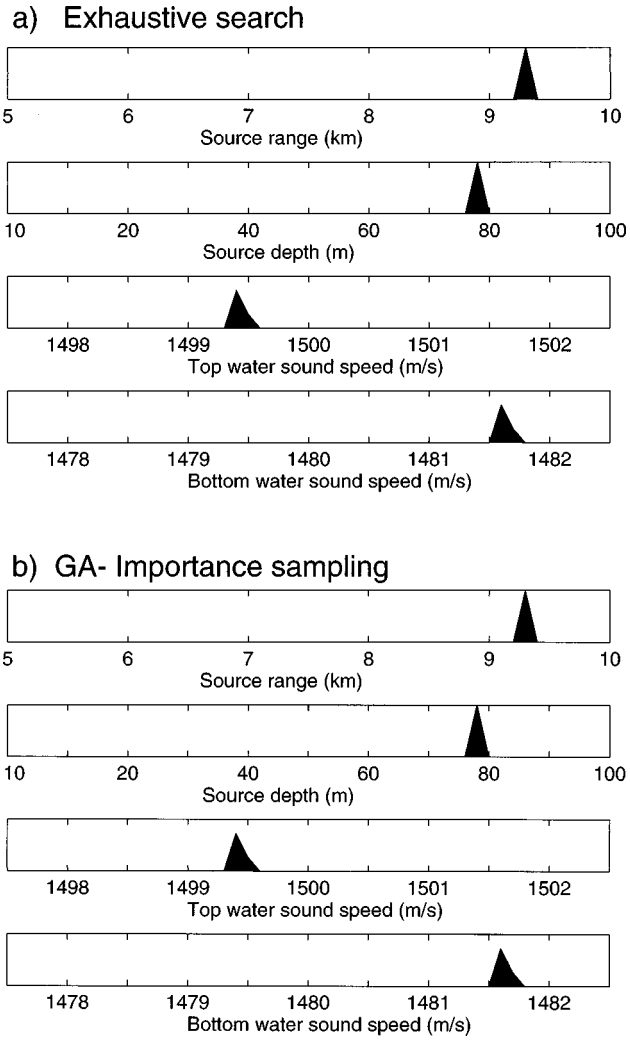

FIG. 2. The estimated *a posteriori* distribution for a SNR of 40 dB for the sspmis case. (a) using numerical integration, (b) using importance sampling.

of this integration is shown in Figs. 2(a) and 3(a). In generating these plots, the noise was assumed to be unknown.

When carrying out the optimization by SAGA,[31] 20 parallel runs, each sampling 2000 models with a population size of 64 were used. One result is the ML estimate of parameters which corresponds to the best obtained fit.

During this optimization the last population (64 individuals) in each of the 20 runs is saved in order to estimate the integrals. Thus the estimation of the integral is based on $20\times64=1280$ model vectors. It is seen in Figs. 2(b) and 3(b) that the evaluation of the integral resembles the distributions obtained when evaluating the integrals based on an exhaustive search. The use of all the GA-evaluated forward models ($20\times2000=4\times10^4$) in the evaluation of the integral did not have any effect. For practical reasons, it is preferred to base the evaluated integral on the last population in each run.

Note that for both SNR=40 and 10 dB the source range and depth are estimated quite accurately, whereas for more noise, the ability to resolve the sound-speed parameters is lost when the SNR is relaxed to 10 dB. The reason for this poor resolution of the parameters is due to a strong correlation between the ocean sound speed at the bottom with that at the top; see Fig. 4, where the two-dimensional marginal

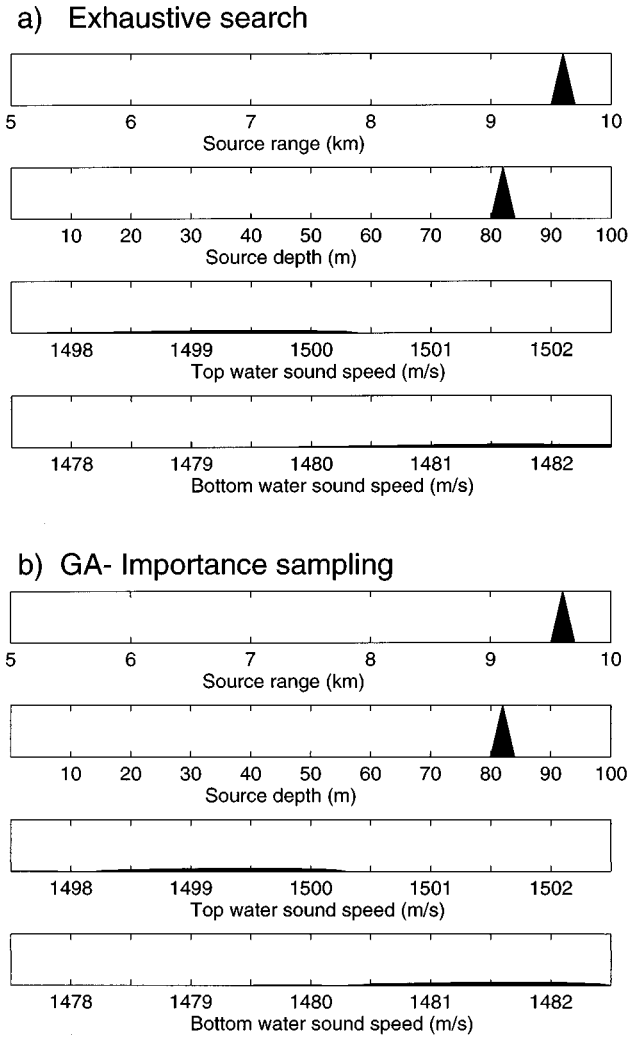

FIG. 3. The estimated *a posteriori* distribution for a SNR=10 dB for the sspmis case. (a) Using numerical integration, (b) using importance sampling.

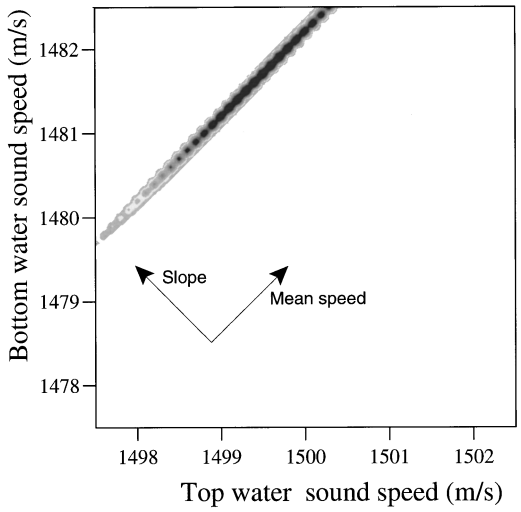

FIG. 4. The estimated marginal 2-D *a posteriori* distribution between the upper and lower ocean sound speed using a full search for a SNR of 10 dB. It is based on the same data as Fig. 3(a). The marginal 1-D distribution for each parameter is displayed on the top and to the right. By reparametrizing the sound speed as slope and mean a better resolution is obtained.

distribution is shown. From this figure it is clear that a better parametrization would be the mean sound speed and the gradient of the sound speed, as indicated in the figure and also discussed in Ref. 12. The difference in ambiguity for the sound speeds estimated at SNR of 40 dB (Fig. 2) and 10 dB (Fig. 3) is due to the fact that at 40 dB, slope and mean sound speed are well resolved, whereas at 10 dB SNR only the slope is well resolved.

2. Optimizing coupled parameters

Coupled parameters usually render an optimization problem slightly more difficult. Parameter coupling has been observed by several researchers.[12,33–35] Coupling can be detected by plotting either the ambiguity function or, alternatively, the 2-D marginal *a posteriori* distribution of the parameters. The advantage of the second approach is that it provides an integrated (global) value across the remaining parameters. However, both approaches have limitations when several parameters are strongly coupled.

For a gradient method coupled parameters do not pose a major problem. A difficulty with gradient methods is the numerical computation of the gradient. When using finite differences for computing, the gradient methods tend to be unstable due to a too small or large step size. Fortunately, it is possible to compute the gradient analytically for a wavenumber integration approach[30] and for a normal-mode approach.[36,37]

Some global search methods additionally exploit gradient information. In ocean acoustics this has been proven successful in Refs. 30 and 34. In Ref. 30, the optimization is a hybrid method combining the global genetic algorithm (GA) with the local Gauss–Newton method. This is implemented by taking several gradient steps between each update of the object function for each individual in the GA population. This approach is quite general but requires a careful analysis of the gradient computation, which was done analytically (in order to avoid huge numerical errors). In Ref. 34, a parameter rotation approach was suggested. The eigenvectors of the *a priori* second moment of the objective function gradient define the transformation for rotating the parameter space. The second moment is defined by implicitly assigning a uniform *a priori* density to the parameters. The computed eigenvectors provide some insight into the geometry of parameter space. After reparametrization, the search proceeds using SA. This approach is efficient if the parameter space is characterized by a few local minima with prominent features in one direction. In cases where the gradient information averages out, this will not provide an improvement. Such cases include circular shaped valleys, landscapes with several valleys, or landscapes with several valleys, or landscapes that are hilly without trend.

3. Including the a priori distribution

A priori knowledge is incorporated using Eq. (28) and based on the former example. In this case the *a priori* knowledge has a maximum at the true value. Initially only prior information of the top sound speed is used, Fig. 5(b). It is seen that this increases the peak of both the upper and lower

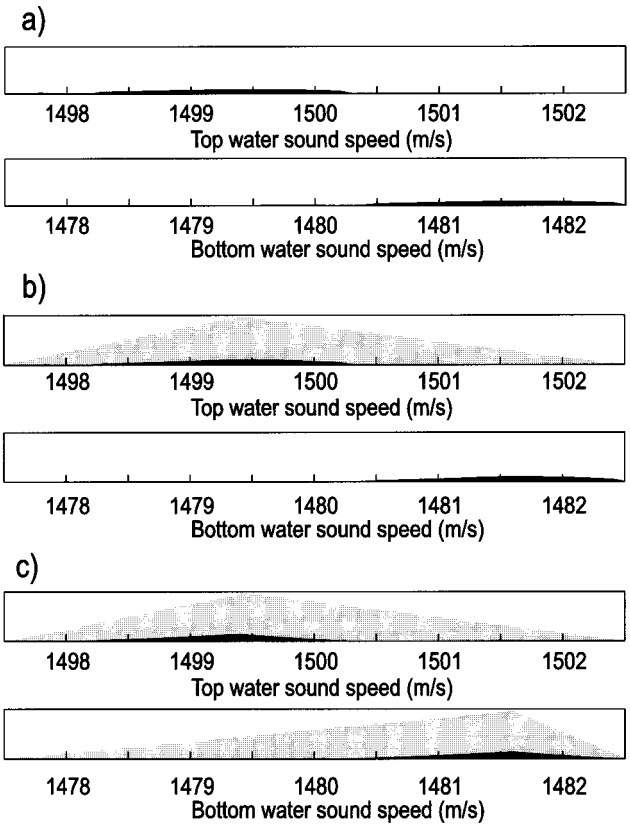

FIG. 5. The estimated *a posteriori* distribution using GA for SNR=10 dB. Only the two sound-speed parameters are displayed. (a): no *a priori* information is used [similar to Fig. 3(b)] in (b) *a priori* knowledge (grey area) about the top sound speed is included and in (c) *a priori* knowledge (grey area) about both top and bottom sound speeds are included. The use of *a priori* knowledge has sharpened the peaks marginally.

sound-speed point. This is because *a priori* knowledge is multiplied on the full *a posteriori* distribution. When using prior information for the lower and upper sound speed, the peak in the distribution becomes more pronounced, Fig. 5(b). It is clear that wrong prior information must bias the estimate.

Prior information about the environment, i.e., measured sound speeds, and the main parameters in terms of their search interval is important for obtaining good inversion results. Incorporation of smooth *a priori* distributions such as Eq. (28) does not seem significant, as the *a posteriori* distribution does not change much.

B. Yellow Shark data

This example is based on the SACLANTCEN Yellow Shark 94 (YS-94) experiment. YS-94 was a carefully designed major experiment in shallow water (100 m) south of Elba in the Mediterranian Sea. A fixed source–receiver geometry was used and a comprehensive environmental data set was available: Sea surface temperature, sea surface motion, currents, 2D temperature/salinity structure along transect, cores, and high resolution seismics. For a detailed description see Ref. 38. In the data used here the source was located at a 9-km range from a vertical array extending the complete depth of the water column, it transmitted energy at 7 frequencies: 200, 250, 315, 400, 500, 630, and 800 Hz. The

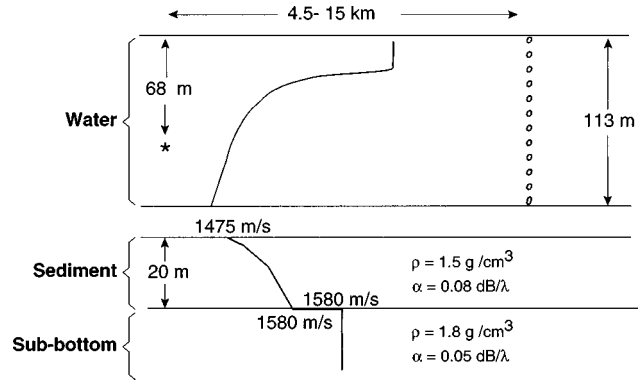

FIG. 6. **ysmodels**. The baseline environmental model used in the inversion of the YS-94 data Ref. 38.

vertical array consisted of 32 hydrophones. The SNR was estimated to about 30 dB.[38] The environment is shown in Fig. 6. The covariance matrix estimate was based on $K=17$ time frames and $P=4$ orthogonal windows, as described in Sec. 1 C 3.

1. Single frequency

First it will be discussed how the *a posteriori* distribution is constructed. This was done from a theoretical point of view in Sec. I, but here a more practical approach is taken by (a) discussing of the convergence of the objective function, (b) constructing the likelihood function from the objective function and, (c) construction of *a posteriori* distribution from the likelihood function.

To investigate the above, a single frequency inversion for the model in Fig. 6 is performed as it is much faster than the more accurate broadband inversion. The unknown part of the environment is represented by either 5, 7, or 10 parameters, as indicated in Table I. Clearly, which parameter sets are found depends on the number of iterations in a search. The search is performed with either 5000 forward modeling runs (split into ten independent populations each with 500

TABLE I. Parameter search bound for the YS-94 case. Each parameter was discretized into 64 values. The 5, 7, and 10 parameters refers to the number of parameters used in the inversion. The bottom sound-speed profile was modeled using the increase from the previous sound-speed point, as is common in SAGA. The receiver depth is the depth of the deepest hydrophone, this controls the vertical position of the entire vertical array in the water column.

Parameter	Lower	Upper
5, 7, and 10 parameters:		
Source range (m)	7	11
Source depth (m)	65	75
Tilt (m)	−3	3
Water depth (m)	110	118
Receiver depth (m)	96	104
7 and 10 parameters:		
Bottom sound speed at interface (m/s)	1460	1500
Bottom sound-speed increase at 5 m (m/s)	10	50
10 parameters:		
Bottom sound-speed increase at 10 m (m/s)	10	50
Bottom sound-speed increase at 20 m (m/s)	10	50
Bottom attenuation (dB/λ)	0	0.4

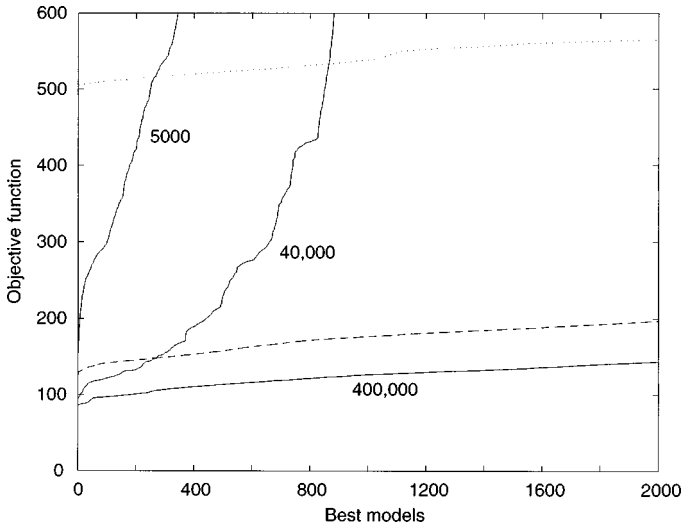

FIG. 7. Sorted values of the objective function, Eq. (17), for the best estimated models for each optimization. The best models are the ones that gave the lowest value of the objective function. Solid lines: The best values of the objective function based on either 4×10^5, 4×10^4, or 5×10^3 evaluations of the forward model with ten unknown parameters. Dashed line: based on 400 000 evaluations with seven unknown parameters. Dotted line: based on 400 000 evaluations with five unknown parameters.

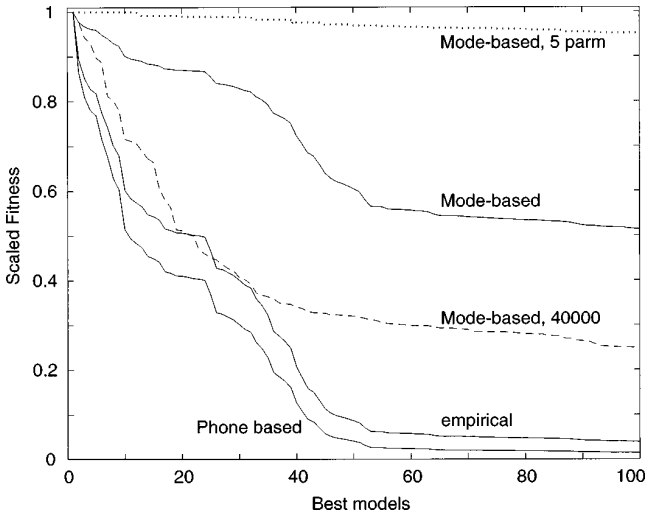

FIG. 8. Sorted values of likelihood functions using either an empirical, Eq. (11), a phone-based, Eq. (18), or a mode-based, Eq. (25) with $J=5$, likelihood function. Solid lines: Based on 4×10^5 forward model evaluations and estimation of ten parameters with either empirical, phone-based, or mode-based likelihood function. The dashed line is based on 4×10^4 forward model evaluations and estimation of ten parameters and mode-based likelihood function. The dotted line is based on 4×10^5 forward model evaluations, estimation of five parameters and mode-based likelihood function.

forward modeling runs [10×500]), 40 000 forward modeling runs [20×2000], or 400 000 forward modeling runs [200×2000].

In Fig. 7 the sorted values of the objective function are displayed for the best models. The best models are the one that gave the lowest value of the objective function. It is seen that for ten parameters we obtain a lower value of the objective function than when using seven or five parameters. Clearly, if more free parameters are available it is possible to obtain a better fit. The curve with ten parameters gives the best fit. Whether this improved fit is significant or whether the extra parameters are just fitting additive noise can be tested.[39] When using more forward modeling runs, more samples with a high degree of fit are obtained, as can be seen by comparing the curves for 5000, 40 000, and 400 000 forward modeling runs in Fig. 7.

Based on these values, the likelihood function (weighted fitness) is computed for each of these models, see Fig. 8. It is seen from Eqs. (15) and (18) that the noise estimate depends on the best estimated value of the objective function and, therefore, the value of the likelihood function depends on the search. If this best value is much better that the other value found during the optimization, the likelihood function, Eq. (18), will decrease quite rapidly (compare the curve for five parameters with those for ten parameters). How fast the curve decreases also depends on the number of modes used in the objective function. Note that even though the objective function assumes only a few modes the forward model always includes all propagating modes.

Based on the weighted fitness, as displayed in Fig. 8, the integrals for the marginal distributions, Eq. (5), are estimated. It was found that when using the noise estimate, Eq. (15), with the likelihood function, Eq. (18), to estimate the *a posteriori* distribution that the distributions became single peaked. This is probably due to an underestimation of the noise, because the data on each hydrophone is correlated. For long-range propagation, the pressure field can be described as a sum of modes. Thus it is expected that the denominator in Eq. (15) should express the number of propagating modes, see Eq. (24).

Both the semiempirical weighting and the ML weighting using five modes in the noise estimate and estimating five parameters when 400 000 forward models is used, are shown in Fig. 9(a) and (b) when 400 000 forward models are used in the optimization. It should be noted that the objective function as well as the samples used in the estimation of the objective function are identical for both methods. Thus the difference in the plot is entirely due to different weighting of the objective function when constructing the *a posteriori* distributions. Intuitively, the empirical estimates appear to overestimate the resolution, whereas the ML gives a more realistic estimate of the peak. The empirical estimates of the variance depend on the number of forward modeling runs. The variance will not be as small if a smaller number of forward modeling runs was used during the optimization.

For the results of the optimization with 5 parameters, it is seen that the parameter estimate of the source depth reaches the upper bound. This indicates that the optimization has not performed well, probably because the environment has not been well described. When using nine parameters it is seen that the source depth becomes more stable. Again it is seen that the empirical weighting gives a more optimistic estimate of the uncertainties.

Comparing the likelihood based results with five or nine parameters [Fig. 9(b) and (d)], it is seen that the spread of the distributions is about the same. The estimated parameters are, however, not the same; due to additional parameters for the nine parameter problem. As only one frequency is used in the optimization, more stability is probably obtained by increasing the number of frequencies.

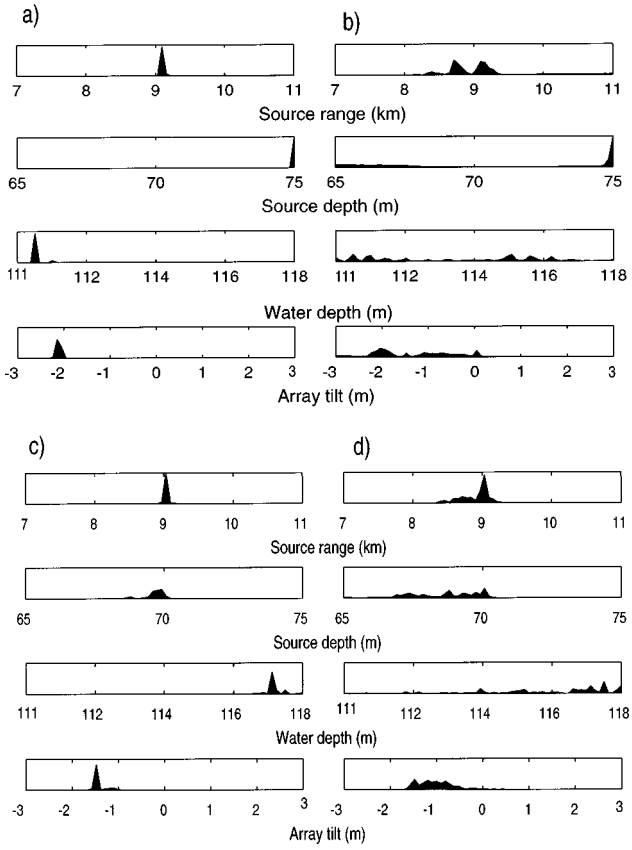

FIG. 9. The estimated *a posteriori* distribution for a search of five or nine parameters. (a) Five parameters, empirical posteriori; (b) five parameters, likelihood based posteriori; (c) nine parameters, empirical posteriori; (d) nine parameters, likelihood based posteriori. Only four parameters are shown in the plot as the fifth parameter was not that well determined.

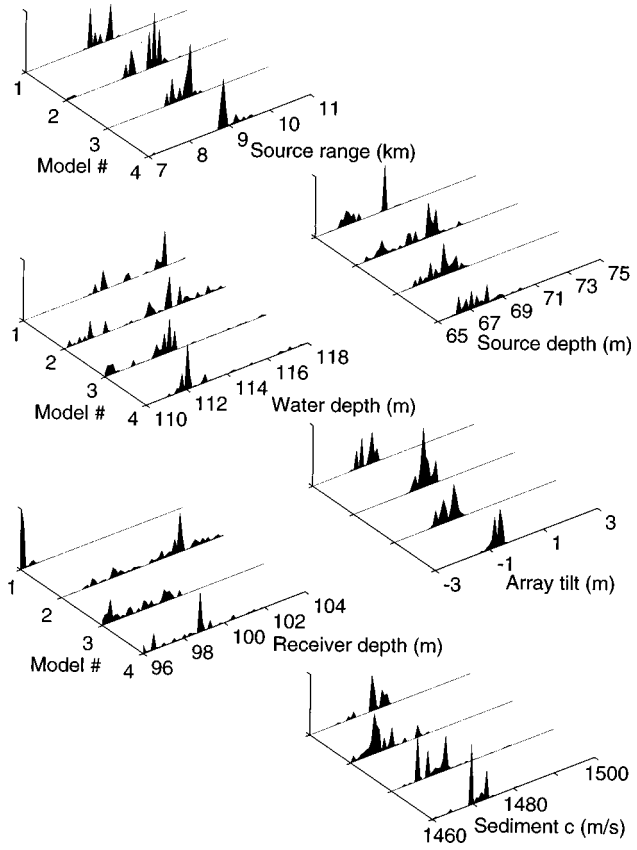

FIG. 10. The estimated *a posteriori* distribution for the YS-94 data. The noise has been estimated using five modes.

2. Multifrequency

By using observations at more frequencies, more information is used and thus a more robust estimation of the underlying parameters is usually obtained. In order to appreciate the value of more frequency observations it is essential to use the ML approach rather than the empirical approach (Sec. I B). The additional information that is gained from using more data is not reflected in the empirically based probability distributions, and thus it cannot be used to study convergence of solutions. The inversion is carried out using the four data models with increasing information:

(1) one frequency at 400 Hz;
(2) three frequencies at 200, 400, and 800 Hz;
(3) five frequencies at 400, 315, 400, 500, and 800 Hz; and
(4) seven frequencies at 400, 250, 315, 400, 500, 630, and 800 Hz.

The corresponding distributions are shown in Fig. 10. In general, as more frequencies are used, the solution seems to converge and the spread of the distributions decreases. One exception is the estimation of receiver depth for one frequency. However, it is clustered at one bound indicating that a solution outside the search bound is preferable. Incoherent averaging over frequency is especially effective if one or two octaves of signal bandwidth are available.

III. CONCLUSIONS

A precise formulation has been given for estimating the *a posteriori* distribution of environmental parameters retrieved from an ocean acoustic experiment. From these distributions, all information about the parameters can be extracted, as mean, higher moments, and marginal distributions. Numerical evaluation of multidimensional integrals over *a posteriori* distributions is required. These integrals can be numerically estimated using samples from global optimization methods. The method is based on importance sampling and requires no additional evaluation of the objective function at the expense of (negligible) bias.

The maximum-likelihood solution to an inversion problem does not provide an estimate of final parameter uncertainty. The likelihood based *a posteriori* distribution shows, however, the improvement in performance when using more frequencies, or differences when using a near or far array. As precise knowledge about the likelihood function is often unavailable for practical problems, the empirical formulation might be preferable, although uncertainty estimates are less accurate.

It is well known that SA and GA have superior performance for ocean geo-acoustic parameter estimations over local deterministic solution strategies due to the large number of secondary local optima of the objective function. Now, uncertainty studies can also be enhanced by a global approach.

The examples illustrate the use of this approach for simulated and real data on a vertical array. Array geometry is

arbitrary to the approach and both frequency and time domain data can be used.

APPENDIX A: OPTIMAL IMPORTANCE SAMPLING

Consider the evaluation of the multidimensional integral Eq. (6). First, the integral is rewritten as an expectation

$$\theta=\int_{\mathscr{M}} \frac{f(\mathbf{m})\sigma(\mathbf{m})}{g(\mathbf{m})}\, g(\mathbf{m})d\mathbf{m}\equiv \mathsf{E}_g\left[\frac{f(\mathbf{M})\sigma(\mathbf{M})}{g(\mathbf{M})}\right], \quad \text{(A1)}$$

where the random parameter vector $\mathbf{M}$ is selected from the generating distribution g. This expectation is estimated by the arithmetic mean $\hat{\theta}$ from Eq. (7). The variance is given by

$$\mathrm{Var}_g\,\hat{\theta}=\left[\mathsf{E}_g\left(\frac{f^2(\mathbf{M})\sigma^2(\mathbf{M})}{g^2(\mathbf{M})}\right)-\theta^2\right]\Big/\, N_{\mathrm{obs}}. \quad \text{(A2)}$$

Notice that the variance decreases as $O(N_{\mathrm{obs}}^{-1})$ with increasing number of samples N_{obs}. Using a variational procedure (with the constraint that g be a probability density) it can be shown that this variance is minimized for

$$g^{\mathrm{MV}}(\mathbf{m})=\frac{|f(\mathbf{m})|\sigma(\mathbf{m})}{\int_{\mathscr{M}}|f(\mathbf{m})|\sigma(\mathbf{m})d\mathbf{m}}. \quad \text{(A3)}$$

APPENDIX B: MATCHED FIELD LIKELIHOOD

Starting from Eq. (12) and using the Gaussianity of $\mathbf{e}(\omega_l)$ as stated in Sec. I C 1, the probability density (for a single time frame $K=1$) given the signal S_l and the noise power spectral density ν_l is given by

$$\mathscr{L}_1(\mathbf{m},S,\nu)=\prod_{l=1}^{L}(\pi\nu_l)^{-N}\exp\left[-\frac{|\mathbf{q}_l-\mathbf{w}_l(\mathbf{m})S_l|^2}{\nu_l}\right]. \quad \text{(B1)}$$

Errors $\mathbf{e}_1$, $\mathbf{e}_2$ at differing frequencies $\omega_1\neq\omega_2$ are assumed uncorrelated. For large observation times it is a good approximation for the noise in the data (but might be violated for deterministic modeling errors, cf. Sec. I C). Measurement data $\mathbf{q}_{l,k}$ from multiple time frames $k=1,\ldots,K$ is incorporated by multiplying the corresponding probability densities (B1) for each single time frame. This gives

$$\mathscr{L}_1=\prod_{k=1}^{K}\prod_{l=1}^{L}(\pi\nu_l)^{-N}\exp\left[-\frac{|\mathbf{q}_{l,k}-\mathbf{w}_l(\mathbf{m})S_{l,k}|^2}{\nu_l}\right]. \quad \text{(B2)}$$

The ML estimate $\hat{\mathbf{m}}^{\mathrm{ML}}$ for $\mathbf{m}$ is obtained by jointly maximizing over the signal and noise parameters $(S_{l,k},\nu_l\forall l,k)$ and the model parameter vector $\mathbf{m}$. The maximization w.r.t. $S_{l,k}$ is obtained by requiring $\partial\mathscr{L}_1/\partial S_{l,k}=0$ in closed form: $\hat{S}_{l,k}=\mathbf{w}_l^{\dagger}(\mathbf{m})\mathbf{q}_{l,k}/|\mathbf{w}_l(\mathbf{m})|^2$. It is seen that $\hat{S}_{l,k}$ depends on $\mathbf{m}$ but not on ν. Inserting this into (B1) yields

$$\mathscr{L}_2(\mathbf{m},\nu)=\prod_{l=1}^{L}(\pi\nu_l)^{-NK}\exp\left[-\frac{\phi_l(\mathbf{m})}{\nu_l}\right] \quad \text{(B3)}$$

with

$$\phi_l=\mathrm{tr}\,\hat{\mathbf{R}}_l-\frac{\mathbf{w}_l^{\dagger}(\mathbf{m})\hat{\mathbf{R}}_l\mathbf{w}_l(\mathbf{m})}{\mathbf{w}_l^{\dagger}(\mathbf{m})\mathbf{w}_l(\mathbf{m})}. \quad \text{(B4)}$$

Optimizing w.r.t. ν_l yields

$$\hat{\nu}_l^{\mathrm{ML}}=\frac{1}{N}\,\phi_l. \quad \text{(B5)}$$

This gives

$$\mathscr{L}_3(\mathbf{m})=\left(\frac{N^K}{e\,\pi^K}\right)^{NL}\left(\frac{1}{\phi(\mathbf{m})}\right)^{N}. \quad \text{(B6)}$$

The ML solution $\hat{m}^{\mathrm{ML}}$ is obtained by maximizing $\mathscr{L}_3$ over all $\mathbf{m}\in\mathscr{M}$. Finally, an estimate for the noise power spectral density (which is assumed independent of $\mathbf{m}$) is obtained from Eq. (B5) and the ML solution $\hat{\nu}_l^{\mathrm{ML}}$ at $\hat{m}^{\mathrm{ML}}$ into the likelihood function, Eq. (B3). From now on, we consider the noise spectral density as known and only keep the free argument $\mathbf{m}$ of the objective function ϕ_l. This approach leads to

$$\mathscr{L}(\mathbf{m})=\prod_{l=1}^{L}(\pi\hat{\nu}_l^{\mathrm{ML}})^{-N}\exp\left[-\frac{\phi_l(\mathbf{m})}{\hat{\nu}_l^{\mathrm{MD}}}\right], \quad \text{(B7)}$$

which results in the definition of Eq. (18).

[1] N. Metropolis and S. Ulam, ''The Monte Carlo method,'' J. Am. Stat. Assoc. **44**, 335–341 (1948).
[2] N. Metropolis, A. W. Rosenbluth, M. N. Rosenbluth, A. H. Teller, and E. Teller, ''Equation of states done by fast computing machines,'' J. Chem. Phys. **1**, 1087–1092 (1953).
[3] Y. Bard, *Nonlinear Parameter Estimation* (Academic, San Diego, 1974).
[4] W. Menke, *Geophysical Data Analysis: Discrete Inverse Theory* (Academic, San Diego, 1989).
[5] S. D. Rajan, J. F. Lynch, and G. V. Frisk, ''Perturbative inversion methods for obtaining bottom geoacoustic parameters in shallow water,'' J. Acoust. Soc. Am. **82**, 998–1017 (1987).
[6] A. Tarantola, *Inverse Problem Theory: Methods for Data Fitting and Model Parameter Estimation* (Elsevier, Amsterdam, 1987).
[7] P. W. Cary and C. H. Chapman, ''Automatic 1-D waveform inversion of marine seismic reflection data,'' Geophys. J. **93**, 527–546 (1988).
[8] M. K. Sen and P. L. Stoffa, ''Nonlinear one-dimensional seismic waveform inversion using simulated annealing,'' Geophysics **56**, 1624–1638 (1991).
[9] K. Mosegaard and A. Tarantola, ''Monte Carlo sampling of solutions to inverse problems,'' J. Geophys. Res. **100**, 12431–12447 (1995).
[10] M. K. Sen and P. L. Stoffa, ''Bayesian inference, Gibbs' sampler and uncertainty estimation in geophysical inversion,'' Geophysical Prospecting **44**, 313–350 (1996).
[11] M. K. Sen and P. L. Stoffa, *Global Optimization in Geophysical Inversion* (Elsevier, Amsterdam, 1995).
[12] P. Gerstoft, ''Inversion of seismoacoustic data using genetic algorithms and *a posteriori* probability distributions,'' J. Acoust. Soc. Am. **95**, 770–782 (1994).
[13] P. Gerstoft and D. F. Gingras, ''Parameter estimation using multi-frequency range-dependent acoustic data in shallow water,'' J. Acoust. Soc. Am. **99**, 2839–2850 (1996).
[14] M. D. Collins, W. A. Kuperman, and H. Schmidt, ''Nonlinear inversion for ocean-bottom properties,'' J. Acoust. Soc. Am. **92**, 2770–2783 (1992).
[15] C. E. Lindsay and N. R. Chapman, ''Matched field inversion for geophysical parameters using adaptive simulated annealing,'' IEEE J. Ocean Eng. **18**, 224–231 (1993).
[16] S. E. Dosso, M. L. Yeremy, J. M. Ozard, and N. R. Chapman, ''Estimation of ocean bottom properties by matched-field inversion of acoustic field data,'' IEEE J. Ocean Eng. **18**, 232–239 (1993).
[17] P. Gerstoft and A. Caiti, ''Acoustic estimation of bottom parameters: error bounds by local and global methods,'' in *Second European Conference on Underwater Acoustics*, edited by L. Bjørnø (European Commission, Luxembourg, 1994), pp. 887–892.
[18] J. M. Hammersley and D. C. Handscomb, *Monte Carlo Methods* (Wiley, New York, 1964).
[19] A. J. W. Duijndam, ''Bayesian estimation in seismic inversion. Part I: Principles,'' Geophysical Prospecting **36**, 878–898 (1988).
[20] J. Lefebvre, H. Roussel, E. Walter, D. Lecointe, and W. Tabbara, ''Pre-

diction from wrong models: The Kriging approach,'' IEEE Antennas Propag. Mag. **38**, 35–45 (1996).
[21] F. B. Jensen and M. C. Ferla, ''SNAP-The SACLANTCEN normal mode acoustic propagation model,'' SACLANT Undersea Research Centre, SM-121, La Spezia, Italy, 1979.
[22] D. H. Johnson and D. E. Dudgeon, *Array Signal Processing* (Prentice-Hall, Englewood Cliffs, NJ, 1993).
[23] D. Maiwald and J. F. Böhme, ''Multiple testing for seismic data using bootstrap,'' IEEE Proc. IEEE ICASSP-94 **6**, 89–92 (1994).
[24] A. Tolstoy, *Matched Field Processing for Underwater Acoustics* (World Scientific, Singapore, 1993).
[25] M. L. Hinich, ''Maximum likelihood estimation of a radiating source in a waveguide,'' J. Acoust. Soc. Am. **66**, 480–483 (1977).
[26] E. C. Shang, ''Source depth estimation in wave guides,'' J. Acoust. Soc. Am. **86**, 1960–1964 (1985).
[27] D. J. Thompson, ''Jacknifing multiple-window spectra,'' IEEE Proc. ICASSP-94 **6**, 73–76 (1994).
[28] C. F. Mecklenbräuker, D. Maiwald, and J. F. Böhme, ''F-Test in matched field processing: identifying multimode propagation,'' IEEE Proc. ICASSP-95, Vol. 5, 3123–3126 (1995).
[29] S. Rajan, ''Waveform inversion for the geoacoustic parameters of the ocean bottom,'' J. Acoust. Soc. Am. **91**, 3228–3241 (1992).
[30] P. Gerstoft, ''Inversion of acoustic data using a combination of genetic algorithms and the Gauss-Newton approach,'' J. Acoust. Soc. Am. **97**, 2181–2191 (1995).
[31] P. Gerstoft, ''SAGA Users guide 2.0, an inversion software package,'' SACLANT Undersea Research Centre, SM-333, La Spezia, Italy, 1997.
[32] M. Porter and A. Tolstoy, ''The matched field processing benchmark problems,'' J. Comput. Acoust. **2**, 161–185 (1994).
[33] H. Schmidt and A. B. Baggeroer, ''Physics imposed resolution and robustness issues in seismo-acoustic parameter inversion,'' in *Full Field Inversion Methods in Ocean and Seismic Acoustics*, edited by O. Diachok, A. Caiti, P. Gerstoft, and H. Schmidt (Kluwer, Dordrecht, 1995), pp. 85–90.
[34] M. D. Collins and L. Fishman, ''Efficient navigation of parameter landscapes,'' J. Acoust. Soc. Am. **98**, 1637–1644 (1995).
[35] Z.-H. Michalopoulou, M. B. Porter, and J. Ianniello, ''Broadband source localization in the Gulf of Mexico,'' J. Comput. Acoust. **4**, 361–370 (1996).
[36] R. T. Kessel, ''The variation of modal wavenumbers with geoacoustic parameters in a layered media,'' J. Acoust. Soc. Am. **102**, 2690–2696 (1997).
[37] O. A. Godin, ''Acoustic mode reciprocity in fluid/solid systems: implications on environmental sensitivity and horizontal refraction,'' International Conference on Theoretical and Computational Acoustics, New Jersey, 1997.
[38] J-P. Hermand and P. Gerstoft, ''Inversion of broadband multitone acoustic data from the Yellow shark summer experiments,'' IEEE J. Ocean Eng. **21**, 324–346 (1996).
[39] C. F. Mecklenbräuker, P. Gerstoft, J. F. Böhme, and Pei-Jung Chung, ''Hypothesis testing for acoustic environmental models using likelihood ratio,'' J. Acoust. Soc. Am. (submitted).

A simplified method for determining sediment size and concentration from multiple frequency acoustic backscatter measurements

Eric D. Thosteson and Daniel M. Hanes
Department of Coastal and Oceanographic Engineering, University of Florida, P.O. Box 116590, Gainesville, Florida 32611

(Received 2 September 1997; accepted for publication 7 May 1998)

Until recently the determination of concentration from acoustic backscatter intensity measurements required an iterative technique due to the implicit form of the acoustic backscatter equation. In this paper, an explicit form of this equation is examined in an effort to simplify the technique of determining size from multifrequency acoustic backscatter data. By retaining the size dependence throughout the derivation for an explicit solution for concentration, a new explicit form results. This new explicit concentration solution improves the technique for determining median sediment size by incorporating sediment attenuation in the calculation. Because this new technique relies on the minimization of the variance in concentration as determined by different frequency transducers, the previous technique of pairing transducers of different frequencies is replaced by a technique making use of any number of different frequency transducers. The new size/concentration inversion technique is tested using both simulated and laboratory data. Numerical precision is shown to be the only source of error with the use of simulated data. Laboratory tests result in less than 20% error in the determination of both concentration and size over a range of nearly one meter. [S0001-4966(98)06108-6]

PACS numbers: 43.30.Pc, 43.30.Xm, 43.30.Ma, 43.30.Gv [DLB]

INTRODUCTION

Use of a high-frequency underwater acoustic transducer to profile the vertical distribution of sediment concentration has been demonstrated under both laboratory and field conditions by several investigators.[1–5] Basically, profiles of the intensity of backscattered sound from suspended sediment are collected, and this intensity is related to the suspended sediment concentration at each point in the profile. A typical technique for determination of concentration from acoustic backscatter data requires inversion of the acoustic backscatter equation for concentration, which yields an implicit equation needing an iterative technique for solution. In order to obtain profiles of concentration from a single transducer operating at a fixed frequency, knowledge of the sediment grain size distribution is required prior to applying the inversion procedure. In addition, the assumption that this size distribution either remains constant with range or with a predetermined form at all ranges is required, as the scattering and absorption properties of the sediment are dependent upon grain size.[6] Recently, several investigators have demonstrated effective measurement of both the profiles of sediment concentration and of the median grain size of the distribution.[3,7] The technique requires the use of multifrequency acoustic transducers. Since the absorbing and scattering properties of sediment depend on both the grain size and upon the frequency of the incident sound, each unique frequency transducer provides an independent measurement of the backscattered intensity profile. Hence, each point in the profile can be described by a number of independent equations equal to the number of coincident and collocated measurements of unique frequency. Typically, three transducers of unique frequency are used to collect coincident intensity profiles. Although in theory, use of three frequencies suggests that at each measured point, concentration and two parameters of the grain-size distribution can be determined, typically, only concentration and one parameter of the distribution are obtained. The sensitivity of the equations to small variations in intensity and also the nonlinearity of the sediment size response functions are responsible for this limitation.

Lee and Hanes[8] presented an explicit solution for concentration, to be referred to in this paper as LH95, from the acoustic backscatter equation, significantly reducing the computational effort by removing the need for iteration. An added benefit derived from use of the explicit solution is removal of the ambiguity in concentration solutions obtained by the iterative solution to the implicit equation. Figure 1 shows the relation between concentration and transducer voltage (proportional to the square root of intensity) as calculated by the acoustic backscatter equation (3) assuming a constant concentration profile. From this figure, it is apparent that a single voltage value from the transducer may result from two different concentrations. Physically, this can be described with the following argument. At low concentrations, the sound attenuation due to sediment in the sound path is low, resulting in an increase in the intensity of the backscattered sound with increasing concentration. As this attenuation becomes more dominant, the intensity of the backscattered sound begins to decrease with increased concentration. So, from the two concentration solutions obtained from the implicit equation, the choice of the correct solution depends upon the magnitude of the attenuation. The explicit solution for concentration yields only one concentration, as

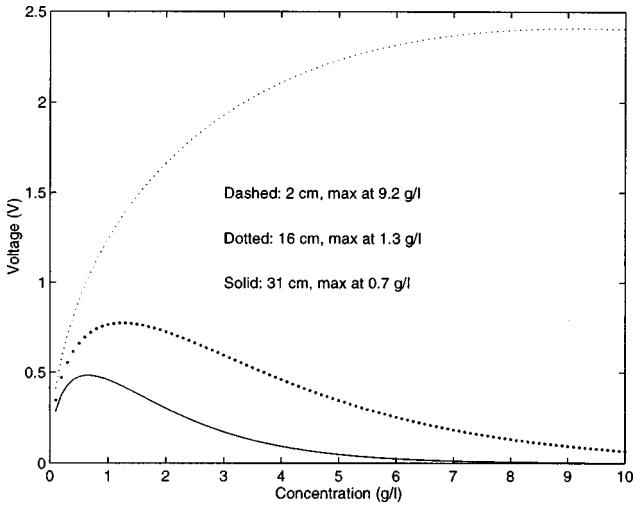

FIG. 1. Expected voltage for given concentrations, 5-MHz transducer.

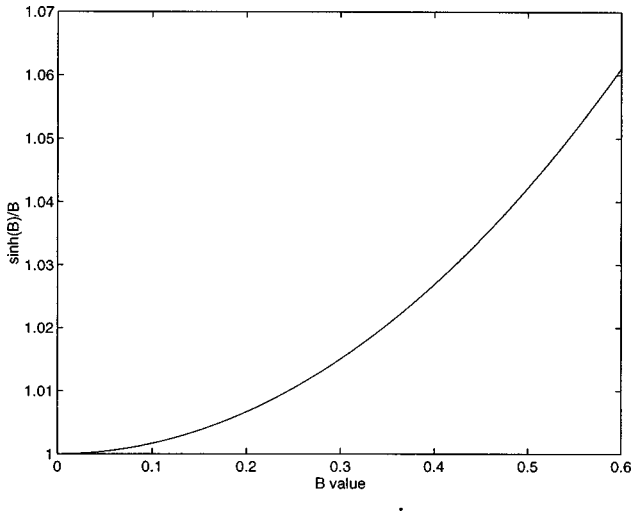

FIG. 2. Significance of $\sinh(B)/B$ term in acoustic backscatter equation.

this dependence on attenuation is accounted for by integration of the intensity profile.

In spite of the benefits presented by use of the LH95 explicit solution, it is restricted in its use to concentration only. Its use requires that the grain-size distribution be known and constant with range. Holdaway and Thorne extended the functionality of the solution by allowing the size distribution to vary but to retain a predetermined form with range from the transducer.[9] In the following derivation, a similar explicit solution for concentration retaining the dependence on the grain-size distribution is found by following the LH95 development. Based on this explicit form, the methods used for evaluating parameters of the grain-size distribution are re-examined, and an improved method, at least in computational effort, is introduced. In addition, the existing method for evaluating the grain-size parameters by pairing acoustic concentration profilers (ACPs) of different frequencies is extended to utilize an arbitrary number of unique frequency transducers.

I. THEORY

The equation that relates the intensity of the backscattered acoustic signal to the concentration and size distribution of the scatterers in suspension is referred to as the acoustic backscatter equation. This equation has been presented in several forms, each nearly equivalent. Presented here is a general form of the equation, based jointly on the forms presented by Hay[10] and Thorne:[6]

$$V^2 z^2 = (S^2 c \tau)\, \frac{1}{\psi^2(z)}\, F(z) C(z) e^{-4z(\alpha_w + \alpha_s(z))}\, \frac{\sinh B}{B}, \quad (1)$$

$$\alpha_s = \frac{1}{z} \int_{z_0}^{z} \zeta(\hat{z}) C(\hat{z})\, d\hat{z}. \quad (2)$$

The variables in Eqs. (1)–(2) are defined as follows: V = voltage read from transducer, z = distance from transducer, S = system constant, c = speed of sound, assumed constant with distance, τ = acoustic pulse width(s), ψ = near-field correction term (see the Appendix), F = backscatter parameter (see the Appendix), C = mass concentration (sediment density in F), α_w = water attenuation parameter (see the Appendix), α_s = sediment attenuation parameter, $B = (\alpha_w + \zeta(z) C(z))$, z_0 = range from transducer at which first concentration and size is evaluated, and ζ = local sediment attenuation proportionality constant (see the Appendix).

The near-field correction term, ψ, is included here for completeness, and it can easily be included in the following derivation by temporarily absorbing it in the backscatter parameter. Since it is simply another function of z, it does not complicate the derivation. It has not been included in the following derivation, because it was not used in the subsequent numerical simulations or laboratory tests. The complete solution, including this term, is presented in the Appendix. In the key above, it is noted that the speed of sound is assumed constant with distance. In reality, changes in temperature, salinity, and mass concentration will result in small changes in the speed of sound. Such speed of sound changes due to temperature and salinity fluctuations are small in typical applications of the present theory, but should they not be, the speed of sound parameter can be absorbed into the backscatter parameter instead of into the system constant throughout the following derivation. Speed of sound fluctuations from increased mass concentration are also small in the range of concentrations, discussed below, for which the present single-scattering theory holds.

In Eq. (1), the final term on the right side of the equation, $(\sinh B)/B$, presents difficulty when trying to obtain an explicit solution for concentration. This term accounts for the difference in the magnitude of the sediment attenuation from the portion of the sampling volume closest to the transducer to the portion furthest from the transducer. Figure 2 shows the magnitude of this term versus the term B, and Table I shows the magnitude of this term for several cases using a distribution of quartz sand with median grain diameter, $\mu_\phi = 2.65$ and standard deviation, $\sigma_\phi = 0.25$. Note these parameters are given in units of phi, defined as $\phi = -\log_2 d$, where d is the grain diameter in mm. The transducer frequencies listed in Table I are the highest frequencies used in this study. A 30-g/l mass concentration corresponds to roughly a 1% concentration by volume, the approximate upper limit of

TABLE I. Values of $\sinh(B)/B$ for extreme concentrations.

Transducer frequency (MHz)	Concentration (g/l)	B	$\frac{\sinh B}{B}$
5	30	0.5591	1.053
5	5	0.0994	1.002
2.25	30	0.0956	1.002
2.25	5	0.0172	1.000

concentration before multiple scattering must be considered, and the 5-g/l concentrations are the highest tested in this study. From these results, it can be seen that for the highest concentrations for which the present theory applies, this term can be significant when the highest-frequency transducers are used. When operating transducers of lower frequency with suspensions of lower concentration, this term is very close to unity. Additionally, since the sediment attenuation term within the exponential function is an empirically determined parameter, determination of its value without including the $(\sinh B)/B$ term may compensate for its absence. So, for the remainder of this text, the acoustic backscatter equation will be approximated by the following expression:

$$V^2 z^2 = AF(z)C(z)e^{-4z(\alpha_w+\alpha_s(z))}. \tag{3}$$

In Eq. (3), the system sensitivity constant, S, the speed of sound, c, and the pulse width, τ, have been combined into a single system constant, A. The system constant can be later separated back into these constituents in order to correct for temperature variations.

II. DEVELOPMENT

A. Concentration inversion

Beginning with the general form of the acoustic backscatter equation (3), the concentration dependence is removed from the sediment attenuation term, α_s, giving a form in which the multiple term dependence on concentration is more obvious, Eq. (4).

$$AF(z)C(z) = V^2(z)z^2 \exp\left(\int_{z_0}^{z} 4(\alpha_w + \zeta(\hat{z})C(\hat{z}))d\hat{z} \right). \tag{4}$$

Following the LH95 derivation, first, the natural logarithm of the equation is found:

$$\ln A + \ln F + \ln C = 2\ln(Vz) + \int_{z_0}^{z} (4\alpha_w + 4\zeta C)d\hat{z}, \tag{5}$$

and then the derivative:

$$\frac{F'}{F} + \frac{C'}{C} = 2\left[\frac{V'z+V}{Vz}\right] + 4\alpha_w + 4\zeta C. \tag{6}$$

Upon arranging the terms of Eq. (6), a nonlinear differential equation of the Bernoulli type results:

$$C' + \left[\frac{F'}{F} - 2\left(\frac{V'z+V}{Vz}\right) - 4\alpha_w\right]C = 4\zeta C^2. \tag{7}$$

Rewriting in standard form, Eq. (7) becomes the following:

$$C' + p(z)C = Q(z)C^n. \tag{8}$$

Following the standard method of solution for a Bernoulli equation, the following substitutions can be made:

$$t = C^{1-n} = C^{-1}; \quad C = t^{-1}, \tag{9}$$

$$\frac{dC}{dz} = \frac{dC}{dt}\frac{dt}{dz} = -t^{-2}t'. \tag{10}$$

These substitutions result in a readily solved first order linear inhomogeneous differential equation:

$$-t^{-2}t' + pt^{-1} = Qt^{-2}, \tag{11}$$

$$t' + \hat{p}t = \hat{Q}, \tag{12}$$

where in Eq. (12), the following apply:

$$\hat{p} = -p, \quad \hat{Q} = -Q. \tag{13}$$

Solution to Eq. (12) is found by first determining the integrating factor:

$$I = \exp\left(\int \hat{p}dz \right), \tag{14}$$

$$\int \hat{p}dz = -\int \left[\frac{F'}{F} - 2\left(\frac{V'z+V}{Vz}\right) - 4\alpha_w\right]dz$$

$$= -\ln F + 4\alpha_w z + 2\ln(Vz), \tag{15}$$

$$I = \exp(2\ln(Vz) + 4\alpha_w z - \ln F) = \frac{(Vz)^2}{F}\exp(4\alpha_w z). \tag{16}$$

After multiplying the equation by the integrating factor, an exact differential results, which can then be integrated for solution.

$$\frac{d}{dz}\left(\frac{(Vz)^2}{F}\exp(4\alpha_w z)t\right) = -4\zeta\frac{(Vz)^2}{F}\exp(4\alpha_w z), \tag{17}$$

$$\frac{(Vz)^2}{F}\exp(4\alpha_w z)t = -\int_{z_0}^{z} 4\zeta\frac{(V\hat{z})^2}{F}\exp(4\alpha_w\hat{z})d\hat{z} + \gamma. \tag{18}$$

Equation (18) is then solved for t, and then finally for the concentration, C:

$$t = \frac{\gamma - \int_{z_0}^{z} 4\zeta[(V\hat{z})^2/F]\exp(4\alpha_w\hat{z})d\hat{z}}{[(Vz)^2/F]\exp(4\alpha_w z)}, \tag{19}$$

$$C = \frac{1}{t} = \frac{[(Vz)^2/F]\exp(4\alpha_w z)}{\gamma - \int_{z_0}^{z} 4\zeta[(V\hat{z})^2/F]\exp(4\alpha_w\hat{z})d\hat{z}}. \tag{20}$$

Next, boundary conditions (21) are applied for solution of the integration constant:

$$\left.\begin{aligned} C &= C_0 \\ V &= V_0 \\ F &= F_0 \end{aligned}\right\} \quad \text{at} \quad z = z_0, \tag{21}$$

$$\gamma = \frac{(V_0 z_0)^2}{F_0 C_0}\exp(4\alpha_w z_0). \tag{22}$$

The concentration C_0 at range z_0, the closest point to the transducer not in near field, may be estimated in many ap-

plications by assuming the concentration and size are constant within near field. The implicit form of the acoustic backscatter equation, Eq. (4), simplifies somewhat, giving Eq. (23):

$$C_0=\frac{(Vz_0)^2}{AF}\,e^{4z_0(\alpha_w+\zeta C)}. \tag{23}$$

This can be solved iteratively for concentration for a given grain size, using a zero sediment attenuation form of the equation for an initial estimate:

$$C_0=\frac{(Vz_0)^2}{AF}\,e^{4z_0\alpha_w}. \tag{24}$$

B. Size determination

The technique originally introduced by Hay and Sheng[3] for determining the median size of particles in suspension involved first approximating the acoustic backscatter equation (4) by neglecting the sediment attenuation. In this way ratios could be constructed from the approximate equations for any pair of unique frequency transducers. Since the concentration dependence of the attenuation is removed by neglecting the sediment attenuation, the remaining concentration terms in the equation cancel in the formation of the ratio. Hence, the only remaining unknowns in the ratios are functions of the size distribution of the suspended particles. By assuming the particle size can be described by a two-parameter distribution, the log-normal distribution, and by further assuming one parameter is constant, the ratios can be evaluated over a range of the other parameter. The standard deviation is the parameter assumed constant and the ratios are determined over a range of median particle sizes. Median particle size is then found by minimizing the difference between the ratios and its known value with respect to the median particle size. Crawford and Hay improved the technique by solving the approximate equations first for those terms that are not functions of the size distribution or transducer frequency.[7] These terms are equal in all of the equations, regardless of transducer frequency, so equating the remaining terms in the other equations eliminates the concentration dependence. Again, the minimization technique is applied as before to determine the median particle size.

First by solving each transducer's equation only for concentration, and then by minimizing the variance in the concentrations predicted by any number of transducers with respect to median sediment size, Crawford and Hay's[7] technique is here slightly modified. By using the explicit solution for concentration, Eq. (20), there is no longer the need to neglect the sediment attenuation. In addition, once the median particle size is found by the minimization technique, the mean concentration is readily computed from the existing concentration solutions. The exact procedure is as follows.

The explicit solution for concentration derived above is discretized to represent each frequency of m transducers with $n+1$ bins outside the nearfield region of each transducer:

$$C_{i,j}=\frac{[(V_{i,j}z_j)^2/F_{i,j}]\exp(4\alpha_{wi}z_j)}{\gamma_i-I_{i,j}},$$
$$i=1,2,...,m,\quad j=1,2,...,n. \tag{25}$$

In the denominator of this expression, I is the discrete form of the integral, given by the following:

$$I_{i,j}=2\sum_{k=1}^{j}\left(\zeta_{i,k}\frac{(V_{i,k}z_k)^2}{F_{i,k}}\exp(4\alpha_{wi}z_k)+\zeta_{i,k-1}\frac{(V_{i,k-1}z_{k-1})^2}{F_{i,k-1}}\exp(4\alpha_{wi}z_{k-1})\right)\times(z_k-z_{k-1}). \tag{26}$$

The integration constant is defined again at point z_0:

$$\gamma_i=\frac{(V_{i,0}z_0)^2}{F_{i,0}C_{i,0}}\exp(4\alpha_{wi}z_0). \tag{27}$$

It should be mentioned that zero concentration in suspension, which results in zero voltage read at the transducer, will result in an indeterminate value of the integration constant. The location of z_0 should thus be set at the first range with nonzero concentration, determined by the following iterative technique.

The initial concentration in the profile, located at the first point outside all of the transducer near fields, is found for each transducer by the former iterative technique:

$$C_0=\frac{(Vz_0)^2}{AF}\,e^{4z_0(\alpha_w+\zeta C_0)}. \tag{28}$$

Two considerations should be taken when determining this initial concentration. First, because of attenuation, the magnitude of the voltage read from the transducer is limited in magnitude from the above expressions, as is apparent in examination of Fig. 1. Due to the statistical fluctuations in the backscattered signal and also to instrument noise, it is possible that the actual signal is higher in magnitude than this theoretical limit. In such cases, the iterative technique will not converge to a solution. A simple divergence test in the iteration algorithm will reveal this condition. Minimization of the difference between the initial concentration guess and that returned by Eq. (28) will produce a good concentration approximation in such cases. Second, it is important to realize that Eq. (28) will produce two concentration solutions for the reasons discussed previously. For the lowest-frequency transducers typically used, the higher magnitude solution is regularly above the expected range of applicability of the present theory, and can safely be ignored. For the higher-frequency transducers, the decision of which concentration to use must be based on physical arguments or by comparison with the results from lower-frequency transducers. In field measurement of suspended sediment, the transducer is usually a sufficient distance from the bed, such that the higher magnitude solution is again outside the expected range and can be safely ignored.

The complete technique for solution is as follows. Equation (28) is solved iteratively for the initial concentration for each transducer over a range of median grain diameters. Note

that both F and ζ are functions of the grain-size distribution, typically assumed to be log normal. Calculation of these parameters first requires one to determine the distribution based on the given median grain diameter. The form of the log-normal distribution is given in the Appendix. The standard deviation of the grain-size distribution is assumed constant and is determined by other physical arguments. In the case of field measurement of sediment suspension, the standard deviation is assumed equal to that of the distribution of sediment in the seabed below the transducer. For each median grain diameter, the mean concentration and the variance in the concentration between transducers is calculated:

$$\mu_C = \frac{1}{m} \sum_{i=1}^{m} C_i , \tag{29}$$

$$\sigma_C^2 = \frac{1}{m} \sum_{i=1}^{m} C_i^2 - \left(\frac{1}{m} \sum_{i=1}^{m} C_i \right)^2 . \tag{30}$$

The median grain diameter is recognized as that with the minimum concentration variance, and the concentration is given by the corresponding mean concentration. If only two transducers are used, more than one solution for the median grain diameter is possible. In this case, determination of size is still possible if the range of grain sizes is restricted and appropriate transducer frequencies are selected in advance.

After the initial concentration is found, the integration constant, γ, can be found for each transducer from Eq. (27). The solution for the remainder of the bins in the profile proceeds by solving Eq. (25) for each transducer for a range of median grain diameters, and then by selecting the correct grain diameter by minimization of the concentration variance between transducers, given by Eq. (30). Again, the concentration is given by the corresponding mean value from all transducers.

In the present study, the standard deviation of the grain-size distribution is assumed constant. This assumption has been accepted based on the limited existing experimental evidence.[3] In the above procedure, size is found by minimizing the concentration variance while varying a single parameter, the median grain diameter, of the distribution. It is interesting to note that the minimization of the concentration variance could be performed by varying both the standard deviation and mean of the distribution, so the above procedure does not constrain the investigation to a constant standard deviation in the grain-size distribution. Since more than one solution to the nonlinear problem is possible, determination of both parameters would require more than the three discrete frequency transducers utilized in this study in order to produce a unique solution. The simulations performed in this study were designed to mimic the behavior of existing laboratory equipment, so further research is required to verify the capability of the present theory in determining more than a single parameter of the grain-size distribution.

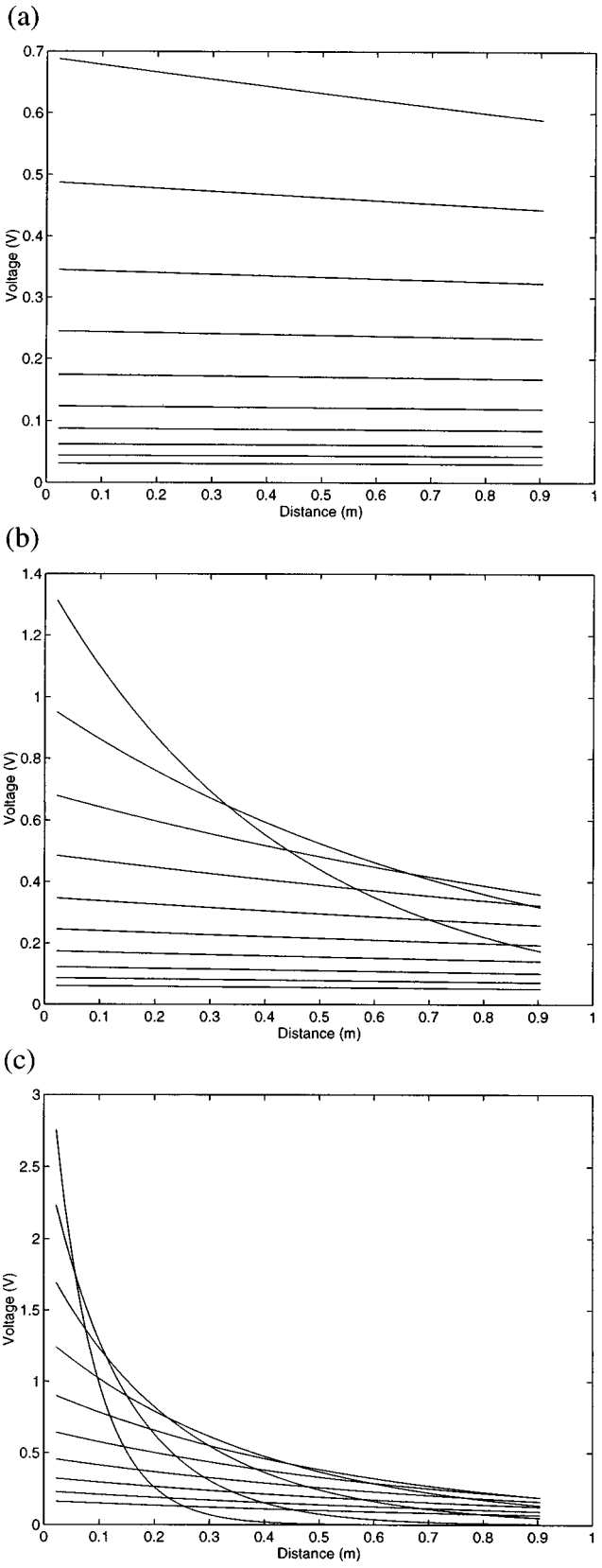

FIG. 3. Numerically generated profiles for (a) 1.0-, (b) 2.25-, and (c) 5.0-MHz transducers.

III. VERIFICATION OF TECHNIQUE

As an initial test of the calibration technique, ideal voltage profiles for 1.0-, 2.25-, and 5.0-MHz transducers were simulated using the acoustic backscatter equation (4) with a predetermined log-normal distribution. For simplicity, the generated profiles contained no near field, or in other words, the acoustic backscatter equation is assumed to be valid at the face of the transducer and beyond. Figure 3 shows these

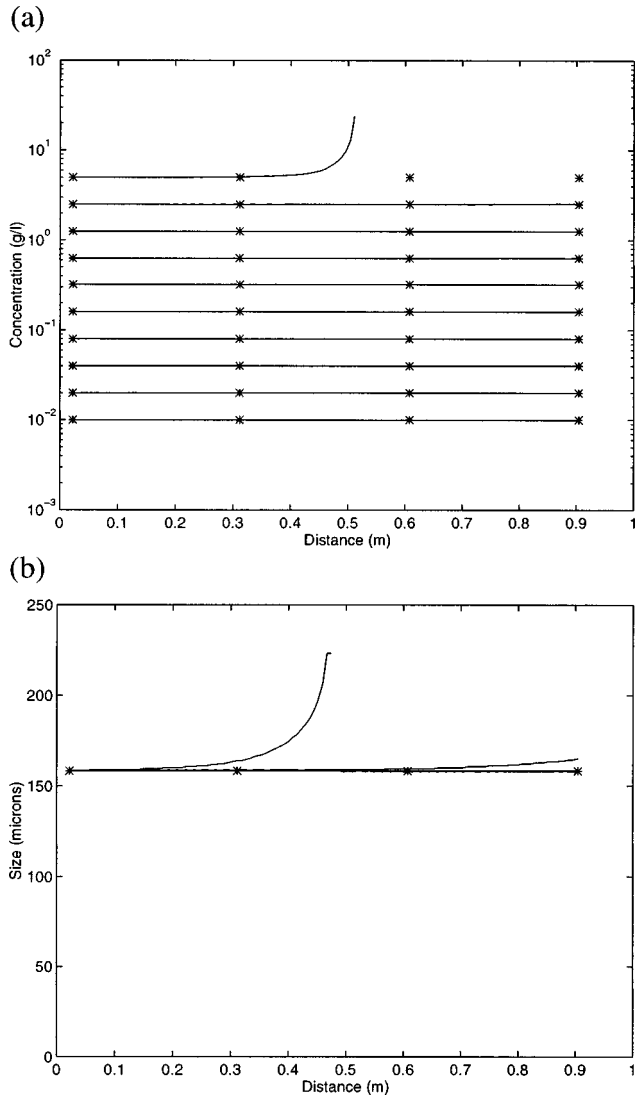

FIG. 4. Resulting (a) concentration and (b) median grain size from inversion technique using 2.25- and 5.0-MHz profiles. Asterisks indicate known values.

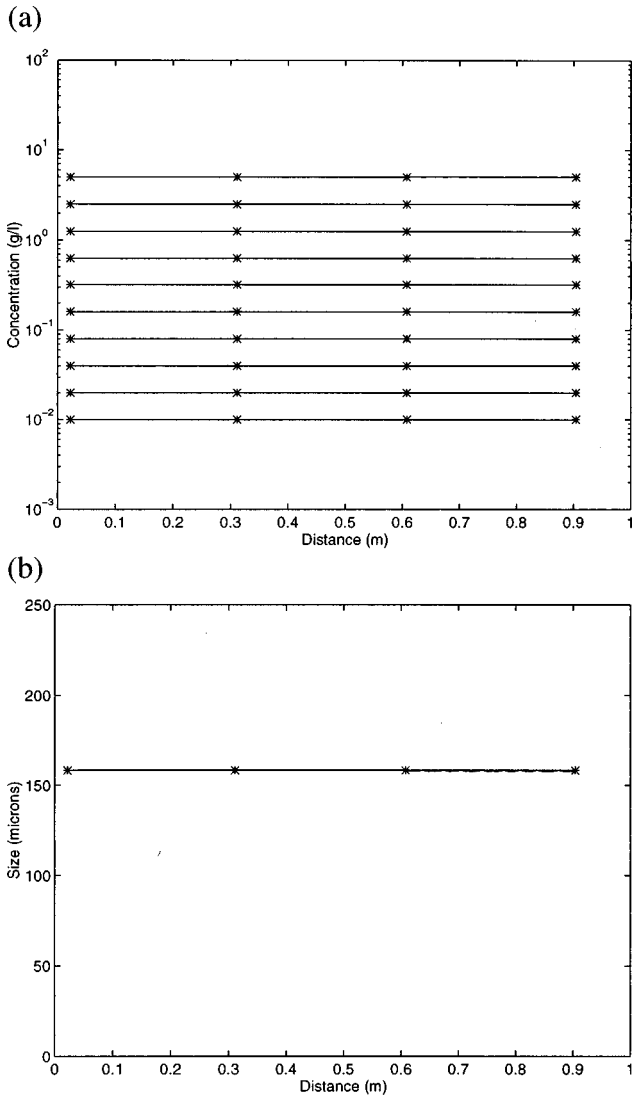

FIG. 5. Resulting (a) concentrations and (b) median grain size from inversion technique using 1.0- and 2.25-MHz profiles. Asterisks represent known values.

numerically generated profiles. The concentrations used were 0.01, 0.02, 0.04, 0.08, 0.16, 0.32, 0.63, 1.25, 2.5, and 5.0 g/l, and the grain-size distribution was assumed to have a median grain diameter $\mu_\phi = 2.66$ and a standard deviation $\sigma_\phi = 0.25$. Since in the absence of attenuation, the voltage read from the transducer increases with increasing suspended particle concentration, the concentrations are easily distinguishable at zero distance. Higher attenuation with higher operational frequency and with higher concentration is apparent from the figures. Particularly, the profiles from the highest concentrations in the 5-MHz simulation are attenuated so heavily that away from the transducer little, if any, signal remains.

Shown in Fig. 4 are the concentration and size profiles resulting from applying the new technique using double precision calculations (64 bit) with only the 2.25- and 5.0-MHz voltage profiles from Fig. 3. Since only two frequencies were used in this test, the range of median grain sizes was restricted within ± 2 standard deviations of the initial known distribution. In Fig. 4(b), the size profiles overlap for all cases except the cases involving the highest two concentrations. Not surprising, the technique accurately produced the initial concentration, as in Holdaway and Thorne's simulations,[9] and size in the majority of the cases. This test does illustrate the difficulty though in using the highest-frequency transducer through significant ranges of high concentrations. As noted before in Fig. 3, at the highest concentrations, the high sediment attenuation results in large signal loss away from the transducer. In Fig. 4, the error induced in evaluating the concentration and size from this small signal is apparent. Figure 5 shows the results from use of the 1.0- and 2.25-MHz signals. The results in this test showed excellent agreement with both the original size and concentrations, even through a 1-m range of relatively high concentration. The next inversion, shown in Fig. 6, uses all three of the simulated signals. Again, because of the signal loss in the high concentration 5-MHz data, the results exhibit similar, but somewhat more erroneous behavior to those in Fig. 4.

This tendency for the results to diverge more from the known concentrations than in the previous cases is best ex-

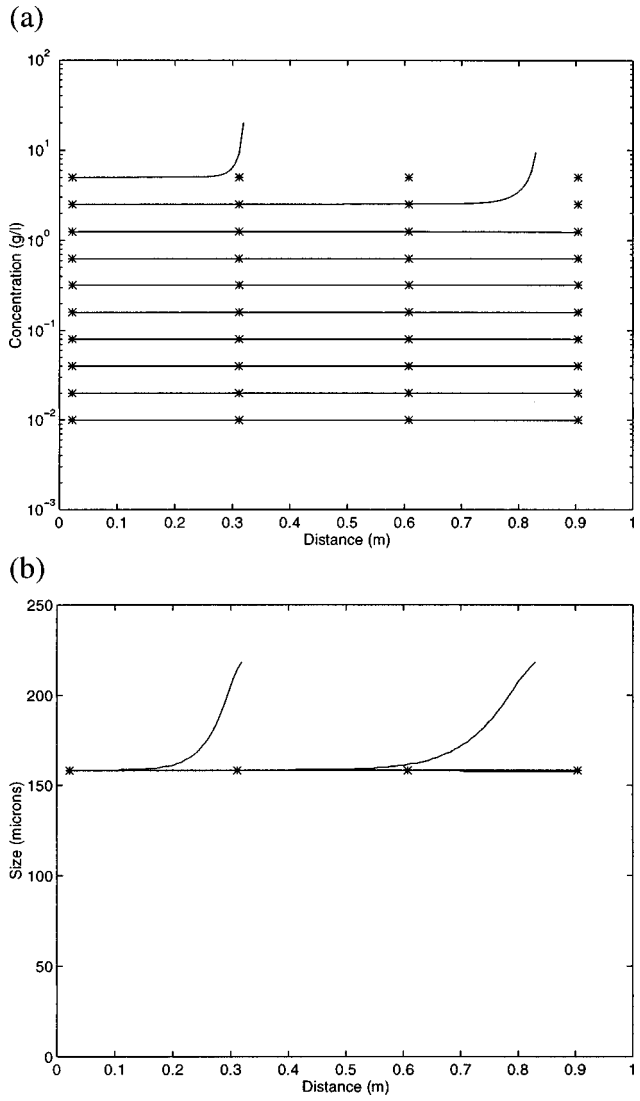

FIG. 6. Resulting (a) concentrations and (b) median grain size from inversion technique using 1.0-, 2.25-, and 5.0-MHz profiles. Asterisks represent known values.

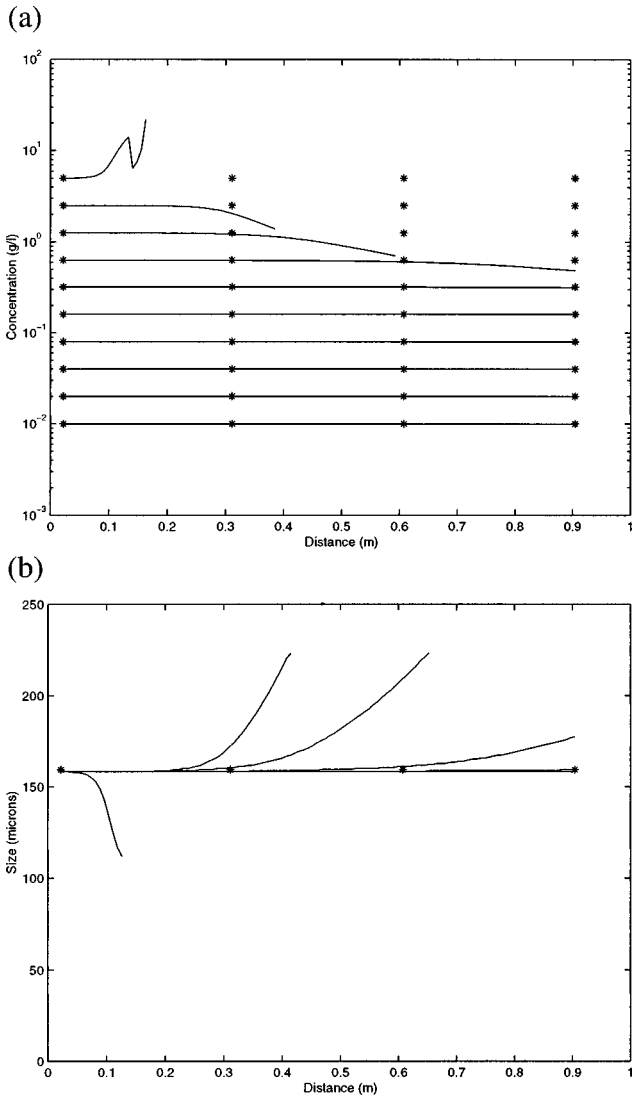

FIG. 7. Resulting (a) concentrations and (b) median grain size from inversion technique using 1.0- and 5.0-MHz profiles. Asterisks indicate known values.

plained by first examining the results from use of the 1-MHz and 5-MHz data. Figure 7 presents this final inversion, which yields the worst results yet presented. Because the inversion technique minimizes the concentration variance between transducers, the solution with the lowest variance is that in which the concentration predicted from a good signal (in this case, the 1-MHz signal) agrees with the concentration predicted from a faulty signal (in this case, the 5-MHz signal). The mechanism by which this agreement is obtained is by adjustment of the median grain size. Such adjustment of grain size in addition to the faulty concentration prediction introduces error, which rapidly accumulates with distance from the transducer. For 1-MHz data from the current test grain size, the faulty adjustment in grain size which forces concentration agreement is large. Re-examination of the inversion from the 2.25-MHz and 5-MHz data, Fig. 4, shows that concentration agreement is achieved between these signals with less adjustment of the grain size. Looking again at Fig. 6, in which all three signals were used, it is apparent that the results, in quality, fall somewhere between those from the 1- and 5-MHz data and the 2.25- and 5-MHz data. It is important to note that the advantage of using multiple frequencies is reduction of the likelihood of obtaining multiple solutions to the nonlinear inversion problem. Only careful data quality testing that reveals excessive signal loss or other signal faults will prevent introduction of these signal errors.

Finally, because the greatest benefit of the present theory is the ability to determine profiles of varying concentration and size, one final simulation is shown in Fig. 8. In this simulation, theoretical signals were generated as before, but from a linearly varying size profile and an exponentially varying concentration profile. The sizes and concentrations determined by this new method are indistinguishable in the figure from the predetermined profiles, indicating that the theory performs well over a wide range of sizes and concentrations.

Laboratory tests were performed in a recirculating calibration chamber, which produces a suspension of sediment of approximately constant concentration and grain-size distribution.[1] Three transducers with transmitted pulse

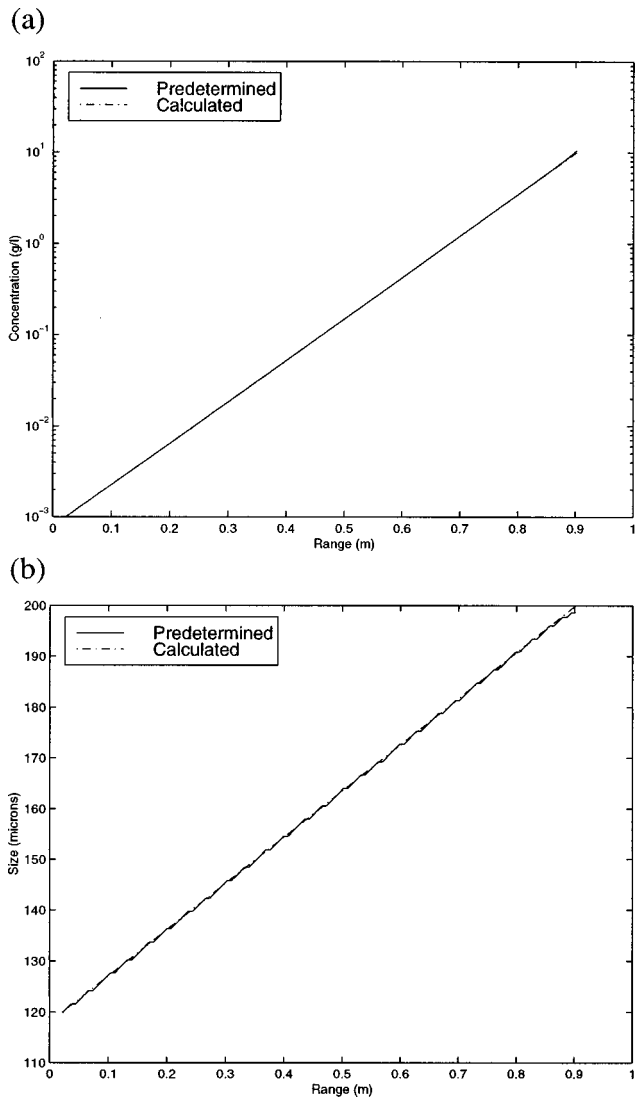

FIG. 8. Comparison of predetermined (a) concentration and (b) size profiles with those predicted by the new inversion technique.

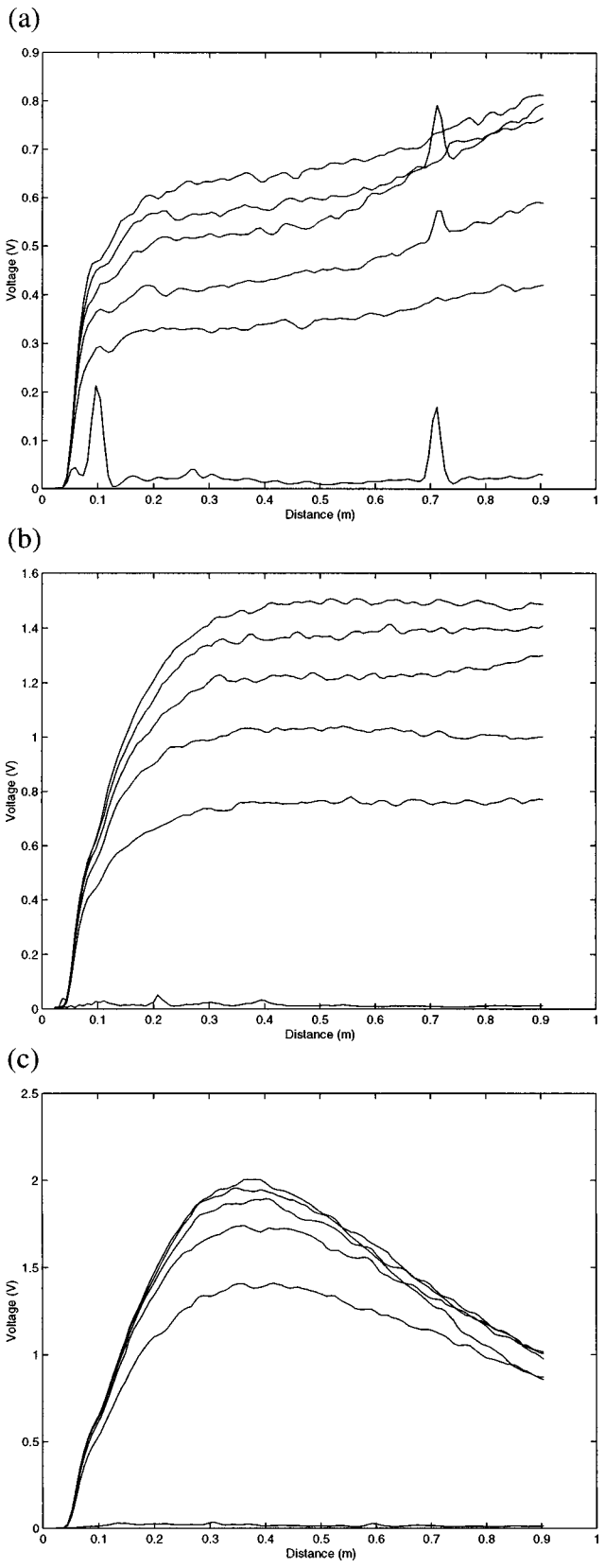

FIG. 9. Raw signal strength profiles for the (a) 1.08-MHz, (b) 2.07-MHz, and (c) 4.70-MHz transducers.

widths of 13 μs each and discrete transmitter frequencies of 1.08, 2.07, and 4.70 MHz, respectively, were used for the measurements. Each transducer utilized a crystal 10 mm in diameter, so the beamwidths decrease with increasing frequency. The three transducers were part of an acoustic backscatter system (ABS) from The Centre for Environment, Fisheries and Aquaculture Science (CEFAS, formerly known as The Fisheries Laboratory). Calibration of the ABS for determination of the system constants is performed in the same tank using real sediments, but the source levels of the transducers can be determined approximately by the electrical characteristics of the system to be 195, 201, and 208 dB/μPa for the 1.08-, 2.07-, and 4.70-MHz transducers, respectively. The receiver bandwidth for each transducer is 100 kHz, and the noise floor, electrically, is below 1 μV. Envelopes of backscattered signal strength were sampled at 100 kHz, with profiles collected at 100 Hz from each transducer. The ensemble rms was determined from 1 minute's data for each concentration. As in the numerical simulations, the distribution parameters for the sediment were a median grain diameter $\mu_\phi = 2.66$ and a standard deviation $\sigma_\phi = 0.25$. The concentration used were 0, 0.1, 0.2, 0.3, 0.4, and 0.5 g/l. In Fig. 9, the raw backscattered signal voltages from the experiments are shown. Note that the system utilized a linear time-varying gain (linear variation) to compensate for

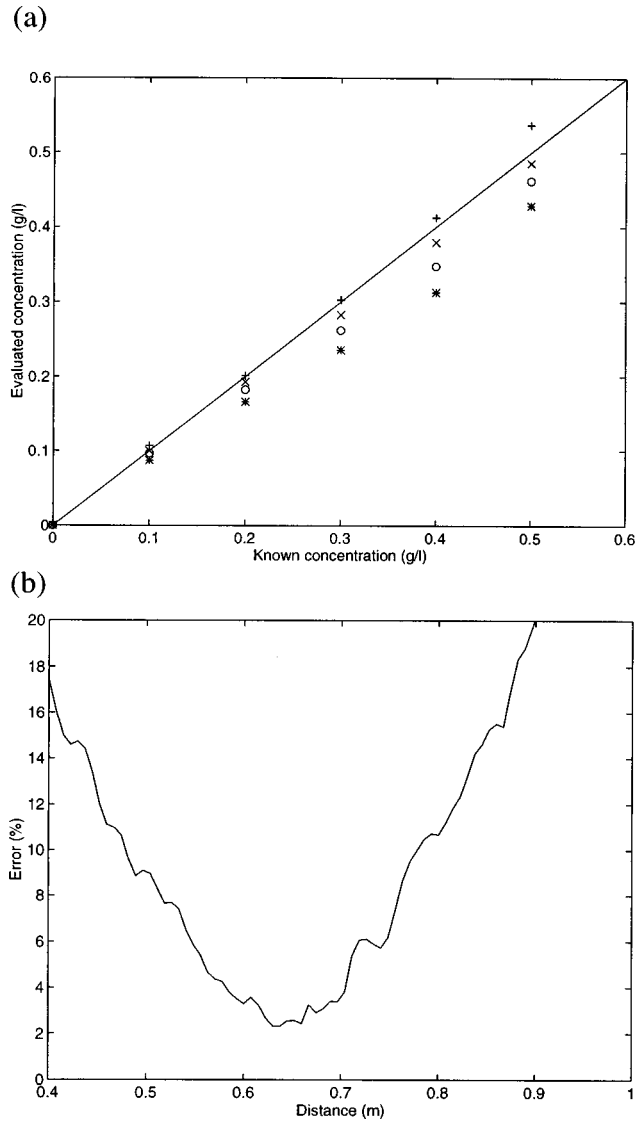

FIG. 10. Comparison of known and calculated concentrations (a) shown at distinct concentrations and ranges of (*) 40 cm, (○) 50 cm, (×) 60 cm, and (+) 70 cm; and (b) shown as the mean error of all concentrations with range.

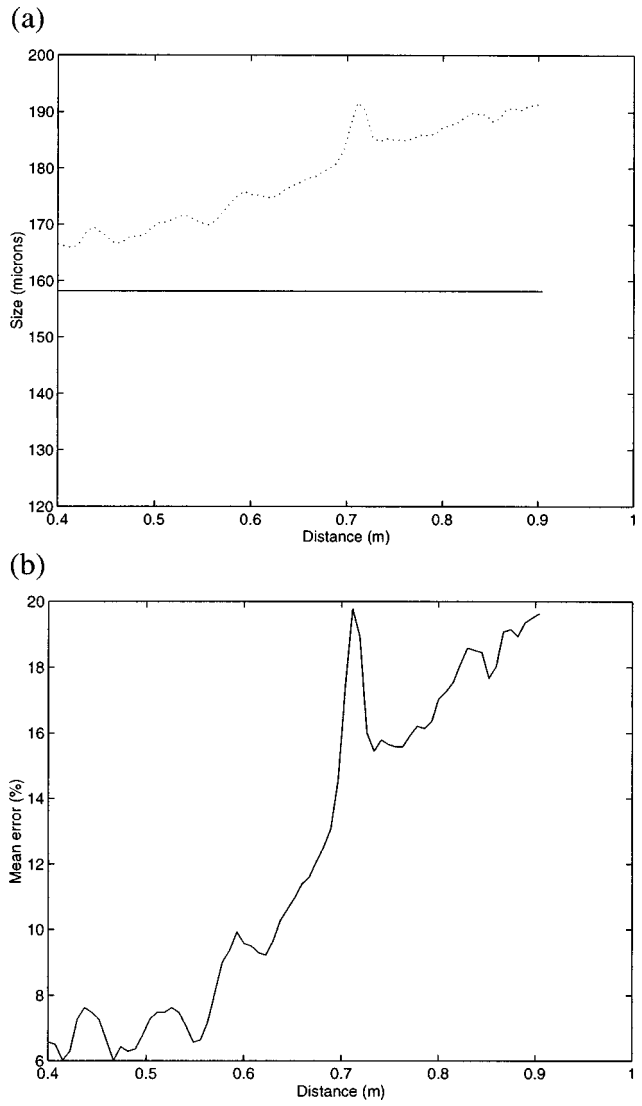

FIG. 11. (a) Comparison of known (solid line) and determined (broken line) median grain size and (b) the resulting error with range.

spherical spreading. Amplifier clipping is apparent near the transducer where the gain is very low.

Figure 10 shows the agreement between the known concentration and that determined with the new inversion technique. Several factors explain the form of the error curve with range. First, concentrations in the chamber were determined by adding calculated dry masses of sediment to the known volume of water. Due to hindered settling within the funnel at the base of the chamber, actual concentrations in the tube may be slightly lower than those calculated. Next, the initial concentration measurement is located 40 cm from the transducer face due to both near-field effects from the transducers and from complications introduced by amplifier saturation at shorter ranges. Determination of the initial concentration must therefore be done with a signal that has already experienced 40 cm of water and sediment attenuation through significant concentrations. The sensitivity of the concentration measurement to attenuation increases the likelihood of error, particularly for high concentrations, long attenuation paths, and high operational frequencies. Finally, for calibration of the acoustic transducers, the error between known and calculated concentrations was minimized in the range from 40 cm to 90 cm. In this minimization technique, approximately half of the calculated concentration profile typically falls below the known value and half above. This effect is apparent in the error profile of the present concentration evaluation, Fig. 10(b), which shows the best agreement in the center portion of the profile. If the transducer calibration were performed at just a single range, as is often described in the literature, and the measurements presented in this text evaluated using the single point calibration information, the error in the determination of concentration is less than 5%.

Figure 11 compares the known median grain size with that measured in the circulation chamber. Again, if the calibration is performed at a single range and the size determined from the single point calibration, the error in evaluation of median grain size is less than 10%. Even in this case, the evaluated median grain size is slightly higher than the known value. Errors result in this evaluation from use of

somewhat low concentrations for determination and from differences in various sediments not accounted for explicitly in the empirical form function. Use of low concentrations was made necessary by operation of the 4.70-MHz transducer with an initial concentration evaluation point located a significant distance from the transducer. Presently, one form function is said to describe noncohesive quartz sediment (see the Appendix), but it is expected that grain properties of a given sediment sample will modify the form function slightly. Empirical evaluation of the form function for a given sediment type would likely improve the error in determination of the median grain size.

It should be noted that evaluating concentration and size with a constant concentration profile is actually a more demanding application of the technique and system than is typically experienced in field measurements, due to the propagation of error through the profile. In measurements of sediment suspension above the seabed, the transducer is typically far enough from the seabed such that the concentrations near the transducer are low.

IV. CONCLUSIONS

A new technique of determining both concentration and the median grain diameter of suspended particles has been presented. The significant advantage of the technique is that by using an explicit solution for concentration, the median grain diameter can be found without having to neglect sediment attenuation. In addition, because incorporating the correct median grain diameter in the explicit solution will produce an identical concentration regardless of the operational frequency of the transducer, the concentration variance between any number of transducers can be minimized to find the median grain diameter. Previous techniques have typically paired transducers and applied an empirical procedure on the results from the pairs to obtain the grain diameter. Numerical simulations were performed to verify the capability of the technique to produce both the expected concentrations and grain diameters. In addition, laboratory results from a recirculating calibration chamber verify that the technique applies well in determining sediment size and concentration from measurements of backscattered acoustic intensity.

ACKNOWLEDGMENTS

The authors wish to acknowledge the support of the Coastal Sciences Program of the Office of Naval Research. For their assistance in the laboratory measurements, the authors are grateful to Craig Conner and Yeon Sihk Chang. Assistance with the ABS operation from Nick Pearson is greatly appreciated.

APPENDIX

In the following, for completeness, the expressions used for calculation of various parameters present in the backscatter equations are presented.

1. Log-normal distribution

If the median grain size, μ_ϕ, and standard deviation, σ_ϕ, are expressed in units of ϕ, the probability distribution in terms of the grain radii, a (in mm), is given in the subsequent formula.

$$p(a)=\frac{1}{\sigma_\phi(\ln 2)\sqrt{2\pi}}\exp\left(\frac{-(1+\ln a/\ln 2+\mu_\phi)^2}{2\sigma_\phi^2}\right)\left(\frac{1}{a}\right). \tag{A1}$$

2. System constant

The system constant, A, is determined by calibrating each transducer in a recirculating calibration chamber with a series of suspensions of constant concentrations of a known grain-size distribution of sediment.

3. Water attenuation

The water attenuation parameter is determined in seawater by the expression of Fisher and Simmons:[11]

$$\alpha_w=(55.9-2.37T+0.0477T^2-0.000384T^3)f_M^2\times 10^{-3}. \tag{A2}$$

In Eq. (A2), f_M is the frequency in MHz and T the temperature in degrees Celsius.

4. Sediment attenuation

The sediment attenuation parameter is determined following the method outlined by Thorne:[6]

$$\zeta=\frac{3}{4\langle a_s\rangle\rho_s}\langle\chi\rangle. \tag{A3}$$

The pointed brackets represent a value representative for a distribution of sediment with probability density function, $p(a_s)$, rather than for a single sediment size, so the representative value for a_s, the particle radius, is given in Eq. (A4):

$$\langle a_s\rangle=\int_0^\infty a_s p(a_s)da_s. \tag{A4}$$

In Eq. (A3), χ is the normalized total scattering cross section, given by the following:

$$\chi=\frac{\frac{4}{3}K_\alpha x^4}{1+x^2+\frac{4}{3}K_\alpha x^4}. \tag{A5}$$

x is the dimensionless particle radius, given as the product of the particle radius and the acoustic wave number. K_α is a constant based on the particle density and compressibility and is equal to 0.18 for quartz sediment. Finally, Eq. (A6) gives the representative value of χ for a distribution of sediment.

$$\langle\chi\rangle=\frac{\int_0^\infty a_s p(a_s)da_s\int_0^\infty a_s^2\chi p(a_s)da_s}{\int_0^\infty a_s^3 p(a_s)da_s}. \tag{A6}$$

5. Backscatter

Equation (A7) gives the backscatter function.

$$F=\frac{\langle f\rangle^2}{\rho_s\langle a_s\rangle}. \tag{A7}$$

In this equation, the form function, as defined by Thorne,[6] is given by

$$f=C_0\left(\frac{K_f x^2}{1+K_f x^2}\right), \tag{A8}$$

with

$$C_0=(1-\nu_1 e^{-[(x-x_1)/\eta_1]^2})(1+\nu_2 e^{-[(x-x_2)/\eta_2]^2}). \tag{A9}$$

In this equation, $\nu_1=0.37$, $\eta_1=0.5$, $x_1=1.4$, $\nu_2=0.28$, $\eta_2=2.2$, $x_2=2.8$ based on an empirical fit to measured data. And based on the compressibility and density of the sediment relative to water, $K_f=1.14$ for noncohesive sedimentary material. The representative value of the form function for a distribution of sediment is given by the following:

$$\langle f\rangle=\left(\frac{\int_0^\infty a_s p(a_s)da_s\int_0^\infty a_s^2 f^2 p(a_s)da_s}{\int_0^\infty a_s^3 p(a_s)da_s}\right)^{1/2}. \tag{A10}$$

6. Near-field correction

Equation (1) presents the acoustic backscatter equation with the near-field correction term, ψ. This term, as defined by Thorne *et al.*,[4] is given as follows:

$$\begin{aligned}&\psi=1, \quad \text{for } r>\epsilon r_n \ \text{(far field)},\\ &\psi=\frac{2+\epsilon r_n/r}{3}, \quad \text{for } r<\epsilon r_n \ \text{(near field)}.\end{aligned} \tag{A11}$$

In the original text, r_n is the theoretical near-field limit and ϵ is set equal to 2. The explicit solution for concentration including the near-field correction is found following the same derivation presented above:

$$C=\frac{[(Vz)^2\psi^2/F]\exp(4\alpha_w z)}{\gamma-\int_{z_0}^{z}4\zeta[(V\hat{z})^2\psi^2/F]\exp(4\alpha_w\hat{z})d\hat{z}}. \tag{A12}$$

In this solution, the integration constant is also slightly modified:

$$\gamma=\frac{(V_0 z_0)^2\psi_0^2}{F_0 C_0}\exp(4\alpha_w z_0). \tag{A13}$$

Like the other subscripted variables, ψ_0 is determined at z_0.

[1] D. M. Hanes, C. E. Vincent, D. A. Huntley, and T. L. Clarke, ''Acoustic measurements of suspended sand concentration in the C^2S^2 experiment at Stanhope Lane, Prince Edward Island,'' Mar. Geol. **81**, 185–196 (1988).

[2] D. M. Hanes, T. H. Lee, and E. D. Thosteson, ''Intermittent near bed sediment suspension,'' Technical Report on the Supertank Laboratory Data Collection Project, edited by N. C. Kraus and J. M. Smith (Coastal Engineering Research Center, U.S. Army Corps of Engineers, Vicksburg, MS, 1993), Chap. 11, pp. 185–210.

[3] A. E. Hay and J. Sheng, ''Vertical profiles of suspended sand concentration and size from multifrequency acoustic backscatter,'' J. Geophys. Res. **97**, 15661–15677 (1992).

[4] P. D. Thorne, C. E. Vincent, P. J. Hardcastle, S. Rehman, and N. Pearson, ''Measuring suspended sediment concentrations using acoustic backscatter devices,'' Mar. Geol. **98**, 7–16 (1991).

[5] M. O. Green and C. E. Vincent, ''Wave entrainment of sand from a rippled bed,'' in *Proceedings of the Coastal Engineering Conference* (ASCE, New York, 1991), Vol. 3, pp. 2200–2212.

[6] P. D. Thorne, ''Measuring suspended sediments using acoustics,'' Technical Report #UFL/COEL-TR/092 (Coastal and Oceanographic Engineering Department, University of Florida, Gainesville, FL, 1993), pp. 1–25.

[7] A. M. Crawford and A. E. Hay, ''Determining suspended sand size and concentration from multifrequency acoustic backscatter,'' J. Acoust. Soc. Am. **94**, 3312–3324 (1993).

[8] T. H. Lee and D. M. Hanes, ''Direct inversion method to measure the concentration profile of suspended particles using backscattered sound,'' J. Geophys. Res. **100**, 2649–2657 (1995).

[9] G. P. Holdaway and P. D. Thorne, ''Determination of a fast and stable algorithm to evaluate suspended sediment parameters from high resolution acoustic backscatter systems,'' The 7th international conference on electronic engineering in oceanography (The Southampton Oceanography Centre, 1997), pp. 86–92.

[10] A. E. Hay, ''Sound scattering from a particle-laden, turbulent jet,'' J. Acoust. Soc. Am. **90**, 2055–2074 (1991).

[11] F. H. Fisher and V. P. Simmons, ''Sound absorption in sea water,'' J. Acoust. Soc. Am. **62**, 558–564 (1977).

The determination of signal coherence length based on signal coherence and gain measurements in deep and shallow water

William M. Carey[a)]
Department of Ocean Engineering, Massachusetts Institute of Technology, Cambridge, Massachusetts 02139

(Received 27 June 1997; revised 30 March 1998; accepted 4 May 1998)

Experimental measurements of signal coherence and array signal gain are presented for both deep- and shallow-water sound channels. The signal gain is related to the transverse horizontal coherence length through relationships from the statistical theory of antennas. Signal gain measurements in the transverse direction are proffered as a practical measure of coherence length for both broadband and narrow-band signals. With this technique, measurements at frequencies near 400 Hz are presented and show for the deep-water cases that lengths on the order of 100 wavelengths can be achieved to ranges of 500 km; while in the variable downward refraction conditions of shallow-water waveguides with sand-silt bottoms, lengths on the order of 30 wavelengths to ranges of 45 km are realized. The measurement of broadband and narrow-band coherence is discussed with emphasis on the role of partly coherent noise backgrounds, multipath interference effects, and averaging constraints. Experimental results are interpreted with deep-ocean coherence models consistent with sound scattering from the ocean volume and Gaussian coherence function for the shallow-water waveguide. © *1998 Acoustical Society of America.* [S0001-4966(98)04208-8]

PACS numbers: 43.30.Re, 43.30.Wi [SAC-B]

INTRODUCTION

The fundamental limit to spatial, coherent signal processing is the coherence length. It is the estimation of the transverse-coherence length that is the subject of this paper. The estimation of this coherence length may be accomplished by measurement of the narrow-band coherence function, broadband correlation function, or the coherent signal gain either from a direct measurement with a filled aperture or the steered beam response from a sparsely filled aperture.

The ocean acoustic environment in the low to mid frequencies complicates the measurement of coherence because the achievable signal-to-noise ratios are limited by a semicoherent noise background.[1] Narrow-band coherence estimates are possible, but the requirements of incoherent averaging result in long analysis times compared with the time during which the medium is stationary. The motion of the receiving system and source also produces a dynamic multipath field that can dominate the coherence measurement. As shown by Carter *et al.*,[2–4] the bounds on the estimation from measurement of either the magnitude or the magnitude squared of the coherence function are large. The measured coherence is a strong function of the signal-to-noise ratio and coherent multipath interference,[5,6] and the estimation requires a large number of samples that must be done in a short time compared with the dynamics of the medium or source–receiver motions. Carter presents as an example a narrow-band coherence estimate of 0.7 using eight fast Fourier transforms with the 95% confidence bounds of 0.3 and 0.86. The corresponding estimation of the $1/e$ point is very uncertain.

On the other hand, the measurement of array signal gain [$\mathrm{ASG}=10\log(\mathrm{asg})$] is performed with an array of sensors. The asg estimate is based on a larger number of degrees of freedom and a larger signal-to-noise ratio that results from the coherent signal summation and the spatial filtering of unwanted noise sources. The measurement of asg with 50 elements and an average element signal-to-noise ratio of 3 dB yields a coefficient of variation of 5%.[7] For most of the experiments reported in this paper the average hydrophone element signal-to-noise ratio ranged between 3 and 10 dB. The individual estimates of ASG are based on a linear average of several asg samples. Because the asg[8] ($\mathrm{asg}=\Sigma_i^N\Sigma_j^N\rho_{sij}$ with ρ_{sij} the pairwise coherence), is proportional to the pairwise coherence functions, a reduction in asg can be related to the coherence length provided the functional form is known and all other causes of gain reduction, gain degradation, are eliminated. Furthermore, the variation of asg with array length in wavelengths should show the point at which the coherent signal gain ($\propto N^2$) changes to incoherent gain ($\propto N$).

The primary causes of signal gain degradation are array shape variations and motion through a range-dependent multipath field.[5,6] These dynamic effects can be compensated using state-of-the-art digital-model-based signal processing systems. Multipath variations are most important for the fore/aft directions because arrivals appear on different beams. Broadside, multipath arrivals are less of a problem because the arrivals can be contained in the near broadside beams. These variations caused by multipath interference act as an amplitude shading, resulting in broadening and bifurcation of the measured beam response. However, these variations are automatically compensated in the estimation of signal gain because (1) the beam response is normalized by the average signal over all of the hydrophones comprising the

[a)]On IPA assignment from the Naval Undersea Systems Center and the Defense Applied Research Projects Agency.

aperture and (2) the gain of arrivals on individual beams can be summed.

The remaining factors, which determine the array signal gain because they produce phase randomness, are refractive and scattering effects attributed to the surface, water-sediment interface, volume, and internal wave structure of the sea. The purpose of this paper is to discuss the practical determination of array signal gain and spatial coherence lengths and to present experimental estimates based on measurements with arrays from several deep- and shallow-water areas. The deep-water measurements are compared to previously published single path results and theoretical estimates.[5] The array signal gain results and those from Ref. 6 are both presented and are shown to produce comparable transverse coherence lengths to the signal path measurements of Stickler and estimates by Moseley[5] using the Beran–McCoy formalism. Finally results from several shallow-water experiments using both explosive, continuous-wave sources and bottom-mounted arrays are presented and discussed.

I. BACKGROUND

The determination of the array signal gain or the array response to a signal with phase randomness is central to the determination of an array length limit. Since the response of a continuous line array is equivalent to a discrete line array with the elements spaced at $\lambda/2$, the work of Shifrin[9] is significant. Shifrin has shown that the mean-squared response function depends on two quantities, the phase variance and the phase correlation function. He also shows closed-form solutions for the exponential and Gaussian correlation forms. The expressions derived by Shifrin define three regions for the variation of array gain as a function of L/λ: the first is a region where the gain varies as $20\log(2L/\lambda)$; the second, a region of gain saturation, gain independent of $10\log(L/\lambda)$; and a third region where gain increases with $20\log(2L/\lambda)$ but attenuated by $20\log(\exp(-\alpha))$, where α is the phase variance. (This third region may not be relevant to sonar.) These results in general mean that sonar arrays are optimal in region one. The analysis that follows is based on the work of Shifrin and is an adaptation of the material found in Ref. 9. The beam pattern for a line array of length L along the y axis with a plane-wave excitation function $P(y)$ is

$$f_{lp}(k\ \sin\ \theta)=\int_{-L/2}^{L/2}P(y)\exp(iky\ \sin\ \theta)dy. \tag{1}$$

With $\psi=\pi L\ \sin\theta/\lambda$ and $x=2y/L$, the pattern becomes

$$f(\psi)=\frac{2\,f_{lp}(\psi)}{L}=\int_{-1}^{1}P(x)\exp(i\psi x)dx. \tag{2}$$

When the excitation is taken as a wave with a deterministic component P_0 and a phase random component $\phi(x)$,

$$P(x)=P_0\ \exp(-i\psi_0 x+i\phi(x)). \tag{3}$$

The expression for the pattern function becomes

$$f(\psi_s)=f(\psi-\psi_0)=\int_{-1}^{1}P_0\ \exp(i\phi(x))\exp(i\psi_s x)dx. \tag{4}$$

The random variable $\phi(x)$ has the following statistical characterization with mean, $\langle\phi(x)\rangle=0$, and variance, $\langle\phi(x)^2\rangle=\sigma^2=\alpha$, and a correlation length, L_ϕ:

$$R_\phi=\langle\phi_1\cdot\phi_2\rangle/\sigma_1\sigma_2=\exp(-(x_1-x_2)^2/C^2),$$
$$C=2L_\phi/L. \tag{5}$$

An interesting result from Shifrin's analysis is that if one takes the expectation values of the pattern function

$$\langle f(\psi_s)\rangle=P_0\ \exp(-\sigma^2/2)\sin\ \psi_s/\psi_s, \tag{6}$$

and its magnitude squared, the expected power,

$$\langle|f(\psi_s)|^2\rangle=\int\int P_0^2\langle\exp(i(\phi_1-\phi_2))\rangle \times\exp(i\psi_s(x_1-x_2))dx_1\ dx_2, \tag{7}$$

$$\langle|f(\psi_s)|^2\rangle=\int\int P_0^2\ \exp(-\alpha(1-R_\phi) +i\psi_s(x_1-x_2))dx_1\ dx_2. \tag{8}$$

At this point some limits are readily apparent. First is the case $C\to 0$; here the response is the line array response $\propto\exp(-\alpha)$. The other extreme is when $C\to\infty$; here the array response is the theoretical response. The special case of transverse arrivals is important and Eq. (8) reduces to the evaluation of the integral

$$\langle|f(0)|^2\rangle=\int\int P_0^2\ \exp(-\alpha(1-R_\phi))dx_1\ dx_2. \tag{9}$$

Shifrin has evaluated this integral numerically; however, an accurate approximation can be derived for the cases where the aperture length is on the order of the correlation length and the phase variance is small. In the region of $C\approx 2$, expanding the phase correlation function in a Taylor series,

$$R_\phi=\exp(-(x_1-x_2)^2/C^2)\cong 1-|x_1-x_2|^2/C^2, \tag{10}$$

$$\alpha[R_\phi-1]=-\alpha|x_1-x_2|^2/C^2=-|x_1-x_2|^2/C^2/\sigma_0^2,$$
$$\alpha=\sigma_0^2=\sigma_i^2(x_i). \tag{11}$$

The accuracy of this expansion can be shown by comparison of the expected mean-squared beam response integral,

$$\langle|f(0)|^2\rangle\cong\int\int P_0^2\ \exp(-\alpha|x_1-x_2|^2/C^2)dx_1\ dx_2, \tag{12}$$

with Shifrin's numerical evaluation of the exact integral, Eq. (9). For values of $C>1.5$ and $\alpha\approx 0.5$–1.0, the expression yields results with errors less than 4% compared with the exact value. In the case considered here, the array length is varied from values less than the correlation length to values greater than the correlation length; consequently, the errors are small. Equation (13),

$$P_0^2\ \exp(-\alpha|x_1-x_2|^2/C^2)=P_0^2\ \exp(-|y_1-y_2|^2/L_h^2) \tag{13}$$

is recognized as the spatial coherence function with a form determined by the phase correlation function, which is consistent with the expectation that the signal gain is propor-

tional to the coherence function. Randomness in phase with a Gaussian correlation function produces a spatial coherence function with a quadratic (Gaussian) form. This result is also true for the exponential correlation function and implies that the $1/e$ spatial correlation length is proportional to the phase correlation-length-squared divided by the phase variance. This quantity is the horizontal coherence length, L_h. The expectation value of the magnitude-squared response function of the line array response is

$$\langle f_{lp}(\psi_s)\cdot f_{lj}^*(\psi_s)\rangle = \int \cdot \int_{-L/2}^{L/2} (4P_p\cdot P_j^*/L^2) \times \exp(-[(y_p-y_j)/L_h]^2) \times \exp(i2\psi_s(y_p-y_j)/L)dy_p\, dy_j. \tag{14}$$

This expression can readily be discretized and placed in matrix notation. The first part of the integrand is recognized as the cross-power spectral density, and the Gaussian exponential is seen to be the spatial coherence function:

$$\begin{aligned} P(k\ \sin\ \theta,\omega) &= \langle f_{lp}(k\ \sin\ \theta,\omega)\cdot f_{lj}^*(k\ \sin\ \theta,\omega)\rangle \\ &= C'\cdot R_{\mathrm{cps}}\cdot C, \\ R_{\mathrm{cps}} &= \|[4P_p\cdot P_j^*/L^2]\exp(-[(y_p-y_j)/L_h]^2)\|, \\ & j,p=1,2,...,N, \\ C &= \|\exp(i2\psi_s y_j)\| = \|\exp(i(2\pi\ \sin\ \theta/\lambda)y_j)\|. \end{aligned} \tag{15}$$

The cumulative distribution of the measurement ensemble yields the mean value SGM (dB), standard deviation s.d. (dB), and the coefficient of variation, COV=s.d./SGM.[6] If the measurement ensemble has been over a depth-time-range interval for which the oceanographic conditions have been stationary, then the mean $\mathrm{SGM}=10\log(sg_m)$ can be related to the expectation value, $\mathrm{SGE}=10\log(\langle \mathrm{asg}\rangle)$. The relative gain is equal to the ratio of the expected gain to the theoretical gain, $\mathrm{RSG}=\mathrm{SGM}-\mathrm{SGT}=10\log(\langle \mathrm{asg}\rangle/\mathrm{asg}_t)$. It can be shown[2] that the expectation of the relative signal gain (rsg) for an aperture, $L_a=(N-1)d$, is

$$\begin{aligned} \mathrm{rsg}=\mathrm{asg}/N^2 &= \left(\frac{1}{N^2}\right)\sum_{j=1}^{N}\sum_{p=1}^{N} \exp[-(|j-p|d/L_h)^n] \\ &= \left(\frac{1}{N^2}\right)\sum_{J=-(n-1)}^{(n-1)} (N-|J|)\exp[-(|J|d/L_h)^n] \end{aligned} \tag{16}$$

and with $y=Jd/L_h$

$$\mathrm{rsg}\cong\left(\frac{L_h}{L_a}\right)^2\int_{-L_0/L_h}^{L_a/L_h}(L_a/L_h-|y|)\exp(-|y|^n)dy,$$

$$\mathrm{ASGD}=-10\log(\mathrm{rsg})$$

with the coherence function exponent of $n=1$,[9,10] $n=1.5$,[11] and $n=2$.[9,12] Shifrin (Ref. 9, Appendix I) has numerically evaluated the integral for $n=2$ and $n=1$. Figure 3 of Ref. 5 shows numerical results for all three values of n. One may also perform the evaluation using the discrete form of Eq. (16) if the number of array elements is known and the functional form n is assumed. On average, the results are a 2-dB degradation in signal gain which corresponds to an array two coherence lengths long.

The line array can be used to measure ASGD and to estimate the signal coherence length, L_h, as a function of frequency and range. The use of L_h in the optimum design of an array requires a criterion, i.e., maximize signal-to-noise ratio, or minimize bearing error. For actual sonars, many factors such as the properties of the noise field both self and ambient must be considered. In this paper the emphasis is placed on the angular spread of the signal arrivals for propagation in both the deep and shallow water. The criterion is to match the 3-dB down points of the signal spread and array beam width. Since the angular spread of the signal can be written as

$$S(k\ \sin\ \theta)=\int_{-\infty}^{\infty}\exp\left(-\left(\frac{y}{L_h}\right)^n\right)\cdot\exp(iky\ \sin\ \theta)dy, \tag{17}$$

and since this can be integrated in closed form for $n=1$, 1.5, 2; the results for matching the 3-dB points of the signal spread and the array beamwidth are easily computed to be for $n=1$, $L_a/L_h=2.72$; $n=1.5$, $L_a/L_h=1.89$, and $n=2$, $L_a/L_h=1.64$ consistent with our previous approximations.

The ratio $L_a/L_h=2.72$ for $n=1$ compares favorably to the estimates of Cox.[10] For example, a 53-element array spaced at $\lambda/2$ with a coherence length of 10λ corresponding to a coherence value between adjacent elements of 0.95 yields a gain of 15 dB according to Cox and yields a gain of 17 dB corresponding to the length of an array based on the factor 2.72. However, Morgan and Smith[13] defined a normalized transition length which varied between 1 and 2 depending on the processor and the value of n. For the value $n=1$, his ratio of $L_a/L_h=1$ as opposed to the above value of 2.72. The conclusion is that the actual coherence length and the form of the coherence function are determined by the scattering in the waveguide, and the optimization criterion using the coherence function determines the sonar processor and the aperture length.

II. EXPERIMENTAL RESULTS

This section discusses measured estimates of coherence lengths for deep and shallow water. The results of Stickler[14] are first discussed and compared with theoretical computations and measured array signal gain estimates. Recent results of signal gain measurements from shallow-water experiments are then discussed and coherence length estimates are presented.

Stickler[14] and his colleagues at the Bell Telephone Laboratories performed experiments during the 1960s near Bermuda, the Plantagenet Bank. A large planar transmit array and 10 ms/400 Hz pulses provided sufficient resolution to measure the normalized acoustic correlation coefficient as a function of transverse sensor separations up to 1200 m and ranges between 137–963 km. Moseley[5] analyzed these results[14] and found that the single path (13° ray) not influ-

TABLE I. Coherence length estimates at 400 Hz.

R(km)	L_h(m)	L_h/λ	$E_{fm}\times 10^{+17}$
137	1143	306	5.9
139	1677	450	3.4
259	1067	286	3.5
268	1067	286	–
507	381	102	8.2
963	350	94	4.96

enced by boundary interaction yielded $1/e$ correlation lengths between 94 and 450 wavelengths as shown in Table I (discussed in more detail in Ref. 5).

Also shown in this table are estimates of an environmental factor E_f as derived by Beran and McCoy[11] using Eqs. (37) and (38) of Ref. 5 and are reproduced below:

$$\Gamma(r,f,y,z)=R_p(r,f,y,z)/I(z)=\exp(-E_f\cdot f^{5/2}\cdot r\cdot y^{3/2}), \tag{18}$$

where

$$E_f=1.7\left(\frac{1}{c_0}\cdot\frac{\partial}{\partial t}c_0\right)^2\cdot A_T\cdot L_{\gamma m}\cdot\left(\frac{2\pi}{c_0}\right)^{5/2}. \tag{19}$$

The values of E_{fm} are found by inserting the range r, frequency f, separation distance $y=L_h$ in the first expression and setting the exponential exponent equal to one. The mean value of $E_{fm}=4.9\times 10^{-17}$ is based on these acoustic measurements. As discussed in Ref. 5, the range dependence is linear. E_f can also be estimated by using of the oceanographic parameters shown in the above expression. Moseley[5,15,16] used the average sound velocity along the ray, $c_0=1517$ m/s; the variation of the speed of sound as a function of temperature from Wilson's equation, $\partial c_0/\partial t=3.6$ m/s/ °C; the single-term-power-law spectrum coefficient for the horizontal temperature fluctuations, $A_T=1.5\times 10^{-7}$ °C^2/m; and a fluctuation length, $L_{\gamma m}=30$ m, to calculate an expected value of $E_f=4.8\times 10^{-17}$.[5]

Deep-water measurements were performed with experimental horizontal arrays in several ocean basins at frequencies between 300 and 400 Hz at ranges between 100 and 600 km, with the sound source transverse to the aperture, low speeds, array tilts less than 2°, and careful ship driving to control motion. Array signal gain results were found to show a departure from coherent gain at 300λ with a degradation of 3.4 dB and at 200λ with a degradation of 2.2 dB. These measurements are consistent with a transverse coherence length of 100λ at 300–400 Hz and a range of 500 km.[6] Average results from several experiments are listed in Table II.

Estimates of the value of E_f based on these estimates of coherence length from moving arrays are between 5×10^{-17} to 10×10^{-17}, results that are larger than Moseley's results, but no correction for array shape and motion has been applied. Nevertheless the array estimates are consistent. These results can be extended to other ocean basins by using Moseley's analysis. Representative values are shown in Table III.[5]

In summary, between 300–400 Hz the measured coherence lengths in deep ocean basins are of the order of 100λ at

TABLE II. Array estimates of L_h/λ.

Basin	Freq.	Range	L_a/λ	ASGD	L_h/λ
Ionian	337	⩽300 km	143	1.5	95
N.W. Atl.	337	582 km	143	1.12	127
N.W. Atl	337	⩽600 km	143	2.0–2.4	72–60
Levantine	323	⩽800 km	112	1.2	96

ranges of 500 km. Calculations using the Beran–McCoy coherence function and the criterion of matching the aperture beamwidth with the angular spread of the signal yield aperture lengths in the absence of motional effects of 189λ. The coherence length decreases as the frequency increases, and the measured values appear consistent with estimates using the Beran–McCoy formalism as well as computations using the quadratic expressions of Dashen.[12]

Shallow-water environments are known for unpredictability, which is partially due to lack of information concerning the key environmental variables such as water depth, range-dependent sound-velocity structure, internal waves, sea-surface roughness, bottom roughness and type, location of currents and eddies, and changes in bathymetry. These characteristics of the shallow-water waveguide make theoretical modeling of signal coherence very difficult, and in general, classification will be based on a few key parameters. Properties of the waveguide which can be used for classification are the type of bottom and the process of formation. With a given bottom type, experiments can be performed using predictable seasonal profile changes to stress specific scattering mechanisms. Upward refracting profiles stress the sea surface; downward refracting profiles stress the bottom. Coastal regions and time of year may be chosen to stress internal wave effects.

Experiments have been performed in sandy-silty areas with known sediment thickness, bathymetry, and measured range-dependent sound velocity profiles, see Table IV.

These experiments were conducted in areas where the sediment layer was formed by deposition, usually found on the eastern continental shelves as opposed to thin sediment layers over volcanic substrata or rock. Additionally these experiments had either isovelocity or variable downward refracting sound-speed profiles. The degree of bottom interaction is determined by the profile, and in the downward refracting cases, the propagation of sound is determined by bottom interaction. However, the role of the variability of the thermocline in both time and range cannot be ignored in the study of coherency.

Wille and Thiele's experiment[17] was in the North Sea using explosives. The results are reported using the ''coherence distance'' as opposed to the value L_h used in this paper

TABLE III. The E parameter and coherence lengths for $R=500$ km.

Basin	Depth	$E\times 10^{17}$	L/λ at 300 Hz	L/λ at 400 Hz	L/λ at 600 Hz
Atlantic	4000 m	4.88	234	145	62
Mediter.	2000 m	4.88	234	145	62
Pacific	3700 m	9.31	152	94	48
Arctic	1600 m	13.1	199	61	31

TABLE IV. Shallow-water coherence length results. SVP=sound velocity profile; ISV=isovelocity; DR=downward refracting; WD=water depth; S=sand; S-SC=sandy-silty-clay; SD=source depth; RD=receiver depth; COV=coefficient of variation in measured results.

Reference	17	19	20	21	21	21	21	21
Location	N. Sea	N.W. Atl.	GM/WFE	GM/FS	NWA/JS	SOK-1	SOK-1	SOK-2
SVP	ISV	DR	DR	DR	DR	DR	DR	DR
WD	65 m	0.1–1 km	0.1–1 km	200 m	100 m	100 m	100 m	100 m
Bottom	S	S-SC	S-SC	S-SC	S-SC	S-SC	S-SC	SC-S
f_1(Hz)	400	135	173–175	200–400	200–400	354	300	354
f_2	800			400–800	400–600	600	500	604
Range km	7.4	100	25	9.3	4–22	7–11	5–45	14–24
$(L_c/\lambda)_1$	18	31	21	30	23	27	29	38
$(L_c/\lambda)_2$	10			32	25	30	31	54
Source	Exp.	CW	CW	Exp.	Exp.	CW	Exp.	CW
sd_0	21 m	18 m	100 m	100 m	52 m	30 m	52 m	33 m
RD	15 m	750 m	400 m	200 m	100 m	101 m	101 m	94 m
COV	8%	4%	6%	4%	4%	4%	5%	2%–4%

(see the Appendix). The propagation path was parallel to the wave crests, 2.5–3 m in height, with an average wind speed of 30 kn over 5 h corresponding to a sea state 4 on the World Meteorological Scale. It is understood that at a frequency of 400 Hz, his estimate is $L_c/\lambda = 18$ representing the combined effects of the sea surface and the bottom. Scholz[18] performed similar measurements in the North Sea during the winter months with a slightly upward refracting profile and low sea state and found $L_h \approx 100\lambda$ at 50 km and during the summer with downward refraction $L_h \approx 23\lambda$ at 50 km. Scholz used these same techniques in the Baltic Sea measurements with a water depth of 90 m in the summer under calm sea conditions and found $L_h \approx 7.9\lambda$ at 250 Hz and $L_h = 1.8\lambda$ at 500 Hz at a range of 13 km. Scholz found that the frequency, source received depths, and range affected his results and that summer conditions produced much shorter coherence lengths. The lack of pertinent environmental information, however, precludes their inclusion in the tabular summary.

This author has reported results[19,20] of coherence lengths estimated from ASGD measurements using a long moving array in deep water from continuous sources on the Scotian Shelf and the Gulf Coast of Florida. These estimates are shown to be $L_c/\lambda = 31$ at 135 Hz and $L_c/\lambda = 21$ at 173 and 175 Hz for moderate sea states of 2 to 3 on the World Meteorological Scale. The assumption in these two experiments was that the ASGD was primarily due to the interaction with the bottom and the effects of coastal currents on the range-dependent sound velocity structure, considering that the corresponding deep-water results previously discussed were consistent with longer coherence lengths.

The remainder of Table IV presents results recently obtained in a series of shallow-water experiments referred to as the ''Area Characterization Tests,'' ACT.[21–24] These experiments were conducted with bottomed horizontal arrays, explosive and continuous wave sources in sea sates less than 3. Both transverse and longitudinal coherencies were measured. Reported in Table IV are the average values of the transverse coherence lengths determined from array signal-gain estimates. The coefficient of variation of these signal-gain measurements was approximately 4% to 5% determined by the ratio of the measurement standard deviation, dB, and the measured signal gain, dB.

The first experiment was conducted on the West Florida Escarpment of the Gulf of Mexico. The environment was weakly range dependent with a downward refracting profile, a mixed layer depth of 30 m followed by a rather constant thermocline with a gradient $\Delta C/\Delta D = -0.36$ m/s/m.[22] The sound propagation and coherency at this site was primarily due to the bottom interaction because the variability in the sound-speed profiles was minimal.

The second experiment was at a site north of the Hudson Canyon on the east coast of the United States. The oceanographic environment was more variable at this site,[23] due to the interaction of three water masses: the shelf water, the Hudson River outflow, and an eddy from the Gulf Stream. Thus this site represented a complicated set of oceanographic conditions. The profiles featured a mixed-layer depth of 27 m followed by a variable thermocline gradient $\Delta C/\Delta D = -0.9$ to -1.4 m/s/m indicative of internal wave activity.[23] The propagation at this site was determined by the bottom, but the coherency was undoubtedly determined by the combined effects of bottom interaction and water column variability.

The final two sites were in the Strait of Korea.[24] The first site was in the vicinity of the South Korean Coastal Front formed by the Tsushima Current and the South Korean Coastal Water. The sound velocity profiles had a mixed-layer depth of 20 m and an isovelocity layer at depths greater than 80 m. The intermediate regions between 20 and 80-m depth of the profiles were variable with gradients between $\Delta C/\Delta D = -0.31$ and -0.9 m/s/m and showed the effects of the interfingering of the two water masses.[24] There the bathymetry and bottom composition were rather uniform. The bottom consisted of three layers, the first of which was approximately 10 m and composed of sand with shells to sand-silt. The second sand layer had an erosion surface caused by low sea-level epochs and averaged 40 m and the third was sedimentary rock, the acoustic basement. The propagation at this site was strongly bottom interacting; however, the oceanographic variations were large. The coherence length estimates of 27–29 wavelengths are remarkable, and broadband acoustic imaging (not reported here) showed resolved targets at ranges of 40 km.

The second site, near Cheju-do, was located on the boundary between the Korean Strait and the Yellow Sea water masses where the major variable was the tidal mixing,

however, the observed variability was larger than expected based on archival data. The bottom water appeared to be Yellow Sea cold water with the intermediate depth waters the result of vertical and lateral mixing of the Tushima Current and Yangtze River water.[24] This mixing results in spatial and temporal variability in the velocity profile between 20 and 80 m. Density differences between these water masses should also result in internal wave activity. The sound-velocity profile at this site had a mixed-layer 20-m depth and an isovelocity layer below 80 m. The second site bottom was again two layers over the acoustic basement. The first layer approximately 5-m deep is composed of a mixture of mud and sand, silty-clay and sand, over a rough layer of sand approximately 15-m deep. Examination of Table IV shows that, on average, longer coherence length estimates resulted from the data gathered from the second site; that is, a horizontal coherence length of 38λ at a range of 24 km compared with 27λ at a range of 11 km. The reason for these different transverse coherence lengths is not understood, but these different transverse coherence lengths must be attributed to the variability of the water column and different bottom properties.

Despite these differences the measurements in this study are very consistent and should be representative of coastal sites with variable oceanography and sandy and silty-clay bottoms. The general trend observed was average coherence lengths of 29λ at 354 Hz and 34λ at 604 Hz for ranges between 9 and 45 km. The loss of coherence was most likely due to oceanographic variability and bottom interaction. These effects were also observed by Wasiljeff[25] in his measurements near Elba in water 115-m deep with clay and clay-sand bottoms. Wasiljeff compared winter and summer coherence measurements at frequencies greater than 800 Hz and observed large coherence lengths during the winter experiments and short coherence lengths, 29λ at 800 Hz, at ranges between 10 and 19 km during the summer downward refraction. In general, Wasiljeff's measured larger coherence lengths at higher frequencies than those reported in this work.

III. SUMMARY AND CONCLUSIONS

The transverse coherence length as a function of range (R/λ) and length (L/λ) is the primary parameter limiting the resolution of sonar arrays. This author contends that the correlative form of the phase randomness introduced in the acoustic field through scattering as the wave propagates determines the coherence functional form and the transverse array signal gain. The relative signal gain was shown to be proportional to the coherence length and an integral of the coherence function over the aperture. Because the measurement of the pairwise coherence is strongly affected by noise and multipath interference effects, the measurement of signal gain is an alternative and it can be measured with a coefficient of variation of approximately 5%. Estimates of coherence lengths derived from the means of measured signal-gain distributions were found to be remarkably consistent for both deep- and shallow-water cases.

Estimates of coherence lengths at a frequency of 400 Hz were made using the deep-ocean pairwise coherence results of Stickler *et al.* and were found to have a coefficient of variation between 12% and 32% with estimated lengths that were between 102λ at 507 km and 94λ at 962 km. When rsg is used as the measure, estimates of coherence lengths averaged 100λ at 300–500 km in agreement with the difficult single-path measurements of Stickler, demonstrating the utility of this measurement technique. Both sets of deep-water measured results are consistent with the Beran–McCoy expression for coherence length variations as a function of frequency with a factor $E_f = 4.8 \times 10^{-17}$.

Estimates of shallow-water coherence lengths were presented for five shallow water sites under variable downward refracting conditions. Results between 300 and 400 Hz with an assumed Gaussian coherence functional form were found to produce average coherence lengths of 30λ to ranges of 45 km with the loss of coherence primarily attributed to the multiple bottom interactions and scattering in water volume.

The major conclusion drawn in this paper is deep-ocean coherence lengths are at least three times the shallow-water lengths at ten times the range. This difference is attributed to the bottom and variable coastal-water column profiles. Second, the measurement of signal gain provides a viable means of estimating the transverse horizontal coherence lengths as a function of frequency and range in noisy shallow-water environments. Future experiments should cover a period of time longer than the experiments discussed in this paper; they, at least, will have a precise knowledge of the source and receiver locations, the sound velocity structure, sea state, and the first λ of the sediment layer.

The measurements reported here, when coupled with a calibrated numerical code, should enable the rank ordering of coherence-loss mechanisms. However the shallow-water waveguide, because of its seasonal variability, may offer a natural means of isolating particular mechanisms. The upward refracting profile of the winter emphasizes the surface; the mixed layer during the spring followed by a variable thermocline emphasizes internal wave effects; and the downward refracting conditions of summer emphasize the bottom. Thus it is concluded that long-term, shallow-water coastal measurements are warranted.

APPENDIX: COHERENCE LENGTHS

In this paper the coherence function is taken as

$$\rho(\Delta x_{ij}) = \exp[-(x_i - x_j|/L_h)^n], \quad n = 1,\ 1.5,\ \text{or}\ 2.$$

The value of n depends on the specific theoretical coherence model. The convention usually employed is to define L_h by $\rho(\Delta x_{ij} = L_h) = \exp(-1)$, which is different than the convention used by Wille (see Ref. 9) where the expression for the coherence function is

$$\rho(\Delta x_{ij}) = \exp[-(2\pi|x_i - x_j|\sigma_\theta/\lambda)^2/2].$$

When $\rho(\Delta x_{ij} = d_c) = \exp(-1/2)$, the ''correlation distance'' is defined as $d_c = \lambda/2\pi\sigma_\theta$ or

$$\rho(\Delta x_{ij}) = \exp[-(|x_i - x_j|/d_c)^2/2].$$

The net result is that $L_h/\lambda = 0.225(2\pi d_c/\lambda)$. Thus a normalized coherence distance of $(2\pi d_c/\lambda) = 100$ corresponds to a normalized coherence length of $L_h/\lambda = 22.5$.

[1] W. M. Carey and R. A. Wagstaff, ''Low frequency noise fields,'' J. Acoust. Soc. Am. **80**, 1523–1526 (1986).
[2] G. C. Carter, C. H. Knapp, and A. H. Nuttall, ''Statistics of the estimate of the magnitude coherence function,'' IEEE Trans. Audio Electroacoust. **AU-21**, 388–389 (1973).
[3] G. C. Carter, C. H. Knapp, and A. H. Nuttall, ''Estimation of the magnitude squared coherence function via overlapped FFT processing,'' IEEE Trans. Audio Electroacoust. **AU-21**, 337–344 (1973).
[4] E. R. H. Scannell and G. C. Carter, ''Confidence bounds for magnitude-squared coherence estimates,'' *Proceedings of the IEEE International Conference on Acoustics, Speech, and Signal Processing* (IEEE, New York, 1978), pp. 670–673.
[5] W. M. Carey and W. B. Moseley, ''Space-time processing, environmental-acoustic effects,'' in *Progress in Underwater Acoustics*, edited by H. M. Merklinger (Plenum, New York, 1987), pp. 743–758, expanded version in IEEE J. Ocean Eng. **16**, 285–301 (1991).
[6] W. M. Carey, J. Reese, and C. Stuart, ''Mid-frequency measurements of array signal and noise characteristics,'' IEEE J. Ocean Eng. **22**, 548–565 (1997).
[7] N. Hastings and J. Peacock, *Statistical Distributions* (Wiley, New York, 1974), p. 13.
[8] R. Urick, *Principles of Underwater Sound*, 2nd ed. (McGraw-Hill, New York, 1974), p. 34.
[9] Y. S. Shifrin, *Statistical Antenna Theory* (Golem, Boulder, CO, 1971).
[10] H. Cox, ''Line array performance when the signal coherence is spatially dependent,'' J. Acoust. Soc. Am. **54**, 1743–1746 (1973).
[11] M. J. Beran, J. J. McCoy, and B. B. Adams, ''Effects of a fluctuating temperature field on the spatial coherence of acoustic signals,'' NRL Tech. Rept. 7809, NRL, Washington, DC 20375, 1975.
[12] R. F. Dashen, S. M. Flatte, W. H. Munk, and F. Zachariasen, ''Limits on coherent processing due to internal waves,'' Standford Research Rep. Tr-JSR-76-14, 1977-(Avail DTIC), Standford Research, Menlo Park, CA 94025.
[13] D. R. Morgan and T. M. Smith, ''Coherence effects on the detection performance of quadratic array processors, with applications to large-array matched-field beamforming,'' J. Acoust. Soc. Am. **87**, 737–747 (1990).
[14] D. C. Stickler and R. D. Worley, and S. S. Jaskot, Bell Telephone Laboratories (unpublished). Summarized by G. H. Robertson, ''Model for spatial variability effects on single path reception of underwater sound at long ranges,'' J. Acoust. Soc. Am. **69**, 112–123 (1981).
[15] W. B. Moseley and D. R. Del Balso, ''Horizontal random temperature structure in the ocean,'' J. Phys. Oceangr. **6**, 267–280 (1976).
[16] W. B. Moseley, ''Acoustic coherence in space time-an overview,'' in Proc. EASTCON'78; ''Geographic variability of spatial signal correlation and subsequent array performance,'' in Proc. Int. Symp. Underwater Acoustics, Tel Aviv, Israel, 1981 (unpublished).
[17] P. Wille and R. Thiele, ''Transverse horizontal coherence of explosive signals in shallow water,'' J. Acoust. Soc. Am. **50**, 348–353 (1971).
[18] R. Scholz, ''Horizontal spatial coherence measurements with explosives and CW sources in shallow water,'' in *Aspects of Signal Processing. Part I*, edited by G. Tacconi (Reidel Dordrecht, Holland, 1977), pp. 95–108.
[19] W. M. Carey, ''Measurement of down-slope sound propagation from a shallow source to a deep ocean receiver,'' J. Acoust. Soc. Am. **79**, 49–59 (1986).
[20] W. M. Carey, I. B. Gereben, and B. A. Brunson, ''Measurement of sound propagation downslope to a bottom-limited sound channel,'' J. Acoust. Soc. Am. **81**, 244–257 (1987).
[21] These results are from the ACT series of experiments conducted by W. Carey, P. Cable, and J. O'Connor on the Florida Shelf in the Gulf of Mexico, on the Jersey Continental Shelf, and in the Straits of Korea. Explosive sources were developed and deployed by W. Marshall and the analysis was performed by Mike Steele, T. Kooij, and J. Angle from BBN Laboratories. In addition the CW sources were deployed by W. Carey and G. Hunsaker, NRAD. Analysis of the Straits of Korea array data was performed by J. Reese, NRAD.
[22] B. Gomes and J. Mathews, ''West Florida Shelf Environment for the Area Characterization Test I (ACT I),'' NRL/MR/7182-93-7061, NRL, Stennis Space Center, MS, 8 July 1994.
[23] O. Marcia, ''Act II Sea Test XBT Results,'' BBN Memorandum to W. Carey, October 1993.
[24] P. Bucca, J. Fulford, J. Lynch, and A. Newhall, ''Environmental variability during the third Acoustic Characterization Test (ACT III) in the Strait of Korea,'' NRL/FR/7182--97-9667, NRL, Stennis Space Center, MS, 28 July 1997.
[25] A. Wasiljeff, ''Spatial horizontal coherence of acoustical signals in shallow water,'' SACLANTCEN SM-68, SACLANT ASW Research Centre, LaSpezia, Italy, May 1975.

Modal analysis of wave fields in range-independent oceanic media

Elias Parastates
Division of Guidance & Control, Materials and Underwater Sensors, National Defense Research Establishment, S-172 90 Stockholm, Sweden

(Received 23 June 1997; revised 13 January 1998; accepted 16 April 1998)

A maximum-likelihood (ML) method for modal analysis of time invariant two-dimensional wave fields in a deterministic layered waveguide is introduced. The Cramer–Rao bounds (CRBs) of the variances of the ML modal parameter estimates are derived from the likelihood function of the wave field sampled in a vertical plane by a rectangular receiver array. The ML estimates are shown to be consistent for a finite array size and a fixed number of sensors as the number of snapshots tends to infinity. The ML method is applied on data collected in the Swedish archipelago, is shown to resolve a high number of modes from moderate length apertures, and to achieve a good agreement between modeled and observed wave fields. © *1998 Acoustical Society of America.*
[S0001-4966(98)05407-1]

PACS numbers: 43.30.Wi, 43.60.Gk [SAC-B]

LIST OF SYMBOLS

$\mathbf{i}$	is the imaginary unit.
$E\{\ \}$	is the expectation operator.

If $\mathbf{B}=(\mathbf{b}_1\cdots\mathbf{b}_M)$ is a $(M\times M)$ complex valued matrix function of real variables $\alpha_1,\ldots,\alpha_K$, then

$\mathbf{B}^T$	is the transpose of $\mathbf{B}$,
$\mathbf{B}^*$	is the conjugate of $\mathbf{B}$,
$\mathbf{B}^H$	is the conjugate transpose of $\mathbf{B}$,
$\|\mathbf{B}\|_F^2$	is the squared Frobenius norm of $\mathbf{B}$,
triu$\{\mathbf{B}\}$	is a $(M\times M)$ matrix with elements triu$\{\mathbf{B}\}(i,j)=\mathbf{B}(i,j)$ for $i\leqslant j$, 0 otherwise,
diagm$\{\mathbf{B}\}$	is an $(M\times M)$ matrix with elements diagm$\{\mathbf{B}\}(i,i)=\mathbf{B}(i,i)\forall i$, diagm$\{\mathbf{B}\}(i,j)=0$, $j\neq i$,
trace$\{\mathbf{B}^H\mathbf{B}\}=\Sigma_{i=1}^M\mathbf{b}_i^H\mathbf{b}_i$	is the trace operator (Ref. 1, p. 332),
vec$\{\mathbf{B}\}=\begin{pmatrix}\mathbf{b}_1\\ \vdots\\ \mathbf{b}_M\end{pmatrix}$	is the vector operator (Ref. 2, p. 18),
$\mathbf{B}_i,\mathbf{B}_{ij}$	with boldface subindexes, are matrix names.
$\mathbf{B}_i+\mathbf{B}_j+(\cdots)^H$	$=\mathbf{B}_i+\mathbf{B}_j+\mathbf{B}_i^H+\mathbf{B}_j^H$
$\mathbf{B}_{\partial i}=\partial\mathbf{B}/\partial\alpha_i$	
$\mathbf{B}_{\partial i\ \partial j}=\partial\mathbf{B}/\partial\alpha_i\ \partial\alpha_j$	

INTRODUCTION

The complex amplitude of an acoustic pressure field excited by a monochromatic point source in a laterally homogeneous oceanic medium, at a great distance, is synthesized by propagating modes. The modal wave numbers and amplitudes are characteristic of the medium and therefore useful in inverse modeling.[3]

Frisk and Lynch[4] suggest the acoustical characterization of a medium, by numerical evaluation of the Hankel transform using data from synthetic apertures, i.e., generated by a source towed away from moored receivers. From the inversion of experimental data taken in Nantucket sound, Frisk *et al.*[5] point out the sensitivity of the Hankel transform to range variations. The need of resolving closely located modes from moderate apertures, arising, for example, in shallow-water applications, makes high-resolution estimators particularly interesting. Chouhan *et al.*[6] suggest multiple signal classification (MUSIC),[7] Rajan *et al.*[8] analyze Nantucket sound data using MUSIC and estimation of signal parameters via rotational invariance techniques (ESPRIT)[9] observing a better performance of the latter. Parastates[10,11] estimates wave numbers, using MUSIC and multidimensional (MD)-MUSIC, processing each sensor depth individually, observing that the multidimensional method offers lower estimate variance.

The statistical efficiency of the high-resolution methods has been the subject of a number of works in the signal-processing area. Stoica and Nehorai[12] investigate the performance of the MUSIC and ML methods in parameter estimation of complex exponential signals in noise, concluding that the latter is more efficient unless the signal amplitudes are uncorrelated. Ottersten *et al.*[13] investigate the asymptotic properties of one- and multidimensional estimators of direction of arrival (DOA) of plane-wave fronts impinging on an array, considering the signal amplitudes as random variables.

This work, an extended and improved version of Ref. 11, introduces a ML method for modal analysis of time invariant two-dimensional wave fields in a deterministic layered waveguide. Applying the theory developed in Ref. 12: (i) The Cramer–Rao bound (CRB) (Ref. 14, p. 9) of the modal wave numbers are derived. (ii) The utilized ML estimators of wave numbers as well as amplitudes are shown to be consistent (Ref. 14, p. 3) for a finite array size and a fixed

number of sensors as the number of snapshots tends to infinity. The ML method is applied on experimental data, is shown to resolve a high number of modes from moderate length apertures, and to achieve a good agreement between the synthesized and the observed wave field.

The theoretical model of the wave field is described in Sec. I. In Sec. II the likelihood function of the wave field, sampled in a vertical plane, and the CRBs of the variances of the estimated modal wave numbers and the noise power are formulated. In Sec. III, a ML estimator is introduced, the consistency of the estimates is established, and the eigenrepresentation of the correlation matrix of the sampled field is discussed. A modal analysis of data collected in the Baltic by two-dimensional (2-D) arrays is presented in Sec. IV. Seabed parameter inversion of the estimated modal parameters will be presented in work in preparation.

I. THE THEORETICAL COMPLEX AMPLITUDE

Consider a laterally homogeneous oceanic medium composed of fluid and solid layers, bounded above by a pressure release surface and below by a penetrable solid half-space. Introduce a cylindrical coordinate system with origo on the water surface, the positive z axis pointing downwards. Designate the (range, depth) domain by (r,z), with the seabed at z_d. The complex amplitude of the acoustic pressure field excited by a submerged monochromatic source at $(0,z_s)$ may, within the water column, be expressed in terms of the inverse Hankel transform (Ref. 15, p. 122)

$$x(r,z)=\frac{1}{2}\int_{-\infty}^{\infty}X(\alpha,z)H_0^{(1)}(\alpha r)\alpha\, d\alpha, \tag{1}$$

where $X(\alpha,z)$ is the complex amplitude as a function of horizontal wave number and depth. $X(\alpha,z)$ is analytic in the entire α plane except for poles at the wave numbers of the normal modes of the medium, and branch points associated with downward moving P and S waves in the solid half-space. Assuming all poles to be simple and applying the residue theorem on (1) yields a representation of the wave field as a sum of normal modes plus branch-cut integrals. At a great distance from the source contributions from branch cuts and damped modes are negligible. Therefore the far-field equivalent of (1), in the presence of additional spatial noise $h(r,z)$, becomes

$$x(r,z)=\frac{1}{\sqrt{r}}\sum_{k=1}^{K}g_k(z)e^{i\alpha_k r}+h(r,z), \tag{2}$$

where

$$g_k(z)=\mathbf{i}\sqrt{2\pi\alpha_k}e^{-\mathbf{i}(\pi/4)}\xi_k(z), \tag{3}$$

$\xi_k(z)=\lim_{\alpha\to a_k}(\alpha-a_k)X(\alpha,z)$ is the kth modal eigenfunction, α_k is the corresponding real valued wave number, and $H_0^{(1)}(\alpha r)$ has been replaced by its asymptotic form for large arguments αr (Ref. 16, p. 364). The noise term is considered as a zero-mean stationary complex Gaussian process (Ref. 17, p. 43) with autocorrelation

$$E\{h(r,z)h(r',z')\}=0, \tag{4a}$$

$$E\{h(r,z)h^*(r',z')\}=\sigma^2\delta(r-r')\,\delta(z-z'). \tag{4b}$$

Sampling (2) on a grid $(r_n,z_j)n=1,...,N,\ j=1,...,J$ leads to

$$\mathbf{X}=\mathbf{AG}+\mathbf{H}, \tag{5}$$

where

$$\mathbf{X}=(\mathbf{x}_1\cdots\mathbf{x}_i\cdots\mathbf{x}_J),$$

$$\mathbf{x}_j=(x(r_1,z_j)\cdots x(r_n,z_j)\cdots x(r_N,z_j))^T,$$

$$\mathbf{A}=(\mathbf{d}_1\cdots\mathbf{d}_k\cdots\mathbf{d}_K),$$

$$\mathbf{d}_k=\left(\frac{e^{\mathbf{i}\alpha_k r_1}}{\sqrt{r_1}}\cdots\frac{e^{\mathbf{i}\alpha_k r_n}}{\sqrt{r_n}}\cdots\frac{e^{\mathbf{i}\alpha_k r_N}}{\sqrt{r_N}}\right)^T,$$

$$\mathbf{G}=(\mathbf{g}_1\cdots\mathbf{g}_j\cdots\mathbf{g}_J),$$

$$\mathbf{g}_j=(g_1(z_j)\cdots g_k(z_j)\cdots g_K(z_j))^T,$$

and

$$\mathbf{H}=(\mathbf{h}_1\cdots\mathbf{h}_j\cdots\mathbf{h}_J),$$

$$\mathbf{h}_j=(h(r_1,z_j)\cdots h(r_n,z_j)\cdots h(r_N,z_j))^T.$$

Whenever $(r_n=r_0+n\Delta r, z_j=z_0+j\Delta z)$ the grid is termed as uniformly spaced. Assume that $\hat{\mathbf{X}}_l=(\hat{\mathbf{x}}_{1,l}\cdots\hat{\mathbf{x}}_{j,l}\cdots\hat{\mathbf{x}}_{J,l})$ $l=1,...,L$ are independent, second-order ergodic, observations (snapshots) of $\mathbf{X}$ of the form

$$\hat{\mathbf{x}}_{j,l}=\mathbf{A}\mathbf{g}_j+\hat{\mathbf{h}}_{j,l} \tag{6}$$

collected by a 2-D array or a vertical line array using a synthetic aperture technique.

II. THE LIKELIHOOD FUNCTION OF THE MODAL WAVE FIELD

Given observations $\hat{\mathbf{X}}_l$ the objective of the modal analysis is to estimate the unknown modal amplitudes $\mathbf{G}$, the wave numbers $\mathbf{a}=(a_1\cdots a_k)^T$, and the noise variance σ^2. Due to (4a) and (4b), the first- and second-order moments of the $[JN\times 1]$ spatial noise vector vec$\{\mathbf{H}\}$ are given by

$$E\{\mathrm{vec}\{\mathbf{X}-\mathbf{AG}\}\}=\mathbf{0}, \tag{7a}$$

$$E\{\mathrm{vec}\{\mathbf{X}-\mathbf{AG}\}\cdot\mathrm{vec}\{\mathbf{X}-\mathbf{AG}\}^T\}=\mathbf{0}, \tag{7b}$$

$$E\{\mathrm{vec}\{\mathbf{X}-\mathbf{AG}\}\cdot\mathrm{vec}\{\mathbf{X}-\mathbf{AG}\}^H\}=\sigma^2\mathbf{I}. \tag{7c}$$

The probability density of (5) is therefore given by

$$f(\mathrm{vec}(\mathbf{X}))=\frac{1}{(\pi\sigma^2)^{JN}}\,e^{-(1/\sigma^2)\Sigma_{j=1}^{J}(\mathbf{x}_j-\mathbf{A}\mathbf{g}_j)^H(\mathbf{x}_j-\mathbf{A}\mathbf{g}_j)}. \tag{8}$$

The log likelihood function conditioned on independent observations $\mathbf{x}_{j,l}$ $l=1,...,L$, regarded as a function of $\mathbf{G}$ and $\mathbf{a}$ becomes

$$\begin{aligned}Y&=Y_{\log}(\hat{\mathbf{X}}_l,l=1\cdots L|\sigma^2,\alpha_1,\ldots,\alpha_K,\mathbf{G})\\&=-JLN\,\ln(\pi\sigma^2)-\frac{1}{\sigma^2}\sum_{l=1}^{L}\sum_{j=1}^{J}(\hat{\mathbf{x}}_{j,l}-\mathbf{A}\mathbf{g}_j)^{\mathbf{H}}\\&\quad\times(\hat{\mathbf{x}}_{j,l}-\mathbf{A}\mathbf{g}_j).\end{aligned} \tag{9}$$

In case of correlated noise (9) still applies if a whitening transformation is utilized, i.e., (5) is multiplied from the left

by the inverse of a square root of the noise covariance matrix (Ref. 17, p. 60). The ML estimates of the unknown parameters are obtained by maximization of the likelihood function. To obtain their least attainable variance proceed as in Ref. 12, where the CRB of the parameters of multiple superimposed complex exponential signals in noise has been derived. Notice that n,j correspond to data indices in Ref. 12 and that the additional index l may be viewed as an experiment number in a sequence of independent experiments performed under identical conditions. For $L=1$ the CRB of the variance of the modal parameters and variance become identical with what is reported in Ref. 12. For $L>1$ the computation of the CRB is straightforward noticing that the mutual independence of the observations (6) implies that the noise vectors $\hat{\mathbf{h}}_{j,l}$ are mutually uncorrelated with respect to l, see also Appendix A.

The CRB of the estimated wave numbers becomes

$$\mathrm{CRB}(\alpha_1,\ldots,\alpha_K,J,L,N)=\frac{\sigma^2}{2L}\left(\sum_{j=1}^{J}\ \mathrm{Re}\{\mathrm{diagm}\{\mathbf{g}_j\}^H\mathbf{D}^H \times(\mathbf{I}-\mathbf{P})\mathbf{D}\mathrm{diagm}\{\mathbf{g}_j\}\}\right)^{-1}, \quad (10)$$

where $\mathbf{D}=(\mathbf{d}_{\partial 1}\ \cdots\ \mathbf{d}_{\partial K})$ and $\mathbf{P}=\mathbf{A}(\mathbf{A}^H\mathbf{A})^{-1}\mathbf{A}^H$ is the orthogonal projector onto the column space of $\mathbf{A}$, the modal space. From (10) it follows that 2-D processing is at least equally efficient as individual processing of each array depth since $\mathrm{CRB}^{-1}(\alpha_1,\ldots,\alpha_K,J+1,L,N)-\mathrm{CRB}^{-1}(\alpha_1,\ldots,\alpha_K,J,L,N)=2L(\mathrm{Re}\{\mathrm{diagm}\{\mathbf{g}_{J+1}\}^H\mathbf{D}^H(\mathbf{I}-\mathbf{P})\mathbf{D}\}\mathrm{diagm}\{\mathbf{g}_{J+1}\})/\sigma^2$ is real symmetric positive semidefinite (Ref. 17, p. 297).

The CRB of the variance becomes

$$\mathrm{CRB}(\sigma^2,J,L,N)=\frac{\sigma^2}{JLN}. \quad (11)$$

Notice that (10) and (11) are valid even when $H_0^{(1)}(\alpha r)$ rather than its asymptotic form is used in (2) and (3). The additional factor $1/L$ appearing in all CRBs compared with Ref. 12 arises from using data from L independent observations in the likelihood function (9).

If the wave field given by (2) is sampled by a uniformly spaced array then

$$\lim_{N\to\infty} JN^2\mathrm{CRB}(\alpha_1,\ldots,\alpha_K,J,L,N)=\frac{\sigma^2}{L\Delta r}\begin{pmatrix}\zeta_{1,1}^{-1} & 0 & 0\\ 0 & \ddots & 0\\ 0 & 0 & \zeta_{K,K}^{-1}\end{pmatrix}, \quad (12)$$

where

$$\zeta_{k,k}=\frac{2\pi\alpha_k}{J}\sum_{j=1}^{J}|\xi_k(z_j)|^2.$$

For a proof of (12) see Appendix B.

If in addition $J\to\infty$ while $z_J=z_c\leqslant z_d$ remains fixed, $1/J=\Delta z/(z_c-z_0)\to 0$ and

$$\lim_{J\to\infty}\zeta_{k,k}=\frac{2\pi\alpha_k}{z_c-z_0}\int_{z_0}^{z_c}|\xi_k(z)|^2\,dz \quad (13)$$

becomes, apart from the scale factor $2\pi\alpha_k$, the averaged elastic energy of the kth modal eigenfunction within the vertical aperture of the array.

Assuming the existence of a minimum variance estimator (Ref. 14, p. 8), the CRB formulas could also be useful for experimental design purposes, i.e., they reflect the influence of the number of sensors and array dimensions upon the estimate accuracy. For horizontally large, vertically dense arrays, possibly implemented by a vertical line array and synthetic aperture processing, (12) and (13) suggest that modal parameter estimates of watermodes having most of their energy concentrated within the vertical aperture of the array will be more accurate than their sediment reciprocals, and that $\mathrm{CRB}(\alpha_k,J,L,N)\sim(\Delta r\alpha_k JLN^2)^{-1}$.

III. THE MAXIMUM-LIKELIHOOD ESTIMATOR

Denote explicitly all functions of wave-number estimators $\hat{\alpha}=(\hat{\alpha}_1,\ldots,\hat{\alpha}_K)$ within this section, by inserting $(\hat{\alpha})$. Assume that the wave numbers are distinct, and that the array is unambiguous, i.e., the columns of $\mathbf{A}(\hat{\alpha})$ are linearly independent for distinct $\hat{\alpha}_k, k=1,\ldots,N$. From the Vandermonde structure (Ref. 1, p. 178) of $\mathrm{diagm}\{(\sqrt{r_1}\cdots\sqrt{r_N})\}\times\mathbf{d}_k(\hat{\alpha}_k)$ follows that a uniformly spaced array with Δr less than one-half of the smallest wavelength is unambiguous if all $\hat{\alpha}_k\leqslant\pi$.

Substitute the modal amplitudes obtained from the least-squares solution of (6) in (A1). Set derivatives (A1)–(A3) equal to zero and rearrange, yields (Ref. 14, p. 38) estimators of amplitudes and variance

$$\hat{\mathbf{g}}_j(\hat{\alpha})=L^{-1}(\mathbf{A}^H(\hat{\alpha})\mathbf{A}(\hat{\alpha}))^{-1}\mathbf{A}^H(\hat{\alpha})\sum_{l=1}^{L}\hat{\mathbf{x}}_{j,l}, \quad (14)$$

$$\hat{\sigma}^2(\hat{\alpha})=\frac{1}{JLN}\sum_{j=1}^{J}\sum_{l=1}^{L}\|(\mathbf{I}-\mathbf{P}(\hat{\alpha}))\hat{\mathbf{x}}_{j,l}\|_2^2 =\mathrm{trace}\{(\mathbf{I}-\mathbf{P}(\hat{\alpha}))\hat{\Xi}\}, \quad (15)$$

where

$$\hat{\Xi}=\frac{1}{JLN}\sum_{j=1}^{J}\sum_{l=1}^{L}\hat{\mathbf{x}}_{j,l}\hat{\mathbf{x}}_{j,l}^H \quad (16)$$

is the sample correlation matrix. The ML estimates of the wave numbers are given by the global minimum of $\hat{\sigma}^2(\hat{\alpha})$, i.e.,

$$\underset{\mathrm{ML}}{\hat{\alpha}}=\arg\min_{\hat{\alpha}}\hat{\sigma}^2(\hat{\alpha}). \quad (17)$$

Inserting $\underset{\mathrm{ML}}{\hat{\alpha}}$ into (14) and (15) immediately yields the ML estimates $\underset{\mathrm{ML}}{\hat{\mathbf{g}}_j},\underset{\mathrm{ML}}{\hat{\sigma}^2}$, of the amplitudes and variance. For the consistency check of the estimates introduce the asymptotic form of the sample correlation matrix

$$\hat{\Xi} = \lim_{L\to\infty} \frac{1}{JLN} \sum_{j=1}^{J} \sum_{l=1}^{L} \hat{\mathbf{x}}_{j,l} \hat{\mathbf{x}}_{j,l}^{H}$$

$$= \frac{1}{JN} \sum_{j=1}^{J} \mathbf{A}\mathbf{g}_j \mathbf{g}_j^H \mathbf{A}^H + \frac{\sigma^2}{N} \mathbf{I}, \tag{18}$$

where the second equality follows by the ergodicity assumption and (6), i.e., $\lim_{L\to\infty}(1/L)\Sigma_{l=1}^{L}\hat{\mathbf{h}}_{j,l} = E\{\mathbf{h}_j\} = 0$ and $\lim_{L\to\infty}(1/L)\Sigma_{l=1}^{L}\hat{\mathbf{h}}_{j,l}\hat{\mathbf{h}}_{j,l}^{H} = E\{\mathbf{h}_j\mathbf{h}_j^H\} = \sigma^2\mathbf{I}$. Inserting (18) into (15) gives the asymptotic variance

$$\lim_{L\to\infty} \hat{\sigma}^2(\hat{\alpha}) = \operatorname{trace}\left\{ (\mathbf{I} - \mathbf{P}(\hat{\alpha}))\left(\frac{1}{JN} \sum_{j=1}^{J} \mathbf{A}\mathbf{g}_j \mathbf{g}_j^H \mathbf{A}^H \right) \right\}$$

$$+ \operatorname{trace}\left\{ (\mathbf{I} - \mathbf{P}(\hat{\alpha}))\left(\frac{1}{N} \sigma^2 \right) \right\} \geqslant \frac{N-K}{N} \sigma^2 \tag{19}$$

with minimum when

$$\operatorname{trace}\left\{ (\mathbf{I} - \mathbf{P}(\hat{\alpha})) \sum_{j=1}^{J} \mathbf{A}\mathbf{g}_j \mathbf{g}_j^H \mathbf{A}^H \right\} = 0. \tag{20}$$

Since the array is assumed unambiguous the minimum is unique and occurs for $\hat{\alpha} = (\alpha_1 \cdots \alpha_K)$. The asymptotic consistency of the ML estimates given by (17) then follows by the uniqueness of the minimum. The asymptotic consistency of the ML amplitudes, (14), follow from

$$\lim_{L\to\infty} \underset{\text{ML}}{\hat{\mathbf{g}}_j} = \mathbf{g}_j + \lim_{L\to\infty} \frac{1}{L} (\mathbf{A}^H\mathbf{A})^{-1}\mathbf{A}^H \sum_{l=1}^{L} \mathbf{h}_{j,l}$$

$$= \mathbf{g}_j + (\mathbf{A}^H\mathbf{A})^{-1}\mathbf{A}^H E\{\mathbf{h}_j\}. \tag{21}$$

In Ref. 12, the asymptotic form of the sample correlation matrix is obtained by increasing N and J. Therefore the corresponding consistency conditions are slightly different (for the frequencies: $J\to\infty$; for the amplitudes: $J\to\infty$, $N\to\infty$ and no damping). The asymptotic ML estimate of the variance

$$\lim_{L\to\infty} \underset{\text{ML}}{\hat{\sigma}^2} = \frac{N-K}{N} \sigma^2 \tag{22}$$

is, however, independently of J, inconsistent unless N tends to infinity.

Introduce the eigenrepresentation of the correlation matrix $\hat{\Xi} = \Sigma_{n=1}^{N} \hat{\lambda}_n \hat{\mathbf{u}}_n \hat{\mathbf{u}}_n^H$, where $\hat{\lambda}_n$ denote the eigenvalues, ordered by decreasing magnitude, $\hat{\mathbf{u}}_n$ are the associated eigenvectors. If $J \geqslant K$ then the K principal eigenvectors of $\hat{\Xi}$ estimate the eigenvectors spanning the modal subspace, the remaining ones are introduced by the noise (Ref. 17, p. 618). Since $\mathbf{P}$ in (20) projects onto the modal subspace, and noise eigenvectors bias $\hat{\Xi}$ by adding components that are not present in the noise free case, $\hat{\Xi}$ in (15) may consistently be replaced by its principal component part $\Sigma_{n=1}^{K} \hat{\lambda}_n \hat{\mathbf{u}}_n \hat{\mathbf{u}}_n^H$.

Remark: Consider an oceanic waveguide under isovelocity conditions, with a perfectly reflecting bottom, and a vertically dense array with $(z_0 = 0, z_J = z_d)$. The Sturm–Liouville orthogonality condition implies then on the off-diagonal entries $\zeta_{k,l} = (1/z_d)\int_0^{z_d} g_k(z) g_l^*(z) dz$ in $\Sigma_{j=1}^{J} \mathbf{g}_j \mathbf{g}_j^H$ to be zero. If in addition the horizontal aperture is large, then MUSIC will be equally efficient as ML according to Ref. 12.

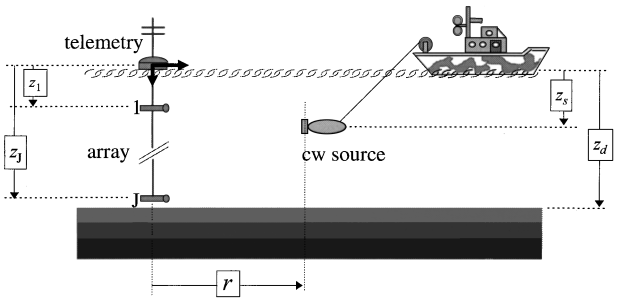

FIG. 1. Experimental setup: A moving cw source, registered by a moored vertical sensor array.

IV. EXPERIMENTAL RESULTS

A shallow-water experiment was carried out in the Swedish archipelago by a crew from the Swedish National Defense Research establishment in Sept. 1992. The overall objective was to obtain measurements of the pressure field as a function of the range for medium inversion and matched field processing. The experimental site, chosen because of its relatively flat topography, was in Kalmarsund, the strait between the island Öland and the mainland of Sweden. A seismic refraction experiment carried out near this site in Sept. 1988 indicated a horizontally stratified seabed composed of sandstone covered by a sediment layer of approximately 15-m thickness.[18] The water column in the area is 40-m deep. The experimental setup consisted of a stationary vertical array with eight hydrophones located at depths $z_j = 5j$ m, $j = 1,...,8$, registering a slowly moving cw source suspended from a ship, see Fig. 1.

The source was towed at a constant depth z_s, at almost constant speed, along a straight line intercepting the sensor array position. The towing lengths varied from 2 to 9 Km. The source strength was approximately 170 dB, and the emitted signal was a single tone with frequency specific for each run, i.e., $L = 1$. Array signals were transmitted to the ship by telemetry; bandpass filtered in parallel with a reference signal from a hydrophone attached 2 m above the source; logged on a Magneto-Optical disk device with a dynamic range of 72 dB. The source–receiver distance, determined by radar ranging, was sampled at 10-s intervals. The echosounder showed a depth of 39–41 m throughout the track.

The registered reference and receiver signals are realizations of

$$s_{\text{ref}}(t) = \varphi_{\text{ref}} \cos(2\pi f_c t) - \psi_{\text{ref}} \sin(2\pi f_c t) + \eta_e(t), \tag{23}$$

$$s_j(t) = \varphi_j(t)\cos(2\pi f_c t) - \psi_j(t)\sin(2\pi f_c t) + \eta_j(t), \tag{24}$$

where $\eta_e(t)$, $\eta_j(t)$ are assumed to be Gaussian processes with symmetric spectrum around the carrier frequency f_c and for low towing speeds

$$x(r_n, z_j) = \frac{\varphi_j(t(r_n)) + \mathbf{i}\psi_j(t(r_n))}{\varphi_{\text{ref}} + \mathbf{i}\psi_{\text{ref}}}. \tag{25}$$

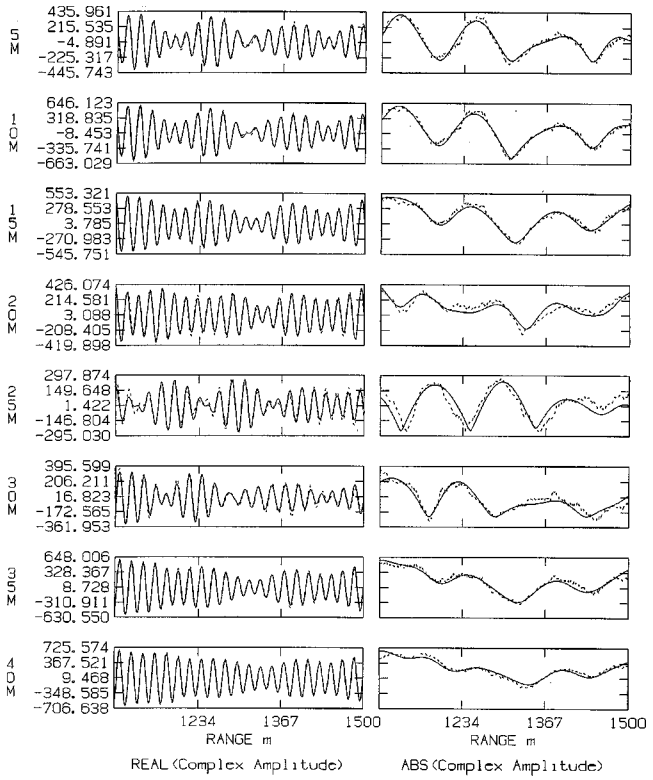

FIG. 2. Observed (dotted lines) and synthesized (solid lines) complex amplitudes as functions of range at $f_c = 80$ Hz, $z_s = 20$ m, $1101 \leqslant r \leqslant 1500$ m.

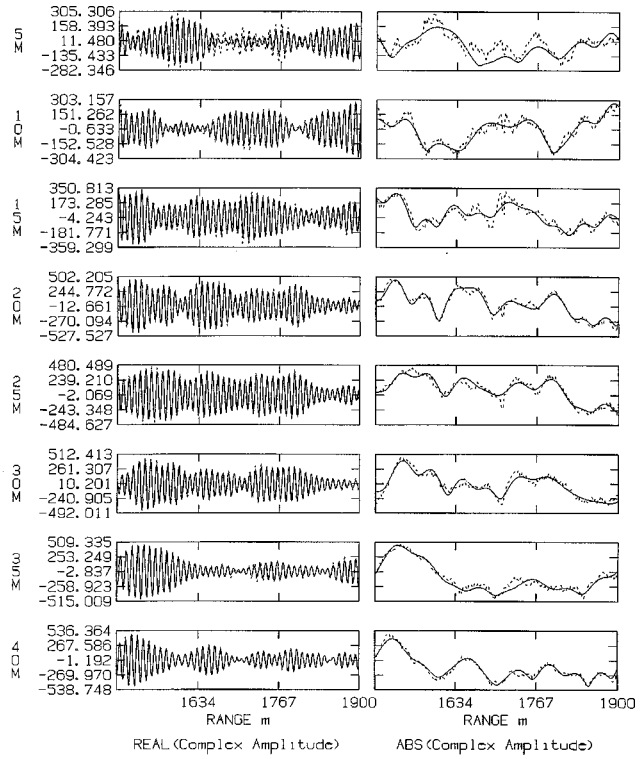

FIG. 3. Observed (dotted lines) and synthesized (solid lines) complex amplitudes as functions of range at $f_c = 161$ Hz, $z_s = 20$ m, $1501 \leqslant r \leqslant 1900$.

Observations $\hat{x}_l(r_n, z_j)$ of (2) on a uniformly spaced grid, at time points $t(r_n)$, are obtained as follows. Introduce relative time for notional convenience. For each one of the emitter frequencies: (a) A smooth approximation of the source–receiver range as a function of continuous time t is obtained by least-squares fitting B-splines to ranging data, removing obvious outliers. The smoothed range function is then interpolated by Hermite polynomials to evaluate $t(r_n)$. (b) Least-squares fits of (23), (24) to data $\hat{s}_{\text{ref},1}(t), \hat{s}_{j,1}(t)$ in short duration time windows centered around $t(r_n)$, representing the receiver in-phase and quadrature components as polynomial functions of time, yields estimates of f_c, φ_{ref}, ψ_{ref}, $\varphi_j(t(r_n)), \psi_j(t(r_n))$. Finally, collect $\hat{x}_l(r_n, z_j)$ $n = 1,...,N$ in $\hat{\mathbf{x}}_{j,1}$ and $\hat{\mathbf{x}}_{j,1}$ $j = 1,...,J$ in $\hat{\mathbf{X}}_1$ which constitutes a 2-D array.

The numerical minimization of the object function in (17), known as the variable projection functional,[19] is done using a trust region method (Ref. 20, pp. 77–88). For numerical stability, the computation of $\mathbf{P}$ is based on the QR decomposition of $\mathbf{A}$, i.e., $\mathbf{A} = \mathbf{QR}$, by the modified Gram–Schmidt orthogonalization (Ref. 1, p. 218) yielding $\mathbf{P} = \mathbf{QQ}^H$. A detailed implementation of the gradient and Hessian of the variable projection functional based on the differentiation of $\mathbf{Q}$ is given in Appendix C. Initial values are provided by FFTs of $\hat{\mathbf{x}}_{1,1} \cdots \hat{\mathbf{x}}_{J,1}$. The K highest peaks in each spectrum indicate the location of the propagating mode wave numbers. Using each one of the resulting J different sets of initial values, the variable projection functional is minimized. Among the resulting J sets of minimizers, those having different modes with almost equal wave numbers and shapes are considered as ''defective'' and deleted. The minimizer yielding minimum variance $\hat{\sigma}^2$ is considered as a maximum-likelihood estimate. Note that defective sets may occur due to mode splitting effects, or when K exceeds the number of modes required for synthesizing the data. Since the number of propagating modes is *a priori* unknown, this procedure is repeated, each time increasing the value of K by one, until the minimum variance ceases to decrease or all minimizers are deleted.

Analysis results from two data sets are presented: $f_c = 80$ Hz, $z_s = 20$ m, $1101 \leqslant r \leqslant 1500$; $f_c = 161$ Hz, $z_s = 20$ m, $1501 \leqslant r \leqslant 1900$. After some experimentation, the in-phase and quadrature components where approximated by fifth degree polynomials, the complex amplitudes were estimated from 1-s sliding time windows on grids where $\Delta r = 1$ m, see the dotted lines in Figs. 2 and 3. The solid lines in Figs. 2 and 3 show the synthesized complex amplitude, see (2), evaluated on the aperture grid using ML estimates of the wave numbers shown in Table I and amplitudes computed using (14). The synthesized field agrees indeed well

TABLE I. Estimated wave numbers (m^{-1}) at: $f_c = 80$ Hz, $z_s = 20$ m, $1101 \leqslant r \leqslant 1500$; $f_c = 161$ Hz, $z_s = 20$ m, $1501 \leqslant r \leqslant 1900$.

Frequency	Mode 1	Mode 2	Mode 3	Mode 4	Mode 5	Mode 6	Mode 7	Mode 8	q_{res}
80 Hz	0.344 07	0.334 76	0.285 33	0.272 22	0.242 86				−18.1
161 Hz	0.695 90	0.684 06	0.661 21	0.643 97	0.636 87	0.607 02	0.562 32	0.555 05	−14.7

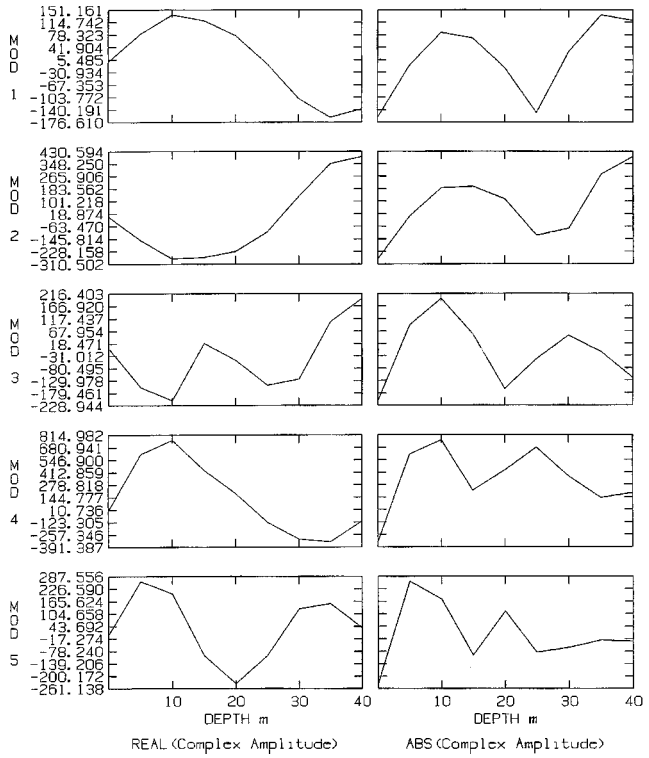

FIG. 4. Estimated modes as functions of depth at $f_c=80$ Hz, $z_s=20$ m, $1101\leqslant r\leqslant 1500$.

with the unprocessed complex amplitude data, offering low residual values $q_{\text{res}}=10\log(JN\hat{\sigma}^2_{\text{ML}}/\|\hat{\mathbf{X}}_1\|_F^2)$. Figures 4 and 5 show the modal eigenfunctions, obtained by linear interpolation of the estimated amplitudes.

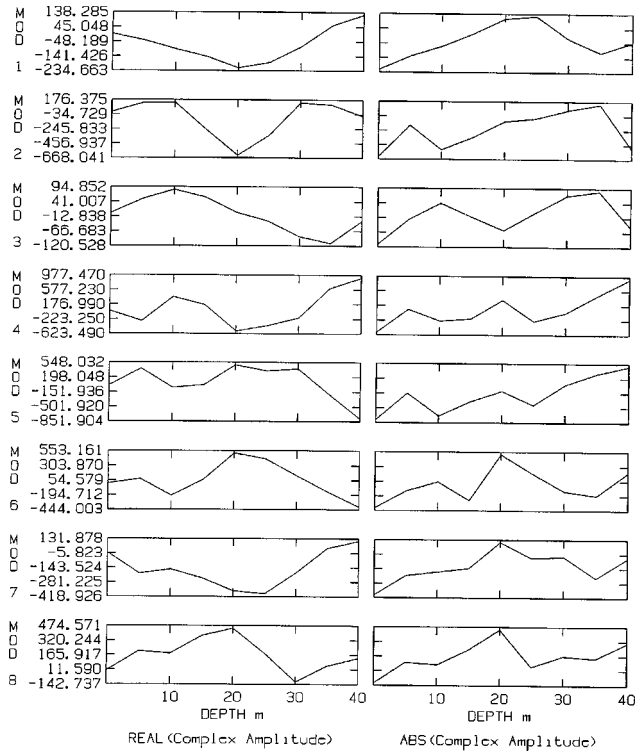

FIG. 5. Estimated modes as functions of depth at $f_c=161$ Hz, $z_s=20$ m, $1501\leqslant r\leqslant 1900$.

V. DISCUSSION

High-resolution model oriented methods of modal decomposition are indisputably superior compared with Hankel transformation. The choice of a particular method strongly depends, however, on the statistical properties of the assumed physical model; its optimality is reflected by the resulting residual between the model and the observations. In this work, it is assumed that the oceanic medium is range independent, the wave field is deterministic and time invariant. A model of the density and likelihood functions of the wave field, excited by a monochromatic source, sampled on a vertical plane by a rectangular receiver array, is formulated. The CRB of the variance of the estimates of wave numbers, and noise variance as functions of array size, number of sensors, and observations is formulated. For arrays with large horizontal aperture, dense in the vertical direction it is shown that the CRB of the wave number variance is inversely proportional to: the portion of the modal energy within the array; the wave number magnitude; the number of observations; the number of sensor depths (i.e., 2-D processing is more efficient than individual processing of each array depth); the squared number of sensors/depth. A ML estimator of modal parameters is proposed and shown to be consistent at finite array size and number of sensors, provided that the number of observations is large. Analytical formulas of the first and second derivative of the associated variable projection functional are provided in purpose of its numerical minimization. It is claimed that the wave-field correlation matrix may consistently be replaced with the eigenrepresentation of its modal part.

The ML estimator is used in a modal analysis of 2-D synthetic apertures collected in Kalmarsund. A high number of modes is resolved from moderate aperture lengths. Good agreement is achieved between the synthesized and observed wave field; confirming the feasibility of the method. An environmental parameter inversion of the Kalmarsund data, based on a distributed genetic algorithm[21] combined with a Gauss Newton method and XFEM,[22] are presented in work in preparation.

ACKNOWLEDGMENTS

I gratefully acknowledge Professor Ilkka Karasalo for helpful and stimulating discussions. Thanks are also due to Dr. John Robinson for his peer review, Dr. Jorgen Pihl who helped me with the implementation of the data logging system, and the FOA crew I joined during the Kalmarsund experiment, including Lennart Berghult, Sixten Erixon, Frank Gustavsson, Arne Gjärdman, Lars Lekzen, Per Moren, Olle Nyström, Jörgen Pihl, and Viggo Westerling. The Swedish Defence Materials Administration supported the experiment by participating with the research vessel H.M.S. Urd under the command of Captain Stang.

APPENDIX A: SOME ISSUES ON THE CRB OF THE WAVE NUMBERS AND THE VARIANCE

Differentiate (9) with respect to the unknown parameters

$$\frac{\partial Y}{\partial \sigma^2}=-\frac{JLN}{\sigma^2}+\frac{1}{\sigma^4}\sum_{l=1}^{L}\sum_{j=1}^{J}\hat{\mathbf{h}}_{j,l}^H\hat{\mathbf{h}}_{j,l}, \tag{A1}$$

$$(\partial/\partial\ \mathrm{Re}\{g_1(z_j)\}\cdots\partial/\partial\ \mathrm{Re}\{g_K(z_j)\})^T\ \ Y$$
$$= \frac{2}{\sigma^2}\sum_{l=1}^{L}\ \mathrm{Re}\{\mathbf{A}^H\hat{\mathbf{h}}_{j,l}\}, \tag{A2}$$

$$(\partial/\partial\ \mathrm{Im}\{g_1(z_j)\}\cdots\partial/\partial\ \mathrm{Im}\{g_K(z_j)\})^T\ \ Y$$
$$= \frac{2}{\sigma^2}\sum_{l=1}^{L}\ \mathrm{Im}\{\mathbf{A}^H\hat{\mathbf{h}}_{j,l}\}, \tag{A3}$$

$$(\partial/\partial\alpha_1\cdots\partial/\partial\alpha_K)^T\ \ Y$$
$$= \frac{2}{\sigma^2}\sum_{l=1}^{L}\sum_{j=1}^{J}\ \mathrm{Re}\{\mathrm{diagm}\{\mathbf{g}_j\}^H\mathbf{D}^H\hat{\mathbf{h}}_{j,l}\}. \tag{A4}$$

To obtain the CRB of the estimates for $L=1$ see Ref. 12. For $L>1$, by the independence assumption, the noise vectors $\hat{\mathbf{h}}_{j,l}$ are mutually uncorrelated with respect to l. When taking the expectation of pair products of (A1)–(A4), needed for the evaluation of the information matrix, the additional summation over l therefore will contribute with an additional factor L.

APPENDIX B: CRB OF WAVE NUMBERS FOR VERTICALLY DENSE HORIZONTALLY LARGE ARRAYS

By (10)

$$\lim_{N\to\infty} N^2\mathrm{CRB}(\alpha_1,\ldots,\alpha_K J,L,N)$$
$$= \lim_{N\to\infty}\frac{\sigma^2}{2JL}\left(\frac{1}{J}\sum_{j=1}^{J}\ \mathrm{Re}\left\{\mathrm{diagm}\{\mathbf{g}_j\}^H\left(\frac{1}{N^2}\,\mathbf{D}^H\mathbf{D}\right.\right.\right.$$
$$\left.\left.\left.-\left[\frac{1}{N}\,\mathbf{D}^H\mathbf{A}(\mathbf{A}^H\mathbf{A})^{-1}\,\frac{1}{N}\,\mathbf{A}^H\mathbf{D}\right]\right)\mathrm{diagm}\{\mathbf{g}_j\}\right\}\right)^{-1}. \tag{B1}$$

Without loss of generality let $r_0=M\Delta r$, where M is a large integer. Since $\lim_{N\to\infty}(\Sigma_{n=1}^{N}(1/n)-\log(N))=C_E$, where C_E designates the Euler constant, it follows that

$$\lim_{N\to\infty}\left((\mathbf{A}^H\mathbf{A})(k,k)-\frac{1}{\Delta r}\log(N+M)\right)$$
$$= \frac{1}{\Delta r}\left(C_E-\sum_{n=1}^{M}\ \frac{1}{n}\right), \tag{B2}$$

$$\lim_{N\to\infty}(\mathbf{A}^H\mathbf{A})(k,l\neq k)$$
$$= -\frac{\ln(2\sin((\alpha_l-\alpha_k)\Delta r/2))}{\Delta r}$$
$$+\frac{\mathbf{i}(\pi-(\alpha_l-\alpha_k))}{2}-\frac{1}{\Delta r}\sum_{n=1}^{M}\ \frac{e^{\mathbf{i}(\alpha_l-\alpha_k)\Delta n}}{n}, \tag{B3}$$

where $(\mathbf{A}^H\mathbf{A})(k,l)$ designates the (k,l)-th element of $\mathbf{A}^H\mathbf{A}$ and (B3) is obtained using (Ref. 16, p. 1005).

Since $\lim_{N\to\infty}(1/N^{m+1})\Sigma_{n=1}^{N}n^m e^{i(\alpha_l-\alpha_k)n}=[1/(m+1)]\times\delta_{k,l}$, see Ref. 12, it follows that

$$\lim_{N\to\infty}\frac{1}{N}(\mathbf{D}^H\mathbf{A})(k,l)=\lim_{N\to\infty}\frac{-\mathbf{i}e^{\mathbf{i}(\alpha_l-\alpha_k)\Delta rM}}{N}\ \sum_{n=1}^{N}\ e^{\mathbf{i}(\alpha_l-\alpha_k)\Delta rn}$$
$$= -\mathbf{i}\delta_{k,l}. \tag{B4}$$

$$\lim_{N\to\infty}\frac{1}{N^2}(\mathbf{D}^H\mathbf{D})(k,l)$$
$$= \lim_{N\to\infty}\frac{\Delta r e^{\mathbf{i}(\alpha_l-\alpha_k)\Delta rM}}{N^2}$$
$$\times\left(M\sum_{n=1}^{N}\ e^{\mathbf{i}(\alpha_l-\alpha_k)\Delta rn}+\sum_{n=1}^{N}\ ne^{\mathbf{i}(\alpha_l-\alpha_k)\Delta rn}\right)$$
$$= \frac{\Delta r}{2}\,\delta_{k,l}\,. \tag{B5}$$

From (B2)–(B3) it follows that, for fix M, diagonal entries in $\mathbf{A^H A}$ grow as $\log(N)$ while off-diagonal entries are bounded. Thus entries in its inverse tend to zero.

For instance

$$\|(\mathbf{A}^H\mathbf{A})^{-1}\|_\infty$$
$$\leqslant\frac{\Delta r}{\ln(N/M)}\left(1+\frac{4(K-1)}{(M+1)\Delta r\Delta\alpha\ \ln(N/M)}\right.$$
$$\left.+O\left(\frac{\|\mathbf{B}\|_\infty^2}{1-\|\mathbf{B}\|_\infty}\right)\right), \tag{B6}$$

where $\Delta\alpha=\min\{|\alpha_l-\alpha_k|\}$, $l\neq k$, $\mathbf{B}=\boldsymbol{\epsilon}^{-1}(\mathbf{A}^H\mathbf{A}-\boldsymbol{\epsilon})$ and $\boldsymbol{\epsilon}=\mathrm{diagm}\{[\mathbf{A}^H\mathbf{A}(1,1)\cdots\mathbf{A}^H\mathbf{A}(K,K)]^T\}$. Since entries in $\mathbf{A}^H\mathbf{D}/N$ remain bounded, entries in $\mathbf{D}^H\mathbf{A}(\mathbf{A}^H\mathbf{A})^{-1}\mathbf{A}^H\mathbf{D}/N^2$ tend to zero. Substituting (B5) in (B1) yields (12).

From (B6) and that off-diagonal entries (B4) tend to zero as $O(1/[N(\alpha_l-\alpha_k)])$ it follows that (12) approximates (10) when $N\gg M$ and $N(\alpha_l-\alpha_k)\gg 1$.

APPENDIX C: GRADIENT AND HESSIAN OF THE VARIABLE PROJECTION FUNCTIONAL

The gradient and the Hessian entries of the variable projection functional, i.e., (17), are

$$(\mathrm{trace}\{(\mathbf{I}-\mathbf{P})\cdot\hat{\boldsymbol{\Xi}}\})_{\partial i}=-\mathrm{trace}\{\mathbf{Q}^H\hat{\boldsymbol{\Xi}}\mathbf{Q}_{\partial i}+(\cdots)^H\}, \tag{C1}$$

$$(\mathrm{trace}\{(\mathbf{I}-\mathbf{P})\cdot\hat{\boldsymbol{\Xi}}\})_{\partial i\ \partial j}=-\mathrm{trace}\{\mathbf{Q}_{\partial j}^H\hat{\boldsymbol{\Xi}}\mathbf{Q}_{\partial i}$$
$$+\mathbf{Q}^H\hat{\boldsymbol{\Xi}}\mathbf{Q}_{\partial i\ \partial j}+(\cdots)^H\}. \tag{C2}$$

Matrices $\mathbf{Q}_{\partial i}$, $\mathbf{Q}_{\partial i\ \partial j}$ are obtained by the following procedure:

Differentiate $\mathbf{Q}^HQ=\mathbf{1}$ once to obtain

$$(\mathbf{Q}^H\mathbf{Q})_{\partial i}=\mathbf{Q}_{\partial i}^H\mathbf{Q}+(\cdots)^H=\mathbf{0}, \tag{C3}$$

$$\mathbf{Q}_{\partial i}^H\mathbf{Q}=-\mathbf{Q}^H\mathbf{Q}_{\partial i}\,. \tag{C4}$$

Differentiate $\mathbf{Q}^H\mathbf{Q}=\mathbf{1}$ twice to obtain

$$(\mathbf{Q}^H\mathbf{Q})_{\partial i\ \partial j}=\mathbf{Q}_{\partial i\ \partial j}^H\mathbf{Q}+\mathbf{Q}_{\partial i}^H\mathbf{Q}_{\partial j}+(\cdots)^H=\mathbf{0}, \tag{C5}$$

$$\mathbf{Q}_{\partial i\ \partial j}^H\mathbf{Q}+(\cdots)^H=-\mathbf{Q}_{\partial i}^H\mathbf{Q}_{\partial j}-(\cdots)^H. \tag{C6}$$

Differentiate $\mathbf{A}=\mathbf{QR}$ to obtain

$$\mathbf{A}_{\partial i}=\mathbf{Q}_{\partial i}\mathbf{R}+\mathbf{Q}\mathbf{R}_{\partial i}\,, \tag{C7}$$

$$\mathbf{Q}^H\mathbf{A}_{\partial i}\mathbf{R}^{-1}=\mathbf{Q}^H\mathbf{Q}_{\partial i}+\mathbf{R}_{\partial i}\mathbf{R}^{-1}, \tag{C8}$$

$$\mathbf{Q}^H\mathbf{A}_{\partial i}\mathbf{R}^{-1}+(\cdots)^H=\mathbf{Q}^H\mathbf{Q}_{\partial i}+\mathbf{R}_{\partial i}\mathbf{R}^{-1}+(\cdots)^H$$
$$=\{\text{due to (C3)}\}=\mathbf{R}_{\partial i}\mathbf{R}^{-1}+(\cdots)^H. \tag{C9}$$

Since: the left-hand side of (C9) is a matrix with real diagonal elements, the inverse of an upper (lower) triangular matrix is upper (lower) triangular, the product of two upper (lower) triangular matrices is upper (lower) triangular; $\mathbf{R}_{\partial i}\mathbf{R}^{-1}$ designated by $\mathbf{M_i}$ becomes

$$\mathbf{M_i}=\mathbf{R}_{\partial i}\mathbf{R}^{-1}=\text{triu}\{\mathbf{Q}^H\mathbf{A}_{\partial i}\mathbf{R}^{-1}+(\mathbf{Q}^H\mathbf{A}_{\partial i}\mathbf{R}^{-1})^H\}$$
$$-\tfrac{1}{2}\,\text{diagm}\{\mathbf{Q}^H\mathbf{A}_{\partial i}\mathbf{R}^{-1}+(\mathbf{Q}^H\mathbf{A}_{\partial i}\mathbf{R}^{-1})^H\}. \tag{C10}$$

Multiplying (C7) from right by $\mathbf{R}^{-1}$, inserting (C10), and rearranging yields

$$\mathbf{Q}_{\partial i}=\mathbf{A}_{\partial i}\mathbf{R}^{-1}-\mathbf{Q}\mathbf{M_i}. \tag{C11}$$

Differentiate (C7) to obtain

$$\mathbf{A}_{\partial i\ \partial j}=\mathbf{Q}_{\partial i\ \partial j}\mathbf{R}+\mathbf{Q}_{\partial i}\mathbf{R}_{\partial j}+\mathbf{Q}_{\partial j}\mathbf{R}_{\partial i}+\mathbf{Q}\mathbf{R}_{\partial i\ \partial j}, \tag{C12}$$

$$\mathbf{Q}^H\mathbf{A}_{\partial i\ \partial j}\mathbf{R}^{-1}=\mathbf{Q}^H\mathbf{Q}_{\partial i\ \partial j}+\mathbf{Q}^H\mathbf{Q}_{\partial i}\mathbf{R}_{\partial j}\mathbf{R}^{-1}+\mathbf{Q}^H\mathbf{Q}_{\partial j}\mathbf{R}_{\partial i}\mathbf{R}^{-1}$$
$$+\mathbf{R}_{\partial i\ \partial j}\mathbf{R}^{-1}, \tag{C13}$$

$$\mathbf{Q}^H\mathbf{A}_{\partial i\ \partial j}\mathbf{R}^{-1}+(\cdots)^H=\mathbf{Q}^H\mathbf{Q}_{\partial i}\mathbf{R}_{\partial j}\mathbf{R}^{-1}+\mathbf{Q}^H\mathbf{Q}_{\partial j}\mathbf{R}_{\partial l}\mathbf{R}^{-1}$$
$$+\mathbf{R}_{\partial i\ \partial j}\mathbf{R}^{-1}+\mathbf{Q}^H\mathbf{Q}_{\partial i\ \partial j}+(\cdots)^H$$
$$=\{\text{due to (C6)}\}=\mathbf{Q}^H\mathbf{Q}_{\partial i}\mathbf{R}_{\partial j}\mathbf{R}^{-1}$$
$$+\mathbf{Q}^H\mathbf{Q}_{\partial j}\mathbf{R}_{\partial i}\mathbf{R}^{-1}+\mathbf{R}_{\partial i\ \partial j}\mathbf{R}^{-1}$$
$$-\mathbf{Q}_{\partial i}^H\mathbf{Q}_{\partial j}+(\cdots)^H. \tag{C14}$$

Introducing

$$\mathbf{G_{ij}}=\mathbf{Q}^H\mathbf{A}_{\partial i\ \partial j}\mathbf{R}^{-1}+\mathbf{Q}_{\partial i}^H\mathbf{Q}_{\partial j}-\mathbf{Q}^H\mathbf{Q}_{\partial i}\mathbf{M_j}-\mathbf{Q}^H\mathbf{Q}_{\partial j}\mathbf{M_i} \tag{C15}$$

and substituting in (C14) yields

$$\mathbf{G_{ij}}+(\cdots)^H=\mathbf{R}_{\partial i\ \partial j}\mathbf{R}^{-1}+(\cdots)^H. \tag{C16}$$

Designate $\mathbf{R}_{\partial i\ \partial j}\mathbf{R}^{-1}$ in (C16) by $\mathbf{M_{ij}}$ and use previously stated properties of triangular matrices to obtain

$$\mathbf{M_{ij}}=\mathbf{R}_{\partial i\ \partial j}\mathbf{R}^{-}=\text{triu}\{\mathbf{G_{ij}}+\mathbf{G_{ij}^H}\}-\tfrac{1}{2}\text{diagm}\{\mathbf{G_{ij}}+\mathbf{G_{ij}^H}\}. \tag{C17}$$

Multiplying (C12) from right by $\mathbf{R}^{-1}$, inserting $\mathbf{M_{ij}}$, and rearranging yields

$$\mathbf{Q}_{\partial i\ \partial j}=\mathbf{A}_{\partial i\ \partial j}\mathbf{R}^{-1}-\mathbf{Q}_{\partial i}\mathbf{M_j}-\mathbf{Q}_{\partial j}\mathbf{M_i}-\mathbf{Q}\mathbf{M_{ij}}. \tag{C18}$$

[1] G. H. Golub and C. F. Van Loan, *Matrix Computations* (Johns Hopkins U.P., Baltimore, 1989).
[2] A. Graham, *Kronecker Products and Matrix Calculation with Applications* (Ellis Horwood, London, 1981).
[3] S. D. Rajan, J. F. Lynch, and G. V. Frisk, ''Perturbative inversion methods for obtaining bottom geoacoustic parameters in shallow water,'' J. Acoust. Soc. Am. **82**, 998–1017 (1987).
[4] G. V. Frisk and J. F. Lynch, ''Shallow water waveguide characterization using the Hankel transform,'' J. Acoust. Soc. Am. **76**, 205–216 (1986).
[5] G. V. Frisk, J. F. Lynch, and S. D. Rajan, ''Determination of compressional wave speed profiles using modal inverse techniques in a range-independent environment in Nantucket Sound,'' J. Acoust. Soc. Am. **86**, 1928–1939 (1989).
[6] H. M. Chouhan and G. V. Anand, ''Normal mode wave-number estimation using a towed array,'' J. Acoust. Soc. Am. **93**, 1807–1814 (1993).
[7] R. O. Schmidt, ''A signal subspace approach to multiple emitter location and spectral estimation,'' Ph.D. thesis, Stanford University, Stanford, CA, 1981.
[8] S. D. Rajan and S. D. Bhata, ''Evaluation of high-resolution frequency estimation methods for determining frequencies of eigenmodes in shallow water acoustic field,'' J. Acoust. Soc. Am. **93**, 378–389 (1993).
[9] R. Roy and T. Kailath, ''ESPRIT-Estimation of signal parameters via rotational invariance techniques,'' IEEE Trans. Acoust., Speech, Signal Process. **ASSP 37**, 984–955 (1989).
[10] E. Parastates, ''Modal structure analysis of experimental data from a shallow water wave guide by use of classical and parametric methods,'' in Proceedings of the Second European Conference on Underwater Acoustics, Lyngby, 1994, pp. 999–1004.
[11] E. Parastates, ''Modal structure analysis of experimental data from a synthetic aperture arrays using a non linear parametric method,'' in Proceedings of the Full Field Inversion Methods in Ocean and Seismo-Acoustics, Lerici, 1994.
[12] P. Stoica and A. Nehorai, ''MUSIC, Maximum Likelihood and Cramer-Rao Bound,'' IEEE Trans. Acoust., Speech, Signal Process. **ASSP-37**, 720–741 (1989).
[13] B. E. Ottersten, ''Parametric subspace fitting methods for array signal processing,'' Ph.D. thesis, Stanford University, Stanford, CA, 1989.
[14] M. Kendall and A. Stuart, *The Advanced Theory of Statistics* (Griffin, London, 1979), Vol. 2.
[15] L. Brekhovskikh and Y. Lysanov, *Fundamentals of Ocean Acoustics* (Springer-Verlag, Berlin, 1982).
[16] M. Abramowitz and I. A. Stegun, *Handbook of Mathematical Functions With Formulas, Graphs, and Mathematical Tables* (National Bureau of Standards, Washington, DC, 1964), Applied Mathematics Series.
[17] C. W. Therrien, *Discrete Random Signals and Statistical Signal Processing* (Prentice-Hall, Englewood Cliffs, NJ, 1992).
[18] J. Pihl, M. Hammarström, and P. Moren, ''Hydroakustiska mätningar med knallskott,'' FOA rapport, 1990, in Swedish.
[19] G. H. Golub and V. Pereyra, ''The differentiation of pseudo-inverses and nonlinear least squares problems whose variables separate,'' SIAM (Soc. Ind. Appl. Math.) J. Numer. Anal. **10**, 413–432 (1973).
[20] P. E. Gill, W. Murray, and M. H. Wright, *Practical Optimization* (Academic, London, 1981).
[21] D. Whitley and T. Starkweather, ''Genitor II: a distributed genetic algorithm,'' J. Exp. Theor. Artif. Intell. **2**, 189–214 (1990).
[22] I. Karasalo, ''Exact finite elements for wave propagation in range-independent fluid-solid media,'' J. Sound Vib. **172**, 671–688 (1994).

Array element localization for horizontal arrays via Occam's inversion

Stan E. Dosso[a] and Mark R. Fallat
School of Earth and Ocean Sciences, University of Victoria, Victoria, BC V8W 3P6, Canada

Barbara J. Sotirin
Cold Regions Research and Engineering Laboratory, US Army Corps of Engineers, 72 Lyme Road, Hanover, New Hampshire 03755-1290

John L. Newton
Polar Associates, Inc., 100 Burns Place, Goleta, California 93117

(Received 22 September 1997; accepted for publication 25 March 1998)

Accurate locations for the individual elements of an acoustic sensor array are required for the application of advanced array processing methods. This paper develops a general method of localizing horizontal line array (HLA) elements which overcomes bandwidth constraints of low-frequency arrays and uncertainty in the experimental configuration. Array elements are localized for two HLA's associated with the Spinnaker Array, a three-dimensional sensor array located in the high Arctic. Recordings were made of imploding glass light bulbs deployed at a series of locations surrounding the array site. Implosion instants were not measured; hence, the data consist of relative travel times. In addition, the source locations were measured only approximately in the field, and are treated as unknown parameters. The inverse problem of determining hydrophone and source locations is nonunique and ill-conditioned. To determine the most physically meaningful solution, an iterative linearized inversion is developed which applies the method of regularization to include *a priori* information about the solution. Available *a priori* information includes source–location estimates from on-ice measurements, depth estimates for the array end points, and the expectation that each HLA is essentially linear. The inversion is formulated to jointly minimize the parameter-estimate residuals and the three-dimensional curvature of each HLA, subject to fitting the array element localization (AEL) data to a statistically appropriate level. Minimizing HLA curvature produces the simplest array shape that is consistent with the data: any deviations from a straight array are definitely required by the data, and are not artifacts of the inversion algorithm or starting model. © *1998 Acoustical Society of America.* [S0001-4966(98)05107-8]

PACS numbers: 43.30.Xm, 43.60.Pt [DLB]

INTRODUCTION

Measuring ocean acoustic fields at an array of sensors allows the application of advanced signal processing methods such as beamforming[1] and matched-field processing and inversion.[2–6] However, the application of such methods requires accurate knowledge of the positions of the individual sensors. For example, as a general rule, in order to achieve a loss of less than 1 dB in array processing gain, the sensor positions must be known to within $\lambda/10$, where λ is the wavelength at the frequency of interest.[7,8] Deploying hydrophone arrays, either at sea or through Arctic ice cover, is not an exact procedure, and sufficiently accurate sensor positions are rarely known after the fact. In most cases, an acoustic survey is required to localize the sensors after deployment, a procedure referred to as array element localization (AEL). AEL surveys generally consist of measuring the travel times of acoustic signals transmitted from a series of known positions to the sensors to be localized. Given knowledge of the ocean sound speed, these travel-time data can then be inverted for estimates of the sensor locations.

In the case of a dynamic array, such as a vertical line array (VLA) that moves with currents in the water column, AEL is required on an on-going basis. AEL systems for VLA's are typically based on continually transmitting signals from a set of acoustic transponders positioned about the array on the seafloor.[9–11] This procedure allows the position of the array elements to be tracked with time.

In the case of a static array, such as a horizontal line array (HLA) fixed to the seafloor, AEL is required only once.[12,13] A simple and practical set of AEL measurements for a static array can be obtained by deploying acoustic sources at a series of positions about the array site and recording the arrivals at the sensors. The sources can be deployed from a ship in open water, or from the ice cover in the Arctic. Synchronization in time between the source transmissions and the recording system is not required (i.e., sensor locations can be determined from relative travel-time measurements, although absolute measurements are superior). Note that in AEL surveys of this nature, the uncertainties in the source positions are often significant, and may introduce greater errors than the uncertainties in the travel-time data themselves. AEL based on relative travel-time

[a]Electronic mail: sdosso@uvic.ca

measurements and an approximate knowledge of source positions is the focus of this paper.

The problem of determining a model for the array element locations based on travel-time measurements represents a nonlinear inverse problem which is inherently nonunique (i.e., an infinite number of acceptable models exist which fit the data). This nonuniqueness is exacerbated when the data represent relative (rather than absolute) travel times and when source positions are only approximately known. Since the data do not uniquely determine the sensor positions, the approach to the inversion can be an important factor influencing the character of the solution. Many inversion algorithms are based on determining the model which minimizes the misfit to the measured data, subject to stability constraints which often serve to keep the solution close to some initial model. Although this provides a mathematical formulation of the inversion, it is not physically meaningful to seek a misfit smaller than that defined by the uncertainty of the data.[14,15] In fact, seeking to fit the data too closely can introduce extraneous (unphysical) structure into the model in an attempt to fit the noise on the data.

This paper develops an inversion algorithm for AEL based on a somewhat different approach. Rather than minimizing the misfit to the data, the inversion is formulated to achieve a misfit that is statistically consistent with the estimated uncertainties of the data, while explicitly applying additional independent information about the solution, known as *a priori* information, to the inversion. To treat the general problem of HLA localization with relative travel-time data and inaccurate source positions, the source–transmission instants and source positions are included along with sensor positions as unknown parameters in the inversion. *A priori* information regarding these parameters is usually available from the array deployment and/or AEL survey. For instance, although the uncertainties in source–position measurements may require that they be treated as unknown parameters, the measurements nonetheless provide useful prior estimates for these parameters. Prior estimates may also be available for some (or all) sensor locations. More typically, for an HLA deployed in a straight line, the *a priori* expectation that the array shape is well approximated by a linear function can be applied by minimizing the three-dimensional curvature of the array. This essentially applies *a priori* information about the correlation between sensor positions, rather than information about the positions themselves. If the HLA is deployed in a series of linear segments, the curvature of each segment can be minimized independently.

In addition to applying the *a priori* expectation of a linear array, minimizing HLA curvature has the benefit of producing the simplest model for the array shape, in the sense that it contains the minimum amount of structure or detail necessary to fit the travel-time data. In this model, any deviations from a straight array are definitely required by the data, and are not simply artifacts of the nonuniqueness or the inversion procedure. The minimum-curvature HLA model may be considered the ''best'' interpretation, in the sense that any other interpretation is unnecessarily complex in satisfying the data. In geophysical inverse theory, the construction of minimum-structure models such as this is often referred to as Occam's inversion,[15] in reference to Occam's Razor which admonishes that hypotheses and interpretations should always be as simple as possible.

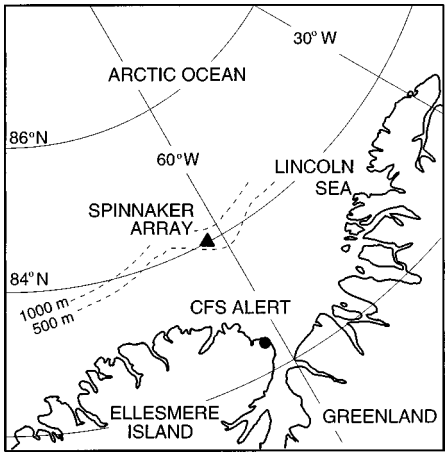

FIG. 1. Location of the Spinnaker Array.

In this paper, an algorithm is developed to apply Occam's inversion to AEL. The inversion is applied to determine sensor locations for a bottom-mounted HLA consisting of two linear segments. The HLA comprises part of the Spinnaker Array, a three-dimensional array of hydrophones deployed through the pack ice of the Lincoln Sea in the high Arctic.[16] Section I of this paper describes the Spinnaker Array and its deployment. Section II describes the AEL survey and subsequent data processing. Section III briefly reviews the inverse theory results that form the basis of the AEL inversion algorithm, describes the implementation of the algorithm, and presents a synthetic inversion example. Finally, Sec. IV presents the AEL inversion and a Monte Carlo uncertainty analysis for the Spinnaker HLA sensor positions.

I. SPINNAKER ARRAY

The Spinnaker Array (SA) was deployed in April 1996 in approximately 570 m of water near the edge of the continental shelf of the Lincoln Sea, north of Ellesmere Island, Canada, as shown in Fig. 1. The array site is within the domain of the permanent polar pack ice, with year-round ice thicknesses of 3–7 m on multiyear ice floes, and considerably more at pressure ridges. A schematic diagram of the SA is shown in Fig. 2. The array consists of a 2.4-km HLA of 80 hydrophones, a 240-m secondary HLA of 8 hydrophones oriented approximately perpendicular to the first HLA, and two

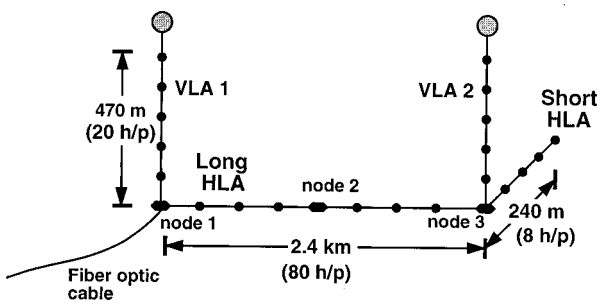

FIG. 2. Schematic diagram of the Spinnaker Array (h/p represents hydrophone).

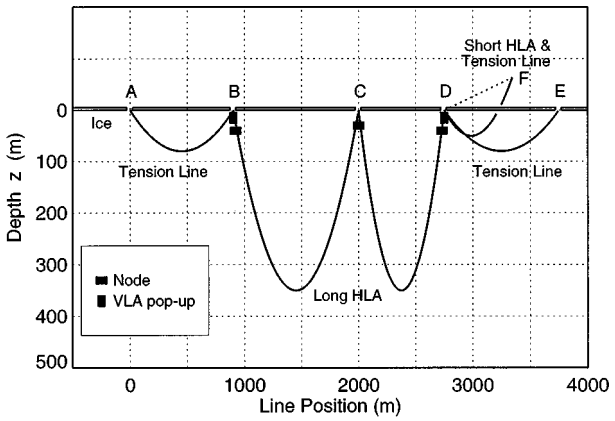

FIG. 3. Profile view of SA deployment procedure. Letters A–F refer to holes through the ice (see text).

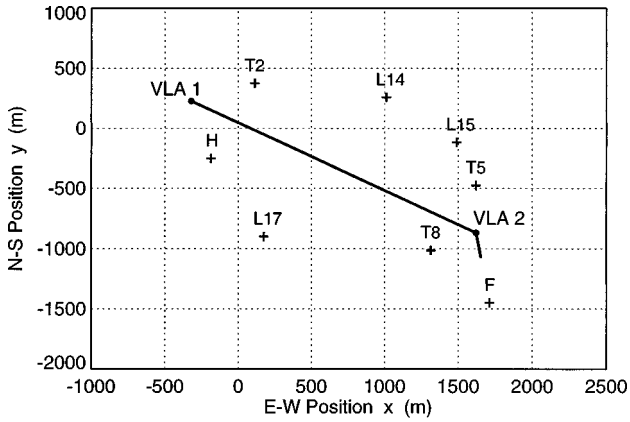

FIG. 4. Geometry of the AEL survey for the HLA sensors. The crosses indicate location of deployment holes for the light bulb sources. The solid line indicates the estimated position of the long and short HLA's. Solid circles indicate locations of the VLA's.

470-m VLA's of 20 hydrophones, one located at each end of the long HLA. The HLA sensors are located directly on the seafloor. The hydrophone signals are sampled at a rate of 256 Hz with a spectrally flat passband of 5–60 Hz. Digital acoustic data from the array are transferred 180 km over a seafloor fiber-optic cable to a land-based recording facility at CFS Alert on Ellesmere Island (Fig. 1). The same fiber also transfers commands and a master clock signal from CFS Alert to the SA. The electronics and optics associated with the SA are contained in three bottom-mounted electronics modules referred to as nodes.

To deploy the SA, an autonomous underwater vehicle (AUV) was used to string the HLA's between a series of holes through the ice, as shown in Fig. 3. At this stage, the two VLA's were contained in ''pop-up'' cannisters which were commanded to release the arrays after deployment was complete. The long HLA was suspended under the ice between three holes (labeled B, C, and D in Fig. 3), with one node suspended below each hole and a VLA cannister below the outer two holes. The short HLA was suspended in an orthogonal orientation at one end of the main HLA (holes D and F). Tensioning lines were strung under the ice from each end of the main HLA (holes A, E, and F). These lines were attached to the VLA cannisters and to one end of the short HLA, and were used to control the position of the cannisters as they were lowered and to ensure that the HLA's were as straight as possible on the seafloor. In order to perform continuous AEL for the VLA's, a high-frequency acoustic transponder system was deployed at each VLA site. Each system consisted of a transponder attached to the base of the VLA and four remote transponders positioned on the seafloor at ranges of $\sim$500 m. The locations of the transponders were determined to high precision by a series of acoustic measurements.[17] In order to localize the sensors of the HLA's, an AEL survey was carried out from the ice surface shortly after deployment of the SA was complete. This survey is described in the following section.

II. AEL SURVEY

A. AEL field work

The AEL survey carried out to determine the HLA sensor positions consisted of deploying impulsive sources at a series of locations around the SA, and recording the acoustic arrivals at the sensors (recording was carried out remotely via the fiber-optic cable at CFS Alert). The impulsive sources consisted of imploding glass light bulbs under hydrostatic pressure in the water column. Imploding light bulbs provide a simple, repeatable acoustic source that is safe and environmentally benign.[18] Light bulbs were deployed through eight holes drilled through the ice. Figure 4 shows the location of the light bulb deployment holes relative to the approximate HLA positions, as estimated from consideration of the deployment hole positions and line lengths (the coordinate system for the experiment was defined with x positive to the East, y positive to the North, and z positive downward). Five of the light bulb sites corresponded to preexisting holes which had been used for the SA deployment, the other three holes (L14, L15, and L17 in Fig. 4) were drilled specifically for the AEL survey. Three light bulbs were imploded at 25- and 50-m depths at each location. The implosion depth was controlled by lowering the light bulb on a line to the desired depth, then dropping a messenger weight along the line which burst the bulb on impact. The time of implosion was not measured in this procedure.

Relevant geometric and environmental parameters were measured at the SA site during the array deployment and AEL survey. The relative locations of all ice holes were measured using a laser surveying instrument (geodimeter). Surveys were carried from a local origin near each VLA site. Relative to the local origin, these measurements are accurate to within approximately ± 0.2 m. However, a number of sightings taken over several days between the two local origins indicated that positioning between the two sites varied by up to 1.5 m. This variation was caused by a series of cracks in the ice between the two sites that opened and closed during the SA deployment and ensuing AEL measurements. Absolute location of the ice floe at the SA site was monitored using time-averaged GPS (Global Positioning System) satellite navigation employing military precision codes (P-codes), which indicated no discernible movement of the sea ice for a period of several days to an uncertainty of ± 5 m. Assuming the ice was stationary during the AEL survey, the uncertainty in the x-y (horizontal) position of the

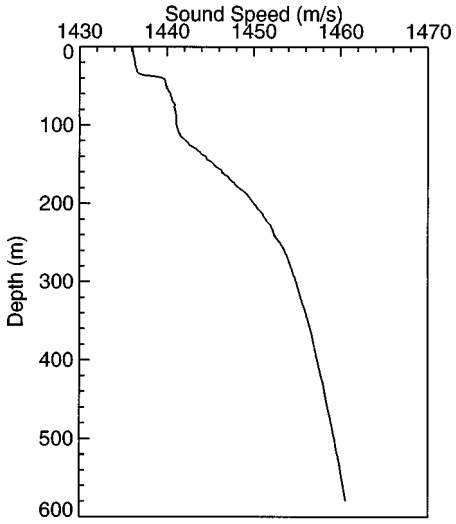

FIG. 5. Sound-speed profile measured by CTD cast at the array site.

sources due to the survey uncertainties and possible effects of currents in the water column was estimated to be ± 2 m. The uncertainty in the z (vertical) source positions was taken to be ± 0.5 m. The water depth at each hole was measured using an echo depth-sounder: measured depths varied from 550 to 580 m, with an estimated accuracy of 1%. Ice thickness was also measured at each hole, and varied from 3 to 4 m. The sound-speed profile over the water column was measured using a CTD (conductivity, temperature, depth) cast at the SA site, and is shown in Fig. 5 (sound speeds are considered accurate to ± 0.1 m/s).

Finally, constraints on the depth of the HLA sensors closest to the two VLA's can be assigned from the known depths of the acoustic transponders attached to the base of each VLA.[17] In particular, hydrophone 1 of the long HLA is located adjacent to VLA 1 (depth 562.8 m), and hydrophones 80 (long HLA) and 81 (short HLA) are adjacent to VLA 2 (depth 571.2 m). Given that these hydrophones are $\leqslant 30$ m from the VLA's and seafloor slopes are relatively gradual at the SA site, the uncertainty of these depth constraints is estimated to be ± 3 m. These HLA end-point depth estimates provide valuable *a priori* information for the AEL inversion.

B. AEL data

An example of the acoustic data from the AEL survey is given in Fig. 6(a), which shows the time series recorded at the HLA sensors for a light bulb implosion at 50-m depth in hole L17. This hole is located approximately broadside to the long HLA (Fig. 4). Hydrophones 1–80 in Fig. 6(a) correspond to the long HLA, while hydrophones 81–88 correspond to the short HLA (hydrophone numbers increase from the northwest to the southeast in Fig. 4). The dominant feature of Fig. 6(a) is the moveout in time of the light bulb arrivals across the arrays. For the long HLA, the moveout approximates the expected hyperbolic shape for an impulsive source broadside to a straight array. The slight undulations in the moveout between hydrophones 40 and 60 indicate that the array is not completely straight in this region. The abrupt

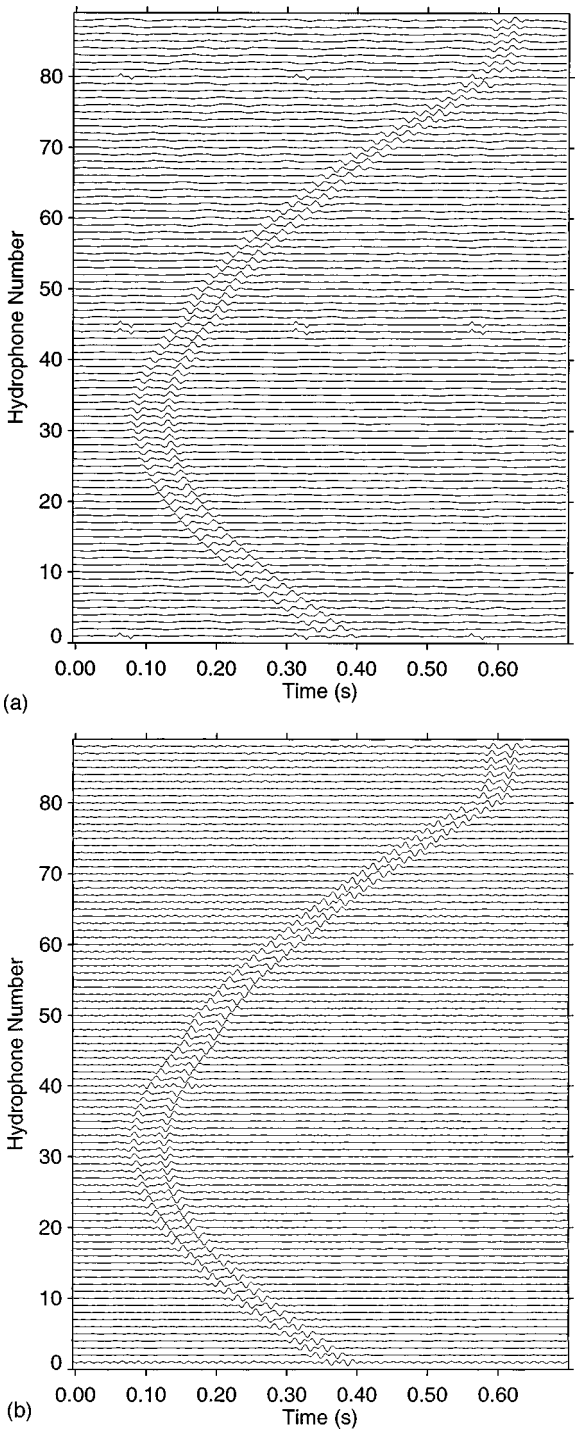

FIG. 6. Time series recorded on the long HLA (hydrophone numbers 1–80) and short HLA (numbers 81–88) for a 50-m light bulb source deployed in hole L17. (a) shows the raw section, (b) shows the processed section.

change in the moveout at hydrophone 81 is due to the different orientations of the long and short HLA's. The light bulb signals themselves consist of two arrivals: a direct arrival, followed shortly by a (phase-inverted) surface-reflected arrival. Higher-order reflections involving both the seafloor and ice surface were recorded, but are not included in the time window shown in Fig. 6. The time separation between the direct and surface-reflected arrivals decreases with increasing offset between source and hydrophone. For the light bulbs deployed at 50-m depth, the two arrivals could be dis-

tinguished at all hydrophones of the two HLA's. However, for the 25-m light bulbs, the two arrivals essentially merged at many hydrophones, precluding useful arrival-time picks. Therefore only the 50-m light bulb recordings are considered in this paper. The spurious pulses appearing every $\sim$0.25 s for hydrophones 1, 44, 45, and 80 in Fig. 6(a) represent electronic noise caused by the three nodes of the SA, which periodically corrupted the acoustic data of the adjacent hydrophones.

Prior to picking light bulb arrival times, a three-step processing sequence was applied to the recorded time series. In the first step, the spurious pulses induced by the nodes were removed by replacing the contaminated samples by values determined via linear interpolation of the adjacent data points. The second step of the processing sequence involved deconvolving the recorded time series to increase the effective bandwidth (the precision to which arrival-times can be picked depends directly on the waveform bandwidth). The raw light bulb recordings for this system have a useful bandwidth of approximately 30–60 Hz. The lower frequency limit is due to the low power of a light bulb source relative to the ambient noise level at low frequencies. The upper frequency limit is due to the anti-aliasing filter applied prior to digitization of the hydrophone signals at the sampling rate of 256 Hz. To increase the useful bandwidth, a deterministic deconvolution was applied to the HLA recordings. This procedure was based on the spectral division[19] of each record by an estimate of the incident light bulb wavelet. The wavelet estimate was taken from a light bulb direct arrival recorded at a VLA hydrophone located near the center of the water column. Since the deconvolution procedure can increase noise as well as signal levels, an optimum (Weiner) filter,[19] designed from samples of both signal and noise, was applied in conjunction with the deconvolution. The deconvolution and filtering procedure increased the useful signal bandwidth to approximately 30–100 Hz. The final processing step involved resampling the time series at a rate of 25 600 Hz (i.e., 100 times the original sampling rate) to better define the features (maxima and minima) of the arrival waveform. An example of the processed time series is given in Fig. 6(b).

To determine relative travel times from the (processed) HLA recordings requires picking the arrival times of the light-bulb signals. Since the HLA localization experiment yielded more than 2000 recordings (88 hydrophones, eight light bulb locations, three 50-m light bulbs at each location), an automated picking scheme was devised. This scheme was based on interactively defining the start and end points of the direct-arrival waveform on one hydrophone record for each light bulb (typically, the recording for the hydrophone closest to the source was selected). An adaptive matched filter was then used to automatically select this waveform on the remaining 87 records. For each record, the time of the waveform peak was picked to define the arrival time. Picking peak times proved to be a robust procedure that was not affected by interference between the tail of the direct arrival and the onset of the reflected arrival.

Since the light bulb implosion instants are not known, the arrival-time picks for each source represent a set of relative travel-time measurements. To compute means and standard deviations for the travel-times from the three 50-m light bulbs deployed at each source location, the three sets of picks must first be aligned in time. The simplest procedure is to align the sets of picks based on one arrival, e.g., aligning the earliest arrival on each set. This simple alignment is not optimal, however, since it is based on exactly aligning one arrival, while ignoring the alignment of all others. To improve on this procedure, alignment corrections were sought that minimized the sum of the arrival-time standard deviations (this sum provides a measure of the simultaneous alignment of all arrivals). Since only two corrections are required to optimally align three sets of picks, the minimization was carried out using a straightforward grid search technique. The alignment corrections typically reduced the standard deviation sum by approximately one third. Using the optimal alignment, travel-time means and standard deviations were computed for the eight source locations. Since the computed standard deviations were based on just three samples, the values tend to fluctuate from sensor to sensor. To obtain more stable estimates, a 15-point median filter was applied to the computed standard deviations for each source location. An additional (independent) uncertainty of 0.2 ms due to variability in the filter delay associated with each hydrophone was added to these standard deviations (values were combined as the square root of the sum of squares). The final standard deviation estimates for the travel-time measurements generally varied from 0.3 to 0.5 ms.

III. INVERSION ALGORITHM

A. General considerations

In this section an inversion algorithm is developed to determine the hydrophone locations for the two HLA's using the travel-time measurements described in Sec. II. In formulating the inversion algorithm, every effort was made to treat the data and available *a priori* information to within their estimated uncertainties. To this end, a forward-modeling study was carried out to investigate the significance of several sources of error relative to the uncertainties of the measured data. The results of the study are as follows. First, errors in the positions of the light-bulb sources of ± 2 m horizontally and ± 0.5 m vertically were found to lead to significant travel-time errors. Therefore the source locations are not treated as known values, but rather are included as unknown parameters in the inversion algorithm. Second, the effect of refraction in the water column was investigated. It was found that for propagation paths $\gtrsim$1000 m, the effects of ray curvature were significant, and therefore a raytracing-based inversion algorithm is developed here. Third, errors of ± 0.1 m/s in the sound-speed profile were found to lead to insignificant travel-time errors. Therefore the measured sound-speed profile is used in the inversion algorithm; however, for completeness, the effects of sound-speed errors are included in the uncertainty analysis of Sec. IV.

A final issue concerns the use of relative travel-time measurements in AEL inversion. Two approaches are possible here. The first approach is to remove the source instants from the problem by considering appropriate differences between the relative travel times as the data to be inverted. The

second approach is to treat the relative travel times as the data, and include each source instant as an unknown parameter to be determined in the inversion. The latter approach is adopted here since it results in data with smaller uncertainties and since it allows the inversion algorithm greater scope in the application of the *a priori* information. Hence the AEL problem considered in this section consists of inverting relative travel-time measurements for the (three-dimensional) locations of the HLA hydrophones, the locations of the light bulb sources, and the implosion instant of each source.

The AEL problem described above represents a nonlinear inverse problem. Such problems are inherently nonunique, and a closed-form expression for the solution generally does not exist. An effective approach to many nonlinear inverse problems is based on local linearization and iteration. This reduces the nonlinear problem to a series of linear inversions (initialized at an arbitrary starting model), which can be solved using methods of linear inverse theory. Given the nonuniqueness of the inverse problem, the approach to the linearization and the linearized inversion are important factors influencing the character of the final solution. The following sections briefly consider two approaches to this problem; more complete reviews of inverse theory can be found elsewhere.[14,19–21]

B. Linearization and the creeping method

Consider a measurement of the arrival time t for the direct signal from an acoustic source to a sensor in the ocean. The dependence of t on the sensor location (x,y,z), source location (x',y',z'), and source instant t_0 can be written

$$t=\tau(x,y,z;x',y',z')+t_0, \tag{1}$$

where τ represents the travel time along the acoustic raypath between the two sets of coordinates (an expression for τ and an efficient method of computing direct-ray travel times are given in the Appendix). For the purposes of inversion, it is advantageous to scale the source instant t_0 in (1) by a representative ocean sound speed $\overline{c}$ and write

$$t=\tau(x,y,z;x',y',z')+(\overline{c}t_0)/\overline{c}. \tag{2}$$

By considering $\overline{c}t_0$ rather than t_0 as the unknown parameter, all parameters in (2) have the same physical units, i.e., distance (scaling parameters in this manner generally improves the numerical stability of inversion algorithms). For an array of H hydrophones and a set of S sources, there are a total of $N=HS$ arrival-time measurements which depend on $M=3H+4S$ parameters (three spatial variables for each hydrophone, and three spatial variables and scaled source instant for each source). The set of equations representing these measurements can be written in general vector form as

$$\mathbf{t}=\mathbf{T}(\mathbf{m}), \tag{3}$$

where $\mathbf{t}$ is the vector of measured travel times, $\mathbf{T}$ represents the forward mapping given by the right side of (2), and $\mathbf{m}$ represents the vector or model of the M parameters

$$\mathbf{m}=\{x_i,y_i,z_i;x_j',y_j',z_j';\overline{c}t_{0_j},\quad i=1,H,\quad j=1,S\}. \tag{4}$$

Equation (3) defines the AEL inverse problem: given a data set of measured travel times $\mathbf{t}$ and knowledge of the forward mapping $\mathbf{T}$, determine the model parameters $\mathbf{m}$ which gave rise to the data. As mentioned previously, this inverse problem is nonlinear; however, a local linearization can be obtained by expanding $\mathbf{T}(\mathbf{m})=\mathbf{T}(\mathbf{m}_0+\delta\mathbf{m})$ in a Taylor series to first order about an arbitrary starting model $\mathbf{m_0}$ to yield

$$\mathbf{t}=\mathbf{T}(\mathbf{m_0})+\mathbf{J}\delta\mathbf{m}, \tag{5}$$

where $\delta\mathbf{m}$ represents an unknown model perturbation to be determined. In (5), $\mathbf{J}$ is the Jacobian or sensitivity matrix which consists of the partial derivatives of the data functionals with respect to the model parameters, $J_{kl}=\partial T_k(\mathbf{m_0})/\partial m_l$ (partial differentiation of the ray travel time τ is summarized in the Appendix). Defining $\delta\mathbf{t}=\mathbf{t}-\mathbf{T}(\mathbf{m_0})$, the expansion can be written

$$\mathbf{J}\delta\mathbf{m}=\delta\mathbf{t}. \tag{6}$$

Equation (6) defines a linear inverse problem for $\delta\mathbf{m}$ which can be solved using methods of linear inverse theory (considered below). Once $\delta\mathbf{m}$ is determined, the corresponding model solution is $\mathbf{m}=\mathbf{m_0}+\delta\mathbf{m}$. Since nonlinear terms are neglected in (6), the model $\mathbf{m}$ may not adequately reproduce the measured data according to the nonlinear forward mapping (3). In this case, the starting model is updated, $\mathbf{m_0}\leftarrow\mathbf{m}$, and the inversion repeated iteratively until an acceptable solution is determined or the iterations converge.

To consider the linear inverse problem (6), assume that the noise (error) on datum t_i is an independent, Gaussian-distributed random variable with zero mean and standard deviation σ_i. For an overdetermined system of equations, the least-squares solution is determined by minimizing the χ^2 misfit

$$\chi^2=|\mathbf{G}(\mathbf{J}\delta\mathbf{m}-\delta\mathbf{t})|^2 \tag{7}$$

with respect to the perturbation $\delta\mathbf{m}$, where $\mathbf{G}$ is a diagonal weighting matrix given by $\mathbf{G}=\mathrm{diag}[1/\sigma_1,\ldots,1/\sigma_N]$. The solution is given by

$$\delta\mathbf{m}=[\mathbf{J}^T\mathbf{G}^T\mathbf{G}\mathbf{J}]^{-1}\mathbf{J}^T\mathbf{G}^T\mathbf{G}\delta\mathbf{t}, \tag{8}$$

provided the matrix in square brackets is nonsingular. The least-squares solution (8) provides an unbiased estimate of the true solution (i.e., the solution to the noise-free problem). In physical problems, the matrix to be inverted in (8) is rarely singular, but is often ill-conditioned. Ill-conditioning is the numerical manifestation of an ill-posed inverse problem, and leads to an unstable solution (i.e., small changes to the data lead to large changes to the solution). In AEL problems, including the source positions as well as the sensor positions as unknowns leads to an ill-posed inverse problem.

Ill-conditioned inverse problems can be addressed using singular value decomposition (SVD). The SVD of an $N\times M$ matrix $\mathbf{GJ}$ is given by

$$\mathbf{GJ}=\mathbf{U}\mathbf{\Lambda}\mathbf{V}^T, \tag{9}$$

where $\mathbf{U}$ and $\mathbf{V}$ are $N\times M$ and $M\times M$ matrices with columns consisting of orthonormal vectors $\mathbf{u}_i$ and $\mathbf{v}_i$, respectively, and $\mathbf{\Lambda}$ is an $M\times M$ diagonal matrix with entries $\lambda_1\geqslant\lambda_2\geqslant\cdots\geqslant\lambda_M\geqslant 0$ known as singular values. Substituting (9) into (8) leads to

$$\delta\mathbf{m}=\mathbf{V}\mathbf{\Lambda}^{-1}\mathbf{U}^T\mathbf{G}\delta\mathbf{t}=\sum_{i=1}^{M}\frac{1}{\lambda_i}\mathbf{v}_i\mathbf{u}_i^T\mathbf{G}\delta\mathbf{t}. \tag{10}$$

If one or more $\lambda_i=0$, the solution given by (10) is undefined: this corresponds to a singular matrix in (8). An ill-conditioned matrix is characterized by one or more of the singular values being very small. It is apparent from (10) that small λ_i can cause errors in the data $\delta\mathbf{t}$ to have a greatly magnified effect on the solution $\delta\mathbf{m}$ (i.e., small singular values cause instability). The condition number defined by $C=\lambda_1/\lambda_M$ gives an indication of the conditioning of the inverse problem: the larger C, the more ill-conditioned the inversion.

Several methods exist to stabilize ill-conditioned linear inversions. One method is to simply set the reciprocals of the small singular values in (10) to zero, thereby removing their effect on the inversion. How small λ_i need be in order to be removed is somewhat arbitrary. For instance, Creager and Dorman[13] removed all λ_i such that $\lambda_i/\lambda_1<0.01$ in their AEL inverse problem. A second method is to add a constant θ to the main diagonal of the matrix in square brackets in (8); the resulting solution can then be expressed as

$$\delta\mathbf{m}=\sum_{i=1}^{M}\frac{\lambda_i}{\lambda_i^2+\theta}\mathbf{v}_i\mathbf{u}_i^T\mathbf{G}\delta\mathbf{t}. \tag{11}$$

For an appropriate choice of θ, when λ_i is small, the factor $\lambda_i/(\lambda_i^2+\theta)$ in (11) is small rather than large, and instability is avoided. This approach forms the basis of Levenberg–Marquardt inversion[22] which has been applied to ill-conditioned AEL problems.[23,24]

The solution obtained with either of the two stabilized inversions described above no longer minimizes the χ^2 misfit. In fact, the misfit increases monotonically with either the number of singular values deleted or the size of the constant θ. Moreover, neither approach provides an unbiased estimate of the true model. Rather, for a given level of misfit, both methods produce the ''smallest'' solution in the sense that $|\delta\mathbf{m}|^2$ is a minimum. Nonlinear inversion based on applying such methods to linearization (6) has been referred to as the ''creeping'' method[14] since it iteratively progresses toward a solution by a series of small perturbations, with the final model retaining a dependence on the initial starting model. Note that since the linear inverse problem (6) is formulated in terms of the model perturbation (not the model), *a priori* information about the model cannot be included directly in the inversion. To our knowledge, all previous linearized AEL algorithms reported in the literature are based on the creeping method.

C. The jumping method and regularized inversion

An alternative to the creeping method can be formulated by substituting $\delta\mathbf{m}=\mathbf{m}-\mathbf{m_0}$ into expansion (6) to obtain

$$\mathbf{J}\mathbf{m}=\delta\mathbf{t}+\mathbf{J}\mathbf{m_0}\equiv\mathbf{d}. \tag{12}$$

This expression relates known quantities (the right side, which may be considered modified data $\mathbf{d}$) directly to $\mathbf{m}$: the linearized inverse problem is formulated in terms of the model, not the model perturbation. In this case, *a priori* information regarding the model can be applied directly to the inversion, often leading to a more physically meaningful solution. This approach has been referred to as the ''jumping'' method,[14] since the size of the model change at each iteration is not constrained and the final solution is generally independent of the starting model. Within the jumping method, the method of regularization provides a particularly useful approach to the linearized inversion at each iteration. Regularization is based on formulating a unique, stable inversion by explicitly including *a priori* information regarding the solution. This is typically accomplished by minimizing an objective function ϕ which combines a term representing the data misfit and a regularizing term that imposes the *a priori* expectation that the model $\mathbf{m}$ in some manner resembles a prior estimate $\hat{\mathbf{m}}$:

$$\phi=|\mathbf{G}(\mathbf{J}\mathbf{m}-\mathbf{d})|^2+\mu|\mathbf{H}(\mathbf{m}-\hat{\mathbf{m}})|^2. \tag{13}$$

In (13), $\mathbf{H}$ represents an arbitrary weighting matrix known as the regularization matrix. The variable μ is a Lagrange multiplier which serves as a trade-off parameter controlling the relative importance assigned to the data misfit and the *a priori* expectation in the minimization. The regularized solution is obtained by minimizing ϕ with respect to $\mathbf{m}$ to yield

$$\mathbf{m}=[\mathbf{J}^T\mathbf{G}^T\mathbf{G}\mathbf{J}+\mu\mathbf{H}^T\mathbf{H}]^{-1}[\mathbf{J}^T\mathbf{G}^T\mathbf{G}\mathbf{d}+\mu\mathbf{H}^T\mathbf{H}\hat{\mathbf{m}}]. \tag{14}$$

The presence of the term $\mu\mathbf{H}^T\mathbf{H}$ within the square brackets in (14) ensures that the matrix to be inverted is well-conditioned. The value for μ is generally chosen so that the χ^2 misfit achieves its expected value of $\langle\chi^2\rangle=N$ for N data. This applies the *a priori* information subject to ensuring that the data are fit to a statistically appropriate level.

The regularization matrix $\mathbf{H}$ in (13) and (14) provides considerable flexibility in the application of *a priori* information in the inversion. For instance, if prior model parameter estimates $\hat{\mathbf{m}}$ are available, an appropriate weighting is given by

$$\mathbf{H}=\mathrm{diag}[1/\xi_1,\ldots,1/\xi_M], \tag{15}$$

where ξ_j represents the uncertainty for jth parameter estimate $\hat{m}_j$. This weighting correctly applies prior parameter estimates which can vary over orders of magnitude in uncertainty. Alternatively, the *a priori* information can be applied to derivatives of the model parameters. For instance, if the *a priori* expectation is that the parameters are well approximated by a linear function (e.g., a straight array of sensors), then an appropriate choice is $\hat{\mathbf{m}}=\mathbf{0}$ and

$$\mathbf{H}=\begin{bmatrix}-1&2&-1&0&0&0&0&\cdots&0\\0&-1&2&-1&0&0&0&\cdots&0\\\vdots&&&&\ddots&&&&\vdots\\0&\cdots&0&0&0&-1&2&-1&0\\0&\cdots&0&0&0&0&-1&2&-1\end{bmatrix}. \tag{16}$$

For this choice of $\hat{\mathbf{m}}$ and $\mathbf{H}$, minimizing (13) effectively minimizes a discrete approximation to the second derivative of $\mathbf{m}$ (i.e., minimizes model curvature), subject to fitting the data.

The AEL inverse problem considered in this paper involves both types of *a priori* information described above. In particular, prior parameter estimates are available for the source locations from the on-ice survey, and the known depths of the transponders at the base of each VLA provide depth estimates for the closest HLA sensors (Sec. II). Reliable prior estimates are not available for the remaining hydrophone position parameters. However, the prior expectation that each HLA is essentially linear can be applied by minimizing the curvature of each array. To simultaneously apply two different types of *a priori* information to a linear inverse problem, an augmented objective function can be formed which includes two regularization terms

$$\phi = |\mathbf{G}(\mathbf{Jm}-\mathbf{d})|^2 + \mu_1|\mathbf{H_1}(\mathbf{m}-\hat{\mathbf{m}}_\mathbf{1})|^2 + \mu_2|\mathbf{H_2}(\mathbf{m}-\hat{\mathbf{m}}_\mathbf{2})|^2. \quad (17)$$

Minimizing this objective function with respect to $\mathbf{m}$ leads to the solution

$$\mathbf{m} = [\mathbf{J}^T\mathbf{G}^T\mathbf{GJ} + \mu_1\mathbf{H}_1^T\mathbf{H}_1 + \mu_2\mathbf{H}_2^T\mathbf{H}_2]^{-1} \times [\mathbf{J}^T\mathbf{G}^T\mathbf{Gd} + \mu_1\mathbf{H}_1^T\mathbf{H}_1\hat{\mathbf{m}}_1 + \mu_2\mathbf{H}_2^T\mathbf{H}_2\hat{\mathbf{m}}_2]. \quad (18)$$

In (17) and (18), the first regularization term is taken to represent the *a priori* parameter estimates for the source locations and for the HLA end-point sensor depths. Hence $\hat{\mathbf{m}}_1$ consists of the prior estimates for these parameters, with zeros for the remaining parameters. The regularization matrix $\mathbf{H}_1$ is of the form of (15) with diagonal elements consisting of the reciprocal of the estimate uncertainty for parameters with prior estimates, and zeros for the remaining parameters. The second regularization term is taken to represent the *a priori* expectation of linear arrays. Hence $\hat{\mathbf{m}}_2$ is taken to be zero, and $\mathbf{H}_2$ is of the form of (16) for the HLA sensor position parameters, with rows of zeros corresponding to the remaining parameters. Rows of zeros are also included in $\mathbf{H}_2$ at appropriate locations to separate the measures of curvature in x, y, and z for each of the two HLA's.

D. Implementation of the inversion algorithm

This section briefly describes the implementation of the inverse-theory results presented above to produce a practical AEL inversion algorithm. The algorithm is based on applying the linear inversion result with two regularization terms given by (18) at a series of iterations initiated from an arbitrary starting model $\mathbf{m}_0$. Convergence of the algorithm is based on two criteria: (i) obtaining a misfit to the measured data of $\chi^2 = N$ for N data, and (ii) obtaining a stable solution such that the rms change in the HLA positions between iterations is less than 0.01 m. In regard to the first criterion, note that although (18) is derived based on the χ^2 misfit for the linear inverse problem (12) that approximates the nonlinear problem (3) at each iteration, the convergence of the inversion algorithm must be judged in terms of the misfit to the nonlinear problem

$$\chi^2 = |\mathbf{G}(\mathbf{T}(\mathbf{m})-\mathbf{t})|^2. \quad (19)$$

The most subtle aspect of implementing the inversion has to do with assigning values to the two trade-off parameters, μ_1 and μ_2, which control the balance between the data misfit and the two types of *a priori* information. This requires a two-dimensional search at each iteration for the μ_1 and μ_2 values that produce the desired data misfit and the appropriate balance between minimizing the array curvature and minimizing the deviation of the source positions and array end-point depths from their prior estimates (referred to as parameter residuals). We have found that a practical and effective procedure is to set

$$\mu_2 = \alpha\mu_1 \quad (20)$$

for a fixed value of α, and solve a one-dimensional problem at each iteration for the value of μ_1 which yields the desired χ^2 misfit (this problem is discussed below). The final model obtained from this procedure can then be examined to ascertain whether the value of α was appropriate based on a comparison of the parameter residuals, $m_j - \hat{m}_j$, and the estimate uncertainties, ξ_j. If the residuals are substantially smaller (an order of magnitude) than the estimate uncertainties, then a smaller value of α is required; if the residuals are substantially larger, a larger value of α is required. The inversion can be repeated with a new value of α until $m_j - \hat{m}_j \lesssim \xi_j$ is achieved. In practice, we have found determining an appropriate value for α to be a straightforward procedure, typically requiring only two or three trial inversions. The value for α need not be refined too highly, since the uncertainties of the parameter estimates are only approximate, and the HLA sensor positions recovered in the inversion are not generally sensitive to changes in α of less than one or two orders of magnitude.

The above procedure reduces the problem of determining two trade-off parameters to a one-dimensional search for the parameter μ_1 that produces the desired χ^2 misfit at each iteration. The trade-off parameter μ_1 is chosen so that the χ^2 misfit is reduced by approximately a factor of 100 at each iteration until $\chi^2 = N$ is achieved. Controlling the change in misfit in this manner limits the change in the model at each iteration. This helps ensure that the linear approximation is valid, and stabilizes the convergence. Since χ^2 increases monotonically with μ_1, it is straightforward to determine the value for μ_1 which produces the desired χ^2 at a given iteration. At early iterations an approximate value for μ_1 is sufficient, and a bisection algorithm is employed. Near convergence, the bisection solution is improved by applying one or more iterations of Newton's method to determine a precise value for μ_1.

E. Synthetic inversion example

Before applying the inversion algorithm developed in the preceding sections to the measured data from the AEL survey, a synthetic inversion example is considered in this section. The example is designed to illustrate Occam's inversion for HLA localization in a case where the models obtained can be compared to the true array configuration. The example is roughly based on the AEL survey described in Sec. II; however, some parameters are altered for simplicity and efficiency, and to illustrate certain aspects of the inversion. The source–location configuration for the synthetic example is identical to that of the actual AEL survey, consist-

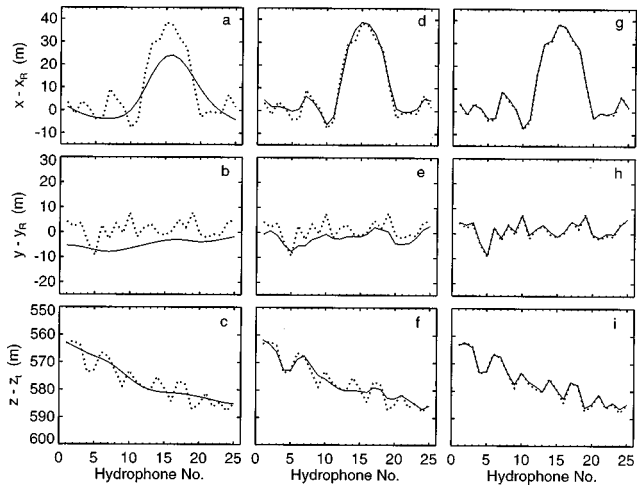

FIG. 7. Synthetic example of Occam's inversion using exact source locations. Solid lines indicate inversion results, dotted lines indicate the true HLA shape. x and y positions are shown relative to the coordinates (x_R, y_R) of a straight reference array (see text). Results are shown for data errors of σ=8 ms in (a)–(c), σ=2 ms in (d)–(f), and σ=0.4 ms in (g)–(i).

ing of eight sources at 50-m depth, as shown in Fig. 4. A single HLA of 25 sensors, ~720 m long, is considered. The end points of the HLA are located at $(x,y)=(300,-200)$, $(1000,-500)$ in Fig. 4. The HLA is predominately, but not completely, straight. The array shape is given by the dotted lines in Fig. 7(a)–(c) in terms of plots of $x-x_R$, $y-y_R$, and z as a function of hydrophone number. In these plots, x_R and y_R represent the coordinates of a perfectly straight reference array of equally spaced sensors extending between the HLA end points. Plotting the difference between the actual array shape and a straight reference array emphasizes deviations from a straight array, and clearly illustrates features of the HLA shape on the scale of meters for an array hundreds of meters long. Figure 7(a) shows that the deviations in x from a straight array include a bulge of ~40 m extending from hydrophones 10–20, together with a number of smaller random features. Figure 7(b) shows that the deviations in y consist of random features of up to 10 m. Figure 7(c) shows that the depth z of the HLA increases from 562 to 586 m, with random deviations of $\lesssim$5 m from a linear slope.

Synthetic (relative) travel-time data were computed for the source and HLA configuration described above (for eight sources and 25 hydrophones, the data set consists of $N=200$ travel times). The data were subsequently contaminated with random errors drawn from a Gaussian distribution with zero mean and standard deviation σ. In Fig. 7, the array shape determined via Occam's inversion of the noisy travel-time data (solid line) is compared to the true HLA shape (dotted line) for three different values of σ. In this example, the exact source positions were assumed to be known, and were not included as parameters in the inversion. In addition, the depth of the sensor at each end of the HLA was considered to be known *a priori* to within 3 m. Figure 7(a)–(c) shows the inversion result for a data uncertainty of σ=8 ms. With this relatively large uncertainty, the HLA sensor positions cannot be recovered accurately. The Occam's inversion result, which minimizes the array curvature, includes only the features in array shape which are resolved by the data.

TABLE I. Summary of χ^2 misfit and rms array curvature S (in x, y, z, and total) for the synthetic examples given in Figs. 7–10 (Fig. 7: Occams inversion, exact source locations; Fig. 8: creeping inversion, exact source locations; Fig. 9: Occams inversion, inaccurate source locations; Fig. 10: Occams inversion, inaccurate source locations included in inversion).

Case		χ^2	S_x (m^{-1})	S_y (m^{-1})	S_z (m^{-1})	S_{total} (m^{-1})
True HLA		166	9.3	9.2	7.1	25.6
Fig. 7	σ=8 ms	200	1.1	0.2	0.2	1.5
	σ=2 ms	200	4.9	2.2	2.5	9.6
	σ=0.4 ms	200	8.4	7.4	6.0	21.8
Fig. 8	σ=8 ms	108	15.9	19.8	23.3	59.0
	σ=2 ms	108	9.9	10.0	8.4	28.3
	σ=0.4 ms	108	9.4	9.1	7.2	25.7
Fig. 9	σ=8 ms	200	1.5	0.3	0.4	2.2
	σ=2 ms	200	7.2	4.9	4.9	17.0
	σ=0.4 ms	1760	9.3	9.2	7.1	25.6
Fig. 10	σ=8 ms	200	1.0	0.2	0.2	1.4
	σ=2 ms	200	4.9	2.2	2.6	9.7
	σ=0.4 ms	200	8.4	7.1	5.9	21.4

For example, the recovered HLA shape includes the bulge in x and the general slope in z, but none of the small-scale random deviations. Of note is the fact that, despite large errors in the data, the inversion result contains no spurious structure. Figure 7(d)–(f) shows the HLA shape recovered by inverting data with a smaller uncertainty of σ=2 ms. In this case, the inversion result begins to resolve the small-scale deviations in HLA shape. However, the inversion result has significantly less structure than the true HLA, reflecting the resolution limit of the data. Figure 7(g)–(i) shows the inversion result for a relatively small data uncertainty of σ=0.4 ms. The recovered HLA shape closely matches the true shape, including the small-scale deviations; however, the deviations are still typically slightly smaller than those of the true HLA. Table I summarizes the synthetic inversion results in this section. Note from this table that the structure of the inversion results in Fig. 7 (as measured by the rms array curvature) is consistently smaller than that of the true HLA.

The Occam's inversion results in Fig. 7 represent the models which minimize array curvature, subject to fitting the data to a statistical level of $\chi^2=N$. For comparison, Fig. 8 shows the results of inverting the same data sets using the creeping method based on minimizing the misfit (Sec. III B). In particular, the models in Fig. 8 were computed using the SVD solution (10) but removing singular values λ_i such that $\lambda_i/\lambda_1<0.01$, and iterating until the rms model change between iterations was less than 0.01 m. Figure 8(a)–(c) shows that inverting data with a relatively large uncertainty of σ=8 ms can lead to significant spurious structure. This structure is not required to fit the data; however, it is also not precluded by the data. Figure 8(d)–(f) and (g) and (h) shows that for more accurate data (σ=2 and 0.4 ms, respectively), the spurious structure is reduced; however, the inversion results still typically have more, rather than less, structure than the true HLA (Table I).

The above inversion examples make use of exact knowl-

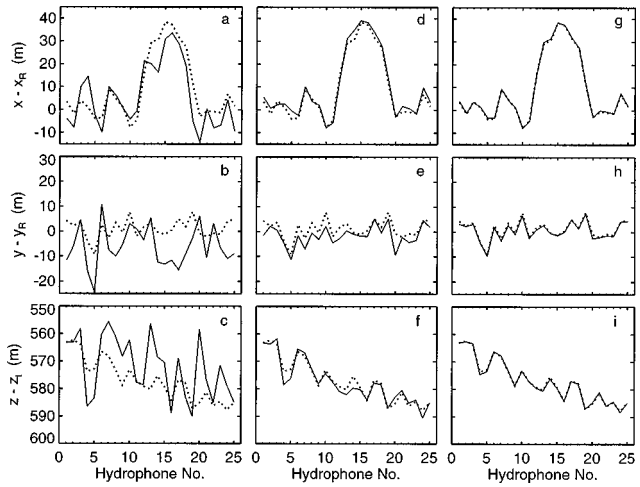

FIG. 8. Synthetic example of minimum-misfit inversion using exact source locations. Solid lines indicate inversion results, dotted lines indicate the true HLA shape. Results are shown for data errors of $\sigma=8$ ms in (a)–(c), $\sigma=2$ ms in (d)–(f), and $\sigma=0.4$ ms in (g)–(i).

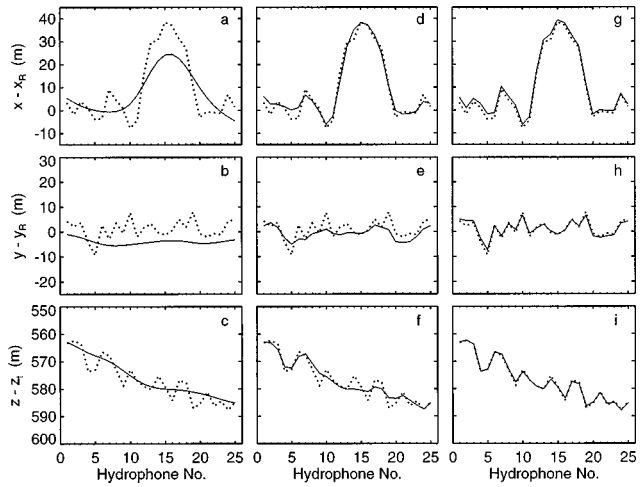

FIG. 10. Synthetic example of Occam's inversion including source locations in the inversion. Solid lines indicate inversion results, dotted lines indicate the true HLA shape. Results are shown for data errors of $\sigma=8$ ms in (a)–(c), $\sigma=2$ ms in (d)–(f), and $\sigma=0.4$ ms in (g)–(i).

edge of the source locations. The effects of errors in source locations are illustrated in Fig. 9, which shows Occam's inversion results for noisy synthetic data ($\sigma=8$, 2, and 0.4 ms) when random (Gaussian) errors are added to the source positions, but the source locations are not included as parameters in the inversion (i.e., the inaccurate source positions are treated as known parameters). The standard deviation of the source–position errors is 10 m in x and y, and 2 m in z (note that these source errors are larger than the uncertainties for the AEL survey in this paper, but would not be large for ship-borne surveys). For the largest data uncertainty, a comparison of Fig. 9(a)–(c) and Fig. 7(a)–(c) shows that the source–location errors have only a minor effect on the recovered HLA shape. For more accurate data, the effects of inaccurate source positions are more pronounced, as shown by comparing Fig. 9(d)–(f) and (g)–(i) to the corresponding cases in Fig. 7. Note from Table I that for $\sigma=0.4$ ms, the inversion algorithm did not converge (i.e., could not achieve the desired misfit of $\chi^2=200$). A major effect of the source–position errors in Fig. 9 are large translations of the HLA position in x and y (depth z is constrained by the known end-point values). In addition, the rms curvature of the solutions in Fig. 9 are significantly larger than those in Fig. 7 for exact source locations (Table I).

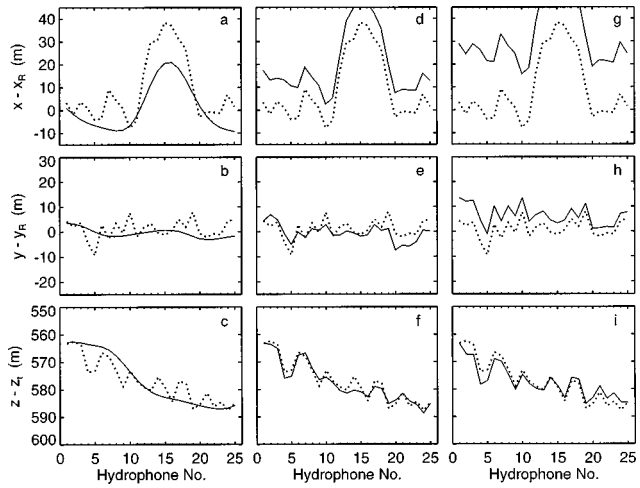

FIG. 9. Synthetic example of Occam's inversion using (fixed) inaccurate source locations. Solid lines indicate inversion results, dotted lines indicate the true HLA shape. Results are shown for data errors of $\sigma=8$ ms in (a)–(c), $\sigma=2$ ms in (d)–(f), and $\sigma=0.4$ ms in (g)–(i).

When the source positions are only approximately known, a significant improvement in HLA localization can be obtained by including the source positions as unknown parameters (with *a priori* estimates) in the inversion, as illustrated in Fig. 10. In particular, Fig. 10(d)–(f) and (g)–(i) shows that the translations in x and y, evident in the corresponding cases in Fig. 9, are substantially reduced when source positions are included in the inversion. Table I indicates that the rms curvature of the solutions in Fig. 10 are slightly lower than those in Fig. 7 (exact source locations), a reflection of the reduced resolving power of the data due to the uncertainty in the source positions. The source locations determined in the inversions of Fig. 10 are illustrated in Fig. 11, which indicates the difference between the recovered source coordinates (x',y',z') and the true source coordinates (x_t',y_t',z_t') by solid lines. The approximate source positions used as the *a priori* estimates are indicated by dashed lines. The source positions recovered in the inversion represent a substantial improvement over the *a priori* estimates, particularly for the smaller data uncertainties. Figures 10 and 11 indicate that excellent AEL results can be obtained with relative travel-time data and only an approximate knowledge of the source locations.

IV. AEL INVERSION FOR SPINNAKER HLA'S

A. Occam's inversion result

In this section, the inversion algorithm for HLA sensor localization developed in Sec. III is applied to the data from the AEL survey for the SA (Sec. II). This involves inverting measured travel times for eight light bulb source locations and a total of 88 hydrophones in order to determine the hydrophone locations, source locations, and the source instants. The (linearized) system of equations representing this in-

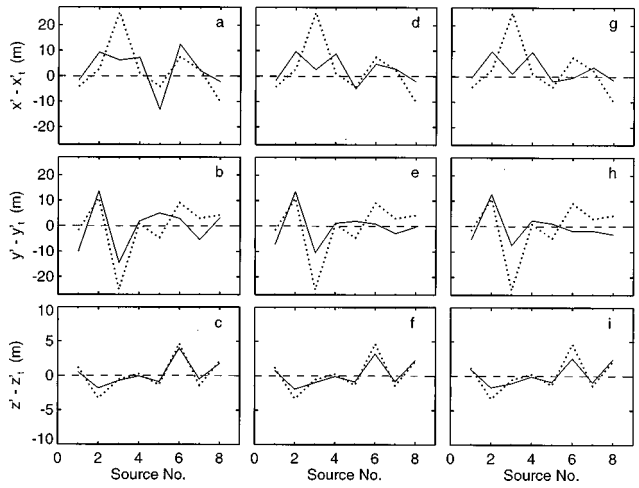

FIG. 11. Source locations determined in the Occam's inversion of Fig. 10. Solid lines indicate inversion results, dotted lines indicate *a priori* estimates. Positions are shown relative to the true source locations (x_t', y_t', z_t'). Results are shown for data errors of $\sigma=8$ ms in (a)–(c), $\sigma=2$ ms in (d)–(f), and $\sigma=0.4$ ms in (g)–(i).

verse problem is formally overdetermined, consisting of $N=704$ equations in $M=296$ unknowns. However, the system is strongly ill-conditioned with a condition number $C\sim 10^{16}$. The instability of the inversion is obviated by the application of *a priori* information consisting of the expectation that each HLA is essentially straight, together with prior estimates for the source locations and for the depths of HLA sensors 1, 80, and 81 (i.e., the sensors immediately adjacent to the VLA's).

Figure 12 illustrates the convergence properties of the inversion algorithm for a starting model corresponding to the estimated HLA location and measured source positions shown in Fig. 4. The χ^2 misfit, shown in Fig. 12(a), decreases by almost four orders of magnitude over the first two iterations. The desired misfit of $\chi^2=704$ is achieved on iteration 3, and maintained for iteration 4 while the rms model change, shown in Fig. 12(b), decreases below the threshold of 0.01 m for convergence. The rms source-positions residuals (difference between recovered source positions and prior

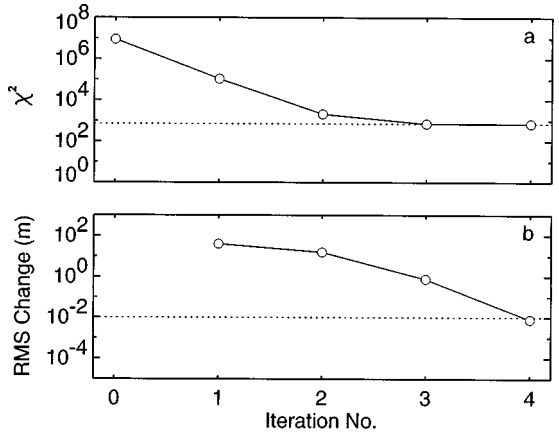

FIG. 12. Convergence properties of inversion of the AEL survey data. (a) shows the χ^2 misfit, (b) shows the rms change in HLA sensor positions between iterations. Dotted lines indicate the values required for convergence.

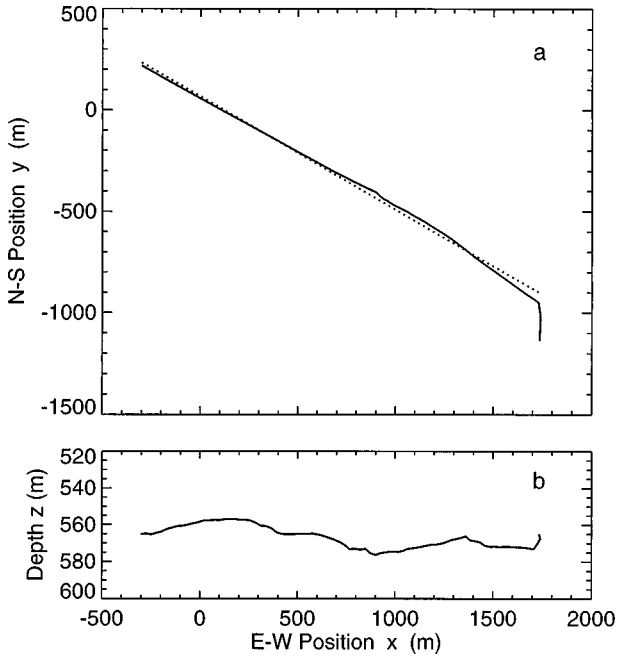

FIG. 13. HLA element locations determined from inversion of AEL data. (a) shows the long and short HLA's (solid line) in the x-y plane. The dotted line represents a least-squares fit to the element locations of long HLA. (b) shows the HLA depths in the x-z plane.

estimates) for the final model were 0.92 m in x, 0.70 m in y, and 0.22 m in z. The residuals in the depth of HLA sensors 1, 80, and 81 were 2.2, 1.8, and -1.8 m. These values are in good agreement in magnitude with the prior estimate uncertainties of 2 m in x and y and 0.5 m in z for the source positions, and 3 m for the sensor depths. This indicates that the value of $\alpha=10$ used in (20) gave an appropriate trade-off between minimizing the array curvature and minimizing the residuals for source positions and sensor depths. Increasing or decreasing α by a factor of 10 had a negligible effect on the HLA element locations determined in the inversion.

The result of the inversion for the HLA sensor locations is shown in Fig. 13. Figure 13(a) shows the long and short HLA's in the horizontal plane. A straight (dotted) line is included as a reference in Fig. 13(a). This line corresponds to a least-squares fit to the sensor locations determined for the long HLA. The HLA's appear to be quite straight, although some deviations are apparent near the center of the long HLA (considered below). The depth of each element of the two HLA's are shown in Fig. 13(b). Essentially identical results for the HLA locations were obtained by initiating the inversion algorithm from a number of different starting models.

To consider the shape of the long HLA in greater detail, Fig. 14 shows the difference between the y (north-south) location of the HLA elements and the least-squares line of Fig. 13(a) as a function of the independent parameter x. Individual sensor positions are indicated by crosses in Fig. 14. Note that the vertical and horizontal scales in this figure greatly exaggerate the deviations from a straight array. This figure shows that the segment of the HLA to the west of the central node ($x<900$ m) is essentially straight, with a small curvature to the northeast. Immediately to the east of the

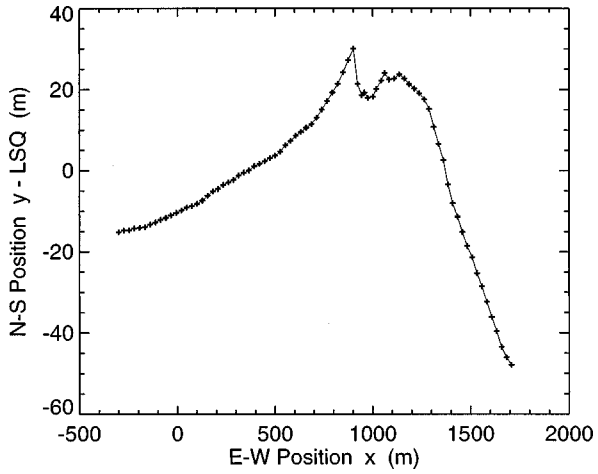

FIG. 14. Deviation of the y element positions of the long HLA from the least-squares line of Fig. 13. Individual hydrophone locations are indicated by crosses.

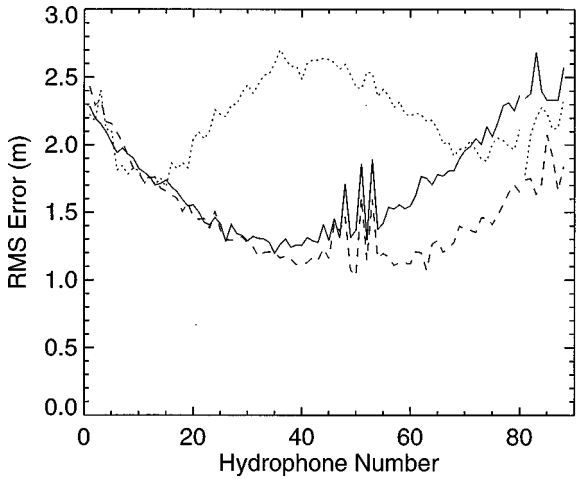

FIG. 15. Standard deviations of sensor positions in x (solid line), y (dashed line), and z (dotted line) from the Monte Carlo simulation. The break in the lines indicates the transition from the long HLA to the short HLA.

central node ($900<x<1200$ m), a section of the array appears to lie in folds on the seafloor. To the east of this section ($x>1200$ m), the array again straightens out, albeit at a slightly different bearing than the western section (the difference in bearing of the straight sections to the east and to the west of the central node is $\sim 6°$). Since the Occam's inversion algorithm explicitly minimizes array curvature, the features of the recovered array shape, including the change in bearing and the small structure of the central folded section, are definitely required to fit the AEL data. In fact, the shape of the long HLA illustrated in Fig. 14 is consistent with what might be expected given the procedure for deploying the SA described in Sec. I. The long HLA was lowered to the seafloor from three points, with tensioning lines attached to each end of the array (Fig. 3). The tension applied to the western end of the HLA resulted in the western half of the array being essentially straight. The tension applied to the eastern end of the HLA straightened the eastern extremity of the array; however, it was not sufficient to remove the slack and completely straighten the array near the central node.

B. Monte Carlo uncertainty estimates

The Occam's inversion result in the previous section provides the minimum-structure HLA model consistent with the AEL survey data. To estimate the uncertainties associated with these sensor locations, a Monte Carlo simulation[19] of the inversion procedure was carried out. In this simulation, the ''true'' hydrophone and source locations were taken to be those determined by the inversion of the measured AEL data. Simulated travel-time data were computed for this configuration using the raytracing algorithm described in the Appendix and the sound-speed profile shown in Fig. 5. Each realization of the Monte Carlo process consisted of adding random errors to the simulated data and to the sound-speed profile, assigning *a priori* parameter estimates based on random perturbations to the true values, and subsequently applying the inversion algorithm initialized from a random starting model. The random error on each datum was drawn from a Gaussian distribution with zero mean and standard deviation equal to that estimated for the corresponding datum of the actual AEL survey described in Sec. II. The sound-speed errors were Gaussian distributed, with a standard deviation of 0.1 m/s, representing the uncertainty of the CTD measurements. The prior estimates for source locations and end-point sensor depths were taken to be the true values plus a random Gaussian error with standard deviation equal to the uncertainty in the parameter estimate (2 m in x and y and 0.5 m in z for source positions, and 3 m for sensor depths). In total, 20 inversion were carried out, and the rms error of each sensor position was computed from the set of solutions.

The rms errors in the x, y, and z sensor coordinates computed from the Monte Carlo process are shown in Fig. 15. The errors for the x and y coordinates are smallest near the center of the long HLA. In this region, the sensors are well surrounded (horizontally) by the light bulb sources, as shown in Fig. 4. The errors of the x and y coordinates in Fig. 15 increase toward either end of the array, probably because the sensors are not as effectively surrounded by sources near the array ends (e.g., for sensors at the western end of the HLA, all sources are to the east). The largest fluctuations in the rms error in x and y occur between hydrophones 45 and 55. This corresponds to the folded region of the long HLA (Fig. 14) where the inversion algorithm particularly concentrates on reducing the high curvature. The errors in z (depth) are largest near the center of the long HLA, where the sources are farthest away, and generally decrease towards the ends, where the sources are closer and therefore more directly overhead. The rms errors of the sensor coordinates in Fig. 15 vary between approximately 1.0 and 2.5 m. This uncertainty is $\lesssim \lambda/10$ at a frequency of 60 Hz, which defines the upper frequency limit of the data passband for the Spinnaker Array.

V. SUMMARY

This paper developed an effective inversion algorithm for localizing the individual elements of an array of sensors

using travel-time measurements from a series of acoustic sources. The general case is considered in which the source instants are not known, and source locations are only approximately known. The nonuniqueness of this inverse problem is addressed by explicitly applying *a priori* information about the solution in an iterative regularized inversion scheme. The *a priori* information includes estimates of the source positions, any available estimates of sensor positions, and the expectation of a linear HLA (or an array consisting of a series of linear segments). The prior expectation of a straight array is applied by minimizing the array curvature, which has the additional benefit of producing the simplest array shape consistent with the AEL data. Deviations in the solution from a straight array are definitely required by the data, and are not simply artifacts of the inversion algorithm or starting model.

The inversion algorithm is applied to localize the elements of a two-segment HLA which forms part of the Spinnaker Array, a three-dimensional sensor array located near the edge of the continental shelf of the Lincoln Sea in the high Arctic. An AEL survey, consisting of imploding light bulbs at a series of locations surrounding the array, was carried out shortly after the SA was deployed. The results of the inversion indicate that the two HLA segments are predominately straight, although several features are observed and related to the array deployment procedure. A Monte Carlo simulation of the inversion indicated that the rms errors of the recovered HLA sensor positions vary from 1.0 to 2.5 m, which is $\lesssim\lambda/10$ at the upper frequency limit for the Spinnaker Array.

Finally, the AEL inversion methodology presented here for an Arctic application is generally applicable to other settings. Examples include the localization of arrays of hydrophones, ocean-bottom seismometers or other instruments in open water using acoustic travel times to a surface vessel whose position is only approximately known.

ACKNOWLEDGMENTS

The first author thanks Mark McDonald, Oleg Godin, and Lothar Jaschke for interesting and helpful discussions. This work was supported by NRaD research Contracts No. N66001-93-O-0114 and No. N66001-93-D-0114, the Office of Naval Research, and the Space and Naval Warfare System Command. Project Spinnaker was supported by ONR, SPAWAR, and CRAD.

APPENDIX: RAY TRAVEL TIMES AND DERIVATIVES

Consider an acoustic source and receiver in the ocean at (x_i, y_i, z_i) and (x_j', y_j', z_j'), respectively, with $z_i < z_j'$. The horizontal range between the two is given by

$$r = \sqrt{(x_i - x_j')^2 + (y_i - y_j')^2}. \tag{A1}$$

Expressions for the range r and travel time τ along a ray path between source and receiver are easily derived by applying Snell's Law to an infinite stack of infinitesimal layers[25]

$$r = \int_{z_i}^{z_j'} \frac{pc(z)\,dz}{[1 - p^2 c^2(z)]^{1/2}}, \tag{A2}$$

$$\tau = \int_{z_i}^{z_j'} \frac{dz}{c(z)[1 - p^2 c^2(z)]^{1/2}}. \tag{A3}$$

In (A2) and (A3), the ray parameter $p = \cos\theta(z)/c(z)$ is constant along a ray path, and defines the take-off (grazing) angle at the source. The ray parameter for an eigenray connecting source and receiver is usually determined by searching for the value of p which produces the correct range (to a specified tolerance) using (A2). The efficiency of this search is key to the efficiency of the ray-tracing algorithm. We have implemented an efficient procedure of determining p for direct-path eigenrays based on Newton's method. An initial estimate p_0 is calculated assuming straight-line propagation with a sound speed c_H representing the harmonic mean of the measured sound-speed profile

$$c_H = (z_j' - z_i) \Big/ \int_{z_i}^{z_j'} \frac{dz}{c(z)}. \tag{A4}$$

An improved estimate p_1 is obtained by expanding $r(p)$ in a Taylor's series about p_0 and neglecting nonlinear terms to give

$$r(p) = r(p_0) + \frac{\partial r(p_0)}{\partial p}(p - p_0), \tag{A5}$$

which has a solution

$$p = p_0 + \left[\frac{\partial r(p_0)}{\partial p}\right]^{-1} (r(p) - r(p_0)). \tag{A6}$$

In (A6), $\partial r/\partial p$ is determined by differentiating (A2) according to Leibnitz's rule to yield

$$\frac{\partial r}{\partial p} = \int_{z_i}^{z_j'} \frac{c^2(z)\,dz}{[1 - p^2 c^2(z)]^{3/2}}. \tag{A7}$$

If $r(p)$ computed from (A2) is within the tolerance of the desired range, the procedure is complete. If not, the starting value is updated, $p_0 \leftarrow p$, and the procedure repeated iteratively until a satisfactory value is obtained. The travel time along the ray path is then computed using (A3). Since Newton's method converges quadratically near the solution, this is an efficient method of determining direct eigenrays to high precision. For all raytracing described in this paper, only one or two iterations of Newton's method were required to determine the ray parameter to a range tolerance of 0.01 m.

In addition to computing travel times, the linearized inversion algorithm requires partial derivatives of travel time with respect to source and receiver coordinates. Consider first the partial derivative with respect to horizontal coordinate x_i. Employing the chain rule

$$\frac{\partial \tau}{\partial x_i} = \frac{\partial t}{\partial p}\frac{\partial p}{\partial r}\frac{\partial r}{\partial x_i} = \frac{\partial \tau}{\partial p}\left[\frac{\partial r}{\partial p}\right]^{-1}\frac{\partial r}{\partial x_i}. \tag{A8}$$

The three partials on the right side of (A8) can be calculated from (A3), (A2), and (A1), respectively, yielding

$$\frac{\partial \tau}{\partial x_i} = p(x_i - x_j')/r. \tag{A9}$$

Similarly, partial derivatives with respect to the other horizontal coordinates are

$$\frac{\partial \tau}{\partial x_j'} = p(x_j' - x_i)/r, \tag{A10}$$

$$\frac{\partial \tau}{\partial y_i} = p(y_i - y_j')/r, \tag{A11}$$

$$\frac{\partial \tau}{\partial y_j'} = p(y_j' - y_i)/r. \tag{A12}$$

The partial derivative of τ with respect to vertical coordinate z_i can be determined by differentiating (A3) to give

$$\frac{\partial \tau}{\partial z_i} = \int_{z_i}^{z_j'} \frac{pc(z)dz}{[1-p^2c^2(z)]^{3/2}} \left(\frac{\partial p}{\partial z_i}\right) - \frac{1}{c(z_i)[1-p^2c^2(z_i)]^{1/2}}. \tag{A13}$$

An expression for $\partial p/\partial z_i$ can be obtained by noting that

$$\frac{\partial r}{\partial z_i} = 0 = \int_{z_i}^{z_j'} \frac{c(z)dz}{[1-p^2c^2(z)]^{3/2}} \left(\frac{\partial p}{\partial z_i}\right) - \frac{pc(z_i)}{[1-p^2c^2(z_i)]^{1/2}}. \tag{A14}$$

Solving for $\partial p/\partial z_i$ and substituting into (A13) yields

$$\frac{\partial \tau}{\partial z_i} = \frac{1}{c(z_i)}[1-p^2c^2(z_i)]^{1/2}. \tag{A15}$$

Similarly,

$$\frac{\partial \tau}{\partial z_j'} = -\frac{1}{c(z_j')}[1-p^2c^2(z_j')]^{1/2}. \tag{A16}$$

[1] W. S. Burdic, *Underwater Acoustic System Analysis* (Prentice-Hall, Englewood Cliffs, NJ, 1994).

[2] A. Tolstoy, *Matched Field Processing for Underwater Acoustics* (World Scientific, Singapore, 1993).

[3] A. B. Baggeroer, W. A. Kuperman, and P. N. Mikhalevsky, ''An overview of matched field methods in ocean acoustics,'' IEEE J. Ocean Eng. **18**, 401–424 (1993).

[4] J. M. Ozard, ''Matched field processing in shallow water for range, depth, and bearing estimates: Results of experiment and simulation,'' J. Acoust. Soc. Am. **86**, 744–753 (1989).

[5] M. D. Collins, W. A. Kuperman, and H. Schmidt, ''Nonlinear inversion for ocean-bottom properties,'' J. Acoust. Soc. Am. **92**, 2770–2783 (1992).

[6] S. E. Dosso, M. L. Yeremy, J. M. Ozard, and N. R. Chapman, ''Estimation of ocean bottom properties by matched field inversion of acoustic field data,'' IEEE J. Ocean Eng. **18**, 232–239 (1993).

[7] B. D. Steinberg, *Principles of Aperture and Array System Design* (Wiley, New York, 1976).

[8] W. S. Hodgkiss, D. E. Ensberg, J. J. Murray, G. L. D'Spain, N. O. Booth, and P. W. Schey, ''Direct measurement and matched-field inversion approaches to array shape estimation,'' IEEE J. Ocean Eng. **21**, 393–401 (1996).

[9] B. J. Sotirin and J. A. Hildebrand, ''Large-aperture digital acoustic array,'' IEEE J. Ocean Eng. **13**, 271–281 (1988).

[10] B. J. Sotirin and J. A. Hildebrand, ''Acoustic navigation of a large-aperture array,'' J. Acoust. Soc. Am. **87**, 154–167 (1990).

[11] B. J. Sotirin, V. K. McDonald, J. R. Olsen, J. M. Stevenson, and G. O. Pickens, ''An integrated array element localization system,'' Proc. Oceans '94 , 727–731 (1994).

[12] W. S. Hodgkiss, ''Shape determination of a shallow-water bottomed array,'' Proc. Oceans '89 , 1199–1204 (1989).

[13] K. C. Creager and L. M. Dorman, ''Location of instruments on the seafloor by joint adjustment of instrument and ship positions,'' J. Geophys. Res. **87**, 8379–8388 (1982).

[14] J. A. Scales, P. Docherty, and A. Gersztenkorn, ''Regularisation of nonlinear inverse problems: Imaging the near-surface weathering layer,'' Inverse Probl. **6**, 115–131 (1990).

[15] S. C. Constable, R. L. Parker, and C. G. Constable, ''Occam's inversion: A practical algorithm for generating smooth models from electromagnetic sounding data,'' Geophysics **52**, 289–300 (1987).

[16] B. J. Sotirin and J. Thorleifson, ''Project Spinnaker: Deployable arrays in the Arctic,'' J. Underwater Acoust. **46**, 679–694 (1996).

[17] S. E. Dosso, G. H. Brooke, S. J. Kilistoff, B. J. Sotirin, V. K. McDonald, M. R. Fallat, and N. E. Collison, ''High-precision array element localization of vertical line arrays in the Arctic Ocean,'' IEEE J. Ocean Eng. (in press).

[18] G. J. Heard, M. McDonald, N. R. Chapman, and L. Jaschke, ''Underwater light bulb implosions: A useful acoustic source,'' Proc. Oceans '97 **2**, 755–762 (1997).

[19] W. H. Press, B. P. Flannery, S. A. Teukolsky, and W. T. Vetterling, *Numerical Recipes* (Cambridge U.P., New York, 1992).

[20] L. R. Lines and S. Treitel, ''Tutorial: A review of least-squares inversion and its application to geophysical inverse problems,'' Geophys. Prospecting **32**, 159–186 (1984).

[21] C. van Schooneveld, ''Inverse problems: A tutorial survey,'' in *Underwater Acoustic Data Processing*, edited by Y. T. Chan (Kluwer, The Netherlands, 1989), pp. 393–411.

[22] D. W. Marquardt, ''An algorithm for least squares estimation of nonlinear parameters,'' ACM Trans. Math. Softw. **7**, 481–497 (1963).

[23] J. C. Osler and D. M. F. Chapman, ''Seismo-acoustic determination of the shear-wave speed of surficial clay and silt sediments on the Scotian shelf,'' Can. Acoust. **24**, 11–22 (1997).

[24] P. H. Milne, *Underwater Acoustic Positioning Systems* (Cambridge U.P., Cambridge, England, 1983).

[25] W. M. Telford, L. P. Geldart, R. E. Sheriff, and D. A. Keys, *Applied Geophysics* (Cambridge U.P., New York, 1976).

Ultrasonic wave generation by time-gated microwaves

Bernard Hosten[a)]
Laboratoire de Mécanique Physique, Université de Bordeaux I, URA C.N.R.S. No. 867, 351, Cours de la Libération, 33405-TALENCE Cedex, France

Pierre Alain Bernard
Laboratoire de Modélisation Avancée des Systèmes Thermiques et des Ecoulements Réels, École Nationale Supérieure de Chimie et de Physique de Bordeaux, Avenue Pey-Berland, B.P. 108, 33402 TALENCE Cedex, France

(Received 26 October 1997; accepted for publication 21 April 1998)

This paper shows how the energy transfer between electromagnetic waves and elastic waves at the surface of fluid or solid materials could constitute a new way to generate ultrasonic waves without contact for the purpose of nondestructive evaluation and control. When time-gated microwaves strike the surface of a material, there is a generation of ultrasonic waves. The times-of-flight of these elastic waves inside the material decrease when the power of the incident microwaves increases. Therefore, the diminution of the propagation path indicates that the energy transformation appears in a volume close to the surface, the depth of which is increasing along with the power of the microwaves and depends on the material properties. Consequently, the elastic wave generation is attributed to the evolution of the power of the microwave during the gate width that governs the frequency content of the ultrasonic waves. The generation of ultrasound is checked in water and polymers. If the microwaves are not too attenuated in the material, the ultrasonic waves can be generated both at input (air–solid) and output (solid–air) interfaces. These peculiarities can generate new applications in the nondestructive evaluation and control of material. © *1998 Acoustical Society of America.* [S0001-4966(98)01308-3]

PACS numbers: 43.35.Cg, 43.35.Mr, 43.35.Zc [HEB]

INTRODUCTION

The nondestructive evaluation and testing (NDE and NDT) of materials commonly involve the use of ultrasonic waves.[1] The standard techniques utilize an immersion medium (usually water) or a coupling agent between the material and the piezoelectric transducer.

For over two decades, techniques that do not need any contact or coupling medium have been developed. The noncontact techniques to generate ultrasound are based on the electromagnetic acoustic transducer (EMAT) air-coupled transducers or laser impact.[1]

Microwaves are frequently used in the nondestructive investigation of materials, like x rays, to produce images of the transmitted intensity.[1] Although the production of ultrasound from laser impact was intensely studied experimentally and theoretically, the microwave impact was not well mentioned in the NDE community. Although R. M. White[2] presented the theoretical background in 1963, the production of elastic waves from modulated microwave energy was essentially noticed for their physiologist effects. Human subjects hear a ''click'' when the head is irradiated with high-energy microwave pulse. These effects were investigated by the microwave community.[3,4]

In 1984 R. L. Nasoni *et al.*[5] presented some preliminary results on the generation of ultrasound from electromagnetic waves through immersed interfaces. To the authors' knowledge, there have been no other attempts to use microwaves as a tool to generate ultrasound without contact. The purpose of this paper is to show the conditions for which microwaves can produce ultrasound at air–liquid, air–solid, and solid–air interfaces, and to describe initial experimental investigations that will help to build the theoretical model of microwave-elastic wave interaction.

First we describe the characteristic of the time-gated microwave source. Second, the generation in a volume close to the air–liquid interface and the linearity of this phenomenon is discussed. It is shown that the ultrasonic wave frequency content is governed by the shape of the temporal gate. Third, we introduce the generation of ultrasound by time-gated microwave near air–solid or solid–air interfaces, showing the potential of this method for NDE and NDT. Finally, some preliminary theoretical explanations are presented.

I. MICROWAVE SOURCE DESCRIPTION

The electromagnetic wave is produced by a magnetron in the frequency range of 5.4–5.9 GHz (C Band) with a peak power of 1 MW. A pulse of 0.56 μs is applied to the cathode of the magnetron. The repetition rate, 585 Hz, is fast enough to permit fast averaging if necessary. The wave is delivered by a standard wave guide R48 (of cross section $=22.15\times47.55$ mm) that imposes the propagation mode (TE10) (Fig. 1). At these frequencies, the microwave wavelength is around 52 mm in vacuum and 62 mm in the waveguide. In order to use the lowest power possible and to prove that compact sources could be designed in the future, a coupler was used to divide the power by 10. The amplitude of the pulse sent to the magnetron was adjusted to furnish a

a)Electronic mail: hosten@lmp.u-bordeaux.fr

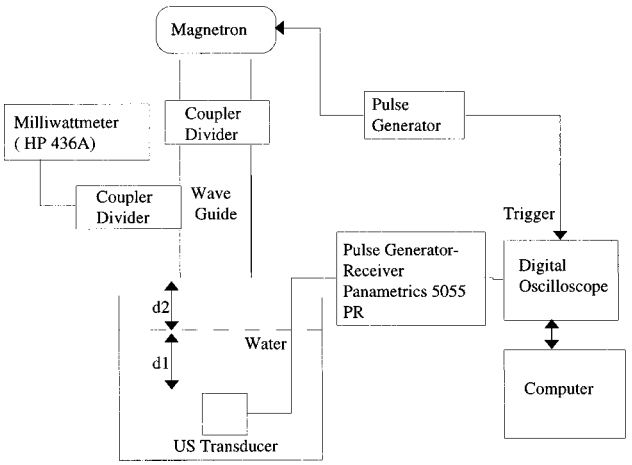

FIG. 1. Experimental arrangement to generate ultrasonic wave in water.

power at the end of the waveguide varying from 0 to 100 kW. Another coupler diverted a small part of this energy to a milliwattmeter (HP 436A) in order to measure the microwave power delivered at the end of the waveguide.

II. EXPERIMENTAL VERIFICATION OF ULTRASONIC WAVE GENERATION

A. Generation at the air–liquid interface

Figure 1 presents the apparatus used to observe the generation of ultrasonic waves in water. Ultrasonic waves are received by an immersion transducer at a central frequency of 1 MHz (Panametrics V302). The distance between the end of the microwave guide and the water surface is $d2$ (20 mm). The distance $d1$ (33 mm) is easily determined using the ultrasonic transducer in pulse-echo mode and measuring the times-of-flight between echoes reflected by the water surface. The time-of-flight between the two first echoes is 44.35 μs (velocity in water 1.49 mm/μs at 22 °C).

Figure 2 presents the time history of the ultrasonic wave generated by the microwave at the interface air–water. The first transmission through the water layer is shown with two successive echoes. The times-of-flight are 44.19 and 44.22 μs, respectively, between the first two echoes and the two subsequent ones. The time is measured with the cross-correlation function between echoes. The difference between the time measurement gives the order of the experimental errors that are mainly due to the slight shape difference of the echoes (Fig. 2). This observation proves that there is a transfer of energy between the time-gated microwave and ultrasonic waves near the air–liquid interface.

B. Frequency domain

The shape of the gate that modulates the microwave was acquired and is shown in Fig. 3(a) and its spectrum in Fig. 3(b). The bandwidth upper limit of this pulse is limited to around 1 MHz. Figure 4 compares the frequency domain of the first echo generated by the microwave and by the generator in the pulse-echo mode. The frequency spectrum of the ultrasonic wave generated by the microwave and filtered by the transducer receiver is comprised (at -6 dB) between 0.1 and 0.8 MHz. Then it seems reasonable to assume that the frequency content of the ultrasonic wave generated by the microwave source is controlled by the shape of the gate. In the future, it will be more convenient to use a broadband receiver, such as a laser probe.

C. Linearity

Figure 5 presents the evolution of the peak amplitude of the first echo generated by the microwave function of the instantaneous power of the microwave, in the range of 0 to 100 kW. This corresponds to a mean power of 0 to 34 W. The energy transformation between microwave and ultrasound is a linear phenomenon in this energy range.

The amplification of the receiver was around 40 dB. Clearly low power sources can be used in the future to generate ultrasonic waves in liquids.

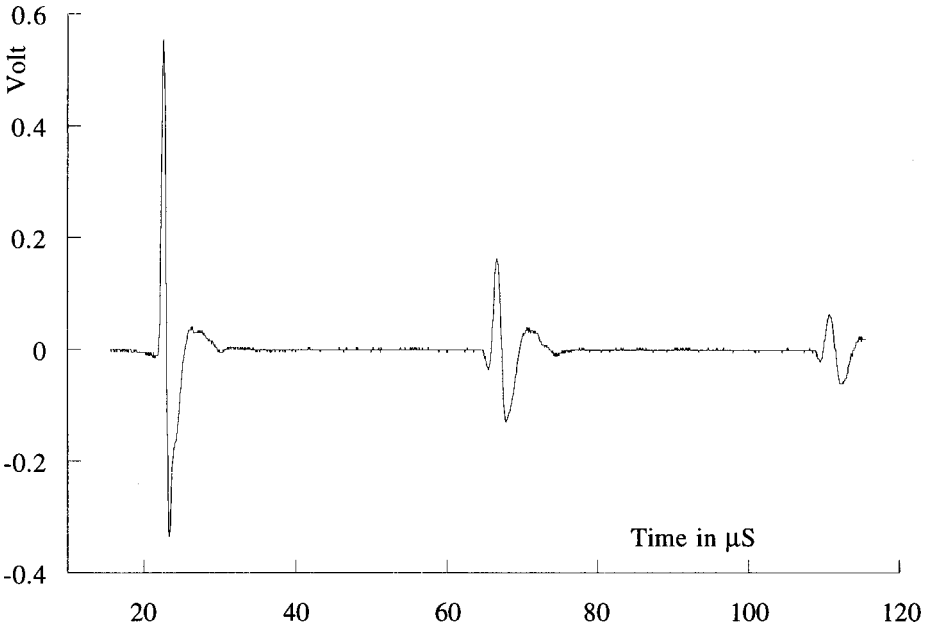

FIG. 2. Ultrasonic waves generated by microwave at the air/water interface.

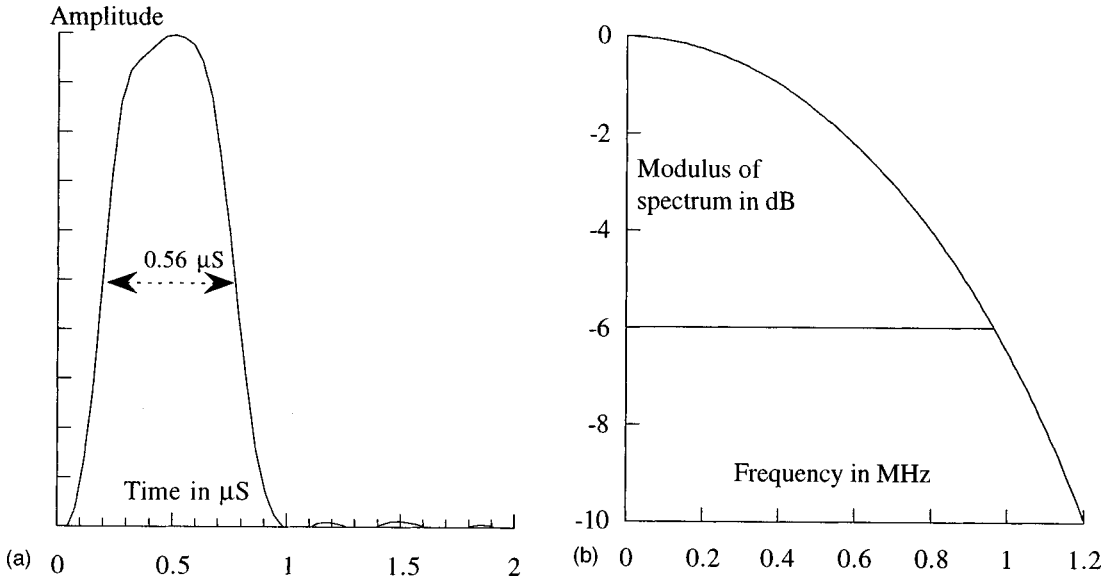

FIG. 3. (a) Time history of the gate. (b) Frequency spectrum of the gate.

D. Shift of the time-of-flight versus power

It is noticeable to consider time-of-flight as a function of source power. This time should be around 22.1 μs according to the previous measurement. This cannot be known absolutely because there is an uncertainty between the trigger position and the beginning of the magnetron oscillation. However, the waveforms at various amounts of power can be compared. As shown in Fig. 6, the times-of-flight decrease as the power increases. If a source region between microwave and elastic wave is considered near the surface, one can assume that the source region depth is increasing with power and the propagation distance of the ultrasonic wave is decreased. This depth can be estimated to around 370 μm (0.25 μs in water) for 50 kW and is about 100 times smaller than the electromagnetic wavelength.

It is important to notice that the oscilloscope was triggered by the gate, with no variation of the trigger position. However, if one expects a slight supplementary delay when the power is increased, the shift would be the reverse of what it is shown in Fig. 6.

III. GENERATION AT THE INTERFACE AIR–SOLID AND SOLID–AIR

A. Weakly absorbing materials

The experimental setup (Fig. 1) is slightly modified to investigate ultrasonic wave generation in a solid. A contact transducer (Panametrics 101; Central frequency 0.5 MHz) is connected to the solid through a coupling medium (Fig. 7). The receiver is replaced by a more powerful amplifier (Panametrics 5058 PR; Gain: 60 dB) since the ultrasonic wave amplitudes in the solid were much smaller than in water.

Using the pulse-echo technique, the time-of-flight for a round trip in a block of PVC was found equal to 25.6 μs. This value corresponds to a thickness of 29.5 mm with a longitudinal wave velocity of 2.3 mm/μs. Figure 8 presents the ultrasonic echoes generated by the microwave source at a power of 100 kW. Although the noise in this waveform could be easily suppressed by averaging, it is presented in this way to estimate the signal-to-noise ratio.

The time-of-flight of the first echo U_1 is about 12 μs. This measurement is not accurate since the beginning of the echo is not well defined, nevertheless it proves that the

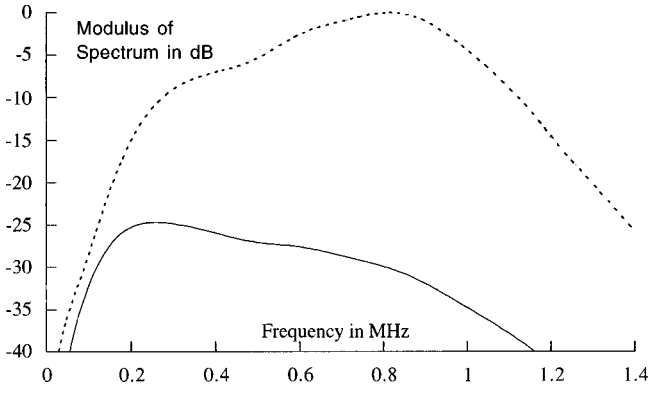

FIG. 4. Modulus of the frequency spectrum. Solid line: first ultrasonic echo generated by the microwave. Dashed line: first ultrasonic echo generated by the generator in the pulse-echo mode.

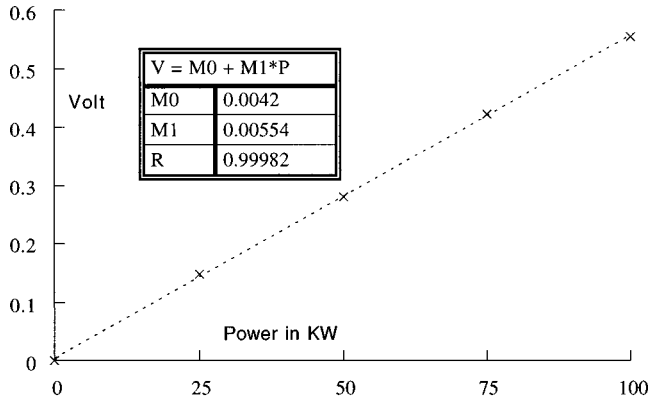

FIG. 5. Peak amplitude of the first echo generated by the microwave versus power.

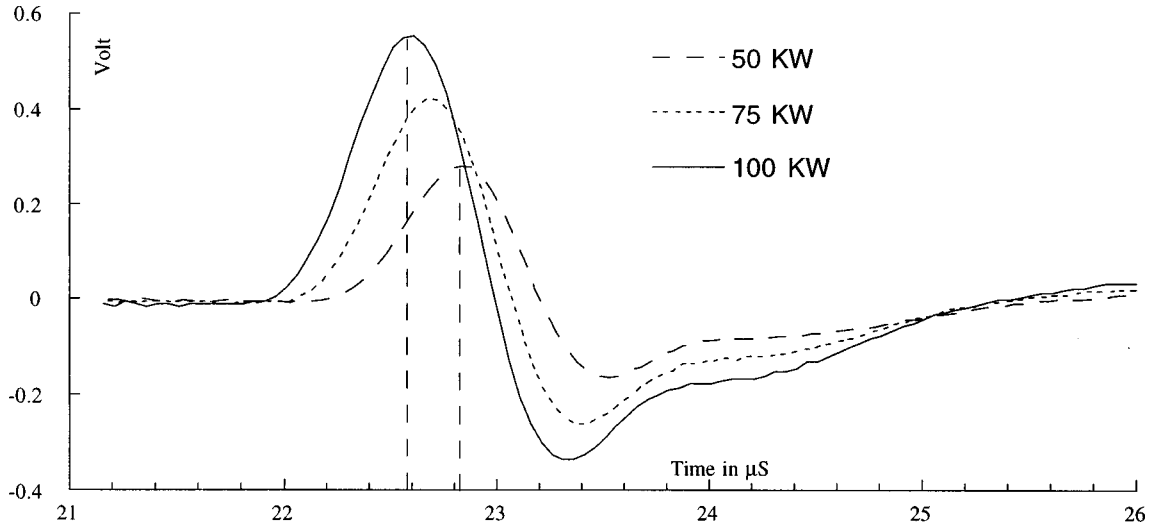

FIG. 6. First echoes generated by the electromagnetic wave for various values of the electromagnetic power.

source is located near the upper surface of the plate. The measurement of the delay between echoes U_1 and U_2 is more accurate since it is possible to isolate each echo with a temporal window and to measure the delay by a standard cross-correlation procedure. The result, 25.6 μs, is identical to the measure made with the pulse-echo technique.

Another echo L_1 appears between U_1 and U_2. The arrival time of this echo, approximately 25 μs, corresponds to a round trip inside the plate. That means there is an important source of ultrasonic waves located near the lower surface. The delay (12.5 μs) between the echoes U_1 and L_1 is slightly less than the time-of-flight for one trip inside the plate. Therefore the sources at upper and lower surfaces are located in a volume with a small thickness. The accurate measurement of the source region depth must be performed with a more precise setup since its value seems much smaller than in the case of water.

By using a more absorbing material, it is easier to reveal the presence of this source region. The PVC is replaced by a 1-cm-thick plate made of paraffin wax with 10% carbon powder. The waveforms, presented in Fig. 9, show the variation of the amplitude and the time-of-flight of one echo as a function of the electromagnetic wave power. As previously, the time-of-flight is decreased when the power is increased. The difference is the order of 1 μs which corresponds to an estimated source region depth of 1 mm (velocity$\approx$1.7 mm/μs) which is much larger than in water. This must be explained by the attenuation of microwaves which is much larger in water than in PVC.

B. Reflecting materials

As for optical waves, metals are almost pure reflectors for electromagnetic waves. To observe the generation of ultrasonic waves in metal, the PVC plate was replaced by a 49.3-mm-thick plate made of aluminum. The corresponding waveform is not shown here because the ultrasonic echoes were corrupted by in the ambient electromagnetic noise, but with a better setup one can imagine producing ultrasonic waves in metals from electromagnetic waves. To enhance the production of ultrasound, a 2-mm-thick water layer was poured on the surface. The waveform is presented in Fig. 10. The ultrasound amplitude was so important that the gain of the receiver was set to 0 dB. The first arrival time ($\approx$8.2 μs) in the first echo is only slightly larger than one trip in the aluminum plate ($\approx$7.8 μs). There is generation of ultrasound everywhere in the water layer and almost at the water–aluminum interface.

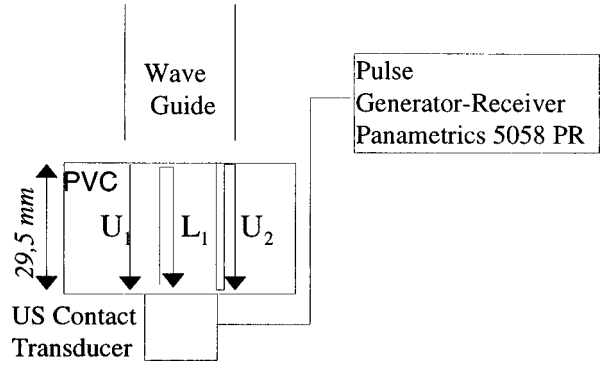

FIG. 7. Experimental setup to generate and receive the ultrasonic wave in solid.

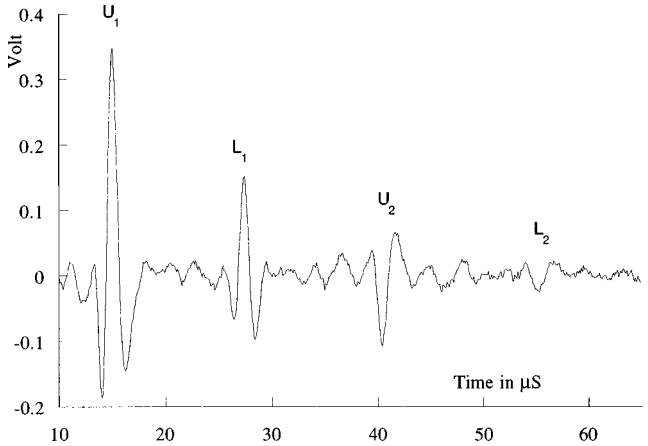

FIG. 8. Ultrasonic waves generated by microwave source at air/solid and solid/air interfaces (electromagnetic power 100 kW).

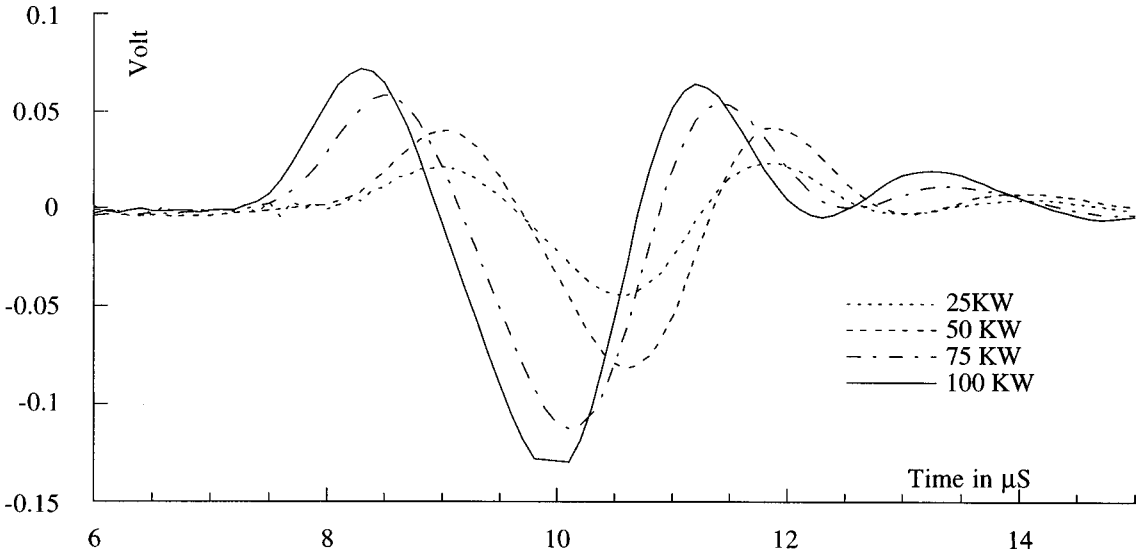

FIG. 9. Ultrasonic wave generated in a plate made of paraffin wax with 10% carbon powder.

In order to explore the possible application to the *in situ* nondestructive evaluation of metallic materials, a very thin layer of paint was sprayed on the aluminum surface. The gain of the receiver was again increased to 60 dB. The waveform in Fig. 11 shows the noise due to the electromagnetic pulse and a first echo arriving at around 8 μs. This result is promising for NDE applications since structures are often painted.

IV. MODEL

To build a model for the interaction between electromagnetic waves and elastic waves more precise experiments and investigations are necessary. However, the following experimental considerations will be useful to develop a model:

(i) The evolution of the electromagnetic wave power creates elastic waves in a frequency domain imposed by the gate width.

(ii) The transduction is linear and occurs in a zone near the interface.

(iii) The source region depth depends on the material properties and the power of the electromagnetic wave. The higher the power or the higher the absorption of the electromagnetic wave, the deeper the source region. Its depth is much smaller than the penetration depth of the microwave inside the material, since the microwave wavelength is much larger than the source region.

Laser impacts also create elastic waves via several mechanisms: radiation pressure, electrostriction, Brillouin scattering, and thermoelastic expansion. The latter is dominant under normal circumstances. These mechanisms and their applications are completely described in literature and textbooks.[6,7] In addition, the presence of a ''precursor'' was observed in laser generation and explained with one- or two-dimensional models,[2,8,9] taking into account the presence of a

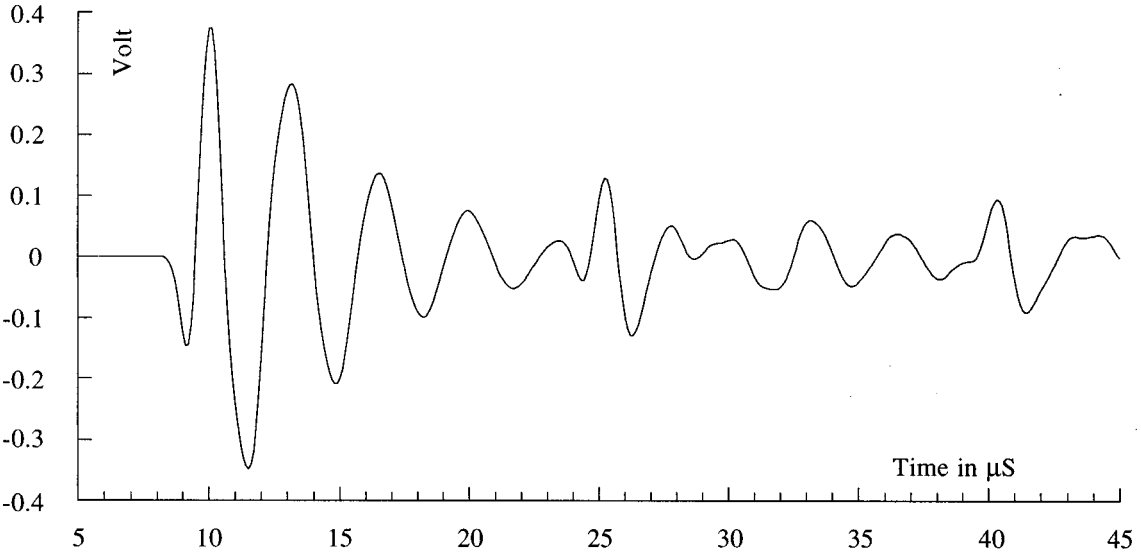

FIG. 10. Ultrasonic wave generated at the water/aluminum surface (electromagnetic power 100 kW).

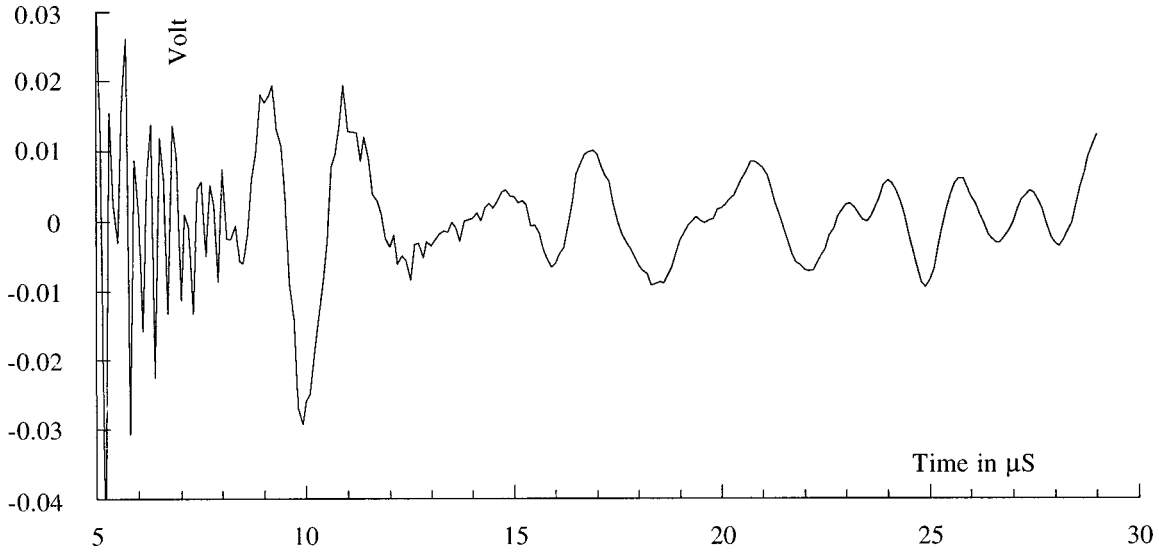

FIG. 11. Ultrasonic wave generated at the paint/aluminum surface (electromagnetic power 100 kW).

source buried below the surface. The ''precursor'' appearance is equivalent to what is observed from the evolution of times-of-flight (Fig. 6). Since the electromagnetic source is large in comparison with the ultrasonic wavelength, it is conceivable that the one-dimensional model would be appropriate.[2,8,9]

As explained in Ref. 9, a nonfocused laser source in the thermoelastic regime generates two waves located at both faces of the plate. A similar analysis would be appropriate for a microwave source. The stress σ induced by a temperature rise ΔT is given by

$$\sigma(x,t)=C\,\frac{\partial u(x,t)}{\partial x}-\lambda\Delta T, \tag{1}$$

where u is the normal displacement in the ultrasonic field, C is the diagonal component of the rigidity tensor in the x direction normal to the interface, and λ is the thermal stress coefficient. The interfaces at $x=0$ and $x=L$ are stress free, then $\sigma(0,t)=0$ and $\sigma(L,t)=0$. Equation (1) implies there is a displacement gradient at $x=0$ and $x=L$. Therefore, two waves are produced at both interfaces if the material does not absorb too much of the electromagnetic energy. If the absorption is negligible, the spatial dependence of ΔT is weak, and the second term on the right-hand side in the wave equation

$$\rho\,\frac{\partial^2 u(x,t)}{\partial t^2}=C\,\frac{\partial^2 u(x,t)}{\partial x^2}-\lambda\,\frac{\partial \Delta T}{\partial x} \tag{2}$$

can be neglected and the waves are produced near the interfaces. If the absorption increases, this term is responsible for the buried sources of ultrasounds and the depth of the generation zone increases.

This model seems even more appropriate for the microwaves than for the optical waves since their wavelengths are much larger. For instance, in this paper the microwave wavelength is larger than the thickness of the tested materials. Comparison between theory and experiment will be presented in a later paper.

V. CONCLUSIONS

This paper highlights the transformation of energy between electromagnetic waves and elastic waves through the surface of liquid or solid materials.

The experimental considerations lead to a one-dimensional thermoelastic model. More experiments must be conducted to link the electromagnetic and elastic material properties to the elastic waves characteristics. These experimental observations will permit us to model the energy transformation in order to estimate the penetration depth, to predict the response of any material and to consider the applications to the nondestructive evaluation of materials.

Ultrasonic waves can be generated at interface air–solid and also solid–air. If the electromagnetic attenuation is not too significant, the electromagnetic wave can generate ultrasound inside the materials in a zone located near a cavity or a delamination. Clearly, some important applications to the nondestructive testing of material can be accomplished.

There is a very large spectrum of applications since the gate width and shape of the microwave can be controlled to produce lower frequency content. In the other way, ultrasonic waves with very high frequency content can be produced with shorter pulses and even a monocycle pulse source.[10]

ACKNOWLEDGMENTS

The authors gratefully acknowledge the CEL (Centre d'Essais des Landes) for supplying the time-gated microwave source and the help of Bernard Desvergnes, Jean Brandier, Jean-Claude Devant and Stephane Lallement.

[1] *Proceedings of Review of Progress in Quantitative NonDestructive Evaluation*, edited by D. O. Thompson and D. E. Chimenti (Plenum, New York), Vols. 1–16.
[2] R. M. White, ''Generation of Elastic Waves by Transient Surface Heating,'' J. Appl. Phys. **34(12)**, 3559–3567 (1963).
[3] J. C. Lin, ''Further Studies on the Microwaves Auditory Effect,'' IEEE Trans. Microwave Theory Tech. **MTT-25(11)**, 939–943 (1977).
[4] D. Borth, ''Theoretical Analysis of Acoustic Signal Generation in Mate-

rials Irradiated with Microwave Energy,'' IEEE Trans. Microwave Theory Tech. **MTT-25(11)**, 945–953 (1977).
[5] R. L. Nasoni, G. A. Evanoff, P. G. Halverson, and T. Bowen, ''Thermoacoustic Emission by Deeply Penetrating Microwave Radiation,'' in IEEE Ultras. Symp. (1984), pp. 633–638.
[6] D. A. Hutchins, ''Ultrasonic generation by pulsed laser,'' *Physical Acoustics*, edited by W. P. Mason and R. N. Thurston (New York, 1988), Vol. XVIII.
[7] C. B. Scruby and L. E. Drain, *Laser Ultrasonics Techniques and Applications* (Hilger, Bristol, 1990).
[8] K. L. Telschow and R. J. Conant, ''Optical and thermal parameter effects on laser-generated ultrasound,'' J. Acoust. Soc. Am. **88**, 1494–1502 (1990).
[9] A. Hénault, A. Cournoyer, F. Enguehard, and J. Bertrand, ''A study of dynamic thermal expansion using a laser-generated ultrasound 1-*d* model,'' Proceedings of the 9th International Conference on Photoacoustic and Photothermal Phenomena, edited by S. Y. Zhang, Nanjing, China (1996), pp. 370–374.
[10] F. C. Chen and W. C. Chew, ''An impulse radar nondestructive evaluation system,'' in *Review of Progress in QNDE* (Plenum, New York, 1997), Vol. 16A, pp. 709–715.

An improved continuum mixture model for wave propagation in fibrous composites

Adnan H. Nayfeh and Wael G. Abdelrahman
Department of Aerospace Engineering and Engineering Mechanics, University of Cincinnati, Cincinnati, Ohio 45221-0070

(Received 25 September 1997; accepted for publication 14 April 1998)

A new improved continuum mixture model is developed for the propagation of axisymmetric longitudinal waves in fibrous composites. The major improvement on the original model of Hegemier, Gurtman, and Nayfeh [Int. J. Solids Struct. **9**, 395 (1973)] is achieved by the inclusion of the axial rate of change of the radial displacement in the shear constitutive relations which was neglected previously. This model has also been extended to treat situations in which the fiber and the matrix are anisotropic. The improved model is found superior to the original one, when compared with the recently acquired experimental data and exact solutions. © *1998 Acoustical Society of America.* [S0001-4966(98)00508-6]

PACS numbers: 43.35.Cg [HEB]

INTRODUCTION

In a recent paper,[1] Huang and Rokhlin presented low-frequency experimental dispersion data for longitudinal wave propagation in a fibrous composite system. The specific composite tested consisted of a titanium alloy matrix reinforced with three-layer concentric cylindrical SiC fibers (SCS-6). Each fiber is about 140 μm in total diameter and consists of a carbon core and a SiC shell separated from the matrix by another thin 3-μm-thick carbon layer. All fiber layers, as well as the matrix, are isotropic materials. Huang and Rokhlin compared this experimental data with the available continuum mixture theory model of Hegemier *et al.*[2] Comparisons were shown to be good at arbitrary low-frequency ranges. At relatively higher frequencies, the discrepancy increases significantly and it was suggested that better agreement with the exact solutions was expected. In a subsequent paper,[3] Huang and Rokhlin derived an exact dispersion relation for a multilayered concentric cylindrical fiber reinforced composite. In their study, all of the fiber components as well as the matrix are assumed isotropic. Concurrent with their study, Nayfeh and Nagy[4] derived exact dispersion relations for a similar system when all individual composite layers are anisotropic. Both of the exact solutions were found to better fit the experimental data.

Due to the comparative simplicity, and ease in utility, of the approximate mixture modeling, we have decided to examine the reason for its inability to better fit the data especially at the moderately higher-frequency ranges. We do this with the intention of improving the previously constructed model in Ref. 2. Before we proceed to derive the new improved continuum mixture model, it is instructive to review the various assumptions and approximations adopted in constructing the original model.

In the original continuum mixture theory, fibers made up of single isotropic material are uniformly distributed in an isotropic material matrix. The resulting hexagonal symmetry of the unidirectionally reinforced composite permitted the isolation of a representative unit cell, which in turn was modeled as a concentric cylinder subjected at its outer boundary to vanishing radial displacement and shear stress. Next, guided by the various symmetries and fiber-matrix interface conditions, certain approximate radial dependencies of some of the field variables are assumed which satisfy these conditions. The only other critical approximation was to neglect the term representing the axial rate of change of the radial displacement from the shear constitutive relation for both the fiber and the matrix. As a consequence, the two-dimensional field equations that hold in both the fiber and the matrix, together with their interface continuity conditions, are reduced to a quasi-one-dimensional system of two coupled partial differential equations that automatically satisfy all interface and radial boundary conditions. By assuming a harmonic solution for the field variables, the characteristic dispersion equation of the system is obtained. This characteristic equation predicts the existence of two modes. The fundamental one, which is the only mode that can propagate at arbitrarily low frequencies, starts from the mixture speed at the zero frequency limit and continuously varies to the high-frequency limit of the bulk wave speed in the matrix. The second mode appears after its cutoff frequency and converges, at high frequencies, to the bulk wave speed in the fiber.

In the present work, we develop an improved mixture model based on retaining the term representing the axial rate of change of the radial displacement, which was neglected in the previous model. Since the continuum mixture solutions are most appropriate for two homogenous phase media, namely for media consisting of single material fiber and matrix, we need to model the multilayered fiber of Ref. 1, as an effective homogenized one. Due to the biased geometry of the fiber layers, the effective fiber will have anisotropic properties or, more precisely, will exhibit transverse isotropy. The effective anisotropic properties of the three-component fiber tested in Ref. 1 will be constructed by a repetitive use of the procedure developed by Nayfeh[5] for deriving effective properties for two-component fibrous composites. Thus, the present situation dictates that the applicable continuum mixture model has to be modified for anisotropic media. For this

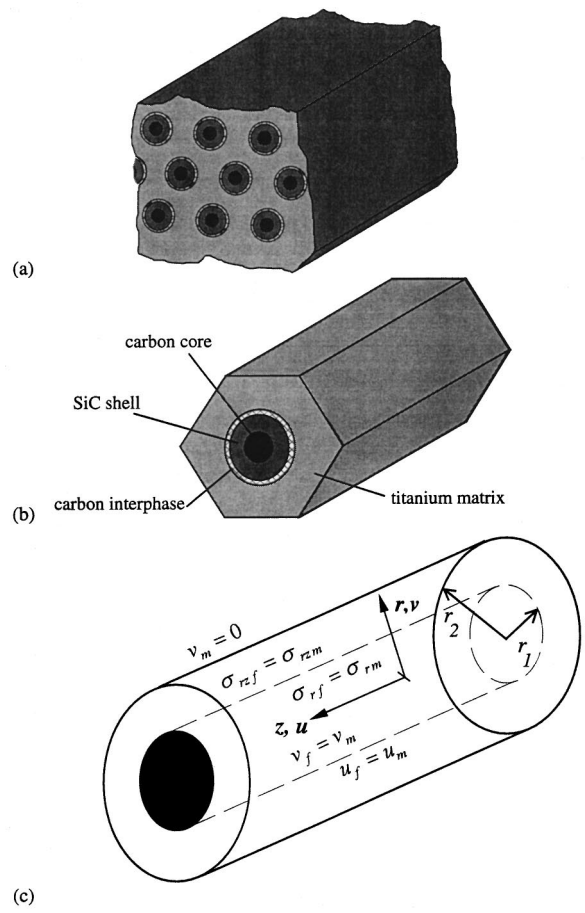

FIG. 1. The composite panel model: (a) the composite panel, (b) the representative unit cell, and (c) the effective fiber concentric cylinder model.

reason, we shall extend the original mixture modeling to include the appropriate transverse anisotropy which is inherent in the tested sample. Moreover, although the matrix in most applications is isotropic, without any extra efforts, we shall also treat it as transversely isotropic. Situations involving isotropic material fibers or matrix can then be easily obtained as special cases by merely imposing the appropriate restrictions on their anisotropic properties.

The dispersion equation, resulting from the improved model, will lead to three modes rather than two as predicted by the original model. The new fundamental mode will show dramatic improvements over its original counterpart in its comparison with the experimental data. As shall also be seen, curious, but interesting, observations are drawn from examining the roles played by the various modes in both models, especially in the high-frequency limits. For completeness, and in order to allow right comparisons, we shall also extend the original continuum mixture model to transversely anisotropic media. This, however, will be deduced as a special case from the results of the present modeling.

I. ANALYTIC MODEL

A. Formulation of the problem

Consider the unidirectionally reinforced periodic composite shown in Fig. 1(a). It has a hexagonal symmetry with a representative unit cell as shown in Fig. 1(b). The specific geometry shown corresponds to the sample tested in Ref. 1. The fiber layers are assumed to be perfectly bonded together and, in turn, to the matrix. To facilitate our analysis, we approximate the unit cell with a concentric cylinder as shown in Fig. 1(c). Here, Fig. 1(c) implies that we have already replaced the discrete fiber with an effective homogenized one. It has an outer radius r_2 with the effective fiber having a radius r_1. The composite symmetry requires the cell in Fig. 1(c) to be subjected to the indicated interface conditions, and also to vanishing radial displacement and shear stress at its outer boundary.

For axisymmetric longitudinal wave propagation, the behavior of the composite is described by the following two-dimensional momentum equations:

$$\frac{\partial \sigma_z}{\partial z} + \frac{1}{r}\frac{\partial}{\partial r}(r\sigma_{rz}) = \rho \frac{\partial^2 u}{\partial t^2}, \tag{1}$$

$$\frac{\partial \sigma_r}{\partial r} + \frac{\partial \sigma_{rz}}{\partial z} + \frac{1}{r}(\sigma_r - \sigma_\theta) = \rho \frac{\partial^2 v}{\partial t^2}. \tag{2}$$

Identifying the fiber and matrix materials with the subscripts f and m, respectively, the fiber and matrix have the transversely isotropic materials constitutive relations taking the form:

$$\begin{Bmatrix} \sigma_z \\ \sigma_\theta \\ \sigma_r \\ \sigma_{r\theta} \\ \sigma_{rz} \\ \sigma_{\theta z} \end{Bmatrix}_f = \begin{bmatrix} f_{11} & f_{12} & f_{12} & 0 & 0 & 0 \\ f_{12} & f_{22} & f_{23} & 0 & 0 & 0 \\ f_{12} & f_{23} & f_{22} & 0 & 0 & 0 \\ 0 & 0 & 0 & f_{44} & 0 & 0 \\ 0 & 0 & 0 & 0 & f_{55} & 0 \\ 0 & 0 & 0 & 0 & 0 & f_{55} \end{bmatrix} \begin{Bmatrix} \varepsilon_z \\ \varepsilon_\theta \\ \varepsilon_r \\ \gamma_{r\theta} \\ \gamma_{rz} \\ \gamma_{\theta z} \end{Bmatrix}_f, \tag{3}$$

$$\begin{Bmatrix} \sigma_z \\ \sigma_\theta \\ \sigma_r \\ \sigma_{r\theta} \\ \sigma_{rz} \\ \sigma_{\theta z} \end{Bmatrix}_m = \begin{bmatrix} m_{11} & m_{12} & m_{12} & 0 & 0 & 0 \\ m_{12} & m_{22} & m_{23} & 0 & 0 & 0 \\ m_{12} & m_{23} & m_{22} & 0 & 0 & 0 \\ 0 & 0 & 0 & m_{44} & 0 & 0 \\ 0 & 0 & 0 & 0 & m_{55} & 0 \\ 0 & 0 & 0 & 0 & 0 & m_{55} \end{bmatrix} \times \begin{Bmatrix} \varepsilon_z \\ \varepsilon_\theta \\ \varepsilon_r \\ \gamma_{r\theta} \\ \gamma_{rz} \\ \gamma_{\theta z} \end{Bmatrix}_m, \tag{4}$$

where

$$\varepsilon_z = \frac{\partial u}{\partial z}, \quad \varepsilon_r = \frac{\partial v}{\partial r}, \quad \varepsilon_\theta = \frac{v}{r}, \quad \gamma_{rz} = \frac{\partial v}{\partial z} + \frac{\partial u}{\partial r} \tag{5}$$

are the axisymmetric strain displacement relations. Here σ_r, σ_z, σ_θ, and σ_{rz} are the nonvanishing components of the stress tensor; u and v are the displacement components in the longitudinal and radial directions, respectively.

We chose to expand the above equations for further use. For axisymmetric longitudinal wave propagation in this system, the applicable constitutive relations are

$$\sigma_z = C_{11}\frac{\partial u}{\partial z} + \frac{C_{12}}{r}\frac{\partial}{\partial r}(rv), \tag{6}$$

$$\sigma_r = C_{22}\frac{\partial v}{\partial r} + \frac{C_{23}}{r}v + C_{12}\frac{\partial u}{\partial z}, \tag{7}$$

$$\sigma_\theta = C_{33}\frac{v}{r} + C_{23}\frac{\partial v}{\partial r} + C_{12}\frac{\partial u}{\partial z}, \tag{8}$$

$$\sigma_{rz} = C_{55}\left(\frac{\partial v}{\partial z} + \frac{\partial u}{\partial r}\right), \tag{9}$$

which hold for the fiber if $C_{ij} = f_{ij}$ and for the matrix if $C_{ij} = m_{ij}$.

The above field equations are supplemented with the following symmetry and continuity conditions:

Symmetry:

$$v_f(z,0,t) = 0, \quad \sigma_{rzf}(z,0,t) = 0, \quad \sigma_{rzm}(z,r_2,t) = 0, \tag{10a}$$

$$v_m(z,r_2,t) = 0, \tag{10b}$$

Continuity (on $r = r_1$):

$$\sigma_{rzf}(z,r_1,t) = \sigma_{rzm}(z,r_1,t), \quad v_f(z,r_1,t) = v_m(z,r_1,t), \tag{10c}$$

$$\sigma_{rf}(z,r_1,t) = \sigma_{rm}(z,r_1,t), \quad u_f(z,r_1,t) = u_m(z,r_1,t). \tag{10d}$$

B. Method of solution

Following the procedure outlined in Ref. 2 if Eqs. (1) and (6) are averaged according to

$$\overline{(\quad)}_f = \frac{1}{\pi r_1^2}\int_0^{r_1} 2\pi(\quad)_f\, dr, \tag{11a}$$

$$\overline{(\quad)}_m = \frac{1}{\pi(r_2^2 - r_1^2)}\int_{r_1}^{r_2} 2\pi(\quad)_m\, dr, \tag{11b}$$

and if the symmetry and continuity conditions (10a)–(10c) are used, one obtains the quasi-one-dimensional momentum equations

$$n_f\frac{\partial \overline{\sigma}_{zf}}{\partial z} = -\tau + n_f\rho_f\frac{\partial^2 \overline{u}_f}{\partial t^2}, \tag{12}$$

$$n_m\frac{\partial \overline{\sigma}_{zm}}{\partial z} = \tau + n_m\rho_m\frac{\partial^2 \overline{u}_m}{\partial t^2}, \tag{13}$$

and the constitutive relations

$$n_f\overline{\sigma}_{zf} = f_{12}S + n_f f_{11}\frac{\partial \overline{u}_f}{\partial z}, \tag{14}$$

$$n_m\overline{\sigma}_{zm} = -m_{12}S + n_m m_{11}\frac{\partial \overline{u}_m}{\partial z}. \tag{15}$$

Here n_f and n_m stand for the volume fractions of the fiber and matrix materials, respectively, and τ and S denote the momentum and the constitutive relations interaction terms, respectively; these quantities are defined as

$$n_f = r_1^2/r_2^2, \tag{16a}$$

$$n_m = (r_2^2 - r_1^2)/r_2^2, \tag{16b}$$

$$\tau = 2n_f\sigma^*/r_1, \tag{17a}$$

$$S = 2n_f v^*/r_1, \tag{17b}$$

where σ^* and v^* are the interface shear stress and radial displacement; namely,

$$\sigma^* = \sigma_{rzf}(z,r_1,t) = \sigma_{rzm}(z,r_1,t), \tag{18}$$

$$v^* = v_f(z,r_1,t) = v_m(z,r_1,t). \tag{19}$$

C. Evaluation of τ and S

The remaining constitutive relations Eqs. (7)–(9) will now be utilized to derive the relevant partial differential equations describing the system in terms of the interaction terms τ and S and the axial displacements $\overline{u}_f$ and $\overline{u}_m$. Once this is done, the problem described by Eqs. (12)–(15) reduces to a quasi-one-dimensional one which retains the integrity of the propagation in the individual fiber and matrix components subject to the interaction terms τ and S. This cannot, however, be done without adopting appropriate approximations. These concern the radial dependence of the radial displacement and the shear stress. Accordingly, we assume

$$v_f(z,r,t) = B(z,t)r, \tag{20a}$$

$$\sigma_{rzf}(z,r,t) = A(z,t)r, \tag{20b}$$

$$v_m(z,r,t) = B(z,t)\frac{n_f}{n_m}\left(\frac{r_2^2}{r^2} - 1\right)r, \tag{21a}$$

$$\sigma_{rzm}(z,r,t) = A(z,t)\frac{n_f}{n_m}\left(\frac{r_2^2}{r^2} - 1\right)r, \tag{21b}$$

chosen to automatically satisfy the symmetry conditions (10a) and (10b) and the interface continuity conditions (10c).

Introducing these approximations into the functions defined in Eq. (17) yields

$$\tau = 2n_f A, \tag{22}$$

$$S = 2n_f B. \tag{23}$$

Using these expressions in Eqs. (12)–(15) leads to

$$n_f\frac{\partial \overline{\sigma}_{zf}}{\partial z} = -2n_f A + n_f\rho_f\frac{\partial^2 \overline{u}_f}{\partial t^2}, \tag{24}$$

$$n_m\frac{\partial \overline{\sigma}_{zm}}{\partial z} = -2n_f A + n_m\rho_m\frac{\partial^2 \overline{u}_m}{\partial t^2}, \tag{25}$$

$$n_f\overline{\sigma}_{zf} = 2n_f f_{12}B + n_f f_{11}\frac{\partial \overline{u}_f}{\partial z}, \tag{26}$$

$$n_m\overline{\sigma}_{zm} = -2m_{12}n_f B + n_m m_{11}\frac{\partial \overline{u}_m}{\partial z}. \tag{27}$$

At once, we notice that two coupled equations can be obtained by substituting $\overline{\sigma}_{zf}$ and $\overline{\sigma}_{zm}$ from Eqs. (26) and (27) into Eqs. (10) and (11), respectively, and using the relations (22) and (23) to eliminate τ and S. This yields

$$n_f f_{11} \frac{\partial^2 \overline{u_f}}{\partial z^2} + 2n_f f_{12} \frac{\partial B}{\partial z} = -2n_f A + n_f \rho_f \frac{\partial^2 \overline{u_f}}{\partial t^2}, \tag{28}$$

$$n_m m_{11} \frac{\partial^2 \overline{u_m}}{\partial z^2} + 2n_f m_{12} \frac{\partial B}{\partial z} = -2n_f A + n_m \rho_m \frac{\partial^2 \overline{u_m}}{\partial t^2}. \tag{29}$$

Next, we start by satisfying the shear constitutive relation (9). Multiplying it with r^2 and integrating by parts in accordance with Eq. (11a), we directly obtain

$$u^* - \overline{u}_f = \frac{r_1^2}{4}\left(\frac{A}{f_{55}} - \frac{\partial B}{\partial z}\right), \tag{30a}$$

where u^* is the interface value of u_f.

Similarly, for the matrix material, if we multiply Eq. (9) by $(r^2 - r_2^2)$, substitute from Eq. (21b), and integrate by parts according to Eq. (11b) we obtain

$$u^* - \overline{u}_m = \frac{r_1^2 Q}{4}\left(\frac{A}{m_{55}} - \frac{\partial B}{\partial z}\right), \tag{30b}$$

where we have used the continuity relation required by Eq. (10d), namely

$$u^*(z,t) = u_f(z, r_1, t) = u_m(z, r_1, t). \tag{31}$$

Here $Q = (1/n_m^2)(n_f^2 - 4n_f + 3 + 2\ln n_f)$ is a function of the volume fractions only. By eliminating u^* from Eqs. (30a) and (30b) we get the important relation

$$\overline{u}_m - \overline{u}_f = \eta_2 A - \eta_1 \frac{\partial B}{\partial z}, \tag{32a}$$

where

$$\eta_1 = \frac{r_1^2}{4}(1 - Q), \quad \eta_2 = \frac{r_1^2}{4}\left(\frac{1}{f_{55}} - \frac{Q}{m_{55}}\right). \tag{32b}$$

Next, we turn our attention to the radial and tangential stresses. Subtracting Eq. (8) from Eq. (7) we obtain

$$\sigma_r - \sigma_\theta = 2C_{55}\left(\frac{\partial v}{\partial r} - \frac{v}{r}\right). \tag{33}$$

Specializing this equation to the fiber using the approximation of Eq. (20a) yields

$$\sigma_{rf} = \sigma_{\theta f}, \tag{34a}$$

and to the matrix, using Eq. (21a), gives

$$\sigma_{rm} - \sigma_{\theta m} = -\frac{4m_{55}}{n_m}\frac{r_1^2}{r^2} B. \tag{34b}$$

Following the above procedure, if we substitute from Eqs. (20b) and (34a) into Eq. (2), multiply the resulting equation by r^2, and integrate according to Eq. (11a), we obtain

$$\sigma_r^* - \overline{\sigma}_{rf} + \frac{r_1^2}{4}\left(\frac{\partial A}{\partial z} - \rho_f \frac{\partial^2 B}{\partial t^2}\right) = 0. \tag{35a}$$

Similarly, substituting from Eqs. (21b) and (34b) into Eq. (2), multiplying the resulting equation by $(r^2 - r_2^2)/(r_2^2 - r_1^2)$, and integrating as per Eq. (11b) we obtain

$$\sigma_r^* - \overline{\sigma}_{rm} + \frac{2m_{55}}{n_m^2}(n_m + n_f \ln n_f)B + \frac{r_1^2 Q}{4}\left(\frac{\partial A}{\partial z} - \rho_m \frac{\partial^2 B}{\partial t^2}\right) = 0, \tag{35b}$$

where

$$\sigma_r^*(z,t) = \sigma_{rf}(z, r_1, t) = \sigma_{rm}(z, r_1, t), \tag{36}$$

is the common interfacial radial stress.

Eliminating σ_r^* from Eqs. (35a) and (35b) yields

$$\overline{\sigma}_{rf} - \overline{\sigma}_{rm} = \frac{r_1^2}{4}\left(\frac{\partial A}{\partial z} - \rho_f \frac{\partial^2 B}{\partial t^2}\right) - \frac{r_1^2 Q}{4}\left(\frac{\partial A}{\partial z} - \rho_m \frac{\partial^2 B}{\partial t^2}\right) - \frac{2m_{55}}{n_m^2}(n_m + n_f \ln n_f)B. \tag{37}$$

We have so far identically satisfied all required interface conditions. We now need to eliminate $\overline{\sigma}_{rf}$ and $\overline{\sigma}_{nm}$ from the above equations. In order to do this, we specialize the constitutive equation (7) for the fiber and matrix by substituting into it from Eqs. (20a) and (21a), respectively, to obtain

$$\sigma_{rf} = (f_{22} + f_{12})B + f_{12}\frac{\partial u_f}{\partial z}, \tag{38a}$$

$$\sigma_{rm} = -\frac{n_f}{n_m}\left(m_{22} + m_{12} + 2m_{55}\frac{r_2^2}{r^2}\right)B + m_{12}\frac{\partial u_m}{\partial z}. \tag{38b}$$

Averaging Eqs. (38) according to Eq. (11) yields, for the fiber and the matrix, respectively,

$$\overline{\sigma}_{rf} = (f_{22} + f_{12})B + f_{12}\frac{\partial \overline{u_f}}{\partial z}, \tag{39a}$$

$$\overline{\sigma}_{rm} = -\frac{n_f}{n_m}\left(m_{22} + m_{12} - \frac{2m_{55}}{n_2}\ln n_f\right)B + m_{12}\frac{\partial \overline{u_m}}{\partial z}. \tag{39b}$$

Eliminating $\overline{\sigma}_{rf}$ and $\overline{\sigma}_{rm}$ between Eqs. (37) and (39a) and (39b) we finally get the following important equation:

$$\xi_1 B + \xi_2 \frac{\partial^2 B}{\partial^2 t} = m_{12}\frac{\partial \overline{u_m}}{\partial z} - f_{12}\frac{\partial \overline{u_f}}{\partial z} + \eta_1 \frac{\partial A}{\partial z}, \tag{40a}$$

where

$$\xi_1 = \frac{1}{n_m}[n_m(f_{22} + f_{12}) + n_f(m_{22} + m_{12}) + m_{55}],$$

$$\xi_2 = \frac{r_1^2}{4}(\rho_f - Q\rho_m). \tag{40b}$$

The behavior of the composite system is completely described by Eqs. (28), (29), (32), and (40). As seen, this system consists of four partial differential equations that couple the two longitudinal averaged displacements, interfacial shear stress and interfacial radial displacement. Before we proceed to derive the characteristic dispersion equation for this improved model we shall summarize the original

continuum mixture model including anisotropic material properties.

II. THE ORIGINAL CONTINUUM MIXTURE MODEL

The relevant mixture equations for the original mixture model can be directly deduced from the results of the present improved model as follows: First we neglect the $\partial v/\partial z$ term from the shear constitutive relation (9). This reduces Eqs. (30a) and (30b) to

$$u^*-\overline{u}_f=\frac{r_1^2}{4}\frac{A}{f_{55}}, \tag{41a}$$

$$u^*-\overline{u}_m=\frac{r_1^2 Q}{4}\frac{A}{m_{55}}. \tag{41b}$$

These two equations can be manipulated to solve for A and u^* as

$$A=\frac{G}{2n_f}(\overline{u}_m-\overline{u}_f), \tag{42}$$

and

$$u^*=\frac{1}{(m_{55}-f_{55}Q)}(m_{55}\overline{u}_m-f_{55}Q\overline{u}_f), \tag{43}$$

where $G=8f_{55}m_{55}/r_2^2(m_{55}-f_{55}Q)$.

Next, specializing Eqs. (38a) and (38b) to $r=r_1$ and invoking the interface continuity equation (10d) yields

$$B=\frac{(m_{12}-f_{12})}{2n_f D}\frac{\partial u^*}{\partial z}, \tag{44a}$$

where

$$D=\frac{1}{2n_f n_m}[n_m(f_{22}+f_{12})+n_f(m_{22}+m_{12})+2m_{55}]. \tag{44b}$$

Combining this equation with Eq. (43) and, by eliminating u^*, we solve for B in terms of the strain components $\partial\overline{u}_f/\partial z$ and $\partial\overline{u}_m/\partial z$ as

$$B=\frac{F}{2n_f}\left(m_{55}\frac{\partial\overline{u}_m}{\partial z}-f_{55}Q\frac{\partial\overline{u}_f}{\partial z}\right), \tag{45a}$$

where

$$F=\frac{(m_{12}-f_{12})}{D(m_{55}-f_{55}Q)}. \tag{45b}$$

Substituting from this equation back into the averaged constitutive relations (26) and (27), combining the resulting equations with Eq. (24) and (25), and using Eq. (32) to eliminate A leads to the two coupled partial differential equations

$$c_{11}\frac{\partial^2\overline{u}_f}{\partial z^2}+c_{12}\frac{\partial^2\overline{u}_m}{\partial z^2}-n_f\rho_f\frac{\partial^2\overline{u}_f}{\partial t^2}-G(\overline{u}_f-\overline{u}_m)=0, \tag{46a}$$

$$c_{22}\frac{\partial^2\overline{u}_m}{\partial z^2}-c_{21}\frac{\partial^2\overline{u}_f}{\partial z^2}-n_m\rho_m\frac{\partial^2\overline{u}_m}{\partial t^2}-G(\overline{u}_m-\overline{u}_f)=0. \tag{46b}$$

Here the coefficients c_{11}, c_{12}, c_{21}, c_{22} are given as combinations of the fiber and matrix properties and volume fractions as

$$c_{11}=n_f f_{11}-f_{12}f_{55}FQ, \quad c_{12}=f_{12}m_{55}F, \tag{47a}$$

$$c_{21}=-m_{12}f_{55}FQ, \quad c_{22}=n_m m_{11}-m_{12}m_{55}F. \tag{47b}$$

III. HARMONIC WAVES

In order to derive the characteristic dispersion behavior of the composite, we assume a steady-state harmonic solution for the system as

$$(\overline{u}_f,\overline{u}_m,A,B)=(X_1,X_2,X_3,X_4)e^{i(kz-\omega t)}, \tag{48}$$

where X_i, $i=1,...,4$ are the amplitudes, k is the wave number, and ω is the circular frequency. Substituting these expressions into the system of equations (28), (29), (32), and (40) and rearranging in matrix form, we obtain

$$\begin{bmatrix} n_f(\rho_f\omega^2-f_{11}k^2) & 0 & 2n_f & 2n_f f_{12}k \\ 0 & n_m(\rho_m\omega^2-m_{11}k^2) & -2n_f & -2n_f m_{12}k \\ -1 & 1 & -\eta_2 & \eta_1 k \\ -f_{12}k & m_{12}k & \eta_1 k & \xi_1-\xi_2\omega^2 \end{bmatrix} \times \begin{Bmatrix} X_1 \\ X_2 \\ X_3 \\ X_4 \end{Bmatrix} = \underline{0}. \tag{49}$$

For nontrivial solutions, the determinant must be zero; this defines the expanded characteristic dispersion equation of the system as

$$a_1k^6-a_2k^4+a_3k^2-a_4=0, \tag{50}$$

where

$$\begin{aligned} a_1&=n_m f_{11}m_{11}\eta_1^2, \\ a_2&=4\eta_1(n_f f_{11}m_{12}+n_m f_{12}m_{11})+2\eta_2(n_f f_{11}m_{12}^2 \\ &\quad +n_m f_{12}^2 m_{11})+n_m\omega^2\eta_1^2(m_{11}\rho_f+f_{11}\rho_m) \\ &\quad -n_m f_{11}m_{11}\eta_2(\xi_1-\xi_2\omega^2), \\ a_3&=4\omega^2\eta_1(n_f m_{12}\rho_f+n_m f_{12}\rho_m)+2\omega^2\eta_2(n_f m_{12}^2\rho_f \\ &\quad +n_m f_{12}^2\rho_m)-4n_f(f_{12}-m_{12})^2+2(n_f f_{11}+n_m m_{11}) \\ &\quad \times(\xi_1-\xi_2\omega^2)-n_m\omega^2\eta_2(m_{11}\rho_f+f_{11}\rho_m) \\ &\quad \times(\xi_1-\xi_2\omega^2), \\ a_4&=\omega^2(2n_f\rho_f+2n_m\rho_m-n_m\rho_f\rho_m\eta_2)(\xi_1-\xi_2\omega^2). \end{aligned}$$

For a given frequency, this resulting equation admits six solutions for k or, more precisely, three solutions for k^2. Thus, solutions for k occur in three pairs, each pair having two k's that are negative of each other. We shall label them k_q, $q=1,2,...,6$. Three values of k represent three wave numbers for three modes propagating in the positive z direction, whereas the others represent three wave numbers of three modes propagating in the negative z direction. The phase velocity of each mode is defined as $c_q=\omega/k_q$. Similar dispersion characteristic equations can be easily obtained for the

TABLE I. Material properties and dimensions for the fiber and matrix materials.

Material	Density (kg/m^3)	C_{11} (GPa)	C_{12} (GPa)	C_{13} (GPa)	C_{44} (GPa)	C_{55} (GPa)	Radius (μm)
Isotropic carbon	1700	49	17	17	16	49	18
SiC	3200	446	92	92	177	446	68
Interphase carbon	2100	31	21.8	21.8	4.6	31	71
Titanium	5400	193	103	103	45	193	132.3

original mixture model by assuming harmonic solutions to Eqs. (46a) and (46b). This, however, lends to only two propagating modes.

Based upon the two models described above, we now proceed to construct dispersion curves for the composite sample tested in Ref. 1. The isotopic material properties and dimensions of both the fiber layers and the matrix are obtained from Ref. 4 and reproduced in Table I.

As mentioned earlier in the Introduction, the effective fiber anisotropic properties are calculated from these individual isotropic properties by a repetitive application of the procedure outlines in Ref. 5, which can handle single material fiber and matrix. The construction procedure is outlined as follows: first, the fiber core is assumed to be immersed in a cladding surrounding and their combined stiffness matrix is obtained. Second, the composite anisotropic combination of core and cladding is assumed to be immersed in an interphase carbon, and their combined stiffness matrix is obtained. The resulting f_{ij} matrix contains the stiffness coefficients of the transversely isotropic effective fiber calculated as

$$f_{ij}=\begin{bmatrix} 381.3 & 58.24 & 58.24 & 0 & 0 & 0 \\ 58.24 & 262.8 & 56.20 & 0 & 0 & 0 \\ 58.24 & 56.20 & 262.8 & 0 & 0 & 0 \\ 0 & 0 & 0 & 37.29 & 0 & 0 \\ 0 & 0 & 0 & 0 & 65.35 & 0 \\ 0 & 0 & 0 & 0 & 0 & 65.35 \end{bmatrix}. \tag{51}$$

The stiffness coefficients of the isotropic titanium matrix is given as

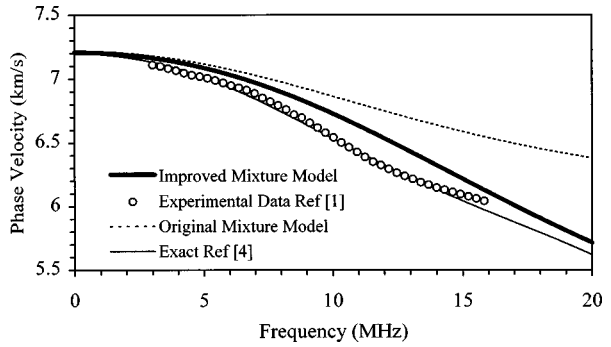

FIG. 2. Fundamental mode comparisons of both mixture models, the exact solution and experimental data.

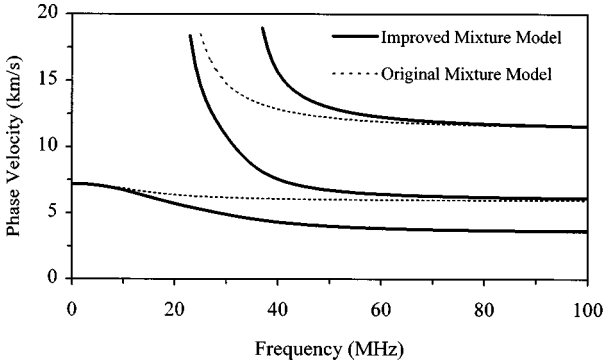

FIG. 3. Extended frequency mode comparisons for the two mixture models.

$$m_{ij}=\begin{bmatrix} 193.0 & 103.0 & 103.0 & 0 & 0 & 0 \\ 103.0 & 193.0 & 103.0 & 0 & 0 & 0 \\ 103.0 & 103.0 & 193.0 & 0 & 0 & 0 \\ 0 & 0 & 0 & 45 & 0 & 0 \\ 0 & 0 & 0 & 0 & 45 & 0 \\ 0 & 0 & 0 & 0 & 0 & 45 \end{bmatrix}. \tag{52}$$

The above stiffness matrices are all that is necessary to generate the dispersion curves, based on solutions of Eq. (50). In Fig. 2 the frequency dependence of the fundamental mode is plotted and compared with results obtained from the exact solutions of Ref. 4 and the experimental data of Huang and Rokhlin. Also included for comparison is the fundamental mode obtained from solution of the characteristic equation which can be easily obtained from Eqs. (46). As can be seen, significant improvements are achieved by the improved mixture model when compared with the experimental data as well as with the exact solution.

Extended frequency-dependent dispersion curves are shown and compared for both mixture models in Fig. 3. Although both mixture models are essentially valid for low-frequency ranges, as this figure shows, the high-frequency limits predict effective bulk waves with wave speeds that are either pure or combinations of the virgin properties of the fiber and matrix and their volume fractions. The original mixture model predicts the two longitudinal pure bulk waves of the fiber and the matrix, individually. These bulk wave limits have previously been observed experimentally.[6] The improved model, on the other hand, predicts three bulk wave limits; the two pure longitudinal and a mixture shear. An analytical expression for this mixture shear wave speed limit can be easily extracted from Eq. (50) as

$$c_s^2=\frac{(1-Q)^2 f_{55} m_{55}}{(\rho_f-\rho_m Q)(m_{55}-f_{55}Q)}.$$

The curious observation here is the manner in which the various modes evolve. Whereas both fundamental modes converge at the zero frequency limit to the same effective mixture wave speed, each converges, as the frequency increases, to a different bulk wave. The mode of the original model converges to a bulk longitudinal and that of the improved model to the bulk mixture shear. Notice also that the

cutoff frequency for the second modes of both models coincide, but converge to the two bulk wave speeds as the frequency increases.

ACKNOWLEDGMENT

This work has been supported by AFOSR Grant No. 95-0269, Dr. Walter Jones, Program Manager.

[1] W. Huang and S. I. Rokhlin, Rev. Prog. Quant. Nondestr. Eval. **14**, 1233–1240 (1995).
[2] G. A. Hegemier, G. A. Gurtman, and A. H. Nayfeh, Int. J. Solids Struct. **9**, 395 (1973).
[3] W. Huang, S. I. Rokhlin, and Y. J. Wang, Ultrasonics **33**, 365–375 (1995).
[4] A. H. Nayfeh and P. B. Nagy, J. Acoust. Soc. Am. **99**, 931–941 (1996).
[5] A. H. Nayfeh, *Wave Propagation in Layered Anisotropic Media with Application to Composites* (Elsevier, Amsterdam, 1995).
[6] C. H. Yew and P. N. Jogi, Int. J. Solids Struct. **12**, 693–703 (1976).

Lamb waves in highly attenuative plastic plates

C. W. Chan and P. Cawley
Department of Mechanical Engineering, Imperial College, Exhibition Road, London SW7 2BX, England

(Received 22 October 1997; accepted for publication 20 April 1998)

The influence of material attenuation on Lamb wave dispersion behavior has been studied analytically. As the attenuation is increased, keeping the ratio of the bulk longitudinal to bulk shear wave attenuation constant at the value measured in high-density polyethylene, the degree of coupling between the shear and longitudinal partial waves decreases and the phase velocity dispersion curves for different modes of the same symmetry can cross; this is not possible for an elastic plate. With increasing attenuation, some modes become asymptotic to the bulk longitudinal velocity at high frequency, rather than to the bulk shear velocity. At high values of attenuation, there is minimal coupling between the longitudinal and shear partial waves and the behavior of the longitudinal modes is analogous to that of a ''fluid plate.'' The predicted group velocities and attenuations of selected modes in a high-density polyethylene plate have been checked experimentally, and good agreement was obtained. © *1998 Acoustical Society of America.* [S0001-4966(98)02508-9]

PACS numbers: 43.35.Pt [HEB]

INTRODUCTION

Most of the literature on Lamb waves has to date concentrated on their propagation in materials which are elastic with very little or no internal (material) damping. Attenuation in Lamb waves can be broadly divided into two categories: attenuation caused as a result of energy transfer from the material of interest into the surroundings (commonly known as ''leakage''), and internal (material) attenuation, for example that which is found in a viscoelastic medium. There has been a considerable amount of work on leakage (see, for example, Refs. 1–5) but relatively little on the effect of material attenuation. Plane waves propagating in a lossy medium have been considered by many authors (see, for example, Ref. 6) and the effect of anelasticity on surface waves propagating on the surface of the earth has been studied by geologists.[7,8] Plate waves in viscoelastic media have been analyzed by Chervinko and Senchenkov[9] and Tanaka and Kon-no.[10] Nkemzi[11] extended the work of Tanaka and Konno, presenting the dispersion curves for a viscoelastic plate, and investigating the relationship between the elastic and viscoelastic solutions. However, the emphasis of the paper is more on the solution technique than on the form of the dispersion curves.

The authors have been investigating different possible methods for inspecting butt welds in plastic water pipes, one possibility being to launch a Lamb wave along the pipe and to monitor any reflection coming from the weld. This has the potential attraction that if a suitable mode is chosen, the whole weld can be inspected in a single test, without the need to scan a transducer around the pipe circumference. A similar technique has been used to detect corrosion and other defects in metal pipes.[12–15] For this technique to be practical, it is necessary to find a mode which will propagate with only modest attenuation and which can be excited as a single mode so that the received signal will not be complicated by the presence of multiple modes.[12]

The families of modes in pipes are strongly related to the Lamb modes in a plate, so it was decided to investigate the simpler case of an attenuative plate in the initial study. This paper considers the effect of attenuation on the Lamb wave dispersion curves of a high-density polyethylene of the type used in water and gas pipes. First the incorporation of attenuation into the dispersion curve calculation is discussed. A simple viscoelastic behavior is assumed and a solution of the wave equation can be found by using a complex wave number, the imaginary part representing the attenuation of the wave. Dispersion curves are then predicted for different levels of attenuation varying from zero to four times that measured in the plastic. Selected points on these curves are then verified experimentally.

I. ATTENUATION MODEL

The software used to predict the dispersion curves was that described by Lowe *et al.*[5,16] For a plate in vacuum, it employs a matrix technique based on satisfying the traction-free boundary conditions at the surfaces of the plate, the wave field being made up of the superposition of partial waves.[5] In the elastic case, the amplitudes of the partial waves are assumed to be constant. In order to study the effects of attenuation, an expression for the attenuation of the partial waves has to be included.

The first step is to decide on an appropriate attenuation model to describe the material behavior. Many models exist for this purpose (see, for example, Refs. 17 and 18). One of the most popular models is the Voigt viscoelastic model[5,19] which is simple to use and has been shown to be fairly representative of the behavior of real, attenuative materials. It is commonly known as the ''spring and dashpot in parallel'' model in which the spring represents the elastic behavior of the material and the dashpot the damping.

The effect of damping is to modify the Lamé constants λ and μ into the following operators:

$$\lambda \text{ becomes } \lambda + \frac{\lambda'}{\omega}\frac{\partial}{\partial t}; \quad \mu \text{ becomes } \mu + \frac{\mu'}{\omega}\frac{\partial}{\partial t}, \quad (1)$$

where λ' and μ' represent the viscoelastic constants of the material and ω is the frequency.

If we substitute these operators into the displacement equation of motion, we get the following equation:

$$\rho \frac{\partial^2 \mathbf{u}}{\partial t^2} = (\lambda+\mu)\boldsymbol{\nabla}(\boldsymbol{\nabla}\cdot\mathbf{u}) + \mu\nabla^2\mathbf{u} + \left(\frac{\lambda'+\mu'}{\omega}\right)\boldsymbol{\nabla}\left(\boldsymbol{\nabla}\cdot\frac{\partial \mathbf{u}}{\partial t}\right) + \left(\frac{\mu'}{\omega}\right)\nabla^2\frac{\partial \mathbf{u}}{\partial t}, \quad (2)$$

where $\mathbf{u}$ is the displacement vector in the cartesian coordinate system $\mathbf{x}$, and ρ is the density.

By using the Helmholtz method (see, for example, Ref. 18) to decouple the motion into scalar dilatational and vector rotational fields, ϕ and ψ, we obtain

$$\rho \frac{\partial^2 \phi}{\partial t^2} = \left(\lambda + 2\mu + \frac{\lambda'+2\mu'}{\omega}\frac{\partial}{\partial t}\right)\nabla^2\phi, \quad (3)$$

$$\rho \frac{\partial^2 \psi}{\partial t^2} = \left(\mu + \frac{\mu'}{\omega}\frac{\partial}{\partial t}\right)\nabla^2\psi. \quad (4)$$

In the problems considered in this paper, only one component of ψ is nonzero; this is the component describing rotation about the normal to the plane containing the direction of propagation and the plate thickness. It can be shown that functions of the form

$$\phi, \psi = C_{1,2} e^{i(\mathbf{k}\cdot\mathbf{x}-\omega t)}, \quad (5)$$

where $C_{1,2}$ are arbitrary constants, satisfy the equations if the wave number $\mathbf{k}$ is complex, i.e., $\mathbf{k} = \mathbf{k}_r + i\mathbf{k}_i$.

Rewriting the above equation yields

$$\phi, \psi = C_{1,2} e^{i(\mathbf{k}_r\cdot\mathbf{x}-\omega t)} e^{-\mathbf{k}_i\cdot\mathbf{x}}. \quad (6)$$

In these equations, the first exponential term describes the propagation of the wave, and the second exponential term describes its decay. By substituting these equations into Eqs. (3) and (4), we obtain complex expressions a and b which are constants for a given material (a and b correspond to α and β, respectively, in Ref. 5):

$$a = \left(\frac{\lambda+2\mu-i(\lambda'+2\mu')}{\rho}\right)^{1/2}, \quad (7)$$

$$b = \left(\frac{\mu-i\mu'}{\rho}\right)^{1/2}. \quad (8)$$

The real parts of a and b are respectively the longitudinal and shear phase velocities in the absence of attenuation. The phase velocities in the presence of attenuation can be written

$$C_{L,S} = \frac{\omega}{|\mathbf{k}_r|}. \quad (9)$$

Given that $C_{L,S}$ are constant for a given material, it may be shown[5] that the imaginary part of the wave number (i.e., the attenuation) is linearly proportional to frequency, as is the real part. This implies that the attenuation per wavelength is constant. The complex longitudinal and shear velocities given by Eqs. (7) and (8) can now be used in the solution of the Lamb wave problem. The solution technique is the same as that used for the elastic plate case, except that both real and imaginary parts of the wave number must be computed.[5]

TABLE I. Material properties measured on high-density polyethylene.

Wave type	Velocity (m/s)	Attenuation (Np/wavelength)
Longitudinal	2340 (±2%)	0.055 (±5%)
Shear	950 (±5%)	0.29 (±10%)

II. THE EFFECT OF MATERIAL ATTENUATION ON DISPERSION CURVES

A. Material properties

The material chosen for study was a high-density polyethylene of the type used for plastic water and gas pipes. The longitudinal and shear velocities and attenuations of the material were measured from simple bulk wave experiments on a cube of the material cut from the plate used in the Lamb wave experiments which will be described in Sec. III, and are shown in Table I. Some slight anisotropy was observed, the difference between the velocities along the three axes of the cube was about 5%. However, it was felt that these differences were small enough to justify treating the material as isotropic. The values given in Table I are those in the direction of propagation of the Lamb waves in the experiments of Sec. III. The attenuations are expressed as nepers per wavelength, indicating that the attenuation increases linearly with frequency. Fourier analysis of the signals received in the bulk wave experiments suggested that this was a good model of the material behavior over the frequency range used in the measurements (2–5 MHz for the shear wave and 2–14 MHz for the longitudinal wave experiments). Since polyethylene is a viscoelastic material, it is reasonable to assume that this behavior is also followed at frequencies down to the 0.1–0.3 MHz used in the Lamb wave experiments.

In the studies of the effect of material attenuation described below, the shear and longitudinal velocities were maintained at the values shown in Table I, while the longitudinal and shear attenuation coefficients were changed from their initial values α_L and α_s to $p\alpha_L$ and $p\alpha_s$, respectively. Four cases, $p=0$, 0.5, 1.0, and 4.0, were investigated. Therefore the ratio of the shear to longitudinal attenuation coefficients was kept constant. However, since the difference between the longitudinal and shear wave attenuation coefficients is proportional to p, as p increases, the reduction in the amplitude of a shear wave over a given propagation path length increases compared to that of a longitudinal wave of the same frequency.

B. Zero attenuation case ($p=0$)

Figure 1(a) shows the phase velocity dispersion curves for the case of zero attenuation ($p=0$). The modes shown in bold correspond to those which are longitudinal through thickness modes at cutoff.[20] It can be seen that the first few non-zeroth-order modes have fairly simple forms and that as

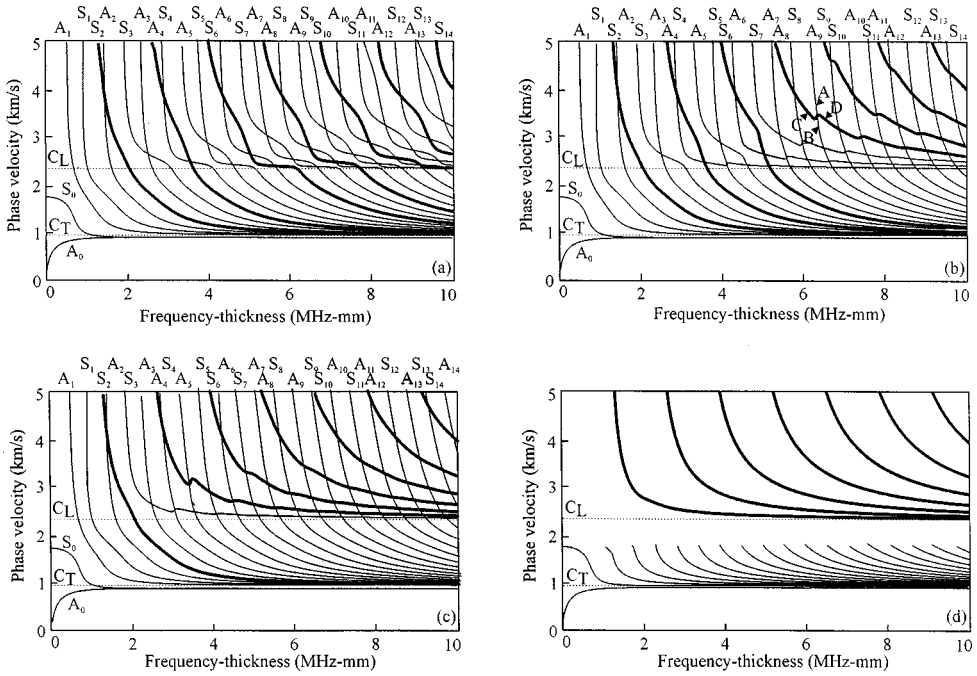

FIG. 1. Phase velocity dispersion curves for four levels of attenuation: (a) zero attenuation; (b) half measured values; (c) measured values; (d) four times measured values. Longitudinal cutoff modes shown in bold.

the frequency increases their phase velocities tend towards the bulk shear velocity. As the mode order increases, modes start to appear that seem to travel towards the bulk longitudinal velocity but only do so temporarily, before continuing down and heading towards the bulk shear velocity. The situation in this asymptotic region corresponds to the longitudinal partial wave becoming parallel to the plate and subsequently becoming inhomogeneous. Similar asymptotic behavior has been observed by Uberall *et al.*[21] and Mindlin.[22]

Uberall *et al.*[21] found that the appearance of the longitudinal asymptotic regions became more pronounced as the bulk shear velocity was reduced while keeping the longitudinal bulk velocity fixed. It has been noted that the physical character of the Lamb modes in these regions is similar to those observed in a fluid plate (i.e., in a material which is unable to support shear motion[23]). The fluid plate is equivalent to the shear bulk velocity being set to zero, in which case all modes tend towards the longitudinal bulk velocity with increasing frequency.

According to Uberall *et al.*,[21] the existence of longitudinal asymptotic regions tends to suggest that in the longitudinal bulk velocity region, the nature of the mode is essentially longitudinal, whereas below the longitudinal bulk velocity region, shear behavior dominates and above the longitudinal bulk velocity the mode can be dominated either by shear or longitudinal motion. This is demonstrated in Fig. 2(a) and (b), which shows the ratio of the amplitudes of the longitudinal and shear partial waves as a function of frequency for the s_3 (shear cutoff) and s_6 (longitudinal cutoff) modes, respectively, together with the corresponding phase velocity dispersion curves. (Strictly there are four partial waves in the plate: shear and longitudinal partial waves propagating in the upwards and downwards directions. However, the upwards and downwards propagating waves of a given type have the same amplitude, so it is only necessary to consider the ratio of the longitudinal and shear amplitudes.) For the shear cutoff mode [Fig. 2(a)], the amplitude ratio is initially very small, as expected; the amplitude ratio then rises when coupling with the partial longitudinal wave occurs. In the region near the bulk longitudinal velocity the amplitude ratio reaches a maximum, indicating the longitudinal nature of the mode in this region; it is also interesting to note that the

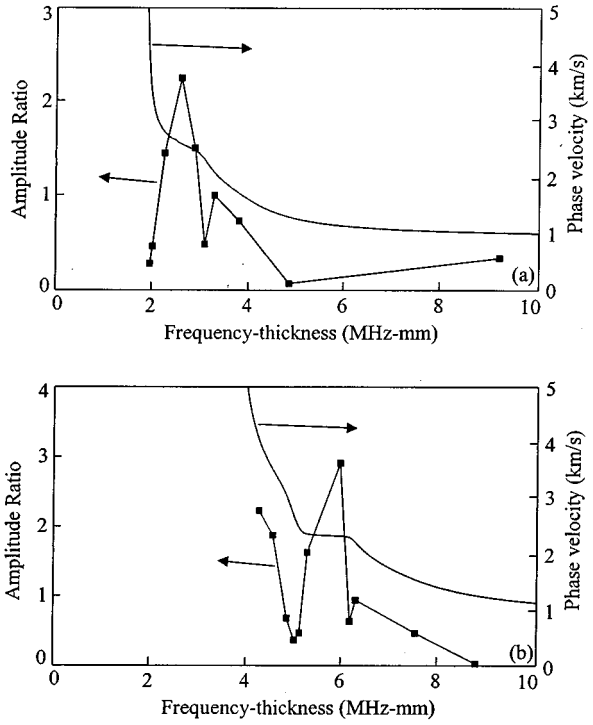

FIG. 2. Ratio of amplitudes of longitudinal and shear partial waves, together with corresponding phase velocity dispersion curves for (a) shear cutoff s_3 mode and (b) longitudinal cutoff s_6 mode.

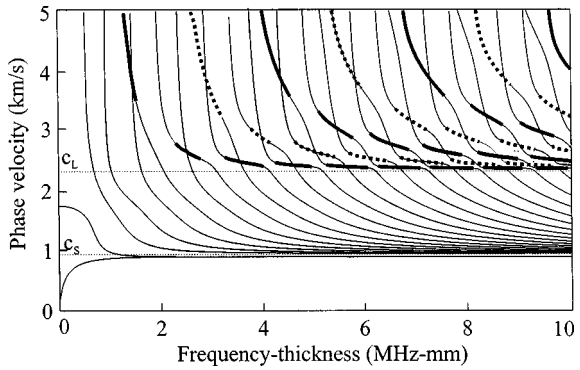

FIG. 3. Phase velocity dispersion curves for elastic plate highlighting plateauing regions. Heavy bold solid line: symmetric modes; heavy bold dashed line: antisymmetric modes.

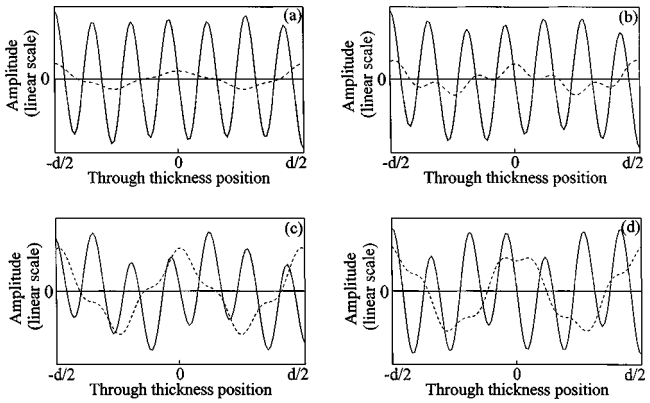

FIG. 4. Mode shapes showing variation of in-plane (———) and out-of-plane (– – –) displacements through the thickness of the plate for the half-attenuation case corresponding to points (a) *A*; (b) *B*; (c) *C*; and (d) *D* on dispersion curves of Fig. 1(b).

phase velocity dispersion curve ''plateaus'' in the vicinity of the bulk longitudinal velocity. Below the longitudinal bulk velocity, the amplitude ratio is small, indicating the dominant shear nature of the mode at high frequency. For the longitudinal cutoff mode [Fig. 2(b)], the amplitude ratio is initially high at cutoff but descends to a minimum; at this point the mode has become shear dominant. As the frequency is increased, the ratio then rises to a maximum in the longitudinal asymptotic region before dropping down as the mode tends towards the shear bulk velocity. Note that, above the longitudinal bulk velocity, the longitudinal cutoff mode is not confined to being a longitudinal dominant mode, as can be seen by the clear minimum in the amplitude ratio.

It is interesting to note in Fig. 1(a) that the longitudinal asymptotic behavior becomes more pronounced as the frequency increases. Also, as the mode order increases, the curve for a given mode passes through more regions of reduced gradient (tending to form plateaux) as it moves from cutoff to its high-frequency asymptote. By joining these regions together, it is possible to visualize a new set of curves as shown in bold in Fig. 3. In this figure, each new curve is a single mode, either symmetric or antisymmetric in nature. These curves all start off at cutoff as longitudinal through-thickness modes and tend towards the longitudinal bulk velocity at high frequency. Bold solid and dotted lines have been used to denote plateauing regions belonging to symmetric and antisymmetric modes, respectively. The case of Lamb modes which are longitudinal at cutoff and tend towards the longitudinal bulk velocity at high frequency are observed in a fluid plate[23] where the bulk shear wave cannot exist. As soon as shear waves can propagate, coupling with the longitudinal waves occurs. Uberall *et al.*[21] suggest that the coupling between longitudinal and shear bulk waves creates a repulsion effect (mode repulsion) whereby neighboring dispersion curves of the same type (symmetric or asymmetric) repel each other and therefore like modes never cross. Similar observations have been made by Mindlin.[22] A simple two degree of freedom spring-mass model for describing the coupling behavior when two Lamb modes approach each other on the dispersion curves has been given by Yapura and Kinra,[24] although this was not for a single layered plate but for a fluid–solid bilayer.

C. Half-attenuation case ($p=0.5$)

Figure 1(b) shows the phase velocity dispersion curves for the case where the shear and longitudinal wave attenuations are half the measured values. At the lower frequency end, the dispersion curves appear to be very similar to those of the zero attenuation case but differences start to appear as the frequency increases. Certain modes (s_4, a_6, s_7, a_8, s_9, a_{11}, s_{13}) now have dispersion curves which are asymptotic to the longitudinal bulk velocity, rather than the bulk shear velocity, at high frequencies. The first three such modes stem from modes which are through-thickness shear modes at cutoff (s_4, a_6, s_7); the rest are from modes which are through-thickness longitudinal modes at cutoff (a_8, s_9, a_{11}, s_{13}). As in the zero attenuation case, at high frequency the other modes are asymptotic to the shear bulk velocity. Therefore, four distinct groups of curves can exist when attenuation is present: shear cutoff modes which are longitudinal asymptotic, longitudinal cutoff modes which are longitudinal asymptotic, longitudinal cutoff modes which are shear asymptotic, and shear cutoff modes which are shear asymptotic. It is interesting to note that there are three longitudinal cutoff modes which are asymptotic to the shear bulk velocity (s_2, a_4, s_6) and there are three shear cutoff modes which are asymptotic to the longitudinal bulk velocity (s_4, a_6, s_7).

Another striking feature of the dispersion curves of Fig. 1(b) is that the curves for different modes of the same symmetry sometimes cross. For example, the a_8 and a_9 curves cross at about 6.4 MHz-mm, whereas this never happens in the zero attenuation case.[22] A study of the mode shapes of each mode at points around the crossing has confirmed that there is a continuous evolution of mode shape along each curve through the crossing region, thus confirming that the curves do indeed cross. For example, Fig. 4 shows the mode shapes corresponding to points A, B, C, and D on the phase velocity dispersion curves of Fig. 1(b). It is clear that points A and B lie on the same mode, while C and D are on a different mode, thus confirming that the modes do cross. Further details of this can be found in Ref. 25. Also, the phase velocity of some modes no longer varies monotonically with frequency, the phase velocity of, for example, the

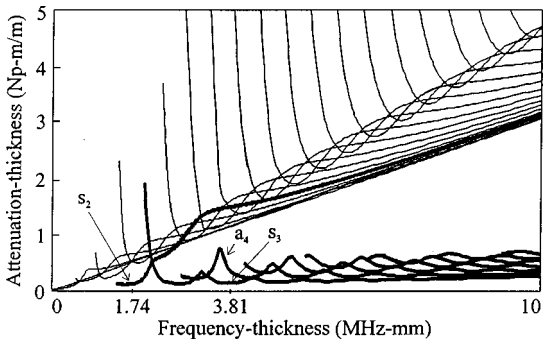

FIG. 5. Attenuation dispersion curves for measured values of attenuation plotted up to phase velocity of 5 km/s. Longitudinal cutoff modes shown in bold.

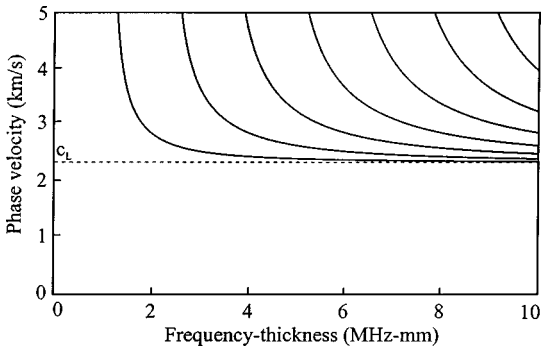

FIG. 6. Phase velocity dispersion curves for a fluid plate having the longitudinal velocity of high-density polyethylene.

a_8 mode rising sharply at 6.4 MHz-mm before falling again. It is interesting that the curves in Fig. 1(b), which cross several other curves (for example, s_7, a_8, a_9), are of a similar form to the curves which would be obtained by joining the plateauing regions in Fig. 3.

These phenomena do not occur at the lower frequency end of the curves, which suggests that they may be associated with the relatively high attenuation of the shear partial wave reducing the degree of coupling between the longitudinal and shear waves as the frequency increases.

D. Full attenuation case ($p=1$)

Figure 1(c) shows the phase velocity dispersion curves for the measured values of attenuation. Only one longitudinal through thickness mode at cutoff is now asymptotic to the bulk shear velocity at high frequency (s_2) and, similarly, the number of shear modes at cutoff which are asymptotic to the longitudinal velocity at high frequency has been reduced to one (s_3). This suggests that the degree of coupling between the longitudinal and shear waves is gradually decreasing as the attenuation increases.

Figure 5 shows the attenuation dispersion curves for the full attenuation case; again, the longitudinal cutoff modes are shown in bold. The vertical scale is attenuation plate thickness per unit propagation distance (Np-m/m). No values have been plotted at phase velocities higher than 5 km/s, corresponding to the phase velocity dispersion curves of Fig. 1. The lower frequency end of each curve is therefore either at a phase velocity of 5 km/s or an attenuation thickness value of 5 Np-m/m (the top of the scale used). The modes which are asymptotic to the bulk longitudinal velocity (one shear cutoff and the rest longitudinal cutoff) all have attenuations which are asymptotic to the bulk longitudinal attenuation, while the modes which are asymptotic to the bulk shear velocity all have attenuations which are asymptotic to the bulk shear attenuation. (The attenuation thickness is plotted as Np-m/m, rather than Np-m/wavelength, so the bulk wave attenuations increase linearly with frequency.) The attenuation dispersion curves show that there are large differences in the attenuation of different modes and this will be a major factor in mode selection for practical testing.

E. Four times attenuation case ($p=4$)

Figure 1(d) shows the phase velocity dispersion curves when the shear and longitudinal attenuations have been increased to four times the experimentally measured values. The shear cutoff modes are now incomplete at high phase velocities. This is because solutions were difficult to find due the very high levels of attenuation. There is now complete separation between the longitudinal and shear cutoff modes, the longitudinal cutoff modes all tending to the longitudinal bulk velocity at high frequencies, while the shear cutoff modes are all asymptotic to the shear bulk velocity. There appears therefore to be minimal coupling between the longitudinal and shear partial waves.

Figure 6 shows the dispersion curves for a ''fluid plate'' (i.e., a plate of a material which does not support a shear wave), the bulk longitudinal velocity having the value measured in high-density polyethylene. The curves are almost identical to those of the longitudinal cutoff modes of Fig. 1(d), confirming that, at high attenuations, the shear and longitudinal modes of the plate are virtually uncoupled. The fluid plate curves are also very similar to those formed by joining the plateauing regions of different modes in the elastic plate case shown in Fig. 3.

III. EXPERIMENTAL VERIFICATION

A. s_2 mode

The experiments were designed both to verify selected points on the dispersion curves, and to identify modes which have potential for use in nondestructive testing. The parameters which can be measured most easily are the group velocity and attenuation, provided we can obtain modes which are not too dispersive. All the tests were carried out on a 12.7-mm-thick high-density polyethylene plate. It is very difficult to measure modes having attenuations over around 200 dB/m, and modes with attenuations higher than this would be of no use in nondestructive testing; in the 12.7-mm-thick plate used in the experiments, this corresponds to an attenuation of 0.28 Np-m/m. Figure 4 shows that this means that it will be difficult to measure any modes except those whose attenuation is asymptotic to the bulk longitudinal attenuation. It is also desirable to measure modes which are well separated from other modes in phase velocity and/or group velocity since if the phase velocity is well separated from other

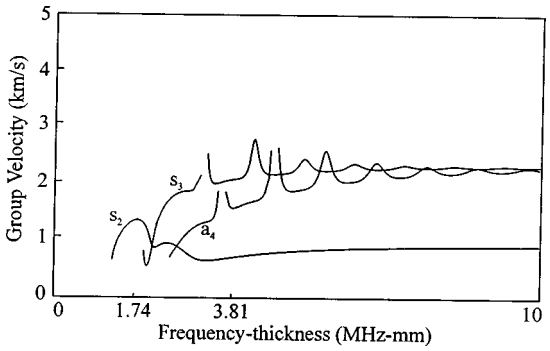

FIG. 7. Group velocity dispersion curves of measured modes.

modes, it is relatively easy to excite a pure mode, while if the group velocity is very different from that of other modes, the signal of interest can be separated by time domain gating of the received signal. Only a small number of modes meet these criteria, so the experiments were limited to three modes.

The first mode to be measured was the s_2 mode, which is the sole longitudinal cutoff, shear asymptotic mode shown in Fig. 1(c). This has a minimum attenuation at about 1.74 MHz-mm (see Fig. 5) which also corresponds roughly to a maximum in its group velocity as shown in Fig. 7. The mode will therefore be relatively nondispersive at around this frequency. The displacement mode shapes also reveal that the mode has significant out-of-plane surface displacement which makes it relatively easy to excite using water-coupled transducers.[26] The program for dispersion curve calculation[5,16] initially computes the wave-number–frequency dispersion relationship, the other types of dispersion curve being obtained from this. The group velocity curves of Fig. 7 were produced using the standard expression (see, for example, Ref. 27)

$$c_g = \frac{d\omega}{d\mathbf{k}}. \tag{10}$$

In this computation, the real part of the wave number was taken. Several gaps can be seen in the curves of Fig. 7; these are regions where the calculation goes unstable. This occurs particularly at the points of the phase velocity dispersion curves of Fig. 1(c) where the phase velocity increases with respect to frequency and then decreases again. The calculation was stable at the frequency–thickness products at which the measurements were taken so sensible comparisons with the experiments can be made. However, there is some uncertainty about the meaning of group velocity in a lossy system and its relationship with the velocity of energy propagation. These issues will be explored in a future paper.

Figure 8 shows a schematic diagram of the equipment used for excitation and reception. Two Panametrics 0.5 MHz center frequency, 25 mm diameter, broadband unfocused transducers were employed. The transducer holders were sealed onto the test plate and filled with water so that coupling between the transducers and the plate could be achieved. The phase velocity of the s_2 mode at 1.74 MHz-mm is 3 km/s so the appropriate angle of incidence in water for excitation and reception is 30°. The frequency required in a 12.7-mm-thick plate was 137 kHz so the input used was a 20-cycle, 137-kHz tone burst in a Hanning window which has a 20-dB down bandwidth of ± 15 kHz. The transducers were sufficiently broadband to give adequate response at this frequency. The excitation signal was fed to the transmitting transducer via a power amplifier which delivered approximately 150 V peak-peak. The received signal was amplified by 60 dB in a Macro Design low-noise amplifier. There is significant beam spreading at such a low frequency with 25-mm-diam transducers, a simple analysis based on a piston source[28] indicating that the 6-dB down points on the main lobe are at $\pm 28°$ from the nominal incident angle. The combined effect of the beam spreading and frequency bandwidth of the input signal is that excitation and reception of a single mode is unlikely. Fortunately, however, the modes neighboring the phase velocity of the s_2 mode at 137 kHz are considerably more attenuative. Therefore, even if these modes are excited, their presence is unlikely to interfere with the measurements because their amplitudes will die away very quickly with propagation distance.

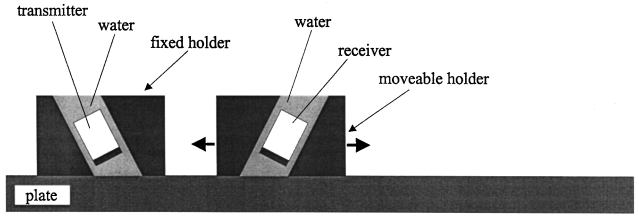

FIG. 8. Schematic diagram of experimental setup.

The received signal for different separation distances between the transmitter and receiver was measured, the transmitter position being fixed. Figure 9(a) and (b) show the

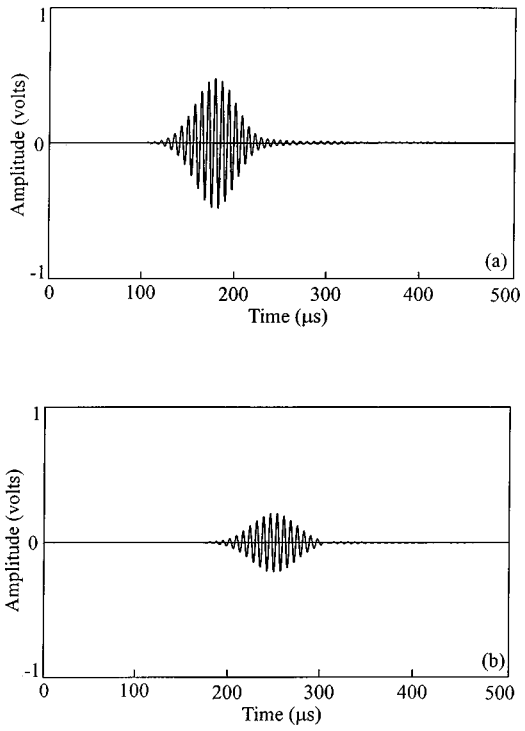

FIG. 9. Time history of received s_2 mode; (a) receiver position 1; (b) receiver position 2.

TABLE II. Comparison of predicted and measured group velocities and attenuations.

Mode	Group velocity (m/s)			Attenuation (Np/mm)		
	Predicted	Measured	% error	Predicted	Measured	% error
s_2	1370	1364	0.4	0.0105	0.009	17
s_3	2101	2121	1	0.01	0.013	23
a_4	1594	1365	17	0.023	0.020	15

received signal at two receiver positions 90 mm apart. The form of the two signals is very similar and shows minimal sign of dispersion, or the presence of other modes which would tend to distort the signal as they would travel at different velocities. It was therefore possible to obtain the group velocity from the difference in the time of flight between the two receiver positions, and the attenuation was calculated from the difference in the amplitudes of the signals.

Table II shows the measured and predicted group velocities and attenuations. The results show an agreement between predictions and measurements of better than 1% in group velocity and 17% in attenuation. Given the difficulties of measuring attenuation reliably (beam spreading, inconsistent coupling etc), this level of agreement is encouraging.

B. s_3 and a_4 modes

The second set of experiments was at a center frequency of 300 kHz, corresponding to a frequency thickness of 3.81 MHz-mm. The angle of incidence used was again appropriate for a phase velocity of 3 km/s. This corresponds to a point on the a_4 dispersion curve, but beam spreading means that the s_3 mode is also likely to be excited strongly. Both modes are asymptotic to the bulk longitudinal velocity at high frequency and are in the group of relatively low attenuation modes in Fig. 5.

The same rig and transducers were used as in the lower frequency experiment and Fig. 10(a) and (b) shows the signals obtained at receiver positions 56 mm apart, the excitation again being a 20-cycle toneburst enclosed in a Hanning window. The signal in Fig. 10(a) when the receiver was closer to the source shows two overlapping signals which have started to separate at the further position shown in Fig. 10(b). Measurement of the group velocities and attenuations of the modes is hampered by the overlapping, but estimates were obtained which agreed quite well with the predictions, as shown in Table II. It seemed desirable to test at greater propagation distances where better separation would have been achieved, but, unfortunately, the signal-to-noise ratio was then degraded by the effects of attenuation, and no advantage was gained when this was attempted.

IV. CONCLUSIONS

The influence of material attenuation on the Lamb wave dispersion behavior in plastic plates has been studied. The shear wave attenuation per wavelength in high-density polyethylene was found to be about five times that of the longitudinal wave, and the effect of varying the values of the two attenuations while keeping their ratio constant has been investigated. As the attenuation increases, the degree of coupling between the shear and longitudinal partial waves decreases and the phase velocity dispersion curves for different modes of the same symmetry can cross; this is not possible for an elastic plate. With increasing attenuation, some modes become asymptotic to the bulk longitudinal velocity at high frequency, rather than to the bulk shear velocity. Where the modes are dominated by the longitudinal partial wave, their attenuation is much lower than that of the shear dominated modes. At high values of attenuation, the modes which are longitudinal through thickness at cutoff are all asymptotic to the bulk longitudinal velocity, while those which are shear through thickness at cutoff are all asymptotic to the bulk shear velocity. There is then minimal coupling between the two types of partial waves and the behavior of the longitudinal modes is analogous to that seen in a ''fluid plate.''

The experimentally measured group velocities and attenuations of the s_2, s_3, and a_4 modes at selected frequencies showed good agreement with the predictions. The modes whose attenuation is asymptotic to that of the bulk longitudinal wave are the only ones which are likely to be useful in practical nondestructive testing. Of these, the s_2 mode can be excited as essentially a pure mode at its maximum group velocity and is the most promising mode for use in the nondestructive testing of high-density polyethylene plates and pipes.

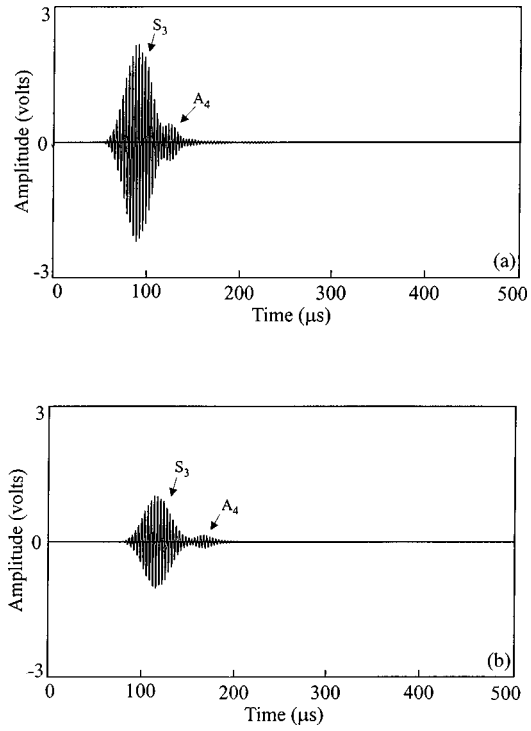

FIG. 10. Time history of received s_3/a_4 modes; (a) receiver position 1; (b) receiver position 2.

ACKNOWLEDGMENTS

The authors are grateful for helpful discussions with Dr. M. J. S. Lowe and Arnaud Bernard. Dr. Chan was supported by an EPSRC postgraduate training partnership award.

[1] L. Alsop, ''The leaky-mode period equation—a plane-wave approach,'' Bull. Seismol. Soc. Am. **6**, 1989–1998 (1970).
[2] T. H. Watson, ''A real frequency complex wave-number analysis of leaking modes,'' Bull. Seismol. Soc. Am. **62**, 369–384 (1972).
[3] P.-C. Xu and A. K. Mal, ''Calculation of the inplane Green's functions for a layered viscoelastic solid,'' Bull. Seismol. Soc. Am. **77**, 1823–1837 (1987).
[4] D. E. Chimenti and A. H. Nayfeh, ''Leaky Lamb waves in fibrous composite laminates,'' J. Appl. Phys. **58**, 4531–4538 (1985).
[5] M. J. S. Lowe, ''Matrix techniques for modelling ultrasonic waves in multilayered media,'' IEEE Trans. Ultrason. Ferroelectr. Freq. Control **42**, 525–542 (1995).
[6] P. W. Bucher, ''Plane waves in linear viscoelastic media,'' Geophys. J. R. Astron. Soc. **23**, 531–542 (1971).
[7] D. L. Anderson and C. B. Archambeau, ''The anelasticity of the earth,'' J. Geophys. Res. **69**, 2071–2084 (1964).
[8] F. Schwab and L. Knopoff, ''Surface waves on multilayered anelastic media,'' Bull. Seismol. Soc. Am. **61**, 893–912 (1971).
[9] O. P. Chervinko and I. K. Senchenkov, ''Harmonic viscoelastic waves in a layer and in an infinite cylinder,'' Soviet Appl. Mech. **22**, 1136–1141 (1987).
[10] K. Tanaka and A. Kon-no, ''Harmonic waves in a linear viscoelastic plate,'' Bull. JSME **23**, 185–193 (1980).
[11] D. Nkemzi, ''The Rayleigh-Lamb dispersion equations for a viscoelastic plate,'' Mechanics Research Communications **20**, 215–222 (1993).
[12] D. N. Alleyne and P. Cawley, ''Long range propagation of Lamb waves in chemical plant pipework,'' Mater. Eval. **55**, 504–508 (1997).
[13] D. N. Alleyne and P. Cawley, ''The effect of discontinuities on the long range propagation of Lamb waves in pipes,'' Proceedings of the Institution of Mechanical Engineers, Part E: Journal of Process Mechanical Engineering **210**, 217–226 (1996).
[14] D. N. Alleyne, P. Cawley, A. M. Lank, and P. J. Mudge, ''The Lamb Wave Inspection of Chemical Plant Pipework,'' in *Review of Progress in Quantitative NDE, Vol. 16*, edited by D. O. Thompson and D. E. Chimenti (Plenum, New York, 1997), pp. 269–1276.
[15] J. L. Rose, J. J. Ditri, A. Pilarski, K. Rajana, and F. T. Carr, ''A guided wave inspection technique for nuclear steam generator tubing,'' NDT & E Int. **27**, 307–330 (1994).
[16] B. Pavlakovic, M. J. S. Lowe, D. N. Alleyne, and P. Cawley, ''Disperse: a general purpose program for creating dispersion curves,'' in *Review of Progress in Quantitative NDE, Vol. 16*, edited by D. O. Thompson and D. E. Chimenti (Plenum, New York, 1997), pp. 185–192.
[17] B. J. Lazan, *Damping of Materials and Members in Structural Mechanics* (Pergamon, London, 1968).
[18] L. E. Malvern, *Introduction to the Mechanics of a Continuous Medium* (Prentice-Hall, Englewood Cliffs, NJ, 1969).
[19] M. Castaings and B. Hosten, ''Delta operator technique to improve the Thomson–Haskell method stability for propagation in multilayered anisotropic absorbing plates,'' J. Acoust. Soc. Am. **95**, 1931–1941 (1994).
[20] C. C. H. Guyott and P. Cawley, ''The measurement of through thickness plate vibration using a pulsed ultrasonic transducer,'' J. Acoust. Soc. Am. **83**, 623–631 (1988).
[21] H. Uberall, B. Hosten, M. Deschamps, and A. Gerard, ''Repulsion of phase-velocity dispersion curves and the nature of plate vibrations,'' J. Acoust. Soc. Am. **96**, 908–917 (1994).
[22] R. D. Mindlin, ''Waves and vibrations in isotropic, elastic plates,'' in *Proceedings of the first Symposium on Naval Structural Mechanics* (Pergamon, Oxford, 1960), pp. 199–232.
[23] M. Redwood, *Mechanical Waveguides* (Pergamon, Oxford, 1960).
[24] C. L. Yapura and V. K. Kinra, ''Guided waves in a fluid-solid bilayer,'' Wave Motion **21**, 35–46 (1995).
[25] C. W. Chan, ''The ultrasonic nondestructive evaluation of welds in plastic pipes,'' Ph.D. thesis, Imperial College, University of London, 1996.
[26] D. N. Alleyne and P. Cawley, ''Optimisation of Lamb wave inspection techniques,'' NDT & E Int. **25**, 11–22 (1992).
[27] L. M. Brekhovskikh and V. Goncharov, *Mechanics of Continua and Wave Dynamics* (Springer-Verlag, Berlin, 1985).
[28] L. E. Kinsler and A. R. Frey, *Fundamentals of Acoustics* (Wiley, New York, 1982).

Surface waves above thin porous layers saturated by air at ultrasonic frequencies

Luc Kelders, Walter Lauriks, and Jean F. Allard[a)]
Laboratorium voor Akoestiek en Thermische Fysica, Departement Natuurkunde, K. U. Leuven, Celestijnenlaan 200 D, B-3001 Leuven, Belgium

(Received 25 June 1997; accepted for publication 8 April 1998)

Experimental evidence of surface waves above thin porous layers of thickness varying from 1.8 to 6 mm of plastic foams having a porosity close to one is presented. Phase velocity measurements at 40 kHz indicate the presence of waves propagating slower than homogeneous plane waves. The pole of the reflection coefficient related to these waves is detected by near-field holography at 20 kHz. The different experimental results are compared with predictions obtained by replacing the air inside the layers by an equivalent fluid, and using methods developed in the context of electromagnetism to localize the poles of the reflection coefficient. © *1998 Acoustical Society of America.* [S0001-4966(98)00208-2]

PACS numbers: 43.35.Pt [HEB]

INTRODUCTION

Surface waves can propagate above comblike structures and honeycombs, and their main characteristics have been measured.[1] These structures are anisotropic porous media, the ''airborne'' surface wave is created by a sound source in air, the frame of the structure being motionless. Other kinds of surface waves related to ultrasound propagation in the elastic frame of porous media have been predicted[2,3] and detected.[4,5] The presence of an ''airborne'' surface wave above usual porous medialike reticulated foams (in a reticulated foam, the membranes of the cells have been removed) has never been detected by direct measurement of the phase velocity in the direction parallel to the surface, and of the exponential decay with increasing distance to the surface.[6] The localization of a pole of the reflection coefficient, related to an airborne surface wave, has been performed recently[7] for the case of thin layers at low and medium frequencies, with the near-field acoustical holography method[8,9] (NAH) developed by Tamura. In the present study, the presence of a surface wave is suggested at 40 kHz, over thin samples of plastic foam, from time-of-flight measurements. The NAH method has been used at 20 kHz to localize the pole, this frequency being now approximately the highest limit of reliability. The NAH method is used for the first time to detect poles at high frequencies. The modeling of the experiments at 20 and 40 kHz is performed by using classical methods and concepts. The air in the porous medium is replaced by an equivalent fluid,[10] and the properties of the leaky waves and the surface waves are investigated with methods previously developed for the similar case, never transposed to acoustics as far as we know, of transverse magnetic waves over a grounded dielectric.[11]

[a)]On leave from Laboratoire d'Acoustique de l'Université du Maine, UMR 6613, Avenue Olivier Messiaen, Le Mans, France.

I. EQUIVALENT FLUID IN POROUS MEDIA

For the materials considered in the present work, which have a low flow resistivity and a density much larger than the air density, the vibrations of the frame induced by an acoustic field in air can be neglected at high frequencies. A detailed study at high and low frequencies of the decoupling of the frame has been performed by Bardot *et al.*[12]

Sound propagation in the air in a porous medium is modified by the interactions between air and the motionless porous frame. Air can be replaced by an equivalent fluid, characterized by an effective complex density ρ_1 being different from the air density ρ, which takes into account the inertial and the viscous interaction, and a bulk modulus χ_1 which is not the adiabatic bulk modulus χ of the free air ($\chi=\gamma P$ where γ is the ratio of the specific heats and P the static atmospheric pressure), due to the thermal exchanges with the frame. Let $\mathbf{v}$ and p be the macroscopic air velocity and pressure. The bulk modulus and the effective density are related by

$$\rho_1 \frac{\partial \mathbf{v}}{\partial t} = -\nabla p, \tag{1}$$

$$\frac{\partial p}{\partial t} = -\nabla \cdot \mathbf{v}. \tag{2}$$

Sound propagation in air in the layer is characterized by the wave number k_1 and the characteristic impedance Z_1, given by

$$k_1 = \omega(\rho_1/\chi_1)^{1/2}, \tag{3}$$

$$Z_1 = (\rho_1\chi_1)^{1/2} \tag{4}$$

that are different from the wave number k and the characteristic impedance Z in the free air. The effective density ρ_1 and the bulk modulus χ_1 can be written [with the time dependence $\exp(-j\omega t)$], respectively,[10]

$$\rho_1 = \alpha_\infty \rho \left[1 + j \frac{\sigma \phi}{\omega \rho \alpha_\infty} \left(1 - \frac{4 j \alpha_\infty^2 \eta \rho \omega}{\sigma^2 \Lambda^2 \phi^2} \right)^{1/2} \right], \tag{5}$$

$$\chi_1 = \frac{\gamma P}{\gamma - (\gamma - 1)[1 + (8 j \eta / \Lambda'^2 \ \mathrm{Pr}\ \omega \rho)(1 - j \rho(\omega \ \mathrm{Pr}\ \Lambda'^2 / 16 \eta))^{1/2}]^{-1}}. \tag{6}$$

In these equations, α_∞ is the tortuosity, Λ and Λ' the viscous and thermal characteristic lengths, ϕ the porosity, σ the flow resistivity, η the viscosity, and Pr the Prandtl number for air. It may be recalled that Λ is a pore-size parameter[13] related to the viscous interaction, and is equal, like Λ', to the radius of the pores for identical circular cross-sectional shaped pores. Equations (5) and (6) represent reasonable approximations which have been used successfully for different kinds of porous media, including reticulated foams.[14–17] At high frequencies, when the viscous skin depth $\delta = (2\eta/\rho\omega)^{1/2}$ is much smaller than the viscous dimension Λ, Eqs. (5) and (6) can be rewritten

$$\rho_1 = \alpha_\infty \rho \left[1 + (1 + j) \frac{\delta}{\Lambda} \right], \tag{7}$$

$$\chi_1 = \frac{\gamma P}{\gamma - (\gamma - 1)[1 - (1 + j)(\delta / \mathrm{Pr}^{1/2} \Lambda')]}. \tag{8}$$

These simple asymptotic expressions have precise physical justifications.[14,15] It may be noticed that the damping, related to the imaginary parts of ρ_1 and χ_1 decreases when frequency increases, and if tortuosity is close to one, the equivalent fluid is not very different from air at high frequencies. The validity of these expressions is limited at high frequencies[16] by scattering. The limit depends on the dimensions that characterize the cross section of the solid bonds. Foams similar to material A have been studied in Ref. 16. Equations (5) and (6) are valid at frequencies lower than 100 kHz.

Two foams were used in the present work. One is a completely reticulated foam denoted as material A. For this material, all the parameters of Eqs. (5) and (6) have been evaluated, from time-of-flight and attenuation measurements[18,19] for tortuosity α_∞ and characteristic dimensions Λ and Λ', and by classical methods for the other parameters. The second material, denoted as material B, is a partially reticulated foam. Due to scattering around 100 kHz, where ultrasonic measurements are performed, Λ and Λ' are not measurable and have been adjusted. The acoustic parameters are given in Table I for both materials. The predicted values of $m = \rho_1/\rho$ and $n = k_1/k$ at 40 kHz are also given in Table I.

The measured tortuosity for material A is equal to 1.05, and equal to 1.28 for material B. This difference will provide an illustration of the influence of tortuosity on the properties of the airborne surface wave. Different layers of material A and material B are used in what follows. Their thicknesses are equal to 6 mm (A1), 5 mm (A2), 2.5 mm (A3), 1.8 mm (A4), and 2 mm (B1).

II. SURFACE AND LEAKY WAVES ABOVE A POROUS LAYER

Surface waves in this work are similar to the waves defined by Tolstoy,[20] that exist over motionless rough surfaces, and are always related to a pole of the reflection coefficient. A porous layer on a rigid impervious backing is represented in Fig. 1(a). A plane wave impinges upon the layer with an angle of incidence θ which can be complex if the wave is inhomogeneous, and a related refraction angle θ_1 which is complex, due to the damping. A detailed description of inhomogeneous waves and of the use of complex angles has been performed by Deschamps.[21] Like in the work by Brekhovskikh and Godin,[22] the wave-number components of the reflected wave are $k_z = k \cos\theta$, $k_x = k \sin\theta$. The surface impedance Z_s of the layer, i.e., the ratio of the acoustic pressure to the z component of acoustic velocity in the frequency domain, is given by

$$Z_s = -j \frac{Z_1}{\cos\theta_1} \cot(k_1 l \cos\theta_1), \tag{9}$$

where l is the thickness of the sample. For materials with a large $|n|$, θ_1 is close to zero in a large range of variation for θ, and Z_s is close to $-jZ_1 \cot(k_1 l)$. A simplified model where the porous layer is replaced by an impedance plane can be used. The impedance plane is not a suitable representation in our case. The reflection coefficient is given by

TABLE I. The acoustical parameters for material A and material B, and the ratios $n = k_1/k$ and $m = \rho_1/\rho$ at 40 kHz. For material A the thicknessess of the layers are 6 mm (A1), 5 mm (A2), 2.5 mm (A3), 1.8 mm (A4), and for material B 2 mm (B1).

	Tortuosity α_∞	Porosity ϕ	Flow resistivity Nsm^{-4} σ	Characteristic dimensions mm Λ	Λ'	Refraction index n and normalized effective density m at 40 kHz n	m
A	1.05	0.98	2800	0.25	0.65	$1.05 + j0.026$	$1.1 + j0.047$
B	1.28	0.97	3370	0.05	0.30	$1.27 + j0.12$	$1.56 + j0.28$

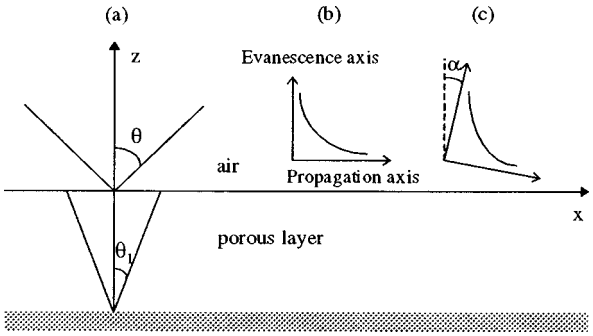

FIG. 1. Plane waves above a porous layer: (a) the classical representation of the incident, reflected, and refracted field, (b) surface waves when losses in the layer are removed ($\theta=\pi/2-j\varphi$), (c) actual surface wave ($\theta=\pi/2+\alpha-j\varphi$).

$$R(\cos\ \theta)=\frac{m\ \cos\ \theta+jn\ \cos\ \theta_1\phi\ \tan(k_1 l\ \cos\ \theta_1)}{m\ \cos\ \theta-jn\ \cos\ \theta_1\phi\ \tan(k_1 l\ \cos\ \theta_1)}. \tag{10}$$

The poles correspond to a zero of the denominator and are solutions of

$$\cos\ \theta=j\ \frac{n}{m}\ \cos\ \theta_1\phi\ \tan(k_1 l\ \cos\ \theta_1), \tag{11}$$

where $\cos\ \theta$ and $\cos\ \theta_1$ are related by

$$\cos^2\ \theta=1-n^2+n^2\ \cos^2\ \theta_1. \tag{12}$$

These poles correspond to surface waves or leaky waves. The distinction in the present work is the same as in the book by Collin (Ref. 11, p. 493) and the work by Tamir and Oliner,[23] where the surface wave, in the absence of losses, is related to pure positive imaginary quantities for the z component k_z of the wave-number vector. Then the x component k_x is real and larger than k ($k_x^2=k^2-k_z^2$). If $\sin\ \theta_p$ is the pole related to the surface wave in the complex $\sin\ \theta$ plane, $\sin\ \theta_p$ is imaginary and $\cos\ \theta_p$ larger than one. Always for lossless media, poles with complex values of $\sin\ \theta_p$ are related to leaky waves. When the condition of zero loss is removed, poles related to the surface waves become complex. Air can be considered as lossless, and the direction of evanescence and of propagation are always perpendicular in air. A representation of the surface wave for an hypothetical lossless layer is given in Fig. 1(b), and for the case of a weak damping in Fig. 1(c). The slight clockwise rotation of the wave-number vector results in a x component k_x (or a $\sin\ \theta_p$) with a small positive part. The x dependence of the amplitude is $\exp(jk\sin\ \theta_p x)$. The phase velocity c_p in the x direction is $\omega/(k\ \mathrm{Re}\sin\ \theta_p)$ and $\mathrm{Re}\sin\ \theta_p=c/c_p$. The wave is damped in the x direction with a damping coefficient $k\ \mathrm{Im}(\sin\ \theta_p)$.

Equations similar to Eqs. (11) and (12) give the location of the poles of the reflection coefficient for transverse magnetic (TM) waves over a grounded dielectric sheet.[11] A method described by Collin[11] can be used to find the poles related to the surface waves when damping is removed. Damping at high frequencies is small in the studied porous materials, and the location of the poles is not strongly modified if damping is removed. Let u and v be the parameters

$$u=-jkl\ \cos\ \theta, \tag{13}$$

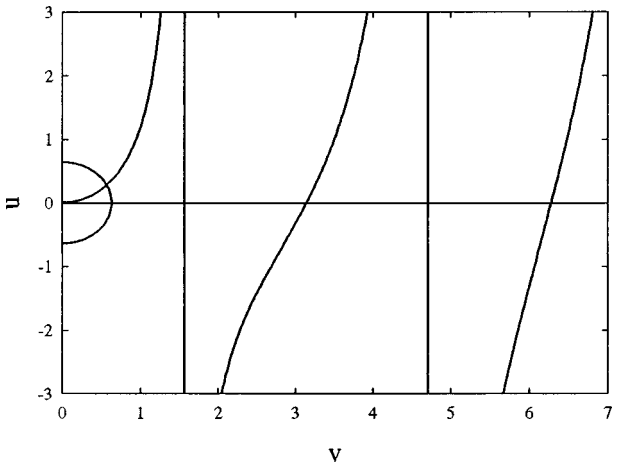

FIG. 2. Graphical localization of the poles related to the surface waves when damping is removed. The curves with the two asymptotes and the circle are related to Eqs. (15) and (16), respectively.

$$v=k_1 l\ \cos\ \theta_1. \tag{14}$$

Equations (11) and (12) can be rewritten, with the help of Eqs. (13) and (14)

$$u=\frac{\phi v}{m}\ \tan\ v, \tag{15}$$

$$u^2+v^2=(k_1^2-k^2)l^2, \tag{16}$$

where all the parameters are real if damping is removed. In that case, a circle in the (u,v) plane represents Eq. (16), and the surface waves correspond to the intersections of the circle with the curve related to Eq. (15) such as $u>0$.

A graphical representation of Eqs. (15) and (16) is given in Fig. 2 for a layer of thickness $l=2$ mm of material B at 40 kHz, the damping is removed by setting $\sigma=0$, and Λ and Λ' infinite. Then $k_1=\alpha_\infty^{1/2}k$, and $m=\alpha_\infty$. There is always at least one intersection, and the number of intersections and of surface waves increases with the radius of the circle. It can be shown that only one surface wave can propagate over the porous layers studied, at 20 kHz and also at 40 kHz. This is still true when the small damping is not neglected. The complex angle related to this wave will be denoted as θ_p.

When $|k_1 l|\ll 1$, the pole of the existing surface wave is located at $\sin\ \theta_p$ given, at the second-order approximation in $k_1 l$, by[7]

$$\sin\ \theta_p=1+\frac{\phi^2 k_1^2 l^2(n^2-1)^2}{2n^2 m^2}. \tag{17}$$

In order to obtain more precise evaluations of $\sin\ \theta_p$, Eq. (17) can be used for a very small thickness, and the solution modified progressively by an iterative process when l increases, so that it remains a solution of Eqs. (11) and (12).

When $|k_1 l|\ll 1$, the pole is close to the real $\sin\ \theta$ axis in the complex $\sin\ \theta$ plane. It has been detected previously at low frequencies.[7] This pole is studied with the Tamura method in Sec. IV at 20 kHz, and the related surface wave with the time-of-flight measurements in Sec. V at 40 kHz. It may be noticed that the surface wave is related, for the case of the grounded dielectric, to a trapped wave inside the dielectric, which undergoes total reflection at the contact sur-

TABLE II. The poles related to the leaky waves for a layer of thickness $l=0.5$ cm of material A at 20 kHz.

$\sin\theta=1.073+j0.57$ $\cos\theta=0.85-j0.74$	$\sin\theta=0.76+j2.26$ $\cos\theta=2.45-j0.71$	$\sin\theta=0.702+j4.05$ $\cos\theta=0.85-j0.68$
$\sin\theta'=1.005-j0.68$ $\cos\theta'=0.97-j0.70$	$\sin\theta'=0.724-j2.45$ $\cos\theta'=-2.63-j0.67$	$\sin\theta'=0.68-j4.23$ $\cos\theta'=-4.23-j0.66$

faces with ground and with air. The surface wave is the evanescent field related in air to the totally reflected field. The situation is similar for the porous layer, there is no surface wave inside the layer. The surface waves, when damping is removed, correspond to real solutions (u,v) of Eqs. (15) and (16). An infinite number of complex solutions exists, related to leaky waves.[11,22] The complex solution can be calculated, like for the case of electromagnetic waves over a grounded dielectric sheet,[11] by setting $k_1 l\cos\theta_1=hl=a+jb$, and eliminating $\cos\theta$ between Eqs. (11) and (12). The resulting equation can be written

$$\cos^2(a+jb)=\frac{-\phi^2n^2}{m^2}\left[\frac{(1-n^2)k_1^2l^2}{a+jb}+n^2\left(1-\frac{\phi^2}{m^2}\right)\right]^{-1}. \tag{18}$$

The solutions of Eq. (18) can be calculated easily when $l\rightarrow 0$. This equation can be replaced by

$$\tan(a+jb)=\pm j\,\frac{m}{\phi}, \tag{19}$$

and $a+jb$ is given by

$$a+jb=\pm 0.5j\,\log((1-m/\phi)/(1+m/\phi))+K\pi, \tag{20}$$

K being any integer. The solutions of Eq. (20) with the minus sign before the log function can be removed, because opposite values of $\cos\theta_1$ are related to the same couple $(\sin\theta, \cos\theta)$. The solutions of Eq. (20) can be modified progressively, like for the case of the surface wave, in order to remain solutions of Eq. (18) when l increases. In the absence of damping, leaky waves can be associated by couples (θ,θ') such as

$$\sin\theta=\sin^*\theta, \tag{21}$$

$$\cos\theta'=-\cos^*\theta. \tag{22}$$

This property of the leaky waves has been previously noticed by Tamir and Oliner[23] in the context of electromagnetic waves. Each pair is related to an intersection of the circle [Eq. (16)] and a branch of the curve [Eq. (15)]. When the circle intersects a branch of the curve, two real solutions of Eqs. (15) and (16) exist. When the radius of the circle is too small for an intersection to occur, these solutions become complex and correspond to a couple of leaky waves. The location of the six leaky waves closest to the real $\sin\theta$ axis is given in Table II for a layer of material a of thickness $l=0.5$ cm at 20 kHz. Relations (21) and (22) are approximately verified, due to the weak damping. These waves are improper, i.e., the imaginary part of $\cos\theta$ is negative and they increase exponentially far away from the layer. This property was also noted by Tamir and Oliner[23] in the context of electromagnetic waves.

III. THE SURFACE WAVE IN THE FAR FIELD OF A POINT SOURCE

A modeling of the far field of a monopole over a porous layer is performed in this section. It is shown that at grazing incidence, the surface wave provides the main contribution to the far field. The source S and the receiver M are represented in Fig. 3 over a porous layer. The distance between the source and the receiver is R_1, and the angle of specular reflection is θ_0. The cylindrical coordinates of the source and the receiver are (z_0,o) and (z,r), respectively. The direct and the reflected field, p_i and p_r, can be written[22]

$$p_i=(\exp(ikR_1))/R_1, \tag{23}$$

$$p_r=\frac{j}{2}\int_{-\infty}^{+\infty}H_0^{(1)}(\xi)R(\mu)\exp[j\mu(z+z_0)]\,\frac{\xi\,d\xi}{\mu}, \tag{24}$$

where

$$\mu=\sqrt{k^2-\xi^2},\quad \xi<k,\quad \mu=j\sqrt{\xi^2-k^2},\quad \xi>k,$$

$R(\mu)$ is the reflection coefficient for plane waves given by Eq. (10) with $\cos\theta=\mu$, and $H_0^{(1)}$ is the Hankel function of the first kind. The far reflected field can be calculated with the saddle point method by using previous results obtained by Brekhovskikh and Godin.[22] The integral in Eq. (24) is performed over the path of steepest descent defined in the complex $q=\sin\theta$ plane by

$$q\,\sin\theta_0+(1-q^2)^{1/2}\cos\theta_0=1+js^2,\quad -\infty<s<\infty. \tag{25}$$

The limit of the path when the specular reflection angle θ_0 is equal to $\pi/2$ is a vertical line $\mathrm{Re}\,q=s$, limited by $\mathrm{Im}\,q=0$. This path, and the path related to $\theta_0=4\pi/9$, are represented

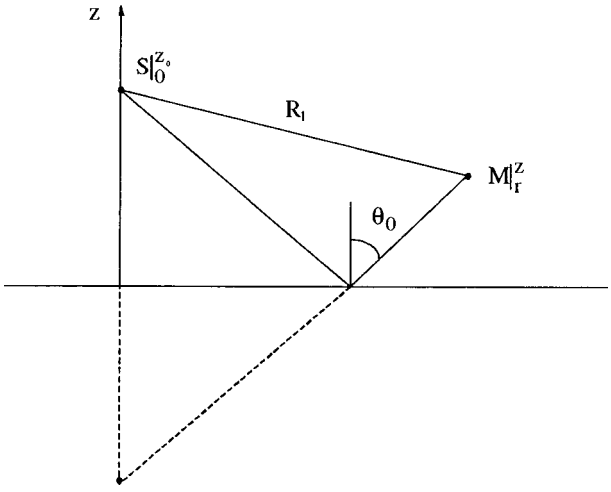

FIG. 3. The source S and the receiver M over a porous layer. The angle of specular reflection is θ_0, the distance from M to S is R_1.

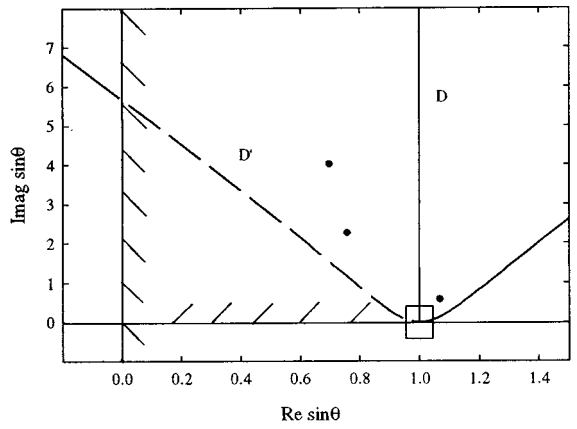

(a)

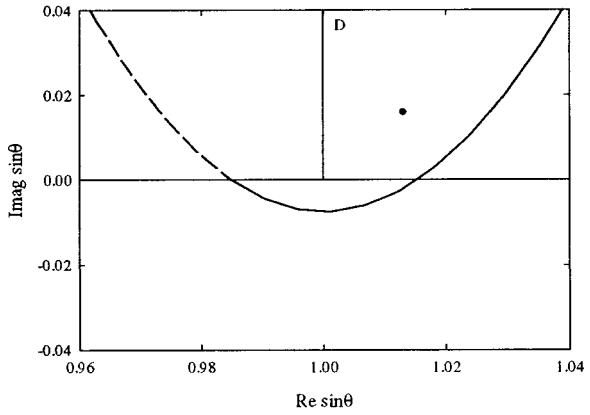

(b)

FIG. 4. (a) The complex sin θ plane. Two paths of steepest descent are represented, $D(\theta=\pi/2)$ and $D'(\theta_0=4\pi/9)$. The cut is shown by strokes on the axes. The portion of D' in the unphysical Riemann sheet is shown by dashes. Poles of Table II with the Re sin $\theta>0$ related to the leaky waves are shown with ●. (b) Zoom of (a). Pole related to the surface wave for material A3 at 20 kHz ($\sin\theta=1.013+j1.58\times10^{-2}$) is shown with a ●.

in Fig. 4. The saddle point is located on the path at $q=\sin\theta_0$. A cut must be set in the q plane, because cos θ is not single valued. It may be defined by[22]

$$\mathrm{Im}(1-\sin^2\theta)=u, \quad 0\leqslant u<\infty. \tag{26}$$

It consists in the real axis from sin $\theta=-1$ to sin $\theta=1$, and the imaginary axis. The left-hand branch of the path, between the positive imaginary axis and the crossing with the real axis for sin $\theta<1$, lies in the unphysical Riemann sheet where Im(cos θ)<0. This part of the path is indicated by dashes in Fig. 4. Poles in the q plane which are crossed when the path of steepest descent is deformed into the initial path (the real sin θ axis) are related to surface and leaky waves in the far field. Poles of Table II with Im(sin θ)>0 are represented in Fig. 4(a), the pole related to the surface wave for layer A3 at 20 kHz is represented in Fig. 4(b). In Fig. 4(a) two poles such as $0<\mathrm{Re}(\sin\theta_p)<1$ can be crossed, because the left-hand side branch of the path and the pole are in the unphysical Riemann sheet. The contribution of the related waves can be neglected, due to the strong damping [Im(sin θ)>2], and it can also be neglected at 40 kHz for the different layers considered. For thicker layers these poles can be closer to the real axis and their contribution non-

TABLE III. Measured location of the maximum of the reflection coefficient on the real sin θ axis (sin θ_M) and predicted pole related to the surface wave (20 kHz).

Layer	sin θ_M	Predicted sin θ_p (surface wave)
A_1	1.027 ± 0.005	1.017 ± 0.003 $+j(2\times10^{-2}\pm10^{-2})$
A_3	1.013 ± 0.005	1.004 ± 0.001 $+j(0.55\times10^{-2}\pm2\times10^{-2})$
B_1	1.052 ± 0.005	$1.04+j3.8\times10^{-2}$

negligible. The presence of the poles related to the leaky waves and their possible contribution are taken into account in similar electromagnetic problems.[11,23] In our case, only the contribution of the pole related to the surface wave has to be taken into account. This pole is close to sin $\theta=1$ for the thin layers studied (see Table III) and can be crossed only if θ_0 is close to $\pi/2$. The pole and the saddle point are close to each other at grazing incidence. The standard steepest descent method must be modified if the pole and the saddle point are close to each other,[22] and the calculation is not easy, due to the involved dependence of R on sin θ.

An approximation can be performed by using a simplified expression for R valid on the portion of the path of steepest descent close to the pole and the saddle point, which provides the major contribution to the integral. When sin θ is very close to 1, $\cos^2\theta_1$ is close to $1-1/n^2$, and $|\cos\theta|\ll1$ for the materials concerned in this study. A development at the first-order approximation of $\tan(k_1 l\cos\theta_1)$ in Eq. (10) gives

$$R(\cos\theta)=\frac{\left(j\frac{m}{n}\cos\theta+\phi k_1 l\left(1-\frac{1}{n^2}+\cos^2\theta\right)\right)}{\left(j\frac{m}{n}\cos\theta-\phi k_1 l\left(1-\frac{1}{n^2}+\cos^2\theta\right)\right)}. \tag{27}$$

Neglecting $\cos^2\theta$ provides

$$R(\cos\theta)=\frac{\left(\cos\theta-j\frac{n}{m}\phi k_1 l\left(1-\frac{1}{n^2}\right)\right)}{\left(\cos\theta+j\frac{n}{m}\phi k_1 l\left(1-\frac{1}{n^2}\right)\right)}. \tag{28}$$

Equation (28) yields the reflection coefficient of an impedance plane, the impedance Z_p being given by

$$Z_p=-j\frac{Z_1}{\phi}\left(k_1 l\left(1-\frac{1}{n^2}\right)\right)^{-1}, \tag{29}$$

which is the first-order approximation of the surface impedance Z_s of the layer in the vicinity of the pole and the saddle point. The location of the pole for this impedance plane is θ_p such as

$$\sin\theta_p=(1-Z^2/Z_p^2)^{1/2}. \tag{30}$$

This equation gives the same location as Eq. (17).

The far-field reflected pressure p_r has been calculated by Breskhovskikh and Godin[22] for an impedance plane when the pole is close to the saddle point. In Ref. 22, p_r is given by

$$p_r = \frac{\exp(jkR_1)}{R_1} R(\cos\ \theta_0) + \left[\frac{2k\ \cos^2\ \theta_p}{r\ \sin\ \theta_p}\right]^{1/2} \exp\left(jkR_1\ \cos(\theta_p - \theta_0) - j\ \frac{\pi}{4}\right) \times\{\sqrt{\pi}(1+\text{erf}\ u + u^{-1}\ \exp(-u^2))\}, \quad (31)$$

where u is given by

$$u = j\{kR_1(j - j\ \cos(\theta_p - \theta_0))\}^{1/2}. \quad (32)$$

The second term on the right-hand side of Eq. (31) is related to the surface wave. This term disappears when the pole lies far enough from the domain where it can be crossed by the path of steepest descent. The surface wave also disappears when the thickness $l \to 0$ because $\cos\theta_p \to 0$. When $\theta_0 \to \pi/2$, $R(\cos\theta_0) = -1$, and the first term on the right-hand side of Eq. (31) cancels the direct field. At grazing incidence, the one surface wave for the case of thin layers provides the main contribution to the far field, and p_t is given by

$$p_t = \frac{2k\ \cos^2\ \theta_p}{R_1\ \sin\ \theta_p} \exp(jkR_1 \sin\ \theta_p) 2\sqrt{\pi}\ \exp\left(-j\ \frac{\pi}{4}\right). \quad (33)$$

Equation (31) can be valid for $|kR_1| \gg 1$. At 40 kHz for $R_1 = 10$ cm, $|kR_1| = 74$. In Sec. V, the distance between the receiver and the source is always larger than 10 cm.

IV. EXPERIMENTAL EVIDENCE OF THE POLE RELATED TO THE SURFACE WAVE

Experiments have been performed at 20 kHz to detect the poles of the reflection coefficient with the Tamura method. The method has been used previously in the audible frequency range to detect a pole over a porous layer[7] and a honeycomb structure.[24] A sound source creates an axisymmetric field over the porous layer. Measurements of the pressure on two axial lines at $z = z_1$, and $z = z_2$ can provide an evaluation of the plane-wave reflection coefficient sin θ real < 1 (ordinary plane waves), and sin θ real > 1 (evanescent waves). If a pole is located close to the real sin θ axis, the reflection coefficient can present a peak for sin θ real in the neighborhood of the pole. Measurements have been performed on three layers at 20 kHz, at the upper limit where the method can provide reliable measurements.

Simplifications were done on the original setup used at audible frequencies. The source is a tube of diameter equal to 4 mm, fed by a tweeter, and the receiver is a B&K 4170 microphone, with a probe of diameter equal to 1.4 mm. A pure-tone signal is used. The dimensions of the layers are about 40×40 cm. The height of the source is 5 mm, and the two measurement lines are at 0.7 and 2.0 mm from the layer. The interval between the measured points is 1 mm, and measurements were performed at 150 points on each line. The location of the poles in the sin θ plane for the surface waves, obtained with the parameters of Table I, is indicated in Table III. The uncertainty on sin θ_p is indicated for the layers made of material A, for which all parameters have been measured. It has been obtained from the uncertainties $\Delta\Lambda = \Delta\Lambda' = 0.025$ mm, $\Delta\sigma = 500$ Nsm^{-4}, $\Delta\alpha_\infty = 0.015$, and $\Delta l = 0.1$ mm. The poles are close to the Re sin θ axis, and the reflection coefficient, measured with the Tamura method on the Re sin θ axis, must present a maximum for sin θ close to the abscissa of the pole. The location of the measured maximum on the Re sin θ axis is denoted as sin θ_M in Table III. The uncertainty on sin θ_M, obtained from repeated measurements performed in slightly different conditions is 0.005. The method has not been used for layer A2 and A4, the lateral dimensions of the sample being too small. For layer A4, the predicted value for Re sin θ_p at 20 kHz is 1.002, and the Tamura method would not have provided significant information. A systematic difference about 10^{-2} exists between both quantities, but the behavior of sin θ_M and predicted Re sin θ_p is the same when l increases. Moreover, it appears that an increase in tortuosity creates a noticeable increase of the real part of sin θ_p, and a similar shift of sin θ_M. The measured and predicted reflection coefficients are represented for sin θ real up to sin $\theta = 1.4$ in Figs. 5 and 6

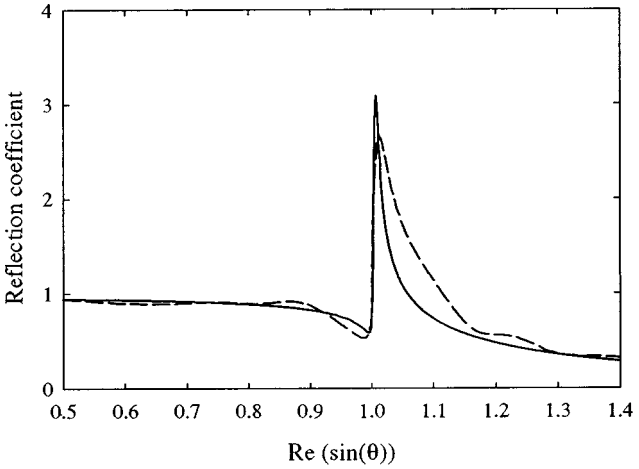

FIG. 5. Modulus of the reflection coefficient for layer A_3 at 20 kHz on the real sin θ axis. Measurement ----, prediction ———.

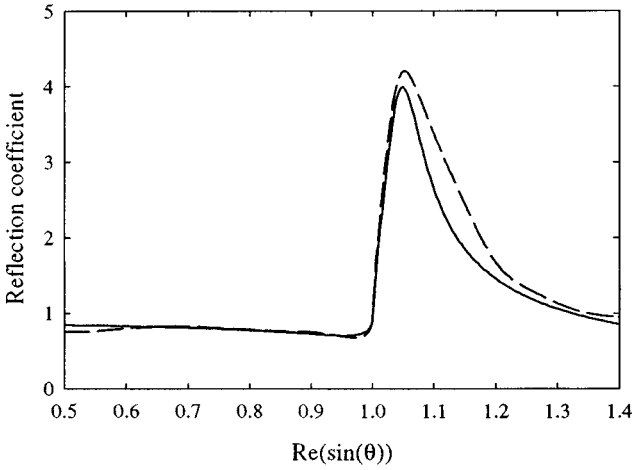

FIG. 6. Modulus of the reflection coefficient for layer B_1 at 20 kHz on the real sin θ axis. Measurement ----, prediction ———.

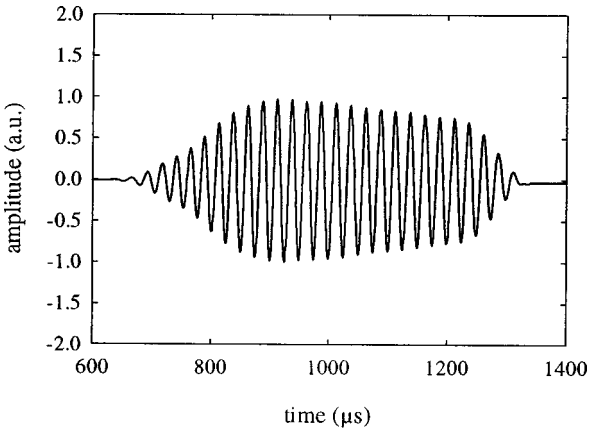

FIG. 7. The burst used for time-of-flight measurements.

for layer A3 and layer B1, respectively. For layer A3, the measured peak is significantly broader than the predicted one. The predicted peaks can be broadened by decreasing the characteristic dimensions, but the maximum is shifted far from the measured values. The broadening could be due to the fact that the layer is not perfectly homogeneous, but the effect cannot be modelized. It may be noticed that the predictions are obtained without an adjustable parameter for this layer. For the layer B1, the characteristic dimensions have been adjusted, and the tortuosity was evaluated only in the direction normal to the faces of the layer. The angle θ_1, related to the pressure field of the surface wave is not close to 0. Prediction and measurements would be in a better agreement with a planar tortuosity larger than the normal tortuosity. We have preferred not to use too many unknown parameters in the modeling. The peaks of $|R|$ in the vicinity of the predicted poles are a striking evidence of the presence of the pole. In the audible frequency range, which is the usual frequency range of the Tamura method, measured and predicted values of sin θ_M for a fibrous layer[7] are very close to each other. Another manifestation of the surface wave is presented in the next section.

V. TIME-OF-FLIGHT MEASUREMENT

At 40 kHz, the Tamura method cannot be used, and time-of-flight measurements are performed. The incident field is created by a tweeter at grazing incidence. A receiver (B&K 4138 microphone) is set successively at 15 and 18 cm from the tweeter. As pointed out by Brekhovskikh and Godin (Ref. 22, p. 60), due to diffraction, the actual field has a structure similar to the one of a cylindrical wave which has, like a line source, inhomogeneous components. For a line source, like for a monopole source, poles in the unphysical Riemann sheet can be captured by the steepest descent path,[11,23] but for the layer used in the present work, the related leaky waves disappear in the far field. In the far field, sufficiently close to the layer, the direct and the reflected field cancel, and the main contribution can be provided by the surface wave. It can be expected that this is also true for our experiment. Two signals are used successively, a long tone burst represented in Fig. 7 which has a narrow spectrum in the frequency domain, and a sine signal. There is no noticeable modification of the shape of the burst depending on the location of the microphone over the porous layer. The time of flight of the burst between the two positions of the microphone is measured, and a measurement of the phase velocity c_p is performed with the sine signal. The first measurement allows a unique choice between the infinite number of possible results with the sine signal. A calibration is performed by measuring the sound speed c by removing the porous layer. From Sec. II, Re sin $\theta_p = c/c_p$. The precision on c/c_p, obtained from different measurements performed with slightly different conditions, is 2×10^{-3}. The measured values for Re sin θ_p are given in Table IV for a distance equal to 0.5 mm between the receiver and the layer. There is a good agreement between measurement and prediction, except for layer A4 such as the order of magnitude of sin $\theta_p - 1$ is comparable to the uncertainty on sin θ_p. The measured values of c_p are stationary when the receiver is located at distances from the porous layer smaller than 0.4 cm, but for a distance larger than 1 cm, c_p and c become indistinguishable. A reasonable interpretation is that the surface wave is the main component of the field close to the layer, and that at distances larger than 1 cm, the direct and the reflected field become more important than the surface wave. Precise measurements of the damping perpendicularly to the layer are not possible, because the distance where the surface wave is dominant is too small. There is no measurement reported for layer A1 in Table IV, the measured velocity is equal to the sound speed in free air. The thickness of layer A2 (5 cm) is the upper limit where the surface wave has been detected. It may be noticed that for layers having a tortuosity close to 1, sin θ_p is very close to 1 for the small thicknesses, and when sin θ_p is significantly different from 1, when l increases sufficiently, the damping in the x direction becomes nonnegligible. This appears clearly in Table IV where predicted sin θ_p are given for layers of material A for different thicknesses. Due to this damping, it is difficult, in the far field, to observe a surface wave having a phase velocity significantly different from the one of an ordinary propagating wave.

TABLE IV. Measured Re sin θ_p and predicted sin θ_p at 40 kHz.

Layer	Measured Re sin θ_p	Predicted sin θ_p
A_2	1.036 ± 0.002	1.025 ± 0.005 $+j(2\times10^{-2}\pm0.2\times10^{-2})$
A_3	1.01 ± 0.002	1.01 ± 0.003 $+j(0.99\times10^{-22}\pm0.1\times10^{-2})$
A_4	1.0023 ± 0.002	1.006 ± 0.002 $+j(6\times10^{-3}\pm0.5\times10^{-3})$
B_1	1.088 ± 0.002	$1.1+j7.6\times10^{-2}$

VI. CONCLUSION

Poles of the reflection coefficient of a thin porous layer, related to the surface and leaky waves, have been predicted by using methods previously developed in the domain of electromagnetic waves. Measurements of the reflection coefficient of inhomogeneous waves confirm the presence of a pole related to a surface wave. Measurements of the phase

velocity in the far field close to the layer indicate the presence of a wave propagating at the velocity predicted for the surface wave. The main problem related to the observation of these waves is explained.

[1] K. M. Ivanov-Shits and F. V. Rozhin, ''Investigations of surface waves in air,'' Sov. Phys. Acoust. **5**, 510–512 (1960).
[2] S. Feng and D. L. Johnson, ''High-frequency acoustic properties of a fluid/porous solid interface. I. New surface mode,'' J. Acoust. Soc. Am. **74**, 906–914 (1983).
[3] S. Feng and D. L. Johnson, ''High-frequency acoustic properties of a fluid/porous solid interface. II. The 2D reflection Green's function,'' J. Acoust. Soc. Am. **74**, 915–924 (1983).
[4] M. J. Mayes, P. B. Nagy, L. Adler, B. P. Bonner, and R. Streit, ''Excitation of surface waves of different modes at fluid-porous solid interface,'' J. Acoust. Soc. Am. **79**, 249–251 (1986).
[5] P. B. Nagy, ''Observation of a new surface mode on a fluid-saturated permeable solid,'' Appl. Phys. Lett. **60**, 2735–2737 (1992).
[6] G. Daigle, M. R. Stinson, and D. I. Havelock, ''Experiment on surface wave over a model impedance plane using acoustical pulses,'' J. Acoust. Soc. Am. **99**, 1993–2005 (1996).
[7] J. Tizianel, J. F. Allard, W. Lauriks, and L. Kelders, ''Experimental localization of a pole of the reflection coefficient of a porous layer,'' J. Sound Vib. **202**, 600–604 (1997).
[8] M. Tamura, ''Spatial Fourier transform method of measuring reflection coefficient of porous layers at oblique incidence,'' J. Acoust. Soc. Am. **88**, 2259–2264 (1990).
[9] B. Brouard, D. Lafarge, J. F. Allard, and M. Tamura, ''Measurements and prediction of the reflection coefficient of porous layers at oblique incidence and for inhomogeneous waves,'' J. Acoust. Soc. Am. **99**, 100–107 (1996).
[10] J. F. Allard, *Propagation of Sound in Porous Media: Modelling Sound Absorbing Materials* (Chapman & Hall, London, 1993).
[11] R. E. Collin, *Field Theory of Guided Waves* (McGraw-Hill, New York, 1960).
[12] A. Bardot, B. Brouard, and J. F. Allard, ''Frame decoupling at low frequencies in thin porous layers saturated by air,'' J. Appl. Phys. **79**, 8223–8229 (1996).
[13] D. L. Johnson, J. Koplik, and L. M. Schwarz, ''New pore size parameter characterizing transport in porous media,'' Phys. Rev. Lett. **57**, 2564–2567 (1986).
[14] D. L. Johnson, J. Koplik, and R. Dashen, ''Theory of dynamic permeability and tortuosity in fluid saturated porous media,'' J. Fluid Mech. **176**, 379–402 (1987).
[15] Y. Champoux and J. F. Allard, ''Dynamic tortuosity and bulk modulus in air-saturated porous media,'' J. Appl. Phys. **70**, 1975–1979 (1991).
[16] P. Leclaire, M. Kelders, W. Lauriks, J. F. Allard, and C. Glorieux, ''Ultrasonic wave propagation in reticulated foams saturated by different gases: High frequency limit of the classical models,'' Appl. Phys. Lett. **69**, 2641–2643 (1997).
[17] M. Henry, P. Lemarinier, J. F. Allard, J. L. Bonardet, and A. Gedeon, ''The evaluation of the characteristic dimensions for porous sound absorbing materials,'' J. Appl. Phys. **77**, 17–20 (1995).
[18] J. F. Allard, B. Castagnède, M. Henry, and W. Lauriks, ''Evaluation of tortuosity in acoustic porous materials saturated by air,'' Rev. Sci. Instrum. **65**, 754–755 (1994).
[19] P. Leclaire, L. Kelders, W. Lauriks, M. Melon, N. Brown, and B. Castagnède, ''Determination of the viscous and thermal characteristic lengths of plastic foams by ultrasonic measurements in helium and air,'' J. Appl. Phys. **80**, 2009–2012 (1996).
[20] I. Tolstoy, ''Smoothed boundary conditions, coherent low-frequency scatter, and boundary modes,'' J. Acoust. Soc. Am. **75**, 1–22 (1984).
[21] M. Deschamps, ''Reflection and refraction of the inhomogeneous wave,'' in *Acoustic Interaction with Submerged Elastic Structure*, edited by D. Inman and A. Guran (World Scientific, Singapore, 1996).
[22] L. M. Brekhovskikh and O. A. Godin, *Acoustics of Layered Media II, Point Source and Bounded Beams* (Springer series on wave phenomena, Springer-Verlag, New York, 1992).
[23] T. Tamir and A. A. Oliner, ''Guided complex waves. Part I. Fields at an interface,'' Proc. IEEE **110**, 310–324 (1963).
[24] J. Tizianel, J. F. Allard, and B. Brouard, ''Surface waves above honeycombs,'' J. Acoust. Soc. Am. (submitted).

Photoacoustic waves excited in liquids by fiber-transmitted laser pulses

G. Paltauf[a] and H. Schmidt-Kloiber
Institute of Experimental Physics, Karl-Franzens-University Graz, Universitaetsplatz 5, A-8010 Graz, Austria

M. Frenz
Institute of Applied Physics, University of Berne, Sidlerstrasse 5, CH-3012 Berne, Switzerland

(Received 27 October 1997; accepted for publication 20 April 1998)

The acoustic wave field generated in front of a submerged fiber tip by short laser pulses is theoretically and experimentally studied by fast imaging and optical pressure measurements. It is shown that the finite size of the fiber causes strong tensile stress leading to cavitation. Depending on the absorption coefficient of the laser radiation, cavitation-induced bubble formation occurs inside (low absorption) or outside (high absorption) the volume of heat deposition. The results are used to characterize the cavitation bubble formation mechanisms and to predict possible consequences for applications of fiber-guided short-pulsed laser sources in medicine. © *1998 Acoustical Society of America.* [S0001-4966(98)02408-4]

PACS numbers: 43.35.Ud [HEB]

INTRODUCTION

The increasing employment of pulsed laser sources for medical applications has fostered the study of photomechanical aspects of laser–tissue interaction. Regardless of their origin, such as thermoelastic expansion, explosive vaporization, cavitation, or stress wave emission, photomechanical effects have been recognized of being important both for supporting tissue ablation and for causing unwanted side effects.[1–5] The relative importance of photomechanical versus photothermal effects depends on the ratio of pulse duration to relaxation times of stress (t_{ac}) and temperature (t_{th}), given by

$$t_{ac}=\frac{\delta}{c} \quad \text{and} \quad t_{th}=\frac{\delta^2}{4\kappa}, \tag{1}$$

where δ is the smallest dimension of the irradiated volume (either the laser beam radius or the optical penetration depth), κ is the thermal diffusivity, and c is the speed of sound. If the pulse duration is shorter than t_{th}, the interaction is thermally confined and the maximum possible average temperature is obtained in the target volume. In this case the distribution of thermal energy is determined by the laser light distribution. Short laser pulses fulfilling the condition of thermal confinement are successfully applied in minimally invasive surgery, because with each laser pulse sufficient energy can be delivered to precisely ablate tissue before heat is transferred to surrounding tissue. This limits the extent of thermal damage adjacent to the ablation crater. If the laser pulse is also shorter than t_{ac}, the condition of stress confinement is satisfied, leading to a high-amplitude thermoelastic stress wave. When generated at a boundary to a medium with lower acoustic impedance (e.g., tissue–air), this wave contains, owing to reflection at the interface, both compressive and tensile stresses. The interaction of such a bipolar stress wave with tissue can lead to rupture and subsequent ejection of tissue fragments, a process called spallation.[6–8] In comparison with a purely thermal evaporation process, photomechanical ablation needs much less energy per unit volume for material removal. Therefore, generally, the ablation threshold for short pulses is much lower than for long pulses, where heat and stress are not confined.[9,10]

For the use in minimally invasive surgery, laser pulses are mostly delivered to the treatment site via optical fibers. During treatment, the fiber tip is either in direct contact with the tissue (contact mode) or is held at a certain distance (noncontact mode). If the fiber tip borders on an absorbing medium, the thermoelastic stress wave caused by absorption of a short laser pulse is launched from a volume directly adjacent to the fiber tip. This volume, which forms the acoustic source, is the region where laser energy is deposited. Its size is given by the cross-sectional area of the optical fiber times the optical penetration depth ($1/\mu_a$) in the absorber. Due to the material properties and the usually cylindrical shape of the fiber, the wave is influenced by very specific boundary and starting conditions:

(i) The fiber has a higher acoustic impedance than the medium into which the wave is emitted (usually water or tissue with high water content). Therefore a part of the wave is reflected at the fiber tip with positive sign.
(ii) The stress wave source has circular symmetry.
(iii) Since multimode fibers are used to transmit high-power laser radiation, the radial distribution of laser radiation at the fiber tip has an extreme top-hat profile with a more or less homogeneous spatial intensity distribution, depending on the mode structure of the laser beam.

As any wave emitted from a source of finite size, thermoelastic stress waves generated at a fiber tip are subject to diffraction. Together with conditions (i)–(iii), this has a strong influence on the temporal and spatial evolution of the

[a]Electronic mail: guenther.paltauf@kfunigraz.ac.at

acoustic field in front of the fiber. One of the most important features of this field is the occurrence of strong tensile stresses near the fiber tip. This has been observed experimentally in time-resolved schlieren images, where we found cavitation near the symmetry axis of the fiber shortly (within a few hundred nanoseconds) after the laser pulse.[11] Since the cavitation zone was outside the heated volume, we could exclude thermal effects as the origin of these bubbles. First theoretical calculations and the visual observation of stress wave propagation have confirmed the hypothesis that tensile stresses and cavitation are due to diffraction of the thermoelastic wave at the circular boundary of the acoustic source in front of the fiber tip.

Acoustic diffraction effects have been widely investigated, mainly in the context of experimental techniques that derive information about the optical properties and the structure of samples from measurements of optoacoustic waves. In these applications, diffraction plays an important role as it changes both the shape and the amplitude of the acoustic wave during propagation. The most obvious of these changes is the transformation of a wave emitted from a cylindrical disc into its derivative at some distance from the source.[12] Such a transformation has to be taken into account in measuring techniques such as optoacoustic tomography[13] or measurements of tissue optical properties,[14–17] where the main information is contained in the temporal profile of the recorded stress. The potential destructive effect of diffracted optoacoustic waves has been recognized in ophthalmology, where the tensile stresses can cause damage to ocular structures.[18]

In this study we will concentrate on the evolution of the acoustic field near the optical fiber tip where the cavitation effect is observed. For the characterization of a point in the acoustic field relative to the source, usually the concept of near and far field is used. If the diameter of the source is much larger than the acoustic wavelength, then the border between near and far field is located at a distance z_f from the fiber tip,[12] defined by

$$z_f = \frac{D^2}{4\lambda_{ac}}, \tag{2}$$

where D is the diameter of the source and λ_{ac} is the acoustic wavelength, given by twice the optical penetration depth. Qualitatively, the near field can be described as the zone where at any point on the symmetry axis the plane wave that propagates in axial direction passes before the signal from the lateral boundary of the source arrives. According to this definition, there is no such boundary if the acoustic wavelength is larger than the radius of the source.

Cavitation strongly influences the mechanical and optical properties of the medium in front of the fiber tip and thereby determines the physical interaction processes and also the outcome of a surgical procedure. It is therefore of importance to know the origin as well as the temporal and spatial development of tensile stresses that are responsible for cavity formation. In this study we present a thorough analysis of the stress wave emission from a liquid volume in contact with an optical fiber tip after absorption of a short laser pulse. In the theoretical part we use a model that describes the pressure–time history at an arbitrary point in, or outside, the laser-irradiated volume. Additionally, experimental observations of cavitation and stress wave propagation will be presented and compared with theoretical findings.

I. GENERATION OF PHOTOACOUSTIC WAVES IN LIQUIDS

In the regime of thermal confinement and in the absence of viscous damping, the photoacoustic wave equation in terms of the velocity potential ψ has the form[19]

$$\nabla^2\psi - \frac{1}{c^2}\frac{\partial^2\psi}{\partial t^2} = \frac{\beta}{\rho C_p} S, \tag{3}$$

where β is the thermal expansion coefficient, ρ is the density, C_p is the specific heat capacity at constant pressure, and S is the heat generated per unit volume and time. The pressure p and the velocity of a volume element $\mathbf{u}$ can be obtained from ψ by the relations

$$p = -\rho\frac{\partial\psi}{\partial t} \quad \text{and} \quad \mathbf{u} = \text{grad}\ \psi. \tag{4}$$

The heat source term S can be an arbitrary function of time and space. However, we will first concentrate on the case of instantaneous heat deposition where S can be expressed as

$$S(\mathbf{r},t) = W(\mathbf{r})\,\delta(t); \tag{5}$$

$W(\mathbf{r})$ is the absorbed volumetric energy density and $\delta(t)$ the Dirac delta function. In this case, a solution of the wave equation can be derived from the following formula:[20]

$$\psi(\mathbf{r},t) = -\frac{t}{4\pi\rho}\frac{\beta c^2}{C_p}\int\int_{|\mathbf{r}-\mathbf{r}'|=ct} W(\mathbf{r}')\ ds, \tag{6}$$

where $\mathbf{r}'$ denotes a point in the source volume, ds is the surface element on a unit sphere, and the integration has to be carried out on the surface of a sphere with radius ct around the observation point $\mathbf{r}$. For a cylindrical symmetry (using r and z for the radial and axial coordinates), the energy density in a pure absorber can be written as

$$W(r,z) = \mu_a H_0 f(r)\exp(-\mu_a z), \tag{7}$$

where H_0 is the incident radiant exposure at the surface ($z=0$) of the absorbing liquid, μ_a is the absorption coefficient, and $f(r)$ is a dimensionless function describing the radial laser beam profile. Instantaneous heating causes a distribution of photoacoustic pressure at time zero $p_0(r,z)$ that is proportional to the energy density:

$$p_0(r,z) = \frac{\beta c^2}{C_p} W(r,z) = \Gamma W(r,z), \tag{8}$$

where Γ is the Grüneisen coefficient. Substituting (8) and (4) into (6) yields

$$p(r,z,t) = \frac{\partial}{\partial t}\left[\frac{t}{4\pi}\int\int_{R=ct} p_0(r',z')\ ds\right]. \tag{9}$$

Here R is the radius of the sphere around the observation point over which the integration is performed. The acoustic field in front of the fiber tip contains contributions from reflection at the water–glass interface. These can be taken into account by assuming an image distribution $p_0^*(r',z')$ at $z'<0$, given by

$$p_0^*(r',z')=R_{ac}p_0(r',-z') \tag{10}$$

with R_{ac} the acoustic reflectivity of the interface. R_{ac} is equal -1 for a free surface and $+1$ for a rigid surface. The acoustic reflectivity depends, in general, on the angle of incidence θ and is given by the relation[20]

$$R_{ac}=\frac{\rho_2 c_2 \cos\theta-\rho_1\sqrt{c_1^2-c_2^2\sin^2\theta}}{\rho_2 c_2 \cos\theta+\rho_1\sqrt{c_1^2-c_2^2\sin^2\theta}}. \tag{11}$$

For a water–quartz interface with $\rho_2=2500$ kg/m^3, $c_2=5200$ m/s, $\rho_1=1000$ kg/m^3 and $c_1=1500$ m/s, the value of R_{ac} varies between 0.8 at normal incidence and 1 at $\theta>16°$.

Let us first consider the case of a perfect top-hat beam profile (fiber radius a) with

$$\begin{aligned} &f(r')=1, \quad r'\leqslant a,\\ &f(r')=0, \quad r'>a. \end{aligned} \tag{12}$$

If we further assume a constant R_{ac} and limit ourselves to a point on the positive z axis, integration of (9) is straightforward and yields for $z>a$

$$\begin{aligned} p(z,t)&=\frac{\Gamma\mu_a H_0}{2}(p_1+p_2), \quad \text{range } 1: ct\leqslant a,\\ p(z,t)&=\frac{\Gamma\mu_a H_0}{2}(p_1+p_2-p_4-p_5),\\ &\quad \text{range } 2: a<ct\leqslant z,\\ p(z,t)&=\frac{\Gamma\mu_a H_0}{2}(R_{ac}p_3+p_2-p_4-p_5),\\ &\quad \text{range } 3: z<ct\leqslant\sqrt{z^2+a^2},\\ p(z,t)&=\frac{\Gamma\mu_a H_0}{2}[R_{ac}(p_3-p_6)+p_2-p_5],\\ &\quad \text{range } 4: ct>\sqrt{z^2+a^2}, \end{aligned} \tag{13a}$$

with

$$\begin{aligned} &p_1=\exp(\mu_a(ct-z)), \quad p_2=\exp(-\mu_a(ct+z)),\\ &p_3=\exp(-\mu_a(ct-z)),\\ &p_4=\frac{ct}{\sqrt{c^2t^2-a^2}}\exp(\mu_a(\sqrt{c^2t^2-a^2}-z)),\\ &p_5=\frac{ct}{\sqrt{c^2t^2-a^2}}\exp(-\mu_a(\sqrt{c^2t^2-a^2}+z)),\\ &p_6=\frac{ct}{\sqrt{c^2t^2-a^2}}\exp(-\mu_a(\sqrt{c^2t^2-a^2}-z)). \end{aligned} \tag{13b}$$

For $z<a$, the boundaries of the ranges change to

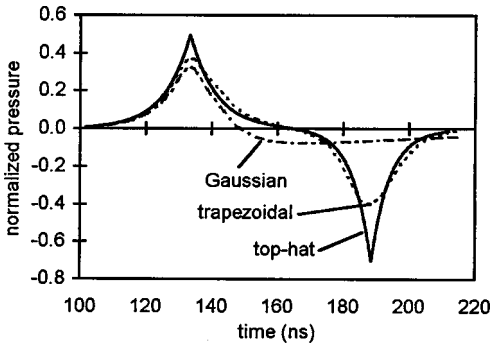

FIG. 1. Photoacoustic signals in water calculated for a point on the fiber axis, 200 μm away from the fiber tip, assuming an absorption coefficient of $\mu_a=840$ cm^{-1} and different beam profiles and pulse durations: top-hat ($a=200$ μm, $d=0$, delta-pulse), trapezoidal ($a=180$ μm, $d=20$ μm, $t_p=6$ ns) and Gaussian ($a=0$, $d=200$ μm, $t_p=6$ ns).

$$\text{range } 1: ct\leqslant z; \quad \text{range } 2: z<ct\leqslant a;$$

$$\text{range } 3: a<ct\leqslant\sqrt{z^2+a^2}; \quad \text{range } 4: ct>\sqrt{z^2+a^2},$$

and the signal in range 2 becomes

$$p(z,t)=\frac{\Gamma\mu_a H_0}{2}(R_{ac}p_3+p_2). \tag{14}$$

As required for a purely one-dimensional wave ($a=\infty$) all factors depending on the beam diameter vanish and the solution is given by a combination of simple exponential functions (p_1,p_2,p_3). The one-dimensional solution can therefore be obtained by translating with the speed of sound half of the initial pressure distribution in the positive z direction and the other half in the negative z direction, taking into account the reflection of the latter at the interface. Measurement of the one-dimensional portion of a wave outside the source volume provides an accurate method to derive the optical absorption coefficient. Since the first part of such a wave is proportional to p_1, a linear fit to the logarithm of the signal has a slope equal to the product $\mu_a c$.

For the calculation of off-axis signals, Eq. (9) has to be integrated numerically. A more realistic beam profile is

$$\begin{aligned} &f(r')=1, \quad r'\leqslant a,\\ &f(r')=\exp(-(r'-a)^2/d^2), \quad r'>a, \end{aligned} \tag{15}$$

where d characterizes the falling slope of the beam profile at the fiber edge. Measurements of the beam profile in front of the fiber tip with a CCD camera suggest a ratio $a/d\approx 10$. Also, the finite pulse duration can be taken into account by convolution of the delta-pulse solution with the temporal profile of the laser pulse. For a Gaussian pulse we obtain

$$p(r,z,t)=\frac{\int_{-\infty}^{+\infty}e^{-(2t'/t_p)^2}p_\delta(r,z,t-t')\,dt'}{\int_{-\infty}^{+\infty}e^{-(2t'/t_p)^2}\,dt'}, \tag{16}$$

where $p_\delta(r,z,t)$ is the solution that was obtained by assuming delta-pulse irradiation and t_p is the pulse duration.

In the following, all calculated signals will be presented in terms of normalized pressure, given as the absolute pressure divided by the factor $\Gamma\mu_a H_0$. Figure 1 shows the temporal development of the normalized pressure for three cases: An analytical solution for a perfect top-hat beam pro-

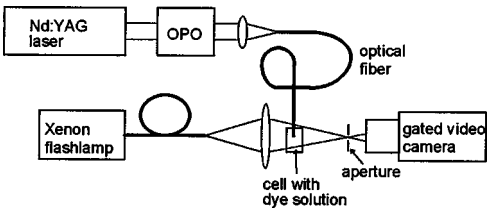

FIG. 2. Experimental setup for time-resolved imaging of the region below a fiber tip submerged in a dye solution.

file and instantaneous heat deposition is compared with two numerical solutions for a finite pulse duration of 6 ns, one for a trapezoidal radial profile ($a=180$ μm and $d=20$ μm) and the other one for a Gaussian profile ($a=0$, $d=200$ μm). All signals were calculated for a point in the near field ($z=200$ μm) of a source with 400-μm diameter. The positive peak represents the plane wave propagating in the axial direction, whereas the negative peak comes from the edge of the source. Stress relaxation during the finite pulse duration causes some minor changes to the compressive part of the waves. The tensile part, however, strongly depends on the radial beam profile and is highest for the perfect top-hat distribution.

II. EXPERIMENTAL METHODS

Pulses with a duration of 6 ns from an optical parametric oscillator (OPO) were coupled into an optical fiber. The distal end of the fiber was submerged in an aqueous solution of 10 g/l Orange G. This dye has a strong absorption peak at 490 nm with a sharply falling slope towards longer wavelengths. By tuning the OPO from 490 to 555 nm we could vary the absorption coefficient of the dye solution from $\mu_a=840\ \mathrm{cm}^{-1}$ to $\mu_a=26\ \mathrm{cm}^{-1}$. Absorption coefficients were determined from the rising slope of stress signals, measured with a pressure detector made of a 9-μm-thick piezoelectric polyvinylidenefluoride (PVDF) film. Before the experiments the dye solution was filtered through a 200-nm pore diameter filter. For time-resolved observation of cavitation and stress wave propagation the region below the submerged fiber tip was imaged with a time-gated video camera using an exposure time of 10 ns. The delay time between laser pulse and video exposure could be varied between 0 and 1000 μs. An illumination pulse with a duration of 1 μs was created by a xenon lamp at appropriate delay after the laser pulse and was guided to the sample via a 400 μm core diameter fiber. The tip of the illuminating fiber was imaged onto an aperture in front of the camera objective to enhance the contrast of pressure gradients (Fig. 2).

For temporally and spatially resolved detection of acoustic waves we used an optical transducer that has been described previously.[21] It is based on changes of reflectance of a glass–water boundary during passage of a pressure wave. The fast variations of reflectance are probed with a continuous HeNe laser that is focused onto the interface. The small elliptical detector spot with principal diameters of approximately 150 and 300 μm is imaged with a lens onto the active area of a fast photodiode. A high sensitivity for the detector is achieved by using an incident angle slightly smaller than

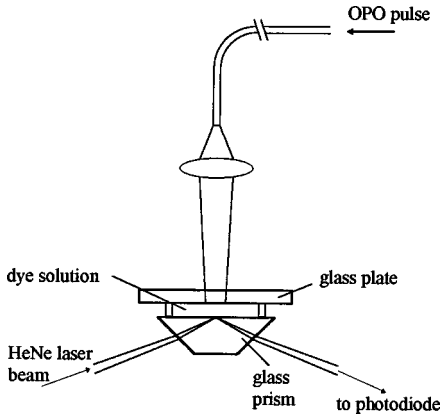

FIG. 3. Experimental arrangement for measurements of photoacoustic waves in a dye solution below an enlarged image of a fiber tip. HeNe laser beam, glass prism, and photodiode belong to the optical stress sensor.

the critical angle of total internal reflection. Spatially resolved detection of thermoelastic stress waves in the near field is only possible if the source is much larger than the detector spot. Therefore we used an enlarged image of a 1-mm core diameter optical fiber for irradiation of the liquid surface. To simulate the boundary condition at a fiber tip, the liquid was covered with a 4-mm-thick glass plate (Fig. 3). Since both the prism and the glass plate reflect the acoustic wave, a minimum thickness of the liquid layer had to be chosen (1 mm in our experiments) in order to avoid an interference of the direct wave with reflected waves.

III. RESULTS

The series of pictures (Fig. 4) taken at different delay times after transmitting an OPO pulse of 490-nm wavelength through a 400-μm core diameter fiber shows stress wave propagation, cavitation, and vapor bubble formation in the liquid in front of the fiber tip. The absorption coefficient of the dye solution at this wavelength is $\mu_a=840\ \mathrm{cm}^{-1}$. The schlieren setup makes it possible to see the structure of the stress wave that consists of a plane wave part, marked by the thick shadow parallel to the fiber exit surface, and a toroidal wave, seen as two circles with their centers at the left and right edges of the fiber core (picture at $t=120$ ns). Cavitation is generated when the circles overlap at the fiber axis, which happens 140 ns after the laser pulse. The zone where cavitation appears is limited to the region near the fiber axis and is well outside the heated volume. The optical penetration depth amounts only to 12 μm. The radiant exposure of $1.27\ \mathrm{J/cm}^2$ leads to a maximum theoretical average temperature rise in the heated volume of $\Delta T=255\ ^\circ\mathrm{C}$ (assuming constant specific heat capacity and no vaporization). The average temperature rise ΔT in the absorbing liquid is calculated by

$$\Delta T=\frac{\mu_a H_0}{\rho C_\nu}, \tag{17}$$

where H_0 is the radiant exposure, ρ is the density of the liquid, and C_ν is the specific heat capacity at constant volume. This leads to an explosive vaporization of a water layer adjacent to the fiber tip, generating the vapor bubble that

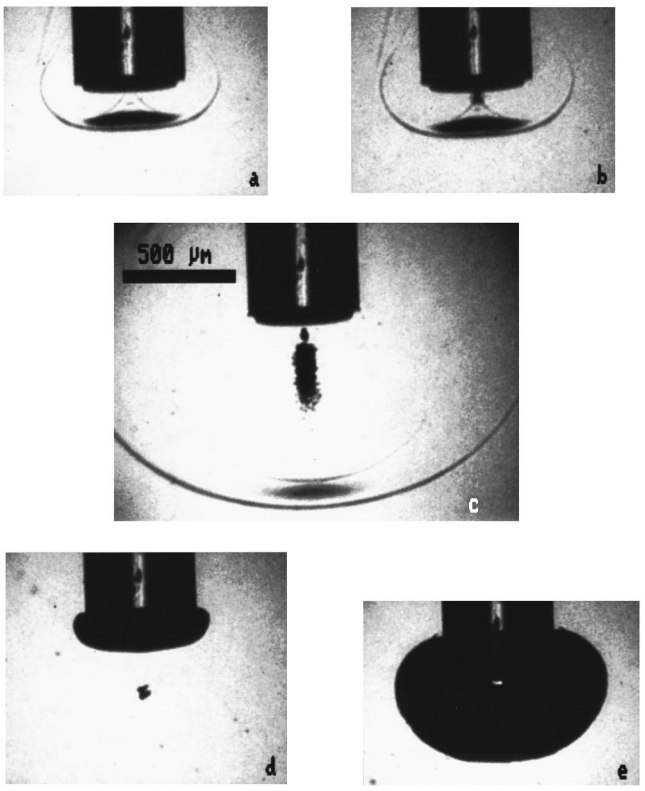

FIG. 4. Images of stress wave propagation, cavitation, and vapor bubble formation below a 400-μm core diameter fiber tip after transmission of an OPO pulse with $\lambda = 490$ nm and $H_0 = 1.27$ J/cm^2 into a dye solution with $\mu_a = 840$ cm^{-1}. Images were taken at different delay times after beginning of the laser pulse: (a) 120 ns, (b) 140 ns, (c) 570 ns, (d) 5.1 μs, (e) 50 μs.

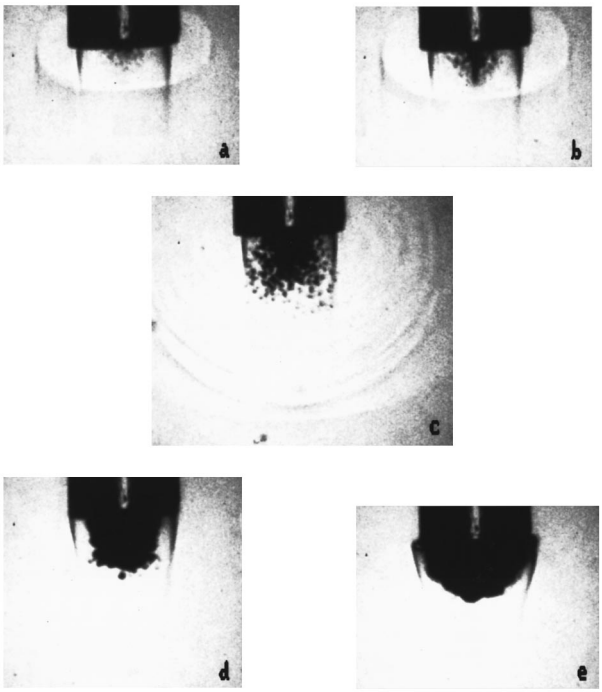

FIG. 5. Stress wave propagation and cavitation below a 400-μm core diameter fiber tip. OPO wavelength $\lambda = 555$ nm, $H_0 = 5.25$ J/cm^2, and $\mu_a = 26$ cm^{-1}. Delay times: (a) 120 ns, (b) 140 ns, (c) 570 ns, (d) 5.1 μs, (e) 20 μs.

appears a few microseconds after the laser pulse and reaches its maximum expansion at about 50 μs. The small dark spot below the vaporization bubble (seen at $t = 5.1$ μs) is the remnant of the collapsing cavitation bubbles.

Figure 5 shows stress wave-induced cavitation in a dye solution with an absorption coefficient of 26 cm^{-1}. In this case, cavitation occurs mainly inside the $1/e$ depth of the heated volume. However, the radiant exposure of 5.25 J/cm^2 leads only to a maximum average temperature rise of 33 °C, what excludes vaporization as the main origin of the cavities. In contrast to the cavitation bubbles generated in a liquid with high absorption coefficient, the cavitation bubbles in a weakly absorbing liquid persist longer and coalesce to a large bubble (see picture at $t = 20$ μs). The two dark lines at the core-cladding boundary of the fiber result from the two-dimensional projection of the cylindrical temperature gradient of the heated volume. Due to the long thermal relaxation time of 221 ms the temperature gradient stays almost confined during the time of observation.

The stress wave propagation and the cavitation bubble formation at a free surface for high and low absorption are shown in Fig. 6. The fiber tip was held slightly above the liquid surface as seen in the pictures. At high absorption, there is a clear difference to the image taken with the fiber submerged: below a free boundary, cavitation spreads over nearly the whole fiber diameter. This difference is less pronounced at low absorption.

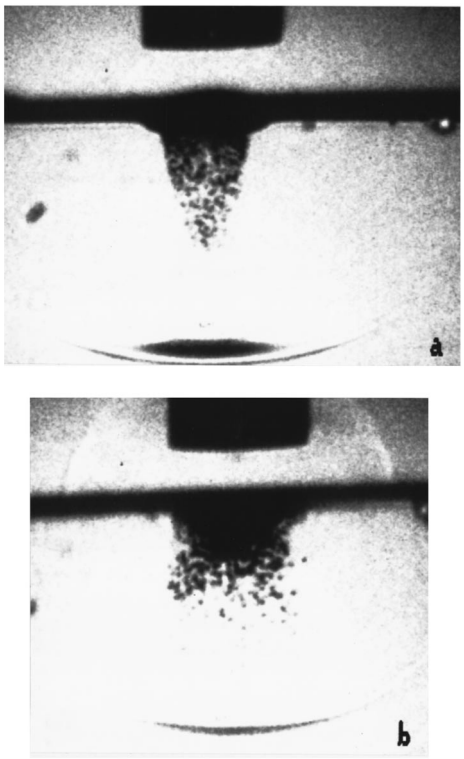

FIG. 6. Photoacoustic cavitation below a free surface at (a) high absorption ($\mu_a = 840$ cm^{-1}, $H_0 = 1.27$ J/cm^2) and (b) low absorption ($\mu_a = 26$ cm^{-1}, $H_0 = 5.25$ J/cm^2). Delay time: 570 ns.

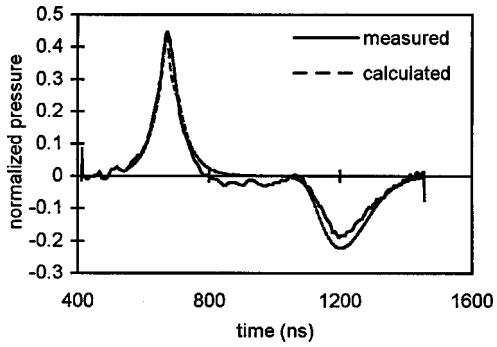

FIG. 7. Measured and calculated photoacoustic signals in dye solution below a threefold enlarged image of a 1-mm core diameter fiber tip. The liquid surface was covered with a glass plate. The detector was centered at $z=1$ mm below the liquid surface. OPO wavelength $\lambda=525$ nm, $\mu_a=178\ \mathrm{cm}^{-1}$. The origin of the time axis coincides with the start of the laser pulse.

Figures 7 and 8 show signals measured with the experimental setup shown in Fig. 3 in comparison with theoretical results. In the experiments the thickness of the liquid layer between the prism and the glass plate was either 1 or 5 mm. The diameter of the laser-irradiated area was 3 mm and the optical sensor was centered below the circular source. An OPO wavelength of 525 nm yielded an optical absorption coefficient of $\mu_a=178\ \mathrm{cm}^{-1}$. According to definition (2), both positions ($z=1$ mm and $z=5$ mm) of the detector are in the acoustic near field. The signals consist of a positive and a negative part, separated by a delay time that decreases with increasing distance from the source. Superimposed on the measured signals are the corresponding calculated signals. In the calculation we assumed a beam profile with $a=1.3$ mm and $d=0.25$ mm. These values were taken from images of the irradiated area obtained with a CCD camera. There is quite a good accordance between measured and calculated signals. We believe that the small deviations that are visible are due to slight differences in theoretical and experimental beam profiles. Figure 9 shows the measured and calculated signals of the temporal development of the normalized stress 1 mm below the liquid surface but at a point $r=0.75$ mm off-axis. It is remarkable that although the positive part of the wave has not changed in comparison with the signals on the symmetry axis, there is only a small, sustained tensile phase.

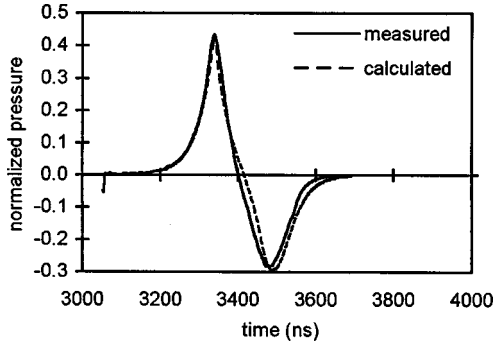

FIG. 8. Photoacoustic signals taken under same experimental parameters as in Fig. 7, but with $z=5$ mm.

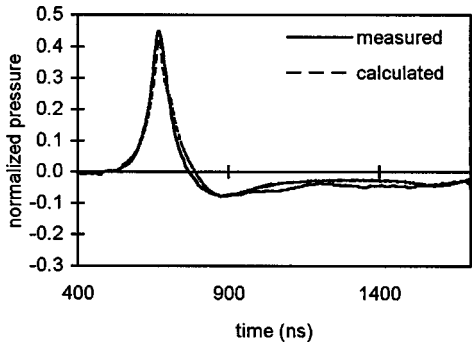

FIG. 9. Photoacoustic signals taken under same experimental parameters as in Fig. 7. The detector was positioned 0.75 mm off-axis, at $z=1$ mm below the surface.

IV. DISCUSSION

Although the analytical solution in (13) and (14) is based on some idealized assumptions (i.e., ideal top-hat beam profile and instantaneous heat deposition), it gives us a good opportunity to study the composition of the acoustic field in front of a submerged fiber tip. In the case of a plane wave ($a=\infty$), the wave consists only of the three components p_1, p_2, and $R_{ac}p_3$, where p_1 and p_2 denote the waves traveling in the liquid in positive and negative z directions, respectively, and $R_{ac}p_3$ is the reflected wave. In the case of a finite source diameter, components p_4, p_5, and $R_{ac}p_6$ are waves originating at $r=a$. Since these waves always have an opposite sign to that of their plane wave counterparts, they are the sources of tensile stress below a submerged fiber, where $R_{ac}>0$ (rigid boundary). The singularity of p_4 and p_5 at $ct=a$ corresponds to the arrival of the collapsing cylindrical wave at $r=0$. For a point inside the irradiated volume, this is the main reason for the generation of tensile stress. If the point is outside the irradiated volume, the maximum tensile stress originates at $z'=0$ and $r'=a(ct=\sqrt{z^2+a^2})$.

It is very informative to look at radial pressure distributions calculated for different times and fixed z. Figure 10(a) shows such distributions, derived for a distance $z=100\ \mu$m from a 400-μm core diameter fiber tip, $\mu_a=840\ \mathrm{cm}^{-1}$ and $t_p=6$ ns (the same experimental parameters under which the images in Fig. 4 where taken). In the diagram the approach of a tensile wave component towards $r=0$ can be seen. As could be anticipated from the spatial and temporal initiation of cavitation in the video images, the maximum negative pressure is reached at the symmetry axis after a time $t=150$ ns. In contrast, below a free surface [Fig. 10(b)], a first rarefaction arrives after 80 ns. It is due to the negative reflection at the water–air interface and is equally distributed over nearly the entire diameter of the irradiated spot. A second rarefaction arrives at the symmetry axis at $t=150$ ns. As in the case of a rigid boundary, it originates at the radial limit of the acoustic source, at $z'=0$ and $r'=a+d$. Since cavitation can be seen over nearly the entire fiber diameter (Fig. 6), it can be concluded that these bubbles are created by the first rarefaction wave.

At low absorption considerable relaxation of pressure occurs through radial propagation. Therefore in both cases of free and rigid surface, strong tensile stresses are created in-

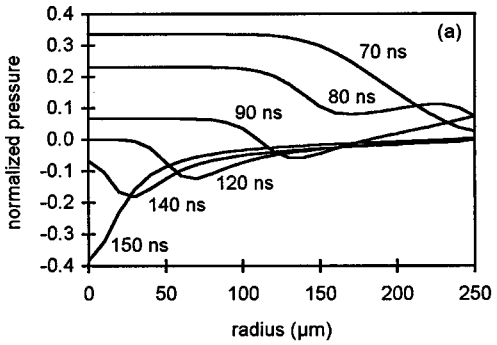

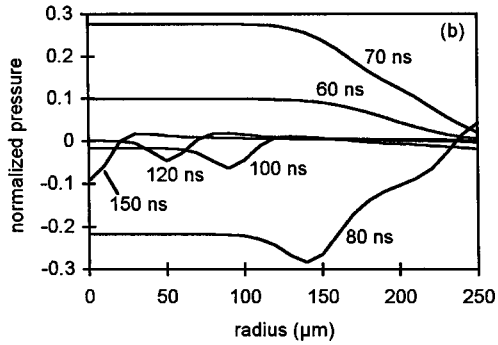

FIG. 10. Dependence of the photoacoustic pressure in water with $\mu_a = 840\ \mathrm{cm}^{-1}$ on the radial distance from the fiber axis, calculated for different times after the laser pulse and a fixed depth of $z = 100\ \mu$m. (a) Rigid surface (water–glass), (b) free surface (water–air). Fiber diameter: 400 μm ($a = 180\ \mu$m, $d = 20\ \mu$m).

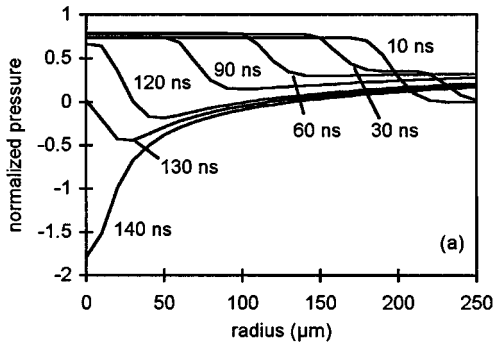

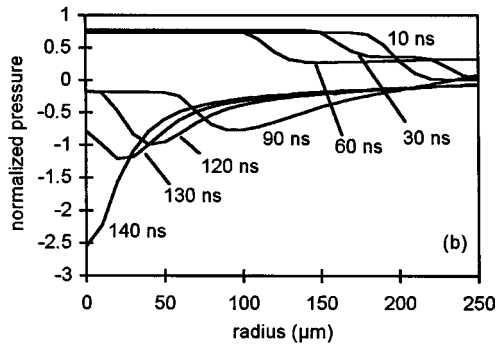

FIG. 11. Dependence of the photoacoustic pressure in water with $\mu_a = 26\ \mathrm{cm}^{-1}$ on the radial distance from the axis of a 400-μm core diameter fiber, calculated for different times after the laser pulse and a fixed depth of $z = 100\ \mu$m. (a) Rigid surface (water–glass), (b) free surface (water–air).

side the source volume by the collapsing cylindrical wave, and the contribution of negative reflection of the axially propagating wave components at the free boundary is small [compare Fig. 11(a) and (b)].

Time-resolved stress measurements with an enlarged source and a small detector area support the findings derived from theory. As is shown in Figs. 7 and 8, a detector centered in the near field of the source records two distinct phases of the photoacoustic wave having different polarity. The negative signal cannot be resolved accurately if the source is not large compared to the detector size. In this case only the plane, positive wave will be recorded correctly, because it arrives at each point on the detector plane at the same time. The tensile components, however, hit different radial positions of the detector at different times [Fig. 10(a)]. Therefore, a detector that is larger than the fiber diameter can only record strong tensile waves at some distance from the source, where compressive and tensile components propagate in nearly the same direction.[11] This is an important finding of our study for measuring techniques where the information is obtained from the temporal profile of the recorded stress wave.

The amplitude of the photoacoustic pressure generated under conditions of stress confinement is given by the product $\Gamma \mu_a H_0$. Using the temperature-dependent Grüneisen coefficient of water,[22] and an energy density $\mu_a H_0$ that raises the temperature from 20 °C to 100 °C, a calculation of the amplitude yields 900 bar. As has been shown above, a negative pressure even exceeding the initial positive amplitude can be created in front of an optical fiber tip (Fig. 11). This can cause damage to the material in which the wave propagates. If the material is water as in our experiments, photomechanical damage starts with the opening of cavities that subsequently grow and may coalesce into a larger bubble. The threshold for cavitation depends strongly on the state of the water. In our experiments, where no strong efforts have been made to highly purify the water, the onset of cavitation is determined by heterogeneous nucleation at small particulate impurities, for which the threshold lies near -10 bar.[23] In highly purified water, however, the threshold for homogeneous cavitation may be as high as -1 kbar.[24]

V. IMPLICATION FOR MEDICAL APPLICATIONS

Cavitation in water might be important for medical applications of infrared laser pulses. Since near-infrared radiation is strongly absorbed by tissue water, IR pulses transmitted through optical fibers are very effective for precise, minimally invasive tissue ablation.[25–28] However, some surgical procedures require a liquid environment, which mostly consists of water, blood, or a mixture of both, and therefore the radiation may be blocked before it can reach the tissue. This can be avoided by using a part of the laser pulse or a prepulse to create a transparent vapor channel between the fiber tip and the tissue surface.[29–33] In order to optimize this effect energetically, it might be advantageous to initiate the formation of the channel by photoacoustic cavitation, which needs less energy than pure thermal vaporization. For example, cavitation in front of a 400-μm fiber at μ_a

$=26\ \mathrm{cm}^{-1}$ could be created at a maximum average temperature rise of 33 °C. Similar conditions are achieved with a *Q*-switched Holmium laser ($\lambda=2.12\ \mu$m) in an aqueous environment (water or blood).

If the optical fiber tip is in direct contact with the tissue, the irradiated tissue volume becomes the source of the photoacoustic wave. Owing to its high water content, the maximum thermoelastic pressure in biological tissue is similar to that in water (about 800 bar at a temperature rise from body temperature to the boiling point). Even if the tensile strength of tissue is higher than that of water, the high negative stresses generated in front of an optical fiber are likely to cause damage. As the photographs in Fig. 4 have shown, cavitation can reach to a depth that is much larger than the optical penetration depth. Therefore it can be expected that at high absorption the photoacoustic damage range largely exceeds the thermally affected zone. If the absorption coefficient is so low that the optical penetration depth is comparable to the fiber diameter, the tensile stress amplitude exceeds the initially generated photoacoustic stress. Therefore it is likely that photoacoustic damage might occur at temperatures below the boiling point of the tissue water. In both cases, low and high absorption, the weakening of the mechanical integrity of the tissue by the photoacoustic wave may have an influence on the surgical procedure. This influence can be positive, because it can lower the ablation threshold. However, the generation of additional mechanical damage may also be an unwanted side effect.

VI. CONCLUSION

The generation of a photoacoustic wave by transmitting a short laser pulse through an optical glass fiber into an absorbing liquid has been investigated. Owing to acoustic diffraction at the edge of the finite-size fiber, the wave contains tensile stress and causes cavitation near the rigid liquid–glass interface, both in the near and far fields of the acoustic source. The diffraction influences the temporal profile of the acoustic stress wave and has important consequences when determining optical properties of a medium by optoacoustic methods. Depending on the optical penetration depth of the laser radiation, the formation of cavitation can lead either to a desired side effect by decreasing the threshold for ablation or to an undesired one when the mechanical tissue damage exceeds the extent of the thermal damage.

ACKNOWLEDGMENTS

This work has been supported by the Austrian Science Foundation FWF (Project P10769-Med) and the Swiss Science Foundation SNF.

[1] G. Paltauf, M. Frenz, and H. Schmidt-Kloiber, in *Laser-Tissue Interaction and Tissue Optics*; Proc. SPIE 2624, edited by H. J. Albrecht, G. Delacrétaz, T. H. Meier, R. W. Steiner, L. O. Svaasand, and A. Katzir (SPIE, Bellingham, 1995), pp. 72–82.

[2] R. S. Dingus, D. R. Curran, A. A. Oraevsky, and S. L. Jacques, in *Laser-Tissue Interaction V*; Proc. SPIE 2134A, edited by S. L. Jacques and A. Katzir (SPIE, Bellingham, 1994), pp. 434–445.

[3] T. G. van Leeuwen, J. H. Meertens, E. Velema, M. J. Post, and C. Borst, Circulation **87**, 1258–1263 (1993).

[4] Y. Yashima, D. J. McAuliffe, S. L. Jacques, and T. J. Flotte, Lasers Surg. Med. **11**, 62–68 (1991).

[5] M. Ith, H. Pratisto, H. U. Stäubli, H. J. Altermatt, M. Frenz, and H. P. Weber, Sports Exercise and Injury **2**, 207–209 (1996).

[6] R. S. Dingus and R. J. Scammon, in *Laser-Tissue Interaction II*; Proc. SPIE 1427, edited by S. L. Jacques and A. Katzir (SPIE, Bellingham, 1991), pp. 45–54.

[7] G. Paltauf and H. Schmidt-Kloiber, Lasers Surg. Med. **16**, 277–287 (1995).

[8] A. A. Oraevsky, S. L. Jacques, and F. K. Tittel, J. Appl. Phys. **78**, 1281–1290 (1995).

[9] F. Könz, M. Frenz, H. Pratisto, H. P. Weber, A. S. Silenok, and V. I. Konov, J. Appl. Phys. (to be published).

[10] Y. Domankevitz, M. S. Lee, and N. S. Nishioka, in *Laser-Tissue Interaction III*; Proc. SPIE 1646, edited by S. L. Jacques and A. Katzir (SPIE, Bellingham, 1992), pp. 42–45.

[11] M. Frenz, G. Paltauf, and H. Schmidt-Kloiber, Phys. Rev. Lett. **76**, 3546–3549 (1996).

[12] M. W. Sigrist, J. Appl. Phys. **60**, R83–R121 (1986).

[13] A. A. Karabutov, N. B. Podymova, and V. S. Letokhov, Appl. Phys. B: Lasers Opt. **63**, 545–563 (1996).

[14] P. C. Beard and T. N. Mills, Phys. Med. Biol. **42**, 177–198 (1997).

[15] A. A. Oraevsky, S. L. Jacques, and F. K. Tittel, Appl. Opt. **36**, 402–415 (1997).

[16] G. Paltauf, H. Schmidt-Kloiber, and H. Guss, Appl. Phys. Lett. **69**, 1526–1528 (1996).

[17] S. Lohmann, C. Ruff, and C. Schmitz, in *Laser-Tissue Interaction and Tissue Optics II*; Proc. SPIE 2923, edited by H. J. Albrecht, G. Delacretaz, and T. H. Meier (SPIE, Bellingham, 1996), pp. 2–11.

[18] S. Siano, R. Pini, P. G. Gobbi, R. Salimbeni, M. Vannini, F. Carones, G. Trabucchi, and R. Brancato, Lasers Surg. Med. **20**, 416–425 (1997).

[19] G. J. Diebold and T. Sun, Acustica **80**, 339–351 (1994).

[20] L. D. Landau and E. M. Lifschitz, *Hydrodynamics* (Akademie, Berlin, 1981).

[21] G. Paltauf and H. Schmidt-Kloiber, J. Appl. Phys. **82**, 1525–1531 (1997).

[22] G. Paltauf and H. Schmidt-Kloiber, Appl. Phys. A: Mater. Sci. Process. **62**, 303–311 (1996).

[23] G. Paltauf, E. Reichel, and H. Schmidt-Kloiber, in *Laser-Tissue Interaction III*; Proc. SPIE 1646, edited by S. L. Jacques and A. Katzir (SPIE, Bellingham, 1992), pp. 343–352.

[24] J. C. Fisher, J. Appl. Phys. **19**, 1062–1067 (1948).

[25] J. A. Izatt, D. Albalgli, I. Itzkan, and M. S. Feld, in *Laser-Tissue Interaction I*, Proc. SPIE 1202, edited by S. L. Jacques and A. Katzir (SPIE, Bellingham, 1990), pp. 133–140.

[26] S. M. Shapshay, H. T. Aretz, and S. E. Setzer, Otolaryngol.-Head Neck Surg. **102**, 251–256 (1990).

[27] R. Kaufmann, A. Hartmann, and R. Hibst, J. Dermatol. Surg. Oncol. **20**, 112–118 (1994).

[28] A. D. Zweig, B. Meierhofer, O. M. Muller, C. Mischler, V. Romano, M. Frenz, and H. P. Weber, Lasers Surg. Med. **10**, 262–274 (1990).

[29] H. Loertscher, W. Q. Shi, and W. S. Grundfest, IEEE Trans. Biomed. Eng. **39**, 86–87 (1992).

[30] T. G. van Leeuwen, M. J. van der Veen, R. M. Verdaasdonk, and C. Borst, Lasers Surg. Med. **11**, 26–34 (1991).

[31] M. Ith, H. Pratisto, H. J. Altermatt, M. Frenz, and H. P. Weber, Appl. Phys. B: Lasers Opt. **59**, 621–629 (1994).

[32] H. Pratisto, M. Ith, M. Frenz, and H. P. Weber, Appl. Phys. Lett. **67**, 1963–1965 (1995).

[33] M. Frenz, H. Pratisto, F. Könz, E. D. Jansen, A. J. Welch, and H. P. Weber, IEEE J. Quantum Electron. **32**, 2025–2036 (1996).

Experimental determination of the total vibratory power transmission in an elastic beam

Jie Pan[a] and Ruisen Ming
Department of Mechanical and Materials Engineering, The University of Western Australia, Nedlands WA 6907, Australia

Colin H. Hansen
Department of Mechanical Engineering, The University of Adelaide, Adelaide SA 5001, Australia

Robert L. Clark
Department of Mechanical Engineering and Materials Science, Duke University, Durham, North Carolina 27708-0300

(Received 29 September 1997; accepted for publication 29 April 1998)

A structure can simultaneously support different types of structural waves. For active control of vibration in a beam structure, it is necessary to consider all wave types simultaneously. Thus it is necessary to be able to measure the vibration amplitude associated with all wave types at any beam cross section as well as the total vibratory power transmission associated with all wave types. In this paper, the theoretical basis is outlined for a new method which allows measurement of all the required quantities using appropriately oriented and located accelerometers. Experimental results are also provided to illustrate the usefulness of this method. © *1998 Acoustical Society of America.* [S0001-4966(98)04408-7]

PACS numbers: 43.40.At, 43.40.Cw [CBB]

INTRODUCTION

The development of an accurate technique for the measurement of vibratory power transmission in structures has the potential to influence the field of structural acoustics in much the same way that the development of the sound intensity technique influenced the field of airborne acoustics. Unfortunately, the measurement of vibratory power transmission is often hampered by the simultaneous presence of several structural wave types. However, in spite of the complexity involved in its determination, the vibrational intensity in a structure is a very useful cost function for active vibration control systems.[1,2] The accurate measurement of vibratory power transmission in a structure is directly related to the controllability of the structure. Several studies[3–6] have shown that it is necessary to consider the total vibratory power transmission due to all wave types when the active control of beam vibration is considered.

There has been a significant amount of research undertaken in the past on the measurement of structural intensity which is directly related to vibratory power transmission. However, most of the work has concentrated on the measurement of only one wave type in beams, plates, and cylindrical shells.[7–14] A few related to the measurement of power flow in coupled one-dimensional structures carrying more than one wave type.[15–18] Horner and White[15,16] compared the theoretical predictions with the measured power flows carried by longitudinal and flexural waves in a branched pipe with anechoic terminations. Farag and Pan[17,18] assessed the accuracy in the measurement of power flow of different wave-types in coupled finite beams. They separately measured the power flows carried by different wave types by using different accelerometer configurations.

In this paper a new technique is demonstrated and its theoretical basis is outlined for the simultaneous measurement of the structural intensity of all wave types (bending, quasilongitudinal, and torsional waves) in a one-dimensional beam. The technique uses a number of accelerometers appropriately oriented and located around the beam at two (far field) different axial locations to determine the vibration field and stress field at these cross sections due to all wave types. This information is then used to determine the vibratory power transmission components for each wave type. Experimental data is provided to validate the method for the measurement of total power transmission and the methods for the measurement of individual power flow components.

I. THEORETICAL BACKGROUND

Consider a uniform beam lying along the X direction of a Cartesian coordinate system, as shown in Fig. 1. When the beam is excited, the total vibratory power transmission in the beam is, in general, carried by four wave types. These are quasilongitudinal waves in the X direction, bending waves vibrating in the Y and Z directions, respectively, and a torsional wave with rotational vibration around the X axis.

It is of interest to be able to determine the displacement field of any beam cross section by using vibration measurements on the beam surface, thus allowing the structural intensity to be determined for each wave type simultaneously.

The beam surface displacement vectors can be measured by using an accelerometer configuration as shown in Fig. 1. Three displacement components at each location can be measured simultaneously by three accelerometers oriented along

[a]Electronic mail: pan@mech.uwa.edu.au

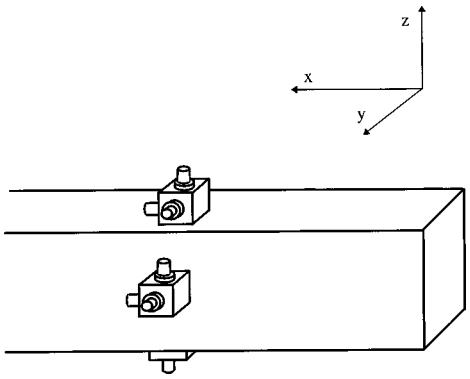

FIG. 1. Diagram of the accelerometer configuration being used in the measurement of acceleration vectors on a beam.

three orthogonal axes. However, to accurately interpret the internal displacement field of the beam, the following two factors must be taken into account.

(1) The measured displacements at each location on the beam surface are the displacements contributed by all the possible wave motion in the beam.

(2) The output of an accelerometer is not only related to the main axis displacement, but also to the transverse axis displacements. For a given acceleration in one direction, the measured value would be a_M if the main axis of the accelerometer is in the same direction as the acceleration. If the transverse axis of the accelerometer is in the same direction as the given acceleration, the measured value would be a_C. The transverse sensitivity α is thus defined as

$$\alpha = a_C / a_M . \tag{1}$$

The transverse sensitivity is frequency dependent and may be a complex value depending upon the relative phase between a_C and a_M. It is worth noting that the problem of cross sensitivity is most acute in conventional piezoelectric accelerometers.

A. Displacement components of a cross section

According to classical beam vibration theory (Bernoulli–Euler beam theory) the beam displacement field at any cross section can be described by six complex modal displacement components denoted by a displacement matrix $[S_0]=[u_0, v_0, w_0, \theta_x, \theta_y, \theta_z]^T$. Three components are used to describe the translations of the cross section along the three orthogonal axes and the others are used to describe the rotations of the section about the three axes. Once these modal displacement components are known, the displacement vector (u_0, v_0, w_0) at any location (y,z) on that cross section can be determined by:

$$\begin{pmatrix} u \\ v \\ w \end{pmatrix} = \begin{pmatrix} 1 & 0 & 0 & 0 & z & -y \\ 0 & 1 & 0 & -z & 0 & 0 \\ 0 & 0 & 1 & y & 0 & 0 \end{pmatrix} [S_0]. \tag{2}$$

Note that the (u, v, and w) components are complex; that is, they are characterized by an amplitude and phase, as are the components of $[S_0]$.

The measurement of (u, v, and w) at two or more locations on the beam surface of a particular cross section allows the vector $[S_0]$ to be determined. This can then be used with Eq. (2) to calculate the displacements (u, v, and w) at any point on the cross section, and not necessarily on the surface.

Two methods may be used to determine the vector $[S_0]$. The first method involves measuring the amplitude and phase of the displacement components u, v, and w at a number of locations around the beam cross section. The complex components of $[S_0]$ are then adjusted until the following function e is minimized.

$$e = \sum_{i=1}^{M} \{[u_i - u(y_i, z_i)]^2 + [v_i - v(y_i, z_i)]^2 + [w_i - w(y_i, z_i)]^2\}, \tag{3}$$

where M is the total number of measurement locations on the beam cross section; u_i, v_i, w_i are the measured values at location y_i, z_i, and $u(y_i, z_i)$, $v(y_i, z_i)$, $w(y_i, z_i)$ are the values at y_i, z_i calculated using Eq. (2). This method may be useful for investigating the vibration field distribution on a cross section of a structure. However, this method is not suitable for the design of a sensor to determine the total power transmission for use as a cost function in the active control of beam vibration, because it may need many measurement points to obtain accurate results.

The second method for determining $[S_0]$ involves the use of a minimum number of measurement locations and a minimum number of accelerometers. As will be discussed latter, three accelerometers are needed to identify three true acceleration components at each location. There are six unknown components of $[S_0]$ in Eq. (2), and in general six measurements are sufficient to uniquely determine $[S_0]$. The total acceleration measurement (three orthogonal axial components) at two locations on the same cross section will provide six equations. These six equations can be written as:

$$\begin{pmatrix} u_1 \\ v_1 \\ w_1 \\ u_2 \\ v_2 \\ w_2 \end{pmatrix} = \begin{pmatrix} 1 & 0 & 0 & 0 & z_1 & -y_1 \\ 0 & 1 & 0 & -z_1 & 0 & 0 \\ 0 & 0 & 1 & y_1 & 0 & 0 \\ 1 & 0 & 0 & 0 & z_2 & -y_2 \\ 0 & 1 & 0 & -z_2 & 0 & 0 \\ 0 & 0 & 1 & y_2 & 0 & 0 \end{pmatrix} \begin{pmatrix} u_0 \\ v_0 \\ w_0 \\ \theta_x \\ \theta_y \\ \theta_z \end{pmatrix}, \tag{4}$$

where u_1, v_1, w_1 are measured at the first location (y_1, z_1) and u_2, v_2, w_2 are measured at the location (y_2, z_2). However, the determinant value of the coefficient matrix is zero, which indicates that the configuration with six accelerometers and two locations is not able to determine completely all the elements in $[S_0]$. Another set of measurements (u_3, v_3, w_3) at another location (y_3, z_3) is necessary to completely determine $[S_0]$. The resultant equation can be written as:

TABLE I. Calculation of $\det(A^TA)$ for given accelerometer configurations.

Locations	$\det(A^TA)$
(1,2,3)	2.5635×10^{-9}
(1,2,4)	4.7607×10^{-9}
(1,3,4)	4.7607×10^{-9}
(2,3,4)	2.5635×10^{-9}

$$\begin{pmatrix} u_1 \\ v_1 \\ w_1 \\ u_2 \\ v_2 \\ w_2 \\ u_3 \\ v_3 \\ w_3 \end{pmatrix} = \begin{pmatrix} 1 & 0 & 0 & 0 & z_1 & -y_1 \\ 0 & 1 & 0 & -z_1 & 0 & 0 \\ 0 & 0 & 1 & y_1 & 0 & 0 \\ 1 & 0 & 0 & 0 & z_2 & -y_2 \\ 0 & 1 & 0 & -z_2 & 0 & 0 \\ 0 & 0 & 1 & y_2 & 0 & 0 \\ 1 & 0 & 0 & 0 & z_3 & -y_3 \\ 0 & 1 & 0 & -z_3 & 0 & 0 \\ 0 & 0 & 1 & y_3 & 0 & 0 \end{pmatrix} \begin{pmatrix} u_0 \\ v_0 \\ w_0 \\ \theta_x \\ \theta_y \\ \theta_z \end{pmatrix}$$

$$= [A][S_0], \tag{5}$$

where $[A]$ is a 9×6 location matrix. The unique solution for Eq. (5) exists only when the matrix $[A]^T[A]$ is not singular. If the locations of the accelerometers are selected so that $[A]^T[A]$ is not singular, $[S_0]$ can be calculated by

$$[S_0]=([A]^T[A])^{-1}[A]^T \times[u_1,v_1,w_1,u_2,v_2,w_2,u_3,v_3,w_3]^T. \tag{6}$$

In the following experiment the displacement components were measured at four locations $[(u_1,v_1,w_1)$ at location $(0,L_z/2)$, (u_2,v_2,w_2) at location $(L_y/2,0)$, (u_3,v_3,w_3) at location $(-L_y/2,0)$, and (u_4,v_4,w_4) at location $(0,-L_z/2)]$. Table I shows the numerical calculation of the determinant values of matrix $[A]^T[A]$ for any three out of the four locations. The results show that the matrix $[A]^T[A]$ is not singular for this accelerometer arrangement.

B. Transverse sensitivity of the accelerometers

The nonzero transverse sensitivity of each accelerometer indicates that the output of the accelerometer will be not only related to its main axis acceleration but also to the transverse axis accelerations. Usually, when three axial displacement components are present, the displacement component measured by an accelerometer is related to all three axial displacement components (u,v,w) at the accelerometer location. Assuming that (u_m,v_m,w_m) are the displacements measured by three accelerometers with their main axes directed along the *X*, *Y*, and *Z* axes of the beam, respectively (see Fig. 1), then they are related to the local displacement components (u,v,w) by:

$$\begin{pmatrix} u_m \\ v_m \\ w_m \end{pmatrix} = \begin{pmatrix} 1 & \alpha_{xy} & \alpha_{xz} \\ \alpha_{yx} & 1 & \alpha_{yz} \\ \alpha_{zx} & \alpha_{zy} & 1 \end{pmatrix} \begin{pmatrix} u \\ v \\ w \end{pmatrix}, \tag{7}$$

where α_{xy} is the *y* component of the transverse sensitivity of the accelerometer whose main axis is directed along the *X* axis. The transverse sensitivity components of each accelerometer can be determined experimentally; therefore, (u,v,w) can be determined at each location from the measured displacements (u_m,v_m,w_m).

C. Total power transmission

The time average complex power transmission $\overline{P}$ in the *X* direction evaluated on the $x=x_s$ plane is directly related to cross-section displacement modal components $[S_0]$ by

$$\overline{P}=[S_0]^H[\Lambda][S_0], \tag{8}$$

where $[\ ]^H=[\ ]^{*T}$ (the complex conjugate and transpose of a matrix) and $[\Lambda]$ is a (6×6) matrix given by

$$[\Lambda]=\frac{j\omega}{2}\begin{pmatrix} EA\dfrac{\partial}{\partial x} & & & & & \\ & -EI_{zz}\dfrac{\partial^3}{\partial x^3} & & & 0 & \\ & & -EI_{yy}\dfrac{\partial^3}{\partial x^3} & & & \\ & & & D\dfrac{\partial}{\partial x} & & \\ & 0 & & & EI_{yy}\dfrac{\partial}{\partial x} & \\ & & & & & EI_{zz}\dfrac{\partial}{\partial x} \end{pmatrix}, \tag{9}$$

where I_{yy} and I_{zz} are the moments of inertia of the cross section around the *Y* and *Z* axes, respectively, *D* is the torsional rigidity of the beam, *E* is Young's modulus, and *A* is the area of the cross section. The real part of $\overline{P}$ represents the

power transmission through the $x=x_s$ plane. The imaginary part of $\bar{P}$ represents the local stored energy. Equations (8) and (9) show that the total power transmission consists of six components. Four are related to the first-order derivative with respect to x of the cross section modal components. These terms can be determined by the measurement of $[S_0]$ at two closely spaced cross sections and by using the finite difference relations to approximate their derivatives.[7,8] The remaining two power transmission components are related to the third-order derivative of the cross-section components v_0, w_0. In general the values of v_0 and w_0 at four cross sections have to be measured[4] to approximate the third-order derivative. However, if the measurement is conducted in the far field of the vibration source, the power transmission measurement process can be simplified. In this case, the power transmission component of the bending waves vibrating in the Z direction can be expressed as:

$$\bar{P}_{Bz}=\frac{j\omega}{2}EI_{yy}\left(w_0^*\frac{\partial^3 w_0}{\partial x^3}-\frac{\partial w_0^*}{\partial x}\frac{\partial^2 w_0}{\partial x^2}\right). \tag{10}$$

If the near-field components of bending waves can be neglected, the following relationship will hold

$$\frac{\partial^2 w_0}{\partial x^2}=-k_w^2 w_0, \tag{11}$$

where k_w is the z-axial component of the bending wave number. Using the above expression, the real part of P_{Bz} can be written as

$$\begin{aligned}P_{Bz}&=-\mathrm{Re}\left\{\frac{j\omega}{2}EI_{yy}k_w^2\left(w_0^*\frac{\partial w_0}{\partial x}-\frac{\partial w_0^*}{\partial x}w_0\right)\right\}\\&=\omega^2\sqrt{m_bEI_{yy}}\,\mathrm{Im}\left\{w_0^*\frac{\partial w_0}{\partial x}\right\}\\&=-\omega^2\sqrt{m_bEI_{yy}}\,\mathrm{Im}\{w_0^*\theta_y\}\\&=\frac{2\sqrt{m_bEI_{yy}}}{\omega^2}\,\mathrm{Im}\{G(a_{y\theta},a_w,\omega)\},\end{aligned} \tag{12}$$

where m_b is the mass per unit length of the beam; $G(a_{\theta y},a_w,\omega)$ is the cross spectral density of the rotational acceleration $a_{\theta y}$ in the y-axial direction and the translational acceleration a_w in the z-axial direction. Similarly, for the bending vibration in Y direction, the real part of P_{By} can be expressed as

$$\begin{aligned}P_{By}&=\omega^2\sqrt{m_bEI_{zz}}\,\mathrm{Im}\{v_0^*\theta_z\}\\&=\frac{2\sqrt{m_bEI_{zz}}}{\omega^2}\,\mathrm{Im}\{G(a_v,a_{\theta z},\omega)\}.\end{aligned} \tag{13}$$

Therefore the two components of the far-field bending wave power transmission can be determined using four elements $(v_0,w_0,\theta_y,\theta_z)$ in $[S_0]$ at one beam cross section.

The quasilongitudinal and torsional wave powers can be expressed as

$$\bar{P}_{Lx}=-\frac{j\omega}{2}EA\frac{\partial u_0^*}{\partial x}u_0, \tag{14}$$

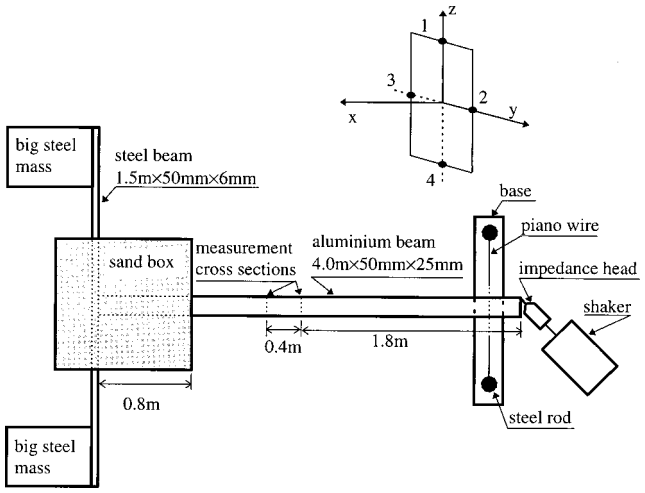

FIG. 2. Schematic diagram of experimental setup.

$$\bar{P}_{Tx}=-\frac{j\omega}{2}D\frac{\partial\theta_x^*}{\partial x}\theta_x. \tag{15}$$

The estimation of $\partial\theta_x/\partial x$ and $\partial u_0/\partial x$ can be made from two elements in $[S_0]$ in two closely spaced beam cross sections on the basis of the finite difference principle.

II. EXPERIMENTAL RESULTS

A. Experimental arrangement

As shown in Fig. 2, a 4-m-long aluminum beam of cross section dimensions $L_z=50$ mm and $L_y=25$ mm was used in the experiment. The beam was lying along the X direction of a Cartesian coordinate system. One end of the beam was bolted to the middle of a 1.5-m-long steel beam with the cross section of 50×6 mm and buried (0.8 m) in a box which was full of dry sand. Each end of the steel beam was bolted to one big steel mass. The use of the steel beam and the sand box was intended to provide an effectively absorptive termination for all wave types. The other end of the beam was supported by a piano wire and attached with a mechanical shaker. The force from the shaker was oriented in an arbitrary direction (elevation and the azimuth angle of 45°, respectively) and attached to the right corner of the beam end cross section. The location and orientation of the shaker allow the excitation of all wave types (bending, quasilongitudinal, and torsional waves) in the beam.

The shaker was driven with pseudorandom noise. The frequency of analysis was up to 1.6 kHz because the exciting force decayed rapidly after 1.1 kHz. To compare the power transmission with the input power, an impedance head was mounted at the driving location. The shaker and the impedance head were connected by a steel rod of 30 mm in length and 1 mm in diameter to avoid the transmission of possible transverse force which would cause errors in the input power measurement. The total input power can be calculated using the force and acceleration signals, F and a, output from the impedance head

$$P_{\text{input}}=\frac{1}{2}\mathrm{Re}\{F^*v\}=\frac{1}{\omega}\mathrm{Im}\{G(F,a,\omega)\}. \tag{16}$$

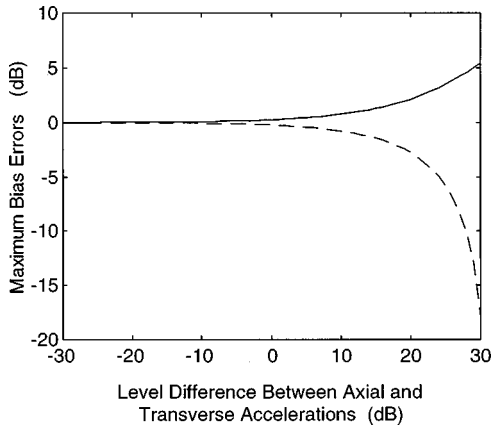

FIG. 3. Predicted bias error limits due to the presence of transverse sensitivity (2.75%) in the measurement of translational acceleration in the aluminum beam. ———: $\alpha = 2.75\%$; – – – – –: $\alpha = -2.75\%$.

To measure the acceleration vectors, three phase matched (the phase differences were less than 0.3° at frequencies below 2 kHz) B&K4375 accelerometers were mounted on one aluminum cube of 10-mm side dimensions to construct a triaxial accelerometer, as shown in Fig. 1. During the measurement, the triaxial accelerometer was used to pick up the acceleration signals in three axial directions at the measurement positions $[(y,z)=(0,L_z/2),(L_y/2,0),(-L_y/2,0),(0,-L_z/2)]$ which were located at the beam cross sections $x=1.8$ m and $x=2.2$ m, respectively. The measured signals were free from the effects of decaying waves above 7 Hz. Every acceleration component (both real and imaginary parts) was recorded using the transfer function mode of an FFT analyzer with the force signal from the impedance head as the reference.

B. Determination of the transverse sensitivity of an accelerometer

The transverse sensitivities of the accelerometers being used in the measurements were measured using a B&K4294 Calibration Exciter and an aluminum cube. The measured values ranged from 0.92% to 2.75% at 159 Hz. The bias error associated with the transverse sensitivity depends on the ratio of the main axial signal to its transverse axial signal. For example, if the actual acceleration levels, L_{a1} and L_{a2}, at two orthogonal directions are 80 and 60 dB, respectively, the maximum variation of the measured acceleration levels will be from -2.79 to 2.11 dB for a_1 and ± 0.024 dB for a_2. Figure 3 shows the predicted bias error limits due to the presence of transverse sensitivity (2.75%) in the measurement of translational acceleration in the beam. It is shown that the bias error can be neglected if the acceleration level in the main axis of the accelerometer is larger than that in the transverse axis, or less than 0.8 dB if the acceleration level in the main axis of the accelerometer is less that 10 dB lower than that in the transverse axis. The measured data could be totally corrupted if the ratio of the main axial signal to its transverse axial signal is close to the transverse sensitivity in magnitude but different in sign. For example, if the ratio u/v is close to $-\alpha_x$, the measured value u_m will be approximately equal to $\alpha_x w$ [seeing Eq. (7)] which is the contribution from the vibration in the Z direction rather than the X direction.

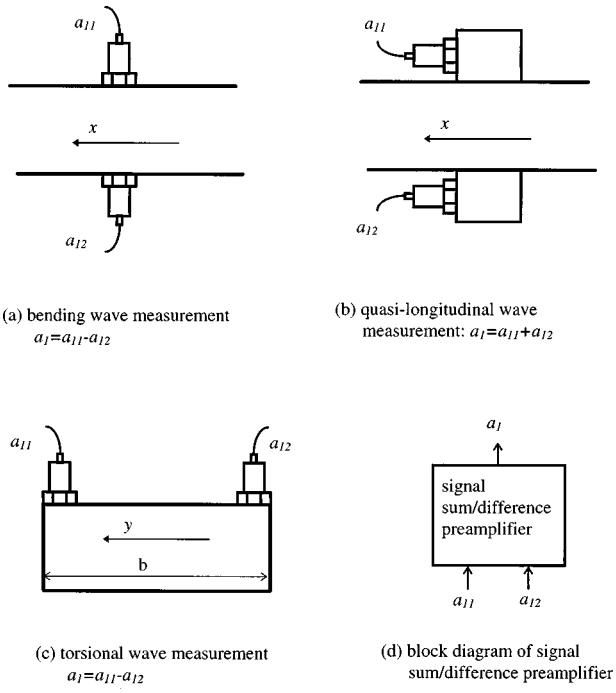

FIG. 4. Accelerometer configurations in the measurement of: (a) bending wave acceleration; (b) quasilongitudinal wave acceleration; (c) torsional wave acceleration, and (d) signal sum/difference preamplifier.

C. Measurement of structural intensity

To verify the method proposed in this paper, the power transmissions obtained were compared with those measured using the structural intensity technique.[8] As bending, quasi-longitudinal and torsional waves were simultaneously present in the beam, two phase-matched accelerometers were used with a signal sum/difference preamplifier to reduce the cross effects between different structural waves.[9] Figure 4 shows the accelerometer configurations for measuring acceleration signals of different wave types in a beam. The accelerometer configuration shown in Fig. 4(a) is designed to eliminate the effects of quasilongitudinal waves for the measurement of bending wave acceleration. Care should be taken to ensure that two accelerometers were located on the center positions of opposite sides of the same beam cross section. The difference between the signals output from the accelerometers should not contain any contribution from torsional waves, and it gives twice the bending wave acceleration component in the direction parallel to the main axis of the accelerometers. For the measurement of quasilongitudinal wave acceleration, the accelerometer configuration described by Verheij in Ref. 9 was used. The accelerometers were mounted on the aluminum cubes and then placed parallel to the beam surface along the beam (X) direction, as shown in Fig. 4(b). There should be no torsional wave contribution in the measured data because the accelerometers were located at the center points of opposite sides of the same beam cross section. The contribution of bending waves measured by the accelerometers should be the same in magnitude but opposite

in sign and thus should cancel when added together. For the measurement of rotational acceleration, two accelerometers were located on the edges of the same side of the beam cross section, as shown in Fig. 4(c). (This is a modified accelerometer configuration described by Verheij in Ref. 9.) The difference between the two acceleration signals should not contain any contribution from bending or quasilongitudinal waves. It gives the rotational acceleration when it is divided by the accelerometer separation (beam width). However, the accelerometer configurations shown in Fig. 4 cannot eliminate the effects of the accelerometer transverse sensitivities on the intensity measurements. Two orthogonal transverse axes of each accelerometer were chosen. The corresponding transverse sensitivity to each transverse axis is determined prior to the measurements. During the intensity measurements, attention has been paid to ensure that these two chosen transverse axes were parallel to the coordinate axes of the beam. The measured data were then theoretically corrected during data processing using Eq. (7).

To avoid the phase-mismatch error, structural intensity can be estimated from the measured frequency response function with reference to the force signal.[10] In the far-field, structural wave power transmission can be expressed as[10]

$$P=\frac{\alpha m_b}{\omega^3\Delta}\,\mathrm{Im}\{H^*(F,a_1,\omega)H(F,a_2,\omega)\}G(F,\omega), \quad (17)$$

where $H(F,a_1,\omega)$ represents the transfer function between acceleration a_1 and force F; $G(F,\omega)$ is the autospectral density of the input force; Δ is the separation between two beam cross sections where the accelerometers were located; a_1 and a_2 are the acceleration signals output from the signal sum/difference preamplifier, respectively; $\alpha=c_b^2/2$ for bending waves; $\alpha=c_L^2/4$ for quasilongitudinal waves; $\alpha=0.3bc_T^2$ for torsional waves; c_b, c_L, and c_T are the bending, quasilongitudinal, and torsional wave speeds, respectively; and b is the accelerometer separation, as shown in Fig. 4(c).

The quantity Δ should be kept within 5% to 15% of the wavelength of interest. The error due to the finite difference can be accurately predicted and corrected using the following expression during data processing,[19,20]

$$P_{\text{corrected}}=\frac{k\Delta}{\sin(k\Delta)}\,P_{\text{measured}}, \quad (18)$$

where P_{measured} and $P_{\text{corrected}}$ represent the measured power transmission and the power transmission free from the finite-difference error; k is the wave number of interest.

D. Results and discussion

Figure 5 shows the bias errors due to the presence of transverse sensitivity in the measurement of three axial components of the vibrational acceleration in the aluminum beam. The transverse sensitivities of the accelerometers being used in the orthogonal transverse axes were measured and marked, respectively. The marked points were in the axial directions during the measurement. It can be seen that the bias error can be negligible for the measurement of bending wave acceleration components. This is because each of the bending wave acceleration components is comparable or larger than the acceleration components in the accelerometer transverse axial directions. However, for the measurement of quasilongitudinal wave acceleration, the bias error is not negligible at most frequencies. This is because the quasilongitudinal wave acceleration is much smaller than the bending wave acceleration components in the accelerometer transverse axial directions at most frequencies, especially at frequencies below its first resonance frequency ($f_1=644$ Hz). The conclusion could be drawn from this figure that the transverse sensitivity must be taken into account when the acceleration component along the main axis of the accelerometer is much smaller than the components along its transverse axes.

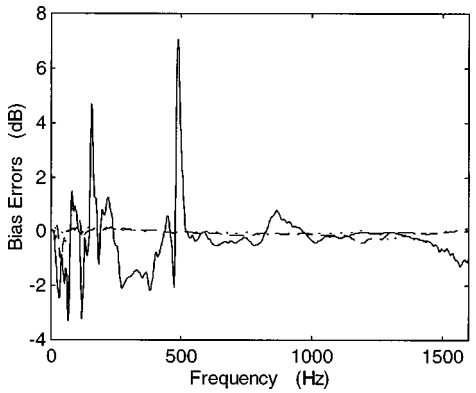

FIG. 5. Measured bias errors due to the presence of transverse sensitivity in the measurement of the quasilongitudinal wave acceleration in X direction (———) and the bending wave acceleration components in Y direction (– – – –) and Z direction (----------).

Figure 6 shows the structural wave power transmissions calculated using Eqs. (7) and (12)–(15) from two sets of data measured at positions $(y,z)=(0,L_z/2),(L_y/2,0),(-L_y/2,0)$ and at positions $(y,z)=(0,L_z/2),(L_y/2,0),(0,-L_z/2)$, respectively. It can be seen that the results calculated using the two different groups of data are different, but the difference between them is very small at most frequencies. At most frequencies below 150 Hz, the measured bending wave power transmissions become negative (which are not shown in Fig. 6 and also the reason for the discontinuity of the curves) or very large, and the agreement between two sets of measured results is very poor. This could be due to the errors in the measurement of the rotational acceleration components $a_{\theta x}$ and $a_{\theta y}$ because they are small in comparison with the background noise. For the measurement of quasilongitudinal and torsional wave power transmissions, the negative values and poor agreement at low frequencies could result from very small power transmissions. For a simply supported beam, the predicted first resonance frequency is about 644 Hz for quasilongitudinal waves and 400 Hz for torsional waves. It is usually difficult to generate quasilongitudinal or torsional waves at frequencies below the first resonance frequency. Therefore the measurement error is large.

Figure 7 shows the comparison between the bending (vibrating in Y direction) wave power transmissions measured at different beam cross sections ($x=1.8$ and 2.2 m). Two results agree well and they can be considered to be identical. This means that this proposed method can be used to mea-

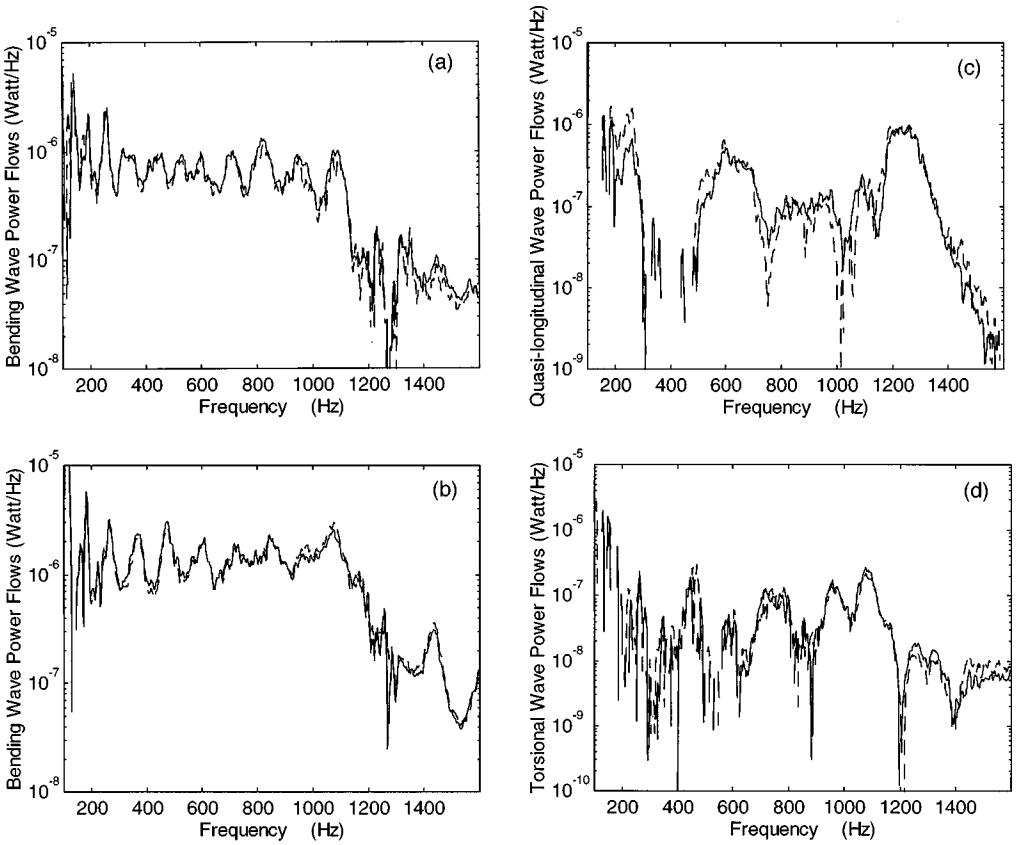

FIG. 6. Power transmissions calculated using the data measured at positions [———: $(y,z)=(0,L_z/2),(L_y/2,0),(-L_y/2,0)$] and at positions [– – – –: $(y,z)=(0,L_z/2),(L_y/2,0),(0,-L_z/2)$]. (a) Bending vibration in Y direction; (b) bending vibration in Z direction; (c) quasilongitudinal vibration; (d) torsional vibration.

sure structural wave power transmissions at any beam cross section of the far field.

Figure 8 shows the comparisons of structural wave power transmission components measured using the proposed method and the structural intensity technique [calculated using Eq. (17)]. The error due to the finite difference approximation has been theoretically corrected using Eq. (18) during data processing. At frequencies below the first resonance frequency, the results measured by the two techniques are different. This is because the power transmission is very small compared with background noises and it cannot be measured using any of these two techniques in this frequency range. However, when the power transmission increases and can be accurately measured using the structural intensity technique, the proposed method can also accurately measure it. The proposed method and the structural intensity technique give ''identical'' results.

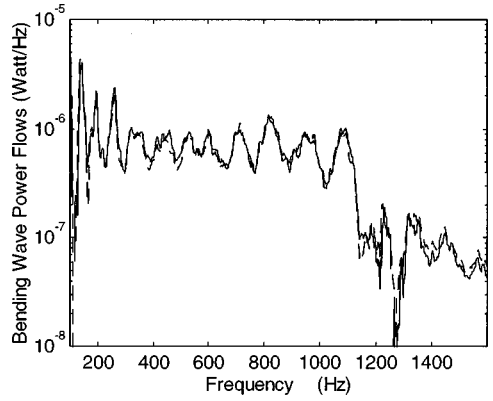

FIG. 7. Bending (vibration in Y direction) wave power transmissions measured at beam cross sections $x=1.8$ m (———) and $x=2.2$ m (– – – –).

Figure 9 compares the total vibratory power transmission measured using the proposed method with the results directly measured using the impedance head [calculated using Eq. (16)]. It can be seen that the agreement between two measured results is quite good except at frequencies below 180 Hz. The reasons for the poor agreement at the low frequencies could be that the y- and z-axial components of the rotational acceleration are small in comparison with the background noise and cannot be accurately measured, and that the measured values of the quasilongitudinal and torsional wave power transmissions did not represent the actual values. They were corrupted by background noise. The summation of actual bending wave power transmission and noise (which were assumed to be quasilongitudinal and torsional wave power transmissions) produced a wrong answer. At frequencies above 1.1 kHz, both measured results decay with frequency. This is because the exciting force decayed rapidly with frequency. At frequencies above 1.27 kHz the direct measurement gives slightly (less than 2 dB) higher values than the proposed method, but the curve shapes are similar. The reason could be that the total power transmission became small and comparable with the energy losses in part of

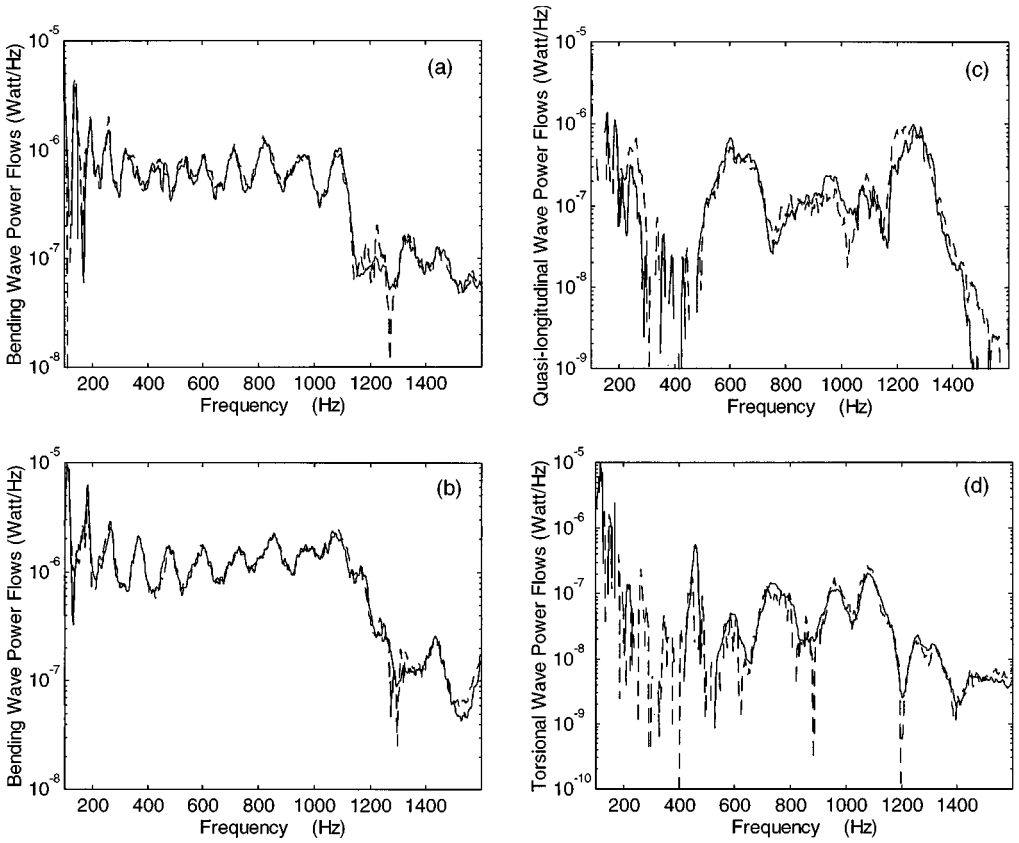

FIG. 8. Bending [vibration in Y (a) and Z (b) directions], quasilongitudinal (c) and torsional (d) wave power transmissions measured using the structural intensity technique (———) and the new method (– – – –).

the beam (between the excitation position and the measurement position) and the support.

III. CONCLUSIONS

A new method is proposed in this paper for the measurement of structural wave power transmission. The outlined theory is experimentally verified on a uniform aluminum beam. The measured results showed that this new method can be used to accurately measure the total vibratory power transmission and its components. However, this method may not be applicable at frequencies below the first resonance frequency of the structure under study or at low frequencies where the rotational acceleration is small in comparison with background noise for the measurement of bending wave power transmission.

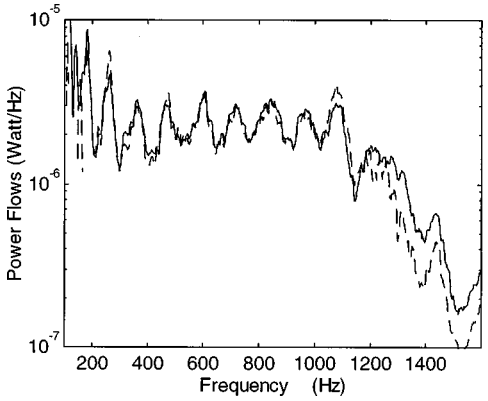

FIG. 9. Total vibratory power transmissions measured using the impedance head (———) and the new method (– – – – –).

This new method can provide detailed information of both vibration and stress fields. It is suitable to apply in active vibration control where the measured total vibratory power transmission is used as a cost function. For the case of bending waves only, the total vibratory power transmission can be determined from the data measured at one cross section of the structure under study. This means that this method can be easily implemented.

Both theoretical predictions and experimental results showed that the accelerometer transverse sensitivity becomes important and must be taken into account when the signal in the main axis of the accelerometer is much (more than 10 dB) lower than the signals in its transverse axes. When the ratio of the main axial signal to its transverse axial signal is close to the transverse sensitivity, the measured data could be corrupted and the power transmission cannot be measured.

[1] W. Redman-White, P. A. Nelson, and A. R. D. Curtis, ''Experiments on the active control of flexural wave power transmission,'' J. Sound Vib. **121**, 187–191 (1987).
[2] L. O. Gonidou, ''Active control of flexural power transmission in elastic thin beams,'' Master of Science thesis, Virginia Polytechnic Institute and State University, 1988.
[3] J. Pan and C. H. Hansen, ''Active control of total power transmission along a beam,'' Proceedings of International Congress on Recent Developments in Air and Structure Borne Sound and Vibration, Mechanical Engineering Department, Auburn University, AL, 1990, pp. 229–236.

[4] C. R. Fuller, G. P. Gibbs, and R. J. Silcox, ''Simultaneous active control of flexural and extensional power transmission in beams,'' Proceedings of International Congress on Recent Developments in Air and Structure Borne Sound and Vibration, Mechanical Engineering Department, Auburn University, AL, 1990, pp. 657–662.
[5] C. H. Hansen and J. Pan, ''Active control of beam vibration,'' Proceedings of the Australian Vibration and Noise Conference, Melbourne, The Institution of Engineers, Australia, 1990.
[6] R. L. Clark, Jr., J. Pan, and C. H. Hansen, ''An experimental study on the active control of multiple-wave types in an elastic beam,'' J. Acoust. Soc. Am. **92**, 871–881 (1992).
[7] D. U. Noiseux, ''Measurement of power transmission in uniform beams and plates,'' J. Acoust. Soc. Am. **47**, 238–247 (1970).
[8] G. Pavic, ''Measurement of structure-borne wave intensity, part I: formulation of the methods,'' J. Sound Vib. **49**, 221–230 (1976).
[9] J. W. Verheij, ''Cross spectral density methods for measuring structure borne power transmission on beams and plates,'' J. Sound Vib. **70**, 133–149 (1980).
[10] J. Linjama and T. Lahti, ''Estimation of bending wave intensity in beams using the frequency response techniques,'' J. Sound Vib. **153**, 21–36 (1992).
[11] E. Williams, ''Structural intensity in thin cylindrical shells,'' J. Acoust. Soc. Am. **89**, 1615–1622 (1991).
[12] X. Pan and C. H. Hansen, ''Active control of vibratory power transmission along a semi-infinite plate,'' J. Sound Vib. **184**, 585–610 (1995).
[13] X. Pan and C. H. Hansen, ''An experimental study of active control of vibratory power transmission in a cylindrical shell,'' J. Acoust. Soc. Am. **99**, 2519(A) (1996).
[14] A. R. Briscoe and R. J. Pinnington, ''Axisymmetric vibrational power measurement in empty and fluid filled pipes,'' J. Sound Vib. **192**, 771–791 (1996).
[15] J. L. Horner and R. G. White, ''Techniques for measuring vibrational power transmission in beam-like structures carrying two types of waves,'' CETIM, Senlis, France, Centre Technique des Industries Mécaniques, 1990, pp. 273–279.
[16] J. L. Horner and R. G. White, ''The measurement of vibrational power in pipe systems at low frequencies,'' NOISE-93, St. Petersberg, Russia, Interpublish Ltd., 1993, pp. 43–48.
[17] N. H. Farag and J. Pan, ''Dynamic response and power flow in 3-dimensional coupled beam structures, part 2: Factors affecting power flow measurements,'' J. Acoust. Soc. Am. (submitted).
[18] N. H. Farag and J. Pan, ''Dynamic response and power flow in 3-dimensional coupled beam structures, part 3: Experimental assessment,'' J. Acoust. Soc. Am. (to be published).
[19] W. Redman-White, ''The measurement of structural wave intensity,'' Ph.D. thesis, The University of Southampton, 1982.
[20] J. W. Verheij and C. J. M. van Ruite, ''On the measurement of structure-borne sound energy flow along pipes, part 3: analysis of systematic and random errors,'' Report 308.785/1, Institute of Applied Physics, TNO-TH, Delft, Holland, 1983.

Condenser microphone model. I. Application of the T-matrix method of Waterman to acoustic scattering from an elastic obstacle

Wolfgang Kainz
Institut für Kernphysik der Technischen Universität Wien, Wiedner Haupstr. 8-10, A-1040 Vienna, Austria

(Received 7 November 1997; accepted for publication 8 May 1998)

Acoustic scattering of a plane wave from a condenser microphone is investigated and the eigenfrequencies of this coupled acoustic system are calculated. The wave is incident parallel to the axis of a rigid cylinder, closed at the bottom by an elastic membrane. To take into account the normal modes inside the cylinder a Green's function method is applied. Outside the scattering and interaction of the incident plane wave with the microphone is treated analytically using the transfer-matrix method of Waterman. Good agreement of the eigenfrequencies with measurement is achieved, but only for obstacles which are not too small, i.e., the wavelength is comparable to the dimensions of the microphone (radius a of the microphone membrane is greater than 0.015 m). [S0001-4966(98)05908-6]

PACS numbers: 43.40.Dx, 43.38.Bs [PJR]

LIST OF SYMBOLS

a	radius of membrane
A_n	expansion coefficients, Eq. (10)
a_n	expansion coefficient, Eq. (18)
A_{ni}	expansion coefficients, Eq. (20)
A	matrix with elements A_{ni}
A^T	transpose of A
B_{ni}	expansion coefficients, Eq. (20)
B_n	expansion coefficients, Eq. (30)
c_a	speed of sound in air
C	vector with element C_n, Eq. (30)
C_n	elements of vector C
c	wave velocity in membrane
d	differential symbol
dS'	surface element
f	frequency
$f(r)$	source term of a sound wave
$f_{n,R}$	expansion coefficient, Eq. (18)
$G(r,\varphi\|r',\varphi')$	Green's function of membrane
$g(r\|r')$	$=g(r,0,0\|r',0,0)$ Green's function of inner part of cylinder (Appendix A)
$p(r)$	pressure of sound wave
$p_-(r)$	incoming plane wave
p_m	pressure in Eq. (15)
p_u	pressure inside the cylinder
$P_n(\cos\theta)$	Legendre polynom
r,r'	radial coordinate
$\mathbf{r}_s$	coordinate of cylinder surface
S	symbol for surface
T	tension of membrane
t	time
T^T	transpose of transfer matrix
T_{pn}	elements of transfer matrix
u	particle velocity
U_{mn}	def. in Eq. (23)
U	matrix with elements U_{mn}
V_{mn}	def. in Eq. (24)
V	matrix with elements V_{mn}
W_{mn}	def. in Eq. (24)
$g(r,\varphi,z\|r'\varphi',z')$	Green's function of cylinder (Appendix A)
$g(\mathbf{r}\|\mathbf{r}')$	$=g(r,\varphi,z\|r'\varphi',z')$
$h_n^{(1)}(kr)$	Hankel function of 1st order
i	integer
$\|i\rangle$	state vector, $\langle i\|\mathbf{r}\rangle=\varphi_i(\mathbf{r})$
$J_m(z)$	Bessel function of order m
$j_n(z)$	spherical Bessel function of order n
k	$=\omega/c$ wave number of membrane
k_{mn}	zero of Bessel function, Eq. (2a)
k_n	zero of Bessel function $J_0(k_n a)=0$
k_a	$=\omega/c_a$ wave number in air
l_n	$=z_{n0}=k_n a$
L	height of cylinder
m	integer
n	integer
P_{inc}	incoming plane wave
P	net pressure on membrane
P_i	amplitude of P_{inc}
W	matrix with elements W_{mn}
x	$=\cos\theta$, integration variable
z_{mn}	$J_m(z_{mn})=0$
$\alpha_n(\mathbf{r}_s)$	def. in Eq. (18)
$\beta_n(\mathbf{r}_s)$	def. in Eq. (18)
β	$=P_i a/T$
Δ	Laplacian
δ_{ij}	Kronecker delta
δ	$=\rho\omega^2 a^3/T$
ϵ_m	$=1$, if $m=0$, $=2$, if $m>0$
η	displacement of membrane
λ_i	$=1/(k_i^2-k^2)$
μ	$=ka$
$\Psi_n(\mathbf{kr}_s)$	solution of wave equation

φ, φ'	angular coordinate
$\varphi_{mni}(r,\varphi)$	eigenfunction of membrane, Eq. (2a)
ρ	density of air
σ	mass density of membrane

INTRODUCTION

This is the first of a series of papers on condenser microphone models. The problem of the vibration of an elastic membrane with air loading[1–3] and coupled to a cavity[4] was treated some years ago. Some condenser microphone models have been treated by the author,[5,6] but the exact treatment of acoustic scattering was not taken into account. In Refs. 5 and 6 the inner part of the microphone (electrode with a pattern of small apertures) was treated and the eigenfrequencies calculated. In this paper the inner part of the microphone is simply an air-filled cylinder, closed at one side by an elastic membrane. A more complicated inner part (electrode with an aperture) will be considered in a forthcoming publication. The essential topic is the scattering of a plane wave incident parallel to the axis of a rigid cylinder with an elastic membrane at on end (Fig. 1). In a classical paper Waterman[7] introduced the transfer-matrix approach for acoustic scattering. This method overcomes the difficulty of ill-conditioned matrices which appear, when the problem is solved by a series expansion of the incoming and scattered wave and the displacement function of the membrane. Thus the problem is reduced to handle infinite matrices. Using the method of Waterman these ill-conditioned matrices will be conditioned and then truncated. On the other hand, the matrices of the inner part of the microphone are not ill-conditioned and can therefore be truncated without further manipulations.

The paper is organized as follows: After an Introduction, Sec. I deals with the vibrations of a membrane coupled to a rigid, air-filled cylinder. The Green's function of the membrane of the inner part of the cylinder are repeated from an earlier publication. Section II introduces the transfer-matrix method of Waterman applied to acoustic scattering from an elastic obstacle, which in this case is the air-filled cylinder with the elastic membrane. Section III is dedicated to the calculation of the matrix elements of the problem, and Sec. IV to the analytic solution of the problem, which consists of calculating the mean displacement of the membrane as a function of the frequency of the incident plane wave. In Sec. V the results are presented and compared to the experimental measurements and to other calculations with a membrane with air loading in a rigid panel. A conclusion is given in Sec. VI.

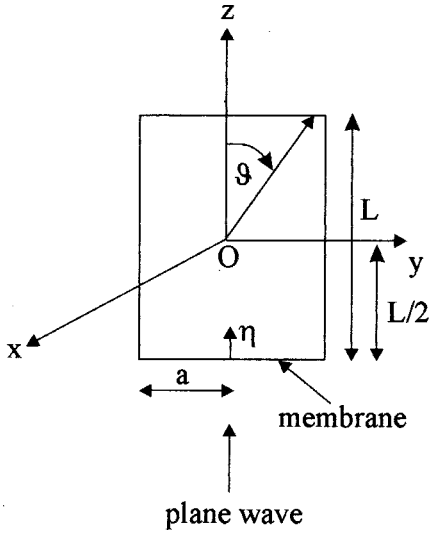

FIG. 1. Condenser microphone (kettledrum) with plane wave.

I. VIBRATION OF A MEMBRANE COUPLED TO A RIGID AIR-FILLED CYLINDER

The wave equation of an elastic membrane is[8]

$$(\Delta + k^2)\,\eta = -\frac{1}{T}P, \quad k = \frac{\omega}{c}, \quad \omega = 2\pi f, \tag{1a}$$

$$c = \sqrt{\frac{T}{\sigma}}. \tag{1b}$$

Because of perpendicular incidence of the wave the problem has azimuthal symmetry. A factor $e^{-i\omega t}$ is omitted. If P was known, the solution of Eq. (1) would be

$$\eta(r,\varphi) = \frac{1}{T}\int G(r,\varphi|r',\varphi')P(r',\varphi')r'\,dr'\,d\varphi'. \tag{2a}$$

G is the Green's function of the membrane[9] and is given by

$$G(r,\varphi|r',\varphi') = \sum_{n=1,m=0,i=1}^{n=\infty,m=\infty,i=2} \frac{1}{k_{mn}^2 - k^2}\,\varphi_{mni}(r,\varphi)\varphi_{mni}(r',\varphi'),$$

$$J_m(k_{mn}a) = 0 \tag{2b}$$

which defines the zeros of the Bessel function of order m:

$$\varphi_{mni}(r,\varphi) = \frac{1}{a}\sqrt{\frac{\epsilon_m}{\pi}}\,\text{trig}\; m\varphi \cdot \frac{J_m(k_{mn}r)}{J_{m-1}(z_{mn})},$$

$$J_m(z_{mn}) = 0,$$

$$\epsilon_m = \begin{cases} 1,\ldots,m=0 \\ 2,\ldots,m>0, \end{cases} \quad \text{trig}\;\alpha = \begin{cases} \cos\alpha,\ldots,i=1 \\ \sin\alpha,\ldots,i=2. \end{cases} \tag{3}$$

Equation (3) defines the eigenfunctions of the membrane of radius a. For azimuthal symmetry we have

$$G(r,r') = \sum_{n=1}^{\infty} \frac{\varphi_n(r)\varphi_n(r')}{k_n^2 - k^2} \tag{4}$$

$$J_0(k_n a) = 0, \quad \varphi_n(r) = \frac{J_0(k_n r)}{a\sqrt{\pi}J_{-1}(l_n)}, \quad l_n = z_{0n}. \tag{5}$$

Equation (5) defines an orthonormal system of eigenfunctions. In reality P is not known, but η-dependent:

$$P(r) = 2P_i + \rho\omega^2\int g(r|r')\,\eta(r')\,r'\,dr'\,d\varphi'. \tag{6}$$

Equation (6) can be deduced from the Helmholtz integral equation[10]

$$p(\mathbf{r})=\int\int\int f(\mathbf{r})g(\mathbf{r}|\mathbf{r}')dv+\int\int\left[g(\mathbf{r}|\mathbf{r}')\frac{\partial}{\partial n'}\right.$$
$$\left.\times\, p(\mathbf{r}')-p(\mathbf{r}')\frac{\partial}{\partial n'}g(\mathbf{r}|\mathbf{r}')\right]dS'. \tag{7}$$

Here g is the Green's function for the inner part of the cylinder (see Appendix A) with $\partial g/\partial n|_S=0$ and the source term $f=0$. Also the acoustic equation

$$\frac{\partial p}{\partial n}=-\rho\frac{\partial u}{\partial t},\quad u=\frac{\partial \eta}{\partial t} \tag{8}$$

is used. Equations (6) and (2) give the following integral equation for the displacement of the membrane η:

$$\eta(r)=\frac{1}{T}\int G(r|r')r'dr'd\varphi'$$
$$\times\left[2P_i+\rho\omega^2\int g(r'|r'')\eta(r'')r''dr''d\varphi''\right]. \tag{9}$$

The incident plane wave is $p_-(z)=P_ie^{ik_az}$, $k_a=\omega/c_a$. The air loading in the outer space is not taken into account. This will be done later. Equation (9) is solved by expansion of $\eta(r)$ in terms of the eigenfunctions of the membrane vibration *in vacuo*:

$$\eta(r)=\sum_{n=1}^{\infty}A_n\varphi_n(r). \tag{10}$$

Equation (9) can be written in terms of Dirac-kets[5,6] and operators G,g in a Hilbert space with the same notation of operators as the corresponding Green's function:

$$|\eta\rangle=\frac{2}{T}G|P_i\rangle+\frac{\rho\omega^2}{T}Gg|\eta\rangle, \tag{11}$$

$$|\eta\rangle=A_n|n\rangle,\ \langle r|n\rangle=\varphi_n(r),\ \langle r|P_i\rangle=P_i. \tag{12}$$

A summation over repeated subscripts is understood. More about this notation will be explained in Refs. 5 and 6. Inserting Eq. (12) in Eq. (11) gives

$$A_i|i\rangle=\frac{2}{T}G|P_i\rangle+\frac{\rho\omega^2}{T}GgA_i|i\rangle. \tag{13}$$

After multiplication by $\langle j|$ we get with

$$\langle i|j\rangle=\delta_{ij},$$

$$A_i\delta_{ij}=\frac{2}{T}\langle j|G|P_i\rangle+\frac{\rho\omega^2}{T}\langle j|Gg|i\rangle A_i,$$

$$G|i\rangle=\lambda_i|i\rangle,\ \lambda_i=\frac{1}{k_i^2-k^2},$$

$$A_i\delta_{ij}=\frac{2}{T}.\lambda_j\langle j|P_i\rangle+\frac{\rho\omega^2}{T}.\lambda_j\langle j|g|i\rangle A_i.$$

Exchange of $i\leftrightarrow j$:

$$A_j\delta_{ij}=\frac{1}{k_i^2-k^2}\left(\frac{2}{T}\langle i|P_i\rangle+\frac{\rho\omega^2}{T}\langle i|g|j\rangle A_j\right),$$

With

$$ka=\mu,\ \frac{\rho\omega^2a^3}{T}=\delta,$$

and

$$k_ma=l_m,$$

$$i\to m,j\to n\to$$

$$\left[\delta_{mn}(l_m^2-\mu^2)-\delta\frac{1}{a}\langle m|g|n\rangle\right]A_n=\frac{2a^2}{T}\langle m|P_i\rangle. \tag{14}$$

The matrix $\langle m|g|n\rangle$ will be given in Appendix B. Equation (14) is an algebraic equation for the expansion coefficients A_n.

II. RAYLEIGH METHODS AND T-MATRIX APPROACH OF WATERMAN FOR ACOUSTIC SCATTERING

Equation (14) can be written shortly as

$$Z_{mn}A_n=\frac{a^2}{T}p_m,\quad p_m=\int p_-\varphi_n(r)rdrd\varphi,$$
$$P=p_--p_u, \tag{15}$$

with P the total pressure on the membrane, p_- the pressure outside, and p_u inside the microphone. From the acoustical equation

$$\frac{\partial p}{\partial n}=-\rho\omega^2\eta\ \text{ and }\ \eta=A_m\varphi_m, \tag{16}$$

we have from Eq. (15)

$$\frac{\partial p_-}{\partial n}=-\frac{\rho\omega^2a^2}{T}\varphi_mZ_{mn}^{-1}p_n. \tag{17}$$

Following the paper of Kazandjian,[11] who shows that the Rayleigh methods are equivalent to the T-matrix approach of Waterman, we write for the wave outside the microphone (the first part at the right hand side of p_- is the incoming plane wave, the second the scattered wave):

$$p_-(\mathbf{r}_s)=a_n\ \mathrm{Re}\ \Psi_n(k\mathbf{r}_s)+f_{n,R}\Psi_n(k\mathbf{r}_s),$$

$$\frac{\partial p_-}{\partial n}(\mathbf{r}_s)=a_n\alpha_n(\mathbf{r}_s)+f_{n,R}\beta_n(\mathbf{r}_s),$$

$$\alpha_n(\mathbf{r}_s)=\left(\frac{\partial}{\partial n}\mathrm{Re}\ \Psi_n(k\mathbf{r})\right)_{r=r_s},$$

$$\beta_n(\mathbf{r}_s)=\left(\frac{\partial}{\partial n}\Psi_n(k\mathbf{r})\right)_{r=r_s}. \tag{18}$$

From Eq. (17) we get

$$a_n\alpha_n+f_{n,R}\beta_n=-\frac{\rho\omega^2a^2}{T}\times\int(a_n\ \mathrm{Re}\ \Psi_n'+f_{n,R}\Psi_n')\varphi_n'Z_{mn}^{-1}\varphi_m. \quad (19)$$

The prime denotes an integration variable as argument with prime. Projecting this equation onto an orthogonal system of functions defined on the surface of the microphone Φ_i we get

$$\begin{aligned}
&a_nA_{ni}=f_{n,R}B_{ni},\\
&A_{ni}=\int\alpha_n\Phi_i+\frac{\delta}{a}\int\int\Phi_i\varphi_mZ_{ml}^{-1}\varphi_l'\ \mathrm{Re}\ \Psi_n',\\
&B_{ni}=-\int\beta_n\Phi_i-\frac{\delta}{a}\int\int\Phi_i\varphi_mZ_{ml}^{-1}\varphi_l'\Psi_n',\\
&\varphi_m=\frac{1}{a\sqrt{\pi}}\frac{J_0\left(l_m\frac{r}{a}\right)}{J_{-1}(l_m)},\\
&\Phi_i=\alpha_i=\left(\frac{\partial}{\partial n}\ \mathrm{Re}\ \Psi_i\right)_{r=r_s},\quad \beta_i=\left(\frac{\partial}{\partial n}\ \Psi_i\right)_{r=r_s}, \qquad (20)\\
&\Psi_n=\sqrt{\frac{2n+1}{4\pi}}\,h_n^{(1)}(kr)P_n(\cos\vartheta),\\
&\int\ldots dS=\int\sqrt{r^2+r_\vartheta^2}r\sin\vartheta d\vartheta d\varphi;
\end{aligned}$$

$$\frac{\partial}{\partial n}=\frac{r}{\sqrt{r^2+r_\vartheta^2}}\left(\partial_r-\frac{r_\vartheta}{r^2}\,\partial_\vartheta\right),$$

$$r_\vartheta=\frac{\partial r(\vartheta)}{\partial\vartheta}.$$

Summation over twice subscripts is always understood. The usual symbols for Bessel-(J), Hankel-(h), and Legendre functions (P) are used. $r(\vartheta)$ describes the rotational symmetric surface of the microphone. From the above equations the unknown expansion coefficients $f_{n,R}$ of the scattered wave can be calculated from the known coefficients a_n of the incoming plane wave

$$P_{\mathrm{inc}}(\mathbf{r})=a_n\ \mathrm{Re}\ \Psi_n(k\mathbf{r}). \quad (21)$$

III. CALCULATION OF THE MATRIX ELEMENTS

The function $r(\vartheta)$ for the surface (the origin in in the center of the cylinder) is given by

$$\begin{aligned}
&0<\vartheta<\vartheta_1:\quad r=\frac{L}{2\cos\vartheta},\\
&\vartheta_1<\vartheta<\vartheta_2:\quad r=\frac{a}{\sin\vartheta}, \qquad (22)\\
&\vartheta_2<\vartheta<\pi:\quad r=-\frac{L}{2\cos\vartheta}.
\end{aligned}$$

The matrix elements are

$$\begin{aligned}
U_{mn}=\int\beta_m\Phi_n=&\frac{\sqrt{(2m+1)(2n+1)}}{2}\left\{\int_{\cos\vartheta_1}^1\frac{dx}{x}\left[\frac{Lk_a}{2}\,h_m^{(1)'}\left(\frac{k_aL}{2x}\right)P_m(x)+(1-x^2)h_m^{(1)}\left(\frac{k_aL}{2x}\right)P_m'(x)\right]\right.\\
&\times\left[\frac{Lk_a}{2}\,j_n'\left(\frac{k_aL}{2x}\right)P_n(x)+(1-x^2)j_n\left(\frac{k_aL}{2x}\right)P_n'(x)\right]\\
&+\int_{\cos\vartheta_2}^{\cos\vartheta_1}\frac{dx}{\sqrt{1-x^2}}\left[ak_ah_m^{(1)'}\left(\frac{ak_a}{\sqrt{1-x^2}}\right)P_m(x)-x\sqrt{1-x^2}h_m^{(1)}\left(\frac{ak_a}{\sqrt{1-x^2}}\right)P_m'(x)\right]\\
&\times\left[ak_aj_n'\left(\frac{ak_a}{\sqrt{1-x^2}}\right)P_m(x)-x\sqrt{1-x^2}j_n\left(\frac{ak_a}{\sqrt{1-x^2}}\right)P_m'(x)\right]\\
&+\int_{-1}^{\cos\vartheta_2}\frac{dx}{x}\left[\frac{Lk_a}{2}\,h_m^{(1)'}\left(-\frac{k_aL}{2x}\right)P_m(x)-(1-x^2)h_m^{(1)}\left(-\frac{k_aL}{2x}\right)P_m'(x)\right]\\
&\left.\times\left[-\frac{Lk_a}{2}\,j_n'\left(-\frac{k_aL}{2x}\right)P_n(x)+(1-x^2)j_n\left(\frac{k_aL}{2x}\right)P_n'(x)\right]\right\}; \qquad (23)
\end{aligned}$$

$$V_{mn}=\int\Phi_m\varphi_n=\frac{\sqrt{2m+1}}{J_1(l_n)}\int_{-1}^{\cos\vartheta_2}\frac{dx}{2x^2}\frac{L}{a}\left[\frac{-Lk_a}{2}\,j_m'\left(\frac{-Lk_a}{2x}\right)P_m(x)+(1-x^2)j_m\left(\frac{-Lk_a}{2x}\right)P_m'(x)\right]J_0\left(\frac{-l_n\sqrt{1-x^2}}{2ax}\right),$$

$$W_{mn}=\int\varphi_m\frac{\Psi_n}{a}=\frac{\sqrt{2n+1}L^2}{J_1(l_m)a^2}\int_{-1}^{\cos\vartheta_2}\frac{dx}{4x^3}J_0\left(\frac{-l_mL\sqrt{1-x^2}}{2ax}\right)h_n^{(1)}\left(\frac{-k_aL}{2x}\right)P_n(x). \qquad (24)$$

IV. ANALYTIC SOLUTION AND MEAN DISPLACEMENT OF THE MEMBRANE

As now the expansion coefficients of the scattered wave are known, we can evaluate the mean displacement of the membrane as a function of the frequency of the incoming plane wave. We start with Eq. (2) and insert the complete wave

$$P=a_n \,\mathrm{Re}\,\Psi_n+f_{n,R}\Psi_n. \tag{25}$$

From Eqs. (20), (23), and (24) we have the relation between the coefficients of the incoming plane wave and the scattered wave

$$\mathrm{Re}\,A^T a=-A^T f_R, \quad Ta=f_R, \quad T^T=-\mathrm{Re}\,A.A^{-1}. \tag{26}$$

T is the so-called transfer matrix of Waterman. Since matrix A is ill conditioned (the imaginary part of the matrix elements in the lower part of matrix A grow to infinity), these imaginary parts are set to zero by Gaussian elimination. This can be thought to be done by a real triangular matrix, which does not change the value of T^T. Then matrix T^T can be inverted by Schmidt orthogonalization, and also this step can be done by a triangular matrix. It should be emphasized that this last step is one of the most important steps in this paper and has been introduced by Waterman. We have from Eqs. (23) and (24)

$$A=-U-\delta(VZ^{-1}W)^T. \tag{27}$$

Now the mean displacement of the membrane as a function of the frequency is calculated. From the acoustic equation we have for the displacement of the membrane

$$\eta=-\frac{1}{\rho\omega^2}\frac{\partial p_-}{\partial n}. \tag{28}$$

The mean displacement is obtained by integrating over the area of the membrane and dividing by the area of the membrane.

$$\begin{aligned}\overline{\eta}&=-\frac{1}{\rho\omega^2}\frac{1}{a^2\pi}\int\frac{\partial p_-}{\partial n}\,dS\\&=-\frac{1}{\rho\omega^2 a^2\pi}\int\frac{\partial}{\partial n}\,(a_n\,\mathrm{Re}\,\Psi_n+f_{R,n}\Psi_n)dS\\&=-\frac{1}{\rho\omega^2 a^2\pi}\left(a_n\int\mathrm{Re}\,\frac{\partial\Psi_n}{\partial n}+T_{nl}a_l\int\frac{\partial\Psi_n}{\partial n}\right)\\&=-\frac{1}{\rho\omega^2 a^2\pi}\,a_n(\mathrm{Re}\,\overline{B}_n+T_{ln}\overline{B}_l),\end{aligned}$$

$$a_n=\sqrt{2n+1}\,i^n\sqrt{4\pi}, \tag{29}$$

$$\overline{B}_n=\int\frac{\partial}{\partial n}\sqrt{\frac{2n+1}{4\pi}}\,[h_n^{(1)}(k_a r)P_n(\cos\vartheta)]dS,$$

$$\overline{\eta}\approx\frac{\beta}{\mu^2}\,C.(\mathrm{Re}\,B+T^T.B), \tag{30}$$

$$C_n=i^n(2n+1),$$

$$\begin{aligned}B_n=\int_{\xi=0}^{\xi=1}d\xi\Bigg[&\frac{L}{2\sqrt{a^2\xi^2+\frac{L^2}{4}}}\\&\times h_n^{(1)\prime}\left(\sqrt{a^2\xi^2+\frac{L^2}{4}}.k_a\right)k_a P_n\left(-\frac{1}{\sqrt{1+\frac{4a^2\xi^2}{L^2}}}\right)\\&-\frac{a^2\xi^2}{\sqrt{a^2\xi^2+\frac{L^2}{4}^3}}\,h_n^{(1)}\left(k_a\sqrt{a^2\xi^2+\frac{L^2}{4}}\right)\\&\times P_n'\left(-\frac{1}{\sqrt{1+\frac{4a^2\xi^2}{L^2}}}\right)\Bigg].\end{aligned}$$

V. RESULTS

In Tables I–VII the results of Ref. 4 and of this paper are presented and compared. Figures 3–6 show the mean displacement of some kettledrums and some microphones. Figure 2 gives the mean displacement of the membrane of a kettledrum as a function of the frequency of the incoming

TABLE I. Here the eigenfrequencies of a kettledrum are given for comparison with experiment. n is the number of mode. Radius of the membrane is $a=0.328$ m, height of the cylinder $L=0.414$ m. Column 1: experimental values of the resonances in Hz of Ref. 4. Column 2: Calculated values in Ref. 4. Column 3: Calculated eigenfrequencies by the author for a kettledrum *in vacuo*. Column 4: Calculated eigenfrequencies by the author for a kettledrum with air loading in a rigid panel to avoid scattering. Column 5: Calculated eigenfrequencies by the author of a kettledrum with scattering. $T=3710$ N/m.

	$T=3710$ N/m				
n	1	2	3	4	5
0	128	126	160	126	128
1	235	244	276	244	232
2	383	405	431	407	400
3	⋯	⋯	500	488	488
4	⋯	⋯	⋯	595	⋯

TABLE II. Same as Table I. $T=1960$ N/m.

	$T=1960$ N/m				
n	1	2	3	4	5
0	94	⋯	138	110	110
1	179	181	205	181	172
2	286	302	328	312	312
3	⋯	⋯	488	464	464
4	⋯	⋯	595	566	513

TABLE III. Same as Table I. $T=5360$ N/m.

	$T=5360$ N/m				
n	1	2	3	4	5
0	140	138	177	138	141
1	284	291	320	297	269
2	467	⋯	476	442	442
3	⋯	511	552	512	539
4	⋯	⋯	⋯	⋯	⋯

TABLE IV. Eigenfrequencies of a condenser microphone (with scattering) calculated by the author. Radius of the membrane $a=0.0328$ m, height of the cylinder $L=0.0414$ m. Tension $T=3710$ N/m.

	$T=3710$ N/m
n	
0	1380
1	3047
2	4999
3	6728
4	9056
5	13458

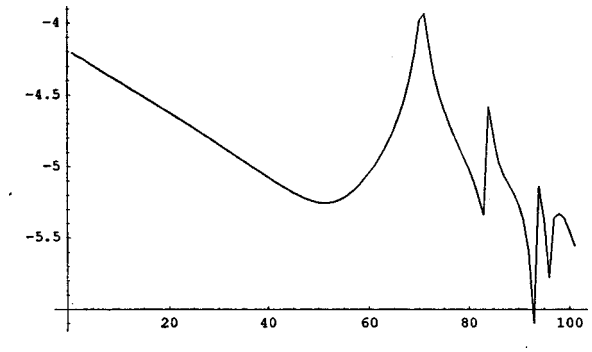

FIG. 2. Mean displacement of the membrane of a kettledrum in dependence of the frequency of the incoming plane wave. The curve is realistic for $i>50$, because otherwise the wavelength is too large compared to the dimensions of the obstacle. Resonance frequencies are at 141 Hz, 269 Hz, 442 Hz, 538 Hz.

TABLE V. Same as in Table IV. $T=1960$ N/m.

	$T=1960$ N/m
n	
0	1025
1	2263
2	4999

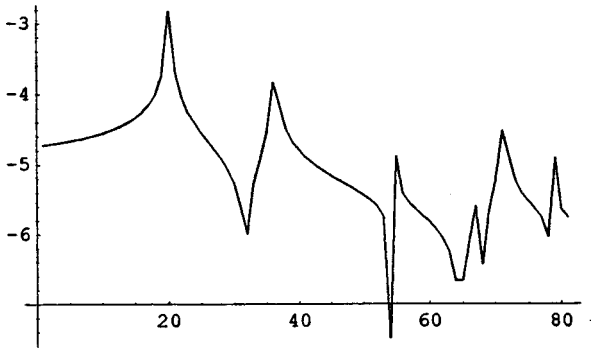

FIG. 3. Mean displacement for a kettledrum *in vacuo*, i.e., without air loading. Same geometry as in Fig. 2. $T=1960$ N/m. Resonances at 138 Hz, 205 Hz, 328 Hz, 442 Hz, 488 Hz, 595 Hz.

TABLE VI. Same as in Table IV. $T=5360$ N/m.

	$T=5360$ N/m
n	
0	1602
1	3714
2	4528
3	6094
4	8202
5	11040
6	13458

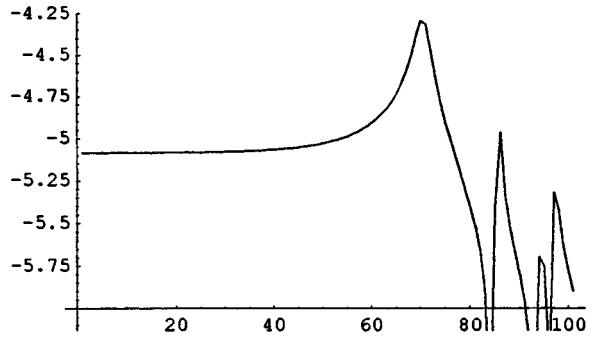

FIG. 4. Kettledrum with air loading in a rigid panel to avoid scattering. Same geometry as in Fig. 2. $T=5360$ N/m. Resonances at 138 Hz, 297 Hz, 442 Hz, 512 Hz.

TABLE VII. Eigenfrequencies of a condenser microphone calculated by the author. Radius of the membrane $a=0.015$ m, height of the cylinder $L=0.02$ m. Tension $T=5360$ N/m. Column 1: With scattering. Column 2: Microphone in a rigid panel to avoid scattering.

	$T=5360$ N/m	
n	1	2
0	3580.5	3584
1	8129.5	8166
	8743	8756
	8769	8778
2	13 974	13 000
	14 023	14 023
	15 134	

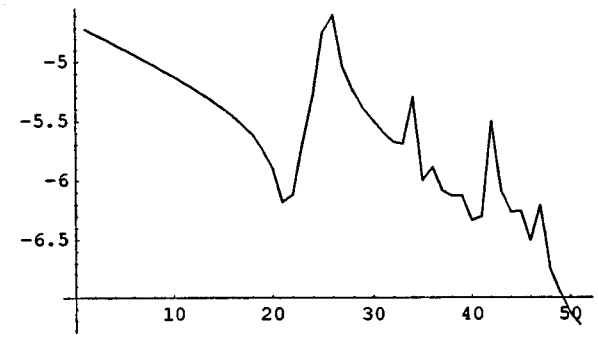

FIG. 5. Mean displacement of the membrane for scattering from a cylindrical condenser microphone. $T=5360$ N/m, $a=0.0328$ m, $L=0.0414$ m. ρ, σ and c_a are the same as in Fig. 2. The curve is realistic for $i>20$. Resonances at 1602 Hz, 3714 Hz, 6094 Hz, 8202 Hz, 11040 Hz, 13458 Hz.

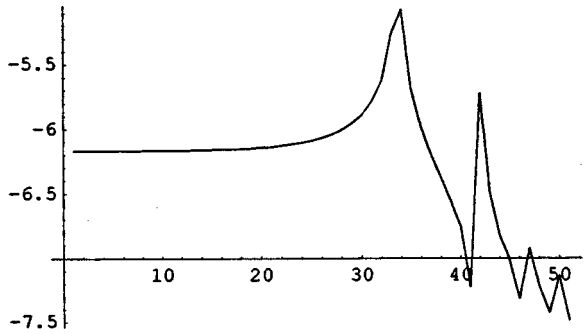

FIG. 6. Mean displacement of the membrane for a small cylindrical condenser microphone in a rigid panel to avoid scattering. $a=0.015$ m, $L=0.02$ m, $T=5360$ N/m. Other parameters as in Fig. 5. The complete curve is realistic. Resonance at 3584 Hz, triple resonance at 8166 Hz, 8756 Hz, 8778 Hz, double resonance at 13 000 Hz, 14 023 Hz, resonance at 17 803 Hz.

plane wave; $a=0.328$ m, $L=0.414$ m, $T=5360$ N/m, $\sigma=0.262$ kg/m^3, $c_a=344$ m/s, $\rho=1.2$ kg/m^3. There is a logarithmic scale on both axes. The values $i=1,...,100$ on the abscissa correspond to the frequencies $f=4.4$ Hz,...,624 Hz. The correspondence is given by the formula $f=10^{4.30103(3000+100i)/20000}$.

This formula guarantees a logarithmic scale on the abscissa. The ordinate is log η in dB. The curve is realistic for $i>45$, which corresponds to $f>41$ Hz. This means that for $\lambda>8.4$ m the curve does not show the measured values. The diameter of the membrane in this case is $d=0.66$ m. One can see that for $\lambda>10d$ the theory fails. The giant resonance at 141 Hz is compared in Table III with experimental values of Ref. 4. This reference gives a value of 140 Hz, so that agreement is very good. Also the calculated value of 138 Hz of Ref. 4 shows good agreement. Column 3 of Table III gives also the calculated eigenfrequencies of a kettledrum *in vacuo* by the author: $f=177$ Hz. This deviation of 21% can be understood by the absence of air loading. Column 4 compares with a kettledrum in a rigid panel (without scattering). The value $f=138$ Hz shows that there is only a 1.4% difference to the case with scattering. This means that for these dimensions of the obstacle scattering does not play an important role. The second resonance in Fig. 2 is calculated at $f=269$ Hz (see Table III, Column 5). The measured value of $f=284$ Hz shows a deviation of 5%. This means that for $\lambda=1.2$ m, which is of order $2d$ (diameter), other effects must be taken into account for complete agreement. The calculated value of Ref. 4 gives $f=291$ Hz in good agreement with the author's calculation of $f=297$ Hz (1% difference). Also the next resonance calculated at $f=442$ Hz agrees with the measured value of $f=467$ Hz fairly good (5% difference). The effect of air loading $f=476$ Hz *in vacuo* (2% deviation) is much smaller at this frequency than for $f=140$ Hz. Column 4 of Table III shows that scattering does not play any role for this wavelength. Figure 5 shows the mean displacement of a membrane for scattering from a condenser microphone of radius $a=0.032$ m. This is a large microphone, but the theory is not accurate if $a<0.02$ m. And for $a<0.015$ m the theory completely fails. So one can clearly see that the analytic solution of the scattering problem by the method of Waterman and the Green's function approach of the author is only possible if the length scale of the obstacle is in the range of the wavelength of $0.03\text{ m}<\lambda<0.3$ m.

VI. CONCLUSION

In this paper the scattering of a plane wave from a kettledrum and from a condenser microphone model is investigated. The eigenfrequencies of these coupled acoustic systems are calculated by applying the so-called transfer-matrix method of Waterman and by a Green's function approach. A comparison of the results is made with a calculation of the modal frequencies of a plane wave striking a kettledrum (condenser microphone) in a rigid panel to avoid scattering. As a result, the modal frequencies of these two models show good agreement. The approach of Waterman shows for scattering also good agreement with experiment. For a small condenser microphone the agreement is only good if the wavelength of the plane wave is comparable to the dimensions of the microphone. So one can conclude that the T-matrix approach of Waterman for scattering fails, if the dimension of the obstacle is smaller than the wavelength of the incoming plane wave. On the other hand, one can see that the Green's function approach and the eigenfunction expansion to solve the coupled scattering problem leads to very convincing results. Also the calculations of the wave striking an obstacle in a rigid panel show nearly the same results as the measurements and calculations of Ref. 4.

APPENDIX A

The Green's function for the cylinder is with the notation of Ref. 5:

$$g(r,\varphi,z|r_0,\varphi_0,z_0)=\sum_{m,n,n'}\frac{\epsilon_{n'}\epsilon_m\cos m(\varphi-\varphi_0)J_m(k_{rmn}r)J_m(k_{rmn}r_0)\cos(k_{zn'}z)\cos(k_{zn'}z_0)}{L\pi a^2(k_{rmn}^2+k_{zn'}^2-k_a^2)J_m^2(k_{rmn}a)\left(1-\frac{m^2}{k_{rmn}^2a^2}\right)}. \tag{A1}$$

APPENDIX B

The matrix elements of Green's function (A1) are given by the following formula. As in Appendix A, the notation is explained in Refs. 5 and 6:

$$\langle m|g|n\rangle = \delta_{mn}\frac{\operatorname{cth}\left(\frac{L}{a}\sqrt{l_m^2-\alpha^2}\right)}{\sqrt{l_m^2-\alpha^2}} - \frac{2a l_m l_n}{L}\sum_{n'=0}^{n'=\infty}\frac{\epsilon_{n'}J_0\left(\sqrt{\alpha^2-\frac{n'^2\pi^2a^2}{L^2}}\right)}{\left(l_m^2-\alpha^2+\frac{n'^2\pi^2a^2}{L^2}\right)\left(l_n^2-\alpha^2+\frac{n'^2\pi^2a^2}{L^2}\right)\sqrt{\alpha^2-\frac{n'^2\pi^2a^2}{L^2}}\,J_1\left(\sqrt{\alpha^2-\frac{n'^2\pi^2a^2}{L^2}}\right)}. \tag{B1}$$

[1] H. P. W. Gottlieb and H. A. Aebischer, Acustica **61**, 223–232 (1986); Acustica **65**, 2–10 (1987).
[2] P. M. Morse and K. U. Ingard, *Theoretical Acoustics* (McGraw-Hill, New York, 1968).
[3] P. M. Morse, *Vibration and Sound* (Acoustical Society of America, New York, 1953), 2nd ed. reprint.
[4] R. S. Christian, R. E. Davis, A. Tubis, C. A. Anderson, R. I. Mills, and T. D. Rossing, J. Acoust. Soc. Am. **76**, 1336–1345 (1984).
[5] W. Kainz, J. Acoust. Soc. Am. **100**, 2156–2165 (1996).
[6] W. Kainz, J. Acoust. Soc. Am. **100**, 2166–2169 (1996).
[7] P. C. Waterman, J. Acoust. Soc. Am. **45**, 1417–1429 (1969); **60**, 567–580 (1976); **63**, 1320–1325 (1978); Phys. Rev. D **3**, 825–839 (1971); in *Computer Techniques for Electromagnetics*, edited by R. Mittra (Pergamon, Oxford, 1973), p. 97.
[8] P. M. Morse and K. U. Ingard, *Theoretical Acoustics* (McGraw-Hill, New York, 1968), p. 193.
[9] P. M. Morse and K. U. Ingard, in Ref. 8, p. 643.
[10] P. M. Morse and K. U. Ingard, in Ref. 8, p. 321.
[11] L. Kazandjian, J. Acoust. Soc. Am. **93**, 3139–3148 (1993).

Full numerical solution for the far-field and near-field scattering from a fluid-loaded elastic plate with distributed mass or stiffness inhomogeneity

J. M. Cuschieri
Center for Acoustics and Vibration, Department of Ocean Engineering, Florida Atlantic University, Boca Raton, Florida 33431

D. Feit
Carderock Division, NSWC, David Taylor Research Center, Bethesda, Maryland 20817

(Received 1 April 1997; accepted for publication 21 April 1998)

The scattering of a plane acoustic wave by a fluid-loaded thin elastic plate of infinite extent with a distributed mass or stiffness inhomogeneity is investigated. This paper is a follow up to previous work done by the same authors on the scattering from a fluid-loaded plate with a distributed mass inhomogeneity. In this paper both stiffness and mass distributed inhomogeneities are considered and a complete description of the full numerical solution is presented. Furthermore, both near-field and far-field scattering results are presented in this paper. The presence of the distributed inhomogeneity modifies the wave number transform of the equation of motion of the fluid-loaded plate to a Fredholm integral equation. This integral equation has singularities at the roots of the dispersion equation. To obtain a complete numerical solution of the Fredholm integral equation, a singularity subtraction technique is used, which is similar in essence to the hybrid analytic/numerical approach for the solution of the scattering from a fluid-loaded elastic plate [J. Acoust. Soc. Am. **95**, 1998–2005 (1994)]. The solution to the resulting Fredholm integral equation of the second kind is obtained using the Nyström approximation. The results for the far-field scattering are for an oblique angle of incidence and for monostatic scattering. The results show that mass distributed inhomogeneities are stronger scatterers than distributed stiffness inhomogeneities for frequencies below the critical frequency of the plate. Above the critical frequency, both types of inhomogeneities have similar scattering strengths. Also included are results for different types of inhomogeneity distributions. This work was sponsored by ONR. [S0001-4966(98)01708-1]

PACS numbers: 43.40.Rj [CBB]

INTRODUCTION

The importance of the scale of an inhomogeneity on the scattering from a fluid-loaded structure is a classical problem in structural acoustics. The scale of the homogeneity relative to the acoustic wavelength will determine whether the inhomogeneity can be modeled by a point (or line) load, or the actual spatial-distribution of the inhomogeneity has to be taken into account. Scale is important in determining the accuracy by which the spatial distribution of the inhomogeneity must be known and modeled to capture the relevant scattering and radiation characteristics. Also, of interest is the influence of the type—stiffness or mass—of the inhomogeneity on the relative scattering strength. These issues of scale and type can be investigated by analytically solving for the response Green's function and the scattered pressure from a fluid-loaded structure with a distributed inhomogeneity. An approximate analytical solution to this problem is presented in Ref. 1. In this paper, a complete solution is presented. The fluid-loaded plate (Fig. 1) is assumed infinite and the solution is obtained using wave number transforms. In this paper, thin plate equations of motion are used. While Mindlin plate equations of motion would have a more accurate representation of the coincidence effects,[2] the added complexity would have detracted from the objective of this paper, which is the analysis of the influence on the scattering of the type and ''smoothness'' of the inhomogeneity.

In a previous paper,[1] the scattering from a fluid-loaded elastic plate with a distributed mass inhomogeneity was considered. In that paper the emphasis was on comparing the results from a series solution, where only the first few terms are considered, to a full numerical solution. However, very little detail was provided on the full numerical solution. In this paper a more complete description of the full numerical solution is provided together with a generalization of the formulation to consider the scattering from both stiffness and mass distributed inhomogeneities. Results for the near-field and far-field scattering are obtained. In the formulation of the problem, the elastic plate is considered to lie in the $y=0$ plane and the inhomogeneity is of length l. Three different forms of inhomogeneity distributions are considered together with the special case of a line discontinuity, which can be considered as a concentrated inhomogeneity, the same as in Ref. 1. A schematic view of the problem is shown in Fig. 1. The total net change in the mass or stiffness of the plate due to the presence of the inhomogeneity is kept constant between all distributions, that is, the integral over the extent of the inhomogeneity is a constant for both the mass or stiffness inhomogeneities.

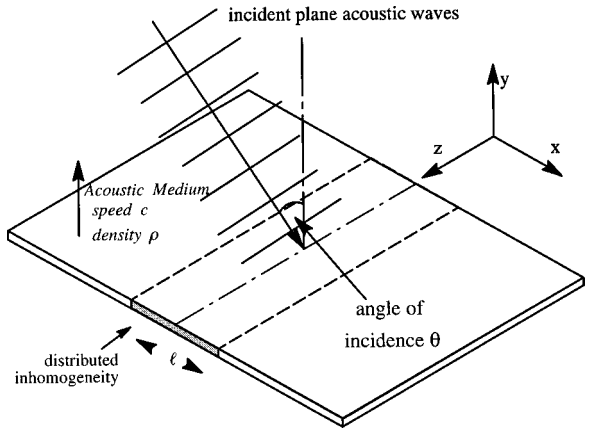

FIG. 1. Plate configuration with distributed mass or stiffness inhomogeneity.

The complete solution is obtained in two steps. The first step consists of numerically solving the Fredholm integral equation which describes the solution of the inhomogeneous plate in the wave number domain. This first step gives the response or the scattered pressure as a wave number function. In the second step, the inverse transform from the wave number to the spatial domain is performed using the hybrid numerical–analytical approach.[3] This is an efficient way of performing this inverse transform, as compared to a contour integral approach,[2] and it does not require the introduction of structural damping. Response Green's function and scattered pressure results are obtained for spatial distributions that extend over a length equivalent to 20 times the thickness of the plate. This is the only length of inhomogeneity considered. In the case of the mass inhomogeneity, the special case of a concentrated line distribution, which is equivalent to a line discontinuity, is also considered. The distributions have varying degrees of end ''smoothness.'' [1]

The inhomogeneity distributions considered are: a concentrated line, a uniform distribution, a quadratic distribution, and a biquadratic distribution. The inhomogeneities' functional forms were given in Ref. 1 and are repeated in Eqs. (1)–(4),

$$z_1(x) = Z_0 \delta(x), \tag{1}$$

$$z_2(x) = \frac{Z_0}{l}\,[H(x+l/2) - H(x-l/2)], \tag{2}$$

$$z_3(x) = 6\,\frac{Z_0}{l^3}\left(\frac{l^2}{4} - x^2\right)[H(x+l/2) - H(x-l/2)], \tag{3}$$

$$z_4(x) = 30\,\frac{Z_0}{l^5}\left(\frac{l^2}{4} - x^2\right)^2 [H(x+l/2) - H(x-l/2)], \tag{4}$$

where l is the extent of the inhomogeneity and Z_0 is the impedance change introduced by the inhomogeneity. The form of Z_0 depends on the type—stiffness or mass—of the inhomogeneity. These four distributions are shown in Fig. 2, and Fig. 3 shows the wave number transform of the inhomogeneity distributions.

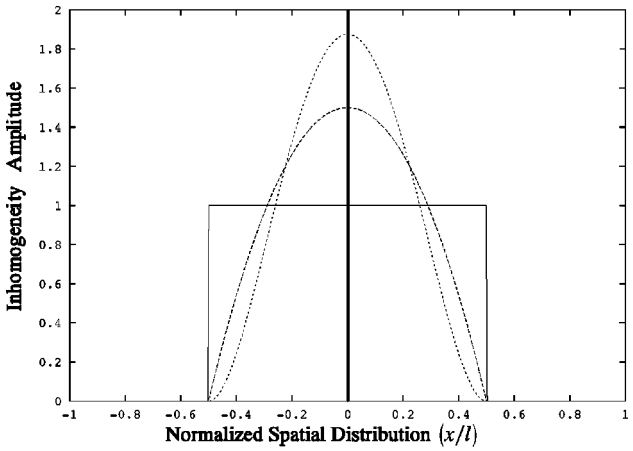

FIG. 2. Inhomogeneities distributions: ———: concentrated (line); ———: uniform; – – – –: quadratic; ------: biquadratic. The inhomogeneity amplitude is the normalized amplitude given by $(z(x)l/Z_0)$.

I. FORMULATION OF THE SOLUTION

If the plate is assumed to lie in the x-z plane, with the inhomogeneity distributed along the x-direction, the equation of motion of the plate when excited by an incident plane wave, with angle of incidence θ to the y-axis and moving in the positive x-direction, using an $e^{-j\omega t}$ time dependency, is given by:

$$\left(\frac{\partial^2}{\partial x^2}\left[(b'+b)\,\frac{\partial^2}{\partial x^2}\right] - (m'+m)\omega^2\right)\frac{\nu(x)}{-j\omega} + p_s(x,0) = -p_b(x,0), \tag{5}$$

where $m' = \rho_s h$ is surface mass density of the plate, $b' = Eh^3/[12(1-\upsilon^2)]$ is the plate bending stiffness, and ρ_s, E, υ, and h are, respectively, the plate material density, Young's modulus of elasticity, Poisson's ratio, and thickness. $m = m(x)$ and $b = b(x)$ are the inhomogeneity mass and stiffness distributions, respectively. If the incident pressure is given by

$$p_i(x,y) = P_0 e^{jk_0(x\,\sin\,\theta - y\,\cos\,\theta)} \tag{6}$$

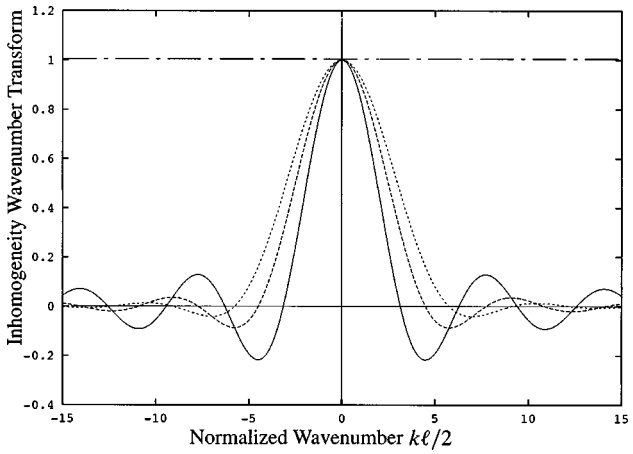

FIG. 3. Representation of the spatial Fourier transform of the distributed inhomogeneities. ———: Uniform distribution; – – – –: quadratic distribution; ------: biquadratic distribution; — – —: concentrated line distribution. The plotted amplitude is $(Z(k)/Z_0)$.

then in Eq. (5)

$$p_b(x,0) = 2P_0 e^{jk_0 x \sin\theta} \tag{7}$$

and the scattered component $p_s(x,0)$ must satisfy the continuity condition at the plate acoustic medium interface, given as follows:

$$\frac{\partial p_s}{\partial y}(x,0) = j\rho\omega v(x), \tag{8}$$

where $k_0 = \omega/c = 2\pi/\lambda_0$, is the acoustic wave number, c is the sound speed in the acoustic medium, λ_0 is the acoustic wavelength, and ρ is the density of the acoustic medium.

The solution to the above equations is sought using a spatial Fourier transform over the x-domain. This procedure transforms the equation of motion (5) from the spatial to the wave number domain or the spectral domain. Following this transformation, Eq. (5) becomes:

$$\begin{aligned}&[\tilde{Z}_s(\bar{k}) + \tilde{Z}_a(\bar{k})]\tilde{V}(\bar{k},\omega) + 4\pi\delta(\bar{k} - \alpha \sin\theta) \\ &\quad + \frac{j\bar{k}^2}{2\pi}\int_{-\infty}^{\infty} \bar{k'}^2 \left[\frac{L\tilde{b}(\bar{k}-\bar{k'})}{lb'}\right]\tilde{V}(\bar{k'},\omega)d\bar{k'} \\ &\quad - \frac{j}{2\pi}\int_{-\infty}^{\infty}\left[\frac{L\tilde{m}(\bar{k}-\bar{k'})}{lm'}\right]\tilde{V}(\bar{k'},\omega)d\bar{k'} = 0,\end{aligned} \tag{9}$$

where L is the length of the inhomogeneity normalized by the elastic plate flexural wave number $\gamma = \sqrt[4]{\omega^2/(b'/m')}$, that is, $L = \gamma l$. Furthermore, it should be noted that the mass and stiffness inhomogeneity distributions ($\tilde{b}$ and $\tilde{m}$) are also scaled by the plate flexural wave number γ. It is shown later on in this paper that this scaling will result in the normalized magnitude of the inhomogeneity being a function of the normalized frequency parameter α, defined in the following paragraph.

The tilde above the variables in Eq. (9) indicates that the variable is defined in the wave number space. The expression that relates the surface pressure to the normal velocity of the plate when transformed to the wave number domain has the form

$$\tilde{P}_{sc}(\bar{k},Y) = \tilde{Z}_a(\bar{k})\tilde{V}(\bar{k})e^{jY\sqrt{\alpha^2-k^2}}. \tag{10}$$

In Eqs. (9) and (10), the following parameters have been introduced. Y is the normalized distance along the normal to the plate defined by $Y = \gamma y$, $\tilde{Z}_s(\bar{k}) = -j(1-k^4)$ is the plate spectral impedance, $\tilde{Z}_a(\bar{k}) = (\epsilon/\alpha)/\sqrt{\alpha^2-k^2}$ is the acoustic spectral impedance, $\tilde{V}(k) = \tilde{\nu}(k)/[P_0/(m'\omega)]$ is the normalized surface velocity response, $\tilde{P}_{sc}(k,Y) = \tilde{p}_s(k,Y)/P_0$ is the normalized scattered pressure, ϵ is the fluid-loading parameter as defined in Ref. 4 and given by $\epsilon = (\rho c)/(m'\omega_c)$, which is equal to $\epsilon = 0.129$ for a water-loaded steel plate, $k = k/\gamma = \sqrt{\omega/\omega_c}$ is the Mach number also defined in Ref. 4 and $(\rho\omega^2)/(b'\gamma^5) = \epsilon/\alpha$.

II. NUMERICAL SOLUTION

Rearranging Eq. (9), a Fredholm integral equation of the third kind is obtained, for which a solution is sought to obtain the wave number spectral response of the surface velocity. Equation (9) can be reduced to a Fredholm integral equation of the second kind by using the substitution,

$$\tilde{W}(\bar{k}) = \tilde{Z}(\bar{k})\tilde{V}(\bar{k}) + 4\pi\delta(\bar{k} - \alpha \sin\theta), \tag{11}$$

where $\tilde{Z}(\bar{k}) = [\tilde{Z}_s(\bar{k}) + \tilde{Z}_a(\bar{k})]$. From Eq. (11) the solution for the normal spectral velocity response can be obtained from the relationship,

$$\tilde{V}(\bar{k}) = -\frac{4\pi\delta(\bar{k} - \alpha \sin\theta)}{\tilde{Z}(\bar{k})} + \frac{\tilde{W}(\bar{k})}{\tilde{Z}(\bar{k})}, \tag{12}$$

where the first term on the RHS of Eq. (12) is the velocity response of the homogeneous plate induced by the incident acoustic wave, while the second term is the velocity response due to the presence of the inhomogeneity. Substituting Eq. (12) into Eq. (9) and rearranging,

$$\begin{aligned}&\tilde{W}(\bar{k}) + \frac{1}{2\pi}\int_{-\infty}^{\infty}\tilde{Z}_d(\bar{k},\bar{k'})\frac{\tilde{W}(\bar{k'})}{\tilde{Z}(\bar{k'})}d\bar{k'} \\ &\quad = \frac{2}{\tilde{Z}(\alpha \sin\theta)}\tilde{Z}_d(\bar{k},\alpha \sin\theta),\end{aligned} \tag{13}$$

where $\tilde{Z}_d(\bar{k},\bar{k'})$ is either $[j\bar{k}^2\bar{k'}^2 L\tilde{b}(\bar{k}-\bar{k'})/(lb')]$ for a stiffness inhomogeneity or $[-jL\tilde{m}(k-k')/(lm')]$ for a mass inhomogeneity. The kernel of the integral in Eq. (13) has singularities at the zeros, and branch points (if a contour integral approach is used), of the denominator $\tilde{Z}(\bar{k}) = [\tilde{Z}_s(\bar{k}) + \tilde{Z}_a(\bar{k})]$, which is the dispersion equation of the fluid-loaded plate. The integrals cannot therefore be directly evaluated.[2] A solution is developed using a singularity subtraction technique,[5,6] which is very similar in essence to the hybrid approach presented in Ref. 3. The zeros of the dispersion equation cannot be located analytically and a numerical approach has to be used.[3] Thus if singularities exists at $\bar{k} = \pm\bar{k}_a$, then

$$\begin{aligned}&\frac{1}{2\pi}\int_{-\infty}^{\infty}\frac{\tilde{Z}_d(\bar{k},\bar{k'})}{\tilde{Z}(\bar{k'})}\tilde{W}(\bar{k'},\omega)d\bar{k'} \\ &\quad = \frac{1}{2\pi}\int_{-\infty}^{\infty}\left[\frac{\tilde{Z}_d(\bar{k},\bar{k'})}{\tilde{Z}(k')} - \left(\frac{\tilde{Z}_d(\bar{k},\bar{k}_a)(\bar{k'}+\bar{k}_a)}{2k_a\tilde{g}(k_a)(k'^2-k_a^2)}\right.\right. \\ &\qquad \left.\left. + \frac{\tilde{Z}_d(\bar{k},-\bar{k}_a)(\bar{k'}-\bar{k}_a)}{2(-k_a)\tilde{g}(k_a)(k'^2-k_a^2)}\right)\right]\tilde{W}(\bar{k'})d\bar{k'} \\ &\qquad + \frac{j}{2}\left[\frac{\tilde{W}(\bar{k}_a)\tilde{Z}_d(\bar{k},\bar{k}_a)}{k_a\tilde{g}(k_a)} + \frac{\tilde{W}(-\bar{k}_a)\tilde{Z}_d(\bar{k},-\bar{k}_a)}{(-k_a)\tilde{g}(k_a)}\right],\end{aligned} \tag{14}$$

where

$$g(\bar{k}_a) = \lim_{\bar{k}\to\bar{k}_a}\frac{\tilde{Z}(\bar{k})}{(\bar{k}^2-\bar{k}_a^2)} = \frac{\partial(\tilde{Z}(\bar{k}_a))/\partial\bar{k}}{2\bar{k}_a}. \tag{15}$$

The singularities (zeros) of $\tilde{Z}(\bar{k}) = [\tilde{Z}_s(\bar{k}) + \tilde{Z}_a(\bar{k})]$ occur in pairs. If $\tilde{Z}(k) = [\tilde{Z}_s(\bar{k}) + \tilde{Z}_a(k)]$ has more than one pair of singularities on or close to the real axis, which would be the case at frequencies above the critical frequency, then the procedure is repeated until all pairs of singularities close or

on the real axis are removed. Having removed the singularities from the integral, the integral can be evaluated numerically using a Gauss quadrature approach. Substituting for the integral in Eq. (13) by its numerical equivalent, including the singularity subtraction of Eq. (14), then Eq. (13) results in

$$\tilde{W}(\bar{k})+\frac{1}{2\pi}\sum_{i=1}^{N} w_i\left[\frac{\tilde{Z}_d(\bar{k},\bar{k}_i)}{\tilde{Z}(\bar{k}_i)}-\left(\frac{\tilde{Z}_d(\bar{k},\bar{k}_a)(\bar{k}_i+\bar{k}_a)}{2\bar{k}_a\tilde{g}(\bar{k}_a)(\bar{k}_i^2-\bar{k}_a^2)}+\frac{\tilde{Z}_d(\bar{k},-\bar{k}_a)(\bar{k}_i-\bar{k}_a)}{2(-\bar{k}_a)\tilde{g}(\bar{k}_a)(\bar{k}_i^2-\bar{k}_a^2)}\right)\right]\tilde{W}(\bar{k}_i)$$
$$+\frac{j}{2}\left[\frac{\tilde{W}(\bar{k}_a)\tilde{Z}_d(\bar{k},\bar{k}_a)}{\bar{k}_a\tilde{g}(\bar{k}_a)}+\frac{\tilde{W}(-\bar{k}_a)\tilde{Z}_d(\bar{k},-\bar{k}_a)}{(-\bar{k}_a)\tilde{g}(\bar{k}_a)}\right]=2\,\frac{\tilde{Z}_d(\bar{k},\alpha\,\sin\,\theta)}{\tilde{Z}(\alpha\,\sin\,\theta)}, \tag{16}$$

where w_i are the Gauss quadrature weights and $\bar{k}_i$ are the Gauss nodes. This expression can be evaluated at the discrete values $\bar{k}_n$, that is,

$$\tilde{W}(\bar{k}_n)+\frac{1}{2\pi}\sum_{i=1}^{N} w_i\left[\frac{\tilde{Z}_d(\bar{k}_n,\bar{k}_i)}{\tilde{Z}(\bar{k}_i)}-\left(\frac{\tilde{Z}_d(\bar{k}_n,\bar{k}_a)(\bar{k}_i+\bar{k}_a)}{2\bar{k}_a\tilde{g}(\bar{k}_a)(\bar{k}_i^2-\bar{k}_a^2)}+\frac{\tilde{Z}_d(\bar{k}_n,-\bar{k}_a)(\bar{k}_i-\bar{k}_a)}{2(-\bar{k}_a)\tilde{g}(\bar{k}_a)(\bar{k}_i^2-\bar{k}_a^2)}\right)\right]\tilde{W}(\bar{k}_i)$$
$$+\frac{j}{2}\left[\frac{\tilde{W}(\bar{k}_a)\tilde{Z}_d(\bar{k}_n,\bar{k}_a)}{\bar{k}_a\tilde{g}(\bar{k}_a)}+\frac{\tilde{W}(-\bar{k}_a)\tilde{Z}_d(\bar{k}_n,-\bar{k}_a)}{(-\bar{k}_a)\tilde{g}(\bar{k}_a)}\right]=2\,\frac{\tilde{Z}_d(\bar{k}_n,\alpha\,\sin\,\theta)}{\tilde{Z}(\alpha\,\sin\,\theta)}. \tag{17}$$

If the discrete values $\bar{k}_n$ take the same values as the Gauss quadrature nodes $\bar{k}_i$, then a set of M linear equations are obtained, where $M=N+N_p$, N being the number of Gauss nodes and N_p being the number of singularities. This set of M linear equations can be represented in a matrix format,

$$\begin{bmatrix}\tilde{W}(\bar{k}_1)\\ \tilde{W}(\bar{k}_2)\\ \tilde{W}(\bar{k}_3)\\ \tilde{W}(\bar{k}_4)\\ \tilde{W}(\bar{k}_5)\\ \vdots\\ \tilde{W}(\bar{k}_N)\\ \tilde{W}(\bar{k}_a)\\ \tilde{W}(-\bar{k}_a)\end{bmatrix}+\begin{bmatrix}\tilde{\mathcal{K}}(\bar{k}_1,\bar{k}_1) & \tilde{\mathcal{K}}(\bar{k}_1,\bar{k}_2) & \tilde{\mathcal{K}}(\bar{k}_1,\bar{k}_3) & \tilde{\mathcal{K}}(\bar{k}_1,\bar{k}_4) & \cdots & \tilde{\mathcal{K}}(\bar{k}_1,\bar{k}_N) & \tilde{\mathcal{Z}}(\bar{k}_1,\bar{k}_a) & \tilde{\mathcal{Z}}(\bar{k}_1,-\bar{k}_a)\\ \tilde{\mathcal{K}}(\bar{k}_2,\bar{k}_1) & \tilde{\mathcal{K}}(\bar{k}_2,\bar{k}_2) & \tilde{\mathcal{K}}(\bar{k}_2,\bar{k}_3) & \tilde{\mathcal{K}}(\bar{k}_2,\bar{k}_4) & \cdots & \tilde{\mathcal{K}}(\bar{k}_2,\bar{k}_N) & \tilde{\mathcal{Z}}(\bar{k}_2,\bar{k}_a) & \tilde{\mathcal{Z}}(\bar{k}_2,-\bar{k}_a)\\ \tilde{\mathcal{K}}(\bar{k}_3,\bar{k}_1) & \tilde{\mathcal{K}}(\bar{k}_3,\bar{k}_2) & \tilde{\mathcal{K}}(\bar{k}_3,\bar{k}_3) & \tilde{\mathcal{K}}(\bar{k}_3,\bar{k}_4) & \cdots & \tilde{\mathcal{K}}(\bar{k}_3,\bar{k}_N) & \tilde{\mathcal{Z}}(\bar{k}_3,\bar{k}_a) & \tilde{\mathcal{Z}}(\bar{k}_3,-\bar{k}_a)\\ \tilde{\mathcal{K}}(\bar{k}_4,\bar{k}_1) & \tilde{\mathcal{K}}(\bar{k}_4,\bar{k}_2) & \tilde{\mathcal{K}}(\bar{k}_4,\bar{k}_3) & \tilde{\mathcal{K}}(\bar{k}_4,\bar{k}_4) & \cdots & \tilde{\mathcal{K}}(\bar{k}_4,\bar{K}_N) & \tilde{\mathcal{Z}}(\bar{k}_4,\bar{k}_a) & \tilde{\mathcal{Z}}(\bar{k}_4,-\bar{k}_a)\\ \tilde{\mathcal{K}}(\bar{k}_5,\bar{k}_1) & \tilde{\mathcal{K}}(\bar{k}_5,\bar{k}_2) & \tilde{\mathcal{K}}(\bar{k}_5,\bar{k}_3) & \tilde{\mathcal{K}}(\bar{k}_5,\bar{k}_4) & \cdots & \tilde{\mathcal{K}}(\bar{k}_5,\bar{k}_N) & \tilde{\mathcal{Z}}(\bar{k}_5,\bar{k}_a) & \tilde{\mathcal{K}}(\bar{k}_5,-\bar{k}_a)\\ \vdots & \vdots & \vdots & & \vdots & & \vdots & \vdots\\ \tilde{\mathcal{K}}(\bar{k}_N,\bar{k}_1) & \tilde{\mathcal{K}}(\bar{k}_N,\bar{k}_2) & \tilde{\mathcal{K}}(\bar{k}_N,\bar{k}_3) & \tilde{\mathcal{K}}(\bar{k}_N,\bar{k}_4) & \cdots & \tilde{\mathcal{K}}(\bar{k}_N,\bar{k}_N) & \tilde{\mathcal{Z}}(\bar{k}_N,\bar{k}_a) & \tilde{\mathcal{Z}}(\bar{k}_N,-\bar{k}_a)\\ \tilde{\mathcal{K}}(\bar{k}_a,\bar{k}_1) & \tilde{\mathcal{K}}(\bar{k}_a,\bar{k}_2) & \tilde{\mathcal{K}}(\bar{k}_a,\bar{k}_3) & \tilde{\mathcal{K}}(\bar{k}_a,\bar{k}_4) & \cdots & \tilde{\mathcal{K}}(\bar{k}_a,\bar{k}_N) & \tilde{\mathcal{Z}}(\bar{k}_a,\bar{k}_a) & \tilde{\mathcal{Z}}(\bar{k}_a,-\bar{k}_a)\\ \tilde{\mathcal{K}}(-\bar{k}_a,\bar{k}_1) & \tilde{\mathcal{K}}(-\bar{k}_a,\bar{k}_2) & \tilde{\mathcal{K}}(-\bar{k}_a,\bar{k}_3) & \tilde{\mathcal{K}}(-\bar{k}_a,\bar{k}_4) & \cdots & \tilde{\mathcal{K}}(-\bar{k}_a,\bar{k}_N) & \tilde{\mathcal{Z}}(-\bar{k}_a,\bar{k}_a) & \tilde{\mathcal{Z}}(-\bar{k}_a,-\bar{k}_a)\end{bmatrix}$$
$$\times\begin{bmatrix}\tilde{W}(\bar{k}_1)\\ \tilde{W}(\bar{k}_2)\\ \tilde{W}(\bar{k}_3)\\ \tilde{W}(\bar{k}_4)\\ \tilde{W}(\bar{k}_5)\\ \vdots\\ \tilde{W}(\bar{k}_N)\\ \tilde{W}(\bar{k}_a)\\ \tilde{W}(-\bar{k}_a)\end{bmatrix}=\begin{bmatrix}\tilde{\mathcal{R}}(\bar{k}_1)\\ \tilde{\mathcal{R}}(\bar{k}_2)\\ \tilde{\mathcal{R}}(\bar{k}_3)\\ \tilde{\mathcal{R}}(\bar{k}_4)\\ \tilde{\mathcal{R}}(\bar{k}_5)\\ \vdots\\ \tilde{\mathcal{R}}(\bar{k}_N)\\ \tilde{\mathcal{R}}(\bar{k}_a)\\ \tilde{\mathcal{R}}(-\bar{k}_a)\end{bmatrix}, \tag{18}$$

where

$$\mathscr{K}(\bar{k}_n,\bar{k}_i)=\frac{1}{2\pi}\,w_i\left[\frac{\tilde{Z}_d(\bar{k}_n,\bar{k}_i)}{\tilde{Z}(\bar{k}_i)}-\left(\frac{\tilde{Z}_d(\bar{k}_n,\bar{k}_a)(\bar{k}_i+\bar{k}_a)}{2\bar{k}_a\tilde{g}(\bar{k}_a)(\bar{k}_i^2-\bar{k}_a^2)}+\frac{\tilde{Z}_d(\bar{k}_n,-\bar{k}_a)(\bar{k}_i-\bar{k}_a)}{2(-\bar{k}_a)\tilde{g}(\bar{k}_a)(\bar{k}_i^2-\bar{k}_a^2)}\right)\right], \tag{19}$$

$$\mathscr{Z}(\bar{k}_n,\bar{k}_a)=\frac{j}{2}\,\frac{\tilde{W}(\bar{k}_a)\tilde{Z}_d(\bar{k}_n,\bar{k}_a)}{\bar{k}_a\tilde{g}(\bar{k}_a)}$$

and (20)

$$\mathscr{Z}(\bar{k}_n,-\bar{k}_a)=\frac{j}{2}\,\frac{\tilde{W}(-\bar{k}_a)\tilde{Z}_d(\bar{k}_n,-\bar{k}_a)}{(-k_a)\tilde{g}(k_a)},$$

and

$$\mathscr{R}(\bar{k}_n)=2\,\frac{\tilde{Z}_d(\bar{k}_n,\alpha\,\sin\,\theta)}{\tilde{Z}(\alpha\,\sin\,\theta)}. \tag{21}$$

Equation (18) represents a set of M linear equations which can be solved for the variable $\tilde{W}(\bar{k}_n)$ at the Gauss nodes and the singularities. That is, the solution of the Fredholm integral equation degenerates into a solution of the matrix equation (18). From the solution of the above matrix equation, other values for $\tilde{W}(k)$, apart from those at the Gauss nodes, can be obtained by interpolation. This interpolation process to obtain the value of the function at any value of k is generally referred to as the Nyström interpolation and details on its features and convergence properties can be found in Ref. 5.

From the solution for the spectral domain surface velocity response, the spatial domain response is obtained by inverse Fourier transforming the spectral domain solution. The inverse Fourier transform is performed using the hybrid numerical/analytic techniques,[3] since from Eq. (12) the spectral domain velocity response has singularities at the roots of the dispersion equation.

The normalized scattered pressure ($\tilde{P}_s=\tilde{p}_s/P_0$) is given by combining Eqs. (10) and (12), which after substituting for the spectral domain velocity response is inverse Fourier transformed to obtain the spatial domain scattered pressure. That is, starting from

$$\tilde{P}_s(\bar{k},Y,\omega)=\frac{\epsilon/\alpha}{\sqrt{\alpha^2-\bar{k}^2}}\,e^{jY\sqrt{\alpha^2-\bar{k}^2}}\times\left[-\frac{4\pi\delta(\bar{k}-\alpha\,\sin\,\theta)}{\tilde{Z}(\bar{k})}+\frac{\tilde{W}(\bar{k})}{\tilde{Z}(\bar{k})}\right], \tag{22}$$

the inverse Fourier transform of the first term in the square parenthesis represents the specular component of the scattered pressure,[1] which when combined with the normalized reflected component from Eq. (7), can be written in the form,[1]

$$\tilde{P}_{sp}(X,Y)=R(\theta)e^{j\alpha(X\,\sin\,\theta+Y\,\cos\,\theta)}, \tag{23}$$

where

$$R(\theta)=\frac{\tilde{Z}_s(\alpha\,\sin\,\theta)-\tilde{Z}_a(\alpha\,\sin\,\theta)}{\tilde{Z}_s(\alpha\,\sin\,\theta)+\tilde{Z}_\alpha(\alpha\,\sin\,\theta)}. \tag{24}$$

The inverse Fourier transform of the second term in the square parenthesis is the nonspecular component,

$$P_{sc}(X,Y)=\frac{1}{2\pi}\int_{-\infty}^{\infty}\frac{\epsilon/\alpha}{\sqrt{\alpha^2-\bar{k}^2}}\,\frac{\tilde{W}(\bar{k})}{\tilde{Z}(\bar{k})}\,e^{jY\sqrt{\alpha^2-\bar{k}^2}}e^{j\bar{k}X}\,d\bar{k} \tag{25}$$

for which a numerical or hybrid numerical–analytical inverse Fourier transform has to be used. In Eqs. (23) and (25), X is the normalized distance along the surface of the plate defined by $X=\gamma x$.

III. FAR-FIELD AND NEAR-FIELD SCATTERING

The normalized (with respect to P_0) far-field scattered pressure, neglecting the specular component, can be obtained from Eq. (25) using a stationary phase approximation,[1–3]

$$\tilde{P}_{sc}(R,\phi)f=\frac{\alpha^3}{\epsilon}\,\sqrt{\frac{2}{\pi\alpha R}}\,e^{j(\alpha R-\pi/4)}D(\theta)D(\phi)\times\tilde{Z}_d[\alpha(\sin\,\phi-\sin\,\theta)]-\frac{\alpha}{2\pi}\,\sqrt{\frac{1}{2\pi\alpha R}}\,e^{j(\alpha R-\pi/4)}D(\phi)\times\sum_{i=1}^{N}a_i\,\frac{\tilde{Z}_d(\alpha\,\sin\,\phi-\bar{k}_i)}{\tilde{Z}(\bar{k}_i)}\,\tilde{W}(\bar{k}_i), \tag{26}$$

where

$$D(\theta)=\frac{\cos\,\theta}{[1-(\alpha^2/\epsilon)j\,\cos\,\theta(1-\alpha^4\,\sin^4\,\theta)]}. \tag{27}$$

The near-field scattered pressure is not possible to obtain using a stationary phase approach, hence a solution to the inverse Fourier transform of Eq. (25) is required. The inverse Fourier transform is obtained using the hybrid technique,[3] that is,

$$\tilde{P}_{sc}(X,Y)=\frac{1}{2\pi}\int_{-\infty}^{\infty}\left[\frac{\epsilon/\alpha}{\sqrt{\alpha^2-\bar{k}^2}}\,\frac{\tilde{W}(\bar{k})}{\tilde{Z}(\bar{k})}-\tilde{W}(\alpha)\right]\times e^{j\sqrt{\alpha^2-\bar{k}^2}Y}e^{j\bar{k}X}\,d\bar{k}+\frac{j\alpha Y\tilde{W}(\alpha)}{2\sqrt{X^2+Y^2}}\times H_1^{(1)}[\alpha\sqrt{X^2+Y^2}]. \tag{28}$$

IV. RESULTS

Scattering results are generated for the four distributions, for both mass and stiffness inhomogeneities. The results are presented in the form of contour plots, one for each inhomogeneity type and distribution. The abscissa of these plots represents the angle of scatter while the ordinate represents the normalized frequency, where the maximum frequency considered is five times the critical frequency. The

TABLE I. The characteristics of the inhomogeneity at two selected frequencies.

Ω	α	L	l/λ_s	l/λ_0	$1/(19.8\alpha)$
0.2	0.45	8.85	1.41	0.63	11%
2.0	1.41	28.0	4.46	6.29	4%

extent of the inhomogeneity is 20 times the thickness of the plate, which when nondimensionalized, the extent of the inhomogeneity satisfies the relationship:

$$L=\gamma l=\frac{20h\,\rho\alpha}{\epsilon m'}=19.8\alpha. \tag{29}$$

The characteristics of the inhomogeneity at two selected frequencies are summarized in Table I.

The magnitude of the inhomogeneities is selected such that the following ratios are satisfied:

$$\left[\frac{L\tilde{b}(\bar{k}=0)}{lb'}\right]=1\Rightarrow\left[\frac{\tilde{b}(\bar{k}=0)}{lb'}\right]=\frac{1}{19.8\alpha}, \tag{30}$$

$$\left[\frac{L\tilde{m}(\bar{k}=0)}{lm'}\right]=1\Rightarrow\left[\frac{\tilde{m}(\bar{k}=0)}{lm'}\right]=\frac{1}{19.8\alpha}. \tag{31}$$

Using this representation, the magnitude of the nondimensionalized inhomogeneity changes with frequency and as observed from Table I decreases to about a 4% change at a normalized frequency of 2.0. Figure 4 shows the variation of the extent and normalized magnitude of the inhomogeneity as a function of normalized frequency.

Figure 5 shows the far-field scattering from a mass inhomogeneity for an incidence angle of 45 degrees. This figure has similar features to the scattering results presented in Ref. 1 for normal angle of incidence, mainly that at low frequencies, where the length of the inhomogeneity is less than or on the order of an acoustic wavelength, the inhomogeneity scattered field is nondirective, while at high frequencies a highly directive field with a lobe structure dependent on the smoothness of the distributions at their end points, is observed. At low frequencies, the scattering from each distribution does not significantly vary as one progresses from the uniform distribution to the biquadratic distribution. That

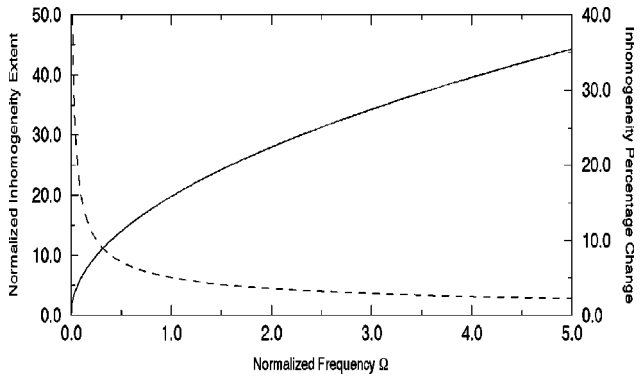

FIG. 4. Variation of the extent and nondimensionalized magnitude (as a percentage of the plate impedance) of the inhomogeneity. ———: Inhomogeneity extent L; – – – –: Ratio (in percent) of total mass or stiffness introduced by inhomogeneity to the plate nominal mass or stiffness within the extent of the inhomogeneity.

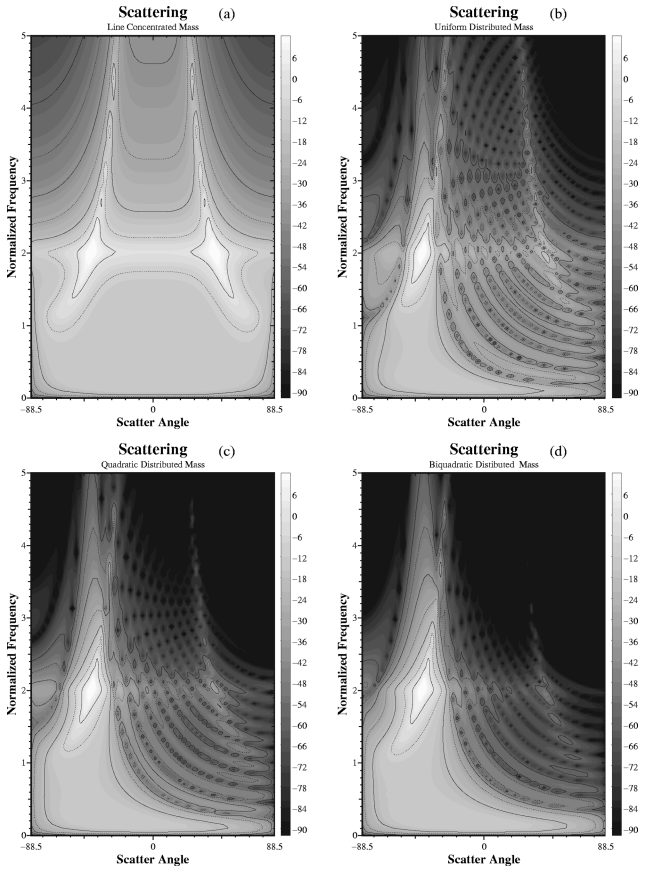

FIG. 5. Bistatic far-field scattering for 45 degree incidence for mass inhomogeneities, (a) line concentrated distribution; (b) uniform distribution; (c) quadratic distribution; (d) biquadratic distribution.

is, smoothness does not seem to play a significant role. However, the scattering is different from that of the concentrated line inhomogeneity. Furthermore, a coincidence peak, characteristic of high frequency radiation from a plate above the critical frequency, is observed, and the amplitude of this peak is enhanced by the less smooth distributions. In fact, the scattering along the coincidence angle is masking some of the features observed in Ref. 1 for normal incidence. As will be shown later, in the monostatic results, for oblique angles of incidence, the peak along the coincidence direction dominates the scattering pattern.

For a stiffness inhomogeneity, and for normal incidence, a stiffness inhomogeneity will not have any scattering strength because of the presence of $\bar{k}^2\bar{k}'^2$ in the distributed impedance term $\tilde{Z}_d(\bar{k},\bar{k}')$. For normal incidence $\theta=0$ and $\alpha\sin\theta=0$. Thus the RHS of Eq. (13), which is the forcing term associated with the inhomogeneity impedance, is equal to zero, resulting in no additional response (apart from that associated with the homogeneous plate) in the behavior of the plate from the presence of the inhomogeneity. The physical interpretation of this result is as follows. At normal incidence the waves induced in the plate originate from the area of the inhomogeneity. Since the inhomogeneity has no inertia associated with it, the response of the plate will follow the excitation. The consequence of this is that no perturbation in the surface response of the plate is induced, apart from the component associated with the response of the homogeneous

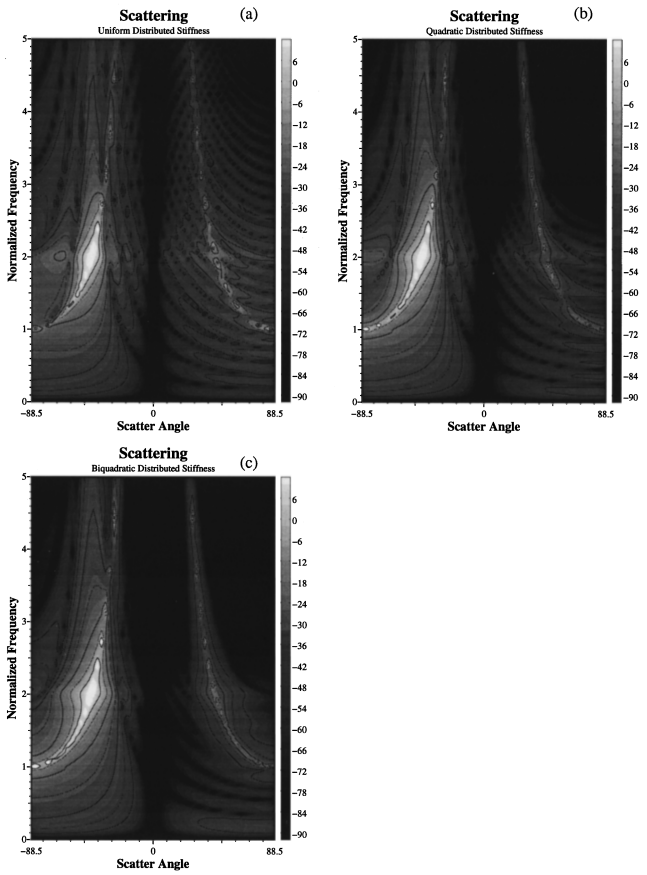

FIG. 6. Bistatic far-field scattering for 45 degree incidence for stiffness inhomogeneities, (a) uniform distribution; (b) quadratic distribution; (c) biquadratic distribution.

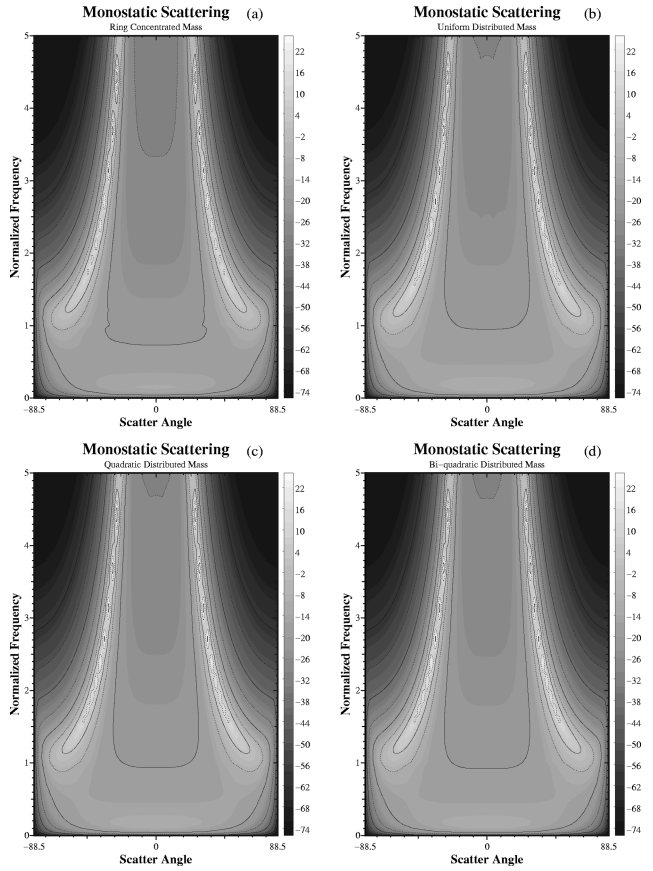

FIG. 7. Monostatic far-field scattering mass inhomogeneities, (a) line concentrated distribution; (b) uniform distribution; (c) quadratic distribution; (d) biquadratic distribution.

plate which has the same trace wave number as the incident wave. This component, part of the specular component [Eq. (23)], is not included in the far-field scattering results. This result is also consistent with the fact that the stiffness inhomogeneity has a quadrupolelike scattering while the mass inhomogeneity has a dipolelike scattering due to the fact that the inertia of the inhomogeneity generates a reaction force on the fluid.

Figure 6 shows the far-field scattering from a stiffness inhomogeneity for a 45 degree incidence angle. In the case of a stiffness inhomogeneity, a concentrated line inhomogeneity does not contribute to the scattering and hence only three scattering plots are shown in Fig. 6, corresponding to the uniform, quadratic, and biquadratic distributions. The quadrupolelike characteristics are clearly evident in these scattering plots, due to the presence of the null in the far-field pressure in the normal direction.

Clearly observable in Fig. 6 is the strong scattering at the coincidence frequency of $\Omega = 2.0$. Because of the null in the scattered pressure, the scattering along the coincidence direction is more evident in this case. At high frequencies, the lobe structure associated with the distribution end smoothness becomes apparent and the scattering becomes more directive, with reduced side lobe levels. Similar to the mass inhomogeneity, at low frequencies, the scattering from each distribution does not significantly vary between distributions.

The significance of the scattering at the coincidence frequency can be seen from the far-field monostatic scattering results shown in Figs. 7 and 8, for, respectively, mass and stiffness inhomogeneities. As can be observed from these figures, above the critical frequency ($\Omega = 1.0$), there is very little difference in the monostatic scattering between mass and stiffness inhomogeneities. There is somewhat of a difference in the normal direction between the different distributions, but this difference is masked by the strong scattering along coincidence. Furthermore, stiffness and mass inhomogeneities are equally strong scatterers for frequencies above the critical frequency. Below the critical frequency, stiffness inhomogeneities are generally weaker scatterers. This is also observable from the near-field scattering results.

Near-field scattering results and velocity response Green's functions are presented for two representative normalized frequencies of 0.2 and 2.0, that is, one below and one above the critical frequency. The black strip along the bottom axis of each of the scattering plots shows the extent but not shape of the inhomogeneity. Figure 9 shows the near-field scattering and response Green's function for the four distributions of a mass inhomogeneity for normal incidence at $\Omega = 0.2$. The response Green's function plots show the magnitude, real, and imaginary components of the velocity response. The inhomogeneity distribution plays a significant role in the shape of the scattering and as the smoothness of the inhomogeneity increases, the closer is the similarity of the scattering pattern to that of a piston in a baffle. The

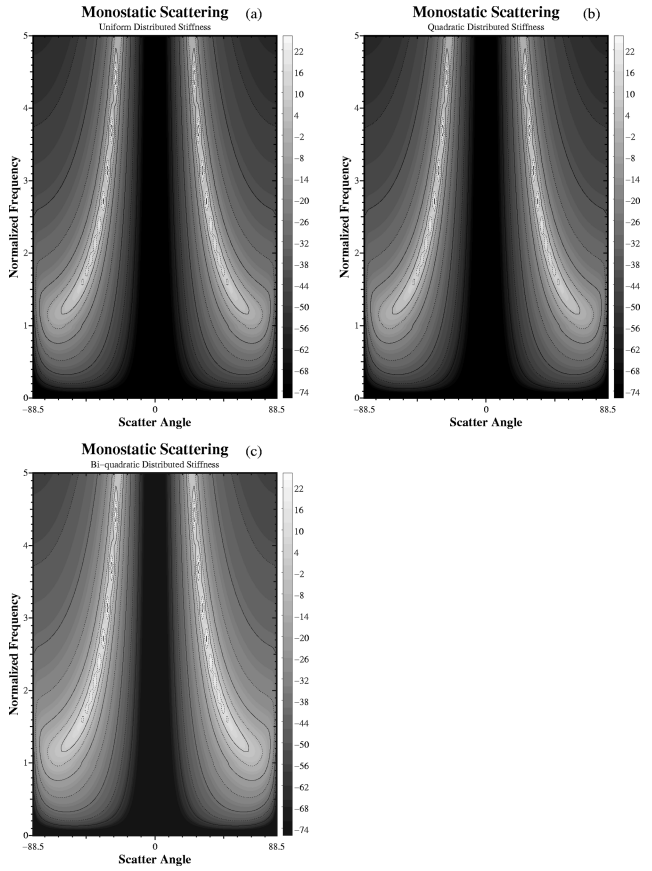

FIG. 8. Monostatic far-field scattering for stiffness inhomogeneities, (a) uniform distribution; (b) quadratic distribution; (c) biquadratic distribution.

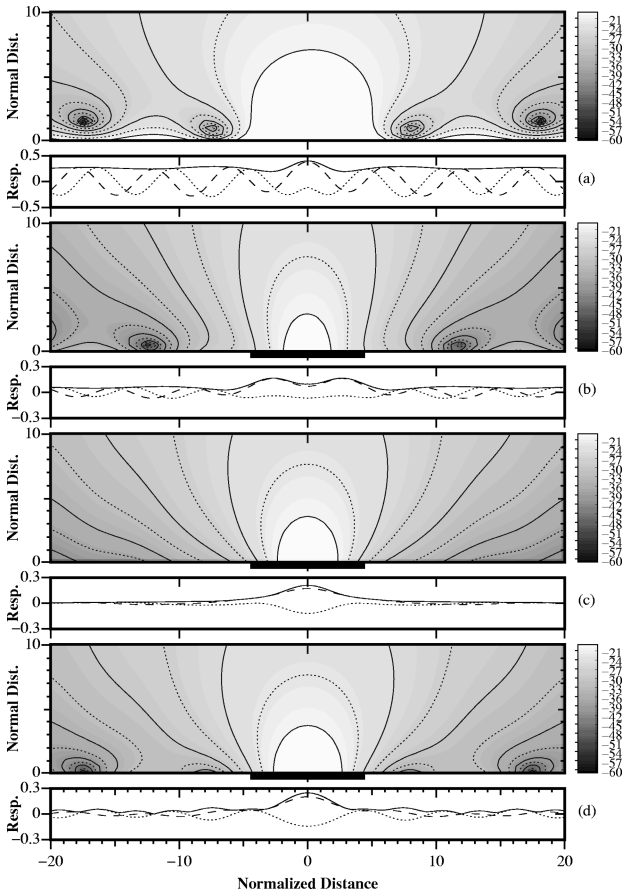

FIG. 9. Bistatic near-field scattering and associated response Green's function for normal incidence for mass inhomogeneities, at a normalized frequency of 0.2. (a) Line concentrated distribution; (b) uniform distribution; (c) quadratic distribution; (d) biquadratic distribution. The response plots show the ———: magnitude; ------: real; and – – – –: imaginary components of the velocity response.

nondirective quality of the scattering can also be observed in these results. Figure 10 shows the near-field scattering and response Green's function for a uniform, quadratic, and biquadratic mass inhomogeneities for a 45 degree angle of incidence for $\Omega = 0.2$. The scattering pattern does not significantly change except that it gets skewed in the direction of the angle of incidence. The dipolelike characteristics are still preserved.

Figure 11 shows the scattering and the response Green's function for the same three distributions as in Fig. 10 but this time for stiffness inhomogeneities. The differences in the scattering and the response patterns between the stiffness and mass inhomogeneities at low frequencies are clearly evident from comparison of Figs. 10 and 11. The far-field null near normal is somewhat masked in the stiffness inhomogeneity results by the near-field scattered pressure contributions. However, one can observe the starting of the null toward the top end ($Y = 10.0$) of the scattering diagram. The much lower scattering strength at low frequencies of the stiffness inhomogeneities, when compared to the mass inhomogeneities, can also be clearly observed.

In Fig. 12 the near-field scattering and velocity Green's function response from a mass inhomogeneity at a frequency of twice the critical frequency ($\Omega = 2.0$) for normal incidence is shown for the four inhomogeneity distributions including the concentrated line inhomogeneity. It should be noted that the scale of the scattering plot for the concentrated line inhomogeneity is 20 dB higher than for the scattering from the other distributions. For a concentrated line inhomogeneity, the scattering along the coincidence direction, which for $\Omega = 2.0$ are at 45 degrees is clearly evident. The increased directivity of the scattering due to the extent of the inhomogeneity which is consistent with the far-field scattering results is also evident for the uniform, quadratic, and biquadratic distributions. The dependency on the smoothness of the ends of the inhomogeneity can be clearly seen in these near-field scattering plots. For the uniform inhomogeneity, the abrupt changes at the inhomogeneity endpoints gives rise to a stationary wave-type pattern, which can be attributed to the predominant influence, hence scattering, from the ends of the inhomogeneity. As the smoothness of the inhomogeneity increases, the scattering becomes less directive, with the associated reduction in the significance of the scattering from the inhomogeneity ends. This is analogous to the radiation from a shaded array, where the increased end smoothness of the shading widens the main lobe but reduces the side lobes.

Figures 13 and 14 show the near-field scattering and response Green's function at a frequency above the critical frequency ($\Omega = 2.0$) for a 45 degree angle of incidence for, respectively, mass and stiffness inhomogeneities. There is not much of a difference between these two scattering patterns, which reinforces the observation made from the analy-

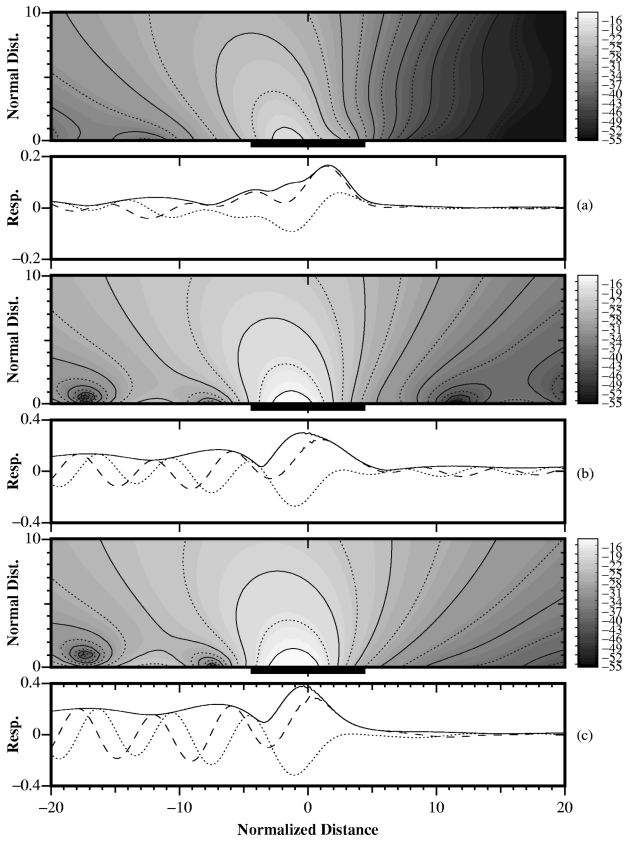

FIG. 10. Bistatic near-field scattering and associated response Green's function for 45 degree incidence for mass inhomogeneities, at a normalized frequency of 0.2. (a) Uniform distribution; (b) quadratic distribution; (c) biquadratic distribution. The response plots show the ———: magnitude; ------: real; and – – – –: imaginary components of the velocity response.

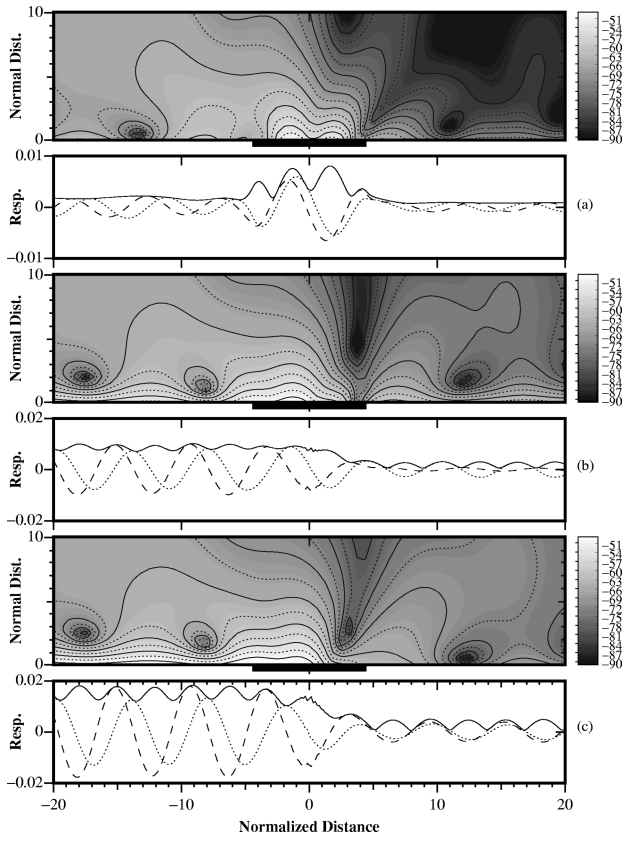

FIG. 11. Bistatic near-field scattering and associated response Green's function for 45 degree incidence for stiffness inhomogeneities, at a normalized frequency of 0.2. (a) Uniform distribution; (b) quadratic distribution; (c) biquadratic distribution. The response plots show the ———: magnitude; ------: real; and – – – –: imaginary components of the velocity response.

sis of the monostatic scattering results. Above the critical frequency, the scattering strength of mass and stiffness inhomogeneities are comparable. Furthermore, the smoothness of the inhomogeneity only plays a role away from the coincidence angle. The scattering pattern is, however, dominated by the scattering along the coincidence direction and therefore for oblique incidence the smoothness of the inhomogeneity ends plays only a minor role, unlike for normal incidence.

V. CONCLUSION

A full numerical solution has been obtained for the response and near-field and far-field scattering from a fluid-loaded plate with a distributed mass or stiffness inhomogeneity. The distributions considered for the mass inhomogeneity are concentrated line, uniform, quadratic, and biquadratic. For the stiffness inhomogeneity, the concentrated line distribution is not considered since this type of inhomogeneity distribution has no scattering strength. Far-field bistatic scattering results are presented for a 45 degree incidence angle, together with monostatic far-field scattering. Furthermore, near-field scattering for normal and 45 degree incidence are also presented.

The scattering results show that for both types of inhomogeneities, the scale of the inhomogeneity is not very important when the extent of the inhomogeneity is much less than an acoustic wavelength. However, when the extent of the inhomogeneity is larger than an acoustic wavelength, the shape of the inhomogeneity distribution becomes significant. Also, for normal incidence, only the distributed mass inhomogeneity contributes to the scattering. Distributed stiffness inhomogeneities do not induce any forces on the fluid-loaded plate structure, resulting in no scattered waves. For oblique angles of incidence, both mass and stiffness inhomogeneities generate a scattered acoustic field. The mass inhomogeneities generate a dipolelike acoustic scattering pattern, while the stiffness inhomogeneities generate a quadrupolelike scattering pattern. In general, for frequencies below the critical frequency, the stiffness inhomogeneities are weaker scatterers compared to the mass inhomogeneities, while above the critical frequency both types of inhomogeneities have similar scattering strength. The relative scattering strength between mass and stiffness inhomogeneities have also been considered by Steinberg and McCoy.[7,8] In their work they consider the influence of microstructure within the inhomogeneity. In the absence of the microstructure within the macrostructure of the inhomogeneities, their conclusion that a mass inhomogeneity is generally a stronger scatterer when compared to a stiffness inhomogeneity agrees with the results obtained here.

At low frequencies, the scattering from the mass inhomogeneities decreases with increased smoothness, while the

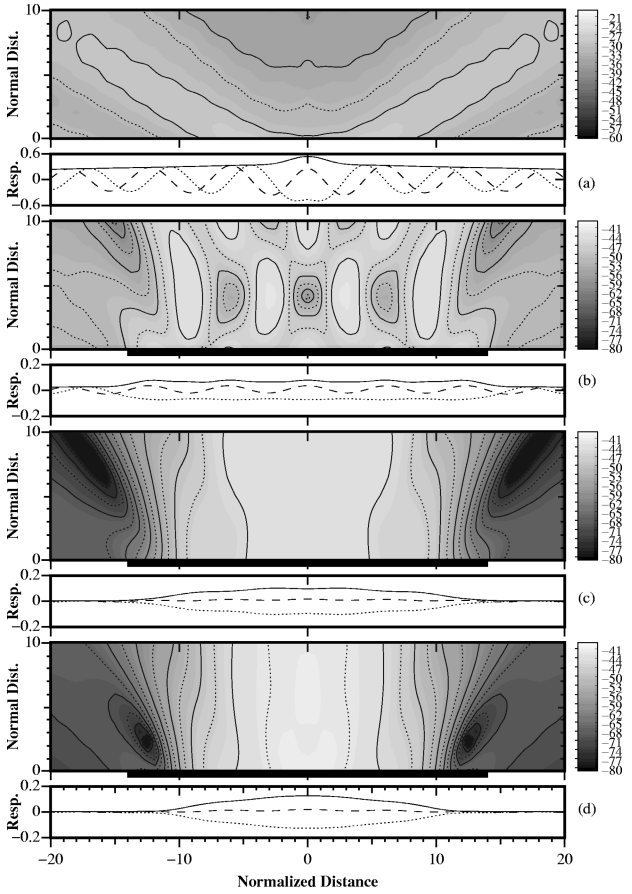

FIG. 12. Bistatic near-field scattering and associated response Green's function for normal incidence for mass inhomogeneities, at a normalized frequency of 2.0. (a) Line concentrated distribution; (b) uniform distribution; (c) quadratic distribution; (d) biquadratic distribution. The response plots show the ———: magnitude; ------: real; and – – – –: imaginary components of the velocity response.

scattering from the stiffness inhomogeneities is predominantly at grazing angles, with most of the scattering propagating close to the plate surface. At high frequencies the scattering mainly occurs from the edges of the inhomogeneities. The scattering from either the stiffness or mass inhomogeneities are very similar and the scattering increases with decreased smoothness.

Regarding directivity, at very low frequencies and for angles of incidence other than normal, both the far-field and near-field scattering patterns are generally nondirective, that is, the scattering is not along any specific scattering angle. Inhomogeneity end ''smoothness'' in this case plays only a minor role in the directivity of the scattered field, with increased smoothness resulting in somewhat less directionality. This result has also been observed in Ref. 1 and in the near-field scattering for normal incidence. As the frequency increases, but still below the critical frequency, the near- and far-field scattering are slanted toward the angle of incidence. At high frequencies (above the critical frequency) and oblique incidence, the far-field scattering, for both the mass and stiffness inhomogeneities, is predominantly along the coincidence angles. This is different from the results obtained in Ref. 1 for normal incidence, where the predominant direction of far-field scattering was in the normal direction, along the incidence angle. The near-field scattering results are for an incidence angle of 45 degrees and a normalized frequency of 2.0, which corresponds to a coincidence angle of 45 degrees. Hence, for these results the incidence and scattering angle are the same. Furthermore, the near-field scattering from both mass and stiffness inhomogeneities predominantly comes from the discontinuities at the ends of the inhomogeneity. Apart from the scattering along the coincidence angle, the far-field scattering has a lobe structure which is dependent on the end point ''smoothness'' of the inhomogeneity

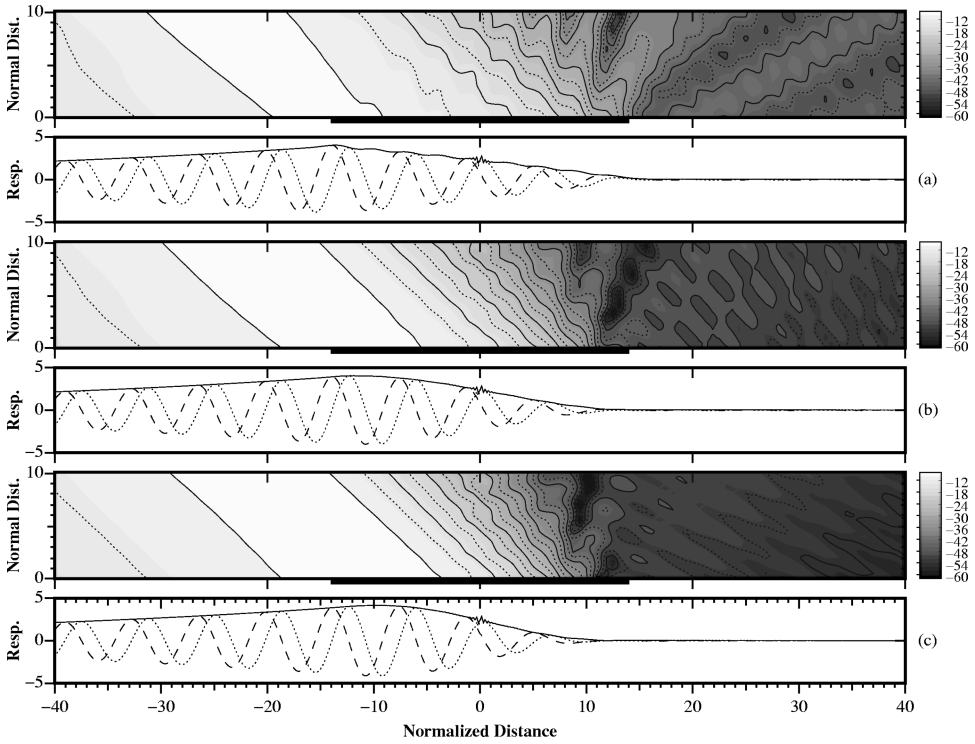

FIG. 13. Bistatic near-field scattering and associated response Green's function for 45 degree incidence for mass inhomogeneities, at a normalized frequency of 2.0. (a) Uniform distribution; (b) quadratic distribution; (c) biquadratic distribution. The response plots show the ———: magnitude; ------: real; and – – – –: imaginary components of the velocity response.

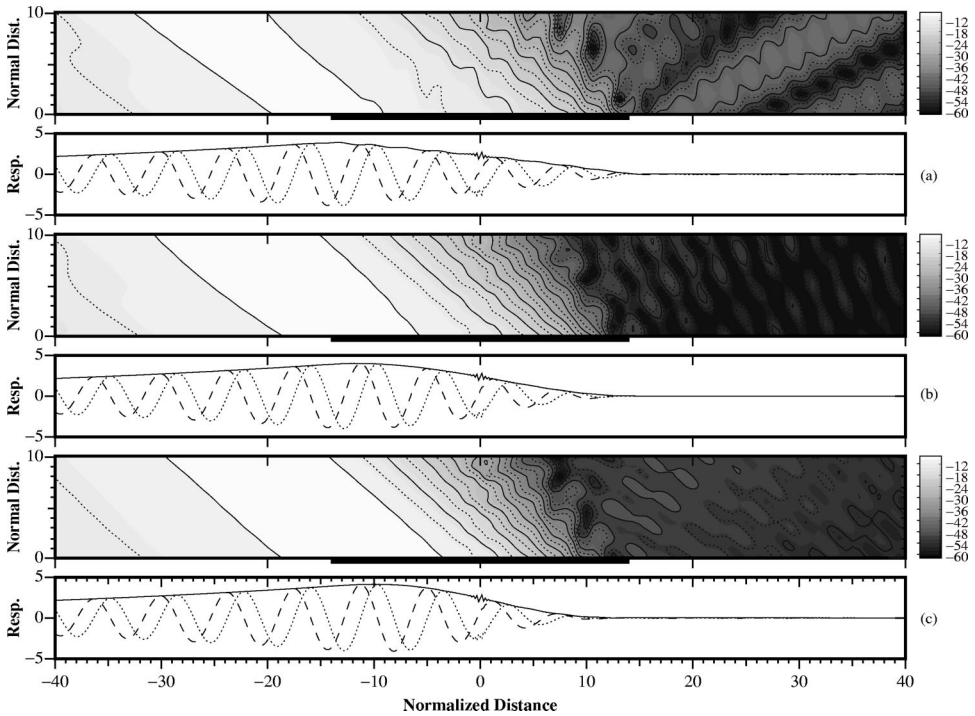

FIG. 14. Bistatic near-field scattering and associated response Green's function for 45 degree incidence for stiffness inhomogeneities, at a normalized frequency of 2.0. (a) Uniform distribution; (b) quadratic distribution; (c) biquadratic distribution. The response plots show the ———: magnitude; ------: real; and – – – –: imaginary components of the velocity response.

distribution. This lobe structure, and its dependence on the inhomogeneity distribution smoothness, was also observed in Ref. 1 for normal incidence. The near-field scattering from the uniform mass inhomogeneity, for normal incidence, exhibits a form of a standing wave pattern within the region of the inhomogeneity. This is attributed to the sharp terminations of the uniform inhomogeneity distribution, and is related to the strong lobe structure of the far-field scattering.[1]

ACKNOWLEDGMENTS

The authors would like to acknowledge the U.S. Office of Naval Research, Code 34, for the support of this work. The authors would also like to acknowledge Dr. A. Tucker who motivated this work through his questions regarding the scattering from distributed structural inhomogeneities.

[1] D. Feit and J. M. Cuschieri, ''Scattering of sound by a fluid-loaded plate with a distributed mass inhomogeneity,'' J. Acoust. Soc. Am. **99**, 2686–2700 (1996).
[2] M. C. Junger and D. Feit, *Sound, Structures, and Their Interaction*, 2nd ed. (MIT, Cambridge, MA, 1986).
[3] J. M. Cuschieri and D. Feit, ''A hybrid numerical analytical solution for the Green's function of a fluid-loaded elastic plate,'' J. Acoust. Soc. Am. **95**, 1998–2005 (1994).
[4] D. G. Crighton, ''Approximations to the admittances and free wave numbers of fluid-loaded panels,'' J. Sound Vib. **68**, 15–33 (1980).
[5] K. E. Atkinson, *A Survey of Numerical Methods for the Solution of Fredholm Integral Equations of the Second Kind* (SIAM, Philadelphia, 1976).
[6] L. M. Delves and J. L. Mohamed, *Computational Methods for Integral Equations* (Cambridge U.P., Cambridge, MA, 1985).
[7] B. Z. Steinberg and J. J. McCoy, ''Toward local effective parameter theories using multiresolution decomposition,'' J. Acoust. Soc. Am. **96**, 1130–1143 (1994).
[8] B. Z. Steinberg and J. J. McCoy, ''Effective measures for nonstationary microscale stiffness variation using multiresolution decomposition,'' J. Acoust. Soc. Am. **96**, 1130–1143 (1994).

Structural-acoustic control system design by multi-level optimization

Héctor M. Rodríguez
Department of General Engineering, University of Puerto Rico, Mayagüez Campus, Mayagüez, Puerto Rico 00681-9044

Ricardo A. Burdisso
Vibration and Acoustics Laboratories, Department of Mechanical Engineering, Virginia Polytechnic Institute and State University, Blacksburg, Virginia 24061-0238

(Received 29 August 1997; accepted for publication 2 April 1998)

A multi-level optimization approach for the design of feedforward active structural acoustic control (ASAC) systems is presented. The formulation takes advantage that both the structural response and the acoustic radiation from a controlled structure can be completely defined in the modal domain. All the physical parameters that define the control inputs and the error sensors are defined in the modal domain in terms of the unit modal control forces and the modal error sensor components, respectively. The upper level of the optimization solves for the optimum modal parameters that minimize the total radiated acoustic power. Then, these optimum modal parameters are used in a set of lower level or physical domain optimization problems to determine the physical characteristics of the actuators and sensors to be implemented. Since the response of the system is evaluated in the upper level using a modal approach, the formulation permits the implementation of numerical techniques and/or experimental data during the design process. Therefore, the proposed methodology can be used for the design of control systems for realistic structures with complex disturbances in an efficient manner. The design formulation is illustrated for the case of a simply supported plate excited by an off-resonance disturbance.
[S0001-4966(98)03707-2]

PACS numbers: 43.40.Vn [PJR]

INTRODUCTION

An approach for the attenuation of structurally radiated noise consists in modifying the vibration behavior of the structure by applying control force inputs directly to the structure. This technique is known as Active Structural Acoustic Control (ASAC) and was first introduced by Fuller.[1] The combination of this technique in conjunction with new developments in specialized actuators and sensor materials have permitted the implementation of the concept of ''smart'' or adaptive systems where the transducers being an integral part of the structure. At present, such advanced control systems have been successfully implemented to control sound radiation from plates and cylinders; sound transmission/radiation from single and double panels; and interior noise from cylindrical structures among others.[2]

Although the concept of ASAC systems along with ''smart'' structures has been successfully tested, the design aspects of such systems is still under much investigation. A formal optimization approach in ASAC implementations was first introduced by Wang and co-workers.[3] This investigation consisted in the direct optimization of the location of rectangular piezoelectric (PZT) actuators to minimize the sound radiation from a simply supported plate. The results demonstrated that optimally located actuators provided a far better sound reduction, at both on- and off-resonance excitations, than actuators whose position were chosen based in some physical consideration. More recently, other optimum design approaches for structural-acoustic control systems have been proposed such as using subset selection techniques,[4] cluster analyses,[5] eigenproperty assignments,[6] and genetic algorithms.[7] These previous works have demonstrated that optimally designed actuators and sensors can have a significant impact on the performance of active control systems to reduce both sound radiation and acoustic fields inside enclosures. They have shown that significant levels of attenuation can be obtained with far fewer optimally located transducers, thus reducing the dimensionality and complexity of the control system. However, there are still limitations that prevent the same approaches from being implemented in the design of complex realistic structures.

For the case of minimizing sound radiation from complex structures, the design approach of ASAC systems is virtually nonexistent. In most of the previous optimization approaches, the design formulation consisted of using a nonlinear optimization algorithm to minimize an expression related to the total radiated acoustic power as a function of the physical characteristics (i.e., location, size, etc.) of the actuators and sensors. The main problem with this straightforward approach is that the computation of the acoustic response for complex structural systems as a function of the physical characteristics of the actuators and sensors results in a computationally expensive procedure.

In this work an efficient formulation for the design of feedforward ASAC systems to suppress acoustic radiation from complex structural systems under light fluid loading (i.e., no acoustic feedback) is presented. The approach consists in a two-stage multi-level optimization scheme. The for-

mulation takes advantage of the fact that both the structural response and the acoustic radiation from a controlled structure can be completely defined in terms of modal quantities. All the physical parameters that define the control inputs and the error sensors have their counterpart in the modal domain through the unit modal control forces and the modal error sensor components, respectively. Therefore, the upper level of the optimization is defined in the modal domain and solves for the optimum unit modal control forces and modal error sensor components that minimize the total radiated power. Then, these optimum modal parameters are used in a set of lower level optimization problems to determine the physical characteristics of the actuators and sensors to be implemented. Since in the formulation the response is evaluated in the upper level or modal domain, it permits the implementation of numerical techniques and/or experimental data during the design process. In addition, since the upper level optimization problem is universal for any type of structure/transducer combination, a previously developed general analytical sensitivity formulation[8] is implemented to improve the performance of the optimization algorithm during the solution process. Therefore, the formulation is capable to handle complex structures with complex disturbances (e.g., multiple frequencies) in an efficient manner. Once the optimum modal parameters are obtained, different types of transducers can be investigated with a minimum computational effort. The proposed approach is illustrated for the case of a simply supported plate excited by an off-resonance disturbance. The study of a plate will serve as a benchmark to implement the design methodology for more complex systems.

I. STRUCTURAL-ACOUSTIC RESPONSE

A. Structural response

The response of a structure can be obtained by modal superposition once the eigenproperties of the system (i.e., natural frequencies and mode shapes) are known. These eigenproperties can be estimated using numerical techniques such as the finite element method (FEM) or experimentally using modal analysis techniques. For the case of sound radiation from structures submerged in light fluids such as air, it is necessary to consider only the vibration in which the response normal to the radiating surface is dominant.[9] The Fourier transform (FT) of the response in the direction normal to the structural surface can be obtained as a linear combination of the modes as

$$w(\mathbf{r}_s,\omega)=\sum_{n=1}^{N} q_n(\omega)\phi_n(\mathbf{r}_s) = \sum_{n=1}^{N} F(\omega) f_n H_n(\omega)\phi_n(\mathbf{r}_s), \tag{1}$$

where ω is the excitation frequency, $\phi_n(\mathbf{r}_s)$ is the nth mode shape, N is the total number of modes included in the analysis, $\mathbf{r}_s$ is a point on the structure, and $q_n(\omega) = F(\omega) f_n H_n(\omega)$ is the FT of the nth modal displacement where $F(\omega)$ is the amplitude of the external excitation and f_n is the nth unit modal force defined as

$$f_n=\int_S \phi_n(\mathbf{r}_s) f(\mathbf{r}_s)\, dS, \tag{2}$$

where the integral is extended over the structural domain S and $f(\mathbf{r}_s)$ is a function that defines the spatial distribution of the excitation. Finally, $H_n(\omega)$ is the nth modal frequency response function defined as $H_n(\omega)=(\omega_n^2-\omega^2+2j\beta_n\omega_n\omega)^{-1}$, where j is the imaginary number and β_n is the nth modal damping ratio.

B. Acoustic response

The acoustic radiation $p(\mathbf{r},\omega)$ from a harmonically vibrating structure can be obtained after solving the Helmholtz wave equation[10]

$$\nabla^2 p(\mathbf{r},\omega)+k^2 p(\mathbf{r},\omega)=0 \tag{3}$$

in conjunction with the boundary conditions

$$\nabla p(\mathbf{r}_s,\omega)=\omega^2\rho w(\mathbf{r}_s,\omega) \tag{4a}$$

and

$$\lim_{|\mathbf{r}|\to\infty} p(\mathbf{r},\omega)\to 0, \tag{4b}$$

where $\mathbf{r}$ is a field point location; $\nabla(.)$ is the Laplacian operator; $k=\omega/c$ is the acoustic wave number; and c and ρ are the phase speed and density in the fluid that surrounds the structure, respectively. Equation (4a) relates the structural response with the acoustic pressure at the structural surface while Eq. (4b) represents the Sommerfeld far-field condition that requires that the acoustic pressure decreases as the field point is moved away from the structure. Equations (3) and (4) do not possess closed-form solution for any but very simple cases. For the case of structures with complex geometries, they are solved using numerical techniques such as the boundary element method (BEM).[11]

The strategy in this work is to obtain the acoustic response by considering the contributions of each of the structural modes separately. By substituting the modal expansion in Eq. (1) into Eq. (4), the acoustic pressure field can be obtained as a linear contribution of the structural modes as

$$p(\mathbf{r},\omega)=\sum_{n=1}^{N} q_n(\omega) p_n(\mathbf{r},\omega), \tag{5}$$

where $p_n(\mathbf{r},\omega)$ is the acoustic pressure at $\mathbf{r}$ due to the nth mode shape, i.e., modal pressure.

The total acoustic radiated power can be estimated by integrating the far-field acoustic intensity over a sphere of surface area A that surrounds the structure as

$$\Pi(\omega)=\int_A \frac{|p(\mathbf{r},w)|^2}{2\rho c}\, dA. \tag{6}$$

Replacing Eq. (5) into Eq. (6), the acoustic power can be written in a general quadratic form as

$$\Pi(\omega)=\sum_{n=1}^{N}\sum_{m=1}^{N} q_n(\omega)q_m^*(\omega)\int_A \frac{p_n(r,\omega)p_m^*(r,\omega)}{2\rho c}dA$$

$$=\{q(\omega)\}^H[K(\omega)]\{q(\omega)\}, \tag{7}$$

where the superscripts (*) and H imply complex conjugate and conjugate transpose, respectively; and the elements of matrix $[K(\omega)]$ are given by the integral in Eq. (7).

The diagonal elements of the matrix $[K(\omega)]$ represent the power radiated due to the direct contributions of the modes, while the off-diagonal terms contain the power radiated due to the coupling of the modes. In particular, the off-diagonal terms could be either positive or negative depending if the interaction between the modes is constructive or destructive. For the case of complex structures, this matrix has to be evaluated by numerical techniques and therefore represents the highest computational effort during the evaluation of the acoustic response. Finally, $\{q(\omega)\}$ is the vector of modal displacements.

Equation (7) defines the total radiated power at a single frequency. The general case of multiple frequency excitations is expressed as a linear combination of the contributions due to each frequency as

$$\Pi_T(\omega)=\sum_{i=1}^{N_F}(\{q(\omega_i)\}^H[K(\omega_i)]\{q(\omega_i)\})=\sum_{i=1}^{N_F}\Pi(\omega_i), \tag{8}$$

where N_F is the total number of frequencies.

Inspection of Eqs. (7) and (8) show that the relative contributions to the acoustic power due to the modes depend on two factors: the complex amplitudes of the modal displacements $\{q(\omega_i)\}$ and the relative values of the modal power matrices $[K(\omega_i)]$. The modal displacements $\{q(\omega_i)\}$ depend on the dynamics of the structure under a particular disturbance $F(\omega)$. In the same way, the matrices $[K(\omega_i)]$ depend on the capacity of the structural modes to generate sound and their coupling characteristics. For a mode excited on-resonance, its modal displacement will be significantly larger than the other ones and therefore this mode will most likely dominate the acoustic field. On the other hand, at off-resonance conditions the acoustic field will probably be mainly due to the radiation of the modes with the higher radiation efficiency.

C. Optimum feedforward control inputs

Equation (1) represents the steady-state or frequency domain structural response due to an external disturbance $F(\omega)$. The response due to this disturbance can be controlled by applying N_c secondary control forces $U_k(\omega)$ where $k=1,...,N_c$. The response of the controlled system can be expressed as[6]

$$w^c(\mathbf{r}_s,\omega)=\sum_{n=1}^{N} q_n^c(\omega)\phi_n(\mathbf{r}_s), \tag{9}$$

where, using the principle of superposition, the nth modal displacement of the controlled system is

$$q_n^c(\omega)=q_n(\omega)+H_n(\omega)\sum_{k=1}^{N_c} U_k(\omega)u_{nk}, \tag{10}$$

where $U_k(\omega)$ and u_{nk} are the amplitude and the nth unit modal control force of the kth control input, respectively. As can be seen in Eq. (10), the unit modal control forces u_{nk} dictate the relative *controllability* of the different modes by the control inputs $U_k(\omega)$. Similarly to the unit modal disturbances, the unit modal control forces are given as

$$u_{nk}=\int_S \phi_n(\mathbf{r}_s)u_k(\mathbf{r}_s)dS, \tag{11}$$

where $u_k(\mathbf{r}_s)$ defines the spatial distribution of the control forces. Similar to the unit modal disturbances, the unit modal control forces depend completely on the physical implementation of the actuators, e.g., shakers, PZT ceramics, etc.

In feedforward control, the complex amplitude of the control inputs $U_k(\omega)$ are obtained by ''feeding forward'' a reference signal $x(\omega)$, fully coherent to the original disturbance $F(\omega)$, through an array of compensators. The compensators are designed such that a measurable control cost function is minimized. This cost function is usually obtained as the sum of the mean-square-value (msv) of the response at the error sensors as

$$J=\sum_{s=1}^{N_s}|E_s(\omega)|^2, \tag{12}$$

where $E_s(\omega)$ is the FT of the response due to the sth error sensor output and N_s is the total number of error outputs.

In ASAC applications, the error signals could be obtained by measuring directly the acoustic field using microphones or the structural vibration using structural sensors. In many applications the use of far-field microphones as error sensors is not practical. Since one of the objectives in this work is to eliminate the need for the use of microphones and design a completely adaptive system with the actuators and sensors integrated to the structure, only structural sensors are considered here. For the case of such sensors, the response can always be expressed as a linear combination of modal terms as[6]

$$E_s(\omega)=\sum_{n=1}^{N} q_n^c(\omega)\xi_{ns}, \tag{13}$$

where ξ_{ns} is the nth modal component of the sth error sensor. Again, the modal error components are related to the physical implementation of the sensors and they dictate the relative *observability* of the different modes

By differentiating Eq. (13) with respect to the real and imaginary part of the control inputs $U_k(\omega)$ and setting them to zero, it can be shown that the set of the optimum control inputs is the solution of the following linear system of equations

$$[T_{ce}(\omega)]\{U(\omega)\}=-F(\omega)\{T_{de}(\omega)\}, \tag{14}$$

where vector $\{U_k(\omega)\}$ contains the N_c control inputs, the elements of matrix $[T_{ce}(\omega)]$ are the transfer functions be-

tween the control inputs and the error outputs and the elements of vector $\{T_{de}(\omega)\}$ contain the transfer functions between the disturbances and the error outputs.

Once the optimum feedforward control inputs $U_k(\omega)$ are obtained from the solution of Eq. (14) they are substituted into Eq. (10) to compute the modal displacements of the controlled system $q_n^c(\omega)$. Finally, the controlled modal displacements can be substituted for the uncontrolled modal displacements in Eq. (7) to yield the total radiated power of the controlled system as

$$\Pi^c(\omega)=\{q^c(\omega)\}^H[K(\omega)]\{q^c(\omega)\}, \tag{15}$$

where $\{q^c(\omega)\}$ is the vector of controlled modal displacements. In the same way, the total controlled radiated power due to the contribution of N_F frequencies is given as

$$\Pi_T^c(\omega)=\sum_{i=1}^{N_F}(\{q^c(\omega_i)\}^H[K(\omega_i)]\{q^c(\omega_i)\}) = \sum_{i=1}^{N_F}\Pi^c(\omega_i). \tag{16}$$

Equation (16) describes the acoustic response of a feedforward controlled structure. This equation clearly shows the advantage of evaluating the response as a combination of modal contributions, especially in terms of the computational effort. This advantage is specially critical during the design of the control system. This design procedure involves a systematic update of the physical characteristics of the transducers (i.e., type, size, number, location, etc.) and the evaluation of the acoustic response for each configuration. This process is continued until the desired attenuation is obtained. Using Eq. (16), the evaluation of the acoustic response is just a matter of simple algebraic manipulations once the elements of matrices $[K(\omega_i)]$ are known.

II. CONTROL SYSTEM DESIGN BY MULTI-LEVEL OPTIMIZATION

As shown in Eq. (16), the total radiated power from the controlled system is a function of the forces $U_k(\omega)$ which in turn are defined from the modal characteristics of the uncontrolled system, i.e., $F(\omega)f_n$ and $H_n(\omega)$, and of the actuators and sensors, i.e., u_{nk} and ξ_{ns}. The unit modal control forces u_{nk} and modal error sensor components ξ_{ns} are directly related to the physical implementation of the actuators and sensors, respectively. Therefore, the design of the control system consists in finding the transducers that, when implemented, yield the proper unit modal control forces u_{nk} and modal error sensor components ξ_{ns}. The significance of the unit modal control forces and the modal error sensor components in the response of the controlled system is that they represent the relative *controllability* and *observability* of the modes by the control actuators and the error sensors, respectively. Regardless of the type of actuators and sensors, the unit modal control forces and the modal error sensor components play the role of weighting coefficients that can be normalized between ± 1.

The fact that the response of the controlled system can be obtained without the knowledge of the physical characteristics of the transducers but from their effect on the different modes brings out the opportunity of designing the control system using a multi-level optimization approach. In multilevel optimization a complex problem is broken into a set of simpler problems that offers computational advantages. The process of decomposition consists of separating the optimization process in an upper level problem, in which a global cost function is minimized with respect to global design variables, and a set of lower level problems, in which a set of local design variables are related to all the global design variables or a subset of them. The upper level or modal domain optimization consists in finding the optimum unit modal control forces and modal error sensor components that minimize the total radiated acoustic power. Therefore, at the upper level optimization, the global cost function is the total radiated acoustic power as presented in Eq. (16) and the global design variables are the modal quantities u_{nk} and ξ_{ns}. Once the optimum modal parameters are obtained, a set of lower level or physical domain optimization problems can be solved in which the actuators and sensors that yield the optimum unit modal control forces u_{nk} and modal error sensor components ξ_{ns} are obtained. Therefore, the local design variables at the lower level are the physical parameters that define the actuators and sensors, i.e., number, size, location, etc., while the local cost functions are the sum of the squares of the differences between the optimum modal quantities and the ''actual'' modal parameters due to the implementation of a particular transducer. The outcome of this procedure is an optimally designed control system.

The main advantages of the proposed design approach can be listed as:

(1) The design process is broken into the solution of two simple problems. The modal domain or upper optimization problem consists in the minimization of a continuous function of the modal control parameters. On the other hand, the physical domain or lower level formulations consist in a set of much simpler problems that involves matching the ''actual'' modal parameters of the transducers as closely as possible to the ''ideal'' modal parameters. The simplicity in the solution in this two-level approach should be contrasted to the difficulty in solving a straightforward optimization problem in which the acoustic response is directly expressed in terms of the physical characteristics of the transducers.

(2) Since the upper level is solved in the modal domain, the formulation is applicable to the design of any complex structure modeled using FEM/BEM codes or using experimental modal analysis data. The highest computational effort at this level is in computing the matrices $[K(\omega_i)]$ using Eq. (7). The computation of these matrices has to be carried out only once for each disturbance frequency during the design process.

(3) Since the modal domain is universal for any type of structure, a sensitivity analysis of the cost function and the constraints can be developed in this stage. The use of

analytical sensitivities instead of numerical approximations greatly improves the performance of optimization algorithms.[8]

(4) Since the response of the controlled system is completely defined in the modal domain, the upper level formulation can be used to investigate and evaluate the performance of different control system configurations. At this level, the designer can decide with relative ease the required number of control inputs N_c and error outputs N_s that are necessary to obtain a desired attenuation.

(5) Since the design of the transducers to be implemented in the control system is carried out after solving simple sets of optimization problems, different models of actuators and sensors can be easily investigated at the lower level without the need to recompute the response of the structure.

A. Upper level or modal domain optimization

The modal domain or upper level optimization problem is posed as follows:

$$\text{Min } R(u_{nk},\xi_{ns})=\frac{\Pi_T^c(\omega)}{\Pi_T(\omega)} \tag{17a}$$

such that

$$g_m^c(u_{nk},\xi_{ns})=\sum_{n=1}^{N}\frac{|U_k(u_{nk},\xi_{ns},\omega_i)\cdot u_{nk}|^2}{|F(\omega_i)\cdot f_n|^2}\leqslant\lambda_m,$$

$$i=1,...,N_F \quad m=N_c\times N_F \tag{17b}$$

$$g_k^n(u_{nk})=\sum_{n=1}^{N}u_{nk}^2=1, \quad k=1,...,N_c \tag{17c}$$

$$g_s^{\xi}(\xi_{ns})=\sum_{n=1}^{N}\xi_{ns}^2=1, \quad s=1,...,N_s. \tag{17d}$$

The optimization problem stated in Eq. (17) seeks to minimize the ratio $R(u_{nk},\xi_{ns})$ of the total radiated power of the controlled system $\Pi_T^c(\omega)$ to the total radiated power of the uncontrolled system $\Pi_T(\omega)$. The inequality constraints in Eq. (17b) impose restrictions on the effort, through the penalty parameter λ_m. By setting the penalty parameter λ_m to less than one, Eq. (17b) implies that the modulus square of each one of the modal control forces, $|U_k(\omega_i)u_{nk}|^2$, will be in a weighted average sense less than the modulus square of the modal disturbances, $|F(\omega_i)f_n|^2$. Therefore, by satisfying these constraints the control force applied to each mode will be less than the modal force due to the disturbance. There is an inequality constraint of this type for each one of the N_c control inputs at each one of the N_F frequencies. It is important to mention that the constraints in the control effort Eq. (17b) could also be implemented as a penalty in the cost function. Finally, the equality constraints in Eqs. (17c), (17d) imply a normalization of the design variables since the only relevant information is their relative values, which defines the relative *controllability* and *observability* of the modes, respectively. This continuous optimization problem in the upper level or modal domain can be solved by any constrained optimization algorithm in conjunction with previously developed analytical sensitivity formulations.[8]

B. Lower level or physical domain optimization

Once the optimum modal parameters are obtained they are used as goals to reach in a set of physical domain optimization problems. The purpose of the optimization problems at this level is to find the physical characteristics of the desired actuators and sensors that when implemented in the real structure induce unit modal control forces and modal error sensor components as close as possible to the optimum values obtained from the upper level optimization. For the sake of clarity, from now on the optimum modal parameters obtained in the upper level are denoted as ''ideal'' while the modal parameters of the physical transducers are denoted as ''actual.'' The ''actual'' modal parameters are functions of the physical design parameters of the transducers such as type, location, dimensions, etc. Hence, the first requirement at this level is to have mechanical models for the transducers that relate the modal parameters to the physical design variables. In addition, a single control input (error output) can be implemented using multiple actuators (sensors) wired in- or out-of-phase. Therefore, the cost functions at this level are a measure of the difference between the ''ideal'' and ''actual'' modal parameters while the design variables are the physical characteristics of the implementation of the transducers (i.e., size, location, relative phases, etc.).

1. Optimum actuator design

The set of lower level or physical domain optimization problems to obtain the optimum physical design parameters $\{a\}$ for the control actuators can be expressed in formal optimization notation as

$$\min C_k(\{a\})=\sum_{n=1}^{N}|u_{nk}-\hat{\Psi}_{nk}(\{a\})|^2, \tag{18}$$

where the cost function $C_k(\{a\})$ represents a measure of the error between the ''ideal'' optimum unit modal control forces u_{nk} and the ''actual'' unit modal control forces given by the function $\hat{\Psi}_{nk}(\{a\})$ for the kth control input. Then, the nth component of the ''actual'' unit modal control force $\hat{\Psi}_{nk}(\{a\})$ driven by the kth control signal is obtained by including the contributions of all the nth unit modal forces produced by each one of the N_A actuators as

$$\hat{\Psi}_{nk}(\{a\})=\sum_{i=1}^{N_A}\Psi_{ni}(\{a\}_i), \tag{19}$$

where $\Psi_{ni}(\{a\}_i)$ is the mechanical model that defines the nth unit modal force produced by the ith actuator and vector $\{a\}_i$ contains the design variables for the ith actuator.

2. Optimum sensor design

Similarly, the set of lower level or physical domain optimization problems to obtain the optimum physical design parameters for the error sensors can be expressed as

TABLE I. Modal properties of simply supported plate and modal control components.

Mode (n_x, n_y)	Nat. freq. Hz	f_n	''Ideal'' u_{nl}	''Ideal'' ξ_{nl}	''Actual'' u_{nl}	''Actual'' ξ_{nl}
(1,1)	85.9	1.370	−0.070	0.161	0.144	0.380
(2,1)	184.9	−1.100	−0.166	−0.235	−0.290	−0.069
(1,2)	244.8	0.570	0.005	0.359	−0.022	−0.146
(2,2)	343.8	−0.460	−0.002	−0.102	0.050	−0.274
(3,1)	349.9	−0.480	−0.002	0.186	−0.048	0.096
(3,2)	508.5	−0.200	0.001	0.094	−0.053	−0.295
(1,3)	509.5	−1.130	−0.154	−0.143	−0.122	−0.124
(4,1)	581.0	1.490	0.963	−0.460	0.927	0.451
(2,3)	608.5	0.910	0.127	0.455	0.130	0.500
(4,2)	739.8	0.620	0.002	0.534	−0.036	−0.218
(3,3)	773.5	0.400	0.001	−0.110	0.030	0.380

$$\min C_s(\{b\}) = \sum_{n=1}^{N} |\xi_{ns} - \hat{\Omega}_{ns}(\{b\})|^2, \tag{20}$$

where C_s is the cost function relating the difference between the optimum modal error sensor components ξ_{ns} and the ''actual'' modal error sensor components given by $\hat{\Omega}_{ns}(\{b\})$ connected to the sth error channel. Similar to the case of the unit modal control forces, the nth component of the ''actual'' modal error sensor component due to the sth error signal $\hat{\Omega}_{ns}(\{b\})$ can be obtained by including the contributions of all the nth modal error sensor components due to each one of the N_E error sensors as

$$\hat{\Omega}_{ns}(\{b\}) = \sum_{j=1}^{N_E} \Omega_{nj}(\{b\}_j), \tag{21}$$

where $\Omega_{nj}(\{b\}_j)$ is the nth modal error sensor component of the jth error sensor and vector $\{b\}_j$ contains the design variables for the jth sensor.

Equations (18) and (21), solved for each one of the N_c control and N_s error channels, define completely the set of lower level or physical domain optimization problems. As can be seen, once the optimum modal parameters are obtained in the upper level optimization different actuators and sensor models can be investigated with a minimum computational effort.

III. NUMERICAL RESULTS

This section illustrates the implementation of the proposed multi-level optimization design approach for the design of an optimum control system for a baffled simply supported plate. Since both the structural and acoustic responses of a simply supported plate can be obtained analytically, the study of this structure is ideal as a benchmark for more complex systems. The plate is made of steel with a modulus of elasticity $E = 2\times10^{11}$ N/m^2, mass density $\rho_s = 7800$ Ns^2/m^4, and Poisson's ratio $\nu = 0.28$. The dimensions of the plate are $L_x = 0.38$ m, $L_y = 0.30$ m, and thickness $h = 0.002$ m. The plate is assumed to be vibrating in air with a density $\rho = 1.21$ kg/m^3 and phase speed $c = 343$ m/s. The disturbance is assumed to be a point force with amplitude $F(\omega) = 1N$ and frequency $\omega = 3454$ rad/s (i.e., 550 Hz) and located at $x_f = 0.24$ m, $y_f = 0.13$ m. The case of multiple frequency excitations has already been studied[12] and will be reported in a future publication.

A. Uncontrolled system response

For the case of a simply supported plate, the natural frequency and mass normalized mode shape, identified by their modal indices (n_x, n_y), are easily computed.[10] In the present case, it is assumed a modal damping ratio of 1% (i.e., $\beta_n = 0.01$) for all the modes. A total of 11 modes (i.e., $N = 11$) are considered in the analysis. The natural frequencies and unit modal disturbance force, f_n, are summarized in the second and third column in Table I. From the values of the natural frequencies, it can be seen that the disturbance excitation is off-resonance between the (1,3) and the (4,1) modes. In addition, the values of the unit modal disturbances indicate that the disturbance couples well with modes (4,1), (1,1), (1,3), and (1,2) while is less effective in driving, for example, modes (3,2) and (3,3).

Similarly, the far-field acoustic response due to the nth mode of a baffled simply supported plate can also be obtained analytically from the solution of the Raleigh integral as[9]

$$p_n(r,\theta,\gamma,\omega) = -\omega^2\rho \frac{L_x L_y}{2\pi r n_x n_y} \sqrt{\frac{4}{\rho_s h L_x L_y}} \left(\frac{(-1)^{n_x} e^{-j\tau_1} - 1}{(\tau_1/n_x\pi)^2 - 1}\right) \times \left(\frac{(-1)^{n_y} e^{-j\tau_2} - 1}{(\tau_2/n_y\pi)^2 - 1}\right) e^{-jkr}, \tag{22}$$

where $k = \omega/c$; $\tau_1 = kL_x \sin\theta\cos\gamma$ and $\tau_2 = kL_y \times \sin\theta\sin\gamma$; and θ and γ are the angles defining the far-field direction.

Using Eq. (22), the contribution due to the modes, both direct and cross terms, to the total radiated power at 550 Hz including the dynamics of the system can be presented graphically. To this end, each one of the elements in the double summation in Eq. (7) is shown in Fig. 1. The results are presented in decibels (dB ref 1×10^{-12} W) where the negative contributions (i.e., light shaded columns) are included in the figure as the dB of the absolute value. This figure shows that mode (4,1) is the highest contributor to the

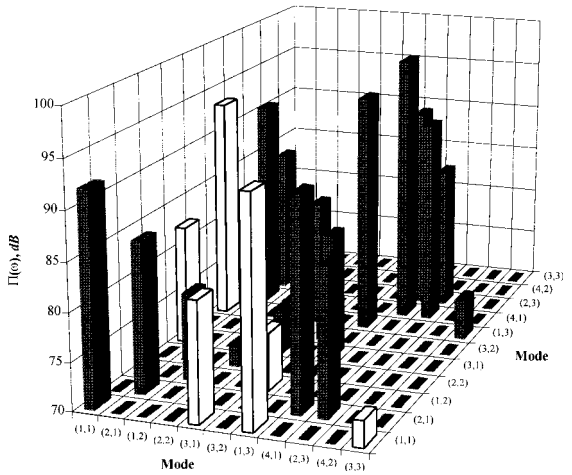

FIG. 1. Modal contributions to total radiated power. Total radiated power: 101.8 dB.

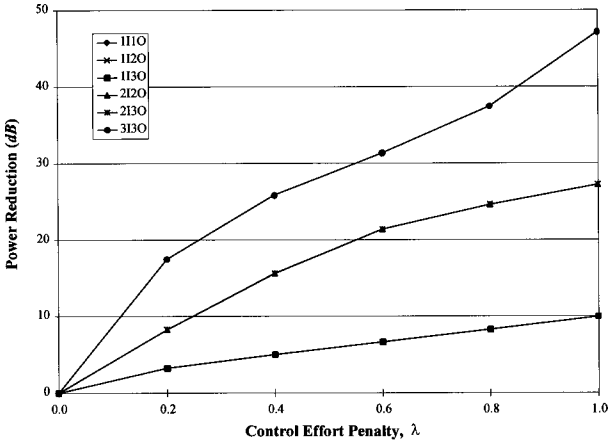

FIG. 2. Reductions in total radiated power.

total radiated power in spite of having low radiation efficiency. This is due to the fact that the force strongly drives this mode. These results demonstrate the significant effect that the disturbance plays in the modal contributions to the total radiated power, in particular for spectrally white inputs. On the other hand, the effect of the radiation efficiency can be observed in the fact that even though the excitation frequency is far away from the resonance of the (1,1) mode the power due to this mode is only about 6 dB below the power produced by mode (4,1). Thus this shows that both the dynamics and the radiation properties of the modes are important in the modal breakdown of the total acoustic power.

B. Control system design: Results and discussion

1. Modal domain design

The goal in the upper level or modal domain optimization is to find the optimum values of the unit modal control forces and modal error sensor components that minimize the total radiated power of the controlled system $\Pi_T^c(\omega)$ in the presence of designer selected constraints in the modal control effort. In the present example, this optimization problem has been solved using the Goal Attainment Method.[13] Six different control configurations were studied: 1I1O, 1I2O, 1I3O, 2I2O, 2I3O, and 3I3O where ''I'' and ''O'' denote control and error channels, respectively. The acoustic power reduction for each of the six control configurations as a function of the penalty in the control effort are shown in Fig. 2. Each one of the configurations in the figure represents a set of optimum unit modal control forces u_{nk} and optimum modal error sensor components ξ_{ns}. It can be observed that for a particular number of control channels, there is no increase in the reduction in the total radiated power by increasing the number of error outputs. For that reason, the curves for configurations with identical number of control inputs are overlapped in the figure (e.g., curves 1I1O, 1I2O, and 1I3O). As can be seen in the figure, the reduction in the total radiated power can be accomplished by relaxing the constraint in the control effort and/or increasing the number of control channels. The results in Fig. 2 are very useful during the design process since the designer can decide at a very early stage how many control channels are needed and what relative expense (modal control effort) is required to accomplish a desired attenuation. Since the acoustic response (before and after control) is expressed in terms of modal parameters, the same reductions will be expected for any type of actuator/sensor configuration that yields the same unit modal control forces and modal error sensor components as the optimum ones. This is one of the main advantages of the present approach versus optimizing directly the physical characteristics of the transducers.

In order to investigate in detail the optimum results, the values for the optimum modal parameters for the 1I1O configuration with a $\lambda=1.0$ are also presented in the fourth and fifth columns of Table I. As shown in the table, the optimum unit modal control forces, u_{nk}, suggest that most of the control effort should be dedicated to mode (4,1) with significantly less effort into modes (2,1), (1,3), (2,3), and (1,1). This behavior is explained by plotting the modal contributions to the controlled total radiated power. This is shown in Fig. 3. Comparison of this figure and Fig. 1 shows that the mechanism of control is by mainly reducing the contribution due to mode (4,1). As shown in Fig. 1, mode (4,1) is the

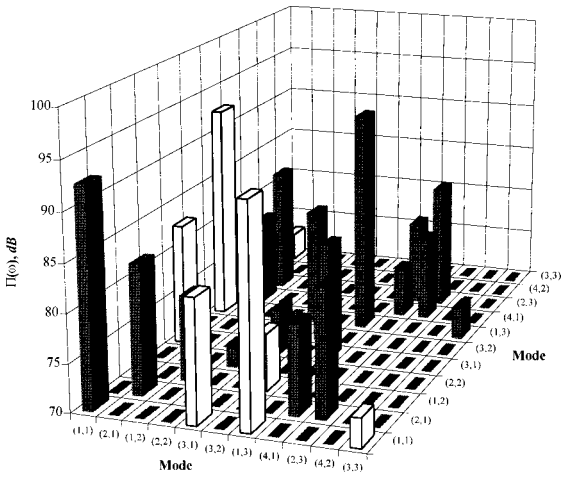

FIG. 3. Modal contributions to controlled power using the 1I1O configuration and $\lambda=1.0$. Total radiated power: 91.8 dB.

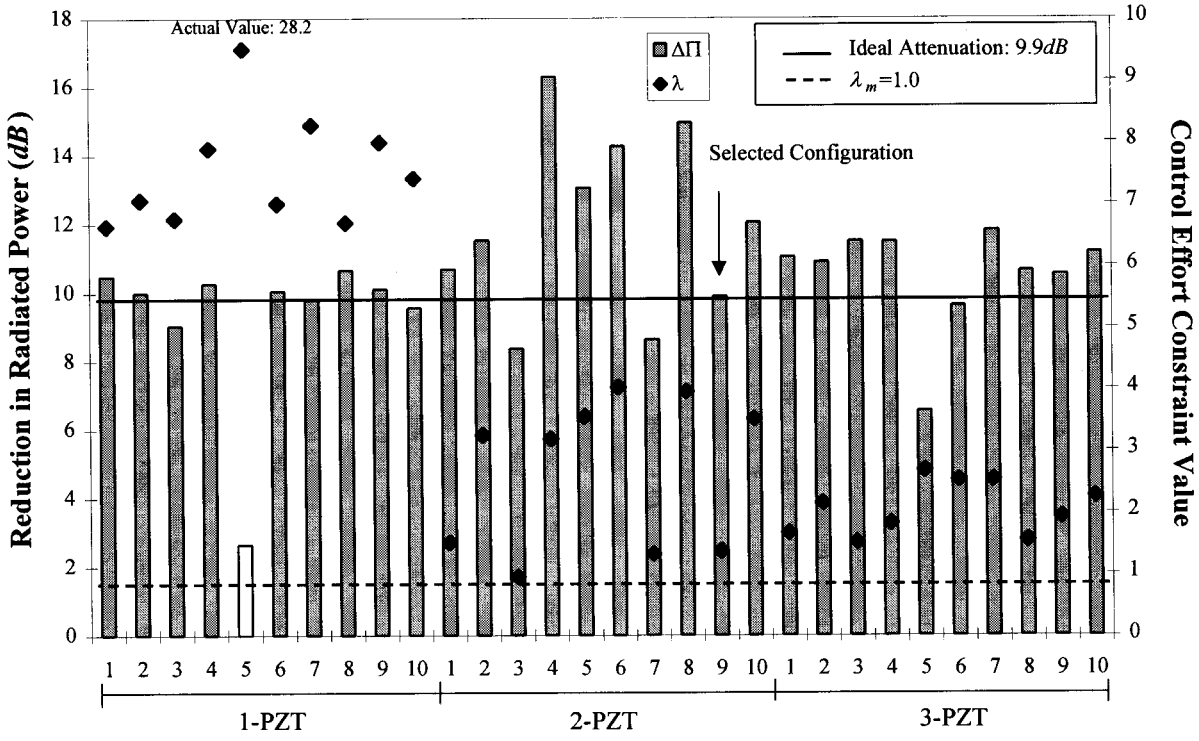

FIG. 4. Performance of optimum actuator configurations (using ''ideal'' sensor).

highest contributor to the uncontrolled sound field and therefore it is trivial that this mode has to be highly controlled as implied in Table I. On the other hand, modes (1,1) and (1,3) are virtually left unaffected by the control system as indicated by the low values of the unit modal control forces for these modes in Table I. This is because in the uncontrolled system the direct power radiated by these modes is canceled by their negative cross-radiation terms as shown in Fig. 1. On the other hand, Fig. 1 also shows that modes (2,1) and (2,3) do not have a significant direct term contribution to the total power. However, these modes couple acoustically with the (4,1) mode as shown by the important positive cross terms in the same figure. Thus the control system attenuates the (2,1) and (2,3) modes to reduce these cross terms.

The previous results show that the optimization process is successful in identifying only those modes that had to be controlled to reduce the total radiated power. On the other hand, the optimum modal error sensor components in Table I do not seem to observe the more important modes in the total radiated power, where the highest value of the modal error components is for mode (4,2) which is barely excited by the disturbance and do not contribute at all to the acoustic field. This is explained by looking once more at the form of Eq. (10). If the values of the control inputs $U_k(\omega)$ are fixed in this equation, as is the case when the modal control effort constraints are active, the only control parameters that change from mode to mode are the unit modal control forces u_{nk}. Therefore, the selection of the correct unit modal control forces has a direct impact on the total radiated acoustic power. On the other hand, the relevance of the optimum modal error sensor components stands in providing the correct complex amplitudes for the control inputs and not in observing a particular mode due to its radiation characteristics. This also explains why there is no improvement in the reduction in the radiated power by simply increasing the number of error signals. Having more error signals will only provide different means to satisfy the required control effort constraints.

At this point, the major aspects of the modal domain optimization results have been covered. In a typical implementation of the proposed design approach, the designer investigates at the modal domain level many configurations, as shown in Fig. 2, and selects the one that best fits the particular situation (i.e., attenuation, number of control channels, control effort, etc.). Then, the optimum unit modal control forces and modal error sensor components of the selected configuration are used in the physical domain level to design the physical characteristics of the actuators and sensors.

2. Physical domain design

The first step in the lower level or physical domain design is the selection of the type of transducers to be used. One of the advantages of the present design approach is that different models of actuators and sensors can be investigated with a low computational effort. In the present work, the design formulation is demonstrated only for one type of actuator and one type of sensor. The control actuators will be PZT patches while the error sensors are assumed to be accelerometers.

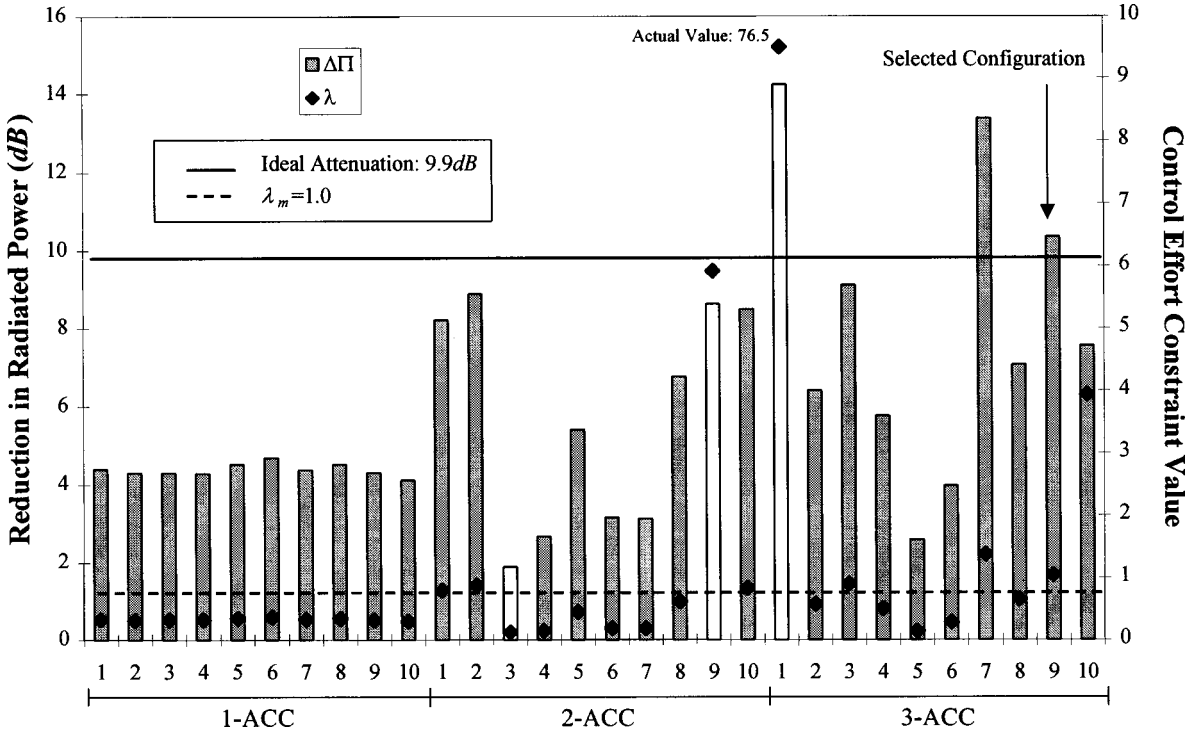

FIG. 5. Performance of optimum sensor configurations (using ''ideal'' control forces).

a. Optimum actuator design. A mechanical model for the PZT elements that relates the physical to the modal parameters is required. As shown in the literature, if two PZT patches are symmetrically bonded to both sides of the structure and wired out-of-phase, their effect can be approximated as line moments applied to the middle surface of the structure along the edges of the patches.[12] In the present example, this configuration (i.e., a PZT pair wired out-of-phase) is denoted as a single actuator. For the case of a simply supported plate, the line moments along the edges of the ith PZT actuator will yield an nth unit modal force in the form of[14]

$$\Psi_{ni}(x_{ci},y_{ci},l_{xi},l_{yi},P_i) = P_i C_0 \frac{k_{xn}^2+k_{yn}^2}{k_{xn}k_{yn}}(\cos(k_{xn}(x_{ci}-l_{xi})) - \cos(k_{xn}(x_{ci}+l_{xi})))(\cos(k_{yn}(y_{ci}-l_{yi})) - \cos(k_{yn}(y_{ci}+l_{yi}))), \quad (23)$$

where $P_i=\pm 1$ is the relative phase between actuators; the constant C_0 is a function of the thickness and material properties of the plate and the PZT elements; $k_{xn}=n_x\pi/L_x$ and $k_{yn}=n_y\pi/L_y$; and (x_{ci},y_{ci}) and (l_{xi},l_{yi}) are the coordinates of the central location and dimensions of the ith PZT pair, respectively. Using this configuration for the unit modal control forces, the optimum control inputs $U_k(\omega)$ will be the voltages to be applied to the actuators. The properties of the PZT patches used in this example are: piezoelectric strain coefficient $d_{31}=171\times10^{-12}$ m/V, Poisson's ratio $v_p=0.31$, Young's modulus $E_p=6.1\times10^{10}$ N/m^2, and thickness $h_p=0.0002$ m. Finally, Eq. (23) is used to obtain the nth unit modal force due to N_A actuators driven in- or out-of-phase by the control input.

As implied in Eq. (23), the actuator design variables [i.e., the elements of $\{a\}_i$ in Eq. (18)] are the central location (x_{ci},y_{ci}), the dimensions (l_{xi},l_{yl}), and the relative phase P_i for the ith PZT pair. In the present example, up to three PZT pairs (i.e., $N_A=1$, 2 or 3) were considered in the design formulation. A genetic algorithm[15] (GA) was used to solve this problem. Ten different GA analyses were carried out for each one of the PZT configurations. The best solution from each analysis was selected that yielded a final set of thirty possible control implementations.

The performance of these thirty control configurations is summarized in Fig. 4. The ''actual'' modal error sensor components are not known at this stage, therefore the results shown in this figure are obtained out using the ''ideal'' values of the modal error components ξ_{ns} given in Table I. In this figure, the horizontal axis represents the 30 control configurations, e.g., the first ten are the best solutions for each one of the GA analyses with a single actuator and so forth. The columns represent the power reduction achieved for each configuration. For comparison purposes, the solid horizontal line represents the predicted power attenuation from the modal domain optimization [i.e., $\Delta\Pi(\omega)=9.9$ dB]. The control effort constraint given in Eq. (17b) is also plotted (dotted line) to illustrate the performance of the actuator configurations. The limit of this constraint (i.e., $\lambda=1.0$) is indicated by the horizontal dotted line. Thus any value higher that 1.0 indicates that the constraint is violated.

The results in Fig. 4 show that good attenuation in the total radiated power is obtained even when using a single PZT. The fifth case gives an increase in the power (i.e., clear column implies negative reduction) but since there are many other alternate solutions, the designer just needs to discard that one. The good performance of the single PZT is at the

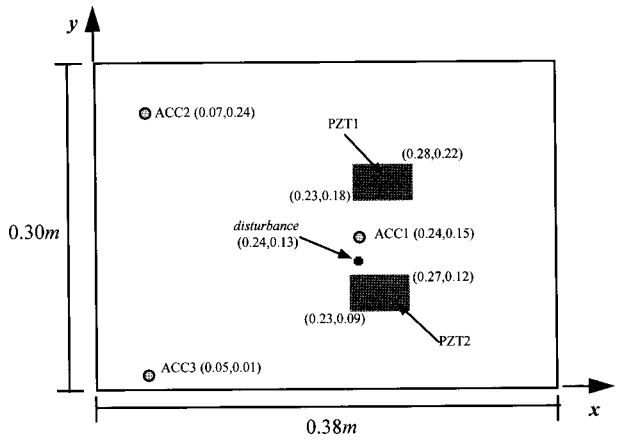

FIG. 6. Optimum actuator/sensor configuration (coordinates in meter).

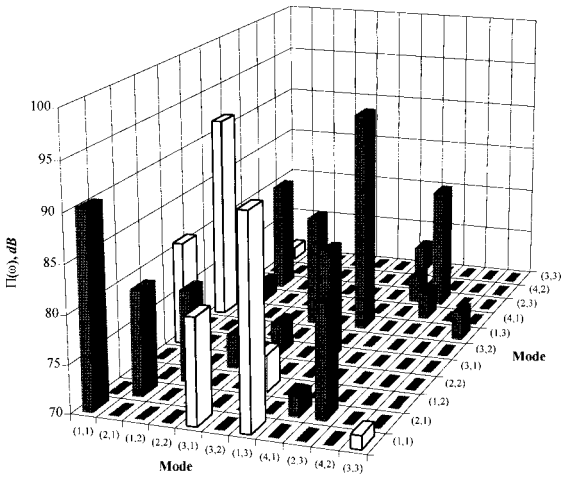

FIG. 7. Modal contributions to controlled power using the 1I1O ''actual'' configuration. Total radiated power: 91.1 dB.

expense of a significant violation in the control effort penalty. On the other hand, the control effort is reduced (i.e., the value of the constraint approaches the ''ideal'' value of 1.0) as the number of PZT patches is increased. This is because as the number of actuators is increased the match between the ''ideal'' and ''actual'' unit modal control forces is better and the control spillover to undesired modes is reduced.

From the 30 available solutions, the ninth configuration when using two PZTs is selected to be implemented in this example. In this configuration both actuators are driven inphase which yields a reduction of 9.9 dB in the total radiated power and a small violation in the control effort limit of 1.5.

b. Optimum sensor design. The mechanical model of accelerometer sensors is simply given as the value of the mode shape at the sensor location. The design variables in this optimization problem [i.e., the elements of $\{b\}$ in Eq. (20)] are the coordinates of the sensors (x_{sj}, y_{sj}) for $j = 1,...,N_E$. The physical domain optimization problem to design the sensors is again exactly in the same form as the case of the actuator design using the GA. Results are obtained for sensing configurations consisting of one, two, and three accelerometers (i.e., $N_E = 1,...,3$). The performance of the best solutions of ten GA analyses is again evaluated in the same way as for the case of the actuators. Figure 5 shows the power reduction and control effort constraint for the 30 sensing configurations. To obtain these results, the ''ideal'' unit modal control forces found in the modal domain optimization are used (see Table I). The results in the third figure show that using only one sensor (i.e., minimizing the error at only one location) does not yield enough amplitude to the control input $U_k(\omega)$ to induce a significant attenuation in the total radiated power. The attenuation for this case is about 4 dB. It can also be observed that the control effort constraint is not active [i.e., $g_1^c(u_{nl}, \xi_{nl}) = 0.5 < 1.0$]. As can be seen, as the number of sensors is increased there is an increase (in the average) in the reduction of the total radiated power. On the other hand, the modal control effort is very low with one sensor and also increases with the number of sensors. Based on these results the ninth configuration with three accelerometers is selected. This configuration (in conjunction with the ''ideal'' control forces) yields a power reduction of 11.0 dB and again a small control effort violation [i.e., $g_1^c(u_{nl}, \xi_{nl}) = 1.2 > 1.0$].

3. Optimum actuator/sensor configuration

A schematic of the selected actuator/sensor configuration [i.e., 2-PZT(9) and 3-ACC(9) in Figs. 10 and 11] is shown in Fig. 6. The ''actual'' modal control and modal error sensor components are again presented in Table I. As can be seen, the ''actual'' unit modal control forces show a very good agreement to the ''ideal'' values. The most significant discrepancy between the ''actual'' and ''ideal'' values is the change in phase in the first component. On the other hand, when compared to the ''ideal'' values, the ''actual'' modal error parameters show some differences in terms of the relative *observability* of the modes and phases. From the results in the previous section, these differences do not seem to affect the performance of the control system. Once the actuators and sensors are designed, the performance of the complete ''actual'' system is then compared to the performance of the ''ideal'' one obtained in the modal domain optimization.

The magnitude of the control input using the selected ''actual'' configuration is 19.1 V. This configuration yields a total reduction in the radiated power of 10.7 dB that is very close to the ''ideal'' attenuation predicted in the modal domain of 9.9 dB. The modal contributions to the total radiated power when implementing the ''actual'' control system are shown in Fig. 7. This figure can be compared to the ''ideal'' reductions previously shown in Fig. 3. As can be seen, both results are very similar. Note that the selected actuators/sensor configuration is only one of the 900 available combinations. In practice, the designer could check the performances of several configurations. Here, only one configuration was investigated to illustrate the method.

IV. CONCLUSIONS

A new approach for the optimum design of actuators and error sensors to be implemented in ASAC applications has been developed. The formulation is based in a multi-level optimization procedure. The upper level is defined in the modal domain and solves for the optimum relative *controllability* and *observability* of the modes that the control system should implement in order to minimize the total radiated

acoustic power. The optimum results at the upper level are used in the lower level or physical domain optimization problems in order to find the actuators and sensors to be implemented in the structure. The formulation allows the use of either numerical techniques or experimental results during the design process. Therefore, the proposed design approach can be readily applied for the design of control systems for complex structures with complex excitations. In this paper, the developed optimum design formulations were implemented for the case of a simply supported plate. The simply supported plate was studied because both its structural and acoustic responses are well understood which permitted to obtain a better understanding of results and the evaluation of the performance of the design method.

ACKNOWLEDGMENTS

The authors gratefully acknowledge the support of this work by the Office of Naval Research (Grant No. ONR-N00014-92-J1170) and the State Council of Higher Education for Virginia (Commonwealth Graduate Fellowship).

[1] C. R. Fuller, ''Apparatus and methods for global noise reduction,'' U.S. Patent No. 4,715,599 (1987).
[2] C. R. Fuller, S. J. Elliot, and P. A. Nelson, *Active Control of Vibration* (Academic, San Diego, CA, 1996).
[3] B. T. Wang, R. A. Burdisso, and C. R. Fuller, ''Optimal placement of piezoelectric actuators for active control of sound radiation from elastic plates,'' Proceedings of Noise-Con 91, Tarrytown, New York, 14–16 July 1991, 267–275 (1991).
[4] C. E. Ruckman and C. R. Fuller, ''Using multiple regression and subset selection to optimize actuator locations in feedforward active control systems'', J. Acoust. Soc. Am. **92**, 2410(A) (1992).
[5] R. H. Cabell, H. C. Lester, G. P. Mathur, and B. N. Tran, ''Optimization of actuator arrays for aircraft interior noise control,'' 15th AIAA Aeroacoustics Conference, Long Beach, California, 25–27 October 1993, 1–10 (1993).
[6] R. A. Burdisso and C. R. Fuller, ''Design of active structural acoustic control systems by eigenproperty assignment,'' J. Acoust. Soc. Am. **96**, 1582–1591 (1994).
[7] M. T. Simpson and C. H. Hansen, ''Use of genetic algorithms for optimizing vibration actuator placement for minimizing sound transmission into enclosed spaces,'' Proceedings of Smart Structures and Materials, San Diego, California, 26–29 February 1996.
[8] H. M. Rodriguez and R. A. Burdisso, ''Sensitivity analysis for feedforward control system design,'' J. Acoust. Soc. Am. **98**, 3352–3359 (1995).
[9] F. Fahy, *Sound and Structural Vibration* (Academic, Orlando, FL, 1985).
[10] M. C. Junger and D. Feit, *Sound, Structures and Their Interaction* (Acoustical Society of America, Woodbury, NY, 1993).
[11] R. D. Ciskowski and C. A. Brebbia, *Boundary Element Methods in Acoustics* (Comp. Mechanics Publications, Boston, 1991).
[12] H. M. Rodríguez, ''Optimum design for feedforward structural-acoustic control of complex structural systems,'' Doctor of Philosophy Dissertation, Department of Mechanical Engineering, VPI&SU (1996).
[13] The MathWorks, Inc., *Optimization Toolbox User's Guide* (Natick, MA, 1992).
[14] E. K. Dimitriadis, C. R. Fuller, and C. R. Rogers, ''Piezoelectric actuators for distributed vibration excitation of thin plates,'' J. Vib. Acoust. **113**, 100–107 (1989).
[15] D. E. Goldberg, *Genetic Algorithms in Search, Optimization and Machine Learning* (Addison-Wesley, Reading, MA, 1989).

Wave-based matching-pursuits detection of submerged elastic targets

Mark McClure and Lawrence Carin
Department of Electrical and Computer Engineering, Box 90291, Duke University, Durham, North Carolina 27708-0291

(Received 9 January 1997; revised 24 February 1998; accepted 17 April 1998)

Matching pursuits is a nonlinear algorithm which iteratively projects a given signal onto a complete dictionary of vectors. The dictionary is constructed such that it is well matched to the signals of interest and poorly matched to the noise, thereby affording the potential for denoising, by adaptively extracting an underlying signature from a noisy waveform. In the context of wave scattering and propagation, there are basic constituents that can be used to construct most measured waveforms. A dictionary of such constituents is used here, in the context of wave-based matching-pursuit processing of acoustic waves scattered from submerged elastic targets. It is demonstrated how wave-based matching pursuits can be utilized for denoising as well as to effect a detector, the latter being parametrized via its receiver operating characteristic (ROC). Results are presented using measured aspect-dependent (orientation-dependent) scattered waveforms, for the case of a submerged elastic shell. © *1998 Acoustical Society of America.* [S0001-4966(98)05707-5]

PACS numbers: 43.60.Pt, 43.60.Gk, 43.30.Wi [SAC-B]

INTRODUCTION

The acoustic waves scattered from a complex submerged elastic target are generally strongly dependent on the orientation (aspect) of the target relative to the sensor, thereby significantly complicating target detection and identification. Consequently, prohibitive computational resources are required to effect matched-filter detection, since this requires storing all of the aspect-dependent scattered waveforms. To mitigate this problem, a set of eigenvectors (or other basis) could be derived which spans the space of all such waveforms,[1] and this (hopefully smaller) set of vectors could be used to perform detection. Alternatively, or additionally, compression algorithms (e.g., wavelets[2–4]) could be used to reduce the storage requirements, thereby significantly reducing the memory constraints incurred in utilizing all aspect-dependent target signatures. However, in practice, it is difficult to have *a priori* knowledge of all aspect-dependent scattered waveforms for targets of interest. This issue is exacerbated by the fact that the signature is often strongly dependent on the surrounding environment, which is generally not known in advance.

Alternatively, instead of requiring knowledge of all aspect-dependent waveforms that can be scattered from a given target, one could simply use *any* complete basis. For example, a Gabor or wavelet[2–5] basis could be employed for such purposes. If one has no *a priori* knowledge of the target-signature properties, such a procedure reduces to an energy detector for the case of additive white Gaussian noise. However, if one had knowledge of which *subset* of the basis are most important for a given class of targets, a detector that exploits this information effectively can be realized.[5] Unfortunately, as demonstrated subsequently, the scattered signatures from complex elastic targets are often too complicated and aspect dependent to admit robust detection based on a subset of filter elements.

To ameliorate these difficulties, adaptive algorithms which decompose the unknown scattered waveform into basic constituent features have been investigated. One could, for example, devise a model to which a general scattered waveform could be fit,[6] and then perform a maximum likelihood (ML) parameter estimation. In the context of detection, this results in a generalized likelihood ratio test (GLRT).[6] However, the appropriate model is often difficult to know *a priori* and the ML search can be computationally intensive. As an alternative, Altes[7] has considered the development of a detector based on reflections of the incident-pulse shape, as well as differentiations and integrations thereof. Detectors based on the incident-pulse shape are often used in classical matched-filter detectors and range-compression algorithms,[6] which assume that the target or target features behave as point scatterers. The additional set of differentiated and integrated incident waveforms, however, are based on the characteristics of scatterings from local features on the target, taking proper account of the waveshape distortion incurred by such diffraction.

In this paper, we formalize some of the concepts originally proposed by Altes[7] and develop a new wave-based matching-pursuits scheme in which these ideas are exploited, thereby effecting an efficient and flexible signal-processing algorithm. In particular, Altes' concept of building a detector which utilizes differentiated and integrated versions of the incident-pulse shape was based on insight garnered by studying biological underwater sensing systems (animals). However, based on previous forward modeling, it is well known that scattering from and propagation along several elastic and inelastic structures can yield significant pulse distortion (dispersion). For example, the geometrical theory of diffraction (GTD)[8,9] analysis of scattering from inelastic edges, tips, and finite flat surfaces yields diffraction coefficients (reflection coefficients) which are proportional to $(j\omega)^{-1/2}$, $1/j\omega$, and $j\omega$, respectively, where ω represents the angular frequency–the two latter expressions representing integration

and differentiation, respectively. Moreover, Lamb waves[10–12] propagating along an elastic plate can also experience significant dispersion, depending on material properties and the frequency of operation. To account for such distortion, we have constructed a dictionary composed of wavefronts $w_{\alpha\tau}(t)$ with Fourier transforms given by $\hat{w}_{\alpha\tau}(\omega)=\hat{g}(\omega)(j\omega)^{\alpha}\exp(-j\omega\tau)$, where $\hat{g}(\omega)$ represents the Fourier transform of the incident pulse $g(t)$. Altes[7] considered integer values of α, while we generalize this to account for a more-general class of dispersive phenomena. Thus our dictionary D is composed of the incident pulse and appropriate distortions thereof (dictated by physically motivated dispersion), each of which are shifted in time by the parameter τ.

To efficiently utilize the physically based dictionary D in a detector, we have developed what we have termed a ''wave-based matching pursuits'' algorithm. In particular, D is used here as the dictionary for the matching-pursuits scheme developed originally by Mallat and Zhang.[13] This algorithm projects a given waveform onto each element in D, selecting that dictionary element with which there is the highest correlation. The selected component is subtracted from the signal, and the procedure is then repeated on the remaining waveform. If the dictionary is complete, as is our wave-based dictionary,[14] the algorithm is guaranteed to converge (fully represent the signal in terms of dictionary elements) after sufficient iterations. It is important to note, however, that our motivation is not to fully reconstruct a waveform that is already known (measured). Rather, by building a dictionary that is closely matched to the underlying wave physics, we anticipate that the dictionary will initially be most correlated with the underlying target signature, rather than to the noise. Thus by stopping the algorithm properly (to be discussed further below), one ideally can extract the target signature, while leaving behind (in the remainder) the noise/clutter. Thus, instead of storing all the aspect-dependent signatures from a set of targets, we use the wave-based matching-pursuits algorithm to adaptively extract such waveforms from measured data (with no *a priori* knowledge of whether a target is present or, if so, the target orientation).

The wave-based matching-pursuits algorithm is driven by the design of a dictionary D that is matched to the underlying wave phenomenology. Therefore, when a target is present, we expect the algorithm to initially extract the target signature from noisy data, in a highly convergent manner (with a precipitous decline in the energy of the aforementioned remainder). After the target response has been so removed, the algorithm proceeds with the slowly convergent task of reconstructing the noise (because our dictionary is complete), and it is at this point that the algorithm is (ideally) stopped. However, if there is no target present, there will be no initial precipitous decline in the energy of the remainder, since the algorithm is processing noise/clutter from the outset. This dichotomy between the signal-plus-noise and noise-only cases is exploited here in the context of detection. It is important to note that, in addition to providing detection, the matching-pursuits scheme also extracts the underlying waveform, which can be used subsequently in the context of identification.

The remainder of the paper is organized as follows. In Sec. I we give a summary of the matching-pursuits algorithm, with emphasis on its applicability and limitations with regard to noisy data and its use in the context of detection. In Sec. II we demonstrate algorithm performance by considering measured data for acoustic scattering from a submerged elastic shell. Issues addressed include denoising, criteria with which to stop the iterative matching-pursuits scheme, and detector performance [presented in the form of receiver operating characteristic (ROC)]. Finally, in Sec. III we conclude by summarizing the results of this work, limitations of the algorithm, and future directions.

I. WAVE-BASED MATCHING-PURSUITS DENOISING AND DETECTION

A. Basic algorithm

The matching-pursuits algorithm was developed originally in Ref. 13 and is summarized here, wherein the unique feature of using a wave-based dictionary is highlighted. Let D represent a finite set (dictionary) of normalized vectors which are complete (and possibly redundant). We project a measured (noisy) waveform $f(t)$ onto all elements in D, and choose that function, denoted $b_1(t)$, which is best matched to the signal $f(t)$:

$$f(t)=\langle f|b_1\rangle b_1(t)+R_1(t), \quad S(f,b_1)\geqslant S(f,b_k)\forall b_k\in D, \tag{1}$$

where $S(f,b_k)$ is a selection criterion,

$$\langle f|b_k\rangle\equiv\int f(t)b_k(t)dt, \tag{2}$$

and $R_1(t)$ is the remainder after the first matching-pursuits iteration. The measured waveform and the dictionary elements are assumed to be real-valued functions. The original selection criterion[13] was $S(f,b_k)=|\langle f|b_k\rangle|$. However, this criterion emphasizes large-amplitude portions of $f(t)$ over other regions of $f(t)$ which have smaller amplitudes but may be better correlated to a member of D. Therefore, as an alternative, we have found $S(f,b_k)=|\langle f|b_k\rangle|/E_k^{1/2}$ to be useful, where E_k represents the energy in $f(t)$ over the nominal support of $b_k(t)$. This latter criterion emphasizes those portions of the waveform $f(t)$ that are most correlated with elements in D, independent of their excitation strength. The procedure in Eq. (1) is repeated on $R_1(t)$, and after N iterations

$$f(t)=\sum_{n=1}^{N}\langle R_{n-1}|b_n\rangle b_n(t)+R_N(t), \quad R_0(t)\equiv f(t) \tag{3}$$

and

$$\langle f|f\rangle=\sum_{n=1}^{N}\langle R_{n-1}|b_n\rangle^2+\langle R_N|R_n\rangle. \tag{4}$$

As alluded to above, when D is complete, $\langle R_N|R_N\rangle\rightarrow 0$ as $N\rightarrow\infty$.[13] Additionally, although the decomposition is implemented in a nonlinear fashion [dictated by the criterion $S(f,b_k)$], the energy decomposition in Eq. (4) is analogous

to that of an orthonormal basis. In the above discussion, as in the rest of the paper, we use $b_k(t)$ to denote a general dictionary element and $b_n(t)$ to represent that element selected on the nth matching-pursuit iteration.

Any complete dictionary D can be used in the above algorithm. However, as will be discussed further subsequently, the utility of matching pursuits to provide effective denoising (and therefore detection) is predicated on $|\langle s|b_k\rangle|^2 > \sigma^2$ for one or more $b_k \in D$, where $f(t)=s(t)+n(t)$, with $s(t)$ denoting the signature scattered from the target and $n(t)$ representing additive (assumed) noise/clutter with variance σ^2. It is therefore essential to compose the dictionary in terms of elements that can parsimoniously and robustly represent general scattered waveforms $s(t)$ (such that the waveforms in D selected for representation of $s(t)$ have sufficient energies relative to σ^2). While the Gabor representation proposed in Refs. 5 and 13 is attractive for general signals for which no *a priori* knowledge is available, in the case of acoustic scattering from elastic and inelastic structures, tremendous insight is available and should be exploited. In particular, from decades of forward modeling[8–12,15,16] it is known that the scattered waveform from general targets can always be represented as a summation of (possibly distorted) wavefronts scattered from localized scattering centers on the target and/or wavefronts radiated by multiple creeping-wave circumnavigations along smooth elastic or inelastic surfaces.[17,18] Each of these is localized in time and nonlocalized in frequency. At late times, multiple reflections or circumnavigations can be repackaged in the form of damped oscillations (resonances),[17,18] which are localized in frequency and nonlocalized in time. Which of these two representations is most appropriate is dictated in large part by convenience (and the degree of *a priori* knowledge available). While the wavefront representation is always valid, the resonant parametrization is appropriate only at late times.[17,18] Moreover, the particular resonant frequencies are determined by the detailed target properties and may be subject to change within a variable environment. We have exploited resonant signatures when appropriate,[14] but here we assume very little *a priori* knowledge of the target, and our dictionary is therefore composed exclusively of shifted versions of the incident waveform and several distortions thereof (each of which is based on a physical scattering mechanism).

Distortion of the incident pulse can occur due to diffraction at localized scatterers (edges, corners, tips, etc.), structural dispersion, and/or dispersive material parameters. The latter case can often be ignored. Over the last several decades the geometrical theory of diffraction (GTD)[8,9] has been used to catalogue the diffraction coefficients for scattering from a wide class of localized scattering centers. Frequency-dependent (dispersive) diffraction coefficients imply a corresponding distortion of the incident-pulse shape, and here we utilize several important GTD-derived frequency dependencies to account for dispersion incurred at localized scattering centers. With regard to structural dispersion, such as elastic propagation along a thin (possibly curved) plate,[10–12] the sensor will only detect such when the plate modes are fast waves with respect to the surrounding media (water), such that energy can be leaked back to the observer at the appropriate angle.[19,20] Moreover, such modes are dispersed continuously as they propagate, and therefore the degree of pulse distortion will depend on the size of the target, as well as on the number of possible target circumnavigations incurred. Thus it is difficult to account in the dictionary for all possible forms of structural-dispersion-induced distortions, but we endeavor to build as much flexibility in D as possible to accommodate such physics.

As discussed in the Introduction, our dictionary D is composed of shifted wavefronts. In particular, if $g(t)$ represents the incident pulse, with Fourier transform $\hat{g}(\omega)$, the basis elements are represented by the dual-parameter wavefronts

$$b_{\alpha,\tau}(t)=\frac{1}{2\pi}\int_{-\infty}^{\infty}\hat{g}(\omega)(j\omega)^{\alpha}\exp[j\omega(t-\tau)]d\omega, \qquad (5)$$

which is a detailed representation of the generalized $b_k(t)$ used in Eq. (1). Although Eq. (5) is expressed in terms of continuous times t and τ, in practice both parameters are discretized (with discretization significantly smaller than the Nyquist rate). To accommodate the breadth of wave phenomenology discussed above, we consider all half-integer increments of α between -2.5 and 2.5. This dictionary is compact enough such that all variables (α,τ) are tested on each matching-pursuits iteration (using a personal computer); however, if one desired, coarse sampling could be used for τ, to find temporal regions of interest, followed by a localized search (e.g., Newton method[13]) for the optimal shift.

B. Denoising

As discussed above, the dictionary has been designed to be well matched to a waveform $s(t)$ scattered from a general underwater target. We demonstrate the importance of this for denoising and detector applications. Assume we measure a waveform $f(t)=s(t)+n(t)$, where $n(t)$ is additive zero-mean white Gaussian noise with variance σ^2. Considering the first matching-pursuit iteration, the dictionary elements have projections $\langle f|b_k\rangle=\langle s|b_k\rangle+\langle n|b_k\rangle$, $\forall b_k \in D$, and the expectation $E\{\langle f|b_k\rangle\}=\langle s|b_k\rangle$ with variance σ^2. If there is no scattered waveform, $s(t)=0$ and $E\{\langle f|b_k\rangle\}=0$ with variance σ^2, $\forall b_k \in D$. We see that it is only possible for the matching-pursuits algorithm to consistently distinguish between the signal-plus-noise and the noise-only cases if $|\langle s|b_k\rangle|$ is large relative to σ, for *some* $b_k \in D$. Therefore, it is essential that the dictionary represent $s(t)$ in as compact a manner as possible, such that significant energy $|\langle s|b_n\rangle|^2$ is associated with each b_n selected for its representation. For subsequent matching-pursuits iterations, one subtracts from $f(t)$ the selected $\langle f|b_n\rangle b_n(t)$, which complicates matters slightly. Nevertheless, similar signal-to-noise-ratio (SNR) requirements still apply for matching-pursuits iterations $n>1$.

For perspective, recall that the performance of a matched-filter-based detector is dictated exclusively by the figure of merit $\langle s|s\rangle/\sigma^2$, independent of the shape of the scattered signal $s(t)$. Unfortunately, for complex elastic targets, it is very difficult (if not impossible) to have *a priori*

knowledge of the complicated, aspect-dependent scattered signatures $s(t)$, necessitating the matching-pursuits scheme presented here. However, it is important to note that one pays a price for the flexibility of the matching-pursuits algorithm. In particular, while a matched-filter detector works well for large $\langle s|s\rangle/\sigma^2$, the matching-pursuits algorithm requires large $|\langle s|b_n\rangle|^2/\sigma^2$. Except for very simple special cases, $|\langle s|b_n\rangle|^2 \ll \langle s|s\rangle$, such that smaller σ^2 will be required for the matching-pursuits scheme, relative to the matched filter.

C. Detection statistic

Below we derive a test statistic which is used subsequently in a matching-pursuits detector. Throughout this discussion, approximations are made such that a compact (but suboptimal) statistic can be realized. We consider a binary hypothesis test, letting H_0 denote $f(t)=n(t)$ (noise only) and H_1 denote $f(t)=s(t)+n(t)$ (unknown signal plus noise), where $n(t)$ represents zero-mean white Gaussian noise with variance σ^2.

We first address the case of hypothesis H_1, and assume that σ^2 is sufficiently small such that the matching-pursuits scheme works properly (see Sec. I B). Moreover, we assume that the dictionary elements *selected* by the algorithm are relatively invariant to the particular noise realization, the latter only influencing the *amplitude* of the elements selected, $\langle f|b_n\rangle$. Therefore, if the algorithm is stopped after N iterations, the probability density $p(\mathbf{c},\mathbf{m}|H_1)$ is

$$p(\mathbf{c},\mathbf{m}|H_1)=\frac{1}{\sqrt{2\pi}^N|\Lambda|^{1/2}}\exp\left[-\frac{1}{2}(\mathbf{c}-\mathbf{m})^T\Lambda^{-1}(\mathbf{c}-\mathbf{m})\right], \tag{6}$$

where $\mathbf{c}$ is an $N\times 1$ dimensional vector, the nth element of which represents $\langle f|b_n\rangle$; $\mathbf{m}$ is an $N\times 1$ dimensional vector, the nth element of which represents $\langle s|b_n\rangle$, the mean of the nth element selected from the dictionary; and Λ represents the $N\times N$ covariance matrix $E\{(\mathbf{c}-\mathbf{m})(\mathbf{c}-\mathbf{m})^T\}$. It is straightforward to demonstrate that the components of Λ satisfy $\Lambda_{nm}=\sigma^2\int b_n(t)b_m(t)dt$. The principal assumption (simplification) used in deriving Eq. (6) is that the same dictionary *elements* are always selected for the noise variance σ^2 under consideration (with variable *amplitudes*, denoted by the vector $\mathbf{c}$); this assumption allows us to consider a fixed covariance matrix Λ.

Under hypothesis H_0, there is no underlying signal $s(t)$ in $f(t)$ for the matching-pursuits algorithm to home in on. For simplicity, we assume that the matching-pursuits selection criterion in Eq. (1) is $S(f,b_k)=|\langle f|b_k\rangle|$. Therefore, on the first matching-pursuits iteration, the algorithm chooses from $N_D(N_D\gg N)$ random variables $|\langle n|b_k\rangle|$, where N_D is the total number of shifted-wavefront dictionary elements in D. Note that, unlike under H_1, under H_0 the algorithm will not select the same dictionary elements for each noise realization, since there is no underlying signal $s(t)$ to guide the algorithm. On iteration one, the probability that $\zeta_1=\langle n|b_1\rangle$ will be selected is the probability that $|\langle n|b_1\rangle|\geq|\langle n|b_k\rangle|$, $\forall b_k\in D$, or[21]

$$\begin{aligned}p(\zeta_1|H_0,\ \text{iteration one})&=\frac{1}{2}\frac{|\Lambda_D|^{-1/2}}{\sqrt{2\pi}^{N_D}}\frac{d}{d|\zeta_1|}\int_{-|\zeta_1|}^{|\zeta_1|}dz_1\int_{-|\zeta_1|}^{|\zeta_1|}dz_2\cdots\int_{-|\zeta_1|}^{|\zeta_1|}dz_{N_D}\\&\quad\times\exp[-\tfrac{1}{2}\mathbf{z}^T\Lambda_D^{-1}\mathbf{z}],\end{aligned} \tag{7}$$

where Λ_D is the $N_D\times N_D$ matrix $E\{\mathbf{z}\mathbf{z}^T\}$, where the $N_D\times 1$ dimensional vector $\mathbf{z}$ has zero-mean elements $z_k=\langle n|b_k\rangle$. Because of the narrow temporal support of the wavefronts composing D, most of the z_k will be uncorrelated. Therefore, to yield a usable result we *approximate* Λ_D as a diagonal matrix with $\Lambda_{Dkk}=\sigma^2$. Subsequently,

$$\begin{aligned}p(\zeta_1|H_0,\ \text{iteration one})&\approx\frac{N_D}{\sqrt{2\pi}^{N_D}\boldsymbol{\sigma}^{N_D}}\exp\left(-\frac{1}{2}\frac{\zeta_1^2}{\boldsymbol{\sigma}^2}\right)\left[\int_{-|\zeta_1|}^{|\zeta_1|}dz\right.\\&\quad\left.\times\exp\left(-\frac{1}{2}\frac{z^2}{\sigma^2}\right)\right]^{N_D-1}.\end{aligned} \tag{8}$$

Continuing this process for N iterations, and denoting the N components ζ_n by the $N\times 1$ vector $\boldsymbol{\zeta}$, we have

$$\begin{aligned}p(\boldsymbol{\zeta}|H_0)\approx&\left[\frac{N_D}{\sqrt{2\pi}^{N_D}\boldsymbol{\sigma}^{N_D}}\right]^N\exp\left(-\frac{1}{2}\frac{\boldsymbol{\zeta}^{\mathbf{T}}\boldsymbol{\zeta}}{\boldsymbol{\sigma}^2}\right)\\&\times\left[\int_{-|\zeta_1|}^{|\zeta_1|}dz\ \exp\left(-\frac{1}{2}\frac{z^2}{\boldsymbol{\sigma}^2}\right)\right]^{N_D-1}\\&\times\left[\int_{-|\zeta_2|}^{|\zeta_2|}dz\ \exp\left(-\frac{1}{2}\frac{z^2}{\sigma^2}\right)\right]^{N_D-1}\\&\times\cdots\left[\int_{-|\zeta_N|}^{|\zeta_N|}dz\ \exp\left(-\frac{1}{2}\frac{z^2}{\sigma^2}\right)\right]^{N_D-1}.\end{aligned} \tag{9}$$

We reiterate the distinction between $\mathbf{c}$ and $\boldsymbol{\zeta}$ in Eqs. (6) and (9), respectively. Under hypothesis H_1, we assume that the same dictionary *elements* $\mathbf{c}$ are selected for each noise realization, with random *amplitudes*; while under hypothesis H_0, there is no underlying signal $s(t)$ to guide the matching pursuits, so $\boldsymbol{\zeta}$ represents a vector of N random variables (amplitudes) selected by the algorithm, with no distinction attributed for the particular (random) dictionary elements they represent. In both cases, however, $\mathbf{c}$ and $\boldsymbol{\zeta}$ represent the first N elements selected by the matching-pursuits algorithm. For a given realization, one does not know whether the waveform under consideration corresponds to H_0 or H_1, and therefore, to simplify notation, for the general case we denote the first N elements $\langle f|b_n\rangle$ selected by the matching-pursuits algorithm by the $N\times 1$ dimensional vector $\mathbf{r}$.

To derive a detector test statistic, we consider the ratio $p(\mathbf{r},\mathbf{m}|H_1)/p(\mathbf{r}|H_0)$.[6] Unfortunately, to obtain $\mathbf{m}$, one requites *a priori* knowledge of the unknown signal $s(t)$. The maximum-likelihood (ML) estimate of $\mathbf{m}$ is $\mathbf{m}=\mathbf{r}$, which yields $p(\mathbf{r},\mathbf{m}|H_1)=1$, a natural consequence of the fact that we assume no knowledge of the underlying signal. Alternatively, one could use a fixed basis (e.g., Gabor or wavelet[3,5]) that is the same for each waveform tested (as compared to the adaptive nature of the matching-pursuits algorithm). In

this case, *a priori* knowledge of the signal $s(t)$ is not required; rather, one can exploit information on which *subset* of bases functions[5] in the (fixed) complete set can robustly represent $s(t)$. While detector performance is improved by such a scheme, for the case of scattering from a submerged elastic target, the signature will often be too aspect- and environment-dependent to be represented robustly by a fixed subset of basis elements. Moreover, as discussed in the Introduction, it is unlikely in practice that one will have *a priori* access to all the aspect-dependent signatures from a complex elastic target.

Using the ML estimate $p(\mathbf{r},\mathbf{m}|H_1)=1$, the log of the likelihood ratio $p(\mathbf{r},\mathbf{m}|H_1)/p(\mathbf{r}|H_0)$ yields the statistic

$$l=\frac{1}{2}\frac{\mathbf{r^T r}}{\boldsymbol{\sigma}^2}-(N_D-1)\sum_{n=1}^{N}\ \ln\left[\int_{-|r_n|}^{|r_n|}dz\ \exp\left(-\frac{1}{2}\frac{z^2}{\boldsymbol{\sigma}^2}\right)\right]\begin{matrix}H_1\\ >\\ <\\ H_0\end{matrix} t, \tag{10}$$

where t is a threshold. While this result is relatively simple in form, it does require knowledge of the noise variance. Therefore, in the subsequent results, we have used the simpler, suboptimal statistic $l_N=\mathbf{r}^T\mathbf{r}$, where again $\mathbf{r}$ is a vector representing the first N dictionary elements $\langle f|b_n\rangle$ selected by the matching-pursuits algorithm (independent of whether f represents H_0 or H_1).

It should be pointed out that the choice of the statistic $l_N=\mathbf{r}^T\mathbf{r}$ is motivated by more than just simplifying Eq. (10). As discussed in Sec. I A, the dictionary D is designed to be matched to a waveform scattered from a general submerged elastic/inelastic target. Thus when an underlying target signature $s(t)$ is present (H_1) and the SNR is appropriate (see Sec. I B), then one expects a precipitous increase in $l_N=\mathbf{r}^T\mathbf{r}$ as the underlying signal is extracted (with matching-pursuits iteration). However, for the case of noise only (H_0), the dictionary is poorly matched to the noise ($E\{\langle n|b_k\rangle\}=0$), and therefore one would expect $l_N=\mathbf{r}^T\mathbf{r}$ to be relatively small, compared to the latter case (assuming σ^2 is sufficiently small). Thus the statistic $l_N=\mathbf{r}^T\mathbf{r}$, which has been derived above on mathematical grounds, based on several simplifying assumptions, could easily be justified on physical grounds, due to the relative match and mismatch of the dictionary to hypotheses H_1 and H_0, respectively.

D. Model order

In Sec. I C we derived the test statistic $l_N=\mathbf{r}^T\mathbf{r}$, based on the first N elements selected by the wave-based matching-pursuits algorithm. It is therefore of interest to choose the model order N judiciously. When a target is present, $l_N=\mathbf{r}^T\mathbf{r}$ will increase quickly as the underlying signal is extracted (assuming sufficient SNR). After the scattered signal is largely extracted from the measured waveform, the matching-pursuits algorithm will undertake the slowly convergent reconstruction of the noise (recall that our dictionary is complete), characterized by a relatively slow increase in $l_N=\mathbf{r}^T\mathbf{r}$. By comparison, for the case of noise only, the algorithm will perform the noise reconstruction from the outset. Thus one method of selecting N involves tracking the increase in $l_N=\mathbf{r}^T\mathbf{r}$ as a function of matching-pursuits iteration, and stopping the algorithm (thereby selecting N) when the ratio $\Delta_N=(l_N-l_{N-1})/l_N$ is sufficiently small. As discussed when presenting the results below, we have found it useful to use a simple ARMA filter to smooth Δ_N as a function of N, and then the stop point is then selected based on the smoothed statistic.

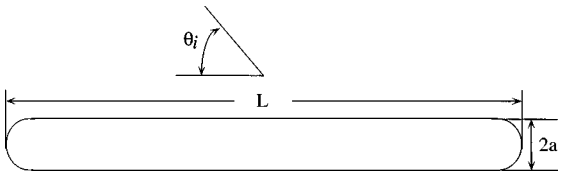

FIG. 1. Schematic of steel shell used in underwater acoustic-scattering measurements. Dimensions: $L=154.7$ cm, $a=9.43$ cm, and plate thickness $t=0.229$ cm.

Assume that the appropriate stop point (for an unknown signal) is iteration N_s. This implies that after N_s iterations the statistic $l_N=\mathbf{r}^T\mathbf{r}$ is sufficiently distinct statistically, for H_1 and H_0, to provide useful discrimination. If the matching-pursuits algorithm is run for iterations $n>N_s$, the algorithm will (ideally) be operating on noise alone under both H_1 and H_0. Thus for $N>N_s$, $l_N=\mathbf{r}^T\mathbf{r}$ should increase in a similar manner statistically for H_1 and H_0, and there should therefore be little change in detector performance (relative to stopping the algorithm at N_s). Consequently, we have found it prudent to bias the selection of N_s to be larger than what otherwise might seem necessary, to assure that all of $s(t)$ has been extracted prior to stopping the algorithm. This said, it may appear wise to make N_s as large as possible. However, while this may improve detector performance slightly, it will cause a significant increase in computation time, and therefore a balance must be reached between detector performance and algorithm run time. Finally, we note that one might also consider a sequential detector,[22] with which the algorithm is terminated after reaching a certain threshold. Although not investigated here, this is a potentially useful direction of future research.

II. EXAMPLE RESULTS

We consider acoustic scattering from an $L=154.7$ cm long (end to end) cylindrical steel shell of $a=9.43$ cm outer radius and plate thickness $t=0.229$ cm (Fig. 1). The scattering data were measured at the Naval Research Laboratory (see, for example, Refs. 23, 24), in the $1\leqslant ka\leqslant 16$ range, where k represents the acoustic wave number in water. The scattered waveforms were measured using a chirped input pulse, and, in the subsequent processed data, we replace this experimentally transmitted waveform with the Raleigh wavelet[25] shown in Fig. 2 (using standard deconvolution techniques). Although algorithm performance is independent of the input-pulse shape, we use the Raleigh wavelet because it is compact temporally, and therefore the various wave species are generally nononverlapping and thus easily discernable.

A. Denoising results

As discussed in Secs. I A and I B, the wave-based matching-pursuits algorithm employs a dictionary which is

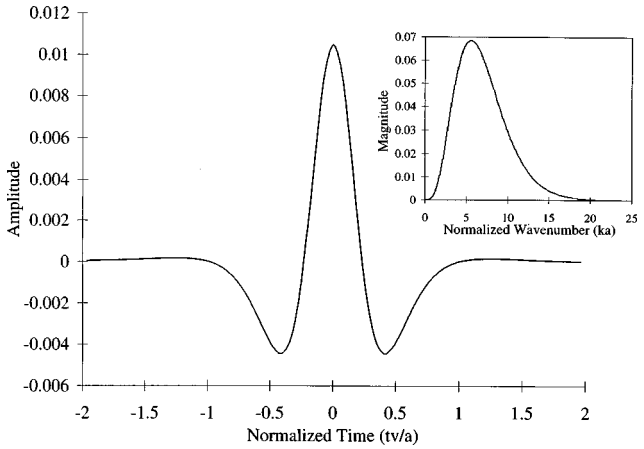

FIG. 2. Rayleigh wavelet (Ref. 25) used as the incident pulse for all scattering data (imposed after deconvolving the chirped pulse used in the measurements), with spectrum shown inset. The time and frequency are normalized with respect to a and v, where a is shown in Fig. 1 and $v = 1500$ m/s is the sound speed in water.

matched to the underlying wave physics, thereby providing the potential for denoising. In particular, if the SNR is sufficiently high (to be quantified below), the matching-pursuits scheme will initially extract the underlying waveform, rather than the additive noise. Therefore, by stopping the iterative algorithm appropriately, match pursuits can be utilized to separate an underlying scattered waveform from noise/clutter.

To illustrate the denoising performance achieved by wave-based matching pursuits, consider the backscattered waveform shown in Fig. 3(a), which corresponds to $\theta_i = 75°$ (see Fig. 1). The initial scattered signal in Fig. 3(a) represents the specular response, followed subsequently by a series of strong waveforms due to helical-wave excitation. We corrupt the scattered waveform in Fig. 3(a) by additive zero-mean white Gaussian noise, with variance σ^2 [see Fig. 3(b)]. The scattered waveform $s(t)$ in Fig. 3(a) is discretized with

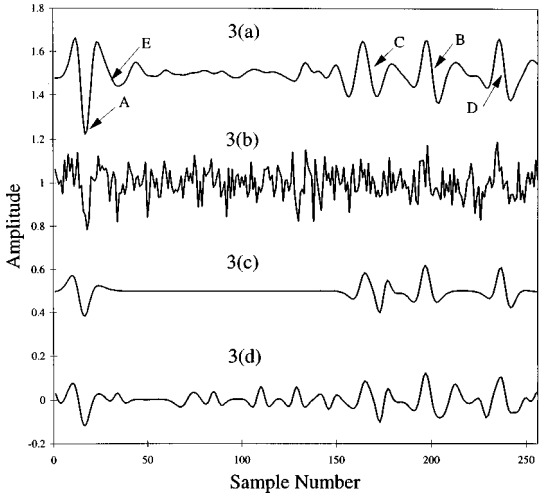

FIG. 3. Example results for denoising waveforms scattered from the target in Fig. 1 (with the addition of white Gaussian noise). (a) Backscattered waveform from target in Fig. 1, at angle $\theta_i = 75°$. (b) Waveform in (a), with one realization of 18-dB additive white Gaussian noise. (c) Signal extracted from (b) after five wave-based matching-pursuits iterations. (d) Signal extracted from (b) after 15 matching-pursuits iterations.

TABLE I. Relative energies in the first five dictionary elements selected via matching pursuits, for representation of the signal in Fig. 3(a) [wavefront positions are labeled A–E in Fig. 3(a)]. Additionally, for 18-dB and 12-dB SNR, the signal-component SNR (SC-SNR) for each of the five wavefronts A–E is given, defined as $\langle s|b_n\rangle/\sigma^2$, where b_n represents the nth wavefront selected and $s(t)$ represents the signal in Fig. 3(a).

Label	Relative energy (dB)	SC-SNR (dB)	
		18-dB SNR	12-dB SNR
A	−4.23	13.85	7.85
B	−7.98	10.10	4.10
C	−8.08	10.00	4.00
D	−8.19	9.89	3.89
E	−15.52	2.56	−3.44

N_p data points, and Fig. 3(b) corresponds to an SNR of 18 dB, with SNR defined here as $\langle s|s\rangle/\sigma^2$. As discussed in Sec. I B, effective matching-pursuit denoising is dictated by the signal-component SNR (denoted SC-SNR) being relatively large, i.e., $|\langle s|b_k\rangle|^2 > \sigma^2$, for some $b_k(t) \in D$. If we assume $b_n(t)$, $n = 1 \rightarrow N$ represent the N elements of D which principally constitute $s(t)$, we can estimate the SC-SNR, $|\langle s|b_n\rangle|^2/\sigma^2$, by first applying the wave-based matching-pursuits algorithm on the noiseless waveform in Fig. 3(a) (to compute $\langle s|b_n\rangle$). In Table I we list the SC-SNR for the five principal elements extracted by the matching pursuits algorithm, for SNRs of 18 and 12 dB. The temporal location of these components are denoted in Fig. 3(a).

For an SNR of 18 dB [Fig. 3(b)], we have found the results of the denoising procedure to be very repeatable, with example results plotted in Fig. 3(c) and (d) for $N = 5$ and $N = 15$ iterations, respectively. In Fig. 3(c), we see that the principal constituents have been extracted in the first 5 iterations, while after 15 iterations [Fig. 3(d)] noise contributions [not seen in Fig. 3(a)] are becoming evident. After the principal components of $s(t)$ have been extracted (after the first $N_s = 5$ iterations), for iterations $n > N_s$ the algorithm will ideally process noise alone. Thus the energy $|\langle f|b_n\rangle|^2$ in the elements selected for $n > N_s$ will be dictated by the noise variance σ^2, since the expectation $E\{|\langle n|b_k\rangle|^2\} = \sigma^2$, $\forall b_k \in D$. The results in Fig. 3(c) and (d) demonstrate the difficulty of stopping the algorithm properly for denoising purposes, under the case of large noise variance. However, as discussed in Sec. II B, this is less of an issue for detection. Our experience with the data set examined here indicates that, after detection, one can generally have confidence that the first several dictionary elements selected to represent $f(t) = s(t) + n(t)$ are representative of $s(t)$, while elements selected subsequently are more tenuous. An issue for future study involves the development of schemes to put confidence bounds on the accuracy of elements selected from the dictionary D, as a function of matching-pursuits iteration n. Finally, we note that the relatively high noise case addressed in Fig. 3 has been selected because in Sec. II B detector performance is examined at such SNRs. For higher SNRs, at which the denoising is less sensitive to the stop point, the detector false alarm rate is too low to be quantified accurately with a reasonable number of Monte Carlo realizations.

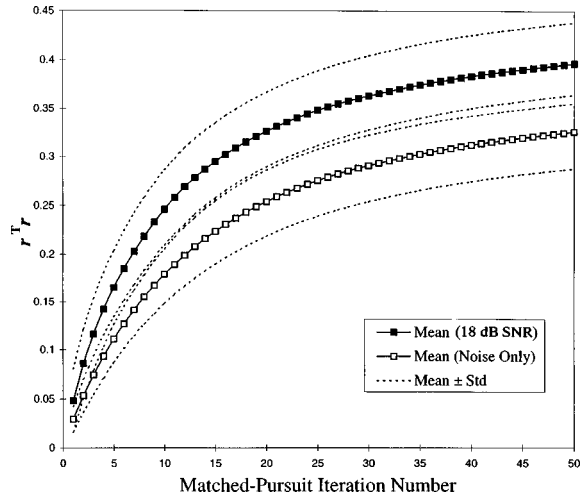

FIG. 4. Expectation of $\mathbf{r}^T\mathbf{r}$ as a function of matching-pursuits stop point N. Results are shown for the waveform in Fig. 3(a), with 18-dB additive white Gaussian noise, and for the case of noise alone. The standard deviations for each of these results are depicted via the dashed curves. In both cases, 1000 Monte Carlo realizations were utilized.

Denoising results have only been presented for the case of $\theta_i = 75°$. This angle was selected because it demonstrates the interesting effects of helical-wave excitation (which are only seen over a limited range of incident angles). However, we have tested the denoising scheme for incident angles over the complete range of $\theta_i = 0°$ to 359°, and our investigations indicate that the results in Fig. 3 are representative of what is found for a general θ_i. In the detection examples considered in the next section, we examine algorithm robustness as a function of incident angle θ_i.

B. Detection

Assume under hypotheses H_1 (signal plus noise) that there is a stop point N_s at which, on average, the underlying signal $s(t)$ is largely extracted. If $(\mathbf{r}^T\mathbf{r}|H_0)$ represents $\mathbf{r}^T\mathbf{r}$ under hypothesis H_0 (noise only), with $(\mathbf{r}^T\mathbf{r}|H_1)$ representing the same under H_1, after $N = N_s$ iterations, the expectation $E\{(\mathbf{r}^T\mathbf{r}|H_1) - (\mathbf{r}^T\mathbf{r}|H_0)\}$ is approximately $\langle s|s\rangle + N_s\sigma^2 - E_{Ns}$, where E_{Ns} represents the mean noise energy extracted after N_s iterations, under H_0. Moreover, for $N > N_s$ the matching-pursuits algorithm will ideally be processing noise only, for both hypotheses H_0 *and* H_1. Thus one would expect that $E\{(\mathbf{r}^T\mathbf{r}|H_1) - (\mathbf{r}^T\mathbf{r}|H_0)\}$ will remain relatively constant for stop points $N > N_s$. This explains the results in Fig. 4, in which the difference in $\mathbf{r}^T\mathbf{r}$ between H_0 and H_1 is relatively constant for sufficiently large N (results are shown for $\theta_i = 75°$, although similar results were found for all θ_i considered). The performance of a detector based on the statistic $\mathbf{r}^T\mathbf{r}$ will be relatively insensitive to the stop point N for $N > N_s$ [assuming that the *distributions* of $(\mathbf{r}^T\mathbf{r}|H_1)$ and $(\mathbf{r}^T\mathbf{r}|H_0)$ are relatively constant for $N > N_s$], and therefore it is this regime in which we wish to operate the detector. Finally, we note that at relatively high SNRs there is generally a pronounced difference between $E\{(\mathbf{r}^T\mathbf{r}|H_1)\}$ and $E\{(\mathbf{r}^T\mathbf{r}|H_0)\}$,[13,14] since $E\{|\langle n|b_k\rangle|^2\} = \sigma^2 \ll |\langle s|b_n\rangle|^2$ for $n \leqslant N_s$. Again, the relatively high noise cases considered here were selected such that ROC curves could be calculated accurately with a reasonable number of Monte Carlo realizations.

The parameter N_s is dependent on the particular scattered waveform $s(t)$, which, for complex submerged elastic targets, can vary substantially as a function of aspect angle. However, it is reasonable to assume that one might have *a priori* knowledge of the range of N_s required to robustly represent the waveform scattered from a given target. Alternatively, to adaptively sense when the matching-pursuits algorithm has decomposed the signal, we can observe, for example, the change (gradient) in $\mathbf{r}^T\mathbf{r}$ as a function of N, as described in Sec. I D. Defining $l_N = \mathbf{r}^T\mathbf{r}$ as the test statistic calculated after N matching-pursuits iterations, we define $\Delta_N = (l_N - l_{N-1})/l_N$. To smooth Δ_N we employ the simple ARMA filter $b_0\Delta_N + a_1\Delta_{N-1}$, with coefficients $b_0 = 0.8$ and $a_1 = 0.2$. Many more sophisticated filters could be used to smooth Δ_N; however, the very simple one used here was selected because it does not exploit *a priori* information that might unfairly bias the detector performance (i.e., one may be able to design a more complex filter that optimizes performance for a particular target; however, the results may be misleading, since the filter may not be relevant to a general class of targets).

To quantify detector performance, we first plot in Fig. 5 the receiver-operating characteristic (ROC) for the $\theta_i = 75°$ case examined in Fig. 3, for SNRs of 18, 15, and 12 dB. The matching-pursuit characteristics were computed via 1000 Monte Carlo realizations, with the stop point fixed at $N_s = 15$. These results demonstrate that at SC-SNRs for which the matching-pursuits-based detector is appropriate, there is substantially improved detector performance relative to an energy detector (the ROC for which are calculated analytically[6]). The matching-pursuits-based detector and the energy detector employ the same underlying assumptions: no *a priori* knowledge of the particular scattered signal $s(t)$. Although the matching-pursuits employs an energy-based statistic $l_N = \mathbf{r}^T\mathbf{r}$, the algorithm yields improved performance relative to a classical energy detector by utilizing a dictionary based on the underlying wave physics, for scattering from a *general* submerged target. Finally, we also computed ROCs for stop points $N = 20$, 30, and 40, in addition to the $N = 15$ considered in Fig. 5. As expected from the previous discussion, the detector performance was nearly invariant to N for $N > 15$.

The ROC results plotted in Fig. 6 were computed by applying the adaptive stop criterion discussed above, for the $\theta_i = 75°$ scattered waveform, with the algorithm stopped when $b_0\Delta_N + a_1\Delta_{N-1} < t_s$. We arbitrarily set the stop threshold as $t_s = 0.01$, with better results expected for smaller t_s (to assure the algorithm stops in the region $N > N_s$). However, the number $t_s = 0.01$ was selected as what we deemed to be a reasonable stop criterion, if no *a priori* knowledge were available (in an effort, as above, to not bias algorithm performance too favorably, based on *a priori* information one may not have in practice). Nevertheless, despite the conservative t_s, we note by comparing Figs. 5 and 6 that the adaptive scheme only suffers a small degradation in performance, relative to the fixed stopped criterion $N = 15$, which

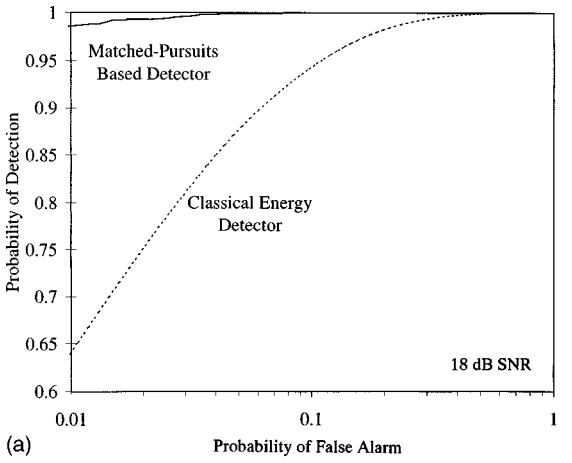

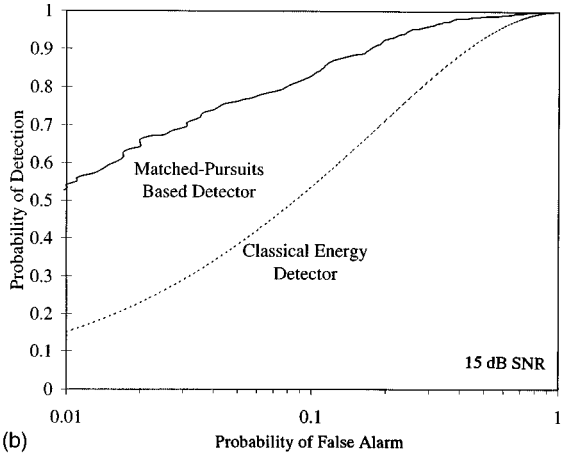

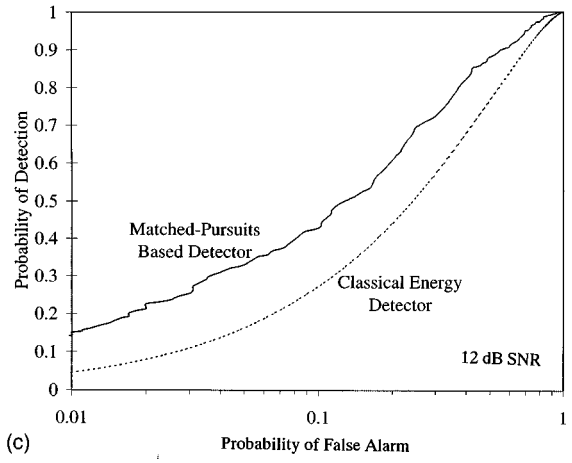

FIG. 5. Receiver operating characteristic (ROC), using the target signature in Fig. 3(a). A comparison is shown between results of the matching-pursuits detector and an energy detector. With regard to the former, the algorithm is stopped after $N_s = 15$ iterations. (a) 18-dB SNR, (b) 15-dB SNR, and (c) 12-dB SNR.

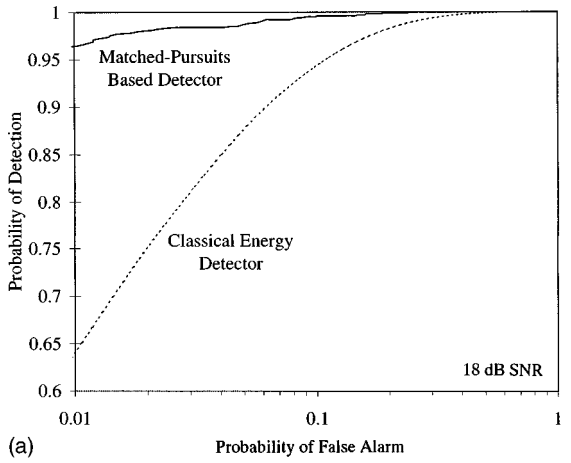

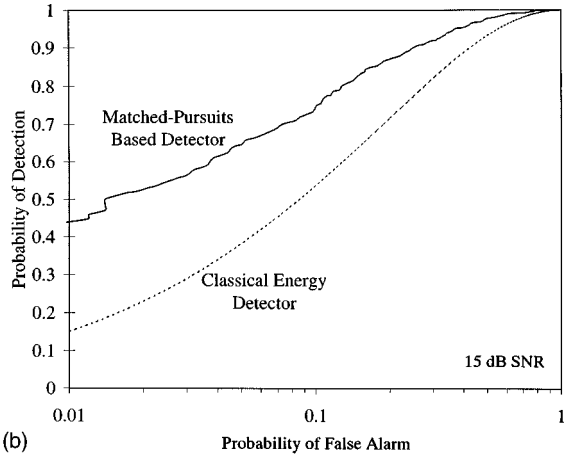

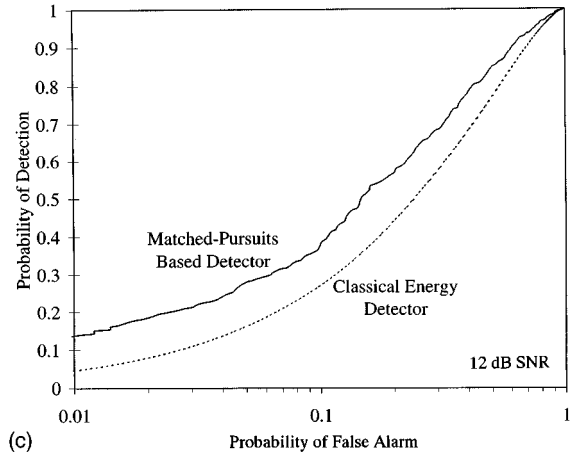

FIG. 6. As in Fig. 5, but now the adaptive stop criterion in Secs. I D and II B is applied.

exploited *a priori* knowledge of N_s. As a comparison with the fixed stop point considered in Fig. 5, the *mean* stop point for the *adaptive* stop procedure was $E\{N_s\} = 17.9$, with a variance of 3.0.

Thus far all results have been presented for the particular backscatter angle of $\theta_i = 75°$. However, as discussed in the Introduction, the matching-pursuits algorithm requires no *a priori* knowledge of the particular scattered waveform $s(t)$ under consideration, and therefore algorithm performance should be largely independent of the backscattered angle θ_i. After testing our algorithm on most of the 720 aspect angles (0.5° angular discretization) measured by the Naval Research Laboratory, we have found the expected aspect-independent property generally realized in practice. As an example, in Fig. 7 we plot the waveforms scattered from the target in Fig. 1 for $\theta_i = 60°$ and 90° (the signals scattered at these angles, along with 75°, are representative of typical waveforms scattered from the target in Fig. 1). The 90° angle of incidence, for example, is characterized, after the initial strong re-

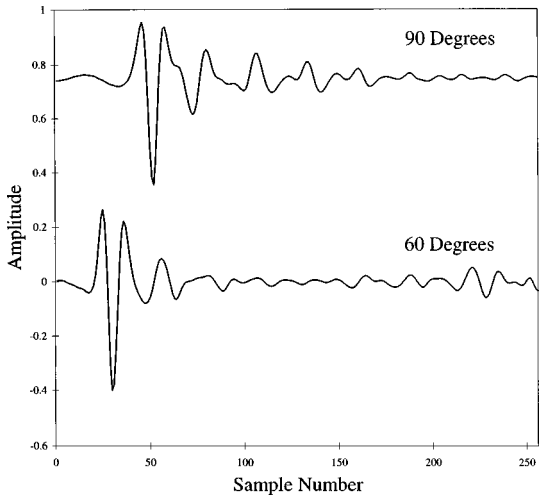

FIG. 7. Waveforms scattered from the target in Fig. 1, at angles $\theta_i = 60°$ and $\theta_i = 90°$.

sponse, by a series of decaying wavefronts, sequenced nearly periodically. This latter phenomenon is due to energy leaked to the observer, from multiple circumnavigations of curved-plate leaky waves.[19,20] This physical phenomenon is fundamentally different than that of the helical wave seen for $\theta_i = 75°$, but both waveforms can be represented compactly in terms of the wave-based elements in D.

A comparison of detector performance is shown in Fig. 8 for $\theta_i = 60°$, 75°, and 90°, using the adaptive stop criterion, at SNRs of 18 and 15 dB. The results in Fig. 8 were computed using 1000 Monte Carlo iterations. At both 18-dB and 15-dB SNR, the detector performs essentially the same for each waveform. This substantiates the relative aspect-independent performance of the matching-pursuits detector, despite the fact that $s(t)$ may depend strongly on aspect. Moreover, at both these SNRs the matching-pursuit detector well out performs an energy detector.

Finally, a comment should be made concerning the noisy waveforms processed in Fig. 8. By normalizing the scattered waveforms, we considered identical SNRs for each

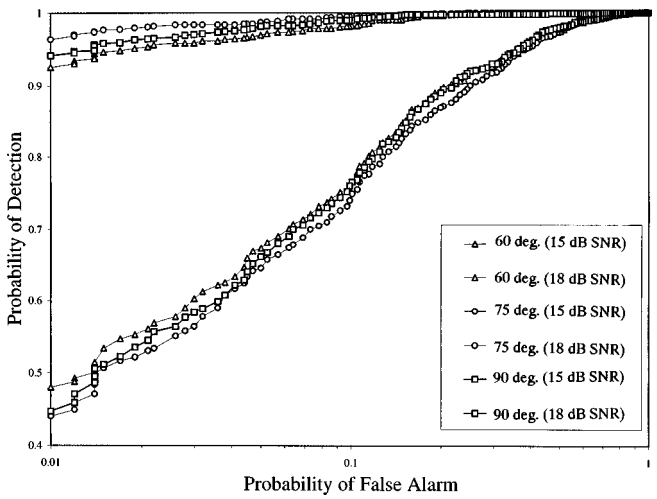

FIG. 8. Comparison of the receiver operating characteristics using the matching-pursuits detector, for waveform scattered from $\theta_i = 60°$, 75°, and 90°. Results are shown for SNRs of 18 dB and 15 dB.

of the angular-dependent scattered signals $s(t)$. However, in practice, the actual SNR will also be aspect dependent, since the *amplitude* (strength) of the scattered waveforms will vary with angle θ_i (in addition to the shapes, as was considered in Fig. 8). For example, the peak scattered field at $\theta_i = 0°$ (not considered here) is considerably smaller than that at $\theta_i = 90°$. This underscores the necessity for an adaptive algorithm, which does not exploit *a priori* knowledge of the SNR, the latter being strongly aspect dependent and thus not known in advance.

III. CONCLUSIONS

A wave-based matching-pursuits algorithm has been developed for denoising and detecting waveforms scattered from general submerged targets. The algorithm has been demonstrated through the processing of measured acoustic data scattered from a submerged elastic shell. Algorithm performance for noisy data is dictated by the signal-component signal-to-noise ratio, denoted here as SC-SNR. The matching-pursuits algorithm iteratively decomposes the general scattered signal $s(t)$ into components $b_k(t)$ catalogued in a dictionary D. For the case of additive noise $n(t)$ with variance σ^2, the matching-pursuits algorithm operates as designed when at least some of the $b_n(t)$ selected from D for representation of the noisy waveform $s(t)+n(t)$ are characterized by ''large'' SC-SNR $|\langle s|b_n\rangle|^2/\sigma^2$. In the context of the research reported here, we have found effective denoising and detector performance when the $|\langle s|b_n\rangle|^2/\sigma^2$ are in excess of approximately 5 dB. This underscores the need for a dictionary D which can represent the scattered field in a compact, parsimonious manner (such that as much energy as possible is contained in each $|\langle s|b_n\rangle|^2$ extracted by the algorithm).

As discussed in the Introduction, all waveforms scattered from general submerged targets can be decomposed in terms of a series of (generally) dispersed wavefronts, motivating the wavefront-based dictionary applied here. However, often successive wavefronts can be repackaged compactly in terms of resonances and/or chirps. Such wave objects generally require some *a priori* knowledge of the target, which we sought to avoid in the context of the research presented here. However, by so repackaging such successive wavefronts into resonances/chirps, the composite bases $b_n'(t)$ will necessarily have a larger $|\langle s|b_n'\rangle|^2/\sigma^2$ than any of the wavefronts alone, thereby improving robustness in noise. In future work, we will explore such repackaging, in a manner that minimizes the extent of *a priori* knowledge one must possess.

Finally, the examples presented here considered measured acoustic scattering data from a submerged elastic shell, with the shell placed in a uniform, time-independent background. The effects of a shallow-water waveguide and of time-varying and inhomogeneous sound speeds have not been considered. While such effects will clearly complicate matters and must be addressed for many applications of interest, the purpose of the present paper was simply to present a new algorithm, wave-based matching pursuits, and demonstrate its applicability for scattering from submerged elastic

targets. The efficacy of this algorithm has been examined particularly in the context of target detection (and subsequent identification). Shallow-water waveguide effects and time-varying media represent significant escalations in problem complexity, and future research is underway to handle such in the context of the general matching-pursuits paradigm.

ACKNOWLEDGMENTS

The authors wish to thank Dr. Luise Couchman and Dr. Brian Houston of the Naval Research Laboratory for providing the acoustic scattering data. This research has been sponsored in part by the Office of Naval Research under Grant No. N00014-96-1-0861 and the Naval Research Laboratory under Grant No. N00014-96-C-6033.

[1] G. Golub and C. Van Loan, *Matrix Components* (Johns Hopkins U.P., Baltimore, MD, 1989), 2nd ed.
[2] S. G. Mallat, ''Multifrequency channel decomposition of images and wavelet models,'' IEEE Trans. Acoust., Speech, Signal Process. **37**, 2091–2110 (1989).
[3] S. G. Mallat, ''A theory for multiresolution signal decomposition: The wavelet representation,'' IEEE Trans. Pattern. Anal. Mach. Intell. **11**, 674–693 (1989).
[4] I. Daubechies, ''The wavelet transform, time-frequency localization and signal analysis,'' IEEE Trans. Inf. Theory **36**, 961–1005 (1990).
[5] B. Friedlander and B. Porat, ''Detection of transient signals by the Gabor representation,'' IEEE Trans. Acoust., Speech, Signal Process. **37**, 169–180 (1989).
[6] H. L. Van Trees, *Detection, Estimation, and Modulation Theory, Part 1* (Wiley, New York, 1968), pp. 261–264.
[7] R. A. Atles, ''Sonar for generalized target description and its similarity to animal echolocation systems,'' J. Acoust. Soc. Am. **59**, 97–105 (1976).
[8] J. B. Keller, ''Geometrical theory of diffraction,'' J. Opt. Soc. Am. **52**, 116–130 (1962).
[9] P. L. Marston, ''GTD for backscattering from elastic spheres and cylinders in water and the coupling of surface elastic waves with the acoustic field,'' J. Acoust. Soc. Am. **83**, 25–37 (1988).
[10] G. S. Sammelmann, D. H. Trivett, and R. H. Hackman, ''The acoustic scattering by a submerged, spherical shell. I: The bifurcation of the dispersion curve for the spherical antisymmetric Lamb wave,'' J. Acoust. Soc. Am. **85**, 114–124 (1989).
[11] M. F. M. Osborne and S. D. Hart, ''Transmission, reflection, and guiding of an exponential pulse by a steel plater in water. I: Theory,'' J. Acoust. Soc. Am. **17**, 1–18 (1945).
[12] S. G. Kargl and P. L. Marston, ''Observations and modeling of the backscattering of short tone bursts from a spherical shell: Lamb wave echoes, glory, and axial reverberations,'' J. Acoust. Soc. Am. **85**, 1014–1028 (1989).
[13] S. G. Mallat and Z. Zhang, ''Matching pursuits with time-frequency dictionaries,'' IEEE Trans. Signal Process. **41**, 3397–3415 (1993).
[14] M. McClure and L. Carin, ''Matched pursuits with a wave-based dictionary,'' IEEE Trans. Signal Process. **45**, 2912–2927 (1997).
[15] L. B. Felsen, ''Observable-based wave modeling: Wave objects, spectra and signal processing,'' in *Huygens' Principle 1690–1990: Theory and Applications*, edited by H. Bolk, H. A. Ferwarda, and H. K. Kuiken (Elsevier, New York, 1992).
[16] L. B. Felsen, ''Progressing and oscillatory waves for hybrid synthesis of source excited propagation and diffraction,'' IEEE Trans. Antennas Propag. **32**, 775–796 (1984).
[17] E. Heyman and L. B. Felsen, ''A wavefront interpretation of the singularity expansion method,'' IEEE Trans. Antennas Propag. **33**, 706–718 (1985).
[18] L. Flax, G. C. Gaunaurd, and H. Uberall, ''Theory of resonant scattering,'' in *Physical Acoustics XV* (Academic, New York, 1981).
[19] M. C. Junger and D. Feit, *Sound Structures and Their Interaction*, 2nd ed. (MIT, Cambridge, MA, 1986).
[20] L. B. Felsen and N. Marcuvitz, *Radiation and Scattering of Waves* (Prentice-Hall, Englewood Cliffs, NJ, 1973).
[21] A. Papoulis, *Probability, Random Variables, and Stochastic Processes*, 3rd ed. (McGraw-Hill, New York, 1991).
[22] A. Wald, *Sequential Analysis* (Dover, New York, 1973).
[23] D. M. Drumheller, D. H. Hughes, B. T. O'Connor, and C. F. Gaumond, ''Identification and synthesis of acoustic scattering components via the wavelet transform,'' J. Acoust. Soc. Am. **97**, 3649–3656 (1995).
[24] N.-C. Yen, L. R. Dragonette, and S. K. Numrich, ''Time-frequency analysis of acoustic scattering from elastic objects,'' J. Acoust. Soc. Am. **87**, 2359–2370 (1990).
[25] P. Hubral and M. Tygel, ''Analysis of the Raleigh pulse,'' Geophysics **54**, 654–658 (1989).

Minimum variance distortionless response beamforming of acoustic array data

Brian G. Ferguson
Maritime Operations Division, Defence Science and Technology Organisation, PO Box 44, Pyrmont NSW 2009 Australia

(Received 5 July 1995; accepted for publication 22 April 1998)

An array of hydrophones is towed below the sea surface so as to sample the underwater acoustic pressure field in both space and time, while a land-based array of microphones is used to sense the atmospheric acoustic environment which, at the time, was dominated by a single source of broadband energy. After transformation from the time domain to the frequency domain, the sensor outputs from each array are weighted and combined in the spatial domain (beamformed) so as to produce a frequency–wave number power spectrum, which displays the power spectral density distribution of the various signal and noise sources as a joint function of frequency and wave number. The frequency-domain beamforming (or spatial filtering) process enables both conventional and optimal estimation of the frequency–wave number power spectrum. The optimal spatial filtering technique used here is commonly referred to as the Minimum Variance Distortionless Response (MVDR) beamformer which requires inversion of the observed narrow-band cross-power spectral matrix at each frequency of interest. A comparison of the frequency–wave number power spectra estimated by the two spatial filtering techniques shows that the MVDR beamformer enables the various sources of acoustic energy to be more clearly delineated in frequency–wave number space. The MVDR beamformer is a data-adaptive spatial filter which is observed to suppress sidelobes, to enhance the spatial resolution of an array through narrower beamwidths, and to provide superdirective array gain at frequencies well below the design frequency of an array. By extending the processing to include the data from another type of towed array, it is shown that frequency–wave number analysis, when incorporated with MVDR beamforming, constitutes a powerful diagnostic tool for studying the self-noise characteristics of towed arrays. [S0001-4966(98)02108-0]

PACS numbers: 43.60.Gk, 43.30.Yj [JLK]

INTRODUCTION

Arrays of acoustic sensors are used to detect weak signals, to resolve closely spaced sources and to estimate the bearing and other properties of a signal source. The array of sensors samples the acoustic field at different (discrete) points in space, then a beamformer appropriately weights the sensor outputs prior to summation so as to enhance the detection and estimation performance of the acoustic system by improving the output signal-to-noise ratio. The outputs of a spatially distributed array of sensors are combined by the beamformer so that signals from a chosen direction are coherently added while the effects of noise and interference from other directions are reduced by destructive interference.

The arrays considered in this paper consist of a line array of microphones, which formed part of an experimental land-based acoustic surveillance system, and a horizontal line array of hydrophones towed below the sea surface. In addition, another type of towed array is considered briefly to highlight the general utility of the techniques presented in this paper for analyzing the self-noise in towed arrays.

Rather than restricting the beamforming process to real angles of arrival, the spatial filtering of the acoustic array data is extended to include the whole of wave number space (real angles of arrival form a subspace within wave number space) so that the wave vector **k** is used here instead of angular coordinates. Note that the term ''wave number'' refers to the magnitude of the wave vector, the direction of which is orthogonal to the wavefront of the incident plane wave. The wave number is the number of wavelengths per unit distance (that is, the spatial frequency) in the direction of propagation.

The total power incident on an array may be estimated as a function of both the frequency f and the wave vector components k_x, k_y, and k_z. For the linear arrays considered here, only the component of the wave vector in the direction of the array's axis (denoted k_x) is required where $k_x=(\sin\theta)/\lambda=(f\sin\theta)/c$; θ is the angle of incidence (measured from the normal to the array axis: $-90°\leqslant\theta\leqslant+90°$), f and λ are the frequency and wavelength (respectively) of the plane-wave arrival, and c is the speed of sound propagation in the medium. The parameter k_x represents the spatial frequency of the incident plane wave in the direction of the array axis. (Note that alternate definitions of k_x include a factor of 2π.)

If plane waves of different frequencies (emanating from a broadband source located in the far field) arrive at the array from the same direction, say θ_0, then the frequency–wave number coordinates for these waves lie on a straight line that runs radially outward from the origin of the frequency–wave number plot with a slope (dk_x/df) of $\sin\theta_0/c$ (see Fig. 1). The area of the frequency–wave number plot for which $|k_x|\leqslant f/c$ (that is, $|\sin\theta|\leqslant 1$) is referred to as the ''physical

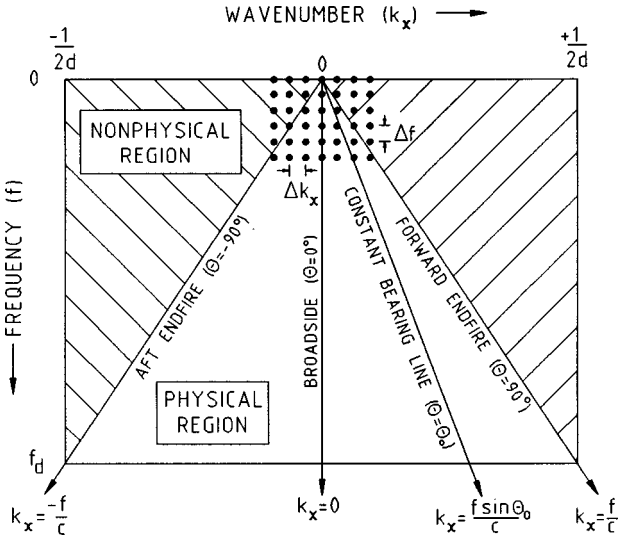

FIG. 1. Generic frequency–wave number plot, where f_d is the design frequency of the array. The design frequency of an array with equally spaced sensors is the frequency whose corresponding wavelength is equal to twice the separation distance between adjacent sensors, that is, $f_d=c/(2d)$.

region.'' (Note that the physical region is also commonly referred to as the ''acoustic region.'') Figure 1 shows that the physical region (unhatched area) is bounded by the forward endfire direction ($\theta=+90°$) and the aft endfire direction ($\theta=-90°$). Plane waves traveling with a velocity c that are incident on the array at angles between the aft and forward endfire directions (that is, $-90°\leqslant\theta\leqslant+90°$) have frequency–wave number coordinates that are restricted to this region. The remaining (hatched) areas in Fig. 1 represent the ''nonphysical region,'' waves propagating in an axial direction along the array with a speed less than c have frequency–wave number coordinates that lie in this region.

In Fig. 1, f and k_x have been treated as continuous variables. However, for sampled data, a matrix of discrete data points is superimposed on the diagram in which the vertical and horizontal spacings between adjacent points correspond to the respective wave number and frequency bin widths (Δk_x and Δf); a subset of these points is represented by the rectangular grid of points in Fig. 1.

I. FREQUENCY–WAVE NUMBER TRANSFORM

The acoustic pressure field in which the array of sensors is immersed is assumed to consist of a superposition of traveling waves that sweep across the array as plane wavefronts.[1] The frequency–wave number power spectral density provides the mean square value for the amplitudes of these waves as a function of both frequency and wave number. In other words, frequency–wave number analysis assumes that the acoustic pressure field can be decomposed into a sum of complex exponentials that are mathematically equivalent to plane waves. For a linear array of equispaced sensors, the decomposition of the acoustic pressure field into a wave number spectrum of plane-wave components is mathematically equivalent to the Fourier transformation of a sampled time series into a spectrum of single-frequency components. Thus an isomorphism exists between the time–frequency transform and the space–wave number transform.

For a linear array of equispaced sensors, the frequency–wave number spectrum can be evaluated by using a two-dimensional discrete Fourier transform of a matrix having the spatial samples of the acoustic pressure field as rows and the temporal samples as columns.[2,3] The frequency–wave number power spectral density $S(\mu\Delta k_x,\nu\Delta f)$, denoted $S_{\mu\nu}$, is given by

$$S_{\mu\nu}=X_{\mu\nu}X^*_{\mu\nu}, \tag{1}$$

where $X_{\mu\nu}=\Sigma_{j=0}^{N-1}\Sigma_{l=0}^{M-1}x_{jl}\exp(-i2\pi\mu j/N)\exp(-i2\pi\nu l/M)$, $X^*_{\mu\nu}$ is the complex conjugate of $X_{\mu\nu}$, μ is the wave number index, ν is the frequency index, j is the sensor (or spatial sample) index, N is the number of sensors, l is the time sample index, M is the number of time samples, $x_{jl}=x_j(l\tau_0)$ is the lth time sample from the jth sensor, τ_0 is the temporal sampling period, Δf is the frequency bin width, and Δk_x is the wave number bin width.

The quantity $S_{\mu\nu}\Delta k_x\Delta f$ represents the power incident on the array within a frequency range of $(\nu\pm1/2)\Delta f$ and the wave number range of $(\mu\pm1/2)\Delta k_x$. Now $X(\mu\Delta k_x,\nu\Delta f)$, denoted $X_{\mu\nu}$, is a two-dimensional discrete Fourier transform that represents the decomposition of the matrix $\{x_{jl}\}$ into a set of orthogonal plane waves. If $X(k_x,f)$ is a continuous function of k_x and f, then not all the values of $X(k_x,f)$ will be independent. The value of $X(k_x,f)$ for an arbitrary k_x and f can be expressed as a linear combination of a set of orthogonal vectors consisting of $M/2$ sine and cosine waves having temporal periods that are integer subdivisions of the observation interval and N complex spatial frequencies whose spatial periods are integer subdivisions of the array aperture.

II. ESTIMATION OF THE FREQUENCY–WAVE NUMBER POWER SPECTRUM

In this paper, the frequency–wave number power spectrum is estimated using both conventional and optimal spatial filtering techniques, which are implemented in the frequency domain. The conventional method, which corresponds to unshaded delay-and-sum beamforming in the time domain, uses a fixed wave number window, and its resolution in wave number space is determined by the beamwidth of the main lobe of the array's beam pattern. (The secondary lobes of the beam pattern are called ''sidelobes.'') Alternatively, with the optimal method of estimation, a variable wave number window is used whose shape is a function of the wave number at which the estimate is obtained.

The output power of the optimal spatial filter is minimized subject to the constraint of a unity power response at the wave number of interest. This spatial filter is commonly referred to in the literature as the Minimum Variance Distortionless Response (MVDR) beamformer, or the Capon beamformer. Thus a traveling wave with the wave number of interest is considered to be a ''signal'' by the spatial filter and is unaffected as it passes through the spatial processor, whereas traveling waves with other wave numbers are considered as ''noise'' and are suppressed by spatial filtering. The optimal filter senses the wave number distribution of the

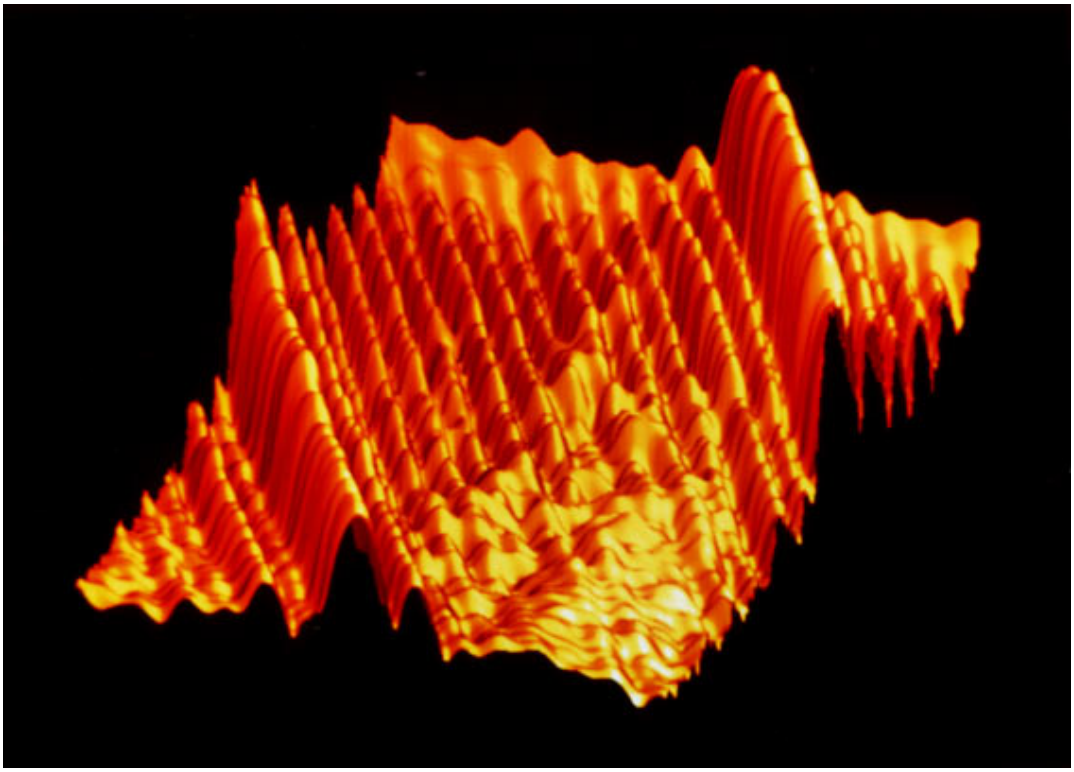

FIG. 2. Frequency–wave number power spectrum for the microphone array estimated using the conventional frequency-domain beamforming technique. The dominant feature in the spectrum shows the variation with frequency and wave number of the acoustic energy received by the array from a stationary jet engine operating near the forward endfire direction. The orientation of the axes is shown in Fig. 4 and the frequency–wave number power spectral density is in logarithmic units. The maximum frequency is equal to twice the design frequency of the array. The discontinuity in the line of constant bearing is due to spatial aliasing.

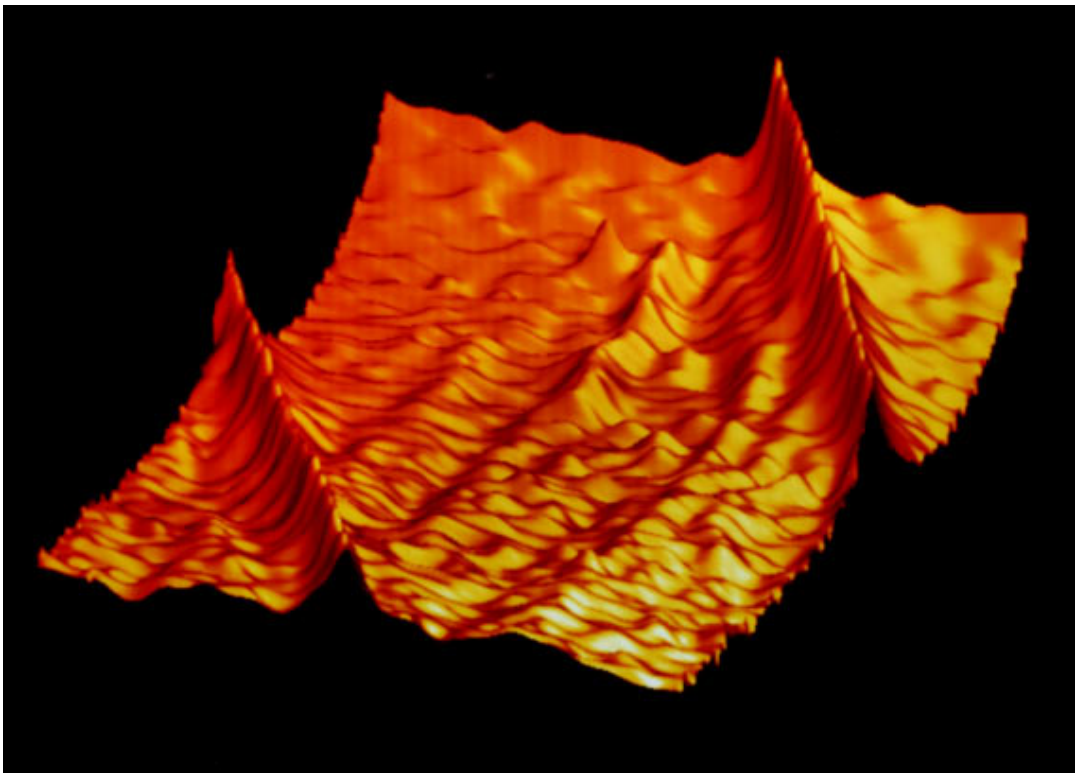

FIG. 3. Same as Fig. 2 but the MVDR beamforming technique is used instead of the conventional method.

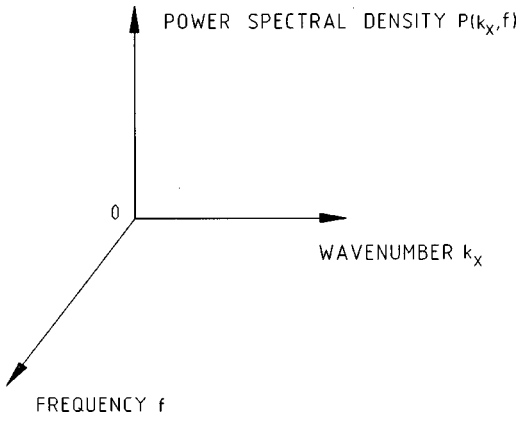

FIG. 4. Rectangular Cartesian coordinate system showing the orientation of the axes for the frequency–wave number power spectra displayed in this paper.

noise sources and then adjusts its spatial response (beam pattern) so that the beamformer's output noise power is a minimum. The performance of such a beamformer is optimum in the sense that the output signal-to-noise ratio (or equally, the array gain) is a maximum. (Note that the array gain is defined as the beamformer's output signal-to-noise ratio divided by the signal-to-noise ratio of a single sensor.) This technique of wave number filtering has proven to be extremely useful for the estimation of frequency–wave number spectra when the incoherent noise power is relatively small compared with the power of the propagating waves.[4] In an incoherent noise field, the optimal technique is equivalent to the conventional technique.

Since the spatial filtering is implemented in the frequency domain, the time waveform of each sensor is decomposed into its complex spectral components by using a fast Fourier transform routine. With $X_j(f)$ denoting the complex narrow-band output of the jth sensor, then the observed cross-power spectral matrix, denoted by $\mathbf{R}(f)$, is given by[5]

$$R_{ij}(f)=\langle X_i(f)X_j^*(f)\rangle, \quad \text{for } i,j=1,2,...,N, \tag{2}$$

where N is the total number of sensors in the array and $\langle\ \rangle$ indicates that the direct segment, or block averaging, method is used to estimate R_{ij}.

The conventional estimate of the wave number spectrum for an unshaded array is given by

$$P_c(k_x,f)=\mathbf{w}_c^H(k_x)\mathbf{R}(f)\mathbf{w}_c(k_x), \tag{3}$$

where $\mathbf{w}_c(k_x)=\mathbf{v}(k_x)/N$ is the conventional weight vector, $\mathbf{w}_c^H(k_x)$ is the complex conjugate transpose of $\mathbf{w}_c(k_x)$, and $\mathbf{v}(k_x)$ is the vector of phase delays required to bring into phase those spectral components of the sensor outputs that have the same wave number k_x at a given frequency f. For the present case of a linear array with equispaced sensors, the jth element of $\mathbf{v}(k_x)$ is given by

$$v_j(k_x)=\exp(-i2\pi k_x jd), \tag{4}$$

where d is the intersensor spacing (or the spatial sampling interval, which is equal to the reciprocal of the spatial sampling frequency).

The optimal estimate of the wave number spectrum is given by

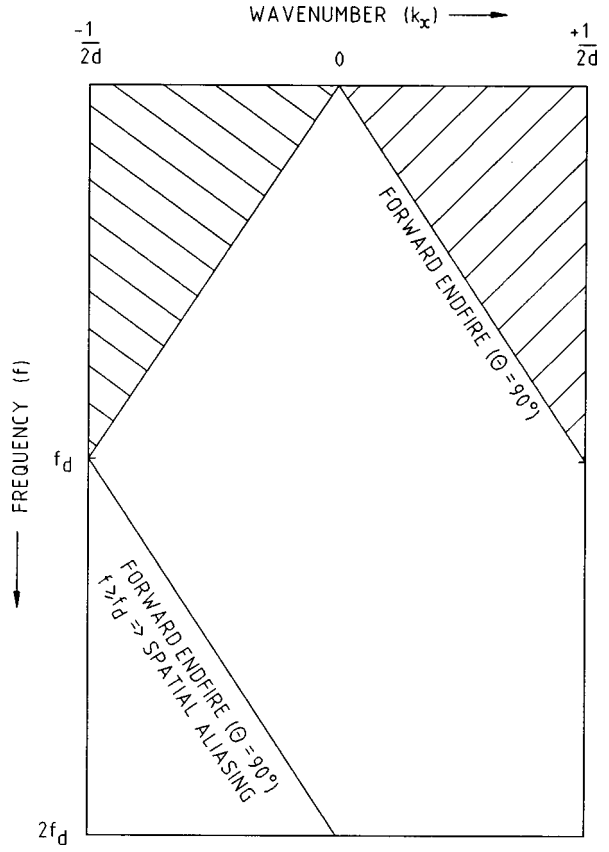

FIG. 5. Frequency–wave number plot showing the effect of spatial aliasing for a broadband source at forward endfire when the frequency of interest (f) exceeds the design frequency of the array (f_d); $f=f_d$ marks the onset of spatial aliasing for the endfire directions, that is, it is impossible to distinguish between a plane-wave arrival at forward endfire and one at aft endfire. The maximum frequency corresponds to twice the design frequency of the array.

$$\begin{aligned} P_0(k_x,f)&=\mathbf{w}_0^H(k_x,f)\mathbf{R}(f)\mathbf{w}_0(k_x,f)\\ &=\{\mathbf{v}^H(k_x,f)\mathbf{R}^{-1}(f)\mathbf{v}(k_x,f)\}^{-1}, \end{aligned} \tag{5}$$

where $\mathbf{w}_0(k_x,f)=\mathbf{R}^{-1}(f)\mathbf{v}(k_x)/(\mathbf{v}^H(k_x)\mathbf{R}^{-1}(f)\mathbf{v}(k_x))$ is the weight vector for the constrained optimal (or MVDR) beamformer. This equation is derived either by minimizing the output noise power, or by maximizing the array gain, subject to the constraint

$$\mathbf{v}^H\mathbf{w}_0=1. \tag{6}$$

The cross-power spectral matrix plays an important role in frequency domain beamforming. Conceptually, the optimal beamformer may be thought of as using the cross terms $(R_{ij}, i\neq j)$ to sense the wave number distribution of the noise sources and then shading the array by multiplying the sensor outputs by a set of complex weights prior to summation so that the array gain is maximized.

Note that for an unconstrained optimal beamformer, the set of weights that maximizes the output signal-to-noise ratio by minimizing the beamformer's output noise power is given by[6]

$$\mathbf{w}_u(k_x,f)=\mathbf{Q}^{-1}(f)\mathbf{v}(k_x,f), \tag{7}$$

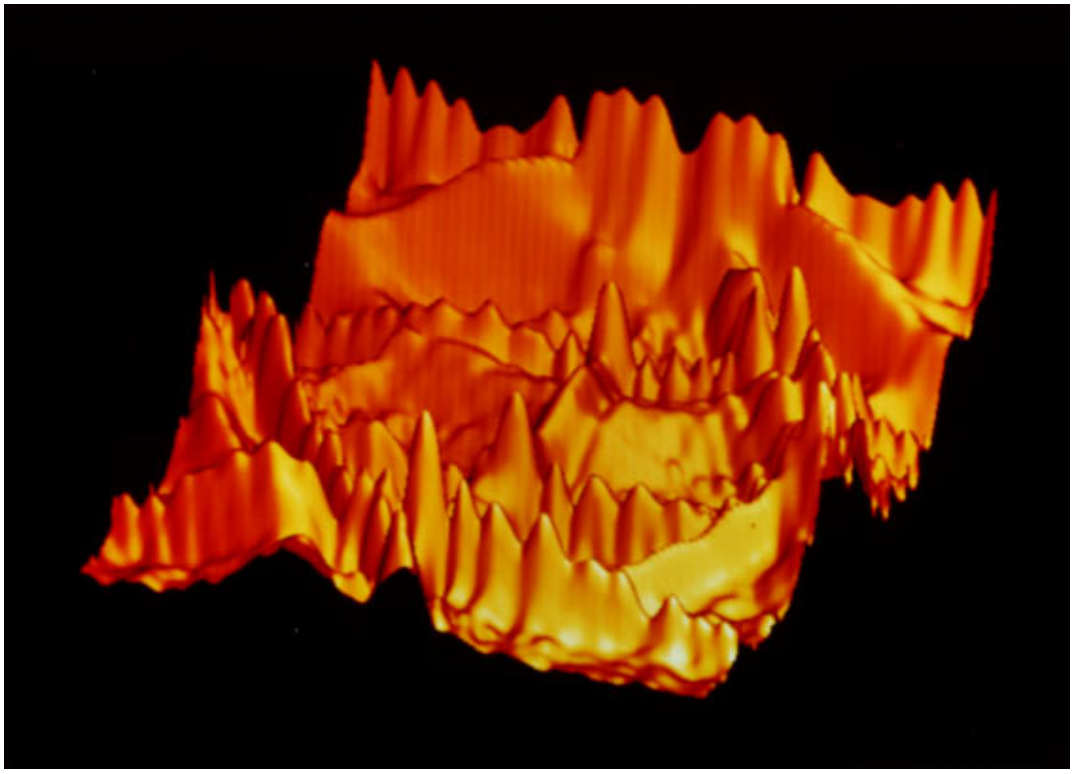

FIG. 6. Frequency–wave number power spectrum for the towed array of hydrophones estimated using the conventional frequency-domain beamforming technique. The orientation of the axes is shown in Fig. 4 and the frequency–wave number power spectral density is in logarithmic units. Acoustic energy surfaces associated with the array self-noise, the tow vessel (both direct path and multipath propagation are evident), and various surface ship contacts are prominent. Spatial aliasing can also be observed. The maximum frequency corresponds to twice the design frequency of the array.

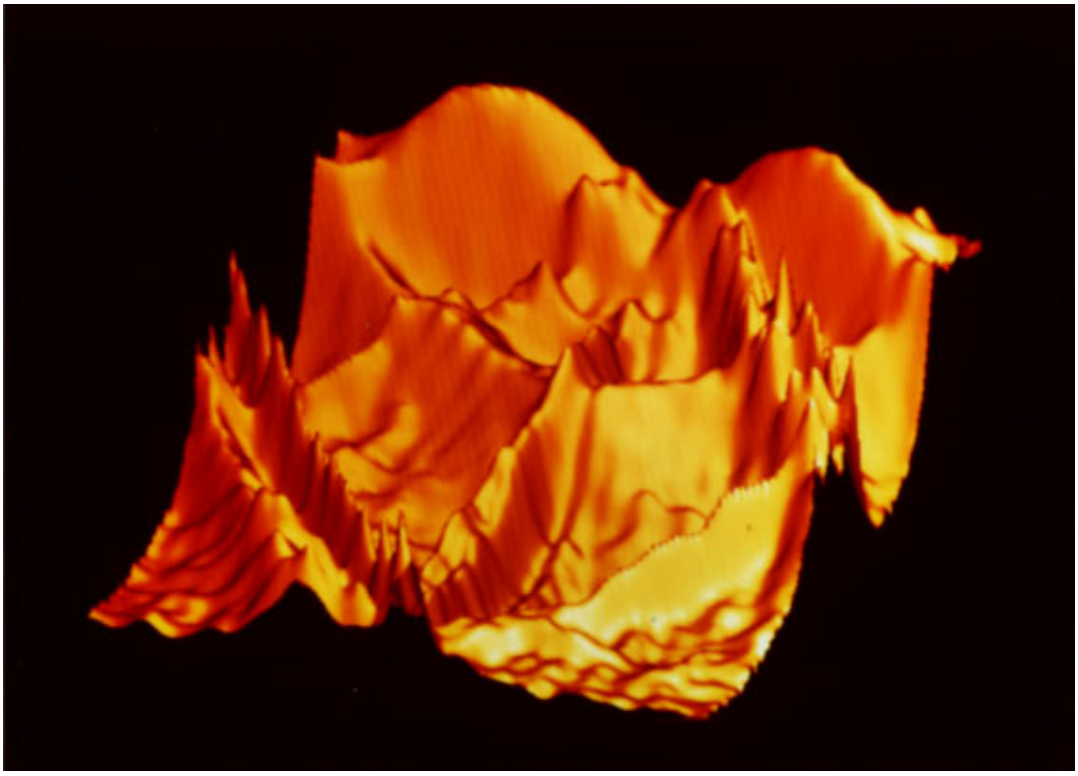

FIG. 7. Same as Fig. 6 but the MVDR beamforming technique is used instead of the conventional method.

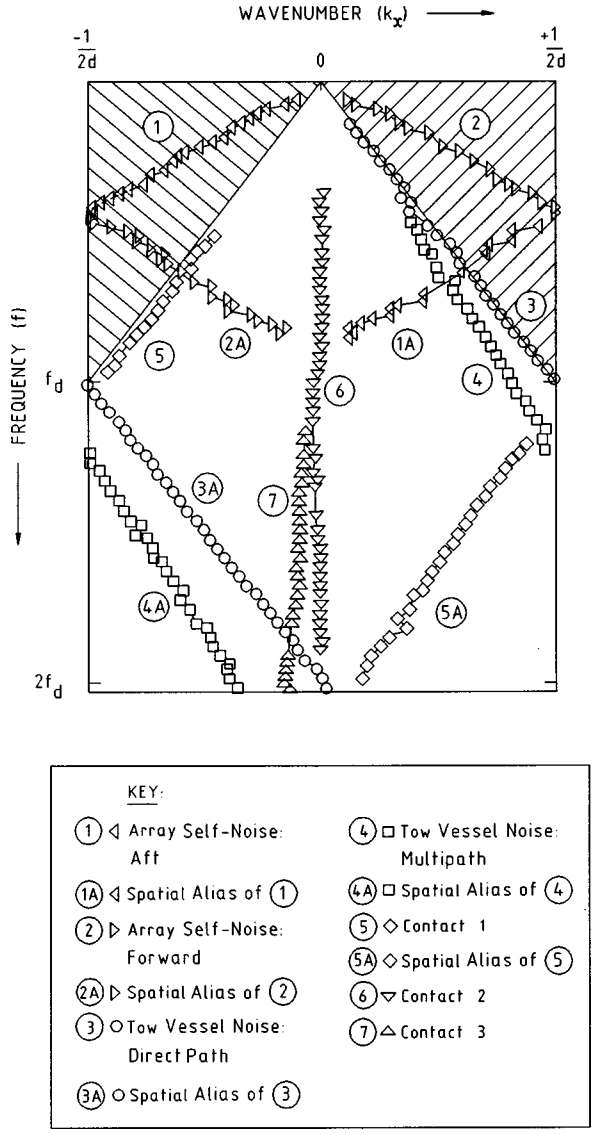

FIG. 8. Frequency–wave number plot showing the frequency and wave number coordinates (ordinates and abscissae, respectively) of the various sources contributing energy to the acoustic field which is sampled by the towed array of hydrophones. This diagram is useful in ascribing each surface in the frequency–wave number power spectrum displayed in Fig. 7 to a particular source of acoustic energy.

where $\mathbf{Q}(f)$ is the cross-power spectral matrix of the noise, normalized so that all of its diagonal elements are unity. The unconstrained optimal beamformer uses prior knowledge of the noise cross-power spectral matrix to suppress the noise. Unfortunately, $\mathbf{Q}(f)$ is not usually known and needs to be estimated when the signal is absent. However, if the estimate of $\mathbf{Q}(f)$ inadvertently contains a contribution due to the wanted signal, then the signal itself will be treated as noise and will also be suppressed. The MVDR beamformer, which is a constrained optimal (or adaptive) beamformer, overcomes this difficulty by selecting the set of weights, $\mathbf{w}_0(k_x, f)$ given above, so that the output power of the beamformer is minimized while the spatial response at the wave number of interest is constrained to unity. In practice, the observed cross-power spectral matrix, $\mathbf{R}(f)$, has both signal and noise components.

III. FREQUENCY–WAVE NUMBER POWER SPECTRUM ESTIMATION FOR THE MICROPHONE ARRAY

The microphone array consisted of 15 equally spaced sensors with the separation between adjacent sensors corresponding to a half-wavelength at the array's design frequency of 190 Hz. The output for each sensor was sampled at 7 kHz. The digital time series information was transformed into the frequency domain using a 4096-point fast Fourier transform routine. The transformed data were then processed using both conventional and optimal spatial filtering methods with the respective frequency–wave number power spectra being displayed in Figs. 2 and 3; the abscissae correspond to the wave number (k_x) coordinates, the ordinates correspond to the frequency (f) coordinates, with the power spectral density, $P(k_x, f)$ comprising the third coordinate. The orientation of the axes for the frequency–wave number power spectral density displays presented in this paper is shown in Fig. 4.

The dominant feature in the frequency–wave number power spectrum is the surface associated with intense broadband acoustic energy emitted by a stationary jet engine operating in a direction toward forward endfire. The upper frequency of the display corresponds to twice the array's design frequency. The sidelobe structure of the conventional spatial filter (see Fig. 2) is suppressed by the optimal spatial filter (see Fig. 3). Also, the beamwidth of the main lobe is much narrower in the case of the MVDR beamformer.

Both displays show the effect of the spatial aliasing as a discontinuity in the line of constant bearing that occurs when the wave number exceeds the spatial Nyquist frequency, that is, $k_x > 1/(2d)$. [The spatial Nyquist frequency, k_c, is equal to half the spatial sampling frequency, that is, $k_c = 1/(2d)$.] With spatial aliasing, a wave number with magnitude greater than $1/(2d)$ is transformed so that its magnitude is below $1/(2d)$, and the sign of the wave number is reversed. Aliasing in the frequency domain is analogous in one respect: a frequency above the temporal Nyquist frequency, f_c, is folded back into the frequency range from 0 to f_c; but it is dissimilar in another respect: the sign is not reversed. [The temporal Nyquist frequency is equal to half the temporal sampling frequency, that is, $f_c = 1/(2\tau_0)$.] Spatial aliasing results in a line of constant bearing becoming discontinuous at the point where the wave number is equal to half the spatial sampling frequency, so that the line no longer runs radially outward from the origin. Instead, the line is displaced in wave number (by $1/d$) but remains inclined at the same characteristic angle (see Fig. 5).

IV. FREQUENCY–WAVE NUMBER POWER SPECTRUM ESTIMATION FOR THE HYDROPHONE ARRAY

Figures 6 and 7 show the conventional and optimal estimates of the frequency–wave number power spectrum for the towed array data. The upper frequency corresponds to twice the design frequency of the array. Each of the surfaces in these displays is associated with either the array self-noise, the tow vessel, or contacts (surface vessels). A comparison

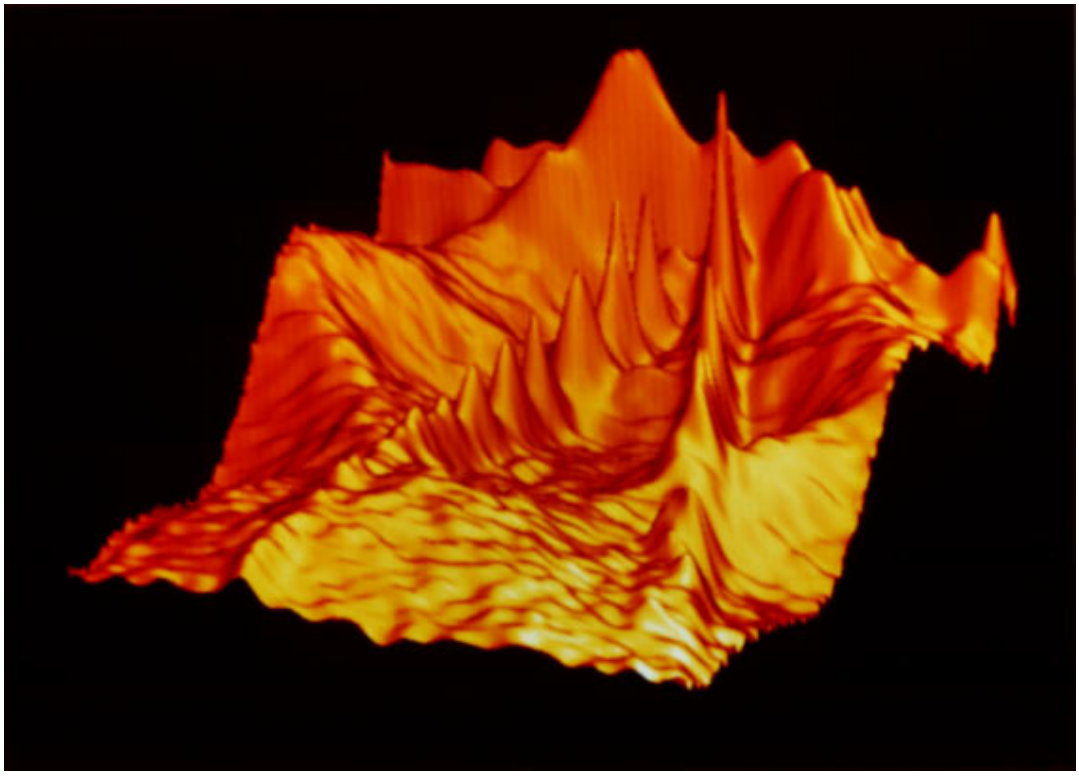

FIG. 9. Frequency–wave number power spectrum when the MVDR beamforming method is used to process the acoustic data from another type of hydrophone array towed at high speed. The orientation of the axes is shown in Fig. 4 and the frequency–wave number power spectral density is in logarithmic units. The maximum frequency corresponds to the design frequency of the array. Prominent features in the display are associated with the correlated self-noise (or structural wave) propagating both fore and aft along the array, the noise radiated by the tow vessel, and the sound received from a surface ship contact. Spatial aliasing of the structural waves is evident.

of Figs. 6 and 7 demonstrates the advantages of invoking the optimal estimation technique to suppress the spatial leakage (sidelobes) and to improve the spatial resolution performance of the array. Spatial aliasing is also evident in the frequency–wave number power spectra.

Projecting the maxima in Fig. 7 onto the frequency–wave number plane produces a frequency–wave number plot. The coordinates of the points on the frequency–wave number plot shown in Fig. 8 are derived by detecting the peaks in the optimal wave number spectrum for a given frequency bin; the wave number bins corresponding to peaks in the wave number spectrum constitute the abscissae, with the frequency bin number representing the common ordinate. The optimal wave number spectrum is preferred because the secondary maxima associated with sidelobes in the conventional wave number spectrum are suppressed, thus substantially reducing the number of peak detections. The frequency–wave number plot shows the broadband acoustic energy radiated by the tow vessel, which is received directly by the array's sensors from the forward endfire direction; this energy arrives at the array via direct path propagation. The tow vessel's radiated noise is also reflected at the sea surface before arriving at the array; this is an example of multipath propagation. There is a strong broadband source at aft endfire (a merchant vessel designated ''contact 1'') and also two weaker broadband sources just near broadside (''contact 2'' and ''contact 3''). The tow vessel and surface ship contacts are broadband sources of acoustic energy and so display a characteristic linear relationship in the frequency–wave number plane. The frequency–wave number coordinates lie on a line of constant bearing that runs radially outward from the origin with the rate of change of wave number with respect to frequency being equal to $\sin\theta/c$, where c is the velocity of sound propagation in the medium and θ is the angle of incidence measured from broadside. The wedge-shaped physical region is bounded by two lines of constant bearing corresponding to the aft and forward endfire directions, and the energy associated with plane-wave signals incident on the array from angles lying between $-90° \leqslant \theta \leqslant +90°$ occurs inside this region. Outside, there is the array self-noise that propagates along the array structure with a phase speed (derived from Fig. 8) that is about half the speed of sound propagation in the underwater medium. Array self-noise phenomena are common in all hydrophone arrays, whether hull-mounted or towed, and are observed when vibrations of the array structure propagate along the array and excite the hydrophones. The array self-noise is symmetric in wave number space because the vibrations correspond to structural (extensional) waves propagating with the same speed along the array in both axial directions.

V. OPTIMAL ESTIMATION OF THE FREQUENCY–WAVE NUMBER POWER SPECTRUM FOR ANOTHER TOWED ARRAY

Frequency–wave number analysis is a powerful diagnostic tool for monitoring the effects of self-noise on towed array performance.[7] Figure 9 shows the optimal estimate of

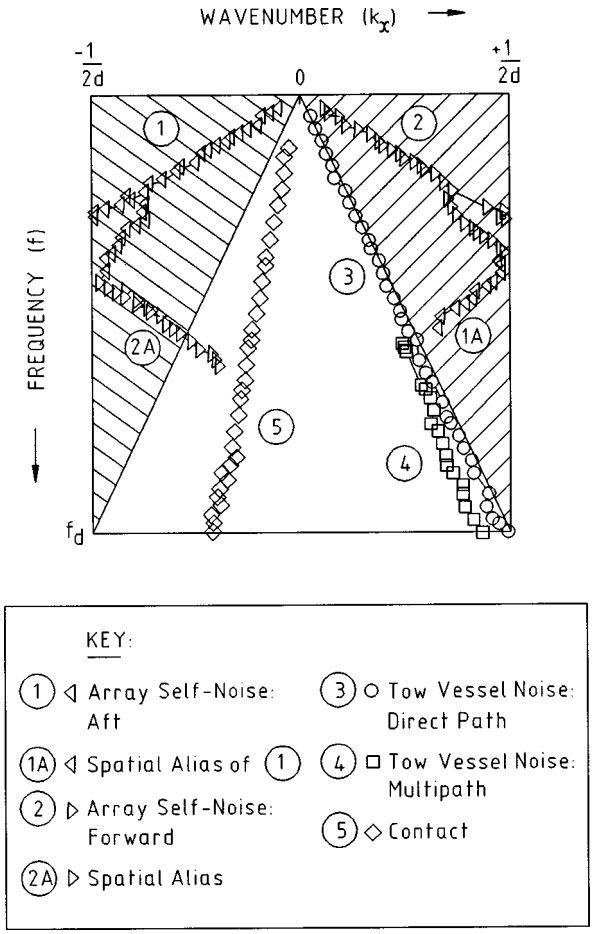

FIG. 10. Frequency–wave number plot showing the frequency and wave number coordinates (ordinates and abscissae, respectively) of the various sources contributing energy to the acoustic field which is sampled by an array of hydrophones towed at high speed. This diagram is useful in matching each source of acoustic energy to its corresponding surface in the frequency–wave number power spectrum displayed in Fig. 9.

the frequency–wave number power spectrum for another type of towed array. The maximum frequency is equal to the array's design frequency (f_d). The corresponding frequency–wave number plot, shown in Fig. 10, can be used to identify the various sources of acoustic energy in the frequency–wave number power spectrum.

The correlated component of the self-noise, which manifests itself as a structural wave in the nonphysical region of frequency–wave number space, is large because the tow speed is high. Structural waves propagate along the array in both axial directions (that is, forward and aft). Spatial aliasing of the structural waves is also evident.

The interference pattern observed in Fig. 9 (which is associated with the acoustic energy received from a surface ship contact) is an example of the Lloyd's mirror effect.[8] This phenomenon is caused by constructive and destructive interference between the sound waves that propagate directly to the array and those that propagate via a boundary-reflected path (that is, multipath propagation caused by reflection of the sound energy from either the sea surface or the sea bottom), which leads to amplitude modulation of the resultant wave. The amplitude modulation is observed to have a regular variation with frequency.

VI. CONCLUSIONS

Optimal estimation of the frequency–wave number power spectrum by the MVDR beamformer enables the sources of acoustic energy to be readily discerned in frequency–wave number space (especially the correlated component of the self-noise in the towed arrays) and the temporal and spatial frequency characteristics of each acoustic source to be quantified. The MVDR beamformer is preferred to the conventional beamformer for frequency–wave number analysis because it suppresses sidelobes, improves the spatial resolution of the array, and provides array gain at frequencies well below the design frequency of each of the arrays considered here.

ACKNOWLEDGMENTS

The author gratefully acknowledges the contributions that Gary Speechley, Lionel Criswick, and Helen Lawless (DSTO Sydney) made to this paper. This work was supported by the Cooperative Research Center for Robust and Adaptive Systems which is funded by the Australian Government under the Cooperative Research Centers Program.

[1] R. N. McDonough, ''Application of the maximum-likelihood method and the maximum-entropy method to array processing,'' in *Non-Linear Methods of Spectral Analysis*, edited by S. Haykin (Springer-Verlag, New York, 1983), pp. 181–244.

[2] D. A. Gray, ''Frequency wave number beamforming by use of the two dimensional Fourier transform,'' in Technical Report WSRL-0162-TR, dated July 1980.

[3] B. Maranda, ''Efficient digital beamforming in the frequency domain,'' J. Acoust. Soc. Am. **86**, 1813–1819 (1989).

[4] J. Capon, ''High-resolution frequency wave number spectrum analysis,'' Proc. IEEE **57**, 1408–1418 (1969).

[5] D. A. Gray, ''Some applications of parametric and non-parametric spectral estimation techniques to passive sonar data,'' J. Electron. Elec. Eng. Aust. **5**, 112–119 (1985).

[6] H. A. d'Assumpcao and G. E. Mountford, ''An overview of signal processing for arrays of receivers,'' J. Electron. Elec. Eng. Aust. **4**, 6–19 (1984).

[7] L. R. LeBlanc and J. I. Salisbury, ''High-resolution wave number frequency methods for towed arrays,'' J. Acoust. Soc. Am. **90**, 3155–3160 (1991).

[8] R. J. Urick, *Principles of Underwater Sound* (McGraw-Hill, New York, 1983), pp. 131–133.

Optimal and wavelet-based shock wave detection and estimation[a)]

Brian M. Sadler, Tien Pham, and Laurel C. Sadler
Army Research Laboratory, Adelphi, Maryland 20783

(Received 15 May 1997; revised 15 April 1998; accepted 27 April 1998)

Detection and estimation of aeroacoustic shock waves generated by supersonic projectiles are considered. The shock wave is an N-shaped acoustic wave emanating in the form of an acoustic cone trailing the projectile. An optimal detection/estimation scheme is considered based on a parametric signal plus white Gaussian noise model. To gain robustness and reduce complexity, we then focus on gradient estimators for shock wave edge detection, exploiting the very fast shock rise and fall times. The approach is cast in terms of a wavelet transform where the level of smoothing corresponds to scale. A multiscale analysis is described, consisting of multiscale products, to enhance edge detection and estimation. This method is effective and robust with respect to unknown environmental interference that will generally not exhibit singularities as sharp as the N-wave edges. Experimental results are presented for discriminating N waves in the presence of vehicle noise. Results are also shown, as a function of miss distance, for gradient-based detection of simulated small projectile shocks inserted into recorded tank noise. [S0001-4966(98)03008-2]

PACS numbers: 43.60.Cg, 43.28.Mw [JLK]

INTRODUCTION

We consider optimal and gradient-based detection and estimation of aeroacoustic shock waves generated by supersonic projectiles. This problem arises in military, law enforcement, and other cases. It is desired to detect the presence of a bullet or other projectile, and to estimate the parameters of the shock wave. Detection is useful in a variety of scenarios with application in sniper location as well as on vehicles and aircraft. Of particular interest are robust methods that will work at moderate signal-to-noise ratio (SNR) in the presence of platform noise.

The shock wave is an ''N-shaped'' wave emanating in the form of an acoustic cone trailing the projectile.[1] The cone angle is given by $\arcsin(c/v)=\arcsin(1/M)$, where c is the velocity of sound in air, v is the projectile velocity, and $M=v/c$ is the Mach number. Letting ΔP denote the pressure jump at the start of the N wave, and P_0 denote ambient atmospheric pressure, then[2]

$$\frac{\Delta P}{P_0}=0.53d\,\frac{(M^2-1)^{1/8}}{x^{3/4}l^{1/4}}, \tag{1}$$

where d and l are the projectile diameter and length, respectively, and x is the perpendicular distance from the projectile trajectory to the sensor (the nearest point of approach or miss distance). Denoting the length of the N wave as L, then

$$L=1.82d\,\frac{Mx^{1/4}}{(M^2-1)^{3/8}l^{1/4}}\approx 1.82d\left(\frac{Mx}{l}\right)^{1/4}. \tag{2}$$

In Eq. (2) $L=cT$ is the N-wave length, where T is the N-wave time duration observed by a single sensor. An alternative form, often used in supersonic aircraft studies, gives the length of the observed shock wave along the ground as $L'=LM$, e.g., see Gierke.[3] Although somewhat complex in nature when first formed, the shock wave assumes the N shape after propagating ≈ 50 projectile diameters, so that Eqs. (1) and (2) are approximations that hold for x sufficiently large.[2] From Eqs. (1) and (2) we see that the primary factors affecting amplitude and length are d and x (x can be relatively large); amplitude and length are otherwise weakly dependent on the projectile's overall shape and velocity. Experiments show reasonably good agreement with Eqs. (1) and (2), e.g., see Bass *et al.*[4] and Stoughton.[5]

Theoretical characterization of the N-wave rise time is somewhat more problematic. Weak-shock predictions agree qualitatively with measurements, but tend to significantly underestimate rise times.[5] Issues include the shock strength, turbulence effects, and molecular vibrational relaxation.[4,5] Experiments with small caliber shocks consistently show rise times ranging from less than 1 μs for small x, to greater than 100 μs for $x>100$ m.

The very fast rise and fall of the shock wave edges leads to the observed N-wave characteristic, and the linear slope between the edges is generally not dependent on the projectile shape at large miss distances.[2] Thus the observed shock wave shape is largely independent of the projectile shape and velocity after a short propagation distance (see also Refs. 6 and 7). This in turn implies that a general purpose detector can be developed that is applicable to a wide variety of projectiles.

Note that the magnitude of the shock decreases with the miss distance as $x^{-3/4}$, while the length increases as $x^{1/4}$. We assume that the miss distance x is not known *a priori* and this, coupled with the direct dependence on projectile diameter d, implies that an observed N-wave may have been generated by a continuum of different size projectiles at different

[a)]Part of the results in this paper were presented in the 130th meeting of the Acoustical Society of America, St. Louis, MO, November 1995 [J. Acoust. Soc. Am. **98**, 2968(A) (1995)]; and at the Intl. Conf. Acoust., Speech, and Signal Process. (ICASSP-97), Munich, Germany, April 1997 [Proc. Intl. Conf. Acoust. Speech, and Signal Process. Vol. 3, pp. 1889–1992 (1997)].

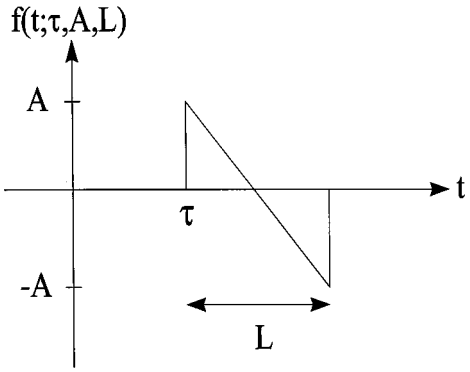

FIG. 1. Ideal parameterized shock wave (or N-wave) $f(t)$.

ranges. For example, one cannot necessarily discriminate between a larger projectile further away versus a smaller projectile that is closer to the sensor. Estimation of x, v, and projectile type from a single sensor are generally not possible without *a priori* knowledge or constraints on the problem. It is possible, however, to estimate these quantities in some scenarios, especially with multiple sensors. An example is a firing range application.[8,9] Here the angle of arrival is known, allowing estimation of the projectile velocity via the change in L versus time, obtained with multiple sensors along the projectile path. The velocity and length estimates may then be used to classify projectiles. We also note that low precision microphones may be used in practice, reducing system cost but making absolute determination of shock wave pressure unreliable.

The N-wave can be parameterized in terms of time of arrival τ, amplitude A, and length L. In the following, for convenience, we use amplitude A rather than pressure ΔP. An idealized constant slope N wave is shown in Fig. 1 and described by (e.g., see Pierce,[10] Chap. 11)

$$f(t;\theta)=Af\left(\frac{t-\tau}{L}\right), \quad \tau\leqslant t\leqslant \tau+L, \tag{3}$$

where

$$f(t)=1-2t, \quad 0\leqslant t\leqslant 1, \tag{4}$$

is the amplitude and length-normalized signal, and $\theta=[\tau,A,L]$ denotes the parameter vector. Acceptable ranges for θ are assumed to be known from context, based on Eqs. (1) and (2).

In the following we discuss two approaches for detecting $f(t;\theta)$ and estimating τ, A, and L. First, we consider the optimal detection-estimation scheme based on a Gaussian noise assumption, leading to a matched filter-type implementation. This approach has high complexity and does not model interference. Next, as an alternative, we consider the use of gradient estimators as a means of detecting the rising and falling edges of the N wave, an approach that requires sufficient SNR but has much lower complexity and is robust to interference. Smoothed gradient estimators are described in the context of wavelets, and a multiscale analysis is described that exploits multiple levels of smoothing simultaneously. Simulations and experiments with measured N-waves and vehicular interference sources complete the paper.

I. OPTIMAL DETECTION AND ESTIMATION IN GAUSSIAN NOISE

In this section we consider optimal Bayes and maximum-likelihood methods for detection of the shock wave and estimation of its parameters. These methods rely on an additive Gaussian noise assumption, leading to a parameterized matched filter-bank approach. However, as often happens under an additive Gaussian noise assumption, the resulting detector is generally not robust to violations of this assumption, such as in the presence of strong interfering acoustic sources.

Consider the binary hypothesis test

$$\begin{aligned} H_1&: \quad r(t)=f(t;\theta)+n(t), \quad 0\leqslant t\leqslant T\gg L, \\ H_0&: \quad r(t)=n(t), \end{aligned} \tag{5}$$

where $n(t)$ is white Gaussian noise with variance N_0. We assume that $f(t;\theta)$ is completely contained in the interval T. This problem is well studied in the context of radar where $f(t)$ is typically a narrow-band sinusoidal pulse of possibly unknown time-of-arrival, frequency, and phase; e.g., see Helstrom.[11] If θ were known then the optimal decision would be based on the matched filter. The Bayes-optimal decision rule is based on the likelihood ratio

$$\lambda(\mathbf{r})=\frac{\int_\theta p_1(\mathbf{r}|\theta)w_\theta(\theta)d\theta}{p_0(\mathbf{r})}\underset{H_0}{\overset{H_1}{\gtrless}}\lambda_0, \tag{6}$$

where $w_\theta(\theta)$ is the *a priori* joint probability density of θ, $p_i(\cdot)$ is the likelihood function under the ith hypothesis, and $\mathbf{r}$ is the set of samples of $r(t)$, $0\leqslant t\leqslant T$. We further assume that the unknown parameters in θ are independent. This last assumption is not strictly true: A and L both depend on the same parameters in Eqs. (1) and (2). However, we are assuming the quantities d, v, l, and x are unknown.

Next we consider the form of the optimal detection receiver. We begin by assuming L is random, and then broaden the analysis to allow τ and then A also to be random. Suppose that L is random with τ and A known, and assume a uniform prior probability density on L, so that $L\sim\mathcal{U}[L_0,L_1]$, with $0<L_0<L_1$. Now,

$$p_1(\mathbf{r})=c_0\int_{L_0}^{L_1}\exp\left\{\frac{-1}{N_0}\int_0^T[r(t)-f(t;L)]^2\,dt\right\}\frac{dL}{L_1-L_0}, \tag{7}$$

while under H_0

$$p_0(\mathbf{r})=c_0\exp\left\{\frac{-1}{N_0}\int_0^T[n(t)]^2\,dt\right\}, \tag{8}$$

with c_0 a constant. Defining the signal energy

$$E_f=\int_0^T[f(t)]^2\,dt=\frac{LA^2}{3}, \tag{9}$$

and also defining

$$q(L)=\int_0^T r(t)f(t;L)dt, \tag{10}$$

then we can write the likelihood ratio as

$$\lambda(\mathbf{r}) = \int_L \lambda(\mathbf{r}|L) w(L) dL$$

$$= \int_{L_0}^{L_1} \exp\left\{ \frac{-E_f}{N_0} + \frac{2A}{N_0} q(L) \right\} \frac{dL}{L_1 - L_0}. \tag{11}$$

For the purposes of implementation we partition the uniform density for L into a discrete set of equally likely lengths L_i, $i=1,...,M$, so that we may replace the integration of Eq. (11) by the summation

$$\lambda(\mathbf{r}) \approx \frac{1}{M} \sum_{i=1}^{M} \lambda(\mathbf{r}|L_i). \tag{12}$$

A similar argument for the time of arrival τ may be applied, where we take $\tau \sim \mathcal{U}[0,\tau_1]$. For L and τ random and assuming A known, then

$$\lambda(\mathbf{r}) = \int_0^{\tau_1} \lambda(\mathbf{r}|\tau) \frac{d\tau}{\tau_1}$$

$$= \int_0^{\tau_1} \int_{L_0}^{L_1} \exp\left\{ \frac{-E_f}{N_0} + \frac{2A}{N_0} q(L) \right\} \frac{dL}{L_1 - L_0} \frac{d\tau}{\tau_1}, \tag{13}$$

where $\lambda(\mathbf{r}|\tau)$ is now given by Eq. (11). Partitioning the delays τ into an equally likely set τ_j, $j=1,...,N$, then

$$\lambda(\mathbf{r}) \approx \frac{1}{MN} \sum_{i=1}^{M} \sum_{j=1}^{N} \lambda(\mathbf{r}|L_i, \tau_j), \tag{14}$$

with

$$\lambda(\mathbf{r}|L_i, \tau_j) = \exp\left\{ \frac{-E_f}{N_0} + \frac{2A}{N_0} q(L) \right\}. \tag{15}$$

Note that for L and/or A random $E_f = LA^2/3$ is not constant from realization to realization. Thus in the implementation based on Eq. (14) the correction term $-E_f/N_0$ is applied in each branch for normalization.

Finally, consider the effects of A, L, and τ random. Now $\lambda(\mathbf{r}|A)$ is given by Eq. (13), and we note that $\lambda(\mathbf{r}|A)$ is maximized for any fixed $A>0$ if q is maximized. Note from Eq. (10) that $q(L)$ is a simple correlation between the model and the received data. Thus a decision may be made by comparing the correlation q to a threshold, and q provides a uniformly most powerful (UMP) test with respect to amplitude A. Note that we are exploiting the fact that $A>0$; if A is bipolar then no UMP test exists and we must resort to a suboptimal two-sided test.

An alternative to Eq. (14) is the ''maximum-likelihood'' (ML) detector, which is an approximation to Eq. (14). This detector proceeds by taking the maximum of the M paths, as shown in Fig. 2, and corresponds to a bank of matched filters matched to the various lengths L [denoted MF (L_i) in the figure]. It arises from the multiple hypothesis test

$$\begin{aligned} H_0&: \quad r(t) = n(t), \quad 0 \leqslant t \leqslant T \gg L, \\ H_i&: \quad r(t) = f(t;\theta_i) + n(t) \end{aligned} \tag{16}$$

for $i=1,...,MN$, where θ_i is the ith parameter vector out of the MN possible choices. The ML detector also corresponds

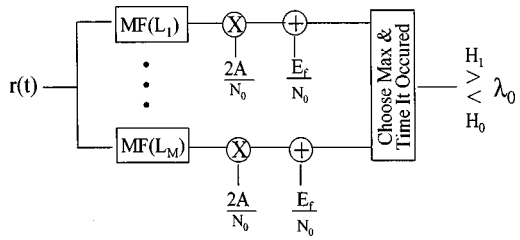

FIG. 2. Maximum-likelihood shock wave detector in white Gaussian noise.

to forming the maximum-likelihood estimates of the parameters and then using these in the likelihood ratio as if they were the true θ. Thus the detector of Fig. 2 is appealing for our problem because it simultaneously yields estimates $\hat{\tau}$ and $\hat{L}$. Given $\hat{\tau}$ and $\hat{L}$ an optimal estimate of A is easily obtained via linear regression over $\hat{\tau} \leqslant t \leqslant \hat{\tau} + \hat{L}$. Because E_f can change, a normalization is required before applying the common threshold λ_0. Alternatively, the correlation statistic q in Eq. (10) can be employed requiring a separate threshold for each channel.

Note that the complexity of the scheme in Fig. 2 is proportional to $M \times N$ [see Eq. (14)]. With fast implementation of the matched filters (via the FFT) the complexity is therefore of order $O(M \times T \log T)$, where T is the data record length [see Eq. (5)]. Thus the search over M different shock wave lengths creates significant complexity in the detector.

Without knowledge of the prior probabilities of H_1 vs H_0 it is prudent to select the decision threshold λ_0 via the Neyman–Pearson criterion so as to maximize the probability of detection for a fixed probability of false alarm. This assumes that N_0 is known or can be estimated. Here, H_0 is a simple hypothesis, so that for τ known the probability of false alarm P_{fa} is given by

$$P_{fa} = \int_{R_1} \rho_0(y) dy = \frac{1}{(2\pi)^{1/2}} \int_{\gamma}^{\infty} e^{-y^2/2} dy, \tag{17}$$

where $\rho_0(y)$ is the Gaussian pdf of the noise and the last equality assumes unit variance. Given a desired P_{fa}, γ may be obtained from Eq. (17). This, together with known or estimated values for N_0 and E_f, are sufficient to set the detection threshold; for example, see Ref. 12, Sec. 6.2. In the more general case of the ML detector in Fig. 2 with unknown arrival time, P_{fa} and the probability of detection P_{det} are more difficult to calculate. When the SNR is large enough to be useful in practice then P_{det} can be approximated by the detection probability arising as if the arrival time τ were known *a priori*. P_{fa} can be approximated using the rate at which the detection statistic crosses the threshold, e.g., see Ref. 11, Chap. 7.

II. EDGE DETECTION AND MULTISCALE WAVELET ANALYSIS

In this section we consider gradient-based detection and estimation schemes as an alternative to the optimal Gaussian noise solution of the previous section. This approach exploits the very fast rise and fall times of the shock wave edges. We are motivated by reduced complexity implementation, as

well as the desire to be robust to strong interferers, such as platform noise. With strong unknown interference an optimal solution will generally be unavailable.

A. Edge detection

Gradient operators are a classical means of estimating step changes in signals and images, and may be applied for detection of shock edges. Commonly used 2-D operators such as Roberts, Prewitt, and Sobel reduce to an FIR filter with impulse response $[-1,0,1]$ in one dimension (e.g., see Jain[13]). More general extensions, so-called filtered derivative methods, combine smoothing with gradient estimation to reduce noise effects, and are more effective when higher noise levels are encountered. These methods are attractive due to low complexity linear implementation. They also tend to be localized, providing robustness to highly varying backgrounds and multiple change points. Alternative step-change detection methods are based on detecting changes in statistical distributions, such as a step change in the mean, and typically require a moderate to large sample size around a single point of change, e.g., see Basseville and Nikiforov.[14] Thus the latter may be difficult to apply in the present context.

A filtered derivative method that has received a lot of attention is the derivative of Gaussian (dG), which estimates the gradient after smoothing with a Gaussian function. The level of smoothing is determined by the variance of the Gaussian. The dG approach can be derived under criteria of detection and localization (see Canny,[15] Tagare and deFigueiredo,[16] and Koplowitz and Greco[17]). The problem can also be formulated in terms of zero crossings of the second derivative, such as the Laplacian of Gaussian approach which is equivalent to dG in 1-D. Attempting to achieve simultaneous detection and estimation results in a tradeoff between the level of smoothing and the variance of the estimated step location, and this tradeoff is sensitive to the edge shape and SNR. On the one hand, only very local information is required for optimal estimation of the edge location.[18,19] On the other hand, a large data window is desired to detect step changes, in essence allowing sufficient smoothing to estimate signal levels before and after the change. In addition, the optimal smoothing level is not typically known *a priori*.

B. A wavelet framework

The problems with choosing *a priori* the level of smoothing appropriate for gradient estimation can be overcome to some extent by employing a multiscale analysis, i.e., combining results over multiple levels of smoothing. It is well known that wavelets may be used for detecting and characterizing singularities.[20] This has been applied to edge detection in images via analysis across scale space, putting earlier work of Canny[15] and others into the wavelet transform framework.[21]

Consider a wavelet $\psi(t)$ that consists of the first derivative of a smoothing function $u(t)$, given by $\psi(t) = du(t)/dt$. With easily achievable constraints on $\psi(t)$ then, for some function of interest $g(t)$, it is straightforward to show that[20]

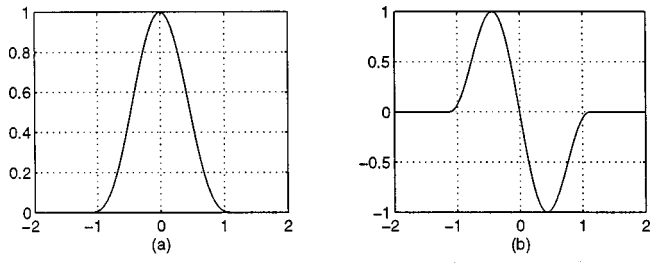

FIG. 3. (a) A cubic spline smoothing function $u(t)$ that is approximately Gaussian, and (b) its derivative $\psi(t)=du(t)/dt$. $\psi_s(t)=(1/s)\psi(t/s)$ is a wavelet yielding a filter bank that estimates the derivative at a level of smoothing increasing with the scale s.

$$W_s\, g(t) = g(t) * \left(s\, \frac{du_s}{dt} \right)(t) = s\, \frac{d}{dt}\, (g * u_s)(t), \tag{18}$$

where $u_s(t)=(1/s)u(t/s)$ and $*$ denotes convolution. Thus for appropriate choice of $u(t)$, $W_s\, g(t)$ can be interpreted as a derivative of a local average of $g(t)$ where the degree of smoothing depends on s. The result is estimation of the derivative of $g(t)$ at various levels of smoothing (scales). In Ref. 21 Mallat and Zhong developed a nonorthogonal DWT based on $u(t)$ being a cubic spline approximation to a Gaussian, shown in Fig. 3. We refer to this particular DWT as the MZ-DWT (Matlab code for this algorithm is listed in Ref. 22). Thus the MZ-DWT implements the dG algorithm at various smoothing levels. We note that the discretization here is dyadic in scale ($s=2^j$, $j \in \mathbb{Z}$) but is not dyadic in time (shift), which corresponds to a filter bank with no down sampling. The MZ-DWT of $g(n)$, $1 \leqslant n \leqslant N$, consists of

$$W_{2^j}\, g(n), \quad j = 1,2,\ldots,J-1, \tag{19}$$

where $J=\log_2 N$, plus the remaining coarse scale information denoted by $S_J(n)$. Thus the MZ-DWT, consisting of $J \times N$ points, is overcomplete (nonorthogonal). This contrasts with the (perhaps more commonly encountered) orthogonal wavelet transforms where the number of coefficients decreases with scale. The inverse DWT may also be readily computed, enabling filtering and reconstruction.

The impulse responses of the MZ-DWT filter bank over several scales are shown in Fig. 4. Some frequency responses are illustrated in Fig. 5; the linear slope region of each filter yields an approximation to differentiation in the various passbands. From now on we use $W_s\, g(n) = W_{2^j}\, g(n)$ to specifically denote the MZ-DWT at scale $s=2^j$, $j=1,2,\ldots$, and at sampling time n.

C. Multiscale analysis

A detection strategy may be based on one or more scales of $W_s\, g(n)$. We emphasize that the lowest scale corresponds to a simple two-point gradient estimator [see Fig. 4(a)]. Various multiscale strategies are possible, e.g., Li *et al.* developed *ad hoc* modifications for the ECG problem.[23]

Consider a multiscale analysis by forming the product

$$p(n) = \prod_{j=j_0}^{j_1} W_{2^j}\, g(n), \tag{20}$$

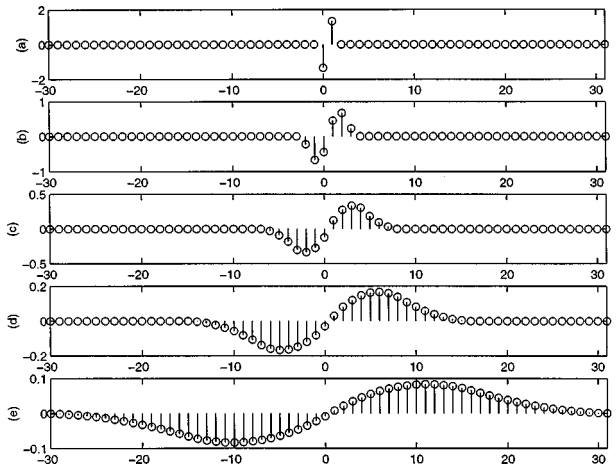

FIG. 4. The impulse responses of Mallat's discrete wavelet transform (MZ-DWT) for the first five scales, panels (a) through (e), respectively. These approximate derivative-of-Gaussian (dG) gradient estimation for various levels of smoothing. Note that (a) corresponds to unsmoothed estimation.

illustrated in Fig. 6. This is a distinctly nonlinear function of the input time series $g(n)$. The function $p(n)$ will show peaks at the N-wave edges, and will have relatively small values elsewhere. The idea of a cross-scale correlation was developed by Rosenfeld for edge detection in images,[24,25] and recently used in the wavelet framework for signal and image denoising by Xu *et al.*[26] The use of $p(n)$ for detection exploits the MZ-DWT response to the signal and noise in a beneficial way. Singularities produce cross-scale peaks in $W_{2^j} g(n)$, and these are reinforced in $p(n)$. Although particular smoothing levels may not be optimal, the nonlinear combination tends to reinforce the peaks while suppressing spurious noise peaks. The signal peaks will align across scale for the first few scales, but not for all scales because increasing the amount of smoothing will spread the response and cause singularities separated in time to interact. Thus choosing j_1 too large will result in misaligned peaks in $p(n)$. In practice the choice of j_1 is limited to roughly $j_1 \leqslant 5$; in our examples we use $j_0=1$ and $j_1=3$. An odd number of terms in $p(n)$ preserves the sign of the edge. The complexity of the

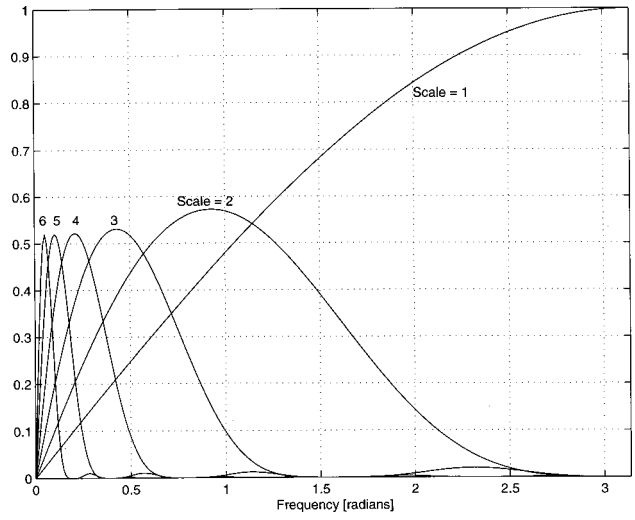

FIG. 5. The frequency response of the MZ-DWT arising from the filters of Fig. 4, shown for the first six scales.

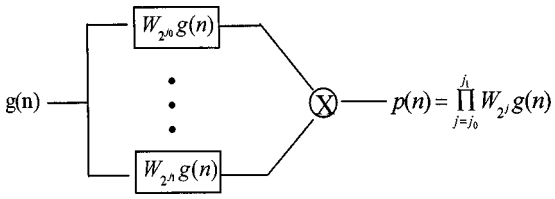

FIG. 6. Computation of $p(n)$, the discrete-wavelet transform cross-scale product.

edge detection approach is low. Each scale of $W_s\, g(n)$ requires an FIR filter, and formation of $p(n)$ requires $j_1 - j_0 + 1$ multiplies per sample, with $j_1 - j_0 + 1 = 3$ in our examples.

Also motivating use of $p(n)$ is the MZ-DWT response to white noise across scales. Let $v(n)$ denote a white noise random process, and $W_{2^j}\, v(n)$ its MZ-DWT. It can then be shown that the expected number of maxima of $W_{2^{j+1}}\, v(n)$ is one half the expected number of maxima in $W_{2^j}\, v(n)$.[20] Thus due to the increased smoothing at each successive scale, as the scale increases by one the number of maxima decreases by half. The result is that maxima in the cross-scale product $p(n)$ due to noise are strongly suppressed, while maxima due to the signal are reinforced.

Statistical analysis of $p(n)$ is given in Ref. 27, with performance analysis for step changes in additive independent Gaussian and non-Gaussian noise. For white noise input to the DWT, we have shown that

$$r_p(m) \triangleq \frac{E[p(n)p(n+m)]}{E[p^2(n)]} \approx \delta(m), \tag{21}$$

for $j_0=1$, $j_1 - j_0 \geqslant 2$, where $\delta(m)$ is the delta function. Thus $p(n)$ is a whitened process, despite its nonlinear nature. This is intuitively apparent from study of Fig. 5. The time domain product of the outputs of the DWT filters corresponds to convolution in the frequency domain; convolution of these filter shapes results in a largely flat spectrum for $p(n)$. We have also shown that the probability density function of $p(n)$ is in general heavy tailed non-Gaussian.

D. Two experimental examples

Figures 7 and 8 illustrate the application of the MZ-DWT to obtain $p(n)$. Figure 7(a) shows both an experimentally measured shock wave and a simulated shock wave time series concatenated together. The measured shock wave (the first 200 points) was obtained from a 38-mm-diam projectile (a tank round) at a sampling rate of 48 kHz; this represents a high quality, high SNR measurement. The noise-free simulated shock wave ($n=201-400$) was generated by sampling Eq. (3) to approximately match the measured one, with amplitudes normalized for display. Also shown in Fig. 7(b)–(e) are $W_{2^j}\, g(n)$ for the first four scales ($j=1,...,4$). The increase in smoothing with scale is apparent, and the resulting smoothed derivative estimates show the N-wave edges clearly. The resulting normalized cross-scale product $p(n)$ is shown in Fig. 7(f), for $j_0=1$ and $j_1=3$, depicting clean peaks aligned with the shock wave edges. Note that both the

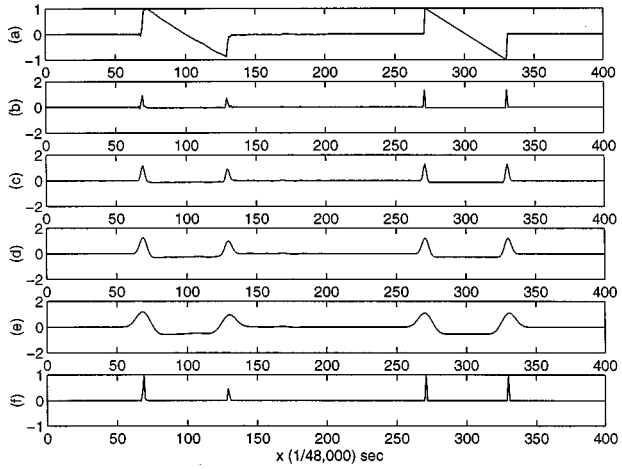

FIG. 7. Measured ($n=1-200$) and simulated ($n=201-400$) shock wave for $d=38$ mm projectile at 48 kHz sampling rate: (a) time series; (b)–(e) first 4 scales of MZ-DWT; (f) normalized product of first 3 MZ-DWT scales.

leading and trailing edge of the N wave are positive going, resulting in positive peaks in $W_{2^j} g(n)$, hence in this application we can reject negative peaks in $p(n)$.

Figure 8 depicts similar results based on a recorded shock wave of a 12.7-mm projectile at a 48-kHz sampling rate (note the two echoes following the original shock). This noisy, low SNR recording results in many false peaks in the lower MZ-DWT scales. If one were restricted to a single scale for analysis, this might be the third [Fig. 8(d)]. However, $p(n)$ taken over the first three scales shows distinct peaks for the initial pulse and the echoes, despite the numerous false peaks in the lower scales of the MZ-DWT.

E. Estimation and reconstruction

As in the ML detection scheme of Fig. 2, DWT-based detection simultaneously yields estimates $\hat{\tau}=n_1$ and $\hat{L}=n_2-n_1$, where n_1 and n_2 are the estimated shock edge times. Based on the parametric signal model it remains to estimate A. Because of the assumed linear slope then, in white Gaussian noise, the optimal estimate of the entire waveform $f(n)$

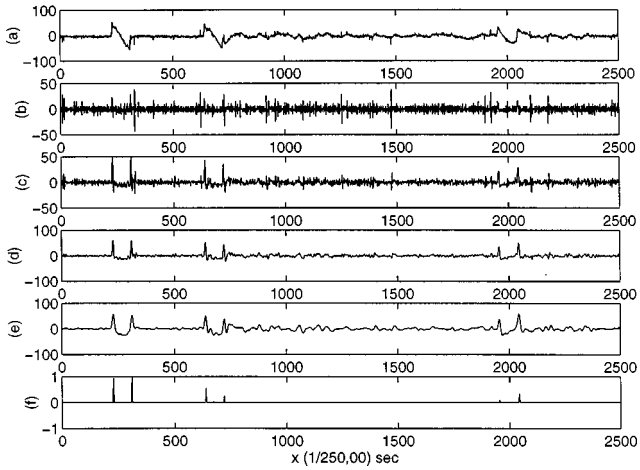

FIG. 8. Measured shockwave for $d=12.7$ mm projectile at 48 kHz sampling rate: (a) time series; (b)–(e) first 4 scales of DWT; (f) normalized product of first 3 DWT scales.

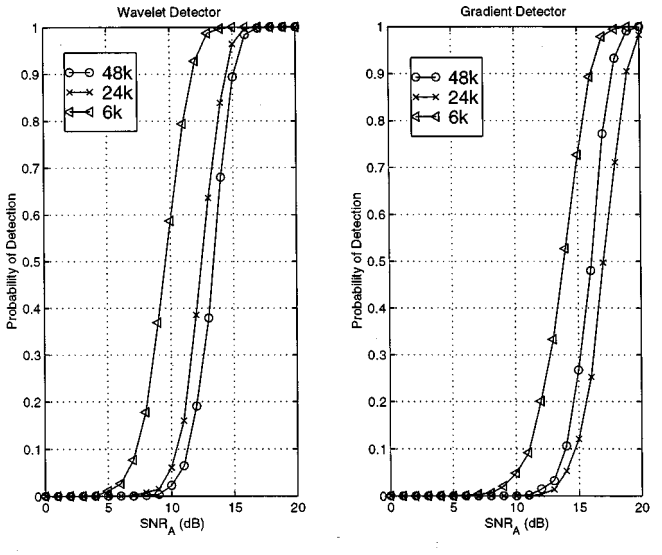

FIG. 9. Detection simulation for a shockwave in additive white Gaussian noise comparing multiscale wavelet-product detection and unsmoothed gradient detection. Here SNR_A depends on shock amplitude versus additive white noise variance.

is simply obtained via least-squares line fitting (linear regression) over the noisy observations for $n\in[n_1,n_2]$. In practice the N-wave peaks will not be strictly equal in magnitude; estimates of these N-wave maxima and minima arise from the endpoints of the linear fit to the data. Another simple estimate of A is to form $\hat{A}=0.5[f(n_1)-f(n_2)]$. The latter estimate may be more appropriate under heavy interference.

Wavelet denoising (i.e., filtering for noise removal via the WT) can be achieved with the DWT employed here.[20,26] These edge-preserving denoising algorithms rely on signal reconstruction from the DWT maxima via alternating projection methods, and do not assume knowledge of the time domain waveform.[21,28]

III. SIMULATION AND EXPERIMENTAL RESULTS

A. Shock detection in Gaussian noise

In this example we consider gradient estimation of simulated shock waves in additive white Gaussian noise. Detection results are shown in Fig. 9. The shock wave was constructed using Eq. (3), with length L established from Eq. (2) using the parameters in Table I, corresponding to a small projectile ($d=5.56$ mm) at a moderate miss distance (50 m). A sampling rate of 125 000 samples/s was assumed, with $y(n)=Af(n)+v(n)$, the ideal shock wave $f(n)$ plus additive noise $v(n)$. Table I values lead to a shock duration of about 36 samples. The signal-to-noise ratio was defined as

$$\mathrm{SNR}_A=10\log_{10}\frac{A^2}{\sigma_v^2}, \tag{22}$$

TABLE I. Shock wave simulation parameters for example 1.

c (m/s)	M	d (mm)	l (mm)	x (m)
355	2.7	5.56	$3d$	50

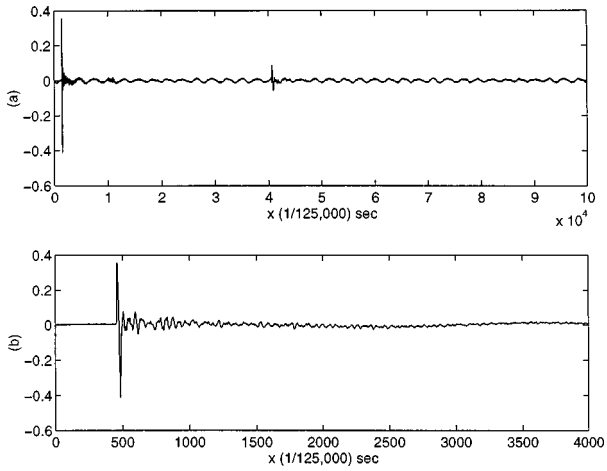

FIG. 10. Measured shock wave for $d=5.56$ mm projectile at 125 kHz sampling rate in presence of idling vehicle: (a) 0.8 s of time series showing shock (near $n=0$) and muzzle blast (after $n=40\,000$); (b) zoom of time series showing shock wave.

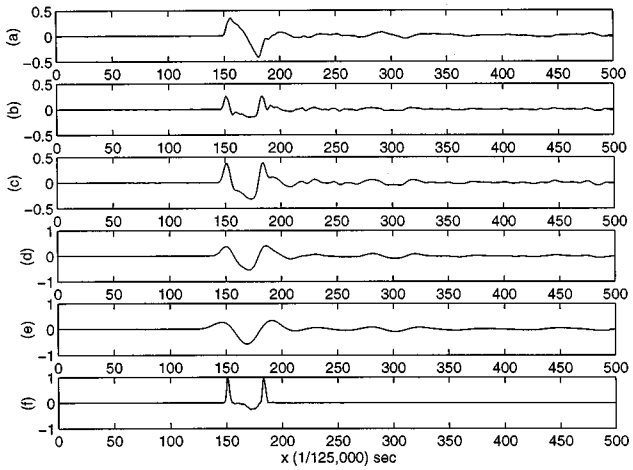

FIG. 11. Zoom of measured shock wave time series from the previous figure: (a) shock wave time series; (b)–(e) first 4 scales of DWT; (f) normalized product of first 3 DWT scales.

where A is the shock amplitude and σ_v^2 is the noise variance. The definition of SNR_A shows the detection performance as a direct function of the amplitude, as opposed to the more standard definition based on the signal energy. The use of SNR_A is more appropriate in this case as the detectors rely on the local edge information only, and do not exploit the entire shock waveform.

To simulate rise time and system bandwidth effects, three low-pass filters were designed with bandwidths of 6, 24, and 48 kHz, respectively. Each filter was designed using the Remez exchange algorithm with 50-dB stop-band suppression and a 1-kHz roll-off region, and each had 170 taps. The noisy signal $y(n)$ was then passed through each filter and detection tests carried out using (i) $p(n)$ in Eq. (20) with $j_0=1$ and $j_1=3$, and (ii) a simple gradient operator with impulse response $[-1,0,1]$. Data records of length $3\times512=1536$ were used with the shock wave centered in the record to insure the low-pass filters were in steady state before and after the shock. Detection thresholds were established yielding no false alarms over 100 000 noise training samples. Successful detection was declared if both N-wave edges were detected above threshold. Results in Fig. 9 are averages over 1000 Monte Carlo trials for each value of SNR_A. The results show a 4–5 dB performance gain in using $p(n)$ over a simple unsmoothed gradient estimator, reflecting the benefits of smoothing at lower SNR_A.

B. Experimental shock detection in platform noise

Next we show results based on experimentally collected data on a noisy platform. Figure 10(a) shows a time series collected from a microphone placed 5 ft off the ground and 3 ft behind a military HMMWV (jeep) with its diesel engine idling. The data were collected with a sampling rate of 125 kHz, such that the time series in Fig. 10(a), which is composed of 100 000 samples, represents 0.8 s elapsed time. A high velocity rifle with projectile diameter $d=5.56$ mm was fired past the HMMWV at various miss distances. The data shown here correspond to a miss distance x of approximately 22 m. The shock wave is evident early in Fig. 10(a), and the muzzle blast follows near the center of the data record. The engine and exhaust sounds are also apparent in the waveform away from the shock and muzzle blast occurrences.

Figure 10(b) is an enlargement of the time series, and the shock wave is now evident. We apply the DWT and form $p(n)$ via Eq. (20) with $j_0=1$ and $j_1=3$. Results are shown in Fig. 11. Here, Fig. 11(a) is a further enlargement of the time series over 500 samples around the N wave, (b)–(e) show the first four scales of the MZ-DWT, and (f) shows $p(n)$ with its peak normalized to unity. Note the sharpening of the peaks in $p(n)$ versus the unsmoothed gradient estimate [panel (f) versus panel (b), respectively].

We have repeated this experiment with both larger projectiles and smaller miss distances, hence the data shown are the worst case (i.e., smallest amplitude) within the confines of our parameters for this experiment. The engine noise is relatively low pass in comparison to the fast rise time of the N wave, such that the engine noise does not generally produce significant peaks in $p(n)$. Also, the exhaust noise, while of higher bandwidth than the engine sound, is of sufficiently less amplitude than the shock wave in this scenario and hence does not seriously restrict the detection process.

C. Simulated shock in experimentally collected platform noise

In this example we insert simulated shockwaves into experimentally recorded sound from a moving tank to obtain detection performance as a function of miss distance. Detection results are shown in Fig. 12. An overview of the proce-

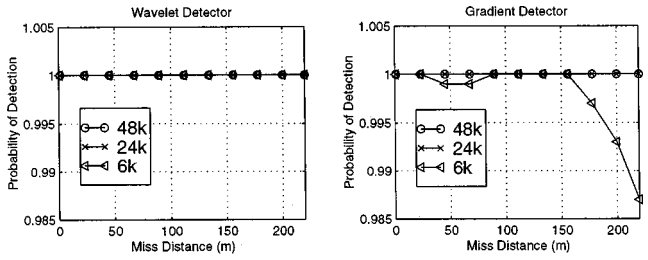

FIG. 12. Detection of simulated N-wave in recorded tank noise.

TABLE II. Overview of example 3.

1	Shock wave simulation (using parameters from Table III): Find L from Eq. (2). Find shock SPL by linearly interpolating data from Table IV. Find rise-time by interpolating experimental data from Ref. 5, Fig. 6. Filter ideal shock to simulate rise time, yielding $s(n)$.
2	Form $y(n)=s(n)+x(n)+v(n)$. Randomly select tank sound segment $x(n)$ from 1.6 s recording. Add white Gaussian noise $v(n)$ at 20 dB ($10\log_{10}\lvert P_x/P_v\rvert$).
3	Simulate system bandwidth for three cases: Pass $y(n)$ through low-pass filters with cutoffs of 48, 24, and 6 kHz.
4	Monte Carlo trials: Repeat steps 1–3, 1000 trials for each miss distance and each LPF. Two different detectors compared in Fig. 12.

dure used for this experiment is given in Table II, with parameters given in Table III.

The time series is given by

$$y(n)=s(n)+x(n)+v(n), \tag{23}$$

where $s(n)$ is a simulated shock, $x(n)$ is recorded tank sound, and $v(n)$ is white Gaussian noise. The recording was made with a sampling rate of 125 kHz by driving a tank past a fixed microphone. For this experiment the recording was composed of 200 000 samples (1.6 s) taken when the tank was within roughly one meter of the sensor. The tank SPL was measured by taking the worst case peak-to-peak (p-p) amplitude; for the time series in this experiment this p-p SPL was 132 dB. Each realization of $y(n)$ was formed by adding $s(n)$ and $v(n)$ to the tank recording with the time-of-arrival τ randomly selected within the 200 000 samples, and detection results averaged over 1000 Monte Carlo trials for each miss distance. Each realization was of length 1536 samples, with the shock centered in the record. This length was used to insure the low-pass filters described below (and example 1 above) reached steady state response. Additive white Gaussian noise $v(n)$ was included to further simulate sensor and other noise. The noise $v(n)$ was added at a fixed power ratio of 20 dB, given by $10\log_{10}\lvert P_x/P_v\rvert$, where P_x is the average power in the 1.6 s of recorded tank sound and P_v is the Gaussian noise power.

The shock was simulated as follows. The projectile diameter $d=5.56$ mm, length l, Mach number M, and the speed of sound in air c, are given in Table III. The shock duration was obtained via Eq. (2), and rounded to the nearest sample time, with sampling rate matching the recorded tank data at 125 000 samples per second. The shock amplitude was obtained from a linearly interpolated curve based on experimentally collected shock pressure levels. The SPLs are shown in Table IV, obtained by averaging over several shots for each miss distance. These were representative measurements over several trials with different (separately calibrated) microphones. The measurements were conducted in a benign outdoor environment with minimal acoustic interference. The miss distances x in Table IV are approximate within the experimental error of a marksman firing past a designated point from a range of roughly 200 m. SPLs for arbitrary miss distances in the range $1\leqslant x\leqslant 220$ m were obtained by interpolating a linear least-squares fit to the data in Table IV, while enforcing a slope proportional to $x^{-3/4}$ as required by Eq. (1). An ideal shock was then simulated via Eq. (3), where the amplitude was determined with reference to the calibrated shock SPL and the duration in samples determined as described above.

TABLE III. Shock wave parameters in example 3.

c (m/s)	M	d (mm)	l (mm)	x (m)	Samples/s
355	2.7	5.56	$3d$	$1\leqslant x\leqslant 220$	125 000

TABLE IV. Average measured peak-to-peak sound pressure levels for $d=5.56$ mm diameter projectile shock waves.

Miss distance (m)	1	7	22
SPL (dB)	150	142	134

The ideal shock was then filtered to simulate the rise time. The appropriate rise time was obtained by piecewise interpolating the experimental measurements for a 5.56-mm projectile provided by Stoughton (see Fig. 6 of Ref. 5). Experimental results were incorporated due to the lack of a sufficiently accurate theoretical rise time prediction. Rise times for this case varied from less than 1 μs at $x=1$ m miss distance to greater than 40 μs at $x=220$ m. The ideal simulated shock was then passed through a smoothing filter whose coefficients were all equal to one, with filter extent equal to twice the estimated rise time (quantized to the sampling rate). For example, at $x=200$ m the rise time is 40 μs, corresponding to five samples at the sampling rate of 8 μs per sample. So, the ideal shock was smoothed with an FIR filter of length $2\times 5=10$ with all the filter weights equal to one. This approach to simulating the rise time is conservative in that it overly smooths the shock and results in rise times slower than those observed experimentally.

Each realization of $y(n)$ was passed through one of three low-pass filters, as in example 1 above, simulating various system bandwidths. Detection results in Fig. 12 are shown for an unsmoothed gradient with impulse response $[-1, 0, 1]$, as well as for the wavelet product detector $p(n)$, with $j_0=1$ and $j_1=3$ in Eq. (20). Detection thresholds were set to yield no false alarms over a 200 000 sample training set consisting of $x(n)+v(n)$ for one realization of $v(n)$. Detection was declared only if both the leading and trailing N-wave edges were detected.

Detection results in Fig. 12 predict nearly perfect detection using gradient estimation, out to a miss distance of 220 m. Note that, for a system bandwidth of 6 kHz, the unsmoothed gradient begins to show a loss of performance beyond 150 m. The reduced gradient response is brought on by excessive smoothing. This effect is not evident in the wavelet-product detector, which is able to maintain detection even at the lower system bandwidth of 6 kHz. Thus a higher system bandwidth may be employed that better preserves the rise time, which in turn enables a lower complexity detector. Conversely, a lower system bandwidth may be used with a somewhat more complex detector.

This experiment is intended to be conservative with respect to rise time and the level of additive Gaussian noise. We note, however, that the tank sounds were recorded from a microphone not on the moving platform. Placing the sensor on the tank might lead to somewhat higher noise levels due to vibration, wind, or other effects. The simple gradient-based approach to shock detection appears functional and robust to platform noise due to the fast rise time and relatively large shock amplitude. We also note that larger projectiles will produce louder shocks with faster rise times, hence the detection results will improve in such cases.

IV. DISCUSSION

Based on our experimental and simulation results, gradient estimation appears to be a viable low complexity method for detection and estimation of shocks on noisy platforms. Our ability to simulate realistic shocks is limited by the inability to accurately predict rise time. So, the last example of the previous section was intentionally conservative, utilizing a small projectile, a very noisy platform, and significant additive white noise. A larger projectile or quieter platform will improve detectability. While it is important to preserve the rise time to enable accurate edge detection, our results indicate that the relatively loud shock waves can be detected with system bandwidths that are readily achievable.

In its simplest form, gradient estimation can be accomplished with very low complexity. The multiscale wavelet approach provides a technique that incorporates smoothing in the gradient estimation process, without knowing *a priori* what the optimal smoothing level may be. The addition of smoothing provides increased protection against additive noise. The wavelet approach is computationally simple and straightforward to implement in real time applications.

Gradient-based performance depends on the fast rise time and amplitude of the shock edges. This is in contrast to optimal matched filter performance which is theoretically insensitive to the signal shape in additive white Gaussian noise, provided the signal shape is known precisely. Thus in Gaussian noise, the matched filter will generally out perform any other scheme. However, the signal form is only parametrically known, so that a search of the parameter space is necessary, resulting in higher complexity. And, additive interference will quickly degrade the matched filter performance.

The gradient-based approach might be used as a front end to other system layers. In particular the important problem of angle of arrival estimation, requiring multiple sensors, will typically require accurate detection and time-of-arrival estimation at each sensor.

[1] G. B. Whitham, ''Flow patterns of a supersonic projectile,'' Commun. Pure Appl. Math. **5**, (1952).

[2] G. B. Whitham, ''The behaviour of supersonic flow past a body of revolution, far from the axis,'' Proc. R. Soc. London, Ser. A **201**, 89–109 (1950).

[3] H. von Gierke, ''Aircraft noise sources,'' in *Handbook of Noise Control*, edited by C. Harris (McGraw-Hill, New York, 1957), Chap. 33.

[4] H. E. Bass, B. A. Layton, L. N. Bolen, and R. Raspet, ''Propagation of medium strength shock waves through the atmosphere,'' J. Acoust. Soc. Am. **82**, 306–310 (1987).

[5] R. Stoughton, ''Measurements of small-caliber ballistic shock waves in air,'' J. Acoust. Soc. Am. **102**, 781–787 (1997).

[6] J. Dumond, E. Cohen, W. Panofsky, and E. Deeds, ''A determination of the wave forms and laws of propagation and dissipation of ballistic shock waves,'' J. Acoust. Soc. Am. **18**, 97–118 (1946).

[7] K. Friedrichs, ''Formation and decay of shock waves,'' Commun. Pure Appl. Math. **1**, 211–245 (1948).

[8] R. Loucks, B. Davis, L. Moss, T. Pham, and M. Fong, ''A method of identifying supersonic projectiles using acoustic signatures,'' Army Research Laboratory Technical Report, ARL-TR-859, September 1995.

[9] T. Pham, M. Fong, J. Gerber, and K. Tran, ''Brassboard design for round discrimination system,'' Army Research Laboratory Technical Report, ARL-TR-332, February 1994.

[10] A. D. Pierce, *Acoustics, An Introduction to Its Physical Principles and Applications* (McGraw-Hill, New York, 1981).

[11] C. Helstrom, *Elements of Signal Detection and Estimation* (Prentice-Hall, Englewood Cliffs, NJ, 1995).

[12] C. Weber, *Elements of Detection and Signal Design* (Springer-Verlag, New York, 1987).

[13] A. K. Jain, *Fundamentals of Digital Image Processing* (Prentice-Hall, Englewood Cliffs, NJ, 1989).

[14] M. Basseville and I. V. Nikiforov, *Detection of Abrupt Changes, Theory and Application* (Prentice-Hall, Englewood Cliffs, NJ, 1993).

[15] J. Canny, ''A computational approach to edge detection,'' IEEE Trans. Pattern. Anal. Mach. Intell. **PAMI-8**, 679–698 (1986).

[16] H. D. Tagare and R. J. P. deFigueiredo, ''On the localization performance measure and optimal edge detection,'' IEEE Trans. Pattern. Anal. Mach. Intell. **12**, 1186–1190 (1990).

[17] J. Koplowitz and V. Greco, ''On the edge location error for local maximum and zero-crossing edge detectors,'' IEEE Trans. Pattern. Anal. Mach. Intell. **16**, 1207–1212 (1994).

[18] R. Kakarala and A. O. Hero, ''On achievable accuracy in edge localization,'' IEEE Trans. Pattern. Anal. Mach. Intell. **14**, 777–781 (1992).

[19] A. M. Reza and M. Doroodchi, ''Cramer-Rao lower bound on locations of sudden changes in a steplike signal,'' IEEE Trans. Signal Process. **44**, 2551–2556 (1996).

[20] S. Mallat and W. L. Hwang, ''Singularity detection and processing with wavelets,'' IEEE Trans. Inf. Theory **38**, 617–643 (1992).

[21] S. Mallat and S. Zhong, ''Characterization of signals from multiscale edges,'' IEEE Trans. Pattern. Anal. Mach. Intell. **14**, 710–732 (1992).

[22] B. M. Sadler and A. Swami, ''Analysis of wavelet transform multiscale products for step detection and estimation,'' Army Research Laboratory Technical Report, to appear 1998.

[23] C. Li, C. Zheng, and C. Tai, ''Detection of ECG characteristic points using wavelet transforms,'' IEEE Trans. Biomed. Eng. **42**, 21–28 (1995).

[24] A. Rosenfeld, ''A nonlinear edge detection technique,'' IEEE Proc. **58**(5), 814–816 (1970).

[25] A. Rosenfeld and M. Thurston, ''Edge and curve detection for visual scene analysis,'' IEEE Trans. Comput. **20**, 562–569 (1971).

[26] Y. Xu, J. Weaver, D. Healy, and J. Lu, ''Wavelet transform domain filters: A spatially selective noise filtration technique,'' IEEE Trans. Image Process. **3**, 747–758 (1994).

[27] B. M. Sadler and A. Swami, ''On multiscale wavelet analysis for step estimation,'' Proc. Intl. Conf. Acoust., Speech, and Sig. Process (ICASSP98), to appear; also ''On multiscale products for step detection and estimation,'' IEEE Trans. Info. Theory, submitted 1998.

[28] Z. Cvetkovic and M. Vetterli, ''Discrete-time wavelet extreme representation: Design and consistent reconstruction,'' IEEE Trans. Signal Process. **43**, 681–693 (1995).

On the existence of an age/threshold/frequency interaction in distortion product otoacoustic emissions

Patricia A. Dorn,[a] Pawel Piskorski, Douglas H. Keefe, Stephen T. Neely, and Michael P. Gorga
Boys Town National Research Hospital, Omaha, Nebraska 68131

(Received 3 February 1998; accepted for publication 8 May 1998)

Interactions among age, threshold, and frequency in relation to distortion product otoacoustic emissions (DPOAE) have yet to be resolved. The effects of these variables were explored by analyzing DPOAEs in ears with thresholds not exceeding 20 dB HL. Multivariate regression analyses were performed in two different ways. For data to be included in the first analysis, audiometric threshold had to be 20 dB HL or better only at the particular frequency under study, but might exceed 20 dB HL at other half-octave frequencies. Significant main effects were found for age, threshold, and frequency. There was also an age-by-frequency interaction, but a significant age-by-threshold interaction was not observed. DPOAE amplitudes decreased as either age, frequency, or threshold increased. In the second analysis, when a more stringent inclusion criterion was applied (normal thresholds at all frequencies), the main effects for age, threshold, and frequency were not significant. The significant age-by-frequency interaction remained, whereby DPOAE amplitudes decreased as age and frequency increased, but the age-by-threshold interaction again was not significant. The magnitude of DPOAE amplitude change across age, threshold, and frequency and for the age-by-frequency interaction was small but similar for both groups of subjects. Age in association with threshold did not account for observed changes in DPOAE amplitudes for either group. Importantly, the lack of a significant age-by-threshold interaction indicates that there may be processes intrinsic to aging alone that act on DPOAE generation. [S0001-4966(98)05108-X]

PACS numbers: 43.64.Ha, 43.64.Jb [BLM]

INTRODUCTION

Distortion product otoacoustic emission (DPOAE) measures are a nonbehavioral method to obtain frequency specific information about cochlear status. As audiometric thresholds become poorer, reflecting increased outer hair cell (OHC) damage, the magnitude of the DPOAE response decreases and is ultimately eliminated (e.g., Martin *et al.*, 1990; Gorga *et al.*, 1993a, 1996, 1997; Kimberley *et al.*, 1994). With increasing age, there is an increased likelihood of reduced hearing, particularly in the higher frequencies. One might conclude, therefore, that DPOAE magnitudes decrease as age increases; however, this effect may not be solely a consequence of aging, but rather reflect the fact that older individuals are more likely to experience hearing loss. There are other factors that make it difficult to understand the influence of age on DPOAEs. For example, age effects on DPOAE amplitudes might depend on frequency, such that aging (and interactions between aging and hearing loss) differ for lower frequencies compared to higher frequencies. Understanding the contributions of age, threshold, and frequency to measured DPOAEs has important basic implications for describing how cochlear responses change with age. In addition, knowledge of how these variables interact has potential clinical significance with respect to how DPOAE measures are used to identify hearing loss across the life span.

One approach that might lead to a better understanding of age, threshold, and frequency effects is to evaluate DPOAEs in subjects from different age groups, while controlling for the influence of auditory sensitivity. A number of studies have explored the effects of age on otoacoustic emissions (Arnold *et al.*, 1996, as described in Lonsbury-Martin *et al.*, 1997; Strouse *et al.*, 1996; Prieve and Falter, 1995; Kimberley *et al.*, 1994; Whitehead *et al.*, 1994; Stover and Norton, 1993; Lonsbury-Martin *et al.*, 1991; Collet *et al.*, 1990; Bonfils *et al.*, 1988).

Bonfils *et al.* (1988) and Collet *et al.* (1990) found age-related changes in click-evoked otoacoustic emissions (CEOAE). Both studies included subjects into the 8th decade of life. With increasing age, CEOAEs had a lower incidence, higher absolute threshold (in dB HL), and a response with a lower peak frequency. In one study (Bonfils *et al.*, 1988), subject inclusion allowed for ''normal age-corrected'' audiometric thresholds. This means that subjects differed not only in age but also in threshold, making it impossible to accurately attribute any effects on OAEs to either age or threshold. Collet *et al.* (1990) used ''audiometrically normal'' subjects, although specific details of inclusion criteria were not provided. Thus there is some ambiguity as to how well the influences of threshold differences were minimized.

Both Stover and Norton (1993) and Prieve and Falter (1995) observed that CEOAE thresholds were not significantly related to age. In these studies, stricter audiometric threshold requirements had to be met. Prieve and Falter (1995) required thresholds of 15 dB HL or better from 250 to

[a]Electronic mail: dornp@boystown.org

8000 Hz. Subjects in the Stover and Norton (1993) study had thresholds of 20 dB HL or better from 250 to 4000 Hz.

DPOAE studies also reported conflicting outcomes regarding the significance of age. Both Kimberley *et al.* (1994) and Whitehead *et al.* (1994) noted a trend for normal hearing older subjects to exhibit reduced DPOAE amplitudes at higher frequencies. Lonsbury-Martin *et al.* (1991) and Arnold *et al.* (1996) found a decrease in DPOAE amplitudes at higher frequencies with increasing age. In the 1996 study, age effects for DPOAE and audiometric thresholds were found in the higher frequencies for a relatively young subject group ($\geqslant$35 years, with 2 ears above age 50), as compared to 15- to 24-year-olds and 25- to 34-year-olds. Although all subjects had hearing within normal limits, differences among groups were present, with older subjects having higher thresholds. Additionally, in the 1991 study, some subjects aged 50 and above had elevated high-frequency thresholds. As a consequence, these data do not allow one to conclude that there is an aging effect on DPOAE amplitude independent of sensitivity loss. Stover and Norton (1993) found that DPOAE thresholds were significantly related to hearing sensitivity and frequency, but not to age, and that more of the variance in OAE data could be explained by sensitivity than by age. Unfortunately, their observations were based on data from a small number of subjects, and those from the older subject groups (60's and 70's) had elevated thresholds at higher frequencies. Strouse *et al.* (1996) found no consistent age effects on DPOAE thresholds; however, their control group of 20-year-olds exhibited large intersubject DPOAE threshold variability, potentially obscuring any age/DPOAE threshold interactions. DPOAE amplitudes, obtained at a fixed primary level (65 dB SPL), were smaller in older subjects (70-year-olds) at lower frequencies, while younger subjects (50-year-olds) exhibited smaller DPOAEs at higher frequencies. This outcome is difficult to explain, especially in relation to aging effects, because increased age is normally associated with decreased auditory function at higher frequencies.

The findings from these reports do not provide a clear picture as to whether age alone, or age in conjunction with threshold shifts, significantly affects otoacoustic emissions (OAE). Clinically, this is an important issue to resolve, as the presence of an age effect would mean that adjustments should be applied to DPOAE measures (Lonsbury-Martin *et al.*, 1997) for use in diagnostic and screening programs. The present study was undertaken to evaluate the main and combined effects of age, threshold, and frequency on DPOAE amplitude measures. With increasing age, reduced auditory sensitivity is common, and initially occurs in the higher frequencies. DPOAEs are sensitive to auditory status, as the nonlinear response properties of the cochlea are compromised when OHC damage occurs. If DPOAE measures are to be used as diagnostic and screening tools, it is important to know if these measures should be adjusted for age before making clinical judgements about auditory status. In order to assess age effects, two subject groups were constructed on the basis of meeting either a more stringent or less stringent interpretation of normal hearing sensitivity. The more stringent criterion required normal audiometric thresholds over a wide range of frequencies. The less stringent criterion allowed for data to be included if threshold was normal at a particular frequency, regardless of sensitivity at other frequencies. Through this process, two groups of subjects were constructed, with similar auditory status and representing a wide range of ages.

In our groups of audiometrically equivalent subjects, where two clearly stated threshold criteria have been applied, one might not anticipate finding main effects for age. A main effect of threshold is anticipated, even for the range of thresholds not exceeding 20 dB HL (e.g., Allen *et al.*, 1991; Gorga *et al.*, 1997), regardless of subject age. In the context of the present question, however, insight into underlying processes may be gained by explaining the age-by-threshold interaction. A significant age-by-threshold interaction would complicate interpretations of any observed age effects. In contrast, the absence of such an interaction, especially in the presence of a main effect for age, would suggest that aging results in changes in DPOAE responses independent of the threshold effect.

In the presence of normal hearing, DPOAE amplitude is relatively independent of frequency, although slightly reduced DPOAE amplitudes have been observed around 3000 Hz (e.g., Lonsbury-Martin *et al.*, 1991; Gorga *et al.*, 1993a). As a result, a main effect of frequency, in combination with a significant frequency-by-threshold interaction, would suggest that DPOAEs differed because threshold differed across frequency. Likewise, a main effect of frequency, if the frequency-by-threshold interaction is not significant, would suggest that the effect cannot be accounted for in differences in thresholds across frequencies. An examination of age-by-frequency interactions would be useful under these conditions. A significant interaction between these variables would suggest that DPOAEs are affected by age but only for certain frequencies. The analyses to follow address each of these questions and were designed to evaluate age effects on DPOAEs, while controlling for the potential influences of threshold and frequency. With this study we seek to clarify what (if any) main or combined effects of age, threshold, and frequency act on DPOAE measures.

I. METHOD

A. Subjects

Subjects were culled from a larger database where DPOAEs were measured in over 1200 ears of over 800 subjects. These data, which were described in a previous report (Gorga *et al.*, 1997), were concerned with the extent to which DPOAEs accurately identify hearing loss under routine clinical conditions. The methods under which those data were collected are summarized therein, and will be reviewed here only briefly.

All subjects had to present normal middle-ear function (based on tympanometry, and/or otologic examination, and comparison of air and bone conduction thresholds) at the time of test. In addition, a pure-tone audiogram was available on all subjects. Audiometric thresholds (in dB HL *re*: ANSI, 1996) were measured at octave and half-octave frequencies from 250 to 8000 Hz, using standard age-appropriate clinical

TABLE I. Number of ears in the normal-per-frequency group in each decade for each frequency.

	Frequency							
Age	750	1000	1500	2000	3000	4000	6000	8000
5–9.9	23	50	30	38	28	41	31	40
10–19.9	24	40	28	40	36	29	20	31
20–29.9	57	61	62	61	56	62	52	56
30–39.9	55	71	63	69	56	58	48	52
40–49.9	92	133	113	125	94	97	72	83
50–59.9	56	81	70	66	53	53	23	27
60–69.9	72	112	97	85	55	50	24	30
70–79.9	48	79	64	56	27	21	5	6

TABLE II. Number of ears in the normal-across-frequency group in each decade for each frequency.

	Frequency							
Age	750	1000	1500	2000	3000	4000	6000	8000
5–9.9	16	19	19	19	19	19	19	19
10–19.9	10	13	13	14	14	14	13	12
20–29.9	42	43	43	43	43	44	44	43
30–39.9	37	43	42	41	41	42	42	41
40–49.9	35	44	48	49	49	49	49	39
50–59.9	12	14	16	16	16	16	16	12
60–69.9	6	8	8	10	10	10	10	9

procedures, with a minimum step size of 5 dB. A more precise threshold estimate could have been obtained by using psychophysical methods such as adaptive forced-choice procedures. However, in this study data collection was performed under routine clinical conditions. Audiometric frequencies corresponded to the f_2 frequencies used during DPOAE measurements, with the exception of 250 and 500 Hz. Interpretable DPOAE measurements were not possible at f_2 frequencies of 250 and 500 Hz due to high noise levels.

To assess the effects of age, threshold, and frequency on DPOAEs, audiometric thresholds were used to construct two groups of ''normal-hearing'' subjects by applying a less stringent and then a more stringent inclusion criterion. Analyses were performed separately on these groups. In the first group, audiometric status was treated on an individual frequency basis. Data were included only at those frequencies for which audiometric thresholds were 20 dB HL or better, without regard to sensitivity at other frequencies. We refer to this set as the normal-per-frequency group. A more stringent criterion for normal hearing was applied to create the second group. Only those subjects with audiometric thresholds of 20 dB HL or better at all octave and half-octave frequencies from 250 to 8000 Hz were included, representing a restricted subset of the first group. We refer to this set as the normal-across-frequency group. In both cases, the audiogram served as the ''gold standard'' of auditory function. This approach is consistent with our previous efforts to describe the relations between DPOAEs and cochlear status (Gorga *et al.*, 1993a, b, 1996; Stover *et al.*, 1996). Our previous work demonstrated that 20 dB HL (the inclusion criterion for the present paper) results in optimal separation between ears with normal hearing (thresholds up to 20 dB HL) and ears with hearing loss (Gorga *et al.*, 1993a), even though this criterion does not necessarily result in a homogeneous group of subjects (see Fig. 9, Gorga *et al.*, 1997).

As expected, the normal-per-frequency group (Table I) had larger numbers of ears per age group, compared to the normal-across-frequency group (Table II). Ears represented in the normal-across-frequency group were also represented in the normal-per-frequency group. Within the normal-per-frequency group, the number of ears at each frequency were uneven because audiometric data could not always be obtained at all eight frequencies and/or DPOAE amplitudes did not meet inclusion criteria in every subject. In the normal-across-frequency group uneven numbers of ears were due to the fact that DPOAE inclusion criteria were not always met. For example, the number of ears in the normal-per-frequency group ranged from 5 (6000 Hz, 70–79 years) to 133 (1000 Hz, 40–49 years), whereas the comparable range for the normal-across-frequency group varied from 6 (750 Hz, 60–69 years) to 49 (3000, 4000, and 6000 Hz in the 40–49 year group). There were sufficient observations for data analyses up to the 60–69.9 decade in the normal-across-frequency group, and up to the 70–79.9 decade in the normal-per-frequency group, reflecting the more restrictive nature of the inclusion criteria for the first group. Finally, there were scattered observations for subjects in the 80–89.9 and 90–99.9 age decades for both groups; however, the numbers per frequency cell were small and there were cells with no observations. As a consequence, analyses were limited to the range of ages shown in Tables I and II.

B. Stimuli

DPOAEs were measured in response to pairs of primary tones (f_1 and f_2, $f_2/f_1=1.22$), with f_2 frequencies ranging from 750 to 8000 Hz in half-octave steps. Due to the step size, this study was not designed to assess DPOAE microstructure. Primary tones were presented at intensity levels of $L_1=65$ dB SPL and $L_2=55$ dB SPL. These stimulus levels were selected because previous data have shown that they result in the most accurate classifications of auditory status (e.g., Gaskill and Brown, 1990; Whitehead *et al.*, 1995; Stover *et al.*, 1996) when the dividing line between normal and impaired hearing was drawn at 20 dB HL.

C. Procedures

Following audiometric and middle-ear assessments, DPOAE data were collected in a quiet room adjacent to the clinic, using a Bio-logic Scout system. Measurement-based stopping rules were used such that data collection at any f_2 frequency was terminated if the noise level was less than -30 dB SPL, or after 32 s of artifact-free averaging time, whichever occurred first. While the noise-floor stopping rule allows us to resolve small DPOAEs, caution is necessary when interpreting any DPOAE less than -20 dB SPL, which is a conservative estimate of the level of distortion produced by the measurement system (Gorga *et al.*, 1994). As a result, data were included in subsequent analyses only if the DPOAE amplitude was not less than -20 dB SPL and only

TABLE III. Multivariate regression analysis outcome for each group.

Normal-per-frequency variables	p value	Normal-across-frequency variables	p value
Age	0.010[a]	Age	0.166
Threshold	0.000[a]	Threshold	0.103
Frequency	0.012[a]	Frequency	0.973
Age×Threshold	0.526	Age×Threshold	0.629
Age×Frequency	0.000[a]	Age×Frequency	0.000[a]
Threshold×Frequency	0.672	Threshold×Frequency	0.216

[a]Significant effects at levels $p<0.05$.

if this amplitude exceeded the noise floor, regardless of the extent to which its amplitude exceeded the noise.

DPOAE amplitude was defined as the level in the $2f_1-f_2$ bin, while noise estimates were based on the average level at three frequency components above and three below (24.8-Hz separation between components) the $2f_1-f_2$ frequency. Comparisons were always made between audiometric data and DPOAE data when audiometric and f_2 frequencies were equal.

D. Statistical analysis

Preliminary statistical treatment of the data was done with analysis of variance (ANOVA) prior to initiating any linear regression analyses. The ANOVAs strongly indicated the presence of a threshold effect and to a lesser extent an age and a frequency effect. Given these outcomes we felt confident that it would be appropriate to perform regression analyses on these data. Multivariate regression analyses were performed on the dependent variable of DPOAE amplitude with independent variables of age, audiometric threshold, and frequency. Main effects for age, threshold, and frequency, as well as interactions among these variables were evaluated. The first analysis involved the normal-per-frequency group and the separate second analysis was performed on data from the normal-across-frequency group.

II. RESULTS

Results of multivariate regression analysis for both subject groups are displayed in Table III. In the normal-per-frequency group, where a less stringent inclusion criterion was applied, there were significant main effects for age, audiometric threshold, and frequency. There was also an interaction effect between age and frequency. No other significant interactions were observed. In particular, there was no interaction between age and threshold. We take this latter observation to mean that thresholds across age groups did not differ. In the normal-across-frequency group, where a more stringent inclusion criterion was applied, only the interaction between age and frequency remained significant. No main effects for age, threshold, or frequency were present. As with the previous subject group, there was no interaction between age and threshold.

In contrast to the differences in the level of significance across the two subject groupings, the trends in the data relating DPOAE amplitudes to age, threshold, and frequency were strikingly similar. Figures 1–3 represent DPOAE data related to each of these three variables (age, frequency, and threshold) for both subject groups. In each figure, the data from the normal-per-frequency group are shown with filled symbols, while the data for the normal-across-frequency group are shown as open symbols. In each case, mean values are plotted, along with the standard error of the mean.

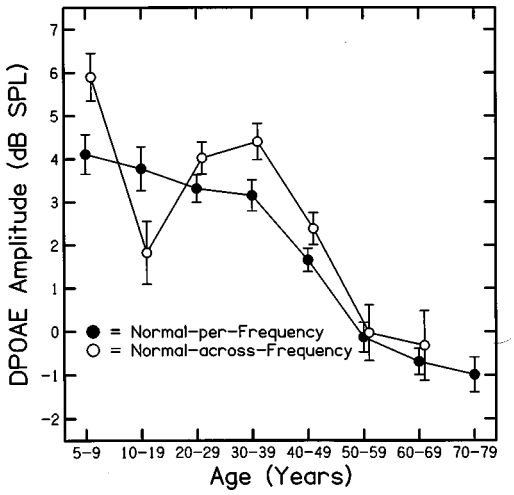

FIG. 1. Mean DPOAE amplitudes and standard errors by age, in decades, across all threshold levels and frequencies. The normal-per-frequency group is depicted with filled symbols and the normal-across-frequency group is shown with open symbols. DPOAE amplitude decreased as age increased.

Figure 1 relates DPOAE amplitude to age, collapsing across thresholds and frequency. The observation of a significant effect in the normal-per-frequency group and nonsignificant effect in the normal-across-frequency group may be a result of the unusual observation (reduced mean DPOAE amplitude in relation to older age groups) for the decade from 10 to 19.9 years in the normal-across-frequency group (open symbol, Fig. 1). This nonmonotonicity may be a consequence of sampling error. However, there are about 13 ears per frequency in this group (see Table II), amounting to a total number of 103 observations (across all eight frequencies). With the exception of this point (for which we have no

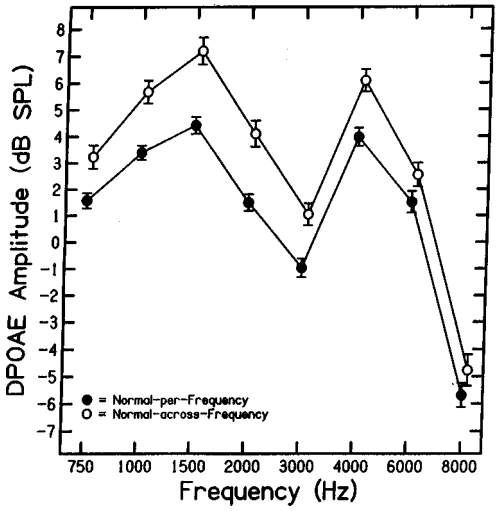

FIG. 2. Mean DPOAE amplitudes and standard errors for each of eight frequencies across all threshold levels and age decades. The normal-per-frequency group is depicted with filled symbols and the normal-across-frequency group is shown with open symbols. Generally, DPOAE amplitude decreased as frequency increased.

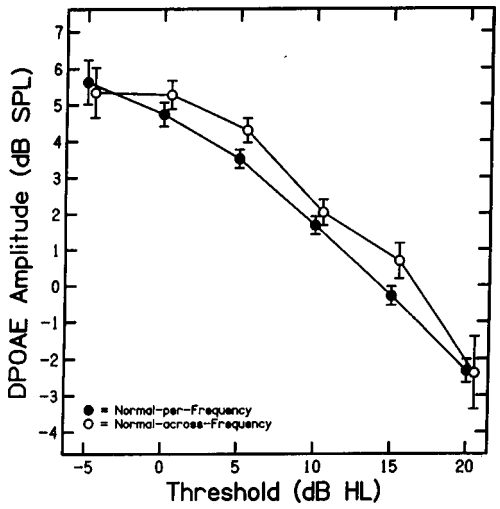

FIG. 3. Mean DPOAE amplitudes and standard errors for the six audiometric threshold levels across all frequencies and age decades. The normal-per-frequency group is depicted with filled symbols and the normal-across-frequency group is shown with open symbols. DPOAE amplitude decreased as threshold increased.

other explanation), the overall trends are comparable to those seen in the normal-per-frequency group. Indeed, the DPOAE amplitude range across the decades tested is 5.10 dB in the normal-per-frequency group and 6.22 dB in the normal-across-frequency group. Also, the function for the normal-across-frequency group is slightly higher, indicating that this group (with the exception of the 10–19.9 decade) produced slightly larger DPOAEs.

The effects of frequency on DPOAE amplitude are shown in Fig. 2, following the convention used in Fig. 1. There is a tendency for larger response amplitudes in the normal-across-frequency group (open symbols), with differences on the order of 1–3 dB. This finding is not surprising if one accepts the view that the subject inclusion criterion was more stringent for this group, and thus, auditory function was ''more normal.'' The overall pattern of the response across frequency, however, is similar for both groups. For example, both groups demonstrate relatively constant amplitudes across frequency, with the exception of a dip at 3000 Hz. This frequency pattern has been observed by others as well (Arnold *et al.*, 1996; Strouse *et al.*, 1996; Lonsbury-Martin *et al.*, 1991; Gorga *et al.*, 1993a). Standard errors are smaller across frequency in the normal-per-frequency group (filled symbols). The reduced amplitude for both groups at 8000 Hz might be related to reduced reliability of measurements at this frequency because of standing wave problems in stimulus calibration at high frequencies (Siegel, 1994), or due to smaller DPOAE signals produced within the cochlea in response to the 8000-Hz tone.

Figure 3 plots mean DPOAE amplitude as a function of audiometric threshold. Data exist at each 5-dB step from −5 to 20 dB HL, consistent with the way these data were collected in the clinic. As in our previous examples for age and frequency, the trends across the two subject groupings are similar. The DPOAE amplitude range is 7.96 dB in the normal-per-frequency group and 7.73 dB in the normal-across-frequency group. Yet, in spite of this apparent similarity, the threshold effect was significant in the normal-per-frequency, but not in the normal-across-frequency group (see Table III). Interestingly, DPOAE amplitude decreases monotonically as a function of threshold, even over the range of thresholds that are ordinarily considered within normal limits. These observations are similar to those made previously (see for example, Lonsbury-Martin *et al.*, 1997; Allen and Fahey, 1992), although the size of the present effect appears larger than previously reported.

Figure 4 represents the condition for which the final significant effect was observed. In this figure, DPOAE amplitudes are plotted as a function of age for each of eight test frequencies. For clarity, data are shown with two frequencies plotted per panel. Data from the normal-per-frequency group are shown with filled symbols and data for the normal-across-frequency group are shown with open symbols. The age-by-frequency interaction was significant for both subject groups (see Table III). It appears to be due mainly to the patterns observed at 8000 Hz, although a similar pattern is also evident at 6000 Hz (bottom right panel, Fig. 4).

III. DISCUSSION

Significant main effects were found for age, threshold, and frequency in the normal-per-frequency group. This outcome was not anticipated for age and frequency. DPOAE amplitudes were reduced with increased age, increased threshold levels, and higher frequencies. However, in the normal-across-frequency group there were no main effects. This may be due to the occurrence of a type II error, and/or inadequacies of fitting the data with a linear model, and/or the number of subjects was insufficient, which may have prevented the main effects from reaching significance. Should these hypotheses be correct, given that main effects were significant in the ANOVAs, it suggests that DPOAE amplitude may have varied for age, threshold, and frequency in the normal-across-frequency group. Statistical analyses revealed a significant interaction between age and frequency for both groups, with older subjects exhibiting decreased DPOAE amplitudes at higher frequencies. This finding is consistent with observations made by Arnold *et al.* (1996), Kimberley *et al.* (1994), and Whitehead *et al.* (1994). As might be expected from subject selection criteria, significant threshold-by-frequency and age-by-threshold interactions were not observed in the present data for either group. Importantly, the lack of an age-by-threshold effect in the present analyses indicates that age and threshold act independently on DPOAE amplitude measures, when threshold is controlled.

In both of the present subject groups, the age range under consideration was wide, extending into the 70's in the normal-per-frequency group and into the 60's in the normal-across-frequency group. The upper age bounds are likely a good representation of the age range that can be evaluated, while still controlling for auditory sensitivity. Undoubtedly there exist people in their 70's and beyond who have normal audiometric thresholds up to and including 8000 Hz, and likewise there are people in their 80's and above who have individual frequencies at which audiometric thresholds are normal. In fact, there were several subjects in the larger da-

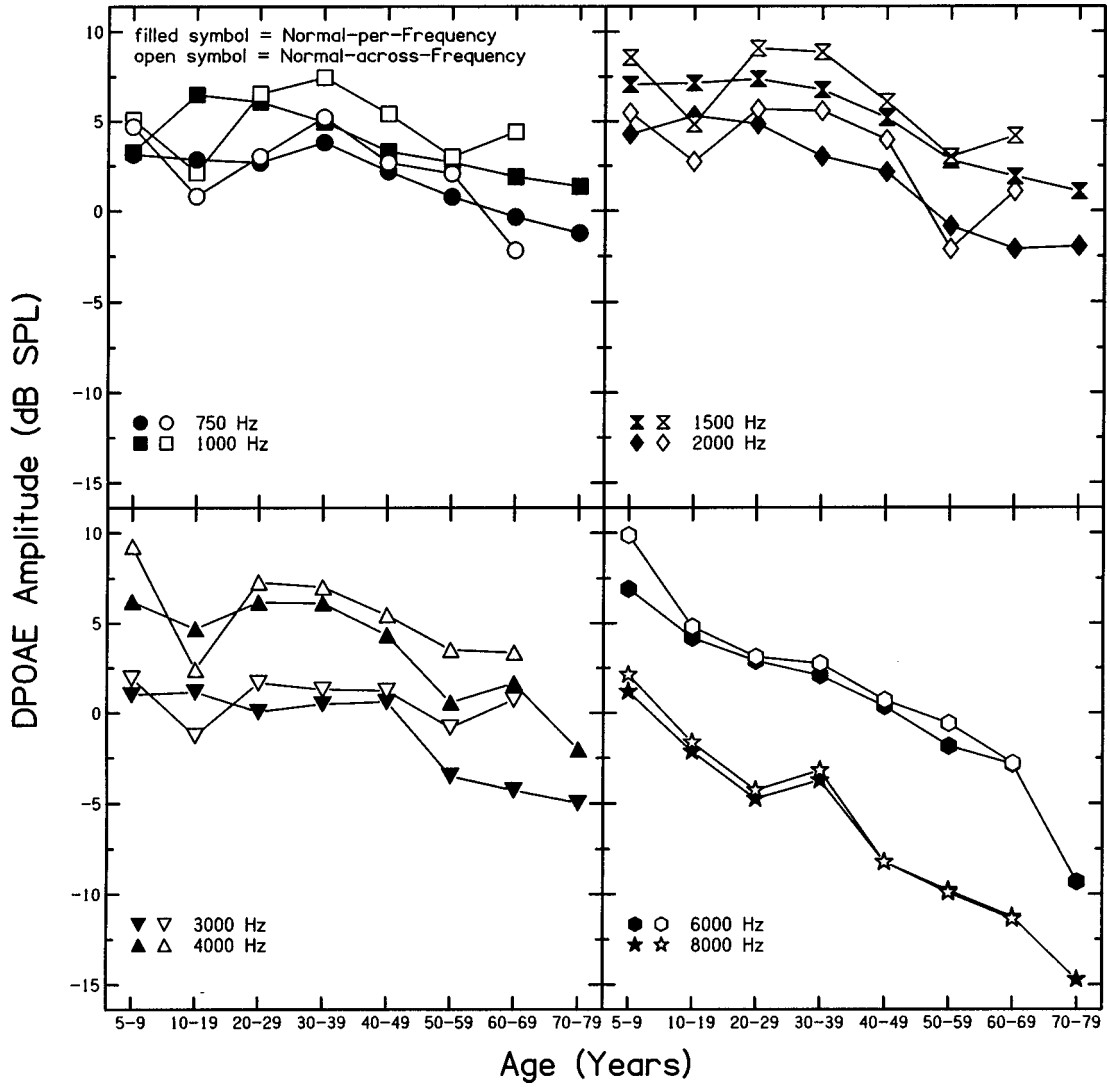

FIG. 4. The age-by-frequency interaction is depicted. Mean DPOAE amplitudes by age (in decades) for the four octave and four interoctave frequencies evaluated are shown. Two frequencies are plotted per panel. The normal-per-frequency group is depicted with filled symbols in each panel, while the normal-across-frequency group is shown with open symbols in each panel. Generally, DPOAE amplitude decreased as age and frequency increased.

tabase that met these criteria. The difficulty comes in finding sufficient numbers of these people to allow for statistical analyses. In other OAE studies where normal hearing older adults were used, Strouse *et al.* (1996) had subjects to age 79. Arnold *et al.* (1996) and Stover and Norton (1993) had normal hearing subjects into their 50's, while Prieve and Falter (1995) had normal hearing subjects to age 61. Our subjects were drawn from a large database and we feel confident that a reasonable upper age range for normal hearing was represented in this study.

The range of DPOAE amplitudes across decades of life (5.1 and 6.22 dB), across thresholds (7.96 and 7.73 dB), and across frequency (7.26 and 8.0 dB), was of a small magnitude for both ''normal hearing'' groups (see Figs. 1–3). All of these represented significant main effects for the normal-per-frequency group (first value in each pair), but not for the normal-across-frequency group (second value in each pair). With minor exceptions, the patterns relating DPOAE amplitudes to any of these variables were similar across groups. This observation suggests to us that there may be real effects of age, threshold, and frequency. A possible explanation for the different statistical outcomes may relate to differences in sample size and standard error. The number of ears in the normal-per-frequency group was often 1.5 to several times larger per decade, per frequency, or per threshold than in the normal-across-frequency group. Additionally, smaller standard errors were present in the normal-per-frequency group, which may be a consequence of the larger samples in this group.

The statistically different main effects across groups may be due to other factors beside sample size differences. It was not uncommon for subjects in the normal-per-frequency group to have elevated thresholds at frequencies other than the frequency (ies) at which the present analyses were performed. While the present analyses required that threshold be normal for data to be included at a particular frequency, threshold elevations were possible at other frequencies, including adjacent frequencies. The fact that the sample sizes across groups differed in the way they did is consistent with this view. Perhaps the amount of distortion generated within the cochlea or its reverse transmission out of the cochlea can be adversely affected by dysfunction at cochlear regions

other than the region associated with the f_2 under direct study. A study by Avan *et al.* (1991) suggests that CEOAEs may be influenced by the cochlear status at regions outside of the frequency range of CEOAEs. Another explanation is that the use of a linear regression model may have been appropriate for the normal-per-frequency data, but may not have been the best fit for the normal-across-frequency data. ANOVA results indicated significant effects for age, threshold, and frequency in the normal-across-frequency group. Unlike the multivariate regression analysis, which assumed that the data could be fit to a straight line, the ANOVA made no such assumption about the data.

A significant age-by-frequency interaction was present, regardless of differences in sample size or how the two groups were constructed. Lonsbury-Martin *et al.* (1991) and Arnold *et al.* (1996) also reported that an age effect was present at higher frequencies. From Fig. 4 (bottom right panel), it is clear that the responses at 6000 and 8000 Hz have a large impact on mean DPOAE amplitude across age. Again, the magnitude of decrease in the DPOAE amplitude at these frequencies (2.2 dB per decade of life for both groups) was larger than at any other frequency. This outcome could reflect the general pattern of how cochlear degeneration is manifested, with higher frequency regions affected first in an aging population. Additionally, OAEs sometimes are considered to be more sensitive indicators of cochlear status, as compared to audiometric thresholds. Thus decrements may be observed in high-frequency DPOAEs (due either to aging or subclinical cochlear damage) prior to a time when sensitivity loss is evident.

Age and threshold did not significantly interact, regardless of sample size or group construction (see Table III). These results suggest that when auditory sensitivity was controlled, age and threshold acted independently on DPOAE measures. This represents an important finding, since hearing loss is so closely linked with the aging process. When subject groups representing a wide age range, but narrow sensitivity range are constructed, the independence of these two variables can be seen.

In summary, we observed changes in DPOAE amplitude with age, threshold, and frequency. The magnitude of DPOAE amplitude change for these main effects was small, but consistent. However, we do not feel that corrections to DPOAE measures for these variables are warranted at this time. Further, an age-by-frequency interaction was observed at higher frequencies. We do feel that age-by-frequency dependent criteria for DPOAE testing, at least over the age range included in this study, should be considered for 6000 Hz and above. Age and threshold did not significantly interact. We conclude that age does affect DPOAEs, but that this variation with age is independent of threshold. Evidence of aging may be found in DPOAE amplitude measures, without a concomitant change in sensitivity.

ACKNOWLEDGMENTS

This work was supported by grants from NIH/NIDCD (R01 DC002251, 5 T32 DC00013, and P01 DC00520). We thank Dr. Pat Stelmachowicz for her helpful suggestions in the preparation of this manuscript. We also thank two anonymous reviewers for their helpful suggestions on our earlier version of this manuscript.

Allen, J. B., Connington, M., and Levitt, H. (**1991**). ''A comparison of pure tone and distortion product audiometric thresholds'' (unpublished manuscript).

Allen, J. B., and Fahey, P. F. (**1992**). ''Using acoustic distortion products to measure the cochlear amplifier gain on the basilar membrane,'' J. Acoust. Soc. Am. **92**, 178–188.

ANSI (**1996**). ANSI S3.6-1996, ''Specifications for Audiometers'' (American National Standards Institute, New York).

Arnold, D. J., Lonsbury-Martin, B. L., Martin, G. K., and Stagner, B. B. (**1996**). ''Influence of ultra-high frequency hearing on distortion product otoacoustic emission levels in humans,'' in *Abstracts of the Nineteenth MidWinter Meeting*, edited by G. R. Popelka (Association for Research in Otolaryngology, Des Moines, IA), pp. 19, 25.

Avan, P., Bonfils, P., Loth, D., Narcy, Ph., and Trotoux, J. (**1991**). ''Quantitative assessment of human cochlear function by evoked otoacoustic emissions,'' Hearing Res. **52**, 99–112.

Bonfils, P., Bertrand, Y., and Uziel, A. (**1988**). ''Evoked otoacoustic emissions: normative data and presbycusis,'' Audiology **27**, 27–35.

Collet, L., Moulin, A., Gartner, M., and Morgan, A. (**1990**). ''Age-related changes in evoked otoacoustic emissions,'' Ann. Otol. Rhinol. Laryngol. **99**, 993–997.

Gaskill, S. A., and Brown, A. M. (**1990**). ''The behavior of the acoustic distortion product, $2f_1-f_2$, from the human ear and its relation to auditory sensitivity,'' J. Acoust. Soc. Am. **88**, 821–839.

Gorga, M. P., Neely, S. T., Bergman, B., Beauchaine, K. L., Kaminski, J. R., and Liu, Z. (**1994**). ''Towards optimizing the limits of distortion product otoacoustic emission,'' J. Acoust. Soc. Am. **96**, 1494–1500.

Gorga, M. P., Neely, S. T., Bergman, B., Beauchaine, K. L., Kaminski, J. R., Peters, J., and Jesteadt, W. (**1993a**). ''Otoacoustic emissions from normal-hearing and hearing-impaired subjects: distortion product responses,'' J. Acoust. Soc. Am. **93**, 2050–2060.

Gorga, M. P., Neely, S. T., Bergman, B. M., Beauchaine, K. L., Kaminski, J. R., Peters, J., Schulte, L., and Jesteadt, W. (**1993b**). ''A comparison of transient-evoked and distortion product otoacoustic emissions in normal-hearing and hearing-impaired subjects, J. Acoust. Soc. Am. **94**, 2639–2648.

Gorga, M. P., Neely, S. T., Ohlrich, B., Hoover, B., Redner, J., and Peters, J. (**1997**). ''From laboratory to clinic: a large scale study of distortion product otoacoustic emissions in ears with normal hearing and ears with hearing loss,'' Ear Hearing **18**, 440–455.

Gorga, M. P., Stover, L. J., Neely, S. T., and Montoya, D. (**1996**). ''The use of cumulative distributions to determine critical values and levels of confidence for clinical distortion product otoacoustic emission measurements,'' J. Acoust. Soc. Am. **100**, 968–977.

Kimberley, B. P., Hernadi, I., Lee, A. M., and Brown, D. K. (**1994**). ''Predicting pure tone thresholds in normal and hearing-impaired ears with distortion product otoacoustic emissions and age,'' Ear Hearing **15**, 199–209.

Lonsbury-Martin, B. L., Cutler, W. M., and Martin, G. K. (**1991**). ''Evidence for the influence of aging on distortion-product otoacoustic emissions in humans,'' J. Acoust. Soc. Am. **89**, 1749–1759.

Lonsbury-Martin, B. L., Martin, G. K., and Whitehead, M. L. (**1997**). ''Distortion product otoacoustic emissions,'' in *Otoacoustic Emissions Clinical Applications*, edited by M. S. Robinette and T. J. Glattke (Thieme, New York), pp. 83–109.

Martin, G. K., Ohlms, L. A., Franklin, D. J., Harris, F. P., and Lonsbury-Martin, B. L. (**1990**). ''Distortion product emissions in humans III. Influence of sensorineural hearing loss,'' Ann. Otol. Rhinol. Laryngol. **99**, 30–42.

Prieve, B. A., and Falter, S. R. (**1995**). ''COAEs and SSOAEs in adults with increased age,'' Ear Hearing **16**, 521–528.

Siegel, J. H. (**1994**). ''Ear-canal standing waves and high-frequency sound calibration using otoacoustic emission probes,'' J. Acoust. Soc. Am. **95**, 2589–2597.

Stover, L., Gorga, M. P., Neely, S. T., and Montoya, D. (**1996**). ''Towards optimizing the clinical utility of distortion product otoacoustic emission measurements,'' J. Acoust. Soc. Am. **100**, 956–967.

Stover, L., and Norton, S. J. (**1993**). ''The effects of aging on otoacoustic emissions,'' J. Acoust. Soc. Am. **94**, 2670–2681.

Strouse, A. L., Ochs, M. T., and Hall, J. W. (**1996**). ''Evidence against the influence of aging on distortion-product otoacoustic emissions,'' J. Am. Acad. Audiol. **7**, 339–345.

Whitehead, M. L., McCoy, M. J., Lonsbury-Martin, B. L., and Martin, G. K. (**1995**). ''Dependence of distortion product otoacoustic emissions on primary levels in normal hearing and impaired ears. I. Effects of decreasing L_2 below L_1,'' J. Acoust. Soc. Am. **97**, 2346–2358.

Whitehead, M. L., Stagner, B. B., Lonsbury-Martin, B. L., and Martin, G. K. (**1994**). ''Measurement of otoacoustic emissions for hearing assessment,'' IEEE Eng. Med. Biol. Mag. Apr/May, 210–226.

Effects of loop diuretics on the suppression tuning of distortion-product otoacoustic emissions in rabbits

Glen K. Martin,[a] David Jassir, Barden B. Stagner, and Brenda L. Lonsbury-Martin
Department of Otolaryngology, University of Miami School of Medicine, P.O. Box 016960, Miami, Florida 33101-6960

(Received 10 November 1997; revised 25 March 1998; accepted 18 May 1998)

The suppression tuning of distortion-product otoacoustic emissions (DPOAEs) is commonly assumed to measure frequency selectivity, because the dominant features of suppression-tuning curves (STCs) are similar to the principal properties of the neural-tuning curves (NTCs) of single auditory-nerve fibers. In the present study, several common loop diuretics were used to affect the DPOAE-generation process to determine if reversible ototoxicity could adversely modify the characteristics of STCs, in a manner similar to that shown previously for NTCs. Contour plots of DPOAE level in the presence of a series of variable-level suppressor tones were obtained before and after administering diuretic drugs that reversibly reduced or eliminated DPOAEs. Primary-tone pairs were centered at 2.8 or 4 kHz, with $L_1=L_2$, or $L_2<L_1$. From the resulting plots, STC parameters including tip frequency, threshold at the tip frequency, and $Q_{10\,\mathrm{dB}}$ measures of tuning were extracted for four suppression criteria of 3, 6, 9, and 12 dB. In the pre-drug nonototoxic state, suppression tuning depended on both primary-tone level (L_1,L_2), and the relative levels of the primaries (L_1-L_2), with tuning being sharper for lower- than for higher-level equilevel primaries, and sharpest for offset-level primary tones. Following drug injection, the expected decrease in sharpness of tuning evidenced by changes in $Q_{10\,\mathrm{dB}}$ as well as the dramatically elevated tip thresholds normally seen for NTCs under similar conditions, were not observed. Overall, $Q_{10\,\mathrm{dB}}$ increased or decreased more or less randomly, with a slight tendency for STCs to become sharper than prior to drug dosing, for the two highest suppression criteria. The STC-tip frequencies demonstrated significant decreases following diuretic administration that were weakly correlated with the associated decreases in DPOAE amplitude. The most consistent changes in response to the drug-induced reduction in DPOAE level were increases in the STC-tip thresholds. However, these changes were relatively small and rarely exceeded 10 dB. In the absence of notable changes in overall STC shape, a major finding was a change in the effectiveness of suppression following ototoxic insult. However, when the amount of suppression was expressed as a percentage of the DPOAE remaining, the effects of diuretic dosing were often almost completely obscured. Overall, the results demonstrated that when the generation of DPOAEs was interfered with by the introduction of a suppressor tone to produce STCs that resemble NTCs, STCs behaved quite differently following reversible cochlear insult than their previously documented neural counterparts. These findings imply that STCs do not assess the frequency-selective aspects of the cochlear amplification process in a manner similar to NTCs.
 [S0001-4966(98)06808-8]

PACS numbers: 43.64.Jb, 43.64.Bt, 43.64.Kc [RDF]

INTRODUCTION

Since Kemp's (1978) discovery of otoacoustic emissions (OAEs), it has become almost universally accepted (e.g., Kummer *et al.*, 1995) that these responses arise from the compressive nonlinearity responsible for the frequency-selective gain described for the mechanical response of the basilar membrane (Rhode, 1971; Sellick *et al.*, 1982; Johnstone *et al.*, 1986; Robles *et al.*, 1986). This frequency-selective amplification of basilar-membrane vibration has become known as the cochlear amplifier (CA) (Davis, 1983). Presumably, the CA is based in the electromotility of outer hair cells (OHCs), and is responsible for the various OAEs that can be detected noninvasively in the ear canal (Brownell, 1990). When the nonlinear CA is stimulated by two tones at frequencies f_1 and f_2 ($f_1<f_2$), various even- and odd-order distortion-product OAEs (DPOAEs) result (Kemp, 1979), with the largest and most frequently studied one being the $2f_1-f_2$ DPOAE.

Similar to two-tone suppression in auditory-nerve fibers (Delgutte, 1990), it was soon established that OAEs, in general, and DPOAEs, in particular, could also be suppressed by the introduction of a third, or suppressor tone (Kemp and Chum, 1980; Kemp and Brown, 1983; Brown and Kemp, 1984; Martin *et al.*, 1987; Harris *et al.*, 1992; Koppl and Manley, 1993). If the suppressor tone is varied in frequency and level, while the primary tones are held constant, a suppression-tuning curve (STC) can be obtained for various criterion amounts of DPOAE-amplitude reduction. These STC functions have ''best'' tip or center frequencies (CFs), tip thresholds, low-frequency tails, and steep high-frequency slopes, which, in many ways, closely resemble the features of the neural tuning curves (NTCs) commonly described for single auditory-nerve fibers. These observations raise two different, but related, experimental questions. First, do

[a]Electronic mail: gmartin@mednet.med.miami.edu

DPOAE STCs behave similarly to NTCs following cochlear insults, and, second, if STCs do not behave like STCs, do they nevertheless reflect some aspect of cochlear-frequency selectivity?

Several studies in laboratory animals have implied, by way of comparison (Koppl and Manley, 1993; Frank and Kossl, 1995), that STCs can be employed as noninvasive measures of cochlear-frequency selectivity in a manner similar to the NTCs obtained from animals. For example, in the bat, Frank and Kossl (1995) noted that, as the tuning characteristics of neurons in the ventral cochlear nucleus changed within various specialized frequency regions, DPOAE STCs obtained across corresponding frequency extents in an additional group of bats demonstrated similar alterations in tuning properties. Specifically, in the frequency region between 62 and 72 kHz which represents a region of specialized thickening of the bat basilar membrane, the low-frequency tails of both NTCs and STCs reversed direction. These findings were interpreted by the authors as providing evidence that STCs reflect the underlying tuning characteristics of auditory-nerve fibers. Similarly, in the bobtail lizard, comparisons of the distributions of $Q_{10\,\mathrm{dB}}$ values revealed a close relationship between NTC and STC measures of frequency selectivity (Koppl and Manley, 1993). Together, these observations in animal models support the assumption that the dominant features of STCs are similar to the tuning characteristics of single nerve fibers.

Recently, in the first detailed study of STCs in humans, Kummer *et al.* (1995) reported that, for low primary-tone levels ($L_1=55$, $L_2=40$ dB SPL), STC sharpness increased with the increasing frequencies of the primaries. These investigators noted that, around 4–6 kHz, the low-frequency tails of the STCs had slopes of 30–40 dB/octave, whereas the high-frequency limb exhibited slopes of approximately 230 dB/octave. From 1 to 4 kHz, $Q_{10\,\mathrm{dB}}$, a standard measure of frequency tuning (i.e., CF/bandwidth at 10 dB above tip threshold), increased as a function of frequency with values ranging from 1.69 to 7.87. Moreover, tip thresholds ranged from 26 to 52 dB SPL, with a mean of 38 dB SPL, which was slightly below the level of the f_2 primary. Overall, these findings for STCs compared favorably with the trends described earlier for single auditory-nerve fibers (Kiang *et al.*, 1965), and suggested that STCs in humans reflect the frequency-selective aspects of the nonlinear amplification of basilar-membrane vibration.

Several recent studies in humans from Abdala and colleagues have assumed that DPOAE STCs can provide objective estimates of the frequency selectivity of the peripheral hearing apparatus (Abdala *et al.*, 1996; Abdala and Sininger, 1996; Abdala and Luckoski, 1997). Based upon this notion, these investigators have thoroughly examined STCs in adults, neonates, and premature infants. Interestingly, they found differences between premature neonates and adults in STCs low-frequency slope and suppression growth. Measures of $Q_{10\,\mathrm{dB}}$ were significantly sharper for premature neonates than adults, opposite to what might be expected if the cochlea were still developing.

In adults, Abdala *et al.* (1996) performed comparisons between the tuning features of STCs and psychoacoustic tuning curves (PTCs), and discovered that PTCs were more sharply tuned. These findings are consistent with prior observations in the guinea pig (Ryan and Dallos, 1975; Dallos *et al.*, 1977), in which the $Q_{10\,\mathrm{dB}}$ for PTCs was approximately twice the $Q_{10\,\mathrm{dB}}$ values measured for the NTCs of single nerve fibers. Because of the many differences between PTCs, STCs, and NTCs (see Abdala *et al.*, 1996), the ability of STCs to index frequency selectivity as measured by PTCs remains unclear.

One approach toward indirectly testing the hypothesis that STCs reflect the frequency selectivity of the peripheral auditory system in a way similar to NTCs would be to examine STCs in laboratory animals before and after a manipulation known to dramatically affect both NTCs and the mechanical tuning of the basilar membrane. This goal can be accomplished by administering reversibly ototoxic diuretics, such as ethacrynic acid or furosemide, which are well-known to significantly elevate NTC tip thresholds and, consequently, reduce the frequency selectivity of both NTCs (Evans and Klinke, 1982; Sewell, 1984), and the pattern of basilar-membrane vibration (Ruggero and Rich, 1991). It is also well-established that reversible ototoxins dramatically reduce low-level, ''active'' DPOAEs (Whitehead *et al.*, 1992; Mills *et al.*, 1993; Mills and Rubel, 1994), which is consistent with the notion that low-level DPOAEs arise from the same sensitive, physiologically vulnerable CA that is responsible for the frequency-selective amplification of basilar-membrane vibration, and the sharp tuning of auditory-nerve fibers. To determine the ability of DPOAE STCs to reflect changes in the cochlea's amplification process in a manner similar to NTCs, the present study in rabbits examined DPOAE STCs elicited by primary-tone levels known to be operating in the ''active,'' physiological vulnerable region of DPOAE generation, before and after injections of the loop diuretics, ethacrynic acid, or furosemide. The outcome of these manipulations revealed that DPOAE STCs do not behave like NTCs, but do not rule out the possibility that DPOAE STCs measure some aspect of cochlear-frequency selectivity.

I. METHODS

A. Experimental animals

Subjects were nine young, adult pigmented rabbits weighing between 2.5 and 4 kg, seven of which produced reliable data following diuretic administration. Prior to any DPOAE measurements, each animal was anesthetized (ketamine 50 mg/kg, xylazine 10 mg/kg) and surgically fitted with a permanent headmount device. The DPOAE measurements were carried out a few days later in a soundproofed booth, with the rabbit secured in a standard plastic restrainer, and its head held firmly in position by a bracket fixed to the restrainer, and attached to the head mount. To reduce the effects of the acoustic reflex (Whitehead *et al.*, 1991), as well as to prevent potential changes in position of the probe, $2f_1-f_2$ DPOAEs were obtained during the ototoxicity experiments with the animals anesthetized as described above. Anesthesia was also helpful for inserting an indwelling intravenous (IV) catheter in the marginal ear vein for ease of

ototoxic-drug administration, and for avoiding any pain or discomfort that might be caused by the injection of the relatively high doses of diuretic drugs. The experimental-animal protocol was reviewed and approved locally by the Institutional Animal Care and Use Committee of the University of Miami School of Medicine.

B. DPOAE measurement procedures

The measured DPOAE responses included DP-grams, i.e., DPOAE level as a function of frequency, with primary-tone levels held constant, and the suppression response areas (SRAs) described below. The DP-grams were collected at geometric-mean (GM) frequencies [$\mathrm{GM}=(f_1\times f_2)^{0.5}$], in 0.1-octave steps, from 1.414 to 18.37 kHz, using procedures previously described in detail elsewhere (Whitehead *et al.*, 1995). Briefly, the f_1 and f_2 primary tones were generated by a 16-bit digital signal processing (DSP) board (Digidesign, Audiomedia), mounted in a Macintosh llci personal microcomputer, and presented over ER-2 (Etymotic Research) loudspeakers. Ear-canal sound pressure, which was measured by an ER-10 (Etymotic Research) microphone, was sampled and synchronously averaged ($n=4$) by the DSP board. From a 4096-point fast Fourier transform (FFT) of the time sample, the levels of the $2f_1-f_2$ DPOAE, and the related noise floor, were extracted.

C. Suppression-response areas (SRAs)

The SRAs were obtained for each ear at the GM frequencies of 2.828 ($f_1=2.53$, $f_2=3.16$ kHz) and 4 kHz ($f_1=3.59$, $f_2=4.47$ kHz). The primary tones ($f_2/f_1=1.25$) were either equilevel at $L_1=L_2=45$, 50, 55, 60, or 65 dB SPL, or with L_2 lower than L_1 by an amount that depended on the level of L_1, i.e., $L_1/L_2=50/35$, 55/45, and 60/55 dB SPL, which had previously been determined from a DPOAE growth function that maximized sensitivity to cochlear insult (Whitehead *et al.*, 1995). For each primary-tone pair, the suppressor tone, which was digitally added to the f_1 channel, was swept in 10 steps/octave, from 0.25 to 10 kHz, with the suppressor being systematically increased in 5-dB steps, from 35 to 85 dB SPL. Data were collected in a matrix of 324 frequency/level combinations, in which the amount of suppression was calculated relative to DPOAE level in the absence of the suppressor tone. This reference nonsuppressed DPOAE level was based upon the mean of all control DPOAE levels measured at the end of each frequency column in the suppression matrix. It was found that the use of mean-control DPOAE-amplitude values reduced noise in the SRAs, when DPOAE amplitude was reduced toward the noise floor following diuretic administration. This procedure, however, did not adversely affect STC parameters as judged by inspection of the outcomes yielded by selecting the ''individual'' controls option of the analysis software. The amount of suppression was limited so as not to exceed the average control amplitude minus the average noise floor, plus 2 standard deviations (s.d.'s). This procedure prevented spurious amounts of suppression when the suppressor reduced DPOAEs to values near the noise floor. The SRA data were displayed as contour plots (Microsoft, Excel v5.0) in which successive contours represented increasing iso-suppression, in 3-dB steps.

D. Suppression-tuning curves (STCs)

A spreadsheet algorithm was developed to extract iso-suppression tuning curves (STCs) from the SRA contour plots, and to automatically calculate the tip frequency, threshold at the tip, and $Q_{10\,\mathrm{dB}}$ (i.e., STC-tip frequency/bandwidth at 10 dB above STC-tip threshold), for the suppression criteria of 3, 6, 9, and 12 dB. In a second analysis procedure, the data in the suppression matrix were smoothed once, prior to the STC extraction, to remove anomalies that could affect estimates of the STC-tip frequency, threshold, or $Q_{10\,\mathrm{dB}}$. The smoothing procedure used a common image-analysis method in which each point in the matrix was replaced by the average of itself and its eight neighbors. Although this procedure produced somewhat ''idealized'' suppression contours (see Figs. 3 and 4), it surprisingly had only minor effects on STC characteristics and, thus, ensured that the data were relatively uncontaminated by aberrant points that can adversely affect the STC-extraction process. Although both procedures appeared to produce comparable results, to avoid any bias, data are presented below for both unsmoothed and smoothed data points.

E. Experimental protocol

Following acquisition of the control measures, rabbits were given an IV injection of either ethacrynic acid (40 mg/kg) or furosemide (100 mg/kg), with four rabbits receiving ethacrynic acid, and the remaining five rabbits being administered furosemide. There were no apparent differences noted between the effects of the two diuretics on DPOAEs in the present study, which is consistent with a similar lack of obvious differences between the two diuretics noted previously in several other studies in which loop diuretics were used to reduce DPOAE level (Whitehead *et al.*, 1992; Mills and Rubel, 1994). To observe dynamic changes, as the animals recovered from the effects of the diuretic agent, both DP-grams and STCs, typically at four primary-tone level combinations were regularly remeasured, whenever possible, at ~20-min intervals over the post-drug period that lasted for about 80–120 min. These procedural steps resulted in a complex repeated-measures experimental design in which multiple primary-tone level combinations, obtained at four time periods during recovery, were derived from the same rabbit. This experimental design was necessary to avoid testing unreasonably large numbers of rabbits in order to obtain completely independent samples at every primary-tone level combination. To circumvent the majority of problems created by a within-subjects' paradigm, all relevant STC parameters were computed and expressed as post-drug minus pre-drug (i.e., pre/post) differences. These difference scores were then plotted as a function of DPOAE amplitude change, because this is likely the relevant variable that reflects alterations in the active process that presumably underlies the well-described changes observed for single auditory-nerve fibers, as well as for basilar-membrane vibration patterns obtained under similar conditions.

One potential problem with this approach was the possibility that DPOAE variability, or changing DPOAE amplitude following diuretic administration, could affect STC pa-

rameters. Because only 4–5 min were required to collect a complete suppression-matrix, it was expected that DPOAE amplitude would remain relatively stable throughout the collection period. To be certain that this was the case, the s.d.'s of the control DPOAE amplitudes were computed for both the pre- and post-diuretic administration periods. As was expected based on a large laboratory database of rabbit DPOAEs, the pre-diuretic control DPOAE levels were very stable, with a mean s.d. of 0.60 dB (range 0.01–1.45 dB SPL). Post-drug control DPOAE amplitudes were only slightly more variable and exhibited a mean s.d. of 0.69 dB (range 0.01–2.41 dB SPL). Overall, when post-drug s.d.'s were plotted as a function of DPOAE-amplitude change, they clearly became more variable as DPOAE level was reduced toward the noise floor. Inspection of plots of the control DPOAE amplitude over time, for cases with the largest s.d.'s, revealed only one instance in which control levels showed a conspicuous trend as though recovering from diuretic administration. To control for this changing baseline, these particular suppression data were calculated based upon individual control measures.

F. Statistical analyses

For comparisons between the pre- versus post-drug DPOAE and STC parameters, nonparametric paired-sign tests were used to test the statistical significance of any noted changes (Siegel, 1956). Similarly, to determine the relationship between the DPOAE level and the STC parameter under study, nonparametric Spearman-rank correlation coefficients (r_s), corrected for ties, were computed, based upon the differences in rank ordering of the pre/post-difference pairs. To be conservative, nonparametric statistical analyses were selected, because the data did not meet all the assumptions necessary for performing parametric statistical tests. In other words, the data for the various suppression criteria and primary-tone levels did not represent independent samples from different rabbits. The various statistical tests were performed using a commercially available software package (Abacus, StatView v4.0), with the adopted level of statistical significance being $p<0.05$.

II. RESULTS

A. Control STC characteristics

The STCs properties were highly dependent on the parameters of the eliciting primary tones. Such influences are readily observable in the bargraphs of Fig. 1, which display the mean values obtained from unsmoothed contour plots, across the four suppression criteria. Figure 1(A) illustrates the effects of primary-tone level on STC-tip thresholds. It is clear that, as the level of f_1 increased (from left to right), the corresponding tip threshold also increased, for both the 2.828- (open bars) and 4-kHz (solid bars) STCs. It is also apparent that tip thresholds were typically about 3–5 dB lower than the corresponding level of f_2.

The bargraph plot of Fig. 1(B) shows the tendency for the STC-tip frequency to depend upon the level of f_2. For primaries with a GM of 2.828 kHz, the restricted range of f_2 levels failed to reveal any apparent trend. However, for the

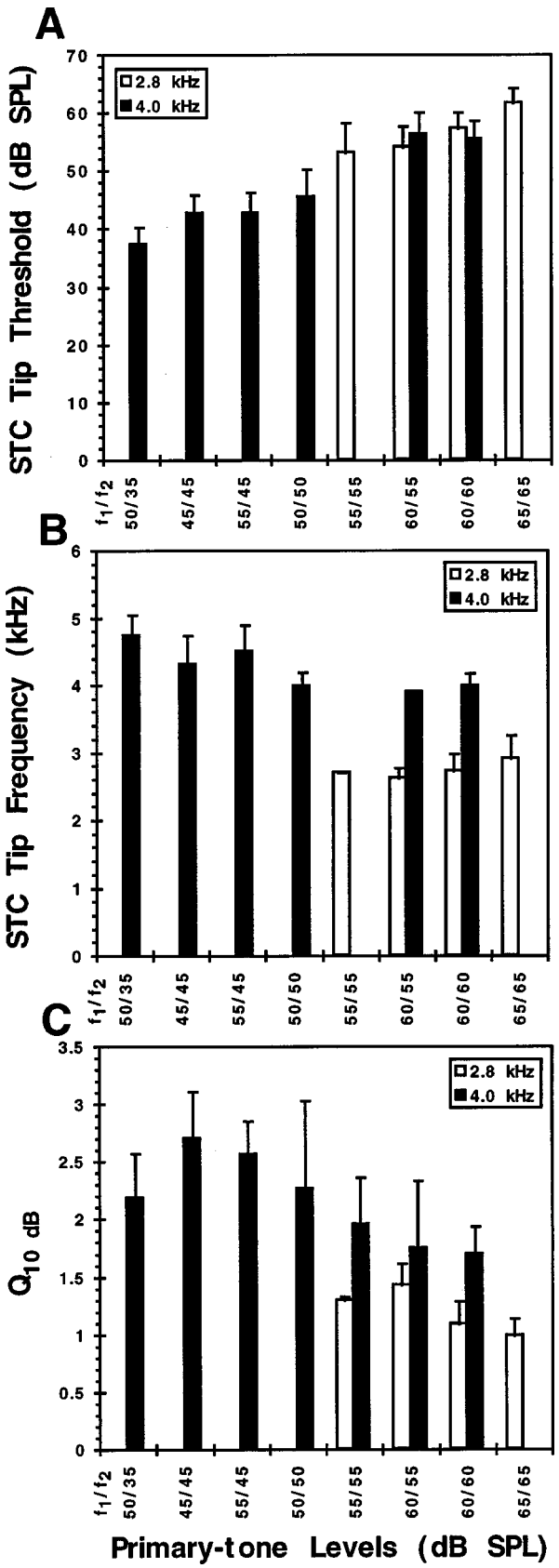

FIG. 1. Bargraphs relating mean STC-tip thresholds (A), STC-tip frequencies (B), and STC $Q_{10\,dB}$ (C), across the four suppression criteria, at the GMs of 2.828 (open bars) and 4 kHz (solid bars), to $L_1=L_2$ and $L_2<L_1$ primary-tone levels. Plots are arranged from left to right in ascending order, first by the level of f_2, and then by the level of f_1. Plots show the trend for lower primary-tone levels to be associated with: (A) lower tip thresholds; (B) a shift of tip frequency towards f_2, particularly for the 4-kHz STCs; and (C) increased $Q_{10\,dB}$. Error bars represent +1 s.d.

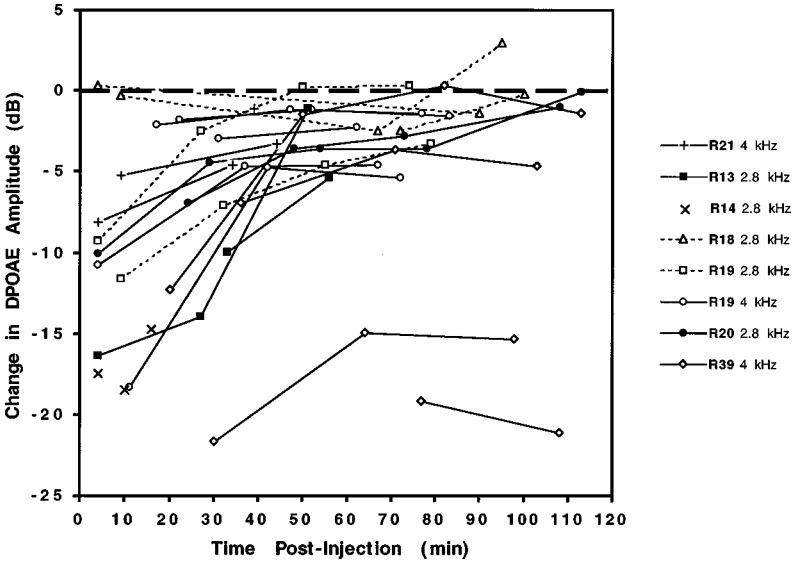

FIG. 2. Changes in DPOAE amplitude as a function of time post-injection for individual rabbits. Lines with similar symbols reflect different primary-tone level combinations for a particular rabbit.

STCs evoked by the 4-kHz GM primaries, the tip frequency was closer to the GM of 4 kHz for the higher-level primaries (e.g., 50/50, 60/55, 60/60 dB SPL), at the right. In contrast, it tended to move toward, or above, the f_2 frequency of 4.47 kHz, as the overall primary-tone level decreased, a trend which was particularly clear as the level of f_2 was dramatically reduced below f_1 (e.g., at 50/35 dB SPL).

Finally, Fig. 1(C) illustrates the influence of the primary-tone GM frequency and f_2 level on $Q_{10\,\mathrm{dB}}$ for the 2.828- and 4-kHz STCs. When both were measured at the same primary-tone level combinations, the 2.828-kHz STCs tended to have lower $Q_{10\,\mathrm{dB}}$ values than those obtained at 4 kHz. For the GM of 4 kHz, it is clear that, overall, lowering of primary-tone level, as well as the level of f_2, in particular, increased the sharpness of tuning as measured by $Q_{10\,\mathrm{dB}}$. The basis of the reversal of this trend at the f_1 and f_2 combination of 50/35 dB SPL is unclear. However, inspection of the contour plots revealed that it could not be attributed to a ''floor'' effect caused by the knowledge that the suppressor level did not extend below 35 dB SPL.

Obscured by these mean plots is the influence of suppression criterion on the measured STC parameters. As might be expected, there was an orderly progression of this effect with the 3-dB criterion STCs having the lowest thresholds, and the 12-dB criterion STCs yielding, on average, the highest thresholds by approximately 10 dB, for all primary-tone levels. Also, with respect to the $Q_{10\,\mathrm{dB}}$, on average, higher suppression criteria resulted in sharper tuning (i.e., higher $Q_{10\,\mathrm{dB}}$ values), but this difference was less apparent as the level of f_2 increased. Considering the complex influences of primary-tone level on STC features, the present study represented an attempt to sample a broad range of conditions to determine the sensitivity of the various DPOAE-tuning properties that correspond reasonably well to those traditionally measured for NTCs.

B. DPOAE amplitude changes

Following diuretic administration, DPOAE levels typically decreased substantially, and then gradually returned toward normal levels. The amount of reduction in DPOAE amplitude depended upon both the levels of the primary tones, with low-level primary-tone combinations being most affected, and with the time post-injection that measurements were obtained. Figure 2 shows these changes in DPOAE amplitude as a function of time post-injection for individual rabbits. Each point represents a time at which an STC was collected. From this figure, it is clear that STC parameters cannot be meaningfully compared as a function of time post-injection because each STC was collected at a slightly different point during the recovery process. Consequently, to control for the fact that the amount of DPOAE change depended upon primary-tone levels and time post-injection, all changes in STCs parameters were analyzed as a function of DPOAE-amplitude change. To the extent that STC parameters are sensitive to reversible cochlear dysfunction, it would be expected that the largest DPOAE changes would be associated with the largest changes in STC characteristics. Similarly, significant diuretic effects on STCs would also be expected to result in overall pre/post-changes that were significantly different from zero, i.e., the ''no change'' condition.

The overall distribution of DPOAE amplitude changes ($n=67$) produced across the four post-drug measurement periods peaked in a range from 0 to -6 dB ($n=40$, 60%), which presumably encompassed either the time interval when the drug was beginning to take effect, or the recovery period. The majority of the remaining reductions in DPOAE levels ($n=22$, 33%) were more or less evenly distributed across a broad range of amplitude changes extending from -7 to -22 dB. These diminished DPOAEs likely represented the time interval when the diuretic effect was maximal. Except for a small number of DPOAE increases ($n=5$, 7%), the majority of the STC measurements ($n=62$, 93%) were performed when cochlear function was either moderately, or severely compromised by the reversible influences of the diuretic agents.

C. Effects of DPOAE decreases on STC parameters

The plots of Fig. 3 show a representative sample of the effects of the diuretics on DPOAE tuning at the GM fre-

quency of 2.8 kHz, at fairly low primary-tone levels ($L_1 \neq L_2 = 60/55$), which would be expected to be most sensitive to cochlear insult. These examples for rabbit R14 show DPOAE SRAs in the form of contour plots in 3-dB increments, or the STCs extracted from these plots for suppression criteria of 3–12 dB. The left half of the figure (A, C, E, G) shows tuning responses prior to diuretic administration, whereas the right portion (B, D, F, H) depicts data collected following a large drug-induced reduction in DPOAE level of 17.5 dB. The top (A–D) and bottom (E–H) halves of the figure compare the same data, before and after, one pass of the smoothing algorithm, respectively. In this example, the smoothing procedure was particularly helpful in extracting reliable STC parameters at a time when the DPOAE amplitude was dramatically reduced.

In the top half of Fig. 3[(A)–(D)], it is clear that, following the dramatic reduction in DPOAE amplitude, the overall amount of suppression that could be obtained was reduced. That is, only the 3- and 6-dB criterion amounts of suppression were calculable before the measurement system's noise floor was reached. However, for these remaining amounts of suppression, clearly, there is little change in the anticipated direction for overall shape of the SRA (A vs B), or in the general profile of the STCs extracted from these data (C vs D). This observation is most evident in the smoothed data shown below in panels (E)–(H). Here, for the smoothed 3-dB data depicted in Fig. 3(G) and (H), the STC-tip frequency changed from about 2.84 to 3.26 kHz, while threshold remained essentially unchanged from 48 to 47 dB SPL. In addition, the $Q_{10\,\mathrm{dB}}$ was reduced slightly from 1.89 to 1.79. In contrast, for the 6-dB suppression criterion, the $Q_{10\,\mathrm{dB}}$ was actually sharpened substantially as it changed from a pre-drug value of 1.05 to a post-drug score of 2.05.

In Fig. 4, similar pre/post-drug comparisons are made in rabbit R19 for DPOAE tuning for primary tones with a GM of 4 kHz ($L_1 \neq L_2 = 55/35$). Again, even with a drug-induced DPOAE reduction of 20.5 dB, for the 3-, 6-, and 9-dB amounts of suppression, little difference can be seen between the pre/post-STCs (C vs D) for the unsmoothed data. For the unsmoothed 3-dB criterion data shown in Fig. 4(C) and (D), $Q_{10\,\mathrm{dB}}$ increased from 1.76 to 2.23, which was also reflected in the corresponding smoothed data of Fig. 4(G) and (H) (i.e., $Q_{10\,\mathrm{dB}}$ of 1.42 vs 1.88). In this example, the unsmoothed STC-tip frequency decreased slightly (4.6 vs 3.9 kHz), whereas the threshold remained essentially the same (35 vs 35 dB SPL). Smoothing lowered the 3-dB contour below the 35 dB SPL suppressor level and, therefore, this STC was omitted. For the other suppression criteria, STC-tip thresholds increased approximately 5 dB, and $Q_{10\,\mathrm{dB}}$, decreased slightly for the unsmoothed data (C vs D), but increased somewhat for the smoothed data (G vs H).

In order to better observe general trends in the data, all the post-diuretic differences for STC-tip frequency, threshold, and $Q_{10\,\mathrm{dB}}$ were diagramed as scatterplots by comparing the difference scores with their corresponding DPOAE-amplitude changes. These data were statistically tested for the significance of the pre/post-changes, and correlations between the two variables were also computed. Figure 5 summarizes the influence of drug-induced reductions in DPOAE level on the $Q_{10\,\mathrm{dB}}$ measured for each of the four suppression criteria. From inspection of these plots, it is clear that there were no striking effects of DPOAE-amplitude changes on STC $Q_{10\,\mathrm{dB}}$. For the most part, it was equally likely that $Q_{10\,\mathrm{dB}}$ would either increase or decrease, regardless of the magnitude of the DPOAE-amplitude shift (i.e., the data points were equally distributed around the dashed horizontal line representing ''0'' change). These impressions were substantiated in all but two instances by statistical tests that revealed no consistent pre/post-differences (i.e., the ''ns'' noted at the bottom left of each plot), as well as by the lack of significant rank-order correlations (r_s) with DPOAE amplitude (indicated at the bottom right of each plot). The only consequential findings included an observed increase in $Q_{10\,\mathrm{dB}}$ for the 9-dB smoothed (open circles) data ($p < 0.01$), and the 12-dB unsmoothed (solid circles) data ($p < 0.05$). Overall, there is little indication in Fig. 5 that STC $Q_{10\,\mathrm{dB}}$ was systematically altered, at least, in the expected direction of a decrease in the sharpness of tuning, even when DPOAE amplitudes were significantly reduced by diuretic administration. If any trends existed at all, $Q_{10\,\mathrm{dB}}$ seemed to become slightly sharper, contrary to what would be anticipated from the comparable NTC literature. These comprehensive findings agree with the more restricted examples presented above in Figs. 3 and 4, which were obtained for two of the most sensitive primary-tone levels used to elicit DPOAEs in the present study.

The data of Fig. 6 illustrate findings for STC-tip frequencies that were obtained in a similar manner as the tuning results described in Fig. 5. Here, except for the unsmoothed (solid circles) 6-dB suppression data, a consistent and significant pre/post-decrease in tip frequency was noted. In addition, a significant, but weak, correlation with DPOAE-amplitude change was also uncovered for either smoothed or unsmoothed data, for the 6- and 9-dB conditions, thus, suggesting that the STC-tip frequency tended to decrease somewhat as DPOAE amplitude was reduced.

Measures of changes in STC-tip thresholds as a function of DPOAE-amplitude change are plotted in Fig. 7. These scatterplots revealed that, for all but the 12-dB criterion, overall significant pre/post-increases in the tip threshold occurred for one or both of the smoothing conditions. In addition, for all suppression criteria, except for the 3-dB unsmoothed data, elevations in STC-tip thresholds were significantly correlated with decreases in DPOAE amplitude. Overall, the tip thresholds showed maximum threshold elevations of only about 10 dB, even in the presence of DPOAE-amplitude decreases of 15–25 dB.

One interesting question that can be examined with respect to these data concerns how the suppression process was influenced by changes in the overall DPOAE amplitude following diuretic administration. More specifically, the substantial difference between the remaining amount of suppressible DPOAE amplitude, which was much smaller following drug administration than in the control condition, was taken into account by applying a normalization procedure. Figure 8 shows the consequences of this treatment of the data, which expressed the amount of suppression as a percent of the DPOAE amplitude remaining above the noise

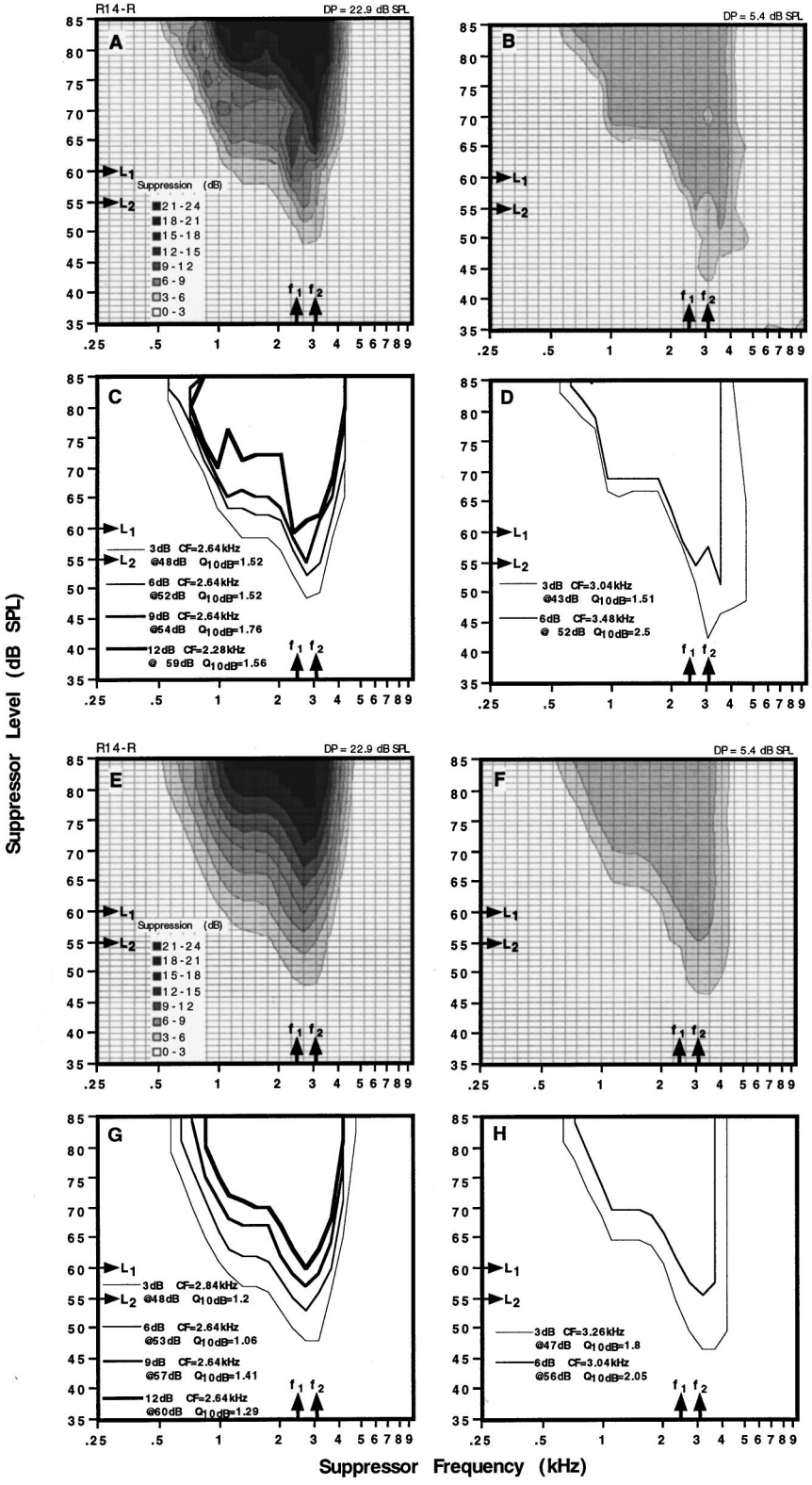

FIG. 3. Examples from the right ear of rabbit #14 (R14-R) of DPOAE tuning measured before (left column) and following (right column) drug injection with SRAs (A, B, E, F) and STCs (C, D, G, H), which were extracted from the SRAs, for the GM frequency of 2.828 kHz. Panels (A)–(D) (top) show unsmoothed raw data, and panels (E)–(H) (bottom) illustrate the effects of one smoothing pass on the data. This example clearly illustrates the minimal effects of a diuretic agent on the STCs for suppression criteria of 3 and 6 dB, at the time when DPOAE amplitude was reduced 17.5 dB from pre-drug control levels. For SRAs, the legends show the amount of suppression in 3-dB steps, in increasing amounts of shading, for criteria of 3, 6, 9, and 12 dB, and up to 24 dB. For STCs, the legends provide the STC-tip or center frequency (CF), threshold (@), and the computed $Q_{10\,\mathrm{dB}}$ tuning factor, as a function of the suppression criterion, in lines of increasing boldness that represent the various iso-suppression contours. Arrows on the ordinates and abscissas of each plot indicate the levels (L_1, L_2) and frequencies (f_1, f_2), respectively, of the primary tones. The unsuppressed level of the DPOAE is indicated at the top right of each SRA plot.

floor (i.e., the signal-to-noise ratio). For increased clarity, these data were based upon the smoothed SRAs for R19 that were described above in Fig. 4. The panels at the top left [Fig. 8(A), (B)] show pre- and post-drug SRA contours at the post-diuretic STC-tip frequency of 3.9 kHz, with suppression expressed in the usual 3-dB bands, along with a plot of the growth of suppression in dB at the right [Fig. 8(C)]. In the bottom panels [Fig. 8(D)–(F)], these same data are expressed in 10% bands as a percent of the DPOAE amplitude above the noise floor. It is clear from the post-drug data in Fig. 8(E) that this transformation essentially eliminated the effects of reducing DPOAE amplitude from 27 to 6.5 dB SPL, in terms of the effectiveness of suppression. In fact, from inspection of the data of Fig. 8(D) and (E), it would be difficult to determine which SRA represents the condition when cochlear function was abnormal. On the far right [Fig. 8(F)],

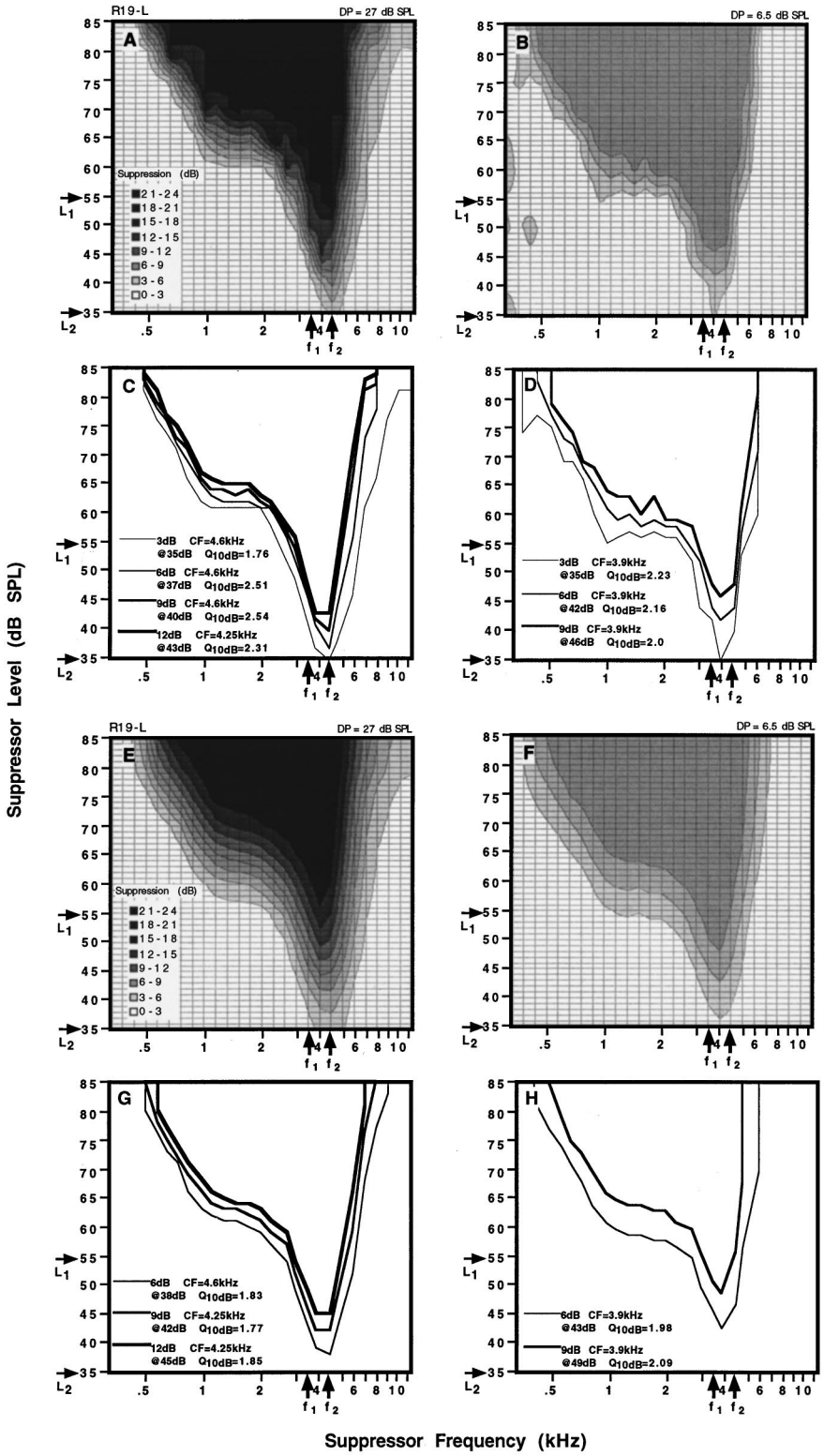

FIG. 4. Changes in SRAs and associated STCs for the left ear of rabbit #19 (R19-L) before (left column) and after (right column) diuretic administration for primary tones at the GM frequency of 4 kHz. In this example, a decrease in DPOAE amplitude of 20.5 dB was again accompanied by very small changes in the measured STC parameters. The specific details of the plots are identical to those described for Fig. 3. Note that the 3-dB STC is omitted for the smoothed data (G and H), because the 3-dB contour extended below the 35 dB SPL suppressor level.

the pre/post-growth of suppression functions taken at the STC-tip frequency are plotted in percent units. Post-drug dosing, it can be seen that the same suppressor level expressed in dB [Fig. 8(C)] was much less effective in reducing DPOAE level than it was during the pre-drug period. For example, for a suppressor level of 50 dB SPL, prior to drug administration, DPOAE amplitude was reduced approximately 19 dB, whereas after dosing, the same suppressor produced only an 11-dB reduction in DPOAE level. However, when the amount of suppression was expressed in Fig. 8(F) as a percentage of the post-drug DPOAE remaining above the noise floor, the two pre/post-growth of suppression functions became quite similar. It should be noted that these curves did not reach the 100% value, because it was necessary for the DPOAE remaining to be 2 s.d.'s above the average noise floor to be considered a real emission.

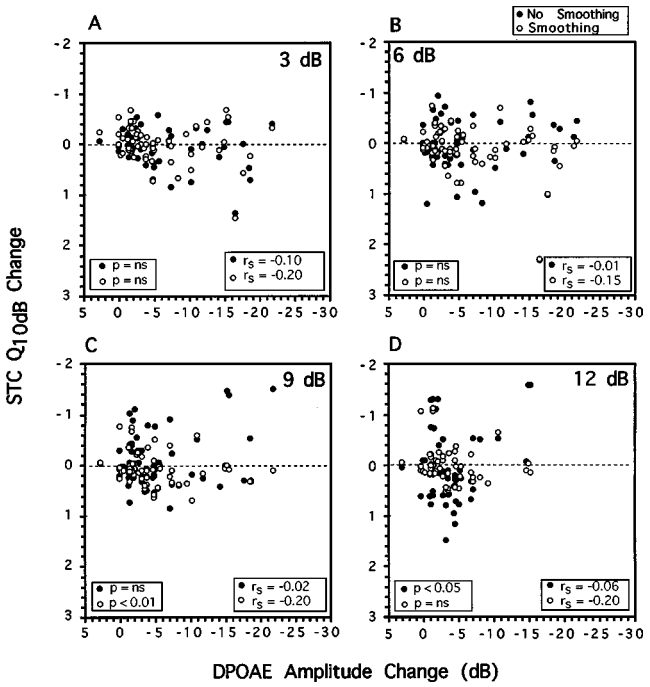

FIG. 5. Scatterplots showing all STC $Q_{10\,\mathrm{dB}}$ measurements paired with the corresponding post-drug diuretic change in DPOAE amplitude for each of the four suppression criteria. It is clear that, overall, $Q_{10\,\mathrm{dB}}$ values were equally distributed above and below the dashed zero line representing no drug-induced changes and, thus modifications to DPOAE tuning were poorly correlated with alterations in DPOAE amplitude. Raw unsmoothed data (solid circles) as compared to smoothed data (open circles) show the same trends. The ''*p*'' values at the lower left of the plots indicate the level of statistical significance for paired-sign tests that evaluated the amount of pre/post-changes in $Q_{10\,\mathrm{dB}}$. The Spearman-rank correlation coefficients (r_s) at the bottom right of each plot provide the correlations obtained between the $Q_{10\,\mathrm{dB}}$ factor and the corresponding decrement in DPOAE level. Asterisks in this figure, and in Figs. 6 and 7 below, indicate the degree of significance for the r_s metric (*=$p<0.05$, **=$p<0.01$, ***=$p<0.001$), and ''ns''=not significant.

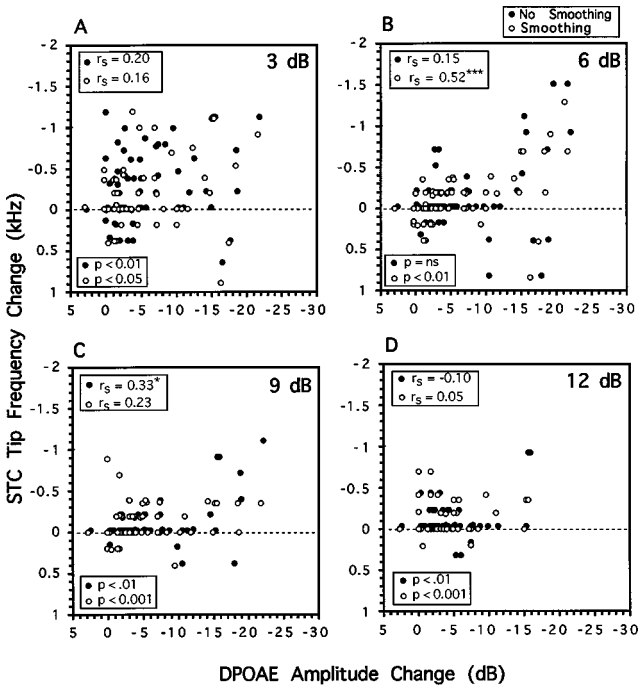

FIG. 6. Scatterplots of STC-tip frequency paired with the corresponding drug-induced changes in DPOAE level for each suppression criterion. Overall, there was consistent pre/post-decreases in the tip frequencies following diuretic administration. As indicated by the r_s factor values (top left), this decrease in the tip frequency was weakly correlated for the majority of the suppression criteria with changes in DPOAE level. The specific details of the plots are as described above for Fig. 5.

III. DISCUSSION

A. Comparison of STCs to NTCs

The present study examined three characteristics of STCs including tip threshold, best tip frequency, and $Q_{10\,\mathrm{dB}}$ following reversible ototoxicity induced by two common loop diuretics. A major finding was that $Q_{10\,\mathrm{dB}}$ was not significantly decreased as might be expected under these pathological conditions, even for DPOAE-amplitude reductions of about 20 dB. Surprisingly, the 9- and 12-dB criteria showed small but significant increases in $Q_{10\,\mathrm{dB}}$. Although the STC-tip frequency was found to decrease slightly during the ototoxicity episodes, the most significant finding was that the tip threshold showed a consistent elevation, although the maximum threshold shifts were on the order of about 10 dB. Overall, any slight differences noted between the various suppression criteria were not particularly remarkable.

The above results obtained for STCs can be contrasted to those observed in previous studies of NTCs for auditory-nerve fibers following similar cochlear insults. For example, Evans and Klinke (1982) showed that, following furosemide administration, cat NTCs exhibited dramatic elevations in tip thresholds (see their Fig. 3), which clearly would have been associated with substantial changes in $Q_{10\,\mathrm{dB}}$. Similarly, Sewell (1984) discovered that, following furosemide injections in cats, NTC-tip thresholds were elevated in some cases by as much as 60 dB, with almost all the reported threshold

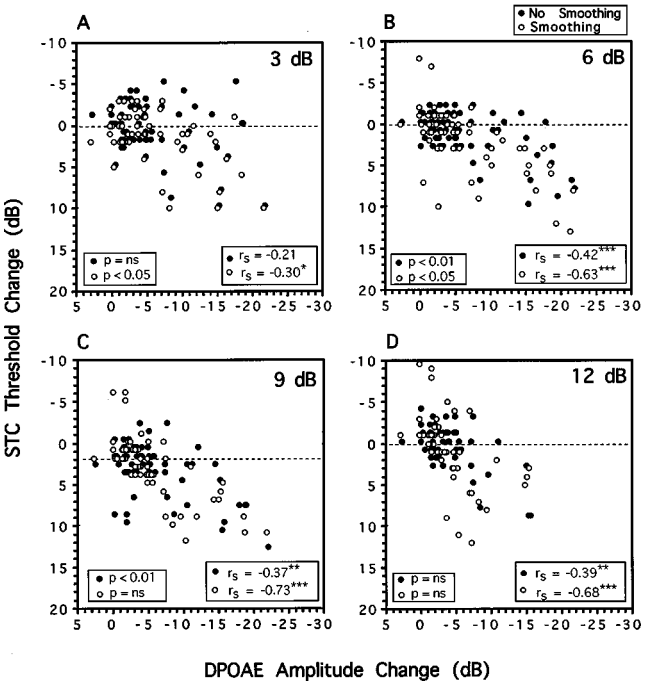

FIG. 7. Scatterplots of STC-tip threshold changes associated with the corresponding change in DPOAE level for each criterion suppression. These plots demonstrate a consistent increase in the tip threshold associated with a decrease in the drug-related DPOAE amplitude. The specific details of the plots are as described above for Fig. 5.

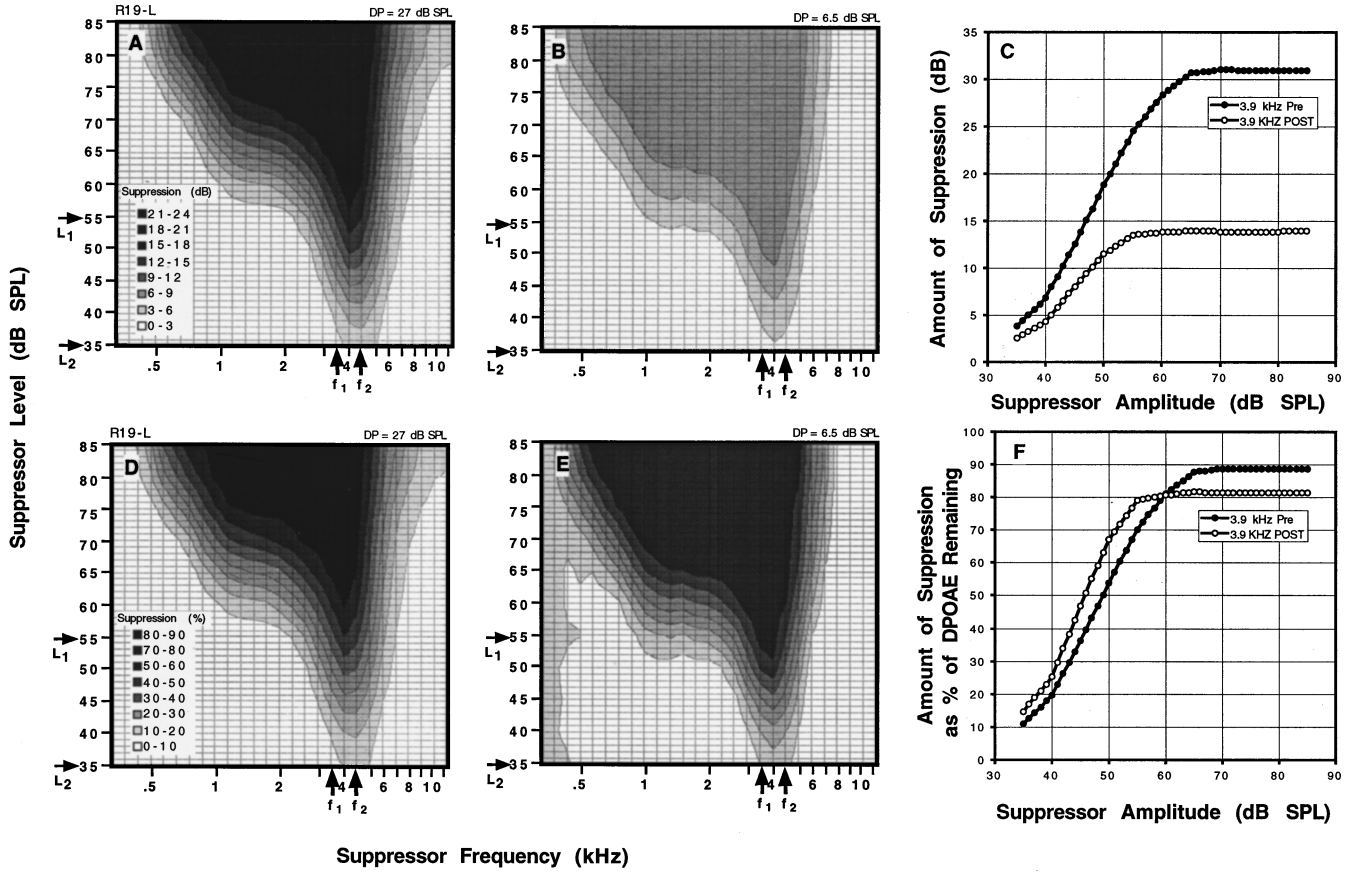

FIG. 8. Smoothed data for rabbit R19 from Fig. 4 in which the amount of suppression before (A) and after (B) diuretic administration, or the growth of suppression in dB (C) before (solid circles) and after (open circles) drug administration are plotted. In the panels below (D–F), DPOAE suppression is transformed into a percentage of the DPOAE remaining. Replotting the data in percentage units essentially eliminated the influence of the 20.5-dB decrease in DPOAE amplitude (D vs E, and F).

shifts being >10 dB. As might be expected, this elevation in tip threshold was accompanied by qualitative decreases in the sharpness of tuning. Although the changes in $Q_{10\,\mathrm{dB}}$ that were obtained for cat NTCs following furosemide administration were not quantitatively determined in either study, it is clear that NTC-tip elevations of 50–60 dB would result in substantial decreases in the sharpness of tuning as reflected by low $Q_{10\,\mathrm{dB}}$ values.

Several recent studies have either made the assumption based upon the similarity of the morphology and behavior of STCs to NTCs (Abdala *et al.*, 1996; Abdala and Sininger, 1996; Abdala and Luckoski, 1997), or inferred by comparison of STC characteristics to NTC features (Koppl and Manley, 1993; Frank and Kossl, 1995), that STCs provide a noninvasive means of measuring the frequency-selective characteristics of the auditory system. To our knowledge, there have been no direct comparisons between NTCs and STCs recorded from the same normal animal, or from the same preparation before and after such experimental manipulations as ototoxicity or noise overexposure, both of which are known to alter NTC measures. The present study shares one of these shortcomings in that the rabbit STCs were not directly compared to corresponding NTCs. However, the STCs were collected before and after conditions shown by a substantial body of literature to drastically influence NTC characteristics, including tip thresholds and qualitative estimates of the sharpness of tuning. On the whole, the present findings, indicate that STCs, in contrast to NTCs, are relatively insensitive to both changes in STC-tip thresholds and frequency selectivity as measured by $Q_{10\,\mathrm{dB}}$.

B. Effects of STCs parameters

One potential problem in comparing NTCs to STCs concerns determining the optimal parameters under which to obtain STCs, considering that STCs are elicited by bitonal stimuli, whereas NTCs are based on the application of single pure tones. For example, it is known that STCs in both gerbils and humans increase in sharpness as the f_2/f_1 ratio used to obtain these measures is decreased (Brown and Kemp, 1984). In the Frank and Kossl (1995) bat study noted above, the f_2/f_1 ratios were extremely small, averaging 1.033 (i.e., the primary tones were very near to one another in the frequency domain), which may explain the close resemblance of the STCs to single-tone elicited NTCs. Unlike NTCs, the tip thresholds from the pre-drug control STCs of the present study depended upon primary-tone levels. Also, although similar to NTCs, the $Q_{10\,\mathrm{dB}}$ depended upon the STC-test frequency. However, it was also influenced by the lowering of the f_2 level. These results in rabbits agree with the findings of recent human studies showing a dependence of STC-tip thresholds on primary-tone levels (Kummer *et al.*, 1995), and $Q_{10\,\mathrm{dB}}$ on test frequency (Abdala *et al.*, 1996). Other human studies of DPOAE tuning also demonstrated that low-

ering the level of f_2, i.e., L_2, significantly increased the sharpness of tuning that can be obtained with STCs (Lecusay *et al.*, 1996).

In an attempt to overcome, to some extent, the problems associated with the effects of primary-tone parameters on STC properties, the present study examined STCs elicited by a variety of primary-tone level combinations, at two test frequencies, using four distinct suppression criteria. However, none of these variables appeared to dramatically increase the STC's sensitivity to the reversible effects of common loop diuretics. In fact, as shown in Figs. 3 and 4, the very low-level and sensitive primary-tone combinations of 60/55 or 50/35 dB SPL, respectively, failed to reveal significant changes in either 3- or 6-dB STCs, even in the presence of a drug-induced 17–20 dB decrease in DPOAE amplitude.

Recently, it has been suggested that the precipitous drop in DPOAE level following furosemide administration corresponds closely to a decrease in the gain of the CA (Mills, 1997). This decrease in CA gain is presumably responsible for the changes in NTCs, as well as in alterations to the organ of Corti's mechanical tuning ability at the level of the basilar membrane. However, the present results suggest that the STC indices employed in the present study, unlike similar measures for NTCs, are not particularly sensitive to dramatic alterations in the CA, and, are not, as has been implied in the literature, capable of providing measures of frequency selectivity or threshold shifts analogous to the related responses of auditory-nerve fibers.

Based upon the effects of primary-tone parameters alone, there are several reasons to believe that STCs may not directly assess the frequency selectivity of the CA, which is apparently the case for NTCs. Both decreasing the primary-tone ratio, or lowering the level of L_2, significantly increases the $Q_{10\,\mathrm{dB}}$ of STCs. It seems reasonable to view such manipulations as reducing or restricting the region of the cochlear partition over which DPOAEs are generated. However, it seems less rational to assume that the apparent change in frequency selectivity ($Q_{10\,\mathrm{dB}}$) produced by these manipulations actually reflects a change in the underlying sharply tuned basilar-membrane amplification process. Considering that STCs represent a complicated response generated by a three-tone stimulus complex, i.e., the two primary plus the suppressor tones, the finding that they do not exactly mimic NTCs is not too surprising.

C. Potential factors contributing to STC shape

The major finding of the present study was that, although STCs exhibit the general features of neural-tuning curves, they do not appear to directly measure cochlear-frequency selectivity as evidenced by measures at the level of the basilar membrane or single auditory-nerve fibers. This interpretation is not too unexpected considering that STCs probably represent the suppression of DPOAE-generation processes that are elicited by the two-tone stimulus complex. It would, in fact, be surprising if this measure equaled or exceeded the frequency selectivity observed for single-tone tuning. One way to view the DPOAE-suppression process is to assume that the suppressor tone acts to drive the OHCs into saturation in a manner similar to that assumed in models of two-tone suppression for auditory-nerve fibers (e.g., Yates *et al.*, 1989; Geisler *et al.*, 1990). In this type of model, suppression describes the region of relative importance of the CA in generating a DPOAE. Thus the sensitive STC-tip portion can be viewed as indicating the frequency locus on the cochlear partition from which a DPOAE arises. This information can be contrasted to the DP-gram, which may or may not permit the site of DPOAE generation to be determined. For example, suppression paradigms have been used successfully to determine the region of generation along the cochlear partition of the $2f_1-f_2$ vs $2f_2-f_1$ DPOAE (Martin *et al.*, 1987, 1998), whereas the DP-gram of either of these emission types cannot provide such information.

Based upon this formulation, the shape of the STC is similar to that of the NTC, because this contour arises primarily from the properties of the stimulating tone for NTCs, or the suppressor tone for STCs, which interferes with the DPOAE-generation process (Harris *et al.*, 1993). Thus the steep apical slope of the traveling-wave envelope of the suppressor tone defines the high-frequency slope of the STC, whereas the tail of the suppressor-tone traveling-wave envelope defines the region of interference with the generation of the DPOAE on the low-frequency side of the STC.

These notions help explain the results of Fig. 8 in which the influence of diuretic administration was removed by expressing suppression as a percentage change of the remaining DPOAE. At first glance, these findings seem paradoxical in that it might have been anticipated that a DPOAE from a compromised cochlea would be more easily suppressed and, consequently, the DPOAE reduced to the noise floor for even very low-level suppressors. However, if diuretic administration can be viewed as decreasing the gain of the CA (Mills, 1997), these effects are then not limited to the primary tones, but also affect the amplitude and the effectiveness of the suppressor. Because the amount of suppression is approximately proportional to the relative amplitude of the suppressor, at least for two-tone suppression in auditory-nerve fibers (Yates *et al.*, 1989; Geisler *et al.*, 1990), expressing the amount of suppression as a percentage, to a large extent, compensates for the decreased gain of the CA and, thus restores the STCs to normal.

When pathological factors influence DPOAE generation, such as during the reversible episodes of ototoxicity performed here, as long as the DPOAE is generated, i.e., measurable, the amount of suppression may diminish, but the overall form of the STC will remain similar to that recorded during the control period. However, if the region of DPOAE generation is dramatically reduced, it could be predicted that the STC would become sharper, as observed at times in the present study. Exactly how diuretics, which appear to have a relatively uniform effect, would reduce the region of DPOAE generation is not clear. It may happen, for example, by changing the region of effective overlap between f_1 and f_2, similar to the sharpening effects of lowering L_2 on STC tuning as observed in Fig. 1. Overall, it appears that STCs do not provide very satisfactory measures of NTC parameters in that their basic characteristics, in the form of the tip frequency, threshold, and $Q_{10\,\mathrm{dB}}$, are relatively unchanged, even in cases of substantial DPOAE reduction. However, it

must be cautioned that the present results are based upon the effects of reversible ototoxic diuretics that probably affect the entire cochlea relatively uniformly. Thus, it is possible that following other cochlear insults, such as noise overstimulation, that typically produce more localized effects on OHC function, STCs may reveal tuning abnormalities that were not observed here.

ACKNOWLEDGMENTS

This research was supported in part by funds from the Public Health Service (DC00313, DC00613, DC03114), and funds from the University of Miami Chandler Chair. The computer programming of Michael E. Knapp M.D., the technical assistance of Geoffrey M. Waxman, the secretarial assistance of Mayte Ruiz, and the helpful suggestions of two anonymous reviewers are gratefully acknowledged.

Abdala, C., and Luckoski, C. (**1997**). ''Distortion product otoacoustic emission ($2f_1-f_2$) suppression tuning curves in human adults and premature neonates,'' Abstr. Assoc. Res. Otolaryngol. **20**, 24.

Abdala, C., and Sininger, Y. S. (**1996**). ''The development of cochlear frequency resolution in the human auditory system,'' Ear. Hear. **17**, 374–385.

Abdala, C., Sininger, Y. S., Ekelid, M., and Zeng, F-G. (**1996**). ''Distortion product otoacoustic emission suppression tuning curves in human adults and neonates,'' Hearing Res. **98**, 38–53.

Brown, A. M., and Kemp, D. T. (**1984**). ''Suppressibility of the $2f_1-f_2$ stimulated acoustic emissions in gerbil and man,'' Hearing Res. **13**, 29–37.

Brownell, W. E. (**1990**). ''Outer hair cell electromotility and otoacoustic emissions,'' Ear Hear. **11**, 82–92.

Dallos, P., Ryan, A., Harris, D., McGee, T., and Ozdamar, O. (**1977**). ''Cochlear frequency selectivity in the presence of hair cell damage,'' in *Psychophysics and Physiology of Hearing*, edited by E. F. Evans and J. P. Wilson (Academic, London), pp. 249–258.

Davis, H. (**1983**). ''An active process in cochlear mechanics,'' Hearing Res. **9**, 79–90.

Delgutte, B. (**1990**). ''Two tone rate suppression in auditory-nerve fibers: Dependence on suppressor frequency and level,'' Hearing Res. **49**, 225–246.

Evans, E. F., and Klinke, R. (**1982**). ''The effects of intracochlear and systemic furosemide on the properties of single cochlear nerve fibres in the cat,'' J. Physiol. (London) **331**, 409–428.

Frank, G., and Kossl, M. (**1995**). ''The shape of $2f_1-f_2$ suppression tuning curves reflects basilar membrane specialization in the mustached bat, *Pteronotus parnellii*,'' Hearing Res. **83**, 151–160.

Geisler, C. D., Yates, G. K., Patuzzi, R. B., and Johnstone, B. M. (**1990**). ''Saturation of outer hair cell receptor currents causes two-tone suppression,'' Hearing Res. **44**, 241–256.

Harris, F. P., Probst, R., and Xu, L. (**1992**). ''Suppression of the $2f_1-f_2$ otoacoustic emission in humans,'' Hearing Res. **64**, 133–141.

Harris, F. P., Probst, R., Plinkert, P., and Xu, L. (**1993**). ''Influence of interference tones on $2f_1-f_2$ acoustic distortion products,'' in *Proceedings of the International Symposium on Biophysics of Hair Cell Sensory Systems*, edited by H. Duifhuis, J. W. Horst, P. van Dijk, and S. M. van Netten (World Scientific, London), pp. 87–93.

Johnstone, B. M., Patuzzi, R., and Yates, G. K. (**1986**). ''Basilar membrane measurements and the traveling wave,'' Hearing Res. **22**, 147–153.

Kemp, D. T. (**1978**). ''Stimulated acoustic emissions from within the human auditory system,'' J. Acoust. Soc. Am. **64**, 1386–1391.

Kemp, D. T. (**1979**). ''Evidence of mechanical nonlinearity and frequency selective wave amplification in the cochlea,'' Arch. Otorhinolaryngol. **224**, 37–45.

Kemp, D. T., and Brown, A. M. (**1983**). ''A comparison of mechanical nonlinearities in the cochleae of man and gerbil from ear canal measurements'' in *Hearing—Physiological Bases and Psychophysics*, edited by R. Klinke and R. Hartmann (Springer-Verlag, Berlin), pp. 82–88.

Kemp, D. T., and Chum, R. (**1980**). ''Observations on the generator mechanism of stimulus frequency acoustic emissions, two-tone suppression,'' in *Psychophysical, Physiological and Behavioural Studies in Hearing*, edited by G. van den Brink and F. A. Bilsen (Delft U.P., Delft, The Netherlands), pp. 34–41.

Kiang, N. Y. S., Watanabe, T., Thomas, E. C., and Clark, L. F. (**1965**). *Discharge Patterns of Single Fibers in the Cat's Auditory Nerve* (MIT, Cambridge, MA), Res. Monogr. 35.

Koppl, C., and Manley, G. A. (**1993**). ''Distortion-product otoacoustic emissions in the bobtail lizard. II: Suppression tuning characteristics,'' J. Acoust. Soc. Am. **93**, 2834–2844.

Kummer, P., Janssen, T., and Arnold, W. (**1995**). ''Suppression tuning characteristics of the $2f_1-f_2$ distortion-product emissions in humans,'' J. Acoust. Soc. Am. **98**, 197–210.

Lecusay, R. A., Fletcher, C. A., Lonsbury-Martin, B. L., Stagner, B. B., Waxman, G. M., and Martin, G. K. (**1996**). ''Otoacoustic emissions in normal-hearing humans: Musicians vs non-musicians,'' Abstr. Assoc. Res. Otolaryngol. **19**, 25.

Martin, G. K., Probst, R., Scheinin, S. A., Coats, A. C., and Lonsbury-Martin, B. L. (**1987**). ''Acoustic distortion products in rabbits. II. Sites of origin revealed by suppression and pure-tone exposures,'' Hearing Res. **28**, 191–208.

Martin, G. K., Jassir, D., Stagner, B. B., Whitehead, M. L., and Lonsbury-Martin, B. L. (**1998**). ''Locus of generation for the $2f_1-f_2$ vs $2f_2-f_1$ distortion-product otoacoustic emissions in normal-hearing humans revealed by suppression tuning, onset latencies, and amplitude correlations,'' J. Acoust. Soc. Am. **103**, 1957–1971.

Mills, D. M. (**1997**). ''Interpretation of distortion product otoacoustic emission measurements I. Two stimulus tones,'' J. Acoust. Soc. Am. **102**, 413–429.

Mills, D. M., and Rubel, E. W. (**1994**). ''Variation of distortion product otoacoustic emissions with furosemide injection,'' Hearing Res. **77**, 183–199.

Mills, D. M., Norton, S. J., and Rubel, E. W. (**1993**). ''Vulnerability and adaptation of distortion product otoacoustic emissions to endocochlear potential variation,'' J. Acoust. Soc. Am. **94**, 2108–2122.

Rhode, W. S. (**1971**). ''Observations of the vibration of the basilar membrane in squirrel monkey using the Mossbauer technique,'' J. Acoust. Soc. Am. **49**, 1218–1231.

Robles, L., Ruggero, M. A., and Rich, N. C. (**1986**). ''Basilar membrane mechanics at the base of the chinchilla cochlea. I. Input–output functions, tuning curves, and response phases,'' J. Acoust. Soc. Am. **80**, 1364–1374.

Ruggero, M. A., and Rich, N. C. (**1991**). ''Furosemide alters organ of Corti mechanics: Evidence for feedback of outer hair cells upon the basilar membrane,'' J. Neurosci. **11**, 1057–1067.

Ryan, A., and Dallos, P. (**1975**). ''Effect of absence of cochlear outer hair cells on behavioral auditory threshold,'' Nature (London) **253**, 44–46.

Sellick, P. M., Patuzzi, R. B., and Johnstone, B. M. (**1982**). ''Measurement of basilar membrane motion in the guinea pig using the Mossbauer technique,'' J. Acoust. Soc. Am. **72**, 131–141.

Sewell, W. F. (**1984**). ''The effects of furosemide on the endocochlear potential and auditory-nerve fiber tuning curves in cats,'' Hearing Res. **14**, 305–314.

Siegel, S. (**1956**). *Nonparametric Statistics For the Behavioral Sciences* (McGraw-Hill, New York), pp. 68–75, 202–213.

Whitehead, M. L., Martin, G. K., and Lonsbury-Martin, B. L. (**1991**). ''Effects of the crossed acoustic reflex on distortion-product otoacoustic emissions in awake rabbits,'' Hearing Res. **51**, 55–72.

Whitehead, M. L., Lonsbury-Martin, B. L., and Martin, G. K. (**1992**). ''Evidence for two discrete sources of $2f_1-f_2$ distortion-product otoacoustic emission in rabbit: II. Differential physiological vulnerability,'' J. Acoust. Soc. Am. **92**, 2662–2682.

Whitehead, M. L., McCoy, M. J., Lonsbury-Martin, B. L., and Martin, G. K. (**1995**). ''Dependence of distortion-product otoacoustic emissions on primary levels in normal and impaired ears: I. Effects of decreasing L_2 below L_1,'' J. Acoust. Soc. Am. **97**, 2346–2358.

Yates, G. K., Geisler, C. D., Patuzzi, R. B., and Johnstone, B. M. (**1989**). ''Saturation of receptor currents accounts for two-tone suppression,'' in *Cochlear Mechanisms—Structure, Function and Models*, edited by J. P. Wilson and D. T. Kemp (Plenum, New York), pp. 177–188.

Temporal gap detection measured with multiple sinusoidal markers: Effects of marker number, frequency, and temporal position[a)]

C. Formby and L. P. Sherlock
Division of Otolaryngology-HNS, Department of Surgery, 16 South Eutaw Street, Suite 500, University of Maryland School of Medicine, Baltimore, Maryland 21201

S. Li
AT&T Bell Laboratories, 200 Laurel Avenue, Middletown, New Jersey 07748

(Received 6 June 1997; accepted for publication 30 April 1998)

Detection thresholds were measured for silent temporal gaps within combinations of two, three, or four sinusoidal markers (i.e., combinations of one or two pre-gap markers with one or two post-gap markers). The markers were selected from the frequency range 2000–3100 Hz. Sinusoidal frequencies F_1 and F_4 were used as pre-gap markers, while F_2 and F_3 served as post-gap markers. Temporal gap detection (TGD) thresholds were measured from sets of three normal-hearing adults who tracked 70.7% correct detection thresholds adaptively across blocks of 50 two-interval, two-alternative, forced-choice trials. For symmetric marker conditions, where pre- and post-gap markers were equivalent in frequency (e.g., $F_1=F_2$ or $F_1=F_2$ and $F_3=F_4$), TGD thresholds were <10 ms. However, for asymmetric marker frequency alignments across the silent gap, including stimulus configurations where only three markers were presented on a trial (e.g., $F_1=F_2$, $F_2 \neq F_3$, no F_4), performance was highly variable and was dramatically disrupted by the presentation of a second post-gap marker. The multiple-marker results reveal that TGD depends greatly on the number of markers presented, both in terms of the marker temporal position before and after the silent gap signal and the marker frequency alignment (symmetry) across the gap. These results, which cannot be predicted from models of the auditory periphery, may reflect perceptual mechanisms that are important in grouping and organizing auditory images. [S0001-4966(98)04108-3]

PACS numbers: 43.66.Ba, 43.66.Lj, 43.66.Mk [JWH]

INTRODUCTION

The ability to detect temporal gaps in time-varying acoustic signals is important for segmenting virtually all biologically significant complex sounds. The standard task for assessing auditory temporal acuity in the laboratory is one in which a listener reports the briefest detectable silent temporal gap between a pair of otherwise continuous, acoustically similar sounds. Temporal acuity as measured for these constrained conditions is typically reported to be a few milliseconds (see Green, 1971; Moore, 1989; Viemeister and Plack, 1993). Simple laboratory conditions, however, are inherently atypical of the real-world listening experience in which listeners are routinely expected and required to resolve brief silent temporal gaps within complex multiple-component species-specific signals such as human speech (Bullock, 1977; Harnad, 1987; Yost and Watson, 1987; Bregman, 1990). Relatively few reports have described temporal gap detection (TGD) measured directly within multiple-component stimuli (e.g., Green and Forrest, 1989; Grose and Hall, 1988; Grose, 1991; Grose and Hall; 1996; Hall *et al.*, 1996). More common are reports in which temporal gaps and spectral properties have been manipulated parametrically to evaluate a listener's ability to resolve or group the component parts of complex and tonal sequences (see Bregman, 1990). In this study, we compare TGD thresholds measured with one or two pre-gap sinusoidal markers presented in various combinations and frequency relations with one or two post-gap sinusoidal markers, which served to mark the onset and offset of the silent gap signal. The resulting TGD thresholds reveal a surprisingly large range of performance across our sample of stimulus conditions, and in some cases, sizable variation in performance across listeners for the same condition of stimulus parameters. These findings highlight some of the intricacies of auditory temporal processing and provide clues about the perceptual organization of complex sounds.

PRIMARY EXPERIMENTS

I. METHOD

A. Subjects

The subjects who participated in this study were adults between the ages of 21 and 52 years. Each subject had audiometrically normal-hearing sensitivity and was paid to participate in these experiments. Three listeners provided results for each stimulus configuration in this report. The same listeners did not participate in all experiments, but individual performance can be compared for a given participant across relevant conditions by noting the two-letter identification code in the respective panels. Each subject received several

[a)]Some of these results were presented at the 129th meeting of the Acoustical Society of America in Washington, DC [J. Acoust. Soc. Am. **97**, 3329(A) (1995)].

hours of practice on these or related gap detection tasks before beginning formal data collection. Some of the subjects had more experience than others and had previously participated in gap detection experiments with conventional two-marker stimuli. None of the listeners had experience with multiple-marker conditions prior to this study.

B. Apparatus and stimuli

The sinusoidal markers were generated with a microcomputer and played through a 16-bit digital-to-analog converter (DAC) (TDT, model DA1) (61-μs sampling period). The DAC output was low-pass filtered (TDT, model FT5-9) below 7500 Hz to prevent aliasing. The attenuation provided by the filter was about 60 dB at 1.15 times the filter cutoff frequency. Silent gaps were introduced instantaneously (i.e., without a rise/fall time) in the signal waveforms by placing zeros in the buffer. The sinusoids were attenuated (TDT, model PA4) and mixed (TDT, model SM3) with a noise masker. The broadband masker was a temporally continuous white noise (TDT, model WG1) that was low-pass filtered (TDT, model FT5-9) with a cutoff frequency of 7500 Hz. The sinusoids and noise masker were presented monaurally to each listener's right ear via an earphone (Telephonics, model TDH-39). Each listener was seated in a sound-attenuating double-wall room during the listening periods.

The stimulus configurations paired either one (F_1) or two (F_1 and F_4) pre-gap markers with either one (F_2) or two (F_2 and F_3) post-gap markers. The frequency of F_4 was always greater than or equal to F_1 and the frequency of F_3 was always greater than or equal to F_2. The markers were selected in various combinations from the frequencies 2000, 2040, 2100, 2200, 2980, and 3100 Hz, and presented with the broadband masker ($N_0 = 50$ dB) at an average signal-energy to noise power-density ratio of 39 dB. These markers were chosen to span a range of frequencies extending across three critical bands (Zwicker and Feldtkeller, 1967), which enabled us to evaluate within- and across-channel effects on TGD (see Formby *et al.*, 1996; Phillips *et al.*, 1997). The overall duration of each marker was varied randomly and independently over a range from 100 to 900 ms in each of the two observation intervals of a trial. The onset phases of the post-gap markers were randomly varied between 0° and 360° in both the signal and standard intervals. The purpose of presenting the masker and randomizing overall marker duration and onset phase was to minimize the consistent use of alternative cues that otherwise might confound TGD. These alternative cues have been discussed elsewhere (Formby and Forrest, 1991; Formby *et al.*, 1996). Whenever two pre-gap markers or two post-gap markers were presented in combination, the respective marker pairs were gated on and off simultaneously. The standard and signal markers were ramped with 10-ms raised cosine rise/fall times at the onset and offset of each observation interval.

C. Procedure

The general task and procedures used in this study are similar to those described by Formby *et al.* (1996) to measure TGD within a pair of tonal markers. The stimuli were presented in blocks of two-interval, two-alternative, forced-choice (2I, 2AFC) trials. Across each block of 50 trials, both the signal and the standard used the same combination of marker components for a given condition. The signal and standard were comparable in all respects except that the signal had the silent temporal gap inserted between the pre- and post-gap markers, whereas the standard was presented without a gap but with a random phase transition. The listener's task on each trial was to indicate by computer keyboard which observation interval contained the gap signal. Each observation interval was cued visually on the subject's computer monitor and the listener received visual feedback of the correct observation interval after a response on each trial. He or she tracked the duration of the silent gap adaptively according to a one up/two down rule to obtain a 70.7% correct detection threshold for the block of 50 trials. The tracking procedure used logarithmic steps. The first three reversals were implemented with the equivalent of a 3-dB step size in duration, which was followed by the equivalent of a 1-dB step in duration for subsequent reversals. The TGD threshold for a given block of trials was based on the geometric mean of the last even number of reversals for the small adaptive steps, and typically three estimates of threshold from three consistent blocks were averaged for each subject for each TGD condition.

The TGD thresholds were measured in stimulus configurations that paired one or two pre-gap sinusoidal markers with one or two post-gap sinusoidal markers. The markers were combined and presented in various pre- and post-gap temporal positions and frequency relations to mark the onset and offset of the silent gap signal. For a given stimulus configuration, the frequency parameters for one or more of the markers were constant across all blocks of trials. These ''fixed'' frequencies were either 2000, 3100 Hz, or the combination of these two frequencies. Within each stimulus configuration, ''variable'' pre-gap and/or post-gap marker components were selected for presentation from one of the six frequencies between 2000 and 3100 Hz. The variable marker (or markers) was (were) always the same constant frequency value across all 50 trials of a block. TGD thresholds were measured separately for each of the six conditions of ''variable'' marker frequency. Thus ''fixed''-frequency marker components remained constant values across all conditions within a given stimulus configuration, whereas ''variable''-frequency marker components were invariant in frequency within a given block of 50 trials but were changed from block to block within the stimulus configuration. To help clarify which components were ''fixed''- and which ones were ''variable''-frequency markers, an idealized acoustic schema (displayed in the form of a spectrogram) for each stimulus configuration will be shown along with the corresponding TGD thresholds in subsequent presentation of the results.

II. RESULTS AND DISCUSSION

A. Statistical analysis

The data were analyzed by marker configuration, e.g., two-marker, three-marker, and four-marker, using separate

mixed effects linear models for each configuration. Each model included a random effect for subject and additional random effects for each variable marker subject/frequency/stimulus configuration combination. These additional random effects were needed in order to fit the data well. The models were fit using restricted maximum-likelihood estimation performed by SAS proc Mixed (SAS Institution, Inc., 1989). In the context of these linear models, p values were computed to determine the degree to which the TGD thresholds were significantly different between each pair of variable marker frequencies for each stimulus configuration. The nominal p values for these tests are reported in Table I. The variable marker frequencies for each stimulus configuration in Table I are indicated beneath the respective stimulus configuration A–L in the first column. The respective pairings of the variable marker frequencies for each stimulus configuration are shown across the top of the table. To take into account the fact that multiple comparisons were performed, a given comparison can be considered statistically significant if the p value is 0.05/15 (15 comparisons per condition) using the Bonferoni method ($\alpha = 0.003$).

In the two-marker analysis, there is a significant main effect for variable marker frequency ($F = 19.62$; df $= 5,27$; $p = 0.0001$), but not for marker configuration ($F = 0.66$; df $= 1,27$; $p = 0.4237$). This indicates that variable marker frequency affected TGD thresholds in approximately the same manner between configurations A and B. By contrast, there is a significant interaction effect between variable marker frequency and marker configuration for the three-marker configurations ($F = 9.23$; df $= 24,45$; $p = 0.0001$) and four-marker configurations ($F = 5.01$; df $= 36,69$; $p = 0.0001$). This result suggests that the effect of variable marker frequency on TGD threshold differed depending upon the marker stimulus configuration condition. Again, the nominal p values for these pairwise comparisons as a function of variable marker frequency are reported in Table I. The differences are evident in the corresponding figures and will be discussed in detail in the following sections.

B. Two-marker configurations

In previous studies (Formby and Forrest, 1991; Formby *et al.*, 1996; Forrest and Formby, 1996; Heinz *et al.*, 1996), we evaluated in detail and now understand well most of the factors that influence the measurement of TGD thresholds for simple two-marker stimulus conditions. The TGD thresholds measured for the pair of two-marker stimulus configurations (A and B) shown in Fig. 1 are typical of our past results. These data serve as reference conditions with which to compare subsequent results measured in three- and four-marker stimulus configurations.

Shown by the filled symbols in the lower four panels of Fig. 1 are TGD thresholds that were measured for stimulus configuration A (for which the idealized acoustic schema is presented in the top left panel). The continuous line at 2000 Hz in the idealized acoustic schema represents the frequency of post-gap marker F_2, which was always fixed. TGD thresholds were measured as a function of the frequency of the pre-gap marker F_1. The value of F_1 was selected for a block of trials from one of the six variable frequencies shown by dashed lines. Within a block of trials, only one of these values of F_1 was presented as a pre-gap marker in combination with F_2 at 2000 Hz. The resulting individual TGD thresholds (and standard deviation bars) for each of three listeners are presented in separate panels, along with the group results which are shown in the lower right data panel. The TGD thresholds are displayed in milliseconds as a function of each of the six variable-frequency F_1 markers. For these results and all results presented in this report, each listener contributed three consistent estimates to each TGD threshold value.

The TGD thresholds for stimulus configuration A were typically less than 10 ms when the frequencies of the pre- and post-gap markers were similar. As a group, TGD thresholds increased dramatically as the marker frequency separation approached 1000 Hz. Performance across listeners varied widely for large marker frequency separations and, in some instances, TGD threshold differences were as much as 70 ms (compare results for listeners DD and EK). TGD thresholds tended to become asymptotic for marker frequency separations of about half an octave or more.

Essentially the same pattern of TGD thresholds was measured for another set of stimulus conditions that reflect the mirror-image of stimulus configuration A. This is stimulus configuration B, for which the acoustic schema is shown in Fig. 1 in the top right panel. The corresponding TGD results are denoted by the unfilled symbols in the lower four data panels. In stimulus configuration B, TGD thresholds were measured as a function of the frequency of post-gap marker F_2, with pre-gap marker F_1 fixed in frequency at 2000 Hz for all measurements. It is this stimulus configuration (B) that we have implemented in most of our previous attempts to measure TGD for silent gaps in pairs of sinusoidal markers (e.g., Formby and Forrest, 1991; Formby *et al.*, 1996). TGD thresholds have previously been measured and reported for conditions similar to stimulus configuration A (Collyer, 1974; Neff *et al.*, 1982; Grose and Hall, 1996). The similarity of these two sets of results indicates that for TGD threshold measurements with simple two-marker stimuli, it matters little whether the frequency of the pre-gap marker is varied relative to the fixed post-gap marker or the frequency of the post-gap marker is varied relative to the fixed frequency of the pre-gap marker. Accordingly, both the individual and group results shown in Fig. 1 corroborate our past findings for simple two-marker stimulus configurations. The general patterns reflect (1) increasing TGD thresholds as a function of increasing marker frequency separation, (2) asymptotic TGD thresholds at large marker frequency separations, and (3) increased absolute variability in individual performance across listeners for large marker frequency separations (see Formby and Forrest, 1991; Formby *et al.*, 1996). Other reports (e.g., Formby *et al.*, 1993; Grose and Hall, 1996; Phillips *et al.*, 1997) have described some of these same trends for TGD thresholds measured in simple pairs of narrow-band noise markers that differed in center frequency.

In the next set of measurements, we measured TGD thresholds with a third (fixed-frequency) marker added in combination with each pair of pre- and post-gap markers

TABLE I. Paired comparisons for each marker stimulus configuration for corresponding pairs of variable marker frequencies. Significant p values ($\alpha = 0.003$) are shown in bold type.

Marker stimulus config. (Variable marker)	Paired variable marker frequencies														
	2000 vs 2040 Hz	2000 vs 2100 Hz	2000 vs 2200 Hz	2000 vs 2980 Hz	2000 vs 3100 Hz	2040 vs 2100 Hz	2040 vs 2200 Hz	2040 vs 2980 Hz	2040 vs 3100 Hz	2100 vs 2200 Hz	2100 vs 2980 Hz	2100 vs 3100 Hz	2200 vs 2980 Hz	2200 vs 3100 Hz	2980 vs 3100 Hz
A (F_1)	$F=0.01$ $p=0.942$	$F=0.06$ $p=0.810$	$F=3.48$ $p=0.076$	$F=29.22$ **p=0.000**	$F=17.01$ **p=0.000**	$F=0.03$ $p=0.866$	$F=3.21$ $p=0.087$	$F=28.44$ **p=0.000**	$F=16.41$ **p=0.001**	$F=2.63$ $p=0.119$	$F=26.65$ **p=0.000**	$F=15.06$ **p=0.001**	$F=12.54$ **p=0.002**	$F=5.11$ $p=0.034$	$F=0.07$ $p=0.795$
B (F_2)	$F=0.02$ $p=0.895$	$F=0.04$ $p=0.835$	$F=1.52$ $p=0.231$	$F=13.92$ **p=0.001**	$F=15.95$ **p=0.001**	$F=0.12$ $p=0.734$	$F=1.86$ $p=0.186$	$F=14.94$ **p=0.001**	$F=17.03$ **p=0.000**	$F=1.04$ $p=0.318$	$F=12.40$ **p=0.002**	$F=14.31$ **p=0.001**	$F=6.25$ $p=0.020$	$F=7.63$ $p=0.011$	$F=0.07$ $p=0.795$
C (F_2)	$F=0.00$ $p=0.993$	$F=0.14$ $p=0.706$	$F=0.02$ $p=0.880$	$F=0.58$ $p=0.451$	$F=4.85$ $p=0.033$	$F=0.15$ $p=0.700$	$F=0.02$ $p=0.887$	$F=0.59$ $p=0.445$	$F=4.89$ $p=0.032$	$F=0.28$ $p=0.598$	$F=0.15$ $p=0.705$	$F=3.32$ $p=0.075$	$F=0.83$ $p=0.366$	$F=5.54$ $p=0.023$	$F=2.08$ $p=0.157$
D (F_3)	$F=4.93$ $p=0.032$	$F=1.34$ $p=0.234$	$F=7.47$ $p=0.009$	$F=3.86$ $p=0.056$	$F=6.11$ $p=0.017$	$F=1.13$ $p=0.293$	$F=0.26$ $p=0.610$	$F=0.07$ $p=0.799$	$F=0.06$ $p=0.802$	$F=2.49$ $p=0.122$	$F=0.65$ $p=0.423$	$F=1.73$ $p=0.195$	$F=0.59$ $p=0.446$	$F=0.07$ $p=0.795$	$F=0.26$ $p=0.614$
E (F_1)	$F=0.15$ $p=0.703$	$F=0.00$ $p=0.959$	$F=2.22$ $p=0.144$	$F=22.10$ **p=0.000**	$F=35.91$ **p=0.000**	$F=0.19$ $p=0.666$	$F=3.51$ $p=0.068$	$F=25.85$ **p=0.000**	$F=40.66$ **p=0.000**	$F=2.07$ $p=0.158$	$F=21.62$ **p=0.000**	$F=35.30$ **p=0.000**	$F=10.32$ **p=0.002**	$F=20.29$ **p=0.000**	$F=1.67$ $p=0.203$
F (F_4)	$F=0.18$ $p=0.670$	$F=0.17$ $p=0.681$	$F=0.04$ $p=0.852$	$F=0.09$ $p=0.771$	$F=0.05$ $p=0.819$	$F=0.00$ $p=0.987$	$F=0.06$ $p=0.810$	$F=0.02$ $p=0.891$	$F=0.04$ $p=0.843$	$F=0.05$ $p=0.822$	$F=0.01$ $p=0.904$	$F=0.03$ $p=0.856$	$F=0.01$ $p=0.917$	$F=0.00$ $p=0.966$	$F=0.00$ $p=0.951$
G (F_1 and F_2)	$F=0.04$ $p=0.844$	$F=0.01$ $p=0.917$	$F=0.02$ $p=0.894$	$F=0.03$ $p=0.863$	$F=0.00$ $p=0.978$	$F=0.01$ $p=0.925$	$F=0.00$ $p=0.949$	$F=0.00$ $p=0.980$	$F=0.05$ $p=0.822$	$F=0.00$ $p=0.976$	$F=0.00$ $p=0.946$	$F=0.02$ $p=0.895$	$F=0.00$ $p=0.969$	$F=0.03$ $p=0.872$	$F=0.04$ $p=0.842$
H (F_3 and F_4)	$F=0.11$ $p=0.736$	$F=0.01$ $p=0.909$	$F=0.10$ $p=0.755$	$F=0.08$ $p=0.773$	$F=0.10$ $p=0.756$	$F=0.21$ $p=0.652$	$F=0.42$ $p=0.517$	$F=0.40$ $p=0.532$	$F=0.42$ $p=0.518$	$F=0.04$ $p=0.843$	$F=0.03$ $p=0.861$	$F=0.04$ $p=0.844$	$F=0.00$ $p=0.982$	$F=0.00$ $p=0.999$	$F=0.00$ $p=0.983$
I (F_1)	$F=0.00$ $p=0.964$	$F=0.12$ $p=0.735$	$F=0.09$ $p=0.767$	$F=8.35$ $p=0.005$	$F=0.76$ $p=0.388$	$F=0.09$ $p=0.769$	$F=0.06$ $p=0.802$	$F=8.09$ $p=0.006$	$F=0.68$ $p=0.413$	$F=0.00$ $p=0.966$	$F=6.50$ $p=0.013$	$F=0.28$ $p=0.598$	$F=6.72$ $p=0.012$	$F=0.33$ $p=0.569$	$F=4.08$ $p=0.047$
J (F_2)	$F=0.01$ $p=0.936$	$F=0.00$ $p=0.966$	$F=0.15$ $p=0.702$	$F=23.33$ **p=0.000**	$F=0.70$ $p=0.407$	$F=0.02$ $p=0.902$	$F=0.22$ $p=0.644$	$F=24.12$ **p=0.000**	$F=0.84$ $p=0.364$	$F=0.12$ $p=0.734$	$F=22.92$ **p=0.000**	$F=0.63$ $p=0.432$	$F=19.77$ **p=0.000**	$F=0.20$ $p=0.654$	$F=15.97$ **p=0.000**
K (F_3)	$F=5.18$ $p=0.026$	$F=2.24$ $p=0.139$	$F=1.50$ $p=0.226$	$F=1.76$ $p=0.189$	$F=0.00$ $p=0.992$	$F=0.61$ $p=0.438$	$F=1.11$ $p=0.296$	$F=0.90$ $p=0.345$	$F=5.22$ $p=0.025$	$F=0.07$ $p=0.785$	$F=0.03$ $p=0.867$	$F=2.27$ $p=0.137$	$F=0.01$ $p=0.917$	$F=1.52$ $p=0.222$	$F=1.79$ $p=0.185$
L (F_4)	$F=7.41$ $p=0.008$	$F=2.19$ $p=0.144$	$F=0.33$ $p=0.565$	$F=4.92$ $p=0.030$	$F=5.02$ $p=0.028$	$F=1.54$ $p=0.218$	$F=4.59$ $p=0.036$	$F=24.40$ **p=0.000**	$F=24.63$ **p=0.000**	$F=0.81$ $p=0.371$	$F=13.67$ **p=0.000**	$F=13.84$ **p=0.000**	$F=7.82$ $p=0.007$	$F=7.95$ $p=0.006$	$F=0.00$ $p=0.982$

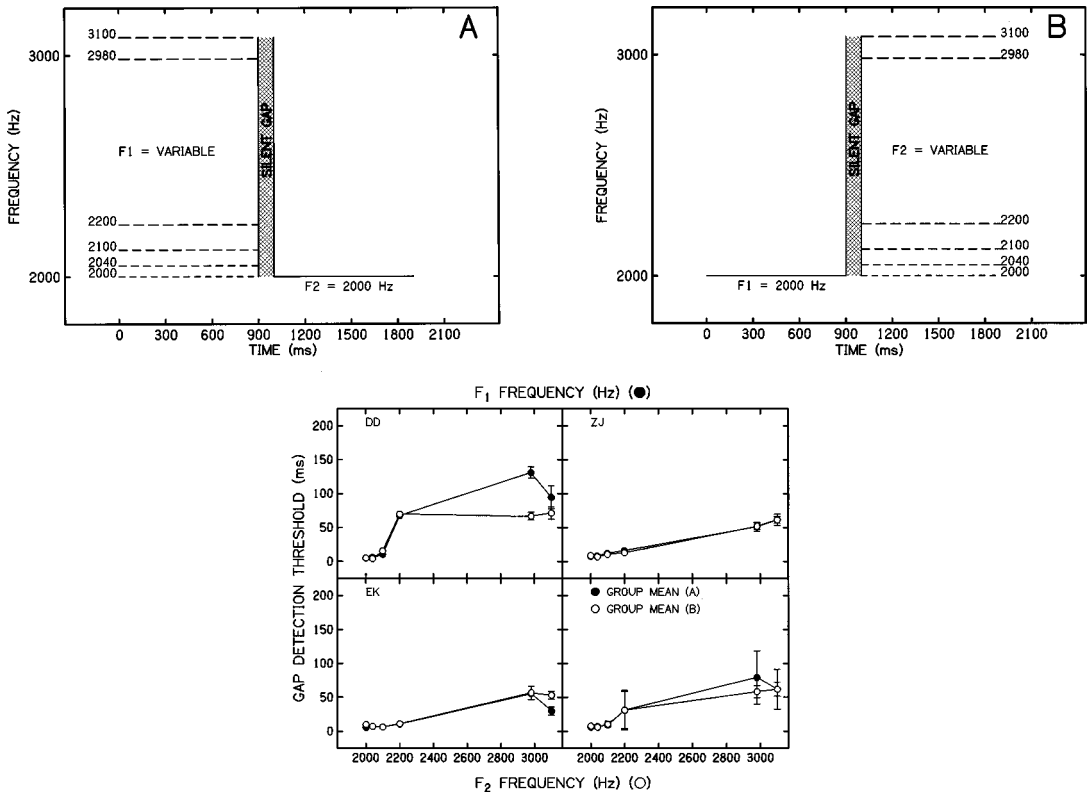

FIG. 1. Idealized acoustic schema for the two-marker stimulus configurations A and B are shown in the top left and right panels, respectively. In stimulus configuration A, TGD thresholds were measured for each variable-frequency pre-gap marker (graded dashed lines) paired separately with the fixed-frequency post-gap marker (solid line). The temporal positions (pre- and post-gap) of the fixed- and variable-frequency markers were simply reversed in stimulus configuration B. The individual and group mean TGD thresholds (and ± 1 standard deviation bars) are shown in the lower four data panels for stimulus configurations A (filled circles) and B (open circles) as a function of the frequency of the variable marker F_1 and F_2, respectively.

used in stimulus configurations A and B. This variation on the seemingly routine two-marker experiment yielded some surprising results.

C. Three-marker configurations

In this series of experiments, we measured TGD thresholds for four different stimulus configurations (C, D, E, and F) that used three markers in various pre- and post-gap temporal positions and fixed- and variable-frequency combinations. The idealized acoustic schema and corresponding TGD results for each of these stimulus configurations are shown in Fig. 2.

In stimulus configuration C, the frequencies of pre-gap marker F_1 and post-gap marker F_3 were fixed at 2000 and 3100 Hz, respectively. TGD thresholds were measured separately for each of the six variable post-gap marker frequencies F_2 (presented progressively in sequence from 2000 to 3100 Hz) in combination with the fixed-frequency markers. Prior to this experiment, we anticipated that because F_3 was appreciably remote in frequency from F_1 (i.e., outside the critical band that passed $F_1 = 2000$ Hz), the listeners would ignore F_3 and the results would resemble those for the two-marker stimuli shown in Fig. 1. Such was not the case, however, as TGD thresholds for all three listeners were uniformly elevated across all values of post-gap marker F_2. Most surprising is that, even for the condition where $F_1 = F_2$, the group TGD threshold in Fig. 2 was about 50 ms. This value was approximately the minimum value across the function. The largest TGD thresholds for the three listeners were obtained for the condition of maximum frequency separation between markers F_1 and F_2. The average threshold for this condition for the group of three listeners exceeded 80 ms, but was of similar magnitude to TGD thresholds shown in Fig. 1 for comparable frequency separations between markers F_1 and F_2 in the simple two-marker configurations.

We measured TGD thresholds for a second arrangement of the three markers that were combined as shown in the idealized acoustic schema for stimulus configuration D in Fig. 2. The frequencies of the pre- and post-gap markers F_1 and F_2 were fixed at 2000 Hz and TGD thresholds were measured as a function of post-gap marker frequency F_3 in declining sequence from 3100 to 2000 Hz. The resulting TGD thresholds revealed patterns of individual and group performance that were similar to those presented for stimulus configuration C. With one main exception, the TGD thresholds for stimulus configuration D were uniformly elevated by 30–50 ms across the range of F_3 frequencies. TGD thresholds for the marker condition F_3 presented at 2000 Hz were routinely less than 10 ms. For the latter condition, markers F_1, F_2, and F_3 were all presented at 2000 Hz and this condition was effectively a control condition (equivalent to $F_1 = F_2$).

In stimulus configurations C and D, we always presented the third marker, F_3, in the post-gap position along with markers F_1 and F_2. In the next pair of three-marker configu-

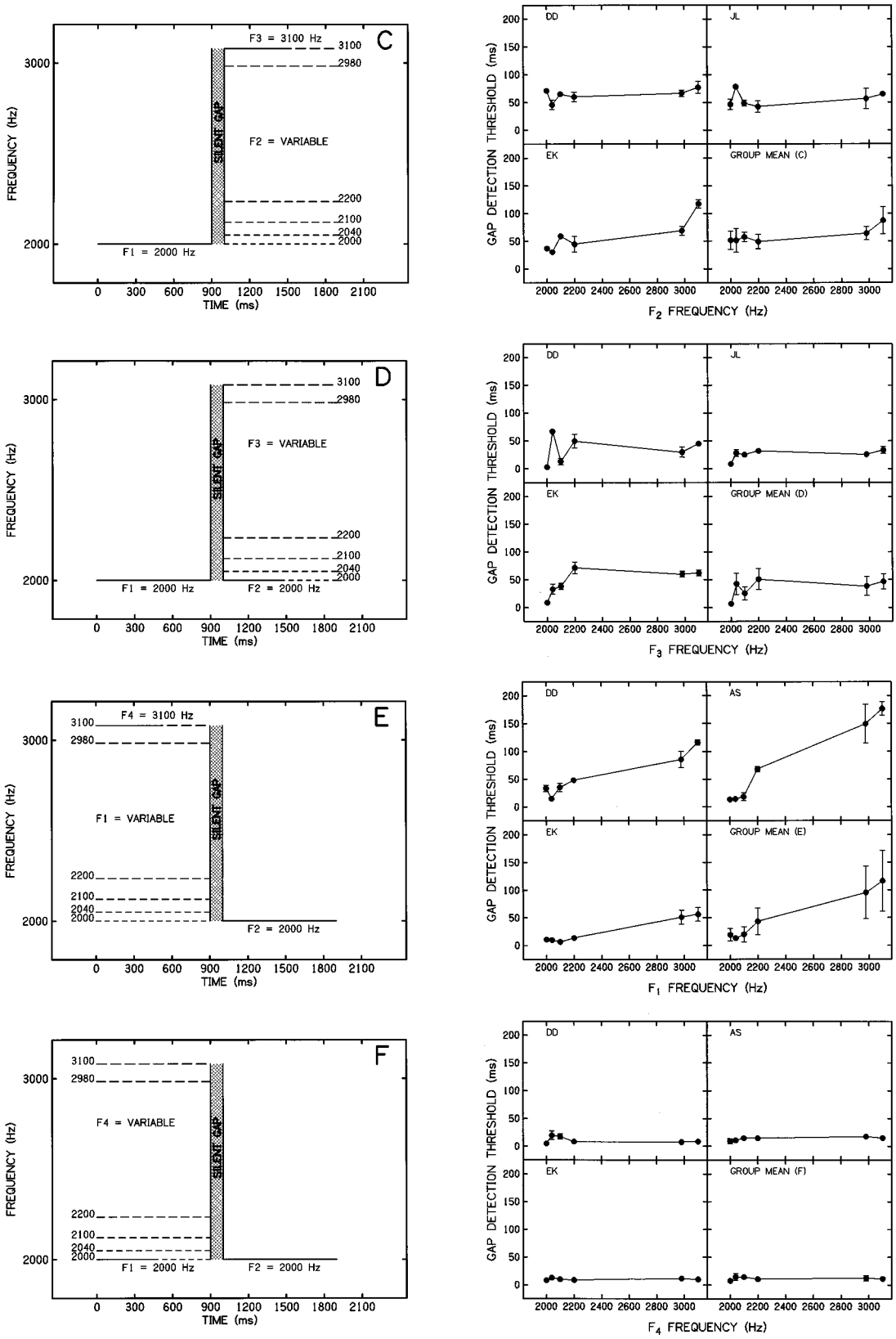

FIG. 2. An idealized acoustic schema for each three-marker stimulus configuration (C, D, E, and F) is shown in the left column. Fixed-frequency markers across all blocks of a given condition are indicated by solid lines at either 2000 and/or 3100 Hz and variable-frequency markers are shown by graded dashed lines. Fixed- and variable-frequency pre- and post-gap marker components are partially coded together whenever the frequencies were in common and presented simultaneously. The individual and group mean TGD thresholds are shown in the data panels in the right column alongside the corresponding configuration. The thresholds are shown as a function of the frequency of the variable pre- or post-gap marker identified for each data set. Error bars are ± 1 standard deviation.

rations (E and F), we replaced post-gap marker F_3 with pre-gap marker F_4. The resulting TGD thresholds are shown in Fig. 2 for stimulus configuration E, in which the frequencies of pre-gap marker F_4 and post-gap marker F_2 were fixed at 3100 and 2000 Hz, respectively. TGD thresholds were measured as a function of the frequency of pre-gap marker F_1, which was presented in progressive sequence from 2000 to 3100 Hz. On average, TGD thresholds increased systematically as the frequency of F_1 was increased. The resulting values ranged from 10–20 ms for F_1 frequencies presented around 2000 Hz to about 120 ms for F_1 presented at 3100 Hz. Pairwise comparisons reveal statistical significance (see Table I). TGD thresholds for variable frequency marker $F_1 = 2000$, 2040, 2100, and 2200 Hz were significantly lower than those for $F_1 = 2980$ and 3100 Hz.

The general trend of the TGD thresholds in Fig. 2 for stimulus configuration E is reminiscent of that measured in Fig. 1 for the two-marker conditions shown in stimulus configuration A. In fact, the two sets of results for listeners DD and EK, who contributed threshold values for both stimulus configurations A and E, are very similar in trend. This similarity is not too surprising because in stimulus configuration E we repeated the same basic stimulus paradigm that we used for stimulus configuration A. That is, in both stimulus configurations the frequency of pre-gap marker F_1 was varied with respect to post-gap marker F_2, which was fixed at 2000 Hz for all blocks of trials. The only difference in the two sets of experiments was that pre-gap marker F_4 was included as an additional fixed frequency component at 3100 Hz in stimulus configuration E. Because the results are so similar for stimulus configurations A and E, we may reasonably conclude that F_4 had little or no influence on our listeners' TGD performances in stimulus configuration E.

The role of pre-gap marker F_4 was also found to be insignificant in affecting TGD thresholds measured in stimulus configuration F. Stimulus configuration F and the corresponding results are shown in Fig. 2. In this set of experiments, we measured TGD thresholds as a function of the frequency of pre-gap marker F_4 (presented in declining sequence from 3100 to 2000 Hz) while holding the frequencies of pre- and post-gap markers F_1 and F_2 constant at 2000 Hz. On average, the resulting TGD thresholds were about 10 ms, and performance was statistically invariant with changes in F_4 frequency. The pattern of results suggests that our listeners largely ignored the presence of F_4. This is not surprising unless one considers the findings for stimulus configuration F in relation to the results for the mirror-image stimulus configuration D. For configuration D, the presentation of the variable frequency post-gap marker F_3 over the frequency range from 2000 to 3100 Hz dramatically elevated TGD thresholds measured between pre- and post-gap marker frequencies fixed at 2000 Hz. In contrast, the presentation of pre-gap marker F_4 in stimulus configuration F, over the same range of variable frequencies and in exactly the same fixed-frequency marker context, had no effect on TGD. Thus for the same three-marker set of variable and fixed marker frequencies, simply interchanging the temporal position of one marker before and after the silent gap significantly altered TGD performance. In the next set of experiments, we increased the complexity of the stimulus configuration by adding a fourth marker to the mix.

D. Four-marker configurations

In this series of experiments, we evaluated six different stimulus configurations (G, H, I, J, K, and L) that variously combined a pair of pre-gap markers with a pair of post-gap markers. The idealized acoustic schema and corresponding results for each marker stimulus configuration are shown in Fig. 3.

Two of the stimulus configurations, which are identified in panels G and H of Fig. 3, yielded virtually identical sets of TGD thresholds. The corresponding results are shown alongside the respective stimulus configuration. For stimulus configuration G, F_1 and F_2 were variable-frequency markers presented in progressive sequence from 2000 to 3100 Hz. The variable-marker frequencies were jointly varied together, and these were always the same value within a given block of trials. The markers F_4 and F_3 were both fixed at 3100 Hz. Stimulus configuration H simply reversed the roles of the marker pairs such that markers F_1 and F_2 were both fixed at 2000 Hz and markers F_4 and F_3 were the variable-frequency components, presented in declining sequence from 3100 to 2000 Hz in tandem. The individual and group TGD thresholds were routinely less than 10 ms across the range of variable-frequency markers between 2000 and 3100 Hz. The results for stimulus configurations G and H are remarkable when compared with the TGD thresholds shown in Fig. 2 for the three-marker configurations. The resulting TGD thresholds in Fig. 3 reflect sizable improvements in detection after adding a fourth marker to the mix to create a symmetric frequency alignment of the pre- and post-gap markers across the silent gap. For example, the TGD thresholds measured for configuration H are 15–40 ms lower (better) than the corresponding values shown earlier in Fig. 2 for configuration D. The two marker configurations are otherwise identical except for the added pre-gap marker in configuration H.

One way to explain the appreciable improvement in TGD performance in stimulus configurations G and H is to suppose that the listeners took advantage of synchronous gap information that was available from another pair of symmetric markers in a second independent channel. This additional information was unavailable to the listeners in the three-marker stimulus configurations C and D. Several studies have reported that TGD may improve dramatically when the gap information is carried by more than one pair of markers (Green and Forrest, 1989; Grose, 1991; Hall *et al.*, 1996). This explanation alone, however, appears inadequate to account for the sizable differences in TGD performance measured in our respective three- and four-marker stimulus configurations. Consider again stimulus configurations G and H, shown in Fig. 3, which were characterized by marker frequency symmetry between corresponding pairs of pre- and post-gap markers across the silent temporal gap. For the six variable-frequency marker conditions in each configuration, group TGD thresholds were routinely near the small control values for $F_1 = F_2$ measured in configurations A (6.17 ms) and B (7.96 ms). Indeed, pooled values averaged across the group mean thresholds for the six variable-frequency marker

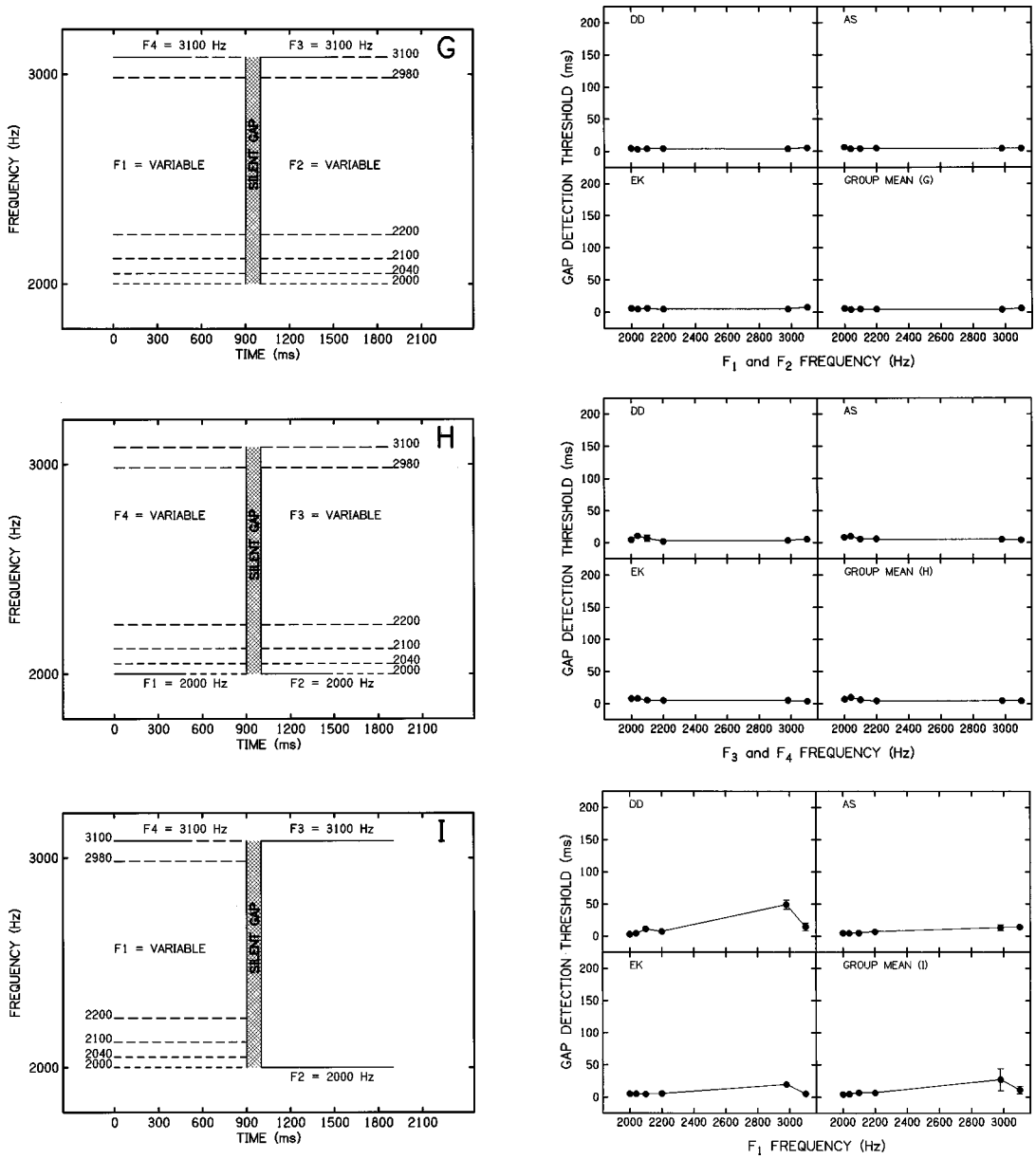

FIG. 3. An idealized acoustic schema for each four-marker stimulus configuration (G, H, I, J, K, and L) is shown in the left column. Fixed- (solid lines) and variable- (graded dashed lines) frequency markers are indicated for each configuration. The individual and group mean TGD thresholds are shown in the data panels in the right column alongside the corresponding configuration. The thresholds are presented as a function of the frequency of the variable pre- and/or post-gap markers identified for each data set. Error bars are ±1 standard deviation.

conditions in configurations G (5.01 ms) and H (6.06 ms) were only slightly better than the simple control thresholds. These results do not indicate an appreciable improvement in TGD performance for the gap information carried simultaneously by pairs of symmetric markers at two independent frequencies relative to performance measured for one pair of symmetric markers presented at a single common frequency. The slight advantage for our symmetric multiple-marker conditions is consistent, however, with studies that measured TGD thresholds for synchronous gaps in multiple ($\geqslant$5) symmetric pairs of sinusoids (Green and Forrest, 1989) and in multiple symmetric bands of noise (Grose, 1991; Hall *et al.*, 1996). These studies found consistently better performance for multiple symmetric pairs of markers than for gap detection measured in a single pair of symmetric markers. Our results also are consistent with the finding that TGD performance is essentially independent of the frequency separation between pairs of symmetric markers that carry synchronous gaps (Hall *et al.*, 1996). Thus the addition of the third asymmetric post-gap marker in stimulus configurations C and D appears to be much more detrimental to TGD performance than is the advantage gained by increasing gap information from an additional pair of symmetric markers in configurations G and H.

A pair of stimulus configurations (I and J) are also shown in Fig. 3 for which the frequency symmetry across the silent temporal gap was altered between one of the pairs of pre- and post-gap markers. In both configurations, the frequency symmetry was maintained for a second pair of pre- and post-gap markers. TGD thresholds in configuration I were measured as a function of the variable-frequency pre-gap marker F_1 presented progressively in sequence from

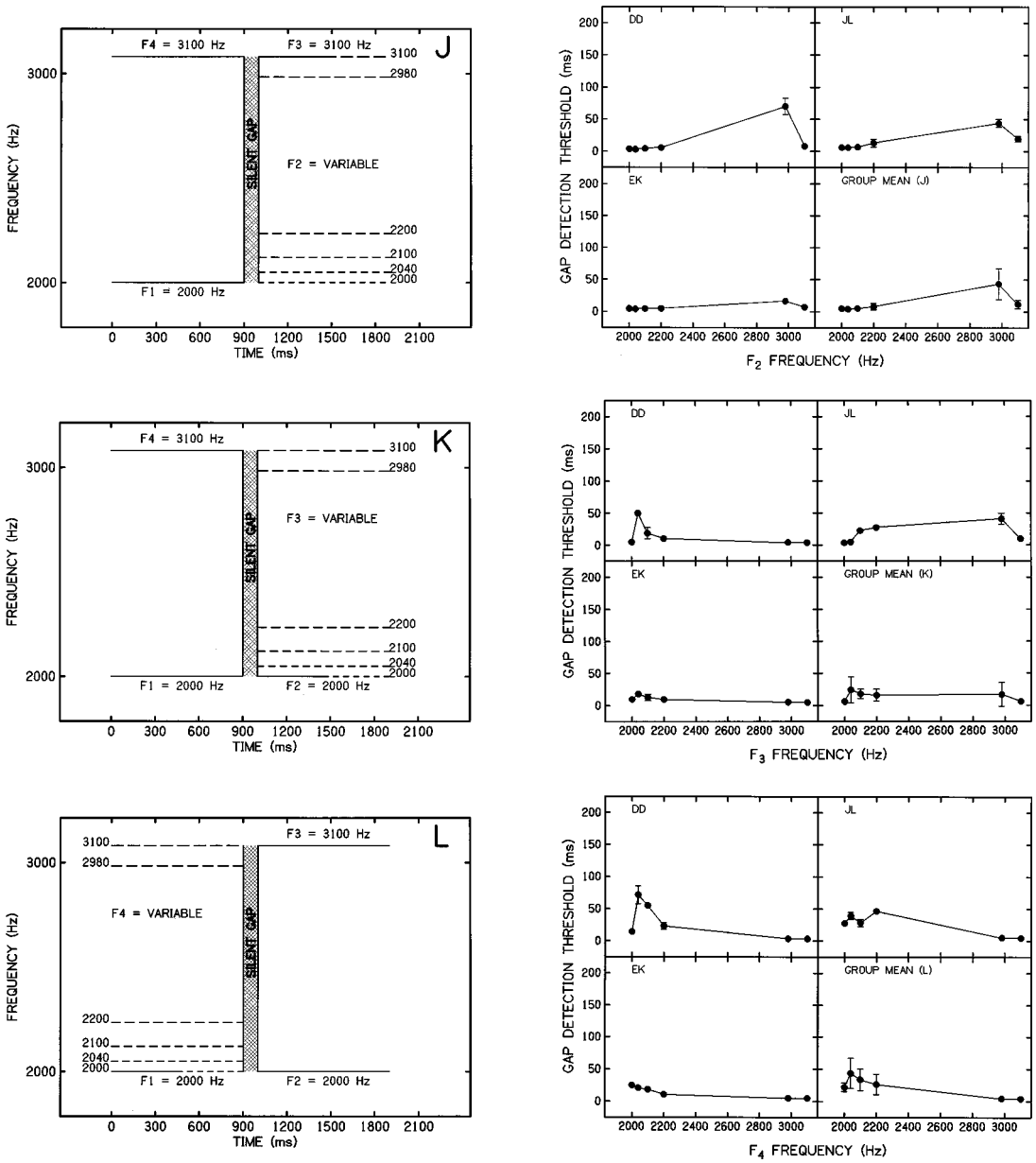

FIG. 3. (*Continued.*)

2000 to 3100 Hz. A post-gap marker F_2 was fixed at 2000 Hz, and pre-gap marker F_4 and post-gap marker F_3 were fixed at 3100 Hz. The marker arrangement and presentation sequence for configuration J were the same as those for configuration I except that pre-gap marker F_1 was fixed at 2000 Hz and post-gap marker F_2 was the variable-frequency parameter. The trend of the results was very similar for these two stimulus configurations. The corresponding TGD results are shown in Fig. 3 alongside the respective configuration as a function of the variable-frequency marker (F_1 in configuration I and F_2 in configuration J). For both configurations I and J, threshold values were usually at or below 10 ms across the set of variable-frequency marker conditions for all listeners. The chief exception is for the 2980-Hz F_2 marker in stimulus configuration J, for which paired comparisons on the group data confirmed statistical differences. The TGD thresholds were elevated by differing amounts depending upon the listener in configurations I and J. For example, for configuration J, the average TGD threshold for listener EK was only slightly elevated above control values to about 18 ms, whereas the TGD threshold for listener JL exceeded 40 ms. The corresponding threshold for listener DD was about 70 ms. The fact that these TGD thresholds were elevated for any condition of the F_2 marker in configuration J (and F_1 marker in configuration I) is noteworthy because the frequencies of the F_4 and F_3 markers were always constant at 3100 Hz, and yet the temporal information provided by these markers was not used optimally. If the listeners had used this information optimally, then we would have anticipated control threshold values below 10 ms across F_1 frequency in configuration I and across F_2 frequency in configuration J.

In another pair of four-marker stimulus configurations, which are identified as K and L in Fig. 3, we reversed the roles of the fixed- and variable-frequency markers previously presented in stimulus configurations I and J. Markers F_1 and F_2 were fixed at 2000 Hz in both configurations K and L,

whereas pre-gap marker F_4 in configuration K and post-gap marker F_3 in configuration L were fixed-frequency values that were set at 3100 Hz. The variable-frequency markers were F_3 and F_4 in configurations K and L, respectively. TGD thresholds were measured as a function of the variable-frequency marker in declining order from 3100 to 2000 Hz in each configuration.

The individual and group results in the four data panels for stimulus configurations K and L are shown alongside the respective configurations. Despite some statistical fluctuations in group TGD performance across the range of the variable marker frequencies for stimulus configuration L (see Table I), the overall patterns of results for stimulus configurations K and L were similar on average. The highest TGD thresholds for the group mean data in both configurations were measured for either F_3 or F_4 near $F_1=F_2=2000$ Hz. This trend reverses the patterns measured for stimulus configurations I and J, which yielded the highest thresholds for the variable frequencies F_1 or F_2 presented near $F_3=F_4=3100$ Hz. This pattern reversal may reflect the reversed order in which the variable-frequency markers were presented in stimulus configurations I and J versus K and L. For configurations I and J, the variable marker frequencies were presented progressively from 2000 to 3100 Hz, whereas the declining sequence was presented for the variable-frequency markers in configurations K and L. Alternatively, a plausible and perhaps more satisfying explanation may be offered for the opposing trends in TGD performance for stimulus configurations I and J versus K and L. This explanation assumes that beating between marker components, which are close in frequency, creates the perception of roughness and this beating percept somehow obscures the salience of the gap. This explanation would account well for the deterioration in performance in configurations I and J for variable-frequency markers F_1 and F_2 near fixed-frequency markers F_4 and F_3 at 3100 Hz and, conversely, for the decline in performance in configurations K and L for variable-frequency markers F_3 and F_4, respectively, presented at frequencies proximal to fixed-frequency markers F_1 and F_2 at 2000 Hz. It is noteworthy, however, that our listeners never reported nor described any beating percept for these conditions.

Whatever the explanation ultimately may be for these opposing trends, it is probably not a simple one because the individual results for each listener are idiosyncratic, with listener DD yielding qualitatively similar TGD functions for both stimulus configurations K and L. His results were characterized by elevated TGD thresholds for F_3 and F_4 presented at 2040 Hz. The respective thresholds were about 50 and 70 ms. Otherwise, his performance was relatively uniform across the range of variable marker frequencies, and thresholds were usually less than 20 ms. Among the three listeners, EK yielded the lowest thresholds and the most uniform performance across the set of variable marker frequencies. EK's thresholds were typically less than 20 ms, except in configuration L for the condition of F_4 presented at 2000 Hz, for which the TGD threshold was about 25 ms. The results for listener JL did not follow the same trends for stimulus configurations K and L. TGD thresholds in configuration K were near control values for the extreme ends of the F_3 variable frequency range, but exceeded 20–40 ms for F_3 presented at 2100, 2200, and 2980 Hz. JL's results for configuration L were about 5 ms for F_4 presented at 2980 and 3100 Hz, but the TGD thresholds were between about 25 and 50 ms for F_4 marker frequencies $\leqslant$2200 Hz.

It is remarkable that TGD thresholds were elevated for any of the variable-frequency marker conditions presented in stimulus configurations I, J, K, and L because one pair of pre- and post-gap marker frequencies was always fixed at either 2000 or 3100 Hz. Thus the pre- and post-gap marker alignment across the silent temporal gap was always symmetric in frequency for one pair of markers on every trial. *A priori*, we expected this information alone would be adequate for the listeners to achieve small control TGD threshold values. This expectation was not met.

SECONDARY EXPERIMENT

I. MOTIVATION AND RATIONALE

There were a number of surprising findings in our primary experiments. Among the most surprising finding was the detrimental influence on TGD of adding a second, remote-frequency, post-gap marker in the three-marker stimulus configurations. For example, consider again configuration C shown in Fig. 2. This was the stimulus configuration in which the frequencies of pre-gap marker F_1 and post-gap marker F_3 were fixed at 2000 and 3100 Hz, respectively, and TGD thresholds were measured as a function of F_2, the variable-frequency post-gap marker. We found for all values of F_2, including F_2 presented at 2000 Hz, that the group average TGD thresholds exceeded 50 ms. This latter marker condition was more than 1000 Hz below F_3 and was the same frequency as marker F_1. Thus the disruptive effect of F_3 on TGD was robust over a broad range of frequencies. The deleterious influence of F_3 (a second, fixed-frequency post-gap marker) is indeed a remarkable finding from the standpoint of auditory filter theory. Consider that TGD thresholds from Fig. 1, when transformed in terms of a frequency domain (roex filter) representation of the results, reveal $F_3=3100$ Hz to be well outside of the nominal auditory filter bandwidth expected for a listener attending to the silent gap between markers F_1 and F_2 at 2000 Hz. Roex functions fitted to these two sets of TGD thresholds (for configurations A and B), using transformation methods described by Formby and Forrest (1991), are shown in Fig. 4 for the upper side of the auditory filter. As expected, the fitted roex functions shown in Fig. 4 are very similar for the two sets of TGD thresholds irrespective of whether the pre-gap marker (unfilled circles) or post-gap marker (filled circles) was fixed at 2000 Hz (or was variable in frequency). We have shown that the patterns of these roex functions mirror some of the attenuation properties of the peripheral auditory filter (Formby *et al.*, 1996). Specifically, TGD thresholds are typically less than 10 ms when the frequencies of the pre- and post-gap markers are similar and fall within the 3-dB passband of an auditory filter containing both markers. TGD thresholds tend to increase systematically as the frequency separation between the pair of markers is increased further, and to a first approximation, the attenuation pattern of the

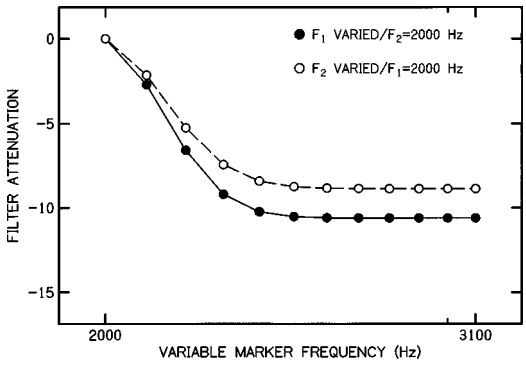

FIG. 4. Roex filter functions fitted to the two sets of normalized TGD thresholds from Fig. 1. Functions represented by filled and open circles correspond to fitted conditions for the normalized thresholds from stimulus configurations A and B, respectively.

normalized TGD thresholds mirrors a compressed form of the auditory filter shape for marker frequency separations within about half an octave. The TGD thresholds tend to become asymptotic for greater marker frequency separations. This latter result is reflected in Fig. 4 by the flat skirts of the fitted roex functions.

On the basis of the roex functions shown in Fig. 4 and, more generally, our understanding of classical auditory filter and critical band theory, we had no reason to expect any effect of marker F_3 on TGD when markers F_1 and F_2 were both presented at 2000 Hz in configuration C. The anticipated absence of an effect for marker F_3 on TGD was also confirmed in simulation experiments. Heinz *et al.* (1996) recently demonstrated that TGD can be simulated qualitatively well, for configurations similar to A and B (shown in Fig. 1), with a multichannel model of the auditory periphery. We would expect this same model to be insensitive to remote frequency effects of post-gap marker F_3 on TGD measured between markers F_1 and F_2 presented at 2000 Hz. Heinz (1997, unpublished findings) has confirmed this prediction for the model. He reports that small TGD thresholds (less than 10 ms) are simulated by the model for simple $F_1=F_2$ marker conditions presented with or without the remote-frequency F_3 marker.

In light of the unexpected influence of marker F_3 on TGD in our configuration C, we performed an additional experiment to try to understand better the influence of the remote-frequency F_3 marker on TGD. In this new experiment, we investigated two issues: (1) the time course or temporal pesistence of marker F_3 in disrupting TGD, and (2) the extent to which the disruptive influence of marker F_3 was dependent on synchronous presentation with post-gap marker F_2 (i.e., whether the disruptive effect on TGD performance was dependent on the temporal onset/offset of post-gap marker F_3 being coincident with post-gap marker F_2).

II. METHOD

The dependent variable in this new experiment was the TGD threshold, which three adult listeners estimated by tracking adaptively the onset delay of marker F_2 relative to the temporal offset of marker F_1 in blocks of 50 2I, 2AFC trials. The three listeners in this experiment were the same ones who contributed the TGD threshold estimates for our original stimulus configuration C in Fig. 2. In this new experiment, the F_1 and F_2 markers were both fixed in frequency and presented at 2000 Hz across each block of trials. The independent variable was the fixed delay of the temporal onset of post-gap marker F_3 relative to the temporal offset of pre-gap marker F_1. The frequency of the F_3 marker was fixed for all conditions at 3100 Hz. The F_3 delay values included 20, 40, 60, 80, 100, and 200 ms. These markers and delay values are shown in Fig. 5 in an idealized acoustic schema (stimulus configuration M) for the gap signal condition. The temporal offset of F_3 was independent of the temporal offset of post-gap marker F_2. Thus the listeners tracked the onset delay of F_2 adaptively with respect to F_1 offset to estimate the TGD threshold for each F_3 onset delay value, which we fixed across each block of trials. This experiment contrasts with our earlier experiment using stimulus configuration C in that those TGD thresholds were measured with simultaneous delays of the temporal onsets of post-gap markers F_2 and F_3 with respect to the offset of pre-gap marker F_1. The two post-gap markers in the original experiments also had coincident offsets. Thus in the earlier measurements, the onsets and offsets were changed simultaneously for F_2 and F_3 as the TGD threshold was tracked adaptively across trials. In the new experiment, the gating on and off of post-gap markers F_2 and F_3 were independent in each interval of a trial and their overall durations were also independent. The adaptive protocol, general methods, and stimuli used in the new experiment were otherwise similar, including random variation of all marker durations between 100 and 900 ms.

III. RESULTS AND DISCUSSION

The individual and group TGD thresholds (and standard deviations) for the three listeners are shown by filled circles in Fig. 5 as a function of the temporal onset delay of post-gap marker F_3 (relative to the offset of pre-gap marker F_1). The TGD thresholds for each of the three listeners from Fig. 2 for stimulus configuration C, for markers F_1 and F_2 presented at 2000 Hz in combination with F_3 presented at 3100 Hz, are shown again by the unfilled circles.

The performance trends were similar for listeners DD and JL. Their TGD thresholds were at maximum values (50–70 ms) for F_3 onset delays in the range of 20–40 ms. Threshold values for an F_3 onset delay of 60 ms were only slightly better (about 40 ms). TGD thresholds for both listeners were very close to control values (typically at or below 10 ms) for F_3 onset delays $\geqslant$80 ms. The results for listener EK were never asymptotic and were characterized by a systematic improvement in TGD as a function of increasing F_3 onset delay. His TGD thresholds varied from about 50 to 21 ms over the range of F_3 onset delays between 20 and 200 ms. Thus for listener EK, the effect of the remote post-gap marker F_3 on TGD persisted for onset delays throughout the 200-ms delay range. In contrast, the presentation of the same F_3 marker had no influence on TGD for listeners DD and JL for F_3 onset delays $\geqslant$80 ms.

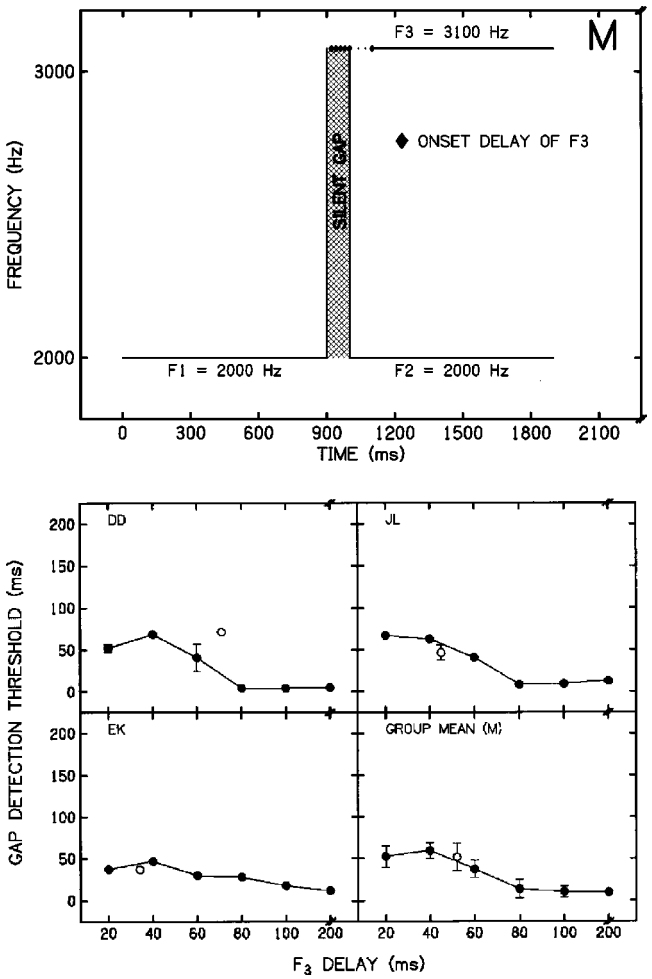

FIG. 5. The idealized acoustic schema for stimulus configuration M is shown in the top panel. Onset delay values for post-gap marker F_3 are depicted by diamond symbols. Pre-gap marker F_1 and post-gap marker F_2 were both presented at 2000 Hz and post-gap marker F_3 was presented at 3100 Hz. Individual and group mean TGD thresholds (± 1 standard deviation) are shown by filled circles in the lower set of data panels. Thresholds are shown as a function of the fixed onset delay of post-gap marker F_3 (with respect to the temporal offset of F_1). TGD thresholds shown by open circles are the original values for each listener for the corresponding condition of markers presented in Fig. 2 for stimulus configuration C.

The original TGD threshold value shown by the unfilled circle for each listener is generally consistent with the new TGD threshold results over the range of F_3 onset delays <80 ms. These original thresholds for configuration C from Fig. 2 for listeners DD, JL, and EK were 71, 46, and 39 ms, respectively. These values, which also are the corresponding average values of F_3 onset delay measured at TGD threshold, agree well with the 30–70-ms threshold range measured for the same listeners in this experiment for F_3 onset delays <80 ms.

We may conclude from the results of this experiment that the influence of marker F_3 persists over a sizable range of onset delays relative to the offset of marker F_1. This temporal effect differs across listeners, but on average, most of the effect subsides for F_3 onset delays >80 ms. Moreover, the temporal effect appears to be largely independent of whether the onset or offset of the F_3 marker coincides with the onset or offset of F_2. Thus the detrimental effect of post-gap marker F_3 on TGD is generally robust in time as well as frequency.

GENERAL DISCUSSION

I. MARKER TEMPORAL POSITION AND TGD INTERFERENCE: PRE- VERSUS POST-GAP EFFECTS

Two trends in these results deserve special consideration. First, our listeners' performances were vastly different depending on the temporal position (i.e., pre- or post-gap) of the third marker (either F_3 or F_4) in the three-marker configurations. The influence of marker temporal position on TGD can be best appreciated by considering once again three-marker configuration C and the corresponding results shown in Fig. 2. For this condition, TGD thresholds were measured as a function of post-gap marker F_2 frequency. Pre-gap marker F_1 was fixed at 2000 Hz and post-gap marker F_3 was fixed at 3100 Hz. This situation was effectively a repeat of two-marker configuration B (shown in Fig. 1), but with post-gap marker F_3 added into the mix in stimulus configuration C. We saw earlier for the two-marker stimulus configuration B that the TGD thresholds increased systematically as the frequency separation between markers F_1 and F_2 was increased, and for small marker frequency separations, the TGD thresholds were less than 10 ms. However, with marker F_3 added in the post-gap position in configuration C, TGD thresholds were elevated to at least 50 ms for F_2 frequency values identical or similar to marker F_1. These results are in marked contrast to those measured for configuration E in Fig. 2, which is the mirror-image condition for configuration C. We substituted pre-gap marker F_4 for post-gap marker F_3 in configuration E and measured the TGD thresholds as a function of pre-gap marker F_1 frequency for marker F_2 fixed at 2000 Hz. The resulting TGD thresholds for three-marker configuration E yielded the same general pattern that we measured in Fig. 1 for two-marker configuration A (and B), with thresholds increasing systematically as the frequency separation between markers F_1 and F_2 was increased. The results for configuration E were predictable because we expected the presentation of a remote pre-gap marker to have little effect on the general pattern of TGD measured for a set of conditions that were otherwise comparable to our two-marker configuration A. In contrast, we had no reason to anticipate that the presentation of the remote post-gap marker in stimulus configuration C would dramatically disrupt TGD under virtually the same set of two-marker conditions (as configurations A and B). Thus the temporal (pre- or post-gap) position of a remote-frequency third marker, when presented in the post-gap position, was detrimental to the TGD performance that we expected for a simple two-marker stimulus configuration. However, a remote-frequency third marker, presented in the pre-gap position under similar conditions, was effectively ignored by our listeners.

Results for the mirror-image three-marker configurations D and F shown in Fig. 2 led to the same conclusion. In both of these three-marker configurations, markers F_1 and F_2 were fixed at 2000 Hz. TGD was measured as a function of marker F_3 frequency in configuration D and as a function of

marker F_4 frequency in configuration F. The TGD thresholds measured for configuration D revealed a significant influence of post-gap marker F_3 on TGD, but the thresholds measured for configuration F reflected little or no influence of pre-gap marker F_4 on performance. Indeed, the latter results were near the small (<10 ms) control TGD thresholds measured for $F_1=F_2$.

A comparison of the TGD data from the three-marker stimulus configurations C and D versus E and F (in Fig. 2) appears to eliminate the idea of a ''cueing'' process as a possible explanation for the performance patterns. Consider first the stimulus configurations C and D, which included the condition where $F_1=2000$ Hz, $F_2=2000$ Hz, and $F_3=3100$ Hz. One might have expected the listeners to do well for this condition because the temporal gap occurs in its entirety within a single-frequency ''channel'' at $F_1=F_2=2000$ Hz, and the single-component F_1 could potentially have served to cue the listener to monitor that channel. The resulting TGD thresholds, however, were elevated well above the control thresholds measured for the simple two-marker condition $F_1=F_2=2000$ Hz. On the other hand, for the condition where $F_1=2000$ Hz, $F_4=3100$ Hz, and $F_2=2000$ Hz in stimulus configurations E and F, one might have expected poorer performance than for the condition above because pre-gap marker F_1 never occurred in isolation to cue the channel to which the listener should attend. Nonetheless, the TGD thresholds were uniformly low for the latter condition. Thus these trends are inconsistent with a ''cueing'' model as a scheme to account for the TGD patterns.

II. MARKER FREQUENCY ALIGNMENT: EFFECT OF SYMMETRIC VERSUS ASYMMETRIC STIMULUS CONFIGURATIONS

The second trend of note in these TGD data is that the listeners' performances were highly dependent on whether the pre- and post-gap marker configurations were presented in a symmetric or an asymmetric frequency alignment across the silent temporal gap. For the asymmetric three-marker configurations C and E (shown in Fig. 2), which we considered above, TGD thresholds were in some cases appreciably elevated relative to control threshold values expected for the simplest stimulus condition pairing markers $F_1=F_2$. The latter result was usually less than 10 ms. Our listeners yielded comparably small TGD thresholds for those four-marker stimulus configurations (G and H in Fig. 3) that maintained the frequency symmetry between corresponding pairs of pre- and post-gap markers by matching the frequencies of markers F_1 and F_2 and the frequencies of markers F_4 and F_3. This outcome is typical of previous findings measured with multiple markers (Green and Forrest, 1989; Grose and Hall, 1988; Grose, 1991; Hall *et al.*, 1996). It appears that to optimize TGD, our listeners attempted to group like-frequency components across time. This process of grouping spectrally similar components appears to be an important preliminary process that precedes the TGD decision. When the frequency-grouping process cannot readily be performed, because the components differ appreciably in frequency, TGD may suffer as shown in Fig. 3 for stimulus configurations I, J, K, and L. Other investigators have arrived at a similar general conclusion, namely that sequential auditory information is preprocessed and segregated on the basis of spectral coherence prior to processing by a central timing mechanism (Bregman and Campbell, 1971; Fitzgibbons *et al.*, 1974; Van Noorden, 1975; Watson *et al.*, 1975; Dannenbring and Bregman, 1976; Divenyi and Danner, 1977; Neff *et al.*, 1982; Bregman, 1990; Grose and Hall, 1996). In the simplest form of the model, this segregation or grouping process is a consequence of the peripheral frequency-channel architecture of the auditory system, which accounts well for ''within-channel'' processing of synchronous gap information in symmetric multiple pairs of markers. Moreover, we may conclude that the process of grouping marker frequency components across time takes precedence over grouping temporal components across frequency. The latter conclusion follows directly from the finding that TGD thresholds were sometimes appreciably elevated when the frequency symmetry between two pre-and two post-gap marker components was altered (in stimulus configurations I, J, K, and L). Under these conditions, the gap information across the two pairs of markers was gated synchronously in terms of the marker offsets and onsets; yet, in some cases, TGD performance declined dramatically with changes only in marker frequency asymmetry.

Examine again the group TGD results shown for stimulus configuration J in Fig. 3, which provides a good example of one of the asymmetric four-marker configurations. We earlier suggested two possible explanations for these results: (1) a marker-frequency presentation order effect, and (2) an effect of beating (roughness) that may obscure the salience of the gap. Consider a third explanation for the trend measured for configuration J. In this configuration, marker F_1 was fixed at 2000 Hz, markers F_4 and F_3 were fixed at 3100 Hz, and TGD thresholds were measured as a function of marker F_2 frequency. The TGD thresholds for these conditions increased subtly with increasing marker F_2 frequency to a maximum value near 50 ms at 2980 Hz. The listeners effectively ignored the presence of markers F_3 and F_4 over this range of F_2 frequency. (This pattern is reminiscent of the results for configuration B in Fig. 1 in which TGD thresholds increased as marker F_2 frequency was increased with respect to marker F_1 at 2000 Hz.) Only when the frequencies of markers F_2, F_3, and F_4 were all presented at 3100 Hz in configuration J did markers F_3 and F_4 play a significant role in TGD. Then, and only then, did the listeners disregard marker F_1 at 2000 Hz, as TGD thresholds were restored to control values near 10 ms. To perform this TGD task, the listeners continued to maintain focus, apparently within a single channel, as marker F_2 was systematically increased in frequency with respect to marker F_1. That focus was apparently activated or attracted initially by small frequency separations between the two markers, and was maintained as the marker frequency separation between markers F_1 and F_2 was increased over a range of almost 1000 Hz. Marker frequency differences between F_1 and F_2 over this range confounded an otherwise easy TGD task between the F_4 and F_3 markers at 3100 Hz. For whatever reason, the listeners' attention to the F_1 and F_2 marker frequency differences took precedence over a much simpler TGD task

within a second, apparently unactivated auditory channel centered on 3100 Hz. One interpretation of this perplexing result is that our listeners effectively attenuated simple temporal information within an inactive perceptual channel in order to attend to complex temporal information, across frequency, within an active channel. This idea of filtering ''off-target'' marker frequencies has previously been proposed as a possible mechanism in temporal gap discrimination (Divenyi and Danner, 1977). Other ''attentional'' filter models may also be relevant (see Dai *et al.*, 1991; Botte, 1995). In fact, roex filter models of attention yield the same effective range of attenuation (7–10 dB) that we estimated from roex functions fitted to our TGD data in Fig. 4.

III. PHENOMENOLOGICAL MODEL

The TGD patterns measured here, with asymmetric three and four marker stimuli, were not always predictable from the knowledge of TGD for simple (symmetric) pairs of sinusoidal markers. The nature of the multiple-marker processing task reflects a higher level of complexity and cognitive function than the simple measurement task for detection of a silent gap between a pair of sinusoidal markers. The latter TGD task appears to be controlled largely by peripheral processes (Williams and Perrott, 1971; Williams and Elfner, 1976; Formby and Forrest, 1991; Formby *et al.*, 1996), and models are currently available to predict these results (Forrest and Formby, 1996; Heinz *et al.*, 1996). These models, however, cannot predict the full range of TGD results measured for our multiple-component marker conditions.

The most parsimonious explanation that we can offer at this time for multiple-marker TGD results like those measured in Fig. 2 for stimulus configuration C is a phenomenological model of the perceptual process. After informal listening to assess potential TGD cues, we believe it is likely that the presence or absence of the silent gap in the signal or standard observation intervals of a trial is judged on the basis of the relative smoothness of the transition between the pre- and post-gap markers. In terms of this strategy, the listeners will usually judge the interval containing the silent gap to have a more abrupt transition than that for the standard interval. This perceptual distinction between the signal and standard decreases systematically as the frequency separation is increased between a simple pair of markers. The problem is that the perceptual transition becomes noticeably more abrupt (or less smooth) in both the signal and standard intervals for marker frequency separations exceeding the nominal passband of the listener's effective auditory filter [which he or she may attempt to center midway between the frequencies of the pre- and post-gap markers to optimize performance (Forrest and Formby, 1996; Heinz *et al.*, 1996)]. The idea here is that the focus of the listener is somehow being shifted from one cochlear location to another by passive peripheral filtering and/or active selective attentional processes (see Phillips *et al.*, 1997). As a consequence, the TGD task becomes more challenging and the TGD thresholds increase accordingly. However, if a remote post-gap (but not pre-gap) marker is included with the simple pair of pre- and post-gap markers (as in stimulus configuration C in Fig. 2), then the listener hears an abrupt perceptual transition in both the signal and standard intervals for all conditions of the variable-marker frequency. In turn, the resulting TGD thresholds increase for all conditions of the variable post-gap marker frequency. The relative increase, however, is most notable for those frequencies of the variable post-gap marker most closely matching the frequencies of the fixed-frequency pre- and post-gap markers. The perceptual transition is reduced to a minimum when the frequencies of one or two pre-gap markers are matched with the frequencies of the corresponding one or two post-gap markers as in configurations G and H (shown in Fig. 3). The listener can then readily group these marker components spectrally. In turn, the TGD task becomes relatively easy, which is reflected by the small TGD thresholds across the range of the variable-frequency markers. It is also evident from the results of our secondary experiment that listeners are compelled to group spectrally disparate (post-gap) markers in time even when this perceptual grouping process is detrimental to TGD performance.

Heinz's (1997, unpublished findings) failure to simulate TGD performance for our configuration C (shown in Fig. 2) with a multichannel model of the auditory periphery is significant. This result suggests that the surprising variation in TGD performance among our multiple-marker conditions depends on stimulus interactions that are organized and combined perceptually at higher levels of the central auditory nervous system. The idea of ''central processes'' in the detection and discrimination of gaps in acoustically dissimilar narrow-band markers is not new (Divenyi, 1985) and most recently has been promoted by Phillips *et al.* (1997). Whatever the mechanism or level of processing, these interactions presumably alter the perceived temporal envelope of the gap signal and marker complex. The general perceptual effects are probably akin to auditory phenomena that depend on cross-spectral processing of relatively slow temporal envelopes (see Yost and Sheft, 1993). Models relevant to understanding these related stimuli and perceptual tasks may also find application in explaining detection of silent temporal gaps in our multiple-marker stimuli.

SUMMARY

A variation on a seemingly routine experiment, with an obvious outcome, yielded a set of findings that challenges our current understanding of auditory temporal acuity. The unexpected results reveal that detection thresholds for a silent temporal gap may increase by an order of magnitude depending upon the number, temporal position, and frequency relations of the components that mark the temporal onset and offset of the gap signal. These results, which are not intuitive and cannot be predicted with existing models, provide a novel perspective on the complexity of auditory temporal gap detection within a multiple-marker complex.

ACKNOWLEDGMENTS

This research was supported by NIH Grant No. DC00951 from the National Institute of Deafness and Other Communication Disorders and the Center for Language and Speech Processing, Johns Hopkins University. We gratefully acknowledge statistical assistance from L. Magder and J.

Hall in the analysis of these data. We thank J. Grose and D. P. Phillips, along with P. Nelson and M. H. Goldstein, Jr., for reading this manuscript and providing editorial suggestions. D. M. Green, R. J. Dooling, G. R. Price, K. Abouchacra, and M. Nola also provided constructive comments in the preparation of an abbreviated version of this manuscript. This brief report (''Auditory temporal acuity and the perceptual organization of complex sounds'') was included in the *Proceedings of the Workshop on the Auditory Basis of Speech Perception*, edited by W. Ainsworth and S. Greenberg (Keele University, U.K.). We thank and acknowledge A. Shutt for editorial assistance in preparing drafts of this manuscript.

Botte, M. C. (**1995**). ''Auditory attentional bandwidth: Effect of level and frequency range,'' J. Acoust. Soc. Am. **98**, 2475–2485.

Bregman, A. S. (**1990**). *Auditory Scene Analysis* (MIT, Cambridge, MA).

Bregman, A. S., and Campbell, J. (**1971**). ''Primary auditory stream segregation and perception of order in rapid sequences of tones,'' J. Exp. Psychol. **89**, 244–249.

Bullock, T. H. (**1977**). *Recognition of Complex Acoustic Signals* (Abakon Verlagsgessellschaft, Berlin).

Collyer, C. E. (**1974**). ''The detection of a temporal gap between two disparate stimuli,'' Percept. Psychophys. **16**, 96–100.

Dai, H., Scharf, B., and Buus, S. (**1991**). ''Effective attenuation of signals in noise under focused attention,'' J. Acoust. Soc. Am. **89**, 2837–2842.

Dannenbring, G. L., and Bregman, A. S. (**1976**). ''The effect of silence on auditory stream segregation,'' J. Acoust. Soc. Am. **59**, 987–989.

Divenyi, P. L. (**1985**). ''Auditory discrimination of brief time intervals: A matter of cues,'' Abstracts of the 8th Midwinter Meeting of the Association for Research in Otolaryngology, p. 170.

Divenyi, P. L., and Danner, W. F. (**1977**). ''Discrimination of time intervals marked by brief acoustic pulses of various intensities and spectra,'' Percept. Psychophys. **21**, 125–142.

Fitzgibbons, P. J., Pollatsek, A., and Thomas, I. B. (**1974**). ''Detection of temporal gaps within and between perceptual tonal groups,'' Percept. Psychophys. **16**, 522–528.

Formby, C., and Forrest, T. G. (**1991**). ''Detection of silent temporal gaps in sinusoidal markers,'' J. Acoust. Soc. Am. **89**, 830–837.

Formby, C., Barker, C., Abbey, H., and Raney, J. J. (**1993**). ''Detection of silent temporal gaps between narrowband noise markers having second-formant-like properties of voiceless stop/vowel combinations,'' J. Acoust. Soc. Am. **93**, 1023–1027.

Formby, C., Sherlock, L. P., and Forrest, T. G. (**1996**). ''An asymmetric roex filter model for describing detection of silent temporal gaps in sinusoidal markers,'' Aud. Neurosci. **3**, 1–20.

Forrest, T. G., and Formby, C. (**1996**). ''Temporal gap detection thresholds in sinusoidal markers simulated with a single-channel envelope detector model,'' Aud. Neurosci. **3**, 21–33.

Green, D. M. (**1971**). ''Temporal auditory acuity,'' Psychol. Rev. **78**, 540–541.

Green, D. M., and Forrest, T. G. (**1989**). ''Temporal gaps in noise and sinusoids,'' J. Acoust. Soc. Am. **86**, 961–970.

Grose, J. H. (**1991**). ''Gap detection in multiple narrow bands of noise as a function of spectral configuration,'' J. Acoust. Soc. Am. **90**, 3061–3068.

Grose, J. H., and Hall, J. W. (**1988**). ''Across-frequency processing in temporal gap detection,'' in *Basic Issues in Hearing*, edited by H. Duifhuis, H. P. Wit, and J. P. Horst (Academic, New York), pp. 308–316.

Grose, J. H., and Hall, J. W. (**1996**). ''Perceptual organization of sequential stimuli in listeners with cochlear hearing loss,'' J. Speech Hear. Res. **39**, 1149–1158.

Hall, J. W., Grose, J. H., and Joy, S. (**1996**). ''Gap detection for pairs of noise bands: Effects of stimulus level and frequency separation,'' J. Acoust. Soc. Am. **99**, 1091–1095.

Harnad, S. (**1987**). *Categorical Perception* (Cambridge U.P., Cambridge, UK).

Heinz, M. G. (**1997**). Unpublished findings.

Heinz, M. G., Goldstein, Jr., M. H., and Formby, C. (**1996**). ''Temporal gap detection thresholds in sinusoidal markers simulated with a multi-channel, multi-resolution cochlear model,'' Aud. Neurosci. **3**, 35–56.

Moore, B. C. J. (**1989**). *An Introduction to the Psychology of Hearing* (Academic, New York).

Neff, D. L., Jesteadt, W., and Brown, E. L. (**1982**). ''The relation between gap discrimination and auditory stream segregation,'' Percept. Psychophys. **31**, 493–501.

Phillips, D. P., Taylor, T. L., Hall, S. E., Carr, M. M., and Mossop, J. E. (**1997**). ''Detection of silent intervals between noises activating different perceptual channels: Some properties of central auditory gap detection,'' J. Acoust. Soc. Am. **101**, 3694–3705.

SAS Institute, Inc. (**1989**). *SAS/STAT User's Guide, Version 6, 4th ed., Vol. 1* (SAS Institute, Inc., Cary, NC).

Van Noorden, L. P. A. S. (**1975**). ''Temporal coherence in the perception of tone sequences,'' Ph.D. thesis, Eindhoven University of Technology.

Viemeister, N. F., and Plack, C. J. (**1993**). ''Time analysis,'' in *Human Psychophysics*, edited by W. A. Yost, A. N. Popper, and R. R. Fay (Springer-Verlag, New York), pp. 116–154.

Watson, C. S., Wroton, H. W., Kelly, W. J., and Benbasset, C. A. (**1975**). ''Factors in discrimination of tonal patterns. I. Component frequency, temporal position, and silent intervals,'' J. Acoust. Soc. Am. **57**, 1175–1185.

Williams, K. N., and Elfner, L. F. (**1976**). ''Gap detection with three auditory events: A single-channel process,'' J. Acoust. Soc. Am. **60**, 423–428.

Williams, K. N., and Perrott, D. R. (**1971**). ''Temporal resolution of tonal pulses,'' J. Acoust. Soc. Am. **51**, 644–647.

Yost, W. A., and Sheft, S. (**1993**). ''Auditory perception,'' in *Human Psychophysics*, edited by W. A. Yost, A. N. Popper, and R. R. Fay (Springer-Verlag, New York), pp. 193–236.

Yost, W. A., and Watson, C. S. (**1987**). *Auditory Processing of Complex Sounds* (Erlbaum, Hillsdale, NJ).

Zwicker, E., and Feldtkeller, R. (**1967**). *Das Ohr als Nachrichtenempfänger* (Hirzel Verlag, Stuttgart).

Temporal integration of loudness under partial masking[a)]

Mary Florentine
Communication Research Laboratory, Department of Speech-Language Pathology and Audiology (133FR), Northeastern University, Boston, Massachusetts 02115

Søren Buus
Communication and Digital Signal Processing Center, Department of Electrical and Computer Engineering (409DA), Northeastern University, Boston, Massachusetts 02115

Monica Robinson
Communication Research Laboratory, Department of Speech-Language Pathology and Audiology (133FR), Northeastern University, Boston, Massachusetts 02115

(Received 21 July 1997; revised 10 February 1998; accepted 23 April 1998)

This paper tests the hypothesis that the loudness ratio between equal-SPL tones with different durations is the same at all SPLs. Detection thresholds and levels required to produce equal loudness for 5- and 200-ms tones presented in quiet or in broadband noise were measured using adaptive, two-interval, two-alternative forced-choice procedures. Tone levels ranged from 5 dB SL to 90 dB SPL for the long tones and about 100 dB SPL for the short tones. Results from six listeners with normal hearing show that the amount of temporal integration, defined as the level difference between equally loud 5- and 200-ms tones, varies nonmonotonically with level and is greatest at moderate levels. The average amount of temporal integration in quiet is about 15 dB near threshold, increases to a peak of 27 dB when the 5-ms tone is about 58 dB SPL, and decreases to about 15 dB near 100 dB SPL. For masker levels of 40, 60, and 80 dB SPL, the amount of temporal integration near masked threshold remains near 15 dB. The maximum amount of temporal integration decreases as masker level increases and occurs at progressively higher levels. At high levels, the amount of temporal integration is nearly the same as in the quiet for all masker levels. Loudness functions derived by applying the equal-loudness-ratio hypothesis to the data yield excellent predictions of loudness matches between tones in the quiet and partially masked tones with the 40- and 60-dB maskers. For the 80-dB masker, clear deviations are present. These results support the equal-loudness-ratio hypothesis, but suggest that intense masking may alter the loudness ratio between 200- and 5-ms tones. [S0001-4966(98)01508-2]

PACS numbers: 43.66.Cb, 43.66.Dc, 43.66.Mk, 43.66.Ba [RVS]

INTRODUCTION

Knowledge of the loudness function for brief sounds in the presence of background noise is important for understanding perception in natural listening situations. Background noise is present in most natural situations and many natural sounds (including speech) are characterized by events of short duration. A search of the literature revealed only one study of temporal integration for loudness in background noise (i.e., Richards, 1977). Because he obtained measurements at only three levels, the present research was initiated to examine more closely the effect of level on temporal integration of loudness for tones presented in quiet and under conditions of partial masking using many levels spanning the listeners' dynamic range.

Apart from their practical significance, measurements on how the amount of temporal integration (defined as the level difference between equally loud short and long tones) depends on level under conditions of partial masking also have considerable theoretical significance. Previous measurements in the quiet show that the amount of temporal integration depends strongly on level and is largest at moderate levels (Florentine *et al.*, 1996; Buus *et al.*, 1997). To explain the effect of level, it was necessary to alter at least one basic assumption about how loudness increases with increasing intensity. Either the loudness functions [in terms of log(loudness) as a function of SPL] for short-duration tones were not parallel to the loudness functions for long-duration tones, or they did not follow a power function even at levels well above threshold—contrary to Stevens's (1955, 1957) power law. A careful examination of the literature revealed parallel loudness functions for short- and long-duration noises (Stevens and Hall, 1966). Parallel loudness functions for stimuli of different durations also are inherent to Zwislocki's (1969) model of temporal integration. In addition, several investigators have noted that loudness functions for 1-kHz tones show small, but consistent, deviations from a power law and are flatter at moderate levels than at low and high levels (e.g., Fletcher and Munson, 1933; Robinson, 1957; Stevens, 1972).

Accordingly, Florentine *et al.* (1996) maintained the assumption that the loudness function for short- and long-duration tones are parallel (i.e., that the loudness ratio between equal-SPL long and short tones is the same at all

[a)]Part of this paper was presented at the 133rd meeting of the Acoustical Society of America, State College, Pennsylvania, June 1997 [J. Acoust. Soc. Am. **101**, 3170 (A) (1997)].

SPLs). This equal-loudness-ratio hypothesis predicts that the slope of the loudness function should be approximately inversely proportional to the amount of temporal integration. In fact, when Florentine *et al.* (1996) assumed that a 200-ms tone at any SPL was about three times as loud as a 5-ms tone at the same SPL, loudness functions calculated from their temporal-integration data were in good agreement with generally accepted loudness functions (e.g., Hellman and Zwislocki, 1963; Hellman, 1994), but were flatter at moderate levels than at low and high levels. Buus *et al.* (1997) derived loudness functions for a 1-kHz tone and for broadband noise from temporal-integration data and showed that the derived loudness functions predicted loudness matches between tones and broadband noises as a function of level. These findings offer considerable support for the equal-loudness-ratio hypothesis. Nevertheless, further testing of the equal-loudness-ratio hypothesis is desirable.

According to the equal-loudness-ratio hypothesis, the amount of temporal integration is inversely related to the local slope of loudness plotted on a logarithmic scale as a function of SPL. The slope is shallow if the amount of temporal integration is large and steep if the amount of temporal integration is small. Therefore, the equal-loudness-ratio hypothesis permits the logarithm of the loudness functions to be derived (except for a scale factor and an additive constant) from measurements of temporal integration. If temporal integration is measured in quiet and under partial masking, the derived loudness functions may be used to predict loudness matches between tones in quiet and tones under partial masking. Because the slope of the loudness function is steeper under partial masking than in quiet (e.g., Steinberg and Gardner, 1937; Gleiss and Zwicker, 1964; Hellman and Zwislocki, 1964; Scharf, 1964; Stevens and Guirao, 1967; Richards, 1968), partial masking offers an opportunity to test if a direct relation exists between the slope of the loudness function and the amount of temporal integration. Accordingly, the present study measured the amount of temporal integration as a function of level using 5- and 200-ms tones presented in quiet and in white-noise maskers at various levels. To test the hypothesis for individual listeners, loudness balances between 200-ms tones in quiet and under partial masking were also measured in two listeners.

I. METHOD

A. Stimuli

The stimuli were 1-kHz tones presented in quiet or in continuous white-noise maskers with overall levels of 40, 60, or 80 dB SPL (spectrum levels of -3, 17, and 37 dB SPL). The tones had equivalent rectangular durations of 5 and 200 ms. The 1-kHz test frequency and the durations of 5 and 200 ms were chosen to make the measurements directly comparable with a previous study (Florentine *et al.*, 1996).

The tones had a 6.67-ms raised-cosine rise and fall. Durations measured between the half-amplitude points were 1.67 ms longer than the nominal durations. Accordingly, the 5-ms stimuli consisted only of the rise and fall, whereas the 200-ms stimuli had a 195-ms steady-state portion. These envelope shapes ensured that almost all the energy of the tone bursts was contained within the 160-Hz-wide critical band centered at 1000 Hz (Scharf, 1970; Zwicker and Fastl, 1990). Even for the 5-ms tone burst, the energy within the critical band was only 0.3 dB less than the overall energy. The masker, when present, was turned on at the beginning and turned off at the end of a block of trials.

Five to nine test levels were used for each duration of the fixed-level stimulus. They ranged from 5 dB SL to 90 dB SPL for the long tones. Typically the maximum sensation levels were 80 dB SL in quiet and 70, 50, or 25 dB SL in continuous white-noise maskers with overall levels of 40, 60, or 80 dB SPL, respectively.

B. Procedure

1. Absolute thresholds

In the first part of the experiment, absolute thresholds were measured for both stimuli using an adaptive procedure in a two-interval, two-alternative forced-choice paradigm. Each trial contained two observation intervals, which were marked by lights. The pause between them was 500 ms. The signal was presented in either the first or the second observation interval with equal *a priori* probability. The listener's task was to indicate which interval contained the signal by pressing a key on a small computer terminal. Two hundred milliseconds after the listener responded, the correct answer was indicated by a 200-ms light. Following the feedback, the next trial began after a 500-ms delay.

The level of the signal initially was set approximately 15 dB above the listener's threshold. It decreased following three consecutive correct responses and increased following one incorrect response. The step size was 5 dB until the second reversal after which it was reduced to 2 dB. Reversals occurred when the direction of change of the signal level changed from increasing to decreasing or *vice versa*. This procedure converges on the signal level yielding 79.4% correct responses (Levitt, 1971).

A single threshold measurement was based on three interleaved adaptive tracks. On each trial, the track for that trial was selected at random among the tracks that had not yet terminated, which they did after five reversals. The threshold for one track was calculated as the average signal level at the fourth and fifth reversals and one threshold measurement was taken as the average threshold across the three tracks. At least three such threshold measurements (for a total of at least nine tracks) were obtained for each listener and condition. The average across all measurements was used as the reference to set the sensation level for each listener and condition in the second part of the experiment.

2. Loudness matches

In the second part of the experiment, the 5- and 200-ms tones were matched in loudness using an adaptive procedure. Measurements with both the long and the short tone varied were obtained in mixed order. The stimuli were presented in a two-interval, two-alternative forced-choice paradigm. On each trial, the listener heard two sounds separated by 500 ms.

The fixed-level sound preceded or followed the variable sound with equal *a priori* probability. The listener's task was to indicate which sound was louder by pressing a key. The response initiated the next trial after a 700-ms delay. The level of the variable sound was adjusted according to a simple up–down procedure (Jesteadt, 1980).[1] If the listener indicated that the variable sound was the louder one, its level was reduced, otherwise it was increased. The step size was 5 dB until the second reversal after which it was reduced to 2 dB. This procedure converges at the level corresponding to the 50% point on the psychometric function (Levitt, 1971).

A single match was based on two interleaved adaptive tracks. One track started 10 dB above the expected equal-loudness level and the other track started 10 dB below it. [If the nominal starting level for the 5-ms tone exceeded 110 dB SPL, the starting level was set to 110 dB SPL. This maximal level ensured that listeners' sound exposure was well below the limit recommended by OSHA (1994).] On each trial, the track for that trial was selected at random until one track terminated; then, the remaining track was used until it terminated. Each track terminated after nine reversals. The equal-loudness level for one track was calculated as the average of the last four reversals and the result of one match was taken as the average equal-loudness level for the two tracks. Three or four such matches were obtained for each listener and condition. Therefore, a total of 12 or 16 tracks was obtained for each pair of stimuli: six or eight with the short stimulus fixed and six or eight with the long stimulus fixed.

In the final part of the experiment, partially masked 200-ms tones were matched in loudness to 200-ms tones presented in quiet. Measurements were obtained from two listeners using the procedure described above. Both the tone in quiet and the tone in noise were varied.

C. Apparatus

A PC-compatible computer with a signal processor (TDT AP2) generated the stimuli via a 16-bit D/A converter (TDT DD1) with a 50-kHz sample rate. It also sampled the listeners' responses and executed the adaptive procedure. The output of the D/A converter was attenuated (TDT PA4), low-pass filtered (TDT FT5, $f_c = 20$ kHz, 135 dB/oct), and attenuated (TDT PA4) before it was added (TDT SM3) to the masker, and led to a headphone amplifier (TDT HB6), which fed one earphone of the Sony MDR-V6 headset. This setup ensured that the stimulus level could be controlled linearly by the attenuators over at least a 130-dB range. Spectral analysis of the 1-kHz tone at its maximal output level of 110 dB SPL showed that distortion consisted mostly of second and third harmonics, which were at least 63 dB below the fundamental.

The masking noise was produced by a waveform generator (TDT WG2), attenuated (TDT PA4), and then added (TDT SM3) to the signal. For routine calibration, the output of the headphone amplifier was led to an A/D converter (TDT DD1), such that the computer could sample the waveform, calculate its spectrum and rms voltage, and display the results before each set of matches.

D. Listeners

Six female listeners, five Caucasians and one African American (listener L3), were tested on all conditions. All listeners had audiometric thresholds within 10 dB of ANSI (1989) standard at octave frequencies from 0.125 to 8 kHz and had medical histories consistent with normal hearing. They ranged in age from 22 to 29 years. Four listeners had previous experience making loudness judgments. All listeners were paid for their services. Listener L3 is the third author.

E. Data analysis

Level differences were calculated between the 5- and 200-ms tones that were judged to be equally loud. Two separate points of subjective equality were calculated for each stimulus pair: the average of the measurements with the short tone fixed and the average of the measurements with the long tone fixed.

For each listener, polynomial fits were made to the combined data obtained with the long and the short tone varied. Such fits were used because they provide a good description of the entire data set, while avoiding problems of how to average measurements taken at different loudness levels. Visual inspection was used to determine a range of polynomial orders that provided a good fit to the data. The lowest-order polynomial within the range was used unless a higher-order polynomial decreased the least-squared error considerably. For one listener, L6, the large differences between the long tone varied and short tone varied in the 80-dB-SPL masker made it necessary to average the level differences before fitting the polynomial.

To examine the statistical significance of the effects of stimulus variables and differences among listeners, a four-way ANOVA (stimulus level×masker level×long or short variable×listener) for repeated measures was performed (Data Desk 5.0, Data Description, Inc., Ithaca, NY, 1995). The dependent variable for this analysis was the level difference ($L_{\text{short}} - L_{\text{long}}$) between two equally loud 5- and 200-ms stimuli. Scheffé *post hoc* tests for contrast (Data Desk 5.0, 1995) were performed when appropriate to explore sources of significant effects and interactions. Differences were considered significant when $p \leqslant 0.05$.

II. RESULTS

A. Individual data

The amounts of temporal integration for tones presented in quiet and in three levels of broadband masking are shown in Fig. 1. For each of the six listeners, the level differences required to obtain equal loudness between 5- and 200-ms tones are plotted as a function of the level of the 5-ms tone. The unfilled symbols show results with the 5-ms tone varied; the filled symbols show results with the 200-ms tone varied.

For five of the six listeners there is reasonable similarity of the loudness matches with the 5-ms tones and with the 200-ms tones varied. The exception is listener L6, who consistently required a larger level difference at the moderate and high levels to obtain equal loudness between the 5- and the 200-ms tones when the 200-ms tone was varied than

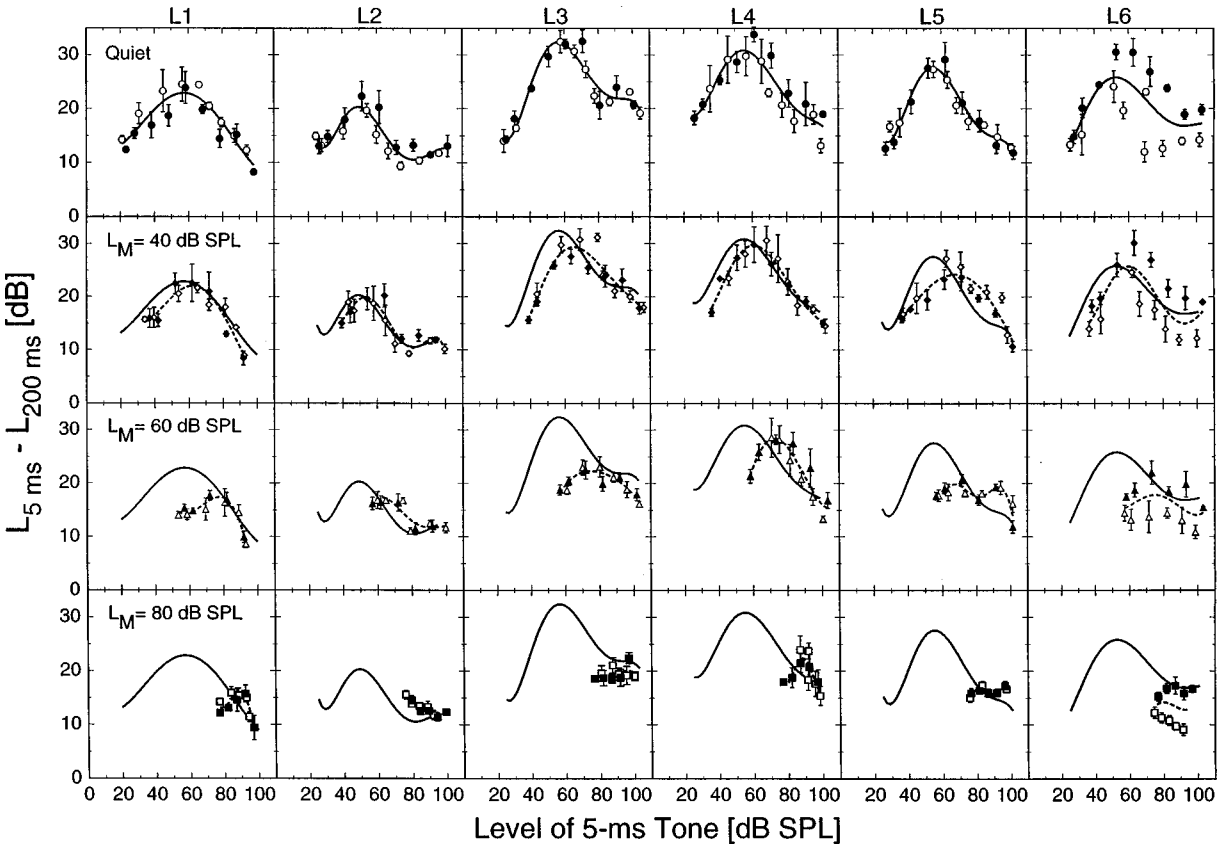

FIG. 1. Temporal integration of loudness for six listeners. The level differences between 5- and 200-ms tones needed to obtain equal loudness are plotted as a function of the level of the 5-ms tone. The four panels in each column show results obtained in quiet and in three levels of broadband masking (40, 60, and 80 dB SPL) for one listener. The unfilled symbols show results with the 5-ms tone varied; the filled symbols show results with the 200-ms tone varied. The vertical bars show plus and minus one standard error of the mean. The solid and dashed lines show polynomial fits to the data (see text).

when the 5-ms tone was varied. The reason for this difference is unclear, but biases of similar magnitude have been observed in another listener (see listener LH in Florentine *et al.*, 1996, p. 1636). For all individual listeners, the matching data are reasonably consistent as indicated by the small standard errors (average is 1.4 dB; range is from 0.1 to 4.5 dB).

The solid and dashed lines in Fig. 1 show the polynomial fits to the temporal-integration data. Although the functions vary somewhat in shape among the listeners, they clearly show a level dependence and a maximum for temporal integration of loudness at moderate levels for all listeners. The maximal amount of temporal integration in quiet varies greatly, ranging from about 20 dB for listener L2 to about 33 dB for listener L3. This large range is consistent with data from Florentine *et al.* (1996). As the level of the background masker increases, the amount of temporal integration decreases and the peak shifts to higher levels. At the highest levels, the amounts of temporal integration obtained at the three masker levels are similar to one another and to those obtained in quiet.

Temporal integration for detection thresholds for the 5- and 200-ms tones hovers around 15 dB with no obvious differences across listeners or masking conditions. The lack of effect of the masker on temporal integration for detection agrees with previous data (Florentine *et al.*, 1988). Across all listeners and levels of partial masking, the threshold data appear to be reasonably close to that obtained for loudness around 5 dB SL.

B. Group data

The average data from the six listeners, plotted in the same manner as Fig. 1, are shown in Fig. 2. Data obtained in the quiet and in the presence of broadband noise at 40, 60, or 80 dB SPL are shown by different symbols. The data obtained by varying the 5-ms tones (open symbols) agree well with the data obtained by varying the 200-ms tones (filled symbols). The standard deviations—calculated across the means for the six listeners—are not shown in the figure. They showed no systematic variation across stimulus conditions and averaged 4.1 dB. The various lines show the amounts of temporal integration predicted from the best-fitting loudness functions derived by applying the equal-loudness-ratio hypothesis to the data, as discussed later. Clearly, the equal-ratio loudness functions can account for the data.

As the level of the background masker increases from 40 to 80 dB SPL, the amount of temporal integration decreases and the shape of the temporal-integration function changes. The functions become flatter and peak at increasingly higher levels and they merge at the highest levels. These observations are supported by the ANOVA shown in Table I. The effects of the stimulus variables are shown in the top half of

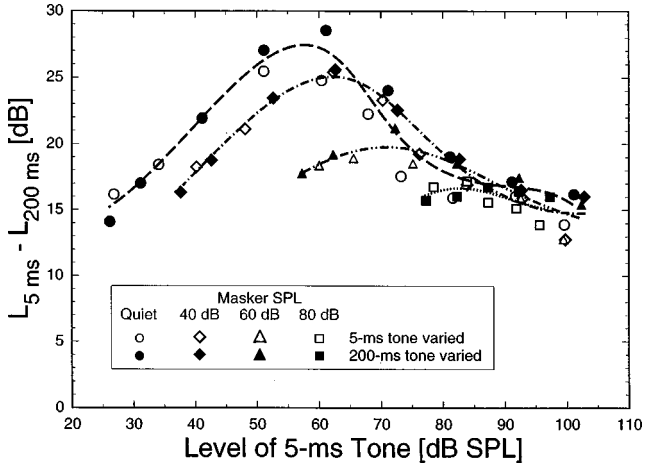

FIG. 2. Average temporal integration of loudness for tones obtained in quiet and in broadband noise at 40, 60, or 80 dB SPL. The level differences between 5- and 200-ms tones needed to obtain equal loudness are plotted as a function of the level of the 5-ms tone. The unfilled symbols show results with the 5-ms tone varied; the filled symbols show results with the 200-ms tone varied. The various lines show the amounts of temporal integration predicted from the best-fitting equal-ratio loudness function.

the table and individual differences (i.e., the effect of and interaction with listener) in the bottom half. As shown at the top, the effects of masker level and sensation level are highly significant. The Scheffé tests for contrast show that the amount of temporal integration is generally larger at 20 and 30 dB SL than at 5 dB SL and high sensation levels (i.e., 60, 70, and 80 dB SL). As indicated by the highly significant interaction between masker level and sensation level, these effects depend on masker level. In quiet, the amounts of temporal integration at 30 and 40 dB SL are the largest and are larger than those at 5, 10, 50, 60, 70, and 80 dB SL. The amount of temporal integration is also larger at 20 dB SL than at 5, 10, 60, 70, and 80 dB SL. With the 40-dB masker, the amounts of temporal integration at 20 and 30 dB SL are largest and are significantly larger than those at 5, 10, 50, 60, and 70 dB SL. In addition, the amount of temporal integration with the 40-dB masker is larger at 40 than at 60 dB SL. There are no significant differences among SLs with the 60- and 80-dB maskers.

TABLE I. Four-way analysis of variance for repeated measures of loudness matching. The dependent variable is the level difference between equally loud 5- and 200-ms tones. The stimulus variables Variable Duration (Vrb; 2 levels: 5 or 200 ms), Masker Level (ML; 4 levels: Quiet, 40, 60, and 80 dB SPL), and Sensation Level (SL; 11 levels: 5, 10,..., 25, 30, 40,..., 70, and 80 dB) are fixed factors. Listener (Lsr; 6 levels: L1 to L6) is random factor.

Source	df	Error df	Sums of squares	Mean square	*F*-ratio	Prob
Const	1	5	442 426	442 426	1036	≤0.0001
Vrb	1	5	4.980	4.980	0.03	0.87
ML	3	15	1874	624.8	28.31	≤0.0001
Vrb*ML	3	15	106.2	35.39	4.17	0.025
SL	10	50	4329	432.9	10.03	≤0.0001
Vrb*SL	10	50	901.1	90.11	4.00	0.0005
ML*SL	14	70	3619	258.5	17.54	≤0.0001
Vrb*ML*SL	14	66	558.1	39.86	3.73	0.0001
Lsr	5	942	2135	427.0	39.80	≤0.0001
Vrb*Lsr	5	942	794.8	159.0	14.81	≤0.0001
ML*Lsr	15	942	331.1	22.07	2.06	0.010
Vrb*ML*Lsr	15	942	127.6	8.484	0.79	0.69
SL*Lsr	50	942	2159	43.17	4.02	≤0.0001
Vrb*SL*Lsr	50	942	1127	22.54	2.10	≤0.0001
ML*SL*Lsr	70	942	1032	14.74	1.37	0.026
Vrb*ML*SL*Lsr	66	942	705.7	10.69	1.00	0.49
Error	942		10 107	10.73		
Total	1273		46 645			

The Scheffé tests also show that the amount of temporal integration is larger in quiet than in 60- or 80-dB maskers, but this effect depends on the sensation level. No effect of masker level is present at 5 and 10 dB SL. At 20 dB SL, the amount of temporal integration with the 40-dB masker is larger than that with the 60-dB masker, which is larger than that with the 80-dB masker, and the amount of temporal integration in the quiet is larger than that with the 80-dB masker. At 30 dB SL, the amount of temporal integration is larger in the quiet and with the 40-dB masker than with the 60-dB masker. At 40 dB SL, the amount of temporal integration in the quiet is larger than that with the 40-dB masker, which is larger than that with the 60-dB masker.

Variable duration alone has no significant effect, but it does interact with masker level and sensation level in a complex manner. This finding probably reflects that equal sensation level is not equal loudness for the two durations. Therefore, the SPL of the short tone and the amount of temporal integration will differ depending on whether the short tone or the long tone is varied.

The lower half of Table I shows that the amount of temporal integration differs across listeners. The Scheffé tests for contrast show that, in general, the amount of temporal integration for listeners L3 and L4 is larger than the amount of temporal integration for L5 and L6, which is larger than that for L1 and L2. These differences depend on stimulus condition in a complex manner as indicated by the numerous highly significant interactions between listener and stimulus variables.

III. DISCUSSION

A. Comparison with data in the literature

The group data obtained in quiet are in qualitative agreement with other data (see Florentine *et al.*, 1996). However, the amount of temporal integration in the present study is about 40% greater than that obtained using identical stimuli and procedures with a different group of normal-hearing listeners. This difference is not surprising given the large differences among listeners.

The effects of partial masking and of stimulus level also agree qualitatively with Richards's (1977) data. Quantitative comparisons are inappropriate because the method and stimuli differ from those in the present study. Richards used an adjustment procedure and his listeners adjusted only the variable-duration stimuli (with or without masking) to sound as loud as a fixed-level 500-ms tone presented in quiet. His shortest duration was 10 ms and the masker was a one-octave band of noise, whereas the present study used a broadband noise. Finally, he tested only three loudness levels for each

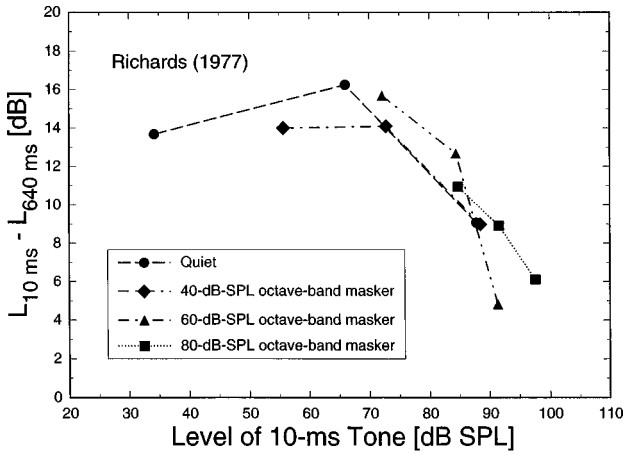

FIG. 3. Average data from Richards (1977) are plotted in the same manner as Fig. 2. The amount of temporal integration (i.e., the level difference between equally loud 10- and 640-ms tones) is plotted as a function of the SPL of the 10-ms tone. As shown by the legend, different symbols show data obtained in quiet and in octave-band noise at 40, 60, or 80 dB SPL.

masker condition, which are too few to allow derivation of loudness functions and testing the equal-loudness-ratio hypothesis. Nevertheless, the effects of stimulus level and masker levels in Richards's (1977) data are similar to those in the present data. This is illustrated in Fig. 3, which shows Richards's (1977) data in the format of Fig. 2. The level difference required to obtain equal loudness between 10- and 640-ms tones is plotted as a function of the level of the 10-ms tone. The amount of temporal integration is clearly largest at moderate levels and decreases with increasing level at high levels. As the level of the background noise increases from 40 to 80 dB SPL, the maximal amount of temporal integration generally decreases, but at high levels the amount of temporal integration is about the same for all masker conditions. These trends all agree with the present data.

B. Testing the equal-loudness-ratio hypothesis

The primary purpose of the present experiment was to test the hypothesis that the loudness ratio between equal-SPL long and short tones is independent of the SPL. If this hypothesis is true, measurements of temporal integration can be used to derive loudness functions (to within a multiplicative and an additive constant for the logarithm of loudness). These loudness functions then can be used to predict loudness matches between tones in quiet and tones under masking. Therefore, the hypothesis can be tested by comparing the predictions to Stevens and Guirao's (1967) data for loudness matches between tones presented in quiet and in broadband maskers.

To this end, loudness functions are first derived from the average temporal-integration data in Fig. 2. According to the equal-loudness-ratio hypothesis, the slope of the loudness function should be approximately inversely proportional to the amount of temporal integration. More precise estimates of the loudness functions were obtained by modeling the logarithm of the loudness function as a sixth-order polynomial. The loudness function for the 5-ms tone was assumed to be a constant amount below (on a logarithmic axis of loudness) that for the 200-ms tone and the amount of temporal integration was predicted as the horizontal distance between the two functions. The six coefficients of the sixth-order polynomial (the constant term does not affect the predictions of temporal integration) were then varied to minimize the squared error between the predicted amounts of temporal integration and the data in Fig. 2. As shown in Fig. 2, the best-fitting polynomials provide an excellent account of the temporal-integration data.

The polynomials determined in this manner describe the logarithms of the loudness functions (as approximated by the sixth-order polynomial) except for one additive and one multiplicative constant. To determine these constants for the loudness function in quiet, one additive and one multiplicative constant were applied to the least-squared error polynomial determined from the temporal-integration data; these constants were then set to minimize the squared difference between the logarithm of Zwislocki's (1965) modified power function $(N=0.076*[(1+0.4*(I/I_{\mathrm{th}}))^{0.27}-1])$ and the polynomial. This fixed the loudness ratio between the 200- and 5-ms tones to be 4.4 at any SPL. This ratio was then used to determine the values of the multiplicative constants for the polynomials fitted to the data for the partially masked tones.

To complete the derivation of the loudness functions, the additive constants to be applied to the polynomials for the partially masked tones also had to be determined. The amounts of temporal integration obtained at high levels were practically identical for all conditions, which indicates that the slopes of the loudness functions at high levels are the same in quiet and under the various levels of masking. This does not mean that the loudness functions coincide at high levels, however. The broadband masker obscures the excitation from the tone over a broad range of frequencies and reduces the overall loudness, even of intense tones. This effect is readily apparent in Stevens and Guirao's (1967) data for loudness balances between tones in quiet and under partial masking, which show that partially masked tones have to be somewhat more intense than tones in quiet to obtain equal loudness, even at high levels. To account for this effect, the additive constant for the polynomials had to be determined individually for each level of masking and provided one free parameter, which was used to minimize the squared error between Stevens and Guirao's (1967) data for a particular masker level and loudness matches predicted from the model loudness functions.

This procedure resulted in the loudness functions shown in Fig. 4. To avoid extrapolating the data, the loudness functions are only shown for the range of levels encompassed by the temporal-integration measurements. For each masking condition, the lowest SPL generally corresponds to 5 dB SL for the 200-ms tone and the highest SPL is the highest level used for the 5-ms tones, which is approximately 100 dB SPL. As expected, the loudness functions are shallower at moderate than at low and high levels, although the loudness function for a tone in the 80-dB masker is close to a power function. The local exponents [i.e., the derivative of 10*log(loudness) vs SPL] of these loudness functions reach minima of 0.21 at 43 dB SPL in quiet, 0.24 at 49 dB SPL

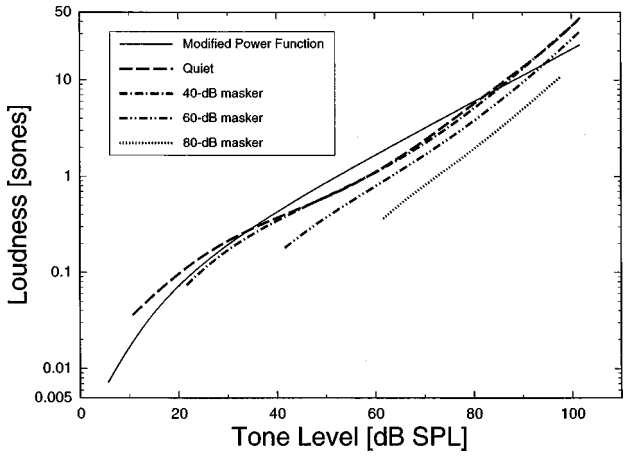

FIG. 4. Loudness functions obtained from temporal integration in quiet and in three levels of broadband white noise at 40, 60, and 80 dB SPL. A modified power function (Zwislocki, 1965) describing the loudness of a 200-ms tone presented in quiet is shown for comparison.

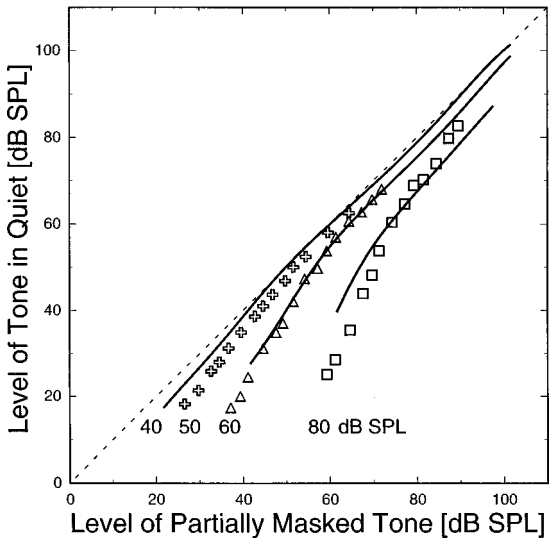

FIG. 5. Loudness-matching functions showing the level of a tone in quiet as a function of the level of an equally loud partially masked tone. Masker level is the parameter. The lines show predictions obtained from the temporal-integration data. The symbols show a subset of the data from Stevens and Guirao (1967).

with the 40-dB masker, 0.32 at 60 dB SPL with the 60-dB masker, and 0.38 at 73 dB SPL with the 80-dB masker. Therefore, the minimal slope becomes increasingly larger and occurs at increasingly higher levels as the masker level increases. This simply reflects the finding that the maximal amounts of temporal integration decreased and the level at which the maximum occurred increased as the masker level increased. At 95 dB SPL, the local exponent is about 0.43 for all the loudness functions. The local exponents obtained for the tones in quiet are similar to those obtained in our previous study (Florentine *et al.*, 1996), which yielded a minimal exponent of 0.25 at 46 dB SPL and an exponent of 0.45 at 95 dB SPL.

If the loudness functions shown in Fig. 4 for tones in quiet and tones under partial masking are correct, they should predict the steepening of loudness-matching functions between tones under partial masking and tones in quiet. The predictions are shown by the lines in Fig. 5. Again, the range of levels encompassed by the predicted matching functions are limited to the ranges of levels tested in the temporal-integration experiment. Because the lowest level was 5 dB SL, predictions for the lowest loudness levels in the 60- and 80-dB-SPL maskers cannot be obtained. The symbols show a subset of the data from Stevens and Guirao (1967). The 40-dB predictions fit well next to the 50-dB data. The predictions and the data follow closely at 60 dB. However, the predictions for the 80-dB masker deviate somewhat from the data. Whereas the predictions for the 40- and 60-dB maskers offer considerable support for the equal-loudness-ratio hypothesis, the predictions at 80 dB indicate that modifications may be required.

The failure to fit the data for the 80-dB masker does not necessarily indicate that the equal-loudness-ratio model fails under intense masking. It seems possible that auditory-nerve adaptation may change under intense masking. If loudness is related to the amount of neural activity evoked by the stimulus (up to some maximum integration time),[2] a reduction of the rapidly decaying onset response would cause a proportionally larger reduction of loudness for a brief tone than for a long tone. Accordingly, intense masking could cause the loudness ratio between the long and the short tone to be larger than that in quiet or under low and moderate levels of partial masking. In fact, if the level-independent loudness ratio were assumed to increase under high levels of masking, a substantially better fit to Stevens and Guirao's (1967) data could be obtained. Therefore, the equal-loudness-ratio model may hold even under intense masking, but the loudness ratio may not be the same as in quiet and under low and moderate levels of partial masking. This indicates that the equal-loudness-ratio hypothesis may be modified to state that the loudness ratio between equal-SPL long and short tones presented in a given masker is independent of the tones' level, but may depend on the masker level when the masker is intense.

Given the substantial differences in the individual data for temporal integration of loudness shown in Fig. 1, it seems that individual differences also should be present in the loudness functions for the various masking conditions. If so, loudness matches between tones in quiet and under partial masking also would be likely to differ among individuals. Therefore, we sought to determine if such individual differences exist and if they can be predicted by the individual differences in the temporal-integration functions. To this end, loudness matches between 200-ms tones presented in quiet and under partial masking were obtained for listeners L1 and L3. (The other four listeners were no longer available for testing.)

The loudness matches are shown by the various symbols in Fig. 6. They generally follow the trends shown by Stevens and Guirao's (1967) data in Fig. 5. At low levels, the matching functions become increasingly steep as the masker level increases. At high levels, all the matching functions have a slope close to unity, but the broadband masker reduces the loudness level by an amount that increases with the masker level. However, the data show differences between the two listeners both in the amount of loudness-level reduction at

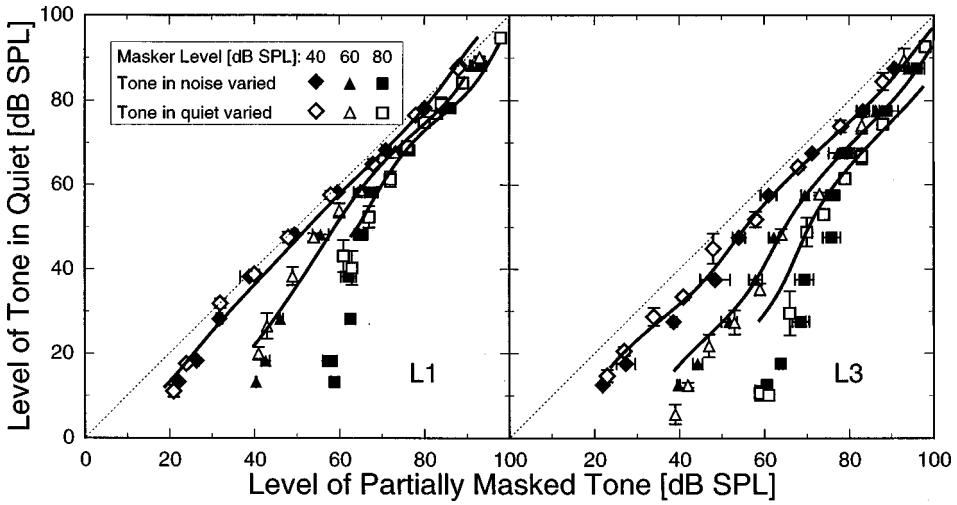

FIG. 6. Measured and predicted loudness-matching functions for individual listeners. The level of a tone in quiet is plotted as a function of the level of an equally loud partially masked tone. Masker level is the parameter. The left panel is for listener L1 and the right panel is for listener L3. The unfilled symbols show results obtained by varying the tone in quiet; the filled symbols show results obtained by varying the partially masked tone. The vertical and horizontal bars show plus and minus one standard error of the mean. The solid lines show predictions obtained from the individual listener's temporal-integration data.

high levels and, more importantly, in the details of the curvature of the matching functions, especially at moderate loudness levels. Whereas the loudness reduction at high levels can be fitted by varying the single free parameter available for a masking condition, the curvature of the predictions depends almost entirely on the temporal-integration functions. For listener L1 (left panel), the matching functions tend to show a monotonically decreasing slope and have a downward-concave curvature at moderate loudness levels. For listener L3 (right panel), the slope varies nonmonotonically with level and the matching functions have an upward-concave curvature when the tone in quiet is between 20 and 50 dB SPL. The solid lines show loudness matches predicted from the individual temporal-integration functions in the manner described above for the average data. Again, the ranges of the predictions are limited to encompass stimulus levels used in the temporal-integration experiment. The predictions closely follow the data, except at the 80-dB-SPL masker level for L3. It appears that the predicted functions replicate most of the details that differ between L1 and L3. In particular, they show the upward-concave curvature found for L3 and the downward-concave curvature found for L1. These findings support the contention that the individual differences in the temporal-integration functions are also observed in the loudness functions and provide further support for the equal-loudness-ratio hypothesis. However, as was noted for the comparison with average data, intense masking may increase the loudness ratio, which may explain the mediocre fit obtained for L3 with the 80-dB-SPL masker.

IV. CONCLUSIONS

The present study measured temporal integration of loudness for 1-kHz tones presented over a wide range of levels in quiet and under three levels of white-noise masking. The results from six listeners with normal hearing show that

(1) The amount of temporal integration for loudness is largest at moderate loudnesses. As the level of partial masking increases, the maximal amount of temporal integration decreases and occurs at higher SPLs.

(2) Loudness functions obtained by applying the equal-loudness-ratio hypothesis to temporal-integration data are flatter at moderate levels than at low and high levels. Therefore, loudness may not follow a power law even at levels well above threshold.

(3) The equal-ratio loudness functions predict loudness matches between partially masked tones and tones in quiet for masker levels of 40 and 60 dB SPL, but not 80 dB SPL. The discrepancy for the 80-dB-SPL masker may indicate that the loudness ratio is altered by intense masking. Therefore, the present results generally support the equal-loudness-ratio hypothesis.

(4) The equal-loudness-ratio hypothesis is further supported by two individual listeners' loudness matches between a tone in quiet and partially masked tones. The loudness matches differed between the two listeners and the differences were apparent in the predictions obtained from their temporal-integration data. However, the fit was mediocre for one listener with the 80-dB-SPL masker as may be expected if the loudness ratio between a long and a short tone is altered by intense masking.

ACKNOWLEDGMENTS

Hannes Müsch, Andrew Oxenham, Robert Shannon, and two anonymous reviewers provided valuable comments. This research was supported by Grant No. NIH-NIDCD RO 1 DC02241.

[1]The present procedure differs from that used by Buus *et al.* (1997). They used a roving-level procedure with a two-down, one-up adaptive rule, which caused the variable stimulus to converge to a level at which it was just noticeably louder than the fixed stimulus. Although this procedure gave reliable results and appeared to eliminate biases that often affect loudness judgments, we chose not to use it for the present study because extensive modeling was required to separate the loudness jnds from the equal-loudness function. To measure the equal-loudness function directly, we

preferred to use a one-up, one-down procedure identical to that used by Florentine *et al.* (1996).

[2]The relation between loudness and the amount of auditory-nerve activity may be complex (see Relkin and Doucet, 1997).

ANSI (**1989**). ANSI S3.6-1989, ''Specifications for audiometers'' (American National Standards Institute, New York).

Buus, S., Florentine, M., and Poulsen, T. (**1997**). ''Temporal integration of loudness, loudness discrimination, and the form of the loudness function,'' J. Acoust. Soc. Am. **101**, 669–680.

Fletcher, H., and Munson, W. A. (**1933**). ''Loudness, its definition, measurement and calculation,'' J. Acoust. Soc. Am. **5**, 82–108.

Florentine, M., Fastl, H., and Buus, S. (**1988**). ''Temporal integration in normal hearing, cochlear impairment, and impairment simulated by masking,'' J. Acoust. Soc. Am. **84**, 195–203.

Florentine, M., Buus, S., and Poulsen, T. (**1996**). ''Temporal integration of loudness as a function of level,'' J. Acoust. Soc. Am. **99**, 2367.

Gleiss, N., and Zwicker, E. (**1964**). ''Loudness function in the presence of masking noise,'' J. Acoust. Soc. Am. **36**, 393–394.

Hellman, R. P. (**1994**). ''Relation between the growth of loudness and high-frequency excitation,'' J. Acoust. Soc. Am. **96**, 2655–2663.

Hellman, R. P., and Zwislocki, J. J. (**1963**). ''Monaural loudness function at 1000 cps and interaural summation,'' J. Acoust. Soc. Am. **35**, 856–865.

Hellman, R. P., and Zwislocki, J. J. (**1964**). ''Loudness function of a 1000-cps tone in the presence of a masking noise,'' J. Acoust. Soc. Am. **36**, 1618–1627.

Jesteadt, W. (**1980**). ''An adaptive procedure for subjective judgments,'' Percept. Psychophys. **28**, 85–88.

Levitt, H. (**1971**). ''Transformed up-down methods in psychoacoustics,'' J. Acoust. Soc. Am. **49**, 467–477.

OSHA (**1994**). ''Occupational noise exposure,'' in *Code of Federal Regulations* (Office of the Federal Register, National Archives and Records Administration, Washington, DC), Title 29, Chap. XVII, § 1910.95, pp. 198–213.

Relkin, E. M., and Doucet, J. R. (**1997**). ''Is loudness simply proportional to the auditory nerve spike count,'' J. Acoust. Soc. Am. **101**, 2735–2740.

Richards, A. M. (**1968**). ''Monaural loudness functions under masking,'' J. Acoust. Soc. Am. **44**, 599–605.

Richards, A. M. (**1977**). ''Loudness perception for short-duration tones in masking noise,'' J. Speech Hear. Res. **20**, 684–693.

Robinson, D. W. (**1957**). ''The subjective loudness scale,'' Acustica **7**, 217–233.

Scharf, B. (**1964**). ''Partial masking,'' Acustica **14**, 17–23.

Scharf, B. (**1970**). ''Critical bands,'' in *Foundations of Modern Auditory Theory, Vol. 1*, edited by J. V. Tobias (Academic, New York), pp. 157–202.

Steinberg, J. C., and Gardner, M. B. (**1937**). ''The dependence of hearing impairment on sound intensity,'' J. Acoust. Soc. Am. **9**, 11–23.

Stevens, S. S. (**1955**). ''The measurement of loudness,'' J. Acoust. Soc. Am. **27**, 815–827.

Stevens, S. S. (**1957**). ''Concerning the form of the loudness function,'' J. Acoust. Soc. Am. **29**, 603–606.

Stevens, S. S. (**1972**). ''Perceived level of noise by Mark VII and decibels (E),'' J. Acoust. Soc. Am. **51**, 575–601.

Stevens, S. S., and Guirao, M. G. (**1967**). ''Loudness functions under inhibition,'' Percept. Psychophys. **2**, 459–465.

Stevens, J. C., and Hall, J. W. (**1966**). ''Brightness and loudness as a function of stimulus duration,'' Percept. Psychophys. **1**, 319–327.

Zwicker, E., and Fastl, H. (**1990**). *Psychoacoustics. Facts and Models* (Springer-Verlag, New York).

Zwislocki, J. J. (**1965**). ''Analysis of some auditory characteristics,'' in *Handbook of Mathematical Psychology*, edited by R. D. Luce, R. R. Bush, and E. Galanter (Wiley, New York), pp. 1–97.

Zwislocki, J. J. (**1969**). ''Temporal summation of loudness: an analysis,'' J. Acoust. Soc. Am. **46**, 431–441.

Across-channel intensity discrimination in the presence of an interferer

Nicholas I. Hill[a] and Peter J. Bailey
Department of Psychology, University of York, York YO10 5DD, United Kingdom

(Received 8 July 1997; accepted for publication 22 April 1998)

Listeners' thresholds for discriminating changes in the relative intensities of two octave-spaced pure tones were measured in three conditions using a 2AFC procedure. In the baseline condition the tone pair was presented alone, while in the two *interference* conditions the tone pair was accompanied by four additional tones, with the frequency separation between adjacent components of the resultant six-component complex being one octave. In the interference conditions the flanking components were either gated synchronously with the target pair, or began 200 ms ahead. The level of the flanking components relative to the target was randomized on each presentation. The overall stimulus level was also randomized on each presentation to reduce the effectiveness of within-channel comparisons. Threshold elevations in the synchronous condition relative to the baseline ranged from approximately 5 to 17 decibels. By contrast, in the asynchronous condition only one listener showed significant (although substantially reduced) interference. The results complement previous observations that across-channel intensity comparisons are poorer between components that begin or end at different times, and are qualitatively consistent with the hypothesis that temporal misalignment promotes the perceptual segregation of simultaneous frequency components. [S0001-4966(98)02708-8]

PACS numbers: 43.66.Dc, 43.66.Fe, 43.66.Ba [JWH]

INTRODUCTION

It is widely accepted, based on considerable psychophysical and physiological evidence, that the auditory periphery functions as a frequency analyzer with energy in different spectral regions being processed in distinct, frequency-specific channels (e.g., Fletcher, 1940; Scharf, 1970). This raises the question of whether and to what extent information in the different channels interacts at higher levels in the auditory system. Among the paradigms that have been used to investigate this issue is that of auditory profile analysis pioneered by Green and colleagues (Spiegel *et al.*, 1981; Green *et al.*, 1983; see Green, 1988 for a review). In a typical profile analysis experiment, a multitone complex is presented in each of two observation intervals, with listeners required to indicate the interval in which the relative level of one component (the target) was increased. To reduce the effectiveness of loudness cues, the overall level of the stimulus is randomized between presentations. The results from such studies indicate that under conditions of minimal uncertainty, thresholds for detecting across-frequency differences in intensity are similar to those obtained in traditional intensity discrimination tasks using sequential presentation and no within-trial randomization of level (e.g., Jesteadt *et al.*, 1977).

Consistent with the hypothesis that the auditory system only combines information fully across those frequency components for which there is evidence of a common source (e.g., Bregman and Pinker, 1978; Darwin, 1984; Darwin and Ciocca, 1992), several profile analysis studies have reported results which suggest that the ability of listeners to compare relative intensities across frequency is impaired by manipulations which promote perceptual segregation of the target and flanking components. Such manipulations include presenting the target and flanking components to different ears (Green and Kidd, 1983; Bernstein and Green, 1987), applying different patterns of frequency modulation to the target and flanking components (Green and Nguyen, 1988; Dai and Green, 1991), and gating the target and flanking components on at different times (Green and Dai, 1992; Hill and Bailey, 1997, 1998). Conversely, Green and Forest (1986) found that in the absence of cues to segregation, listeners were apparently unable to ignore the presence of a random-amplitude frequency component when detecting an increment in the central component of a 21-component complex. The effectiveness of the masker component increased with increasing proximity to the target, the average increase in threshold attributable to the uncertainty in spectral shape being approximately 5 dB.

While the issue of across-frequency interference effects in profile analysis has been largely ignored, there have been numerous demonstrations and investigations of other interference phenomena. These include so-called binaural interference (e.g., Dye, 1990; Trahiotis and Bernstein, 1990; Woods and Colburn, 1992), and modulation detection/discrimination interference (e.g., Yost and Sheft, 1989; Yost *et al.*, 1989; Bacon and Moore, 1993). The presence of extraneous frequency components has also been shown to impair the detection of tones in noise (e.g., Neff and Green, 1987; Neff and Callaghan, 1988) and affects adversely traditional intensity discrimination when the frequencies of the extraneous components are selected randomly on each presentation (Neff and Jesteadt, 1996). In many cases the detrimental effect of extraneous energy can be reduced either by

[a]Corresponding author, Electronic mail: nih1@york.ac.uk

gating the interferer asynchronously (e.g., Hall and Grose, 1991; Moore and Jorasz, 1992; Neff, 1995) or else presenting the interferer continuously throughout a block of trials (Hall and Grose, 1990; Bernstein and Trahiotis, 1995).

The first objective of the current experiment was to determine whether, as suggested by the results of Green and Forest (1986), listeners' ability to discriminate the relative levels of a pair of tones was impaired by the presence of an interfering signal. Assuming that interference did result, the second objective was to assess whether interference could be reduced by gating the interferer on ahead of the tone pair. Three conditions were tested: a baseline condition in which only the target tone and a single referent tone were presented, a *synchronous* interferer condition in which a four-component interferer began and ended at the same time as the target and referent tones, and an *asynchronous* interferer condition in which the interferer was gated on ahead of the other tones. The amplitudes of the components of the interferer were equal to one another, but variable with respect to the target and referent. If listeners were able to compare the levels of the target and referent even in the presence of extraneous energy, then there should be little difference in threshold between the three conditions. However, if listeners combine information across all components for which there is evidence of a common source, then one would expect thresholds to be elevated in the synchronous interferer condition relative to the other two.

I. EXPERIMENT

A. Listeners

The four listeners were aged between 20 and 30 years. All listeners had normal pure-tone thresholds over the range of frequencies used in this experiment. All participants were experienced profile listeners. Listener NH was the first author. The remaining listeners were students at the university and received payment.

B. Stimuli and equipment

The stimulus in the baseline condition consisted of a 1200-Hz target tone and a 600-Hz referent. In the two interference conditions this tone pair was accompanied by four equal-level interferer tones at frequencies of 150, 300, 2400, and 4800 Hz. In all three conditions, the signal was an increment in the level of the 1200-Hz target component. Except in the asynchronous interferer condition, all tones had a duration of 200 ms and were gated on and off at the same time. In the asynchronous condition, the duration of the interferer tones was increased to 400 ms, with the onset of the interferer preceding that of the target and referent by 200 ms. All durations included 10-ms $\cos^2$ onset and offset ramps. To render comparisons of intensity between the target and interferer tones unreliable, the level of the interferer relative to the target was selected randomly on each presentation from a uniform distribution spanning a 20-dB range. The mid-point of the distribution of interferer levels corresponded to the level of the unincremented target such that the maximum level difference between the target component and a component of the interferer in the nonsignal interval was ± 10 dB. To reduce the effectiveness of within-channel loudness cues, the overall level of the stimuli was also selected randomly on each presentation. These levels were again selected from a uniform distribution spanning a 20-dB range, with the level of the target and referent components at the mid-point of this range being 55 dB SPL. The starting phases of the tones were randomized on each presentation.

Stimuli were synthesized in real time at a sampling rate of 20 kHz using custom software running on an IBM-compatible PC. The resulting waveforms were converted to voltages using 16-bit DACs (TDT model DD1) and were low-pass filtered at 8 kHz (TDT model FT5). The overall level of the stimuli was controlled using a pair of attenuators (TDT model PA4) having a resolution of 0.1 dB. The level of the interferer relative to the referent was adjusted in software. Stimuli were presented diotically over Sennheiser HD414 headphones. Listeners were run individually in a sound-attenuating enclosure.

C. Procedure

Thresholds were determined using a two-alternative, forced-choice, adaptive procedure employing a 3-down, 1-up rule which targeted the level increment corresponding to 79% correct responses (Levitt, 1971). Each 80-trial run began with the size of the intensity increment, defined as $10\log(1+\Delta I/I)$, set to 10 dB. During a run the magnitude of the increment was varied logarithmically with an initial ratio of 0.7225. This ratio was increased to 0.85 following the first error so as to increase the resolution of the adaptive procedure near threshold. For example, if the first three responses in a run were correct, the level increment would be reduced to 7.225 dB (0.7225×10.0 dB). An error on the following trial would result in the increment being set to 8.50 dB (7.225 dB/0.85). The data corresponding to the first three or four reversals in each run were ignored, estimated threshold being based on the average intensity increment over the remaining even number of reversals. A typical threshold estimate was based on an average of 8–14 reversals. In each session listeners completed eight runs of the adaptive procedure, which lasted approximately 45 mins.

The beginning of each trial was signaled by the presentation of a visual alerting signal in the center of a computer screen for 200 ms. In the baseline and synchronous interferer conditions, the first observation interval followed 700 ms after the offset of the alerting signal, and the inter-stimulus interval was also 700 ms. In the asynchronous interferer condition these intervals were reduced to 500 ms so that the overall duration of a trial was fixed across the three conditions. Listeners were given an unlimited time in which to respond, immediately after which they were presented with feedback for 400 ms. The next trial began 1 s after the termination of feedback.

So far as was possible listeners participated five days per week over a period of approximately four weeks. On any given session the same condition was presented on each of the eight runs in order to minimize effects of uncertainty. Listeners completed six sessions (3840 trials) in each condition with the conditions rotated daily. For consistency with the majority of profile analysis studies the threshold level

TABLE I. Threshold signal-to-pedestal ratio and associated standard error for each listener and condition derived from the final two sessions of data collection per condition. Also shown are the pairwise differences between performance in the three conditions.

Listener	Threshold (dB)						Difference (dB)		
	Sync		Async		None		Sync-None	Async-None	Sync-Async
AC	−9.47	(0.58)	−13.83	(0.41)	−14.37	(0.55)	4.90	0.54	4.36
NH	−6.59	(0.76)	−13.98	(0.29)	−15.72	(0.60)	9.13	1.74	7.39
HB	4.58	(0.71)	−14.12	(0.61)	−12.35	(0.86)	16.93	−1.77	18.70
AK	4.82	(0.70)	−5.48	(0.48)	−12.16	(0.34)	16.98	6.68	10.30

increment for each run was converted to the corresponding signal-to-pedestal ratio in decibels [defined as $20 \log(\Delta A/A)$] before averaging.

D. Results

Table I shows the threshold signal-to-pedestal ratio and associated standard error for each listener and condition derived from the final two sessions per condition. Also shown are the pairwise differences between performance in the three conditions. For all listeners, discrimination thresholds were higher in the synchronous interferer condition than in the baseline condition, the magnitude of the impairment ranging from approximately 5 dB for listener AC up to almost 17 dB for listeners AK and HB. Gating the interferer on 200 ms ahead of the target and referent resulted in improved performance for all listeners, with only AK having thresholds more than 2 dB higher than in the baseline condition.

For a 3-down, 1-up adaptive procedure and a level variation of 20 dB, the theoretical lower limit on threshold for a listener basing his/her decision purely on across-interval comparisons of loudness is 2.13 dB.[1] With the exception of listeners HB and AK in the synchronous interferer condition, all thresholds were below this limit indicating that in most cases some use was being made of within-interval, across-frequency comparisons of intensity (i.e., spectral cues). Since the level of the interferers relative to the target was roved independently of the overall level, listeners could theoretically achieve a threshold below 2.13 dB without utilizing the referent tone, by combining both level and spectral cues. Such a strategy would predict a lower limit on performance of −2.45 dB.[2] Since the highest threshold in the asynchronous interferer condition was −5.48 dB, all listeners must have been utilizing the referent tone in this condition. Overall performance in the baseline condition was comparable to that reported by Dai and Green (1992) and Versfeld and Houtsma (1995) for similarly spaced two-tone complexes after correcting for differences in targeted threshold.

Listener AC showed the largest effects of practice, with thresholds in all three conditions improving over the six sessions. This improvement ranged from approximately 8 dB in the synchronous interferer condition to just under 3 dB in the asynchronous interferer condition. Of the remaining listeners, NH displayed an improvement of approximately 4 dB in the synchronous interferer condition, while HB improved by nearly 6 dB in the asynchronous interferer condition. The relatively small effects of practice probably reflect the fact that these listeners had considerable prior experience in profile analysis tasks, albeit using different stimuli.

E. Discussion

Thresholds for all listeners were elevated when the interferer was gated synchronously with the target and referent. This result replicates the earlier finding of Green and Forest (1986) and suggests that such interference cannot be overcome even with substantial practice using the same interferer. By comparison with performance in the baseline condition, there were marked quantitative differences in the amount of masking in the synchronous interferer condition. Similar variability has also been observed in other interference paradigms (e.g., Neff and Callaghan, 1988), and may reflect the use of different strategies on the part of the listeners. For example, listeners could base their decision on spectral cues, level cues, or a combination of the two.

Given that the frequency components were spaced at octave intervals, it would appear unlikely that the increase in threshold in the synchronous interference condition resulted entirely from within-channel masking. For example, masking pattern data (Egan and Hake, 1950) and estimates of auditory filter shape derived from the notched-noise method (Moore *et al.*, 1990) suggest that the masking effect of the 300-Hz component of the interferer would have been reduced by approximately 30 dB at the frequency of the referent tone. A more likely explanation for the observed pattern of results is that listeners were unable to exclude the synchronously gated interferer components from the decision process. That is, in the absence of cues to segregation, listeners were basing their decision on a perceptual attribute derived from an integration of intensity information across all frequency components. This interpretation is qualitatively consistent with the model of auditory object formation proposed by Woods (1990). According to this model, the perceptual attributes of an object are derived from a weighted average of auditory information across frequency, the weight assigned to a given component reflecting the probability of that component belonging to the attended object. This probability is hypothesized to depend on such factors as similarity of onset, and harmonicity.

The reduction in the effect of the interferer when it was gated on ahead of the target and referent is consistent with a number of previous demonstrations of beneficial effects of asynchrony in other across-frequency interference paradigms including modulation detection and discrimination interference (Hall and Grose, 1991; Moore and Jorasz, 1992) and

informational masking (Neff, 1995). However, the result contrasts with the failure to find consistent effects of asynchrony in binaural interference paradigms (e.g., Woods and Colburn, 1992; Stellmack and Dye, 1993; Bernstein and Trahiotis, 1995).

Previous studies of the effect of asynchrony in profile analysis tasks have shown that the presence of an asynchrony between the spectral components or regions being compared leads to an elevation in threshold relative to the situation in which all components begin and end at the same time (Green and Dai, 1992; Hill and Bailey, 1997, 1998). The present experiment complements these earlier studies, providing further evidence that, in the case of timbre perception, onset asynchrony is an effective cue for segregating concurrent frequency components. The results of the present experiment also suggest that the reduction in performance as a result of asynchrony observed in previous profile analysis studies was not due to a simple distracting effect, since in the present experiment thresholds were actually lower in the asynchronous condition.

While the present experiment used stimuli that were harmonically related, the result of Green and Forest (1986) suggests that this is an unnecessary condition for interference. Nonetheless, it is possible that the magnitude of the interference in the present experiment was enhanced by the existence of a harmonic relationship. Conversely, presenting the interferer with a different fundamental frequency to the target pair may be an effective way of reducing interference even when the extraneous energy is gated synchronously (e.g., Buell and Hafter, 1991).

In summary, the results of the present experiment indicate that listeners' ability to discriminate the relative intensities of frequency components in one frequency region is impaired by the presence of synchronously gated energy elsewhere in the frequency spectrum. The interference persisted despite nearly 4000 trials of practice, although there was some improvement for two of the four listeners. Gating the extraneous energy on ahead of the critical components either reduced (one listener) or abolished (three listeners) the interference. The results are consistent with an explanation in terms of perceptual grouping of simultaneous frequency components.

ACKNOWLEDGMENTS

The authors would like to thank the two anonymous reviewers for their constructive comments on an earlier version of this manuscript. Financial support was provided by the U.K. Medical Research Council, Grant No. G9436832N.

[1]This limit is based on the assumption that the loudness of the target tone is used as the cue to detection (Green, 1988). If the overall loudness of the stimulus is used as the cue, then the theoretical lower limit would be elevated for the interference conditions due to the additional variability in the level of the interferer.

[2]The two cues could be combined using a decision rule which selected whichever of the two measures (target level versus target *re*: interferer level) differed most across the two intervals. The probability of correctly identifying the target interval using this strategy, p, is given by

$$p=(1/6)(12r^4-16r^3+8r+3),$$

where $r=$ target increment in decibels /20, $0\leqslant r\leqslant 0.5$.

Solving this equation numerically with $p=0.7937$ yields a lower limit on threshold of -2.45 dB using the signal-to-pedestal measure.

Bacon, S. P., and Moore, B. C. J. (**1993**). ''Modulation detection interference: Some spectral effects,'' J. Acoust. Soc. Am. **93**, 3442–3453.
Bernstein, L. R., and Green, D. M. (**1987**). ''The profile-analysis bandwidth,'' J. Acoust. Soc. Am. **81**, 1888–1895.
Bernstein, L. R., and Trahiotis, C. (**1995**). ''Binaural interference effects measured with masking-level difference and with ITD- and IID-discrimination paradigms,'' J. Acoust. Soc. Am. **98**, 155–163.
Bregman, A. S., and Pinker, S. (**1978**). ''Auditory streaming and the building of timbre,'' Can. J. Psychol. **32**, 19–31.
Buell, T. N., and Hafter, E. R. (**1991**). ''Combination of binaural information across frequency bands,'' J. Acoust. Soc. Am. **90**, 1894–1900.
Dai, H., and Green, D. M. (**1991**). ''Effect of amplitude modulation on profile detection,'' J. Acoust. Soc. Am. **90**, 836–845.
Dai, H., and Green, D. M. (**1992**). ''Auditory intensity perception: Successive versus simultaneous, across-channel discriminations,'' J. Acoust. Soc. Am. **91**, 2845–2854.
Darwin, C. J. (**1984**). ''Perceiving vowels in the presence of another sound: Constraints on formant perception,'' J. Acoust. Soc. Am. **76**, 1636–1647.
Darwin, C. J., and Ciocca, V. (**1992**) ''Grouping in pitch perception: Effects of onset asynchrony and ear of presentation of a mistuned component,'' J. Acoust. Soc. Am. **91**, 3381–3390.
Dye, R. H. (**1990**). ''The combination of interaural information across frequencies: Lateralization on the basis of interaural delay,'' J. Acoust. Soc. Am. **88**, 2159–2170.
Egan, J. P., and Hake, H. W. (**1950**). ''On the masking pattern of a simple auditory stimulus,'' J. Acoust. Soc. Am. **22**, 622–630.
Fletcher, H. (**1940**). ''Auditory patterns,'' Rev. Mod. Phys. **12**, 47–65.
Green, D. M. (**1988**). *Profile Analysis: Auditory Intensity Discrimination* (Oxford U.P., Oxford).
Green, D. M., and Dai, H. (**1992**). ''Temporal relations in profile comparisons,'' in *Auditory Physiology and Perception*, edited by Y. Cazals, L. Demany, and K. Horner (Pergamon, Oxford), pp. 471–477.
Green, D. M., and Forest, T. G. (**1986**). ''Profile analysis and background noise,'' J. Acoust. Soc. Am. **80**, 416–421.
Green, D. M., and Kidd, Jr., G. (**1983**). ''Further studies of auditory profile analysis,'' J. Acoust. Soc. Am. **73**, 1260–1265.
Green, D. M., and Nguyen, Q. T. (**1988**). ''Profile analysis: Detecting dynamic spectral changes,'' Hearing Res. **32**, 147–164.
Green, D. M., Kidd, Jr., G., and Picardi, M. C. (**1983**). ''Successive versus simultaneous comparison in auditory intensity discrimination,'' J. Acoust. Soc. Am. **73**, 639–643.
Hall, J. W., and Grose, J. H. (**1990**). ''Comodulation masking release and auditory grouping,'' J. Acoust. Soc. Am. **88**, 119–125.
Hall, J. W., and Grose, J. H. (**1991**). ''Some effects of auditory grouping factors on modulation detection interference (MDI),'' J. Acoust. Soc. Am. **90**, 3028–3035.
Hill, N. I., and Bailey, P. J. (**1997**). ''Profile analysis with an asynchronous target: Evidence for auditory grouping,'' J. Acoust. Soc. Am. **102**, 477–481.
Hill, N. I., and Bailey, P. J. (**1998**). ''Relative intensity comparisons between a tone and spectrally remote noise: Effects of onset asynchrony,'' J. Acoust. Soc. Am. **103**, 1075–1079.
Jesteadt, W., Wier, C. C., and Green, D. M. (**1977**). ''Intensity discrimination as a function of frequency and sensation level,'' J. Acoust. Soc. Am. **61**, 169–177.
Levitt, H. (**1971**). ''Transformed up-down methods in psychoacoustics,'' J. Acoust. Soc. Am. **49**, 467–477.
Moore, B. C. J., and Jorasz, U. (**1992**). ''Detection of changes in modulation depth of a target sound in the presence of other modulated sounds,'' J. Acoust. Soc. Am. **91**, 1051–1061.
Moore, B. C. J., Peters, R. W., and Glasberg, B. R. (**1990**). ''Auditory filter shapes at low center frequencies,'' J. Acoust. Soc. Am. **88**, 132–140.
Neff, D. L. (**1995**). ''Signal properties that reduce masking by simultaneous, random-frequency maskers,'' J. Acoust. Soc. Am. **98**, 1909–1920.
Neff, D. L., and Callaghan, B. P. (**1988**). ''Effective properties of multicomponent simultaneous maskers under conditions of uncertainty,'' J. Acoust. Soc. Am. **83**, 1833–1838.
Neff, D. L., and Green, D. M. (**1987**). ''Masking produced by spectral uncertainty with multicomponent maskers,'' Percept. Psychophys. **41**, 409–415.
Neff, D. L., and Jesteadt, D. M. (**1996**). ''Intensity discrimination in the

presence of random-frequency, multicomponent maskers and broadband noise,'' J. Acoust. Soc. Am. **100**, 2289–2298.
Scharf, B. (**1970**). ''Critical bands,'' in *Foundations of Modern Auditory Theory*, Vol. I, edited by J. V. Tobias (Academic, New York), pp. 159–202.
Spiegel, M. F., Picardi, M. C., and Green, D. M. (**1981**). ''Signal and masker uncertainty in intensity discrimination,'' J. Acoust. Soc. Am. **70**, 1015–1019.
Stellmack, M. A., and Dye, R. H. (**1993**). ''The combination of interaural information across frequencies: The effects of number and spacing of components, onset asynchrony, and harmonicity,'' J. Acoust. Soc. Am. **93**, 2933–2947.
Trahiotis, C., and Bernstein, L. R. (**1990**). ''Detectability of interaural delays over select spectral regions: Effects of flanking noise,'' J. Acoust. Soc. Am. **87**, 810–813.
Versfeld, N. J., and Houtsma, A. J. M. (**1995**). ''Discrimination of changes in the spectral shape of two-tone complexes,'' J. Acoust. Soc. Am. **98**, 807–816.
Woods, W. S. (**1990**). ''Development and test of a model of auditory segregation of a harmonic component,'' unpublished masters dissertation, Boston University.
Woods, W. S., and Colburn, H. S. (**1992**). ''Test of a model of auditory object formation using intensity and interaural time difference discrimination,'' J. Acoust. Soc. Am. **91**, 2894–2902.
Yost, W. A., and Sheft, S. (**1989**). ''Across-critical-band processing of amplitude-modulated tones,'' J. Acoust. Soc. Am. **85**, 848–857.
Yost, W. A., Sheft, S., and Opie, J. (**1989**). ''Modulation interference in detection and discrimination of amplitude modulation,'' J. Acoust. Soc. Am. **86**, 2138–2147.

Psychophysical suppression as a function of signal frequency: Noise and tonal maskers[a)]

Jungmee Lee and Sid P. Bacon[b)]
Psychoacoustics Laboratory, Department of Speech and Hearing Science, P.O. Box 871908, Arizona State University, Tempe, Arizona 85287-1908

(Received 28 July 1997; revised 10 November 1997; accepted 13 April 1998)

Physiological studies have suggested that the basal region of the cochlea is more nonlinear than the apical region. To evaluate this possibility psychophysically, suppression was investigated across signal frequency (250, 500, 1000, 2000, and 4000 Hz) in a forward-masking paradigm using both noise and tonal maskers/suppressors. Masker duration was 200 ms, signal duration was 20 or 40 ms, and signal delay was 0 or 20 ms; the longer delay was necessary to eliminate potential confusion effects observed with the (narrow-band) noise masker. When using a noise masker (spectrum level of 40 dB), suppression was determined by comparing the threshold in the presence of a broadband masker with that in the presence of a critical band (ERB) masker. When using a tonal masker (masker level of 50 dB SPL, suppressor level of 70 dB SPL, with the suppressor frequency being 1.2 times the masker/signal frequency), suppression was determined by comparing the threshold in the presence of the masker plus suppressor with that in the presence of the masker alone. The magnitude of suppression was determined either by the measured change in signal threshold or by the inferred change in masker level. Regardless of how suppression was quantified, for both masker types, the amount of suppression increased as signal frequency increased up to about 1000 Hz, but then reached an asymptote or decreased somewhat as signal frequency increased to 4000 Hz. The magnitude of suppression was much larger with a noise masker than with a tonal masker, which could be a result of the different number of components in the masker which might serve as a suppressor. [S0001-4966(98)02308-X]

PACS numbers: 43.66.Dc, 43.66.Mk [RVS]

INTRODUCTION

Since Rhode's (1971) important demonstration of nonlinear basilar membrane motion in the squirrel monkey, it has become increasingly clear that the healthy peripheral auditory system is highly nonlinear. The results of physiological studies have suggested that the basal regions of the basilar membrane behave more nonlinearly than the apical regions (e.g., Rhode, 1977; Ruggero *et al.*, 1992; Rhode and Cooper, 1993; Cooper and Rhode, 1995). Because most studies of basilar membrane nonlinearity have concentrated on the basal region (e.g., Rhode, 1977; Ruggero *et al.*, 1992; Rhode and Cooper, 1993), however, it is difficult to determine if there are differences in the extent of the nonlinearity at the basal and apical regions of the cochlea. However, Cooper and Rhode (1995) recently studied basilar membrane mechanics at the apical regions (characteristic frequencies were between 200 and 350 Hz) of the guinea pig cochlea, and found compressive input–output functions above 80 dB SPL in only 5 of 17 preparations, and two-tone suppression in only 1 of 5 preparations. Their results contrast with those observed in other studies at the basal region, where compressive input–output functions were observed at levels above 60–70 dB SPL and two-tone suppression was observed in most preparations. Their results suggest, therefore, that the nonlinearity may be more dominant at the basal region than at the apical region of cochlea.

Insight into basilar membrane nonlinearity can be obtained by studying firing rate responses of auditory nerve fibers (e.g., Schmiedt *et al.*, 1980; Delgutte, 1990; Yates *et al.*, 1990; Javel, 1994). Schmiedt *et al.* (1980) measured two-tone suppression in the gerbil auditory nerve using excitor tones at characteristic frequencies (CFs) ranging from about 1000–12 000 Hz, and suppressor tones located above CF. They found that the amount of suppression increased with increasing CF, and, in particular, that fibers with CFs between 4000 and 12 000 Hz showed the strongest suppression. Consistent with those results, Delgutte (1990) found that two-tone suppression varies as a function of CF in the cat auditory nerve. Using suppressor frequencies below CF, he found that fibers with CFs greater than 2000 Hz showed as much as 40–50 dB of suppression, whereas fibers with CFs less than 2000 Hz showed less than 20–30 dB of suppression. Finally, Javel (1994) measured tuning curves in cat auditory nerve fibers, and fitted those curves with a computational model. He found that the magnitude of the compressive component in his model had to increase with increasing CF in order to fit his tuning curve data.

Psychophysical suppression can be observed when the effectiveness of a masker is reduced by the presence of an additional stimulus (suppressor). Since Houtgast (1973) investigated two-tone suppression using the pulsation threshold technique, it has been extensively studied using several different psychophysical paradigms and various stimuli (e.g., Shannon, 1976; Terry and Moore, 1977; Weber, 1978; We-

[a)]Portions of this research were presented at the 133rd meeting of the Acoustical Society of America [J. Lee and S. P. Bacon, ''Psychophysical suppression as a function of signal frequency,'' J. Acoust. Soc. Am. **101**, 3148(A) (1997)].

[b)]Corresponding author; electronic mail: spb@asu.edu

ber and Green, 1978; Stelmachowicz *et al.*, 1982; Fastl and Bechly, 1983; Moore and Glasberg, 1983). Most studies have concentrated on the effects of the temporal, intensive, and spectral relationship between masker and suppressor. Relatively little research has concentrated on the effect of signal frequency. Such research, however, might provide some insight into whether the degree of nonlinearity differs between the basal and apical regions of the cochlea.

In Shannon's study (1976) with tonal maskers, some subjects showed more suppression at higher signal frequencies than at lower frequencies, but others showed no effect of signal frequency on suppression. Because different signal durations were used for different signal frequencies (40, 20, 10, 5, and 3 ms for 500, 1000, 2000, 4000, and 6000 Hz, respectively), it is difficult to interpret his results in terms of the effect of signal frequency on suppression: the smaller amount of suppression at lower frequencies may have been due to the longer signal duration. Recently, Thibodeau and Fagelson (1993) investigated suppression at two signal frequencies (500 and 2000 Hz) using noise and tonal maskers. Consistent with the results from at least some of Shannon's subjects, they found that suppression was larger at the higher signal frequency. On the other hand, Moore and Glasberg (1983) measured suppression using noise maskers, and found more suppression at 2000 Hz than at 4000 Hz. Thus, the results in the literature suggest that there may be an effect of frequency on suppression, although that effect is unclear. To gain a better understanding of the effect of signal frequency on suppression, the present study measured psychophysical suppression over a wide range of signal frequencies (from 250–4000 Hz) with both noise and tonal maskers.

When using a noise masker, suppression was determined by comparing the threshold in the presence of a broadband masker with that in the presence of an ERB (equivalent rectangular bandwidth) masker. When using a tonal masker, suppression was determined by comparing the threshold in the presence of a two-tone masker (consisting of masker plus suppressor) with that in the presence of a one-tone masker (masker alone). The magnitude of suppression was determined either by the measured change in signal threshold or by the inferred change in masker level. The latter may provide a more accurate estimate of suppression magnitude, inasmuch as suppression may represent a reduction in the effective level of the masker (Houtgast, 1974; Shannon, 1976; Moore and Glasberg, 1983). To express suppression as a change in masker level, growth-of-masking functions for the different signal frequencies were measured for both the ERB and tonal maskers. Because growth of masking in forward masking is typically nonlinear (i.e., the slope is usually less than 1 dB/dB), the two measures of suppression will not yield identical estimates of suppression magnitude. Moreover, if the slope of the growth-of-masking function varies systematically as a function of masker/signal frequency, the pattern of results representing suppression versus frequency may depend upon whether suppression is defined as a change in threshold or a change in masker level.

I. EXPERIMENT 1: SUPPRESSION ACROSS SIGNAL FREQUENCY WITH A NOISE MASKER

A. Method

1. Subjects

Three normal-hearing subjects participated. They ranged in age from 24–31 yr. Each subject's absolute thresholds were not worse than 10 dB HL (ANSI, 1989) at any of the octave frequencies from 250–8000 Hz. All subjects had experience in other psychoacoustic experiments. One of the subjects (S1) was author JL; the other two subjects were paid an hourly wage for their participation.

2. Apparatus and stimuli

A forward-masking paradigm was used: a noise masker was followed by a sinusoidal signal. The signal frequency was 250, 500, 1000, 2000, or 4000 Hz. The signals were digitally generated and produced (TDT DA1) at a 20-kHz sampling rate. The output of the 16-bit digital-to-analog converter was low-pass filtered at 8 kHz (Kemo VBF 25.01, 135 dB/oct). The bandwidth of the noise masker was one ERB (Glasberg and Moore, 1990) or broadband (BB; 10 kHz wide). The bandwidths (in Hz) for the ERB masker at the various signal frequencies were: 60 at 250 Hz; 80 at 500 Hz; 140 at 1000 Hz; 240 at 2000 Hz; and 460 at 4000 Hz. The noise masker was created by multiplying a sinusoid (HP 8904A synthesizer) whose frequency was equal to the signal frequency (for the ERB masker) or to 5000 Hz (for the BB masker) by a low-pass-filtered (Kemo VBF 25.01) random noise (GenRad 1381).

The onsets and offsets of both masker and signal were shaped by a cosine-squared function (the analog masker was gated with a digital gating function). The duration of the masker was 200 ms, including rise/fall times of 10 ms. The duration of the signal was 20 or 40 ms, including rise/fall times of 10 or 20 ms, respectively. The 40-ms duration was used to reduce the likelihood of off-frequency listening to splatter in the signal spectrum, which could especially be a problem for the 20-ms signal at the lower signal frequencies (Moore, 1981). The delay (0-voltage points) between the masker offset and signal onset was 0 or 20 ms. The 20-ms delay was employed to effectively eliminate any ''confusion'' effects that could contaminate the threshold measurement at the 0-ms delay (Moore, 1981; Neff, 1985). Signal level was varied adaptively whereas the spectrum level of the masker was fixed at 40 dB SPL.

The growth-of-masking functions were obtained for the 20-ms signal at all signal frequencies. The spectrum level of the ERB masker ranged from 0–40 dB SPL. The delay (0-voltage points) between the masker offset and signal onset was 0 or 20 ms.

An independent BB noise was presented in the nontest ear (contralateral cue). It was gated synchronously with the masker to provide a temporal cue for the onset and, more importantly, the offset of the masker (Moore and Glasberg, 1982). The spectrum level of the cue was 10 dB SPL for the suppression phase of the experiment, and was 30 dB less than the spectrum level of the ERB masker for the growth-of-masking phase of the experiment. Because this cue was

generated by a different noise source from that which generated the masker at the test ear, there is no possibility of a masking level difference.

3. Procedure

A two-interval, forced-choice paradigm employing a three-down, one-up adaptive rule estimating 79.4% correct (Levitt, 1971) was used to measure threshold. Each run consisted of 60 trials. The initial step size of 4 dB was reduced to 2 dB after the first two reversals. The first two or three reversals were discarded (two if the total number of reversals was even, three if it was odd) and the remaining reversals were averaged to obtain the threshold estimate for that run. Threshold estimates were discarded on the rare occasions when the standard deviation of the reversals was greater than 5 dB or when there were fewer than six reversals in the mean. Each threshold reported is the mean of the estimates from at least three runs. When the standard deviation of this mean exceeded 3 dB, an additional estimate was obtained, and all estimates were averaged. This continued until the standard deviation of the estimates was less than 3 dB or until six estimates were obtained. All of the thresholds reported here had standard deviations less than 3 dB.

Subjects listened through TDH-49P headphones while seated in a soundproof room and responded by pushing one of two buttons on a response panel. Lights were used to indicate the warning interval, the two observation intervals, the response interval, and then to provide correct-response feedback.

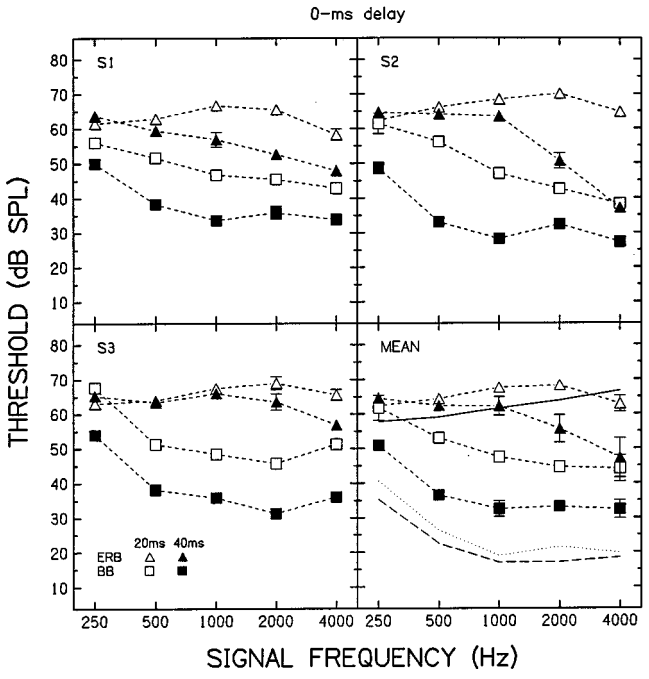

FIG. 1. Detection thresholds as a function of signal frequency for a 0-ms delay between masker offset and signal onset. The open symbols are for a 20-ms signal, and the closed symbols are for a 40-ms signal. Different symbols in each panel represent different masker conditions: triangles for the ERB masker, and squares for the BB masker. In the bottom right panel, the short- and long-dashed lines without symbols represent the group mean absolute threshold for the 20- and 40-ms signal durations, respectively. The solid line represents the overall level of the ERB masker. Error bars indicate plus and minus one standard error. Error bars for some conditions are not visible because they are smaller than the size of the symbols.

B. Results and discussion

Figure 1 shows detection thresholds as a function of signal frequency for the 0-ms signal delay condition. The individual results are shown in three panels, and the mean results in the fourth. The open symbols represent the 20-ms signal duration, and the closed symbols represent the 40-ms signal duration; the triangles are for the ERB masker, and the squares are for the BB masker. In the bottom right panel, the short- and long-dashed lines without symbols represent the group mean absolute thresholds for the 20- and 40-ms signal durations, respectively. The solid line represents the overall level of the ERB masker. Because the pattern of results was similar across subjects, only the mean data will be discussed.

In general, thresholds for the ERB masker are higher than those for the BB masker for both signal durations. The lower thresholds for the BB masker could be interpreted as reflecting suppression (Weber, 1978; Moore, 1981; Moore and Glasberg, 1983), although this interpretation should be made with some caution. Previous studies have indicated that the inherent fluctuations of a narrow-band masker can be confused with the brief signal immediately following the masker, resulting in artificially high thresholds in, for example, the ERB condition (Fastl and Bechly, 1981; Moore, 1981; Moore and Glasberg, 1982, 1983, 1985; Neff and Jesteadt, 1983; Neff, 1985, 1986). The lower thresholds for the BB condition might, therefore, simply reflect the lack of such a confusion effect. Although a contralateral cue was used here to eliminate such confusion, it may have been ineffective. It is, therefore, necessary to examine if the measurements for the ERB masker in the present study were affected by confusion.

Notice that for both signal durations, the thresholds for the BB masker follow the pattern for the absolute thresholds very well, whereas those for the ERB masker do not. Moreover, most of the thresholds for the ERB masker are higher than the overall level of the ERB masker (solid line), particularly at the lower signal frequencies. These results suggest that a confusion effect influenced the thresholds for the ERB masker, but not for the BB masker (Pastore and Freda, 1980; Moore and Glasberg, 1983; Neff, 1986), indicating that the contralateral cue was not effective in eliminating the confusion (see the Appendix for further evidence that confusion effects influenced the results for the ERB masker). Another, probably more effective, way to eliminate the confusion between the ERB masker and sinusoidal signal is to introduce a delay between the two (Moore, 1981; Neff, 1985). Based on the results of Moore (1981) and Neff (1985), a 20-ms delay was introduced between masker and signal to resolve the confusion effects that apparently influenced the results in Fig. 1. These results are shown in Fig. 2. Because the results are similar across subjects, only their mean results are discussed.

For the ERB masker, the thresholds for both the 20- and 40-ms signals are lower than the overall level of the ERB masker and follow the absolute thresholds reasonably well. These results indicate that the confusion effect was elimi-

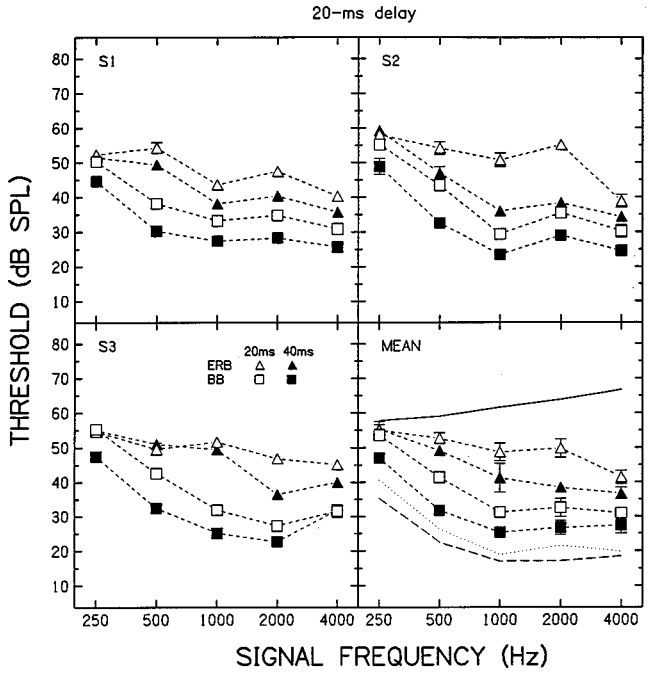

FIG. 2. As for Fig. 1, but for a 20-ms delay between masker offset and signal onset.

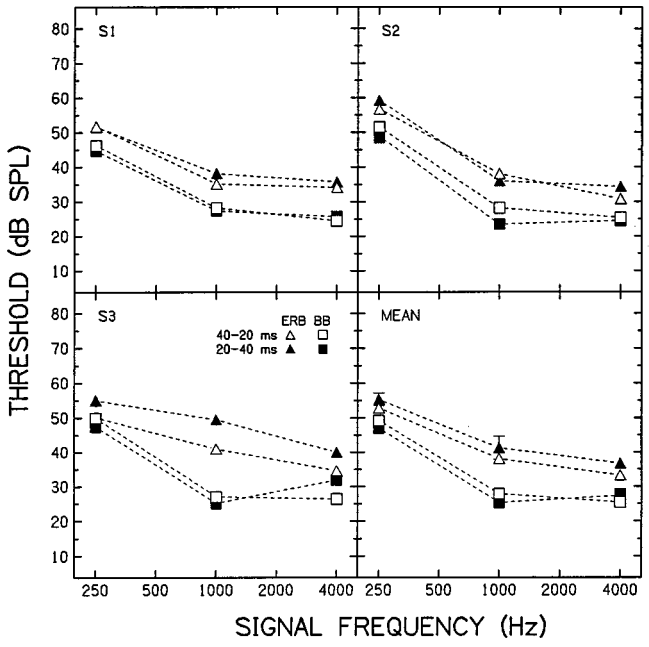

FIG. 3. Comparison between thresholds obtained with a 40-ms signal at a 20-ms delay (closed symbols), and those obtained with a 20-ms signal at a 40-ms delay (open symbols). Triangles are for the ERB masker, and squares are for the BB masker. Error bars indicate plus and minus one standard error.

nated by inserting the delay between masker offset and signal onset, consistent with the findings of Moore (1981) and Neff (1985).

The 40-ms signal was used in the present experiment in order to minimize off-frequency listening due to the detection of signal splatter, which may have been most prominent at the low signal frequencies in the presence of the ERB masker. The consequence of such off-frequency listening would be to reduce the estimate of suppression at low frequencies, and consequently invalidate the comparison of suppression across frequency. If subjects were listening off frequency in the 20-ms condition, then those thresholds might be expected to be lower than those in the 40-ms condition. In fact, thresholds for the 20-ms signal are never lower than those for the 40-ms signal at either delay (see Figs. 1 and 2), suggesting that off-frequency listening may not have been a problem after all for the 20-ms signal.

According to an energy-detection model, there should be a 3-dB decrease in threshold as the signal duration is increased from 20 to 40 ms. The absolute thresholds are in good agreement with this. The masked thresholds, however, show an improvement of anywhere from 0 to 14 dB. Although some of the change in the masked thresholds may be understood by the change in signal energy, it may be better explained by the change in *effective* signal delay that accompanies a change in signal duration. The effective signal delay may be defined as the time from masker offset to signal *offset* (recall that the delay reported here is from masker offset to signal *onset*). To evaluate whether the effect of signal duration on masked threshold can be accounted for quantitatively by a change in effective signal delay, thresholds were measured for a 20-ms signal at a 40-ms (offset to onset) delay and compared with those in Fig. 2 with a 40-ms signal at a 20-ms delay.[1] The results are shown in Fig. 3. Important here is the overlap between the open and closed symbols for a given symbol type (triangles for the ERB masker, squares for the BB masker). The results thus suggest that most of the change in masked thresholds with signal duration in Fig. 2 reflects the concomitant change in effective signal delay.

Given the possible influence of confusion effects at the 0-ms delay, suppression was calculated only for the 20-ms delay condition. The results are shown in Fig. 4. The amount of suppression was calculated by subtracting the thresholds obtained with the BB masker from those obtained with the ERB masker. Although there are some differences within and across subjects, the amount of suppression generally increases with increasing signal frequency up to 500 or 1000 Hz, and then decreases somewhat as signal frequency increases to 4000 Hz. Moore and Glasberg (1983) have also observed a smaller amount of suppression at 4000 Hz compared to 2000 Hz. The cause of this decrease in suppression at high frequencies is unclear, although it may be related to a decrease in energy at high frequencies due to the middle ear transfer function or the rolloff of the headphones at high frequencies (also see Moore and Glasberg, 1983): for these higher signal frequencies, the high-frequency (suppressor) energy in the BB masker that lies above the critical band centered at the signal frequency would be attenuated, and thus less effective. Regardless, the results from this experiment show that the amount of suppression depends on signal frequency.

The amount of suppression in Fig. 4 was defined as the difference between the thresholds in the ERB and BB conditions. If suppression, however, represents a reduction in the effective level of the masker (Houtgast, 1974; Shannon, 1976; Moore and Glasberg, 1983), it may be more appropri-

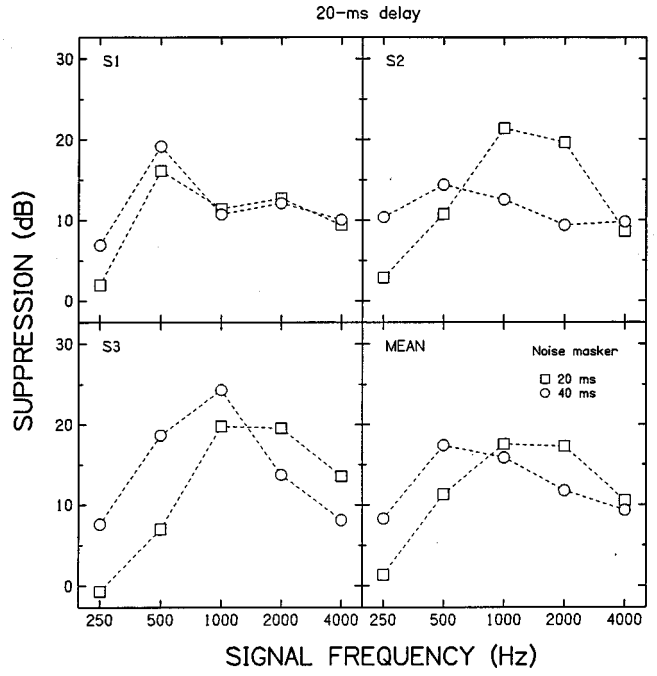

FIG. 4. Suppression as a function of signal frequency for the 20-ms delay condition. Signal duration was either 20 ms (squares) or 40 ms (circles). Suppression is calculated as the difference between threshold in the presence of the ERB masker and threshold in the presence of the BB masker.

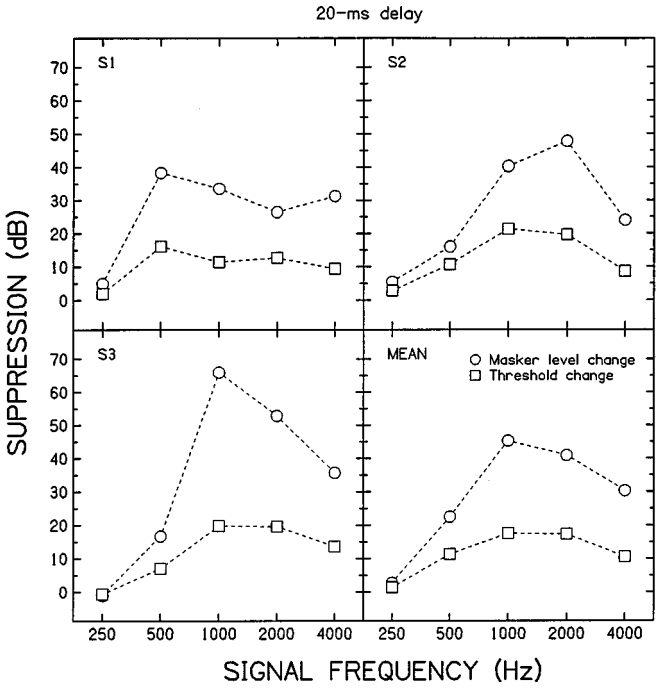

FIG. 5. Suppression as a function of signal frequency for the noise masker. Signal delay was 20 ms, and signal duration was 20 ms. Suppression is calculated in terms of a threshold change (squares, from Fig. 4) and in terms of a masker level change (circles).

ate to define suppression as a change in masker level. This can be done here by taking into account the growth-of-masking functions obtained with the ERB masker. Note, however, that these functions were obtained only for the 20-ms signal, and thus this measure of suppression is confined here to this duration. Each growth-of-masking function was fitted with a least-squares procedure including only those thresholds representing at least 5 dB of masking. Table I shows the resulting slope, y intercept, and variance (R^2) accounted for. There is no systematic change in slope across signal frequency (see Moore and Glasberg, 1983). Importantly, this suggests that the pattern reflecting the amount of suppression as a function of signal frequency will not depend upon how suppression is defined. This is shown in Fig. 5, where suppression is plotted both as a change in threshold (squares, from Fig. 4) and as a change in masker level (circles, defined as a change in threshold divided by the slope of the masking function). Although the pattern of results across signal frequency is similar for the two ways of calculating suppression, the amount of suppression is generally greater when expressed in terms of a change in masker level.

TABLE I. Individual results of the least-squares fits to the growth-of-masking functions for the ERB masker. Signal duration was 20 ms.

	Signal frequency	0-ms delay			20-ms delay		
		Slope	y intercept	R^2	Slope	y intercept	R^2
S1	250	0.82	29.2	0.97	0.40	40.2	0.97
	500	0.93	27.1	0.99	0.42	33.3	0.97
	1000	0.94	28.9	0.99	0.34	29.3	0.98
	2000	0.75	34.0	0.94	0.48	27.7	0.98
	4000	0.69	35.6	0.95	0.30	28.4	0.98
S2	250	0.57	42.3	0.97	0.52	38.4	0.99
	500	0.72	36.8	0.95	0.67	27.8	0.99
	1000	0.78	37.0	1.00	0.53	27.1	1.00
	2000	0.80	37.5	0.98	0.41	34.7	0.95
	4000	0.78	33.7	0.93	0.36	28.1	0.99
S3	250	0.76	32.5	0.98	0.63	34.0	1.00
	500	0.75	32.3	0.97	0.42	30.3	0.94
	1000	0.89	30.7	0.99	0.30	33.2	0.99
	2000	1.00	28.7	1.00	0.37	26.6	0.88
	4000	0.71	35.3	0.95	0.38	29.5	0.88

II. EXPERIMENT 2: SUPPRESSION ACROSS SIGNAL FREQUENCY WITH A TONAL MASKER

A. Method

1. Subjects

The subjects were the same as in experiment 1.

2. Apparatus and stimuli

The same forward-masking paradigm was used as in experiment 1, except that the masker was a tone. The stimuli were digitally generated and produced (TDT DA 1) at a 20-kHz sampling rate. The output of the 16-bit digital-to-analog converter was low-pass filtered at 8 kHz (Kemo VBF 25.01, 135 dB/oct).

The masker and signal frequencies were the same as one another and were equal to 250, 500, 1000, or 4000 Hz. The suppressor frequency was 1.2 times the frequency of the masker (and signal). The onsets and offsets of all stimuli were shaped by a cosine-squared function. The duration of the masker (and synchronously gated suppressor, when present) was 200 ms, including the rise/fall times of 10 ms. The duration of the signal was 20 or 40 ms, including the

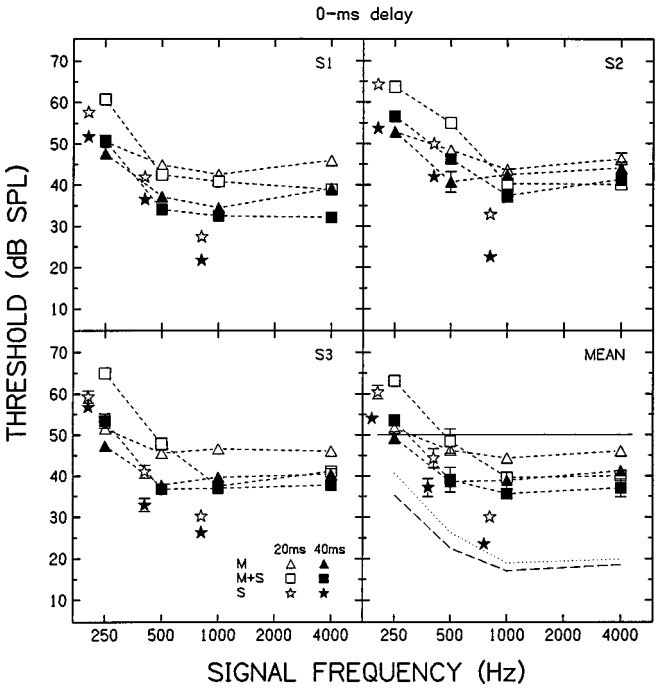

FIG. 6. Detection threshold as a function of signal frequency for a 0-ms delay condition. The open symbols are for a 20-ms signal duration, and the closed symbols are for a 40-ms duration. Different symbols in each panel represent different masker conditions: triangles for masker alone (M); squares for masker plus suppressor ($M+S$); and stars for suppressor alone (S). In the bottom right panel, the short- and long-dashed lines without symbols represent the group mean absolute threshold for the 20- and 40-ms signal durations, respectively. The solid line represents the level of the masker. Error bars indicate plus and minus one standard error.

rise/fall times of 10 or 20 ms, respectively. The delay (0-voltage points) between the masker offset and signal onset was 0 or 20 ms. Signal level was varied adaptively whereas masker and suppressor levels were fixed at 50 and 70 dB SPL, respectively.[2]

The growth-of-masking functions were measured for signal frequencies of 250, 500, 1000, or 4000 Hz. The delay (0-voltage points) between the masker offset and signal onset was 0 or 20 ms. The level of the masker ranged from 30–70 dB SPL.

The contralateral cue that was employed in experiment 1 was not used for the suppression phase of the experiment, because it did not appear effective in experiment 1, and the temporal confusion that might exist for narrow-band noise maskers and sinusoidal signals should not exist for sinusoidal maskers and signals (Neff and Jesteadt, 1983; Neff, 1986).[3] The contralateral cue was used for the growth-of-masking functions, and the spectrum level of the cue was 20 dB less than the level of the masker.

3. Procedure

The procedure was the same as in experiment 1.

B. Results and discussion

Detection thresholds for the 0-ms delay condition are plotted as a function of signal frequency in Fig. 6. The individual and mean results are shown in separate panels. The open symbols depict the results for the 20-ms signal, and the closed symbols depict those for the 40-ms signal: the triangles are for the masker alone (M), the squares are for the masker plus suppressor ($M+S$), and the stars are for the suppressor alone (S).[4] In the bottom right panel, the short- and long-dashed lines without symbols indicate the group mean absolute thresholds for the 20- and 40-ms signals, respectively. The solid line indicates the masker level. Because the results are similar across subjects, only the mean data will be discussed. Furthermore, the results obtained for the two signal durations were similar, and thus will not be described separately.

Overall, it appears that confusion effects did not affect the threshold measurements here with the 0-ms delay. In general, the masked thresholds follow the same trend across frequency as do the absolute thresholds, which is expected given that the amount of forward masking is approximately independent of frequency for a fixed-SPL masker (Jesteadt *et al.*, 1982). Moreover, most thresholds in the M condition are lower than the masker level (solid line). The exception to this is at 250 Hz, where the relatively high masked threshold may be due to the relatively high absolute threshold.

For signal frequencies of 1000 and 4000 Hz, the thresholds obtained in the $M+S$ condition are lower than those obtained in the M condition, suggesting a certain amount of suppression at these frequencies. For signal frequencies of 250 and 500 Hz, the thresholds obtained in the $M+S$ condition are nearly the same or even higher than those obtained in the M condition, suggesting that the suppressor may be producing significant amounts of masking. This is confirmed by noting that, at 250 and 500 Hz, the thresholds in the S condition (stars) are similar to those in the $M+S$ condition, indicating that the suppressor dominates the masking in the latter condition. The larger amount of masking by the suppressor at the lower frequencies is probably related to the fact that the distance on the basilar membrane between places representing the suppressor and signal (for a fixed frequency ratio) is smaller at lower frequencies than at higher frequencies (Greenwood, 1990).

Figure 7 shows the results obtained with a 20-ms delay between the masker and signal. The thresholds obtained in the M condition are lower than the level of the masker at all frequencies. The thresholds obtained in the $M+S$ condition are still clearly higher than those obtained in the M condition at 250 Hz, at least with the 20-ms signal. Thresholds obtained in the S condition indicate that this is due to masking by the suppressor.

For the most part, at both signal delays, the masked thresholds for the 40-ms signal were more than 3 dB lower than those for the 20-ms signal. As argued previously in the context of similar findings in experiment 1, this probably reflects the longer effective signal delay for the 40-ms signal. The lower thresholds for the longer signal also suggest that off-frequency listening to signal splatter probably did not influence the results presented here.

Figure 8 shows suppression as a function of signal frequency for both the 0-ms (closed symbols) and 20-ms delay (open symbols). The amount of suppression was calculated by subtracting the thresholds obtained in the $M+S$ condition from those obtained in the M condition. In general, the

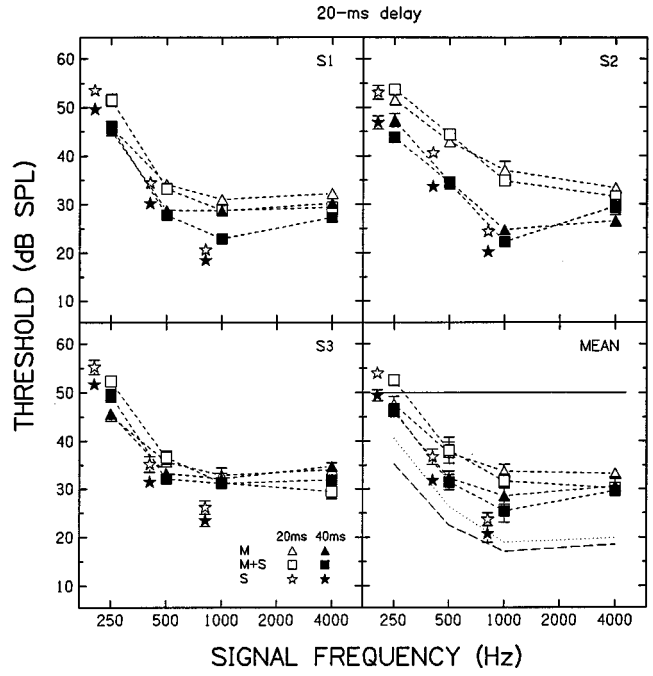

FIG. 7. As for Fig. 6, but for a 20-ms delay between masker offset and signal onset.

amount of suppression increases as the signal frequency increases from 250 to 1000 Hz, and then it remains the same (20-ms signal) or decreases slightly (40-ms signal) as frequency increases to 4000 Hz. The maximum amount of suppression was about 10 dB for the 0-ms delay and about 5 dB for the 20-ms delay, which is in line with other estimates of two-tone suppression. The negative value of suppression at 250 Hz is due to the fact that the suppressor produces more masking than the masker. This raises the question of whether

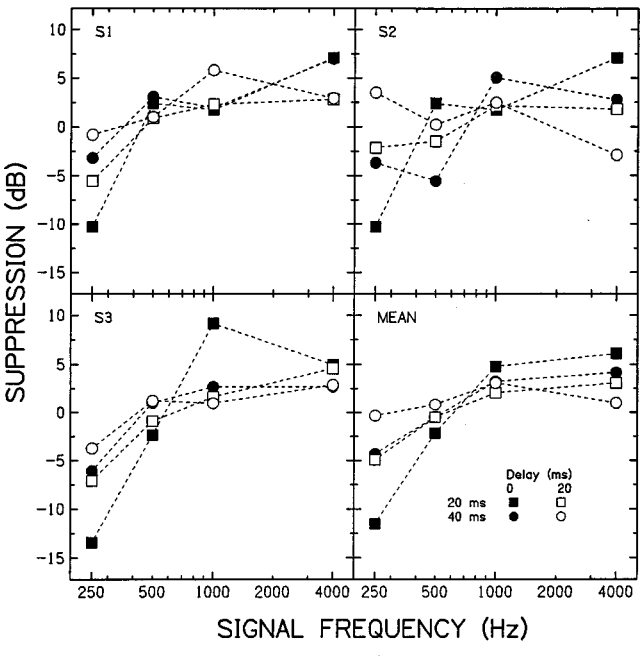

FIG. 8. Suppression as a function of signal frequency for both 0-ms (closed symbols) and 20-ms delays (open symbols). Signal duration was either 20 ms (squares) or 40 ms (circles). Suppression is calculated as the difference between threshold in the M condition and threshold in the $M+S$ condition.

TABLE II. Individual results of the least-squares fits to the growth-of-masking functions for the tonal masker. Signal duration was 20 ms.

	Signal frequency	0-ms delay			20-ms delay		
		Slope	y intercept	R^2	Slope	y intercept	R^2
S1	250	0.74	12.7	1.00	0.53	22.3	0.98
	500	0.64	13.9	0.96	0.27	24.5	0.99
	1000	0.79	7.6	1.00	0.39	16.2	0.96
	4000	0.81	9.6	0.99	0.30	20.5	0.85
S2	250	0.70	18.6	0.98	0.41	32.7	0.94
	500	0.52	21.2	0.98	0.42	19.3	0.98
	1000	0.65	12.6	0.99	0.50	10.1	0.99
	4000	0.71	11.4	0.99	0.27	19.7	0.95
S3	250	0.82	11.2	1.00	0.46	23.4	0.89
	500	0.72	8.8	0.98	0.59	7.0	0.97
	1000	0.76	7.7	1.00	0.40	16.0	0.97
	4000	1.01	−0.9	0.99	0.44	13.4	0.96

a positive amount of suppression could be measured at 250 Hz using larger suppressor/masker frequency ratios, where masking by the suppressor should be reduced. To address this, pilot data from one subject (S1) were obtained with a suppressor/masker frequency ratio ranging from 1.1–1.7. The threshold in the $M+S$ condition decreased as the ratio increased from 1.1 to 1.4, and then it remained nearly constant at a value similar to the threshold obtained in the M condition as the ratio increased to 1.7. These results suggest that the lack of suppression at 250 Hz was not due to our choice of a suppressor/masker frequency ratio of 1.2.

Suppression also can be calculated as a change in effective masker level, by taking into account the growth-of-masking functions for the masker alone. As in experiment 1, these functions were fitted with a least-squares procedure including only those thresholds representing at least 5 dB of masking. Table II shows the resulting slope, y intercept, and variance accounted for (R^2). Consistent with previous results (Jesteadt *et al.*, 1982; Moore and Glasberg, 1983), there is no systematic change in the slope of the masking function across signal frequency. Figure 9 shows suppression magnitude plotted both as a change in masker level and as a change in threshold (replotted from Fig. 8). The effect of signal frequency is similar, regardless of how suppression is defined, although the amount of suppression is generally greater when suppression is expressed as a change in masker level.

The amount of suppression observed in experiment 2 with a tonal masker is smaller than that observed in experiment 1 with a noise masker (compare Figs. 4 and 8). The difference may be related to the number of components in the masker, and in particular to the number of components in the masker which might serve as a suppressor.[5] Duifhuis (1980) compared the amount of suppression produced by two suppressors with that produced by either suppressor alone. He sometimes found more suppression with two suppressor components than with either one by itself (also see Weber, 1984). Viemeister and Bacon (1982) also found more suppression with a multicomponent harmonic complex than with a four-component harmonic complex. To evaluate the possibility that the larger amounts of suppression observed with the noise masker were due to the larger number of com-

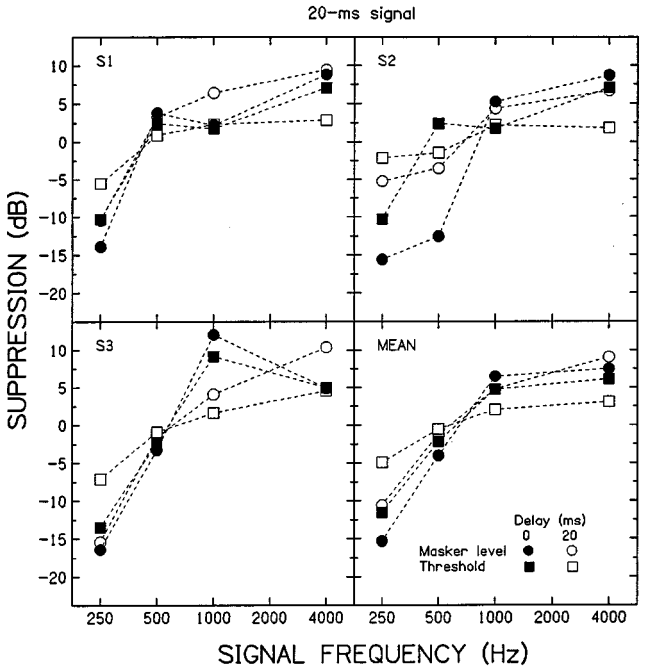

FIG. 9. Suppression as a function of signal frequency for the tonal masker for both 0-ms (closed symbols) and 20-ms delays (open symbols). Signal duration was 20 ms. Suppression is calculated in terms of a threshold change (squares, from Fig. 8) and in terms of a masker level change (circles).

ponents in the masker, pilot data on the effects of number of components were obtained from two subjects (S1 and S2). The masker and signal frequency was 1000 Hz, and the masker level was 40 dB SPL. Three suppression conditions were run. In the first, there was only one suppressor component (1200 Hz). In the second, there were 102 suppressor components, 51 on each side of the masker, spaced at 2-Hz intervals (700–800 Hz on the low side; 1200–1300 Hz on the high side). In the third, there were 202 suppressor components, 101 on each side of the masker, spaced at 2-Hz intervals (600–800 Hz on the low side; 1200–1400 Hz on the high side). When there was only one suppressor component, its level was 60 dB SPL; when there were multiple components, the level of each component was 40 dB SPL. Thus, the overall level of the suppressor was about the same in all conditions. The masker duration was 200 ms, and the signal duration was 20 ms. The average amount of suppression (measured as a change in signal threshold) in the three conditions was 2.6, 5.2, and 12 dB, respectively. In terms of a change in effective masker level, this would correspond to a change in suppression from about 5 to 28 dB. These results are thus consistent with the possibility that the difference in amount of suppression between experiments 1 and 2 is due to the number of suppressor components in the masker.[6]

III. GENERAL DISCUSSION

The major purpose of this study was to investigate the effect of signal frequency on psychophysical suppression. The results from experiments 1 (noise masker) and 2 (tonal masker) suggest that suppression increases as a function of frequency from 250 to about 1000 Hz, beyond which it either decreases slightly (noise masker) or remains the same (tonal masker).[7] These results are consistent with those of Thibodeau and Fagelson (1993), who found smaller amounts of suppression at 500 Hz than at 2000 Hz. They are also consistent with the results of some of the subjects in Shannon (1976).

Before considering the implication of the present results, it is worth considering whether they reflect ''true'' differences in suppression across frequency, or whether they might instead reflect some other differences across frequency. An obvious concern is that they could reflect differences in the sensation level (SL) of the masker, given the form of the normal audibility curve. In particular, if the amount of suppression increased with increasing (sensation) level, then one would expect greater suppression at mid to high frequencies, simply because the SL of the masker (and suppressor) would be higher at those frequencies than it would be at low frequencies. The literature suggests, however, that suppression is not strongly influenced by SL. For example, for suppressor/masker frequency ratios greater than 1.0, Shannon (1976) found a roughly constant amount of suppression as the masker level increased from 30 to 70 dB SPL (suppressor level always 20 dB greater than the masker level, as in the present study). Furthermore, Moore and Glasberg (1983) reported that the slopes of the growth-of-masking functions for narrow-band and broadband maskers were not significantly different from one another, and thus the estimate of suppression (either as a threshold change or a masker level change) would not be expected to depend upon noise level. However, according to Weber's data (1978), the growth of masking may be steeper for narrow-band than for broadband maskers, suggesting that suppression might increase with increasing noise level. Thus, to evaluate the possibility that SL may have influenced our comparison of suppression across frequency, we obtained pilot data from one subject (S1) in a condition where the SL of the noise masker at the 1000-Hz signal frequency was equated to the SL of the noise at the 250-Hz signal frequency.[8] The amount of suppression at 1000 Hz was unaffected by the decrease in level, suggesting that the larger amount of suppression at higher frequencies was not due to the higher SL of the masker at those frequencies.

Given the apparent lack of an effect of level on suppression, it is logical to assume that the difference in suppression across frequency with the noise masker also cannot be explained by differences in the effective level at the output of the auditory filter centered at the signal frequency (i.e., in the level per ERB): because the auditory filter is narrower at low frequencies, the level per ERB is less there than it is at higher frequencies. Nevertheless, to test this possibility, pilot data from one subject (S1) were obtained in conditions where the level per ERB was constant (66.6 dB) across signal frequency. The results did not differ significantly from those where the spectrum level of the masker was held constant. Again, the smaller amount of suppression at lower frequencies does not appear to be due to differences in effective level across frequency.

Another possibility is that the pattern of suppression across signal frequency is dependent upon the choice of

suppressor/masker frequency ratio or masker level, and that different choices from the ones used here could yield a different pattern of results. This seems unlikely, however, given recent results from another study from our laboratory. Hicks (1997) measured two-tone suppression for signal frequencies from 375 to 3000 Hz using suppressor/masker frequency ratios of 1.1, 1.2, and 1.3, and masker levels of 40, 50, and 60 dB SPL (the suppressor level was always 20 dB higher than the masker level), and showed that suppression increases with signal frequency for all conditions. Moreover, she showed that the maximum amount of suppression at a given signal frequency (collapsing across all conditions) increased as a function of signal frequency. Her results suggest that the use of different stimulus parameters would not have influenced our conclusion regarding the influence of signal frequency on psychophysical suppression.

Inasmuch as we can rule out factors that might ''contaminate'' our estimates of suppression, or influence our estimate of how suppression varies with signal frequency, we suggest that our results are consistent with a ''true'' increase in suppression, at least from low to mid frequencies. Our results are thus consistent with a growing body of physiological work (reviewed in the Introduction) that indicates that the basal region of the cochlea is more nonlinear than the apical region.

IV. SUMMARY AND CONCLUSIONS

Psychophysical suppression was measured for both noise and tonal maskers across different signal frequencies. Growth-of-masking functions were also obtained in order to quantify suppression as a change in masker level. The following conclusions may be drawn.

(1) For both noise and tonal maskers, psychophysical suppression increased with signal frequency up to about 1000 Hz, and then stayed constant or decreased somewhat as signal frequency increased to 4000 Hz. This result suggests that the nonlinearity underlying psychophysical suppression is less prominent at the apical end of the cochlea, consistent with some physiological data (Schmiedt *et al.*, 1980; Delgutte, 1990; Javel, 1994; Cooper and Rhode, 1995).
(2) The pattern of results describing the amount of suppression across signal frequency was similar regardless of whether suppression was defined in terms of a change in signal threshold or a change in masker level. The only difference was in the magnitude of suppression, which was larger when suppression was defined as a change in masker level.
(3) At a 0-ms delay, the thresholds in the presence of an ERB masker seemed to be contaminated by ''confusion'' effects; the confusion effects were eliminated by inserting a 20-ms delay between masker offset and signal onset. This is consistent with the findings of Moore (1981) and Neff (1985).
(4) The amount of suppression was larger with a noise than with a tonal masker. This may be due to the larger number of components in the noise masker which might serve as a suppressor.

ACKNOWLEDGMENTS

This research was supported by a grant from NIDCD (DC01376). Two anonymous reviewers provided helpful feedback on previous versions of this manuscript.

APPENDIX: ADDITIONAL TEST OF CONFUSION EFFECTS

One of our reviewers suggested an additional way to evaluate whether a confusion effect may have influenced our results with an ERB masker at the 0-ms delay. If there were no confusion effects, then the amount of suppression *expressed as a change in masker level* should be independent of signal delay. Because growth-of-masking functions were measured in both the 0- and 20-ms delay conditions (see Tables I and II), it was possible to evaluate the potential influence of confusion in this way. The results for the noise masker, averaged across the three subjects, are shown in the left panel of Fig. A1. The results for the two delay conditions nearly overlap at the lowest and highest signal frequencies, but clearly diverge at the mid-frequencies, indicating that confusion effects probably did influence some of our thresholds in the presence of the ERB masker. This confusion can be explained by the relation between signal duration and the average time between minima in the envelope of the narrow-band noise masker (Neff, 1986). Neff (1986) showed that for a 60-Hz-wide narrow-band noise, confusion effects can influence performance for signal durations ranging from 10 to 60 or 70 ms, which is roughly one-half to twice the mean time (26 ms) between envelope minima. The calculated mean time between envelope minima for the ERB masker (Rice, 1954) used in experiment 1 at the various center frequencies was: 26 ms for 250 Hz; 19.5 ms for 500 Hz; 11.1 ms for 1000 Hz; 6.5 ms for 2000 Hz; and 3.4 ms for 4000 Hz. Based on Neff (1986), we conclude that confusion may have influenced the threshold measurements at all signal frequencies except 4000 Hz. This is certainly consistent with data shown in the left panel of Fig. A1, where the data points diverge at all frequencies except 4000 and 250 Hz. It is unclear why there were apparently no confusion effects at 250 Hz.

The average results for the tonal masker are shown in the right panel of Fig. A1. In this case, the results nearly

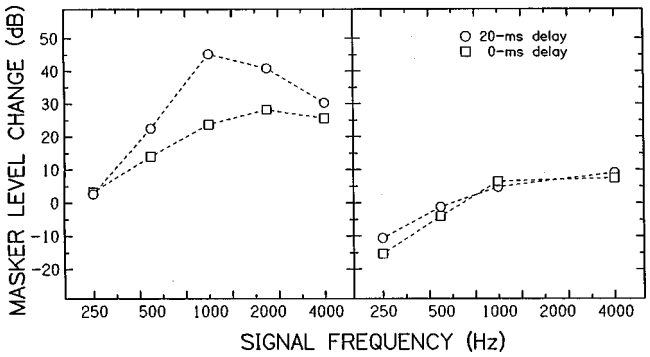

FIG. A1. Suppression as a function of signal frequency for both the 0-ms (squares) and 20-ms delay conditions (circles), averaged across the three subjects. Suppression is calculated as a change in masker level. The results for the noise masker are shown in the left panel and the results for the tonal masker are shown in the right panel.

overlap at all signal frequencies, indicating an absence of confusion effects with the tonal masker.

[1]Additional thresholds were measured for this comparison, rather than using the thresholds for the 40-ms signal at a 0-ms delay (Fig. 1) to compare with the 20-ms signal at a 20-ms delay (Fig. 2), because of the possible confusion effects that may have influenced the thresholds at a 0-ms delay.

[2]The suppressor/masker frequency ratio of 1.2 and level difference of 20 dB were chosen based on the results of Shannon (1976), who found that these conditions produced maximum or nearly maximum amounts of suppression.

[3]Terry and Moore (1977), however, suggested that a confusion effect may arise in the case of a sinusoidal masker and signal, based on the lack of a salient pitch difference between the two. Data obtained here suggest that such a confusion did not exist. Thresholds for the masker level of 50 dB SPL were compared both without a contralateral cue (from the suppression phase of the experiment) and with a cue (from the growth-of-masking phase of the experiment) for signal and masker frequencies of 250, 500, 1000, and 4000 Hz. There were no statistically significant differences ($p > 0.05$) between thresholds obtained with and without the cue.

[4]The 4000-Hz case was not included because it was obvious from the results at 1000 Hz that the suppressor would produce considerably less masking than the masker at 4000 Hz.

[5]One reviewer noted that the comparison between the noise and tonal maskers ''would be more fair if the maskers had been equated in terms of amount of masking.'' Although in general this may be true, there are several instances from the present study where the ERB and on-frequency tonal masker produced comparable amounts of masking, and yet the amount of suppression was greater for the noise masker (e.g., compare the open symbols for S2 at 1000 Hz in Figs. 3 and 7).

[6]To ensure that the considerably larger amount of suppression observed with the 202-component suppressor was not due to its wider frequency range or slightly greater overall level, an additional condition was run with a four-component suppressor. The components were located at 600, 800, 1200, and 1400 Hz, and each was presented at a level of 57 dB SPL. Thus the four-component suppressor had the same frequency range and overall level as the 202-component suppressor. The four-component suppressor, however, produced only 4.8 dB of suppression compared to the 12 dB of suppression produced by the 202-component suppressor.

[7]The finding that suppression decreases at 4000 Hz only for the noise masker is at least consistent with the possibility (discussed in Sec. 1 B) that the decrease is due to the attenuation of important suppressive components in the BB masker located somewhat above the signal frequency. The 4800-Hz tonal suppressor, on the other hand, would not be attenuated much.

[8]This was accomplished by reducing the spectrum level of the noise by the difference between the absolute thresholds at 1000 Hz (17.7 dB SPL) and 250 Hz (40.7 dB SPL). Thus, while the spectrum level of the masker remained at 40 dB SPL when estimating suppression at 250 Hz, the spectrum level of the masker decreased to 17 dB SPL when estimating suppression at 1000 Hz. The masker duration was 200 ms and signal duration was 20 ms. The delay between the offset of masker and onset of signal was 20 ms.

ANSI (**1989**). ANSI S3.6-1989, *Specifications for Audiometers* (American National Standards Institute, New York).

Cooper, N. P., and Rhode, W. S. (**1995**). ''Nonlinear mechanics at the apex of the guinea-pig cochlea,'' Hearing Res. **82**, 225–243.

Delgutte, B. (**1990**). ''Two-tone rate suppression in auditory-nerve fibers: Dependence on suppressor frequency and level,'' Hearing Res. **49**, 225–246.

Duifhuis, H. (**1980**). ''Psychophysical three-tone suppression,'' in *Psychophysical, Physiological, and Behavioural Studies in Hearing*, edited by G. van den Brink and F. A. Blisen (Delft U.P., Delft, The Netherlands).

Fastl, H., and Bechly, M. (**1981**). ''Post masking with two maskers: Effects of bandwidth,'' J. Acoust. Soc. Am. **69**, 1753–1757.

Fastl, H., and Bechly, M. (**1983**). ''Suppression in simultaneous masking,'' J. Acoust. Soc. Am. **74**, 754–757.

Glasberg, B. R., and Moore, B. C. J. (**1990**). ''Derivation of auditory filter shapes from notched-noise data,'' Hearing Res. **47**, 103–138.

Greenwood, D. D. (**1990**). ''A cochlear frequency-position function for several species-29 years later,'' J. Acoust. Soc. Am. **87**, 2592–2605.

Hicks, L. M. (**1997**). ''Psychophysical measures of auditory nonlinearities in individuals with normal hearing and temporary, aspirin-induced hearing loss,'' Doctoral dissertation, Arizona State University.

Houtgast, T. (**1973**). ''Psychophysical experiments on 'tuning curves' and 'two-tone inhibition,' '' Acustica **29**, 168–179.

Houtgast, T. (**1974**). ''Lateral suppression and loudness reduction of a tone in noise,'' Acustica **30**, 214–221.

Javel, E. (**1994**). ''Shapes of cat auditory nerve fiber tuning curves,'' Hearing Res. **81**, 167–188.

Jesteadt, W., Bacon, S. P., and Lehman, J. R. (**1982**). ''Forward masking as a function of frequency, masker level, and signal delay,'' J. Acoust. Soc. Am. **71**, 950–962.

Lee, J., and Bacon, S. P. (**1997**). ''Psychophysical suppression as a function of signal frequency,'' J. Acoust. Soc. Am. **101**, 3148.

Levitt, H. (**1971**). ''Transformed up-down methods in psychoacoustics,'' J. Acoust. Soc. Am. **49**, 467–477.

Moore, B. C. J. (**1981**). ''Interaction of masker bandwidth with signal duration and delay in forward masking,'' J. Acoust. Soc. Am. **70**, 62–68.

Moore, B. C. J., and Glasberg, B. R. (**1982**). ''Contralateral and ipsilateral cueing in forward masking,'' J. Acoust. Soc. Am. **71**, 942–945.

Moore, B. C. J., and Glasberg, B. R. (**1983**). ''Growth of forward masking for sinusoidal and noise maskers as a function of signal delay; implications for suppression in noise,'' J. Acoust. Soc. Am. **73**, 1249–1259.

Moore, B. C. J., and Glasberg, B. R. (**1985**). ''The danger of using narrow-band noise maskers to measure suppression,'' J. Acoust. Soc. Am. **77**, 2137–2141.

Neff, D. L. (**1985**). ''Stimulus parameters governing confusion effects in forward masking,'' J. Acoust. Soc. Am. **78**, 1966–1976.

Neff, D. L. (**1986**). ''Confusion effects with sinusoidal and narrow-band noise forward maskers,'' J. Acoust. Soc. Am. **79**, 1519–1529.

Neff, D. L., and Jesteadt, W. (**1983**). ''Additivity of forward masking,'' J. Acoust. Soc. Am. **74**, 1695–1701.

Pastore, R. E., and Freda, J. S. (**1980**). ''Contralateral cueing effects in forward masking,'' J. Acoust. Soc. Am. **67**, 2104–2105.

Rhode, W. S. (**1971**). ''Observations of the vibration of the basilar membrane in squirrel monkeys using the Mössbauer technique,'' J. Acoust. Soc. Am. **49**, 1218–1231.

Rhode, W. S. (**1977**). ''Some observations on two-tone interaction measured with the Mössbauer technique,'' in *Psychophysics and Physiology of Hearing*, edited by E. F. Evans and J. P. Wilson (Academic, London), pp. 27–41.

Rhode, W. S., and Cooper, N. P. (**1993**). ''Two-tone suppression and distortion production on the basilar membrane in the hook region of cat and guinea pig cochleae,'' Hearing Res. **66**, 31–45.

Rice, S. O. (**1954**). ''Mathematical analysis of random noise,'' in *Selected Papers on Noise and Stochastic Processes*, edited by N. Wax (Dover, New York), pp. 133–294.

Ruggero, M. A., Robles, L., and Rich, N. C. (**1992**). ''Two-tone suppression in basilar membrane of the cochlea: Mechanical basis of auditory-nerve rate suppression,'' J. Neurophysiol. **68**, 1087–1099.

Schmiedt, R. A., Zwislocki, J. J., and Hamernik, R. P. (**1980**). ''Effect of hair cell lesions on responses of cochlear nerve fibers. I. Lesions, tuning curves, two-tone inhibition, and responses to Trapezoidal-wave patterns,'' J. Neurophysiol. **43**, 1367–1389.

Shannon, R. V. (**1976**). ''Two-tone unmasking and suppression in a forward-masking situation,'' J. Acoust. Soc. Am. **59**, 1460–1470.

Stelmachowicz, P. G., Small, A. M., and Abbas, P. J. (**1982**). ''Suppression effects for complex stimuli,'' J. Acoust. Soc. Am. **71**, 410–420.

Terry, M., and Moore, B. C. J. (**1977**). ''Suppression effects in forward masking,'' J. Acoust. Soc. Am. **62**, 781–784.

Thibodeau, L. M., and Fagelson, M. A. (**1993**). ''Comparison of suppression across frequencies,'' J. Acoust. Soc. Am. **93**, 2314(A).

Viemeister, N. F., and Bacon, S. P. (**1982**). ''Forward masking by enhanced components in harmonic complexes,'' J. Acoust. Soc. Am. **71**, 1502–1507.

Weber, D. L. (**1978**). ''Suppression and critical bands in band-limiting experiments,'' J. Acoust. Soc. Am. **64**, 141–150.

Weber, D. L. (**1984**). ''Combined effect of two suppressors,'' J. Acoust. Soc. Am. **75**, 1563–1569.

Weber, D. L., and Green, D. M. (**1978**). ''Temporal factors and suppression effects in backward and forward masking,'' J. Acoust. Soc. Am. **64**, 1392–1399.

Yates, G. K., Winter, I. M., and Robertson, D. (**1990**). ''Basilar membrane nonlinearity determines auditory nerve rate-intensity functions and cochlear dynamic range,'' Hearing Res. **45**, 203–220.

Masking patterns for sinusoidal and narrow-band noise maskers

Brian C. J. Moore and Joseph I. Alcántara
Department of Experimental Psychology, University of Cambridge, Downing Street, Cambridge CB2 3EB, England

Torsten Dau
Carl von Ossietzky Universität Oldenburg, Graduiertenkolleg Psychoakustik, AG Medizinische Physik, D-26111 Oldenburg, Germany

(Received 7 March 1997; revised 14 April 1998; accepted 24 April 1998)

The masking patterns produced by narrow-band maskers can show distinct irregularities. These experiments attempted to clarify the relative importance of factors contributing to these irregularities. A three-alternative adaptive forced-choice method with feedback was used, to promote use of the optimal detection cues. The masker and signal were either a sinusoid or a band of noise that was 80 Hz wide, giving four possible combinations of masker and signal type. In experiment 1, masking patterns were measured for maskers centered at 1 kHz, for all combinations of masker and signal type (tone or noise). The masking patterns showed irregularities (dips or ''shoulders'') above the masker frequency, and the irregularities were larger for the sinusoidal than for the noise masker. Experiment 2 was similar to experiment 1, except that low-pass noise was added to mask combination products. For the noise masker, the low-pass noise slightly increased thresholds, and largely eliminated the irregularities in the patterns, but for the tone masker, the irregularities persisted. Experiment 3 used a noise signal with tone and noise maskers centered at 250, 1000, and 4000 Hz. The tone masker produced less masking than the noise masker for masker-signal frequency separations of 150–250 Hz, regardless of masker frequency. Experiment 4 used an additional masker tone to introduce beats similar to those produced by the interaction of the signal and (main) masker, and to mask combination products. This largely eliminated the dips in the masking patterns for both the noise and tone maskers. Experiment 5 used an additional pair of high-frequency tones to introduce beats, with similar results. We conclude that temporal fluctuations (beats) have a strong influence on the masking patterns for sinusoidal maskers, for masker-signal frequency separations up to a few hundred Hz. Beats may also have some influence on the masking patterns for noise maskers. The detection of combination products also plays a role. © *1998 Acoustical Society of America.* [S0001-4966(98)02808-2]

PACS numbers: 43.66.Dc, 43.66.Ba [JWH]

INTRODUCTION

Masking patterns (also called masked audiograms) are plots of the amount of masking (or the threshold) of a signal as a function of signal frequency in the presence of a masker with fixed frequency and level. The masking patterns of narrow-band sounds, either sinusoids or bands of noise, have been measured in many experiments. Early work on masking patterns was particularly concerned with using the patterns as a tool for estimating the spread of excitation of the masker within the cochlea (Wegel and Lane, 1924; Fletcher and Munson, 1937; Egan and Hake, 1950; Zwicker, 1956). It was thought that the signal threshold might be directly related to the amount of excitation evoked by the masker at the place whose characteristic frequency (CF) corresponds to the signal frequency. However, it soon became apparent that the masking patterns showed a variety of complex features that could not be readily explained in terms of spread of excitation. Also, there were systematic differences between the shapes of masking patterns obtained using sinusoidal and narrow-band noise maskers, even though these are generally assumed to produce similar long-term-average excitation patterns.

The masking patterns for sinusoidal maskers published by Wegel and Lane (1924), by Fletcher and Munson (1937), and by Egan and Hake (1950) showed distinct nonmonotonicities. The peaks in the masking patterns were usually, but not always centered close to the masker frequency, although the data of Wegel and Lane (1924) and of Egan and Hake (1950) showed a local minimum immediately around the masker frequency, which was explained in terms of the detection of beats (envelope fluctuations) between the signal and masker. These researchers suggested that beats only played a role when the signal frequency was within about 100 Hz of the masker frequency. Similar peaks with local minima were observed at twice the masker frequency. These were attributed to the presence of aural harmonics.

Later, Ehmer (1959) and Greenwood (1971) presented extensive measurements of masking patterns for sinusoidal maskers. The masking patterns often showed nonmonotonicities, with local peaks above the masker frequency, but these peaks were often not centered at integer multiples of the masker frequency, as would be expected if they were caused by aural harmonics. Ehmer concluded that ''Aural harmonics are not responsible for the extension of masking to the octaves above the masking tone...'' (page 1120), except perhaps for very high masker levels (100 dB SL). He

also concluded that difference tones play only a minor role, except for very high masker levels. However, he was probably thinking only of the simple difference tone, f_2-f_1, and did not consider the possible contribution of the cubic difference tone, $2f_1-f_2$ (see below for more discussion of this). He argued that the masking patterns of sinusoidal maskers depend mainly on the spread of excitation within the cochlea, and that most of the irregularities in the masking patterns could be explained in terms of beats. The ''dips'' in the patterns for signal frequencies above the masker frequency were assumed to be due to the detection of beats or roughness. In this region, he suggested that ''...the height of the masking pattern does not truly show the amount of activity...'' (evoked by the masker) (page 1119). On the other hand, when beats and roughness could not be detected, because the masker-signal frequency separation was too large, then he argued that ''...the masking pattern is thought to reflect accurately the level of masking-tone activity in the cochlea'' (page 1119). If these arguments are correct, then the detection of beats and roughness would have to play a role over a much larger range of masker-signal frequency separations than assumed by Wegel and Lane (1924) and by Egan and Hake (1950); the ''dips'' in the masking patterns extend to signal frequencies over 1000 Hz above the masker frequency.

The masking patterns for narrow-band noise maskers are generally much more regular than those for sinusoids, and they often do not show secondary maxima well above the masker frequency (Fletcher and Munson, 1937; Egan and Hake, 1950; Zwicker, 1956; Zwicker and Fastl, 1990). It has been argued that the greater regularity is due to the fact that narrow-band noise has inherent random amplitude fluctuations, which cause beats between the signal and masker to be less regular and less salient than when sinusoidal maskers are used (Fletcher and Munson, 1937; Egan and Hake, 1950; Zwicker and Fastl, 1990). If this is the case, then the masking patterns for narrow-band noise might give a better representation of the spread of excitation of the masker (Zwicker, 1970; Zwicker and Fastl, 1990). However, temporal interactions between the masker and signal may still play some role (Egan and Hake, 1950). Also, masking patterns for narrow-band noises can show a small ''dip'' for signal frequencies just above the masker frequency, and Greenwood (1971, 1972) has presented extensive evidence that such dips are at least partly due to the detection of combination products produced by the interaction of signal and masker, particularly products of the type $2f_1-f_2$. These combination products also play a role in tone-on-tone masking, and contribute to the minima in the masking patterns for signal frequencies above the masker frequency (Greenwood, 1971; Smoorenburg, 1972; Zwicker and Fastl, 1990). It should be noted that combination tones may themselves be detected by virtue of the beats that they produce by interaction with the masker (Greenwood and Joris, 1996). However, in this paper, when we refer to beats, this will usually mean beats produced by the interaction of the masker and signal. When we refer to cues produced by combination tones, this will refer to any case where combination tones result in lower thresholds, either because the combination tones are themselves heard as separate tones, or because the combination tones produce beats with the masker. The relative role of beats and combination tones in producing dips in masking patterns remains uncertain.

One curious feature of masking patterns is that sinusoidal maskers often produce more masking than narrow-band noise maskers when the masker level is high and the signal frequency is well above the masker frequency (Egan and Hake, 1950; Greenwood, 1971; Buus, 1985; Mott and Feth, 1986; Zwicker and Fastl, 1990). A possible explanation for this is that, for a narrow-band noise masker, subjects may ''listen in the dips'' of the masker envelope (Buus, 1985; Moore and Glasberg, 1987; van der Heijden and Kohlrausch, 1995; Nelson and Schroder, 1996). The envelope fluctuations are compressed more at places with CFs close to the masker frequency than at places with CFs well above the masker frequency; see Nelson and Schroder (1996). If this explanation is correct, then, for signal frequencies well above the masker frequency, the masking pattern for a sinusoidal masker would give a better indication of the average masker excitation than the masking pattern for a narrow-band noise masker.

For signal frequencies below the masker frequency, sinusoidal maskers usually give less masking than narrow-band noise maskers (Greenwood, 1961, 1971; Mott and Feth, 1986; Glasberg and Moore, 1994). Also, on their low-frequency sides, the masking patterns for sinusoidal maskers tend to become steeper with increasing level, while the masking patterns for narrow-band noise maskers have slopes that are almost invariant with level (Zwicker, 1954; Zwicker and Feldtkeller, 1967; Zwicker and Jaroszewski, 1982; Zwicker and Fastl, 1990). Most of the narrow-band noises used by Zwicker and co-workers had bandwidths of about one critical band (160 Hz at 1 kHz). Greenwood (1971) and Glasberg and Moore (1994) presented evidence that for such noises, combination products produced by the interaction of components within the noise masker may have a masking effect. Glasberg and Moore found that when the noise masker had a very small bandwidth (16 Hz) then similar masked thresholds were obtained for a sinusoidal and narrow-band noise masker, for signal frequencies below the masker frequency. However, thresholds were still slightly lower for the sinusoidal masker, suggesting that some factor other than combination products played a role.

In summary, masking patterns for narrow-band maskers may be affected by a large variety of different factors. The relative importance of these factors is not well established. Although it is often assumed that the masking patterns for narrow-band noise maskers give a better indication of the spread of excitation within the cochlea than the masking patterns for sinusoidal maskers (Zwicker, 1970; Zwicker and Fastl, 1990), this may not be the case for signal frequencies well above the masker frequency, or for signal frequencies below the masker frequency.

The present study was undertaken in an attempt to clarify the relative importance of the factors influencing masking patterns for sinusoidal and narrow-band noise maskers. In contrast to the great majority of previous studies of masking patterns, we used an adaptive forced-choice

method with feedback, as opposed to Békésy tracking or the method of adjustment. We used a three-interval task, in which subjects simply had to indicate the interval that sounded different. This was done to allow subjects to ''home in'' on the optimal detection cues for each masker-signal combination. In previous studies, subjects were sometimes instructed to listen for a specific cue (e.g., the pitch of the signal) and to ignore other cues (Zwicker and Fastl, 1990). Even when they were instructed to use ''any cue'' it is not clear that they selected the cue that would have yielded the lowest threshold.

A second feature of our study was that we compared masking patterns for sinusoidal and narrow-band noise maskers using the same subjects. Only a few previous studies have done this (Egan and Hake, 1950; Greenwood, 1971; Buus, 1985; Mott and Feth, 1986). This is important, as the shapes of masking patterns can vary markedly across subjects, especially for sinusoidal maskers.

A third feature of our study was that we used as signals both sinusoids and narrow bands of noise. This was done in an attempt to tease out the importance of temporal cues. Consider a signal added to a sinusoidal masker. If the signal is itself a sinusoid, then this produces regular beats. If the signal is a narrow-band noise, then the signal will cause fluctuations in the temporal envelope of the total stimulus; but the fluctuations will not be regular. Thus a difference between these two cases would indicate a role for the regularity of the fluctuations.

A fourth feature of our study was that the stimuli were digitally generated. This allowed us to control the relative phase of the signal and masker in the special case when the signal and masker were sinusoids with equal frequency. We used a phase of 90°, so that the power of the masker and signal would add. Most previous studies of masking patterns have not controlled the phase in this way, and this would almost certainly have influenced the tips of the masking patterns.

In a series of experiments we explored the role of various cues by manipulation of the characteristics of the signal and masker, and by adding extra components to the masker, to mask combination tones and/or to disrupt temporal cues caused by the interaction of the signal and the masker.

I. GENERAL METHOD

A. Procedure

Thresholds were estimated using a three-alternative forced-choice adaptive procedure. The masker was presented in three observation intervals and the signal was gated on synchronously with the masker in one of those intervals, chosen randomly. The subject indicated, by pressing one of three buttons, which interval was thought to contain the signal. Immediate feedback was provided by lights on the response box. A run was started with the signal at a level about 10 dB above the expected threshold value, as determined in practice trials. After three successive correct responses the signal level was decreased, while after a single incorrect response it was increased. This procedure tracks the signal level corresponding to 79.4% correct. The initial step size was 5 dB. After four reversals the step size was decreased to 2 dB and eight further reversals were obtained. The threshold was estimated as the mean of the signal levels at the last eight reversal points. Runs were discarded when the standard deviation (s.d.) of the levels at the last eight reversals exceeded 5 dB. Initially, two threshold estimates were obtained for each condition. If the two estimates differed by more than 2 dB, at least one additional estimate was obtained and the two closest estimates were averaged. Absolute thresholds were estimated using a similar procedure; observation intervals were marked by lights on the response box.

B. Stimuli

The masker was either a sinusoid or a Gaussian band of noise that was 80 Hz wide. The signal was also either a sinusoid or a band of noise that was 80 Hz wide. For brevity, these will be referred to as ''tone'' and ''noise'' maskers and signals. The starting phase of the tone masker was 0° and the tone signal had a starting phase of 90° relative to the masker. Hence, when the tone signal and the tone masker had the same frequency, the powers of the signal and masker added. When the signal and masker were both noises with the same center frequency, the two noises were independent of one another. The three masker bursts each had a steady state duration of 200 ms, and 10-ms raised-cosine rise/fall times. The inter-stimulus interval was 500 ms. The signal was gated synchronously with one of the masker bursts.

All stimuli were generated digitally using a Tucker-Davis Technologies (TDT) System II, controlled by a PC. The noise bands were generated by adding sinusoids spaced at 5-Hz intervals, with equal component amplitudes and phases drawn randomly from a uniform distribution in the range 0°–360°; this gives a good approximation to Gaussian noise (Hartmann, 1987). However, unlike true Gaussian noise, the overall energy of the noise bands did not vary significantly from stimulus to stimulus. The spectral slopes were essentially infinite. When noise bands were used, a different randomly generated noise was used for every stimulus. The sampling rate was 25 kHz and stimuli were converted to analog form using two channels of a TDT DD1, one for the signal and one for the masker. The levels were controlled by TDT PA4 programmable attenuators, and signal and masker were mixed (TDT SM3) before being passed to a headphone buffer (TDT HB6), a final manual attenuator (Hatfield 2125) and one earpiece of a Sennheiser HD414 headphone. Sound levels are specified as levels close to the eardrum. The calibration was based on average measurements for three subjects (not those of the present experiments), using a Rastronics Portarem 2000 system with a probe microphone within 4 mm of the eardrum. The positioning of the probe was determined as recommended by the manufacturer, using the on-screen display to monitor standing waves in the ear canal and to place the valley in the frequency response curve above 8 kHz (Siegel, 1994). For a fixed input voltage, the standard deviation of the sound level across subjects was typically about 1 dB for frequencies up to 1 kHz, about 2 dB for frequencies from 2 to 6 kHz, and about 3 dB from 6 to 8 kHz. Subjects were tested in an IAC double-walled sound-attenuating chamber.

To check that the results would not be unduly influenced by distortion products generated in the earphones, measurements were made of the earphone output using a Bruel & Kjær 4153 artificial ear, fitted with a Bruel & Kjær 4134 microphone, connected to a Hewlett-Packard 35670A dynamic signal analyzer. For a sinusoidal input, harmonic distortion occurred mainly for the odd harmonics, and all harmonics had levels at least 62 dB down from the level of the primary tone. We also checked for intermodulation distortion products, especially of the type $2f_1 - f_2$. These were at least 82 dB lower in level than the more intense of the two primary tones. Simple difference tones were at least 78 dB lower in level than the primary tones.

II. EXPERIMENT 1. MASKING PATTERNS AT 1 kHz FOR SINUSOIDAL AND NOISE MASKERS AND SINUSOIDAL AND NOISE SIGNALS

A. Stimuli

In this experiment, the masker center frequency was fixed at 1 kHz. The masker overall level was 45, 65, or 85 dB SPL. Signal frequencies of 0.25, 0.5, 0.75, 0.9, 1.0, 1.1, 1.25, 1.5, 2, 3, and 4 kHz were used. One subject (JA) was also tested using signal frequencies of 0.95 and 1.05 kHz. The masker was either a sinusoid or an 80-Hz-wide band of noise. The signal was also either a sinusoid or an 80-Hz-wide band of noise. All four masker-signal combinations were used.

B. Subjects

Three normally hearing subjects were used. None had any history of hearing problems. All had absolute thresholds less than 10 dB HL at all audiometric frequencies. One subject was author JA who was highly experienced in psychoacoustic tasks, including masking. The other two subjects performed the experiment as part of an undergraduate project. All subjects were given practice until their performance appeared to be stable. This took only 2–3 h. No systematic changes in performance were observed during the course of the experiment.

C. Results

Absolute thresholds did not differ systematically for the noise signal and for the tone signal. Hence, means of the thresholds for the two signal types are given in Table I for each subject, HF, BM, and JA (the table also shows absolute thresholds for the subjects used in subsequent experiments; note that, for each subject, absolute thresholds were only measured for frequencies for which a masked threshold was also measured). The absolute thresholds show a small peak close to 2000 Hz for all three subjects. This is typical for thresholds specified in terms of sound level at the eardrum (Killion, 1978).

Figures 1–3 show results for the individual subjects; amount of masking is plotted as a function of signal frequency. The abscissa is scaled in ERB units (Glasberg and Moore, 1990), with the corresponding frequency shown at the top. The equation relating ERB number to frequency is:

TABLE I. Absolute thresholds for each subject at each tested signal frequency, specified as dB SPL at the eardrum.

Frequency (Hz)	Subject					
	JA	AO	BM	HV	DAV	OM
50	47	35				
100	32	26				
150	28	23				
200	22	19				
250	19	16	11	12	15	
300	19	15				
350	18	15				
500	17	13	4	9	12	2
750	14	11	4	7	11	7
900	13	13	5	5	13	
950	14					
1000	11	10	3	8	12	8
1060	8	7				6
1100	14	12	8	6	11	11
1170	10	11				4
1250	16	10	11	8	11	2
1500	17	11	18	11	13	12
1750	19	14			21	3
2000	22	16	14	18		3
3000	7	3	10	7		0
3500	9	6				
3900	13	8				
4000	17	13	10	8		
4100	20	9				
4500	20	11				
5000	21	13				
6000	17	24				
7000	17	22				
8000	29	16				

$$\text{ERB number} = 21.4 \log_{10}(4.37F + 1), \quad (1)$$

where F is the frequency in kHz.

Consider first the results for the noise masker (upper panels). Generally, the pattern of results is similar for the tone and noise signals (left and right panels, respectively). The only difference is for subject BM, for whom the high-frequency sides of the masking patterns are slightly less regular for the tone signal than for the noise signal. The signal levels at the peaks of the masking patterns are close to or a few decibels below the overall masker levels. This is typical of what is observed for narrow-band noise maskers (Fletcher and Munson, 1937; Fletcher, 1940; Egan and Hake, 1950; Zwicker and Fastl, 1990) and it is consistent with the idea that the main detection cue in this case was the change in overall level produced by adding the signal to the masker (Greenwood, 1961; Bos and de Boer, 1966), although other cues may also be used, especially when the overall level is roved; see Kidd (1989). On average, the level at threshold for the noise signal was 1.2 dB below the masker level, while the threshold for the tone signal was 1.9 dB below the masker level. It should be noted that while the overall level of the noise masker did not vary from one stimulus to the next, the *change* in level produced by adding the signal to the masker did vary randomly from trial to trial, as a different sample of random noise was generated for every masker presentation.

As previously reported for narrow-band noise maskers

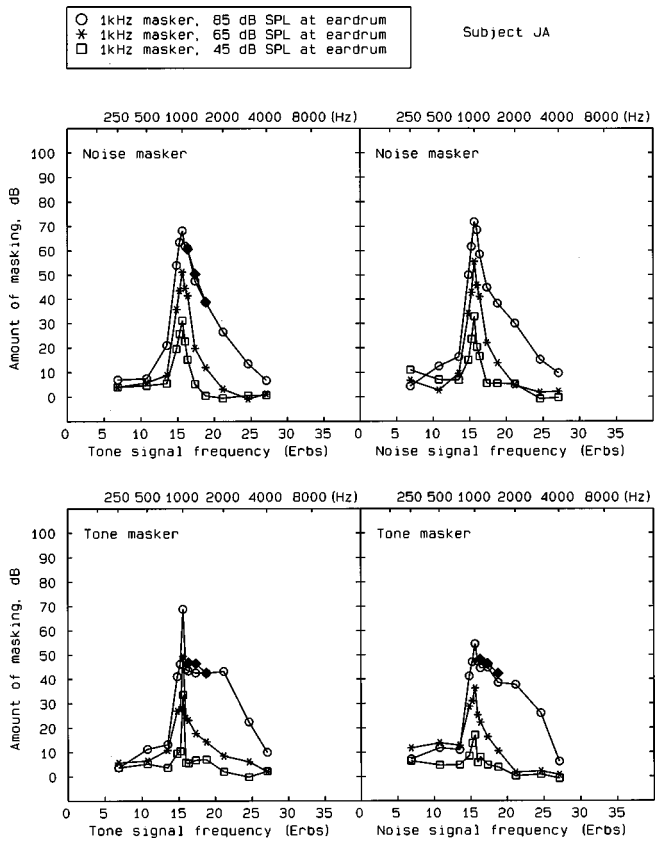

FIG. 1. Results of experiment 1 for subject JA. The amount of masking is plotted as a function of number of ERBs (bottom axis) with the corresponding frequency shown at the top. Each panel shows results for a different masker-signal combination. Open symbols show the amount of masking for each masker level. The filled diamonds show results from experiment 2, obtained using an extra low-pass noise to mask combination tones.

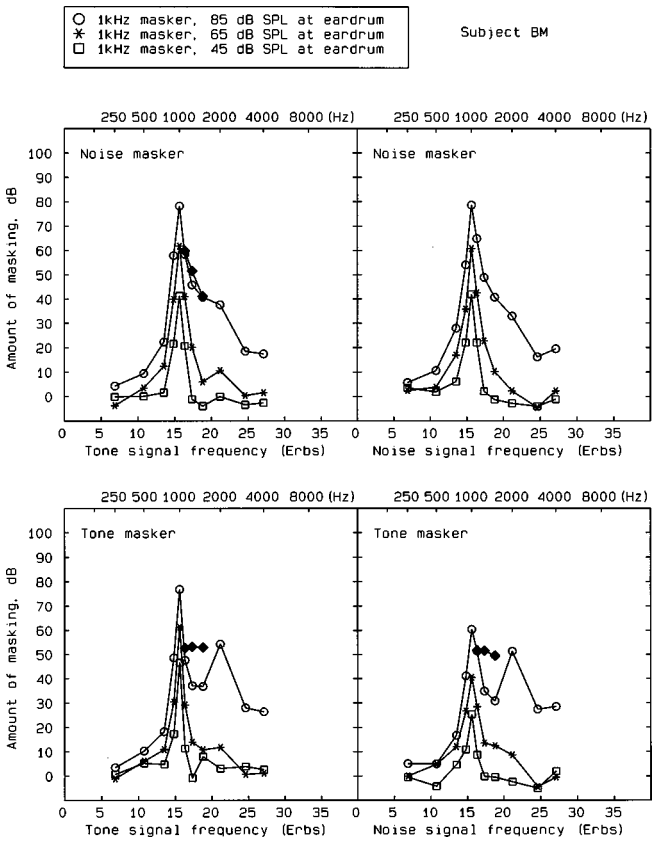

FIG. 2. As Fig. 1 but for subject BM.

(Zwicker, 1980; Zwicker and Fastl, 1990), the masking patterns are reasonably symmetrical (on an ERB scale which approximates a log-frequency scale above 500 Hz) for the lowest masker level, but become distinctly asymmetric for the highest masker level. The slopes of the masking patterns on the low-frequency sides, over the range where the amount of masking exceeds 15 dB, are almost invariant with level. In contrast, the slopes on the high-frequency side become less steep with increasing level, reflecting the classic ''upward spread of masking.''

Consider now the masking patterns for the tone maskers (lower panels). These are much less regular than for the noise maskers, and individual differences are also larger. For the highest masker level, the patterns show distinct irregularities (dips, peaks, and shoulders) above the masker frequency. The dips and shoulders might be due to the detection of beats between signal and masker, to the detection of combination products produced by the interaction of signal and masker, to the detection of beats between a combination tone and the masker, or all three; we will return to this point later.

The signal levels at the tips of the patterns for the tone masker are much higher for the tone signal (left panels) than for the noise signal (right panels). For the former, the only detection cue was the change in level produced by adding the signal to the masker. The signal threshold in this case was generally close to the masker level, and the signal-to-masker

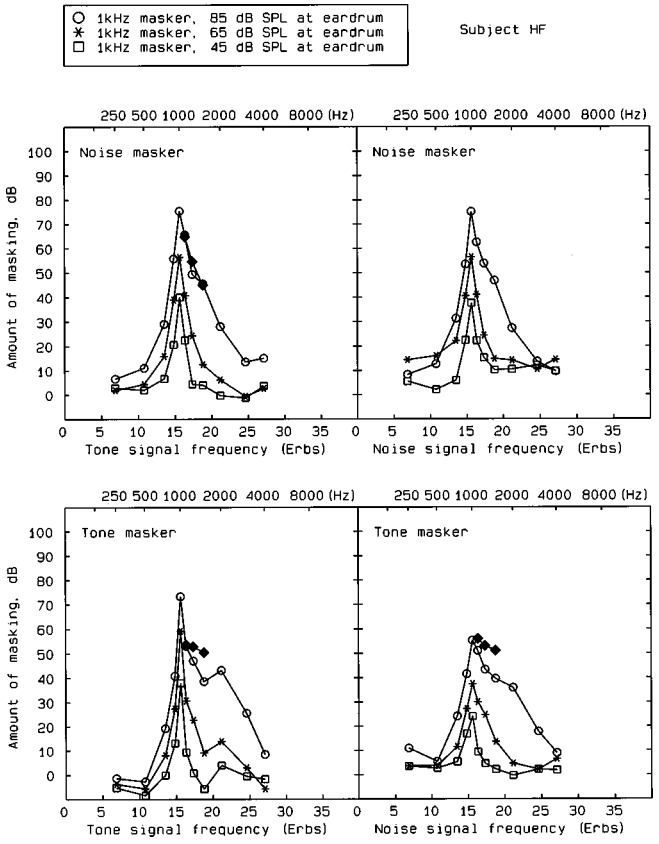

FIG. 3. As Fig. 1 but for subject HF.

ratio at threshold decreased with increasing masker level, consistent with the familiar ''near miss'' to Weber's law for the intensity discrimination of sinusoids (McGill and Goldberg, 1968; Viemeister, 1972; Moore, 1997); the mean signal-to-masker ratio at threshold was +1.5, −1.2, and −4.8 dB for masker levels of 45, 65, and 85 dB, respectively. For the noise signal, an additional detection cue was available, namely the within-interval fluctuation in level produced by adding the signal to the masker. This cue was evidently very effective, since the signal-to-masker ratios at threshold were rather low; average values were −16.3, −19.5, and −20.7 dB for masker levels of 45, 65, and 85 dB, respectively. These values are comparable to those reported by Greenwood (1961, 1971) for a noise signal and tone masker.

For the case where the signal was centered at the masker frequency, the signal thresholds were similar for three of the masker-signal combinations: noise–tone, noise–noise, and tone–tone. These are all cases where the main detection cue was probably the change in overall level produced by adding the signal to the masker. The case with the tone masker and noise signal gives clearly lower thresholds as this is the one case where the signal adds a within-interval cue of a fluctuation in level. The asymmetry of masking between a noise masker and tone signal and vice versa has been reported previously (Hellman, 1972; Hall, 1997) and explained in a similar way. In particular, Hall (1997) presented evidence that, when the signal bandwidth was less than the masker bandwidth, detection was based on differences in overall energy or level. When the signal bandwidth was greater than the masker bandwidth (as for our tone masker and noise signal), detection was based on the temporal structure of the stimuli.

For the tone masker, thresholds are reasonably similar for the tone signal and the noise signal, except when the signal frequency equals the masker frequency. For signal frequencies close to the masker frequency, the cue of a within-interval fluctuation in level would have been present for both masker-signal combinations. The similarity of the patterns in this region suggests that the regularities of the fluctuations are not critical; the tone signal would have produced regular fluctuations (beats) while the noise signal would have produced irregular fluctuations. The very sharp tip of the masking pattern for the tone–tone combination can be attributed to the lack of within-interval fluctuations for the specific case where the signal frequency equals the masker frequency.

The dips and shoulders in the masking patterns for the tone masker extend to signal frequencies up to 1500 Hz; possibly, they would extend to somewhat higher frequencies, but we did not include any signal frequencies between 1500 and 2000 Hz. While these dips were probably partly or mainly caused by the detection of combination products, it is possible that the detection of beats also contributed to the dips and plateaus in the masking patterns; beats in sinusoidal signals are highly detectable for rates up to about 100 Hz, but they become less detectable for higher rates, and are almost undetectable for rates of 1000 Hz or higher (Yost and Sheft, 1988; Zwicker and Fastl, 1990; Dau *et al.*, 1997; Fassel *et al.*, 1998). For signal frequencies above 2000 Hz, it seems likely that beats did not provide a useful cue. It is noteworthy that, in this region, the tone masker generally produced more masking than the noise masker, both for the tone signal and for the noise signal. As noted in the Introduction, the better performance with the noise masker can probably be explained by subjects ''listening in the dips'' of the envelope of the noise masker.

In summary, the shapes of the masking patterns for signal frequencies above and below the masker frequency seem to be determined mainly by the characteristics of the masker rather than by the characteristics of the signal. The masking patterns for both types of masker show irregularities above the masker frequency, which may be attributed partly to the detection of combination products. The dips and shoulders for the tone masker are much larger and extend to higher signal frequencies. When the signal frequency is equal to the masker frequency, thresholds are similar for all masker-signal combinations except the tone masker and noise signal, which gives much lower thresholds. The lower thresholds can be attributed to the availability of a within-channel cue of a fluctuation in level.

III. EXPERIMENT 2. EFFECTS OF USING NOISE TO MASK COMBINATION PRODUCTS

A. Method

This experiment explored the role of combination products in producing the dips and shoulders in the masking patterns described above. This was done by using an additional noise to mask the combination products. The subjects were the same as for experiment 1. The main masker level was always 85 dB SPL, the level for which the dips and shoulders were most pronounced. The additional noise was white noise low-pass filtered at 800 Hz (360 dB/octave slope). It was generated using a Hewlett-Packard 3722A noise generator and four sections of two Kemo VBF8/04 filters.

The level of the low-pass noise was determined as follows. The level of the signal in the region of the dips in the masking patterns (as determined in experiment 1) was used as a starting point. It was reasoned that the level of any combination products would be at least 10 dB below this level (Smoorenburg, 1972; Zwicker, 1981). Hence we adjusted the level of the low-pass masking noise so that, on its own, it would just mask a 750-Hz signal (i.e., a signal in the frequency range where combination products were expected for a 1250-Hz primary signal and a 1000-Hz masker) at a level 10 dB below the level of the dips in the original masking patterns. For all three subjects, this was achieved using an overall noise level of 55 dB SPL (a spectrum level of 26 dB). A check was made that this noise had a negligible effect on the masked threshold for a signal at 1 kHz, when the main masker was present. This was the case for all three subjects.

The experiment was conducted using the three masker-signal combinations that gave rise to dips or shoulders in experiment 1, namely noise–tone, tone–tone, and tone–noise. The signal frequencies were 1100, 1250, and 1500 Hz.

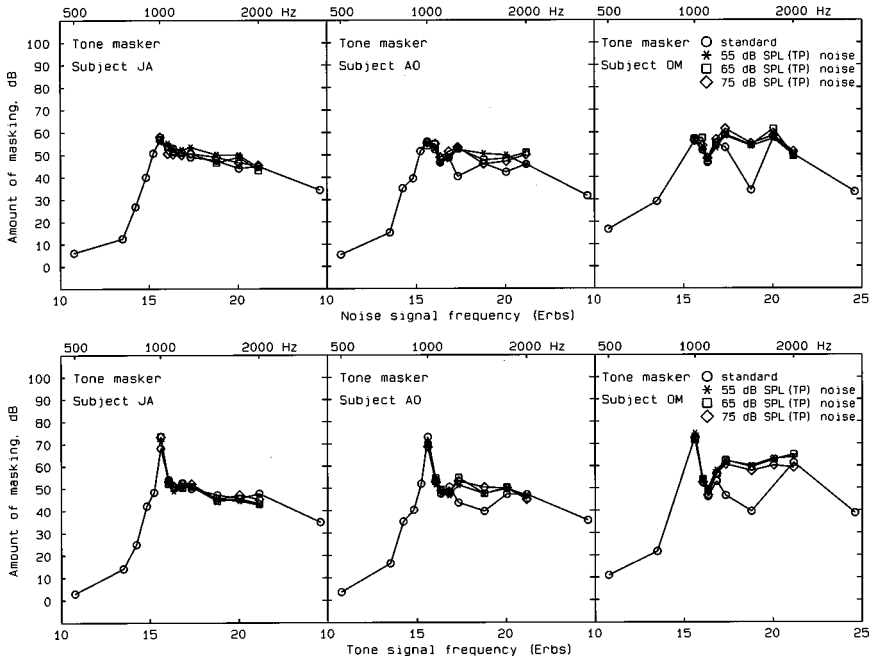

FIG. 4. Masking patterns for three subjects for a tone masker and noise signal (top) or tone signal (bottom). Results are shown for the tone masker alone (standard condition—open circles) and for that masker together with low-pass noise at three different overall levels.

B. Results

The results are shown as the filled diamonds in Figs. 1–3. For the noise masker and tone signal, the added low-pass noise slightly increased thresholds. For the tone masker, the added low-pass noise produced greater threshold elevations, especially for BM and HF. This is consistent with results of Greenwood (1971), obtained under similar but not identical conditions. However, the masking patterns for JA and BM still showed shoulders or dips. Note that for the next higher signal frequency used (2000 Hz), the combination product $2f_1-f_2$ would have fallen at zero frequency, while f_2-f_1 would have fallen at the masker frequency.

It is possible that the shoulders and dips still occurred when the noise was present because the noise level was not sufficiently high to mask combination products for all masker-signal frequency separations. To check on this, the experiment was rerun using both the original low-pass noise levels and two extra noise levels, 10 and 20 dB higher than the original. Unfortunately, subjects BM and HF were no longer available, so two new subjects, AO and OM, were run, together with subject JA. AO was highly experienced in psychoacoustic tasks, including masking. OM had some previous experience in psychoacoustical tasks. AO and OM were trained for this experiment for 2–3 h. Both subjects were paid for their services. Absolute thresholds for these subjects are shown in Table I. Data were gathered for the 1000-Hz 85-dB tone masker using both noise and tone signals. Extra signal frequencies of 1060, 1170, and 1750 Hz were used, so as to map out any irregularities in the masking patterns more precisely. The results are shown in Fig. 4.

For subject JA, the added low-pass noise had very little influence on the amount of masking, even for the highest level used. This is consistent with his earlier results, and may indicate that combination products did not provide useful detection cues for him. For the other subjects, the low-pass noise increased the amount of masking, mainly over the range 1250–1750 Hz. However, the level of the low-pass noise did not have any clear influence on the amount of masking, suggesting that the original overall noise level of 55 dB SPL was sufficient to mask combination products. The masking patterns for AO and OM show distinct dips just above the masker frequency, extending up to about 1170 Hz. The amount of masking in this frequency range was not affected by the low-pass noise. However, the most intense noise should have masked combination tones produced by signals with frequencies of 1100 Hz and above. Consider, for example, the 1170-Hz and 1100-Hz signals, which would have produced combination tones at 830 Hz and 900 Hz, respectively. The excitation level produced by the 75-dB low-pass noise masker, calculated using the program of Glasberg and Moore (1990), was about 62 dB at 830 Hz and 56 dB at 900 Hz. Since the signal thresholds were about 60 dB SPL for AO and OM at both 1170 and 1100 Hz, it seems likely that the effective levels of the combination tones at 830 Hz and 900 Hz were below 50 dB, so they should have been masked by the low-pass noise. We cannot be certain that, for the 1060-Hz signal frequency, the combination tone at 940 Hz was completely masked by the low-pass noise. Also, it is possible that beats produced by the interaction of a combination tone and the masker provided a detection cue for small masker-signal frequency separations. However, the finding that the low-pass noise had *no* effect on signal thresholds for signal frequencies up to 1170 Hz, suggests that combination tones did not influence thresholds in this frequency region. If combination tones did play a role, then the low-pass noise would surely have somewhat reduced the detectability of the combination tones, and it would also have reduced the salience of beats produced by the interaction of combination tones with the masker. Probably, the dips in the masking patterns for signal frequencies up to 1170 Hz arose from temporal interactions between the signal and masker, rather than from the detection of combination products.

Overall, these results suggest that the detection of com-

bination products cannot account completely for the shoulders and dips in the masking patterns for the tone masker. Even under conditions where the combination tones would have been masked, the thresholds did not decline smoothly and progressively with increasing masker-signal frequency separation. It seems likely that temporal interactions (beats) between the signal and masker played a strong role, at least for the tone masker. The detectability of beats depends on their rapidity; fast beats are less detectable than slow ones, at least for rates above about 100 Hz. (Yost and Sheft, 1988; Zwicker and Fastl, 1990; Dau *et al.*, 1997). It appears that beats provide a dominant detection cue for masker-signal frequency separations up to about 200 Hz, and that combination tones can play an important role above that. It is noteworthy, however, that when combination products are masked, the masking patterns for the tone masker still tend to show a plateau in the range from about 1250 Hz to 2000 Hz. It is possible that, when combination products do not provide useful cues, the detection of beats plays some role even for masker-signal frequency separations above 200 Hz.

IV. EXPERIMENT 3. MASKING PATTERNS FOR DIFFERENT MASKER FREQUENCIES

A. Rationale and method

In this experiment, masking patterns were measured for both the tone and noise maskers using masker center frequencies of 250, 1000, and 4000 Hz and masker levels of 45, 65, and 85 dB SPL. For the noise masker and the noise signal, the bandwidth was fixed at 80 Hz for all center frequencies. Only the noise signal was used. The signal frequency covered a wide range above and below each masker frequency. Our goal was to assess whether the difference in the results for the tone and noise maskers was mainly due to the greater detectability of beats for the former or to the greater detectability of combination products for the former.

Consider the effect predicted on the basis of the detection of beats between the signal and the masker. We assume that beats are much more salient for the tone masker than for the noise masker, since the inherent fluctuations in the noise masker make beats harder to detect (although the dominant frequencies in the spectrum of the envelope of the noise masker differ progressively more from the beat rate as the beat rate increases, which might make beats usable even for the noise masker at intermediate beat rates; see Sec. VII for further discussion of this point). Hence, masked thresholds should be lower for the tone masker than for the noise masker over the range of signal frequencies for which beats are audible. For small masker-signal frequency separations, the beats are slow and highly salient. As the masker-signal frequency separation is increased, the beats become more rapid, and, for beat rates above 100 Hz, they would be expected to become progressively less salient, and so less useful as a detection cue (Dau *et al.*, 1997; Fassel *et al.*, 1998). For very large masker-signal frequency separations, greater than about 1000 Hz, the beats would probably be too fast to be detectable. The beat rate depends on the *absolute* value of the masker-signal frequency separation in Hz, not on the masker-signal frequency ratio. Therefore, the tone masker should give less masking than the noise masker over a fixed absolute range of masker-signal frequency separations; this range should not vary with the masker frequency. Also, the range over which thresholds are lower for the tone than for the noise masker should be reasonably symmetrical about the signal frequency.

Consider now predictions based on the assumption that thresholds are lower for the tone than for the noise masker because combination products, or beats between combination products and the masker, are more detectable for the former. Firstly, combination products probably only play a role for signal frequencies above the masker frequency (Greenwood, 1971; Zwicker and Fastl, 1990). Therefore, an asymmetry is predicted: Thresholds should be lower for the tone than for the noise masker by a greater amount for signal frequencies above the masker frequency than for signal frequencies below the masker frequency. In addition, the relative levels of combination products produced by the interaction of signal and masker depend more on the frequency *ratio* between signal and masker than on their absolute frequency separation (Goldstein, 1967; Smoorenburg, 1972; Zwicker, 1981). Hence, if the detectability of combination products determines masked threshold, the tone masker should lead to lower thresholds than the noise masker over a fixed ratio of signal/masker frequencies, and this ratio should be the same for each masker frequency.

In summary, by using a wide range of masker center frequencies, we hoped to tease out the relative roles of beat detection and combination-product detection in producing the difference between the noise and tone maskers.

Two subjects were used. One was author JA. The other was AO, who was also used in experiment 2. Absolute thresholds for both subjects are shown in Table I.

B. Results

The results are plotted as amount of masking in Figs. 5 (subject JA) and 6 (subject AO). The data for subject JA for the 1-kHz maskers are taken from experiment 1. The masking patterns for the noise masker (upper panels) mostly show a peak at, or very close to, the masker frequency, and the amount of masking declines monotonically with increasing masker-signal frequency separation. However, the masking patterns for JA for the 4-kHz masker show some dips on the high-frequency side. The masking patterns may be less regular at 4 kHz because the relative bandwidth of the noise is smallest at that frequency and the effects of combination products are strongest when the relative bandwidth is small (Greenwood, 1971, 1972). Consistent with earlier work (Egan and Hake, 1950; Zwicker, 1956; Zwicker and Fastl, 1990), the masking patterns are reasonably symmetrical for the lowest masker level, but become increasingly asymmetric as the masker level increases. The slopes of the masking patterns hardly vary with level on the low-frequency side. The patterns become shallower with increasing level on the high-frequency side.

In theory, if the masking patterns for the noise masker reflect the shapes of the excitation pattern of the maskers (Zwicker and Fastl, 1990), then the patterns should be similar in shape for the different masker frequencies when plot-

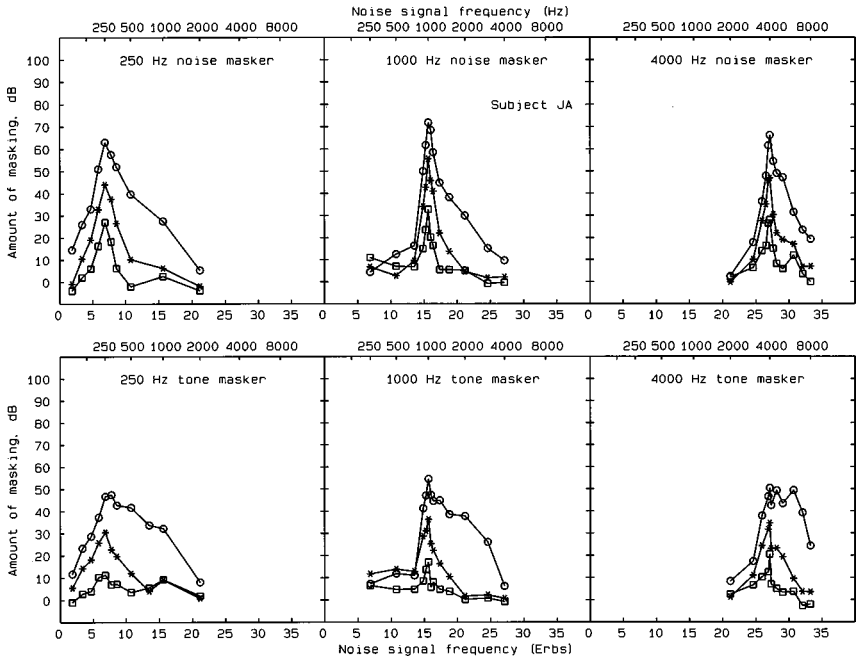

FIG. 5. Results of experiment 3 for subject JA, showing the amount of masking of a noise signal by a noise masker (top) or a tone masker (bottom). Each column shows results for a different masker frequency.

ted on an ERB scale, as in Figs. 5 and 6 (Moore and Glasberg, 1983; Glasberg and Moore, 1990). This is approximately true, although the patterns for JA at 250 Hz are slightly broader than at the two higher frequencies, while the patterns for AO at 4000 Hz are slightly sharper than at the two lower frequencies. The greater breadth at 250 Hz may reflect the fact that the noise bandwidth of 80 Hz was somewhat greater than the ERB at 250 Hz, which is about 52 Hz (Glasberg and Moore, 1990); at 1000 and 4000 Hz the noise bandwidth was less than the ERBs, which are 132 Hz and 456 Hz, respectively.

The masking patterns for the tone masker (lower panels) are generally less regular than for the noise masker, especially for the 4-kHz masker at 85 dB SPL. The changes in the masking patterns across frequency are similar to those reported by Ehmer (1959). The tips of the masking patterns for the tone masker generally fall well below the tips of the patterns for the noise masker, as was also reported by Greenwood (1971) and by Hellman (1972) for tone signals. This is true for signal frequencies adjacent to the masker frequency as well as for the case where the signal frequency equals the masker frequency.

For the 85 dB SPL masker level, the frequency range over which the tone masker produced less masking than the noise masker (by 2 dB or more) corresponded roughly to a constant masker-signal frequency separation of 100–250 Hz, regardless of masker frequency. The mean (regardless of sign) was 163, 187, and 163 Hz, for masker frequencies of

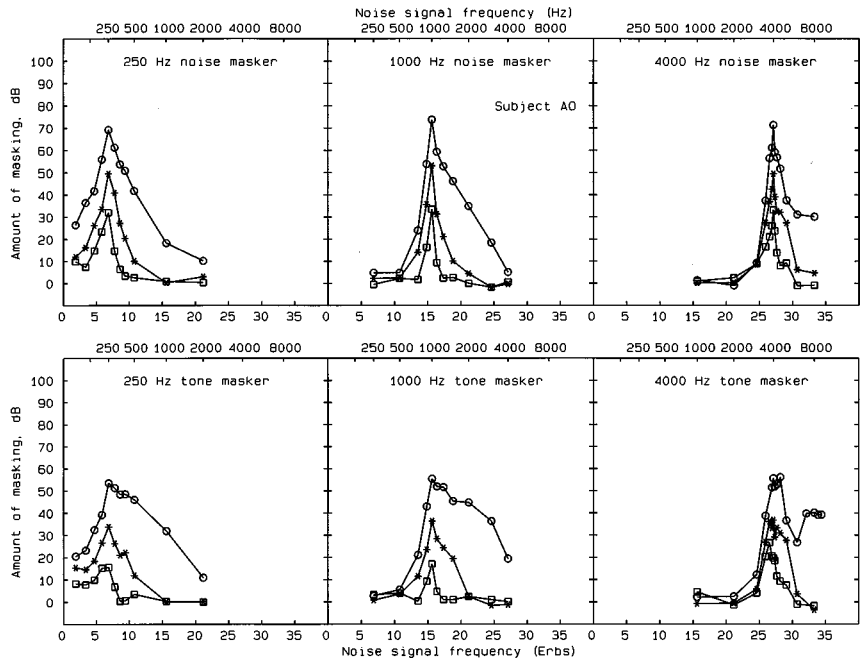

FIG. 6. As Fig. 5, but for subject AO.

250, 1000, and 4000 Hz, respectively. The corresponding mean differences for the 65 dB SPL masker level were 144, 243, and 238 Hz, respectively (it was not possible to conduct a similar analysis for the lowest masker level, as masking occurred only over a limited frequency range). Also, the size of the differences was similar for signal frequencies above and below the masker frequency. These two findings support the idea that the lower thresholds for the tone masker depend upon temporal fluctuations produced by the interaction of signal and masker. The fluctuations become more rapid, and less perceptually salient, as the masker-signal frequency separation increases. If the lower thresholds produced by the tone masker depended on greater detectability of combination products, one would expect the frequency range of the effect to correspond to roughly a constant masker-signal frequency ratio at each level, rather than a constant separation in Hz. If the effect depended on the detection of beats produced by the interaction of a combination product with the masker, one would expect the size of the effect to be greater for signal frequencies above the masker frequency, which is not the case.

For the highest masker level, and for signal frequencies more than 500 Hz above the masker frequency, the tone masker produced more masking than the noise masker. This is consistent with what has been reported previously for tone signals (Buus, 1985; Mott and Feth, 1986; Zwicker and Fastl, 1990; Nelson and Schroder, 1996), and can be explained in terms of ''listening in the dips'' of the noise masker.

The masking patterns for the 4-kHz tone masker at 85 dB show distinct irregularities for both subjects. However, the patterns differ across subjects. The masking pattern for JA has a peak at 6 kHz, while the pattern for AO has a dip at 6 kHz and a peak at 7 kHz. The frequencies of these peaks and dips did not change when the masked thresholds were expressed as SPL, rather than amount of masking. Note that the peaks are not at twice the masker frequency, as would be expected if they were produced by aural harmonics. The dip for AO is very unlikely to be due to the detection of beats between signal and masker, as the beat rate of 2 kHz would be too high for the beats to provide a useful cue. The individual differences in the masking patterns for masker-signal frequency separations exceeding 1000 Hz are probably due to individual differences in the perceptibility of combination products.

In summary, the results suggest that fluctuations in level produced by adding the signal to the masker can play a substantial role for the tone masker for signal frequencies within a few hundred hertz of the masker frequency. Such fluctuations provide an effective detection cue, as fluctuations are completely absent in the nonsignal intervals. However, the fluctuations are less effective for the noise masker, as the inherent fluctuations of the masker are present in all observation intervals. Combination products produced by the interaction of the masker and signal may also play a role, and these are probably the dominant cause of dips in the masking patterns for the 85 dB SPL tone masker for signal frequencies well above the masker frequency.

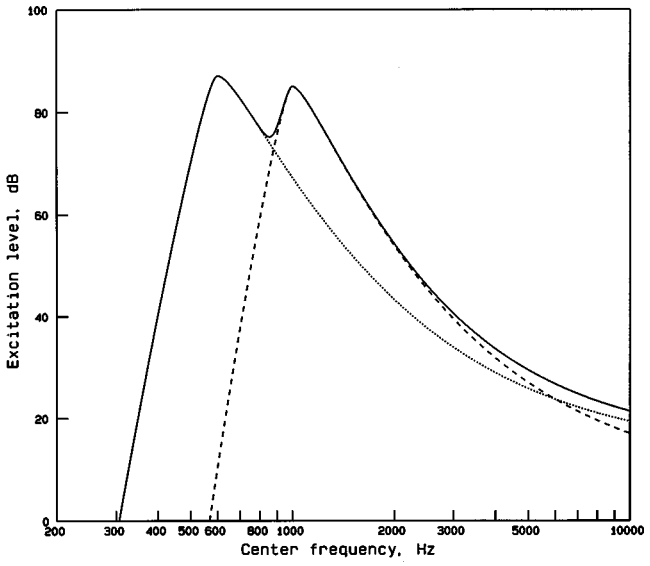

FIG. 7. Illustration of the rationale for experiment 4. The long-dashed line shows the excitation pattern of a 1000-Hz tone at 85 dB SPL. The dotted line shows the excitation pattern for a 600-Hz tone at 85 dB SPL. The solid line shows the excitation pattern produced by combining the two tones.

V. EXPERIMENT 4. THE EFFECT OF ADDING AN ADDITIONAL TONE TO THE MASKER

A. Rationale and method

The goal of this experiment was to see if the distinct dips in the masking patterns for the tone masker and tone signal and the smaller dips for the noise masker and tone signal, as observed in experiment 1, could be eliminated by adding an extra sinusoidal component to the masker to mask combination tones and to reduce the effectiveness of beats as a cue. The added tone was as far below the masker frequency as the signal frequency was above it and thus was coincident with the $2f_1-f_2$ combination tone. The rationale of the experiment is illustrated in Fig. 7.

Consider as an example a 1-kHz tone masker at 85 dB, and a tone signal at 1400 Hz. The excitation pattern produced by the masker, calculated according to the procedure described by Glasberg and Moore (1990), is shown by the dashed curve in Fig. 7. The combination tone $2f_1-f_2$, produced by the interaction of the signal and masker, would fall at 600 Hz. To mask the combination tone, a 600-Hz tone is added to the masker at a level of 85 dB SPL. Its excitation pattern is shown by the dotted line. The excitation pattern produced by combining the two maskers is shown by the solid line. Note that the added tone produces a negligible increase in the excitation evoked by the masker in the frequency region of the 1400-Hz signal. Hence, there should not be any extra masking of the signal caused by an increase in the effective excitation evoked by the masker around 1400 Hz.

The added 600-Hz tone served a second purpose. It would interact with the 1000-Hz tone to give beats at a 400-Hz rate. These beats would be strongest at the outputs of auditory filters tuned around 850 Hz, where the excitation evoked by the two masker components is almost equal. These beats would be expected to make it more difficult to detect the beats due to the interaction of the 1000-Hz masker

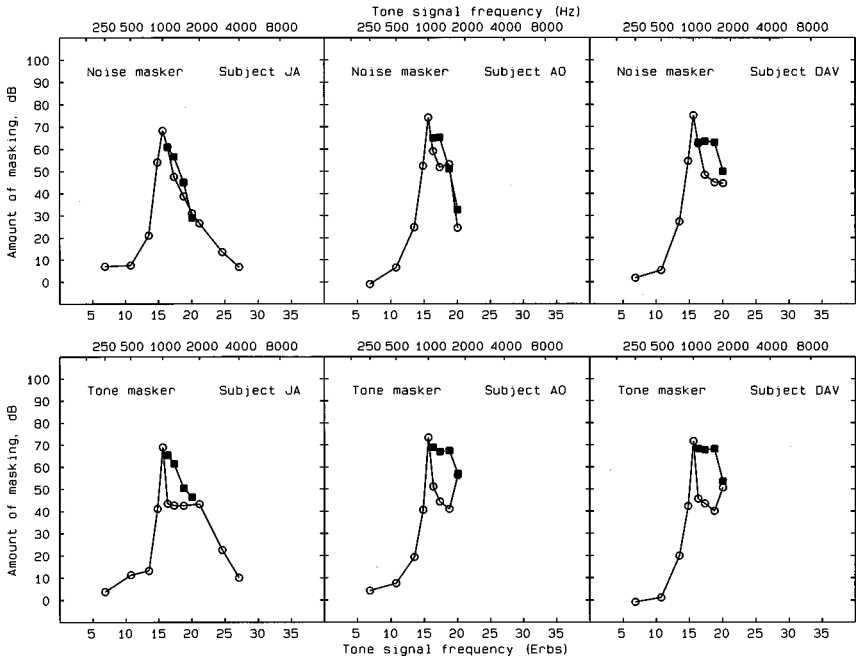

FIG. 8. Results of experiment 4, for three individual subjects. The masker was either a noise (upper panels) or a tone (lower panels). The signal was a tone. The filled squares show results with the added tone. The open circles show results without the added tone. Results for subject JA are reproduced from experiment 1.

component and the signal, because of an effect known as modulation detection interference (MDI) (Yost and Sheft, 1989; Yost *et al.*, 1989). MDI appears to be at least partly an across-channel process, whereby modulation in one frequency region makes it harder to detect modulation in another frequency region. Hence, the added 600-Hz tone would be expected largely to eliminate both of the sources of the dips in the masking patterns.

In the experiment, the main masker was a sinusoid or an 80-Hz-wide band of noise centered at 1 kHz, and it always had a level of 85 dB SPL. The added tone also had a level of 85 dB SPL. For a signal frequency f_s, the added tone had a frequency of $2000-f_s$. The signal frequency ranged from 1100 to 1750 Hz.

Three subjects were used. These were the two subjects of experiment 3 (AO and JA), plus a new normally hearing subject (DAV) who was highly experienced in psychoacoustic tasks, including masking. Absolute thresholds for all subjects are shown in Table I.

B. Results

Figure 8 shows individual results for three subjects. The open symbols show the amount of masking without the added tone; results for JA are taken from experiment 1. The filled squares show the amount of masking with the added tone. Upper panels show results for the noise masker and lower panels show results for the tone masker.

Consider first the results for the tone masker. The added tone produced marked increases in the signal threshold, ranging up to about 20 dB. The added tone eliminated the dips in the masking patterns on the high-frequency side. This is consistent with our expectation that the added tone would both mask the $2f_1-f_2$ combination tone (and any beats produced by the interaction of the combination tone with the 1-kHz masker) and make beats between the signal and masker ineffective as a cue. Hence, the masking patterns obtained in the presence of the added tone may give a reasonably accurate indication of the spread of excitation evoked by the masker for frequencies above the masker frequency.

Consider now the results for the noise masker (upper panels). The added tone resulted in elevated thresholds, the elevations ranging up to about 17 dB. When the added tone was present, the dips in the masking patterns were largely eliminated, although some slight irregularities remained for subjects AO and DAV.

Thresholds obtained with the added tone were 3–8 dB higher for the tone masker than for the noise masker. This difference between the two maskers was small for signal frequencies just above the masker frequency, but tended to increase with increasing signal frequency. The difference can probably be explained in terms of subjects listening in the dips of the noise masker, as described earlier. In the absence of the added tone, the tone masker is *not* more effective than the noise masker for signal frequencies in the range up to 1500 Hz, probably because beats and combination tones produced by interaction of the signal and tone masker provide salient detection cues. The added tone makes these cues less salient, and this allows the effect of dip listening to be revealed over a wider range of signal frequencies.

VI. EXPERIMENT 5. THE INFLUENCE OF A PAIR OF HIGH-FREQUENCY TONES ON MASKING PATTERNS

A. Rationale and method

As a further method for assessing the influence of beat detection on the masking patterns, we measured the effect of adding to the main masker a pair of high-frequency tones, whose frequency separation was equal to that of the main masker and signal. The lower of these two tones had a frequency of 4000 Hz and each tone had a level of 82 dB SPL. For example, if the masker frequency was 1000 Hz, and the signal frequency was 1250 Hz, the two additional tones had frequencies of 4000 Hz and 4250 Hz. The basic idea was that

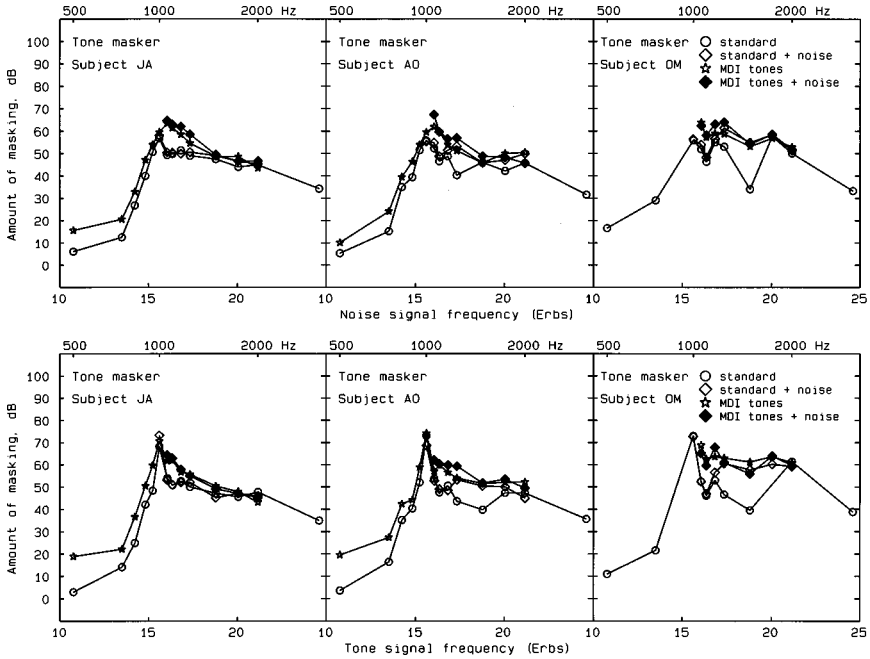

FIG. 9. Results of experiment 5 for three individual subjects. The main masker was a 1000-Hz tone, and the signal was either a noise (upper panels) or a tone (lower panels). Results are shown for: Main masker alone, referred to as ''standard'' (circles); Main masker together with a lowpass noise with an overall level of 75 dB SPL (diamonds); Main masker together with a pair of high-frequency tones, referred to as ''MDI tones'' (stars); Main masker together with a 75 dB SPL low-pass noise and the MDI tones (filled diamonds).

the two high-frequency tones would produce beats, and that these beats would interfere with the detection of beats of the same rate produced by the interaction of the main masker and signal, because of the phenomenon of MDI (Yost and Sheft, 1989; Yost *et al.*, 1989). The beats produced by the high-frequency tones would also interfere with the detection of beats produced by the main masker and the $2f_1-f_2$ combination tone. When the signal frequency was equal to the masker frequency, a single 4000-Hz tone was added to the masker with a level of 85 dB SPL.

The experiment was run following the supplementary experiment described in Sec. III B, and the same subjects were used as in that experiment. The 85-dB tone masker was used with both the tone signal and the noise signal. The following conditions were run:

(1) Main masker alone, referred to as ''standard.''
(2) The main masker together with a low-pass noise with an overall level of 75 dB SPL; this noise was the same as the most intense noise used in the supplementary experiment described in Sec. III B.
(3) The main masker together with the pair of high-frequency tones, referred to as ''MDI tones.''
(4) The main masker together with a 75 dB SPL low-pass noise and the MDI tones.

Initially, we only used signal frequencies above the masker frequency, since we were mainly interested in the irregularities in the masking patterns in that region. However, subsequently, two of the subjects were also run using signal frequencies below the masker frequency (subject OM was no longer available at this stage). In this case, only conditions (1) and (3) were run; it would not have been sensible to include the conditions using low-pass noise, as that noise would have masked the signal.

B. Results

The results are shown in Fig. 9. Note that in this figure the frequency range plotted is smaller than in the previous figures. This was done to display more clearly the frequency region of interest. Consider first the results for signal frequencies above the masker frequency. For subject JA, the masking pattern was essentially the same for the main masker alone and the main masker plus the low-pass noise, for both the noise signal and tone signal. For the two conditions with MDI tones, thresholds were somewhat elevated. The elevation occurred over the frequency range 1060 Hz–1500 Hz for the tone signal, suggesting that beats played a role for masker-frequency separations up to 500 Hz. However, for the noise signal, the elevation only occurred for signal frequencies up to 1250 Hz.

For subjects AO and OM, adding the MDI tones to the tonal masker elevated thresholds more than adding only the low-pass noise, for signal frequencies up to about 1250 Hz. This suggests that detection of beats between the masker and signal played a role for signal frequencies up to 1250 Hz. Interestingly, thresholds obtained with the MDI tones added generally did not change much when the low-pass noise was also added. At first sight, it may appear surprising that adding the MDI tones resulted in masked thresholds around 1500 Hz that were similar to those obtained when low-pass noise was added; one would expect the MDI tones to hinder beat detection, but not to mask the $2f_1-f_2$ combination product. The similarity of thresholds produced by the addition of the low-pass noise and the MDI tones around 1500 Hz probably happened because the MDI tones gave rise to a simple difference tone which acted as a masker of the cubic difference tone produced by the interaction of the main masker and signal. For example, when the signal frequency was 1500 Hz, $2f_1-f_2$ would have fallen at 500 Hz, the same frequency as the simple difference tone produced by the 4000-Hz and 4500-Hz MDI tones. When listening to the

MDI tones alone, subjects reported that they could indeed hear a low-frequency tone with pitch corresponding to the simple difference tone.

Note that masking by a simple difference tone would not be significant for signal frequencies of 1250 Hz and below; indeed such masking may have been negligible for signal frequencies more than about 100 Hz above or below 1500 Hz. For example, for a signal frequency of 1250 Hz, $2f_1 - f_2$ would have fallen at 750 Hz, but the difference tone produced by the MDI tones would have fallen at 250 Hz. A low-level 250-Hz tone would be expected to produce very little masking of a 750-Hz combination product. Two findings suggest that, for signal frequencies up to 1250 Hz, detection of beats between the signal and masker rather than combination-product detection (or detection of beats between $2f_1 - f_2$ and the masker), was responsible for the masked threshold in the standard condition (main masker alone). First, the amount of masking was almost unaffected by the lowpass noise alone. Second, the MDI tones produced threshold elevations, but masked thresholds in the presence of the MDI tones were almost unaffected by the presence or absence of the low-pass noise.

In the presence of the MDI tones, the masking patterns were generally reasonably smooth, except for small dips in the patterns for subject OM around 1100 Hz. These small residual dips probably occurred because the MDI tones did not make beats completely undetectable; modulated interfering sounds can make it more difficult to detect beats, but they do not mask beats completely (Yost and Sheft, 1989; Yost *et al.*, 1989).

For the noise signal, the amounts of masking for signal frequencies just above the masker frequency were actually greater than when the signal frequency equaled the masker frequency. This probably happened because, for the noise signal, there was a within-interval cue of a fluctuation in level when the signal frequency equaled the masker frequency. This cue would not have been disrupted by the extra high-frequency component, because in this special case the extra component was a single tone at 4000 Hz. For the tone signal, the amount of masking was always greatest when the signal frequency equaled the masker frequency.

Consider now the results for signal frequencies below the masker frequency. The MDI tones resulted in amounts of masking that were typically about 5–10 dB higher than for the standard condition. However, the extra masking was greater, especially for JA, when the signal frequency was 500 Hz. This probably happened because, in this special case, the simple difference tone produced by the MDI tones had a frequency of 500 Hz; this tone probably contributed to the masking of the signal. For higher signal frequencies, the simple difference tone would have fallen at lower frequencies, and would have contributed less to the masking of the signal. The extra masking produced by the MDI tones for signal frequencies of 750 Hz and above (for which the simple difference tone produced by the MDI tones would have fallen at 250 Hz or below) was almost certainly produced by disruption of the ability to detect beats between the primary masker and signal.

In summary, the addition of the MDI tones to the main masker produced higher thresholds than obtained in the presence of a low-pass noise for signal frequencies from 1060 to 1250 Hz. The MDI tones also increased the amount of masking for signal frequencies below the masker frequency. The results suggest that beats between the masker and signal influenced the masking patterns for the main masker alone for signal frequencies within 250 Hz of the masker frequency.

VII. DISCUSSION

The results indicate that the masking patterns for tone maskers can be strongly influenced both by the detection of combination products and by temporal interactions between the signal and masker (beats). The temporal interactions seem to play a role not only for signal frequencies very close to the masker frequency, as assumed by Wegel and Lane (1924) and by Egan and Hake (1950). Rather, they probably play a role for masker-frequency separations up to about 250 Hz. This is indicated by the results of experiment 2, which showed that when a low-pass noise was added to an 85 dB SPL tone masker to mask combination products, dips, and/or irregularities in the masking patterns persisted for signal frequencies up to about 250 Hz above the masker frequency. It is also indicated by the results of experiment 3, which showed that thresholds for a noise signal were higher for a narrow-band noise masker than for a tone masker over a range of 100–250 Hz on either side of the masker frequency, regardless of the masker frequency, for masker levels of 65 and 85 dB SPL. Finally, it is indicated by the results of experiment 5, which showed that the addition of a pair of high-frequency beating tones to the 85 dB SPL main masker produced higher thresholds than obtained in the presence of a low-pass noise (or the main masker alone for signal frequencies below the masker frequency) for signal-masker frequency separations up to 250 Hz.

It is generally assumed that beats play little role in the detection of a narrow-band signal in a noise masker, since the inherent random amplitude fluctuations in the masker make beats less salient as a cue (Egan and Hake, 1950). However, this may not be completely true. One might think of this in terms of masking in the modulation domain (Bacon and Grantham, 1989; Houtgast, 1989; Dau, 1996; Dau *et al.*, 1997). The inherent fluctuations in the masker will be most effective in masking the beats when the modulation spectrum of the masker contains strong components at the beat frequency. The modulation spectrum of the masker depends on its bandwidth; the narrower the bandwidth, the more the modulation spectrum is concentrated at low frequencies. For the 80-Hz-wide noise masker used by us, the modulation spectrum is mainly concentrated below 80 Hz (Lawson and Uhlenbeck, 1950). Hence, assuming that there is some frequency selectivity in the modulation domain, the effectiveness of the inherent fluctuations of the masker in masking the beats would have decreased as the masker-signal frequency separation (corresponding to the average beat rate) increased above 80 Hz. If this argument is correct, then temporal interactions between the signal and masker may have influenced a considerable portion of the masking patterns for the noise masker.

It is of interest to consider which, if any, of the masking patterns give the most accurate indication of the spread of excitation evoked by the masker. As described earlier, it has often been assumed that masking patterns for narrow-band noise maskers are the best for this purpose. However, this may not be the case for two reasons. First, as discussed immediately above, temporal interactions between the signal and masker may influence the masking patterns for signal frequencies up to a few hundred hertz from the masker frequency. Second, subjects may ''listen in the dips'' of the masker envelope, an effect which is especially large for signal frequencies well above the masker frequency, but which probably occurs to some extent even for small masker-signal frequency separations (Buus, 1985). Zwicker and Feldtkeller (1967) and Buus (1985) suggested that masking patterns for sharply filtered low-pass noise maskers would give a good indication of the spread of excitation above the masker cutoff frequency. However, even for such maskers, there would be some envelope fluctuations at the outputs of auditory filters tuned above the signal frequency, which would give opportunities for dip listening. This would be especially true for low cutoff frequencies of the masker, as the bandwidth of the auditory filter is small at low center frequencies (Peters and Moore, 1992; Rosen and Stock, 1992; Moore and Sek, 1995).

The most accurate indication of the spread of masker excitation to frequencies above the masker frequency might be given by the masking pattern for a tone masker and tone signal obtained in the presence of an additional tone, as was done in experiment 4. The additional tone was placed at a frequency $2f_m - f_s$ and it served both to mask the $2f_1 - f_2$ combination tone and to make beats between the masker and signal less effective as a cue. Once the signal frequency is more than twice the masker frequency, then beats and combination tones probably play little role, and the additional tone is unnecessary. However, in this case an additional factor, namely suppression, may complicate the interpretation of the masking pattern. It has been suggested that, for masker frequencies well below the signal frequency, the masking of the signal is determined mainly by suppression of the signal, rather than by spread of masker excitation (Kiang, 1974; Delgutte, 1990, 1996). The data of Moore and Vickers (1997) suggest that suppression plays a strong role in this situation but is not completely responsible for the masking of the signal. In any case, it seems likely that the masking pattern for a sinusoidal masker, for signal frequencies well above the masker frequency, overestimates the spread of excitation of the masker.

Estimating the spread of masker excitation to frequencies below the masker frequency is also problematic. The masked thresholds in this frequency range are probably not influenced by the detection of combination products produced by the interaction of signal and masker. However, for a noise masker thresholds may be influenced by the combination products produced by the interaction of components within the masker, unless the masker bandwidth is very small (Bilger and Hirsh, 1956; Greenwood, 1971; Glasberg and Moore, 1994). For both noise and tone maskers, thresholds may be influenced by the presence of beats between the signal and the masker, the effect being more pronounced for the tone masker. The technique used in experiment 5, of adding a pair of high-frequency MDI tones to the main masker, may be effective in reducing the detectability of beats. However, when the signal frequency is well below the masker frequency, the simple difference tone produced by the MDI tones may contribute to the masking of the signal.

VIII. SUMMARY AND CONCLUSIONS

Experiment 1 examined the shapes of masking patterns for sinusoidal and narrow-band noise maskers, and sinusoidal and narrow-band noise signals, using masker levels of 45, 65, and 85 dB SPL. The shapes of the masking patterns for signal frequencies above and below the masker frequency were determined mainly by the characteristics of the masker rather than by the characteristics of the signal. The masking patterns for both types of masker showed dips immediately above the masker frequency, which can be attributed partly to the detection of combination products. The dips for the tone masker were much larger than those for the noise masker. When the signal frequency was equal to the masker frequency, thresholds were similar for all masker-signal combinations except the tone masker and noise signal, which gave much lower thresholds. The lower thresholds can be attributed to the availability of a within-channel cue of a fluctuation in level.

Experiment 2 examined the effect of adding low-pass noise to the 1-kHz 85 dB SPL masker, to mask combination products produced by the interaction of signal and masker. The noise largely eliminated the dips in the masking patterns for the noise masker. The dips for the tone masker were reduced, but not eliminated. For the tone masker, the noise had no effect on masked thresholds for signal frequencies between 1100 Hz and 1170 Hz, even though the highest noise level used should have been sufficient to mask combination products produced by signals at those frequencies. This suggests that some other factor, presumably beats between the signal and masker, contributed to the dips in the masking patterns for signal frequencies close to the masker frequency.

Experiment 3 compared masking patterns using a noise signal with tone or noise maskers using a wide range of masker frequencies and masker levels of 45, 65, and 85 dB SPL. The tone masker produced less masking than the noise masker for signal frequencies within 100–250 Hz of the masker frequency, for all masker frequencies and for signal frequencies both below and above the masker frequency. This suggests that the lower thresholds produced by the tone masker result mainly from more effective beat detection rather than from greater detectability of combination products. However, combination products produced by the interaction of the masker and signal are probably the dominant cause of dips in the masking patterns for the tone masker for signal frequencies well above the masker frequency.

Experiment 4 examined how adding an extra sinusoid with frequency below that of the main 85 dB SPL masker affected detection of signals above the masker frequency. This tone was intended both to mask combination products and to reduce the salience of beats produced by the interac-

tion of the signal and main masker. For both tone and noise maskers, the added tone largely eliminated the dips in the masking patterns. When the added tone was present, the tone masker produced more masking than the noise masker, consistent with the idea that subjects can listen in the dips of the noise masker.

Experiment 5 explored the effect of adding a pair of high-frequency tones to the main 85 dB SPL masker; the frequency separation of these tones was equal to the separation of the main masker and signal, so the added tones produced beats at the same rate as those produced by the interaction of the main masker and signal. A low-pass noise designed to mask combination tones was also presented in some conditions. The addition of the high-frequency tones to the main masker produced higher thresholds than did addition of a low-pass noise for masker-signal frequency separations up to 250 Hz. This suggests that beats between the masker and signal influenced the masking patterns for the main masker alone over this frequency range.

It is suggested that the spread of masker excitation to frequencies above the masker frequency may best be estimated by using a sinusoidal masker in the presence of an extra tone, as in experiment 4. Estimating the spread of masker excitation to lower frequencies may best be done in the presence of a pair of high-frequency MDI tones, as in experiment 5.

ACKNOWLEDGMENTS

This work was supported by Phonak AG (Switzerland), by the Medical Research Council (UK), and by the European Union (SPACE project). We thank Hiva Fassihi and Bhashkar Mukherjee for gathering some of the data reported in this paper, Brian Glasberg for writing the computer program to run the experiments, and Tom Baer, Stefan Launer, Søren Buus, Joseph L. Hall, Joseph W. Hall, and an anonymous reviewer for helpful discussions and comments on an earlier version of this paper.

Bacon, S. P., and Grantham, D. W. (**1989**). ''Modulation masking: Effects of modulation frequency, depth and phase,'' J. Acoust. Soc. Am. **85**, 2575–2580.

Bilger, R. C., and Hirsh, I. J. (**1956**). ''Masking of tones by bands of noise,'' J. Acoust. Soc. Am. **28**, 623–630.

Bos, C. E., and de Boer, E. (**1966**). ''Masking and discrimination,'' J. Acoust. Soc. Am. **39**, 708–715.

Buus, S. (**1985**). ''Release from masking caused by envelope fluctuations,'' J. Acoust. Soc. Am. **78**, 1958–1965.

Dau, T. (**1996**). ''Modeling auditory processing of amplitude modulation,'' Ph.D. Thesis, University of Oldenburg.

Dau, T., Kollmeier, B., and Kohlrausch, A. (**1997**). ''Modeling auditory processing of amplitude modulation: I. Detection and masking with narrowband carriers,'' J. Acoust. Soc. Am. **102**, 2892–2905.

Delgutte, B. (**1990**). ''Physiological mechanisms of psychophysical masking: Observations from auditory-nerve fibers,'' J. Acoust. Soc. Am. **87**, 791–809.

Delgutte, B. (**1996**). ''Physiological models for basic auditory percepts,'' in *Auditory Computation*, edited by H. L. Hawkins, T. A. McMullen, A. N. Popper, and R. R. Fay (Springer-Verlag, New York).

Egan, J. P., and Hake, H. W. (**1950**). ''On the masking pattern of a simple auditory stimulus,'' J. Acoust. Soc. Am. **22**, 622–630.

Ehmer, R. H. (**1959**). ''Masking patterns of tones,'' J. Acoust. Soc. Am. **31**, 1115–1120.

Fassel, R., Kohlrausch, A., and Dau, T. (**1998**). ''The influence of carrier level and frequency on modulation and beat-detection thresholds for sinusoidal carriers,'' J. Acoust. Soc. Am. (submitted).

Fletcher, H. (**1940**). ''Auditory patterns,'' Rev. Mod. Phys. **12**, 47–65.

Fletcher, H., and Munson, W. A. (**1937**). ''Relation between loudness and masking,'' J. Acoust. Soc. Am. **9**, 1–10.

Glasberg, B. R., and Moore, B. C. J. (**1990**). ''Derivation of auditory filter shapes from notched-noise data,'' Hearing Res. **47**, 103–138.

Glasberg, B. R., and Moore, B. C. J. (**1994**). ''Growth-of-masking functions for several types of maskers,'' J. Acoust. Soc. Am. **96**, 134–144.

Goldstein, J. L. (**1967**). ''Auditory nonlinearity,'' J. Acoust. Soc. Am. **41**, 676–689.

Greenwood, D. D. (**1961**). ''Auditory masking and the critical band,'' J. Acoust. Soc. Am. **33**, 484–501.

Greenwood, D. D. (**1971**). ''Aural combination tones and auditory masking,'' J. Acoust. Soc. Am. **50**, 502–543.

Greenwood, D. D. (**1972**). ''Masking by combination bands: Estimation of the levels of the combination bands $(n+1)f_l - nf_h$,'' J. Acoust. Soc. Am. **52**, 1144–1154.

Greenwood, D. D., and Joris, P. X. (**1996**). ''Mechanical and ''temporal'' filtering as codeterminants of the response by cat primary fibers to amplitude-modulated signals,'' J. Acoust. Soc. Am. **99**, 1029–1039.

Hall, J. L. (**1997**). ''Asymmetry of masking revisited: Generalization of masker and probe bandwidth,'' J. Acoust. Soc. Am. **101**, 1023–1033.

Hartmann, W. M. (**1987**). ''Temporal fluctuation and the discrimination of spectrally dense signals by human listeners,'' in *Auditory Processing of Complex Signals*, edited by W. A. Yost and C. S. Watson (Erlbaum, Hillsdale, NJ).

Hellman, R. P. (**1972**). ''Asymmetry of masking between noise and tone,'' Percept. Psychophys. **11**, 241–246.

Houtgast, T. (**1989**). ''Frequency selectivity in amplitude-modulation detection,'' J. Acoust. Soc. Am. **85**, 1676–1680.

Kiang, N. Y.-S. (**1974**). ''Tails of tuning curves of auditory-nerve fibers,'' J. Acoust. Soc. Am. **55**, 620–630.

Kidd, G., Mason, C. R., Brantley, M. A., and Owen, G. A. (**1989**). ''Roving level tone-in-noise detection,'' J. Acoust. Soc. Am. **86**, 1310–1317.

Killion, M. C. (**1978**). ''Revised estimate of minimal audible pressure: Where is the 'missing 6 dB'?,'' J. Acoust. Soc. Am. **63**, 1501–1510.

Lawson, J. L., and Uhlenbeck, G. E. (**1950**). *Threshold Signals (Volume 24 of Radiation Laboratory Series)* (McGraw-Hill, New York).

McGill, W. J., and Goldberg, J. P. (**1968**). ''A study of the near-miss involving Weber's law and pure-tone intensity discrimination,'' Percept. Psychophys. **4**, 105–109.

Moore, B. C. J. (**1997**). *An Introduction to the Psychology of Hearing* (Academic, San Diego), 4th ed.

Moore, B. C. J., and Glasberg, B. R. (**1983**). ''Suggested formulae for calculating auditory-filter bandwidths and excitation patterns,'' J. Acoust. Soc. Am. **74**, 750–753.

Moore, B. C. J., and Glasberg, B. R. (**1987**). ''Factors affecting thresholds for sinusoidal signals in narrow-band maskers with fluctuating envelopes,'' J. Acoust. Soc. Am. **82**, 69–79.

Moore, B. C. J., and Sek, A. (**1995**). ''Auditory filtering and the critical bandwidth at low frequencies,'' in *Advances in Hearing Research*, edited by G. A. Manley, G. M. Klump, C. Köppl, H. Fastl, and H. Oeckinghaus (World Scientific, Singapore).

Moore, B. C. J., and Vickers, D. A. (**1997**). ''The role of spread of excitation and suppression in simultaneous masking,'' J. Acoust. Soc. Am. **102**, 2284–2290.

Mott, J. B., and Feth, L. L. (**1986**). ''Effects of the temporal properties of a masker upon simultaneous masking patterns,'' in *Auditory Frequency Selectivity*, edited by B. C. J. Moore and R. D. Patterson (Plenum, New York).

Nelson, D. A., and Schroder, A. C. (**1996**). ''Release from upward spread of masking in regions of high-frequency hearing loss,'' J. Acoust. Soc. Am. **100**, 2266–2277.

Peters, R. W., and Moore, B. C. J. (**1992**). ''Auditory filter shapes at low center frequencies in young and elderly hearing-impaired subjects,'' J. Acoust. Soc. Am. **91**, 256–266.

Rosen, S., and Stock, D. (**1992**). ''Auditory filter bandwidths as a function of level at low frequencies (125 Hz–1 kHz),'' J. Acoust. Soc. Am. **92**, 773–781.

Siegel, J. H. (**1994**). ''Ear-canal standing waves and high-frequency sound calibration using otoacoustic emission probes,'' J. Acoust. Soc. Am. **95**, 2589–2597.

Smoorenburg, G. F. (**1972**). ''Audibility region of combination tones,'' J. Acoust. Soc. Am. **52**, 603–614.
van der Heijden, M., and Kohlrausch, A. (**1995**). ''The role of envelope fluctuations in spectral masking,'' J. Acoust. Soc. Am. **97**, 1800–1807.
Viemeister, N. F. (**1972**). ''Intensity discrimination of pulsed sinusoids: The effects of filtered noise,'' J. Acoust. Soc. Am. **51**, 1265–1269.
Wegel, R. L., and Lane, C. E. (**1924**). ''The auditory masking of one sound by another and its probable relation to the dynamics of the inner ear,'' Phys. Rev. **23**, 266–285.
Yost, W. A., and Sheft, S. (**1988**). ''Detecting amplitude modulation of sinusoidal carriers,'' J. Acoust. Soc. Am. **83**, S35.
Yost, W. A., and Sheft, S. (**1989**). ''Across-critical-band processing of amplitude-modulated tones,'' J. Acoust. Soc. Am. **85**, 848–857.
Yost, W. A., Sheft, S., and Opie, J. (**1989**). ''Modulation interference in detection and discrimination of amplitude modulation,'' J. Acoust. Soc. Am. **86**, 2138–2147.
Zwicker, E. (**1954**). ''Die Verdeckung von Schmalbandgeräuschen durch Sinustöne,'' Acustica **4**, 415–420.
Zwicker, E. (**1956**). ''Die elementaren Grundlagen zur Bestimmung der Informationskapazität des Gehörs,'' Acustica **6**, 356–381.
Zwicker, E. (**1970**). ''Masking and psychological excitation as consequences of the ear's frequency analysis,'' in *Frequency Analysis and Periodicity Detection in Hearing*, edited by R. Plomp and G. F. Smoorenburg (Sijthoff, Leiden).
Zwicker, E. (**1980**). ''Reversed behavior of masking at low levels,'' Audiology **19**, 330–334.
Zwicker, E. (**1981**). ''Dependence of level and phase of the $(2f_1-f_2)$-cancellation tone on frequency range, frequency difference, level of primaries, and subject,'' J. Acoust. Soc. Am. **70**, 1277–1288.
Zwicker, E., and Fastl, H. (**1990**). *Psychoacoustics—Facts and Models* (Springer-Verlag, Berlin).
Zwicker, E., and Feldtkeller, R. (**1967**). *Das Ohr als Nachtrichtenempfänger* (Hirzel-Verlag, Stuttgart).
Zwicker, E., and Jaroszewski, A. (**1982**). ''Inverse frequency dependence of simultaneous tone-on-tone masking patterns at low levels,'' J. Acoust. Soc. Am. **71**, 1508–1512.

The role of excitation-pattern cues and temporal cues in the frequency and modulation-rate discrimination of amplitude-modulated tones

Christophe Micheyl
MRC Cognition and Brain Sciences Unit, 15 Chaucer Road, Cambridge CB2 2EF, England and Department of Experimental Psychology, University of Cambridge, Downing Street, Cambridge CB2 3EB, England

Brian C. J. Moore
Department of Experimental Psychology, University of Cambridge, Downing Street, Cambridge CB2 3EB, England

Robert P. Carlyon
MRC Cognition and Brain Sciences Unit, 15 Chaucer Road, Cambridge CB2 2EF, England

(Received 29 December 1997; revised 25 March 1998; accepted 21 April 1998)

These experiments examine the influence of excitation-pattern cues and temporal-fine-structure cues on frequency difference limens (FDLs) measured as a function of duration. In the first three conditions, listeners were required to detect a change in carrier frequency from a baseline of 250 or 2000 Hz, for stimuli with half-amplitude durations ranging from 5 to 320 ms. In the ''steady'' condition, duration was manipulated by increasing the steady-state portion of the envelope between two 5-ms linear onset and offset ramps. This resulted in spectra and excitation patterns that broadened with decreasing duration. In the ''modulated'' condition, the carrier was amplitude modulated with a triangle function (period 10 ms) and duration was manipulated by varying the number of cycles of the modulator. In this case, the spectral envelope did not vary with duration, but the width of individual spectral lobes broadened with decreasing duration. The ''low-peak-constant'' condition was similar to the modulated condition, except that an increase in carrier frequency was accompanied by a decrease in the period of the modulator, so as to hold constant the frequency of the spectral lobe located roughly 100 Hz below the carrier frequency. In this condition, changes in carrier frequency resulted in minimal changes in excitation level on the low-frequency side of the excitation pattern, but changes on the high-frequency side were larger than for the first two conditions. Both the values of the FDLs, and their variation with frequency and duration, were similar in these three conditions. The fourth, ''modulator varying,'' condition differed in that the carrier frequency was held constant and listeners were required to detect a change in modulator frequency. Thresholds were expressed as the change in frequency of the spectral side lobes adjacent to the carrier frequency (''equivalent'' FDLs). Excitation-pattern cues in this condition were at least as large as in the first three conditions. However, equivalent FDLs were significantly higher than for the other three conditions. The higher FDLs are attributed to the lack of temporal fine-structure cues related to the carrier frequency. Overall, the results suggest that FDLs in the first three conditions were determined by temporal cues rather than by excitation-pattern cues. The increase of the FDLs with decreasing duration did not arise from increasing spectral splatter. [S0001-4966(98)03708-4]

PACS numbers: 43.66.Fe, 43.66.Hg [RVS]

INTRODUCTION

It is well established that frequency difference limens (FDLs) for pure tones increase as stimulus duration decreases (Turnbull, 1944; Konig, 1957; Liang and Chistovich, 1961; Sekey, 1963; Henning, 1970; Moore, 1973; Freyman and Nelson, 1986) and that the increase is more marked at low than at high frequencies (Liang and Chistovich, 1961; Sekey, 1963; Moore, 1973; Freyman and Nelson, 1986). One interpretation of this phenomenon is based on an excitation-pattern model (Zwicker, 1956, 1970). According to this model, frequency discrimination depends on the detection of differences in the patterns of excitation evoked successively in the auditory system by the stimuli to be discriminated. Zwicker (1956, 1970) assumed that a change in frequency can be detected whenever the excitation patterns differ at any point by more than a criterion value. The size of the FDL is predicted to be inversely proportional to the slope of the excitation pattern at its steepest point, and directly proportional to the criterion value.

In the framework of this model, the increase in FDL with decreasing stimulus duration can be accounted for by two factors. The first is that the criterion change in excitation level probably increases with decreasing duration (Henning, 1970; Moore, 1972; Florentine, 1986). The second is that the slopes of the stimulus spectrum become shallower as duration is reduced, an effect known as spectral splatter. Below a critical duration, the slope of the spectrum becomes less than

the slope of the excitation pattern evoked by a long-duration tone, and so the slope of the spectrum becomes a limiting factor (Moore, 1973). Because the slope of the spectrum is independent of frequency, while the slopes of auditory filters, expressed in dB/Hz, increase with decreasing center frequency, then, as duration is decreased, the spectral slope becomes a limiting factor earlier for low frequencies than for high frequencies. This could explain the greater effect of duration on FDLs at low frequencies, and, in particular, the findings that there exist ''kneepoints'' in the functions relating FDLs to duration, and that the durations at these kneepoints increase with decreasing signal frequency (Liang and Chistovich, 1961; Freyman and Nelson, 1986). However, these kneepoints are often not well defined by the data, especially for high center frequencies (Moore, 1973).

Other data have indicated that an excitation-pattern model cannot entirely account for FDLs. In particular, the size of the FDL for low frequencies and short durations is smaller than predicted by the model (Moore, 1973). Moreover, for long-duration tones, the variation of FDLs with frequency does not follow one prediction of the excitation-pattern model (Zwicker, 1956), which is that the FDL should be a constant proportion of the auditory filter bandwidth at the same center frequency (Moore, 1974; Moore and Glasberg, 1986, 1989; Sek and Moore, 1995).

Mechanisms for pitch extraction operating in the temporal domain were suggested many years ago in order to account for the perception of the residue pitch elicited by complex tones (Schouten, 1940, 1970). The basic underlying principle of such temporal mechanisms is the measurement by the auditory system of time intervals between peaks in the fine structure of the stimulus waveform. The increase in FDLs with decreasing duration is explained by this mechanism in terms of the decreasing number of waveform periods that can be sampled (Goldstein and Srulovicz, 1977). Although the model of Goldstein and Srulovicz can account for the greater effect of duration on FDLs at low frequencies, it does this by adjustment of a parameter, τ_m, which represents the upper bound on the processed interspike intervals; the value of τ_m used for each frequency is chosen to give the correct duration dependence. Thus the model fits the data, but it does not actually predict them.

Support for a temporal account of the effect of duration on FDLs comes from an experiment performed by Plack and Carlyon (1995). They showed that the effect of duration on FDLs for (the fundamental frequency of) harmonic complex tones was greater for tones with unresolved harmonics than for tones with resolved harmonics. They argued that, for the latter, listeners could detect changes in the periods of the individual resolved harmonics (Patterson *et al.*, 1983), but that, for unresolved harmonics, they were forced to rely on the periodicity of the envelope. They suggested that, when there are only a few periods in the signal, further decreases in duration produce a larger effect on FDLs than the same proportional decrease in a larger number of periods. In support of this idea, they noted that the variation of FDLs with duration was similar for a group of unresolved harmonics with a fundamental frequency of 250 Hz and for a 250-Hz pure tone (Moore, 1973).

While temporal theories have become more popular over the last two decades, such theories are not universally accepted, and some researchers have concluded that frequency discrimination data are broadly consistent with an excitation-pattern model (Freyman and Nelson, 1986). The present experiment was designed to test the relative importance of temporal fine structure cues and excitation-pattern cues associated with spectral splatter for the frequency discrimination of unmodulated and amplitude-modulated sinusoidal carriers.

I. RATIONALE AND PREDICTIONS

A. Rationale

The stimuli were chosen to manipulate the extent to which excitation-pattern cues and temporal cues were available. If FDLs depend on excitation-pattern cues, then excitation-pattern differences between just-discriminable stimuli should be similar for all conditions. FDLs were measured as a function of duration for 250- and 2000-Hz tones in four different conditions, as illustrated schematically in Fig. 1. The figure is simplified in that, although the time-domain representations (right-hand panels) are for brief stimuli, with total durations of about 20 ms, the spectra are represented by discrete lines rather than by broad lobes (left-hand panels). Also, for the conditions illustrated in panels (b)–(d), the spectra contained multiple side lobes, but only the two side lobes with the highest amplitude are shown. When describing each condition we will also refer to calculated excitation patterns of selected stimuli in those conditions, as shown in Fig. 2. Full details of the calculations, which were implemented using the algorithm described by Glasberg and Moore (1990), are given in the Appendix. The effect of a background pink noise that was present during the experiments was included in the calculations. It has been suggested that the high-frequency slopes of excitation patterns are not as steep as predicted by this algorithm (van der Heijden and Kohlrausch, 1994). If so, the excitation-pattern differences on the high-frequency sides of the excitation patterns would be somewhat smaller than shown in Fig. 2.

The ''steady'' condition [Fig. 1(a)] was an approximate replication of earlier studies (Henning, 1970; Moore, 1973). FDLs were measured for a sinusoid gated on and off with 5-ms linear ramps, and containing a steady-state portion with a duration between 0 and 315 ms. The left-hand part of Fig. 2(a) shows simulated excitation patterns for a 250-Hz standard and a 254-Hz signal having an ''effective'' duration (measured between the half-amplitude points) of 20 ms. These same frequencies will be used in subsequent examples. The small ripples on the skirts of the excitation patterns correspond to the side lobes in the spectra. The difference between these excitation patterns (right-hand side of the figure) is greatest (just over 1 dB) on the low-frequency side. The greatest difference also occurred on the low-frequency side for other durations and frequency differences. In this condition the spectrum broadened with decreasing duration.

The ''modulated'' condition [Fig. 1(b)] was similar to the steady condition, except that the stimuli were 100% amplitude modulated by an integer number of cycles of a dc-

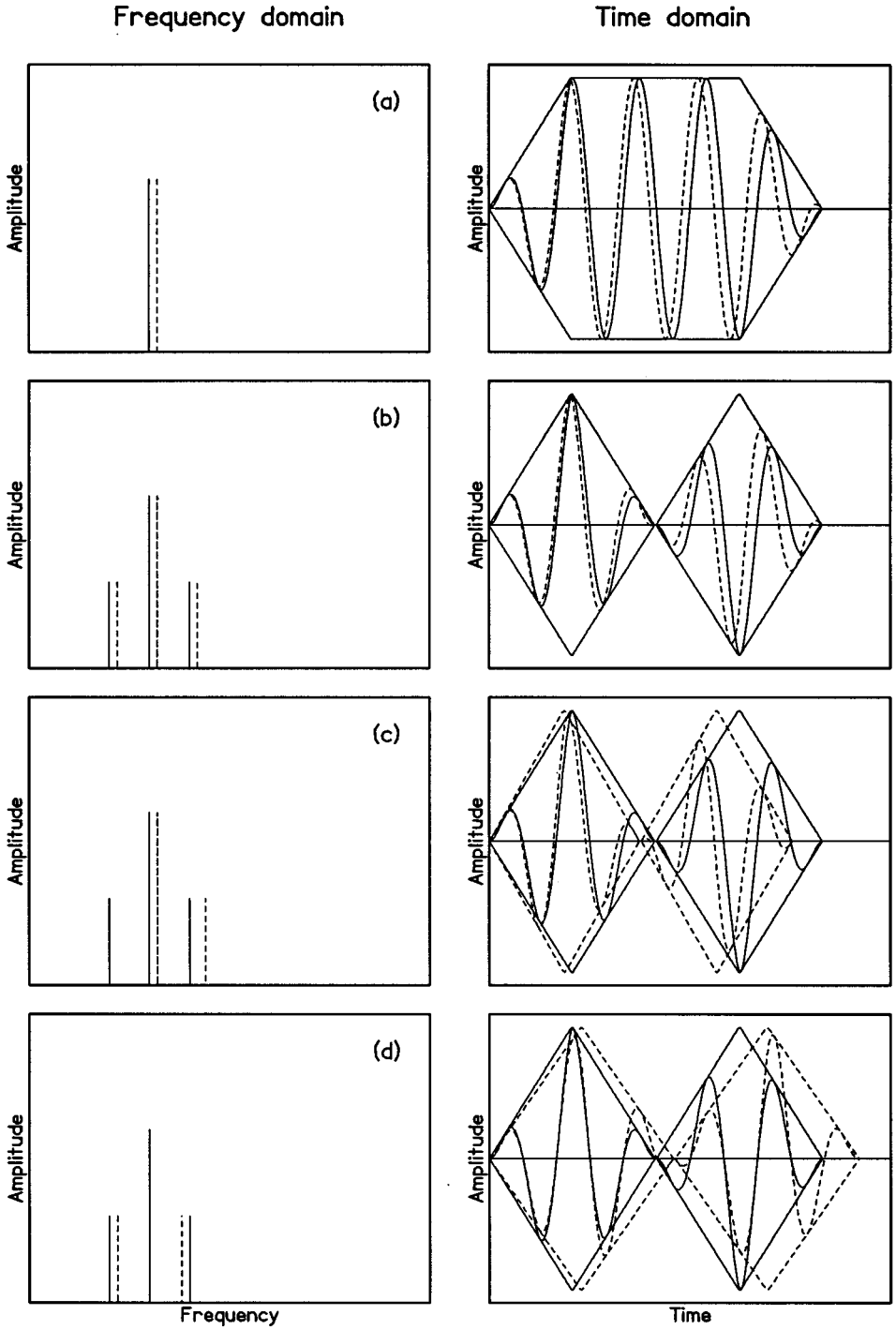

FIG. 1. Schematic representation of the stimuli used in the different conditions. The left-hand column shows simplified spectra, consisting of the main peak and the two most prominent modulation side lobes. The right-hand column shows temporal waveforms, with the envelope superimposed, for the standard (solid line) and signal (dashed line). The four panels illustrate the four conditions: (a) steady, (b) modulated, (c) low-peak-constant, (d) modulator-varying.

shifted triangular waveform having a period of 10 ms. The task was to detect a change in carrier frequency. In this condition, the shortest stimulus was identical to that in the steady condition, and duration was manipulated by varying the number of cycles of the modulator. Again, as can be seen in Fig. 2(b), the greatest changes in excitation (about 1.4 dB) occur on the low-frequency side of the excitation pattern. These changes are strongly influenced by the shift in the frequency of the lower side lobe in the spectrum (centered at about 150 Hz), whose effect is visible as a ''bump'' on the low-frequency sides of the excitation patterns.

The ''low-peak-constant'' condition [Fig. 1(c)] was designed, as its name suggests, to keep the frequency of the side lobe immediately below the carrier frequency fixed, independently of any changes in the carrier frequency. This was achieved by accompanying the increase in carrier frequency between the standard and signal intervals by an increase in the frequency of the triangular modulator. As Fig. 2(c) shows, this greatly reduced the excitation-pattern cues below 250 Hz, even though the change in carrier frequency was the same as in the modulated condition. However, the differences on the high-frequency side of the excitation pattern were larger, amounting to just over 2 dB.

The ''modulator varying'' condition [Fig. 1(d)] differed from the first three conditions in that the carrier frequency was the same in both the standard and signal intervals; in-

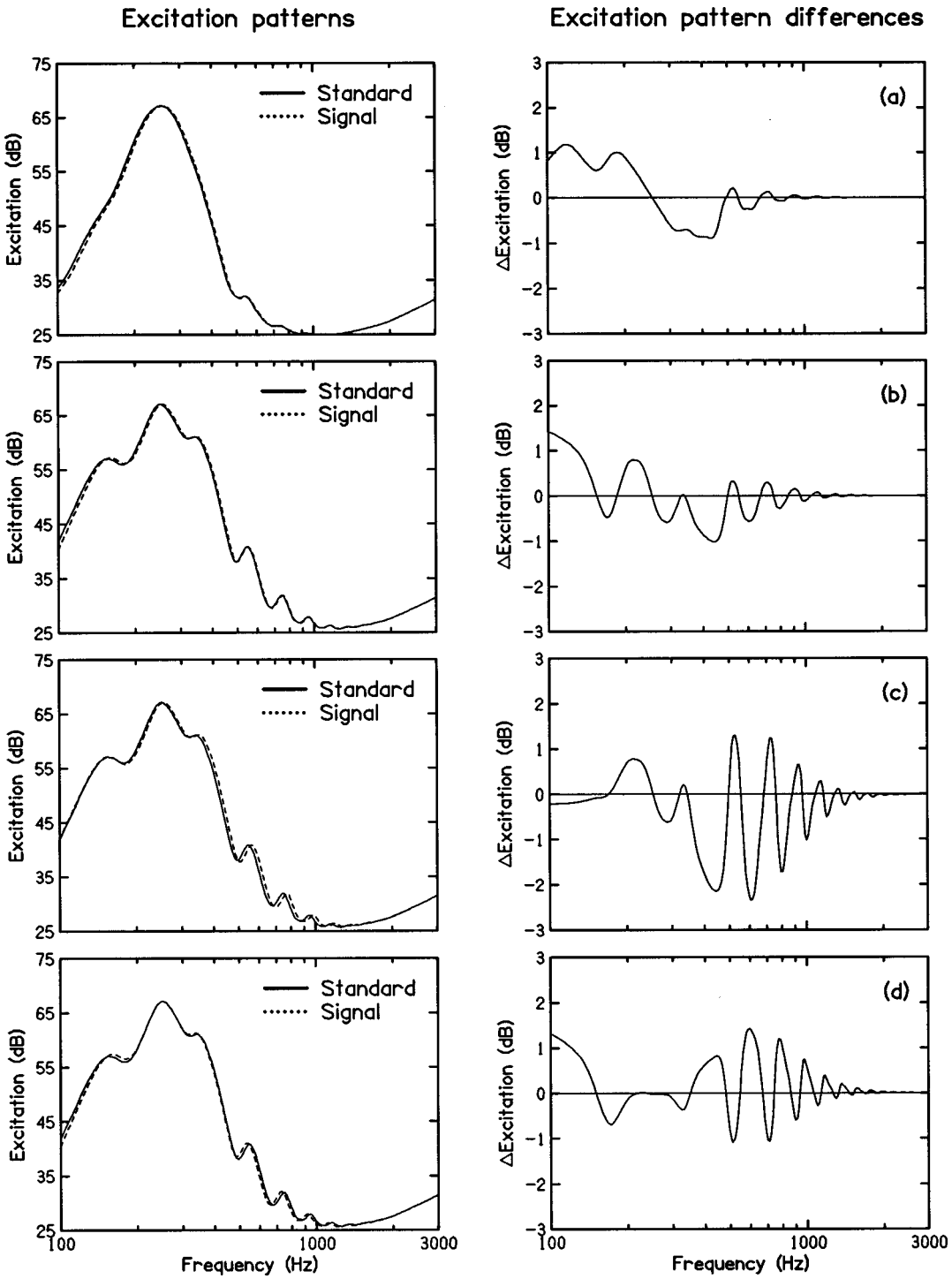

FIG. 2. Calculated excitation patterns (left) and excitation pattern differences (right). The conditions were: (a) steady, (b) modulated, (c) low-peak-constant, (d) modulator-varying. In panels (a)–(c) the carrier frequency was 250 Hz (standard-solid lines) or 254 Hz (signal-dashed lines). In panel (d) the carrier frequency was fixed at 250 Hz and the modulator frequency was either 100 Hz (standard-solid lines) or 96 Hz (signal-dashed lines).

stead, the signal differed from the standard only in the period of the modulator. Figure 2(d) shows the excitation patterns for a signal and standard whose spectral side lobes differed by 4 Hz, the same difference as shown for the modulated condition in Fig. 2(b). It can be seen that this produced excitation-pattern cues both above and below the nominal signal frequency of 250 Hz, and that, on the low-frequency side, these differences were roughly the same in size as those obtained in the modulated condition [Fig. 2(b)]. On the high-frequency side, the differences were slightly smaller than those for the ''low-peak-constant'' condition, amounting to about 1.6 dB, but were larger than those for the steady and modulated conditions.

The spectral envelopes of the stimuli were similar for the last three conditions, and so the excitation-pattern shapes were also similar (although the differences between the standard and signal excitation patterns were not the same across conditions). The spectral envelopes did not change as the

duration was altered, but the widths of individual spectral lobes increased with decreasing duration.

B. Predictions

The excitation-pattern and temporal models make different predictions about the relative size of the FDLs in the four conditions and about how the FDLs vary with frequency and duration.

The excitation-pattern model predicts that the size of the excitation-pattern differences between the standard and signal stimuli at threshold should be similar in each condition. If listeners can monitor any point on the excitation pattern (Zwicker, 1956), or if they can combine information from different parts of the excitation pattern (Florentine and Buus, 1981; Moore and Sek, 1994), performance should be poorest for the steady and modulated conditions, and best for the low-peak constant and modulator-varying conditions. If subjects mainly monitor the low-frequency side of the excitation patterns, then performance should be poorer for the low-peak-constant condition than for any of the other conditions. The excitation-pattern model also predicts that the effect of duration should be greater at 250 Hz than at 2000 Hz in all conditions. This is because the lines in the schematic spectra shown in Fig. 1 would in fact be replaced by lobes which broadened with decreasing duration, and because the maximum slope of the excitation pattern is limited by the width of individual spectral lobes mainly at low frequencies. Because the broadening occurs in all conditions, the effect of duration at 250 Hz should be largely independent of condition.

Temporal models, such as that proposed by Goldstein and Srulovicz (1977), are based on the processing of interspike intervals related to the temporal fine structure of the stimuli. Of our four conditions, the modulator-varying condition [Fig. 1(d)] is the only one in which cues relating to the temporal fine structure of the carrier are not available. If temporal fine-structure information is used in the other three conditions, one would expect that performance would be poorer in the modulator-varying condition than in the other conditions. If a temporal mechanism is used in the modulator-varying condition, then it must be based on analysis of the period of the modulator, or if spectral side lobes are resolved (as they might be for the 250-Hz carrier), on the periodicity of the side lobes. The model of Goldstein and Srulovicz would need to be extended to make quantitative predictions of performance using such cues, and we consider this beyond the scope of this paper. However, it is possible to make some qualitative predictions about the effect of duration. Plack and Carlyon argued that the effect of duration is determined by the number of periods available to the listener; waveform periods when fine-structure cues are available and envelope periods when fine-structure is not available. For a given short duration, the number of envelope periods in our modulator-varying condition was less than the number of fine-structure periods in the other conditions. Hence a temporal model leads to the prediction that, for short durations, the effect of duration should be greatest for the modulator-varying condition.

II. GENERAL METHOD

A. Listeners

The same four listeners took part in all conditions. One was author CM; the others were paid an hourly wage for their services. They had no prior training in psychoacoustic tasks and received a minimum of 12 h training in frequency discrimination before data collection began. During a session, listeners were free to pause whenever they needed and they were advised to do so as soon as they felt tired. Pure-tone absolute thresholds were assessed at octave frequencies between 250 and 8000 Hz using a two-interval forced-choice (2IFC) procedure. All four listeners had absolute thresholds within 15 dB of laboratory norms for young normally hearing subjects (based on measurements in 16 subjects).

B. Stimulus generation and spectral considerations

Signals were generated digitally on an IBM-compatible computer and sent to a CED1401 laboratory interface (12 bit DAC) at a sampling rate of 20 kHz, before being low-pass filtered at 8.6 kHz (Kemo VBF25.01; slope of 100 dB/oct). The signals were based on sinusoidal carriers having a nominal frequency of either 250 or 2000 Hz and a level of 70 dB SPL. A 10-kHz-wide pink noise with a spectrum level of 5 dB SPL at 2000 Hz was presented continuously. This was done to limit the frequency range over which excitation pattern cues might be used, and to mask low-level aural distortion products. The signals and the noise were attenuated separately by Wilsonics PATT or Tucker-Davis Technologies PA3 attenuators and each delivered to one input of a headphone amplifier, being mixed at this stage. All stimuli were presented through one earpiece of a Sennheiser HD414SL headset. They were monitored using a Hewlett-Packard HP3561A spectrum analyzer.

For the steady, modulated, and low-peak-constant conditions, on each trial, the actual carrier frequency was obtained by randomizing the nominal frequency over a 10% range (i.e., $\pm 5\%$ around the carrier frequency). In the signal interval, the actual frequency was the randomized frequency used in the standard interval incremented by Δf. Since Δf was always positive, the carrier frequency was always greater in the signal than in the standard interval. The randomization was introduced to prevent subjects using specific minor features in the spectra of the stimuli, or specific transients, to perform the task (see below for more details).

In the steady condition, duration was manipulated by introducing a steady-state envelope portion between the 5-ms linear onset and offset ramps. For all conditions, we define the nominal ''effective'' duration as the duration over which the amplitude of the waveform is greater than or equal to half the peak amplitude. Overall durations of 10, 15, 25, 45, 85, 165, and 325 ms were used to obtain effective durations of 5, 10, 20, 40, 80, 160, and 320 ms.

The stimuli in the modulated condition were the same as in the steady condition, except that the carriers were multiplied by a dc-shifted triangular modulator having a period of 10 ms (100% modulation depth). In order that an integer number of modulator periods be present in the modulated condition, the overall durations used in this condition were

all multiples of 10 ms. The effective durations used in the modulated condition were the same as for the steady condition; they were one-half of the overall durations. Because the stimuli with only one modulator period (effective duration=5 ms) were identical to the shortest stimuli in the steady condition, those data points are common to the two conditions.

The stimuli for the low-peak-constant condition were similar to those for the modulated condition, except that, on each trial, the modulation rate, f_m, in the signal interval was increased by Δf, to keep constant the frequency of the side lobe immediately below the carrier frequency (at frequency $f_c - f_m$); the frequency of the side lobe immediately above the carrier frequency was shifted by $2\Delta f$. Effective durations of 10, 20, 40, 80, 160, and 320 ms were used.

The stimuli for the modulator-varying condition were similar to those for the modulated condition, i.e., sinusoidal carriers modulated by a triangular waveform. However, in this condition, the standard and signal stimuli differed in modulation period, ΔP, instead of in carrier frequency. The actual carrier frequency was randomized over a range of 10% around the nominal carrier frequency, 250 or 2000 Hz, in each trial, but was the same in both the signal and standard intervals of the trial. Again, this was done to prevent subjects using specific spectral features as a cue. The modulation period was always 10 ms in the standard interval. In the signal interval, it was $10+\Delta P$ ms. Since ΔP was always greater than or equal to 0, the modulation period was always longer in the signal interval. Listeners were instructed to use any cue they wanted, using the visual feedback to help them, to detect the interval in which the modulation period was the longest. Effective durations of 10, 20, 40, 80, 160, and 320 ms were used.

Because the stimuli in the modulator-varying condition always contained an integer number of modulation periods, the overall duration of the stimuli was different for the signal and standard intervals, by an amount depending on ΔP. The overall duration in the signal interval was adjusted upwards or downwards on each trial, by varying the number of modulator cycles, so as to remain as close as possible to that for the standard interval. The effects of this manipulation will be discussed later.

In all conditions the phase of the carrier was randomized from presentation to presentation, in order to prevent listeners from using a particular transient or feature of the spectrum to identify the signal. As Hartmann and Sartor (1991) have demonstrated, the phase at which a sinusoid is turned on and off affects the spectrum for short durations. Calculations for the 250-Hz carrier and the shortest duration in the steady condition showed that: (1) the phase effects were largest when the stimuli contained close to an integer number of periods of the carrier; (2) there were negligible effects of phase on the excitation patterns below 250 Hz; (3) phase affected the magnitude of the difference between standard and signal excitation patterns above 250 Hz, but only rarely the sign of that difference. These effects may have produced some disruption of excitation-pattern cues in the low-peak-constant and modulator-varying conditions, since for these two conditions, the signal was associated with changes on the high-frequency side of the excitation pattern. However, the phase randomization probably had negligible effects for the steady and modulated conditions, and for all conditions at longer durations.

An additional spectral effect occurs specifically for the 250-Hz carrier when, in all except the steady condition, there are side lobes at odd multiples of 100 Hz above and below the carrier frequency. The lobe centered 300 Hz below the carrier frequency ''wraps around'' zero frequency, and appears at 50 Hz. If listeners could detect changes in the frequency of this lobe then this would improve performance in the modulated, low-peak-constant, and modulator-varying conditions, compared to the steady condition. However, given that the level of this lobe is approximately 27 dB below that at the carrier frequency, and 19 dB below that at 150 Hz, it seems unlikely that it would have a substantial effect on performance.

C. Procedure

Thresholds were measured using a 2IFC procedure with visual feedback. A two-down one-up adaptive tracking rule was used which estimated the 71% correct point on the psychometric function (Levitt, 1971). The difference between the two stimuli in a given trial, Δf or ΔP, was changed by a certain factor (step size). Sixteen turnpoints were obtained. A relatively large initial step size of 2.0 was applied until the fourth turnpoint was reached, in order to allow rapid convergence toward the threshold region. After the fourth turnpoint, the step size was reduced to 1.41. Threshold was taken as the geometric mean of the values of Δf or ΔP at the last 12 turnpoints. Nine threshold estimates were made for each condition and the final estimate was the geometric mean of these nine, which was therefore based on 108 turnpoints.

III. RESULTS

The results were similar across subjects for all conditions, so only mean data will be presented. We start by presenting results for the individual conditions and then compare results across conditions. All statistical analyses are based on the logarithms of the FDLs, as the standard deviations of the FDLs were roughly proportional to the mean values of the FDLs.

A. Steady condition

The circles in Fig. 3 show the FDLs in the steady condition as a function of effective duration. For both carrier frequencies, the FDLs decreased with increasing stimulus duration, and this decrease was greater for the 250-Hz carrier (open symbols) than for the 2000-Hz carrier (filled symbols). To assess the statistical significance of these observations, a two-way analysis of variance (ANOVA) was conducted with the logarithm of the FDLs as the dependent variable and frequency and effective duration as factors. This revealed, in addition to significant main effects of frequency [$F(1,3) = 68.84$, $p < 0.005$] and duration [$F(6,18) = 93.70$, $p < 0.001$], a significant interaction between them [$F(6,18) = 15.96$, $p < 0.001$]. As discussed in Sec. I B, this interaction is predicted both by the temporal and by the excitation-

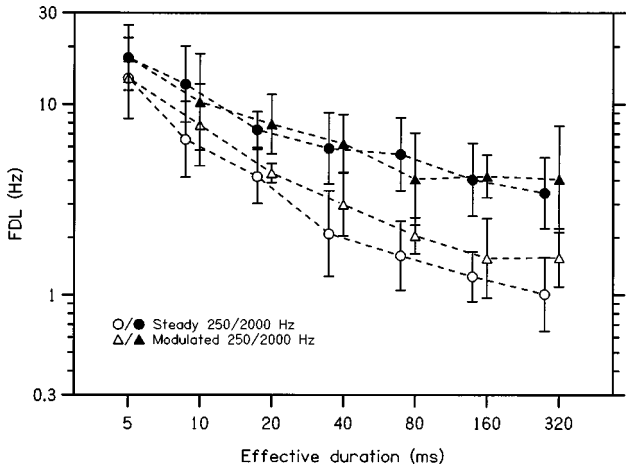

FIG. 3. FDLs as a function of effective duration in the steady (circles) and modulated (triangles) conditions for carrier frequencies of 250 Hz (open symbols) and 2000 Hz (filled symbols). The scales of both axes are logarithmic. The error bars indicate ± one standard deviation across listeners.

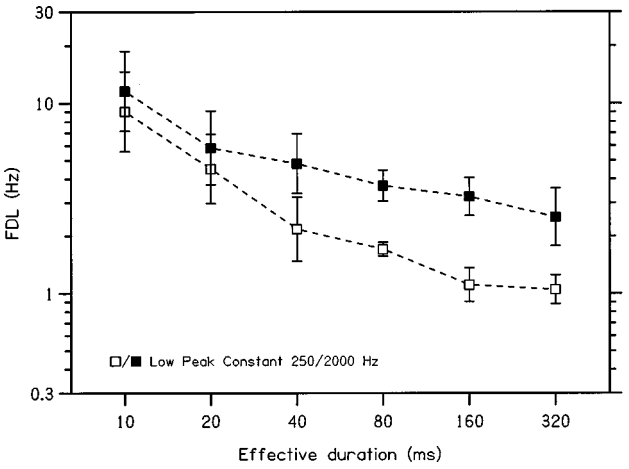

FIG. 4. FDLs as a function of effective duration in the low-peak-constant condition for carrier frequencies of 250 Hz (open symbols) and 2000 Hz (filled symbols). Otherwise as in Fig. 3.

pattern models. The results replicate several aspects of the data in the literature: FDLs are larger at 2000 than at 250 Hz (Henning, 1970; Moore, 1973; Wier *et al.*, 1977; Nelson *et al.*, 1983); FDLs decrease markedly as duration is increased from about 10 to 300 ms (Turnbull, 1944; Konig, 1957; Liang and Chistovich, 1961; Sekey, 1963; Henning, 1970; Moore, 1973; Freyman and Nelson, 1986); and FDLs decrease more as a function of duration at 250 Hz than at 2000 Hz (Liang and Chistovich, 1961; Henning, 1970; Moore, 1973; Freyman and Nelson, 1986).

B. Modulated condition

Results from the modulated condition are shown by the triangles in Fig. 3. As with the steady condition, FDLs increased with decreasing duration [$F(6,18)=77.9$, $p<0.001$], and were higher at 2000 Hz than at 250 Hz [$F(1,3)=46.0$, $p<0.01$]. There was also a significant interaction between frequency and duration [$F(6,18)=3.16$, $p<0.05$], reflecting the greater effect of duration on FDLs at 250 Hz compared to 2000 Hz.

C. Low-peak-constant condition

The open and filled squares in Fig. 4 show the results of the low-peak-constant condition for signal frequencies of 250 and 2000 Hz, respectively. Overall, the results were very similar to those obtained in the steady and modulated conditions, despite the fact that in this condition the excitation-pattern changes were largely above rather than below the carrier frequency, and were therefore affected somewhat by the phase randomization. A two-way ANOVA revealed significant main effects of frequency [$F(1,3)=76.12$, $p<0.005$] and duration [$F(6,18)=53.77$, $p<0.001$]. The two-way interaction was also significant [$F(6,18)=3.38$, $p<0.05$].

D. Modulator varying condition

Thresholds in this condition are expressed as the change in modulation rate; we refer to this as the equivalent FDL, FDLe. When the modulation rate changes by FDLe, the center frequencies of the spectral side lobes adjacent to the carrier frequency also change by FDLe (although the sign of the change is different for side lobes above and below the carrier frequency).

Thresholds (FDLe) in the modulator-varying condition are shown by the diamonds connected by dashed lines in panels (a) and (b) of Fig. 5 for carrier frequencies of 250 and 2000 Hz, respectively. This figure also shows results for the other three conditions. A two-way repeated-measures ANOVA was conducted, with log(FDLe) as the dependent variable and carrier frequency and duration as factors. Not surprisingly, there was a highly significant main effect of duration [$F(5,15)=50.35$, $p<0.0001$]. There was also a significant effect of carrier frequency [$F(1,3)=14.58$, $p<0.05$] indicating that, as in the other conditions, thresholds were lower for the 250-Hz carrier than for the 2000-Hz carrier. However, unlike in the steady, modulated, and low-peak-constant conditions, the interaction between frequency and duration was not significant [$F(5,15)=2.10$, $p=0.122$]. For both frequencies, the values of FDLe reached an asymptote at about 80 ms.

IV. DISCUSSION

A. Comparison between conditions

The most obvious difference between conditions is the markedly worse performance in the modulator-varying condition, compared to the other conditions (Fig. 5). This was confirmed by a three-way (condition×frequency×duration) ANOVA performed on the complete data set. The data for the 5-ms duration were not included, because the data obtained in the steady and modulated conditions for this duration were based on the same blocks of trials. The ANOVA revealed a significant main effect of condition [$F(3,9)=26.49$, $p<0.001$]. A planned comparison between the modulator-varying condition and the mean of the other three conditions showed a significant difference [$F=77.4$, $p<0.001$]. This result is not predictable from the excitation patterns produced by the stimuli in the four conditions. This

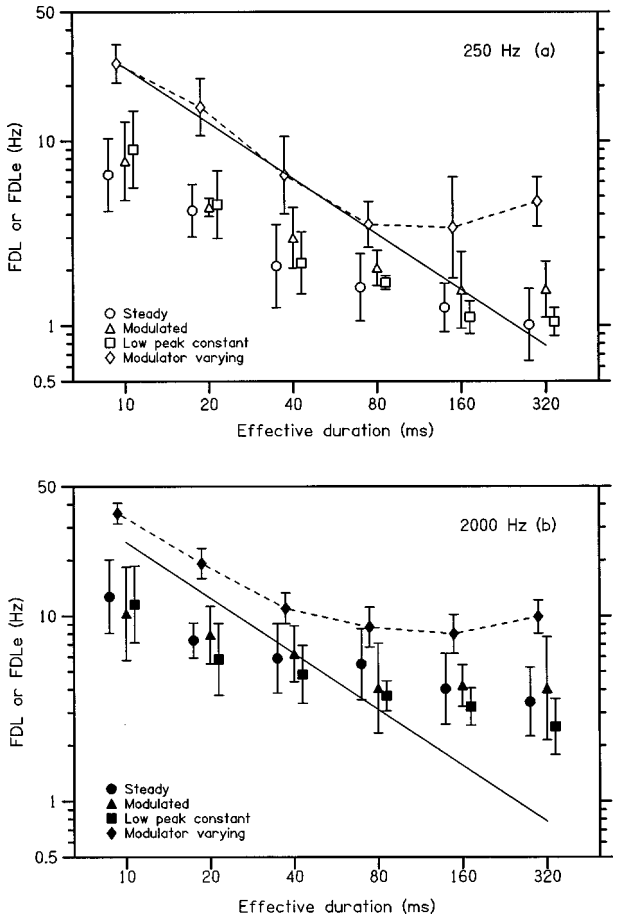

FIG. 5. As in Fig. 4, but showing FDLs as a function of effective duration for all conditions for the 250-Hz carrier (top) and the 2000-Hz carrier (bottom). The conditions were: steady (circles), modulated (triangles), low-peak-constant (squares), and modulator-varying (diamonds connected by dashed lines). The solid line in each panel shows thresholds predicted from use of the ''number of modulator periods'' cue in the modulator-varying condition (see text for details).

is illustrated in Fig. 6, which shows the differences in excitation patterns between standards and signals at threshold in the four conditions, for an effective duration of 20 ms, both at 250 Hz (left-hand panels) and 2000 Hz (right-hand panels). Clearly, the excitation-pattern differences between the standard and signal are much greater in the modulator-varying condition [Fig. 6(d)] than in the steady [Fig. 6(a)], modulated [Fig. 6(b)], and, at 250 Hz, low-peak-constant [Fig. 6(c)] conditions. It is also noteworthy that, for each condition, the excitation-pattern differences were greater at 250 Hz than at 2000 Hz, by a factor of 2 or more. The greater differences at 250 Hz occurred because of the better resolution of spectral side lobes at 250 Hz. It seems likely that excitation-pattern cues associated with spectral side lobes were not used at all for the 2000-Hz carrier, in any condition.

If excitation-pattern differences were being used at all for these short-duration stimuli, then the results for the modulator-varying condition at 250 Hz suggest that the differences needed to be about 5 dB, markedly greater than the criterion value of 1 dB proposed by Zwicker (1956, 1970). This is not surprising, as the 1-dB criterion was intended to apply to long-duration stimuli (or slowly frequency-modulated stimuli). The excitation-pattern differences were markedly smaller than 5 dB for the other three conditions, especially the steady condition and the modulated condition [Fig. 6(a) and (b)]. This suggests that excitation-pattern differences were not being used in those conditions. Also, the excitation-pattern differences at threshold were markedly larger for the low-peak constant condition [Fig. 6(c)] than for the steady or modulated conditions, yet performance was very similar for these three conditions. Again, this suggests that excitation-pattern differences were not used in these three conditions.

Consider now the effects of duration on the FDLs for the steady, modulated, and low-peak-constant conditions. As described in the introduction, the increase of FDLs with decreasing duration for unmodulated tones (our steady condition) has sometimes been explained in terms of the increasing spectral splatter that occurs with decreasing duration, which leads to broader excitation patterns (Freyman and Nelson, 1986). In the modulated and low-peak-constant conditions of our experiment, the spectral envelope did not change with duration, although individual lobes in the spectrum did broaden with decreasing duration. For the 2000-Hz carrier, the individual spectral lobes would have been largely unresolved, so the excitation patterns evoked by the stimuli would hardly have changed with duration. Yet, the variation of the FDLs with duration at 2000 Hz was almost identical for the steady, modulated, and low-peak constant conditions. This suggests that the increase in the FDLs with decreasing duration at 2000 Hz was not due to broadening of the excitation patterns in any of these conditions.

The pattern of results is consistent with a temporal model. In the steady, modulated, and low-peak-constant conditions, the periodicity of the carrier provided a potential cue. Performance was similar for these three conditions. In contrast, in the modulator-varying condition, the periodicity of the carrier did not differ between the signal and the standard. Performance in this condition, expressed as FDLe, was markedly worse than for the other conditions. The results suggest that the periodicity of the carrier was the main cue for the steady, modulated, and low-peak constant conditions. For the modulator-varying condition, performance could have been based either on envelope periodicity cues, or, for the 250-Hz carrier, on excitation-pattern differences or differences in periodicity of resolved spectral side lobes.

The temporal model is also consistent with the finding that, for durations up to 80 ms, thresholds varied more with duration in the modulator-varying condition than in the other three conditions. This was confirmed by a three-way ANOVA based on the four shortest durations only, which showed a significant interaction between duration and condition [$F(9,27)=2.79$, $p<0.0187$]. The ratios of the FDL(e) scores for the 10-ms and 80-ms durations in the steady, modulated, low-peak-constant, and modulator-varying conditions were 4.07, 3.80, 5.28, and 7.47, respectively, at 250 Hz, and 2.32, 2.53, 3.13, and 4.12 at 2000 Hz. The greater effect of duration for the modulator-varying condition is consistent with a temporal model, as, for a given short duration, there are many fewer modulator cycles than carrier cycles. It is noteworthy, however, that performance in the modulator-varying condition did not improve for effective durations

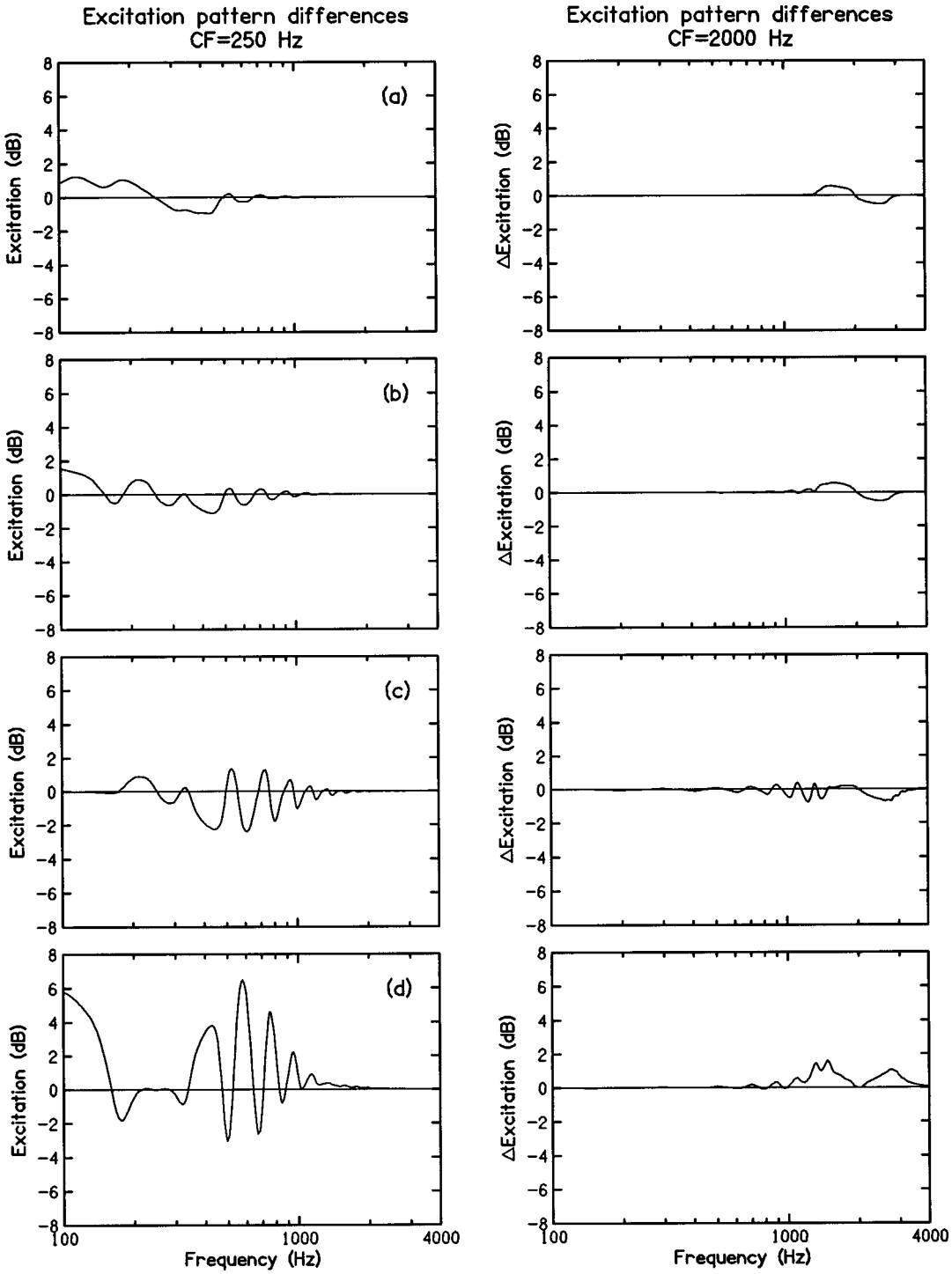

FIG. 6. Differences in excitation patterns between standard and signal stimuli for an effective duration of 20 ms. The frequency differences between the signal and standard were those corresponding to the mean measured threshold. The four rows correspond to the four conditions: (a) steady, (b) modulated, (c) low-peak-constant, (d) modulator-varying. The left and right columns show results for the 250- and 2000-Hz carriers, respectively.

beyond 80 ms (160-ms overall duration). This may reflect a limit on the duration over which temporal integration occurs for modulation discrimination.

In the Introduction, we described the results of Plack and Carlyon (1995), showing that the effect of duration on FDLs for (the fundamental frequency of) harmonic complex tones was greater for tones with unresolved harmonics than for tones with resolved harmonics. They explained this result using a temporal theory, suggesting that the effect of duration is determined by the number of periods available to the listener; waveform periods for resolved components and envelope periods for a complex with unresolved components. Our results for the modulator-varying condition are consistent with this suggestion. For our 250-Hz carrier, the spectral side band at 150 Hz was probably resolved, whereas the side bands for the 2000-Hz carrier were probably not resolved. For a given duration, the number of waveform periods of the 150-Hz side band (of the 250-Hz carrier) is roughly similar

to the number of envelope periods for the 2000-Hz carrier. Hence the effect of duration is predicted to be similar for the two cases, which was indeed the case. Note that it is probably only in the modulator-varying condition that cues relating to the 150-Hz sideband were useable. For the other conditions, cues associated with the temporal fine structure of the 250-Hz carrier would have been much more salient.

B. Additional cues in the modulator-varying condition

In the modulator-varying condition there were three types of additional cues which, although not affecting our main conclusions, need to be considered when interpreting the results.

First, when the carrier frequency was fixed and the modulation period was varied, the center frequencies of side lobes farther from the carrier frequency changed by greater amounts than FDLe. Subjects may have been able to use information from these side lobes for the 250-Hz carrier at short durations, as described above; indeed the large changes in the frequencies of the side lobes are partly responsible for the large excitation-pattern differences shown in Fig. 6(d) for the 250-Hz carrier. However, it seems unlikely that subjects could use this cue for the 2000-Hz carrier. Buus (1983) has presented evidence that discrimination of modulation frequency is based on the modulation *per se*, rather than on spectral cues, at least for modulation rates up to 30%–40% of the carrier frequency and for carrier frequencies above 500 Hz.

The second type of cue arises from our decision always to maintain an integer number of cycles of the modulator, and to adjust the number of modulation cycles in the signal so that its duration was as close as possible to that of standard stimulus. At long durations this produced only small differences in duration (never more than 1% at an effective duration of 320 ms) and in the number of modulator cycles, and the differences in duration did not vary monotonically with ΔP. Therefore differences in duration and/or number of modulator cycles would not have provided a reliable cue. However, this was not necessarily the case for the shorter stimuli. For example, for an effective duration of 10 ms the standard stimulus consisted of two 10-ms periods of the modulator, and, as the modulator period was increased to 13.3 ms, there was a monotonic increase in the overall duration. Beyond this duration the number of modulation cycles would have been reduced from two to one. Listeners may have been able to detect either the increasing duration, or the change in number of modulator periods, or both. The solid lines in Fig. 5 show the performance predicted from the use of the latter strategy, on the assumption that listeners can detect a difference of one modulator cycle at all durations. It can be seen that the line predicts the FDLe values obtained at 250 Hz very well, for effective durations up to 80 ms. Hence at this frequency we cannot rule out the possibility that, at short durations, listeners were using the number of modulation cycles as a cue. If they were doing so, then this cue was presumably more effective than any excitation-pattern cues available at these short durations, and so the effect of the ''number of cycles'' cue would have been to *reduce* the deterioration observed for very brief stimuli. However, it should be borne in mind that the solid line falls below the thresholds obtained at 2000 Hz at all durations, despite the fact that the ''number of cycles'' cue was equally available at both carrier frequencies.

Finally, it is worth mentioning one other unique feature of the modulation-varying condition, which is that the frequencies of the side lobes above and below the carrier frequency changed in opposite directions. According to Zwicker's (1956, 1970) model, this should not have made any difference, since the model assumes that performance is based on changes in the excitation pattern at the single point where the excitation changes the most. Other excitation-pattern models have been proposed which assume that information can be combined from different parts of the excitation pattern (Florentine and Buus, 1981; Moore and Glasberg, 1989; Moore and Sek, 1994). However, even in these models, the direction of the changes is not assumed to matter, provided that the direction is consistent across trials for each point on the pattern. This assumption is essential for excitation-pattern models when trying to account for the detection of mixed amplitude modulation (AM) and frequency modulation (Moore and Sek, 1994). It is also required to account for the finding that the detection of modulation is not affected by whether or not listeners know on a given trial if the modulation will be in amplitude or frequency (Demany and Semal, 1986). Thus the poorer performance found in the modulator-varying condition than in the modulated condition cannot be explained in terms of the different directions of movement of the upper and lower side lobes in the modulator-varying condition.

C. Comparison with previous modulation-discrimination data

It is useful to compare the results from the modulator-varying condition with existing data on AM-rate discrimination. The most comprehensive recent study, which used sinusoidal rather than triangular AM, was performed by Lee (1994). She found that thresholds increased markedly as the number of modulator cycles was reduced below about five, in broad agreement with the large effect of duration observed in the present study. However, Fig. 5 shows that thresholds continue to drop as effective duration is increased up to 80 ms (total duration=160 ms), suggesting that, for our 100-Hz triangular modulator, the ''critical'' number of modulator periods is closer to 16 than to five.

Overall the thresholds measured by us are slightly higher than those measured by Lee (1994). For example, for the 2000-Hz carrier, we found a threshold of about 9 Hz for an effective duration of 80 ms, corresponding to an overall duration of 160 ms. For a similar duration, Lee found a threshold of about 2.5 Hz for a modulation rate of 40 Hz and about 6 Hz for a modulation rate of 160 Hz, when the carrier frequency was randomized (as it was in our experiment, albeit over a smaller range than used by Lee). For the 250-Hz carrier, we found a threshold of about 3 Hz for an overall duration of 160 ms, whereas for a fixed 500-Hz carrier (the lowest used) and a similar duration, Lee found a threshold of about 1 Hz for a 40-Hz modulation rate and about 5 Hz for a 160-Hz modulation rate. The slightly worse overall perfor-

mance found by us might be due to the different modulator waveforms (triangular versus sinusoidal), to individual differences (Lee used three subjects, while we used four), or to our use of a pink noise background; Lee reported that performance worsened for some subjects when low-pass noise was added to the stimuli, when the modulation rate was above 80 Hz, and she attributed this to masking of combination tones.

Lee's data are relevant to our finding that the values of FDLe were higher at 2000 Hz than at 250 Hz. This prediction is not made by the temporal model, but is consistent with an excitation-pattern hypothesis, because excitation-pattern changes associated with changes in spectral side lobes should be larger at the lower carrier frequency [see Fig. 6(d)]. Although Lee found no effect of carrier frequency for 2-s stimuli, her Fig. 3 shows that, for overall durations from 125 to 1000 ms, thresholds were lower for a 500-Hz carrier than for a 4000-Hz carrier. However, this difference only occurred when the modulation rate was 20 or 40 Hz; at a rate of 160 Hz thresholds were similar at the two carrier frequencies. Hence it appears that the effect of carrier frequency is greatest at low modulation rates, where the spectral cues are weakest. We do not have an explanation for this effect, which does not seem to follow from either the temporal or excitation-pattern explanations.

V. SUMMARY AND CONCLUSIONS

This experiment examined the influence of excitation-pattern cues and temporal-fine-structure cues on frequency difference limens (FDLs) measured as a function of duration. FDLs were measured in four conditions, chosen to manipulate the extent to which such cues were available. In the steady condition, duration was altered by increasing the steady-state portion of the envelope between two 5-ms linear onset and offset ramps. In the modulated condition, the carrier was modulated with a triangle function (period 10 ms) and duration was altered by varying the number of cycles of the modulator. The low-peak-constant condition was similar to the modulated condition, except that an increase in carrier frequency was accompanied by a decrease in the period of the modulator, so as to hold constant the frequency of the spectral lobe 100 Hz below the carrier frequency. For a given frequency difference between the standard and signal stimuli, the size and location of the largest excitation-pattern differences varied across conditions. However, both the values of the FDLs, and their variation with frequency and duration, were similar in these three conditions. This suggests that performance depended on the use of temporal fine structure cues, which were similar for the three conditions.

The fourth, modulator varying, condition differed in that the carrier frequency was held constant and listeners were required to detect a change in modulator frequency. Thresholds were expressed as FDLe, the change in frequency of the spectral side lobes adjacent to the carrier frequency. Excitation-pattern cues in this condition were at least as large as in the first three conditions. However, values of FDLe were significantly higher than the FDLs for the other three conditions. The higher values of FDLe are attributed to the lack of temporal fine-structure cues related to the carrier frequency.

The following main conclusions can be drawn from our results:

(1) FDLs in the steady, modulated, and low-peak constant conditions were determined by temporal cues rather than by excitation-pattern cues.

(2) The increase of the FDLs with decreasing duration in the steady, modulated, and low-peak constant conditions did not arise from increasing spectral splatter. It probably occurred because of the decreasing number of periods available for sampling by a temporal mechanism.

(3) Performance in the modulator-varying condition might have been determined by several cues: (a) changes in the modulator period; (b) changes associated with the excitation pattern or periodicity of spectral side lobes (at 250 Hz only); (c) (for short durations) changes in the number of modulator periods.

(4) If excitation-pattern changes are used at all for the frequency discrimination of short-duration stimuli (for example, in the modulator-varying condition), the changes need to be rather large (several decibels).

ACKNOWLEDGMENTS

This work was supported by a Wellcome Trust grant. The authors are grateful to Brian Glasberg and Tom Baer for assistance with computations. We thank Johannes Lyzenga and the two reviewers, Mary Florentine and Armin Kohlrausch, for their constructive comments.

APPENDIX: EXCITATION PATTERN SIMULATIONS

The excitation patterns shown in this paper were calculated using the algorithm described in Glasberg and Moore (1990). The stimuli were generated in the time domain at a sampling frequency of 10 kHz and submitted to fast Fourier transform (FFT) before being processed in the spectral domain. The FFT was based on a rectangular window longer than the stimulus duration. The input level to the excitation-pattern program was adjusted so that the excitation level evoked at the center frequency corresponding to the carrier frequency (250 or 2000 Hz) was the same as would be evoked by a long-duration tone at 70 dB SPL. A pink noise background with a spectrum level of 5 dB SPL at 2 kHz (as in the experiment) was included, the smoothed long-term power spectrum of the noise being added to the stimulus power spectrum. The correction for the external and middle-ear transfer functions described in Glasberg and Moore (1990) as the ELC correction was applied to the stimulus spectrum before this spectrum was fed to the excitation pattern model. Simulated auditory filters with center frequencies between about 3 and 30 ERB (corresponding approximately to 87 and 5577 Hz, respectively) with a spacing of 0.1 ERB were used.

Buus, S. (**1983**). ''Discrimination of envelope frequency,'' J. Acoust. Soc. Am. **74**, 1709–1715.

Demany, L., and Semal, C. (**1986**). ''On the detection of amplitude modulation and frequency modulation at low modulation frequencies,'' Acustica **61**, 243–255.

Florentine, M. (**1986**). ''Level discrimination of tones as a function of duration,'' J. Acoust. Soc. Am. **79**, 792–798.
Florentine, M., and Buus, S. (**1981**). ''An excitation-pattern model for intensity discrimination,'' J. Acoust. Soc. Am. **70**, 1646–1654.
Freyman, R. L., and Nelson, D. A. (**1986**). ''Frequency discrimination as a function of tonal duration and excitation-pattern slopes in normal and hearing-impaired listeners,'' J. Acoust. Soc. Am. **79**, 1034–1044.
Glasberg, B. R., and Moore, B. C. J. (**1990**). ''Derivation of auditory filter shapes from notched-noise data,'' Hearing Res. **47**, 103–138.
Goldstein, J. L., and Srulovicz, P. (**1977**). ''Auditory-nerve spike intervals as an adequate basis for aural frequency measurement,'' in *Psychophysics and Physiology of Hearing*, edited by E. F. Evans and J. P. Wilson (Academic, London).
Hartmann, W. M., and Sartor, D. C. (**1991**). ''Turning on a tone,'' J. Acoust. Soc. Am. **90**, 866–873.
Henning, G. B. (**1970**). ''Comparison of the effects of signal duration on frequency and amplitude discrimination,'' in *Frequency Analysis and Periodicity Detection in Hearing*, edited by R. Plomp and G. F. Smoorenburg (Sijthoff, Leiden).
Konig, E. (**1957**). ''Effect of time on pitch discrimination thresholds,'' J. Acoust. Soc. Am. **29**, 606.
Lee, J. (**1994**). ''Amplitude modulation rate discrimination with sinusoidal carriers,'' J. Acoust. Soc. Am. **96**, 2140–2147.
Levitt, H. (**1971**). ''Transformed up-down methods in psychoacoustics,'' J. Acoust. Soc. Am. **49**, 467–477.
Liang, C.-A., and Chistovich, L. A. (**1961**). ''Frequency difference limens as a function of tonal duration,'' Sov. Phys. Acoust. **6**, 75–80.
Moore, B. C. J. (**1972**). ''Some experiments relating to the perception of pure tones: possible clinical applications,'' Sound **6**, 73–79.
Moore, B. C. J. (**1973**). ''Frequency difference limens for short-duration tones,'' J. Acoust. Soc. Am. **54**, 610–619.
Moore, B. C. J. (**1974**). ''Relation between the critical bandwidth and the frequency-difference limen,'' J. Acoust. Soc. Am. **55**, 359.
Moore, B. C. J., and Glasberg, B. R. (**1986**). ''The role of frequency selectivity in the perception of loudness, pitch and time,'' in *Frequency Selectivity in Hearing*, edited by B. C. J. Moore (Academic, London).
Moore, B. C. J., and Glasberg, B. R. (**1989**). ''Mechanisms underlying the frequency discrimination of pulsed tones and the detection of frequency modulation,'' J. Acoust. Soc. Am. **86**, 1722–1732.
Moore, B. C. J., and Sek, A. (**1994**). ''Effects of carrier frequency and background noise on the detection of mixed modulation,'' J. Acoust. Soc. Am. **96**, 741–751.
Nelson, D. A., Stanton, M. E., and Freyman, R. L. (**1983**). ''A general equation describing frequency discrimination as a function of frequency and sensation level,'' J. Acoust. Soc. Am. **73**, 2117–2123.
Patterson, R. D., Peters, R. W., and Milroy, R. (**1983**). ''Threshold duration for melodic pitch,'' in *Hearing—Physiological Bases and Psychophysics*, edited by R. Klinke and R. Hartmann (Springer-Verlag, Berlin).
Plack, C. J., and Carlyon, R. P. (**1995**). ''Differences in frequency modulation detection and fundamental frequency discrimination between complex tones consisting of resolved and unresolved harmonics,'' J. Acoust. Soc. Am. **98**, 1355–1364.
Schouten, J. F. (**1940**). ''The residue and the mechanism of hearing,'' Proc. K. Ned. Akad. Wet. **43**, 991–999.
Schouten, J. F. (**1970**). ''The residue revisited,'' in *Frequency Analysis and Periodicity Detection in Hearing*, edited by R. Plomp and G. F. Smoorenburg (Sijthoff, Leiden, The Netherlands).
Sek, A., and Moore, B. C. J. (**1995**). ''Frequency discrimination as a function of frequency, measured in several ways,'' J. Acoust. Soc. Am. **97**, 2479–2486.
Sekey, A. (**1963**). ''Short-term auditory frequency discrimination,'' J. Acoust. Soc. Am. **35**, 682–690.
Turnbull, W. (**1944**). ''Pitch discrimination as a function of tonal duration,'' J. Exp. Psychol. **34**, 302–316.
van der Heijden, M., and Kohlrausch, A. (**1994**). ''Using an excitation-pattern model to predict auditory masking,'' Hearing Res. **80**, 38–52.
Wier, C. C., Jesteadt, W., and Green, D. M. (**1977**). ''Frequency discrimination as a function of frequency and sensation level,'' J. Acoust. Soc. Am. **61**, 178–184.
Zwicker, E. (**1956**). ''Die elementaren Grundlagen zur Bestimmung der Informationskapazität des Gehörs,'' Acustica **6**, 356–381.
Zwicker, E. (**1970**). ''Masking and psychological excitation as consequences of the ear's frequency analysis,'' in *Frequency Analysis and Periodicity Detection in Hearing*, edited by R. Plomp and G. F. Smoorenburg (Sijthoff, Leiden).

Modulation rate detection and discrimination by normal-hearing and hearing-impaired listeners

Ken W. Grant, Van Summers, and Marjorie R. Leek
Walter Reed Army Medical Center, Army Audiology and Speech Center, Washington, DC 20307-5001

(Received 25 August 1997; revised 10 February 1998; accepted 31 March 1998)

Modulation detection and modulation rate discrimination thresholds were obtained at three different modulation rates ($f_m = 80$, 160, and 320 Hz) and for three different ranges of modulation depths (m): full (100%), mid (70%–80%), and low (40%–60%) with both normal-hearing (NH) and hearing-impaired (HI) subjects. The results showed that modulation detection thresholds increased with modulation rate, but significantly more so for HI than for NH subjects. Similarly, rate discrimination thresholds (Δr) increased with increases in f_m and decreases in modulation depth. When compared to NH subjects, rate discrimination thresholds for HI subjects were significantly worse for all rates and for all depths. At the fastest modulation rate with less than 100% modulation depth, most HI subjects could not discriminate any change in rate. When valid thresholds for rate discrimination were obtained for HI subjects, they ranged from 2.5 semitones ($\Delta r = 12.7$ Hz, $f_m = 80$ Hz, $m = 100\%$) to 8.7 semitones ($\Delta r = 214.5$ Hz, $f_m = 320$ Hz, $m = 100\%$). In contrast, average rate discrimination thresholds for NH subjects ranged from 0.9 semitones ($\Delta r = 4.2$ Hz, $f_m = 80$ Hz, $m = 100\%$) to 4.7 semitones ($\Delta r = 103.5$ Hz, $f_m = 320$ Hz, $m = 60\%$). Some of the differences in temporal processing between NH and HI subjects, especially those related to modulation detection, may be accounted for by differences in signal audibility, especially for high-frequency portions of the modulated noise. However, in many cases, HI subjects encountered great difficulty discriminating a change in modulation rate even though the modulation components of the standard and test stimuli were detectable. [S0001-4966(98)02208-5]

PACS numbers: 43.66.Mk [RVS]

INTRODUCTION

The most obvious problem faced by hearing-impaired (HI) individuals in understanding speech is inaudibility of speech cues in the acoustic signal. However, even when hearing aids provide sufficient amplification so that speech signals are well above detection thresholds, problems in speech understanding may still persist, especially in noisy backgrounds (Plomp, 1978). Many of these problems appear to be related to signal distortions generated during the processing of sound in the impaired cochlea (Moore, 1995). One such distortion that has received a great deal of attention in recent years is a smearing or smoothing of spectral peaks (e.g., speech formants) making it difficult to discriminate one spectral shape from another (Leek *et al.*, 1987; Baer and Moore, 1993). This type of distortion is associated with the abnormal frequency selectivity and broader-than-normal auditory filter bandwidths often accompanying sensorineural hearing impairment (Summerfield *et al.*, 1985; Leek and Summers, 1993; Summers and Leek, 1994). When there is sufficient hearing loss so that the analysis of spectral detail is impaired, nonspectral cues such as amplitude modulations in the speech waveform may take on added importance for speech perception (Formby, 1987; Rosen and Smith, 1988; Hedrick *et al.*, 1995; Hedrick and Jesteadt, 1996). For some individuals with severe-to-profound sensorineural hearing loss, the cues contained in the gross time-intensity variations in the speech waveform (i.e., the waveform envelope) may be all that are available (Erber, 1972a, b).

Rosen (1989, 1992) identified three basic categories of temporal information in speech that depend primarily on the rate of temporal fluctuation. (1) *From 2–50 Hz*, slow time-varying envelope fluctuations, typically referred to as the *amplitude envelope*, can provide information about manner of articulation, certain vowel contrasts, overall rhythm or tempo, and syllabicity. This information is typically associated with overall duration and amplitude, as well as the rate of amplitude change at syllable onset (i.e., during the attack portion of the syllable). (2) *From 50–500 Hz*, envelope fluctuations provide information about waveform *periodicity* associated with the voice fundamental frequency ($F0$), voicing, intonation, and stress. This information is typically associated with the regularity of waveform fluctuations and the rate of envelope modulation, and is sometimes perceived as a buzz or flutter. (3) *From 600–8000 Hz*, variations in the temporal wave shape can provide information about the place of articulation and vowel quality. This *fine structure* information is typically associated with rapid time fluctuations (e.g., the zero-crossing rate) within a single voiced period or within a short time interval during aperiodic sounds.

A. Previous studies of temporal speech information

Rosen's description of temporal speech cues provides a framework for exploring which of these cues can be perceived by human observers, especially listeners with hearing loss. There have been a number of studies that have directly examined the importance of time-intensity envelope cues for speech perception (Breeuwer and Plomp, 1984, 1986; Van Tasell *et al.*, 1987, 1992; Grant *et al.*, 1985, 1991, 1994;

Shannon *et al.*, 1995). In these studies, envelope signals were extracted from speech by full-wave rectification and low-pass filtering (after Horii *et al.*, 1971) and used to modulate an audible carrier signal (usually a pure tone or noise). The original speech signal was either unprocessed or filtered to limit the spectral regions contributing to the envelope fluctuations. The range of envelope-rate fluctuations was controlled by the cutoff frequency of the low-pass smoothing filter. For the majority of studies, the bandwidths of the envelope signals evaluated were very narrow due to the use of low-pass smoothing filters of 50 Hz or less. Thus, the available cues were probably limited to what Rosen called the amplitude envelope. In only a few studies has the envelope bandwidth been varied systematically (Van Tasell *et al.*, 1987, 1992; Grant *et al.*, 1991), thereby allowing for the possibility that periodicity and some fine structure cues may be transmitted as well. In tests with normal-hearing listeners, increases in envelope bandwidth (accomplished by applying less smoothing to the extracted envelope signal) resulted in improved speech recognition for auditorily presented nonsense syllables (Van Tasell *et al.*, 1987) and for sentences presented audiovisually (Grant *et al.*, 1991). Van Tasell *et al.* (1987, 1992) and Grant *et al.* (1991) suggested that a possible reason for the increase in speech information transmitted with increasing envelope bandwidth was that fundamental frequency cues were made progressively more available in the form of envelope periodicity as the lowpass filter cutoff frequency was increased.

More recently, studies by Turner *et al.* (1995), Souza and Turner (1996), and Van Tasell and Trine (1996) examined the importance of speech waveform information using test signals composed of signal correlated noise [SCN—after Schroeder (1968)]. The SCN signals are generated by multiplying each point of a digitized speech waveform by ± 1 with equal probability. The resulting signals have a flat long-term spectrum and instantaneous amplitude identical to that of the original speech. According to Rosen's taxonomy, SCN signals have both envelope and periodicity information. Fine structure information related to the number of cycles within pitch periods is probably not preserved with SCN signals because of its noise characteristics.

With SCN signals, speech periodicity is well preserved at modulation depths roughly equal to those of the original speech waveform.[1] However, with methods of envelope extraction that include low-pass filtering (Risberg, 1974; Breeuwer and Plomp, 1984, 1986; Grant *et al.*, 1985, 1991, 1994; Shannon *et al.*, 1995), the representation of waveform periodicity varies with the cutoff frequency of the smoothing filter. For example, consider the four waveform examples of the word ''poppy'' shown in Fig. 1. The top panel shows the original speech waveform. The second panel shows the SCN version. Note that the periodicity associated with the voice $F0$ is clearly visible in the SCN signal. The third and fourth panels show envelope signals extracted by rectifying and filtering the speech waveform as described by Horii *et al.* (1971). In the third panel, the smoothing low-pass filter has a cutoff of 100 Hz. Note that the periodicity of the original speech signal is still present but at a much shallower depth than either the original speech waveform or its SCN version.

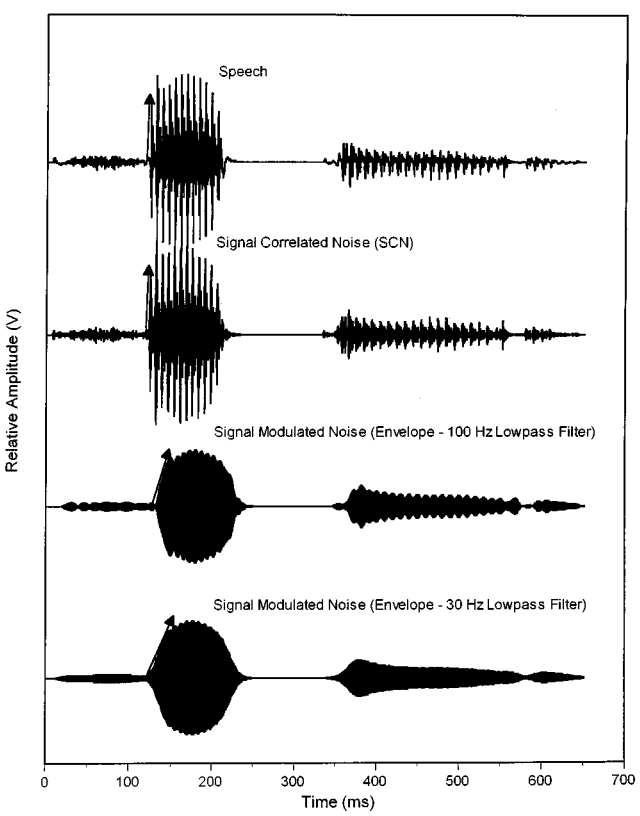

FIG. 1. Original and processed waveforms of the word ''poppy'' spoken by a male speaker. Top panel: original speech waveform. Second panel: Signal correlated noise derived from the original waveform. Third panel: Gaussian noise multiplied by the original speech waveform after full-wave rectification and low-pass filtering with cutoff frequency of 100 Hz. Bottom panel: Gaussian noise multiplied by the original speech waveform after full-wave rectification and low-pass filtering with cutoff frequency of 30 Hz. Arrows indicate changes in the rate of attack at syllable onset resulting from differences in envelope processing.

Also note that the rise time associated with the onset of the vowel /ɑ/ is slower than either the original speech or the SCN signal, as indicated by the slope of the arrows shown on each of the waveforms. The bottom panel shows the speech envelope signal with a low-pass smoothing filter with a 30-Hz cutoff. Whereas some of the waveform periodicity is still visible, the modulation depth is very shallow. In addition, the slope of the envelope at vowel onset is further reduced relative to the waveforms shown in the upper three panels of the figure. Finally, the extreme smoothing at the onset of the first and second syllable obscures voice-onset-time information associated with the consonant /p/.

Results from SCN studies suggest that information about consonant voicing and manner-of-articulation are the most reliably transmitted features of speech envelope signals. Further, there is evidence to suggest that HI individuals are relatively unimpaired, compared to NH subjects, in their abilities to process this temporal speech information (Turner *et al.*, 1995). However, voicing information, according to Rosen's analysis, is related primarily to waveform periodicity. Because the representation of waveform periodicity depends on the methods used to extract envelope cues, the question remains whether listeners are able to detect and discriminate waveform periodicity for modulation depths less than 100%.

In summary, results from studies on temporal speech information demonstrate that listeners can use auditory envelope cues alone and in combination with speechreading to enhance the perception of speech. However, they do not indicate which aspects of the envelope [i.e., amplitude envelope (2–50 Hz) or periodicity (50–500 Hz)] were used. Clearly, the slower varying amplitude-envelope cues are useful when combined with speechreading, and increases in envelope bandwidth tend to improve performance. However, it is uncertain whether this improvement is due to the increased perception of periodicity cues or because of the more clearly represented syllable onset cues. Therefore, the question remains whether listeners can extract and follow changes in periodicity (when made available) from the waveform envelope, and if these cues can be used reliably to benefit speech perception.

B. Detection and discrimination of amplitude modulation by NH subjects

The ability to detect waveform modulations is a function of both the rate of modulation, the depth of modulation, and the shape of the modulating waveform (e.g., Patterson and Johnson-Davies, 1977; Rodenburg, 1977; Viemeister, 1977, 1979; Bacon and Viemeister, 1985; Formby *et al.*, 1992). In general, modulation threshold (i.e., the depth of modulation required for detection) increases with modulation rate. For NH listeners and sinusoidal amplitude modulation at very low rates (1–10 Hz), the modulation depth required for detection is approximately 2%–5% (−33 to 26 dB). Note that these very slow rates of modulation are important for speech in that they reflect the number of syllables spoken per second. At higher rates (e.g., 80 Hz), modulation thresholds are approximately 15%–20% (at about −15 dB), whereas at still higher rates (e.g., above 800–1000 Hz) modulation thresholds are approximately 50% or −6 dB (Rodenburg, 1977; Viemeister, 1977, 1979; Formby, 1985).

To use envelope modulations as a cue for intonation, listeners must be able to track changes in the rate of envelope fluctuation which may require greater depths of modulation than needed for modulation detection. Early studies of modulation rate discrimination for interrupted broadband noise showed that the smallest detectable change in modulation rate (i.e., the difference limen—DL) rose monotonically as the standard modulation rate was increased from 1 to 320 Hz (Miller and Taylor, 1948; Pollack, 1952; Mowbray *et al.*, 1956; Harris, 1963). However, because these studies used interrupted noise, rate DLs could not be related to depth of modulation (in essence, these signals were modulated at depths of 100%).

Patterson and Johnson-Davies (1977) and Patterson *et al.* (1978) measured the modulation depth required to discriminate a fixed 20% modulation rate change as a function of signal bandwidth, spectral location, and type of waveform modulator. They reported that rate discrimination of broadband AM signals with bandwidths $\geqslant$4 kHz required depths of modulation between 15%–30%, and that larger depths of modulation (up to 80%) were required when the listening bandwidth was reduced by the presence of a masking noise. Further, sine-wave modulation required modulation depths approximately 2 dB greater than square-wave modulation. Also reported were large individual differences in rate-threshold data, especially at high modulation rates.

It should be noted that, although Patterson and his colleagues studied discrimination for modulation rates of 40 to 320 Hz, well within the range of rates found in speech *F*0's (i.e., 80–500 Hz), a fixed modulation rate change of 20% is a fairly large step increase with respect to variations in intonation found in speech. Earlier studies have shown that the quantizing of intonation into fewer than 8–12 steps/octave (i.e., frequency differences of 6%–9% per step or 1–1.5 semitones) results in decreases in the ability to track intonation (Hnath-Chisolm and Boothroyd, 1992). To our knowledge, there are no studies that systematically relate modulation depth requirements as a function of modulation rate with stimulus parameters more in keeping with characteristics of typical speech waveforms. In particular, the ability to process modulation rate changes that might serve to encode intonation and stress in speech has not been fully studied.

Rate discrimination thresholds increase with decreases in modulation depth, so that data obtained with modulation depths of 100% can be used to determine the *minimum* discriminable rate change as a function of modulation rate for a given carrier and modulating waveform shape. Formby (1985) measured DLs for modulation rate using a 100% sinusoidally amplitude-modulated broadband noise. Results showed that modulation rate DLs for normal-hearing listeners were relatively flat (1–3 Hz) for modulation rates below 80 Hz. Above 80 Hz, the modulation rate DLs increased with modulation frequency, requiring a rate change in excess of 100 Hz at a modulation frequency of 400 Hz. A similar increase in the modulation rate DL was observed by Hanna (1992) for modulation rates above 100 Hz.

C. Detection and discrimination of amplitude modulation by HI subjects

Modulation detection thresholds for HI listeners tend to be similar to NH listeners at very low modulation rates (below 60 Hz) but deviate more and more from NH thresholds as modulation rate increases (Formby, 1987). These detection threshold differences between NH and HI listeners have been attributed to differences in the audible bandwidth of the modulated signals, with HI listeners having a more spectrally restricted signal due to their hearing loss (Bacon and Viemeister, 1985; Bacon and Gleitman, 1992; Moore, 1995; Turner *et al.*, 1995). When NH listeners are presented with modulated signals with a similarly restricted bandwidth (by using low-pass or bandpass carriers), modulation detection thresholds increase and become more like those for HI listeners (Bacon and Viemeister, 1985; Moore, 1995).

Modulation rate DLs by HI listeners tend to be relatively normal at low modulation rates, below 100 Hz, where modulation detection thresholds are usually less elevated than at higher rates. However, discrimination becomes progressively worse than normal at increasing modulation rates above 100 Hz (Formby, 1986, 1987). Thus, modulation discrimination appears to be constrained by modulation detection thresholds. That is, when modulation detection thresholds are nor-

TABLE I. Better-ear hearing thresholds (dB SPL) for HI subjects.

	Frequency (Hz)								
Subject	250	500	1000	1500	2000	3000	4000	6000	8000
1	45.5	36.5	42.0	61.5	69.0	70.0	69.4	85.5	93.0
2	45.5	41.5	47.0	51.5	64.0	70.0	64.4	80.5	73.0
3	55.5	41.5	27.0	36.5	44.0	85.0	89.4	120.5	113.0
4	40.5	26.5	32.0	36.5	39.0	75.0	69.4	75.5	68.0
5	45.5	36.5	47.0	61.5	79.0	85.0	94.4	80.5	83.0
6	55.5	41.5	47.0	56.5	59.0	60.0	64.4	75.5	53.0
7	55.5	56.5	62.0	61.5	64.0	65.0	84.4	75.5	78.0
8	50.5	46.5	42.0	41.5	49.0	70.0	74.4	110.5	108.0
Mean	49.3	40.9	43.3	50.9	58.4	72.5	76.3	88.0	83.6
s.d.	5.8	8.6	10.6	11.2	13.5	8.9	11.6	17.5	20.3

mal, rate discrimination is near normal; when detection thresholds are elevated, rate DLs are also elevated.

Past studies of modulation rate discrimination by HI listeners have used signals with 100% modulation. Because noise and reverberation serve to reduce the depth of amplitude modulations, it is possible that the depths and rates of modulation found in typical speech environments may provide additional processing challenges to listeners with sensorineural hearing loss. In the present study, modulation rate discrimination abilities were evaluated in normal-hearing and hearing-impaired listeners for rates important for the perception of periodicity in speech (i.e., voicing and intonation). The study is an extension of the work reported by Patterson *et al.* (1978) and Formby (1985, 1986, 1987). However, unlike these earlier studies which limited their exploration to either 100% modulated waveforms or to fixed rate changes of 20%, the present study examined the relation between modulation depth and modulation rate discrimination for rates encompassing the characteristic modulations of speech. Of particular interest are questions regarding the ability of NH and HI listeners to make use of possible cues to voicing and intonation present with varying degrees of clarity in the speech envelope.

I. METHODS

A. Subjects

Four normal-hearing and eight hearing-impaired subjects were tested. The NH subjects had hearing threshold levels better than 15 dB HL at octave frequencies from 250–4000 Hz and better than 20 dB HL at 6000 and 8000 Hz. Their ages ranged from 38–52 years. The hearing-impaired subjects had moderately sloping sensorineural losses typical of noise trauma, with average three-frequency pure-tone thresholds at 500, 1000, and 2000 Hz greater than 30 dB HL but less than 60 dB. The ages of the HI subjects ranged from 58–76 years. Hearing thresholds in dB SPL are shown in Table I for the HI subjects. For NH subjects, testing was conducted on the right ear. For HI subjects, the better ear served as the test ear (six left, two right). Each subject participated in approximately 12 h of testing.

B. Stimuli

Modulation signals were created by digitally multiplying a flat-spectrum Gaussian noise and a dc-shifted square-wave. The square-wave modulator had a peak amplitude of 1.0. To produce different depths of modulation (m), the minimum amplitude of the square-wave was offset from zero by $(100-m)/100$, where m is the desired modulation depth in percent. Thus, for a 100% modulation, the square-wave amplitude varied from 0 to 1; for a 70% modulation depth, the square-wave amplitude varied from 0.3 to 1; for a 30% modulation depth, the square-wave amplitude varied from 0.7 to 1; and so on. Both noise carrier and square-wave modulator were generated digitally at a sampling frequency of 40 kHz (however, the EAR insert phones effectively reduced the audible bandwidth for NH subjects to just over 10 kHz). The frequency of the modulator (f_m) was either 80, 160, or 320 Hz to cover a range of voice fundamental frequencies typical for male, female, and child voices. Square-wave-modulated noise signals were presented monaurally over EAR insert phones at 80 dB SPL (spectrum level $\approx$40 dB). Signal durations were 400 ms with a 50-ms rise/fall.

C. Procedure

A cued two-interval adaptive forced-choice procedure was used to determine the thresholds for modulation detection and modulation discrimination at each of the three modulation rates. Subjects were seated comfortably in a sound-treated booth facing a touch screen response terminal. For modulation detection thresholds, the standard stimulus was unmodulated noise. The comparison stimuli were constructed with modulation depth determined by an adaptive tracking procedure. After presentation of the standard unmodulated noise in interval one, the comparison modulated noise stimulus occurred in either the second or third interval with equal probability, and the standard was presented again in the remaining interval. The subject was instructed to press the appropriate area of the touch screen indicating the interval containing the modulated noise. Depth of modulation was varied according to an adaptive 3-down, 1-up algorithm described by Levitt (1971) targeting 79% correct detections. At the start of the track, the comparison stimulus had a modulation depth of 100%.[2] At first, the step size used to adjust modulation depth was 20%; after two track reversals, the step size was reduced to 5%, after another two reversals, the step size was 2%, continuing until ten more reversals at the smaller step size had occurred. Detection thresholds were determined as the average of the modulation depths on these last ten reversals in the adaptive track. For each adaptive track, the modulation rate was fixed at one of the three modulation frequencies. The three rates were tested in a different random order for each subject. A minimum of three tracks at each modulation rate was used to estimate the final detection threshold for each subject.

For modulation rate discrimination, the standard stimulus consisted of modulated noise at one of three different rates of modulation. For each modulation rate, three modulation depths were chosen, resulting in a total of nine stan-

TABLE II. Modulation rate and depth of standard stimuli used for modulation rate discrimination. Numbers in parentheses indicate the number of HI subjects whose modulation detection thresholds were below the test modulation depth.

	Modulation rate			
	80 Hz	160 Hz	320 Hz	
Modulation depth (%)	40	50 (1)	60 (4)	Low
	70	75	80 (3)	Mid
	100	100	100	High

dard stimuli. Modulation depths were selected based on preliminary results from a modulation detection task with normal-hearing listeners and represent (1) full modulation depth (100%), (2) a depth approximately 15%–30% above detection thresholds (low-depth conditions), and (3) a depth in between these two (mid-depth conditions). It should be noted that for HI subjects, the standard modulation depth for the three low-depth conditions were not all equally above detection thresholds and that for some HI subjects and some modulation rates, the test modulation depth was at or below detection threshold (see Table II).

In each condition, the dependent variable that controlled the adaptive track was the difference in modulation rate necessary for 79% correct discrimination from the standard stimulus. On each trial, the standard stimulus (e.g., $f_m = 80$ Hz, $m = 100\%$) was presented in the first and either the second or third of three sequential time intervals. The comparison stimulus, with the same modulation depth but with the rate determined by the adaptive procedure, occurred in either the second or third interval, selected with equal probability on each trial. Subjects selected the interval (either the second or third) that was different (having a higher rate of modulation) from the other two by touching the appropriate area on the response terminal. Each track began with a comparison modulation rate that was 80% greater than the standard rate. At the beginning of the track, the modulation rate difference between the standard stimulus and the comparison stimulus (Δr) was decreased (for every three consecutive correct responses) or increased (for every incorrect response) by a factor of 2. After four reversals in the direction of the track, Δr was decreased (or increased) by a factor of 1.25. The track continued for ten more reversals at the smaller step size, and a threshold was determined by calculating the geometric mean of the Δr's for the last eight reversals. At least six practice blocks for each of the nine standard stimuli were administered before formal data collection began. Following training, a minimum of three measurements were made for each of the nine standard stimuli, and the mean of these measurements was taken as a final threshold value.

II. RESULTS AND DISCUSSION

A. Modulation detection

Average detection thresholds for NH and HI subjects as a function of modulation rate (f_m) are shown in Fig. 2. As expected, the three-point temporal modulation transfer function, or TMTF, shows that greater modulation depths were required as modulation rate increased from 80 to 320 Hz.

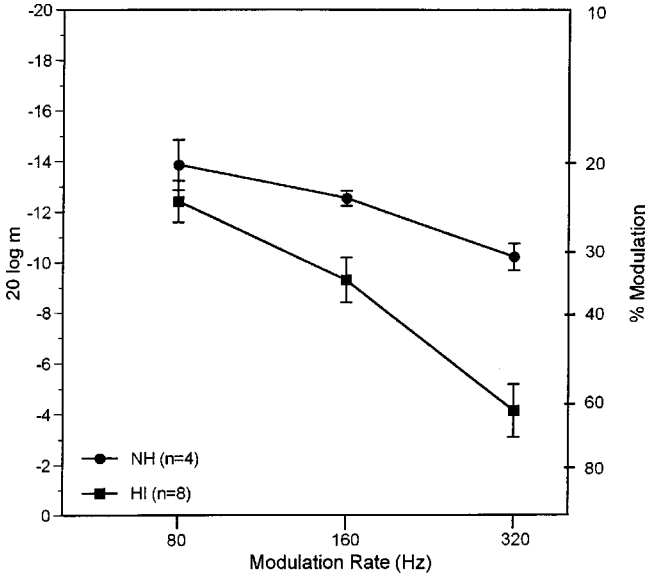

FIG. 2. Mean modulation depth for detection of modulation for normal-hearing (NH) and hearing-impaired (HI) subjects. Error bars represent ± 1 standard error.

Note, however, that the effect of rate was much greater for HI subjects than for NH subjects. At 80-Hz modulation rate, modulation thresholds were similar for NH and HI subjects (20.7% and 24.7%, respectively). In contrast, at 320-Hz modulation rate, NH thresholds were less than half that of HI thresholds (31.1% and 65.3%, respectively). A two-factor (group×rate) repeated measures ANOVA for unbalanced designs (BMDP 5V), using Wald tests of significance, revealed significant effects for group ($\chi^2 = 10.12$, df=1, $p = 0.002$), modulation rate ($\chi^2 = 126.94$, df=2, $p < 0.001$), and their interaction ($\chi^2 = 19.17$, df=2, $p < 0.001$). The interaction was investigated further by calculating regression coefficients for each group and rate in the ANOVA model. The coefficients were tested using z scores. These *post hoc* tests at each modulation rate indicated that detection thresholds for NH and HI subjects were significantly different at modulation rates of 160 and 320 Hz ($z = 2.52$, $p = 0.012$ and $z = 4.73$, $p < 0.001$, respectively). Group differences at 80-Hz modulation rate were not significant ($z = 1.12$, $p = 0.264$).

Bacon and Viemeister (1985) and Formby (1987) noted that the rate at which sensitivity to modulation declines, i.e., the attenuation rate of the modulation transfer function, is steeper above 100-Hz modulation for HI subjects than for NH subjects (approximately 6 and 2.5 dB/oct, respectively). This difference in attenuation slope for the two subject groups is also observed here. The poorer performance by HI subjects can, to a certain degree, be explained by a decrease in audibility of the high-frequency portions of the modulated waveform (Bacon and Viemeister, 1985; Bacon and Gleitman, 1992). To determine the audibility of the amplitude-modulated signals used in this study we measured the peak 1/3-oct band levels of the modulated waveform at the output of the EAR phones and plotted this along with the average NH and HI audiometric thresholds (Fig. 3). Peak 1/3-oct levels were plotted because we assumed that the detection of either a pure tone, as measured in threshold testing, or the AM signals used in the present study, were based primarily

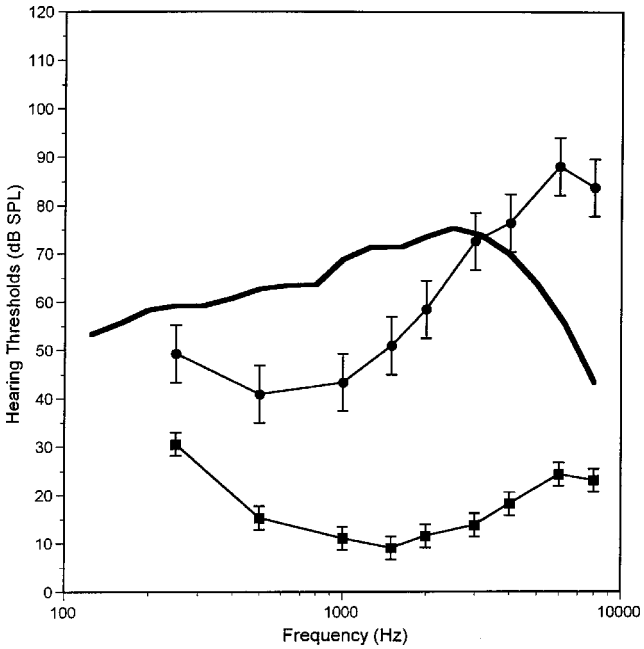

FIG. 3. Comparison of hearing thresholds for NH (squares) and HI (circles) subjects and peak spectrum level of modulated noise signals used to determine thresholds for detection of modulation. Error bars represent ±1 standard error.

on the peak amplitude levels obtained in each critical band (roughly 1/3 oct wide). As Fig. 3 shows, above 3 kHz most of the HI subjects were not able to hear the signal, resulting in a reduced bandwidth of stimulation. Previous studies have shown that modulation thresholds for NH subjects are elevated when the bandwidth of the stimulus is reduced (Patterson *et al.*, 1978; Viemeister, 1979; Bacon and Viemeister, 1985). To the extent that the hearing losses of these listeners acted as a low-pass filter, it is not unexpected that they would show less sensitivity to amplitude modulation than NH subjects listening to an effectively wider-band stimulus.

Bacon and Viemeister (1985) suggested that the steeper slope of the modulation transfer function exhibited by HI subjects (see Fig. 2) may also be related to decreased audibility of the high-frequency portions of the modulated waveform. It was argued that in a modulation detection task with a broadband carrier, the temporal analysis of the signal involves an analysis of the time pattern occurring within each auditory channel (or critical band), and a combination of the time patterns across channels. When the number of critical bands involved in the analysis is reduced, as with low-pass filtering or high-frequency hearing loss, the result is a decreased sensitivity to stimulus modulation. A reduction of the effective listening bandwidth due to low-pass filtering has at least two consequences: listeners are forced to use information from a reduced number of auditory bands in the decision process, and the auditory bands that are used to detect amplitude modulation have a lower center frequency and, presumably, a narrower bandwidth than higher-frequency channels (at least for NH subjects). At high modulation rates, the outputs of auditory channels with narrower bandwidths would be expected to exhibit reduced modulation (relative to higher-frequency auditory channels with broader bandwidths) due to greater attenuation of sideband components.

For HI subjects, the ''effective'' listening bandwidth (i.e., the number of relevant channels of information) depends on the severity and slope of the hearing loss as well as the level of the signal. For our signal levels, the HI subjects were probably limited to an effective overall bandwidth of 3 kHz (compared to 8–10 kHz for NH subjects). Thus, the number of auditory channels used by HI subjects was reduced relative to NH subjects. However, it is not clear that the bandwidth of the remaining auditory channels used by HI subjects were more narrow than the higher-frequency auditory channels available to NH subjects. Typically, broader-than-normal auditory filters accompany sensorineural hearing loss. At the same center frequency, HI subjects with moderate amounts of hearing loss have critical bandwidths roughly two to three times normal when measured at the same SPL (Moore, 1995). Therefore, it is possible that the bandwidth of a moderately impaired auditory channel at 2 kHz could be equal to, or broader than, the bandwidth of a normal auditory channel at 4 kHz. Given this possibility, the argument made by Bacon and Viemeister (1985) that a reduction in modulation thresholds by HI subjects is caused by listening to more narrow auditory channels and a subsequent attenuation of modulation sideband components cannot be made with certainty. Thus, reduction of the effective listening bandwidth (i.e., fewer auditory channels) may explain the general decrease in sensitivity to amplitude modulation in HI subjects (because fewer auditory channels contribute to the decision statistic), but it may not fully explain the steeper slope of the TMTF (relative to NH subjects) for the higher modulation rates.[3]

The decrease in sensitivity in HI subjects at high modulation rates may be more adequately explained by comparing forward masking recovery rates in NH and HI listeners. Glasberg *et al.* (1987) have shown that for signals presented at equal SPL, the rate of recovery from forward masking is much faster for NH subjects than for HI subjects. Similar results have been reported by Nelson and Freyman (1987). These studies suggest that the valleys within modulated waveforms are less well represented in HI listeners, and that this temporal smearing would be worse at faster modulation rates. The present results, along with those of Formby (1987) and Bacon and Viemeister (1985), are consistent with this account.

B. Modulation discrimination

Average thresholds for modulation rate discrimination (Δr) are shown in Fig. 4. In each panel, the change in modulation rate required to produce about 79% discrimination from the standard rate (80, 160, or 320 Hz) is shown in units of Hertz as a function of modulation depth. (Recall that the modulation depths tested varied for the three standard rates, selected according to performance in pilot work.) As expected, Δr increased with increasing rate and decreasing modulation depth for both NH and HI subjects. Several HI subjects were unable to perform the discrimination task at high modulation rates and shallow modulation depths, even though most were able to detect the modulation.[4] This is

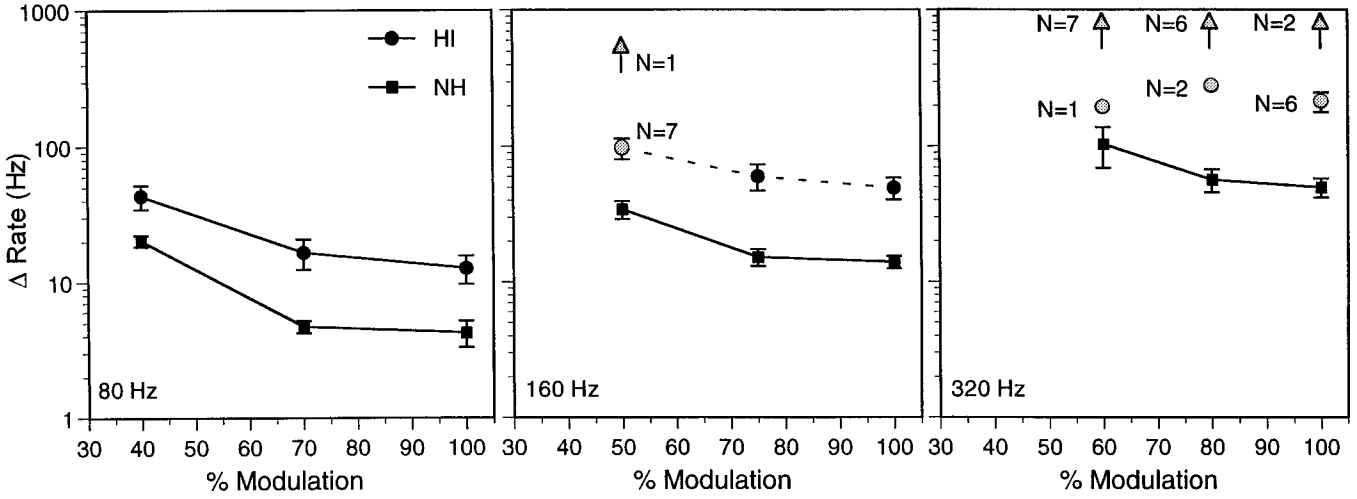

FIG. 4. Mean modulation rate discrimination thresholds for NH and HI subjects. Error bars represent ±1 standard error. The left panel shows data for a modulation rate of 80 Hz; the middle panel shows data for a rate of 160 Hz; the right panel shows data for 320 Hz. Shaded circles indicate missing data. Arrow indicates that thresholds could not be measured within a 2-oct range. N = number of HI subjects that either completed the discrimination task (circles) or that failed to complete the task (arrows).

indicated in Fig. 4 by the shaded circles and upward arrows. Note that for standard modulation rates of 80 and 160-Hz, only one subject could not complete the full set of data (50% modulation depth, 160-Hz modulation rate). However, at 320-Hz modulation rate, HI subjects found the discrimination task quite difficult. Seven HI subjects failed to discriminate at 60% modulation depth, six HI subjects failed to discriminate at 80% modulation depth, and two failed to discriminate at 100% modulation depth.[5] Given the incomplete data set for HI subjects (especially for the 320-Hz modulation rate condition), two different data subsets containing relatively few missing cells were identified for further analysis. A three-factor (group×rate×depth) repeated measures ANOVA was used to analyze group differences for the 80 and 160-Hz conditions together (only one missing cell). In addition, a two-factor (group×rate) repeated measures ANOVA was used to analyze the 100% modulation depth conditions across all three rates (two missing cells). For both analyses, the dependent variable was the logarithm of the mean Δr values. When comparisons were made across rates (80 and 160 Hz), the modulation depth conditions were grouped into low (40%–50%), medium (70%–75%), and high (100%) categories.

Results from the first analysis (two rates, three modulation depths) revealed significant main effects for all three factors ($\chi^2_{\text{Group}}=22.94$, $p<0.001$; $\chi^2_{\text{Rate}}=205.73$, $p<0.001$; $\chi^2_{\text{Depth}}=163.49$, $p<0.001$). Significant interactions included group×rate ($\chi^2=4.43$, $p=0.035$) and rate×depth ($\chi^2=10.81$, $p=0.005$). The remaining interactions (group ×depth and group×rate×depth) were not significant. *Post hoc* tests for comparing group differences for each of the six rate×depth conditions indicated significant group differences for all modulation depth conditions. Results from the second analysis (three rates, 100% modulation depth condition only) revealed significant main effects for group ($\chi^2=31.97$, $p<0.001$) and rate ($\chi^2=369.08$, $p<0.001$). The interaction between group and rate was not significant ($\chi^2=2.02$, $p=0.36$). *Post hoc* test for group differences across the three rates indicated that HI subjects were significantly worse than NH subjects in all three 100% modulation depth conditions.

The present results obtained for the 100% modulation depth condition are in good agreement with previous studies (e.g., Formby, 1985, 1986; Hanna, 1992). The average Δr's for standard rates of 80, 160, and 320 Hz are approximately 3–5 Hz, 10–15 Hz, and 40–50 Hz for NH subjects and approximately 10–15 Hz, 40–50 Hz, and 200–250 Hz for HI subjects. Rate discrimination thresholds for modulation depths less than 100% have not been studied systematically, and not at all in HI listeners. The data obtained for the middle (70%–80%) and low (40%–60%) depth conditions are of particular interest because they represent more realistic conditions of modulation when modulated signals like speech are subjected to noise and/or reverberation. For example, signal-to-noise ratios (S/N) between 3.7–6.0 dB would reduce a signal with 100% modulation to one with 70%–80% modulation (a 20%–30% modulation reduction), whereas S/N's between 1.8 and −1.8 dB would result in modulation reductions of 40%–60% (Houtgast and Steeneken, 1985). Since noise and reverberation are common to most listening environments, rate thresholds obtained at these lower modulation depths are more indicative of subject performance in real-world situations than are thresholds obtained at 100% modulation (which would occur only in nonreverberant quiet settings). Rate discrimination thresholds obtained at 80 and 160 Hz for the middle and low depth conditions showed a similar pattern of performance for NH and HI groups, albeit with the HI subjects performing more poorly. However, at 320-Hz modulation rate, HI subjects could not tolerate any reduction in modulation depth. At modulation depths less than 100%, most HI listeners could not perform the rate discrimination task. These results are consistent with earlier results obtained on a group of patients with Meniere's disease tested at 300-Hz modulation rate and a depth of 100% (Formby, 1986), taking into account the expected threshold differences due to sinusoidal modulation versus square-wave modulation (Patterson *et al.*, 1978).

Previous studies have suggested that rate discrimination (Patterson *et al.*, 1978; Formby, 1987), as well as a similar discrimination of the pitch of amplitude-modulated noise (Burns and Viemeister, 1976), is limited largely by modulation detection thresholds. Our group results support this position with one notable exception. Recall that at a modulation rate of 80 Hz, group differences in modulation detection thresholds were not significant. Nevertheless, modulation rate discrimination thresholds at 80 Hz were significantly different across groups for all modulation depths.

To further explore the presumed relationship between modulation detection and modulation discrimination by listeners with hearing impairment, Pearson correlations were computed across the eight HI subjects. Only one correlation out of nine (modulation detection at 80 Hz versus modulation discrimination at 80-Hz modulation rate with 40% modulation depth) was found to be significant. Thus, whereas detecting modulation is a logical prerequisite for discriminating among different modulation rates, individual differences in modulation detection are not predictive of individual differences in discrimination of modulation rate.

III. GENERAL DISCUSSION

In the present study, we focused on listeners' abilities to detect and discriminate amplitude modulations. The possibility that AM signals are likely to be robust and perceptually salient for hearing-impaired listeners is supported by models of hearing that include an array of bandpass filters as the initial stage of peripheral auditory processing (see, e.g., Patterson *et al.*, 1995). When the impact of sensorineural hearing impairment is incorporated into such models, bandwidths of the auditory filters are broadened to simulate reduced frequency resolution. However, with broader auditory filters, more signal components are expected to interact within a given filter's bandwidth, resulting in more pronounced temporal modulations in the time waveform (de Boer, 1976). Thus, the same basic mechanisms responsible for the decrease in frequency selectivity in impaired listeners logically point to near-normal or better-than-normal acuity for fine temporal discriminations in quiet (Rosen and Smith, 1988; Rosen, 1992). On the other hand, Bacon and Viemeister (1985) have shown that another consequence of the hearing loss is a reduction in audible bandwidth. With sloping losses, this means that the high-frequency portions of the signal will be attenuated or lost entirely unless some form of compensatory spectrum shaping is used. Thus, even though the bandwidths of auditory filters will be broader with hearing loss (allowing for more signal components to interact), the number of active participating bands will be less. The poorer performance of the HI subjects in the present study suggest that reduced access to the high-frequency portions of the AM carrier outweigh any possible enhancement effect that broader-than-normal auditory filters may have on the perception of AM.

One of the goals of the present study was to begin to address claims made in earlier experiments regarding listener access to $F0$ information contained in the speech envelope. Both Van Tasell *et al.* (1987) and Grant *et al.* (1991) suggested that listeners could use envelope modulations associated with the talker's $F0$ to improve their recognition of speech, and that this information would be more available for SCN signals and with envelope signals processed through relatively broad smoothing filters. As described earlier (see Fig. 1), access to this important speech information can occur in two ways: (1) by detecting the presence of fast AM as a cue to voicing, and (2) by tracking variations in AM to indicate changes in intonation and stress (Rosen, 1992). With regard to the detection of voicing information, it appears that the relatively fast envelope modulations associated with typical $F0$ values of male, female, and child speakers can be detected reliably given sufficient modulation depth ($>$40% for NH listeners and $>$70% for HI listeners). Furthermore, voicing detection would likely be best for male voices ($f_m \approx 80$ Hz) and worst for child voices ($f_m \approx 320$ Hz) due to decreased modulation sensitivity with increased f_m.[6] The question remains whether previous studies of temporal information in speech used envelope signals with modulation depths exceeding these critical values. The envelope processing employed by Van Tasell *et al.* and by Grant *et al.* used smoothing filters with low-pass cutoff frequencies of 200 Hz or greater. According to our own measurements, these broad smoothing filters would permit $F0$ envelope modulation depths to exceed 40%, especially for male talkers with average $F0$ near 120 Hz. Since the subjects tested by Van Tasell *et al.* and by Grant *et al.* had normal hearing, it is likely that envelope cues to voicing were indeed enhanced by broadened smoothing filters.

In contrast to voicing information, accessing speech intonation information from envelope cues is far more difficult. The DL for discriminating among $F0$ contours with rise/fall patterns typical of natural speech is approximately 12 Hz for NH subjects and substantially larger (by a factor of 3–5) for HI subjects (Klatt, 1973; Grant, 1987). A typical functional range of $F0$ produced by a female talker (i.e., the range of $F0$ variation for connected speech by a single talker) might be 150–260 Hz, or about 1.5 oct (Hollien and Paul, 1969). That means that NH listeners can utilize approximately 10–15 discriminable steps [roughly the size of a semitone (i.e., 6%)] to monitor changes in the $F0$ of speech. The Δr values shown in Fig. 4 suggest that NH listeners should be able to extract variations in $F0$ near 80 Hz (e.g., low-pitched male voices), so long as the modulation depth was greater than 70%. This is because the DLs for rate discrimination at 80 Hz (70% and 100% modulation depth conditions) were less then one semitone (under 5 Hz). However, for the remaining seven rate discrimination conditions, Δr values were in excess of 1.4 semitones. For HI subjects, the smallest Δr was 2.5 semitones measured at 80 Hz (100% modulation) and increased dramatically for higher rates of modulation.

IV. CONCLUSIONS

Past studies examining the role of amplitude-envelope cues in speech recognition have suggested that information about voicing (periodicity) and intonation ($F0$ variation) may be extracted by detecting and discriminating variations in the rate of envelope ripple (see Fig. 1). The modulation depth of this ripple depends on the signal processing employed to extract speech envelope information. With SCN

signals, or with speech envelopes processed through relatively broad smoothing filters (with low-pass cutoff frequencies greater than 100–200 Hz), the depth of this envelope ripple often exceeds 40%. More typically, the depth of this envelope ripple is much less due to smoothing filters with low-pass cutoff frequencies near 30 Hz.

As a way to address whether envelope ripple can be extracted and used in speech recognition, we determined the detection and discrimination thresholds for variation in the rate of amplitude modulation given modulation rates and modulation depths typically observed in speech. The results showed that with signals presented at an overall level of 85 dB SPL, modulation detection thresholds were significantly better for NH than HI listeners at higher modulation rates (160 and 320 Hz). This implies that while both NH and HI listeners can probably detect speech periodicity in the form of envelope ripple (given sufficient modulation depth), HI listeners would have greater difficulty doing so with female and child talkers. The results for modulation rate discrimination showed that both NH and HI listeners had fairly large threshold values at all modulation rates and modulation depths, with the singular exception of NH subjects at a rate of 80 Hz and a modulation depth of 100%. This implies that envelope cues associated with speech intonation (based on variations in the rate of change of envelope ripple) probably cannot be extracted reliably by either NH or HI listeners.

ACKNOWLEDGMENTS

Portions of this research were presented at the 3rd Joint Meeting of the Acoustical Society of America and the Acoustical Society of Japan, 2–6 December, 1996, Honolulu, Hawaii. This research was supported by Grant Nos. DC00792 and DC00626 from the National Institute of Deafness and Other Communication Disorders to Walter Reed Army Medical Center, and by the Clinical Investigation Service, Walter Reed Army Medical Center, under Work Unit No. 2536. All subjects participating in this research provided written informed consent prior to beginning the study. We would like to thank Sid Bacon and an anonymous reviewer for their helpful comments on an earlier version of this manuscript. The opinions or assertions contained herein are the private views of the authors and are not to be construed as official or as reflecting the views of the Department of the Army or the Department of Defense.

[1]Modulation depth refers to the peak-to-valley ratio of the modulated signal expressed either in dB or in percent. The relation between modulation depth in dB and percent modulation is given by $20 \log m$, where m is the percent modulation divided by 100. Thus, 100% modulation=0 dB, 50% modulation=−6 dB, 10% modulation=−20 dB, etc.

[2]All subjects were able to make the discrimination between an unmodulated noise and a 100% square-wave modulated noise for all modulation rates. If an error occurred at the beginning of the track, the modulation depth of the comparison stimulus remained fixed at 100% until three consecutive correct responses were recorded, at which point the comparison depth was changed to 80%.

[3]To further address this issue, Pearson correlation coefficients were computed to examine the relation between pure-tone thresholds (dB SPL) and modulation detection thresholds ($20 \log m$). Results for the eight HI subjects revealed that audibility in the 3–4-kHz region was significantly correlated with detection thresholds for the 80- and 160-Hz modulation rate conditions ($0.66 < r < 0.81$). However, no significant correlations between pure-tone thresholds and modulation detection thresholds were found for the 320-Hz modulation rate condition, suggesting that the decrease in modulation sensitivity observed for this condition was not determined by audibility alone. However, with only eight HI subjects tested, these correlations should be viewed with caution.

[4]During the rate discrimination task, the adaptive block was terminated whenever a subject made three consecutive wrong discriminations for $\Delta r > 2$ oct (i.e., 24 semitones) above the modulation rate of the standard stimulus. Thus, failure to discriminate was operationally defined as a $\Delta r > 24$ semitones.

[5]It is important to note that many subjects failed to discriminate increases in modulation rate even though their modulation detection thresholds were lower than the modulation depth used in the discrimination tests. For example, at 320 Hz four out of eight HI subjects could detect modulations depths below 60%, five out of eight could detect modulations depths below 75%, and eight out of eight could detect modulation depths below 100%. However, we should also note that although audible, these shallow modulation depths were probably at low sensation levels which may have limited rate discrimination.

[6]This idea is consistent with suggestions in the literature that overall speech intelligibility tends to decline for talkers with elevated fundamental frequency (Eguchi and Hirsh, 1969; Ryles and Lieberman, 1982; Scotto Di Carlo and Germain, 1985). Although there are many reasons given for the decrease in intelligibility with increased $F0$ (e.g., greater spacing of harmonics giving rise to poorer formant definition, greater variability in achieving articulatory targets with child talkers, etc.), it is possible that the reduction (or loss) of AM cues to voicing due to a reduction in modulation sensitivity at higher rates of modulation may also be a contributing factor.

Bacon, S. P., and Viemeister, N. F. (**1985**). ''Temporal modulation transfer functions in normal-hearing and hearing-impaired listeners,'' Audiology **24**, 117–134.

Bacon, S. P., and Gleitman, R. M. (**1992**). ''Modulation detection in subjects with relatively flat hearing losses,'' J. Speech Hear. Res. **35**, 642–653.

Baer, T., and Moore, B. C. J. (**1993**). ''Effects of spectral smearing on the intelligibility of sentences in noise,'' J. Acoust. Soc. Am. **94**, 1229–1241.

Breeuwer, M., and Plomp, R. (**1984**). ''Speechreading supplemented with frequency-selective sound-pressure information,'' J. Acoust. Soc. Am. **76**, 686–691.

Breeuwer, M., and Plomp, R. (**1986**). ''Speechreading supplemented with auditorily presented speech parameters,'' J. Acoust. Soc. Am. **79**, 481–499.

Burns, E. M., and Viemeister, N. F. (**1976**). ''Nonspectral pitch,'' J. Acoust. Soc. Am. **60**, 863–868.

de Boer, E. (**1976**). ''On the 'residue' and auditory pitch perception,'' in *Handbook of Sensory Physiology*, edited by W. D. Keidel and W. D. Neff (Springer-Verlag, Berlin), pp. 479–583.

Eguchi, S., and Hirsh, I. J. (**1969**). ''Development of speech sounds in children,'' Acta Oto-Laryngol. Suppl. **257**, 1–51.

Erber, N. P. (**1972a**). ''Speech-envelope cues as an acoustic aid to lipreading for profoundly deaf children,'' J. Acoust. Soc. Am. **51**, 1224–1227.

Erber, N. P. (**1972b**). ''Auditory, visual, and auditory-visual recognition of consonants by children with normal and impaired hearing,'' J. Speech Hear. Res. **15**, 413–422.

Formby, C. (**1985**). ''Differential sensitivity to tonal frequency and to the rate of amplitude modulation of broadband noise by normally hearing listeners,'' J. Acoust. Soc. Am. **78**, 70–77.

Formby, C. (**1986**). ''Frequency and rate discrimination by Meniere patients,'' Audiology **25**, 10–18.

Formby, C. (**1987**). ''Perception of the temporal envelope of amplitude-modulated noise by hearing-impaired listeners,'' in *Auditory Processing of Complex Sounds*, edited by W. A. Yost and C. S. Watson (Erlbaum, Hillsdale, NJ), pp. 136–146.

Formby, C., Morgan, L. N., Forrest, T. G., and Raney, J. J. (**1992**). ''The role of frequency selectivity in measures of auditory and vibrotactile temporal resolution,'' J. Acoust. Soc. Am. **91**, 293–305.

Glasberg, B. R., Moore, B. C. J., and Bacon, S. P. (**1987**). ''Gap detection and masking in hearing-impaired and normal-hearing subjects,'' J. Acoust. Soc. Am. **81**, 1546–1556.

Grant, K. W. (**1987**). ''Identification of intonation contours by normally hearing and profoundly hearing-impaired listeners,'' J. Acoust. Soc. Am. **82**, 1172–1178.

Grant, K. W., Braida, L. D., and Renn, R. J. (**1991**). ''Single band amplitude

envelope cues as an aid to speechreading,'' Q. J. Exp. Psych. **43**, 621–645.
Grant, K. W., Braida, L. D., and Renn, R. J. (**1994**). ''Auditory supplements to speechreading: Combining amplitude envelope cues from different spectral regions of speech,'' J. Acoust. Soc. Am. **95**, 1065–1073.
Grant, K. W., Ardell, L. H., Kuhl, P. K., and Sparks, D. W. (**1985**). ''The contribution of fundamental frequency, amplitude envelope, and voicing duration cues to speechreading in normal-hearing subjects,'' J. Acoust. Soc. Am. **77**, 671–677.
Hanna, T. E. (**1992**). ''Discrimination and identification of modulation rate using a noise carrier,'' J. Acoust. Soc. Am. **91**, 2122–2128.
Harris, G. G. (**1963**). ''Periodicity perception by using gated noise,'' J. Acoust. Soc. Am. **35**, 1229–1233.
Hedrick, M. S., and Jesteadt, W. (**1996**). ''Effect of relative amplitude, presentation level, and vowel duration on perception of voiceless stop consonants by normal and hearing-impaired listeners,'' J. Acoust. Soc. Am. **100**, 3398–3407.
Hedrick, M. S., Schulte, L., and Jesteadt, W. (**1995**). ''Effect of relative and overall amplitude on perception of voiceless stop consonants by listeners with normal and impaired hearing,'' J. Acoust. Soc. Am. **98**, 1292–1303.
Hnath-Chisolm, T., and Boothroyd, A. (**1992**). ''Speechreading enhancement by voice fundamental frequency: The effects of $F0$ contour distortions,'' J. Speech Hear. Res. **35**, 1160–1168.
Hollien, H., and Paul, P. (**1969**). ''A second evaluation of the speaking fundamental frequency characteristics of post-adolescent girls,'' Lang. Speech **12**, 119–124.
Horii, Y., House, A. S., and Hughes, G. W. (**1971**). ''A masking noise with speech-envelope characteristics for studying intelligibility,'' J. Acoust. Soc. Am. **49**, 1849–1856.
Houtgast, T., and Steeneken, H. J. M. (**1985**). ''A review of the MTF concept in room acoustics and its use for estimating speech intelligibility in auditoria,'' J. Acoust. Soc. Am. **77**, 1069–1077.
Klatt, D. H. (**1973**). ''Discrimination of fundamental frequency contours in synthetic speech: Implications for models of pitch perception,'' J. Acoust. Soc. Am. **53**, 8–15.
Leek, M. R., and Summers, V. (**1993**). ''Auditory filter shapes of normal-hearing and hearing-impaired listeners in continuous broadband noise,'' J. Acoust. Soc. Am. **94**, 3127–3137.
Leek, M. R., Dorman, M. F., and Summerfield, Q. (**1987**). ''Minimum spectral contrast for vowel identification by normal-hearing and hearing-impaired listeners,'' J. Acoust. Soc. Am. **81**, 148–154.
Levitt, H. (**1971**). ''Transformed up-down methods in psychoacoustics,'' J. Acoust. Soc. Am. **49**, 467–477.
Miller, G. A., and Taylor, W. G. (**1948**). ''The perception of repeated bursts of noise,'' J. Acoust. Soc. Am. **20**, 171–182.
Moore, B. C. J. (**1995**). *Perceptual Consequences of Cochlear Damage* (Oxford U.P., Oxford).
Mowbray, G. H., Gebhard, J. W., and Byham, C. L. (**1956**). ''Sensitivity to changes in the interruption rate of white noise,'' J. Acoust. Soc. Am. **28**, 106–110.
Nelson, D. A., and Freyman, R. L. (**1987**). ''Temporal resolution in sensorineural hearing-impaired listeners,'' J. Acoust. Soc. Am. **81**, 709–720.
Patterson, R. D., and Johnson-Davies, D. (**1977**). ''Detection of a change in the pitch of AM noise,'' in *Psychophysics and Physiology of Hearing*, edited by E. F. Evans and J. P. Wilson (Academic, London), pp. 363–371.
Patterson, R. D., Allerhand, M. H., and Giguere, C. (**1995**). ''Time-domain modeling of peripheral auditory processing: A modular architecture and a software platform,'' J. Acoust. Soc. Am. **98**, 1890–1894.
Patterson, R. D., Johnson-Davies, D., and Milroy, R. (**1978**). ''Amplitude-modulated noise: The detection of modulation versus the detection of modulation rate,'' J. Acoust. Soc. Am. **63**, 1904–1911.
Pollack, I. (**1952**). ''Auditory flutter,'' Am. J. Psychol. **65**, 544–554.
Plomp, R. (**1978**). ''Auditory handicap of hearing impairment and the limited benefit of hearing aids,'' J. Acoust. Soc. Am. **63**, 533–549.
Risberg, A. (**1974**). ''The importance of prosodic speech elements for the lipreader,'' in *Visual and Audio-Visual Perception of Speech*, edited by H. B. Nielson and E. Klamp, Sixth Danovox Symposium, Scand. Audiol. Suppl. **4**, 153–164.
Rodenburg, M. (**1977**). ''Investigation of temporal effects with amplitude modulated signals,'' in *Psychophysics and Physiology of Hearing*, edited by E. F. Evans and J. P. Wilson (Academic, London), pp. 429–437.
Rosen, S. (**1989**). ''Temporal information in speech and its relevance for cochlear implants,'' in *Cochlear Implant: Acquisitions and Controversies*, edited by B. Fraysse and N. Cochard (Cochlear AG, Basel), pp. 3–26.
Rosen, S. (**1992**). ''Temporal information in speech: acoustic, auditory, and linguistic aspects,'' Philos. Trans. R. Soc. London **336**, 367–373.
Rosen, S., and Smith, D. A. J. (**1988**). ''Temporally-based auditory sensations in the profoundly hearing-impaired listener,'' in *Basic Issues in Hearing*, edited by H. Duifhius, J. W. Horst, and H. P. Wit (Academic, London), pp. 431–449.
Ryles, J. H., and Lieberman, P. (**1982**). ''Fundamental frequency and vowel perception,'' J. Acoust. Soc. Am. **72**, 1631–1634.
Schroeder, M. R. (**1968**). ''Reference signal for signal quality studies,'' J. Acoust. Soc. Am. **44**, 1735–1736.
Scotto Di Carlo, N., and Germain, A. (**1985**). ''A perceptual study of the influence of pitch on the intelligibility of sung vowels,'' Phonetica **42**, 188–197.
Shannon, R. V., Zeng, F. G., Kamath, V., Wygonski, J., and Ekelid, M. (**1995**). ''Speech recognition with primarily temporal cues,'' Science **270**, 303–304.
Souza, P. E., and Turner, C. W. (**1996**). ''Effect of single-channel compression on temporal speech information,'' J. Speech Hear. Res. **39**, 901–911.
Summerfield, Q., Foster, J., Tyler, R., and Bailey, P. (**1985**). ''Influences of formant bandwidth and auditory frequency selectivity on identification of place of articulation in stop consonants,'' Speech Commun. **4**, 213–229.
Summers, V., and Leek, M. R. (**1994**). ''The internal representation of spectral contrast in hearing-impaired listeners,'' J. Acoust. Soc. Am. **95**, 3518–3528.
Turner, C. W., Souza, P. E., and Forget, L. N. (**1995**). ''Use of temporal envelope cues in speech recognition by normal hearing and hearing-impaired listeners,'' J. Acoust. Soc. Am. **97**, 2568–2576.
Van Tasell, D. J., Soli, S. D., Kirby, V. M., and Widen, G. P. (**1987**). ''Speech waveform envelope cues for consonant recognition,'' J. Acoust. Soc. Am. **82**, 1152–1161.
Van Tasell, D. J., Greenfield, D. G., Logemann, J. J., and Nelson, D. A. (**1992**). ''Temporal cues for consonant recognition: Training, talker generalization, and use in evaluation of cochlear implants,'' J. Acoust. Soc. Am. **92**, 1247–1257.
Van Tasell, D. J., and Trine, T. D. (**1996**). ''Effects of single-band syllabic amplitude compression on temporal speech information in nonsense syllables and in sentences,'' J. Speech Hear. Res. **39**, 912–922.
Viemeister, N. F. (**1977**). ''Temporal factors in audition: A system analysis approach,'' in *Psychophysics and Physiology of Hearing*, edited by E. F. Evans and J. P. Wilson (Academic, London), pp. 419–428.
Viemeister, N. F. (**1979**). ''Temporal modulation transfer functions based upon modulation thresholds,'' J. Acoust. Soc. Am. **66**, 1364–1380.

Loudness perception with pulsatile electrical stimulation: The effect of interpulse intervals[a)]

Colette M. McKay and Hugh J. McDermott
The University of Melbourne, Department of Otolaryngology, Parkville 3052, Australia

(Received 23 June 1997; accepted for publication 16 April 1998)

The effect of interpulse intervals on the perception of loudness of biphasic current pulse trains was investigated in eight adult cochlear implantees at three different stimulus levels encompassing the psychophysical dynamic range. Equal-loudness contours and thresholds were obtained for stimuli in which two biphasic pulses were presented in a fixed repetition period (4 and 20 ms), and also for single-pulse/period stimuli with rates varying between 20 and 750 Hz. All stimuli were of 500-ms duration, and the phase durations of each pulse were 100 μs or less. The results of these experiments were consistent with predictions of a three-stage model of loudness perception, consisting of a peripheral refractory effect function, a sliding central integration time window, and a central equal-loudness decision device. Application of the model to the data allowed the estimation of neural refractory characteristics of the subjects' remaining peripheral neural population. The average neural spike probability for a 50-Hz stimulus was predicted to be about 0.77, with an associated neural refractory time of 7.3 ms. These predictions did not vary systematically with level, implying that the effect of increasing current level on loudness results more from recruitment of neurons than from any increase in average spike probability. © *1998 Acoustical Society of America.* [S0001-4966(98)00708-5]

PACS numbers: 43.66.Mk, 43.66.Cb, 43.66.Ts [JWH]

INTRODUCTION

For electrical stimulation of the acoustic nerve, as for acoustic stimulation, the main parameter which controls the resultant loudness percept is the stimulus magnitude. This is controlled in biphasic pulsatile stimulation by the current amplitude or phase duration of the pulses, with loudness being a monotonic function of both these parameters. In this paper, we investigate the more subtle effects on loudness of temporal parameters of the signal, in particular the effects of interpulse intervals (the time between onsets of successive biphasic pulses). The effect of varying interpulse interval is difficult to study as an independent factor, because there are associated covariables such as rate, number of stimulus pulses, or stimulus duration, which may also affect loudness. For pulse trains that utilize a single interpulse interval and fixed stimulus duration, the rate of stimulation and number of stimulus pulses covary. In stimuli with a fixed number of stimulus pulses, the stimulus duration covaries with interpulse interval.

Pfingst *et al.* (1996) have studied the effect of pulse separation (the time between the end of the first waveform and the onset of the next waveform) on thresholds of detection in human implantees, when pulse separation was varied in stimuli of fixed 500-ms duration (with rate and total number of stimulus pulses covarying). They showed that the threshold versus rate function monotonically decreased for shorter pulse durations (500 μs per phase), but was bowl shaped for longer pulse durations (2 ms). This result was consistent with previous data obtained with monkeys or humans (Shannon, 1985, 1989; Pfingst and Morris, 1993; Moon *et al.*, 1993), except for a species difference affecting the pulse separation at which the 2-ms pulse duration curve reached the minimum threshold. Pfingst *et al.* also measured thresholds for stimuli with a fixed number of pulses (2 or 10) with stimulus duration covarying. In this case, the threshold versus pulse separation functions had the same shape as for the fixed-duration stimuli, for each pulse duration used (500 μs and 2 ms). The main difference between the two-pulse, ten-pulse, and 500-ms stimuli was that stimuli with more pulses had lower thresholds, and produced threshold versus pulse separation curves with steeper slopes. The authors concluded that the pulse separation (or interpulse interval) contributed significantly to the shape of the threshold versus rate curves (as opposed to rate *per se*, or number of stimulus pulses). They stated that their results were consistent with the presence of an integrating mechanism which was most effective within about 5 ms, and that, in the case of very long pulse durations, the non-monotonic threshold versus rate functions were consistent with a neural inhibitory mechanism which operated for short time intervals after long-duration pulses. They suggested that this inhibition may be due to an alteration in the ion channel kinetics of auditory neurons, caused by inactivation of sodium channels for several milliseconds following an action potential, or following a long-duration subthreshold pulse.

The above studies indicate that interpulse interval has a significant effect on detection thresholds. There are several mechanisms which may be involved in temporal interactions

[a)]Some of the data in this paper were presented at the 131st meeting of the Acoustical Society of America, Indianapolis, May 1996 [C. M. McKay and H. J. McDermott (1996) ''The effect on pitch and loudness of major interpulse intervals within modulated current pulse trains,'' J. Acoust. Soc. Am. **99**, 2584(A) (1996)], and at the British Society of Audiology short papers meeting, Nottingham, September 1997 [C. M. McKay and H. J. McDermott (1997) ''A loudness model for electrical stimulation: implications for physiological differences among cochlear implantees''].

between pulses, both at the level of individual neurons, and at the level of central processing of multiple neural responses. At the level of individual neurons, an inhibition of responsiveness (refractoriness) will follow an action potential. For electrically stimulated auditory neurons, an action potential is followed by an absolute refractory time of about 1 ms, and a relative refractory time of up to 6–10 ms, in which the probability of eliciting a second action potential is zero or reduced below its normal value (Stypulkowski and van den Honert, 1984; Parkins, 1989). On the other hand, an excitatory effect on an individual neuron may occur if residual charge remains on the neural membrane following a subthreshold pulse. Such an excitatory effect has been demonstrated by Butikofer and Lawrence (1979) in a simulation using the Frankenhauser–Huxley model of neural stimulation. Since residual charge dissipates quickly, however, these excitatory effects are unlikely to be significant for pulse separations more than about 400 μs.

Mechanisms at a more central level, involving multiple neural responses, are also sensitive to interpulse interval duration. Temporal integration is an example of such a mechanism, and is one of four stages in models which have been commonly applied to account for temporal resolution ability in the auditory system (Viemeister, 1979; Buus and Florentine, 1985; Green and Forrest, 1988; Moore *et al.*, 1988; Plack and Moore, 1990, 1991; Oxenham and Moore, 1994). In these models, the first two stages (auditory filter and compressive nonlinearity) represent the processing which occurs in the periphery and cochlea. The third and fourth stages (sliding temporal integrator with an effective window duration of 3–10 ms and decision device) model more central mechanisms, and are thus likely to be applicable without modification to electrical stimulation. Such a four-stage acoustic model was used in a series of experiments measuring detection of increments and decrements of various durations in sinusoidal stimuli (Moore *et al.*, 1993, 1996; Peters *et al.*, 1995). Those authors found that the model parameters which provided the best fit across frequency and level conditions were an integration time window with equivalent rectangular duration (ERD) of about 7 ms, and a decision device which used a criterion of constant integrator output change (on a dB scale) across conditions to detect changes in intensity (Moore *et al.*, 1996).

Viemeister and Wakefield (1991) proposed an additional feature of central processing to explain the longer term temporal effects such as the decrease in threshold that occurs with increasing signal duration up to about 300 ms. In their model of auditory detection, multiple ''looks'' are stored in memory and can be used selectively to facilitate decisions about detection and discrimination. Each ''look'' involves short-term integration, over about 3 ms, of the output of the auditory filters. The time constant of the ''look'' limits temporal resolution (such as gap detection), but improved information can be obtained by combining ''looks'' over much longer time scales (up to about 300 ms) for tasks such as threshold detection.

The purpose of the experiments reported below was to study the effects on loudness perception of interpulse intervals in current pulse trains at threshold and suprathreshold levels. A model of loudness perception will be used to predict the data and infer predicted physiological differences among implantees based on the data. In the first two experiments, equal-loudness relationships were measured for pulse trains containing pairs of biphasic pulses presented at a fixed repetition rate, but with a variable interpulse interval within each pair. In contrast with previous electrical stimulation experiments described above, interpulse interval was the only variable in these stimuli, but there were necessarily two different interpulse intervals (within the pulse pairs, and between the second pulse and the first pulse of the next pair) which covaried over different ranges. With this stimulus pattern, any overall effect on loudness could then be attributed to differences in the effects of interpulse interval over the two covarying interval ranges. In the third experiment, equal-loudness contours were measured for rates of stimulation between 20 and 750 Hz, in order to compare the effect on loudness of interpulse interval alone to the effect for stimuli of differing overall pulse rate.

In this paper, the stimuli used in the three experiments are described first, and a model of loudness perception is proposed which enables the prediction of the effect on loudness of interpulse intervals in electrical stimuli for the three experimental stimulus paradigms. This model incorporates the refractory effects in electrically stimulated peripheral auditory neurons (stage 1), as well as central integration (stage 2), and decision mechanisms (stage 3), the last two stages being similar to those previously postulated from acoustic experiments. The experimental procedures and results are then presented and compared to the model predictions. The model-fitting procedure results in an inferred description of the refractory characteristics of the subjects' peripheral neurons. In addition, information about the spatial and temporal response patterns of each individual implantee's population of residual auditory neurons is deduced by studying the individual differences in the data.

I. STIMULI AND MODEL

A. Stimuli

The stimuli in these experiments were biphasic current pulse trains, with a total duration of 500 ms, delivered in a bipolar or common-ground stimulation mode. The current amplitude was equal for all pulses in each stimulus. Short duration pulses (50–100 μs) were used throughout these experiments, partly because speech processors used with cochlear implants require these short durations to produce rates that can adequately code temporal information extracted from the speech signal. As pulse duration has been shown to affect the refractory and excitatory state of auditory neurons (see above), it is important to note that this factor was held constant in these experiments, and the conclusions drawn later about neural response characteristics will apply only to short-pulse-duration stimuli, such as those used in speech processors.

The test stimuli for experiments 1 and 2 are illustrated in Fig. 1. They consisted of two biphasic pulses which were repeated with a period of 20 ms (experiment 1) or 4 ms (experiment 2). The test interpulse interval was defined as

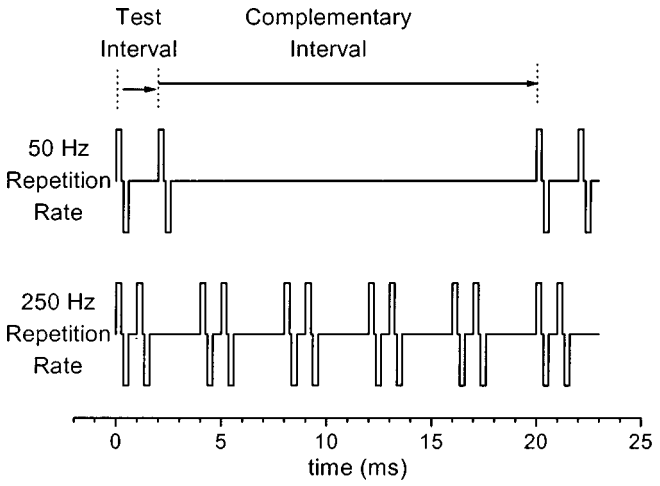

FIG. 1. The test stimuli used in experiments 1 and 2 (23-ms segment). The test interpulse interval was varied between the smallest possible (less than 1 ms) and a maximum of 10 ms for the 50-Hz repetition rate, or 2 ms for the 250-Hz repetition rate. The interphase gap was approximately 43 μs.

the time between the start of the leading phases of the two biphasic pulses, and the complementary (covarying) interpulse interval was the interval between the start of the second pulse and the beginning of the first pulse in the next period. The pulse separation [as defined by Pfingst *et al.* (1996) and described above] can be derived from the interpulse interval by subtracting two phase durations (listed in Table I) and the interphase interval of 43 μs.

The minimum available pulse separation was limited by the fixed data transmission time of the implant (approximately 445 μs). The test interpulse intervals were varied from the minimum (less than 1.0 ms) to a maximum of half the repetition period (10 or 2 ms for experiments 1 and 2, respectively). In addition, pulse trains with a single pulse per period (i.e., a 50-Hz or 250-Hz pulse train) were included. In experiment 3, one-pulse/period pulse trains were also used, with rates between 20 and 750 Hz.

B. The temporal interaction model of loudness

The first stage of our model describes the effects of refractoriness on peripheral neural excitation elicited by the electrical current pulses within a stimulus. This first stage replaces the first two stages of the acoustic models outlined in the Introduction (auditory filter and compressive nonlinearity). The second stage of our model is a sliding temporal integration window, and the third is a central decision device for comparing loudness percepts.

1. Stage 1: Peripheral neural excitation

For the two-pulse stimuli with 20-ms repetition period (experiment 1), we have assumed that the excitation produced by the first of the two biphasic pulses ($E1$) is unaffected by refraction, or other temporal effects, since the no-stimulation period preceding this pulse is always longer than 10 ms. (It follows that the excitation produced by each pulse in the 50-Hz pulse train is also $E1$.) The excitation produced by the second biphasic pulse ($E2$) was assumed to depend on the test interval t, in the following way:

$$E2(t) = E1\left(1 - \frac{R}{1 + e^{(t-T)/0.8}}\right). \quad (1)$$

Here $E2(t)$ is a sigmoid function which was chosen based on the simple assumptions that the activated neurons will have a range of thresholds, leading to a range of spike probabilities and refractory times (since these depend on the signal amplitude relative to the individual thresholds), and that these values are normally distributed. $E2(t)$ has a value close to $E1(1-R)$ for small values of t, rising to a value of $E1$ for large values of t. The parameter R can range from near zero to 1, and can be thought of as the average spike probability for the first pulse for all neurons with thresholds below the stimulus current (and for the second pulse for all such neurons that did not fire on the first pulse). That is, an R near zero would represent a low proportion of available neurons firing on the first pulse, resulting in little decrease of excitation for the second pulse no matter how small the test

TABLE I. Details of subjects who took part in the study. The last two columns list the stimulus parameters used in each experiment. The numbers that describe the electrode specify the two rings comprising the bipolar pair used, or in the case of subjects 6 and 7, the single active ring in common ground mode. The rings of an electrode array are numbered 1 to 22 in the basal-to-apical direction. The sixth column lists the electrical dynamic range of the electrode used, measured using 100-Hz pulse trains with pulse durations as listed for experiment 1.

Subject	Age (yr)	Etiology	Implantation date	Length of profound deafness	Electrical dynamic range for 100 Hz (dB current)	Experiment no.	Pulse duration (μs)	Electrode
1	65	Progressive/genetic	May 1986	30 yr	2.2	1, 3	50	(17,19)
						2	50	(17,19)
2	54	Otosclerosis	October 1990	5 yr	4.3	1	100	(15,19)
						2	70	(16,19)
3	55	Meningitis	September 1990	39 yr	3.0	1, 3	100	(18,20)
						2	50	(18,20)
4	35	Sudden onset/unknown	July 1989	5 months	2.2	1	100	(16,18)
						2	50	(16,18)
5	59	Otosclerosis	February 1992	14 yr	2.7	1, 3	100	(10,12)
6	51	Trauma	November 1988	17 yr	3.1	1, 3	70	20
7	48	Progressive/genetic	January 1987	1 yr	5.5	1	100	15
8	41	Otosclerosis	November 1992	6 yr	3.3	1	70	(18,20)

interval. In contrast, a value of R near 1 would represent a situation where most available neurons fire on the first pulse and are thus in a relative or absolute refractory state for the second pulse, resulting in lower excitation for small test intervals.

The value of T in Eq. (1) specifies the midpoint (in time) of the sigmoid function. It is the average time for which neurons activated on the first pulse remain refractory. Parkins (1989) measured the interspike intervals for 2500-Hz pulse trains in single auditory neurons in squirrel monkeys. He showed that the average time a neuron remains refractory is inversely related to the amount by which the stimulus current exceeds its physiological threshold. The mean interspike times were more than 4 ms for currents within about 1.6 dB of threshold, and reached an asymptote of about 1 ms for currents more than 7 dB above threshold. The standard deviation of refractory times in the population of neurons which responded to the first pulse of our stimulus (which determines the slope of the sigmoid function) was set to 0.8 ms [see Eq. (1)]. Initial analysis of the data showed that goodness-of-fit of the model was insensitive to this parameter within the range 0.5–1.1 ms.

The modeling of relative excitation from the two pulses within the 4-ms repetition period (experiment 2), and for each pulse for the different rates in experiment 3, is more complicated than described above, since, for overall rates exceeding about 100 Hz, every pulse in a stimulus (apart from the first) will be subject to refractory effects. The total effect for any particular pulse will depend on its position within the whole stimulus pulse train. For example, a high-rate pulse train would be expected to produce a large response on the first pulse, followed by a decaying oscillation in response amplitude until a steady-state response occurs [see Javel (1990), Fig. 17.22 for an example]. We will assume for the purpose of our model that the implantee's loudness comparison is based on the steady-state portion of the response. We will also assume that, in the steady part of the response, each stimulus pulse produces the same total excitation which is dependent on the pulse rate (experiment 3), or average pulse rate (experiment 2). Since the range of test interpulse intervals in experiment 2 is small, and the excitation produced by any one pulse will be affected by up to five preceding pulses (occurring within the preceding refractory-time range of about 10 ms), it is expected that the effect of changes to the test interpulse interval on the relative excitation arising from the two pulses will be small, compared to the effect of changing the average interpulse interval (or overall rate).

We will denote the average spike probability for those neurons contributing to the steady-state response to a pulse train of rate r as θ_r. We will assume that the total number of neurons above threshold is dependent only on the current magnitude (and not on the rate). The dependence of total excitation per pulse (E_r) on rate at any particular current can then be expressed as

$$E_r = (\theta_r / \theta_{\mathrm{REF}}) E_{\mathrm{REF}}, \tag{2}$$

where θ_{REF} is the average spike probability and E_{REF} is the total excitation produced by each pulse in the reference stimulus. The ratio of the two spike probabilities was used as a fitting parameter in our model for experiments 2 and 3.

2. Stage 2: Temporal integration window

The relative excitation per pulse given by the refractory model of stage 1 was used as the input to a temporal integrator (stage 2). We have used a sliding, asymmetric, exponential time window $W(t)$, with time constants on each side (τ_1 and τ_2) such that τ_1 is 0.63 times τ_2 [as determined by Oxenham and Moore (1994)], i.e.,

$$\begin{aligned} W(t) &= e^{t/\tau_1}, \quad t<0, \\ W(t) &= e^{-t/\tau_2} \quad t>0, \end{aligned} \tag{3}$$

where t is time (in ms).

The equivalent rectangular duration (ERD), defined as $\tau_1+\tau_2$, was set to 7 ms, based on the parameters found for discrimination of intensity changes in sinusoids by Moore *et al.* (1996). Since this integration most likely occurs more centrally than the acoustic nerve, implantees were assumed to have the same parameters as normally hearing subjects.[1] This assumption may be invalid if the pathology causing deafness in the implantees affected that part of the central auditory pathways which is responsible for the temporal integration. However, our assumption is supported by measurements of temporal resolution in implantees, who have exhibited generally similar performance to that of normally hearing subjects (Shannon, 1993). The suitability of this ERD value for our subjects was supported by initial data fitting procedures in which the ERD was a variable parameter (see Sec. III).

3. Stage 3: Equal-loudness decision criterion

The third stage of our model is analogous to the fourth stage of Moore *et al.*'s (1996) model of intensity discrimination, in which a fixed ratio change of output from the integrator was used as a criterion for detection of intensity change. In our model, a decision of equal loudness is based upon a criterion of equal output from the integrator of stage 2 (or a difference less than that used for detection of intensity difference). Since the stimuli used in our experiment had a fixed duration, we assumed that the longer-term temporal integration (which causes the threshold of stimuli to decrease with increasing stimulus duration up to about 300 ms) would not affect our data. That is, we have assumed that if the output of the short-term integration time window is equal for two stimuli, then the total loudness will be equal after applying the processing of the longer integration time window. The validity of this assumption, as assessed by the results of this study, will be discussed below.

The first two stages of our model predict how the output of the integrator changes when interpulse interval changes, given an invariant stimulus current. For experiments 1 and 2, the ratio change of integrator output (expressed in dB) was calculated for the two-pulse/period stimuli versus the one-pulse/period stimulus, as a function of test interpulse interval. Some examples of these model predictions are shown in

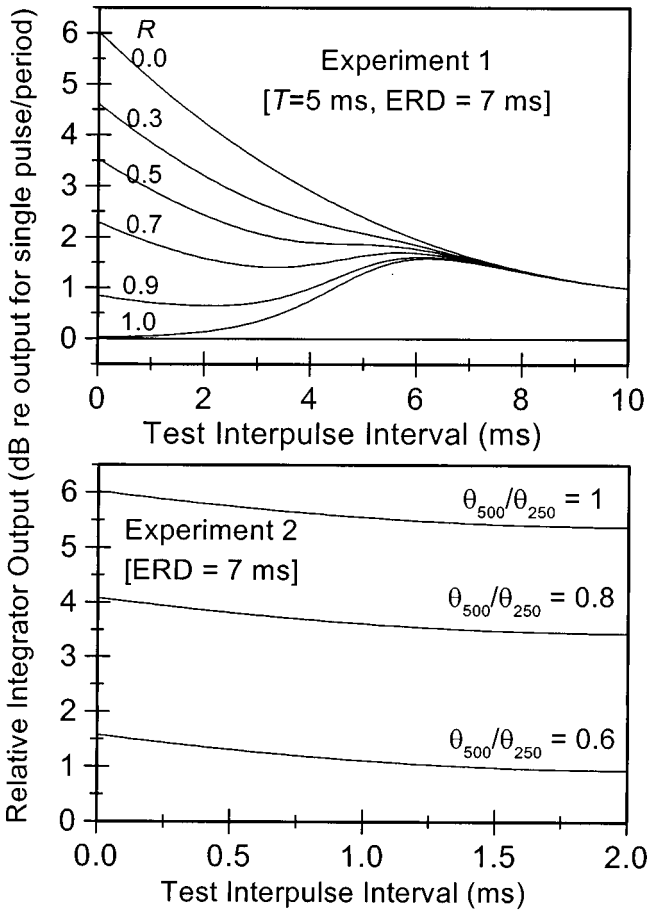

FIG. 2. Some examples of the predicted effect of test interpulse interval on the temporal integration window output for the two-pulse/period stimuli (dB *re*: the output for single-pulse/period stimuli) for 20-ms repetition period (top panel), and 4-ms period (bottom panel). The separate lines show the effect of changing R (top panel) and the ratio $\theta_{500}/\theta_{250}$ (bottom panel), while the other parameters are kept constant as shown.

Fig. 2, where the predicted effects of changing the parameter R in experiment 1, and the ratio $\theta_{500}/\theta_{250}$ in experiment 2, are illustrated.

II. METHODS

A. Subjects and hardware

Eight adult subjects participated in this study, all users of the Mini System 22 implant, manufactured by Cochlear Ltd. All are postlinguistically profoundly deaf, and had no useful hearing before implantation. Details concerning their etiology, length of profound deafness, and implant experience are given in Table I.

The Mini System 22 cochlear implant consists of an intracochlear array of 22 active electrodes, spaced at intervals of 0.75 mm, which are activated by an implanted receiver–stimulator. The receiver–stimulator receives digitally encoded signals from a speech processor via a transcutaneous inductive link. In these experiments the speech processor was interfaced with an IBM-compatible personal computer which, with specifically designed software, was used to control the parameters of stimuli in each experiment and to record the subject's responses. Stimulation current is controlled in this implant in discrete steps, and the current produced at each step was determined from the calibration data obtained from the manufacturer for each subject's implant.

The electrodes used, and their dynamic range for 100-Hz pulse trains, are listed in Table I, along with the pulse durations used. The spatial extent (distance between the component rings of the bipolar pair) was chosen for each subject in each experiment based upon the minimum needed to achieve comfortable loudness without excessive currents. Two subjects used common ground mode.[2]

B. Experimental procedures

1. Experiment 1: 20-ms repetition period

The effect on loudness of varying the interpulse intervals between the pairs of pulses in stimuli with a 50-Hz repetition rate (see Fig. 1) was measured by balancing the loudness of each test stimulus with that of a fixed reference stimulus. The reference stimulus was the two-pulse/period stimulus with the smallest interpulse interval for each subject. This reference was chosen to minimize the perceptual differences (apart from loudness) between the pairs of stimuli being loudness balanced, as any other differences (such as pitch or timbre) could introduce a loudness bias. A 50-Hz pulse train was also balanced with the same reference stimulus. The loudness-balance procedure was conducted at two current levels: first with the reference stimulus at a comfortably loud level, and second with the reference set to half the number of current steps above threshold current compared to the first reference level. Third, the threshold currents for all stimuli were measured using a modified Hughson–Westlake adaptive procedure (Carhart and Jerger, 1959).

The loudness balance procedure was a two-interval forced-choice adaptive procedure, whereby the reference and test stimuli were presented in random order, and the subject was asked whether the first or second stimulus was louder. The current of the test stimulus was initially set so as to produce a percept clearly louder than that of the reference (usually several current steps). The current was then adjusted up or down by one current step (approx. 0.12 dB) whenever the test stimulus was considered softer or louder, respectively, in at least two out of three consecutive trials (see entry 8 in Table I in Levitt, 1971). The procedure continued until 11 turning points were obtained and the last 8 of these were averaged. To overcome potential bias due to the initial loudness or to which stimulus was being adjusted, the procedure was repeated with the two stimuli interchanged (i.e., adjusting the current of the reference stimulus to match the loudness of the test stimulus). In this case, the test stimulus current was set at the previously found equal-loudness current, and the current of the reference stimulus was initially adjusted to produce a loudness greater than that of the test stimulus. Thus two estimates were obtained of the test-stimulus current required for loudness equal to that of the reference stimulus, with the test stimulus starting from above and below the loudness of the reference.

For purposes of comparison with the model predictions, the current reductions (in dB) of the two-pulse/period stimuli

compared to the current of the equally loud one-pulse/period stimulus were calculated by subtracting the average current value for the equally loud one-pulse/period stimulus from each of the current values for the two-pulse/period stimuli.

2. Experiment 2: 4-ms repetition period

The adaptive loudness balancing procedure described above was used to equalize the loudness for pairs of biphasic pulses with 4-ms repetition period, and test interpulse intervals of up to 2 ms. In this experiment, the reference stimulus was selected to be the 250-Hz pulse train. This choice of reference stimulus allowed the reduction in current for the two-pulse/period stimuli compared to the equally loud one-pulse/period stimulus to be obtained directly, and was made possible by the smaller pitch or timbre differences among the stimuli. Subjects 1–4 participated in this experiment, and the equal-loudness relationship was measured at the comfortably loud level only.

3. Experiment 3: Equal loudness for different rates

The equal-loudness relationship for different rates of stimulation between 20 and 750 Hz were obtained at a comfortably loud level for subjects 1, 3, 5, and 6. Each stimulus was loudness balanced with the 50-Hz stimulus. In this case, the loudness balance was obtained using a method of adjustment. The test and reference (50 Hz) stimuli were presented alternating continuously, separated by 500-ms silent intervals, and the subject altered the current of the test stimulus with an unmarked knob, until the loudness was judged equal to that of the reference. An average result of four balances was calculated (two with the reference fixed, and two with the reference adjusted, with the adjustable stimulus always started at a level perceptibly softer than the fixed). This loudness-balance procedure was chosen because it was more time efficient, and the balanced current differences were expected to be larger than in the previous two experiments, thus not needing the greater measurement precision of the adaptive method. Thresholds for all stimuli were obtained as in experiment 1. The reduction of current for the test stimulus relative to that of the equally loud 50-Hz stimulus (in dB) was then calculated.

C. Comparison of experimental data with model predictions

1. Current-to-excitation transformation

In order to quantitatively relate the experimental results to the model output, it is necessary to adopt a transformation between the change in stimulus current and the change in neural excitation. However, the precise nature of the relationship between current and neural excitation is unknown, and it may also be subject, electrode, or level dependent. As a first approximation, we have assumed that the excitation produced by a current pulse can be described by a simple power function of current, with exponent S, at least over the small current range used to balance the loudness in each experiment. In other words, the change in integrator output (in dB) resulting from a current change Δi (in dB) was assumed to be $S\,\Delta i$. This scaling factor was assumed to be constant over small changes of current, and to be stimulus independent, but was allowed to be subject and level dependent.

The model predictions, when divided by S, therefore predict the current increase which would have elicited the same increase in excitation as the change in stimulus type (from one- to two-pulse/period, or 50 Hz to a different rate) while keeping current constant. This is equal to the *reduction* in current (relative to the reference stimulus current) required to reduce the excitation of the test stimulus to a value equal to that of the reference stimulus (as measured in the experiments).

2. Model-fitting procedure

For experiment 1, the prediction for the current increase which would produce the same increase in excitation as the change from one- to two-pulse/period stimuli was fitted to the experimentally measured reduction in current for the two-pulse/period stimuli (relative to the reference stimulus current), to make it equal in loudness to the one-pulse/period stimulus (see above).

The fitting procedure was an iterative χ^2 minimization procedure based on the Levenberg–Marquardt algorithm (Marquardt, 1963). Three fitting parameters were used: R, T, and S. As mentioned above, the integration time window was assumed to have an ERD of 7 ms. Initially, however, fitting was attempted with ERD as a free fourth parameter (but constrained to be equal across the three stimulus levels for each subject) to investigate whether the data were consistent with this 7-ms value. In five out of the eight subjects, the dependence of ERD on the value of at least one other parameter was too great to obtain a valid estimate of ERD. The results for the other three subjects gave estimates for ERD which were generally consistent with the 7-ms value. The ERDs (in ms) and their standard errors were: for $S4$, ERD$=7.5(1.3)$; for $S6$, ERD$=5.3(0.7)$; for $S7$, ERD $=6.8(0.5)$. Based on these results, and their consistency with our initial assumptions about the integration time window, the ERD was fixed at 7 ms for all subjects and stimuli.

In experiment 2, the current-to-excitation exponent, S, which was obtained in the fitting procedure for experiment 1 for each subject at comfortable loudness, was reused. Thus there was a single fitting parameter, $\theta_{500}/\theta_{250}$, used to fit the model predictions to the data.

In experiment 3, S was also constrained to be equal to the values for comfortably loud and threshold stimuli derived by the fitting procedure for experiment 1. The fitting parameter in this case was the ratio θ_r/θ_{50}.

III. RESULTS

A. Experiment 1: 20-ms repetition period

The results of experiment 1 for the eight subjects are shown in Fig. 3, where the reductions in current for the two-pulse/period stimuli (in dB relative to that of the equally loud one-pulse/period stimulus) are plotted against the test interpulse interval for comfortably loud, mid-intensity, and threshold stimuli. It can be seen from the figure that the repeated loudness balancing results at comfortably loud and

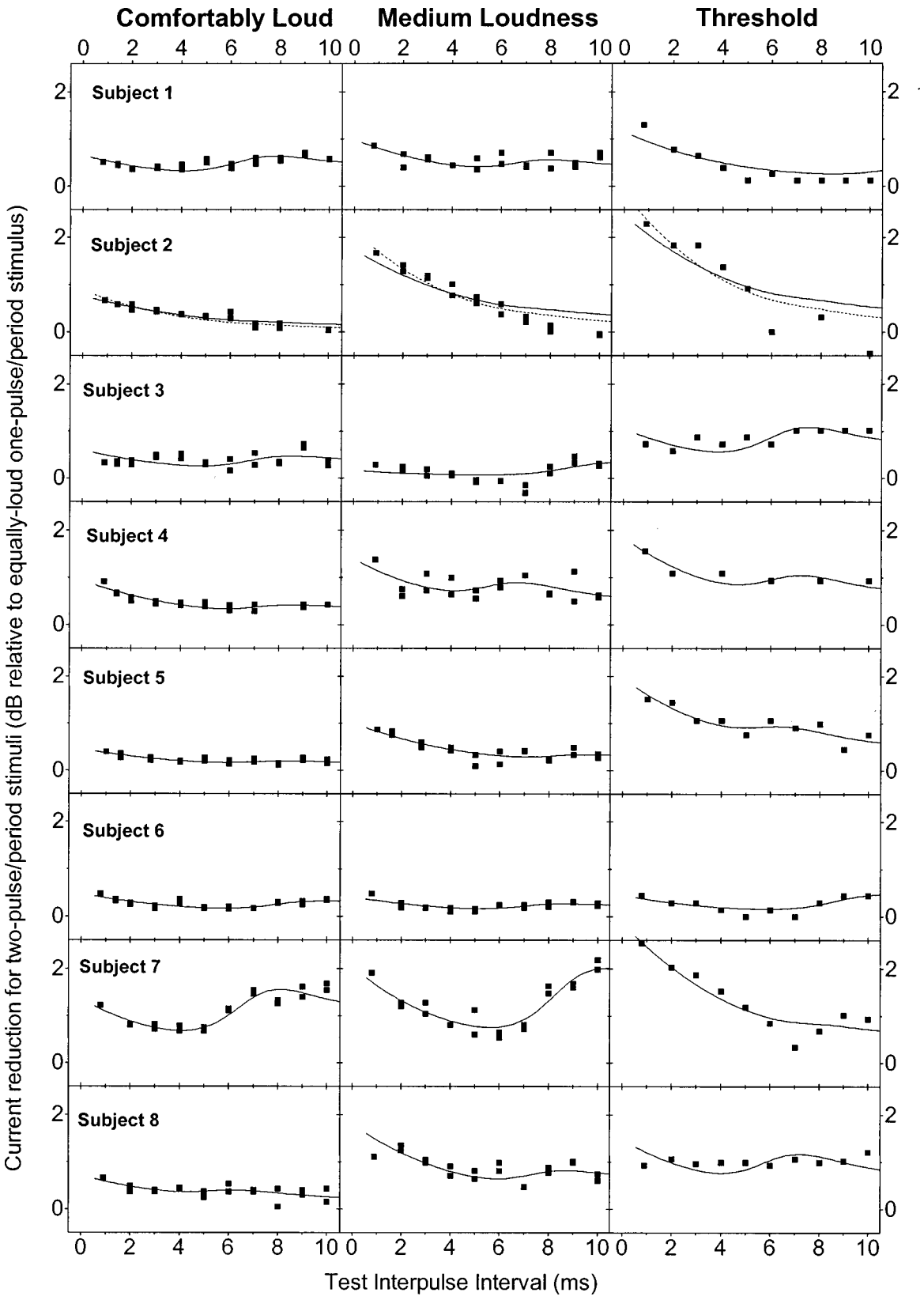

FIG. 3. The threshold and loudness balancing results for different test interpulse intervals in experiment 1, with the best-fit model predictions. Each row contains the data for one subject, and each column the data for each stimulus level. The vertical axes show the current reduction required to make each two-pulse/period stimulus equal in loudness to the one-pulse/period stimulus. The horizontal axes represent the test interpulse interval (see Fig. 1). The pair of symbols at each interpulse interval in the comfortably loud and medium loudness panels show the two loudness balance results (see text). The solid lines represent the best-fit model predictions, using an ERD of 7 ms and the parameter values shown in Table II. The dotted lines for subject 2 represent predictions with a smaller ERD (5.5 ms).

TABLE II. The values of the fitted parameters S, R, and T which gave the best predictions of the data, for each of the eight subjects at the three levels tested. All fitted functions were with a time-window ERD of 7 ms, with the exception of the second set of values for subject 2, where 5.5 ms was used. Asterisks denote the values which were fixed to avoid high dependency among parameters (see text).

Subject	Comfortably loud level fitted parameters (standard errors)	Mid-dynamic range level fitted parameters (standard errors)	Threshold fitted parameters (standard errors)
1	$S=1.85$ (0.17) $R=0.85$ (0.2) $T=6.7$ (0.3) ms	$S=2.05$ (0.3) $R=0.74$ (0.4) $T=7.0$ (0.5) ms	$S=1.41$ (0.18) $*R=0.795$ $T=12$ (5) ms
2	$S=6.1$ (0.9) $*R=0.3$ $*T=7.3$ ms	$S=2.6$ (0.2) $*R=0.3$ $*T=7.3$ ms	$S=1.9$ (0.15) $*R=0.3$ $*T=7.3$ ms
2 ERD=5.5 ms	$S=5.3$ (0.7) $*R=0.3$ $*T=7.3$ ms	$S=2.4$ (0.2) $*R=0.3$ $*T=7.3$ ms	$S=1.7$ (0.1) $*R=0.3$ $*T=7.3$ ms
3	$S=2.3$ (0.4) $R=0.83$ (0.04) $T=7.3$ (0.7) ms	$S=2.6$ (1.0) $R=0.95$ (0.05) $T=9.2$ (1.7) ms	$S=1.15$ (0.12) $R=0.85$ (0.2) $T=8.4$ (0.4) ms
4	$S=2.5$ (0.6) $R=0.69$ (0.08) $T=7.6$ (1.0) ms	$S=1.59$ (0.12) $R=0.71$ (0.03) $T=5.9$ (0.4) ms	$S=1.23$ (0.17) $R=0.70$ (0.05) $T=6.4$ (0.6) ms
5	$S=5.3$ (1.8) $R=0.68$ (0.11) $T=7.5$ (1.3) ms	$S=2.8$ (0.8) $R=0.62$ (0.11) $T=8.5$ (1.1) ms	$S=1.59$ (0.12) $R=0.70$ (0.05) $T=6.4$ (0.6) ms
6	$S=2.9$ (0.5) $R=0.83$ (0.2) $T=8.4$ (0.7) ms	$S=3.8$ (0.6) $R=0.80$ (0.03) $T=7.5$ (0.5) ms	$S=1.85$ (0.5) $R=0.90$ (0.03) $T=5.9$ (0.7) ms
7	$S=0.73$ (0.04) $R=0.88$ (0.01) $T=6.9$ (0.2) ms	$S=0.45$ (0.04) $R=0.89$ (0.01) $T=8.7$ (0.3) ms	$S=1.4$ (0.3) $R=0.40$ (0.15) $*T=7.8$ ms
8	$S=3.85$ (0.7) $R=0.63$ (0.10) $T=5.6$ (1.1) ms	$S=1.27$ (0.15) $R=0.70$ (0.04) $T=7.7$ (0.5) ms	$S=1.12$ (0.12) $R=0.79$ (0.03) $T=6.2$ (0.4) ms

mid-intensity levels were generally within 0.1 dB. Also shown in this figure are the best-fit predictions of the model to these data.

Table II contains the values of the parameters and their confidence limits for the model predictions plotted in Fig. 3. Using the three free parameters R, T, and S, 19 out of the 24 sets of data were successfully fitted with the fitting algorithm without excessive parameter dependence leading to uncertainty about parameter values. Threshold data for subjects 1 and 7, and all three sets of data for subject 2, required at least one of the three parameters to be fixed in order to reduce the parameter dependence. These fixed parameter values were chosen based on the analysis of the remaining data described below, and are marked with an asterisk in Table II.

The 19 sets of data which were successfully fitted with three free parameters were used to investigate the relationships between the parameter values and intensity level. One-way analysis of variance showed that level did not significantly affect R for the five subjects where R was derived for all three levels ($p=0.91$). In addition, paired t tests showed no effect of level on R between comfortably loud and mid-level stimuli for seven subjects ($p=0.93$), and between mid-level and threshold ($p=0.89$) or comfortably loud and threshold stimuli ($p=0.53$) for five subjects. The mean (and standard deviation) of the 19 estimates of R was 0.77 (0.11).

One-way analysis of variance showed that level also did not significantly affect T for the five subjects where T was derived for all three levels ($p=0.47$). Similarly, paired t tests showed no effect of level on T between comfortably loud and mid-level stimuli for seven subjects ($p=0.29$), and between mid-level and threshold ($p=0.33$) or comfortably loud and threshold stimuli ($p=0.37$) for five subjects. The mean (and standard deviation) of the 19 estimates of T was 7.3 (1.1) ms.

One-way analysis of variance showed that level did significantly affect S for the five subjects where S was derived for all three levels ($p=0.02$). Paired t tests for these subjects showed a significant difference in S between comfortably loud and threshold stimuli ($p=0.02$) and between mid-level and threshold stimuli ($p=0.04$), although the difference between comfortably loud and mid-level stimuli did not reach significance for a paired t test with seven subjects ($p=0.24$). The means and standard deviations for S for the five subjects where all three levels were analyzed were: at threshold 1.4 (0.1); at mid-level 2.4 (1.0); and at comfortably loud level 3.3 (1.5).

The above analysis was used to fix various parameters in the five remaining sets of data, in order to obtain the best fit that was consistent with the other data sets. In the case of the threshold data for subjects 1 and 7, initial fitting with all three parameters produced a situation where S was highly dependent on R (and *vice versa*). Based on the insignificant effect of level on R and T values seen in the other subjects, best fits were obtained first with the R value set to the average of the other two R values at the higher levels, and then with the T value similarly fixed. The best outcome of these two fitting procedures is shown in Fig. 3, and the parameters used are in Table II. For subject 1, the best-fitting option was with R fixed, and for subject 7 with T fixed.

Subject 2's data were more difficult to fit, as the initial fitting with all three parameters resulted in S being highly dependent on R for all three stimulus levels. This was due to the monotonic exponential shape of the data. It can be seen from Fig. 2 that this shape is consistent with a low value of R, where refractory effects are likely to have only a small influence. All values of R below about 0.3 produced an equally good fit (with S covarying with the R value). Given that the R values for other subjects were all greater than 0.6 (with one exception), subject 2's R value was set to 0.3, which was the maximum value that produced a reasonable fit. Since T had a very insignificant effect on the model prediction for this R value, it was set to the average (7.3 ms) found for the 19 well-fitted sets of data. It can be seen from Fig. 3 that the model predictions for these values (solid lines) fail to predict the data shape for long interpulse intervals. To improve the model predictions at longer interpulse intervals, it was necessary to narrow the integration time window. The fitting procedure described above for subject 2 was repeated at successively smaller ERDs and the χ^2 values compared. It was found that ERD values within 0.5 ms of 5.5 ms provided the best model predictions. The dotted lines in Fig. 3 show the predictions for an ERD of 5.5 ms for subject 2.

B. Experiment 2: 4-ms repetition period

The results of experiment 2 are shown for subjects 1–4 in Fig. 4, where the reductions in current for the two-pulse/period stimuli (in dB relative to that of the equally loud one-pulse/period stimulus) are plotted against the test interpulse interval. Also shown in this figure are the best-fit predictions of the model for these data. The values of S which were derived from experiment 1 at comfortable loudness were used to make the model predictions. The only fitting parameter was the ratio $\theta_{500}/\theta_{250}$. It should be noted that this parameter influences the vertical position of the predicted curve and not its slope, the latter being determined by S and the ERD of the time window. The two fitted lines for subject 2 correspond to the two ERD values used for this subject in experiment 1. It can be seen in Fig. 4 that the slopes of the predicted curves match the slopes of the data fairly well, thus lending support to the S values obtained from experiment 1. The smaller ERD value of 5.5 ms for subject 2 improved the fit of the slope for these data, as it did in experiment 1. The values of the ratio $\theta_{500}/\theta_{250}$ (and the standard errors) for subjects 1–4 respectively were 0.671 (0.003); 0.69 (0.1); 0.568 (0.003); and 0.655 (0.006). The use

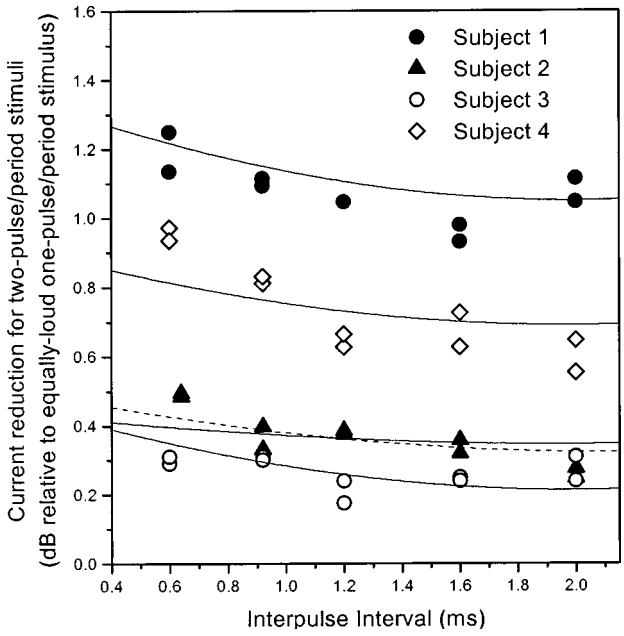

FIG. 4. The current reduction required to make the two-pulse/period stimuli equal in loudness to the one-pulse/period stimulus in experiment 2, along with the best-fit model predictions. As in Fig. 3, the two results for each interpulse interval are represented separately, and the dotted line for subject 2 represents the prediction for ERD=5.5 ms.

of a smaller ERD for subject 2 did not produce a significantly different ratio [0.682 (0.006)]. Thus, for all four subjects, the model predicted that doubling the overall rate from 250 to 500 Hz would lead to a drop in the average spike probability by a factor of approximately $\frac{2}{3}$.

C. Experiment 3: Equal loudness for different rates

The results of experiment 3 are shown in Fig. 5 for subjects 1, 3, 5, and 6, where the current reduction relative to the current for the equally loud 50-Hz stimulus is shown for rates from 20 to 750 Hz. It can be seen that, as rate increased, there was a monotonic increase in the current reduction required to maintain equal loudness. The threshold data are in accordance with previous published results for short duration pulses as described in the Introduction. The comfortably loud data show a similar increase in current reduction for increasing rate, but the magnitude of the effect is smaller than that for threshold, leading to a steadily increasing dynamic range.

Unlike the stimuli in the first two experiments, the total number of stimulus pulses in experiment 3 covaried with interpulse interval for the different rates. The model predicts that there will be two opposing influences on integrator output as rate increases: there will be an increasing number of pulses within the integration window; and there will be a decrease in excitation per pulse caused by a falling spike probability (as seen in experiment 2).

The effect of the increasing number of pulses in the integration time window was first calculated (i.e., keeping spike probability constant). The lines in Fig. 5 show the predicted current reduction due to this effect alone, using an ERD of 7 ms and the values of S derived in experiment 1 for comfortably loud and threshold stimuli. The model predicts

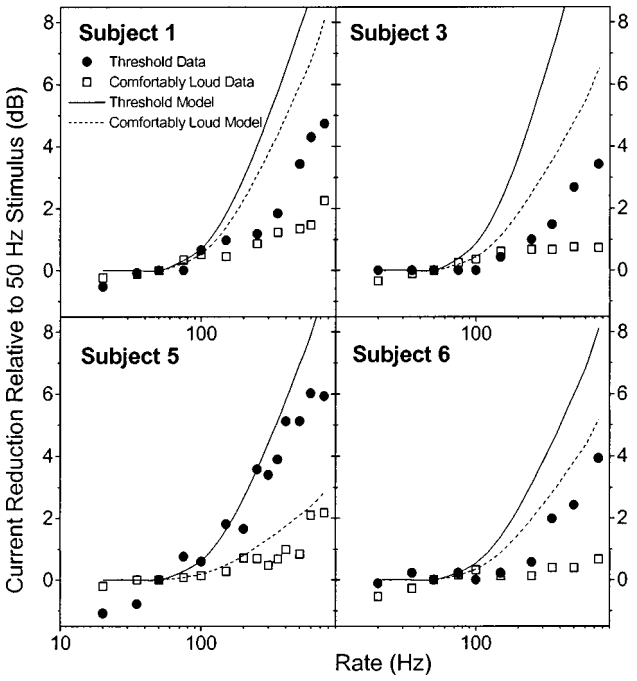

FIG. 5. The loudness balancing results at comfortable loudness and thresholds for stimuli with different rates in Experiment 3. The current reduction relative to the threshold or reference current for the equally loud 50-Hz stimulus is shown, along with the model predictions for the effect of the integration time-window without refractory effects.

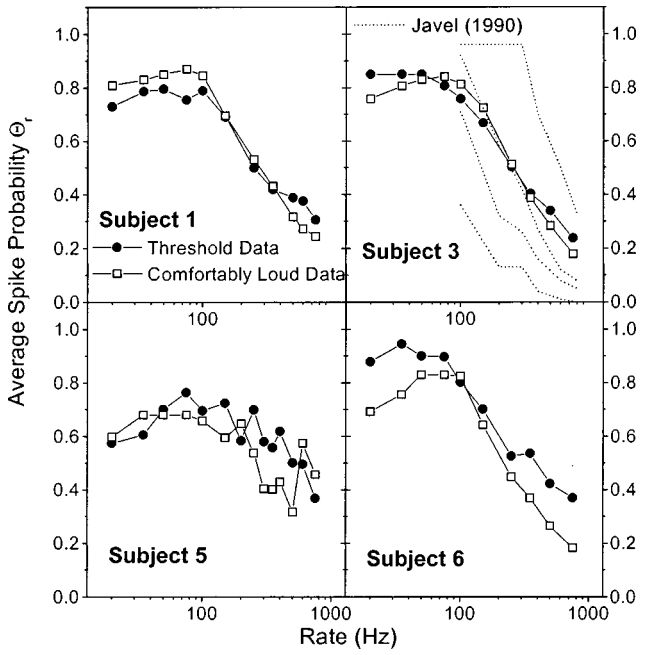

FIG. 6. The predicted effect of rate on θ_r derived from Fig. 5, assuming that the vertical distances between the data and the corresponding line in that figure are due to a reduction in average spike probability, and that θ_{50} is equal to the R value (at threshold or comfortable loudness) determined in experiment 1 (Table II). The four dotted lines in the second panel show the spike probability versus rate functions extrapolated from Fig. 17.21 in Javel (1990), for a single neuron at four different current levels: 51, 51.5, 52, and 54 dB (*re:* 1 μA).

that the actual reduction in current should be less than that given by these lines by an amount given by $(20/S)\log(\theta_r/\theta_{50})$.

The ratios θ_r/θ_{50} were calculated from the vertical distance between each data point and the corresponding curve in Fig. 5. These were then multiplied by the subject's R values (equal to θ_{50}), determined from experiment 1, to create the derived functions of θ_r seen in Fig. 6.

Since θ_r was an arbitrary rate-dependent fitting parameter, which would allow a perfect fit to any data of current adjustment versus rate, the plausibility of our model then rests with the appropriateness of the derived functions of θ_r as descriptions of the averaged spike probabilities across auditory neurons. Javel (1990) measured the spike probability versus intensity for a single auditory neuron in a cat at different stimulation rates. The spike probability versus rate data, interpolated from his Fig. 17.21 for four fixed intensities within about 3 dB of the neuron's threshold of activation, are plotted in Fig. 6, in the same panel as subject 3's data. The behavior of the predicted average spike probability is consistent with these data, given that it represents an average over many neurons all at different levels in their dynamic range. The proportion of neurons that are activated at saturation probability would, in general, make the slope of the average data less steep than for a single neuron near threshold.

There are two further points of interest in the derived average spike probability versus rate functions. First, they predict that spike probability is essentially unaffected by stimulus rates less than 100 Hz, which is consistent with the absence of refractory changes for time intervals longer than about 10 ms. (In some cases, there is a slight drop in derived spike probability below 50 Hz, which will be considered below.) Second, the curves for threshold and comfortably loud levels are similar, implying that the effect of rate on average spike probability is largely independent of stimulation level.

IV. DISCUSSION

The results of experiment 1 have shown that the effect of changing the test interpulse interval within pairs of pulses having a 20-ms repetition period could be successfully accounted for by a model which considered both the effects of refractoriness on the second of the two pulses,[3] and a sliding central integration window with ERD of 7 ms. The application of the model to the experimental results allowed the individual specification of the ''average'' refractory characteristics (R and T), and the transformation between current change and neural excitation change (given by the exponent S). In experiments 2 and 3, the effects of refractoriness were modeled as a reduction of spike probability with increasing rate. The application of the model, using the values of S which were derived in experiment 1, provided good predictions for the results of experiments 2 and 3, and led to a plausible prediction of how spike probability changes with rate. Thus, the model was able to consistently describe the effect of interpulse intervals on loudness for three different stimulus structures.

As mentioned in the Introduction, refractoriness is only one of several factors that can affect the amount of excitation from a pulse which is preceded by another pulse. For stimuli which use very long pulse durations (over 1 ms), there ap-

pears to be an additional inhibitory mechanism which operates after subthreshold pulses, and, for pulses separated by less than 400 μs, there is possibly an excitatory mechanism whereby charge can be integrated on the neural membrane across more than one pulse to achieve a response spike. If either of these stimulus conditions are present (on a single electrode), then these effects would have to be incorporated into the function which describes the excitation for the second pulse compared to that for the first pulse [Eq. (1)]. For the stimuli used in these experiments, and for stimuli typically produced by existing speech processors, these conditions are not expected to arise, and a model based on refractoriness alone is sufficient to describe the peripheral temporal effects.

A. Average peripheral refractory characteristics

If the model assumptions about peripheral neural refractory behavior and the subsequent process of neural spike integration are valid, then it is possible to make inferences from the data about the refractory behavior of the activated neural population of individual subjects who took part in the experiment. Single-neuron spike probabilities are determined by the magnitude of the stimulus current relative to the neural threshold until saturation occurs. Similarly, the value of R is determined by the magnitude of the stimulus current compared to the distribution of neural thresholds that are lower than that current. The R values from experiment 1 (for 19 sets of data) had a mean value of 0.77, and ranged from 0.4–0.9 (although subject 2 may have had values lower than this range). The fact that, on average, R remained constant across the subjects' dynamic ranges implies that, as current increased, and neurons activated at the lower current moved towards a higher or saturated spike probability, the average spike probability remained relatively constant due to other neurons, with higher thresholds, being activated at lower spike probabilities. Thus, for the ''average'' subject, the increase in total excitation per pulse arising from an increase in current is due mostly to an increase in the number of neurons activated, rather than any increase in the average spike probability across those neurons.

The T values (the mean time that neurons which fired on the first pulse remained refractory) depend in a similar fashion on the relative magnitude of the stimulus current compared to the distribution of neural thresholds that are lower than that current. It is not surprising, then, that the mean value of T (7.3 ms) was also not significantly affected by stimulus level. The interspike interval versus ''neural sensation level'' data for single neurons measured by Parkins (1989) indicate that a refractory time of 7.3 ms would be expected for a neuron activated less than 1 dB above its threshold. Thus, the average spike probability and interspike interval data obtained in these experiments support the hypothesis that, as current increases, significant numbers of additional neurons are recruited, leading to large proportions of neurons being activated close to their thresholds, regardless of the stimulus current.

The rate of recruitment of neurons with level is likely to be different for each subject, depending on the local density and type of neural fibers surrounding the stimulation site.

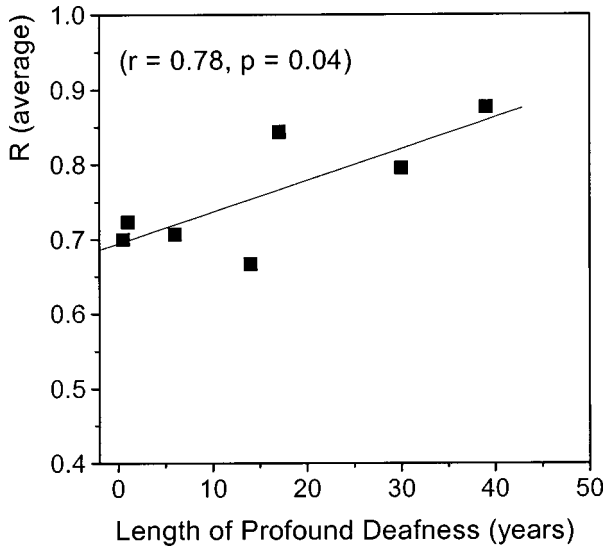

FIG. 7. The relationship of R determined in experiment 1 (averaged over the three levels) to the length of profound deafness prior to implantation, for the seven subjects where R values were uniquely determined. The correlation and statistical significance (r and p) are shown in the panel.

This would lead to individual differences in the way R and T vary with level. For example, subject 7 had a large increase in R (0.4 to 0.9) between threshold and mid-dynamic-range (see Table II). This could be due to a lower density of neural fibers at sites more distant from the stimulation site, so that at higher currents there were not enough neurons being recruited to maintain a low average spike probability.

It is possible that the different average spike probabilities among subjects may reflect the overall density of surviving neural fibers. A subject with a very sparse population of nerve fibers may have a slow rate of recruitment of additional fibers as the current is increased, and this would lead to a higher average spike probability than a subject with a dense population of available nerve fibers. One factor which may affect the density of surviving nerve fibers is the length of profound deafness. For our subjects there was a significant relationship between the R values (averaged across the three levels) and the length of profound deafness before implantation. Figure 7 shows the average spike probabilities and lengths of profound deafness for seven subjects along with the results of linear regression analysis ($r=0.78$, $p=0.04$). (Subject 2 was omitted, as no definite R predictions were obtained for him.) This result supports the proposition that there is a loss of neural density over time in the absence of auditory stimulation, and that this leads to higher average spike probability among the stimulated fibers. Another factor which may influence the density of surviving nerve fibers is the etiology of deafness. Three of the subjects (2, 5, and 8) had a partially conductive deafness (due to otosclerosis), and so may have more surviving nerve fibers than those whose deafness was wholly sensorineural. These three subjects had three out of the four lowest average R values (assuming that subject 2 had a value below 0.65).

In summary, then, the results of the experiments suggest that average spike probability does not change much with level of stimulation, but that there are differences in spike

probabilities among the subjects which are consistent with varying degrees of neural survival.

B. The current-to-excitation transformation

To fit the data from experiment 1 with the model, the scaling factor applied to the current adjustment to transform it into neural excitation units needed to be significantly larger for higher levels of stimulation than that needed at threshold. Given the assumptions of the model, this result suggests that a single simple power function is not appropriate to describe the current-to-excitation transformation over the entire dynamic range. In contrast, the data imply that a ratio current change will cause a larger ratio increase in neural excitation at higher stimulus levels compared to lower levels.

The same conclusion was reached by Nelson *et al.* (1996), who studied the effect of electrical stimulus level on intensity discrimination. They found that, for most subjects, Weber fractions decreased as a power function of intensity (I) relative to absolute threshold. When the electrical intensity was normalized between subjects by using ''percent of the dynamic range'' on a dB scale (%DR), the slope of the Weber function (averaged across seven subjects) was -0.08 dB/%DR, i.e.,

$$Wf_{\mathrm{dB}} = 10 \log (\Delta I/I) = -0.08\{\%\mathrm{DR}\} + 10 \log (\beta). \qquad (4)$$

The 10 log (β) term in the above equation represents the subject's overall sensitivity to intensity change. They interpreted their data as suggesting that the effects of current on neural excitation increased with increasing level. This interpretation was based on the assumption that the central decision device for intensity increment was similar to that in acoustic hearing, and involved a level-invariant criterion based on a set neural excitation ratio increment. It is possible to derive how our scaling factors (of current to neural excitation on log scales) would have changed with level for their seven subjects to produce the relationship in Eq. (4). The derived scaling factors for different points in the dynamic range (as a ratio of the threshold factor) are shown in Fig. 8, along with the ratios from our experiment. The loudness that our subjects called ''comfortably loud'' would probably have been considerably lower than the ''maximum acceptable loudness'' measured by Nelson *et al.*, so we have denoted our data by arrows encompassing 70%–90%DR for ''comfortably loud'' and 35%–45%DR for the ''medium level.'' It can be seen that our results are broadly consistent with, although somewhat lower than, the values derived from the Nelson *et al.* paper. The difference may be due to the considerable variability in both subject groups.

Nelson *et al.* proposed a simple qualitative model in which the relative increase in excitation for higher currents is caused by the stimulation activating peripheral neural processes near threshold, and more distant axonal processes at higher levels. The (presumably) less dense residual peripheral processes would need a larger current increment to recruit more neurons, and have a less steep rate-intensity function, compared to the more dense axonal processes, which would need a smaller current increment to recruit the same number of neurons, and where there is a steeper rate-intensity function. This model is partially consistent with our

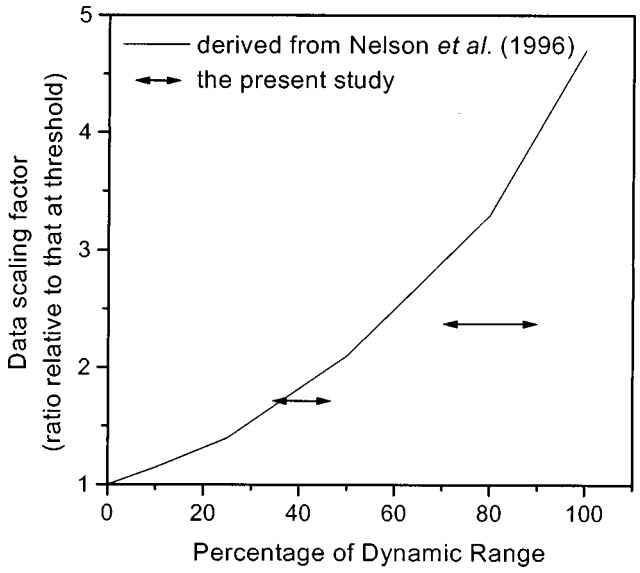

FIG. 8. The change in the power exponent (S) of the current-to-excitation transformation (ratio relative to that at threshold) versus level within the dynamic range, derived from the data presented in Nelson *et al.* (1996) from seven subjects (solid line), along with the ratios of scaling factors (averaged over five subjects) from our experiment 1 (arrows encompassing the most likely regions of the dynamic range for medium and comfortably loud levels).

data. However, we propose that, in the ''average'' subject, the increase in relative excitation at higher levels is due more to increases in the number of neurons activated than any increase in the average spike probability.

In the individual implantee, however, there is a role for both factors in explaining the different patterns of loudness growth. Our subject 5 showed a very large increase in scaling factor between threshold (1.6) and comfortably loud (5.3) (see Table II), indicating a large increase in relative effect of current on excitation. At the same time, the average spike probability changed very little between threshold and comfortably loud levels, indicating that the increase in excitation was mostly due to an increased number of neurons activated. In contrast, subject 7 is atypical of our subject group, in that her scaling factor decreases above threshold, whereas her spike probability more than doubles between threshold and higher levels. This is consistent with the recruitment rate of neurons not being sufficient to maintain a low average spike probability, and in this case, the increase in spike probability would significantly contribute to the total increase in excitation with level. Her large dynamic range (see Table I) may therefore be due to low neural density at sites distant from the electrode.

Nelson *et al.* found that, in their subjects, a flat and very sensitive Weber function (corresponding in our experiment to a large and relatively constant scaling factor) was associated with a smaller dynamic range and superior ability to discriminate electrodes. Our subject 6 would fit this psychophysical description fairly well, and he has both excellent electrode discrimination and speech discrimination ability. However, our subject 7 has similar electrode and speech discrimination abilities to subject 6, but has a very large dynamic range and low sensitivity to level change (inferred from the small scaling factor). Thus the relationship between

intensity discrimination and electrode discrimination may be more complicated than that proposed by Nelson *et al.* More research is needed to define better what neural response characteristics are required for good electrode discrimination. For example, it is not known whether dense and small areas of neural activation would be easier to discriminate than large, partially overlapping regions.

C. The central equal-loudness decision device

As mentioned earlier, the way the central decision device might store or integrate the outputs of the shorter sliding temporal integration window for periods of up to 200 ms was not specifically accounted for in our model. In the case of very low-rate stimulation (experiment 1, and the low rates of experiment 3), where the stimulation period is longer than the ERD, the window output fluctuates with the same period as the rate, and the simplifying assumption was made that the maximum of the output fluctuation is used to compare loudness. If the loudness-decision device used a running average (over about 200 ms) rather than the maximum output, this would have minimal effect on the model predictions for experiments 1 and 2, where the one- and two-pulse/period stimuli have the same period. However, in experiment 3, any ''averaging'' process would reduce the loudness estimation for low rates ($<$about 100 Hz) where the sliding window output fluctuates. Figure 5 shows that, for some of the data, there is a reduction in loudness as rates fall below 50–100 Hz, and this reduction is reflected in a reduction of the inferred average spike probability (Fig. 6). However, the loudness reduction is more likely to be due to an averaging process over longer periods by the central decision device.

V. CONCLUSIONS

These series of experiments have measured and modeled the effect on loudness of varying the interpulse intervals within stimulus pulse trains with short-duration pulses (100 μs and less). The temporal model of loudness perception, which incorporated peripheral refractory effects, a sliding central integration time window, and a central loudness decision device, was able to predict the data from the three experiments in a consistent way. The output of the model allowed comparisons among subjects of the average refractory characteristics of the activated neural population (in terms of average spike probability, and average refractory time). Since these factors were not correlated with stimulus level, it can be concluded that the most significant contributor to increase of total excitation with current is an increase in number of neurons activated, rather than an increase in their average spike probability.

The model predicted that the relationship between change in total excitation and change in current is not a constant power function across the entire perceptual dynamic range. Its prediction that, for most subjects, a specific dB change in current causes an increasing dB change in total excitation as the current increases is analogous to a prediction made from intensity difference limen experiments by Nelson *et al.* (1996).

In summary, the experiments have shown that it is possible to predict neural response behavior from psychophysical performance. This information is potentially useful both in understanding differences in implantees' speech perception performance, and in devising more advanced ways of controlling the stimulus response in order to improve perception of complex signals such as speech.

ACKNOWLEDGMENTS

This research was funded by the Human Communication Research Centre of the University of Melbourne, and the National Health and Medical Research Council of Australia. The authors wish to acknowledge the support and encouragement of Professor Graeme Clark and the patience and cheerful willingness of our subjects, without whom this research would not be possible. We also thank Chris Plack and Leslie Collins for their helpful comments on two earlier versions of the manuscript.

[1]In general, the duration of an integration window depends on the physical quantity being integrated. For example, in some acoustic models the signal intensity is integrated, and in others, the signal intensity is transformed by bandpass filtering and nonlinear compression before integration takes place. The more compression which is applied to the input signal, the smaller the ERD of the integration window which explains the experimental data. The integration window with ERD=7 ms used here (from Moore *et al.*, 1996) was derived from a model with a bandpass filter and nonlinear compression before integration. We have assumed that these initial stages model the transformation, due to cochlear processing, from acoustic intensity to units of peripheral excitation, and hence that the integration window in our model is operating on the same physical units as the acoustical model, when an analogous transformation of current intensity to excitation is applied before the integration window.

[2]These subjects used common-ground stimulation mode (also in their clinical speech processor maps) because there were suspected intermittent shorting problems between particular electrodes (distant from the ones used in this experiment). This electrode configuration will not produce uncomfortable sensations, even if shorting occurs.

[3]It is interesting to ask whether a model which did not include these refractory effects would be able to predict the data consistently across the three experiments. To investigate this question, we fitted the data from experiment 1 to a model where there were two parameters: an integration time-window ERD, which was subject but not level dependent, and the power exponent S. This model will always predict a monotonic decrease in current reduction with widening interpulse interval. For some subjects the goodness-of-fit (as measured by χ^2) was comparable, but in others (such as subject 7), where the data were clearly nonmonotonic, the goodness-of-fit was significantly worse. The derived parameters showed a much larger intersubject variability than for the model with refractory effects: values of ERD varied between 5 ms (subject 2) and infinity (subject 3), and values of S between 2.0 (subject 2, threshold) and 65 (subject 1, mid-level). In the no-refractory-effects model, the ERD and S values completely define the expected results for experiments 2 and 3. In only one case (subject 3) were the predictions of this model for experiment 2 reasonably close to the data. For the other three subjects the slope of the model prediction was too flat (subjects 1 and 4), or gave absolute values about a factor of 2 different from the data (subject 2, half the data values; subject 1, double the data values). The predictions for experiment 3 also failed to match the data accurately for three out of four subjects (1, 3, and 6), with the threshold current changes being underestimated and the comfortable-level changes being overestimated.

Buus, S., and Florentine, M. (**1985**). ''Gap detection in normal and impaired listeners: the effect of level and frequency,'' in *Time Resolution in Auditory Systems*, edited by A. Michelsen (Springer-Verlag, New York).

Butikofer, R., and Lawrence, P. D. (**1979**). ''Electrocutaneous nerve stimulation. II: Stimulus waveform selection,'' IEEE Trans. Biomed. Eng. **BME-26**, 69–75.

Carhart, R., and Jerger, J. (**1959**). ''Preferred method for clinical determination of pure tone thresholds,'' J. Speech Hear. Disord. **24**, 330–345.
Green, D. M., and Forrest, T. G. (**1988**). ''Detection of amplitude modulation and gaps in noise,'' in *Basic Issues in Hearing*, edited by H. Duifhuis, J. W. Horst, and H. P. Wit (Academic, New York).
Javel, E. (**1990**). ''Acoustic and electrical encoding of temporal information,'' in *Cochlear Implants: Models of the Electrically Stimulated Ear*, edited by J. M. Millar and F. A. Spelman (Springer-Verlag, New York), Chap. 17, pp. 247–295.
Levitt, H. (**1971**). ''Transformed up–down methods in psychoacoustics,'' J. Acoust. Soc. Am. **49**, 467–477.
Marquardt, D. W. (**1963**). ''An algorithm for least-squares estimation of non linear parameters,'' J. Soc. Ind. Appl. Math. **11**, 431–441.
Moon, A. K., Zwolan, T. A., and Pfingst, B. E. (**1993**). ''Effects of phase duration on detection of electrical stimulation of the human cochlea,'' Hearing Res. **67**, 166–178.
Moore, B. C. J., Peters, R. W., and Glasberg, B. R. (**1993**). ''Effects of frequency on the detection of decrements and increments in sinusoids,'' J. Acoust. Soc. Am. **94**, 3190–3198.
Moore, B. C. J., Peters, R. W., and Glasberg, B. R. (**1996**). ''Detection of decrements and increments in sinusoids at high overall levels,'' J. Acoust. Soc. Am. **99**, 3669–3677.
Moore, B. C. J., Glasberg, B. R., Plack, C. J., and Biswas, A. K. (**1988**). ''The shape of the ear's temporal window,'' J. Acoust. Soc. Am. **83**, 1102–1116.
Nelson, D. A., Schmitz, J. L., Donaldson, G. S., Viemeister, N. F., and Javel, E. (**1996**). ''Intensity discrimination as a function of stimulus level with electric stimulation,'' J. Acoust. Soc. Am. **100**, 2393–2414.
Oxenham, A. J., and Moore, B. C. J. (**1994**). ''Modeling the additivity of nonsimultaneous masking,'' Hearing Res. **80**, 105–118.
Parkins, C. W. (**1989**). ''Temporal response patterns of auditory nerve fibers to electrical stimulation in deafened squirrel monkeys,'' Hearing Res. **41**, 137–168.
Peters, R. W., Moore, B. C. J., and Glasberg, B. R. (**1995**). ''Effects of level and frequency on the detection of decrements and increments in sinusoids,'' J. Acoust. Soc. Am. **97**, 3791–3799.
Pfingst, B. E., and Morris, D. J. (**1993**). ''Stimulus features affecting psychophysical detection thresholds for electrical stimulation of the cochlea. II: Frequency and interpulse interval,'' J. Acoust. Soc. Am. **94**, 1287–1294.
Pfingst, B. E., Holloway, L. A., and Razzaque, S. A. (**1996**). ''Effects of pulse separation on detection thresholds for electrical stimulation of the human cochlea,'' Hearing Res. **98**, 77–92.
Plack, C. J., and Moore, B. C. J. (**1990**). ''Temporal window shape as a function of frequency and level,'' J. Acoust. Soc. Am. **87**, 2178–2187.
Plack, C. J., and Moore, B. C. J. (**1991**). ''Decrement detection in normal and impaired ears,'' J. Acoust. Soc. Am. **90**, 3069–3076.
Shannon, R. V. (**1985**). ''Threshold and loudness functions for pulsatile stimulation of cochlear implants,'' Hearing Res. **18**, 135–143.
Shannon, R. V. (**1989**). ''A model of threshold for pulsatile electrical stimulation of cochlear implants,'' Hearing Res. **40**, 197–204.
Shannon, R. V. (**1993**). ''Psychophysics,'' in *Cochlear Implants: Audiological Foundations*, edited by R. S. Tyler (Singular, San Diego), Chap. 8, pp. 357–388.
Stypulkowski, P. H., and Van den Honert, C. (**1984**). ''Physiological properties of the electrically stimulated auditory nerve. I. Compound action potential recordings,'' Hearing Res. **14**, 205–223.
Viemeister, N. F. (**1979**). ''Temporal modulation transfer functions based on modulation thresholds,'' J. Acoust. Soc. Am. **66**, 1364–1380.
Viemeister, N. F., and Wakefield, G. H. (**1991**). ''Temporal integration and multiple looks,'' J. Acoust. Soc. Am. **90**, 858–865.

An experimental study of the open end correction coefficient for side branches within an acoustic tube

Jianwu Dang
ATR Human Information Processing Research Laboratories, 2-2 Hikaridai, Seikacho Soraku-gun, Kyoto 619-02, Japan

Christine H. Shadle
Department of Electronics and Computer Science, University of Southampton, Southampton SO17 1BJ, United Kingdom

Yasuhito Kawanishi
Graduate School of Electronic Science and Engineering, Shizuoka University, Japan

Kiyoshi Honda
ATR Human Information Processing Research Laboratories, 2-2 Hikaridai, Seikacho Soraku-gun, Kyoto 619-02, Japan

Hisayoshi Suzuki
Department of Information Engineering, College of Science and Technology, Tohoku, Kunimi 6-45-16, Aoba-Ku, Sendai 982, Japan

(Received 9 June 1997; accepted for publication 15 April 1998)

The open end correction coefficient (OECC) of acoustic tubes has been widely investigated under a free-field condition. This study examines OECCs in confined regions, such as side branches within the vocal tract. To do this, a number of mechanical acoustic models are used to examine the effects of the angle of the branch axis and the proximity of the walls of the main tract to the open end of the branch. The OECC is estimated by matching both the peaks and troughs (i.e., spectral maxima and minima) of the computed and measured transfer functions for each model. The results indicate that the OECC of a side branch depends on L/D, where L is the cross dimension of the main tract at the branching point, and D is the branch diameter. For side branches connected to the main tract through a narrow neck, the OECC of each end of the neck is determined using the ratio of the radius of the neck to that of the adjacent section. Two empirical equations for evaluating the OECC within a tract are derived from the present study. Finally, the range of appropriate OECC values for estimating an accurate vocal tract transfer function is discussed, based on the results presented here and morphologic measurements reported previously. [S0001-4966(98)00408-1]

PACS numbers: 43.70.Bk, 43.70.Jt, 43.70.Aj [AL]

INTRODUCTION

It is well known that sound radiation takes place at any abrupt transition from a smaller cross-sectional area to a larger area in a compound acoustic system. The radiation makes the effective length of the section with the smaller area longer than its actual length. The ratio of the length increment to the radius of the smaller area is referred to as the open end correction coefficient (OECC). It has been proved that the OECC depends on the Helmholtz number kr (cf. Levine and Schwinger, 1948), where k is the wave number and r is the equivalent radius of the open end. In the field of speech production, the OECC is often used as a lumped coefficient in transmission line models for a low-frequency approximation.

Sound radiation at an abrupt area transition has been investigated under several conditions by a number of studies. Among them, Rayleigh (1945) gave theoretical descriptions in which the OECC is 0.785 for each side of an orifice in an infinitely thin plate, and is 0.824 when the plate becomes infinitely thick. Levine and Schwinger (1948) rigorously solved the sound radiation for an unflanged circular pipe. They gave a theoretical value of the OECC, 0.6133, for a low-frequency approximation of the end correction. Nomura *et al.* (1960) examined the sound radiation at the open end of a flanged circular pipe numerically, and showed that the OECC for a flanged pipe is 0.8217 at low frequencies. Ando (1969) employed the same approach to analyze the sound radiation at the open end for various widths of the flange of the pipe, and the OECCs were consistent with the above solutions. Based on experimental data, Hall (1987) suggested the following empirical equation to describe the relation between the OECC and the width of the flange for a low-frequency approximation,

$$\alpha_1 = 0.821 - 0.13[(W/b) + 0.42]^{-0.54}, \tag{1}$$

where b is the radius of the open end and W is the width of the flange. Peters *et al.* (1993) estimated OECCs under conditions in which the geometry at the open end of pipes was varied with and without a mean flow. The OECC obtained for a hornlike open end under the condition with no flow was approximately 0.46 (adjusting their value by taking the

OECC ratio in terms of the horn radius rather than the pipe radius), which is much lower than the previously suggested value of 0.6133. They showed that the OECC changed with geometries at the open end of pipes, larger for a sharp edge and smaller for a rounded one. In other words, the OECC in a compound acoustic system is related to the abruptness of the area transition between the adjacent sections. They also demonstrated that the OECC for large mean flow is low and independent of the flange thickness; for small mean flow the OECC becomes relatively constant, but the value of the constant depends on aspects of the geometry such as flange thickness, ranging between 0.6 and 0.8.

In contrast to free-field conditions, OECCs appropriate for confined regions have not been so extensively studied. Ingard (1953) examined the radiation of sound at the neck of a Helmholtz resonator, and suggested the following formula to evaluate the OECC for the interior end of the neck:

$$\alpha_2 = 0.48(A)^{0.5}[1/r - 1.25/R], \tag{2}$$

where A and r are the area and radius of the smaller-area section. R is the radius of the larger-area section, with r smaller than $0.4R$. El-Raheb and Wagner (1980) examined the effects of the sharp bends and branches of acoustic tubes for a given cross-sectional area and gave distributions of the sound pressure within the acoustic tubes. They showed that some different patterns of the transverse mode occurred for the rectangular pipes and the circular pipes. Since the dimensions of the vocal tract are much smaller than those of their tube models, such phenomena shown in their study would appear in a higher frequency region for a tube with dimensions similar to the vocal tract. However, most of the studies on speech production are more concerned with a low-frequency region which meets the assumption of plane-wave propagation.

In modeling the vocal tract, a number of side branches in the vocal tract such as the nasal tract, paranasal sinuses, and piriform fossa must be taken into account (see Fig. 1). The OECC is a significant factor in accounting for an abrupt area transition, large area ratios, and in most cases, short branch lengths. Partially due to a lack of experimental data for confined regions, however, the OECC values previously used in vocal tract models differ widely.

Fant proposed 0.8 as the OECC for a low-frequency approximation. He also recommended the use of Ingard's equation [Eq. (2)] to compensate for the radiation inductance of an abrupt area transition within the vocal tract such as the area between the teeth (Fant, 1970). Sundberg (1974) employed a value of 0.7 as the OECC to evaluate the acoustic characteristics of the piriform fossa. Dang and Honda (1996b) and Dang *et al.* (1996) estimated an OECC of 0.75 for the piriform fossa using MRI-based mechanical and numerical models. Koyama (1966), in evaluating the antiresonances of the paranasal sinuses, used an OECC value of 1.46 for the abrupt area transition at the two ends of the ostia, 0.73 for each end. On the other hand, Masuda (1992) reported that no end correction was necessary (i.e., the OECC equaled zero) for the ostia of the paranasal sinuses according to a comparison of his morphology-based computation with measured antiresonances.

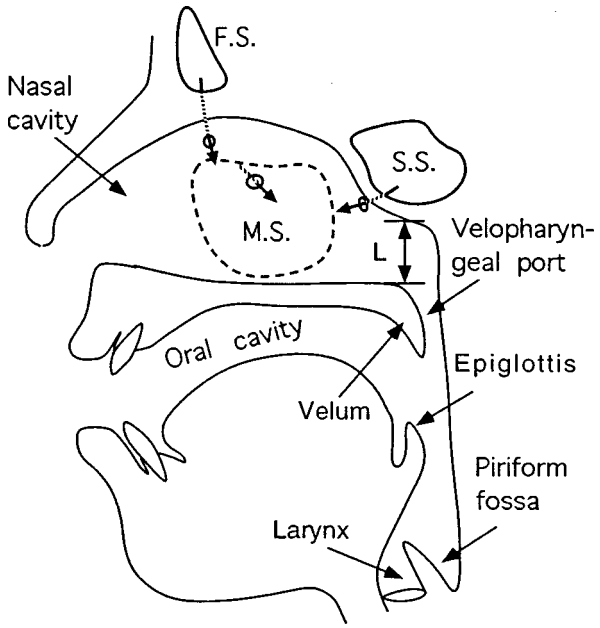

FIG. 1. A diagram of a sagittal view of the vocal tract showing the major side branches. L is the distance from the nasal floor to the ceiling of the nasopharynx. M.S., F.S., and S.S. are the maxillary, frontal, and sphenoidal sinuses.

According to previous studies (Hall, 1987; Peters *et al.*, 1993), the geometry of the open end is a factor affecting the acoustic radiation. This factor is expected to be more dominant in the vocal tract because the geometries around the open end of the side branches are much more complex in the vocal tract than those discussed in the literature cited above. According to MRI-based morphological studies (see Dang *et al.*, 1994; Dang and Honda, 1996c, 1997), the branches show various geometric shapes, and the dimensions of the main tract and the open end of the branches differ significantly from each other. Figure 1 shows a diagram of the major side branches within the vocal tract. At the bifurcation of the nasal and oral tracts, for example, the velopharyngeal port opens into the oral tract at the bend of the velum, and is directed almost opposite to the direction of sound propagation in the vocal tract. Contrarily, the direction of the opening of the piriform fossa is parallel to the direction of sound propagation, and the lateral walls of the fossa are continuous with the posterior and lateral walls of the pharynx. This geometry is expected to enhance the radiation reactance of the open end. The directions of the ostium openings of the paranasal sinuses to the nasal tract differ from one another, and the cross dimension of the main tract is relatively small in the vicinity of the open end. Radiation reactance at the open end of the branches is expected to be different for these different geometries.

In this study, a number of mechanical models with various branches were constructed to imitate the geometries of the side branches in the vocal tract. OECCs were estimated for the side branches within the mechanical models. The purpose of the present study was to provide experimental evidence to support the use of particular values of lumped-coefficient compensation for the radiation at the ends of side branches within the vocal tract model.

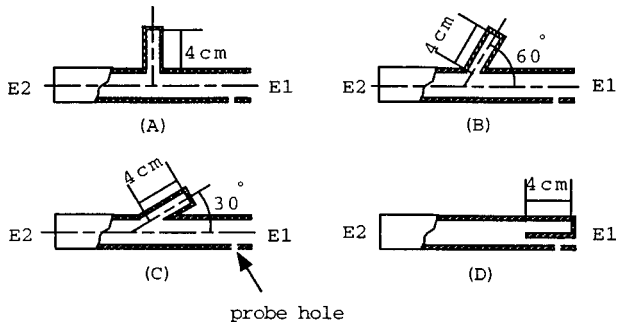

FIG. 2. Diagrams of mechanical models A through D, designed with different branch angles.

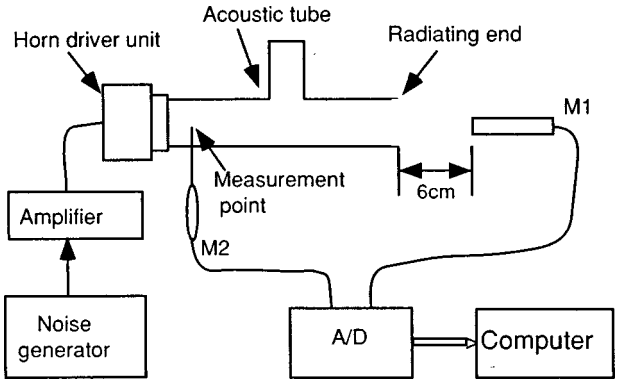

FIG. 3. A diagram of the experimental setup for measuring the transfer function of an acoustic tube.

I. EXPERIMENTAL PROCEDURE

The experimental procedures employed in this study were (1) design and construction of mechanical models with various side branches; (2) measurement and calculation of the transfer functions of the mechanical models; and (3) estimation of the optimal OECC for the side branches based on the computed and measured transfer functions.

A. Construction of the mechanical models

Acoustic experiments were designed to obtain a realistic OECC for vocal tract models. To this end, a number of mechanical models were constructed to imitate the geometries of the side branches in the vocal tract. The main tract was made from hard acrylic plates with a thickness of 0.3 cm. The cross-sectional shape of the main tract was designed to be square, and thus side branches in the tract had a plane opening end. Two types of side branches with a uniform area were employed: a tube with a circular cross section, and a tube with a rectangular cross section. The circular tube was attached about midway along the main tract on the outside of one of the walls. The rectangular tube was placed inside the main tract by partitioning one of the ends.

Figure 2 shows diagrams of four basic models. Models A, B, and C were 18.5 cm long and 2.6×2.6 cm in their inner cross section, while model D was 19.5 cm in length and 2.1×2.1 cm in its inner cross section. The branch in models A, B, and C was a circular tube with a length of 4 cm and a diameter of 1.7 cm, where the length was measured along the branch's central axis from the closed end to the open end. The branch in model D was 4 cm long and 2.1×1.0 cm in its cross-sectional size. The branch angles of the models were 90, 60, 30, and 0 degrees, respectively. These four models were used to examine the effects of different angles of the side branch axis to the main tract. To install the probe tube of a probe microphone for acoustic measurements, holes with a 0.12-cm diameter were drilled in the main tract wall about 1 cm back from either end.

Additionally, three more models, E, F, and G, were constructed for further examinations. Model E (diagramed in Fig. 6) was used for examining effects of the flange of the open end of the side branch, and of the proximity to the main tract wall. Model F (in Fig. 7) was designed to determine effects on the OECC of the branch diameter and the distance between the open end and the opposite wall. Model G (in Fig. 10) was for estimating the OECC of a side branch with a narrow neck. Two identical holes, 1 cm apart, were drilled for the probe tube in the main tract wall near the input end for models E, F, and G.

B. Measurements

The pressure-to-pressure transfer function of the mechanical models was measured using a two-point pressure method, with which the acoustic properties of the side branch can be exactly described by measuring simultaneously the sound pressure in the main tract on the source side of the branch and the sound pressure from the radiating end of the main tract (Dang and Honda, 1996a). A diagram of the experimental setup used for measuring the two pressures is shown in Fig. 3. Microphone 1, B&K 4003, was placed 6 cm away from the radiating end to record the radiated sound. The probe tube of probe microphone 2, B&K 4128, was installed through the hole drilled in the main tract wall on the source side of the branch. A white-noise signal produced by an FG-143 function generator (NF Circuit Design Block Co.) was amplified and fed into an SG-505FRP horn driver unit (Goto Unit Co.) to excite the mechanical model. The join between the model and the neck of the horn driver unit was sealed with plasticine to prevent sound leakage. The outside sound pressure in the vicinity of the join was confirmed to be about 25 dB lower than that at the radiating end. This implies that sound leakage from the join can be considered to be negligible in this measurement. Sound recording was carried out at a sampling rate of 48 kHz in an anechoic room. A room temperature of 20 °C was maintained during the measurement, and therefore the sound velocity used in all calculations was 34 300 cm/s.

The two sound pressures were recorded simultaneously for 5 s for each measurement. Averaged power spectra of the sound pressures were computed using DFT with a 340-ms Hamming window shifting by 85 ms over the entire 5-s signal duration. The ratio of the power spectra of the radiated sound to the internal sound was taken to be the pressure-pressure transfer function of the segment from the internal measurement point to the radiating end.

The antiresonance of the side branch can be identified in the measured transfer function. However, the antiresonance may not appear clearly in the transfer function if it is located

near a resonance. Our previous studies demonstrated that adjusting the location of the internal measurement point can move the resonances in the transfer function without affecting the antiresonance frequencies of the side branch (Dang and Honda, 1996a, c). In essence, the resonances correspond to the resonances of the tube open at both ends, with one end corresponding to the open end and the other to the location of the internal measurement point. For this reason, two probe holes as described previously were designed for models E, F, and G to change the internal measurement point. Thus antiresonances that may be distorted or obscured by nearby resonances for one internal measurement point can be revealed through this procedure.

Strictly speaking, a factor for the transfer from the main tract end to M1, which is in the near field, should be included. As a check, transfer functions were measured for different positions of M1, varying the distance from the open end to M1 from 3.5 to 30 cm. It was found that there were some changes in the amplitude of the baseline of the measured spectra and in the slope of the envelope, but not in the resonance or antiresonance frequencies. Since in this study we are more interested in these frequencies, this factor was omitted.

C. Estimation of OECC

Since the interaction between the resonances and antiresonances in an acoustic system tends to obscure or distort each other, frequencies of maxima and minima in a measured transfer function are usually different from the true resonances and antiresonances to some extent. We therefore refer to maxima and minima in the measured transfer functions as peaks and troughs, respectively, and compare the measured and computed transfer functions in order to establish the frequencies of the true resonances and antiresonances. A transmission-line model was employed to compute the transfer function for the comparison. If both the troughs and peaks in the computed transfer function are matched well to those in the measured one, it is reasonable to assume that the acoustic properties of the computational model are identical to those of the mechanical model.

The transmission-line models had an identical area function to that of the measured tube segment, from M2 to the radiating end, with an adjustable OECC for the branch. The bifurcation point of the branch and main tract in the computational model was at the intersection of the branch's central axis and the open end for models A, B, C, F, and G, and at the edge of the open end of the branch for models D and E. The equivalent radius used for the square openings was approximated by a circular radius of $r=\sqrt{A/\pi}$, where A is the area of the opening. The radiation impedance of the main tract of the computational models was approximated by a cascaded connection of resistance and inductance (Caussé *et al.*, 1984). Losses due to viscosity and heat conduction were implemented in the computation (Flanagan, 1972), while losses due to wall vibrations were ignored for these rigid-walled mechanical models. The validity of the acoustic parameters above was confirmed using a uniform straight tube.

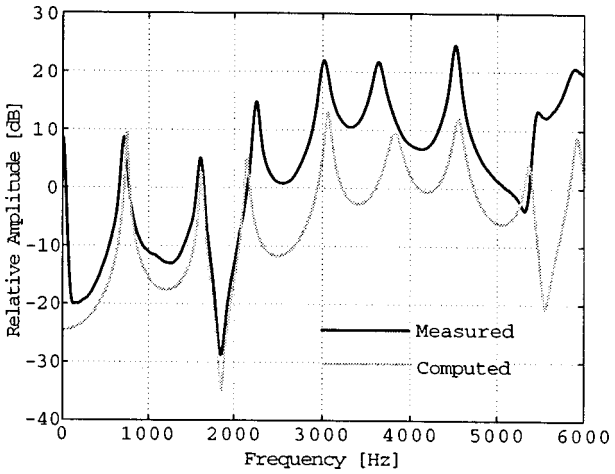

FIG. 4. A typical comparison of measured and computed transfer functions for a tract with a side branch; this case is model D.

In this estimation, the OECC for the branch was adjusted to match the computed troughs and peaks to the measured ones. The optimal OECC value was defined that satisfied the condition that the differences in both the peak and trough frequencies should be less than 3% for frequencies below 3 kHz. The OECC values found in this way will henceforth be referred to as *matched OECC values*, to distinguish them from OECC values derived from empirical formulas. Figure 4 shows an example of the comparisons between the measured and computed transfer functions for model D. In this example, the computation and the measurement are consistent within 3% below 3.5 kHz for the frequencies of the peaks and troughs, and within 5% above. The computed and measured transfer functions demonstrate almost identical spectral shapes at lower frequencies. These two spectra show an increasing disparity at higher frequencies. This is probably caused by the accumulated effects and the assumption of plane-wave propagation in the simulation, where the assumption is not always correct for higher frequencies. For this reason, the above comparison for the troughs was limited to the first trough of the branch, though the second trough was typically visible in the higher frequency region.

Figure 4 shows that as frequency increases, the amplitude difference between the spectra increases. This difference is mainly caused by the different tilts of the two spectra. The tilt is more pronounced for the measured spectrum because microphone 2, B&K 4128, has a decreasing response with increasing frequency (see the instruction manual of B&K 4128), while microphone 1, B&K 4003, has a flat response over a wide frequency region. Since there was no significant effect on the frequencies of the peaks and troughs either with or without calibration, noncalibrated data are used in obtaining the measured transfer function.

II. RESULTS

The results of the experiment are shown for the effects of (1) the angle of the branch to the main tract, (2) the flange of the open end of the branch and the surrounding wall of the

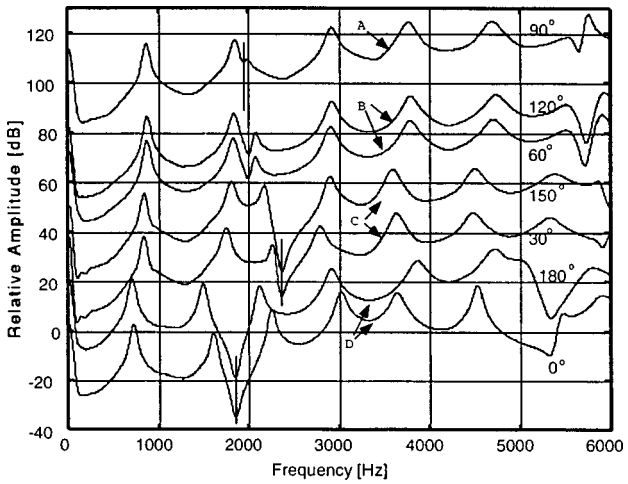

FIG. 5. Transfer functions measured for the mechanical models shown in Fig. 2 with the model label and branch angle for each curve. Successive curves are offset by 20 dB.

main tract, (3) the dimensions of the branch and the main tract at the bifurcation, and (4) a narrow neck within a side branch.

A. Effects of the angle of the side branch axis

Four mechanical models were used experimentally to determine effects of the angle of the side branch axis on the OECC. The mechanical models are shown in Fig. 2. The branch angle is defined as the angle between the central axis of the branch and that of the main tract, using angles in the range of 0–180 degrees. In models A through D, the branch angles are, respectively, 90, 60, 30, and 0 degrees when using E1 as the input end. Treating E2 as the input end, the corresponding branch angles for the same models are 90, 120, 150, and 180 degrees.

The measurements were carried out on the models twice, feeding sound from E1 and then E2. Thus, seven transfer functions were obtained from the models for the angles of 90, 60, and 120, 30 and 150, and 0 and 180 degrees. The measured transfer functions are shown in Fig. 5, given in pairs except for model A. Effects of the angles, if any, can be easily found from each pair for the same model, because the geometries surrounding the branches were exactly the same. The troughs occur at approximately the same frequency for each pair of transfer functions, but their amplitudes are slightly lower (the troughs are deeper) for the obtuse than for the acute angles, and the spectra surrounding the troughs show slightly different shapes. The frequency of the first trough is listed in Table I for each case. The trough frequencies show significant differences for varying branch angles across the four models. As could be predicted theoretically, there is no significant difference in the trough frequencies for the same model regardless of whether its branch angle is obtuse or acute. The consistency of the measurement with the theoretical prediction confirms the accuracy of our experimental procedure.

The OECCs of the branches in the models were also estimated using the method described in Sec. I C. For models B and C, however, the open end of the branch is not simply

TABLE I. Trough frequencies measured from the transfer functions shown in Fig. 5, and matched OECCs (BA: branch angle).

Model	BA (Deg)	Troughs (Hz)	OECC
A	90	1940	0.48
D	0	1848	0.78
	180	1842	0.80
B	60	1991	···
	120	1997	···
C	30	2361	···
	150	2361	···

defined in the computational model since the opening plane of the branch is not parallel to the wavefront for the plane-wave assumption (see El-Raheb and Wagner, 1980). Therefore it is not possible to obtain the OECCs for models B and C using the present method. For this reason, this estimation was limited to models A and D. Matched OECCs are shown in the fourth column of Table I for branch angles of 0, 90, and 180 degrees. The OECCs obtained for 0 and 180 degrees are not significantly different. Contrarily, the OECC for the branch angle of 90 degrees does differ significantly. The value of 0.48 for the 90 degrees case is much smaller than that proposed in previous studies (Rayleigh, 1945; Hall, 1987).

Since the branch angle is not a major factor affecting the OECC, it is suspected that the geometric shapes surrounding the open ends of the branches caused the difference. In model D, but not model A, the branch shares walls with the main tract. This structure may enhance the radiation reactance of the open end. Another difference is that the dimension of the main tract into which the branch opened is larger in model D than that in model A. To clarify the relations between the OECC and these aspects of the geometry, we conducted the following experiments.

B. Effects of the flange of the open end and the main tract wall

A mechanical model with a branch angle of 0 degree (model E, shown in Fig. 6) was used to examine the effects of the flange of the open end of the side branch and the main tract wall. The main tract was 10 cm long, with a cross section of 2.1×2.1 cm. The branch was 4.0 cm in length,

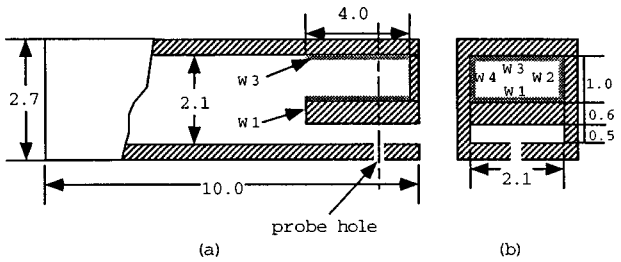

FIG. 6. Model E for examining effects of the flange of the open end of the side branch and the main tract wall. (a) Axial-sectional view; (b) cross-sectional view at the location of the probe hole. The layers added on the original walls are shown by W1, W2, W3, and W4. All dimensions are in cm.

TABLE II. Condition 1: thickening wall W1 in model E. Branch dimensions, measured troughs, and matched OECCs are listed.

W1 thickness (cm)	Branch end area (cm^2)	Troughs (Hz)	OECC
0.6	2.10	1845	0.79
0.7	1.89	1845	0.83
0.8	1.68	1848	0.87
0.9	1.47	1863	0.87
1.0	1.26	1877	0.88
1.1	1.05	1895	0.88

and 2.1×1.0 cm in its cross section. Measurements of the transfer function of this model were made under three conditions:

Condition 1: Vinyl chloride plates with an area of 4.0×2.1 cm and a thickness of 0.1 cm were glued on the partition wall, W1, one by one. This manipulation was done in order to explore effects of the flange width of the open end in a confined region by thickening W1 while retaining the proximity to the main tract walls. The measurement was repeated while the thickness of W1 increased from 0.6 to 1.1 cm in 0.1-cm steps.[1]

Condition 2: Plates identical to those used in condition 1 were glued on the main tract wall (W3, referred to as the back wall) to decrease the effects of the proximity by moving the open end of the branch away from the main tract wall. The measurement was repeated while increasing the thickness of the inserts from 0 to 0.5 cm at 0.1-cm intervals.

Condition 3: Two identical plates with an area of 4.0×1.0 cm and a thickness of 0.1 cm were glued on two opposite sides of the branch simultaneously (W2 and W4) to decrease the proximity to the lateral walls of the main tract. The measurements were carried out while the thickness of each side insert increased from 0 to 0.4 cm with intervals of 0.1 cm.

The measured trough frequencies and matched OECCs are shown in Table II for condition 1. The matched OECCs increase as wall W1 is thickened. This tendency is consistent with those obtained by Ando (1969) and by Hall (1987). Thickening W1 from 0.6 to 1.1 cm increases the OECC from 0.79 to 0.88, a total change of 0.09, or 11%. This implies that the effect of the flange of an open end in a confined space is the same as that in a free field.

The matched OECCs for condition 2 are shown in Table III. At first, the OECC decreases as flange W3 increases from 0.0 to 0.1 cm. It then remains nearly constant as the thickness of W3 increases from 0.1 to 0.4 cm. Changing W3 in this way can apparently be considered to involve two main components: increase of the flange thickness and decrease of the proximity to the main tract wall. According to the result for condition 1, thickening the flange increases the OECC. However, no such tendency was seen under condition 2 even though the thickness of flange W3 was increased by the same amount. It can be concluded that decreasing the proximity to the main wall has the opposite effect, i.e., it tends to decrease the OECC. In other words, when the branch wall continues directly into the main tract, the open end effect of the branch is greatly enhanced.

TABLE III. Condition 2: thickening wall W3 in model E. Branch dimensions, measured troughs, and matched OECCs are listed.

W3 thickness (cm)	Branch end area (cm^2)	Troughs (Hz)	OECC
0.0	2.10	1845	0.79
0.1	1.89	1868	0.76
0.2	1.68	1880	0.76
0.3	1.47	1894	0.76
0.4	1.26	1909	0.76
0.5	1.05	1921	0.77

TABLE IV. Condition 3: thickening walls W2 and W4 in model E. Branch dimensions, measured troughs, and matched OECCs are listed.

W2, W4 thickness[a] (cm)	Branch end area (cm^2)	Troughs (Hz)	OECC
0.0	2.10	1842	0.80
0.1	1.90	1851	0.81
0.2	1.70	1863	0.81
0.3	1.50	1877	0.81
0.4	1.30	1883	0.85

[a]The value shown is the thickness of the insert on each side.

Under condition 3, the matched OECCs increase slightly, unlike in condition 2. This tendency shown in Table IV implies that the effect of decreasing the proximity to the lateral walls is smaller than that of thickening the flanges. The difference between conditions 2 and 3 indicates that the lateral walls had a smaller effect than the back wall, although the length of the boundary between the lateral walls and the branch was about the same as that between the back wall and the branch. If one simply imagines the effective open end of the branch to extend diagonally from W1 to the back wall (so that the length of the back wall effectively ''belonging'' to the branch is longer than the partition wall W1), this phenomenon is easily understood. With this conjecture, the magnitude of the effect of the lateral walls on the OECC is approximately half that of the back wall for the same boundary length.

Summarizing the above results, thickening W1 increases the thickness of the flange and shortens the length of the boundary between the lateral walls and the branch, but it does not change the situation between the back wall and the branch. Therefore it can be concluded that thickening the flange enhances the OECC. Thickening W3 under condition 2 showed a different behavior from that produced by thickening W1 under condition 1. One of the causes may be that an extra abrupt area transition was added to the branch with W3 under condition 2. However, since adding an abrupt area transition should enhance the end radiation and this tendency was not seen in the result, the extra abrupt area transition is not the major cause of the difference. Considering the common results under conditions 2 and 3, the major cause seems to be due to the decrease of the proximity to the main tract wall; it results in acoustically reducing the effective length of the branch. In other words, the proximity to the main tract wall contributes to increasing the effective length of the branch.

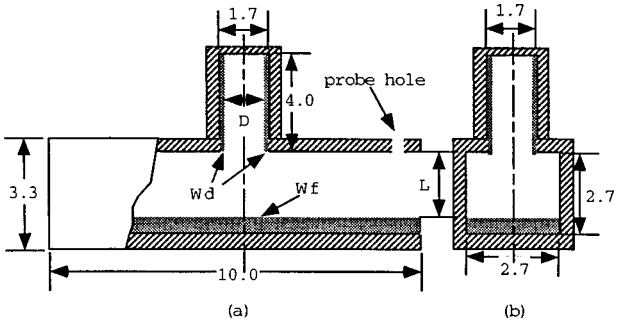

FIG. 7. Model F for investigating the relationship between the OECC and the dimensions of the main tract and the branch at the bifurcation. (a) Axial-sectional shape; (b) Cross-sectional shape. All dimensions are in cm.

C. Effects of the dimensions at the bifurcation

Figure 7 shows a diagram of model F which was used to examine the effects of the dimensions of the main tract and the branch at the bifurcation. The main tract was 10 cm long and 2.7×2.7 cm in its inner cross section. The branch, a circular uniform tube, was 4 cm in length and 1.7 cm in diameter. Effects of the dimensions of the branch and the main tract in the vicinity of the bifurcation were examined by varying two dimensions systematically: the inner diameter of the branch, D, was decreased by increasing the thickness of W_d; and the distance L across the main tract was decreased by increasing the thickness of W_f. D was decreased from 1.7 to 0.7 cm in 0.2-cm steps by gluing layers of stainless steel foil, 0.1 cm thick, on the inner wall of the branch. For each value of D, L was varied from 2.7 to 0.6 cm in 0.3-cm steps by gluing an acrylic plate with an area of 10×2.7 cm and a thickness of 0.3 cm on wall W_f.

Figure 8 shows the matched OECCs for all of the combinations of L and D. The figure demonstrates that OECCs increase with L for a given branch diameter D. For a given L, the OECCs increase as D decreases. The curves of the OECCs move in parallel with D.

The results show that the OECC is approximately proportional to distance L and inversely proportional to the diameter of the open end of the branch. To arrive at a general

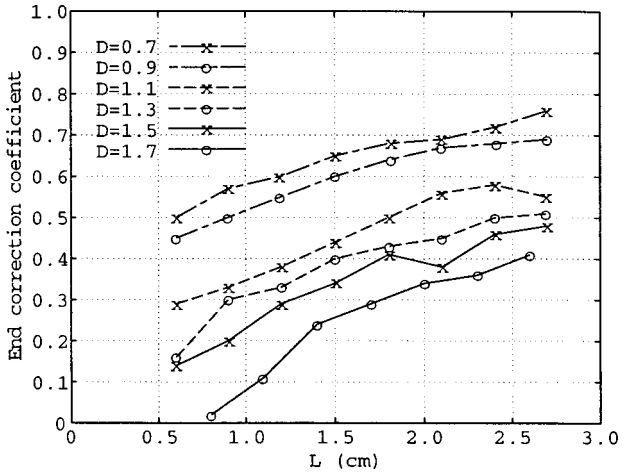

FIG. 8. Matched OECCs for various combinations of L and D for model F, shown in Fig. 7.

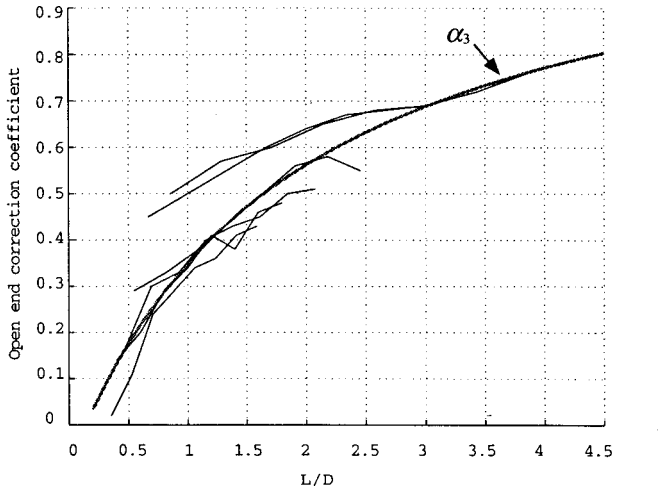

FIG. 9. Matched OECCs of Fig. 8 plotted against dimensionless parameter L/D. See Fig. 7 for the definitions of L and D. The line marked α_3 is the least-squares fit to all of the curves shown.

relationship of the OECCs to the parameters, the data were replotted against a dimensionless parameter L/D. As shown in Fig. 9, the six curves of the matched OECCs collapse approximately onto a curve that is a function of L/D. A least-square method was used to calculate the best-fitting curve. This curve, which we call the *estimated OECC*, is plotted in Fig. 9, and is given by the following empirical formula:

$$\alpha_3=\frac{1.27\xi}{\xi+1.92}-0.086, \quad 0.2<\xi=\frac{L}{D}<4.5, \tag{3}$$

where α_3 is the estimated OECC for model F, D is the inner diameter of the open end of the branch, and L is the distance from the open end to the opposite wall of the main tract. The mean-square error was 0.048 between the measurements and the prediction by this formula. Considering the conditions of the measurement and application, the formula is appropriate to be used in a range of $\xi=L/D$ between 0.2 to 4.5, where α_3 ranges from 0.03 to 0.80.

D. End corrections for a branch with a narrow neck

In the vocal tract, there are a number of branches with a narrow neck, such as the paranasal sinuses in the nasal cavity. A neck has two ends: one opening into the main tract, referred to as the tract end; and the other one opening into the cavity, referred to as the cavity end. Both ends require an end correction for the abrupt area transitions. The tract end of the branch neck has a similar geometry to that discussed for model F. For this end, therefore, the correction coefficient can be evaluated using Eq. (3). In this section we arrive at an estimate for the OECC for the cavity end of the branch neck.

A mechanical model shown in Fig. 10, referred to as model G, was used in this examination. This model consisted of a main tract with a square cross-sectional shape of 2.7×2.7 cm, and a circular branch with a narrow neck. The cavity of the circular branch was 3.8 cm in length and 1.7 cm in inner diameter. The neck length l_N was chosen to be 0.3 cm which is approximately equal to the ostium length of the

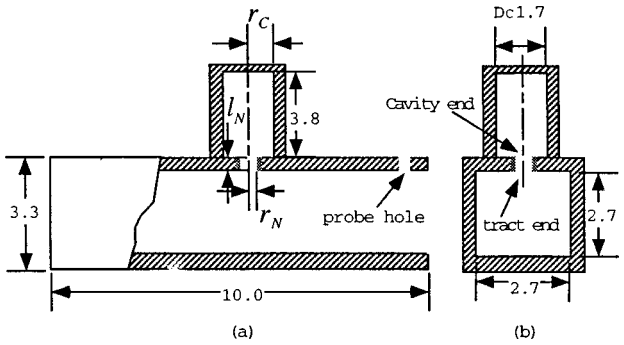

FIG. 10. Model G, used for estimating the OECC for the cavity end of the branch neck as a function of neck diameter $D_N=2r_N$. l_N is the length of the neck. All dimensions are in cm.

maxillary sinus, the biggest side branch in the nasal tract. Diameter, D_N, of the neck was varied as described below.

Transfer functions of model G were measured while varying the diameter of the neck (D_N) from 0.17 to 1.0 cm in 12 steps. In the measured transfer functions, for $D_N > 0.5$ cm, a second trough appeared at a higher frequency. This implies that the branch can no longer be modeled as a simple Helmholtz resonator. Accordingly, this branch was treated as a tract with two cascaded sections in this estimation of the OECC.

As mentioned above, the OECC of the tract end was evaluated using Eq. (3). For $L/D>4.5$, the OECC was reasonably assumed to be 0.80. As shown in Fig. 11 (broken line), this region occurs in model G for $r_N/r_C<0.35$, where r_N=radius of the branch neck and r_C=radius of the branch cavity.

In order to estimate the OECC for the cavity end of the branch neck, the computed transfer function was matched to the measured one while the OECC was adjusted. The optimal OECCs were obtained when the measured and computed transfer functions were consistent with one another within

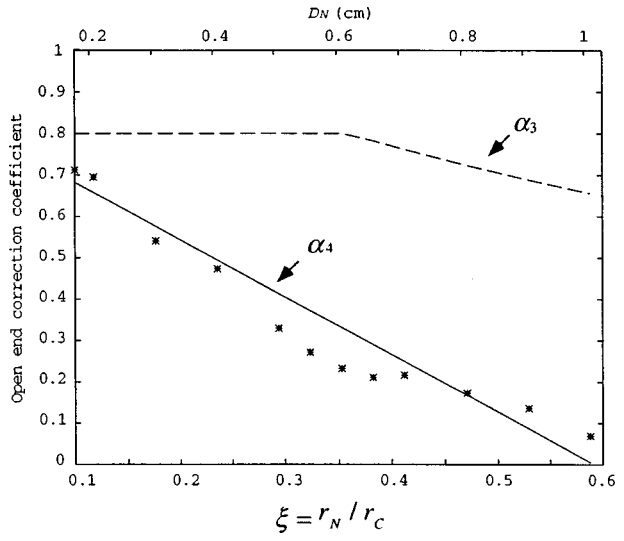

FIG. 11. Predictions and measurements for model G, Fig. 10. With the OECCs of the tract end of the neck evaluated using Eq. (3) (broken line), the OECC of the cavity end of the neck was matched using a cascaded-tube treatment (‘‘*’’), and an empirical approximation [Eq. (4)] to that is shown (solid line). r_N and r_C are defined in Fig. 10. D_N is the diameter of the neck.

1% for the first trough, and within 2% for the first two peaks. Figure 11 shows the matched OECCs for the cavity end (plotted using an asterisk), which decrease monotonically from 0.712 to 0.069 as the ratio of radii increases. To derive a general empirical formula, an expression similar to that used by Ingard (1953) was adopted to describe the experimental data. The parameters in the expression were derived based on the measurements with a constraint that the OECC be equal to 0.821 when $\xi=0$ (Nomura *et al.*, 1960). By minimizing the mean least square of errors between measurement and prediction, we arrive at the expression:

$$\alpha_4=0.821(1-1.69\xi), \quad \xi<0.6, \tag{4}$$

where $\xi=r_N/r_C$. Values of α_4 (solid line) are plotted in Fig. 11 as ξ is varied, which predicts the matched OECCs with a mean-square error of 0.053. This result indicates that the end radiation is negligible when the ratio ξ is larger than 0.6 even if an abrupt area transition exists.

III. DISCUSSION

In this section, we summarize the effects of the geometries on the OECC of a side branch, and compare the predictions of our formulas with previous results. The range of OECCs for the side branches within the vocal tract is also discussed based on the present results and morphologic measurements reported previously.

A. Summary of the measurements

A number of mechanical models were designed with various side branch shapes to imitate the geometries of the side branches within the vocal tract. With these models, acoustic effects of the geometries on the antiresonances and the OECCs of the branches were examined. The angle of the branches with respect to the main tract was varied; this did not show any significant effects on the antiresonance frequencies, nor on the matched OECCs in the cases where they could be estimated. Two cases, i.e., the branches parallel to and perpendicular to the main tract, however, showed different behaviors.

The parallel-branch case (model E) showed an interaction of the effects on the OECC of the branch flange and the proximity to the wall of the main tract. General speaking, the OECC is higher for a branch within a main tract than the same ‘‘branch’’ in a free field. This effect is heightened as the branch open end approaches the main wall of the tract.

The perpendicular-branch case (model F) showed an interaction of the effects on the OECC of the diameter (D) of the branch’s open end and the distance (L) from the end to the far wall of the main tract. This effect was strong enough to allow us to collapse all of the matched OECCs onto one curve using the dimensionless parameter L/D. These collapsed curves can be predicted well using an empirical formula [Eq. (3)]. As shown previously, this formula is derived for a given width of the main tube. What are the possible effects on the formula if the width of the main tube varied? Basically, increasing the width of the main tube has two simultaneous actions: thickening the flange and reducing the proximity of the lateral walls to the branch open end, and

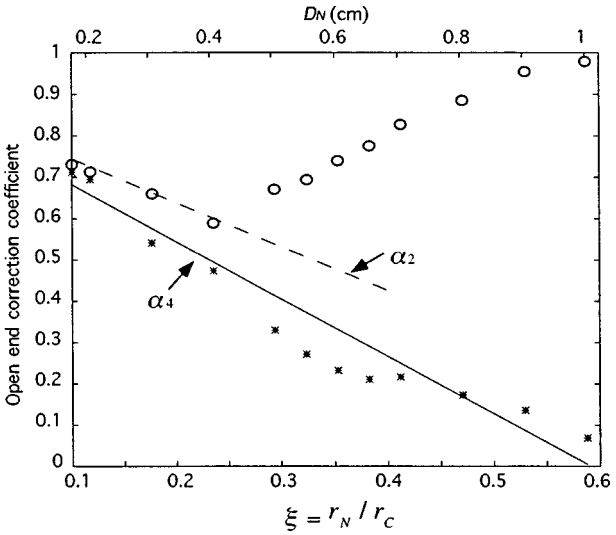

FIG. 12. OECCs for the cavity end of the neck of model G: matched using a Helmholtz resonator treatment (○), using a cascaded-tube treatment (*), and predicted using our formula Eq. (4) (solid line) and Ingard's formula Eq. (2) (dashed line). r_N, r_C, and l_N are defined in Fig. 10. In Ingard's notation, $\xi = r/R$.

vice versa. According to the results obtained in Sec. II B, the OECC increases when widening the flange, and decreases when reducing the proximity of the wall. These two effects occur simultaneously when varying the main tube width, and counteract one another to some extent. This interaction was proved in the results under conditions 2 and 3 of model E, which have a smaller range of variation than that of condition 1, when only the flange is changed. When the width of the main tube becomes wide enough, the effects of both the flange and the lateral wall on the OECC become constant. Accordingly, it can be concluded that the relationship of L and D in this formula is not affected significantly by varying the width of the main tube.

This study also derived an empirical expression [Eq. (4)] from the measurements of model G for predicting the OECC of a side branch with a neck, where the branch was treated as a cascaded tube. The expression has different parameters from Ingard's [Eq. (2)], which was derived for the Helmholtz resonator. To compare these two formulas, the data obtained in Sec. II D were reprocessed by treating the branch as a Helmholtz resonator. Figure 12 shows the matched OECCs obtained from the resonator-treatment (indicated by an open circle), and the OECCs predicted from Ingard's formula (broken line), and our Eq. (4) (solid line). Unlike the cascaded-tube treatment (shown by an asterisk), the OECCs from the resonator-treatment at first decrease and then, for $D_N > 0.5$, increase. This is also the point at which higher-frequency troughs were observed in the transfer functions. Therefore the following discussion is limited to the region where the neck diameter D_N is smaller than 0.5. In this limited region, the matched OECCs (open circle) are consistent with those estimated using Ingard's formula [Eq. (2)] within 2%, and within 15% for our formula [Eq. (4)]. This shows that Ingard's formula gives more accurate estimates than our formula when the branch can be treated as a Helmholtz resonator. However, one can see in Fig. 12 that our formula can offer a good prediction for the more general case. Therefore we conclude that our formula is better in general for the end correction at an abrupt area transition of the vocal tract.

B. The OECC for side branches within the vocal tract

The morphologies of side branches in the vocal tract were investigated by the authors using magnetic resonance imaging (MRI) (Dang *et al.*, 1994; Dang and Honda, 1996c, 1997). In this section we combine vocal tract data with the OECC estimates derived above to arrive at a range of OECCs appropriate for the branches within the vocal tract.

The nasal tract is the largest branch occurring in the vocal tract. When the velum is lowered, an abrupt area transition of the velopharyngeal port occurs on both the oral side and the nasal side as shown in Fig. 1. On the oral side, the geometry is most similar to model E, where the side branch is considered equivalent to the entire nasal tract. Thus the posterior wall of the pharynx, which runs continuously from the ''main tract'' into the ''side branch,'' would be predicted to enhance the radiation from the open end of the nasal tract. According to our measurements from model E, an OECC greater than 0.8 is required to compensate for the open end radiation.

On the nasal side, the geometry surrounding the velopharyngeal port shows features of both model F and model E, i.e., there is a limited distance (corresponding to L) between the open end and a wall of the nasal tract, and this wall is also continuous with the main tract (see Fig. 1). According to Peters *et al.* (1993), the OECC for the open end of the nasal side is smaller than that estimated by the models, because of its horn-shaped edge. In contrast, the posterior wall of the nasopharynx enhances the radiation reaction. Since these two effects are expected to counteract each other to some extent, the OECC of the open end on the nasal side can be approximated using model F. According to our observations (Dang *et al.*, 1994), the distance L from the open end to the ceiling of the nasopharynx was approximately 1.5 cm for nasal sounds, averaging over four subjects. During nasal consonants, the area of the velopharyngeal port is typically about 1.7 cm^2 on the nasal side, and thus the equivalent diameter (D) is about 1.47 cm. An OECC of about 0.35 is predicted using Eq. (3) for an average value. In the transition from a nasal consonant to a nasalized vowel, the area of the velopharyngeal port decreases and the edge of the port gets sharper. In this case, the OECC is expected to increase. For example, when the area of the port is reduced to 0.5 cm^2, the OECC increases to 0.54. The end radiation at both sides of the velopharyngeal port can lower the first nasal formant to some extent. This may explain the fact that the first nasal formant in speech sounds is lower than that in morphology-based synthetic sounds. The discrepancy may be partly due to the OECCs for the branches, in addition to the other acoustic effects of the paranasal sinuses reported previously (Dang *et al.*, 1994; Dang and Honda, 1996c).

In the case of the paranasal sinuses, morphological data of the ostia are available only for the maxillary sinuses (Dang *et al.*, 1994; Dang and Honda, 1996c). The geometry of the nasal side of the ostia is similar to model F. According to our measurements (Dang *et al.*, 1994), the diameter of the

ostia was about 0.38 cm, and the distance from the ostium opening to the opposite wall was about 0.3 cm. The OECC of the ostia on the tract side was predicted to be about 0.28 using Eq. (3). However, the OECC for the cavity side should be about 0.8 since the narrow neck opens to a relatively large cavity.

The geometry of the piriform fossa resembles model E, because the posterior and lateral walls of the pharynx enhance the radiation of the fossa end. However, model E is too simple to account for the geometrical complexity near the open end of the piriform fossa. A detailed discussion is available elsewhere (Dang and Honda, 1996c, 1997; Dang *et al.*, 1996).

Besides the side branches, there are three major abrupt area transitions along the vocal tract: the outlet of the larynx, the region around the epiglottis, and the area between the teeth (the lips are not discussed here because they open to a free field). The abrupt area transition at the epiglottis is obvious for front vowels such as /i/ and /u/, but not evident for back vowels such as /a/. Since front vowels have a relatively large pharynx, the effect of the abrupt area transition in this region is small. In the boundary of the laryngeal and pharyngeal tubes, the ratio of the radii of the larynx's outlet to the pharynx varies with vowels, and ranges from 0.28 to 0.60 for English vowels (Story and Titze, 1996). The OECC based on formula (4) ranges from 0.0 to 0.43, which hardly contributes to the acoustic characteristics of the vocal tract. An end correction of the opening at the teeth can be of more importance than that of the others, since the constriction formed by the teeth is usually short. Empirical formula (4) can be used to estimate the OECC in this case.

Applications of these empirical formulas from the present study have been discussed with regard to the vocal tract. Since details of the vocal tract shape are not completely known and the mean flow within the vocal tract changes during a dynamic articulation, some additional conditions possibly remain to be discovered.

ACKNOWLEDGMENTS

The majority of this study was carried out while the second author was an Invited Researcher, and the third author was a student intern, at ATR. The authors would like to express appreciation to Seiji Adachi and Hani Yehia for their helpful discussions in the analysis of the experimental data. The authors would also like to thank Anders Löfqvist and four anonymous reviewers for comments on previous versions of the manuscript.

[1]The Helmholtz number kr is also a factor affecting the OECC, where k is the wave number and r is the equivalent radius of the open end of the branch. In all of the cases discussed here, trough frequencies ranged from 1842 to 1921 Hz and the equivalent radii were 0.58–0.82 cm (see Tables II–IV). The Helmholtz number kr ranged from 0.20 to 0.29 for the changes in the geometry. According to previous studies (Levine and Schwinger, 1948; Ando, 1969; Peters *et al.*, 1993), the OECC can be considered to be approximately independent of the Helmholtz number for this range of 0.20–0.29.

Ando, Y. (**1969**). ''On the sound radiation from semi-infinite circular pipe of the certain wall thickness,'' Acustica **22**, 219–225.

Caussé, R., Kergomard, J., and Lurton, X. (**1984**). ''Input impedance of brass musical instruments—Comparison between experiment and numerical model,'' J. Acoust. Soc. Am. **75**, 241–254.

Dang, J., and Honda, K. (**1996a**). ''A new method for measuring antiresonance details of the vocal tract transmission characteristics—An experimental study of acoustic tubes,'' J. Acoust. Soc. Jpn. (E) **17**, 93–96.

Dang, J., and Honda, K. (**1996b**). ''Acoustical modeling of the vocal tract based on morphological reality: Incorporation of the paranasal sinuses and the piriform fossa,'' Proceedings of the 1st ESCA Tutorial and Research Workshop on Speech Production Modeling: from Control Strategies to Acoustics & 4th Speech Production Seminar: Models and Data, Autrans, France, pp. 49–52.

Dang, J., and Honda, K. (**1996c**). ''Acoustic characteristics of the human paranasal sinuses derived from transmission characteristic measurement and morphological observation,'' J. Acoust. Soc. Am. **100**, 3374–3383.

Dang, J., and Honda, K. (**1997**). ''Acoustic characteristics of the piriform fossa in models and humans,'' J. Acoust. Soc. Am. **101**, 456–465.

Dang, J., Honda, K., and Suzuki, H. (**1994**). ''Morphological and acoustical analysis of the nasal and the paranasal cavities,'' J. Acoust. Soc. Am. **96**, 2088–2100.

Dang, J., Kawanishi, Y., and Shadle, C. (**1996**). ''Estimation of correction coefficient and location of the radiating end of the piriform fossa,'' Proceedings of the Spring Meeting of Acoust. Soc. Jpn. (in Japanese), pp. 287 and 288.

El-Raheb, M., and Wagner, P. (**1980**). ''Acoustic propagation in rigid sharp bends and branches,'' J. Acoust. Soc. Am. **67**, 1914–1923.

Fant, G. (**1970**). *Acoustic Theory of Speech Production* (Mouton, The Hague), 2nd ed.

Flanagan, J. L. (**1972**). *Speech Analysis Synthesis and Perception* (Springer-Verlag, New York), 2nd ed.

Hall, D. E. (**1987**). *Basic Acoustics* (Wiley, New York).

Ingard, U. (**1953**). ''On the theory and design of acoustic resonators,'' J. Acoust. Soc. Am. **25**, 1037–1061.

Koyama, T. (**1966**). ''Experimental study on the resonance of paranasal sinus,'' J. Otolaryngol. Japan **69**, 1177–1191 (in Japanese).

Levine, H., and Schwinger, J. (**1948**). ''On the radiation of the sound from an unflanged circular pipe,'' Phys. Rev. **73**, 383–406.

Masuda, S. (**1992**). ''Role of the maxillary sinus as a resonant cavity,'' J. Otolaryngol. Japan **95**, 71–80 (in Japanese).

Nomura, Y., Yamamura, I., and Inawashiro, S. (**1960**). ''On the acoustic radiation from a flanged circular pipe,'' J. Phys. Soc. Jpn. **15**, 510–517.

Peters, M., Hirschberg, A., Reijnen, A., and Wijnands, A. (**1993**). ''Damping and reflection coefficient measurements for an open pipe at low Mach and low Helmholtz numbers,'' J. Fluid Mech. **256**, 499–534.

Rayleigh, B. (**1945**). *Theory of Sound* (Dover, New York).

Story, B., and Titze, I. (**1996**). ''Vocal tract area function from magnetic resonance imaging,'' J. Acoust. Soc. Am. **100**, 535–554.

Sundberg, J. (**1974**). ''Articulatory interpretation of the singing formants,'' J. Acoust. Soc. Am. **55**, 838–844.

A microcosm of musical expression. I. Quantitative analysis of pianists' timing in the initial measures of Chopin's Etude in E major

Bruno H. Repp
Haskins Laboratories, 270 Crown Street, New Haven, Connecticut 06511-6695

(Received 16 December 1997; accepted for publication 30 April 1998)

Patterns of expressive timing were measured in bars 1–5 of 115 commercially recorded performances of Chopin's Etude in E major, op. 10, No. 3. These patterns were subjected to principal components analysis, which suggested at least four independent ''timing strategies'': (1) major ritards at the ends of melodic gestures; (2) acceleration within some of these gestures, without final ritards; (3) extreme lengthening of the initial downbeat; and (4) ritards between as well as within melodic gestures. Strategies 1 and 4 respond in different ways to the melodic-rhythmic grouping structure of the music, and strategy 3 merely represents a local emphasis. Strategy 2 is the one most difficult to rationalize; it does not seem to represent an alternative structural interpretation of the music but rather an alternative gestural shaping. Each individual pianist's timing pattern could be described as a weighted combination of these four strategies plus idiosyncratic variation. A wide variety of combinations was represented, and no two individual patterns were exactly the same. In addition, there was a wide range of basic tempi and of degrees of tempo modulation. There were no strong relationships between any of these variables and sociocultural characteristics of the artists, although some weak trends were observed.
[S0001-4966(98)03908-3]

PACS numbers: 43.75.St, 43.75.Mn [WJS]

INTRODUCTION

There is enormous variety in music performance, especially in solo playing where individuality can be given free rein. No two performances of the same work are exactly alike, and this is true even for renditions by the same artist. A musician must exert control over a number of expressive parameters, each of which is continuously variable over time, which results in a combinatorial explosion of possibilities. Yet there are significant constraints on this variety. Infinitely many conceivable performances are never realized because they would be considered bizarre and ''unmusical'' by artists and their audiences. Actual performances thus are only a small subset of the gamut of possible performances. Their variety is hemmed in both by notated instructions (in the Western standard repertoire) and by tacit rules and conventions that define what expressive actions are acceptable, appropriate, and aesthetically pleasing within a given musical structure. Within these constraints (which may vary as a function of style, historical period, and performance tradition), some performances are similar to each other while others are very different; some are conventional or typical (i.e., similar to many others) while others are innovative and original; and some may strike a listener as deficient or crude while others seem sublime.

Judgments about the relative similarity, typicality, and especially the quality of performances are often made by music lovers, critics, or adjudicators on the basis of their auditory impressions, memories, and accumulated knowledge. These judgments may often be very accurate, but they are subject to limits of perception, memory, and attention, and they exhibit considerable individual differences. The goal of objective performance analysis (Seashore, 1936) is to determine the extent to which performances are *actually* similar or typical. (Their quality remains a matter of human aesthetic judgment.) However, even with present-day methods this is a daunting task. Performances not only differ along many dimensions (tempo, timing, dynamics, tone quality, texture, articulation, intonation, etc.) but also vary in most of these dimensions as the music progresses, so that similarity, typicality, and quality change as a function of time: Two performances may be very similar at the beginning but radically different later on, and any single performance may start out conventionally but then continue in a highly original fashion, or it may start brilliantly and then become dull. It would be exceedingly complex and time-consuming to measure and describe all these differences exactly and exhaustively. An objective characterization of performance similarities and differences can be attempted only if the investigation is severely restricted in terms of the length of the music and of the expressive parameters considered. Nevertheless, such a selective analysis can provide interesting information about both general principles and individual strategies underlying expressive performance, information that cannot be obtained easily, if at all, through listening alone.

This study is concerned with acoustic recordings of piano music. This in itself limits the expressive parameters that can be analyzed. Due to its percussive mechanism, the piano only allows expressive variation in timing, dynamics, and articulation. Of these dimensions, horizontal (successive tone onset) timing can be measured with some accuracy in acoustic recordings, but the small intervals involved in vertical timing (the asynchronies among tones in chords) are difficult

to recover. Horizontal dynamics (the peak intensities of successive tones or chords) can be measured, but vertical dynamics (the intensities of the individual tones constituting chords) cannot, at least not with existing methods. Articulation (the degree of separation or overlap of successive tones, which includes the effects of pedaling) is extremely difficult to measure, especially where overlap is concerned. Thus a scientific study of acoustic piano recordings is essentially restricted to measurements of horizontal timing and dynamics. Although more complete and more precise measurements could be obtained from recordings made on a MIDI piano, acoustic recordings have the unique advantage of representing the very best artists and a time span of many decades.

Most previous analyses of acoustically recorded keyboard performances (Povel, 1977; Cook, 1987; Repp, 1990, 1992, 1997a, 1997b) were concerned with timing only. Only Gabrielsson (1987) reported dynamic measurements as well. These earlier studies also had relatively small samples of performances. The largest sample, a collection of 28 recordings of Robert Schumann's ''Träumerei,'' was analyzed by Repp (1992). It became clear from that study and from subsequent investigations (Repp, 1997b, and unpublished timing data obtained from 19 performances of Chopin's Polonaise-Fantasy, op. 61) that, with regard to timing at least, there is an inverse relationship between the length of a musical passage and the diversity of individual performances, as measured by correlational statistics. This is so because all artists tend to respond to major structural breaks in the music by slowing their tempo (see Todd, 1985), and the more such structural boundaries there are in a piece of music, the more similar the overall timing patterns of different artists become. However, within a short passage comprising a single phrase, a considerable variety of expressive detail may be observed, presumably because there are fewer and/or weaker structural imperatives at such a local level. If the passage contains structural ambiguities, some of the expressive variety may be due to different interpretations of the detailed musical structure, and in that case performances by different artists may be expected to fall into clusters or categories, each representing a different interpretation. Alternatively or in addition, however, there may be different ways of expressing the same structure, for example, by varying the allocation of emphasis within the passage or by using different temporal or dynamic shapes to give the music a particular character or to create contrast. While some of this expressive variation may be idiosyncratic, distinct expressive strategies shared by several artists can be revealed by statistical analysis of performance measurements. In addition to the primary question of whether such strategies are categorically distinct or form a continuum of expressive possibilities, a secondary question of interest was whether they are related in any way to sociocultural characteristics of the artists, such as their year of birth, nationality, age at the time of performance, or gender.

Such analyses are really informative only when the sample of performances analyzed is as large as possible, so that many different artists and almost all reasonable ways of playing a musical passage are represented. By focusing on the initial measures of a popular composition by Chopin, it

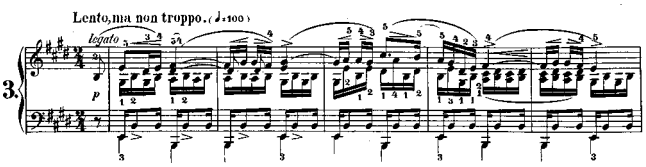

FIG. 1. The initial 5 measures of Chopin's Etude in E major, op. 10, No. 3, copied from the Herrmann Scholtz edition (Leipzig: Peters, 1879).

was possible to assemble 115 different recordings for the present study. Even though some extant recordings were not included, this was as large a sample as could be obtained from a major archive of recorded piano music, and it seemed sufficient for most analyses attempted here. Only questions concerning correlations with artists' sociocultural characteristics really require a much larger sample to receive conclusive answers, and since such large numbers of recordings, especially from earlier decades of this century, simply do not exist, these analyses will have to remain tentative.

The results of this investigation will be reported in three successive articles. The present article, Part I, deals with expressive timing only. Part II (Repp, submitted) will examine expressive dynamics and the relationship between timing and dynamics. Finally, Part III (Repp, in preparation) will investigate the relationship between the objectively measured expressive patterns and aesthetic evaluations of the performances.

I. METHOD

A. The music

The musical passage chosen was the beginning of Chopin's Etude in E major, op. 10, No. 3. The score is shown in Fig. 1.[1] The onset of the second beat of bar 5 defines the end of the excerpt as analyzed here.

There were several reasons for selecting this particular passage. First, it represents one of Chopin's most beautiful melodies (the composer himself apparently thought so; see Eigeldinger, 1986, p. 68), which challenges pianists to do it justice and invites large deviations from exact timing in the service of expression. Second, due to the popularity of the Chopin Etudes in general and the E-major Etude in particular, there are many recordings in existence. Third, the passage has a very slow tempo and, apart from the initial eighth-note upbeat, there are note onsets at every sixteenth-note subdivision of the beat, properties that make it convenient to measure and analyze expressive timing. Finally, the same excerpt was employed in a series of recent studies concerned with timing perception and aesthetic judgment (Repp, 1997a, 1998a, 1998b, 1998c, in press). One of them (Repp, 1997a) included an analysis of the timing of 15 performances, which are also included in the present sample. The results of a principal components analysis indicated that there are at least three quite different ways of timing this passage, although the second of these patterns was represented by only three pianists, and the third by only one. These preliminary findings provided the stimulus to investigate a much larger number of recordings in order to determine more precisely the nature and prevalence of these alternative timing patterns.

B. The recordings

To supplement the 15 recordings whose timing measurements were already available (Repp, 1997a), 102 additional excerpts, copied from LPs and CDs onto digital audio tape, were obtained from the International Piano Archives (IPA) at the University of Maryland. The statistical analysis of the timing measurements later revealed that there were two duplicates among the IPA excerpts (see below), so that there were 115 different performances altogether.[2] A complete list of artists' names, record labels, and recording dates is provided in the Appendix. Seven pianists are represented by two recordings each (Arrau, Ashkenazy, Cortot, Cziffra, Egorov, Horowitz, and Slenczynska). Of the 108 artists, 26 (24%) are female. Many nationalities are represented:[3] American (18), Argentinian (2), Australian (5), Austrian (2), Brazilian (2), British (5), Bulgarian (1), Canadian (3), Chilean (3), Chinese (1), Cuban (1), Czech (1), French (12), German (5), Greek (1), Hungarian (9), Italian (3), Japanese (4), Philippine (1), Polish (9), Portuguese (1), Rumanian (1), Russian/Soviet (21), Spanish (2), Turkish (1), and Uruguayan (1). The recording dates span 68 years, from 1927 to 1995.

C. Measurement procedure

The IPA recordings were input as analog signals from the digital tape to a Macintosh 660AV computer, sampled at a rate of 20.055 kHz, and stored as separate files on a hard disk. A digital waveform editor (SOUNDEDIT16) was used to display the waveforms and to locate and mark event onsets, relying on both visual and auditory cues. An ''event'' comprised all tones with nominally simultaneous onsets, so that the excerpt (Fig. 1) contained 38 event onsets delimiting 37 inter-onset intervals (IOIs). In cases of detectable asynchronies within an event, the onset of the highest tone was marked.[4] Naturally, there was some measurement error, but it was considered negligible for the purposes of this study.

Inter-onset interval durations (in milliseconds) were obtained by calculating the differences between successive event onset times. For reasons explained below, the initial upbeat IOI (corresponding to an eighth-note interval in the score) was analyzed separately from the subsequent sixteenth-note IOIs. Those 36 IOIs constituted the timing pattern or timing profile of a performance. Since these IOIs were all nominally equal, the within-performance variation in IOI duration was almost entirely due to intended tempo modulations in the service of expression. (However, a small part of the observed variability must have been due to measurement error and pianists' limits of motor control.) Throughout this article, expressive timing will be depicted and discussed in terms of IOI durations rather than in terms of local tempo (reciprocals of IOI durations, an alternative preferred by some authors).

D. Principal components analysis

To determine how many truly different types of timing pattern were represented in the sample, the 117 timing profiles were subjected to principal components analysis (PCA). This technique decomposes the many individual timing profiles, which exhibit various degrees of pairwise similarity, into a small number of completely unrelated profiles (the principal components or PCs) and associated weights, so that each individual timing profile can be approximated by a weighted sum of the PCs. Each PC may be considered an independent ''timing strategy.'' The IOI durations are converted into standard scores (mean of zero, standard deviation of one) before analysis, and the PC profiles are likewise expressed in terms of standard scores.

The PCs are determined automatically such that the first PC accounts for the largest amount of variance among the timing profiles, the second PC for the largest amount of the remaining variance, and so on. The first PC is in fact equivalent to the average of all the timing profiles, the second PC is the average of the residuals (after the first PC has been subtracted from the data), and so on. The data can be uniquely and exhaustively described by **m** PCs where **m** is the smaller dimension of the data matrix (36 in the present case). If the individual timing profiles were all quite different from each other, then each of the 36 PCs would account for about 1/36 (2.8%) of the variance. However, if there are significant commonalities among the timing profiles, the first few PCs will account for most of the variance. These PCs may then be considered ''significant,'' and the remaining unexplained variance may be attributed to individual artists' idiosyncrasies and noise in the data. To decide how many PCs are significant, the investigator will first look for a clear discontinuity in a plot of the amounts of variance accounted for by successive PCs. If no such discontinuity is evident, those PCs are usually considered significant that account for more than 1/**m** of the variance (2.8% in the present case). The interpretability of the PCs may also play a role in the decision.

If all timing profiles are highly similar to each other, only a single significant PC will emerge, indicating that there is one basic timing pattern, with the remaining variance being due to idiosyncratic deviations from this standard. However, if the data represent several different types of timing profiles, this will result in the emergence of several significant PCs. In that case, a Varimax rotation often facilitates interpretation of the PCs. This rotation modifies the original PCs in order to maximize the number of timing profiles that are similar to a particular PC (''pure'' cases) and simultaneously minimize the number of those that are equally similar to several PCs (''mixed'' cases). The correlation of an individual timing profile with a PC profile is called its ''loading'' on that PC.

II. RESULTS AND DISCUSSION

A. Three aspects of expressive timing

The sequence of IOIs that constitutes a timing profile subsumes three largely independent aspects of expressive timing. The first of these is the average duration of the IOIs, which is inversely related to the *basic tempo*. In performances with highly modulated tempo, such as the present ones, the reciprocal of the average IOI is not necessarily the best estimate of the basic tempo (see below, but also Repp, 1994b), but it probably reflects differences in basic tempo among performances quite accurately. The second aspect of

timing is the within-performance variability of the (nominally equal) IOI durations, as measured by their standard deviation. The standard deviation will tend to increase with the average IOI duration (see below), but the ratio of these two magnitudes (the coefficient of variation, a measure of *relative modulation depth*) may be more nearly independent of basic tempo (though see Desain and Honing, 1994; Repp, 1994a, 1995b). The third aspect, which is of greatest interest here, is the pattern of IOI durations or the *profile shape*. The PCA is insensitive to differences in basic tempo and relative modulation depth because it converts the IOI durations to standard scores; thus it deals with differences in profile shape only. Similarly, the correlation between two profiles represents only the similarity in profile shape. Therefore, basic tempo and relative modulation depth as well as the timing of the initial upbeat will be considered separately before the PCA of the timing profiles is discussed.

B. Basic tempo

In an earlier empirical study on the problem of estimating the basic tempo of an expressively timed performance, Repp (1994b) found that musically trained listeners' metronome settings matched the reciprocal of the average IOI. However, this result was obtained with performances of a single musical excerpt (the initial 8 measures of Schumann's ''Träumerei''), and its generality is uncertain. In the case of the present excerpt, there were reasons to believe that the basic tempo is underestimated by the reciprocal of the average IOI (see below; also Repp, 1998c). Therefore two alternative estimates were considered as well.[5] One was based on the median rather than the mean IOI, in order to reduce the influence of very long IOIs. (The distribution of IOI durations was skewed to the left.) The other estimate was based on the average duration of eight IOIs (the sixth and seventh IOIs in bars 1–4) that, typically, were the shortest IOIs in a performance. They all represent the timing of the accompaniment during sustained melody tones and thus provide a measure of the baseline (or maximal) tempo. The initial eighth-note upbeat IOI was excluded from all estimates. Each tempo estimate (expressed in quarter-note beats per minute) was obtained by dividing 15 000 (the number of milliseconds in a minute divided by the number of sixteenth notes in a quarter note) by the relevant IOI parameter (mean, median, or minimal mean). Frequency histograms of the three kinds of tempo estimate for the 117 performances are shown in Fig. 2.

As expected, the median-based method yielded slightly higher estimates than the mean-based method, indicating that the within-performance distributions of IOI durations were skewed towards short values. Baseline tempo estimates naturally were even faster. For all estimates, however, the distribution of tempi in the performance sample was roughly normal, despite one abnormally fast performance (Varsi). Deviations from normality (Kolmogorov–Smirnov test, Lilliefors option) were nonsignificant in all three cases. Tempi were most often between 25 and 32 (mean), 27 and 34 (median), or 31 and 38 (baseline) beats per minute.[6] It is noteworthy that these tempi are much slower than the tempo indication found in most Chopin editions, which is 100

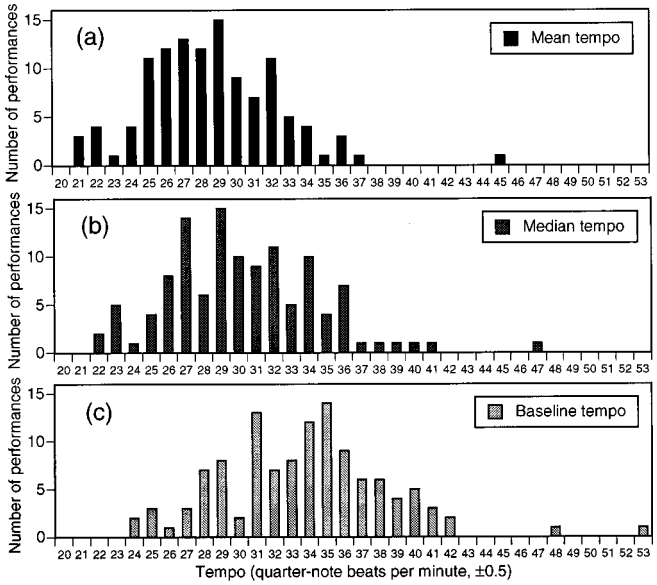

FIG. 2. Frequency distributions of (a) mean tempi, (b) median tempi, and (c) baseline tempi of the 117 performances.

eighth notes (or 50 quarter notes) per minute. (The tempo indication in the German edition shown in Fig. 1 is twice as fast and must be a printer's error.) The fastest performances, after Varsi's, were those by Haase, Renard, Fou Ts'ong, Horowitz-1972, and Paderewski, whereas the slowest ones were those by Katz, Kyriakou, Niedzielski, Pokorna, Goldsand, and Zarankin. The median tempi of all performances are listed in the Appendix.

C. Relative modulation depth

As a measure of absolute modulation depth, the standard deviation of the sixteenth-note IOIs was calculated for each performance. As expected, there was a significant correlation between the average IOI duration and the IOI standard deviation of individual performances ($r=0.43$, $p<0.001$): The absolute magnitude of the timing variation tended to be larger in slow performances. Therefore a measure of relative modulation depth, the coefficient of variation, was calculated for each performance by dividing the standard deviation by the mean IOI. These coefficients did not vary significantly with the mean IOI ($r=-0.17$, $p<0.10$), although the negative correlation almost reached significance, suggesting a slight compression of relative modulation depth at slow tempi, perhaps due to an aesthetic upper limit on the absolute magnitude of timing modulations. The coefficients of variation of the 115 performances ranged from 0.1 to 0.3. The most strongly modulated performances were those by Fou Ts'ong, Pennario, Koyama, Licad, Horowitz-1972, Crown, Sauer, and Koczalski, whereas the least modulated ones were those by Anievas, Székely, Penneys, Murdoch, Duchâble, Iturbi, Egorov-1979, Lortie, Solomon, and Magaloff.

D. The initial upbeat

The initial eighth-note upbeat was excluded from the PCA because its long duration would have had a disproportionate influence on the correlations among the timing pro-

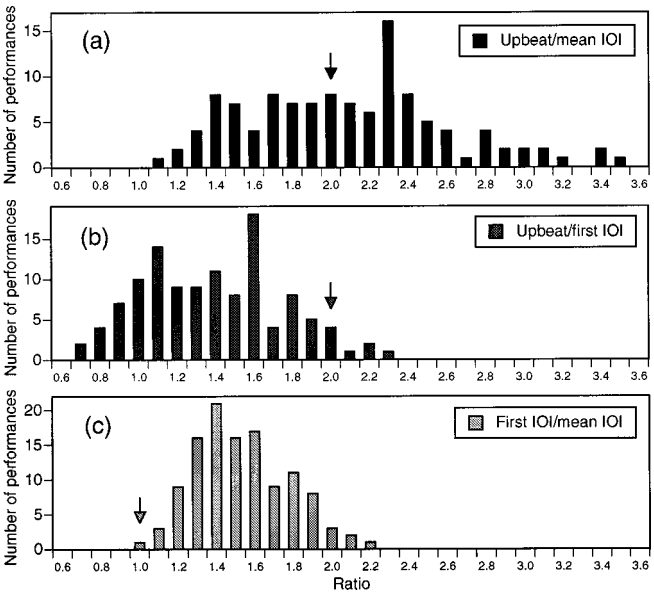

FIG. 3. Frequency distributions of three ratios: (a) upbeat IOI divided by mean sixteenth-note IOI, (b) upbeat IOI divided by first sixteenth-note IOI, (c) first sixteenth-note IOI divided by mean sixteenth-note IOI. Arrows indicate nominal (score-based) ratios.

files. Although this problem could have been circumvented by dividing the upbeat IOI duration in half, there was also enormous individual variation in the duration of this IOI, and quite a few pianists played such a short upbeat as to suggest a sixteenth rather than an eighth note. If some of them actually intended to play a sixteenth note (for whatever reason), division by two would have been inappropriate. Since the pianists' intentions were not known, it seemed best to analyze the upbeat IOI separately.

Not surprisingly, the duration of the upbeat IOI covaried with the average duration of the following 36 sixteenth-note IOIs ($r=0.59$, $p<0.001$). This means that the upbeat duration was not independent of the basic tempo of a performance. A frequency histogram of the ratios between upbeat duration and mean IOI duration is presented in Fig. 3(a). The nominal ratio (arrow) was 2, assuming the upbeat was intended as an eighth note. The most frequently observed ratio was a little higher, 2.3, but the range of values was very wide, extending from 1.1 to 3.5. The ratios at the low end of the distribution, with a small peak at 1.4, could be understood as representing sixteenth-note upbeats. (This is what they sounded like to the author.) However, the broad distribution did not deviate significantly from normality.

The upbeat duration may also be considered in relation to the duration of the sixteenth-note IOI on the immediately following downbeat (the ''first IOI''). Figure 3(b) shows the distribution of the ratios between these two quantities. Here the nominal ratio was 2 also, but nearly all values were smaller, with quite a few falling below 1, the nominal ratio of two sixteenth notes. This was due to the fact that the first IOI tended to be lengthened considerably in relation to the mean IOI. The distribution of a third ratio, the first IOI divided by the mean IOI, is shown in Fig. 3(c). Here the nominal ratio is 1, but the peak of the distribution is at 1.4, with a range from 1.0 to 2.2. Clearly, the upbeat IOI, although it was often lengthened relative to the mean IOI [Fig. 3(a)], was not lengthened as much or as consistently as the first IOI [Fig. 3(c)]. Therefore the peak at a ratio of 1.6 in Fig. 3(b) may be considered representative of pianists' intention to play the upbeat as an eighth note. However, the values at and below the smaller secondary peak at 1.1 (the deviation from normality approached significance, $p<0.07$) suggest that some pianists treated the upbeat intentionally or effectively as a sixteenth note. The artists most representative of this strategy were Varsi, Koczalski, Cziffra-1954, Larrocha, Novaes, Janis, Haase, and Hesse-Bukowska. (Note that five of them are female.) Pianists at the other extreme, who tended to play very elongated upbeats, included Vásáry, Katz, Volondat, Wild, Timofeyeva, Ashkenazy-1974, Magaloff, and Arrau-1930 (only one of whom is female). Gender differences will be discussed in a later section.

E. The grand average timing profile

The timing profiles without the initial upbeat, representing a 117×36 data matrix, were subjected to PCA. The first PC accounted for 61.4% of the variance, which indicated considerable commonality among the performances but left room for alternative patterns. The following six PCs accounted only for 6.2%, 4.5%, 3.7%, 2.8%, 2.5%, and 2.2% of the variance, respectively. There was no clear discontinuity in this series, but the second, third, and fourth PCs exceeded the significance criterion of 2.8% (explained above) and the fifth matched it precisely. Therefore a four- or five-component solution seemed appropriate. Both solutions were compared after Varimax rotation and were found to be quite similar: The first four rotated PCs correlated 0.94, 0.99, 0.98, and 0.92, respectively, between the two solutions. Since the fifth PC was not strongly representative of any individual performances, the four-component solution was preferred. It accounted for 75.9% of the variance in the data. The remaining 24.1% were thus considered unexplained and represented a combination of artists' idiosyncratic intentions, lack of timing control, and measurement error.

The first unrotated PC (UPC-I) represents the average of all timing profiles in standardized form. This grand average profile is shown in Fig. 4. A simplified, computer-generated musical score is shown above the graph for guidance. (The second half of bar 5 has been replaced with a chord, to save space.) Filled circles represent IOIs initiated by melody (soprano) tones, whereas open circles represent IOIs initiated by accompaniment (mezzo/alto) tones during sustained melody tones. In this excerpt, all expressive timing may be considered as lengthening relative to a baseline defined by the IOIs in positions 6 and 7 in each bar, which were used to estimate the baseline tempo [Fig. 2(c)]: These IOIs are the shortest and fall almost on a straight horizontal line in the grand average profile. Regarded in this way, the UPC-I profile represents the average magnitudes of various lengthening tendencies in the sample of performances. The initial downbeat in bar 1 clearly was elongated most. The melody is divided into five or six gestures (or segments, or rhythmic groups, the connected filled circles in Fig. 4), each ending with the onset of a long note that also coincides with a change in harmony. A ritard can be seen at the end of each of these

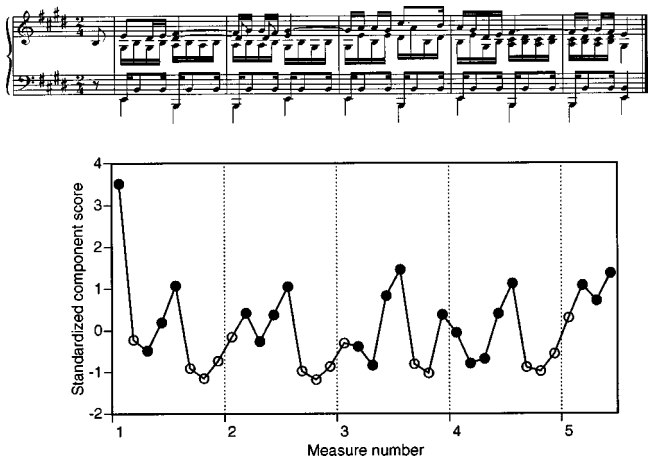

FIG. 4. Standardized grand average timing profile (first unrotated principal component scores, UPC-I). The musical score (without slurs and expression marks, and with a chord substituted for the second half of bar 5) is shown above for guidance. Filled circles represent IOIs initiated by melody tones, open circles IOIs initiated by accompaniment tones.

segments, in sixteenth-note positions 4 and 5 of each bar. (It is doubtful whether the initial two melody notes, upbeat and first downbeat, should be considered a separate gesture, but the great lengthening of the initial downbeat is consistent with such an interpretation.) The melodic segment in bar 4 starts earlier than the others (in position 8 of bar 3) and begins with an acceleration; a small initial lengthening can also be seen in other melodic gestures. Finally, there is also a tendency towards ritards in the accompaniment preceding melodic segments, on the first downbeats of bars 2, 3, and especially 5.

These lengthening tendencies clearly articulate the musical structure, most obviously the melodic segmentation and the alternation of melody and accompaniment, though harmonic change and meter may also play a role. The lingering in position 4 in each bar represents the commonly observed strategy of group-final lengthening (e.g., Povel, 1977; Todd, 1985; Repp, 1992), although it could also be understood as a delay preceding a harmonic change. The slightly greater lingering in position 5 may still be part of a group-final ritard, but it also serves to segregate the temporarily suspended melody from the continuing accompaniment, and it may further be due to the metrical strength of the position. The lengthening of the last IOI in bar 3 could represent group-initial lengthening, or an attempt to maintain continuity with the preceding melodic gesture (which culminates in the melodic peak), or a delay before a harmonic change, or even a momentary dwelling on the note that resolves the dissonance at the melodic peak. The ritards in the accompaniment may prepare the entry of a melodic gesture or segregate the accompaniment from the melody, but they also coincide with a metrically strong position. Thus, even though melodic grouping alone can explain most of the lengthening tendencies in this excerpt, it is more likely that they are a complex function of all structural features of the music.

The question now arises whether the UPC-I pattern is at all representative of individual performances, or whether it is merely a meaningless statistical conglomerate. Repp (1997a) has argued that the average timing profile of a large number

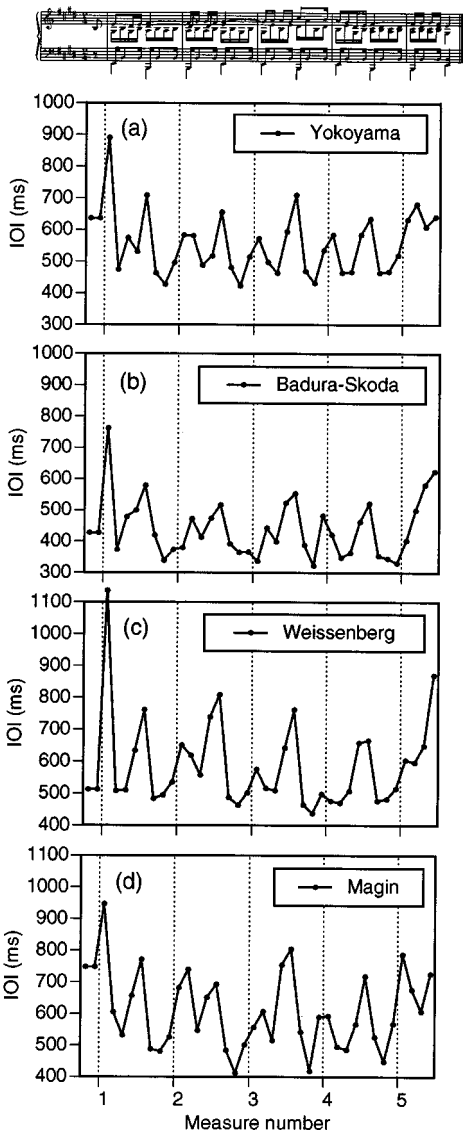

FIG. 5. Four individual timing profiles that correlated highly with the grand average profile (Fig. 4). Initial upbeats are included but shown as two successive sixteenth-note IOIs.

of performances should be regarded as typical and has shown that performances of student and amateur pianists tend to exhibit timing profiles that are highly similar to the grand average profile. The correlations of the present 115 individual timing profiles with the grand average profile (their UPC-I loadings) ranged from 0.94 to 0.31, with only 22 values falling below 0.70, which shows that most performances were fairly similar to the average, and some were highly similar. UPC-I thus may indeed be regarded as a common, typical, or conventional timing profile for this music, and the UPC-I loadings may be interpreted as indices of the typicality (or conventionality) of individual timing profiles. By this criterion, the most conventionally timed performances ($r > 0.9$) were those of Yokoyama, Badura-Skoda, Weissenberg, Magin, Pennario, Solomon, and Kilényi. (This is by no means a value judgment; for aesthetic evaluations, see Part III of this study.) The timing profiles of the first four of these pianists are shown in Fig. 5. The initial eighth-note upbeat durations have been included in these profiles, but for

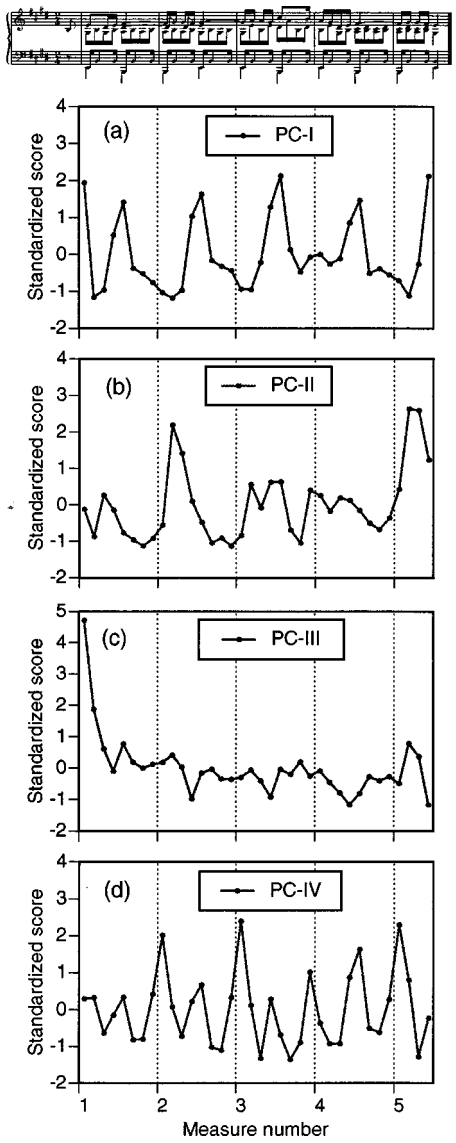

FIG. 6. Standardized scores of the first four rotated principal components.

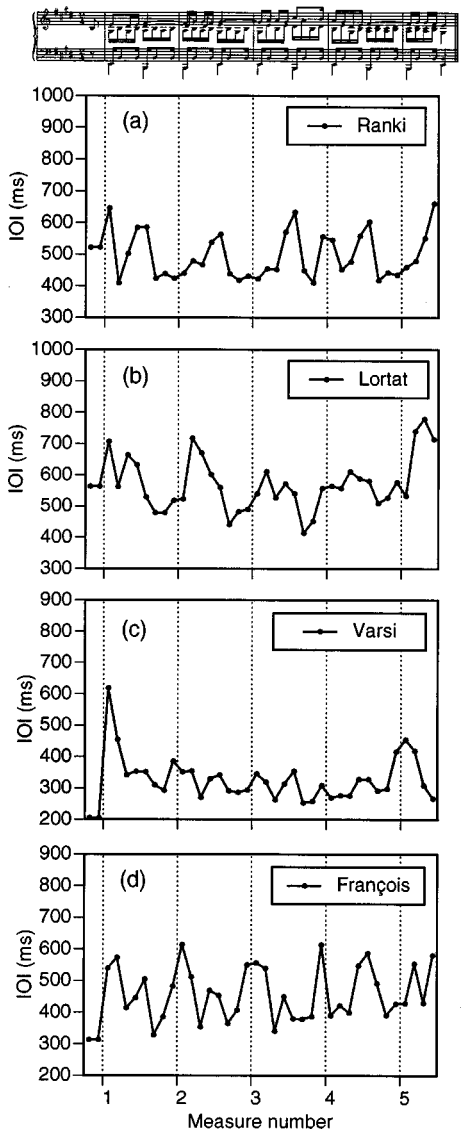

FIG. 7. Individual timing profiles that correlated highly with each of the PC profiles shown in Fig. 6.

graphical reasons they are shown as two successive sixteenth-note IOIs (whose sum constitutes the upbeat duration). The shape similarity of the four profiles to the average profile in Fig. 4 is indeed striking, and they are also fairly similar to each other, though by no means identical: There are individual differences in detail as well as in tempo and modulation depth (which, as pointed out earlier, do not affect correlations). The reader is invited to regard these profiles simply as visual patterns, as it is difficult to ''auralize'' them accurately. It also should be kept in mind that it is the sound that is paced by the timing, and the graphs reveal nothing about the sound (expressive dynamics, texture, etc.) of individual performances.

The most atypical or unconventional timing profiles ($r < 0.6$) were produced by Anda, Horowitz-1972, François, Cortot-1942, Cziffra-1981, Vásáry, Backhaus, Lortat, and Perlemuter; several of them will be presented in later figures. Several of these artists are indeed renowned for their individuality or even eccentricity, and it is interesting to see these reputations supported by objective analysis of such a short musical excerpt.

F. The rotated principal component profiles

To learn more about the different timing strategies of the artists in the sample, the Varimax-rotated PCs were examined. The four rotated PCs accounted for 31.3%, 17.1%, 16.5%, and 11% of the variance, respectively. Rotation does not guarantee the interpretability of the PCs or establish their psychological reality as independent timing strategies; this is a matter of theoretical conjecture and plausibility, as well as perhaps further empirical research. Also, the mathematical constraints of the rotation may introduce some distortions in the shapes of the PC profiles, so it is good to view real timing profiles alongside the statistically extracted ones. The four rotated PC profiles (referred to in the following as PC-I, PC-II, PC-III, and PC-IV) are plotted in Fig. 6, and timing profiles of individual performances loading highly on each

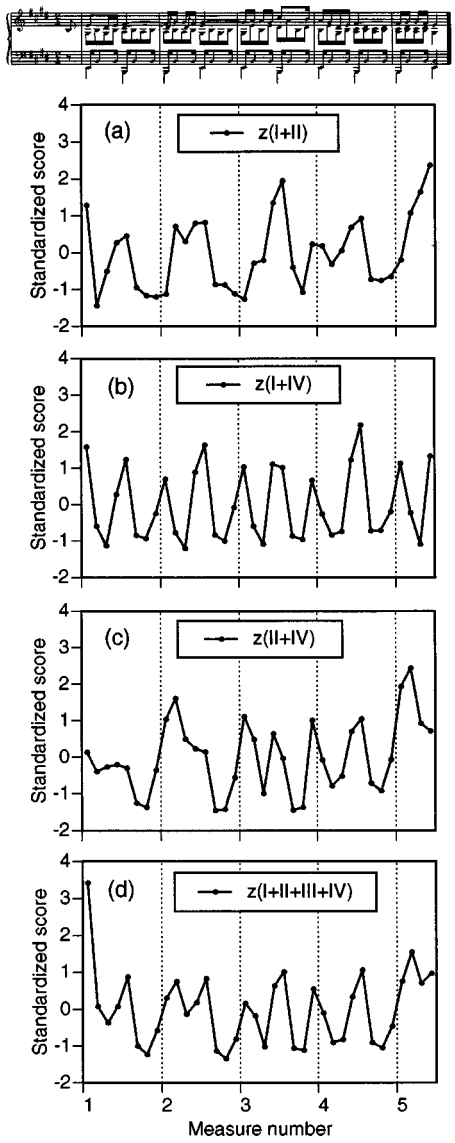

FIG. 8. Standardized scores of some equally weighted combinations of the four PCs.

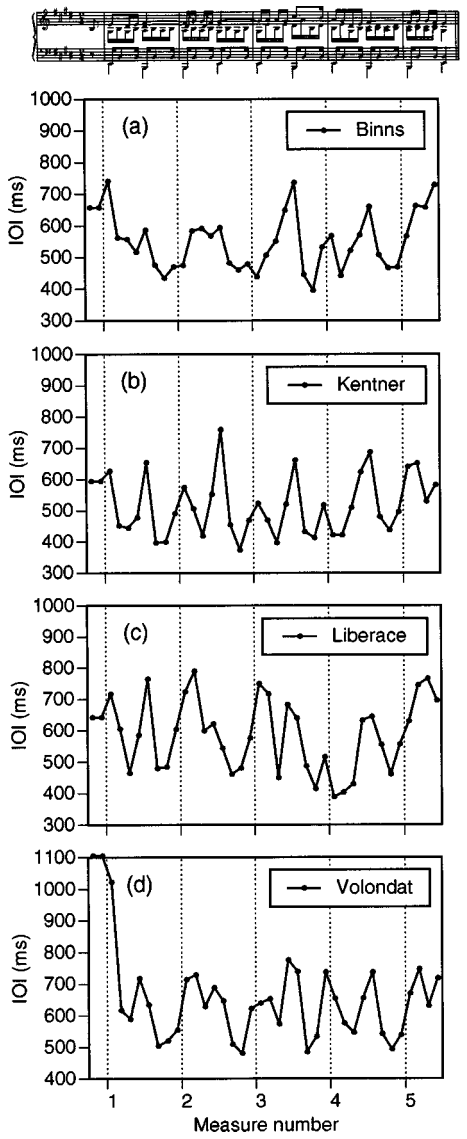

FIG. 9. Four ''hybrid'' timing profiles that correlated about equally with each of the PCs whose combinations are shown in Fig. 8.

PC are shown in Fig. 7. The PC loadings of all performances may be found in the Appendix.

PC-I [Fig. 6(a)] represents the most frequently employed timing strategy. It retains a significant similarity to UPC-I ($r=0.68$, $p<0.001$) and differs mainly in that it emphasizes within-segment ritards but de-emphasizes between-segment ritards and also the segment-initial lengthening at the end of bar 3, which show up strongly in PC-IV instead [Fig. 6(d)]. PC-I also has a long initial downbeat and a ritard during the final melodic gesture. The strategy it represents is mainly one of slowing down at the ends of melodic groups, though the lengthening in the fifth position of each bar may also reflect metrical strength and/or segregation of melody and accompaniment. Loadings on PC-I, which ranged from 0.85 to -0.19, may be considered an alternative measure of typicality. Whereas UPC-I loadings expressed the degree to which a performance represents the *most typical mixture* of timing strategies, PC-I loadings express the degree to which a performance exhibits the *single most common* timing strategy. In terms of this measure, the most typically timed performance was that by Ranki [Fig. 7(a)]. Others who loaded highly on PC-I were Larrocha [see Fig. 11(c) below], Licad, Goldsand, Berezovsky, Hobson, and Mamikonian [see Fig. 11(b) below]. Their timing will be referred to as ''Type I'' in the following. The least typical performances, whose timing was most dissimilar from PC-I, were those by Anda, Cortot-1942, Perlemuter, François, Backhaus, Lortat, and Varsi, largely the same as in terms of UPC-I loadings.

The timing strategy represented by PC-II [Fig. 6(b)] is very different. It dwells on the beginnings of melodic segments, especially in bars 2 and 5, and it completely suppresses the ritards at the ends of melodic gestures. There is no lengthening of the initial downbeat either. In bars 1 and 2 (and probably 5 as well), the pace accelerates during the melodic gesture and continues smoothly into the accompaniment. In bars 3 and 4, the melodic timing is fairly steady, but the two accompaniment notes in bar 3 (positions 6 and 7) are taken very fast. There were quite a few timing profiles that

resembled PC-II, with loadings as high as 0.84. The pianist most representative of this ''Type II'' pattern was Lortat [Fig. 7(b)]. Other high loadings were exhibited by Cortot-1942, Goodman, Magaloff, Pollini, Biret, Slenczynska-1956, Iturbi, Joyce, and Cortot-1933. In an earlier PCA of 28 performances of Schumann's ''Träumerei'' (Repp, 1992), a local timing pattern was identified that was virtually unique to Cortot. The present PC-II strategy seems to be associated with Cortot as well, and it is possible that some of the other pianists were influenced by the example of this highly individual artist.

The timing profile associated with PC-III [Fig. 6(c)] has a single salient feature, the extreme lengthening of the initial downbeat, and is almost flat elsewhere, with a small tendency to shorten the fourth IOI in each bar. Nevertheless, a group of performances showed loadings on PC-III as high as 0.79. These ''Type III'' pianists included Backhaus, Kyriakou, Varsi, Yamazaki, Smith, and Monique Haas. It should be noted that a high correlation can result from a single very large value shared by two data sets. For example, Backhaus's timing profile showed substantial timing modulations which, however, were overshadowed by a greatly elongated initial downbeat. Therefore Fig. 7(c) shows Varsi's profile instead, which does exhibit the relative lack of timing modulation suggested by PC-III, though this is due in part to her very fast tempo.[7] (Note also her very short initial upbeat, a good example of a ''sixteenth-note upbeat.'')

The timing profile associated with PC-IV [Fig. 6(d)] is rapidly and systematically modulated. It shows strong ritards in the accompaniment preceding the onsets of melodic gestures (position 1 in bars 2, 3, and 5), as well as smaller ritards at the ends of segments, as in PC-I. There is no lengthening of the initial downbeat and no final ritard, but a lengthening in position 8 of bar 3, which is inconsistent with the purely metrical explanation that this timing pattern seems to invite. An interpretation in terms of grouping is therefore preferred. Loadings on PC-IV reached only a maximum of 0.72; thus there were no very pure instances of ''Type IV'' performances. Those with loadings above 0.5 included Lortie, François, Székely, Vásáry, Katz, Bingham, Kentner [see Fig. 9(b)], Egorov-1978, Perlemuter, Penneys, and Liberace [see Fig. 9(c)]. Figure 7(d) shows the profile of François who, like Varsi, played an extremely short initial upbeat, suggestive of a (lengthened) sixteenth note.

Although the Varimax rotation maximized the number of performances that closely resembled one or another PC, there were many profiles that loaded nearly equally on two or more PCs. In theory, this could result either from the combination or the alternation of timing strategies, though the following examples suggest that combination is more likely or at least more frequent. Combinations of the Type III strategy with the others are not of great interest because Type III represents only a single salient feature (lengthening of the initial upbeat). Figure 8 shows what the timing profiles of equally weighted combinations of pairs of the other three strategies would look like, as well as the combination of all four strategies [Fig. 8(d)]. In each case, the relevant PC scores were added and then restandardized (i.e., transformed into *z*-scores). These theoretical hybrid profiles may be compared with actual hybrid profiles shown in Fig. 9. Binns [Fig. 9(a)] has a profile with moderate loadings on the first two PCs, a Type I-II profile. It is indeed very similar to the profile in Fig. 8(a) except for bar 1, which seems idiosyncratic. Kentner [Fig. 9(b)] has a Type I-IV profile. It is quite similar to the mixture of PC-I and PC-IV [Fig. 8(b)], though it leans towards Type I in that it shows greater emphasis on within-gesture ritards. (Different mixtures of PC-I and PC-IV result in different relative magnitudes of within- and between-gesture ritards.) Liberace [Fig. 9(c)] exemplifies a Type II-IV profile. It resembles the theoretical mixture [Fig. 8(c)], except in bar 1, which is exaggeratedly Type IV. There is no clear case of a Type I-II-IV profile in the sample, but Volondat's timing [Fig. 9(d)] has nearly equal loadings on all four components and shows the greatly elongated first downbeat characteristic of PC-III as well as an extremely long upbeat. It is very similar to the theoretical mixture of all four PC profiles [Fig. 8(d)] and, not incidentally, to the UPC-I profile (Fig. 4), which is a weighted mixture of all strategies. These examples, at least, look predominantly like combinations rather than alternations of timing strategies.

Whether pianists showing such hybrid timing patterns really entertain several independent cognitive strategies simultaneously remains an open question. Presumably they do not do so consciously, and it may be difficult to prove that they do so subconsciously. What the PC analysis demonstrates is that across different pianists certain timing patterns (the different PCs) are independent of each other while others (the timing of individual gestures within each PC) tend to go together. Thus, for example, the degree of lengthening of the initial downbeat (PC-III) seems to be fairly independent of the timing of later events, and the within-gesture ritards (PC-I) seem to be partially independent of the between-gesture ritards (PC-IV), but within these patterns each type of ritard tends to be applied consistently. However, these are only overall tendencies, and there are numerous individual variations and exceptions.

Two-dimensional scattergrams of the PC loadings for all pairs of PCs are shown in Fig. 10. There is no clear evidence of either clusters or major gaps in these distributions. The space of possible PC combinations seems to be filled fairly evenly by the individual performances. The unidimensional distribution of PC-I loadings is skewed towards high loadings; however, the distributions of the other PC loadings seem fairly symmetrical. The loadings on the different PCs tended to be negatively correlated, for the higher the loading on one PC, the lower the loadings on other PCs must be. The highest negative correlation ($r=-0.42$, $p<0.001$) was between PC-I and PC-II loadings [Fig. 10(a)], due to the relative rarity of performances with low values on both.

Neither the UPC-I loadings nor any of the PC loadings were correlated with median tempo. PC-III loadings, however, showed a positive correlation with relative modulation depth ($r=0.30$, $p<0.01$), and PC-IV loadings a small negative correlation ($r=-0.22$, $p<0.05$). The lengthening of the initial downbeat in PC-III obviously contributed to a measure of overall timing modulation, whereas the rapid modulations characteristic of PC-IV probably required a relatively low amplitude to be aesthetically acceptable.

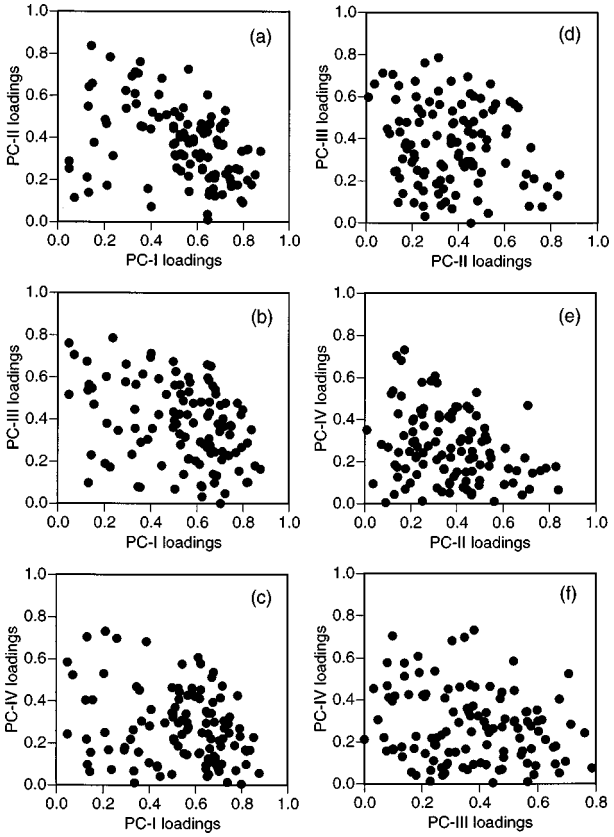

FIG. 10. Scattergrams of positive PC loadings for all pairs of PCs.

G. Similarity among performances

In the course of the PCA the correlations among all possible pairs of timing profiles were computed, a total of $(117\times116)/2=6786$ values, but these were inspected more closely only at a much later stage. Disregarding two outliers (see below), the highest between-performance correlations were 0.929 (Sauer and Mamikonian), 0.921 (Larrocha and Donohoe), 0.920 (Coop and Pokorna), and 0.914 (Weissenberg and Hobson). The first two pairs of profiles are illustrated in Fig. 11. The similarities are indeed striking, although Larrocha and Donohoe have radically different initial upbeat durations and different tempi. Given the large number of correlations computed, it may be concluded that two performances of this excerpt exhibiting a correlation substantially higher than 0.93 are significantly more similar than any two performances by different artists (or, for that matter, by the same artist) are ever likely to be. Even immediately repeated performances by the same pianist may not exhibit such a high correlation, due to uncontrolled timing variation (Repp, 1992, 1995a). When a correlation is higher than 0.99, it is clear that the two performances are identical, with the deviation from a perfect correlation being due to measurement error.[8] This makes it possible to objectively identify copies of a performance (cf. Repp, 1993). The presence of two between-profile correlations of 0.998 in the present sample was a clear indication that there were two pairs of identical performances. One of these turned out to be an accidental substitution of one recording (Aide) for another during preparation of the digital tape at IPA. In the other

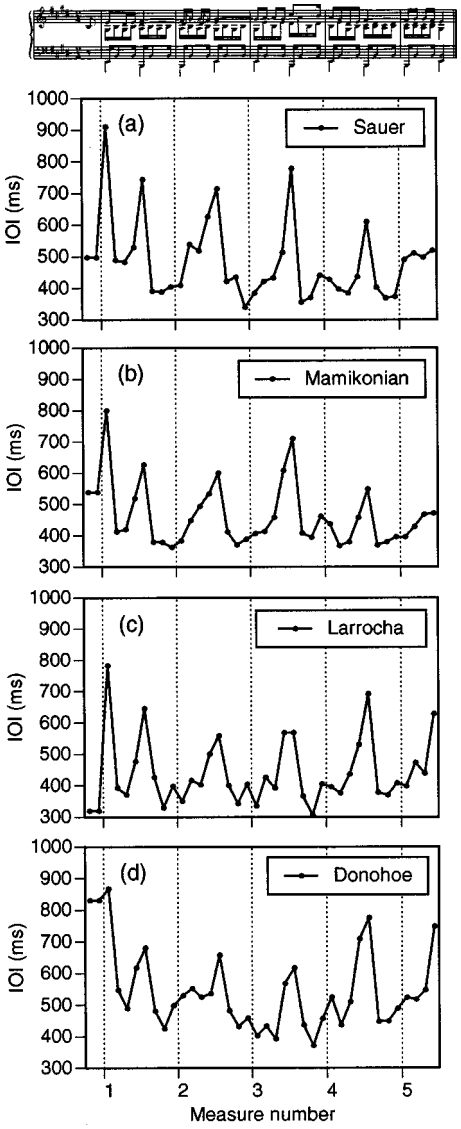

FIG. 11. Two pairs of very similar timing profiles: (a) and (b); (c) and (d).

instance, the performance of a pianist identified on the CD as ''Alexander van der Voss'' turned out to be identical with the performance of Boris Zarankin.[9]

One point of interest was the similarity of different recordings by the same pianist. In an earlier analysis of timing in Schumann's ''Träumerei,'' Repp (1992) found that repeated performances by Cortot and Horowitz, each of whom was represented by three different recordings made years apart, were more similar to each other than to any other pianist's performance in the sample ($n=28$). In the present, much larger sample of much shorter excerpts, seven pianists (Arrau, Ashkenazy, Cortot, Cziffra, Egorov, Horowitz, and Slenczynska) were represented by two recordings each. Egorov's performances were recorded in successive years, Cortot's 9 years apart, and the others 15–30 years apart. The correlation between each pianist's two performances was compared with the $2\times115=230$ correlations between each of his or her two performances and all other performances. In Egorov's case, none of these 230 correlations was larger than his own correlation (0.851), which is impressive evidence of his consistency but is perhaps not surprising in view of the

short interval between his two recordings. In Cortot's case, only seven correlations were higher than his own (0.744). For the other pianists, however, there was not much evidence of consistency in timing. For Arrau, Horowitz, and Slenczynska, the number of correlations exceeding their own (0.713–0.745) ranged from 38 to 66 and thus was still a good deal smaller than the 115 expected by chance. For Ashkenazy (0.648) and Cziffra (0.413), however, there was no statistical evidence at all that their timing came from the same pianist. This indicates that individual timing patterns for the same music can change quite substantially over a number of years. Little is known objectively about the extent to which they can change over shorter time spans, such as months, weeks, or days, though one often hears the informal claim that a particular artist ''never plays the music the same way twice.'' Thus it is not known whether each pianist's recorded timing pattern is representative of his or her approach (at the time of recording, at least) or whether it is merely one of several possible timing patterns that the artist had available simultaneously. This, together with the relatively small sample size, makes it difficult to investigate the relation of timing to sociocultural variables.

H. Sociocultural variables

The investigation of possible influences of artists' year of birth, educational history, age, recording date, nationality, or gender on expressive timing was not a primary purpose of this study, and additional library research would have been necessary to determine biographical information firmly and completely. However, leaving aside educational history (which is difficult to quantify in any case), the artists' gender was certainly known, their nationalities and recording dates were fairly well documented (some were reasonable guesses), and birth dates for a majority of the pianists could be found in books by Methuen-Campbell (1981) and Kehler (1982), with some reasonable guesses added and the remaining dates left blank. Age at the time of recording was, of course, the difference between the recording date and the birth date, if available. Thus it was possible to examine in a preliminary way the relationships between these five sociocultural variables and the objective measurements discussed above: median tempo, relative modulation depth, the initial upbeat ratios (Fig. 3), the typicality index (UPC-I loadings), and the loadings on the rotated PCs.

Recording date was significantly related to three variables. One weak relationship was with the ratio shown in Fig. 3(a) ($r=0.22$, $p<0.05$), indicating a slight tendency for the upbeat to get longer in recent decades. More interestingly, there was a positive correlation with PC-I loadings ($r=0.27$, $p<0.01$) and a negative correlation with PC-II loadings ($r=-0.39$, $p<0.001$). This indicates a trend for Type I timing to increase and for Type II timing to decrease in recent decades. In other words, timing is becoming more typical or mainstream, which is in agreement with many critical writings on modern performance practice. However, the correlation with the UPC-I loadings was not significant. Also, because other sociocultural variables are not equally represented over the decades, it is perhaps safer to conclude merely that, in the present sample, the more recent recordings tended towards the most common timing strategy (PC-I).

Artists' birth dates showed similar correlations with PC-I loadings ($r=0.30$, $p<0.01$) and PC-II loadings ($r=-0.35$, $p<0.01$). Of course, year of birth was highly correlated with year of recording ($r=0.79$, $p<0.001$). In addition, birth date showed a small correlation with PC-IV loadings ($r=0.25$, $p<0.05$), suggesting a tendency for Type IV patterns to be somewhat more common in younger generations.

Pianists' age at the time of recording was negatively correlated with both UPC-I loadings ($r=-0.23$, $p<0.05$) and PC-I loadings ($r=-0.22$, $p<0.05$), which indicates a slight tendency for older artists to exhibit more unusual timing patterns. Pianists' age was unrelated to the year of recording ($r=-0.06$), but it was negatively correlated with their year of birth ($r=-0.66$, $p<0.001$): Pianists born longer ago were generally recorded at a later stage in their career than pianists born more recently. This is largely due to the dual cutoffs imposed by the beginning of acoustic recording (when artists born long ago were already old) and by the present (when artists born recently are still young). In addition, there are now many more opportunities for young artists to be recorded than there were some decades ago.

The effect of gender was assessed by conducting one-way analyses of variance on the various dependent variables. Gender proved to be unrelated to any timing profile characteristics, but there was a significant effect on initial upbeat duration, especially relative to the following downbeat IOI [the ratio shown in Fig. 3(b)]: Men tended to play longer upbeats than women [$F(1,113)=7.6$, $p<0.007$]. In addition, there was a marginally significant tendency for women to play faster than men [$F(1,113)=4.2$, $p<0.05$], and a nearly significant tendency for women to play longer initial downbeats than men [$F(1,113)=3.7$, $p<0.06$], which contributed to the gender difference in relative upbeat duration.

The effect of nationality was difficult to assess because of the many different countries of birth. Therefore the analysis was restricted to those nationalities that were not only well represented in the sample but also have a strong tradition of Chopin performance: French, Polish, and Russian. One-way analyses of variance were conducted accordingly. Only one significant effect emerged, on PC-I loadings [$F(2,39)=4.8$, $p<0.02$]: French pianists were less likely to have Type I timing profiles than their Polish and Russian colleagues.

III. GENERAL DISCUSSION

This study continues a series of investigations of commonalities and differences in distinguished pianists' expressive timing, as measured from commercial acoustic recordings of the same composition (Repp, 1990, 1992, 1997b). The musical excerpt was short, but the sample of recordings was much larger than in previous studies. A mere five bars of music can give rise to a rich diversity of expressive actions, and the large sample made it possible for the first time to map out the ''space'' of aesthetically acceptable timing patterns for a musical passage.

The timing space was defined by six dimensions: basic tempo, relative modulation depth, and the four rotated principal components that describe profile shape. One important finding of this study is that, within this space, there were no distinct clusters of timing patterns. Rather, the space of possibilities seemed to be ''sampled'' by individual performers in a rather continuous way.[10] This suggests that individual differences in timing did not arise from alternative, categorically different structural interpretations of the music. Indeed, the passage does not seem to contain structural ambiguities that need to be resolved by performers. Melodic-rhythmic groups, harmonic progression, and metrical structure are all well defined and mutually supportive. Perhaps the only anomaly is that, due to the final notes of melodic groups and coincident harmonic changes, the second downbeat in each bar (position 5) seems more salient than the first (position 1). However, this does not necessarily reflect a shift in underlying metrical structure, and the data indicate that performers were not faced with a metrical ambiguity requiring a categorical decision. To the extent that interpretation of metrical structure influenced timing at all—and the slow tempo makes that doubtful—it was a matter of deciding on some degree of relative emphasis of first versus second downbeats. Thus, viewed from a metrical perspective, pure Type I profiles focused strongly on second downbeats, whereas pure Type IV profiles gave somewhat more prominence to first downbeats, with many gradations in between.

In view of the relatively homogeneous distribution of individual performances in the timing space, the different profile types (PC patterns) were considered not structural interpretations but timing strategies, i.e., different ways of articulating the same musical structure. In other words, these timing patterns and their combinations primarily convey such things as individuality, motion, and affect within a given structural frame. They give the musical object a particular shape or character (cf. Shaffer, 1996), much as different drawings or paintings of the same object do. The resulting qualities are difficult to describe in words, though some may be captured by imaginative metaphor (which will not be attempted here). The musical structure defines boundaries within which artists' imagination may roam freely.

It is possible to think of structural interpretation in terms of continuously adjustable parameters, and in that case expressive timing may be understood as the parametrization or shaping of a given structure. The grand average timing profile (Fig. 4) may be regarded as a graph indicating the temporal coherence or flexibility of the structure: The higher the value on the ordinate, the more ''stretchable'' the music is at that point, according to the actions taken by a large number of distinguished musicians. Each individual artist, however, creates a personal version of this general temporal shape. While any individual timing pattern could in principle be motivated by explicit or implicit structural considerations—a desire to give more or less emphasis to this or that structural aspect of the music—it is far from clear that this is the motivation behind most artists' expressive strategies. Similarly, there is probably only a small number of music lovers who listen to music in order to be informed about its structure. Although it is always possible to view expression as being *about* the musical structure, this approach misses the essence of musical communication, which is to move listeners and to stimulate their imagination (cf. Cook, 1990; Scruton, 1997). Therefore expression is regarded here as being *constrained* by the musical structure and as communicating living qualities distinct from the structure itself.

The division into two alternating streams, melody and accompaniment, seems to be the most important structural aspect constraining expressive timing in the present Chopin excerpt. When the melody is moving, the accompaniment moves along with it and contributes only to texture and harmony; it comes to the fore only when the melody stands still. Most expressive tempo modulations are nested within the alternating stream segments and employ the conventional strategies of slowing before a boundary and/or accelerating after a boundary. In particular, the pronounced lengthening of the IOI immediately following the onset of a long melody note, which is typical of the Type I timing strategy [Fig. 6(a)] and also can be seen in the Type IV pattern [Fig. 6(d)], helps segregate the melody from the accompaniment. A lengthening of the IOI preceding a melodic gesture is less common but by no means rare and usually occurs together with ritards within melodic gestures. This strategy (Type IV) lends a gestural quality to the accompaniment as well as to the melodic segments and thus elevates the accompaniment from mere background to something like a partner in a dialogue or an echo of the melodic rhythm.

The lengthening of the initial downbeat (Type III) is largely independent of other timing strategies, though it also tends to occur together with within-gesture ritards (Type I). Indeed, it is itself a within-gesture ritard, for the first melodic segment is divided into two smaller gestures, the first of which comprises only the initial upbeat and the following downbeat. The Type III strategy may be considered what Heiles (1964) has called a ''nuance of establishment.'' This designation applies even more, however, to the lengthening of the initial upbeat. Interestingly, that tendency was shown more strongly by male than by female pianists. It may be understood as an attempt to establish control over an audience by capturing its attention through postponement of the anticipated downbeat.

The most interesting timing strategy is the one termed Type II, which (in its ''pure'' form) does entirely without within-gesture ritards and instead shows gesture-initial lengthening followed by acceleration through the following accompaniment in bars 1, 2, and 5, together with a relative lack of temporal modulation in the two linked melodic gestures of bars 3 and 4. It shifts emphasis from the ends of the melodic gestures to their beginnings. Leaving aside subjective judgments for the time being (see Part III of this study), the unusual character of the Type II pattern is suggested by the results of perceptual experiments requiring the detection of small deviations from metronomic timing in the very same Chopin excerpt (Repp, 1998a, 1998b, 1998c, in press). This indirect method revealed that listeners (with or without musical training) have perceptual biases or ''expectations'' of timing modulations that match the ''typical,'' grand average timing profile (Fig. 4). This is the kind of timing that the musical sound structure seems to ''demand'', as it is auto-

matically elicited in listeners' perceptual systems. The Type II pattern is the one most different from the typical profile and from listeners' timing expectations. That it nevertheless can be used with good aesthetic effect is testimony to the inventiveness and skill of the artists who employ it. Clarke (1985, p. 233) has observed that ''a piece with an unambiguous and readily comprehensible structure may encourage a performer to experiment with contradictory expressive elements,'' and the Type II pattern seems to represent such an experimentation.

The four types of timing pattern extracted from the data are descriptive tools, no more. They reduce three-fourths of the variance among 115 different performances to combinations of just four basic patterns. Whether these patterns have any psychological reality as independent cognitive strategies remains uncertain. Most individual timing profiles are mixtures of types, but subjectively they probably appear unified to artists and listeners. Most pianists probably follow their musical instincts, particularly at this level of detail, and simply play with the expression that ''feels right'' for the music. Their musical instincts are shaped in turn by their past experiences as performers and listeners, both with music in general and with the specific passage in particular. Experience increases their explicit and implicit knowledge of the expressive actions that are aesthetically viable within a given musical structure. Inexperienced pianists and amateurs tend to play with conventional expressive timing, the profile that is most compatible with the musical structure (Repp, 1995a, 1997a). Greater experience yields a greater arsenal of options that can be explored.

The smallest unit of expressive action is the gesture, which can be a single note but usually comprises a group of several successive notes. Each expressive gesture in a melody could in principle be shaped differently. However, the regularities within the Type I, II, and IV patterns indicate that similar gestures tend to be shaped similarly. Yet there are many possible individual variants resulting from mixtures of these patterns, and the additional idiosyncratic variance, not accounted for in the PC analysis, should not be forgotten. Also, the Type II pattern is interesting because it does not extend the temporal shaping of bars 1 and 2 to bars 3 and 4. By giving different melodic gestures different expressive characterizations, this timing strategy creates contrast and variety within the phrase.

Todd's (1985) model of expressive timing postulates smooth acceleration–deceleration shapes for whole phrases, so that smaller gestures would be nested in a larger gesture. Although such a large curvilinear trend can be seen in some individual profiles [e.g., Fig. 5(d)], it is not characteristic of most of them. Todd's model tends to be more successful in accounting for the coarse timing patterns in larger hierarchical structures than for the detailed shaping within a phrase (see Windsor and Clarke, 1997; Penel and Drake, 1998).

As already pointed out, the stability of individual artists' timing patterns is essentially unknown. While some pianists may be highly consistent over a number of years, others may be more variable in a deliberate or spontaneous way. The present data provide several examples of artists whose timing profile changed radically over a number of years, but it is unclear how representative the profiles are of the pianist's playing at the time of each recording. Perhaps similarly large changes could be observed within much shorter time spans. This is an interesting topic for further investigation.

While several significant correlations were found between objective parameters of timing and sociocultural variables, they were uniformly small and should be regarded with great caution. The present sample is still quite insufficient for an investigation of that sort, the representativeness of individual artists' profiles is unknown, the sociocultural data are incomplete, and there are numerous confounding variables. At best, the results provide intriguing leads to be followed up in future studies. In seems likely, however, that individual differences far outweigh any sociocultural or historical trends in expression.

Timing is only one aspect of expressive performance, though a very important one. What is being timed or paced are the motor actions that generate the musical sound. The sound heard by a listener is shaped by expressive dynamics (the relative intensities of the notes), articulation, pedaling, instrument acoustics, room acoustics, and sound engineering in recordings. One important question is whether expressive timing is independent of expressive dynamics at the detailed level considered here or whether these two parameters are linked. This issue will be addressed in Part II of this study in the context of a detailed analysis of expressive dynamics in the present sample of performances.

ACKNOWLEDGMENTS

This research was supported in part by an unfunded extension of NIH Grant No. MH-51230. I am grateful to my wife, Norma, whose love and support enabled me to continue my research during this period. Thanks are further due to Donald Manildi (Director, International Piano Archives, University of Maryland) for providing most of the recordings as well as helpful information, to Igor Popovic for writing a valuable piece of software, and to José Bowen, Janet Hander-Powers, David Huron, and Nigel Nettheim for suggestions on how to improve the manuscript. Address correspondence to Bruno H. Repp, Haskins Laboratories, 270 Crown Street, New Haven, CT 06511-6695; Electronic mail: repp@haskins.yale.edu

APPENDIX: RECORDINGS, TEMPI, AND PC LOADINGS

Year=year of recording (~=estimated), MT=median tempo (quarter-note beats per minute), PC-I, PC-II, PC-III, PC-IV=rotated principal component loadings.

Pianist	Label	Year	MT	PC-I	PC-II	PC-III	PC-IV
Aide, William	Musica Viva 1017	1987	25.9	0.650	0.464	0.272	0.042
	(duplicate)			0.656	0.465	0.279	0.052
Anda, Géza	Fonit Cetra CDE 1018	1965	33.3	−0.133	0.485	0.106	0.419
Anievas, Agustin	Seraphim 60081	~1967	26.5	0.331	0.610	0.447	0.264
Arrau, Claudio	Electrola EH 386	~1930	26.0	0.628	0.420	0.284	0.250
	Angel 35413	1956	28.0	0.434	0.606	0.423	0.092
Ashkenazy, Vladimir	Melodiya 10-00511	1959	28.5	0.718	0.473	−0.033	0.222
	London 414 127-2	~1974	30.4	0.691	0.369	0.379	0.094
Backhaus, Wilhelm	Pearl GEMM CD 9902	1927	24.6	0.048	0.255	0.762	0.243
Badura-Skoda, Paul	Westminster XWN-18811	~1960	36.0	0.701	0.445	0.468	0.066
Berezovsky, Boris	Teldec 73129	1991	32.6	0.798	0.092	0.446	0.005
Bingham, John	Meridian 84221	1993	29.5	0.542	0.315	0.139	0.576
Binns, Malcolm	Pearl 9641	1995	27.7	0.645	0.605	0.285	0.091
Biret, Idil	Naxos DDD 8.550364	1990	33.3	0.345	0.707	0.080	0.468
Brailowsky, Alexander	RCA Victor LM-6000	~1947	30.5	0.292	0.624	0.578	0.168
Browning, John	RCA Victrola 60131-2-RV	1968	34.1	0.713	0.369	0.404	0.101
Cherkassky, Shura	HMV ALP 1310	1955	26.5	0.569	0.276	0.577	0.276
Ciani, Dino	Ars Nova VST 6092	1965	27.1	0.156	0.377	0.471	0.406
Ciccolini, Aldo	Capitol SP 8651	1967	25.9	0.504	0.374	0.068	0.222
Cliburn, Van	RCA Victor 60358-2-RG	1961	26.7	0.793	0.336	0.268	0.233
Coop, Jane	Musica Viva 1015	1987	32.3	0.668	−0.001	0.560	0.343
Cortot, Alfred	EMI Classics 2905401	1933	34.9	0.148	0.659	0.548	0.157
	Pathé FJLP 5050	1942	35.7	−0.082	0.828	0.130	0.177
Costa, Sequeira	Supraphon 111 2188	1976	26.5	0.709	0.132	0.248	0.186
Crown, John	Co-Art 5047	~1947	31.8	0.541	0.423	0.488	0.310
Cziffra, György	Philips 6515.005	~1964	35.6	0.357	0.455	0.292	0.452
Cziffra, György	EMI C 167-73103/4	1981	30.0	0.698	−0.319	0.343	0.078
Darré, Jeanne-Marie	Pathé DT 1016	~1953	35.2	0.661	0.500	0.241	0.111
Donohoe, Peter	EMI 54416	1993	29.2	0.745	0.195	0.372	0.249
Drzewiecki, Jaroslav	Canyon 3645	1992	28.7	0.661	0.142	0.654	0.175
Duchâble, François-René	Erato 45178	1981	28.1	0.742	0.209	0.328	0.293
Egorov, Yuri	Peters Int. PLE 121	1978	35.0	0.677	0.124	0.245	0.537
	MHS 4493	1979	34.0	0.675	0.209	0.097	0.395
Ellegaard, France	Siemens 17919	~1939	27.8	0.614	0.440	0.294	0.151
Entremont, Philippe	Sony Classical MLK 64057	~1973	29.3	0.503	0.319	0.563	0.344
Farrell, Richard	EMI 64136	1958	26.5	0.644	0.428	0.268	0.078
Fou Ts'ong	CBS 61886	1980	41.2	0.209	0.467	0.603	0.251
François, Samson	EMI C 163-5323/7	1959	33.5	0.132	0.140	0.098	0.705
Goldenweiser, Alexander	Melodiya M10-42855/6	~1950	27.8	0.595	0.323	0.203	0.423
Goldsand, Robert	Concert Hall H-1632	~1953	23.4	0.819	0.199	0.289	0.099
Goodman, Isador	Austral. Philips 6508 004	1979	30.1	0.225	0.785	0.173	0.169
Haas, Monique	Erato STU 70941	1977	35.8	0.399	0.441	0.696	0.107
Haas, Werner	Philips 836.816	~1965	35.0	0.652	0.210	0.309	0.343
Haase, Erika	Thorofon CTH 2195	1992	40.4	0.681	−0.099	0.521	0.301
Harasiewicz, Adam	Philips Classics 422-282-2	1961	29.0	0.502	0.524	0.395	0.324
Hesse-Bukowska, Barbara	Muza SXL 0611	~1970	29.4	0.652	0.129	0.587	0.044
Hobson, Ian	EMI CFP 4392	1982	31.9	0.791	0.102	0.424	0.270
Horowitz, Vladimir	RCA Victor 60376-2-RG	1951	31.0	0.617	0.326	0.085	0.412
	Sony 53468	1972	38.6	0.686	0.389	0.132	0.131
Iturbi, José	Seraphim S-60186	~1959	30.8	0.447	0.683	0.180	0.042
Janis, Byron	RCA Victor 12-0431	1948	25.8	0.524	0.501	0.425	0.187
Johannesen, Grant	Golden Crest CRS 4101	~1971	30.9	0.529	0.243	0.520	0.444
Joyce, Eileen	EMI OXLP 190 254	1941	30.7	0.319	0.694	0.234	0.219
Kahn, Claude	Epidaure 1946	~1975	31.3	0.508	0.314	0.627	0.211
Karolyi, Julian von	Arkadia 909	1953	31.9	0.654	0.144	0.483	0.127
Katz, Mindru	Pye GGC 4063	1966	22.4	0.611	0.306	0.187	0.608
Kentner, Louis	Capitol GBR 7162	1957	30.4	0.622	0.249	0.080	0.578
Kersenbaum, Sylvia	EMI CFP 40239	1975	30.9	0.467	0.509	0.519	0.297
Kilényi, Edward	APR 7037	1937	29.9	0.558	0.464	0.423	0.340
Koczalski, Raoul	Polydor 67262	1938	31.6	0.134	0.643	0.565	0.099
Koyama, Michie	Sony SRCR 8528	1991	30.1	0.644	0.037	0.661	0.095
Kyriakou, Rena	Vox GBY 12710	1964	22.8	0.237	0.315	0.787	0.075
Larrocha, Alicia de	MHS 1761	~1969	37.1	0.836	0.178	0.352	0.167

Pianist	Label	Year	MT	PC-I	PC-II	PC-III	PC-IV
Levant, Oscar	Columbia ML 4147	~1947	28.9	0.622	0.256	0.032	0.454
Liberace	Columbia ML 4900	~1955	25.3	0.204	0.486	0.191	0.530
Licad, Cecile	MusicMasters MM 67124	~1994	28.7	0.852	0.226	0.180	0.228
Lopes, Fernando	Unicamp LPFL 021/2	1986	26.9	0.748	0.170	0.368	0.325
Lortat, Robert	Dante 025	~1931	26.9	0.144	0.838	0.231	0.065
Lortie, Louis	Chandos CHAN 8482	1986	26.7	0.211	0.174	0.381	0.732
Magaloff, Nikita	Philips 6542 411	1975	29.0	0.354	0.762	0.077	0.158
Magin, Milosz	Festival classique 701	1969	25.9	0.584	0.395	0.384	0.462
Malcuzinsky, Witold	British Columbia LX 1203	~1948	28.8	0.564	0.375	0.532	0.265
Mamikonian, Vardan	Calliope 9220	1993	36.0	0.775	0.177	0.478	0.070
Manz, Wolfgang	Astoria 87008	~1985	33.7	0.646	0.308	0.416	0.296
Murdoch, William	Decca K 704	~1938	32.0	0.294	0.540	0.662	0.180
Niedzielski, Stanislaw	Westminster WL 5340	1955	21.8	0.702	0.455	0.000	0.213
Novaes, Guiomar	Vox PL 10930	~1950	33.7	0.336	0.562	0.566	0.011
Paderewski, Ignace Jan	Pearl 9397	1927	35.8	0.540	0.543	−0.040	0.242
Pennario, Leonard	Capitol P 8391	1957	27.2	0.618	0.467	0.483	0.155
Penneys, Rebecca	Centaur 2210	1993	31.6	0.670	0.160	0.140	0.513
Perahia, Murray	Sony SK 64399	1994	33.4	0.366	0.452	0.615	0.305
Perlemuter, Vlado	Nimbus NI 5095	1983	32.2	0.048	0.289	0.517	0.585
Pokorna, Mirka	Supraphon GMM 90	~1967	23.1	0.646	0.010	0.598	0.352
Pollini, Maurizio	DGG 413 794-2	~1971	34.4	0.562	0.727	0.212	0.146
Ranki, Dezsö	Hungaroton 11555	~1975	32.4	0.876	0.336	0.164	0.057
Renard, Rosita	VAIA/IPA 1028	1949	37.7	0.769	0.255	0.244	0.189
Richter, Sviatoslav	Philips 420 774-2	1958	30.4	0.722	0.530	0.047	0.306
Saperton, David	VAIA/IPA 1037-2	1952	27.1	0.549	0.401	0.317	0.152
Sasaki, Ken	Nimbus 2136	1982	32.3	0.565	0.146	0.214	0.428
Sauer, Emil	Parlophone E 10863	1928	34.5	0.679	0.227	0.543	0.139
Schein, Ann	Japanese CBS WS-10001	~1966	29.5	0.782	0.249	0.154	0.426
Shebonova, Tatiana	Melodiya A10 00217	1985	27.6	0.497	0.455	0.362	0.345
Simon, Abbey	Vox TV-34688	1977	33.5	0.511	0.258	0.378	0.371
Skavronsky, Alexei	Melodiya 10-00249	1986	25.0	0.528	0.325	0.280	0.409
Slenczynska, Ruth	Decca DL 9890	1956	27.3	0.333	0.714	0.358	0.068
	MHS 3216	~1975	30.8	0.434	0.497	0.593	0.087
Slobodyanik, Alexander	Melodiya/Angel SR40204	1977	24.9	0.525	0.403	0.332	0.461
Smith, Ronald	Nimbus 5224	1990	29.3	0.401	0.073	0.714	0.283
Sofronitzky, Vladimir	Melodiya M10 42253/64	1960	34.2	0.130	0.549	0.538	0.219
Solomon	EMI RLS 701	1945	25.9	0.526	0.415	0.565	0.297
Székely, István	Naxos 8.550083	1987	28.6	0.387	0.159	0.305	0.682
Timofeyeva, Lyubov	Melodiya 10-00071	1985	34.5	0.407	0.521	0.357	0.360
Uninsky, Alexander	Epic LC 3065	~1954	33.6	0.563	0.218	0.601	0.299
Varsi, Dinorah	Intercord 160.842	1981	47.4	0.071	0.116	0.707	0.524
Vásáry, Tamás	DGG 2535 266	1965	30.5	0.260	−0.015	0.348	0.698
Vered, Ilana	Connoisseur CS 2045	1972	27.3	0.654	0.147	0.432	0.245
Virsaladze, Elisso	Melodiya C10-05443/6	~1980	26.4	0.716	−0.005	0.368	0.472
Volondat, Pierre-Alain	EMI 173199	1984	23.7	0.498	0.444	0.436	0.464
Weissenberg, Alexis	EMI 69114	1979	28.5	0.724	0.230	0.478	0.272
Wild, Earl	Chesky CD 77	1992	27.2	0.666	0.223	0.252	0.221
Woodward, Roger	Austral. EMI OASD 7560	~1975	32.1	0.707	0.365	0.209	0.416
Woytowicz, Boleslaw	MHS OR C-150/1	~1960	29.6	0.497	0.369	0.675	0.052
Yamazaki, Takashi	Fontec FONC 5027	1980	29.4	0.126	0.213	0.675	0.404
Yokoyama, Yukio	Sony SK 62605	1995	28.5	0.584	0.381	0.477	0.437
Zarankin, Boris	Mastersound 018	1990	23.4	0.816	0.344	0.100	0.168
(duplicate, ''v. d. Voss'')	Orchid 11033	1990	23.3	0.821	0.346	0.101	0.163
Zayas, Juana	Spectrum 165	1983	35.7	0.737	0.251	0.229	0.013

[1]The old edition from which the music has been copied is no longer considered authoritative, and the tempo indication is plainly wrong. However, in the initial bars it does not differ significantly from modern Urtext editions, except in graphic layout and added fingering suggestions. It has the unique advantage of fitting the first five bars into a single system, and it also served as the model for the simplified, computer-generated score used in later figures.

[2]Most analyses include all 117 samples, as they were conducted before the duplication was discovered. It seemed unnecessary to redo the analyses in view of the minimal difference this would have made in the results.

[3]The classification is according to country of birth (which, in some cases, is merely a best guess). No heed was paid to the fact that some of the pianists were trained and/or lived in other countries most of their life (e.g., Arrau, Cherkassky, Fou Ts'ong, Magaloff, Weissenberg), so that they cannot really be considered representative of any pianistic school or performance tradition associated with their country of birth.

[4]A number of performances (at least 29) contained one or more such asynchronies. In nearly all instances, one or several lower tones (played by the left hand) preceded a melody tone, and the majority (59%) occurred on metrical downbeats. Pianists particularly inclined to employ such left-hand-leads (five or more times) were Paderewski (who arpeggiated most chords), Slenczynska (in both of her recordings), Saperton, Ciccolini, Janis, and Liberace. As is well known, this expressive strategy or mannerism tends to be more common in artists of older generations.

[5]A third possibility is to base the tempo estimate on the modal IOI (the peak of the IOI distribution), but this is not very accurate with only 36 IOIs.

[6]In view of the great length of the inter-beat intervals, it may be argued that the primary beat (tactus) is really at the eighth-note level, in which case the tempi should be multiplied by two.

[7]Ideally, to make the profiles more comparable in terms of relative modulation depth, a logarithmic scale should have been used on the *y* axis of the graphs. However, a linear scale proved more convenient in view of certain limitations of the graphics software.

[8]Of course, the two performances would not be identical if they differed in tempo and/or modulation depth and/or initial upbeat duration, but such differences are extremely unlikely in the presence of such a high timing profile correlation and would suggest deliberate manipulation of a sound recording.

[9]The author has not seen these CDs but, according to Donald Manildi of IPA, Zarankin's identity is not in doubt.

[10]Admittedly, this conclusion was drawn on the basis of two-dimensional plots only, but it seems unlikely that a consideration of higher-dimensional spaces would have led to a very different conclusion. Of course, the full six-dimensional timing space is only sparsely ''populated'' and leaves almost infinitely many possibilities for individual timing patterns, without exceeding the constraints defined by the present sample of performances.

Clarke, E. F. (**1985**). ''Structure and expression in rhythmic performance,'' in *Musical Structure and Cognition*, edited by P. Howell, I. Cross, and R. West (Academic, London), pp. 209–236.

Cook, N. (**1987**). ''Structure and performance timing in Bach's C major Prelude (WTCI): An empirical study,'' Music Analysis **6**, 257–272.

Cook, N. (**1990**). *Music, Imagination, and Culture* (Clarendon, Oxford, UK).

Desain, P., and Honing, H. (**1994**). ''Does expressive timing in music performance scale proportionally with tempo?'' Psychol. Res. **56**, 285–292.

Eigeldinger, J.-J. (**1986**). *Chopin: Pianist and Teacher as Seen by His Pupils* (Cambridge U. P., Cambridge, UK).

Gabrielsson, A. (**1987**). ''Once again: The theme from Mozart's Piano Sonata in A major (K.331),'' in *Action and Perception in Rhythm and Music*, edited by A. Gabrielsson (Royal Swedish Academy of Music Publication No. 55, Stockholm), pp. 81–103.

Heiles, W. H. (**1964**). ''Rhythmic Nuance in Chopin Performances Recorded by Moriz Rosenthal, Ignaz Friedman, and Ignaz Jan Paderewski,'' D.M.A. dissertation, University of Illinois.

Kehler, G. (**1982**). *The Piano in Concert* (Scarecrow, Metuchen, NJ).

Methuen-Campbell, J. (**1981**). *Chopin Playing from the Composer to the Present Day* (Taplinger, New York).

Penel, A., and Drake, C. (**1998**). ''Sources of timing variations in music performance: A psychological segmentation model,'' Psychol. Res. **61**, 12–32.

Povel, D.-J. (**1977**). ''Temporal structure of performed music: Some preliminary observations,'' Acta Psychol. **41**, 309–320.

Repp, B. H. (**1990**). ''Patterns of expressive timing in performances of a Beethoven minuet by nineteen famous pianists,'' J. Acoust. Soc. Am. **88**, 622–641.

Repp, B. H. (**1992**). ''Diversity and commonality in music performance: An analysis of timing microstructure in Schumann's 'Träumerei','' J. Acoust. Soc. Am. **92**, 2546–2568.

Repp, B. H. (**1993**). ''Objective performance analysis as a tool for the musical detective,'' J. Acoust. Soc. Am. **93**, 1203–1204.

Repp, B. H. (**1994a**). ''Relational invariance of expressive microstructure across global tempo changes in music performance: An exploratory study,'' Psychol. Res. **56**, 269–284.

Repp, B. H. (**1994b**). ''On determining the basic tempo of an expressive music performance,'' Psychol. Music **22**, 157–167.

Repp, B. H. (**1995a**). ''Expressive timing in Schumann's 'Träumerei': An analysis of performances by graduate student pianists,'' J. Acoust. Soc. Am. **98**, 2413–2427.

Repp, B. H. (**1995b**). ''Quantitative effects of global tempo on expressive timing in music performance: Some perceptual evidence,'' Music Percept. **13**, 39–57.

Repp, B. H. (**1997a**). ''The aesthetic quality of a quantitatively average music performance: Two preliminary experiments,'' Music Percept. **14**, 419–444.

Repp, B. H. (**1997b**). ''Expressive timing in a Debussy Prelude: A comparison of student and expert pianists,'' Musicae Scientiae **1**, 257–268.

Repp, B. H. (**1998a**). ''Variations on a theme by Chopin: Relations between perception and production of deviations from isochrony in music,'' J. Exp. Psychol.: HPP **24** (to be published).

Repp, B. H. (**1998b**). ''Obligatory 'expectations' of expressive timing induced by perception of musical structure,'' Psychol. Res. **61**, 33–43.

Repp, B. H. (**1998c**). ''The detectability of local deviations from a typical expressive timing pattern,'' Music Percept. **15**, 265–290.

Repp, B. H. (**in press**). ''Detecting deviations from metronomic timing in music: Effects of perceptual structure on the mental timekeeper,'' Percept. Psychophys.

Repp, B. H. (**submitted**). ''A microcosm of musical expression: II. Quantitative analysis of pianists' dynamics in the initial measures of Chopin's Etude in E major.''

Repp, B. H. (**in preparation**). ''A microcosm of musical expressions: III. Contributions of expressive timing and dynamics to the aesthetic appeal of the initial measures of Chopin's Etude in E major.''

Scruton, R. (**1997**). *The Aesthetics of Music* (Clarendon, Oxford, UK).

Seashore, C. E. (editor) (**1936**). *Objective Analysis of Musical Performance* (The University Press, Iowa City, IA).

Shaffer, L. H. (**1996**). ''Musical performance as interpretation,'' Psychol. Music **23**, 17–38.

Todd, N. P. [McA.] (**1985**). ''A model of expressive timing in tonal music,'' Music Percept. **3**, 33–58.

Todd, N. P. McA. (**1992**). ''The dynamics of dynamics: A model of musical expression,'' J. Acoust. Soc. Am. **91**, 3540–3550.

Windsor, W. L., and Clarke, E. F. (**1997**). ''Expressive timing and dynamics in real and artificial musical performances: Using an algorithm as an analytical tool,'' Music Percept. **15**, 127–152.

The spectrogram correlation and transformation receiver, revisited

H. Peremans[a)]
Barco M. V., R & D Department, Th. Sevenslaan 106, 8500 Kortrijk, Belgium

J. Hallam
Department of Artificial Intelligence, University of Edinburgh, Forrest Hill, 5, Edinburgh EH1 2Q1, United Kingdom

(Received 1 April 1997; accepted for publication 18 March 1998)

The spectrogram correlation and transformation (SCAT) receiver has been proposed as a model for the receiver structure used by fm bats. The main contribution of this paper lies in the analysis of which features of the proposed model are responsible for its high accuracy in estimating arrival times of overlapping echoes. Apart from providing an answer to this question, the analysis will also indicate the limitations of the SCAT receiver. In particular, it is shown that the temporal block of the SCAT receiver returns erroneous results for interecho delays $<20\ \mu$s and for interecho amplitude ratios >6 dB. It is also shown that the spectral block of the SCAT receiver generates spurious arrival times if more than two overlapping echoes are present. Finally, it is discussed how the characteristic measurement errors predicted by this analysis can be used to further investigate the accuracy of the SCAT receiver as a model of the receiver structure used by fm bats. © *1998 Acoustical Society of America.* [S0001-4966(98)00707-3]

PACS numbers: 43.80.Lb, 43.60.Pt, 43.64.Bt [FD]

INTRODUCTION

In many naturally occurring situations bats seem to show a remarkable capacity to track a single reflecting object among a densely packed group of reflectors (Simmons *et al.*, 1995). Furthermore, in addition to tracking the object of interest, the bats must also have some notion of the positions of the other reflectors as shown by their successful chase of insects in vegetation (Webster, 1967) without colliding with the branches and leaves around them. This seems to indicate that bats are somehow capable of decomposing the summation of highly overlapping echoes picked up by their ears into its constituent parts.

Simmons and his co-workers propose that this decomposition occurs in the temporal domain, i.e., the bat's brain builds a monaural time-domain representation of the signal picked up by each ear (Simmons *et al.*, 1995; Simmons and Chen, 1989; Saillant *et al.*, 1993). In this representation each echo is mapped onto its arrival time. Information about the 3-D position (Suga, 1990; Fuzessery, 1988; Lawrence and Simmons, 1982) of a reflector is derived from the interaural and intra-aural time differences between the arrival times corresponding with that reflector. Because of the smallness of these time differences it has been argued by other authors (Fuzessery *et al.*, 1992; Pollak, 1988; Kuc, 1994) that instead of using time differences bats are more likely to use interaural and intraaural intensity information to derive reliable angular position estimates. However, it should be noted that the mechanisms based on intensities proposed so far (Kuc, 1994) assume isolated echoes and cannot explain the bat's performance in highly cluttered environments. Simmons *et al.* (1995) point out that to derive the intensities of the individual echoes from the composite received signal the arrival times of the echoes should be extracted first. Hence, even if the time differences prove too small to be of use to the bat for position estimation, the time domain decomposition of the signal would still be required to extract reliable intensity information in highly cluttered environments. Experimental evidence for this temporal domain decomposition is derived from two-glint experiments as described by Simmons *et al.* (1995), Simmons (1993), and Saillant *et al.* (1993). These experiments also indicate that the bat is capable of measuring time delays between two overlapping echoes that are as small as 2 μs.

In Saillant *et al.* (1993) proposed a receiver structure (SCAT) that combines a time domain, coarse time information, and frequency domain, fine time information analysis of the received signal to arrive at the temporal decomposition referred to above. The advantages of combining time and frequency domain analyses of the received signals had already been described by Beuter (1980), but the SCAT model introduces the additional assumption that the final representation is solely a time domain one. The model's performance is very similar to the one shown by bats in the two-glint experiments. However, although they show through numerous examples how well the results predicted by the proposed receiver structure match the actual results from experiments performed on bats, the authors do not explain where its resolving power comes from. Hence, to get an improved understanding of where its power comes from we present a formal analysis of this receiver structure which is the main contribution of this paper. However, by analyzing the mechanisms responsible for SCAT's impressive performance we also uncover the assumptions on which the correct operation of those mechanisms is dependent. Exploring the limits of its correct operation allows us to suggest behavioral experiments that can help to decide on the validity of the SCAT as a model for the receiver structure used by fm bats.

So far, we have looked upon the SCAT solely as a model of a biological sonar system. However, our research

[a)]Electronic mail: herbert.peremans@barco.com

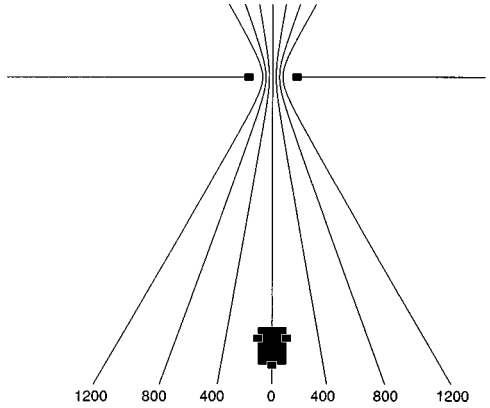

FIG. 1. Different paths the robot can take to drive through an opening. Each path is a hyperbola along which the delay (numbers are in μs) between the echoes from the edges is constant.

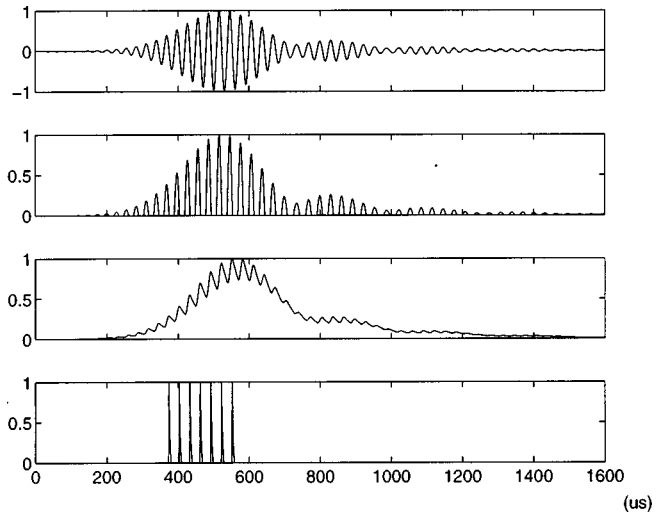

FIG. 2. The outputs at different points in the cochlear block. From top to bottom: the bandpass filter, the half-wave rectifier, the low-pass filter, and the neural coding.

(Peremans *et al.*, 1993; Peremans, 1994) has shown that the sensor interpretation problems encountered by bats are very similar to the ones encountered by mobile robots fitted with ultrasonic sensors. In particular, we have shown that the single most important source of errors is the occurrence of highly overlapping echoes. We have also found, in agreement with Simmons *et al.* (1995), that many frequently occurring situations give rise to such overlapping echoes. Furthermore, particular echoes overlap quite often for considerable periods of time, making it impossible to remove the possibly erroneous measurements by outlier rejection techniques. This can be appreciated by considering a mobile robot driving through an opening while looking at the two edges of the objects defining the opening. As can be seen from Fig. 1, the echoes from the two edges will overlap considerably at both ears along any reasonable path that leads through the opening. Hence, a better understanding of the principles from which the SCAT model derives its resolving power can lead to a significant improvement in robotic sonar systems.

In Section I we briefly describe the spectrogram correlation and transformation receiver. The analysis of the temporal and spectral components of the SCAT is given in Sec. II. This analysis will expose particular assumptions made by the SCAT. Section III contains a discussion of a set of experiments designed to bring out the specific errors resulting from violating those assumptions. These experiments can help decide on the biological plausibility of the SCAT.

I. THE SPECTROGRAM CORRELATION AND TRANSFORMATION RECEIVER

In this section we will summarize the receiver structure proposed by P. Saillant *et al.* (1993) as it was implemented by us. The SCAT receiver consists of three blocks. The cochlear block takes in the signal as received by the ear and analyzes it in a number of frequency channels. The temporal block will use the timing information about corresponding events in the different frequency channels to derive an estimate for the arrival time of a group of overlapping echoes. This arrival time of the group is then further refined by the spectral block which uses the relative amplitudes of the outputs of the different frequency channels to derive estimates for the delays between the individual echoes that make up the group.

In all subsequent examples the transmit cry is a frequency-swept sine wave, its period linearly modulated starting at 110 kHz and going down to 15 kHz in 2.0 ms.

A. The cochlear block

This block derives a spectrogram representation from the original signal. The implementation consists of a filter bank, 81 bandpass filters, a set of half-wave rectifiers, and a low-pass filtering stage. The bandpass filters are tenth-order Butterworth IIR filters with a fixed 3-dB bandwidth of 4 kHz. The central frequencies of the bandpass filters range from 20 to 100 kHz. The frequency scale is hyperbolic, i.e., the center periods of the bandpass filters are linearly spaced. The output of each of the bandpass filters is half-wave rectified and low-pass filtered. The low-pass filter is a first-order Butterworth Infinite Impulse Response (IIR) filter with cutoff frequency equal to 3 kHz.

The outputs of the low-pass filters are then converted into discharge patterns; each discharge is a 1-μs pulse. We will consider ''peak detection'' neurons only. They mark the occurrence of an event by discharging whenever a local peak in the low-pass filter output is above the threshold for that particular frequency channel. During its refractory period, lasting 1 ms, the neuron can only be retriggered by a new local peak if this new peak is larger than the peak that last triggered the neuron.

The outputs at different stages in a particular frequency channel from the cochlear block are shown in Fig. 2.

B. The spectrogram correlation block

This block, also called the temporal block, determines the delay between the emission and the echo by making use of tapped delay lines. If multiple highly overlapping echoes are received, i.e., delays between echoes smaller than the integration time 350 μs, this block returns the delay between the emission and the first echo.

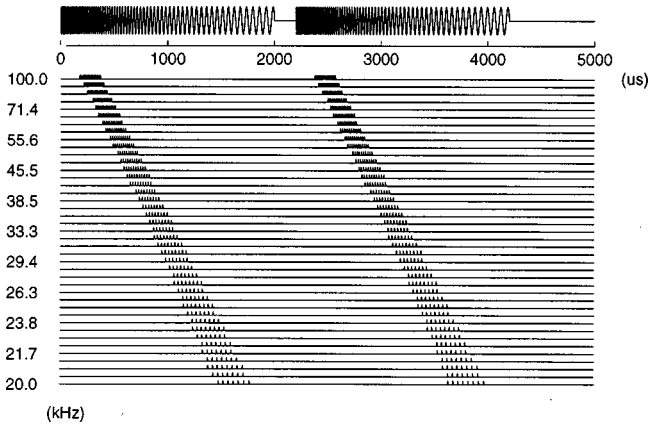

FIG. 3. Activity of the peak detecting neurons due to the emission and a single echo.

First, the sonar emission itself is processed as the model assumes that the ears pick up the emitted cry and use this signal to make the receiver self-calibrating. So, the pulse volleys caused by the emission are fed into a set of tapped delay lines, taps at 1-μs separation, one delay line for each frequency channel. Next, the delay between the volley produced by the emission and the volley produced by the echo is measured (Fig. 3). This is done by a series of coincidence detectors, each tuned to a different delay as shown in Fig. 4. One set of inputs of each coincidence detector is connected to the tapped delay lines. They add together the neural activation, i.e., the pulses caused by the emission, traveling along the different delay lines. The other set of inputs is connected directly to the outputs of the cochlear block and sum the neural activation in the different frequency channels due to the echo. However, because of the fm-swept nature of the cry, the high-frequency channels are activated first as the emission frequency sweeps down (see Fig. 3). Hence, to sum the activity in the different frequency channels due to the same echo these delays have to be compensated for. Therefore the inputs to the coincidence-detecting neuron are taken from points that are shifted by these characteristic delays with respect to each other (Fig. 4).

To implement a variable coincidence-detection resolution the neural pulses (duration 1 μs) are converted into decaying exponentials with a variable time constant before the summation is performed. The default value for this time constant is set to 2 μs. Finally, the summed activity on each set of inputs is compared with a threshold. When the threshold is exceeded on both the delayed emission inputs and the echo inputs, the coincidence detector triggers and signals an echo at the particular delay value represented by it.

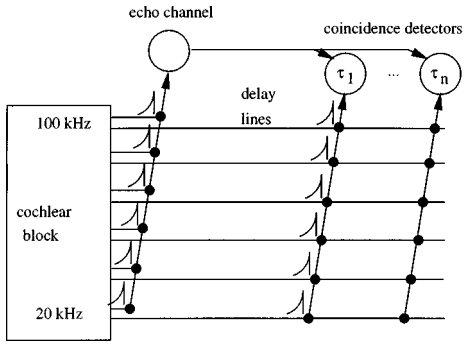

FIG. 4. The architecture of the spectrogram correlation block.

C. The spectrogram transformation block

This block, also called the spectral block, determines the delay between the first and second echo using the outputs of the low-pass filters from the cochlear block. Adding this delay to the arrival time of the first echo extracted by the temporal block results in the arrival time of the second echo. Note that the results from the spectral block are only used when the delay between the two echoes is smaller than the integration time of the cochlear block, i.e., 350 μs. For delays larger than the integration time the temporal block on its own returns accurate estimates for all the arrival times.

Each frequency channel in the spectral block casts a series of votes in favor of certain delays and against other delays between the two echoes. This is implemented by representing the delay dependency of the votes cast by a frequency channel by a cosine wave. The positive regions of the cosine wave correspond with delay values favored by the frequency channel and the negative regions with delay values it disagrees with. The frequency of the cosine wave is equal to the central frequency of the channel. All the cosine waves are started at the time indicated by the temporal block as being the arrival time of the group of echoes. Furthermore, each voting pattern, i.e., cosine wave, is scaled by the strength of the echo at the central frequency of the channel. This strength is determined by integrating the part of the output of the low-pass filter falling within a window with length 350 μs and centered around the arrival time of the first echo as detected by the temporal block. This value is normalized with respect to the emission strength. After adding the voting patterns from the different frequency channels together, the spectral block returns the delays that exceed a threshold.

Finally, the cosine vote patterns are modified somewhat to guarantee good performance of the receiver for very closely spaced echoes as well. Because of the finite frequency range spanned by the frequency channels, the spectral block does not return a single impulse at zero delay when a flat spectral response, meaning only one object is present, is measured. To avoid this phenomenon from interfering with the detection of very small delays (<16 μs), a new set of basis vectors is derived from the cosine waves by adjusting them such that for every delay value their sum equals zero. Furthermore, to compensate for the nonuniform contribution of the energy per frequency caused by the hyperbolic spacing of the constant bandwidth frequency channels, the basis vectors corresponding with the different frequency channels are weighted appropriately.

II. ANALYSIS OF THE SCAT RECEIVER

In this section we want to look at the mechanisms by which the receiver structure described above works as claimed. This analysis will also shed some light on the limits beyond which the receiver will no longer operate correctly. First, we will look at how the temporal block manages to

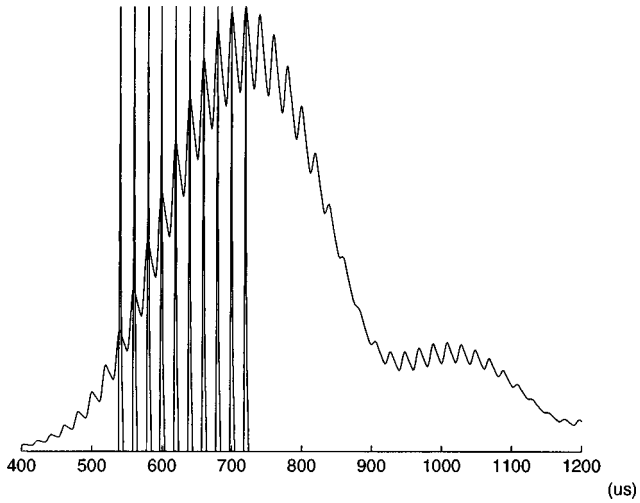

FIG. 5. Activity of the peak detecting neurons is synchronized with the ripple on the outputs of the low-pass filters.

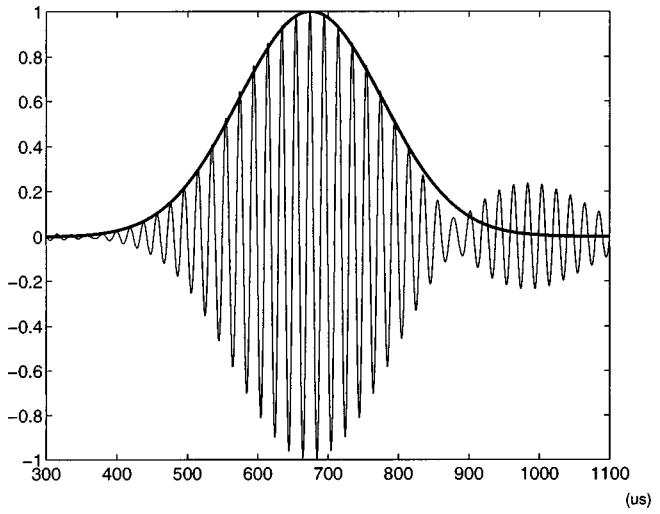

FIG. 6. Approximating the envelope of the output of a cochlear bandpass filter by a Gaussian.

return a remarkably accurate estimate of the arrival time for a group of closely spaced echoes, and next we will see how the spectral block refines this result by providing estimates for the delays between the arrival time of the first echo, i.e., the arrival time of the group, and the arrival times of the subsequent echoes.

A. The temporal block

To help us gain a better understanding of its operation in the presence of multiple, overlapping echoes we look at the temporal block's handling of single echoes first.

1. Nonoverlapping echoes

From Fig. 3 we note that the separation between subsequent pulses from a burst increases along with the center period for the different frequency channels. Looking at Fig. 5, showing the output of the low-pass filter together with the neural pulses triggered by it, we can be even more specific. The pulses generated by the cochlear block are synchronized with the ripple still present on the outputs of the low-pass filtered signals. This behavior is a consequence of the way the ''peak detection'' neurons are defined.

To make the previous statements more precise we now derive the exact positions of the neural pulses when only a single echo is present. The output of each of the bandpass filters in response to an echo (Berkowitz, 1965) can be written as

$$o_i(t)=a(t)\ \cos\ (2\pi f_i t),$$

for $i=1,...,N$, where f_i denotes the central frequency of the ith frequency channel, and $a(t)$ denotes the envelope of this output. To simplify the calculations we approximate the envelope around its maximum $t=t^+$ by

$$|o_i(t)|=a(t)=\exp\left(\frac{(-(t-t^+)^2}{\sigma^2}\right), \tag{1}$$

where σ is determined by the bandwidth of the bandpass filter and the sweep rate of the fm pulse (Menne, 1988), as shown in Fig. 6. The extrema of the output of the bandpass filter occur at times $t=t^*$,

$$0=a'(t^*)\ \cos\ (2\pi f_i t^*)-a(t^*)2\pi f_i\ \sin\ (2\pi f_i t^*), \tag{2}$$

where the prime indicates time derivatives. From Eqs. (1) and (2) we obtain

$$\tan\ (2\pi f_i t^*)=\frac{-2(t^*-t^+)}{2\pi f_i \sigma^2}. \tag{3}$$

Putting $t^*=t^+ +\Delta t$ and $t^+=(m+\alpha)T_i$ with $\alpha \in[-1/2,1/2]$ and m an integer, we want to find the smallest Δt that locally maximizes $o_i(t)$ as this will correspond with the global maximum of $o_i(t)$. From Eq. (3) and approximating $\tan(\theta)\simeq\theta$ for small θ we obtain

$$\Delta t=\frac{-\alpha T_i}{1+2/(2\pi f_i\sigma)^2}\simeq-\alpha T_i\,.$$

Hence $t^*\simeq mT_i$, i.e., the global maximum occurs at the maximum of the modulating cosine wave closest to the maximum of the envelope and all other local maxima coincide with the maxima of the modulating cosine wave. In terms of the phasor representation of the signal $o_i(t)$ (Fig. 7), this means that the maxima occur for the phase of the phasor

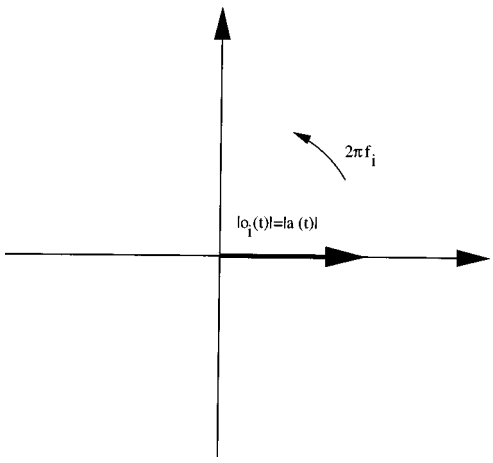

FIG. 7. The phasor representation of the output signal $o_i(t)$ if a single echo is present.

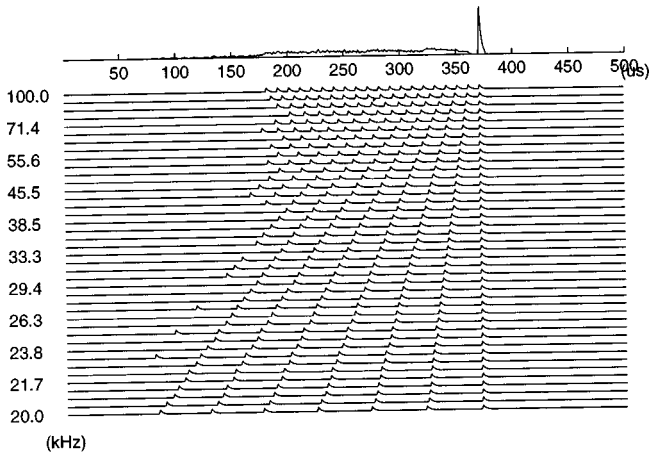

FIG. 8. Activity of the peak detecting neurons due to a single echo (realigned time axes). The top line shows the summed activity.

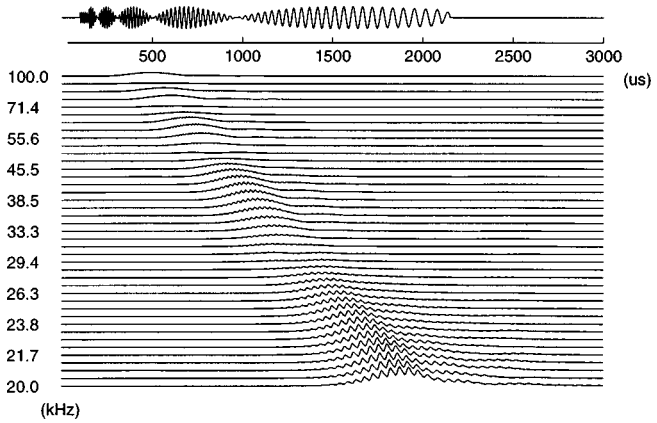

FIG. 9. The outputs of the low-pass filters for two overlapping echoes, $\tau = 50\ \mu$s.

$\gamma = k2\pi$ for $k = 0,1,2,...$, despite the time dependency of the envelope $a(t)$.

Note that we have determined the positions of the maxima of the outputs of the bandpass filters. However, the positions of the neural pulses are determined by the outputs of the low-pass filters (Fig. 5). The latter can be easily derived from the results we have since the half-wave rectifier changes nothing to the positions of the maxima, as can be seen from Fig. 2, and the low-pass filter introduces a constant shift only.

In Fig. 8, we zoom in on the activity burst due to the echo. The time axes are realigned, taking into account the different delays corresponding with the different frequency channels. Note that these delays were arrived at by a self-calibration procedure that measures the delays between the position of the peak (global maximum) of the emission response in the first channel and the position of that same peak in the other channels. Hence, by construction, the pulses produced by the peak (global maximum) of the echo response will be the only ones that line up after realigning the frequency channels. The other pulses, being separated by a multiple of the center period of their frequency channel from the true peak, will be smeared out after realignment, as can be clearly seen from Fig. 8. Hence, the well-defined peak in the summed activity of the different frequency channels will reliably trigger the coincidence detecting neuron in the case of an isolated echo.

2. Two overlapping echoes

We have shown in Fig. 9 the signals at the outputs of the low-pass filterbank when two highly overlapping, i.e., delay $< 350\ \mu$s, echoes occur. Contrary to an isolated echo, there is now no longer a single peak in all frequency channels. Furthermore, in those channels that do contain a single peak the position of that peak has shifted with respect to where it would be if either the first or the second echo were the only echo present. As we saw in the previous section the neural pulses from a burst are separated by the center period of the frequency channel and the last spike from the burst corresponds with the peak itself (Fig. 5). Therefore, shifting the peak will shift all the neural pulses in the burst as well. Since the amount of shift of the peaks will vary from one frequency channel to another, the correct operation of the spectrogram correlation block is no longer guaranteed. However, despite the shifted and possibly doubled peaks the model still returns a surprisingly accurate estimate of the first echo's delay. How is that possible? It turns out that the positions of the shifted peaks, both double and single peaks, are still related to the positions of the peaks that would occur if only one of the two echoes was present. Below we analyze this phenomenon more quantitatively.

In the presence of two echoes the output of the ith bandpass filter from the cochlear block can be written as

$$o_i(t) = a(t)\ \cos\ (2\pi f_i t) + a(t-\tau)\ \cos\ (2\pi f_i (t-\tau)),$$

for $i = 1,...,N$, where τ denotes the delay of the second echo with respect to the first echo. Figure 10 shows the phasor representation of $o_i(t)$, i.e., its squared envelope

$$|o_i(t)|^2 = a^2(t) + a^2(t-\tau) - 2a(t)a(t-\tau)\ \cos\ (\pi - 2\pi f_i \tau), \tag{4}$$

and its phase

$$\gamma_i(t) = \arctan\left(\frac{\sin\ (2\pi f_i \tau)}{\cos\ (2\pi f_i \tau) + a(t)/a(t-\tau)}\right). \tag{5}$$

From the analysis in the previous section we conclude that the phase difference $\gamma_i(t^*)$ corresponds with the time difference between the maxima occurring when a single echo is present and the maxima for a two-echo signal. We have again denoted the times at which $o_i(t)$ is maximal by $t = t^*$. We can derive a number of properties of $\gamma(t^*)$ from Eq. (5), all of which can be verified from the graphical representation shown in Fig. 10. As $2\pi f_i \tau$ varies for different frequency channels, $\gamma_i(t^*)$ will vary as well but we will always have

$$\gamma_i(t^*) \in \left[-\frac{\pi}{2}, \frac{\pi}{2}\right]. \tag{6}$$

For $a(t^* - \tau) \leqslant a(t^*)$ we have

$$\gamma_i(t^*) \leqslant \frac{2\pi f_i \tau}{2}, \tag{7}$$

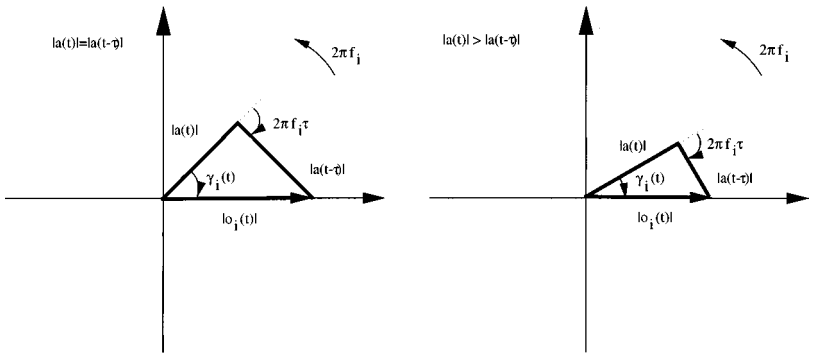

FIG. 10. The phasor representation of the output signal $o_i(t)$ if two echoes are present, for $a(t)=a(t-\tau)$ and for $a(t)>a(t-\tau)$.

and $\gamma_i(t^*)\rightarrow 0$ for $a(t^*-\tau)/a(t^*)\rightarrow 0$. If $a(t^*-\tau) > a(t^*)$, we can redefine $\gamma(t^*)$ to represent the phase difference between the maxima of the second echo and those of the two-echo signal, hence Eq. (7) remains valid.

Equation (6) indicates that the positions of the maxima when two echoes are present are maximally shifted with respect to the maxima for a single echo over $T_i/4$ and most of the time by much less, as shown by Eq. (7). Again, by the same reasoning as described in the previous section, this result about the positions of the maxima of the outputs of the cochlear bandpass filters is equally valid for the maxima of the outputs of the low-pass filters. Hence, we conclude that the positions of the neural pulses when two echoes are present will also be maximally shifted by $T_i/4$ with respect to the neural pulses caused by a single echo. Note that this is not strictly true for the global maximum as in this case there can be an additional shift mT_i, i.e., an unknown but integer multiple of the center period of the frequency channel.

Knowing these properties of the positions of the neural pulses we can explain the robustness of the temporal block in the presence of overlapping echoes. The coincidence detection scheme in the temporal block is a voting scheme with two important features. First, each frequency channel votes for a number, i.e., more than one, of possible peak positions (see Fig. 8). Second, the neural spikes are exponentially decaying pulses (time constant 2 μs), which means that the vote for a particular peak position is actually spread out over its close neighbors in an exponentially decaying fashion. Despite being fed shifted peaks only, the neural pulses are shifted by $(m+\alpha)T_i$, $\alpha\in[-1/4,1/4]$ with respect to the single echo case. These two features allow the temporal block to produce an accurate estimate of the true position of the first echo nevertheless. First, the temporal block compensates for the unknown integer m by casting multiple votes, at multiples of the center period, for each frequency channel. Next, the equally unknown but much smaller, maximally $T_i/4$, shift is compensated for by convolving each vote with an exponentially decaying function. Note that this latter compensation is only a partial one as the decaying exponential has a fixed length. This makes it impossible to spread out each vote over the known uncertainty region $[-T_i/4,T_i/4]$ which increases along with the center period of the frequency channels. Furthermore, whereas the true uncertainty region is symmetrically distributed around the measured pulse position, the decaying exponential is nonzero in the positive half of this region only.

Comparing the summed activity pattern of a single echo shown in Fig. 8 with that of two overlapping echoes ($\tau=25$ μs) shown in Fig. 11, it is clear that it gets increasingly difficult to recognize the peak from the background activity as the delays get smaller. This can be understood by noting that as the delays τ get smaller, the ratio $a(t^*)/a(t^*-\tau)\rightarrow 1$ and $\gamma(t^*)$ increases as can be seen from Eq. (5). When $\gamma(t^*)$ increases, the amount of overlap of the exponential vote patterns decreases, thereby lowering the peak to background ratio. Nevertheless, in this example the temporal block correctly estimates the arrival time of the first echo to be at 1000 μs. The results of a more comprehensive test, Table I, indicate that the temporal block can reliably estimate the first arrival time for delays $\tau\geqslant 25$ μs. If the delays get smaller, errors occur as will be explained below.

3. Limits to the correct operation of the temporal block

From the results in Table I it is clear that as the delays get smaller than 20 μs, the spectrogram correlation block returns the time halfway in between the two echoes instead of the arrival time of the first echo. This behavior can be understood using the results derived above. First, we note that if the envelopes of the outputs of the bandpass filters are symmetrical, the two echo signal will have an extremum at

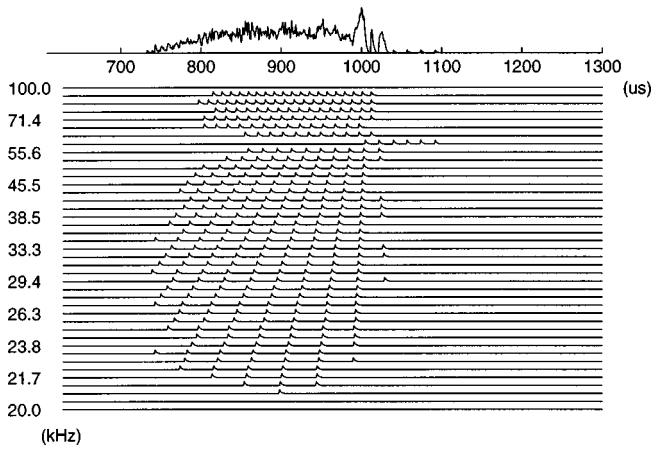

FIG. 11. Activity of the peak detecting neurons due to two echoes at 1000 and 1025 μs (realigned time axes). The top line shows the summed activity.

TABLE I. Comparison of the estimated arrival times of the two echoes and the true ones (arrival time first echo: t_1, delay: τ).

(μs)	t_1	τ	t_1	τ	t_1	τ	t_1	τ	t_1	τ	t_1	τ	t_1	τ
True value	1000	200	1000	100	1000	50	1000	25	1000	20	1000	10	1000	5
SCAT	1001	200	1002	100	1002	50	1000	25	1011	20	1005	11	1003	6

the point halfway in between the two echoes. That the envelopes can in fact be accurately approximated by symmetrical ones over quite a large region around the peak can be verified from Fig. 6. This extremum will be a maximum for all the frequency channels for which the delay $\tau \in [-T_i/2 + 2mT_i, T_i/2 + 2mT_i]$ with T_i the center period of the channel and $m = 0,1,2,\ldots$. If, in addition, $\tau < T_i/2$ for a particular channel, then the global maximum in the two-echo signal coincides with this maximum half-way between the two echoes. After realigning the frequency channels, the peaks generated by these global maxima will all be lined up since they are shifted over a fixed delay $\tau/2$ with respect to the global maxima of the first echo signal. This phenomenon can be clearly observed in Fig. 12. All the frequency channels with center period $T_i/2 > 15$ μs generate a peak half-way between the two echoes that line up perfectly. The frequency channels with center period $T_i/2 < 15$ μs generate peaks that lie around the true arrival time of the first echo. For delays $\tau \leqslant 20$ μs the number of channels that contribute votes to the true arrival time falls below the background vote level. At the same time, the number of channels contributing votes to the time halfway between the two echoes rises. These two effects explain why for $\tau < 20$ μs the peak corresponding with the true arrival time of the first echo is no longer detected and why instead the peak corresponding with the time halfway in between the two echoes is.

Another problem arises if the amplitudes of the overlapping echoes are no longer equal, as they were in all our examples so far. Equation (7) is valid as long as the magnitude of the envelope of the first echo is larger than that of the second echo when the two-echo signal reaches its maxima. This would no longer be guaranteed if the second echo gets stronger than the first one. When the amplitude of the second echo is larger than that of the first echo, Eq. (7), as noted before, remains valid but it now describes the separation of the peaks of the two-echo signal from those of the second echo. Hence, the voting operation performed in the temporal block will favor the arrival time of the second echo in this case. Such a situation is shown in Fig. 13. The amplitude of the second echo is twice that of the first echo, and as expected the arrival time returned is that of the second echo, 1100 μs.

B. The spectral block

This block converts the spectral representation, i.e., magnitude of the outputs of the filterbank, of the composite echo signal into a series of delay values. As mentioned above, the normalized vote patterns, i.e., the warped cosines, are defined such as to transform a flat spectral representation into a zero vote for all possible delays. Hence, in that case a single echo will be detected and its arrival time will be given by the estimate returned by the temporal block. However, all nonflat spectra will result in the detection of multiple echoes and their arrival times will be given by the delay estimates from the spectral block added to the estimate from the temporal block.

1. Two overlapping echoes

We start by examining the spectra of signals consisting of two overlapping echoes. When two echoes $e(t)$, equal magnitude a, and delays τ_1, τ_2 are present, the received signal $s(t)$ is given by

$$s(t) = ae(t-\tau_1) + ae(t-\tau_2),$$

and its spectrum is

$$S(f) = aE(f)\, e^{-j2\pi f\tau_1}(1 + e^{-j2\pi f(\tau_2-\tau_1)}), \tag{8}$$

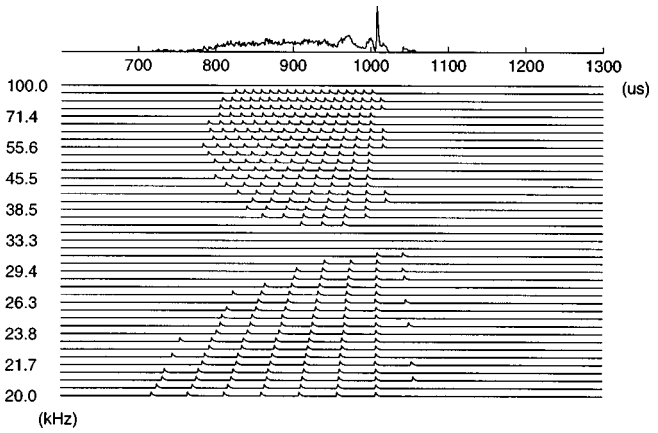

FIG. 12. Activity of the peak detecting neurons due to two echoes at 1000 and 1015 μs (realigned time axes). The top line shows the summed activity.

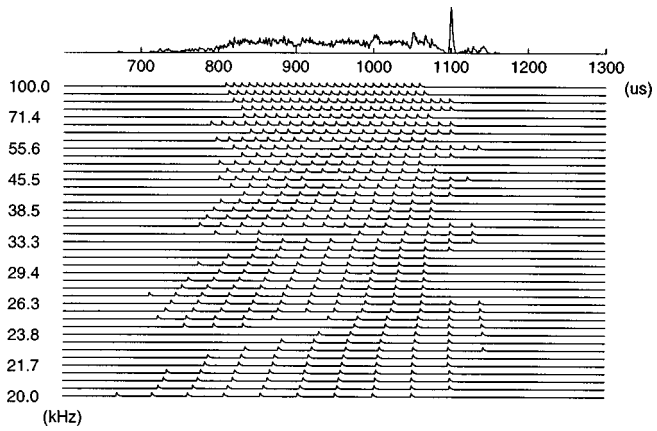

FIG. 13. Activity of the peak detecting neurons due to two echoes at 1000 and 1100 μs (realigned time axes). The amplitude of the second echo is twice that of the first one. The top line shows the summed activity.

with $E(f)$ the spectrum of the echo. From Eq. (8) it is clear that this nonflat spectrum contains notches at frequencies f^- for which

$$f^- = \frac{(2m+1)}{2} \frac{1}{(\tau_2 - \tau_1)}, \tag{9}$$

with m an integer. Hence, from the description of the operation of the spectral block (Sec. I C), we know that the frequency channels corresponding to these particular frequencies will generate no, or only a very weak, cosine wave. Consequently, the delays d corresponding with odd multiples of half the period p^- of those frequency channels

$$d = \frac{2n+1}{2} p^-,$$

with n an integer, will be inhibited less, i.e., supported more. Similarly, the spectrum will contain peaks at frequencies f^+,

$$f^+ = m \frac{1}{(\tau_2 - \tau_1)}. \tag{10}$$

Hence the frequency channels corresponding with those frequencies will generate strong support for the delays

$$d = np^+,$$

with n an integer. Note that Eqs. (9) and (10) guarantee that the true delay $\tau_2 - \tau_1$ will always be among the delays d that are supported more. Hence, adding the voting patterns for all the frequency channels together, the true delay $\tau_2 - \tau_1$ will get the highest support. Table I shows the results of the spectral block on the more comprehensive test. As can be seen from these results, the spectral block returns very good estimates of the delay between the first and second echo down to 5 μs.

However, the conditions as described in this section are quite idealized: echoes have equal amplitudes, echoes are perfect time-delayed copies of emission, and there are only two overlapping echoes. We will see below that the algorithm to convert spectra into delays is quite sensitive to those assumptions.

2. Limits to the correct operation of the spectral block

The result of analyzing the spectrum generated by three overlapping echoes with the spectral block is shown in Fig. 14. The spurious peak in the output of the spectral block corresponds with the delay between the second and the third echo. This behavior of the spectral block can be understood by examining a spectrum of a signal consisting of three overlapping echoes. If three echoes are present,

$$s(t) = ae(t-\tau_1) + ae(t-\tau_2) + ae(t-\tau_3),$$

the spectrum is

$$S(f) = aE(f)\, e^{-j2\pi f\tau_1}(1 + e^{-j2\pi f(\tau_2-\tau_1)} + e^{-j2\pi f(\tau_3-\tau_1)}).$$

The frequencies f^* that maximize this expression have to comply with the combined constraint

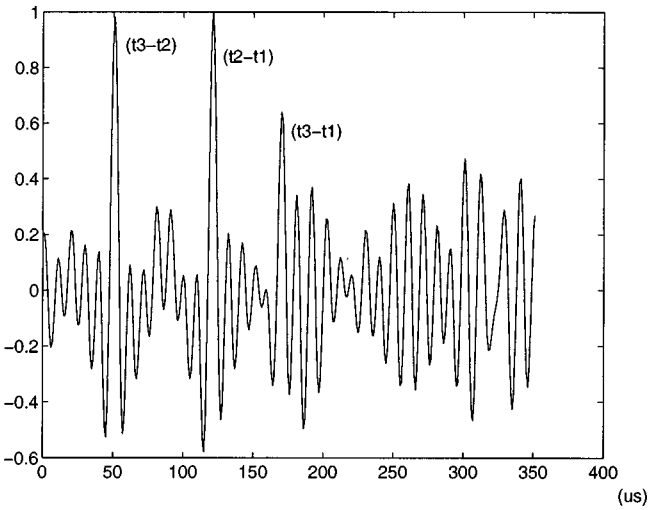

FIG. 14. The peaks in the output of the spectral block, indicating the delays between the three overlapping echoes, contain a spurious delay estimate (true delays: 120 and 170 μs; estimated delays: 50, 120, and 170 μs).

$$2\pi f^*(\tau_2 - \tau_1) = m2\pi, \quad 2\pi f^*(\tau_3 - \tau_1) = n2\pi,$$

with m,n integers. However, all frequencies f^* that do so will also comply with

$$2\pi f^*(\tau_3 - \tau_2) = k2\pi = (n-m)2\pi.$$

Hence, the corresponding frequency channels will not only provide strong support for the delays $\tau_2 - \tau_1$ and $\tau_3 - \tau_1$, but also for the delay $\tau_3 - \tau_2$. Therefore, we conclude that the spectral block will generate spurious delay estimates whenever more than two echoes are present.

As shown by Schmidt (1992), varying the ratio of the amplitudes of the second and the first echo results in a reduction of the depth of the notches and the height of the peaks in the spectrum of the two echo signal. We now analyze how this could affect the delay estimate returned by the spectral block. The strength of the two echo signal, delay τ, at the central frequency f_i of the different frequency channels is given by

$$|o_i| = (1 + a_r^2 + 2a_r \cos(2\pi f_i \tau))^{1/2}, \tag{11}$$

with the amplitude of the first echo $a_1 = 1$ and $a_r = a_2/a_1$. The output of the spectral block is proportional to

$$\sum_{i=1}^{N} |o_i|^2 g_i(t), \tag{12}$$

where the number of filters is denoted by N and the warped basis vectors by $g_i(t)$. For a two-echo signal, the delay estimate is given by the point where this sum reaches its maximum. From Eqs. (11) and (12) and noting that

$$\sum_{i=1}^{N} g_i(t) = 0,$$

by construction, the sum calculated by the spectral block $y(t)$ can be written

$$y(t) = 2\sum_{i=1}^{N} \cos(2\pi f_i \tau) g_i(t),$$

for $a_r=1$. If the two echoes no longer have the same amplitude, the sum calculated by the spectral block can be similarly shown to be proportional to

$$a_r y(t).$$

This scaling, however, will not influence the position of the maximum. Hence, apart from making the delay estimates more susceptible to noise, the scaling will have no direct impact on the results returned by the spectral block.

III. DISCUSSION

The analysis presented above clearly shows that the SCAT receiver as described by Saillant *et al.* (1993) performs very well given the right conditions are fulfilled: not more than two overlapping echoes are present, the echoes have equal magnitudes, and the delay between the echoes is more than 20 μs. Different parts of the SCAT receiver rely to different degrees on those conditions for their correct operation. Violating these conditions results in very specific errors as shown by the analyses from Secs. II A 3 and II B 2. Hence, we propose using the predicted errors to verify the validity of the SCAT as a model for the receiver structure of fm bats.

The temporal block shifts the arrival time of the first echo to the time halfway in between the two echoes if the delay τ gets smaller than 20 μs. According to the SCAT model this phenomenon shifts both arrival times backwards by $\tau/2$. However, experiments like the ones described by Simmons *et al.* (1990, 1995) show that such a shift does not occur with bats. In this type of experiment the arrival time of a single echo probe is varied around the values of the arrival times from a two echo signal. The bats show a marked increase in errors whenever the single echo's arrival time coincides with one of the perceived arrival times from the two-echo signal. This indicates that the SCAT, as a model of the receiver structure of fm bats, will have to be modified to avoid this shift from occurring. One possibility would be that, whenever the delay τ is smaller than 20 μs, the information of the spectral block is used to compensate for this shift. Since the shift is equal to $\tau/2$, the spectral block does indeed provide all the information necessary to perform such a compensation.

The temporal block erroneously takes the arrival time of the second echo to be that of the two-echo signal if the amplitude of the second echo is sufficiently larger than that of the first one. Furthermore, as shown in Sec. III B 2, the delay between the two echoes should not be affected much by varying the amplitude ratio. Hence, as in the previous experiment, the bats should respond as if only the apparent range to the reflecting object was shifted. Previous studies have shown (Moss and Schnitzler, 1995) that many bat species are capable of reliably discriminating between two targets at ranges that differ by less than 100 μs. Hence, one possible way of setting up such an experiment could be to have two target echoes, each one consisting of two copies of the recorded cry separated by 100 μs. For the first target the first echo's amplitude would be twice as large as that of the second one, whereas for the second target it would be the other way around. The target with the loud first echo would be delayed (<100 μs) with respect to the other target to compensate for any amplitude-induced latencies. The SCAT model predicts that despite this delay the target with the loud first echo would still be judged to be the closest target.

The spectral block introduces spurious echoes in situations where more than two overlapping echoes occur. In the simplest case of three overlapping echoes the model predicts that a spurious echo will be detected at $t_1+t_3-t_2$, where t_1, t_2, and t_3 denote the arrival times of the three echoes. As before, an experiment that varies the arrival time of a single-echo probe around the values of the arrival times from the three-echo signal should make it possible to verify this prediction. It should be noted that in a later paper (Simmons *et al.*, 1996) a new version of a SCAT is described which does not suffer from this illusory effect. The occurrence of spurious glints is avoided by making the SCAT model's basis functions phase sensitive. Instead of starting all the basis functions at the same time, as in the spectral block described in this paper, each basis function is made to start when the corresponding frequency channel registers a delay-line coincidence. This way the model produces images containing inpulselike responses, one for each echo, without spurious glints.

As mentioned in the Introduction, apart from the SCAT's relevance for biology, its capability of coping with multiple overlapping echoes would constitute a significant improvement over current ultrasonic sensor systems used for robotic applications. However, to determine whether the SCAT could play such a role we need to replace the simulated echoes used in this study by actually measured ones. Only real world data can tell us whether the limitations of the SCAT, as derived above, are minor inconveniences or whether they present important obstacles to its use by a real robot. Furthermore, all echoes have been taken to be unfiltered copies of the emitted cry so far. But in the real world, absorption, the directivity of emission and reception, and reflection upon a real target will all filter the echo to varying degrees. Since the spectral block translates all deviations from a flat spectrum into hypotheses about particular delays between the echoes it is not clear what will happen when real echoes are processed. Hence we are currently implementing the SCAT on a real sonar system allowing us to verify its usefulness for robotic applications.

ACKNOWLEDGMENT

This work was supported by a Marie Curie fellowship in the framework of the TMR program initiated by the European Commission.

Berkowitz, R. (Editor) (**1965**). *Modern Radar: Analysis, Evaluation and System Design* (Wiley, New York).

Beuter, K. (**1980**). ''A new concept of echo evaluation in the auditory system of bats,'' in *Animal Sonar Systems*, edited by R. Busnel and J. Fish pp. 747–761.

Fuzessery, Z. (**1988**). ''A mechanism for horizontal and vertical target localisation,'' in *Animal SONAR Processes and Performance (NATO ASI Series)*, edited by P. Nachtigall and P. Moore (Plenum, New York), pp. 471–475.

Fuzessery, Z., Hartley, D., and Wenstrup, J. (**1992**). ''Spatial processing within the mustached bat echolocation system: possible mechanisms for optimization,'' J. Comp. Physiol. A **170**, 57–71.

Kuc, R. (**1994**). ''Sensorimotor model of bat echolocation and prey capture,'' J. Acoust. Soc. Am. **96**, 1965–1978.
Lawrence, B., and Simmons, J. (**1982**). ''Echolocation in bats: The external ear and perception of the vertical positions of targets,'' Science **218**(29), 481–483.
Menne, D. (**1988**). ''A matched filter bank for the delay estimation in bats,'' in *Animal SONAR Processes and Performance (NATO ASI Series)*, edited by P. Nachtigall and P. Moore (Plenum, New York), pp. 835–842.
Moss, C., and Schnitzler, H. (**1995**). *Hearing by Bats* (Springer-Verlag, New York), pp. 87–145.
Peremans, H. (**1994**). ''A maximum likelihood algorithm for solving the correspondence problem in tri-aural perception,'' in *IEEE Int. Conf. on Multisensor Fusion and Integration for Intelligent Systems*, Las Vegas, pp. 485–492.
Peremans, H., Audenaert, K., and Campenhout, J. V. (**1993**). ''A high-resolution sensor based on tri-aural perception,'' IEEE Trans. Rob. Autom. **9**(1), 36–48.
Pollak, G. (**1988**). ''Time is traded for intensity in the bat's auditory system,'' Hearing Res. **36**, 107–124.
Saillant, P., Simmons, J., and Dear, S. (**1993**). ''A computational model of echo processing and acoustic imaging in frequency-modulated echolocating bats: The spectrogram correlation and transformation receiver,'' J. Acoust. Soc. Am. **94**, 2691–2712.
Schmidt, S. (**1992**). ''Perception of structured phantom targets in the echolocating bat, megaderma lyra,'' J. Acoust. Soc. Am. **91**, 2203–2223.
Simmons, J. (**1993**). ''Evidence for perception of fine echo delay and phase by the fm bat, eptesicus fuscus,'' J. Comp. Physiol. A **172**, 533–547.
Simmons, J., and Chen, L. (**1989**). ''The acoustic basis for target discrimination by fm echolocating bats,'' J. Acoust. Soc. Am. **86**, 1333–1350.
Simmons, J., Ferragamo, M., Saillant, P., Haresign, T., Wotton, J., Dear, S., and Lee, D. (**1995**). *Hearing by Bats* (Springer-Verlag, New York), pp. 146–190.
Simmons, J., Moss, C., and Ferragamo, M. (**1990**). ''Convergence of temporal and spectral information into acoustic images of complex sonar targets perceived by the echolocating bat, eptesicus fuscus,'' J. Comp. Physiol. A **166**, 449–470.
Simmons, J., Saillant, P., Ferragamo, M., Haresign, T., Dear, S., Fritz, J., and McMullen, T. (**1996**). *Auditory Computation* (Springer-Verlag, New York), pp. 401–468.
Suga, N. (**1990**). ''Cortical computational maps for auditory imaging,'' Neural Networks **3**, 3–21.
Webster, F. (**1967**). ''Performance of echolocating bats in the presence of interference,'' in *Animal Sonar Systems: Biology and Bionics*, edited by R. Busnel (Laboratoire de physiologie acoustique, Jouy-en-Josas, France), pp. 673–713.

LETTERS TO THE EDITOR

Comments on "Acoustic dispersion and attenuation in many spherical scatterer systems and the Kramers–Kronig relations" [J. Acoust. Soc. Am. 101, 3299–3305 (1997)]

Johan L. Leander
Department of Military Technology, National Defence College, P.O. Box 27805, S-11593 Stockholm, Sweden

(Received 24 August 1997; accepted for publication 15 April 1998)

The aim of this Comment is to suggest some possible improvements and developments of the investigation by Zhen Ye [J. Acoust. Soc. Am. **101**, 3299–3305 (1997)]. Particular attention is given to the causality concept and the use of integral theorems. © *1998 Acoustical Society of America.* [S0001-4966(98)00908-4]

PACS numbers: 43.20.Fn, 43.30.Gv [JEG]

I. NUMERICAL EVALUATION OF THE COMPLEX WAVE NUMBER

The first contribution from the investigation by Ye seems to be a numerical evaluation of the complex wave number due to early work by Waterman and Truell which is based on multiple scattering theory.[1] The scattering function is calculated numerically for various types of scatterers such as rigid and elastic spheres and air bubbles. The attenuation and the phase velocity are then calculated for the above types of scatterers for a volume fraction of 0.001. This part of the work is straightforward and significantly simplified since effects of dissipation are neglected.[2,3] The results for the phase velocities for the various systems of scatterers based on the Waterman and Truell theory are then compared with corresponding results based on a time-average equation [Eq. (22) in the work by Ye]. For the case of air bubbles, the difference in the low-frequency regime between the two theories is found to be dramatic. In comparing results from different theories it is of some interest to understand the original assumptions made in the derivations. For the case of air bubbles, for example, there exist a large amount of theoretical approaches.[2,4–9] The equation used by Ye [his Eq. (22)] is frequency independent and, if such a simple theory is to be used in a comparison, it would perhaps have been more appropriate to use the approximate Wood equation which is frequently consulted in bubble acoustics.[6,9] The Wood equation is based on volume averages of the density and the compressibility of the mixture and is here given in the form

$$\frac{c_0^2}{c_m^2}=1+\frac{4\pi NR_0c_0^2}{\omega_b^2}, \tag{1}$$

where c_0 and c_m are the sound speeds in the medium surrounding the scatterers and in the mixture, respectively, R_0 is the equilibrium bubble radius, and N is the number of bubbles per unit volume. The resonance frequency of the bubble reads

$$\omega_b^2=\omega_{\rm iso}^2=\frac{R_{b0}}{\rho_0R_0^2}\left[3-\frac{2\sigma}{R_0P_{b0}}\right], \tag{2}$$

where the subscript iso indicates isothermal conditions.[3] Here, P_{b0}, ρ_0, and σ are the equilibrium pressure in the bubble, the density of the medium surrounding the bubbles, and the surface tension, respectively. Finally, we note that it is readily shown that for the case of air bubbles, the Foldy theory is consistent with the Wood equation in the limit of low frequencies.[4,8,9] This requires, however, that effects of dissipation in terms of heat exchange between the gas and the liquid are included in the analysis.

II. THE CAUSALITY PRINCIPLE AND INTEGRAL THEOREMS

The second contribution from the work by Ye appears to be an analysis concerning the degree of causality of the theory by Waterman and Truell with respect to the type of scatterer considered. We will here expand a little on the causality principle and start by noting that the causality concept is a time domain property.[10] Before we continue, however, it is observed that Ye in his text mixes the numerical evaluation of the complex wave number due to Waterman and Truell and the causality principle. It could perhaps have been

fruitful to postpone the causality discussion and the corresponding equations until the causality test was to be performed.

In looking at linear transient wave propagation problems it is sometimes helpful to use the following Fourier integral,[8,11–14]

$$p(x,t)=\frac{1}{2\pi}\int_{-\infty}^{+\infty}P(0,\omega)\exp(-ik_m x)\exp(i\omega t)\,d\omega, \tag{3}$$

where $p(x,t)$ is the output pulse at position x due to an input pulse at $x=0$. The Fourier transform of the input pulse is denoted $P(0,\omega)$. The medium is modeled by the complex wave number $k_m=\omega/c_m(\omega)-i\alpha_m(\omega)$ where ω is the angular frequency, $c_m(\omega)$ is the phase velocity, and $\alpha_m(\omega)$ is the attenuation.[3] The medium model is said to be causal if it exists a wavefront which is propagating with the speed[11–14]

$$\lim_{\omega\to\infty} c_m(\omega)=c_m(\infty). \tag{4}$$

This time domain property can be expressed in terms of integral relations connecting the frequency domain quantities $c_m(\omega)$ and $\alpha_m(\omega)$.[6,9–11,15] Such integral relations are commonly named as the Kramers–Kronig relations although each investigator, in principle, can derive his own set of causal integral relations.[11] In discussing the Kramers–Kronig relations Ye uses the sentence ''They are, therefore, ideal to test the suitability of...,'' which is identical to what is stated in the work by Temkin which will be of great use in this letter.[6] It would have been nice for the reader if Ye had included the paper by Temkin in his list of references. Temkin presented a theoretical study of the attenuation and the dispersion of sound in bubbly fluids by means of a causality approach. He derived the following set of causal integral relations coupling the attenuation and the phase velocity for a dissipative medium.[6]

$$\frac{1}{c_m^2(\omega)}-\frac{\alpha_m^2(\omega)}{\omega^2}-\frac{1}{c_m^2(\infty)}=\frac{2}{\pi}\int_{-\infty}^{+\infty}\frac{\alpha_m(\Omega)}{c(\Omega)\Omega(\Omega-\omega)}\,d\Omega \tag{5}$$

and

$$2\frac{\alpha_m(\omega)}{\omega c_m(\omega)}=-\frac{1}{\pi}\int_{-\infty}^{+\infty}\frac{c_m^{-2}(\Omega)-c_m^{-2}(\infty)-\alpha_m^2(\Omega)\Omega^{-2}}{(\Omega-\omega)}\,d\Omega. \tag{6}$$

Moreover, Temkin rewrote Eq. (5) as[6]

$$\frac{1}{c_m^2(\omega)}-\frac{\alpha_m^2(\omega)}{\omega^2}-\frac{1}{c_m^2(0)}=\frac{2\omega}{\pi}\int_{-\infty}^{+\infty}\frac{\alpha_m(\Omega)}{c(\Omega)\Omega^2(\Omega-\omega)}\,d\Omega, \tag{7}$$

and we make the observation that the Kramers–Kronig relations connect the attenuation and the phase velocity to within a constant, $c_m(0)$ or $c_m(\infty)$. Actually, this fact forced Temkin to study $c_m(0)$ and $c_m(\infty)$ in a separate investigation where it was found that the Wood equation is approximate.[7] Furthermore, Eqs. (5) and (6) can, after some manipulation, be extracted from the investigation by O'Donnell *et al.*[15] Throughout this letter, the integrals in the relations coupling the attenuation and the phase velocity are Cauchy principal values.[11]

Let us now come back to the work by Ye who used the following form of the Kramers–Kronig relations [Eqs. (4) and (5) in his paper]

$$\mathrm{Re}[n_m^2(\omega)-1]=\frac{2}{\pi}\int_0^{+\infty}\frac{\Omega\ \mathrm{Im}[n_m^2(\Omega)]}{\Omega^2-\omega^2}\,d\Omega \tag{8}$$

and

$$\mathrm{Im}[n_m^2(\omega)]=-\frac{2\omega}{\pi}\int_0^{+\infty}\frac{\mathrm{Re}[n_m^2(\Omega)-1]}{\Omega^2-\omega^2}\,d\Omega, \tag{9}$$

where Re and Im denote real and imaginary parts, respectively. The complex index of refraction is $n_m(\omega)=k_m(\omega)/k_0$ where $k_0=\omega/c_0$. It is of interest here to check the form of the Kramers–Kronig relations Ye used by calling in the results by Temkin. In order to do that we rewrite Eqs. (8) and (9) by means of the complex index of refraction which yields

$$\frac{1}{c_m^2(\omega)}-\frac{\alpha_m^2(\omega)}{\omega^2}-\frac{1}{c_0^2}=\frac{2}{\pi}\int_{-\infty}^{+\infty}\frac{\alpha_m(\Omega)}{c(\Omega)\Omega(\Omega-\omega)}\,d\Omega \tag{10}$$

and

$$2\frac{\alpha_m(\omega)}{\omega c_m(\omega)}=-\frac{1}{\pi}\int_{-\infty}^{+\infty}\frac{c_m^{-2}(\Omega)-c_0^{-2}-\alpha_m^2(\Omega)\Omega^{-2}}{(\Omega-\omega)}\,d\Omega, \tag{11}$$

where we have used that $\alpha_m(\omega)$ and $c_m(\omega)$ are even functions.[16] By direct inspection of Eqs. (5), (6), (10), and (11) it is found that the formulation of the Kramers–Kronig relations in the work by Ye uses $c_m(\infty)=c_0$. Whether this is an assumption made by Ye or not is hard to tell since nothing is said about it in his paper. In any event, the Kramers–Kronig relations used by Ye are not the most general. Moreover, Temkin found that $c_0^2/c_m^2(\infty)=1-V$, where V is the volume fraction.[7] Also, for a Maxwell fluid which satisfies causality, we have with the notation used in this work that $c_0=c_m(0)\neq c_m(\infty)$.[12]

The Kramers–Kronig relations are necessary and sufficient conditions for causality.[10] That is to say, given a causal model, say $k_{\mathrm{Ca}}(\omega)=\omega/c_{\mathrm{Ca}}(\omega)-i\alpha_{\mathrm{Ca}}(\omega)$, then Eqs. (5)–(7) will hold with $\alpha_m(\omega)=\alpha_{\mathrm{Ca}}(\omega)$ and $c_m(\omega)=c_{\mathrm{Ca}}(\omega)$. Also, if a given model is in concordance with the Kramers–Kronig relations, it will correspond to a well-posed transient time domain problem. Now, if a given causal model, $k_{\mathrm{Ca}}(\omega)$, is approximated in some way, it is not obvious (at least not to this author) that the approximation will satisfy the Kramers–Kronig relations. Equations (13) and (14) in the work by Ye are a result of an approximation of the Waterman and Truell theory. It would perhaps have been of some use for the reader if Ye had touched upon this issue while deriving and presenting Eqs. (13) and (14) in his investigation. An analogous situation can be described by considering the regime of small effects in the sense that the attenuation per wave length, $\alpha_m(\omega)c_0/\omega$, and the velocity dispersion, $[c_m(\omega)$

$-c_0]/c_0$, both are small compared to unity. For this case, one could get an approximate version of the Kramers–Kronig relations as

$$\frac{c_0}{c_m^2(\omega)}-\frac{c_0}{c_m^2(\omega)}=\frac{2}{\pi}\int_{-\infty}^{+\infty}\frac{\alpha_m(\Omega)}{\Omega(\Omega-\omega)}\,d\Omega \tag{12}$$

and

$$2\,\frac{\alpha_m(\omega)}{\omega c_m(\omega)}=-\frac{1}{\pi}\int_{-\infty}^{+\infty}\frac{c_m^{-2}(\Omega)-c_m^{-2}(\infty)}{(\Omega-\omega)}\,d\Omega. \tag{13}$$

However, is it always to be expected that the above approximate relations, Eqs. (12) and (13), are consistent with causality? Again, this is not obvious to this author. A final hypothetical situation would be if we used an approximation of a noncausal model and then plugged it into an approximate version of Kramers–Kronig relations and found correspondence. This could perhaps mislead us to argue that the original model is causal. This short and very preliminary discussion is used here so as to demonstrate that it might be of some use to be careful while manipulating with models and equations. Ye also discusses the influence of the scattering function on the causality property. Incidentally, this author studied transient wave propagation in bubbly fluids by means of the Foldy theory for the regime of small effects.[8] In that work it turned out that the scattering function had to be thoroughly examined in order to finally establish that there was causality. Let us here, for the case of demonstration of the importance of the behavior of the scattering function, briefly rehash a simplified version of what took place some time ago. We used the complex wave number

$$k_F(\omega)=k_0\left[1+\frac{2\pi N f(\omega)}{k_0^2}\right], \tag{14}$$

where $f(\omega)=\omega^2 R_0 Q(\omega)$ is the scattering function where

$$Q(\omega)=\frac{1}{\omega_b^2-\omega^2+2i\omega\beta}, \tag{15}$$

where β is the damping function. In our investigation we used the full expressions for ω_b and β by Prosperetti, modeling viscosity of the liquid, heat exchange between the phases, and compressibility of the surrounding liquid.[5] For the present purpose we only consider the adiabatic case where compressibility effects are included. The functions ω_b and β are for this case given by

$$\omega_b^2=\omega_a^2+\frac{\omega^2 k_0^2 R_0^2}{1+k_0^2 R_0^2} \tag{16}$$

and

$$\beta=\left(\frac{\omega^2 R_0}{2c_0}\right)\frac{1}{1+k_0^2 R_0^2}, \tag{17}$$

where the adiabatic resonance frequency, ω_a, is given by Eq. (2) except for the fact that the 3 should be replaced by 3γ where γ is the ratio of specific heats of the enclosed gas. By neglecting terms of order $k_0 R_0$ squared in Eqs. (16) and (17), the function $Q(\omega)$ becomes

$$Q(\omega)=\frac{1}{\omega_a^2-\omega^2+i\omega^3 R_0/c_0}. \tag{18}$$

In trying to find out whether this formulation is causal or not, one can perform an analytic evaluation of the Fourier integral, Eq. (3), with $k_m(\omega)=k_F(\omega)$. In doing that we use the complex plane and set $z=\nu+i\omega$. Let us now omit the details and just state that the model is noncausal if $Q(\omega=z/i)$ is nonanalytic in the right-hand z plane.[11] We are thus led to study the denominator of $Q(z/i)$ and try to locate the zeros in the z plane of the cubic equation

$$z^3-\frac{c_0}{R_0}z^2-\frac{c_0\omega_a^2}{R_0}=0. \tag{19}$$

Now, it turns out that there is one zero in the right-hand z plane and the model is noncausal in its present form. This fact puzzled this author somewhat until it was finally realized that one should not neglect terms of order $k_0 R_0$ squared. By using the full expressions, Eqs. (16) and (17), the function $Q(\omega)$ becomes

$$Q(\omega)=\frac{1+ik_0R_0}{\omega_a^2-\omega^2+i\omega\omega_a^2R_0/c_0}, \tag{20}$$

and we are now led to study the quadratic equation

$$z^2+\frac{\omega_a^2 R_0}{c_0}z+\omega_a^2=0, \tag{21}$$

which has no zeroes in the right-hand z plane so that the model is now causal. The conclusion from this discussion is that it might be critical to manipulate with a model. Another important observation can be made in that the above results are valid for a wide range of bubble sizes. That is to say, the bubble size can be varied and the causality (or noncausality for that matter) is kept. If the full expressions for ω_b and β by Prosperetti are considered, the above causality analysis becomes far more cumbersome.[17] Actually, it becomes so involved and lengthy that in submitting the paper, the referee claimed that it was the most verbose and uninteresting paper he had ever seen. The referee also kindly added that the investigation had nothing to do, whatsoever, with our contemporary understanding of continuum mechanics!

In the last part of his investigation, Ye uses his expressions for the Kramers–Kronig relations [Eqs. (8) and (9) in this letter] so as to test the suitability of the Waterman and Truell model. He finds that the integral relations are not satisfied for the types of scatterers considered. This means, due to the necessity condition, that he finds that there is noncausality and it would here have been convenient if he had stated that explicitly. However, depending on the type of scatterer he considers, the ''capability'' of the Waterman–Truell model to ''reproduce itself'' via the integral relations is changed and Ye argues that this is a measure of the degree of violation of the causality principle. Of course, by pure intuition (whatever that is) one might be willing to say that the ability of a given noncausal model to reproduce itself via the Kramers–Kronig relations is a measure of its ''goodness.'' However, to this author, one cannot talk about gradual causality from the theoretical standpoint. Either we

have causality or not, and there is nothing in between. Either there exists a wavefront propagating with a finite speed relevant for the problem, $c_m(\infty)$, or there is no wavefront at all and the perturbation is felt immediately everywhere in the medium. From the practical point of view, however, one could perhaps give an interpretation of gradual causality. A simple discussion will now be given and, before we do that, it is to be noted that it would have been fruitful if Ye had tried to quantify, in terms of time domain quantities, what is actually to be meant by ''an indication of the degree of violation of causality.''

Now, let us assume that we have two different models, $k_A(\omega)$ and $k_B(\omega)$, which do not satisfy complete causal integral relations such as Eqs. (7) and (8) or (8) and (11). They are thus noncausal, but it turns out that the difference between $k_A(\omega)$ and what comes out of the integral relations while plugging in $k_A(\omega)$ is much smaller than the corresponding difference for the case of $k_B(\omega)$. As stated earlier, one would here perhaps be willing to say the model $k_A(\omega)$ is superior to $k_B(\omega)$ in some time domain sense. Since the two models are noncausal, there is no wavefront but perhaps it can be shown the model, $k_A(\omega)$, yields a pulse for which the major part is traveling with a speed less than $c_A(\infty)$. For the other model, $k_B(\omega)$, we would perhaps find that, in comparison to the case of $k_A(\omega)$, a smaller part of the major part of the pulse would be traveling with a speed less than $c_B(\infty)$. In the above, we have assumed that $c_A(\infty)$ and $c_B(\infty)$ exist. This is not in contradiction with noncausality. The existence of the high-frequency limit of the phase velocity is a necessary but not sufficient condition for causality.[14] This can be understood from the Paley–Wiener condition.[11] The discussion of practical time domain interpretations of the degree of noncausality can be further visualized by means of an alternative form of Eq. (3):

$$p(x,t)=\int_{-\infty}^{+\infty} p(0,t-\tau)h_m(x,\tau)\,d\tau, \tag{22}$$

where $h_m(x,t)$ is the impulse response which characterizes the medium in the time domain.[8,12] This quantity is related to the attenuation and phase velocity by means of the Fourier integral[11]

$$h_m(x,t)=\frac{1}{2\pi}\int_{-\infty}^{+\infty}\exp(-ik_m x)\exp(i\omega t)\,d\omega. \tag{23}$$

Equation (22) says that the output pulse is given by a convolution of the input pulse and the impulse response. Since $k_A(\omega)$ is supposed to be better than $k_B(\omega)$, this can perhaps be related to the corresponding impulse responses, $h_A(x,t)$ and $h_B(x,t)$. A possible relation could be that a larger part of $h_A(x,t)$ is found for times greater than $x/c_A(\infty)$ than is the case for $h_B(x,t)$ for times greater than $x/c_B(\infty)$. The discussion that we present here is obviously very loose and preliminary, but we simply want to stress that there is something important missing in the work by Ye that perhaps would, if properly done, strengthen his test of gradual causality and the corresponding conclusions.

From the work by Ye it seems to be the case that among the types of scatterers considered, air bubbles yield the best ''capability of reproduction'' by the Kramers–Kronig relations. It is confusing to find that this fact should be related to the interest of bubble acoustics, as is stated on p. 3304. To this author, there exist a great number of relevant reasons for an interest in bubble acoustics within the acoustic establishment. Moreover, although it is perhaps obvious, it is here stated that the fact that a given model satisfies the causality principle does not necessarily mean that it has anything, whatsoever, to do with the actual physical processes it is supposed to model. Causality may indeed exist even though the expressions for the attenuation and phase velocity of the model are by no means in agreement with experimental data. Finally, although this author only took into account the monopole part of the bubble scattering function and considered the regime of small effects while proving causality for the Foldy theory, it would not had been a surprise if Ye had found full correspondence in considering the case of air bubbles.[8]

III. SUMMARY

The investigation by Ye deals with such fundamental areas of physics as thermodynamics, the causality principle, and multiple scattering theory. As it stands, however, it is perhaps a little bit more confusing than convincing and also, to some extent, incomplete. The objective of this letter has been to suggest some possible improvements and future developments.

[1] Z. Ye, ''Acoustic dispersion and attenuation in many spherical scatterer systems and the Kramers–Kronig relations,'' J. Acoust. Soc. Am. **101**, 3299–3305 (1997).
[2] G. Gaunard, K. P. Scharnhorst, and H. Uberall, ''Giant monopole resonances in the scattering of waves from gas-filled spherical cavities and bubbles,'' J. Acoust. Soc. Am. **65**, 573–594 (1979).
[3] S. Temkin, *Elements of Acoustics* (Wiley, New York, 1981).
[4] L. L. Foldy, ''The multiple scattering of waves,'' Phys. Rev. **674**, 107–119 (1945).
[5] A. Prosperetti, ''The thermal behaviour of oscillating gas bubbles,'' J. Fluid Mech. **222**, 587–616 (1991).
[6] S. Temkin, ''Attenuation and dispersion of sound in bubbly fluids via the Kramers-Kronig relations,'' J. Fluid Mech. **211**, 61–72 (1990).
[7] S. Temkin, ''Sound speeds in suspensions in thermodynamic equilibrium,'' Phys. Fluids **4**, 2399–2409 (1992).
[8] J. L. Leander, ''Transient wave propagation through bubbly layers via the Foldy-Twersky integral equation,'' J. Acoust. Soc. Am. **95**, 2378–2386 (1994).
[9] J. L. Leander, ''Sound propagation in dilute gas-liquid suspensions: Definition of the regime of noninteracting bubbles via scattering theory and the causality approach,'' J. Acoust. Soc. Am. **97**, 1974–1977 (1995).
[10] J. S. Toll, ''Causality and the dispersion relation: Logical foundations,'' Phys. Rev. **104**, 1760–1770 (1956).
[11] A. Papoulis, *The Fourier Integral and Its Applications* (McGraw–Hill, New York, 1962).
[12] J. L. Leander, ''Acoustic pulse propagation in Maxwell fluids,'' J. Acoust. Soc. Am. **94**, 1643–1650 (1993).
[13] J. L. Leander, ''On the relation between the wave front speed and the group velocity concept,'' J. Acoust. Soc. Am. **100**, 3503–3507 (1996).
[14] J. L. Leander, ''Wave front speed and group velocity in dissipative media: Pulse propagation in relaxing and bubbly fluids'' (submitted).
[15] M. O'Donnell, E. T. Jaynes, and J. G. Miller, ''Kramers-Kroning relationship between ultrasonic attenuation and phase velocity,'' J. Acoust. Soc. Am. **69**, 696–701 (1981).
[16] L. D. Landau and E. M. Lifshitz, *Statistical Physics* (Pergamon, Oxford, 1986).
[17] J. L. Leander, ''Scattering of an acoustic pulse by a small gas bubble in a liquid'' (1993, unpublished).

Response to "Comments on 'Acoustic dispersion and attenuation in many spherical scatterer systems and the Kramers–Kronig relations'" [J. Acoust. Soc. Am. 104, 1111–1114 (1998)]

Zhen Ye
Department of Physics, National Central University, Chung-li, Taiwan, Republic of China

(Received 24 February 1998; accepted for publication 15 April 1998)

This communication replies to some comments in ''Comments on 'Acoustic dispersion and attenuation in many spherical scatterer systems and the Kramers–Kronig relations.' '' © *1998 Acoustical Society of America.* [S0001-4966(98)01008-X]

PACS numbers: 43.20.Fn, 43.30.Gv [JEG]

I thank Johan Leander for useful comments on the paper ''Acoustic dispersion and attenuation in many spherical scatterer systems and the Kramers–Kronig relations'' [J. Acoust. Soc. Am. **101**, 3299–3305 (1997)], referred to as Paper I hereafter. While I agree with many of his comments, a few clarifications seem appropriate.

(1) Paper I is concerned with wave dispersion in random media containing many scatterers. In particular, the dispersion relation derived by Waterman and Truell (1961) is considered. This dispersion relation is applied to a few systems, and examined in the context of the Kramers–Kronig (KK) relations which are a result of causality. Differing from the work of Temkin, who used the KK relations to derive the dispersion from the attenuation or vice versa, in this paper the KK relations are used to examine the known dispersion relations.

(2) The dispersion for an acoustic wave in a bubbly liquid is usually frequency dependent from the multiple scattering theory. In the low-frequency limit (i.e., in the Rayleigh scattering regime), in which the acoustic frequency is much smaller than the natural frequency of the bubbles, it can be shown that the sound speed anomaly predicted from Waterman and Truell (1961) becomes nearly frequency independent, and is approximately given as

$$\Delta c \approx -\frac{\beta \rho_l c_0^3}{2\gamma P_0}, \tag{1}$$

where β is the bubble volume fraction, P_0 is the ambient pressure, and ρ_l is the density of the liquid. This formula is consistent with Eq. (1) of Leander, but differs significantly from the time-average equation (22) in Paper I. However, it can be shown the time-average equation would be in agreement with the multiple scattering theory at low frequencies when and only when the acoustic impedance of the scatterers is close to that of the surrounding medium (Ye and McClatchie, 1998); and under these conditions, it is also consistent with the well-known Wood equation. This is exactly the case for the weak fluid scatterer considered in Paper I.

(3) I appreciate that Leander pointed out that the reference to the work of Temkin (1990) was missing, which has partially motivated the present work.

(4) The KK relation in Paper I takes the assumption $c(\infty)=c_0$ in analogy with the optical situation (Kittle, 1995).

(5) I fully agree with Leander's discussion on the influence of the scattering function on the causality property. It is conceivable that the suitability of a particular dispersion model should not only be tested through the KK relations but be investigated in connection with the time domain analysis.

In my opinion, Johan Leander pointed out some incompleteness in Paper I, and has made good suggestions for possible improvements.

Kittle, C. (**1995**). *Introduction to Solid State Physics* (Wiley, New York).
Temkin, S. (**1990**). ''Attenuation and dispersion of sound in bubbly fluids via the Kramers–Kronig relations,'' J. Fluid Mech. **211**, 61–72.
Waterman, P. C., and Truell, R. (**1961**). ''Multiple scattering of waves,'' J. Math. Phys. **3**, 700–715.
Ye, Z. (**1997**). ''Acoustic dispersion and attenuation in many spherical scatterer systems and the Kramers-Kronig relations,'' J. Acoust. Soc. Am. **101**, 3329–3305.
Ye, Z., and McClatchie, S. (**1998**). ''On inferring sound speed in aquatic animals,'' J. Acoust. Soc. Am. **103**, 1667–1670.

A note about acoustic streaming: Comparison of C. E. Bradley's and W. L. Nyborg's theories

Xiaoliang Zhao, Zhemin Zhu, and Gonghuan Du
Institute of Acoustics, Nanjing University, Nanjing 210093, People's Republic of China

(Received 27 August 1997; accepted for publication 18 March 1998)

Some comparisons of C. E. Bradley's and W. L. Nyborg's theories on acoustic streaming are given.
 [S0001-4966(98)03108-7]

PACS numbers: 43.25.Nm [MAB]

C. E. Bradley derived a system of equations and boundary conditions that describe acoustically driven flow in a very general system.[1] Through careful consideration of boundary conditions at the face of the acoustic radiator, he found a new flow-driven mechanism. Each of the driven mechanisms was analyzed to determine both their physical origins and the structures of the resultant flow. His research is quite useful and necessary, especially in handling the problems of acoustic streaming induced by a radiator whose surface motion is nonrectilinear. Formerly, W. L. Nyborg published an article on acoustic streaming in which a system of equations was also established to predict the acoustic streaming field structure.[2] Noting that this article was not cited by Bradley's paper, we compared them in order to understand the complex streaming problems better.

First, both Bradley and Nyborg started their analysis from equations of conservation of mass and momentum in Eulerian coordinates. The difference is that Bradley considered that entropy does not vary under the first-order approximation in the constitutive relations, while Nyborg assumed that $p_1=c^2\rho_1+R\rho_1$, in which the second term denotes the ''relaxation.'' If we assume $\mathbf{u}_1$ is represented as the real part of a complex number with time factor $e^{i\omega t}$, the equation in Bradley's paper

$$\boldsymbol{\nabla}\boldsymbol{\nabla}\cdot\mathbf{u}_1+\frac{\mu}{\rho_0 c_0^2}\nabla^2\frac{\partial\mathbf{u}_1}{\partial t}+\frac{\mu_B+\mu/3}{\rho_0 c_0^2}\boldsymbol{\nabla}\boldsymbol{\nabla}\cdot\frac{\partial\mathbf{u}_1}{\partial t}-\frac{1}{c_0^2}\frac{\partial^2\mathbf{u}_1}{\partial t^2}=0, \tag{1}$$

reduces to

$$[2k^{-2}+ib\beta^{-2}]\boldsymbol{\nabla}\boldsymbol{\nabla}\cdot\mathbf{u}_1+2\mathbf{u}_1=i\beta^{-2}\boldsymbol{\nabla}\times\boldsymbol{\nabla}\times\mathbf{u}_1, \tag{2}$$

where constants β and b are defined as,

$$\beta^2=\frac{\omega\rho_0}{2\mu},\quad \mu b=[\mu_B+\tfrac{4}{3}\mu]. \tag{3}$$

It is almost the same as Eq. (8) in Nyborg's article, except that $\mu b=[\mu_B+4/3\mu+\rho_0 R]$ by Nyborg's definition, in which the relaxation term affects the first-order sound field as would an increase of the bulk viscosity. In addition, the decomposition process (to the first-order velocity field) made by Bradley and Nyborg agree well, i.e., Eqs. (6) and (7) in Bradley's paper are consistent with Eqs. (12) and (13) in Nyborg's article.

Second, both Bradley and Nyborg dealt with the second-order Eulerian time-averaged velocity $\mathbf{u}_{dc}$ or $\mathbf{u}_2$ similarly. An improvement made by Bradley is that he studied the boundary condition of the radiator in detail and deduced that $\mathbf{u}_{dc}$ commonly is not divergence free. Equations (10) and (11) in Bradley's paper are the same as Eqs. (14) and (15) in Nyborg's article. Nyborg assumes $\boldsymbol{\nabla}\cdot\mathbf{u}_2=0$ while Bradley derived

$$\boldsymbol{\nabla}\cdot\mathbf{u}_{dc}=-\frac{1}{\rho_0 c_0^2}\boldsymbol{\nabla}\cdot\langle\mathbf{I}\rangle, \tag{4}$$

where $\langle\mathbf{I}\rangle=\langle p_1\mathbf{u}_1\rangle$ is the acoustic intensity. Consequently, Eq. (17) in Bradley's paper also resembles Eq. (16) in Nyborg's article, except that an amendment of F is made by Bradley due to the divergence of $\mathbf{u}_{dc}$.

Third, the definitions of mass transport in both articles are similar. Nyborg derived the ''net-mass-flow'' velocity for acoustic streaming in accordance with the nonacoustic situation where an incompressible fluid of constant density ρ_0 flows steadily with velocity $\mathbf{U}$. To be specific, he kept the product of $\rho\mathbf{u}$ up to the second order and took the time average, then obtained

$$\int_S\langle\rho_0\mathbf{u}_2+\rho_1\mathbf{u}_1\rangle\cdot d\mathbf{S}=M, \tag{5}$$

where M represents the time-averaged mass-flow rate. Assuming that $\mathbf{u}_T=\rho_0^{-1}\langle\rho_1\mathbf{u}_1\rangle$, he defined the mass-transport velocity $\mathbf{U}$ as $\mathbf{U}=\mathbf{u}_2+\mathbf{u}_T$. In Bradley's paper, this process may be found in Sec. III A, though $\mathbf{u}_T$ is not defined.

Last, both Bradley and Nyborg have discussed the Lagrangian velocity field to explain why the Eulerian time-average velocity $\mathbf{u}_{dc}$ or $\mathbf{u}_2$ (with nonslip boundary condition at the rest surface of the boundary) is not the velocity commonly determined in experiment; i.e., Eq. (22) in Bradley's paper is the same as Eq. (40) in Nyborg's article. That is,

$$\langle\mathbf{u}(Q,t)\rangle\cong\mathbf{u}_2+\langle\boldsymbol{\xi}_1\cdot\nabla\mathbf{u}_1\rangle. \tag{6}$$

Here $\langle\mathbf{u}(Q,t)\rangle$ is equivalent to $\mathbf{u}_L$, both denoting the time-averaged Lagrangian velocity. Nyborg focused his interest on the rectilinear motion cases, i.e., $\boldsymbol{\xi}_1$ and $\mathbf{u}_1$ are parallel to each other.[2] He concluded that $\mathbf{U}=\langle\mathbf{u}(Q,t)\rangle$ [Eq. (41a), Ref. 2] under that approximation. Bradley, on the other hand, extended the discussion to nonrectilinear ones and found if the neighboring elliptical motion is not uniform, the time-averaged Lagrangian velocity field $\mathbf{u}_L$ differs from mass-transport velocity $\mathbf{U}$. Otherwise, if the field is rectilinear or if the field is elliptical but uniform, $\mathbf{u}_L$ and $\mathbf{U}$ are identical. The results they obtained for rectilinear fluid motion cases also agree.

In conclusion, the processes in which Bradley and Nyborg dealt with the acoustic streaming field structure are found to be similar to each other in some respects. Nyborg

devoted most of his study to rectilinear fluid motion cases, while Bradley extended the theory to nonrectilinear ones. Comparison of these two articles may give readers a better understanding of acoustic streaming field structure.

[1] C. E. Bradley, ''Acoustic streaming field structure: The influence of radiator,'' J. Acoust. Soc. Am. **100**, 1399–1408 (1996).
[2] W. L. Nyborg, in *Physical Acoustics*, edited by W. P. Mason (Academic, New York, 1965), Vol. 2B, pp. 265–331.

Comments on "A unitary model of pitch perception" [J. Acoust. Soc. Am. 102, 1811–1820 (1997)]

Robert P. Carlyon
MRC Cognition and Brain Sciences Unit, 15 Chaucer Road, Cambridge CB2 2EF, England

(Received 18 November 1997; accepted for publication 21 April 1998)

Meddis and O'Mard have recently presented a revised autocorrelogram model of pitch perception, which they claim can account for the different pattern of experimental results obtained for complex tones consisting of resolved and unresolved harmonics. This Letter demonstrates that, in contrast to the experimental data, important features of the model's output and predictions vary with frequency region rather than with resolvability. © *1998 Acoustical Society of America.*
[S0001-4966(98)02608-3]

PACS numbers: 43.66.Nm, 43.66.Ba, 43.66.Hg [JWH]

INTRODUCTION

Meddis and O'Mard (1997) have recently proposed a modification to Meddis and Hewitt's (1991) autocorrelogram model of pitch perception. They argue that the new model is consistent with the different patterns of experimental results which have been obtained for complex tones consisting of resolved and of unresolved harmonics. In particular, they state that it can account for the data reported in two papers by this author and Shackleton (Carlyon and Shackleton, 1994; Shackleton and Carlyon, 1994),[1] and take issue with our conclusion that the $F0$'s of resolved and unresolved harmonics are processed by different mechanisms. They argue instead that the perception of both resolved and unresolved harmonics can be accounted for by a unitary model of pitch.

The experiments we reported used harmonic complex tones which were designed to tease apart the effects of resolvability and of frequency region. This distinction is important because, for a given $F0$, increases in harmonic number are accompanied not only by a decrease in resolvability, but also by an increase in absolute frequency. We therefore varied $F0$ and frequency region orthogonally, by bandpass filtering harmonic complexes with $F0$'s of either 88 or 250 Hz into one of three frequency regions, termed LOW (125–625 Hz), MID (1375–1875 Hz), and HIGH (3900–5300 Hz). Although the harmonics of both $F0$'s were resolved in the LOW region and unresolved in the HIGH region, only the 250-Hz complex was resolved in the MID region. This region therefore played a crucial role in allowing us to investigate the effects of resolvability, independently of frequency region. The experiments revealed three effects which were dependent on resolvability per se, where a complex is defined as ''resolved'' when fewer than two components fall within the 10-dB-down bandwidth of an auditory filter (Glasberg and Moore, 1990) centered on that complex, and ''unresolved'' when more than three components interact within that passband. Meddis and O'Mard claim that their model can account for all three effects. The success of the model with regard to one of these, the effects of phase on pitch, is acknowledged both here and elsewhere (Carlyon and Shackleton, 1994, p. 3545). The remaining two will be considered in the following sections.

I. THE SHAPE OF THE SAC AND THE DETECTION OF *F0* DIFFERENCES

A. Background

Shackleton and Carlyon showed that thresholds for detecting $F0$ differences (''$DLF0$'s'') were higher for unresolved harmonics than for resolved harmonics, independently of $F0$ or frequency region. As shown in Fig. 1(a), $DLF0$'s were low at both $F0$'s (88 and 250 Hz) in the LOW region, high at both $F0$'s in the HIGH region, and, in the MID region, low at an $F0$ of 250 Hz but high at an $F0$ of 88 Hz. Similar findings can be seen in the earlier data of Hoekstra (1979) and in Fig. 1(b), which shows Carlyon and Shackleton's measurements of sensitivity (d') to a fixed $F0$ difference of 3.5%. Although it was pointed out that this did not provide crucial evidence against single-mechanism models in general, it was stated that the findings were inconsistent with a predecessor to Meddis and O'Mard's model (Meddis and Hewitt, 1991), in which the poorer encoding of higher harmonics was due to the higher frequency region rather than to a loss of resolvability. Meddis and O'Mard present two simulations in support of their claim that the new model can account for the superior discriminability of resolved compared to unresolved harmonics. These will be described in turn, together with additional simulations which used stimuli more similar to those in Carlyon and Shackleton's experiments.

B. Simulations

1. Method

To produce the additional simulations described in this section, SACs generated by Meddis and O'Mard's model were obtained for stimuli as close as possible to those used by Carlyon and Shackleton (1994). These differed from the stimuli used in Meddis and O'Mard's simulations in having a 15-dB lower level, bandpass filters with slopes of 48 dB/octave instead of 24 dB/octave, and with the lower baseline $F0$ being 88.4 Hz instead of 100 Hz. Carlyon and Shackleton used this lower $F0$ because, for some listeners, complexes in the MID region with an $F0$ of 100 Hz were not completely unresolved [Shackleton and Carlyon, 1994, Fig. 3(b)].

Complex tones consisting of a large number of consecu-

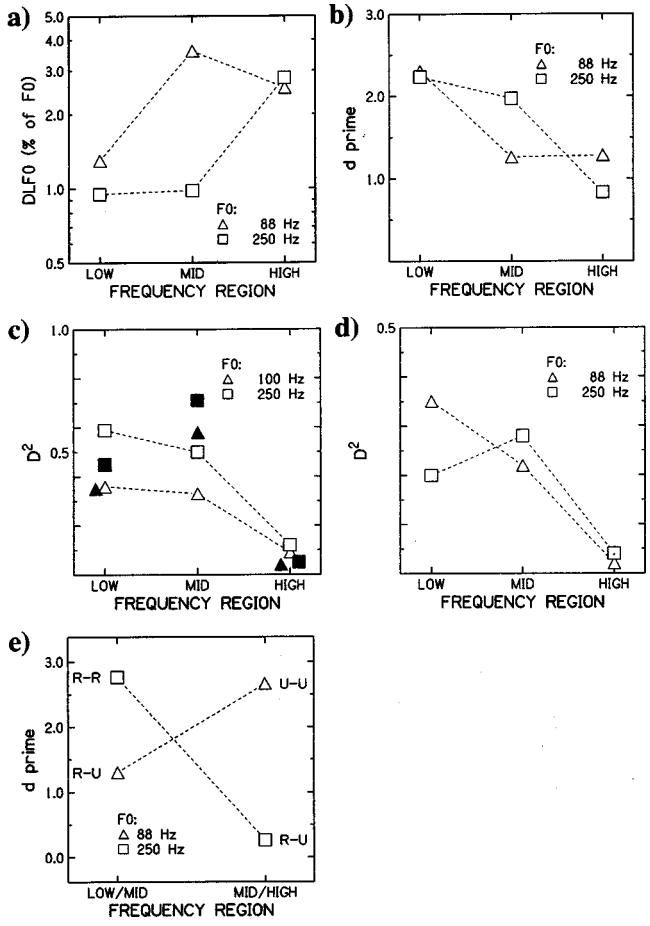

FIG. 1. (a) Mean data for three listeners in the study by Shackleton and Carlyon (1994), showing *DLF*0's for complex tones with *F*0's of 88 and 250 Hz, filtered into the LOW, MID, and HIGH regions. (b) Sensitivity (*d'*) obtained for a 3.5% difference by Carlyon and Shackleton (1994) at the two *F*0's and three frequency regions. Mean data from three listeners. (c) Open symbols: Sensitivity (D^2) predicted by Meddis and O'Mard's simulations for a 2% difference in *F*0 imposed on *F*0's of 100 Hz and 250 Hz in the LOW, MID, and HIGH frequency regions. Closed symbols are for the case where the attenuation rate of the bandpass filters has been changed to 48 dB/octave. (d) As (c), but using stimuli similar to those used by Carlyon and Shackleton; note the change in the scale of the ordinate *re*: part (c). (e) Sensitivity to an across-frequency difference in *F*0 of 7.1% obtained by Carlyon and Shackleton (1994). Mean data from three listeners. See text for details of the simulations.

tive, equal-amplitude harmonics were generated using the same program as used by Carlyon and Shackleton, played out of a 16-bit DAC (CED 1401plus) at a sampling rate of 20 000 Hz, filtered using the same equipment and cutoffs as in the original experiment, and captured using a 16-bit ADC (CED 1401plus). The resulting waveform files were then processed by Meddis and O'Mard's model using the same parameters as described in their article. The stimuli used in the simulations differed from those used by Carlyon and Shackleton in that they were not frequency modulated and were not presented against a background of pink noise.

2. The shape of the SAC

In their Fig. 5, Meddis and O'Mard show that the SAC for a complex tone with an *F*0 of 100 Hz has a sharp peak near 1/*F*0 when filtered into the LOW region, where the harmonics are resolved, but a much broader peak in the HIGH region, where the harmonics are unresolved. Figure 2 here clearly shows that this is an effect of frequency region, rather than of resolvability: Specifically, the shapes of the peaks in the SACs produced by Carlyon and Shackleton's stimuli in the MID region are very similar at the two *F*0's, even though the harmonics in the stimuli are resolved at an *F*0 of 250 Hz but unresolved at an *F*0 of 88 Hz.

3. Simulating sensitivity to F0 differences

Meddis and O'Mard provided a quantitative account of the predictions of the model, by simulating sensitivity to *F*0 differences at baseline *F*0's of 100 and 250 Hz, in the three frequency regions used by Shackleton and Carlyon. When attempting to model discrimination data with a deterministic model such as Meddis and O'Mard's, one must either introduce an explicit source of internal variance, or define some aspect of the difference between the outputs of the model to two stimuli which corresponds to sensitivity. Meddis and O'Mard adopted the latter approach, which, although not making the source of internal variance explicit, is nevertheless valid in that it can produce a set of predictions which can be tested against experimental data. They generated pairs of stimuli, one at the baseline *F*0 and one 2% higher, and calculated the squared Euclidean distance (D^2) between their SACs. The resulting simulations are replotted as the

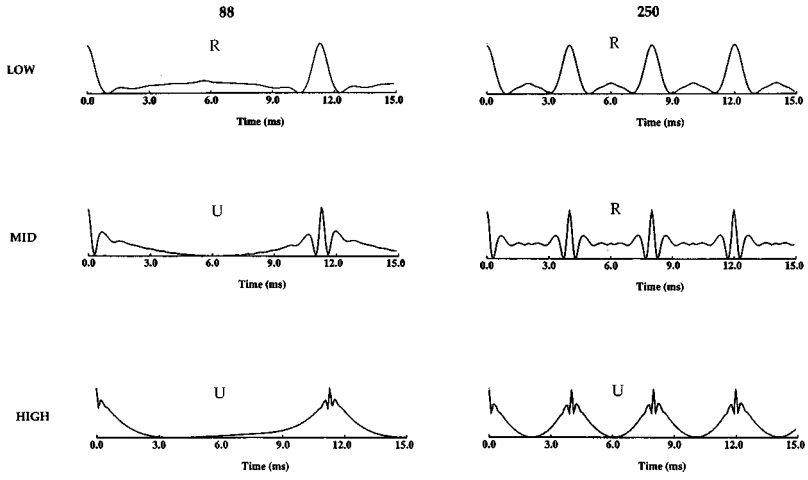

FIG. 2. SACs generated by Meddis and O'Mard's model for the stimuli of Carlyon and Shackleton (1994), at *F*0's of 88 and 250 Hz, filtered into the LOW, MID, and HIGH regions.

open symbols in Fig. 1(c)[2] and show that, in the LOW region, the predicted sensitivity is greater at an $F0$ of 250 Hz than at 100 Hz, with this difference decreasing slightly in the MID region, and with both $F0$'s showing essentially zero sensitivity in the HIGH region. It can be seen that the model fails to account for the main aspect of Carlyon and Shackleton's results, which is that sensitivity is higher at 250 Hz than at 88 Hz only in the MID region [Fig. 1(b)].

A further weakness of the model lies in its sensitivity to fairly modest changes in the stimuli. Figure 1(d) shows that, when Carlyon and Shackleton's stimuli were used, D^2 was not only lower overall, but, in the LOW region, was now lower at 250 Hz than at 88 Hz—the opposite direction to that seen in the data. The difference between the simulations obtained with the two sets of stimuli appears to be due both to the difference in filter slopes and to the difference in level: The solid symbols in Fig. 1(c) show that changing the filter slopes to 48 dB/octave while keeping the level at 60 dB/component predicts a pattern of results which differs both from that obtained in Meddis and O'Mard's original simulation [open symbols, Fig. 1(c)] and with Carlyon and Shackleton's stimuli [Fig. 1(d)]. The predictions were also affected by changing the lower $F0$ in Meddis and O'Mard's simulation from 100 to 88 Hz (not shown). In fact, a number of different simulations were tried by this author, and the only feature of the predictions which remained constant was the very low D^2 produced in the HIGH region.[3] In contrast to this rather labile behavior, Hoekstra (1979) reported that the superior sensitivity for resolved compared to unresolved harmonics (obtained with a fixed filter center frequency and a variable $F0$) was hardly affected by variations in sensation level (pp. 28–29) or filter characteristics (pp. 33–36). It is plausible that the capricious nature of the quantitative simulations could be remedied by a revised decision statistic. However, a great strength of Meddis and O'Mard's approach is the generation of quantitative predictions which can be closely compared to experimental results, and so this matter clearly needs attention. It would be disappointing if evaluation of the model were restricted to a qualitative visual impression of the general form of the SACs.

II. COMPARING THE *F0*'s OF RESOLVED AND UNRESOLVED HARMONICS

Carlyon and Shackleton's strongest evidence against single-mechanism models came from an experiment in which two groups of harmonics were presented simultaneously, and in which listeners were required to detect an $F0$ difference between them. It was predicted that if the $F0$'s of resolved and unresolved harmonics were processed by separate mechanisms, then listeners should have performed poorly when the two groups to be compared differed in resolvability, but well when the two groups were either both resolved or both unresolved. Despite some complications in the interpretations of the results (see Carlyon and Shackleton, 1994; Carlyon, 1998), this prediction was confirmed: As shown in Fig. 1(e), performance was much better when the two groups of harmonics to be compared were either both resolved (250 Hz, LOW vs MID region) or both unresolved (88 Hz, MID vs HIGH) than when they differed markedly in resolvability (88 Hz, LOW vs MID and 250 Hz, MID vs HIGH).

In order to account for Carlyon and Shackleton's results, Meddis and O'Mard refer to the differences in the shapes of the peaks in the simulated SACs for low and high harmonics, as plotted in their Fig. 4. However, inspection of the sine-phase stimuli in that figure shows that the shape of the peak in the SAC varies with frequency region, rather than with resolvability. This can also be seen in Fig. 2 of this paper. Clearly, the peaks of the SACs cannot account for the pattern of results observed by Carlyon and Shackleton, which are dependent on resolvability, rather than on frequency region. In particular, they provide no basis for the finding that listeners could easily compare the $F0$'s of two complexes in the LOW and MID regions when those $F0$'s are close to 250 Hz, but not when they are close to 88 Hz.[4]

III. DISCUSSION

The simulations presented here show that Meddis and O'Mard's model cannot account for the auditory system's superior encoding of resolved compared to unresolved harmonics, but instead predicts a degradation in encoding with increasing frequency, independent of resolvability. As Shackleton and Carlyon pointed out, one cannot rule out the possibility that this difference in the accuracy of encoding will eventually be accounted for by a single-mechanism model. However, it must be concluded that, at present, no such solution has been shown to account adequately for the data.

Finally, it is worth making a comment about the attractiveness of single-mechanism models in general. Given that listeners can encode the $F0$'s of both resolved and unresolved harmonics, either when making sequential (Hoekstra, 1979; Shackleton and Carlyon, 1994) or simultaneous (Carlyon *et al.*, 1992; Carlyon and Shackleton, 1994) comparisons, the idea of a single auditory mechanism which can deal with the two types of harmonic has some intuitive appeal. Two of its potential advantages over the combination of separate mechanisms dealing with resolved (e.g., Goldstein, 1973) and unresolved (Schouten, 1940; Schouten, 1970) harmonics can be described in terms of ''efficiency'' and ''parsimony.'' The efficiency refers to the idea that, when comparing the $F0$'s of resolved and unresolved harmonics, it would be advantageous not to have to translate the outputs of two separate mechanisms into a ''common format'' so that they could be compared. However, Carlyon and Shackleton have shown that listeners are very poor at comparing the $F0$'s of resolved and unresolved harmonics, and have concluded that such a translation does indeed take place. Even if a single-mechanism model could reproduce this poor performance, presumably by producing qualitatively different responses to resolved and unresolved harmonics, it would do so at the expense of the ''efficiency'' aspect of its appeal. The parsimony advantage comes from the argument that the auditory system would not have evolved two distinct mechanisms when a single mechanism could do the job. This advantage, although appealing, should be viewed in the context of the system's willingness to use two distinct mechanisms

when this is necessary to produce good performance. A particularly striking example of this is azimuthal location, with early processing of interaural time and intensity differences being mediated by separate neural populations which, in many mammals (e.g., cat), are anatomically separated into the medial and lateral superior olive respectively (see Irvine, 1992, for a review). The difference between localization and pitch may be that the two localization mechanisms have evolved to exploit different physical cues, whereas two pitch mechanisms have evolved to exploit the different ways in which the auditory periphery responds to resolved and unresolved harmonics. If so, then the approach of looking for a single pitch mechanism may be no more successful than an account of localization which makes no distinction between interaural differences in time and intensity (e.g., Deatherage and Hirsh, 1959).

ACKNOWLEDGMENTS

I am very grateful to Ray Meddis and Lowel O'Mard for generously providing me with their software and parameter files, and for assisting me with their implementation. Hedwig Gockel, Christophe Micheyl, Trevor Shackleton, Ray Meddis, and Adrian Houtsma provided helpful comments on a previous version of this Letter.

[1]In fact, Meddis and O'Mard cite only the article by Carlyon and Shackleton, but, in so doing, erroneously refer to some experiments performed by Shackleton and Carlyon.

[2]After Meddis and O'Mard had kindly provided copies of the parameter files used in their simulations, it was noticed that the slopes of the bandpass filters had erroneously been set to 18 dB/octave in all except the LOW frequency region, instead of the 24 dB/octave cited in their article. The effects of this oversight were minor, but have been corrected in Fig. 1.

[3]One influence on the predicted values of D^2 was noticed when trying out different ways of implementing Meddis and O'Mard's model, which offers two ways of generating simulations from the same stimuli. One may either specify the stimulus parameters and let the software generate the stimuli, or, as has been done in Fig. 1(d), one can input binary waveform files. When the former method was used to approximate Carlyon and Shackleton's stimuli, the results differed from those obtained using the raw waveform files [Fig. 1(d)], in that now D^2 was greater at 88 Hz than at 250 Hz in both the LOW and MID regions. This was presumably due to subtle differences between the two methods of filtering the stimuli. We have also tried measuring D^2 between two LOW region stimuli with the same $F0$ (250 Hz) and which differed only in level (45 dB vs 50 dB/component). This resulted in a D^2 of 0.23, which is of the order of some of the values shown in Fig. 1(d) for stimuli which differ in $F0$.

[4]One feature of the SACs shown in Fig. 2 which *does* differ between resolved and unresolved harmonics is that they drop to zero between the peaks only in the latter case. However, it is unlikely that this is responsible for listeners' inability to compare the $F0$'s of resolved and unresolved harmonics, as these intermediate regions also differ markedly for pairs of stimuli for which listeners do well. An example of this comes from the 250-Hz stimuli in the LOW and MID regions, which are both resolved by the peripheral auditory system. Furthermore, the consistent difference between resolved and unresolved harmonics did not persist when, rather than inputting the raw waveform files, we allowed Meddis and O'Mard's model to generate the stimuli (see footnote 3).

Carlyon, R. P. (**1998**). ''The effects of resolvability on the encoding of fundamental frequency by the auditory system,'' in *Psychophysical and Physiological Advances in Hearing*, edited by A. R. Palmer, A. Rees, A. Q. Summerfield, and R. Meddis (Whurr, London), pp. 246–254.

Carlyon, R. P., and Shackleton, T. M. (**1994**). ''Comparing the fundamental frequencies of resolved and unresolved harmonics: Evidence for two pitch mechanisms?,'' J. Acoust. Soc. Am. **95**, 3541–3554.

Carlyon, R. P., Demany, L., and Semal, C. (**1992**). ''Detection of across-frequency differences in fundamental frequency,'' J. Acoust. Soc. Am. **91**, 279–292.

Deatherage, B. H., and Hirsh, I. J. (**1959**). ''Auditory localization of clicks,'' J. Acoust. Soc. Am. **31**, 486–492.

Glasberg, B. R., and Moore, B. C. J. (**1990**). ''Derivation of auditory filter shapes from notched-noise data,'' Hearing Res. **47**, 103–138.

Goldstein, J. L. (**1973**). ''An optimum processor theory for the central formation of the pitch of complex tones,'' J. Acoust. Soc. Am. **54**, 1496–1516.

Hoekstra, A. (**1979**). ''Frequency discrimination and frequency analysis in hearing,'' Ph.D. Institute of Audiology, University Hospital, Groningen, Netherlands.

Irvine, D. R. F. (**1992**). ''Physiology of the auditory brainstem,'' in *Springer Series in Auditory Research Vol. II. The Mammalian Auditory Pathway: Neurophysiology*, edited by A. N. Popper and R. R. Fay (Springer-Verlag, New York), pp. 153–231.

Meddis, R., and Hewitt, M. (**1991**). ''Virtual pitch and phase sensitivity studied using a computer model of the auditory periphery: Pitch identification,'' J. Acoust. Soc. Am. **89**, 2866–2882.

Meddis, R., and O'Mard, L. (**1997**). ''A unitary model of pitch perception,'' J. Acoust. Soc. Am. **102**, 1811–1820.

Schouten, J. F. (**1940**). ''The residue and the mechanism of hearing,'' Proc. Konikl. Nederl. Wetensc. **43**, 991–999.

Schouten, J. F. (**1970**). ''The residue revisited,'' in *Frequency Analysis and Periodicity Detection in Hearing*, edited by R. Plomp and G. F. Smoorenburg (Sijthoff, Lieden), pp. 41–54.

Shackleton, T. M., and Carlyon, R. P. (**1994**). ''The role of resolved and unresolved harmonics in pitch perception and frequency modulation discrimination,'' J. Acoust. Soc. Am. **95**, 3529–3540.

Elephant hearing

Tom Reuter[a] and Sirpa Nummela
University of Helsinki, Department of Ecology and Systematics, Zoological Laboratory, P.O. Box 17, FIN-00014 Helsinki, Finland

Simo Hemilä
Helsinki University of Technology, Laboratory of Physics, Otakaari 1, FIN-02150 Espoo, Finland

(Received 7 February 1998; revised 9 April 1998; accepted 7 May 1998)

Elephants' vocalizations and movements have recently been shown to produce seismic waves (Rayleigh waves). This may be relevant for the well-known long-distance communication of these animals. It is suggested here that elephants may sense ground vibrations as a result of bone conduction producing a differential vibration of the middle ear ossicles in relation to the skull. This hypothesis is supported by the exceptionally massive ossicles of the Indian and African elephants. The acoustics of bone conduction is reviewed and related to the anatomy of the elephant middle ear.
 [S0001-4966(98)05008-5]

PACS numbers: 43.80.Nd [FD]

We would like to comment on the observations presented by O'Connell, Arnason and Hart at the 134th meeting of the Acoustical Society of America in San Diego in December 1997.[1] O'Connell *et al.* suggest that elephants could base their acoustic long-distance communication on Rayleigh waves propagated in the surface layer of the ground. Such waves could be produced both by stomping the ground and by body vibrations produced by vocalization. In support of this hypothesis we would like to point out that the anatomy of the elephant middle ear shows morphological adaptations suitable for sensing ground vibrations.

Sound information can reach the mammalian inner ear through two main routes. In normal air-conducted hearing sound waves set the tympanic membrane and the middle ear ossicles in vibration, thus producing movements of the oval window and changing pressure gradients in the cochlear fluid. Bone-conducted hearing, on the other hand, is effective in water-living and fossorial mammals for which the difference between the acoustic impedances of the surrounding medium and the body is small. Thus the sound energy efficiently leads to skull vibration. For producing a hearing sensation, clearly a *differential* motion between the skull surrounding the inner ear fluid and the ossicles is needed. If the center of gravity of the ossicular chain lies on the axis of ossicle rotation, then skull vibration produces no such differential motion and no hearing sensation is achieved. Bárány[2] has suggested that such a prevention of bone conduction would be the main evolutionary reason for the mammalian middle ear hinge—it would save them from the noise created by chewing. But if the center of gravity does *not* lie exactly on the rotation axis, then the inertia produced by large ossicles brings about a rotatory movement of the ossicles, and inner ear stimulation and hearing are possible. This type of hearing is analogous to the otolith hearing in some fish.[3,4] In both cases sound brings the whole body into vibration, and the animal detects a motion difference between the head and the stapes or the otolith, respectively.

We have earlier suggested that the true seals (Phocidae) use both air-conducted and bone-conducted hearing, the former in air and the latter in water.[5,6] Among mammals, the ossicles of phocids are very massive and of an unusual shape, suggesting that the ossicle inertia is functional (provided that the rotation axis and the center of gravity do *not* coincide). The middle ear ossicles of the elephants are even more massive than those of the phocids; the combined mass of malleus, incus and stapes (m_{MIS}) is about 650 mg for the Indian elephant, compared with 160–320 mg for five species of phocids.[7] The ossicles of other large herbivores are generally one order of magnitude lighter; the m_{MIS} is 50 mg for the cattle, and 74 mg for the horse,[7] to mention two species for which complete audiograms have been determined.[8] The amphibious hippo might benefit from bone-conducted hearing in water, and indeed morphologically its middle ear ossicles somewhat resemble those of phocids, although they are clearly lighter (125 mg).[6,9]

Light ossicles are a condition for high-frequency hearing in air.[5] However, such ossicles do not *per se* impede low-frequency hearing. The horse and the cattle, for instance, combine rather light ossicles with a reasonably good sensitivity at low frequencies. Massive ossicles seem to occur in animals which receive acoustic information through body vibrations,[10,11] and for this they pay the price of radically reduced hearing at high frequencies.

Elephants have good low-frequency hearing (best sensitivity at 1000 Hz) extending into the infrasound region.[12] Further, they are known to produce infrasounds at high intensities,[13,14] and to use them for instance in mate searching.[15] Low frequencies attenuate less than higher frequencies and they apparently reach especially far when they propagate as Rayleigh waves. This is because Rayleigh waves attenuate as $1/r$, where r is distance, while the intensity of air-borne sound attenuates as $1/r^2$.

The elephant's body with a massive skeleton and pillar-like bones might be suitable for conducting the surface waves to the inner ear. In an elephant's audiogram measured with air-borne sound, the threshold at 100 Hz is quite high,

[a]Electronic mail: tom.reuter@helsinki.fi

ca. 40 dB.[12] However, this high threshold at low frequencies is mainly caused by the limited middle ear air volume and the elastic couplings of the middle ear. In bone-conducted hearing these factors are less relevant. Provided a good inner ear sensitivity, an elephant could use bone conduction in hearing low frequencies. Its heavy ossicles provide the large inertia needed, and the freely mobile type of its middle ear[16] provides soft elastic couplings between the ossicles and the skull. Thus we postulate that an elephant using bone conduction is more sensitive to low frequencies than revealed by ordinary audiogram techniques.

Low-frequency surface waves could act as arousal signals over long distances. For precise sound localization elephants rely on their large pinnae and air-borne sound of higher frequencies.[17,18]

ACKNOWLEDGMENT

S.N. was supported by the Finnish Graduate School of Neurosciences.

[1] C. E. O'Connell, B. T. Arnason, and L. A. Hart, ''Seismic transmission of elephant vocalizations and movement,'' J. Acoust. Soc. Am. **102**, 3124(A) (1997).
[2] E. Bárány, ''A contribution to the physiology of bone conduction,'' Acta Otolaryngologica, Stockholm Suppl. **26** (1938).
[3] R. R. Fay, ''The goldfish ear codes the axis of acoustic particle motion in three dimensions,'' Science **225**, 951–954 (1984).
[4] N. A. M. Schellart and A. N. Popper, ''Functional aspects of the evolution of the auditory system of Actinopterygian fish,'' in *The Evolutionary Biology of Hearing*, edited by D. B. Webster, R. R. Fay, and A. N. Popper (Springer-Verlag, New York, 1992), Chap. 16, pp. 295–322.
[5] S. Hemilä, S. Nummela, and T. Reuter, ''What middle ear parameters tell about impedance matching and high frequency hearing,'' Hearing Res. **85**, 31–44 (1995).
[6] S. Nummela, ''Scaling and modeling the mammalian middle ear,'' Comments Theor. Biol. **4**, 387–412 (1997).
[7] S. Nummela, ''Scaling of the mammalian middle ear,'' Hearing Res. **85**, 18–30 (1995).
[8] R. S. Heffner and H. E. Heffner, ''Hearing in large mammals: Horses (Equus caballus) and cattle (Bos taurus),'' Behavioral Neuroscience **97**, 299–309 (1983).
[9] G. Fleischer, ''Studien am Skelett des Gehörorgans der Säugetiere, einschliesslich des Menschen,'' Säugetierkundliche Mitteilungen **21**, 131–239 (1973).
[10] O. W. Henson, Jr., ''Comparative anatomy of the middle ear,'' in *Handbook of Sensory Physiology*, edited by W. D. Keidel and W. D. Neff (Springer-Verlag, Berlin, 1974), Chap. 3, pp. 39–110.
[11] M. J. Mason, ''Functional anatomy of the middle ear of insectivores,'' J. Acoust. Soc. Am. **103**, 2827(A) (1998).
[12] R. Heffner and H. Heffner, ''Hearing in the elephant,'' Science **208**, 518–520 (1980).
[13] K. B. Payne, W. R. Langbauer, Jr., and E. M. Thomas, ''Infrasonic calls of the Asian elephant (Elephas maximus),'' Behav. Ecol. Sociobiol. **18**, 297–301 (1986).
[14] J. H. Poole, K. Payne, W. R. Langbauer, Jr., and C. J. Moss, ''The social contexts of some very low frequency calls of African elephants,'' Behav. Ecol. Sociobiol. **22**, 385–392 (1988).
[15] J. H. Poole and C. J. Moss, ''Elephant mate searching: group dynamics and vocal and olfactory communication,'' Symp. Zool. Soc. London **61**, 111–125 (1989).
[16] G. Fleischer, ''Evolutionary principles of the mammalian middle ear,'' Adv. Anat., Embryol. Cell Biol. **55**, 1–70 (1978).
[17] R. Heffner, H. Heffner, and N. Stichman, ''The role of elephant pinna in sound localization,'' Anim. Behav. **30**, 628–629 (1982).
[18] R. S. Heffner and H. E. Heffner, ''Hearing in the elephant (Elephas maximus): Absolute sensitivity, frequency discrimination, and sound localization,'' J. Comp. Physiol. Psychol. **96**, 926–944 (1982).

Erratum: "Simulation of ultrasonic pulse propagation through the abdominal wall" [J. Acoust. Soc. Am. 102, 1177–1190 (1997)]

T. Douglas Mast,[a] Laura M. Hinkelman,[b] and Michael J. Orr
Department of Electrical Engineering, University of Rochester, Rochester, New York 14627

Victor W. Sparrow
Graduate Program in Acoustics, The Pennsylvania State University, University Park, Pennsylvania 16802

Robert C. Waag
Departments of Electrical Engineering and Radiology, University of Rochester, Rochester, New York 14627

(Received 21 February 1998; accepted for publication 19 May 1998)
[S0001-4966(98)06708-3]
PACS numbers: 43.80.Cs, 43.20.Fn, 43.58.Ta, 43.10.Vx [FD]

Some incorrect values were included in the paper ''Simulation of ultrasonic pulse propagation through the abdominal wall'' due to minor programming errors. Corrected versions of Tables II and III are shown here and the impact of the errors on the results are discussed below.

The correlation lengths calculated for the arrival time fluctuations produced by the finite-difference time-domain (FDTD) simulation and shown in Table II were incorrect

TABLE II. Statistics of wavefront distortion from measurements (Exp.), finite-difference simulations (FDTD) and straight-ray simulations (S-R).

			Arrival time fluctuations		Energy level fluctuations		
Specimen number	Specimen thickness (mm)	Data source	rms value (ns)	Correlation length (mm)	rms value (dB)	Correlation length (mm)	Waveform similarity factor
75hi	31–34	Exp.	92.7	4.10	3.85	2.99	0.873
		FDTD	53.0	4.70	3.29	1.25	0.957
		S-R	62.3	2.40	0.42	1.92	1.000
77ba	22–29	Exp.	102.7	3.61	3.98	2.38	0.841
		FDTD	59.9	4.05	4.44	1.17	0.951
		S-R	61.6	2.00	0.46	2.09	1.000
87de	26–30	Exp.	73.7	4.74	3.47	2.75	0.866
		FDTD	60.9	8.68	4.18	1.46	0.948
		S-R	66.4	6.89	0.60	10.76	1.000
102gh	17–21	Exp.	38.7	5.56	3.89	3.22	0.943
		FDTD	28.4	3.72	3.10	1.37	0.986
		S-R	31.9	2.44	0.25	2.83	1.000
120de	25–29	Exp.	59.5	5.76	3.07	2.35	0.958
		FDTD	43.6	4.88	3.28	1.38	0.980
		S-R	47.3	3.43	0.38	4.65	1.000
120fe	28–30	Exp.	73.8	8.66	3.66	3.71	0.914
		FDTD	67.1	8.19	3.41	1.30	0.983
		S-R	71.3	8.72	0.51	6.11	1.000

[a]Current affiliation: Applied Research Laboratory, The Pennsylvania State University, University Park, PA 16802.
[b]Current affiliation: Department of Meteorology, The Pennsylvania State University, University Park, PA 16802.

TABLE III. Correlation coefficients between arrival time surfaces and energy level surfaces from FDTD and straight-ray simulations.

Specimen number	Arrival time correlation	Energy level correlation
75hi	0.666	0.363
77ba	0.501	0.572
87de	0.783	0.190
102gh	0.810	0.498
120de	0.787	0.489
120fe	0.872	0.444

because of an arithmetic error. Correct values are given below. These values do not negate any of the conclusions drawn in the original paper. Indeed, they indicate that the results of the finite-difference time-domain simulation are in better agreement with the measurements than previously thought.

The results for the straight-ray simulation were incorrect due to an error in the positioning of the simulated receiving aperture. This error had little impact on the distortion magnitudes and correlation lengths but significantly reduced the level of correlation between the FDTD and straight-ray results. Corrected values for the straight-ray distortion statistics are given here in Table II, while corrected correlation coefficients between the FDTD and straight-ray results are given in Table III.

The increased correlation between the arrival time fluctuations produced by the two simulations for the corrected results strengthens the previous conclusion that ''time-shift aberration in the abdominal wall is, in many cases, principally associated with large-scale variations in sound speed.'' Variations in energy level produced by the two simulations, which correlated poorly before, now correlate significantly in most cases, but the magnitudes of the energy level distortion produced by the two simulation methods still differ greatly. This result affirms that variations in absorption throughout abdominal wall specimens cannot explain the energy level fluctuations observed in the FDTD or measurement results. Instead, it is more likely that the same tissues produce amplitude variations by different mechanisms in each case. Absorption causes the energy fluctuations in the straight-ray simulations, while scattering effects appear to dominate in the FDTD simulations and measurements. This statement is consistent with the conclusions drawn in the original paper.